Transactions of the ASME®

Technical Editor, **LEWIS T. WHEELER (1997)**

Department of Mechanical Engineering,
University of Houston,
Houston, TX 77204-4792

APPLIED MECHANICS DIVISION

Chairman, **C. T. HERAKOVICH**
Secretary, **T. HUGHES**
Associate Technical Editors,
J. R. BARBER (2000)
J. L. BASSANI (1999)
R. C. BECKER (1998)
R. C. BENSON (2000)
M. M. CARROLL (2000)
I. M. DANIEL (1999)
W. J. DRUGAN (2000)
A. A. FERRI (2000)
J. T. JENKINS (1999)
J. W. JU (1998)
V. K. KINRA (1999)
S. KYRIAKIDES (2000)
S. LICHTER (1998)
W. K. LIU (1999)
M. ORTIZ (1998)
N. C. PERKINS (1999)
M.-J. PINDERA (2000)
K. T. RAMESH (2000)
J. N. REDDY (1998)
D. A. SIGINER (2000)
M. TAYA (1999)

BOARD ON COMMUNICATIONS

Chairman and Vice-President
R. MATES

OFFICERS OF THE ASME
President, **K. B. THAYER**
Executive Director, **D. L. BELDEN**
Treasurer, **J. A. MASON**

PUBLISHING STAFF
Managing Director, Engineering
CHARLES W. BEARDSLEY
Director, Technical Publishing
PHILIP DI VIETRO
Managing Editor, Technical Publishing
CYNTHIA B. CLARK
Managing Editor, Transactions
CORNELIA MONAHAN
Production Coordinator
JUDITH SIERANT
Production Assistant
MARISOL ANDINO

Transactions of the ASME, Journal of Applied Mechanics (ISSN 0021-8936) is published quarterly (Mar., June, Sept., Dec.) for $210.00 per year by The American Society of Mechanical Engineers, 345 East 47th Street, New York, NY 10017.

Periodicals postage paid at New York, NY and additional mailing office. POSTMASTER: Send address changes to Transactions of the ASME, Journal of Applied Mechanics, c/o THE AMERICAN SOCIETY OF MECHANICAL ENGINEERS, 22 Law Drive, Box 2300, Fairfield, NJ 07007-2300.

CHANGES OF ADDRESS must be received at Society headquarters seven weeks before they are to be effective. Please send old label and new address. **PRICES:** To members, $40.00; to nonmembers, $230.00; single issue, $92.00. Add $40.00 (airmail $60.00) for postage to countries outside the United States and Canada.

STATEMENT from By-Laws. The Society shall not be responsible for statements or opinions advanced in papers or . . . printed in its publications (B7.1, Para. 3), **COPYRIGHT © 1998** by The American Society of Mechanical Engineers. Authorization to photocopy material for internal or personal use under circumstances not falling within the fair use provisions of the Copyright Act is granted by ASME to libraries and other users registered with the Copyright Clearance Center (CCC). Transactional Reporting Service provided that the base fee of $3.00 per article is paid directly to CCC, Inc., 222 Rosewood Drive, Danvers, MA 01923. Request for special permission or bulk copying should be addressed to Reprints/Permission Department.

INDEXED by Applied Mechanics Reviews and Engineering Information, Inc. Canadian Goods & Services Tax Registration #126148048.

Journal of Applied Mechanics

Published Quarterly by The American Society of Mechanical Engineers

VOLUME 65 • NUMBER 1 • MARCH 1998

TECHNICAL PAPERS

1 **Constructing Exact Dynamic Elasticity Solutions for Axisymmetrically Deformed Plates From Classical Plate Theory Solutions**
Z. Qian and J. G. Simmonds

7 **Compressive Strength Predictions for Fiber Composites**
S.-Y. Hsu, T. J. Vogler, and S. Kyriakides

17 **A Thermoviscoelastic Dynamic Vibration Absorber**
R. Fosdick and Y. Ketema

25 **Asymmetric Shielding Mechanisms in the Mixed-Mode Fracture of a Glass/Epoxy Interface**
J. G. Swadener and K. M. Liechti

30 **A Circular Inclusion With Circumferentially Inhomogeneous Sliding Interface in Plane Elastostatics**
C. Q. Ru

39 **Use of "Simple Solutions" in Regularizing Hypersingular Boundary Integral Equations in Elastoplasticity**
H. Poon, S. Mukherjee, and M. Fouad Ahmad

46 **Inflation of a Thick-Walled Shell Which Exhibits Stress Softening**
J. B. Haddow and J. L. Wegner

51 **Thermal Stresses in a Generally Anisotropic Body With an Elliptic Inclusion Subject to Uniform Heat Flow**
C. K. Chao and M. H. Shen

59 **Toroidal Vibrations of Anisotropic Spheres With Spherical Isotropy**
K. T. Chau

66 **Stress Concentration in an Elastic Cosserat Plate Undergoing Extensional Deformations**
Shankar Krishnaswamy, Z.-H. Jin, and R. C. Batra

71 **Effect of the *T*-Stress in Microcrack Shielding Problems**
LiGuo Zhao and YiHeng Chen

76 **Analysis of Conducting Rigid Inclusion at the Interface of Two Dissimilar Piezoelectric Materials**
Wei Deng and S. A. Meguid

85 **The Energy Release Rate in the General Delamination Problem of Anisotropic Laminates Under Thermomechanical Loads**
Wan-Lee Yin

93 **Kinematic Description of Damage**
Taehyo Park and G. Z. Voyiadjis

99 **The Axisymmetric Deformation of Linearly and Nonlinearly Elastic Spinning Tubes Under End Thrusts and Torques**
T. J. McDevitt and J. G. Simmonds

107 **Large Deflections of Clamped Circular Plates Under Initial Tension and Transitions to Membrane Behavior**
M. Sheplak and J. Dugundji

116 **Critical Speed for Floppy Disks**
A. A. Renshaw

121 **A Theoretical Prediction of Natural Frequency of a Ferromagnetic Beam Plate With Low Susceptibility in an In-Plane Magnetic Field**
You-He Zhou and Kenzo Miya

127 **Property Distribution Determination for Nonuniform Composite Beams From Vibration Response Measurements and Galerkin's Method**
Wei-Hung Chen and R. F. Gibson

134 **On the Eigenvalues and Critical Speed Stability of Gyroscopic Continua**
R. G. Parker

(Contents continued on outside back cover)

This journal is printed on acid-free paper, which exceeds the ANSI Z39.48-1992 specification for permanence of paper and library materials. ♾™

♻ 85% recycled content, including 10% post-consumer fibers.

Downloaded 04 May 2010 to 171.66.16.52. Redistribution subject to ASME license or copyright; see http://www.asme.org/terms/Terms_Use.cfm

CONTENTS (CONTINUED)

141 **Nonlinear Waves in Strings: The Barrage Balloon Problem**
J. F. Hall

150 **Chaotic Motions of a Dual-Spin Body**
A. C. Or

157 **A Parametric Study on the Free Vibration of Noncylindrical Helical Springs**
V. Yıldırım

164 **Numerical Study of Unsteady Flow Around Airfoil With Spoiler**
Cheng Xu and W. W. H. Yeung

171 **A Two-Dimensional Model of the Fluid Dynamics of an Air Reverser**
S. Müftü, T. S. Lewis, K. A. Cole, and R. C. Benson

178 **Three-Dimensional Axisymmetric Piezothermoelastic Solution of a Transversely Isotropic Piezoelectric Clamped Circular Plate**
S. Kapuria, P. C. Dumir, and S. Segupta

184 **Elastodynamic Solution for the Thermal Shock Stresses in an Orthotropic Thick Cylindrical Shell**
H. Cho, G. A. Kardomateas, and C. S. Valle

194 **On-Line Identification of Hysteretic Systems**
A. G. Chassiakos, S. F. Masri, A. W. Smyth, and T. K. Caughey

204 **The Dependence of the Time Scale of Relative Lagrangian Motion on the Initial Separation**
J. C. H. Fung

209 **Canonical Perturbation of a Fast Time-Periodic Hamiltonian via Liapunov-Floquet Transformation**
E. A. Butcher and S. C. Sinha

218 **Paradoxes in Rigid-Body Kinematics of Structures**
L. Mentrasti

223 **On the Dynamics of Vibration Absorbers With Motion-Limiting Stops**
H. Luo and S. Hanagud

234 **Viscoelastic Effects in Modeling Web Handling Systems: Unsteady-State Analysis**
Xiaofeng Guan, M. S. High, and D. A. Tree

242 **A Variational Framework for Solution Method Developments in Structural Mechanics**
K. C. Park and C. A. Felippa

250 **Dynamical Friction Behavior in a Forced Oscillator With a Compliant Contact**
J.-W. Liang and B. F. Feeny

258 **The Transient Response of Structures Using Asymptotic Modal Analysis**
R. R. Reynolds and E. H. Dowell

BRIEF NOTES

Performance Evaluation of Accelerometers to 200,000 G **266**
T. C. Togami, F. A. Brown, M. J. Forrestal, and W. E. Baker

Polycrystalline Plasticity: Application to Earing in Cup Drawing of Al2008-T4 Sheet **268**
S. Balasubramanian and L. Anand

271 Finite Element Analysis of Rolling Contact Problems Using Minimum Dissipation of Energy Principle
S. K. Rathore and N. N. Kishore

273 A Study of Solutions for the Anisotropic Plate Subjected to a Concentrated Force
B. LaMattina, E. C. Klang, and J. W. Eischen

DISCUSSION

277 **Shakedown Analysis for Trusses and Frames, by Pham Duc Chinh—Discussion by P. S. Symonds**

278 **Elastic Fields in a Polygon-Shaped Inclusion With Uniform Eigenstrains, by N. Nozaki and M. Taya—Discussion by G. J. Rodin**

(Contents continued on p. 193)

Downloaded 04 May 2010 to 171.66.16.52. Redistribution subject to ASME license or copyright; see http://www.asme.org/terms/Terms_Use.cfm

ANNOUNCEMENTS AND SPECIAL NOTICES

70	Finite Element Books Bibliography on the Internet
115	Sixth Pan American Congress of Applied Mechanics—Call for Papers
183	Periodicals on ASMENET
257	Symposium on Recent Developments in the Study of Impacts on Composite Materials—Call for Papers
279	Reviewers List
281	Books Received by the Office of the Technical Editor
282	Change of Address Form
283	Worldwide Mechanics Meetings List
286	Information for Authors
287	20th International Congress of Theoretical and Applied Mechanics—Preliminary Announcement
288	Third International Congress on Thermal Stresses—Announcement
289	Fourth Microgravity Fluid Physics & Transport Phenomena Conference—Announcement

Downloaded 04 May 2010 to 171.66.16.52. Redistribution subject to ASME license or copyright; see http://www.asme.org/terms/Terms_Use.cfm

Constructing Exact Dynamic Elasticity Solutions for Axisymmetrically Deformed Plates From Classical Plate Theory Solutions

Z. Qian
Graduate Student.

J. G. Simmonds
Fellow ASME.

Institute of Applied Mathematics
and Mechanics,
University of Virginia,
Charlottesville, VA 22903

This paper addresses the question of how to assess the errors made when the exact three-dimensional linear elasticity solution for the axisymmetric dynamic deformation of an elastic plate is approximated by a solution inferred from the classical plate theory of Kirchhoff. Following the strategy used by Ladevèze and Simmonds for beams, the exact solution of a "nearby" three-dimensional problem, which differs from the original problem by the addition of incremental, computable body forces, face shears, and initial conditions—error increments, for short—is expressed in terms of the solution of a wave equation in which distance normal to the plate's midplane plays the role of a time-like variable while the physical time itself enters only as a parameter. The error increments which, ultimately, can be computed in terms of the solution delivered by plate theory, can be regarded as an "engineering norm" because with them an engineer can decide if such a shift in the external data lies within acceptable bounds.

Introduction

Recently Ladevèze and Simmonds (1996) have presented a method for constructing exact plane stress solutions for the linear dynamic equations of motion of elastically isotropic rectangular beams, starting from the solutions of classical (Euler-Bernoulli) beam theory and using two key ideas: (1) rather than the original two-dimensional plane stress problem, one considers a "perturbed" problem, obtained by adding certain incremental (residual) loads and initial conditions to the original problem; (2) one uses the one-dimensional (approximate) solution delivered by beam theory to reduce finding the exact solution of the perturbed problem to integrating a *spatially* hyperbolic system of equations in which time enters only as a parameter. In the present paper, we apply these ideas to construct exact three-dimensional dynamic elasticity solutions for elastically isotropic circular plates subject to axisymmetric loads, boundary, and initial conditions. The heart of the method lies in constructing an explicit solution of the three-dimensional axisymmetric wave equation with nonhomogeneous terms that depend on the solution of the classical dynamical plate equation of Kirchhoff. As with the beam problem, the only significant incremental loads needed to obtain exact elasticity solutions occur in narrow edge zones, as expected.

The Governing Equations

As shown in Fig. 1, we consider a circular plate of radius a and thickness $2H$. The plate is centered at the origin O of a cylindrical coordinate system (r, θ, z) and its midplane coincides with $z = 0$.

For axisymmetric deformations, the linearized field equations for an elastically isotropic plate comprise the four displacement-stress relations

$$Eu_{,r} = \sigma_r - \nu(\sigma_\theta + \sigma), \quad Er^{-1}u = \sigma_\theta - \nu(\sigma_r + \sigma) \tag{1}$$

$$Ew_{,z} = \sigma - \nu(\sigma_r + \sigma_\theta), \quad G(u_{,z} + w_{,r}) = \tau \tag{2}$$

plus the two equations of motion

$$\sigma_{r,r} + \tau_{,z} + r^{-1}(\sigma_r - \sigma_\theta) + f_r = \rho u_{,tt},$$

$$\tau_{,r} + r^{-1}\tau + \sigma_{,z} + f_z = \rho w_{,tt}. \tag{3}$$

Here, u and w are, respectively, the radial and vertical components of displacement, σ_r, σ_θ, τ, and σ are the nonzero (physical) components of the stress tensor, E is Young's modulus, ν is Poisson's ratio, $G = E/2(1 + \nu)$ is the shear modulus, f_r and f_z are body forces, ρ is the mass density, t is time, and a comma followed by a subscript indicated differentiation with respect to that subscript.

Solving (1) for the in-plane stress components, inserting the resulting expressions into (2) and (3), introducing the notation

$$\bar{f} = \frac{f}{E}, \quad \kappa = \frac{E}{G}, \quad C = \frac{1}{1 - \nu^2}, \quad c^2 = \frac{\nu}{1 - \nu}, \tag{4}$$

and rearranging, we may express our field equations as follows:

$$(1 - \nu)w_{,z} + \nu(u_{,r} + r^{-1}u) = (1 + \nu)(1 - 2\nu)\bar{\sigma},$$

$$u_{,z} + w_{,r} = \kappa\bar{\tau} \tag{5}$$

$$\bar{f}_r = \bar{\rho}u_{,tt} - C(u_{,rr} + r^{-1}u_{,r} - r^{-2}u) - c^2\bar{\sigma}_{,r} - \bar{\tau}_{,z},$$

$$\bar{f}_z = \bar{\rho}w_{,tt} - \bar{\tau}_{,r} - r^{-1}\bar{\tau} - \bar{\sigma}_{,z}. \tag{6}$$

Contributed by the Applied Mechanics Division of THE AMERICAN SOCIETY OF MECHANICAL ENGINEERS for publication in the ASME JOURNAL OF APPLIED MECHANICS.

Discussion on the paper should be addressed to the Technical Editor, Professor Lewis T. Wheeler, Department of Mechanical Engineering, University of Houston, Houston, TX 77204-4792, and will be accepted until four months after final publication of the paper itself in the ASME JOURNAL OF APPLIED MECHANICS.

Manuscript received by the ASME Applied Mechanics Division, Mar. 4, 1997; final revision, Oct. 31, 1997. Associate Technical Editor: R. Abeyaratne.

 Copyright © 1998 by ASME

Downloaded 04 May 2010 to 171.66.16.26. Redistribution subject to ASME license or copyright; see http://www.asme.org/terms/Terms_Use.cfm

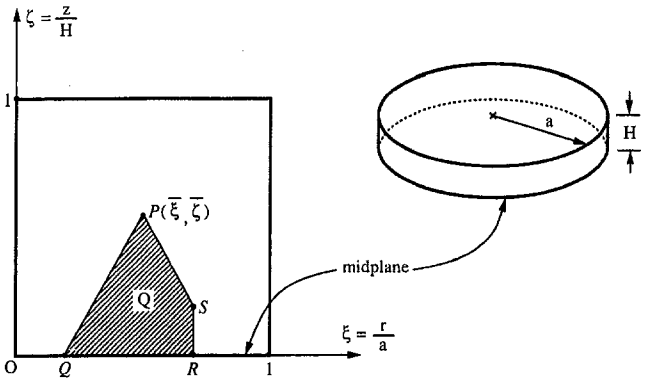

Fig. 1 Geometry and characteristics of an axisymmetric plate

For simplicity, we assume that the plate is clamped along its boundary so that

$$u(a, z, t) = w(a, z, t) = 0 \tag{7}$$

and that the usual regularity conditions hold at $r = 0$. Further, we assume that all external disturbances are such that the plate is in a state of pure bending. That is,

$$\begin{Bmatrix} \bar{\tau}, w, \bar{f}_z \\ \bar{\sigma}, u, \bar{f}_r \end{Bmatrix} \text{ are } \begin{Bmatrix} \text{even} \\ \text{odd} \end{Bmatrix} \text{ functions of } z. \tag{8}$$

Thus, the applied surface tractions may be given the form

$$\bar{\sigma}(r, \pm H, t) = \pm\tfrac{1}{2}\bar{p}_0 p(r, t),$$

$$\bar{\tau}(r, \pm H, t) = \tfrac{1}{2}(\bar{p}_0 a/H) q(r, t), \tag{9}$$

where $p = O(1)$, while the initial conditions read

$$u(r, z, 0) = u^*(r, z), \quad w(r, z, 0) = w^*(r, z) \tag{10}$$

$$u_{,t}(r, z, 0) = u_t^*(r, z), \quad w_{,t}(r, z, 0) = w_t^*(r, z), \tag{11}$$

where the prescribed u^*–and w^*–functions are, respectively, odd and even in z.

Nondimensionalization

If we introduce the parameter and scaled variables[1]

$$\epsilon = H/a, \quad r = a\xi, \quad z = H\zeta, \quad t = (a^2/H)\sqrt{\bar{\rho}}\,\eta \tag{12}$$

$$\bar{f}_r = (\bar{p}_0 a/H^2) F_\xi, \quad \bar{f}_z = (\bar{p}_0/H) F_\zeta, \tag{13}$$

$$w = (\bar{p}_0 a^4/H^3) W, \quad u = (\bar{p}_0 a^3/H^2) U,$$

$$\bar{\tau} = (\bar{p}_0 a/H) T, \quad \bar{\sigma} = \bar{p}_0 S, \tag{14}$$

we may rewrite the reduced field Eqs. (5) and (6) and the associated boundary, parity, and initial conditions (7)–(11) in the form

$$(1 - \nu) W_{,\zeta} + \nu\epsilon^2 (U_{,\xi} + \xi^{-1} U) = (1 + \nu)(1 - 2\nu)\epsilon^4 S,$$

$$U_{,\zeta} = -W_{,\xi} + \epsilon^2 \kappa T \tag{15}$$

$$F_\xi = -C(U_{,\xi\xi} + \xi^{-1} U_{,\xi} - \xi^{-2} U) - T_{,\zeta} + \epsilon U_{,\eta\eta} - \epsilon^2 c^2 S_{,\xi} \tag{16}$$

$$F_\zeta = W_{,\eta\eta} - (T_{,\xi} + \xi^{-1} T) - S_{,\zeta} \tag{17}$$

$$U(1, \zeta, \eta) = W(1, \zeta, \eta) = 0 \tag{18}$$

[1] This scaling is appropriate for the "interior" of the plate. In an edge zone of width $O(H)$, a different scaling is appropriate because, there, $w, u = O(\bar{p}_0 a^2/H)$.

$$S(\xi, \pm 1, \eta) = \pm\tfrac{1}{2} p(\xi, \eta), \quad T(\xi, \pm 1, \eta) = \tfrac{1}{2} q(\xi, \eta), \tag{19}$$

$$U(\xi, \zeta, 0) = U^*(\xi, \zeta), \quad W(\xi, \zeta, 0) = W^*(\xi, \zeta) \tag{20}$$

$$U_{,\eta}(\xi, \zeta, 0) = U_\eta^*(\xi, \zeta), \quad W_{,\eta}(\xi, \zeta, 0) = W_\eta^*(\xi, \zeta) \tag{21}$$

$$\begin{Bmatrix} T, W, F_\zeta \\ S, U, F_\xi \end{Bmatrix} \text{ are } \begin{Bmatrix} \text{even} \\ \text{odd} \end{Bmatrix} \text{ functions of } \zeta, \tag{22}$$

where we have abused the notation by using $p(\xi, \eta)$ and $q(\xi, \eta)$ to denote the dimensionless external pressure and shear functions $p(r, t)$ and $q(r, t)$ under the change of variables (12).

We assume that in the original given three-dimensional elasticity problem, all boundary and initial conditions are homogeneous *except* $(19)_1$. We shall refer to this as the *reference problem.*

Augmented Classical Plate Theory for the Reference Problem

What we call "augmented" classical plate theory for the reference problem is obtained from (15)–(22) by setting $\epsilon = q = F_r = F_z = 0$ (the idea being that, if differentiation with respect to the scaled independent variables ξ, ζ, or η does not change orders of magnitude, then the resulting set of simplified equations should be a close approximation to the full equations. Near edges, near a discontinuous or concentrated load, or for rapid oscillations, these assumptions, which undergird classical plate theory, are not valid.)

Denoting the limiting values of the dependent variables by a hat and solving the resulting set of partial differential differential equations, we find that

$$\hat{W} = V(\xi, \eta), \quad \hat{U} = -\zeta V_{,\xi}(\xi, \eta) \tag{23}$$

$$\hat{T} = (1/2) C(\zeta^2 - 1)(\Delta V)_{,\xi},$$

$$\hat{S} = (1/2)\zeta(\zeta^2 - 1) V_{,\eta\eta} + (1/4)\zeta(3 - \zeta^2) p, \tag{24}$$

where V satisfies the classical (dimensionless) plate equation,

$$-(2/3) C \Delta\Delta V + p = 2V_{,\eta\eta}, \quad \Delta = \frac{\partial^2}{\partial\xi^2} + \frac{1}{\xi}\frac{\partial}{\partial\xi}, \tag{25}$$

and is subject to the boundary and initial conditions

$$V(1, \eta) = V_{,\xi}(1, \eta) = 0 \tag{26}$$

and

$$V(\xi, 0) = V_{,\eta}(\xi, 0) = 0. \tag{27}$$

Further Reduction of the Full Governing Equations

Let us introduce the change of dependent variables

$$T = \tilde{T}(\xi, \zeta, \eta) + (1/2) q(\xi, \eta),$$

$$W = \tilde{W}(\xi, \zeta, \eta) + \epsilon^2 (\kappa/2) \int_1^\xi q(\bar{\xi}, \eta) d\bar{\xi} \tag{28}$$

into our reduced dimensionless governing Eqs. (15)–(22). Then $(15)_2$ yields

$$U_{,\zeta} = -\tilde{W}_{,\xi} + \epsilon^2 \kappa \tilde{T} \tag{29}$$

or, in view of (22),

$$U = -\int_0^\zeta \tilde{W}_{,\xi} d\bar{\zeta} + \epsilon^2 \kappa \int_0^\zeta \tilde{T} d\bar{\zeta}. \tag{30}$$

We now eliminate U from $(15)_1$ by differentiating both sides of this equation with respect to ζ, dividing by $1 - \nu$, and using (29). Noting (4) and $(28)_2$, we have

Downloaded 04 May 2010 to 171.66.16.26. Redistribution subject to ASME license or copyright; see http://www.asme.org/terms/Terms_Use.cfm

$$\tilde{W}_{,\zeta\zeta} - (\epsilon c)^2 \Delta \tilde{W} = \epsilon^4 \left[\frac{(1+\nu)(1-2\nu)}{1-\nu} S_{,\zeta} - \frac{\nu\kappa}{1-\nu} (\tilde{T}_{,\xi} + \xi^{-1}\tilde{T}) \right] \equiv \epsilon^4 f(\xi, \zeta, \eta). \quad (31)$$

This is the *axisymmetric wave equation,* except that the dimensionless vertical coordinate ζ is the "time-like" variable while the real (dimensionless) time η enters only as a parameter.

The zero displacement boundary conditions (18) may be expressed in terms of $\tilde{W}$ only by differentiating the first with respect to ζ and then using $(28)_2$ and (29) to write

$$\tilde{W}(1, \zeta, \eta) = 0, \quad \tilde{W}_{,\xi}(1, \zeta, \eta) = \epsilon^2 \kappa \tilde{T}(1, \zeta, \eta). \quad (32)$$

The Perturbed Problem

We now bring in augmented plate theory by setting $S = \hat{S}$ and $\tilde{T} = \hat{T}$. Thus, the right side of (31) becomes known and the face traction conditions (19) are satisfied. By (22), $(23)_1$, and $(28)_2$, our nonhomogeneous wave Eq. (31) is subject to the "initial conditions"

$$\tilde{W}(\xi, 0, \eta) = V(\xi, \eta) + \epsilon^2(\kappa/2) \int_\xi^1 q(\hat{\xi}, \eta) d\hat{\xi} \equiv \xi^{-1/2} \psi(\xi, \eta), \quad \tilde{W}_{,\zeta}(\xi, 0, \eta) = 0. \quad (33)$$

Our problem has now been reduced to solving (31) for $0 < \xi, \zeta < 1$ and $\eta > 0$, subject to the *overdetermined* boundary/initial conditions (32) and (33). As we shall see in the next section, the problem is rendered well posed by requiring the dimensionless face shear function q to satisfy a certain *consistency condition.* This, in turn, leads to an explicit formula of the form $W = \mathcal{W}(\xi, \zeta, \eta)$ for the dimensionless vertical displacement. The dimensionless radial displacement then follows from (30) in the form $U = \mathcal{U}(\xi, \zeta, \eta)$ and the stress components (if needed) from the inverted form of the displacement-stress relations (1) and (2).

The equations of motion (16) and (17), which, by (23), (24), and $(28)_1$, now take the form

$$F_\xi = C(\Delta - \xi^{-2})(\hat{U} - \mathcal{U}) + \epsilon \mathcal{U}_{,\eta\eta} - \epsilon^2 (c/2)^2 \zeta [2(\zeta^2 - 1) V_{,\eta\eta} + (3 - \zeta^2) p]_{,\xi}. \quad (34)$$

$$F_\zeta = (\mathcal{W} - V)_{,\eta\eta} - (1/2)(q_{,\xi} + \xi^{-1} q) \quad (35)$$

are satisfied simply by taking the right sides as the values of the dimensionless body forces.

As for the initial conditions (20) and (21), we recall that the right sides vanish for the reference problem. Thus, the perturbed problem, whose displacement solutions we have denoted by $\mathcal{W}$ and $\mathcal{U}$, must satisfy nonhomogeneous initial conditions such that the prescribed data are

$$U^*(\xi, \zeta) = \mathcal{U}(\xi, \zeta, 0), \text{ etc.} \quad (36)$$

In outline, therefore, our procedure is the following. Given a reference problem in which (for simplicity) the only external disturbance is a time and spatially varying face pressure, we (1) solve the classical Kirchhoff plate equation, subject to appropriate boundary/initial conditions; (2) next solve the yet-to-be-specified equation for the error (perturbed) load q; (3) then compute $W = \mathcal{W}(\xi, \zeta, \eta)$ and $U = \mathcal{U}(\xi, \zeta, \eta)$; and (4) compute the error (perturbed) body forces f_r and f_z and initial conditions necessary to make $\mathcal{U}$ and $\mathcal{W}$ exact three-dimensional solutions of the equations of elasticity. Collectively, the increments $\{q, f_r, f_z, U^*, \ldots\}$ constitute what we may call an *engineering norm* in the sense that, realizing that the data in any engineering problem are never exact, we replace the given data by perturbed or incremental data which can (in theory) be computed explicitly. The engineer must then decide if these new data fall within the uncertainty bound of the original data. If so, there is nothing more to do; if not, the only recourse—short of solving a three-dimensional problem "exactly"—is to work with a refined plate model in which three-dimensional edge effects are accounted for. (See, for example, Ladevèze (1985) where related work by and references to Goldenveiser, Fredrichs, and Dressler; Precastaings, Gregory, and Wan; van der Heijden; and others may be found.)

Solution of the Spatial Wave Equation and the Consistency Condition

To avoid an unrealistic complication which arises if disturbances from the center of the plate ($\xi = 0$) influence the edge of the plate ($\xi = 1$), we assume that the right-running characteristic $\epsilon c \zeta = \xi$ emanating from the origin intersects the face of the plate and not the edge (see Fig. 1). That is, we assume that the half-thickness of the plate is such that $\nu H < (1 - \nu)a$, a condition certainly satisfied by any structure we would call a plate!

For any point in the open trapezoid $\mathcal{T}$: $\epsilon c \zeta < \xi < 1$, $0 < \zeta < 1$, we shall, in this section, solve (31), subject to $(32)_2$ and (33), by modifying the procedure given by Copson (1975, Chapter 5). Since the dimensionless time η enters all the equations in this section only as a parameter, we shall, in this and the next, drop η from the argument list of any dependent variable. For example, we shall write the dimensionless vertical displacement predicted by classical plate theory as $V(\xi)$. In the next section, we shall solve for $\tilde{W}$ at any point in the open rectangle $0 < \xi < 1 - \epsilon c$, $0 < \zeta < 1$ using an eigenfunction expansion. Obviously there is an overlap where the representation for $\tilde{W}$ delivered by either procedure may be used.

Thus, within the trapezoid $\mathcal{T}$, we first put our wave Eq. (31) into self-adjoint form by introducing the change of variable

$$\tilde{W} = \xi^{-1/2} \omega \quad (37)$$

so that

$$\Box \omega \equiv \omega_{,\zeta\zeta} - (\epsilon c)^2 [\omega_{,\xi\xi} + (1/4)\xi^{-2}\omega] = \epsilon^4 \xi^{1/2} f. \quad (38)$$

Now consider an arbitrary point $P(\bar{\xi}, \bar{\zeta})$ in $\mathcal{T}$. We define a Riemann-Green function for our problem to be any sufficiently smooth function $v(\xi, \zeta; \bar{\xi}, \bar{\zeta})$ that satisfies the homogeneous wave equation $\Box v = 0$ and equals 1 on the two characteristics $\epsilon c(\zeta - \bar{\zeta}) = \pm(\xi - \bar{\xi})$ that pass through P. From problem 5 on p. 89 of Copson (1975), we have

$$v(\xi, \zeta; \bar{\xi}, \bar{\zeta}) = F(\tfrac{1}{2}, \tfrac{1}{2}; 1; \Gamma/4\xi\bar{\xi}) = (2/\pi) K(\sqrt{\Gamma/4\xi\bar{\xi}}), \quad 0 \le \Gamma < 1, \quad (39)$$

where

$$\Gamma = (\epsilon c)^2 (\zeta - \bar{\zeta})^2 - (\xi - \bar{\xi})^2 \quad (40)$$

and F and K are, respectively, the hypergeometric function and the complete elliptic integral of the first kind.

To obtain a representation for $\omega(\bar{\xi}, \bar{\zeta})$, we follow Copson (1975) on pp. 80–81 except, instead of applying the Divergence Theorem to a triangular region, we apply it to the more general quadrilateral region $\mathcal{Q}$ sketched in Fig. 1. Taking into account the conditions (33) along the positive ξ-axis, we have, in an obvious notation,

$$2\omega(\bar{\xi}, \bar{\zeta}) = \epsilon^4 \int_{\mathcal{Q}} v(\xi, \zeta; \bar{\xi}, \bar{\zeta}) \xi^{1/2} f(\xi, \zeta) d\xi d\zeta - \int_{QR} v_{,\zeta}(\xi, 0; \bar{\xi}, \bar{\zeta}) \psi(\xi) d\xi - (\epsilon c)^2 \int_{RS} (\omega v_{,\xi} - v\omega_{,\xi}) d\zeta + (v\omega)_Q + (v\omega)_S, \quad \epsilon c \bar{\zeta} < \bar{\xi} < 1, \quad 0 < \bar{\zeta} < 1. \quad (41)$$

Downloaded 04 May 2010 to 171.66.16.26. Redistribution subject to ASME license or copyright; see http://www.asme.org/terms/Terms_Use.cfm

To find the unknown error load q, we impose on (41) the only conditions we have not yet satisfied, namely the clamped boundary conditions (32). Noting from this latter equation and (37) that

$$\omega(1, \zeta) = 0 \quad \text{and} \quad \omega_{,\xi}(1, \zeta) = \epsilon^2 \kappa \hat{T}(1, \zeta), \tag{42}$$

we obtain the *consistency condition*

$$\int_{1-\epsilon c\bar{\zeta}}^{1} v_{,\xi}(\xi, 0; 1, \bar{\zeta})\psi(\xi)d\xi - v(1 - \epsilon c\bar{\zeta}, 0; 1, \bar{\zeta})\psi(1 - \epsilon c\bar{\zeta})$$
$$= \epsilon^4 \int_0^{\bar{\zeta}} \left[\int_{1-\epsilon c(\bar{\zeta}-\zeta)}^{1} v(\xi, \zeta; 1, \bar{\zeta})\xi^{1/2} f(\xi, \zeta)d\xi \right.$$
$$\left. + c^2 \kappa v(1, \zeta; 1, \bar{\zeta})\hat{T}(1, \zeta) \right] d\zeta \equiv \epsilon^4 g(\bar{\zeta}),$$

$$0 < \bar{\zeta} < 1, \tag{43}$$

where $g(\bar{\zeta})$ is known.

To put this integral equation into standard form, we divide both sides of (43) by $\epsilon^2 v(1 - \epsilon c\bar{\zeta}, 0; 1, \bar{\zeta})$ and set

$$\xi = 1 - \epsilon c x, \quad \psi(1 - \epsilon c x) = \epsilon^4 \Psi(x) \tag{44}$$

$$K(\bar{\zeta}, x) = \frac{v_{,\xi}(1 - \epsilon c x, 0; 1, \bar{\zeta})}{v(1 - \epsilon c\bar{\zeta}, 0; 1, \bar{\zeta})},$$

$$h(\bar{\zeta}) = -\frac{g(\bar{\zeta})}{v(1 - \epsilon c\bar{\zeta}, 0; 1, \bar{\zeta})}. \tag{45}$$

This yields a standard Volterra integral equation of the second kind (with an unsymmetric kernel):

$$\Psi(\bar{\zeta}) = h(\bar{\zeta}) + \epsilon c \int_0^{\bar{\zeta}} K(\bar{\zeta}, x)\Psi(x)dx, \quad 0 < \bar{\zeta} < 1. \tag{46}$$

By iteration, we have the well-known *formal* solution

$$\Psi(\bar{\zeta}) = h(\bar{\zeta}) + \sum_1^{\infty} (\epsilon c)^n \int_0^{\bar{\zeta}} \dots n \text{ times} \dots \int_0^{\bar{\zeta}} K(\bar{\zeta}, x)h(x)dx. \tag{47}$$

However, in practice, one would probably solve (46) numerically.

With $\Psi(\bar{\zeta})$ in hand, we determine q from $(33)_1$ and (44). With the change of variable

$$q = (\epsilon c)^{-1} Q(x), \tag{48}$$

we have

$$\int_0^x Q(\hat{x})d\hat{x} = (2/\kappa)[\epsilon^2(1 - \epsilon c x)^{-1/2}\Psi(x) - \epsilon^{-2} V(1 - \epsilon c x)],$$

$$0 < x < 1. \tag{49}$$

This equation determines (by differentiation) $Q(x)$ and hence $q(\xi)$ on the indicated interval. On $0 < \xi < 1 - \epsilon c$, $q(\xi)$ is arbitrary *so, for simplicity, we set it to zero there.*

With Ψ determined, we may now, using (41), compute ω (and hence $\tilde{W} = \xi^{-1/2}\omega$) at any point in the quadrilateral $\mathcal{Q}$ shown in Fig. 1. The first two lines on the right of (41) are obviously known quantities. As for the last line, the term $(v\omega)_Q$ is now known from (33) and (37) as is $(v\omega)_S$ if S lies on the midplane ($\zeta = 0$) of the plate; if S lies on the edge of the plate ($\xi = 1$), then, by (42), the integral in the last line of (41) reduces to $\epsilon^4 c^2 \kappa \int_0^{\bar{\zeta}} v\omega_{,\xi}\hat{T}d\zeta$, which is known.

An Eigenfunction Expansion for $\tilde{W}$

The eigenvalue problem

$$(\xi\phi')' + \xi\lambda\phi = 0,$$
$$0 < \xi < 1, \quad \phi(0) \text{ bounded}, \quad \phi(1) = 0 \tag{50}$$

has the well-known set of eigensolutions $\{\phi_n(\xi), \lambda_n\}_0^{\infty}$, where

$$\phi_n = \frac{\sqrt{2}J_0(\mu_n\xi)}{J_1(\mu_n)} \quad \text{and} \quad \lambda_n = \mu_n^2. \tag{51}$$

Here, J_0 and J_1 are the Bessel functions of the first kind, order zero and one, respectively, and μ_n is the nth positive root of J_0. Thus, $\tilde{W}$ may be represented in the form

$$\tilde{W} = \sum_{n=0}^{\infty} w_n(\zeta)\phi_n(\xi), \quad 0 < \xi < 1, \quad 0 < \zeta, \tag{52}$$

where, because of the orthogonality condition

$$\int_0^1 \xi\phi_m(\xi)\phi_n(\xi)d\xi = \begin{cases} 1 & \text{if } m = n \\ 0 & \text{if } m \neq n \end{cases}, \tag{53}$$

the coefficients in (52) are given by

$$w_n = \int_0^1 \xi\tilde{W}(\xi, \zeta)\phi_n(\xi)d\xi. \tag{54}$$

Furthermore, because $\tilde{W}$ satisfies the same *homogeneous* boundary condition as does each eigenfunction, namely $(32)_1$, we may differentiate the right side of (52) term by term and substitute the resulting expression into (31) to obtain, by (50) and (51),

$$\sum_{n=0}^{\infty} [w_n''(\zeta) + (\epsilon c\mu_n)^2 w_n]\phi_n(\zeta) = \epsilon^4 f(\xi, \zeta). \tag{55}$$

The orthogonality condition (53) then implies that

$$w_n'' + (\epsilon c\mu_n)^2 w_n = \epsilon^4 f_n(\zeta),$$
$$f_n = \int_0^1 \xi f(\xi, \zeta)\phi_n(\xi)d\xi, \quad 0 < \zeta. \tag{56}$$

From (54) and the "initial conditions" (33), we have

$$w_n(0) = \psi_n, \quad w_n'(0) = 0, \quad \psi_n = \int_0^1 \xi^{1/2}\psi(\xi)\phi_n(\xi)d\xi. \tag{57}$$

Thus,

$$w_n = \psi_n \cos(\epsilon c\mu_n\zeta) + (\epsilon^3/c\mu_n)\int_0^{\zeta} \sin[\epsilon c\mu_n(\zeta - \hat{\zeta})]f_n(\hat{\zeta})d\hat{\zeta} \tag{58}$$

so that the right side of (52) is now completely determined.

The importance of the alternative representation (52) is that it is valid in the whole plate, whereas (41) is valid in the whole plate *excluding* the triangular region $0 < \xi < c\epsilon\zeta$, $0 < \zeta < 1$. However, determining q from the representation (52) by requiring that the coefficients ψ_n in (57) be chosen so that $(32)_2$ be satisfied would involve very very delicate convergence questions. The advantage of (46) is that it leads to a more robust way of determining q.

Asymptotic Solution for Thin Plates

Except for the very mild restriction $\nu H < (1 - \nu)a$ we imposed earlier, we have not taken advantage of the fact that, in practice, $\epsilon = H/a$ is usually small. We now do so to reap the tremendous simplifications that follow in the formulas for the error load q.

In the consistency condition (43), the Riemann-Green function v and its derivatives are evaluated at $\bar{\xi} = 1$. From (39) and the well-known series expansion of the hypergeometric function,

$$v(\xi, \zeta; \bar{\xi}, \bar{\zeta}) = F(\tfrac{1}{2}, \tfrac{1}{2}; 1; \Gamma/4\xi\bar{\xi}) = 1 + (1/16)(\Gamma/\xi\bar{\xi}) + (9/1024)(\Gamma/\xi\bar{\xi})^2 + O(\Gamma/\xi\bar{\xi})^3. \tag{59}$$

Downloaded 04 May 2010 to 171.66.16.26. Redistribution subject to ASME license or copyright; see http://www.asme.org/terms/Terms_Use.cfm

If we make the change of variable $\xi = 1 - \epsilon c x$, as in $(44)_1$, it follows from (40) that

$$\Gamma = (\epsilon c)^2[(\zeta - \bar{\zeta})^2 - x^2] = O(\epsilon^2), \tag{60}$$

so that (59) yields

$$v(1 - \epsilon c x, \zeta; 1, \bar{\zeta}) = 1 + \frac{(\epsilon c)^2[(\zeta - \bar{\zeta})^2 - x^2]}{16(1 - \epsilon c x)} + \frac{9(\epsilon c)^4[(\zeta - \bar{\zeta})^2 - x^2]^2}{1024(1 - \epsilon c x)^2} + O(\epsilon c)^6. \tag{61}$$

Thus,

$$v_{,\zeta}(1 - \epsilon c x, 0; 1, \bar{\zeta}) = -\frac{(\epsilon c)^2\bar{\zeta}}{8(1 - \epsilon c x)}\left[1 + \frac{9(\epsilon c)^2(\bar{\zeta}^2 - x^2)}{32(1 - \epsilon c x)} + O(\epsilon c)^4\right] \tag{62}$$

so that from $(45)_1$,

$$K(\bar{\zeta}, x) = -\frac{(\epsilon c)^2\bar{\zeta}}{8(1 - \epsilon c x)}\left[1 + \frac{7(\epsilon c)^2(\bar{\zeta}^2 - x^2)}{32(1 - \epsilon c x)} + O(\epsilon c)^4\right]. \tag{63}$$

We now make the assumption that *any dependent variable* $M(\xi, \zeta)$ *associated with the classical plate theory solution* $V(\xi)$ *has a finite Taylor expansion about the edge* $\xi = 1$ *of the form*

$$M(1 - \epsilon c x, \zeta) = M(1, \zeta) - \epsilon c M_{,\xi}(1, \zeta)x + (1/2)(\epsilon c)^2 M_{,\xi\xi}(1, \zeta)x^2 - (1/6)(\epsilon c)^3 M_{,\xi\xi\xi}(1, \zeta)x^3 + O(\epsilon c)^4. \tag{64}$$

It then follows from (43), $(44)_1$, and (61) that

$$g = g_0(\bar{\zeta}) + \epsilon c g_1(\bar{\zeta}) + O(\epsilon c)^2, \tag{65}$$

where

$$g_0 = c^2\kappa\hat{T}(1, \bar{\zeta}) \text{ and } g_1 = \int_0^{\bar{\zeta}} (\bar{\zeta} - \zeta) f(1, \zeta) d\zeta, \text{ etc.} \tag{66}$$

Thus, assuming that Ψ has an expansion of the form

$$\Psi = \Psi_0(\bar{\zeta}) + \epsilon c \Psi_1(\bar{\zeta}) + O(\epsilon c)^2, \tag{67}$$

we find that if (45), (61), (63), (65), and (67) are substituted into (46), there follows

$$\Psi_0 = g_0(\bar{\zeta}) \quad \text{and} \quad \Psi_1 = g_1(\bar{\zeta}) - (\bar{\zeta}/8)\int_0^{\bar{\zeta}} g_0(x) dx. \tag{68}$$

Finally, to obtain an expression for q, we substitute (48) and (67) into (49). Noting that the clamped boundary conditions (26) for classical plate theory imply that $V(1 - \epsilon c x) = O(\epsilon c)^2$, we readily find that

$$q = -(c/\kappa)\epsilon^{-1}\mathcal{H}(1 - x)[2V_{,\xi\xi}(1)x - \epsilon c V_{,\xi\xi\xi}(1)x^2 + O(\epsilon c)^2], \tag{69}$$

where $\mathcal{H}$ is the Heaviside step function. As noted in Ladevèze and Simmonds (1996), the incremental face shear stress necessary to obtain an exact three-dimensional solution satisfying the complete clamping conditions (7) is large, of the same order of magnitude as the dominant in-plane stresses. This, of course, is not surprising in view of the well-known boundary layer of width $O(H)$ in three-dimensional plate theory. Note, however, that at a simple supported edge, $V_{,\xi\xi}(1) = 0$ so that (69) suggests that a much milder dimensionless shear load, namely $q = O(1)$, would lead to an exact three-dimensional solution.

Example: A Clamped Plate Under a Constant Normal Pressure

The procedures we have outlined for determining the error load q and thence the radial displacement, the body forces, the incremental initial conditions, and the stresses from, respectively, (30), (34), (35), (36), (1), and (2), must, in practice, be carried out numerically. To give some idea of what is involved, we consider in this last section the simplest possible reference problem, namely a fully clamped plate under a constant surface pressure so that, in $(19)_1$, $p = 1$. The well-known solution of the classical plate equation, subject to (26) and (27), is then (see, for example, Timoshenko and Woinowsky, 1959, p. 55)

$$V = (3/128C)(1 - \xi^2)^2 \tag{70}$$

so that, from (24),

$$\hat{T} = (3/8)\xi(\zeta^2 - 1), \quad \hat{S} = (1/4)\zeta(3 - \zeta^2). \tag{71}$$

Further, if we set $\kappa = 2(1 + \nu)$, the classical value for an elastically isotropic body, then (31) yields

$$f = (3/4)(1 - \zeta^2)(1 + \nu)/(1 - \nu). \tag{72}$$

From (69) and (70),

$$q = -\mathcal{H}(1 - x)(3c^2/32)(1 - \nu)x[2(\epsilon c)^{-1} - 3x + O(\epsilon c)] \tag{73}$$

so that (35) yields

$$F_\zeta = (3/64)(1 - \nu)\epsilon^{-2}\{[2 - 3\epsilon c x + O(\epsilon c)^2]x\delta(1 - x) - 2[1 - 4\epsilon c x + O(\epsilon c)^2]\mathcal{H}(1 - x)\}, \tag{74}$$

upon noting from $(44)_1$ that $\partial/\partial x = -\epsilon c\partial/\partial\xi$. The concentrated load in (74) represented by $\delta(1 - x)$ could be ameliorated by replacing the Heaviside function in (73) by a function that decreased smoothly from 1 to 0 as x went from 1 to 2.

Because our example problem is static, the error load F_ζ is given by the first line of (34), for which we need $\hat{U}$ and $\mathcal{U}$. The former quantity follows from $(23)_2$ and (70) as

$$\hat{U} = (3/32)(1 - \nu^2)\xi(1 - \xi^2)\zeta. \tag{75}$$

To compute $\mathcal{U}$, we use (30). With $\tilde{W} = \xi^{-1/2}\omega$, as in (37), $\tilde{T} = \hat{T} = (3/8)\xi(\zeta^2 - 1)$ as in $(71)_1$, and $\kappa = 2(1 + \nu)$, we have

$$\mathcal{U} = -\left(\xi^{-1/2}\int_0^{\zeta} \omega d\bar{\zeta}\right)_{,\xi} + (1/4)\epsilon^2(1 + \nu)\xi\zeta(\zeta^2 - 3). \tag{76}$$

To compute ω we turn to (41), but confine ourselves to the *edge zone* $1 - \epsilon c \le \bar{\xi} \le 1$ where the deviations from classical plate theory are most pronounced. With the boundary conditions (42), the change of variables (44), the explicit formula (72) for f, and the observation from Fig. 1 that, no matter whether S coincides with R or lies on the edge $\xi = 1$, $\int_{RS} \omega v_{,\xi} d\zeta = 0$, we have

$$2\bar{\omega}(\bar{x}, \bar{\zeta}) \equiv 2\omega(1 - \epsilon c\bar{x}, \bar{\zeta}) = \epsilon^5 c\Big\{(3/4)[(1 + \nu)/(1 - \nu)] \times \int_{Q^*} v(1 - \epsilon c x, \zeta; 1 - \epsilon c\bar{x}, \bar{\zeta})(1 - \epsilon c x)^{1/2}(1 - \zeta^2) dx d\zeta - \int_{(\bar{x}_-)}^{\bar{x}_+} v_{,\zeta}(1 - \epsilon c x, 0; 1 - \epsilon c\bar{x}, \bar{\zeta})\Psi(x) dx\Big\} + (3/4)(1 + \nu)\epsilon^4 c^2 \int_0^{-(\bar{x}_-)} v(1, \zeta; 1 - \epsilon c\bar{x}, \bar{\zeta})(\zeta^2 - 1) d\zeta + (v\omega)_{Q^*} + (v\omega)_{S^*}. \tag{77}$$

Downloaded 04 May 2010 to 171.66.16.26. Redistribution subject to ASME license or copyright; see http://www.asme.org/terms/Terms_Use.cfm

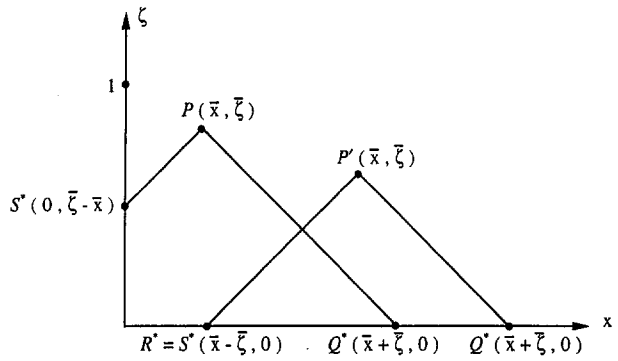

Fig. 2 Characteristics in the transformed $x\zeta$-plane emanating from two different points P and P'

Here, $\mathcal{Q}^*$, Q^*, and S^* are the images in the $x\zeta$-plane of $\mathcal{Q}$, Q, and S, respectively, as in Fig. 2, $x_\pm \equiv x \pm \zeta$, and $\langle a \rangle \equiv \frac{1}{2}(a + |a|)$. If S^* lies on the edge of the plate, $(v\omega)_{S^*} = 0$ because $\omega = 0$ there; if S^* lies in the plane $\zeta = 0$ then, from $(33)_1$, (37), (44), and Fig. 2,

$$(v\omega)^{\mathcal{Q}^*}_{S^*} = \epsilon^4 v(1 - \epsilon c\bar{x}_\pm, 0; 1 - \epsilon c\bar{x}, \bar{\zeta})\Psi(\bar{x}_\pm). \quad (78)$$

If the asymptotic expansions (61), (62), and (67) are substituted into (77) and (78), we find that $\tilde{\omega}(\bar{x}, \bar{\zeta})$ has an expansion of the form

$$\tilde{\omega} = \epsilon^4[\tilde{\omega}_0 + O(\epsilon c)], \quad (79)$$

where, from (66), (68), $(71)_1$, and (72),

$$\tilde{\omega}_0(x, \zeta) = (1/8)(1 + \nu)c^2\{(3 - x_-^2)\langle x_- \rangle + 3[x_+^2 - 1 + (x_-^2 - 1)\mathcal{H}(x_-)]\}. \quad (80)$$

From $(4)_3$, $(44)_1$, (75), (76), (79), and (80),

$$F_\xi = C(\Delta - \xi^{-2})(\hat{U} - \mathcal{U})$$
$$= -(3/4)(1 - \epsilon cx)\zeta - \frac{C}{\epsilon c}\left[\frac{1}{(\epsilon c)^2}\frac{\partial^2}{\partial x^2} - \frac{1}{\epsilon c(1 - \epsilon cx)}\frac{\partial}{\partial x} - \frac{1}{(1 - \epsilon cx)^2}\right] \times \frac{\partial}{\partial x}\left[(1 - \epsilon cx)^{-1/2}\int_0^\zeta \tilde{\omega}(x, \bar{\zeta})d\bar{\zeta}\right]$$
$$= -(3/4)\zeta + \epsilon c\left\{(3/4)x\zeta - (C/c^4)\left[\int_0^\zeta \tilde{\omega}_0(x, \bar{\zeta})d\bar{\zeta}\right]_{,xxx}\right\} + O(\epsilon c)^2$$
$$= -(3/4)\zeta\left\{1 - \epsilon c\left[x + \frac{\mathcal{H}(\zeta - x)}{(1 - \nu)c^2}\right] + O(\epsilon c)^2\right\}. \quad (81)$$

Note that the dimensionless axial error body force above is smaller by an order of magnitude $O(\epsilon c)^2$ than the transverse error body force given by (74).

Conclusions

We have presented a method whereby the errors in the dynamic three-dimensional linear theory of elasticity for axisymmetric plates made by using the classical Kirchhoff model may be assessed by constructing an exact solution of a "nearby" three-dimensional elasticity problem. The errors themselves comprise body and surface shear forces which become large only in a narrow three-dimensional boundary layer of width $O(H)$ at the edge of the plate. While the exact expressions given for the error loads (which involve the solution of an integral equation) probably have to be treated numerically, we have obtained relatively simple analytical *asymptotic* solutions in powers of the half-thickness to radius ratio, $\epsilon = H/a$. We have called our error loads an "engineering norm" because it is the external loads—and their degree of uncertainty—for which the engineer has an immediate physical intuition. If the error loads are unacceptably large, then the plate model must be refined, although a boundary layer correction may be all that is needed, as is abundantly clear from Ladevèze (1985).

Acknowledgments

This work was supported by the US Army Research Office under Grant DAAH04-94-G0189 and by the National Aeronautics and Space Administration under Grant NAG-1-1854.

References

Copson, E. T., 1975, *Partial Differential Equations,* Cambridge University Press, Cambridge, UK.

Ladevèze, P., ed., 1985, *Local Effects in the Analysis of Structures,* Elsevier, Amsterdam.

Ladevèze, P., and Simmonds, J. G., 1996, "Exact Time-Dependent Plane Stress Solutions for Elastic beams: A Novel Approach," ASME JOURNAL OF APPLIED MECHANICS, Vol. 63, pp. 962–966.

Timoshenko, S., and Woinowsky-Krieger, S., 1959, *Theory of Plates and Shells,* 2nd ed., McGraw-Hill, New York.

Downloaded 04 May 2010 to 171.66.16.26. Redistribution subject to ASME license or copyright; see http://www.asme.org/terms/Terms_Use.cfm

S.-Y. Hsu

T. J. Vogler

S. Kyriakides
Fellow ASME

Research Center for Mechanics of Solids, Structures & Materials, W. R. Woolrich 110, The University of Texas at Austin, Austin, TX 78712

Compressive Strength Predictions for Fiber Composites

Introduction

The compressive strength of typical fiber-reinforced matrix composites has been consistently shown to be only 50 to 60 percent of their tensile strength. During the last few years, it has been recognized that compressive strength is governed by plastic buckling of the material (Argon, 1972; Budiansky, 1983) as opposed to elastic microbuckling of the fibers as originally proposed by Rosen (1965). Furthermore, the strength has been shown to be very sensitive to small misalignments of the fibers with the direction of loading ((Budiansky and Fleck, 1993; Kyriakides et al., 1995; Schapery, 1992, 1995; and others) for a more complete historical review, see introductions of these and also Schultheisz and Waas (1996)).

Kyriakides et al. (1995) approached the problem through an idealized model composite consisting of a plane array of alternating fibers and matrix with sinusoidal imperfections (see Fig. 1). Appropriate microsections of this idealized material were discretized by suitably nonlinear finite elements. The fibers were elastic, and the matrix was assumed to be a finitely deforming J_2-flow theory elasto-plastic solid. Such models were then used to analyze the compressive response of the material and to establish in detail the sequence of events that leads to failure. By following the post-buckling response it was also shown that deformation localizes into well-defined bands of bent fibers which are the prelude to fiber kinking. This approach enabled detailed study of the parametric dependence of the failure stress on particular distributions of imperfections found in the AS4-PEEK composite tested (Kyriakides and Ruff, 1997).

Although it has been demonstrated that such plane models are qualitatively representative of fiber composites, some inevitable reservations exist about one-to-one comparison of the failure stresses they yield to measured values. To address this issue, a three-dimensional model of the problem has been developed in which the composite is treated as a hexagonal array of circular, elastic fibers surrounded by an elasto-plastic matrix. This model is outlined below along with a brief review of the plane model. Subsequently, compressive responses calculated for two and three-dimensional microsections with equivalent fiber imperfections are compared. Critical stresses predicted by these models are then compared to corresponding results from simpler models.

Contributed by the Applied Mechanics Division of THE AMERICAN SOCIETY OF MECHANICAL ENGINEERS for publication in the ASME JOURNAL OF APPLIED MECHANICS.

Discussion on the paper should be addressed to the Technical Editor, Professor Lewis T. Wheeler, Department of Mechanical Engineering, University of Houston, Houston, TX 77204-4792, and will be accepted until four months after final publication of the paper itself in the ASME JOURNAL OF APPLIED MECHANICS.

Manuscript received by the ASME Applied Mechanics Division, Feb. 4, 1997; final revision, May, 23, 1997. Associate Technical Editor: L. T. Wheeler.

Large-Scale Micromechanical Models

Two-Dimensional Model. The composite is idealized as a two-dimensional array of alternating fibers and matrix as shown in Fig. 1 (plane-stress and plane-strain cases are considered). Fibers have uniform thickness ($h = 7\ \mu$m) and the matrix layers have the thickness necessary to match the 0.40 matrix volume fraction of the composite. The microsections have finite width (b) defined by the number of fibers, n_f. The fibers have sinusoidal imperfections with amplitude a and wavelength 2λ. In all cases discussed here, the imperfections are uniformly distributed through the microsection width and are represented by

$$\nu_o = a \cos \frac{\pi x_1}{\lambda} \tag{1}$$

(see Fig. 1). If we assume that this periodicity is maintained throughout the deformation history, then it is sufficient to consider a microsection length (L) of just one quarter of the imperfection wavelength. The microsection is discretized by finite elements using eight-node biquadratic elements within the framework of the computer program ABAQUS[1].

Important components of the numerical models are the mechanical properties assigned to the fibers and matrix. These were extracted from a set of measurements made on the composite described in the Appendix of Kyriakides et al. (1995) (these included uniaxial tension and compression tests in the fiber and transverse directions and pure shear tests which yielded the nonlinear shear modulus $\hat{G}_{12}$; the composite elastic properties are listed in Table 1(a)). Although it is well documented that PAN fibers are anisotropic (e.g., see Johnson (1987) and Donnet and Bansal (1990)), as before, the fibers are assumed to be linearly elastic (see Table 1(b)) because the transverse properties are difficult to extract and are thought to have only a minor effect on the composite compressive strength in the fiber direction. Furthermore, the matrix is modeled as a time-independent, isotropic, elasto-plastic solid through the finite deformation J_2-flow theory of plasticity even though PEEK is known to exhibit mechanical characteristics not captured by this simple representation of inelastic behavior.

Compressive strength is strongly dependent on the shear strength of the composite (Argon, 1972; Budiansky, 1983). Thus, when the composite was idealized as a two-dimensional layered material it was necessary that the model have the same shear response as that measured. The matrix stress-strain response shown in Fig. 2 (two-dimensional model) used together with the elastic properties of the fibers in a simple two-dimensional layered solid produces the model composite shear re-

[1] We are greatful to Hibbitt, Karlson and Sorenson, Inc. for making ABAQUS available under academic license.

 Copyright © 1998 by ASME

Downloaded 04 May 2010 to 171.66.16.26. Redistribution subject to ASME license or copyright; see http://www.asme.org/terms/Terms_Use.cfm

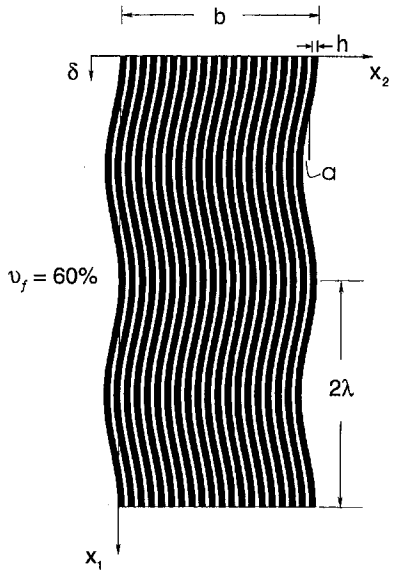

Fig. 1 Geometry of composite microsection idealized as a two-dimensional solid of alternating fibers and matrix with sinusoidal imperfections

sponse shown in Fig. 3(*a*). It can be seen to be in good agreement with the measured shear response of AS4-PEEK.

Three-Dimensional Model. In this case, the fibers were assumed to be circular with diameter h and to have a hexagonal distribution (Fig. 4(*a*)) with a spacing that corresponds to a fiber volume fraction of 0.60 (size of characteristic cell given in Fig. 4(*b*)). As was the case in the two-dimensional models, the composite microsection analyzed has finite width (b) defined by the number of fibers, n_f. The fibers have sinusoidal imperfections in the $x_1 - x_2$ plane which again are described by Eq. (1). Kyriakides and Ruff (1997) reported that in the composite they analyzed typical fiber imperfections were predominantly in two orthogonal planes, the ply plane and the ply stacking plane. Because of this, under compression fibers kinked always in either of these two planes. Motivated by this, we assume the imperfections to have a quasi-planar distribution and require them to remain uniform in the x_3-direction as shown schematically in Fig. 5.

Because of the symmetries in the assumed composite geometry, it is possible to limit attention to a characteristic section

Table 1 Material properties of the composite and its constituents

(a)

APC-2/AS4 Composite				
E_{11} msi (GPa)	E_{22} msi (GPa)	G_{12} msi (GPa)	ν_{12}	ν_f
18.62 (128)	1.533 (10.57)	0.84 (5.79)	0.3	60%

(b)

AS4 Fibers	
E_f msi (GPa)	ν_f
31.0 (214)	0.263

(c)

APC-2 (PEEK) Matrix					
2-D Models			3-D Model		
E_m ksi (GPa)	σ_{om} ksi (MPa)	ν_m	E_m ksi (GPa)	σ_{om} ksi (MPa)	ν_m
893 (6.14)	11.9 (82.1)	0.356	594 (4.10)	10.6 (73.2)	0.356

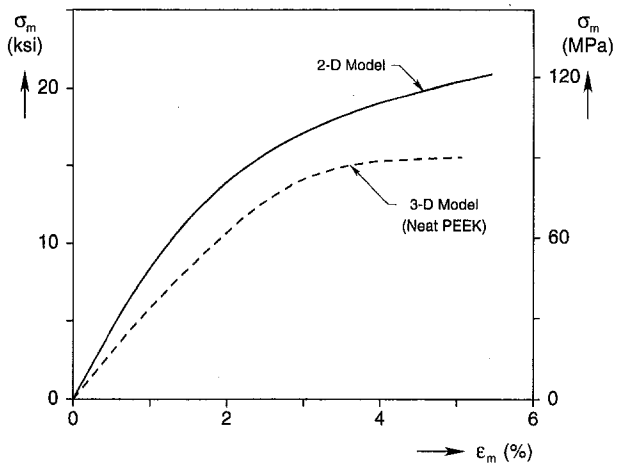

Fig. 2 Stress-strain responses for PEEK used in two-dimensional and three-dimensional models

with a height of λ/2 and width b (see Fig. 5). The two lateral surfaces of the section are assumed to remain plane (i.e., either plane-strain or generalized plane-strain conditions in the x_3-direction), and the deformation is assumed to be antisymmetric at $x_1 = \lambda/2$.

The domain is discretized with 20-node quadratic bricks and 15-node quadratic prisms (full integration was used for both). Typically, the cross section of each half fiber is represented by a single element, while several elements are used to model the matrix between the two rows of half fibers in the characteristic section. In the fiber direction, the element distribution is chosen

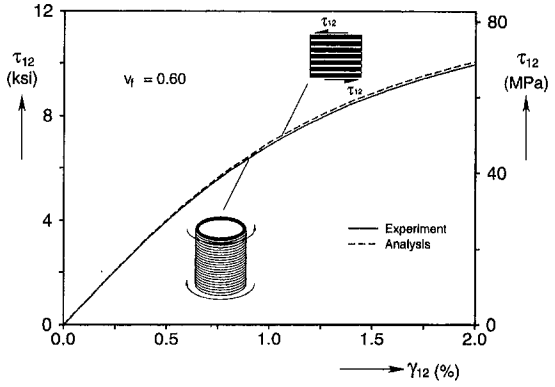

Fig. 3(*a*)

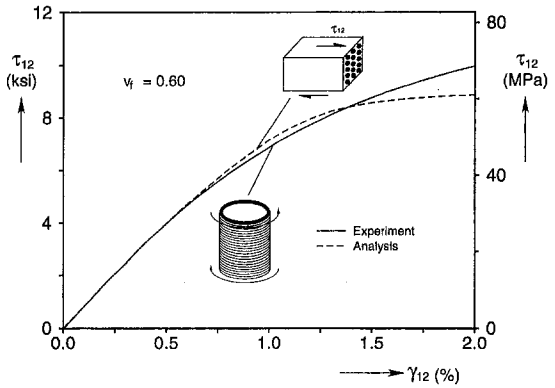

Fig. 3(*b*)

Fig. 3 Comparison of measured composite shear response to numerical simulations for (*a*) the two-dimensional model and (*b*) the three-dimensional model

Downloaded 04 May 2010 to 171.66.16.26. Redistribution subject to ASME license or copyright; see http://www.asme.org/terms/Terms_Use.cfm

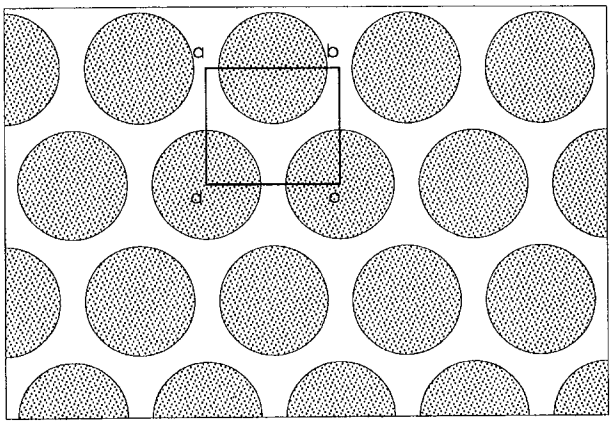

Fig. 4(*a*)

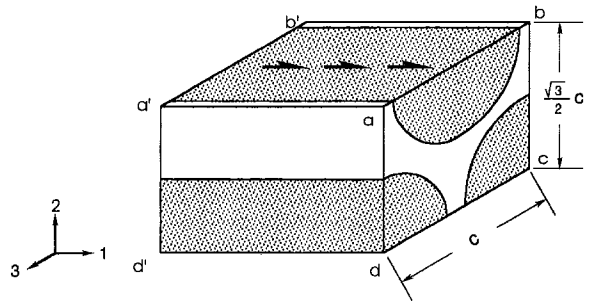

Fig. 4(*b*)

Fig. 4 Composite idealized as a hexagonal array of round fibers in a PEEK matrix. Figures show a representative volume element for three-dimensional numerical simulation of shearing response.

to be more dense in the central third of the domain shown in Fig. 5 as this is the area in which deformation eventually localizes.

The fibers are again assumed to be linearly elastic with the constants given in Table 1(b). The matrix properties used came from a uniaxial tension test on neat PEEK obtained from the same source that supplied the AS4-PEEK composite (see Fig. 2 and Table 1(c)). These constituent properties were used to calculate numerically the pure shear response of this model using the characteristic cell shown in Fig. 4 where the dimension c is related to the fiber diameter and the fiber volume fraction (v_f) by

$$c = h\sqrt{\frac{\pi\sqrt{3}}{6v_f}}. \tag{2}$$

Pure shear was achieved by fixing the surface cdd'c' and displacing uniformly the surface abb'a' as indicated in Fig. 4(b) while requiring that the surfaces abcd and a'b'c'd' have the same displacements. The response calculated is shown in Fig. 3(b) along with the corresponding measured response. The two results are in good agreement up to a shear strain of approximately 1.5 percent beyond which the calculated response is somewhat lower than that measured. The uniaxial tension test on PEEK was limited to a strain of approximately four percent. Beyond this point the stress-strain response was extrapolated so as to asymptotically become perfectly plastic (plateau stress = 15.24 ksi—105.1 MPa). This arbitrary extrapolation is thought to be partly responsible for the disagreement between the predicted and measured shear response in Fig. 3(b) at higher shear strains.

Results

Two-Dimensional Model. The characteristics of the compressive response yielded by the two-dimensional model were discussed in detail in Kyriakides et al. (1995). Here we briefly outline the major features of such responses through an example in order to facilitate comparison with corresponding three-dimensional results. The example chosen involves imperfections uniformly distributed in the x_2-direction with $\lambda = 150h$ and $a = h$. The microsection analyzed is 60 fibers wide and is assumed to be in a state of plane stress. The average axial stress (σ_{11})-end shortening (δ) response calculated is shown in Fig. 6(a). The initial and two deformed configurations of the microsection are shown in Fig. 6(c) (configuration numbers correspond to the points identified by numbers on the $\sigma_{11} - \delta$ response).

The calculated $\sigma_{11} - \delta$ response is initially almost linear and has a stiffness which is very close to the measured compressive modulus of the composite (19 msi—131 GPa). As the compressive stress increases, the matrix is plasticized due to the combination of the axial stress and the shear stress induced by the small inclination of the imperfect fibers. This reduces the shear stiffness of the matrix and eventually results in a limit load at a stress of 220.6 ksi (1.521 GPa) and a strain of 1.168 percent. This represents the critical state of the micromodel. Beyond this point, deformation starts to localize in a narrow band in the central part of the microsection where the fibers undergo significant bending. As the rest of the microsection unloads, the average axial stress and the net axial shortening decrease simultaneously producing the cusp-like part of the response. This, of course, is responsible for the very catastrophic nature of compressive failure of such composites. In configuration ② in Fig. 6(c), the zone of localized deformation is seen to have an inclination of approximately 7 deg to the x_2-axis (β) and a width (w) of approximately 13.5 fiber diameters (the black dots show the locations of maximum moment in each fiber). As the deformation progresses, the shear stress in the matrix approaches the plateau value assumed for larger strains, and the axial stress required for further deformation also asymptotically approaches a value in the neighborhood of 50 ksi (345 MPa). By this time (configuration ⑤), the band has broadened

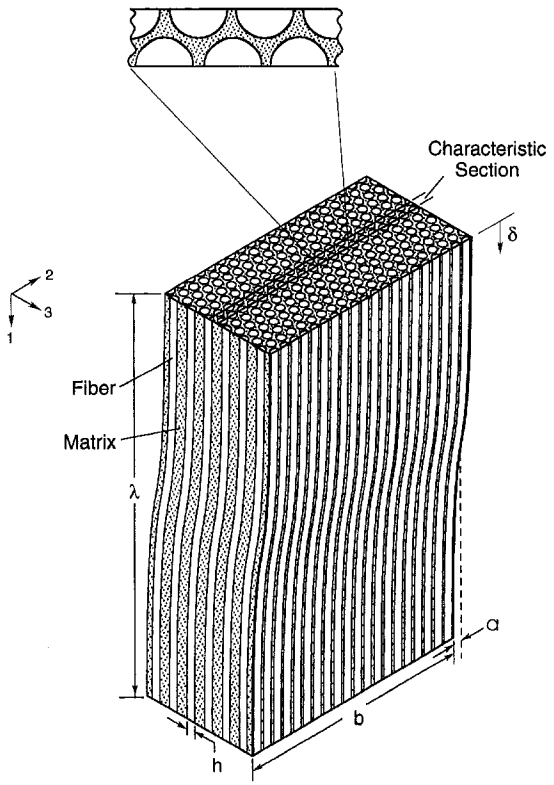

Fig. 5 Geometry of characteristic microsection of composite with sinusoidal imperfection used in a three-dimensional finite element model

Downloaded 04 May 2010 to 171.66.16.26. Redistribution subject to ASME license or copyright; see http://www.asme.org/terms/Terms_Use.cfm

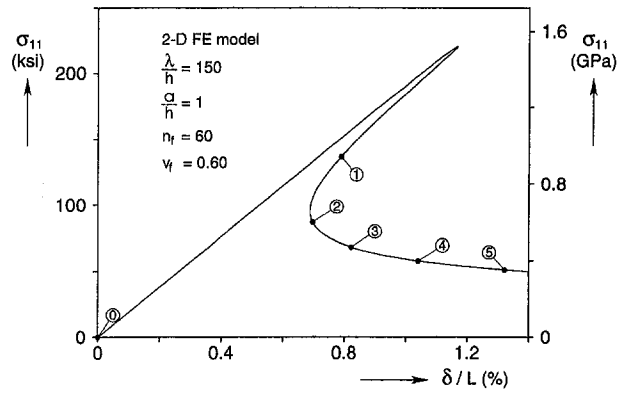

Fig. 6(*a*) Axial stress-end shortening response

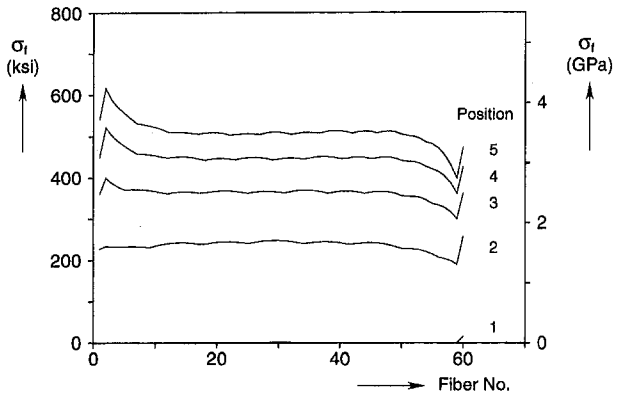

Fig. 6(*b*) Maximum tensile stresses in fibers at several points on response

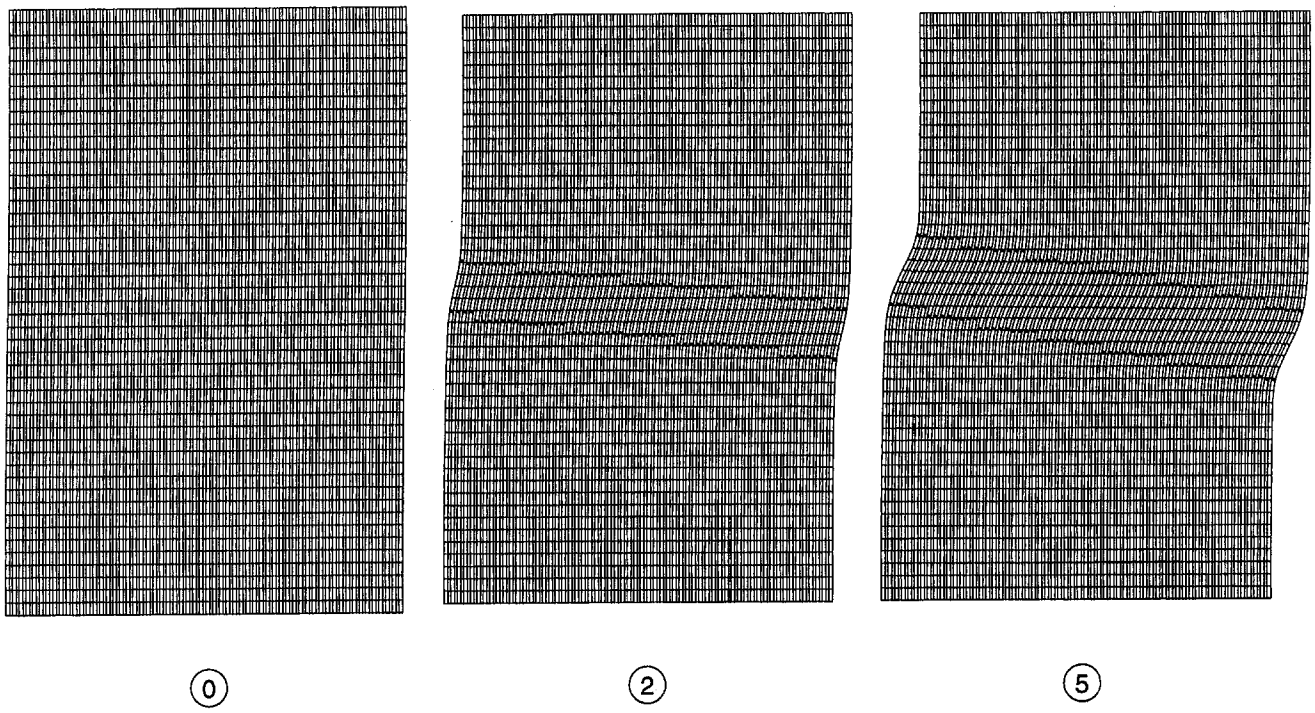

Fig. 6(*c*) Initial and two deformed configurations of the microsection analyzed

Fig. 6 Results of a two-dimensional finite element model with uniform imperfection with $a/h = 1$ and $\lambda/h = 150$

to 19.5 h and increased its inclination to 11.2 deg. A more detailed description of the evolution of the band width and inclination is shown in Fig. 7. (As pointed out in Fig. 22 of Kyriakides et al. (1995), switching to a plane-strain microsection has the effect of increasing somewhat the initial stiffness of the calculated response—in this case to 20.4 msi (140.7 GPa)—but has only a minor effect on the critical stress and on the post-buckling response.)

As mentioned above, the large deformation constitutive behavior of the composite, and by inference that adopted for the matrix, is not well known. As a result, beyond a certain point the post-buckling part of the calculated response should only be considered as an indicator of the expected trend of events. Despite this, the results strongly support the premise of the Argon-Budiansky argument that the compressive strength of such aligned materials is governed by plastic buckling. Furthermore, we clearly see that the band of highly bent fibers developed through a process of localization of deformation. As the deformation progressed, the band broadened and rotated as shown in Figs. 6(c) and 7. Figure 6(b) shows a plot of the maximum tensile stresses in each of the 60 fibers at several points along the response. As the fiber bending increases, the tensile stresses grow to values comparable to the strength of the fibers estimated to be in the neighborhood of 500–600 ksi (3.45–4.14 GPa). At this stage, the fibers break locking in a specific band inclination and width. (Fleck et al. (1995) using an alternate way to analyze the post-buckling response reached similar conclusions.)

This evolution of events is at variance with the assumption made in several recent publications that the band inclination is a characteristic angle inherent to the perfect material and shows up naturally at the onset of failure. The present scenario of events also explains why the lowest bifurcation buckling stress of the perfect system has always been found to correspond to zero band inclination (e.g. Budiansky, 1983; Budiansky and Fleck, 1993; Triantafyllidis, 1994; Jensen and Christoffersen, 1997).

Results for three additional micromodels with the same imperfection wavelength and imperfection amplitudes of a/h = 1, 2 and 3 are shown in Fig. 8. As the imperfection becomes more severe, the critical stress decreases (numerical values of σ_C and ϵ_C are given in Table 2). The lower parts of the post-

Downloaded 04 May 2010 to 171.66.16.26. Redistribution subject to ASME license or copyright; see http://www.asme.org/terms/Terms_Use.cfm

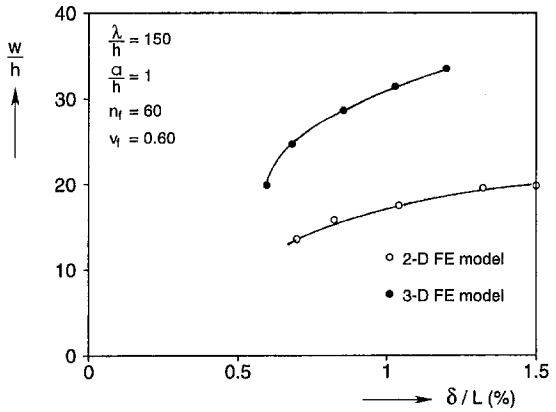

Fig. 7(*a*) Band width

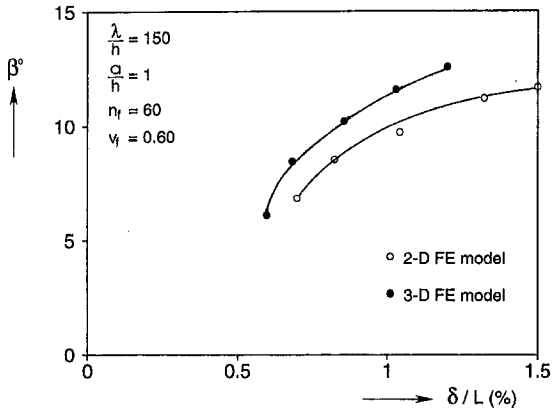

Fig. 7(*b*) Band inclination versus end shortening

Fig. 7 Band characteristics for the two-dimensional and three-dimensional models analyzed in Figs. 6 and 9

buckling responses are seen to coalesce. This suggests that the plateau stress of approximately 50 ksi may be related in some fashion to the axial propagation stress of kinking discussed recently by Moran and Shih (1996) and Vogler and Kyriakides (1997).

Three-Dimensional Model. Figure 9 shows the results from a 60 fibers wide three-dimensional microsection with $\lambda/h = 150$ and $a/h = 1$ (⓪ in Fig. 9(*c*) is a plane view of the undeformed configuration). The slice of the microsection analyzed was laterally restrained such that the net strain in the x_3 direction is zero. The $\sigma_{11} - \delta$ response is shown in Fig. 9(*a*) and two deformed configurations corresponding to it in Fig. 9(*c*). The results are quite similar to those of the corresponding two-dimensional microsection in Fig. 6. The initial stiffness is 18.9 msi (130.3 GPa), a value which again is in good agreement with the measured modulus. The critical stress is 210 ksi (1.448 GPa) and the corresponding strain 1.117 percent, that is, respectively, 4.8 percent and 2.1 percent lower than the corresponding two-dimensional results (the two-dimensional and three-dimensional $\sigma_{11} - \delta$ responses are also plotted together in Fig. 10). We note that the properties of this composite are such that a switch to a microsection restrained to remain plane in a way that makes the average transverse stress $\sigma_{33} = 0$, yields an almost identical response. For an experimental validation of this see Vogler and Kyriakides (1997).

The post-buckling response again traces a cusp-like trajectory which is even sharper than that of the two-dimensional case. In this case, the lower part of the response drops even further than the two-dimensional case as it asymptotically approaches 40 ksi (275 MPa). The unstable post-buckling response is again associated with localization of deformation into a narrow in-

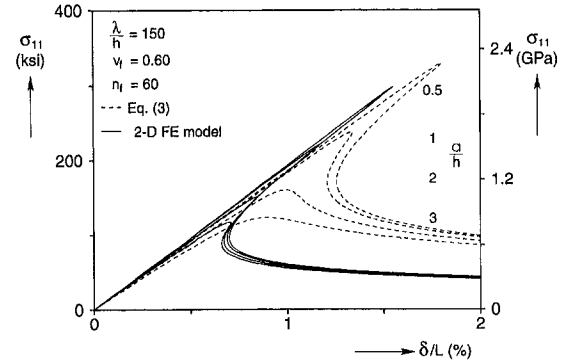

Fig. 8 Compressive $\sigma_{11} - \delta$ responses for four imperfection amplitudes and $\lambda/h = 150$ obtained via the two-dimensional finite element model

clined band of bent fibers shown in the deformed configurations in Fig. 9(*c*). For example, in configuration ② the band has an inclination of just over 6 deg and a width of about $20h$. By configuration ⑤ the inclination has increased to 11.6 deg and the width to $31h$ and in configuration ⑥ the inclination is 12.6 deg and the width $33h$. A graphical representation of the evolution of the β and w with the net shortening is shown in Fig. 7. The band inclination for a given δ is somewhat higher than that calculated in the corresponding two-dimensional case while the width is significantly higher than the two-dimensional width. This difference may be attributed to the difference in the bending rigidity of a round fiber of diameter h and a rectangular one with width h. By contrast, measured values of β reported for this material in Kyriakides et al. (1995) and more recently in Vogler and Kyriakides (1997), are in the neighborhood of 15 deg. Of course, in the experiments the initial kink bands formed dynamically and at their edges the fibers were broken.

Figure 9(*b*) shows a plot of the maximum tensile stresses that develop in the fibers at several of the post-buckling configurations. Clearly, the stresses that develop in the round fibers of the three-dimensional model are higher than those that develop in the two-dimensional microsection for approximately the same values of δ. This again can be attributed to the difference in the fiber bending rigidity in the two models. Higher tensile stresses in the fibers imply that fiber breaking and kinking will occur at a lower value of δ (or earlier in the post-buckling path) than in the two-dimensional microsection.

Results for several other imperfection amplitudes are shown in Fig. 11. The trends are similar to those of the corresponding two-dimensional results. The critical stresses and strains for each case are listed in Table 2. The critical stresses in all cases are between 10.5–11.5 ksi (72–79 MPa) lower than those of the two-dimensional micromodels.

In summary, the results of the three-dimensional composite model are similar to those of the two-dimensional one presented in our earlier work. A three-dimensional microsection with the same number of fibers as a two-dimensional microsection loaded in the same manner yields almost the same initial modu-

Table 2 Critical stresses and strains for imperfections of four amplitudes and $\lambda/h = 150$

a/h	σ_C, ksi (MPa)		ε_C, %	
	2-D	3-D	2-D	3-D
0.5	297.5 (2,052)	285.8 (1,971)	1.546	1.495
1.0	220.6 (1,521)	210.1 (1,449)	1.168	1.117
2.0	151 (1,041)	140.0 (965)	0.845	0.778
3.0	116.9 (806)	105.3 (726)	0.708	0.628

Downloaded 04 May 2010 to 171.66.16.26. Redistribution subject to ASME license or copyright; see http://www.asme.org/terms/Terms_Use.cfm

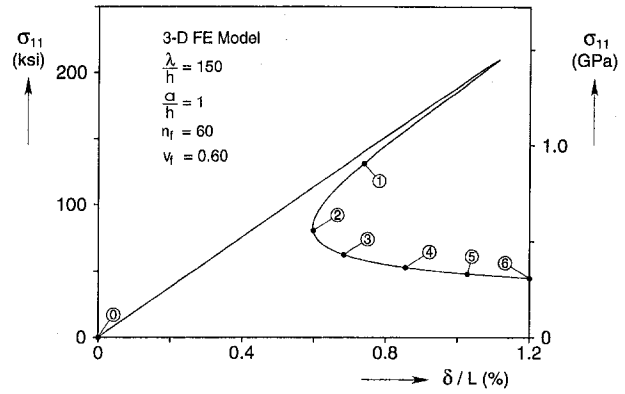

Fig. 9(*a*) Axial stress-end shortening response

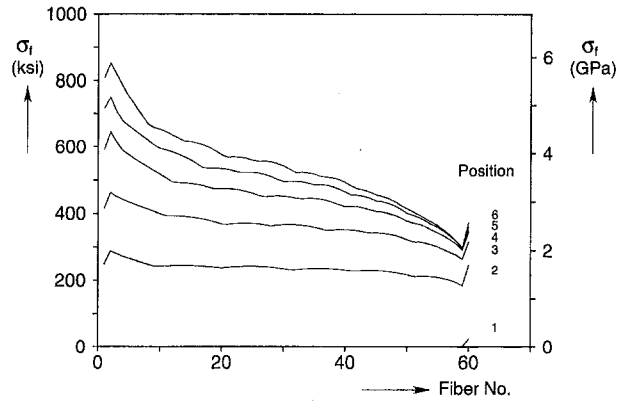

Fig. 9(*b*) Maximum tensile stresses in fibers at several points on response

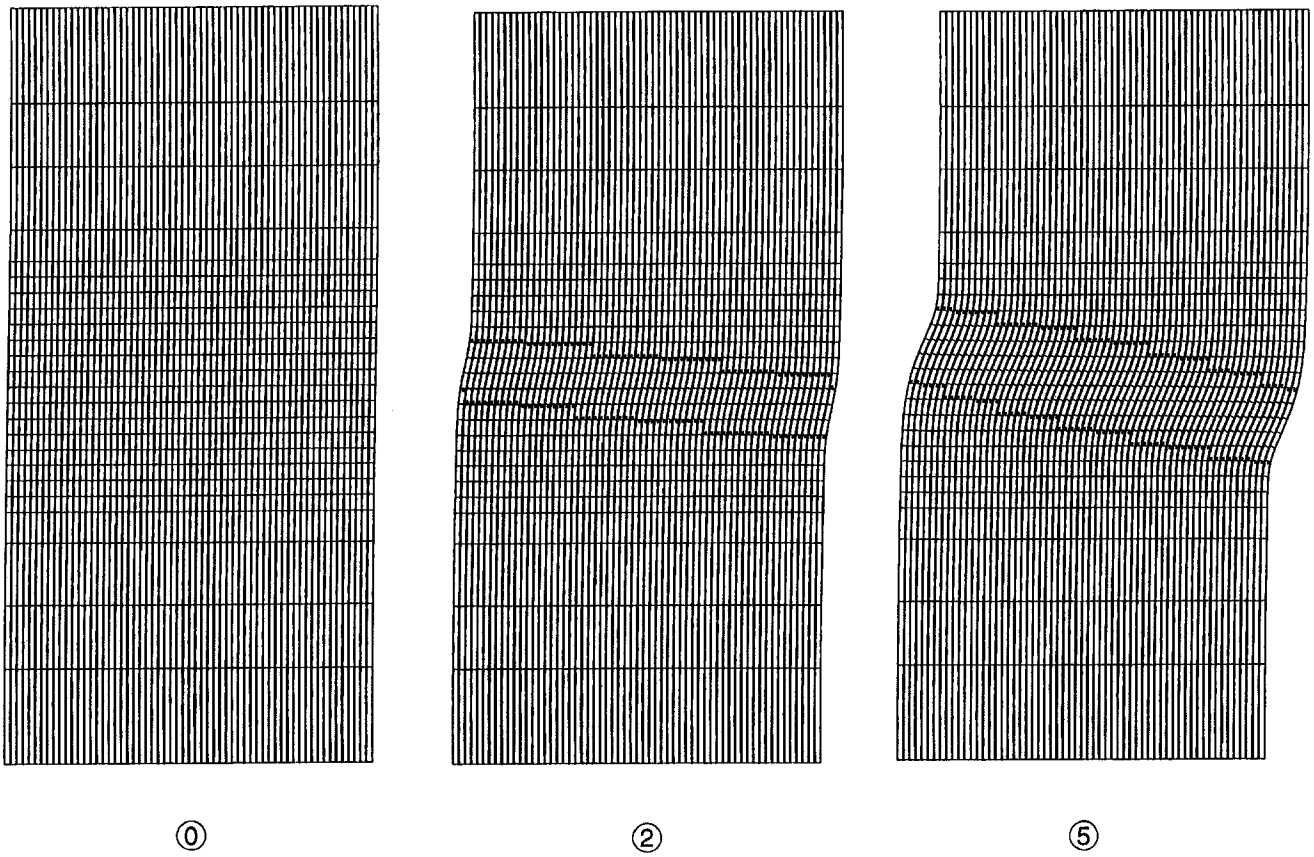

Fig. 9(*c*) Initial and two deformed configurations of the microsection analyzed

Fig. 9 Results of a three-dimensional finite element model with uniform imperfection with $a/h = 1$ and $\lambda/h = 150$

lus and a failure stress which is slightly lower. In the postbuckling regime the band of bent fibers is wider and somewhat more inclined than in the two-dimensional case at the same value of δ. In addition, for the three-dimensional case the stress level of the lower part of the response is somewhat lower than that of the two-dimensional response (Fig. 10). This last difference may be due to the partly erroneous stress-strain response adopted for larger values of matrix strain.

Finally, a comment about the influence of microsection width on the critical stress. The two-dimensional and three-dimensional microsections we have used have stress-free lateral edges where stress concentrations develop (e.g., see Waas et al. (1990) who considered this effect for the linearly elastic case). These edge effects can have significant influence on the calculated response and critical states for microsections of a few fibers as shown in Kyriakides et al. (1995, Section 3.1.1). As the number of fibers is increased the effect on σ_C decays exponentially (approximately). For example, for the problem parameters in Figs. 6 and 9 and $n_f = 60$ the error introduced to σ_C from the edge effect is of the order of five percent for both models.

Straight Fiber Models. The micromechanical models described are capable of predicting the prebuckling response and the critical stress and strain with accuracy. Suitably extended, they can be used to establish the critical stresses and strains of composites with more realistic distributions of imperfections. Indeed, for our composite this was shown in Kyriakides and Ruff (1997) to be essential. In addition, as we have seen, such models are capable of at least qualitative

Downloaded 04 May 2010 to 171.66.16.26. Redistribution subject to ASME license or copyright; see http://www.asme.org/terms/Terms_Use.cfm

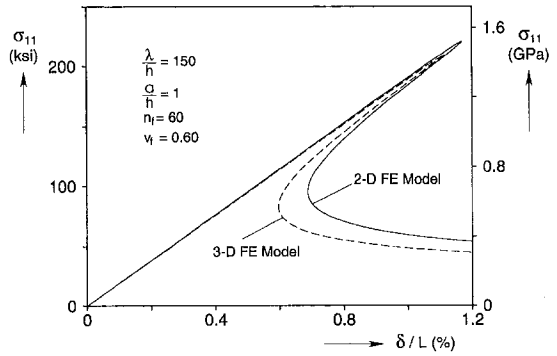

Fig. 10 Comparison of the $\sigma_{11} - \delta$ responses of two-dimensional and three-dimensional finite element models with the same imperfection characteristics

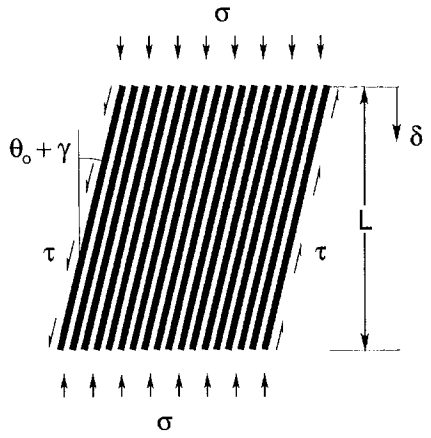

Fig. 12 Geometry of idealized composite used for the straight fiber models

simulation of the post failure events that lead to localization of deformation and eventually to kinking. An essential requirement for proper simulation of the post-buckling behavior is proper modeling of fiber bending (these models are henceforth referred to as bending fiber models—BF). On the other hand, if we limit the objective to predicting just the critical state, the much simpler class of models in which the fibers are assumed to remain straight and uniformly inclined to the direction of the applied load become available (i.e., Argon (1972), Budiansky (1983), Budiansky and Fleck (1993)—henceforth referred to as straight fiber models—SF). We will briefly review these, suggest some modest modifications, and then evaluate their performance by direct comparison to predictions by the two-dimensional and three-dimensional finite element models.

Straight-Inextensional Fibers Model. The simplest model which captures the essence of the problem is the zero kink band angle version of Budiansky's model (1983). The fibers are assumed to be inextensional and to be uniformly inclined by an angle θ_o to the direction of the applied stress (σ) (Fig. 12). If the initial angle θ_o as well as the induced shear strain γ are assumed to be small simple equilibrium considerations of the element relate the applied stress to the induced shear by

$$\sigma = \frac{\tau(\gamma)}{(\theta_o + \gamma)}. \tag{3}$$

$\tau(\gamma)$ is the nonlinear response of the composite to simple shear (for our AS4-PEEK composite shown in Fig. 3). (This expression was also reported in Chatterjee and McLaughlin (1979)). The combination of this material nonlinearity and the geometric nonlinearity in the denominator result in a stress maximum which represents the strength of the composite. If the shear response is assumed to be rigid-perfectly plastic with yield stress τ_o, Eq. (3) reduces to Argon's (1972) expression for the composite strength

$$\sigma_C = \frac{\tau_o}{\theta_o}. \tag{4}$$

In order to facilitate a direct comparison of the composite axial response represented by Eq. (3) with other such results, we will include the elastic deformation of the fibers by assuming that

$$\sigma \approx E_{11}\epsilon \tag{5}$$

but without coupling this to the shear response. The axial shortening of the composite (δ/L) can then be approximated by

$$\frac{\delta}{L} \approx \theta_o\gamma + \tfrac{1}{2}\gamma^2 + \epsilon. \tag{6}$$

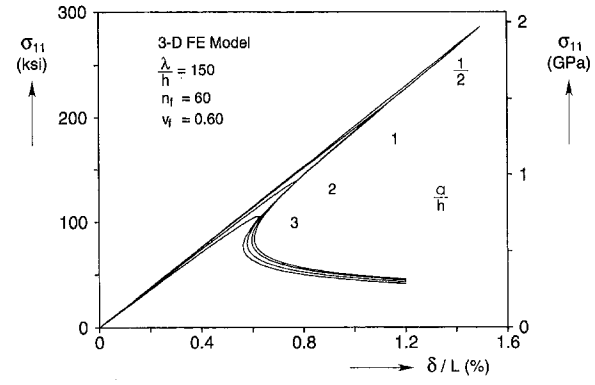

Fig. 11 Compressive $\sigma_{11} - \delta$ responses for four imperfection amplitudes and $\lambda/h = 150$ obtained via the three-dimensional finite element model

Straight-Extensional Fibers Models. A minor deficiency of this model is that as a result of the assumed fiber inextensionality axial deformations do not contribute to the plastification of the matrix. Budiansky and Fleck (1993 last section) addressed this issue by making the fibers linearly elastic, the matrix a J_2 deformation theory elasto-plastic solid, and by using the rule of mixtures to calculate the composite axial and shear response (Christensen and DeTeresa (1997) use a somewhat different approach). For convenience, the relevant equations are summarized in our notation in the Appendix. Budiansky and Fleck incorporated into their extension of Eq. (3) a Ramberg-Osgood representation of the matrix stress-strain response. In our case we use directly the matrix properties extracted from the composite shear response for our two-dimensional models (Fig. 2).

For completeness and in order to be more in concert with the approach taken in the large-scale micromechanical models, the same calculations are repeated using J_2-flow theory. The relevant equations are again summarized in the Appendix.

Results. Typical $\sigma - \delta$ and $\sigma - \gamma$ responses predicted by three SF models are shown in Fig. 13. The case shown had an initial misalignment angle of 0.4 deg. The initial modulus of the $\sigma - \delta$ response yielded by Eq. (3) corresponds to that of the composite (18.6 msi—128 GPa) since this was the value used in Eq. (5). The initial modulus yielded by the other two models corresponds to that obtained by the rule of mixtures

Downloaded 04 May 2010 to 171.66.16.26. Redistribution subject to ASME license or copyright; see http://www.asme.org/terms/Terms_Use.cfm

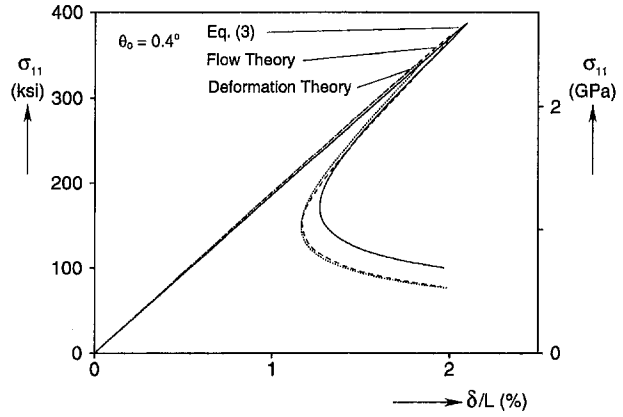

Fig. 13(*a*) Axial stress-end shortening responses

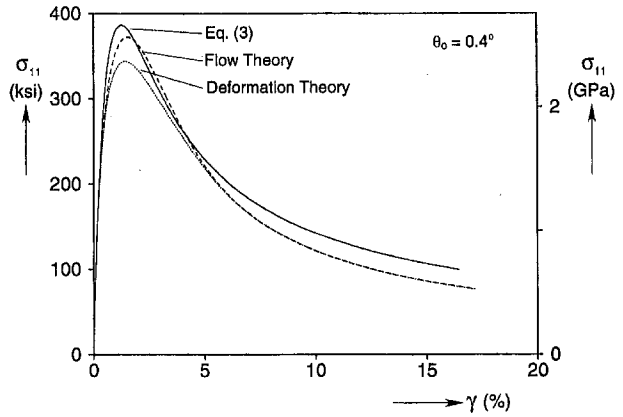

Fig. 13(*b*) Axial stress-shear strain for three straight fiber models

using the matrix and fiber properties in Table 1 (18.94 msi—130.6 GPa).

The responses exhibit limit stresses which are listed in Table 3 along with the corresponding axial strains (here $\epsilon_C = \delta_C/L$) and shear strains. It can be seen that the inextensional model yields the highest critical stress, the deformation theory model the lowest (11 percent lower) and the flow theory model a value in between the other two. The critical shear strain is smallest for the inextensional fiber model and largest for the flow theory model. Interestingly, for this relatively small value of θ_o, the three $\sigma - \delta$ responses exhibit a cusp after the limit stress even without the localization of deformation which is precluded in these SF models. The cusp is formed because of deformation recovered from the elastic unloading of the fibers.

Comparison of Straight Fiber and Bending Fiber Models

In order to enable such a comparison, the single imperfection parameter of the SF models (θ_o) must be related to the two parameters of the sinusoidal imperfections (a and λ) used in the BF models. Provided the sinusoidal imperfections have long wavelength and relatively small amplitude, the following approximation is reasonable:

$$\theta_o \approx \frac{\pi a}{\lambda}. \tag{7}$$

(For more on this see Fig. 23(c) and discussion in Kyriakides et al. (1995).) That is, the maximum misalignment in the sinusoidal imperfection is associated with θ_o. This relationship was used in Eq. (3) to calculate $\sigma - \delta$ responses for the four sets of parameters shown in Fig. 8. The critical stresses and strains predicted by this inextensional SF model are seen to be higher than those of the two-dimensional BF model for all cases, but the difference decreases as the imperfection amplitude increases. The post-buckling responses of the SF models are also included in order to illustrate their difference from the more realistic ones of the BF model where localization of deformation takes place. For the two larger values of a/h, the SF model does not exhibit a cusp after the limit stress whereas the BF results continue to do so. Also, the lower parts of the post-buckling responses tend to a stress which is more than double that of the BF responses.

The numerical values of the critical stresses of the eight responses in Fig. 8 are compared in a master plot of the imperfection sensitivity of σ_C in Fig. 14 (i.e., σ_C versus θ_o). Here we include the imperfection sensitivity predicted by the three SF models (continuous curves) as well as the eight discrete results obtained by the two BF models (in Table 2). Also included is the bifurcation buckling stress (527 ksi—3.634 GPa) of the perfectly aligned composite obtained by assuming the fibers to be linearly elastic and the matrix to be a J_2 deformation theory solid (Budiansky and Fleck, 1993) given by

$$\sigma_{Cb} = \frac{G_m}{(1 - \upsilon_f)\left[1 + 3G_m\left(\frac{1}{E_{ms}} - \frac{1}{E_m}\right)\right]} \tag{8}$$

where $(\bullet)_m$ refers to linearly elastic moduli (Table 1(c)) and $(\bullet)_{ms}$ to the secant modulus which can be obtained from Fig. 2 (two-dimensional model). (By contrast, the elastic buckling stress of the composite of Rosen is 840 ksi (5.8 GPa)). The following observations can be made from these results.

- The imperfection sensitivity of the failure stress is seen once more to be very significant for all models. Misalignment of only 0.5 deg causes a nearly 50 percent reduction in strength.
- The BF models predict somewhat lower critical stresses than all of the SF models with the three-dimensional

Table 3 Problem variables predicted by the three straight fiber models

SF Models	$\theta_o{}^\circ$ (rad)	E_{11} msi	σ_C ksi	ϵ_C %	γ_C%
Inext.	0.4 (0.007)	18.59	386.5	2.092	1.24
Deform. Theory	0.4 (0.007)	18.94	343.9	1.846	1.43
Flow Theory	0.4 (0.007)	18.94	372.3	2.003	1.528

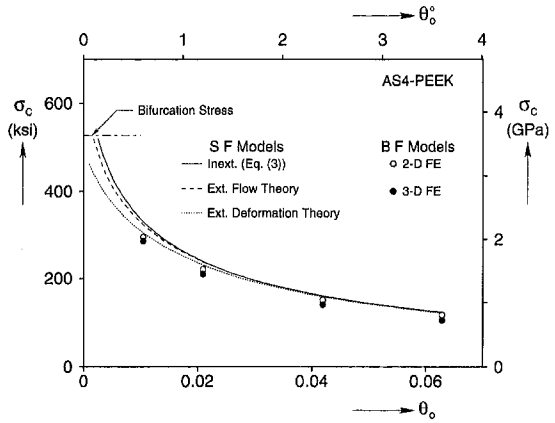

Fig. 14 Comparison of critical stress as a function of initial imperfection amplitude for three straight fiber models and two bending fiber models

Downloaded 04 May 2010 to 171.66.16.26. Redistribution subject to ASME license or copyright; see http://www.asme.org/terms/Terms_Use.cfm

model (which is the most representative of the actual composite) yielding the lowest strength.

- Of the three SF models, the inextensional model yields the highest and the deformation theory model the lowest critical stress. The difference between the three sets of predictions decreases as the imperfection amplitude increases.
- The deformation theory SF model yields results which are quite close to those of the BF models.
- The quality of the predictions of all models is strongly influenced by the accuracy of the representation of the nonlinear shear response of the composite analyzed. For example, optimum results can be expected when the measured shear response is used directly in Eq. (3) as opposed to attempting to fit it with representations with an inadequate number of parameters.
- For this reason, the simpler expression for composite strength of Argon, given in Eq. (4), despite its sound basis was found in practice not to yield dependable predictions of σ_C. Commonly used composites have a very nonlinear shear response which is next to impossible to represent with just one parameter (the yield stress).

Conclusions

A new micromechanical model of fiber-matrix composites has been presented in which the material is represented as a hexagonal array of round elastic fibers in an elasto-plastic matrix. Using the compressive responses of such models, it was confirmed that the prebuckling and critical states predicted earlier by two-dimensional idealizations of the composite are accurate provided the constituent properties are chosen appropriately. Furthermore, the localization of deformation into a narrow inclined band of bent fibers obtained via the two-dimensional model was found to also occur in the more realistic three-dimensional models albeit with some quantitative difference in the band characteristics. As the localization progresses, the zone of bent fibers broadens and increases its inclination in both models. The width and inclination of the bands were found to be larger in the three-dimensional results compared to the corresponding two-dimensional results. Again, as a result of the localized bending, the fibers develop significant tensile stresses and break. The final orientation and width of kink bands seen in controlled compression tests is probably governed by the strength of the fibers.

Critical stresses predicted by these computationally intensive models were compared with three simpler SF models for uniformly distributed fiber imperfections. In general, the SF model which allows for fiber extension and in which the matrix is modeled as a deformation theory solid yielded critical stresses close to those of the finite element models. For fiber misalignment angles larger than approximately 1.2 deg, the strengths predicted by all three SF models were in agreement with the numerical results.

An important aspect of the extensional SF and the two-dimensional finite element models is the way the shear response of the matrix is extracted from the composite. For accurate predictions of compressive strengths the nonlinear stress-strain response of the matrix must be chosen such that the two-dimensional idealized composite has a shear response which matches the measured shear response of the composite. Using the properties measured for neat matrix in such models will result in erroneous predictions of σ_C.

Finally a word of caution. Despite the very good performance of the SF models in predicting σ_C for imperfections with long wavelengths and with uniform transverse distributions, actual imperfections have been shown to have particular geometric characteristics which can hardly be idealized as uniform (e.g., Kyriakides and Ruff, 1997). Use of the present SF models in such cases can result in significant errors in predictions of compressive strength.

Acknowledgments

The financial support of the Office of Naval Research under contract N00014-91-J-4091 acknowledged with thanks. The work of TJV was also supported by the Fannie and John Hertz foundation and the W. M. Keck Foundation.

References

Argon, A. S., 1972, "Fracture of composites," *Treatise on Material Science and Technology,* Vol. 1, H. Herman, ed., Academic Press, New York, pp. 79–114.

Budiansky, B., 1983, "Micromechanics," *Computers & Structures,* Vol. 16, pp. 3–12.

Budiansky, B., and Fleck, N. A., 1993, "Compressive failure of fiber composites," *J. Mechanics & Physics of Solids,* Vol. 41, pp. 183–211.

Chatterjee, S. N., and McLaughlin, P. V., 1979, "Inelastic shear instability in composite materials under compression," *Proc. 3rd. ASCE Eng. Mechanics Div. Specialty Conference,* Sept. 17–19, University of Texas, Austin, TX, pp. 649–652.

Christensen, R. M. and DeTeresa, S. J., 1997, "The Kink Band Mechanism for the Compressive Failure of Fiber Composite Materials," ASME JOURNAL OF APPLIED MECHANICS, Vol. 64, pp. 1–6.

Donnet, J.-B., and Bansal, R. C., 1990, *Carbon Fibers,* 2nd Ed., Marcel Decker, New York.

Fleck, N. A., Deng, L., and Budiansky, B., 1995, "Prediction of Kink Width in Fiber Composites," ASME JOURNAL OF APPLIED MECHANICS, Vol. 62, pp. 329–337.

Fleck, N. A., and Budiansky, B., 1991, "Compressive kinking of fiber composites due to microbuckling." *Proc. IUTAM Symposium on Inelastic Deformation of Composite Materials,* Troy, NY, May 29–June 1, 1990, J. Dvorak, ed., Springer-Verlag, New York, pp. 235–273.

Jensen, H. M., and Christoffersen, J., 1997, "Kink band formation in fiber reinforced materials," *J. Mechanics & Physics of Solids,* Vol. 45, pp. 1121–1136.

Johnson, D. J., 1987, "Structure-property relationships in carbon fibres," *J. Physics D: Applied Physics,* Vol. 20, pp. 286–291.

Kyriakides, S., Arseculeratne, R., Perry, E. J., and Liechti, K. M., 1995, "On the compressive failure of fiber reinforced composites," *Int'l J. Solids & Struct.,* Vol. 32, pp. 689–738.

Kyriakides, S., and Ruff, A. E., 1997, "Aspects of the failure and postfailure of fiber composites in compression," *J. Composite Materials,* Vol. 31, pp. 2000–2037.

Moran, P. M., and Shih, C. F., 1996, "Kink band formation and band broadening in fiber composites under compressive loading: Experiments and Analysis," *Int'l J. Solids & Structures,* Vol. 31, pp. 2000–2037.

Rosen, B. W., 1965, "Mechanics of composite strengthening," *Composite Materials,* American Society of Metals, Metals Park, OH, pp. 37–75.

Schapery, R. A., 1992, "Analysis of local buckling in viscoelastic composites," *Local Mechanics Concepts for Composite Material Systems,* J. N. Reddy and K. L. Reifsnider, eds., Proc. IUTAM Symposium, Blacksburg, VA, Oct. 28–31, 1991, Springer-Verlag, New York, pp. 229–250.

Schapery, R. A., 1995, "Prediction of compressive strength and kink bands in composites using a work potential," *Int'l J. Solids & Structures,* Vol. 32, pp. 739–765.

Schultheisz, C. R., and Waas, A. M., 1996, "Compressive failure of composites, Parts I and II," *Progress in Aerospace Sciences,* Vol. 32, pp. 32–78.

Triantafyllidis, N., 1994–95, private communications.

Vogler, T. J., and Kyriakides, S., 1997, "Initiation and axial propagation of kink bands in fiber composites," *Acta Materialia,* Vol. 45, No. 6, pp. 2443–2454.

Waas, A. M., Babcock, C. D., and Knauss, W. G., 1990, "A Mechanical Model for Elastic Fiber Microbuckling," ASME JOURNAL OF APPLIED MECHANICS, Vol. 57, pp. 138–149.

APPENDIX

The fibers are assumed to be linearly elastic with modulus E_f while the nonlinear matrix is modeled as an elasto-plastic solid through the classical J_2 deformation and J_2 flow theories. The idealized composite element shown in Fig. 12 is again considered. The far-field compressive stress σ and the composite shear stresses τ are related through Eq. (3). We further assume the composite element to be under a state of plane stress and use the rule of mixtures to establish the properties of the composite. The axial stress in the fibers is

$$\sigma_f = E_f \epsilon. \tag{A1}$$

Matrix Modeled as a J_2-Deformation Theory Solid. For this constitutive model, the axial stress in the matrix is related to the axial strain by

Downloaded 04 May 2010 to 171.66.16.26. Redistribution subject to ASME license or copyright; see http://www.asme.org/terms/Terms_Use.cfm

$$\sigma_m = E_{ms}(\sigma_{em})\epsilon \tag{A2}$$

where E_{ms} is the matrix secant modulus which is a function of the equivalent stress

$$\sigma_{em} = (\sigma_m^2 + 3\tau^2)^{1/2}. \tag{A3}$$

Using the rule of mixtures, the axial stress in the composite can then be written as

$$\sigma = [E_f v_f + E_{ms}(1 - v_f)]\epsilon = \sigma_m\left[\frac{E_f}{E_{ms}(\sigma_{em})} v_f + (1 - v_f)\right]. \tag{A4}$$

The rule of mixtures is also used to evaluate the shear strain in the composite as follows:

$$\gamma = \frac{\tau}{\hat{G}_{12}} = \left\{\frac{v_f}{G_f} + \frac{(1 - v_f)}{E_m}\left[3\frac{E_m}{E_{ms}(\sigma_{em})} + (2\nu_m - 1)\right]\right\}\tau. \tag{A5}$$

Using (A.5), (3) is written as

$$\sigma = \frac{\hat{G}_{12}\gamma}{(\theta_o + \gamma)}. \tag{A6}$$

Given the nonlinear uniaxial stress-strain relationship of the matrix and the elastic fiber constants E_f and G_f, Eqs. (A.4), (A.5), and (A.6) are solved iteratively to obtain relationships between σ, ϵ and γ.

Matrix Modeled as a J_2-Flow Theory Solid. In this case the matrix incremental strain-stress relationships are as follows:

$$\begin{Bmatrix} d\epsilon_m \\ d\gamma \end{Bmatrix} = \begin{bmatrix} 1 + q\sigma_m & 3q\sigma_m\tau \\ 3q\sigma_m\tau & 2(1 + \nu_m) + 9q\tau^2 \end{bmatrix}\begin{Bmatrix} d\sigma_m \\ d\tau \end{Bmatrix},$$

$$q = \frac{1}{\sigma_{em}^2}\left(\frac{E_m}{E_{mt}(\sigma_{em})} - 1\right) \tag{A7}$$

where $E_{mt}(\sigma_{em})$ is the matrix tangent modulus which is a function of the equivalent stress (A3). If we identify the diagonal terms of the 2×2 matrix above as A and C and the off-diagonal term as B, then by applying the rules of mixtures incrementally the following relationships are derived:

$$d\sigma = E_f v_f d\epsilon + \frac{E_m(1 - v_f)}{AC - B^2}[Cd\epsilon - Bd\gamma], \tag{A8}$$

$$d\gamma = \frac{d\tau}{G_f} v_f + \frac{(1 - v_f)}{E_m}[Bd\sigma_m + Cd\tau], \tag{A9}$$

and

$$d\sigma = \frac{d\tau}{(\theta_o + \gamma)} - \frac{\tau}{(\theta_o + \gamma)^2}d\gamma. \tag{A10}$$

The nonlinear incremental Eqs. (A8) to (A10) are solved numerically to produce relationships between σ, ϵ, and γ.

Downloaded 04 May 2010 to 171.66.16.26. Redistribution subject to ASME license or copyright; see http://www.asme.org/terms/Terms_Use.cfm

A Thermoviscoelastic Dynamic Vibration Absorber

R. Fosdick

Y. Ketema

Department of Aerospace Engineering and Mechanics, University of Minnesota, Minneapolis, MN 55455

A dynamic vibration absorber with a viscoelastic element is studied. The viscoelastic element is modeled as a material with memory in which the internal dissipative force depends on current, as well as previous deformations. The viscoelastic behavior is governed by two parameters: the relaxation modulus G_0, and the relaxation time γ. We apply the principle of time-temperature superposition to affect a dependence of the relaxation time γ on temperature. This temperature dependence can be used to tune a vibration absorber so as to be effective at more than one excitation frequency.

1 Introduction

Dynamic vibration absorbers are important components in many mechanical devices where vibrations due to external excitation need to be suppressed. Examples of such systems include machines, heavy-duty vehicles, generators, and building structures. For a detailed account of such applications and further references, the reader is referred to Hunt (1979). Though most studies of dynamic vibration absorbers deal with linear vibrations, nonlinear dynamic vibration absorbers have recently received increased attention. Such studies include, for example, Semercigil et al. (1992), where an impact damper is considered. In this case, the impact damper consists of a small rigid mass in a container that is firmly attached to the primary oscillator, the vibrations of which are to be controlled. The mass may collide with the walls of its container during the motion of the system, which accounts for the nonlinearity of this vibration absorber. Another study of a nonlinear dynamic vibration absorber is presented in Natsiavas (1992), where the dynamics of a vibration absorber with a Duffing type of nonlinearity is investigated.

A dynamic vibration absorber is itself an oscillator that is attached to a mechanical system, the vibrations of which are to be suppressed. The mechanical system without the absorber is called the main system, and in this paper, we study a dynamic vibration absorber which consists of a mass which is attached to the main system through a viscoelastic material, see Fig. 1. This will be referred to as a viscoelastic dynamic vibration absorber.

Generally, a dynamic vibration absorber is effective in suppressing vibrations for a specific frequency[1]—its operational frequency. The operational frequency of a dynamic vibration absorber is normally chosen to be equal to the resonance frequency of the main system, since it is at that frequency that the vibrations of the main system are the largest.

For a viscoelastic dynamic vibration absorber, the temperature dependence of the viscoelastic material properties induces a temperature dependence on the optimal operational frequency of the absorber. Consequently, the dynamic vibration absorber is most effective for a limited temperature range of the viscoelastic material, especially when the main system has a fixed resonance frequency. In order to determine the "best" operating conditions, it is important to study the variation of operational frequency with temperature, and thereby characterize the range of admissible temperature variations for the viscoelastic material.

Further, in many practical applications, the resonance frequency of the main system itself may change due to variations in mass, for example. This is the case for heavy-duty trucks and railway wagons, where the resonance frequency for a mode of vibration may change with the amount of load (see, e.g., Settles, 1994). In addition, several modes of vibration with different frequencies may need to be considered (see, e.g., Inoh and Isaka, 1973). In these cases, dynamic vibration absorbers whose operational frequency may be controlled could be of importance. An understanding of how the characteristics of a viscoelastic dynamic vibration absorber depend upon the operating temperature is potentially applicable to the design of such absorbers.

The main purpose of this paper is to study a viscoelastic dynamic vibration absorber whose operational frequency varies with temperature. The viscoelastic material is modeled as a material with fading memory characterized by two material constants: the relaxation time, and the relaxation modulus. We use the principle of time-temperature superposition so that the temperature dependence on the material properties is reduced solely to a dependence of the relaxation time on the temperature.

A similar study of the effect of temperature variations on the characteristics of a dynamic vibration absorber may be found in Satoh (1993). There, three different models for viscoelastic behavior, namely, the Voigt model, the Maxwell model, and the three-element model were used for the viscoelastic material. For each model, the complex modulus was implemented to study the response of the main system for various excitation frequencies. The temperature dependence of the complex modulus is accounted for through the use of the principle of time-temperature superposition.

It can be shown that the three-element model used in Satoh (1993) is equivalent to the linearized material-with-memory model used in the present paper (Fosdick et al., 1997). Nevertheless, when it comes to modeling the temperature dependence of the properties of the viscoelastic material, the material-with-memory model has a clear advantage: as mentioned above, only one material parameter, the relaxation time, depends on temperature. This simplifies the theoretical analysis of the vibration absorber, and may also facilitate experimental investigations. Using this approach, we show in the last section of this paper, how a temperature-dependent viscoelastic dynamic vibration absorber that is effective for two different frequencies may be constructed.

Contributed by the Applied Mechanics Division of THE AMERICAN SOCIETY OF MECHANICAL ENGINEERS for publication in the ASME JOURNAL OF APPLIED MECHANICS.

Discussion on this paper should be addressed to the Technical Editor, Professor Lewis T. Wheeler, Department of Mechanical Engineering, University of Houston, Houston, TX 77204-4792, and will be accepted until four months after final publication of the paper itself in the ASME JOURNAL OF APPLIED MECHANICS.

Manuscript received by the ASME Applied Mechanics Division, Apr. 16, 1997; final revision, July 1, 1997. Associate Technical Editor: R. Abeyaratne.

[1] For this reason, dynamic vibration absorbers are also referred to as tuned vibration absorbers.

 Copyright © 1998 by ASME

Downloaded 04 May 2010 to 171.66.16.26. Redistribution subject to ASME license or copyright; see http://www.asme.org/terms/Terms_Use.cfm

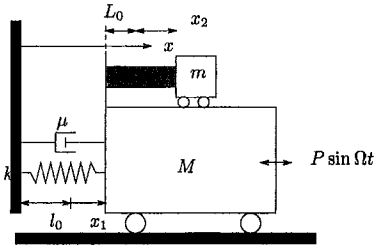

Fig. 1 A dynamic vibration absorber with viscoelastic material

The effect of varying the relaxation time on the dynamic properties of a viscoelastic material has been noted previously by Fosdick et al. (1997). Because, here, only the relaxation time is temperature dependent, these earlier results are directly applicable to the present study.

2 Constitutive Assumptions and Dynamical Equations

Consider the assembly shown in Fig. 1 that consists of an oscillator of mass M, attached to a spring and dashpot, and a dynamic vibration absorber consisting of a mass m attached to the main system through a viscoelastic bar. The stiffness of the spring is denoted by k, and the damping constant of the dashpot is μ. We let $x = \chi(X, t)$ denote the position of a particle X of the viscoelastic bar at time t, with $X = \chi(X, 0)$, both measured relative to the fixed vertical wall in Fig. 1. If we let l_0 and L_0 denote the referential undistorted lengths of the spring and the viscoelastic bar, respectively, then we see that $x_1(t) \equiv \chi(l_0, t) - l_0$ measures the displacement of the spring, and $x_2(t) \equiv \chi(l_0 + L_0, t) - (\chi(l_0, t) + L_0)$ is the intrinsic displacement of the viscoelastic bar, both relative to their undistorted states at $t = 0$, when $x_1(0) = x_2(0) = 0$. The deformation gradient history of the viscoelastic bar is given by $F(X, t - s) \equiv \partial\chi(X, t - s)/\partial X$, $\forall s > 0$. Then, the relative strain history is characterized by

$$J_t(X, t - s) = \frac{[F(X, t - s)]^2}{[F(X, t)]^2} - 1, \quad \forall s \geq 0, \tag{1}$$

and we assume that the constitutive response function for determining the present value of the axial force $f(X, t)$ on the particle X in the viscoelastic bar is of the finite linear form

$$f(X, t) = f^e(F(X, t)) + \int_0^\infty \dot{G}(s) J_t(X, t - s) ds, \tag{2}$$

where $f^e(\cdot)$ denotes an elastic response function and $G(\cdot)$ is the viscoelastic relaxation function for the material.

The Piola-Kirchoff stress in the bar is given by $f(X, t)/A_0$, where A_0 is the referential cross-sectional area of the bar (assumed constant), and the balance of linear momentum requires

$$\frac{1}{A_0} \frac{\partial f(X, t)}{\partial X} = \rho_0 \ddot{\chi}(X, t), \tag{3}$$

where ρ_0 is the constant reference mass density. In this work, we shall neglect the inertia of the viscoelastic bar, so that $f(X, t)$ is independent of X from (3), and assume as an approximation that the deformation of the bar is homogeneous so that we may write

$$x = \chi(X, t) = l_0 + x_1(t) + (X - l_0)x(t), \quad x(0) = 1. \tag{4}$$

Clearly,

$$\begin{aligned} x_2(t) &= \chi(l_0 + L_0, t) - (\chi(l_0, t) + L_0) \\ &= L_0(x(t) - 1). \end{aligned} \tag{5}$$

Then, the deformation gradient $F(X, t) = \partial\chi(X, t)/\partial X = x(t)$ is, in fact, the homogeneous stretch of material filaments so that

$$f^e(F(X, t)) = f^e(x(t)),$$

$$J_t(X, t - s) = \frac{x^2(t - s) - x^2(t)}{x^2(t)}, \tag{6}$$

and from (2) and (6) we have $f(X, t) = f(t)$, where

$$f(t) = f^e(x(t)) + \int_0^\infty \dot{G}(s) \frac{x^2(t - s) - x^2(t)}{x^2(t)} ds. \tag{7}$$

Now, the dynamical equations for the masses M and m are of the form

$$\begin{aligned} M\ddot{\chi}(l_0, t) &= M\ddot{x}_1(t) \\ &= f(t) + P \sin \Omega t - kx_1(t) - \mu\dot{x}_1(t), \end{aligned} \tag{8}$$

and

$$m\ddot{\chi}(l_0 + L_0, t) = m(\ddot{x}_1(t) + \ddot{x}_2(t)) = -f(t), \tag{9}$$

respectively.

3 Time-Temperature Superposition: Reduced Dynamical Equations

Suppose that the relaxation function corresponding to a reference temperature T_0 is given by

$$G(s) = G_0 e^{-(s/\gamma_0)} \tag{10}$$

for $s \geq 0$, where $G_0 > 0$ is the relaxation modulus and $\gamma_0 > 0$ is the relaxation time at this temperature[2]. Then, according to a common application of the time-temperature superposition principle (Christensen, 1982), the relaxation function $G(s; T)$ at temperature T is given by

$$G(s, T) = G\left(s \frac{\gamma_0}{\gamma(T)}\right) = G_0 e^{-(s/\gamma(T))}, \tag{11}$$

where $\gamma(T_0) = \gamma_0$ and $\gamma(T) > 0$ decreases rapidly with increasing temperature, especially for a polymer near its glass transition temperature. This hypothesis has experimental support. In particular, it idealizes the observation that the relaxation modulus, itself, is not heavily sensitive to temperature change and it captures the observation that at elevated temperatures the relaxation time is highly sensitive to such changes. The effect is that at elevated temperatures the relaxation of disturbances in the material takes place on a much faster time scale; $\gamma(T)$ is the temperature-dependent relaxation time.

For polymers, a widely used expression for $\gamma(T)$ is given by the Williams-Landal-Ferry formula (see, e.g., Ferry (1970) and Moore (1993))

$$\gamma(T) = \gamma_0 e^{\psi(T)}, \quad \psi(T) = \frac{c_1(T - T_0)}{c_2 + T - T_0}, \tag{12}$$

where the material constants c_1 and c_2 are positive and dependent on the reference temperature T_0. For rubbers, this expression is fairly well approximated by the form

$$\psi(T) = \frac{-8.86(T - T_s)}{101.6 + T - T_s}, \tag{13}$$

where T_s is a material-dependent reference temperature that normally lies about 50 K above the glass transition temperature, and thus lies roughly in the range of 200 K–300 K. Figure 2 shows a plot of (13) from which we see that $\psi(T)$ decreases

[2] This is a simplifying assumption for the behavior of the viscoelastic material. A more general model would involve a spectrum of relaxation times.

Downloaded 04 May 2010 to 171.66.16.26. Redistribution subject to ASME license or copyright; see http://www.asme.org/terms/Terms_Use.cfm

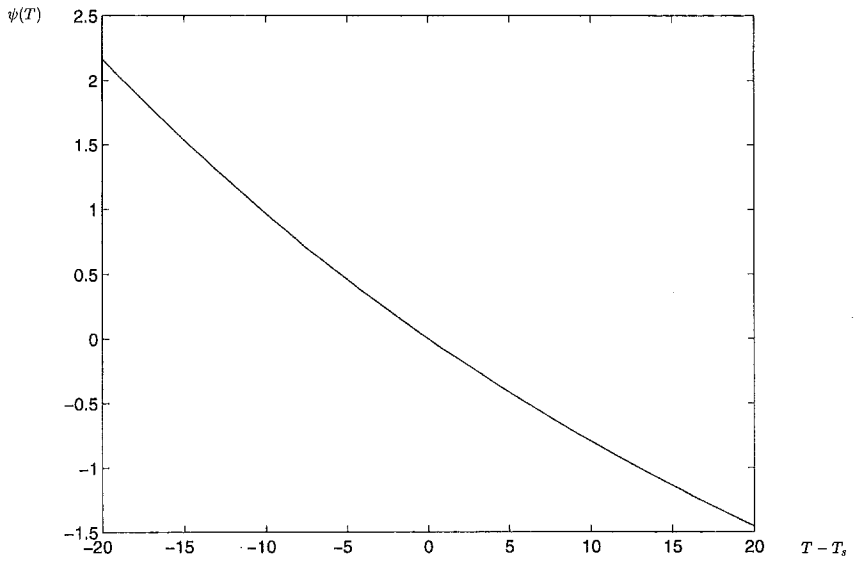

Fig. 2 The function $\psi(T)$ of (13) versus $T - T_s$

monotonically with increasing temperature. The large effect of temperature on the temperature-dependent relaxation time constant $\gamma(T)$ of (12) and (13) is shown in Fig. 3. Clearly, in order to double the value of $\gamma(T)$ with respect to its value at $T = T_s$ a decrease of approximately 7 K is all that is necessary; to cut by one-half the value of $\gamma(T)$ would take only an increase of 10 K.

If we now substitute the relaxation function (11) into (7) and assume that the temperature T is constant, we see that the force throughout the viscoelastic bar is given by

$$f(t) = f^e(x(t)) - \frac{G_0}{\gamma(T)} \int_0^\infty e^{-(s/\gamma(T))} \frac{x^2(t-s) - x^2(t)}{x^2(t)}\, ds, \quad (14)$$

and by introducing the auxiliary function $\zeta(t)$ through

$$\zeta(t) = \int_0^\infty e^{-(s/\gamma(T))} \frac{x^2(t-s) - x^2(t)}{x^2(t)}\, ds, \quad (15)$$

we may rewrite the dynamical equations equivalently as

$$M\ddot{x}_1(t) = -kx_1(t) - \mu\dot{x}_1(t) + P \sin \Omega t + f^e(x(t)) - \frac{G_0}{\gamma(T)}\zeta(t),$$

$$m(\ddot{x}_1(t) + \ddot{x}_2(t)) = -f^e(x(t)) + \frac{G_0}{\gamma(T)}\zeta(t),$$

$$\dot{\zeta}(t) = -\left[\frac{1}{\gamma(T)} + \frac{2\dot{x}(t)}{x(t)}\right]\zeta(t) - \gamma(T)\frac{2\dot{x}(t)}{x(t)}. \quad (16)$$

Due to (5), we see that

$$x(t) = \frac{x_2(t)}{L_0} + 1, \quad \dot{x}(t) = \frac{\dot{x}_2(t)}{L_0}. \quad (17)$$

The dynamic vibration absorber modeled by the system (16) is undistorted at $t = 0$ when $x(0) = 1$, and $x_1(0) = x_2(0) = x_3(0) = 0$. Defining the referential elastic modulus

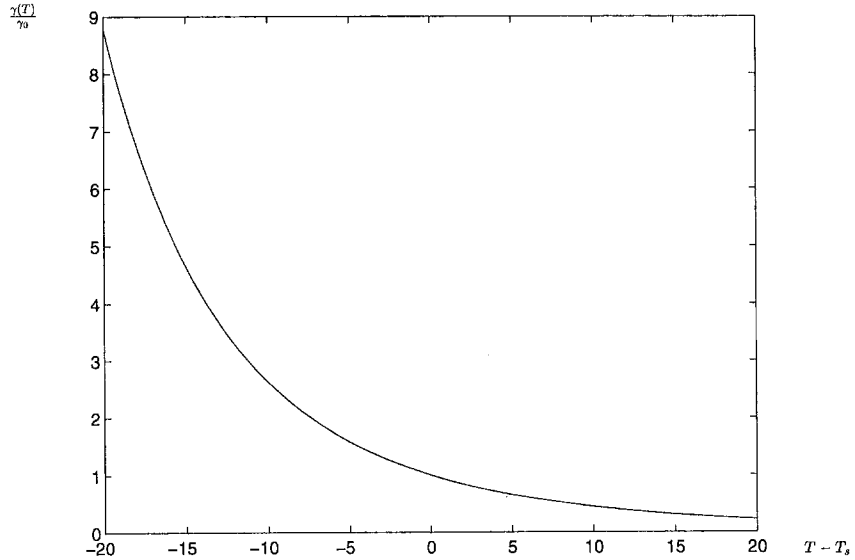

Fig. 3 The function $\gamma(T)/\gamma_0 = e^{\psi(T)}$ of (12)$_1$, (13) versus $T - T_s$

Downloaded 04 May 2010 to 171.66.16.26. Redistribution subject to ASME license or copyright; see http://www.asme.org/terms/Terms_Use.cfm

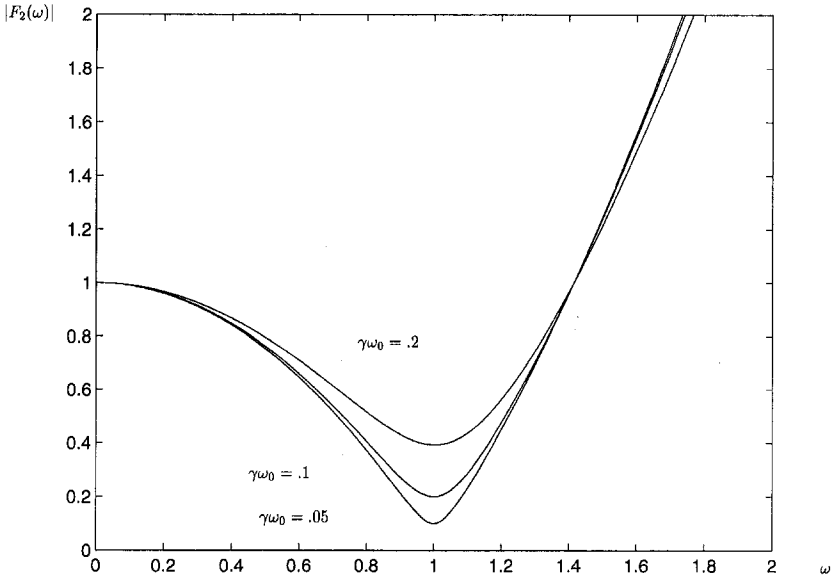

Fig. 4 $|F_2(\omega)|$ **versus** ω **for various values of** $\gamma\omega_0 \ll 1$ **and** $\Phi_0 = 0.1$, $\alpha = 10$, $\kappa = 0.1$

$$k_e \equiv \frac{df^e}{dx}(1) > 0, \tag{18}$$

and linearizing the system (16) about the undistorted state, we readily find

$$M\ddot{x}_1(t) = -kx_1(t) - \mu\dot{x}_1(t) + \frac{k_e}{L_0}x_2(t) + P\sin\Omega t - \frac{G_0}{\gamma(T)}\zeta(t),$$

$$m(\ddot{x}_1(t) + \ddot{x}_2(t)) = -\frac{k_e}{L_0}x_2(t) + \frac{G_0}{\gamma(T)}\zeta(t),$$

$$\dot{\zeta}(t) = -\frac{1}{\gamma(T)}\zeta(t) - 2\frac{\gamma(T)}{L_0}\dot{x}_2(t). \tag{19}$$

4 Dynamic Characteristics of the Absorber

To simplify the study of the dynamic characteristics of the vibration absorber, it is convenient to nondimensionalize the dynamical Eqs. (19). Thus, we introduce a dimensionless time τ through

$$\tau = \omega_0 t \tag{20}$$

where $\omega_0 = \sqrt{k/M}$, i.e., the natural frequency of the undamped main system which consists of the mass M and the spring. Also, we introduce the following dimensionless parameters:

$$\delta = \frac{\mu\omega_0}{k}, \quad \kappa = \frac{k_e}{kL_0}, \quad \Phi_0 = \frac{G_0}{kL_0},$$

$$\alpha = \frac{M}{m}, \quad p = \frac{P}{kL_0}, \quad \omega = \frac{\Omega}{\omega_0}. \tag{21}$$

Then, by normalizing according to

$$\tilde{x}_1(\tau) = \frac{1}{L_0}x_1\left(\frac{\tau}{\omega_0}\right),$$

$$\tilde{x}_2(\tau) = \frac{1}{L_0}x_2\left(\frac{\tau}{\omega_0}\right), \quad \tilde{\zeta}(\tau) = \frac{1}{\gamma(T)}\zeta\left(\frac{\tau}{\omega_0}\right), \tag{22}$$

it is straightforward to transform (19) into the form

$$\frac{d^2\tilde{x}_1(\tau)}{d\tau^2} = -\tilde{x}_1(\tau) - \delta\frac{d\tilde{x}_1(\tau)}{d\tau} + \kappa(\tilde{y}(\tau) - \tilde{x}_1(\tau)) - \Phi_0\tilde{\zeta}(\tau) + p\sin\omega\tau,$$

$$\frac{d^2\tilde{y}(\tau)}{d\tau^2} = -\alpha\kappa(\tilde{y}(\tau) - \tilde{x}_1(\tau)) + \alpha\Phi_0\tilde{\zeta}(\tau),$$

$$\frac{d\tilde{\zeta}(\tau)}{d\tau} = -\frac{1}{\gamma(T)\omega_0}\tilde{\zeta}(\tau) - 2\left(\frac{d\tilde{y}(\tau)}{d\tau} - \frac{d\tilde{x}_1(\tau)}{d\tau}\right), \tag{23}$$

where we have introduced

$$\tilde{y}(\tau) \equiv \tilde{x}_1(\tau) + \tilde{x}_2(\tau). \tag{24}$$

In what follows we will replace $\gamma(T)$ by γ and understand that the value of γ may be changed through a change in the temperature T in accordance with (12), (13). Due to the scaling of the dynamical equations according to (21), the resonance frequency of the main system in (23) is $\omega = 1$. Now, if we denote the transfer functions between the state variables $\tilde{x}_1(\tau)$, $\tilde{y}(\tau)$, and $\tilde{\zeta}(\tau)$ and the input $p\sin\omega\tau$ by $\bar{x}_1(s)$, $\bar{y}(s)$, and $\bar{\zeta}(s)$, respectively, it follows that

$$\bar{x}_1(s) = \frac{H_2(s)}{(s^2 + \delta\omega_0 s + 1)H_2(s) + s^2\left(\kappa - \dfrac{\Phi_0\gamma\omega_0 2s}{1 + s\gamma\omega_0}\right)}, \tag{25}$$

$$\bar{y}(s) = \frac{H_1(s)}{H_2(s)}\bar{x}_1(s), \tag{26}$$

$$\bar{\zeta}(s) = -\frac{\gamma\omega_0 2s}{1 + s\gamma\omega_0}\frac{s^2}{H_2(s)}\bar{x}_1(s), \tag{27}$$

where

$$H_1(s) = \alpha\left(\kappa + \Phi_0\frac{2s\gamma\omega_0}{1 + s\gamma\omega_0}\right), \tag{28}$$

$$H_2(s) = s^2 + H_1(s). \tag{29}$$

Then, we have

Downloaded 04 May 2010 to 171.66.16.26. Redistribution subject to ASME license or copyright; see http://www.asme.org/terms/Terms_Use.cfm

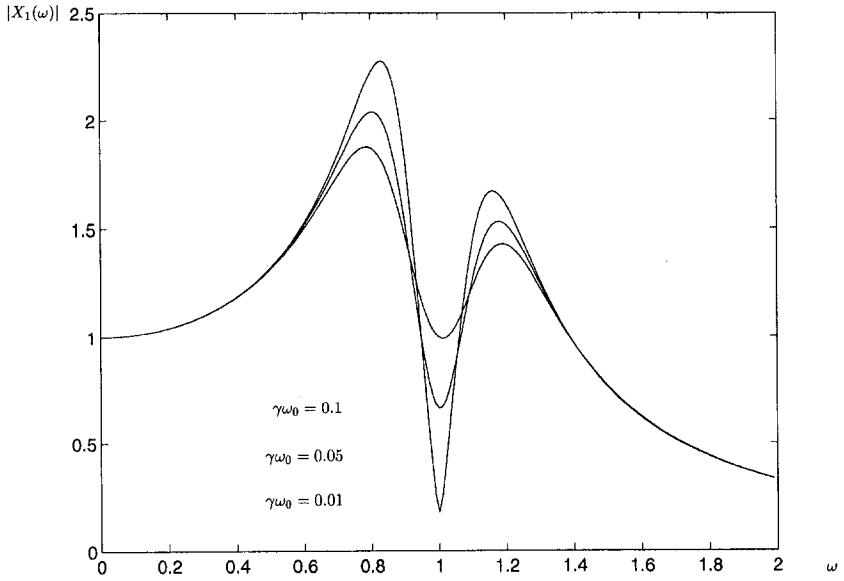

Fig. 5 $|X_1(\omega)|$ **versus** ω **for various values of** $\gamma\omega_0$ **and** $\Phi_0 = 0.1$, $\alpha = 10$, $\kappa = 0.1$, $\delta = 0$

$$\tilde{x}_1(\tau) = X_1(\omega)p \sin \omega\tau,$$
$$\tilde{y}(\tau) = Y(\omega)p \sin \omega\tau,$$
$$\tilde{\zeta}(\tau) = Z(\omega)p \sin \omega\tau, \tag{30}$$

where $X_1(\omega)$, $Y(\omega)$, and $Z(\omega)$ are the sinusoidal transfer functions for $\tilde{x}_1(\tau)$, $\tilde{y}(\tau)$, and $\tilde{\zeta}(\tau)$, respectively, and are given by

$$X_1(\omega) = \bar{x}_1(i\omega),$$
$$Y(\omega) = \bar{y}(i\omega),$$
$$Z(\omega) = \bar{\zeta}(i\omega). \tag{31}$$

Also, we note that (30) can be written in the form

$$\tilde{x}_1(\tau) = |X_1(\omega)|p \sin(\omega\tau + \phi_1(\omega)),$$
$$\tilde{y}(\tau) = |Y(\omega)|p \sin(\omega\tau + \phi_2(\omega)),$$
$$\tilde{\zeta}(\tau) = |Z(\omega)|p \sin(\omega\tau + \phi_3(\omega)), \tag{32}$$

where

$$\phi_1(\omega) = \arctan(\mathrm{Im}(X_1(\omega))/\mathrm{Re}(X_1(\omega))),$$
$$\phi_2(\omega) = \arctan(\mathrm{Im}(Y(\omega))/\mathrm{Re}(Y(\omega))),$$
$$\phi_3(\omega) = \arctan(\mathrm{Im}(Z(\omega))/\mathrm{Re}(Z(\omega))). \tag{33}$$

Clearly, the sinusoidal transfer function $X_1(\omega)$ may be written as

$$X_1(\omega) = \frac{F_2(\omega)}{(-\omega^2 + i\delta\omega_0 + 1)F_2(\omega) - \omega^2\left(\kappa - \dfrac{\Phi_0\gamma\omega_0 2i\omega}{1 + i\omega\gamma\omega_0}\right)}, \tag{34}$$

where

$$F_1(\omega) = \alpha\left(\kappa + \Phi_0 \frac{2i\omega\gamma\omega_0}{1 + i\omega\gamma\omega_0}\right), \tag{35}$$

$$F_2(\omega) = -\omega^2 + F_1(\omega). \tag{36}$$

For $Y(\omega)$ we have

$$Y(\omega) = \frac{F_1(\omega)}{F_2(\omega)} X_1(\omega), \tag{37}$$

and similarly, $Z(\omega)$ is given by

$$Z(\omega) = \frac{-2i\gamma\omega_0\omega^3}{(1 + i\omega\gamma\omega_0)F_2(\omega)} X_1(\omega). \tag{38}$$

4.1 Obtaining Optimal Vibration Suppression. In determining the parameter values for optimal vibration suppression by the viscoelastic damper, we note from (32) and (34) that the amplitude of $\tilde{x}_1(\tau)$ is minimized by choosing $F_2(\omega) = 0$. It is of interest to note that, for the system that consists of the absorber alone, if one had a controlled external sinusoidal excitation in place of $\tilde{x}_1(\tau)$, for example, $\tilde{x}_1(\tau) = C \sin \omega\tau$, resonance would occur for $F_2(\omega) = 0$. This follows from (37) by replacing $F_1(\omega)X_1(\omega)$ by the constant C.

From (35) and (36) it is clear that $F_2(\omega) = 0$ is possible only if $F_1(\omega)$ is real, i.e., if either $\gamma\omega_0 = 0$ or in the limit $\gamma\omega_0 \to \infty$. Since γ and ω_0 are both positive and bounded, these conditions can only be satisfied approximately and in what follows, we shall study the cases $\gamma\omega_0 \ll 1$ and $\gamma\omega_0 \gg 1$ separately.

4.1.1 The case $\gamma\omega_0 \ll 1$. For given ω_0, the case $\gamma\omega_0 \ll 1$ corresponds to high temperature according to (12) and (13), and in this case (35) and (36) yield

$$|F_2(\omega)| \approx \sqrt{(\alpha\kappa - \omega^2)^2 + 4\omega^2\gamma^2\omega_0^2}. \tag{39}$$

Thus, $|F_2(\omega)|$ is minimized at approximately

$$\omega^* = \sqrt{\alpha\kappa - 2\gamma^2\omega_0^2}, \tag{40}$$

and its minimum value is

$$F_2^* = 2\sqrt{\gamma^2\omega_0^2(\alpha\kappa - \gamma^2\omega_0^2)}, \tag{41}$$

which satisfies $\lim_{\gamma\omega_0 \to 0} F_2^* = 0$.

Figure 4 shows the behavior of $|F_2(\omega)|$ versus ω for various values of $\gamma\omega_0 \ll 1$, and for $\Phi_0 = 0.1$, $\alpha = 10$, and $\kappa = 0.1$. The frequency at which $|F_2(\omega)| \to 0$ is $\omega = 1$ which is in agreement with (39).

In choosing parameter values for the absorber to obtain optimal vibration absorption at the resonance frequency of the main system, i.e., $\omega = 1$, we choose $\omega^* \approx 1$. This may be obtained, for example, if one takes $\alpha = 10$ and $\kappa = 0.1$ and $\gamma\omega_0$ small. In Fig. 5, we show the magnitude of the sinusoidal transfer

Downloaded 04 May 2010 to 171.66.16.26. Redistribution subject to ASME license or copyright; see http://www.asme.org/terms/Terms_Use.cfm

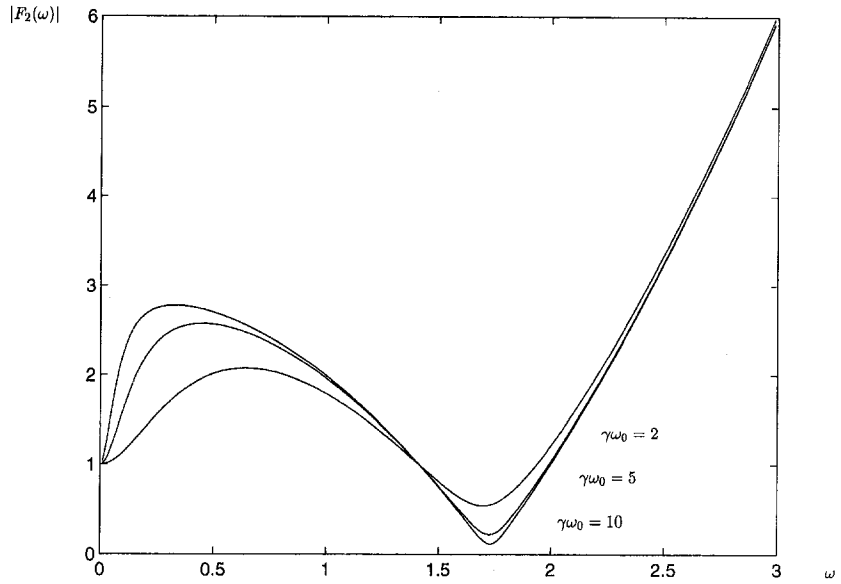

Fig. 6 $|F_2(\omega)|$ versus ω for various values of $\gamma\omega_0$ and $\Phi_0 = 0.1$, $\alpha = 10$, $\kappa = 0.1$

function $|X_1(\omega)|$ as a function of ω for various values of $\gamma\omega_0$ under the assumption that $\gamma\omega_0 \ll 1$. (Note, from (32), that the steady-state amplitude of the main system is amp $\tilde{x}_1(\tau) = |X_1(\omega)|p$.) In this figure and throughout the rest of Section 4.1 we use $\delta = 0$. The effect of nonzero values of δ will be discussed in Section 4.2.

The resonance frequency of the scaled main system is $\omega = 1$, and the idea is to choose the operational frequency of the absorber appropriately. Note that as $\gamma\omega_0$ is decreased, more vibration suppression is obtained near $\omega = 1$ since the error made in the approximation (39) decreases with decreasing $\gamma\omega_0$.

4.1.2 The case $\gamma\omega_0 \gg 1$. The case $\gamma\omega_0 \gg 1$ corresponds to low temperature according to (12) and (13), and in this case (35) and (36) yield

$$F_2(\omega) \approx -\omega^2 + \alpha(\kappa + 2\Phi_0). \tag{42}$$

Thus, in the limit $\gamma\omega_0 \to \infty$, $F_2(\omega)$ vanishes at $\omega = \omega^{**}$, where

$$\omega^{**} = \sqrt{\alpha(\kappa + 2\Phi_0)}. \tag{43}$$

Figure 6 shows the behavior of $|F_2(\omega)|$ versus ω for various large values of $\gamma\omega_0 \gg 1$, and for $\Phi_0 = 0.1$, $\alpha = 10$, and $\kappa = 0.1$. The frequency at which $|F_2(\omega)| \to 0$ is $\omega = \sqrt{3}$, which is in agreement with (42).

In choosing parameter values for the absorber to obtain optimal vibration absorption at the resonance frequency of the main system, i.e., $\omega = 1$, we need to choose $\omega^{**} \approx 1$. This may be obtained if one chooses, for example, $\alpha = 10$, $\kappa = .01$, and $\Phi_0 = 0.045$. Figure 7 shows the magnitude of the sinusoidal transfer function $|X_1(\omega)|$ versus ω for various values of $\gamma\omega_0 \gg 1$. In this case, it is seen that the vibration suppression at $\omega = 1$ becomes better with increasing $\gamma\omega_0$ since here the error in the approximation made in (42) decreases with increasing $\gamma\omega_0$.

It is seen in Fig. 7 that the maximum values of the $|X_1(\omega)|$ decrease as $\gamma\omega_0$ increases and there is more vibration suppression near the resonance frequency. This, in turn, leads to a

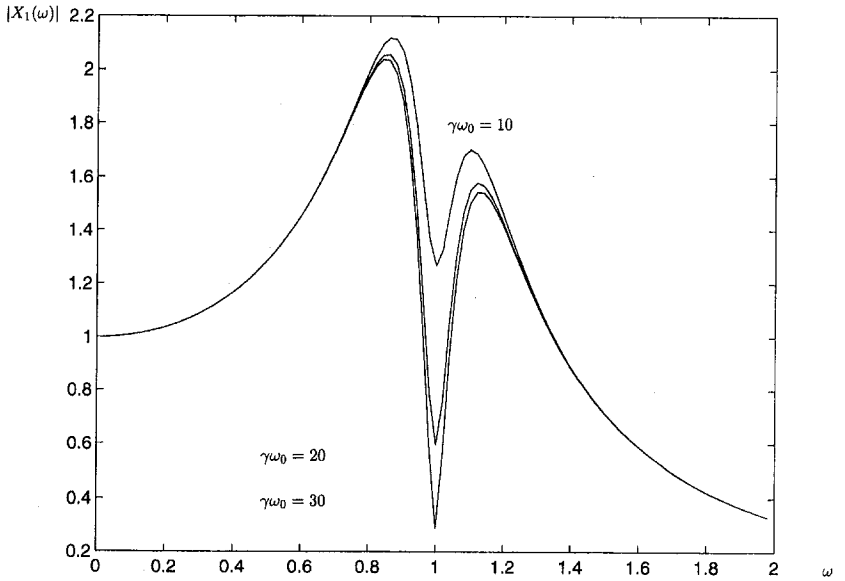

Fig. 7 $|X_1(\omega)|$ versus ω for various values of $\gamma\omega_0$ and $\Phi_0 = .045$, $\alpha = 10$, $\kappa = .01$, $\delta = 0$

Downloaded 04 May 2010 to 171.66.16.26. Redistribution subject to ASME license or copyright; see http://www.asme.org/terms/Terms_Use.cfm

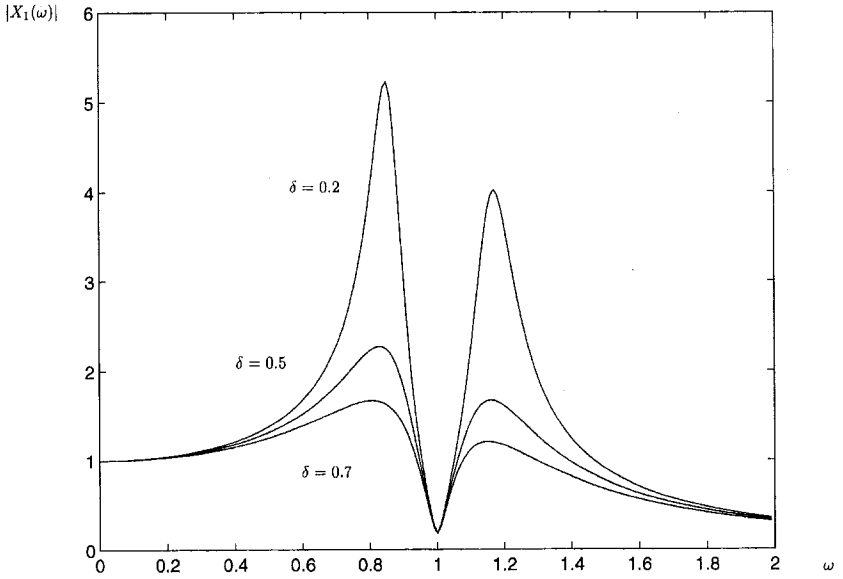

Fig. 8 $|X_1(\omega)|$ **versus** ω **for various values of** δ **and** $\Phi_0 = 0.1$, $\alpha = 10$, $\kappa = 0.1$, $\gamma\omega_0 = 0.01$

widening suppression band, i.e., a larger range of ω for which $|X_1(\omega)| < 1$.

The parameters γ and ω_0 appear together as a product in the above discussion, and this implies that a change in ω_0 may be compensated for by a corresponding change in γ, which may be affected by a change of temperature. In this way, the product $\gamma\omega_0$ may be held constant, which could be of interest in applications where the natural frequency ω_0 may be changed due to a change in mass, M.

4.2 The Effect of External Damping. In the example above, it was assumed that the damping coefficient $\delta = 0$. In Fig. 8, we show $|X_1(\omega)|$ versus ω for $\gamma\omega_0 = 0.01$, $\Phi_0 = 0.1$, $\kappa = 0.1$, and $\alpha = 10$, and for various values of δ. From Fig. 8, we see that for fixed $\gamma\omega_0$, the damping coefficient δ does not affect the maximum vibration absorption but it does influence the suppression bandwidth; as δ increases, the band width increases.

The effect of the damping coefficient on the vibration absorption characteristics of the dynamic vibration absorber for the case $\gamma\omega_0 \gg 1$ is shown in Fig. 9. Again, it is seen that the damping coefficient does not affect the maximum vibration absorption, but the suppression band widens as δ is increased.

5 A Dual-Frequency Vibration Absorber

Suppose the mass of the main system in (19) is changed from M to qM where $q < 1$. Then, the natural frequency $\omega_0 = \sqrt{k/M}$ for the mass M has the form

$$\omega_{0q} = \sqrt{\frac{k}{qM}} \tag{44}$$

for the mass qM. While the parameters δ, Φ_0, κ, and p defined in (21) are not effected by a change of M, α is, and must be replaced by $q\alpha$.

Let us now assume that for the parameters as introduced in (21) there is vibration suppression at $\omega = 1$ with $\gamma\omega_0 \ll 1$. Then, the operational frequency of the vibration absorber is $\omega^* = \sqrt{\alpha\kappa - 2\gamma^2\omega_0^2} \approx 1$, according to (40). When M changes to

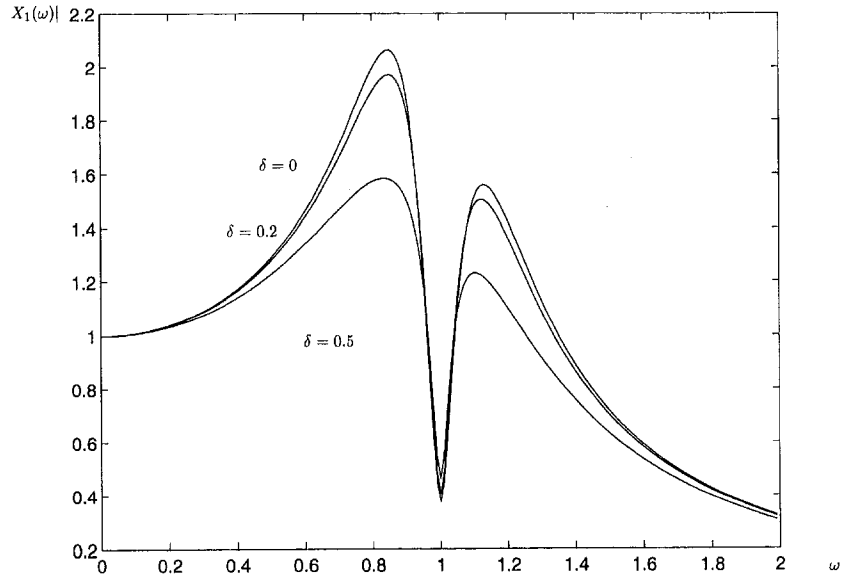

Fig. 9 $|X_1(\omega)|$ **versus** ω **for various values of** δ **and** $\Phi_0 = 0.045$, $\alpha = 10$, $\kappa = 0.01$, $\gamma\omega_0 = 30$

Downloaded 04 May 2010 to 171.66.16.26. Redistribution subject to ASME license or copyright; see http://www.asme.org/terms/Terms_Use.cfm

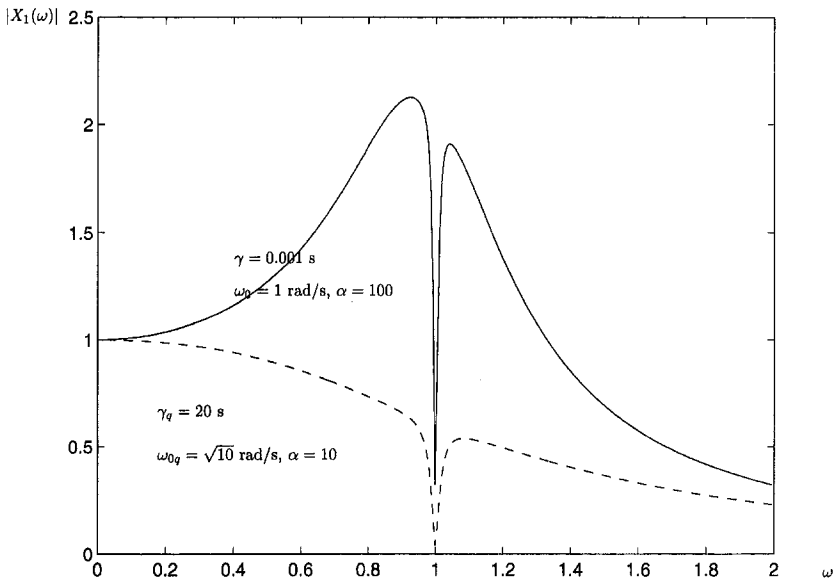

Fig. 10 $|X_1(\omega)|$ versus ω with the dual-frequency dynamic vibration absorber for the case $\gamma\omega_0 \ll 1$, (solid curve), and the case $\gamma_q\omega_{0q} \gg 1$, ($q = 0.1$), (dashed curve); $\Phi_0 = .045$, $\kappa = .01$, $\delta = 0.5$

qM, the goal is to increase γ to, say, γ_q such that $\gamma_q\omega_{0q} \gg 1$, by sufficiently cooling the viscoelastic material. In order to ensure vibration suppression at the new resonance frequency of the main system, which, due to the scaling of the equations, will again be at $\omega = 1$, we obtain from (43)

$$\omega_q^{**} = \sqrt{q\alpha(\kappa + 2\Phi_0)} \approx 1. \tag{45}$$

Thus, a necessary condition for vibration suppression for both the mass M as well as the mass qM is

$$\sqrt{q\alpha(\kappa + 2\Phi_0)} \approx \sqrt{\alpha\kappa - 2\gamma^2\omega_0^2} \approx 1, \tag{46}$$

or, using $\gamma\omega_0 \ll 1$,

$$\sqrt{q\alpha(\kappa + 2\Phi_0)} \approx \sqrt{\alpha\kappa} \approx 1. \tag{47}$$

Using (21) in (47), we find that when the mass of the main oscillator is changed from M to qM, the elastic modulus of the viscoelastic material k_e and the relaxation modulus G_0 must satisfy the relation

$$k_e = 2G_0 \frac{q}{1 - q}, \tag{48}$$

in order for the dual-frequency vibration absorber to be effective. Figure 10 shows an example of dual-frequency vibration absorption obtained according to the discussion above. In this particular example the values $\gamma = 0.001$ s and $\gamma_q = 20$ s are used. The choice of $\delta = 0.5$ in this example only affects the suppression band as explained in Section 4.2.

To get a rough estimate of the temperature changes needed for the dual-frequency vibration absorber, suppose we have a material for which $\gamma = 20$ s at 298 K and that $T_s = 360$ K. Then, (12) gives $\gamma_0 = 1.89 \times 10^{-5}$ s and it follows that $\gamma = .001$ s at approximately $T = 328.5$ K, i.e., for an increase in temperature of 30.5 K.

Acknowledgment

The National Science Foundation Grant DMS 9531925 is gratefully acknowledged for its partial support of this work.

References

Christensen, R. M., 1982, *Theory of Viscoelasticity,* 2nd Ed. Academic Press, New York.

Ferry, J. D., 1970, *Viscoelastic Properties of Polymers,* 2nd Ed., John Wiley and Sons, New York.

Fosdick, R. L., Ketema, Y., and Yu, J. H., 1997, "Vibration Damping through the Use of Materials with Memory," *International Journal of Solids and Structures,* Vol. 35, No. 5–6, pp. 403–420.

Hunt, J. B., 1979, *Dynamic Vibration Absorbers,* Mechanical Engineering Publications, London.

Inoh, T., and Isaka, M., 1973, "Tuning techniques for controlling heavy-duty truck shake-vertical, torsional, and lateral," SAE preprint paper No. 730650 for a meeting on June 18–22.

Moore, D. F., 1993, *Viscoelastic Machine Elements,* Butterworth-Heineman, Oxford, UK.

Natsiavas, S., 1992, "Steady State Oscillations and Stability of Nonlinear Dynamic Vibration Absorbers," *Journal of Sound and Vibration,* Vol. 156, No. 2, pp. 227–245.

Satoh, Y., 1993, "Influence of Temperature Dependence of the Dynamic Absorber Elements on the Vibration Reduction Characteristics," *Nippon Kikai Gakkai Ronbunshu, C Hen.,* Vol. 59, pp. 2968–2974.

Settles, J. C., 1954, "Application of dynamic vibration absorber to vehicles," *Proceedings of the Second United States National Congress of Applied Mechanics,* pp. 111–119.

Semercigil, S. E., Lammers, D., and Ying, Z., 1992, "A New Tuned Vibration Absorber for Wide Band Excitations," *Journal of Sound and Vibration,* Vol. 156, No. 3, pp. 445–459.

Downloaded 04 May 2010 to 171.66.16.26. Redistribution subject to ASME license or copyright; see http://www.asme.org/terms/Terms_Use.cfm

Asymmetric Shielding Mechanisms in the Mixed-Mode Fracture of a Glass/Epoxy Interface

J. G. Swadener
Mem. ASME.

K. M. Liechti
Mem. ASME.

Department of Aerospace Engineering
and Engineering Mechanics,
The University of Texas at Austin,
Austin, TX 78712-1085

An asymmetric increase in the apparent values of the interfacial fracture toughness with increasing mode II component of loading has been observed by several investigators. In this study, cracks were grown in a steady-state manner along the glass/epoxy interface in sandwich specimens in order to determine the mechanisms responsible for the shielding effect. Finite element analysis using a hydrostatic stress and strain rate dependent plasticity model for the epoxy and a cohesive zone model for the interface shows that plastic dissipation in the epoxy accounts for the asymmetric shielding seen in these experiments which cover a wide range of mode mix. Numerical predictions of normal crack-opening displacements yielded results that were consistent with measured values which were made as close as 0.3 μm from the crack tip.

Introduction

Interfacial fractures frequently pose design constraints in composites, microelectronics devices and pressure sensitive adhesives. Cohesive failures near an interface possess many of the same features and are even more common. In this study, the variation in toughness of a relatively weak glass/epoxy interface with mode mix and the underlying causes of the variation are examined.

A number of studies, e.g., Cao and Evans (1989) and Wang and Suo (1990), have determined that interfacial toughness is a function of mode mix. Chai (1992) has observed similar behavior in cohesive failure near an interface. Liechti and Chai (1991, 1992) have considered nearly a full range of mode mix in bimaterial specimens, but the mechanism responsible for toughening remains unclear.

Shih and Asaro (1988) and Zywicz and Parks (1990) laid a theoretical foundation for the plastic contribution to shielding. Tvergaard and Hutchinson (1993) showed numerically that the variation of fracture toughness with mode mix due to plasticity could be asymmetric and have the qualitative features seen in the experiments cited above. Evans and Hutchinson (1989) had earlier proposed a model to account for asperity locking, but this was shown by Liechti and Chai (1992) to be insignificant for their smooth substrate. Needleman (1987, 1990) developed a model for void nucleation, growth, and coalescence, but no voids are observed in these experiments. Crack bridging was observed by Wang and Chiang (1995), but is not seen here. These last two mechanisms may occur in the submicron scale which is beyond the range of our optical resolution. Deng (1994) has included friction in his growing crack analysis. However, in the range of mode mix covered by these experiments, the contact zones are less than 30 nm, and therefore friction effects are negligible. Derjaguin et al. (1982) and Dickinson (1990) observed electrostatic surface charges during fracture, but the electric fields were too small to affect fracture toughness. These mechanisms will be discussed further, but the emphasis will be on plasticity which appears to dominate in the cases studied herein.

A combination of experimental and numerical methods are employed to determine the cause of the shielding. Sandwich specimens are used, because the stiff layers cause an increase in stress concentration for small applied displacements. This allows for better observation of the normal crack-opening displacements near the crack tip. A cohesive zone model was employed in the finite element analysis of steadily growing cracks so that plastic dissipation could be extracted.

Experimental Procedure

The sandwich specimens tested in this study were composed of glass and aluminum with a relatively thin epoxy bond line as shown in Fig. 1. The epoxy height, h_2, ranged from 0.13 to 0.40 mm. The epoxy was composed of a modified bisphenol A resin which contains dibutyl phthalate as a plasticizer and a polyamido amine hardener (CIBA-GEIGY products Araldite GY502 and HY95, mixed 100:40). The epoxy was cured at 20°C for a minimum of eight days. The residual stresses in the epoxy were measured by using a polariscope and found to be less than two percent of the yield stress. The specimens were precracked a minimum of 8 mm along the glass/epoxy interface. For this ratio of a/h_2, fracture parameters have been shown by Knauss (1966) and Rice (1968) to be independent of crack length.

Two loading configurations were used to determine the fracture toughness. First, displacements (u, v) were applied to the specimen via steel grips in both the bond-tangential (x-) direction and the bond-normal (y-) direction in the same manner as described by Liechti and Chai (1991). Using this method, a range of mode mix from −50 deg to 85 deg was achieved. To measure normal crack-opening displacement at higher magnification, some specimens were loaded in four point bending. The mode mix for this configuration was $\psi = 55$ deg.

In both cases, sufficient displacements were applied to initiate and maintain crack propagation. The crack was grown for a few millimeters of self-similar propagation so that steady-state conditions were achieved. The length of crack propagation was also sufficient so that the previous plastic deformations did not affect the current data point. Crack growth was maintained

Contributed by the Applied Mechanics Division of THE AMERICAN SOCIETY OF MECHANICAL ENGINEERS for publication in the ASME JOURNAL OF APPLIED MECHANICS.

Discussion on this paper should be addressed to the Technical Editor, Professor Lewis T. Wheeler, Department of Mechanical Engineering, University of Houston, Houston, TX 77204-4792, and will be accepted until four months after final publication of the paper itself in the ASME JOURNAL OF APPLIED MECHANICS.

Manuscript received by the ASME Applied Mechanics Division, Jan. 6, 1997; final revision, Aug. 14, 1997. Associate Technical Editor: I. M. Daniel.

 Copyright © 1998 by ASME

Downloaded 04 May 2010 to 171.66.16.26. Redistribution subject to ASME license or copyright; see http://www.asme.org/terms/Terms_Use.cfm

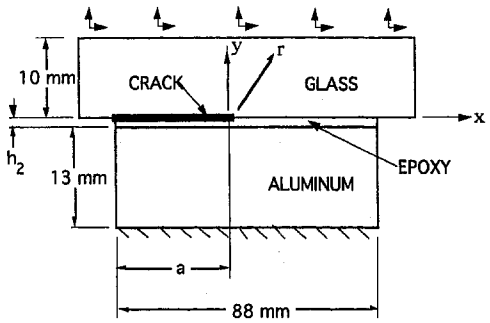

Fig. 1 Sandwich specimen geometry

along the interface. After acquiring data, the displacements were reduced and the crack arrested. Thus it was possible to perform several experiments with different values of mode mix on the same specimen.

Normal crack-opening displacements were measured using crack-opening interferometry (Liechti, 1993). The interference fringes produced by crack opening interferometry were viewed through a microscope and recorded by using a 500-line video cassette recorder. Depending on the magnification used, the spatial resolution ranged from 0.3 to 4.8 μm. A digital image analyzer made possible the determination of normal crack-opening displacements to 1/100 of a fringe order, which gave a resolution of 3 nm. However, uneven reflections from the aluminum adherend (Fig. 3) caused greater scatter in the normal crack-opening displacements measurements, essentially yielding an accuracy of 10 nm.

Analysis

From the invariance of the J-integral under small-scale yielding conditions (Rice, 1968), the energy release rate is found in terms of the displacement of the grips as

$$G = \frac{v^2}{2}\left(\frac{h_1}{\hat{E}_1} + \frac{h_2}{\hat{E}_2} + \frac{h_3}{\hat{E}_3}\right)^{-1} + \frac{u^2}{2}\left(\frac{h_1}{\mu_1} + \frac{h_2}{\mu_2} + \frac{h_3}{\mu_3}\right)^{-1}, \quad (1)$$

where $\hat{E}_i = 2\mu_i/(1-\nu_i)$ for plane stress and $\hat{E}_i = 2\mu_i(1-\nu_i)/(1-2\nu_i)$ for plane strain, μ_i is the shear modulus of component i and ν_i is its Poisson's ratio.

The mode mix is expressed in terms of the angle ψ defined by $\psi = \tan^{-1}(K_2/K_1) + \epsilon \ln(\hat{l}/h_2)$, where ϵ is the bimaterial constant, $\hat{l}$ is a material length parameter which we choose as 100 μm for convenience. For our glass and epoxy materials, ϵ is 0.06. The value of ψ was extracted from finite element analyses using the method of Yau and Wang (1984).

The component of the energy release rate due to plastic dissipation, G_p, was found from finite element analysis of a 48-mm length of the specimen which contained a crack growing at a prescribed constant speed. G_p was calculated as $W_p/b \cdot \Delta a$, where W_p is the plastic dissipation energy, b is the model width, and Δa is the increment of crack growth. The finite element code ABAQUS under academic license from Hibbitt, Karlsson, and Sorensen, Inc. was used. The analysis is quasi-static under the condition of plane strain.

Glass and aluminum components are modeled as elastic elements since they do not exceed the elastic limit in the cases studied. Material properties are shown in Table 1. A user material subroutine is used to capture the hydrostatic stress and strain rate dependencies of the epoxy. The hydrostatic stress dependence is an extended version of the Drucker-Prager model based on the theory given in the ABAQUS Users' Manual (1992), i.e., the flow potential is $g = t - p\tan\phi$, where

Table 1 Material properties

Material	Young's Modulus (GPa)	Poisson's Ratio
Glass	69	0.2
Epoxy	2.03	0.36
Aluminum	70	0.3

$$t = \left(\frac{1}{2}\right)q\left[1 + R - (1-R)\left(\frac{r}{q}\right)^3\right]$$

is an equivalent stress measure, $p = -\text{tr}(\boldsymbol{\sigma})/3$, $q = \frac{3}{2}(\mathbf{s}:\mathbf{s})^{1/2}$, $r^3 = \frac{9}{2}\mathbf{s}:(\mathbf{s}\cdot\mathbf{s})$, $\mathbf{s}$ is the deviatoric stress tensor, R (=1.04) is the ratio of yield strength in triaxial compression to that in triaxial tension, and ϕ is the angle to the t-axis in the p-t plane specifying the direction the yield surface grows. We use fully associated flow with $\phi = \beta = \tan^{-1} 3(R\text{-}1)$, where β is the angle of the slip plane. The strain-rate dependence is given in rate form as

$$\dot{\boldsymbol{\epsilon}}^p = \left[\frac{D}{R\left(1 + \frac{1}{3}\tan\beta\right)}\right]\left(\frac{\sigma_t}{\sigma_0} - 1\right)^n \frac{\frac{\partial f}{\partial \boldsymbol{\sigma}}}{\left(\frac{\partial f}{\partial \boldsymbol{\sigma}} : \frac{\partial f}{\partial \boldsymbol{\sigma}}\right)^{1/2}},$$

where $\dot{\boldsymbol{\epsilon}}^p$ is the plastic strain rate, σ_t is the current equivalent flow stress in tension, σ_0 is the quasi-static flow stress, and $f = t - p\tan\beta$. The values for the material parameters n (=8.98) and D (=0.29 s^{-1}) were found by Liang and Liechti (1996) from shear tests. Hardening is isotropic and follows their plane-strain compression experimental results. The model material response in compression at various strain rates is compared to Liang and Liechti's experimental results (1996) in Fig. 2. The analysis uses the Jaumann stress rate which has been shown by several authors not to be accurate for large strains (for a review see Naghdi, 1990), but should give correct results for the cases we study where the strains do not exceed 30 percent (see Schieck and Stumpf, 1995).

The plasticity equations are integrated using a modified theta scheme developed by Kanchi et al. (1978):

$$\left\{[\mathbf{D}^{\text{el}}]^{-1} + \theta\Delta t \left.\frac{\partial \dot{\boldsymbol{\epsilon}}^p}{\partial \sigma}\right|_t\right\} : \Delta\boldsymbol{\sigma} = \Delta\boldsymbol{\epsilon} - \Delta t\dot{\boldsymbol{\epsilon}}^p|_t,$$

where θ is chosen to be 0.5, $\mathbf{D}^{\text{el}}$ is the elastic compliance matrix, Δt is the time increment, $\Delta\boldsymbol{\epsilon}$ is the increment of strain, and $\Delta\boldsymbol{\sigma}$ is the resulting increment of stress. All quantities are evaluated

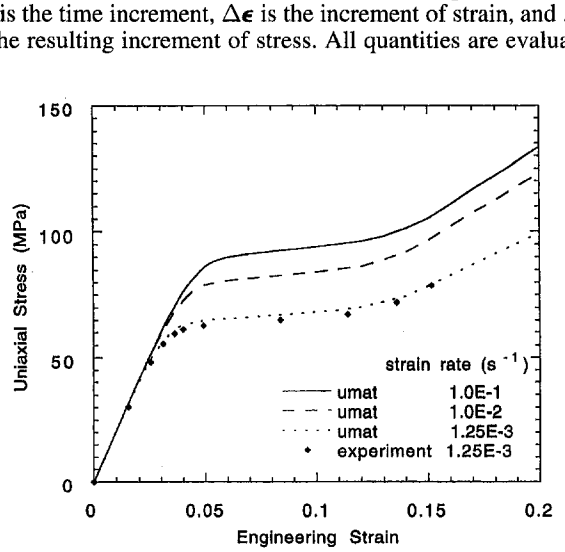

Fig. 2 Comparison of model response in compression at various strain rates with experiments from Liang and Liechti (1996)

Downloaded 04 May 2010 to 171.66.16.26. Redistribution subject to ASME license or copyright; see http://www.asme.org/terms/Terms_Use.cfm

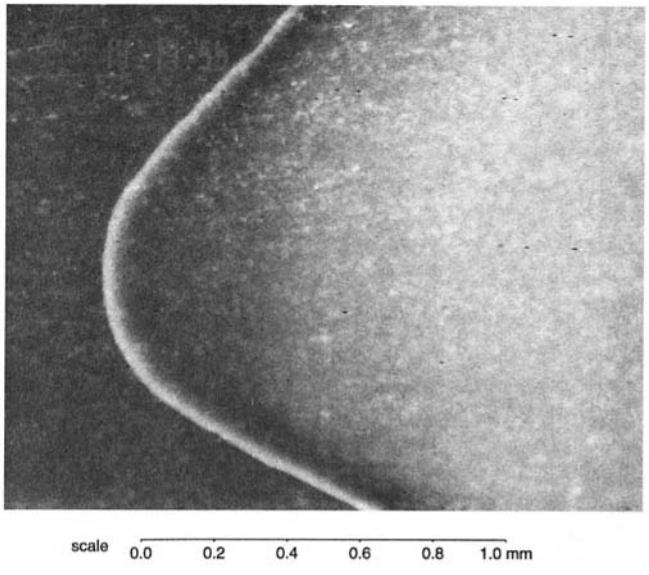

Fig. 3 Fringe patterns obtained by crack-opening interferometry

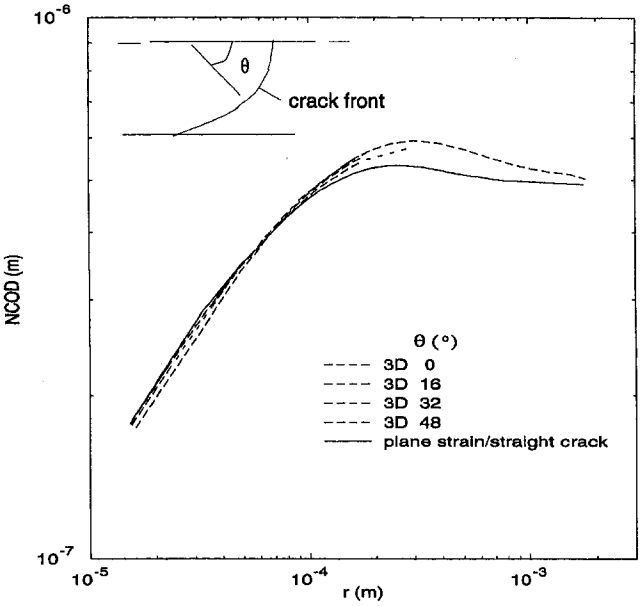

Fig. 4 Comparison of displacements for three-dimensional and plane strain finite element analyses

explicitly at time t. This scheme converges for reasonable values of Δt for our problem.

The debonding process is not well understood and occurs on the nanoscale which is too small to capture completely with a continuum model. Therefore a cohesive zone model was used for debonding. A molecular modeling method might be preferable, but the interaction of glass and epoxy molecules is not yet known. With crack propagation prescribed as a function of time, tractions across the interface are released linearly with time. This results in a nearly linear traction displacement relation on the crack surfaces. We do not propose that this is the actual interaction of the surfaces, but merely that it gives results which are adequate for the evaluation of the shielding mechanisms. Tvergaard and Hutchinson (1994) have shown that fracture toughness results are not significantly affected by the shape of the traction-separation relationship. Ungsuwarungsri and Knauss (1987, 1988a, 1988b) have extracted traction separation laws for cracked joints and crazed cracks. They indicate that certain traction separation laws can give rise to crack growth instabilities. To model the steady-state crack growth in our experiments, the total time to release the tractions was taken to be a constant. This results in a cohesive zone of constant length.

Results and Discussion

An example of the fringe patterns observed is shown in Fig. 3 for a crack propagating from right to left. The crack front is the dark edge ahead of the first bright fringe and is seen to be curved. This was the case for most experiments, with crack front curvature varying with mode mix, as had been noted previously in glass/urethane sandwiches (Liechti and Knauss, 1982) and discussed further in Liechti, Chai, and Liang (1992). Once steady-state conditions were achieved, the crack-front shape remained constant, resulting in self-similar propagation. In order to assess the effects of crack-front curvature, three-dimensional finite element analysis was performed for stationary cracks. The crack front in the model had a radius of curvature of 0.4 mm and was centered 1 mm from the free surface. The crack front intersected the free surface at a 30 deg angle. Displacements were determined at the centerline and for various rays normal to the crack front. The normal crack-opening displacements for three dimensions and plane strain are compared in Fig. 4. The effect of the curved crack front is seen to be localized in the region from 0.1 to 1 mm. The local maximum seen in the three-dimensional analysis is qualitatively similar to the experimental results of Liechti and Knauss (1982). In the K dominant zone ($10 \leq r \leq 50$ μm), the three-dimensional and plane strain results are in agreement. Therefore plain strain analysis is justified for the crack fronts studied which had radii of curvature greater than 0.4 mm.

Normal crack-opening displacement results for two growing cracks are compared to plane strain finite element predictions in Fig. 5. The prediction is for a cohesive zone size of 0.5 μm. A finite element mesh using four-node bilinear quadrilateral elements with a minimum size of 31 nm was used. The experimental results agree with the predictions to within 1.1 μm of the crack tip which was the spatial resolution for these experiments. The fracture toughness varies somewhat from specimen to specimen, but was the same for these two results which were for different bond thicknesses. Tvergaard and Hutchinson (1994) have shown that shielding will be affected when the plastic zone size is greater than 1/5 the bond thickness. However, the largest plastic zone size found in this study was 13 μm which was only 1/20 of the bond thickness. As in the three-dimensional analysis, a zone of K dominance is seen to exist between the region near the crack tip which is dominated by

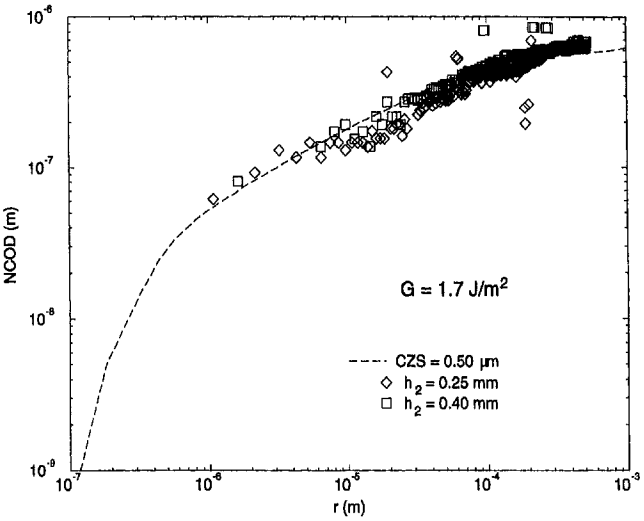

Fig. 5 Normal crack-opening displacement measurements for two growing cracks with different bond thicknesses

Downloaded 04 May 2010 to 171.66.16.26. Redistribution subject to ASME license or copyright; see http://www.asme.org/terms/Terms_Use.cfm

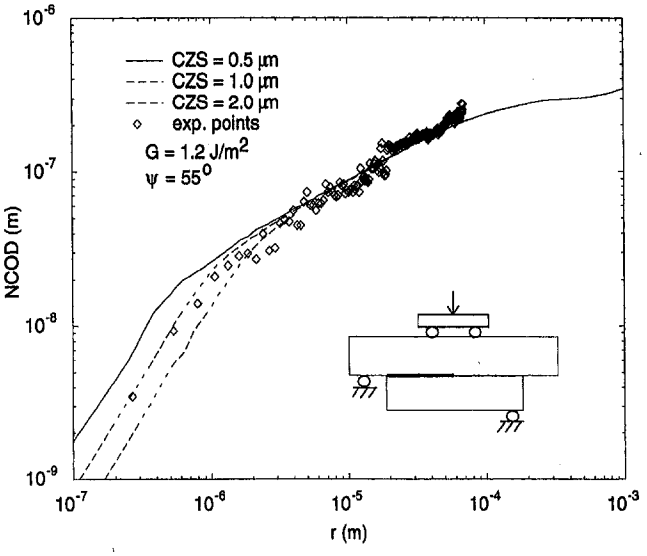

Fig. 6 Comparison of normal crack-opening displacement results from experiment and finite element analysis

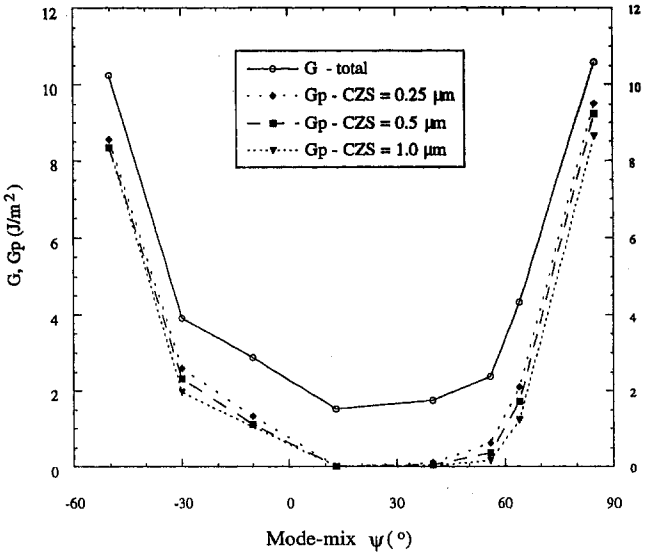

Fig. 7 Plastic dissipation component of fracture toughness

the yielding behavior and the region influenced by the geometry. This zone covers at least $10 \leq r \leq 40$ μm in all cases. The existence of this K dominant zone verifies the small-scale yielding assumption used in Eq. (1) with concomitant extensions to transferability concepts.

Higher magnification was used to obtain the normal crack-opening displacement results shown in Fig. 6. Predictions for three different values of the cohesive zone size are shown for comparison. The predictions match the experimental results, to within 0.3 μm of the crack tip, for a cohesive zone 1.0 μm in length. Due to an uncertainty of 10 nm in the experimental measurements, the range for the cohesive zone size is 0.5 to 2.0 μm (95 percent confidence).

Electrostatic charges have been reported for surfaces in contact by Horn and Smith (1992) and on fracture surfaces by Derjaguin et al. (1982) and Dickinson (1990). The possible effects of electrostatic charges in these experiments were therefore investigated. The air in the vicinity of the crack faces was ionized with a Po-210 α-radiation source and drawn through the crack with suction. This did not cause any observable changes in the normal crack-opening displacements. Therefore, if electrostatic charges exist in these specimens with a sufficient magnitude to affect fracture, the charges must be confined to a region of approximately 1 μm behind the crack tip.

Figure 7 shows the shielding affect of plasticity for selected points, and three values of the cohesive zone size. Convergence of the finite element solution was ± 3 percent of the total fracture toughness for each value of mode mix. When the cohesive zone size is set equal to 0.5 μm, plastic dissipation accounts for the variation of fracture toughness with mode mix. The variation of G_p with ψ also mirrors the asymmetric aspects of the total value of G within the resolution of the experiments. If the cohesive zone size is decreased, the plastic dissipation increases and vice versa. The asymmetry of the toughening curve can be attributed to two factors. First, the yield strength in tension is 13 percent lower than in compression, thus the negative Mode II component which puts the epoxy in tension causes more plastic dissipation than a corresponding positive Mode II component. Secondly, the volume of the plastic zone is larger with a negative Mode II component because it extends ahead of the crack tip along the bimaterial interface and in a larger area behind the crack tip, whereas with a positive Mode II component, the plastic zone is predominantly ahead of the crack tip. These two affects working in combination give rise to the significant asymmetry in the plastic dissipation. Both the volume of the plastic zone and the maximum strain increase with the Mode II component, but the increase is not as dramatic as in the fracture toughness where these effects are combined.

The resultant difference $(G-G_p)$ in Fig. 7 is in the range of 1 to 2 J/m^2. Fracture toughness values versus mode mix are shown in Fig. 8 for the rest of the sandwich specimen experiments. The SL prediction shown in Fig. 8 results from adding the apparent intrinsic toughness, 1.5 J/m^2 to the plastic dissipation using a cohesive zone size of 0.5 μm. A prediction using the Mode I criterion of Charalambides et al. (1992) is shown for comparison. Their prediction is reasonably close for the sandwich results, but is nonconservative for the bimaterial results which cover a wider range of mode mix. The asymmetric character of the shielding and its magnitude are captured by the analysis of this study.

Comparison of the sandwich fracture toughness results with the results for bimaterial specimens from Liechti and Chai (1992) shows similar asymmetric shielding with mode mix. The apparent intrinsic fracture toughness is larger for the bimaterial specimens. This is primarily due to the fact that those toughness values were taken at crack initiation and may have been affected by blunting of the crack tip (Liechti and Chai, 1991). The sandwich specimen curve also appears to be shifted +15 deg

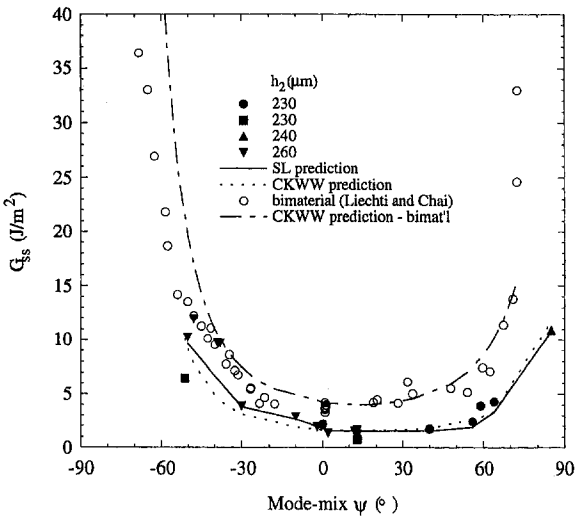

Fig. 8 Fracture toughness values for sandwich and bimaterial specimens

Downloaded 04 May 2010 to 171.66.16.26. Redistribution subject to ASME license or copyright; see http://www.asme.org/terms/Terms_Use.cfm

compared to the bimaterial results. This can be shown pro forma to be the result of including the h_3 term in Eq. (1), although the exact relationship for ψ for three materials has not been obtained. Setting $\hat{l} = 10$ mm would bring the two curves into alignment, but this value is too large for a material length scale.

The apparent intrinsic fracture toughness is too large to be accounted for by surface energy alone which was found to be 84 ± 9 mJ/m^2. This was determined by using the three liquid method of Good et al. (1991) which includes dispersion forces and acid-base interactions. Also, there must be an additional dissipative mechanism to explain the steady-state crack growth observed in the experiments. The strain-rate dependence in the continuum model gives decreased plastic dissipation at higher crack speeds, and therefore cannot account for stable crack propagation. Asperity shielding and linear viscoelastic dissipation were shown by Liechti and Chai (1992) to be negligible. The epoxy material model includes creep when stresses exceed the yield point. Considering the time scales involved in the experiment where the material is loaded and unloaded in a few seconds at strain rates exceeding 1 s^{-1}, nonlinear viscoelastic effects would be expected to be minimal. Friction, electrostatics, and inelastic material deformation on the nanoscale within the cohesive zone region are possible additional mechanisms. Adhesion of up to 0.8 J/m^2 was observed in some recent work (Liechti et al., 1996) with spherical contact between glass and cured epoxy. The materials were not bonded, but simply pressed together. The experiments were Mode I and showed negligible plasticity, but the adhesion mechanism was affected by the deposition of a liquid residue during contact.

Fortunately, however, the energy dissipated by the additional mechanism(s) does not appear to vary with mode mix. Therefore, two simple experiments (one predominantly Mode I and the other with a significant Mode II component) could establish the length to use for the cohesive zone. Then finite element analysis using continuum material models and a simple cohesive zone model could be used to determine the fracture toughness at any desired mode mix.

Conclusions

Interfacial cracks in sandwich specimens have been observed during steady-state self-similar growth with a spatial resolution of as low as 0.3 μm and normal crack-opening displacement resolution of 10 nm. The results indicate that the length of the cohesive zone is approximately 1 μm.

Asymmetric shielding has been observed in these specimens, similar to the results of Liechti and Chai (1992) with bimaterial specimens. Both the quantity of shielding and its asymmetric character can be accounted for by plastic dissipation when hydrostatic stress and strain-rate dependencies are included. A cohesive zone length of 0.5 μm gave the best agreement with experimental data and fits within the range of possible lengths. The plasticity model does not account for all of the energy dissipated during fracture, but the remainder does not appear to vary with mode mix. As a result, it is possible to predict the variation of fracture toughness for the complete range of mode mix from two simple experiments and using continuum models for the materials in interfacial fracture under small scale yielding conditions.

Acknowledgment

The authors would like to acknowledge the financial support for this work provided by the National Science Foundation, grant number CMS-9522964.

References

Cao, H. C., and Evans, A. G., 1989, "An Experimental Study of the Fracture Resistance of Bimaterial Interfaces," *Mechanics of Materials,* Vol. 7, pp. 295–304.

Chai, H., 1992, "Experimental Evaluation of Mixed-Mode Fracture in Adhesive Bonds," *Experimental Mechanics,* Vol. 32, pp. 296–303.

Charalambides, M., Kinloch, A. J., Wang, Y., and Williams, J. G., 1992, "On the Analysis of Mixed-Mode Fracture," *Int. J. Fracture,* Vol. 54, pp. 269–291.

Deng, X., 1994, "An Asymptotic Analysis of Stationary and Moving Cracks with Frictional Contact Along Bimaterial Interfaces and in Homogeneous Solids," *Int. J. Solids and Structures,* Vol. 31, pp. 2407–2429.

Derjaguin, B. V., Krotova, N. A., and Toporov, Y. R., 1982, *Microscopic Aspects of Adhesion and Lubrication,* J. M. George, ed., pp. 471–487.

Dickinson, J. T., 1990, *Non-Destructive Testing of Fiber Reinforced Plastic Composites II,* J. Summerscales, ed., pp. 429–482.

Evans, A. G., and Hutchinson, J. W., 1993, "Effects of Non-Planarity on the Mixed Mode Fracture Resistance of Bimaterial Interfaces," *Acta Metall. Mater.,* Vol. 37, pp. 909–916.

Good, R. J., Chaudhury, M. K., and van Oss, C. J., 1991, "Theory of Adhesive Forces Across Interfaces 2. Interfacial Hydrogen Bonds as Acid-Base Phenomena and as Factors Enhancing Adhesion," *Fundamentals of Adhesion,* L.-H. Lee, ed., Plenum Press, New York, pp. 153–172.

Hibbitt, Karlsson, and Sorensen, Inc., 1992, *ABAQUS User's Manual,* Pawtuket, RI, pp. 4.6.3 1–9.

Horn, R. G., and Smith, D. T., 1992, "Contact Electrification and Adhesion Between Dissimilar Materials," *Science,* Vol. 256, pp. 362–364.

Kanchi, M. B., Zienkiewicz, O. C., and Owen, D. R. J., 1978, "The viscoplastic approach to problems in plasticity and creep involving geometric non-linear effects," *Int. J. Num. Meth. Engrg.,* Vol. 12, pp. 169–181.

Knauss, W. G., 1966, "Stresses in an Infinite Strip Containing a Semi-Infinite Crack," ASME JOURNAL OF APPLIED MECHANICS, Vol. 33, pp. 356–362.

Liang, Y.-M., and Liechti, K. M., 1995, "Toughening Mechanisms in Mixed-Mode Interfacial Fracture," *Int. J. Solids and Structures,* Vol. 32, pp. 957–978.

Liang, Y.-M., and Liechti, K. M., 1996, "On the Large Deformation and Localization Behavior of an Epoxy Resin Under Multiaxial Stress States," *Int. J. Solids and Structures,* Vol. 32, pp. 1479–1500.

Liechti, K. M., Schnapp, S. T., and Swadner, J. G., 1996, "Contact Angle and Contact Mechanics of a Glass/Epoxy Interface," Engineering Mechanics Research Laboratory Report #EMRL 96-11, *Int. J. Fracture,* to appear.

Liechti, K. M., 1993, *Experimental Techniques in Fracture,* J. S. Epstein, ed., VCH Publishers, New York, Chapter 4.

Liechti, K. M., and Chai, Y.-S., 1991, "Biaxial Loading Experiments for Determining Interfacial Fracture Toughness," ASME JOURNAL OF APPLIED MECHANICS, Vol. 58, pp. 680–687.

Liechti, K. M., and Chai, Y.-S., 1992, "Asymmetric Shielding in Interfacial Fracture Under In-Plane Shear," ASME JOURNAL OF APPLIED MECHANICS, Vol. 59, pp. 295–304.

Liechti, K. M., Chai, Y.-S., and Liang, Y.-M., 1992, "Three-Dimensional Effects in Interfacial Crack Propagation," *Experimental Mechanics,* Vol. 32, pp. 218–224.

Liechti, K. M., and Knauss, W. G., 1982, "Crack Propagation at Material Interfaces: II Experiments on Mode Interaction," *Experimental Mechanics,* Vol. 22, pp. 383–391.

Naghdi, P. M., 1990, "A Critical Review of the State of Finite Plasticity," *J. Appl. Math. Phys. (ZAMP),* Vol. 41, pp. 315–394.

Needleman, A., 1987, "A Continuum Model for Void Nucleation by Inclusion Debonding," ASME JOURNAL OF APPLIED MECHANICS, Vol. 54, pp. 525–531.

Needleman, A., 1990, "An Analysis of Tensile Decohesion Along an Interface," *J. Mech. Phys. Solids,* Vol. 38, pp. 289–324.

Rice, J. R., 1968, "A Path Independent Integral and the Approximation Analysis of Strain Concentrations by Notches and Cracks," ASME JOURNAL OF APPLIED MECHANICS, Vol. 35, pp. 379–386.

Schieck, B., and Stumpf, H., 1995, "The Appropriate Corrotational Rate, Exact Formula for the Plastic Spin and Constitutive Model for Finite Elastoplasticity," *Int. J. Solids and Structures,* Vol. 32, pp. 3643–3667.

Shih, C. F., and Asaro, R. J., 1988, "Elastic-Plastic Analysis of Cracks on Bimaterial Interfaces: Part I—Small-Scale Yielding," ASME JOURNAL OF APPLIED MECHANICS, Vol. 55, pp. 299–316.

Tvergaard, V., and Hutchinson, J. W., 1993, "The Influence of Plasticity on Mixed Mode Interface Toughness," *J. Mech. Phys. Solids,* Vol. 41, pp. 1119–1135.

Tvergaard, V., and Hutchinson, J. W., 1994, "Toughness of an Interface along a Thin Ductile Layer Joining Elastic Solids," *Phil. Mag. A,* Vol. 70, pp. 641–656.

Ungsuwarungsri, T., and Knauss, W. G., 1987, "The Role of Damage-Softened Material in the Fracture of Composites and Adhesives," *Int. J. Fracture,* Vol. 35, pp. 221–241.

Ungsuwarungsri, T., and Knauss, W. G., 1988a, "A Nonlinear Analysis of an Equilibrium Craze: Part I—Problem Formulation and Solution," ASME JOURNAL OF APPLIED MECHANICS, Vol. 55, pp. 44–51.

Ungsuwarungsri, T., and Knauss, W. G., 1988b, "A Nonlinear Analysis of an Equilibrium Craze: Part II—Simulations of Craze and Crack Growth," ASME JOURNAL OF APPLIED MECHANICS, Vol. 55, pp. 52–58.

Wang, J.-S., and Suo, Z., 1990, "Experimental Determination of Interfacial Toughness Using Brazil-Nut Sandwiches," *Acta Metall. Mater.,* Vol. 38, pp. 1279–1290.

Wang, Y., and Chiang, F.-P., 1995, "A Photoelastic Study of Extending cracks in Adhesion Joints," *J. Adhesion,* in press.

Yau, Y. F., and Wang, S. S., 1984, "An Analysis of Interface Cracks Between Dissimilar Isotropic Materials Using Conservation Integrals in Elasticity," *Eng. Fracture Mech.,* Vol. 20, pp. 423–432.

Zywicz, E., and Parks, D. M., 1990, "Elastic-Plastic Analysis of Frictionless Contact at Interfacial Crack Tips," *Int. J. Fracture,* Vol. 52, pp. 129–143.

Downloaded 04 May 2010 to 171.66.16.26. Redistribution subject to ASME license or copyright; see http://www.asme.org/terms/Terms_Use.cfm

A Circular Inclusion With Circumferentially Inhomogeneous Sliding Interface in Plane Elastostatics

C. Q. Ru
Department of Mechanical Engineering,
University of Alberta,
Edmonton, Alberta, TGG 2G8,
Canada

A general method is presented to obtain the rigorous solution for a circular inclusion embedded within an infinite matrix with a circumferentially inhomogeneous sliding interface in plane elastostatics. By virtue of analytic continuation, the basic boundary value problem for four analytic functions is reduced to a first-order differential equation for a single analytic function inside the circular inclusion. The finite form solution is obtained that includes a finite number of unknown constants determined by the analyticity of the solution and certain other auxiliary conditions. With this method, the exact values of the average stresses within the circular inclusion can be calculated without solving the full problem. Several specific examples are used to illustrate the method. The effects of the circumferential variation of the interface parameter on the mean stress at the interface and the average stresses within the inclusion are discussed.

1 Introduction

The elastic inclusions with imperfect interface and the effect of the imperfect interface on the overall properties of composites are receiving an increasing amount of attention. Among various mechanical descriptions of an imperfect interface, one of the more widely used models is based on the assumption that tractions are continuous across the interface and displacement discontinuities are proportional to their respective interface tractions in terms of the spring-factor-type interface parameters. Based on this model, Hashin (1991) has examined the case of a spherical inclusion and found that, in contrast to the uniform stress state associated with a perfect interface, the stresses inside the inclusion are not uniform under a remotely uniform stress field. The counterpart of the problem to plane deformations has been examined by Gao (1995) with an analogous conclusion.

The concept of imperfect interface has been developed mainly to account for various damages at the inclusion/matrix interface in composite materials. To simplify the analysis, despite the fact that an interface usually exhibits circumferentially inhomogeneous damage (cf. Tandon and Pagano 1996), the interface parameters appearing in the aforementioned spring-layer model have been assumed to be constant along the entire interface in most of the previous works. To the present author's knowledge, no attempt has been made to analyze the elastic inclusion with a circumferentially inhomogeneous imperfect interface (only a small amount of work has been devoted to the partially debonded elastic inclusion, see, e.g., Karihaloo and Viswanathan (1985) and the composites with radially inhomogeneous interphase, see, e.g., Jasiuk and Kouider (1993)). The main objective of this work is to present a general method for the rigorous solution of a circular inclusion with a circumferentially inhomogeneous sliding interface in plane elastostatics. Several examples are used to illustrate the effect of the circumferential variation of the interface parameter on the stresses in the inclusion.

Contributed by the Applied Mechanics Division of THE AMERICAN SOCIETY OF MECHANICAL ENGINEERS for publication in the ASME JOURNAL OF APPLIED MECHANICS.

Discussion on the paper should be addressed to the Technical Editor, Professor Lewis T. Wheeler, Department of Mechanical Engineering, University of Houston, Houston, TX 77204-4792, and will be accepted until four months after final publication of the paper itself in the ASME JOURNAL OF APPLIED MECHANICS.

Manuscript received by the ASME Applied Mechanics Division, Oct. 15, 1996; final revision, June 2, 1997. Associate Technical Editor: J. W. Ju.

2 Formulation

Let that the elastic inclusion occupy a circular region S_2, with center at the origin of the coordinate system and radius R, and the elastic matrix occupy the exterior of S_2, denoted by S_1. Throughout the paper, unless otherwise stated, all quantities in the region S_1 and S_2 are identified by the subscripts 1 and 2, respectively (see Fig. 1).

For plane deformations, the elastic stresses and the associated displacements can be given in terms of two complex potentials $\phi(z)$ and $\psi(z)$ (Muskhelishvili, 1963)

$$2\mu(u_r + iu_\theta) = e^{-i\theta}[\kappa\phi(z) - z\overline{\phi'(z)} - \overline{\psi(z)}]$$

$$\sigma_{rr} + \sigma_{\theta\theta} = 2[\phi'(z) + \overline{\phi'(z)}]$$

$$\sigma_{rr} - i\sigma_{r\theta} = \phi'(z) + \overline{\phi'(z)} - e^{2i\theta}[\bar{z}\phi''(z) + \psi'(z)] \quad (2.1)$$

where $z = x + iy = re^{i\theta}$ is the complex coordinate, $\kappa = (3 - 4\nu)$ for plane strain and $(3 - \nu)/(1 + \nu)$ for plane stress, and μ and ν are the shear modulus and Poisson's ratio, respectively. Assume that the circular inclusion be bonded to the matrix by a spring-layer imperfect interface, as described in Section 1, then the interface conditions between the inclusion and the matrix are given by

$$[\![\sigma_{rr} - i\sigma_{r\theta}]\!] = 0, \quad z \in \Gamma \quad (2.2)$$

$$\sigma_{rr} = m[\![u_r]\!] - mu_r^0, \quad \sigma_{r\theta} = n[\![u_\theta]\!] - nu_\theta^0, \quad z \in \Gamma \quad (2.3)$$

where Γ is the circular interface, m and n are two non-negative (not constant, in general) interface parameters, $[\![*]\!] = (*)_1 - (*)_2$ denotes the jump across Γ, and u^0 is the displacement induced by the uniform (stress-free) eigenstrains $\{\epsilon_{xx}^0, \epsilon_{yy}^0, \epsilon_{xy}^0\}$ prescribed in the inclusion. Thus

$$-[mu_r^0 - inu_\theta^0] = -m\epsilon_1 R - \frac{m - n}{2z^2} R^3(\epsilon_2 + i\epsilon_3) - \frac{m + n}{2R}(\epsilon_2 - i\epsilon_3)z^2, \quad z \in \Gamma \quad (2.4)$$

where

 Copyright © 1998 by ASME

Downloaded 04 May 2010 to 171.66.16.26. Redistribution subject to ASME license or copyright; see http://www.asme.org/terms/Terms_Use.cfm

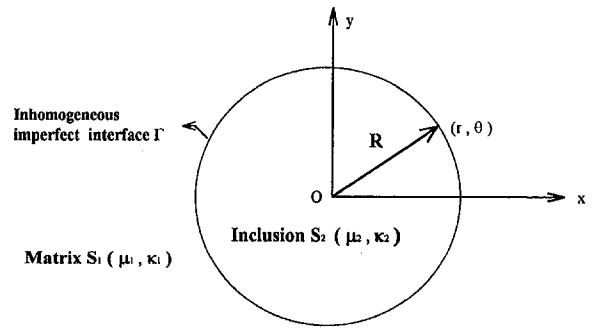

Fig. 1 A circular inclusion with a circumferentially inhomogeneous sliding interface in plane elastostatics

$$\epsilon_1 \equiv \frac{\epsilon^0_{xx} + \epsilon^0_{yy}}{2}, \quad \epsilon_2 \equiv \frac{\epsilon^0_{xx} - \epsilon^0_{yy}}{2}, \quad \epsilon_3 \equiv \epsilon^0_{xy}. \tag{2.5}$$

The asymptotic conditions at infinity are given by

$$\phi_1(z) \cong Az + 0(1), \quad \psi_1(z) \cong Bz + 0(1), \quad |z| \to \infty \tag{2.6}$$

where, without loss of the generality, A is a given real number and B a given complex number. The problem studied in the paper is to determine the four unknown analytic functions $\phi_1(z)$, $\psi_1(z)$, $\phi_2(z)$, and $\psi_2(z)$, complying with the conditions (2.2), (2.3), and (2.6).

Note that $\phi_1(z)$, $\psi_1(z)$, $\phi_2(z)$, and $\psi_2(z)$ admit the following expansions:

$$\phi_1(z) = Az + \sum_{k=0}^{\infty} A_k z^{-k}, \quad \psi_1(z) = Bz + \sum_{k=0}^{\infty} B_k z^{-k}, \quad z \in S_1$$

$$\phi_2(z) = \sum_{k=0}^{\infty} X_k z^k, \quad \psi_2(z) = \sum_{k=0}^{\infty} Y_k z^k, \quad z \in S_2. \tag{2.7}$$

We choose the coordinate system such that $X_0 = Y_0 = 0$. In view of (2.1), the traction continuity conditions (2.2) gives

$$\phi_1' - z\phi_1'' - \frac{z^2}{R^2}\psi_1' - \overline{\phi_2'\left(\frac{R^2}{\bar{z}}\right)}$$

$$= \phi_2' - \overline{\phi_1'\left(\frac{R^2}{\bar{z}}\right)} - z\phi_2'' - \frac{z^2}{R^2}\psi_2', \quad z \in \Gamma. \tag{2.8}$$

The right and the left of (2.8) are analytic in S_2 and S_1, respectively, except at infinity where the left of (2.8) has the asymptotic behavior

$$A - B\frac{z^2}{R^2} - \overline{X_1} + \frac{B_1}{R^2}.$$

Consider the function defined by

$$\Omega(z) = \begin{cases} \phi_1' - z\phi_1'' - \dfrac{z^2}{R^2}\psi_1' - \overline{\phi_2'\left(\dfrac{R^2}{\bar{z}}\right)} \\ \qquad - \left[A - B\dfrac{z^2}{R^2} - \overline{X_1} + \dfrac{B_1}{R^2}\right], \ z \in S_1 \\ \phi_2' - \overline{\phi_1'\left(\dfrac{R^2}{\bar{z}}\right)} - z\phi_2'' - \dfrac{z^2}{R^2}\psi_2' \\ \qquad - \left[A - B\dfrac{z^2}{R^2} - \overline{X_1} + \dfrac{B_1}{R^2}\right], \ z \in S_2. \end{cases} \tag{2.9}$$

It is seen from (2.8) that $\Omega(z)$ is analytic in the whole plane and approaches zero at infinity. Accordingly, $\Omega(z)$ is identically zero and then we obtain the expressions for $\psi_k(z)$ in terms of $\phi_k(z)$ $(k = 1, 2)$ as follows:

$$\psi_1 = Bz + \frac{AR^2 + B_1 - \overline{X_1}R^2}{z} - \left(\frac{\phi_1'}{z}\right)R^2 + \overline{\phi_2}\left(\frac{R^2}{z}\right) + C_1, \quad z \in S_1$$

$$\psi_2 = Bz + \frac{AR^2 + B_1 - \overline{X_1}R^2}{z} - \left(\frac{\phi_2'}{z}\right)R^2 + \overline{\phi_1}\left(\frac{R^2}{z}\right) + C_2, \quad z \in S_2 \tag{2.10}$$

where B_1, C_1, and C_2 are given by (note that A is a real number)

$$2\,\mathrm{Re}[X_1] = 2A + \frac{B_1}{R^2}, \ C_1 = B_0, \ C_2 = 2X_2R^2 - \overline{A_0}. \tag{2.11}$$

Hence, the original problem can be reduced to a problem for the two unknown analytic functions $\phi_1(z)$ and $\phi_2(z)$. To this end, the remaining two displacement interface conditions (2.3) are written into a complex form

$$\sigma_{rr} - i\sigma_{r\theta} = \frac{m-n}{2}[\![u_r + iu_\theta]\!] + \frac{m+n}{2}[\![u_r - iu_\theta]\!] - [mu_r^0 - inu_\theta^0], \quad z \in \Gamma. \tag{2.12}$$

On using (2.1) and (2.10), (2.12) is given in terms of $\phi_k(z)$ $(k = 1, 2)$ as follows:

$$A + \frac{B_1}{R^2} - \frac{B}{R^2}z^2 - \overline{X_1} + \overline{\phi_2'\left(\frac{R^2}{\bar{z}}\right)} + \frac{n-m}{4}\left(\frac{\kappa_1}{\mu_1} + \frac{1}{\mu_2}\right)\frac{R}{z}\phi_1 - \frac{m-n}{4\mu_2}\left[A + \frac{B_1}{R^2} - X_1 + \frac{\bar{B}R^2}{z^2} + \frac{\overline{C_2}}{z}\right]R + \frac{m+n}{4\mu_1 R}[Bz^2 + B_1 + AR^2 - \overline{X_1}R^2 + C_1 z] + \frac{m+n}{4}\left(\frac{\kappa_2}{\mu_2} + \frac{1}{\mu_1}\right)\frac{z}{R}\overline{\phi_2\left(\frac{R^2}{\bar{z}}\right)}$$

$$= -\overline{\phi_1'\left(\frac{R^2}{\bar{z}}\right)} + \frac{n-m}{4}\left(\frac{\kappa_2}{\mu_2} + \frac{1}{\mu_1}\right)\frac{R}{z}\phi_2 - \frac{m-n}{4\mu_1}\left[A + \frac{B_1}{R^2} - X_1 + \frac{\bar{B}R^2}{z^2} + \frac{\overline{C_1}}{z}\right]R + \frac{m+n}{4\mu_2 R}[Bz^2 + B_1 + AR^2 - \overline{X_1}R^2 + C_2 z] + \frac{m+n}{4}\left(\frac{\kappa_1}{\mu_1} + \frac{1}{\mu_2}\right)\frac{z}{R}\overline{\phi_1\left(\frac{R^2}{\bar{z}}\right)} - m\epsilon_1 R - \frac{m-n}{2z^2}R^3(\epsilon_2 + i\epsilon_3) - \frac{m+n}{2R}(\epsilon_2 - i\epsilon_3)z^2, \quad z \in \Gamma. \tag{2.13}$$

Thus, the problem is now reduced to determining the two un-

Downloaded 04 May 2010 to 171.66.16.26. Redistribution subject to ASME license or copyright; see http://www.asme.org/terms/Terms_Use.cfm

known analytic functions $\phi_1(z)$ and $\phi_2(z)$ complying with the interface condition (2.13) and the asymptotic condition (2.6) for $\phi_1(z)$.

3 The Solution for a Homogeneous Imperfect Interface

In this section, we examine briefly a homogeneous spring-layer interface. Hence, the parameters m and n appearing in (2.3) are assumed to be constant along Γ. Although a similar problem has been studied by Gao (1995), where explicit results have been given for the uniaxial tension, the solution given below has a more tractable form and is applicable to any combination of remote uniform stress state and constant eigenstrains $\{\epsilon^0_{xx}, \epsilon^0_{yy}, \epsilon^0_{xy}\}$.

Substituting the expansions (2.7) into (2.13), one can readily see that

$$A_k \equiv 0, \quad k \geq 2$$
$$X_k \equiv 0, \quad k \geq 4. \tag{3.1}$$

Further, we find that $A_0 = X_2 = 0$ and the remaining coefficients A_1, X_1, and X_3 are given by

$$\overline{A_1} = \frac{\dfrac{mnR^2}{4}\left[\dfrac{\kappa_2}{\mu_2} + \dfrac{1}{\mu_1}\right]\left[\dfrac{1}{\mu_1} - \dfrac{1}{\mu_2}\right] - 3 + \dfrac{(m+n)R}{4}\left[\dfrac{2}{\mu_1} - \dfrac{3+\kappa_2}{\mu_2}\right]}{\Delta} B + \frac{3(m+n)R + mnR^2\left(\dfrac{1}{\mu_1} + \dfrac{\kappa_2}{\mu_2}\right)}{2\Delta}(\epsilon_2 - i\epsilon_3), \tag{3.2}$$

$$X_1 = \frac{\dfrac{(\kappa_1+1)}{2\mu_1}A - \epsilon_1}{\left[\dfrac{2}{mR} + \dfrac{1}{\mu_1} + \dfrac{\kappa_2 - 1}{2\mu_2}\right]}, \tag{3.3}$$

$$X_3 = \frac{(n-m)}{2\Delta R^3}\left[\frac{1+\kappa_1}{2\mu_1}B + (\epsilon_2 - i\epsilon_3)\right] \tag{3.4}$$

where

$$\Delta = \frac{3}{R^2} + \frac{(m+n)}{R}\left[\frac{3\kappa_1 + 1}{4\mu_1} + \frac{3+\kappa_2}{4\mu_2}\right] + \frac{mn}{4}\left(\frac{1}{\mu_2} + \frac{\kappa_1}{\mu_1}\right)\left[\frac{\kappa_2}{\mu_2} + \frac{1}{\mu_1}\right] > 0. \tag{3.5}$$

Hence, when m and n are two constants, the general solution is given by

$$\phi_1(z) = Az + \frac{A_1}{z},$$
$$\psi_1(z) = Bz + 2\frac{X_1 - A}{z}R^2 + \frac{A_1R^2 + \overline{X_3}R^6}{z^3}, \quad z \in S_1$$
$$\phi_2(z) = X_1 z + X_3 z^3,$$
$$\psi_2(z) = \left(B + \frac{\overline{A_1}}{R^2} - 3X_3R^2\right)z, \quad z \in S_2. \tag{3.6}$$

In particular, if $m = n$ (it has been assumed by some authors; see, e.g., Achenbach and Zhu (1989)), it is seen from (3.4) that $X_3 = 0$ and then the stress state inside the circular inclusion is uniform. This is in agreement with the results of Hashin (1990, 1991) and Gao (1995).

The solution (3.2)–(3.6) gives a concise expression for the radial stress σ_{rr} on the interface

$$\sigma_{rr}|_{r=R} = 2X_1 - \mathrm{Re}\left[e^{2i\theta}\left(B + \frac{\overline{A_1}}{R^2} - 3X_3R^2\right)\right]. \tag{3.7}$$

For example, for uniaxial tension without any eigenstrain, (3.7) gives

$$\left.\frac{\sigma_{rr}}{m}\right|_{r=R} = \frac{2AR(1+\kappa_1)}{\mu_1}\left[\frac{1}{4 + mR\left(\dfrac{2}{\mu_1} + \dfrac{\kappa_2 - 1}{\mu_2}\right)} + \frac{6 + nR\left(\dfrac{1}{\mu_1} + \dfrac{\kappa_2}{\mu_2}\right)}{4R^2\Delta}\cos[2\theta]\right] \tag{3.8}$$

which is in agreement with Gao's results (see his (27), (28)). For the general case, it is seen from (3.2)–(3.7) that the condition $(\sigma_{rr}/m) \geq 0$ on Γ can be satisfied only when the mean components of the remote stresses and the eigenstrains are dominant over their deviatoric and shear components. Otherwise, the spring-layer model will lead to interpenetration of the materials at the interface (cf. Achenbach and Zhu (1989) and Hashin (1991)). To avoid this unphysical result, some investigators (see, e.g., Benveniste (1984), Thorpe and Jasiuk (1992), and Jun and Jasiuk (1993)) have confined their attention to the sliding interface, obtained by taking $m = \infty$ in (2.2), (2.3). We follow the same strategy in the following sections.

4 A Circular Inclusion With Inhomogeneous Sliding Interface

Now we consider the circular inclusion with a circumferentially inhomogeneous sliding interface. In this case, the interface conditions (2.3) have the forms

$$[\![u_r]\!] - u^0_r = 0, \quad \frac{1}{n(\theta)}\sigma_{r\theta} = [\![u_\theta]\!] - u^0_\theta \tag{4.1}$$

where, $1/n(\theta)$ is a non-negative periodic function given along the interface Γ.

4.1 The Circumferentially Inhomogeneous Sliding Interface. For convenience, we introduce the parameter $\alpha(\theta)$ in place of $n(\theta)$

$$\alpha(\theta) \equiv \frac{n(\theta)R\left(\dfrac{\kappa_1}{\mu_1} + \dfrac{1}{\mu_2}\right)}{2} \tag{4.2}$$

then $1/\alpha(\theta)$ is a non-negative periodic function given on Γ. Further, let

Downloaded 04 May 2010 to 171.66.16.26. Redistribution subject to ASME license or copyright; see http://www.asme.org/terms/Terms_Use.cfm

$$\frac{\alpha_0}{\alpha(\theta)} = 1 + f(\theta), \quad \alpha_0 > 0, \quad -1 < f(\theta) \tag{4.3}$$

where α_0 is a given positive number and $f(\theta)$ is of the form

$$f(\theta) = \sum_{k=1}^{M} (a_k \sin [k\theta] + b_k \cos [k\theta]),$$

$$a_M^2 + b_M^2 \neq 0 \quad \text{unless} \quad f(\theta) \equiv 0 \quad \text{on} \quad \Gamma \tag{4.4}$$

here M is a natural number, and a_k and b_k ($k = 1, 2 \ldots M$) are some given real coefficients. Evidently, if we define

$$f(z) \equiv \frac{1}{2} \sum_{k=1}^{M} \left[ia_k \left(\frac{R^k}{z^k} - \frac{z^k}{R^k} \right) + b_k \left(\frac{R^k}{z^k} + \frac{z^k}{R^k} \right) \right] \tag{4.5}$$

then

$$f(z) = f(\theta), \quad z \in \Gamma.$$

Note that $\alpha(\theta) = \infty$ (or, equivalently, $n(\theta) = \infty$) corresponds to perfect bonding, the interface model (4.3), (4.4) is capable of simulating perfect bonding by choosing a_k and b_k ($k = 1, 2 \ldots M$) in (4.4) such that $f(\theta)$ is close to -1.

4.2 Elimination of $\phi_1(z)$. Now, we first examine the normal displacement continuity condition (4.1_1). In view of (2.10), (4.1_1) can be given in terms of $\phi_1(z)$ and $\phi_2(z)$

$$-\frac{1}{4}\left(\frac{\kappa_1}{\mu_1} + \frac{1}{\mu_2}\right)\frac{R}{z}\phi_1 - \frac{R}{4\mu_2}\left[A + \frac{B_1}{R^2} - X_1 + \frac{\bar{B}R^2}{z^2} + \frac{\overline{C_2}}{z}\right]$$

$$+ \frac{1}{4\mu_1 R}[Bz^2 + B_1 + AR^2 - \overline{X_1}R^2 + C_1 z]$$

$$+ \frac{1}{4}\left(\frac{\kappa_2}{\mu_2} + \frac{1}{\mu_1}\right)\frac{z}{R}\overline{\phi_2\left(\frac{R^2}{\bar{z}}\right)} = -\frac{1}{4}\left(\frac{\kappa_2}{\mu_2} + \frac{1}{\mu_1}\right)\frac{R}{z}\phi_2$$

$$- \frac{R}{4\mu_1}\left[A + \frac{B_1}{R^2} - X_1 + \frac{\bar{B}R^2}{z^2} + \frac{\overline{C_1}}{z}\right] + \frac{1}{4\mu_2 R}[Bz^2 + B_1$$

$$+ AR^2 - \overline{X_1}R^2 + C_2 z] + \frac{1}{4}\left(\frac{\kappa_1}{\mu_1} + \frac{1}{\mu_2}\right)\frac{z}{R}\overline{\phi_1\left(\frac{R^2}{\bar{z}}\right)}$$

$$- \epsilon_1 R - \frac{R^3}{2z^2}(\epsilon_2 + i\epsilon_3) - \frac{z^2}{2R}(\epsilon_2 - i\epsilon_3), \quad z \in \Gamma. \tag{4.6}$$

Using analytic continuation in a manner similar to that used in Section 2, we find two relations between $\phi_1(z)$ and $\phi_2(z)$:

$$-\frac{1}{4}\left(\frac{\kappa_1}{\mu_1} + \frac{1}{\mu_2}\right)\frac{R}{z}\phi_1 - \frac{R}{4\mu_2}\left[\frac{\bar{B}R^2}{z^2} + \frac{\overline{C_2}}{z}\right]$$

$$+ \frac{R}{4}A\left(\frac{\kappa_1}{\mu_1} + \frac{1}{\mu_2}\right) + \frac{R^3}{2z^2}(\epsilon_2 + i\epsilon_3) + \frac{R}{4\mu_1}\left[\bar{B}\frac{R^2}{z^2} + \frac{\overline{C_1}}{z}\right]$$

$$+ \frac{1}{4}\left(\frac{\kappa_2}{\mu_2} + \frac{1}{\mu_1}\right)\frac{z}{R}\overline{\phi_2\left(\frac{R^2}{\bar{z}}\right)} - \frac{R}{4}\overline{X_1}\left(\frac{\kappa_2}{\mu_2} + \frac{1}{\mu_1}\right) = 0,$$

$$z \in S_1 \tag{4.7}$$

and

$$-\frac{1}{4}\left(\frac{\kappa_2}{\mu_2} + \frac{1}{\mu_1}\right)\frac{R}{z}\phi_2 + \left(\frac{R}{4\mu_2} - \frac{R}{4\mu_1}\right)\left[A + \frac{B_1}{R^2} - X_1\right]$$

$$- \epsilon_1 R - \frac{z^2}{2R}(\epsilon_2 - i\epsilon_3) + \frac{1}{4\mu_2 R}[Bz^2 + B_1 + AR^2$$

$$- \overline{X_1}R^2 + C_2 z] - \frac{1}{4\mu_1 R}[Bz^2 + AR^2 + B_1$$

$$- \overline{X_1}R^2 + C_1 z] + \frac{R}{4}A\left(\frac{\kappa_1}{\mu_1} + \frac{1}{\mu_2}\right) - \frac{R}{4}\overline{X_1}\left(\frac{\kappa_2}{\mu_2} + \frac{1}{\mu_1}\right)$$

$$+ \frac{1}{4}\left(\frac{\kappa_1}{\mu_1} + \frac{1}{\mu_2}\right)\frac{z}{R}\overline{\phi_1\left(\frac{R^2}{\bar{z}}\right)} = 0, \quad z \in S_2. \tag{4.8}$$

The compatibility between (4.7) and (4.8) gives the first compatibility condition

$$2A\left(\frac{\kappa_1 - 1}{\mu_1} + \frac{2}{\mu_1}\right) - (\overline{X_1} + X_1)\left(\frac{\kappa_2 - 1}{\mu_2} + \frac{2}{\mu_1}\right) = 4\epsilon_1 \tag{4.9}$$

Next, let us consider the tangential interface condition (4.1_2). Using the relations (2.10) and (4.7), (4.8), the condition (4.1_2) can be given in terms of $\phi_2(z)$ as follows:

$$[1 + f(z)]\left[\frac{A + \frac{B_1}{R^2} + X_1}{2} + \frac{R^2(\epsilon_2 + i\epsilon_3)}{z^2\left(\frac{\kappa_1}{\mu_1} + \frac{1}{\mu_2}\right)}\right.$$

$$\left. + (1 + \eta)\frac{\bar{B}R^2}{2z^2} + \frac{1 + \beta}{2}\overline{\phi_2'\left(\frac{R^2}{z}\right)}\right]$$

$$+ [\alpha_0 - 1 - f(z)]\left[\beta\frac{z}{R^2}\overline{\phi_2}\left(\frac{R^2}{z}\right) + \frac{1}{2}(A + \beta X_1)\right]$$

$$+ \frac{\alpha_0}{2}\eta\left(A + \frac{B_1}{R^2} - \overline{X_1}\right)$$

$$= [1 + f(z)]\left[\frac{A + \frac{B_1}{R^2} + \overline{X_1}}{2} + \frac{z^2(\epsilon_2 - i\epsilon_3)}{R^2\left(\frac{\kappa_1}{\mu_1} + \frac{1}{\mu_2}\right)}\right.$$

$$\left. + (1 + \eta)\frac{Bz^2}{2R^2} + \frac{1 + \beta}{2}\phi_2'(z)\right]$$

$$+ [\alpha_0 - 1 - f(z)]\left[\beta\frac{\phi_2(z)}{z} + \frac{1}{2}(A + \beta\overline{X_1})\right]$$

$$+ \frac{\alpha_0}{2}\eta\left(A + \frac{B_1}{R^2} - X_1\right), \quad z \in \Gamma \tag{4.10}$$

where we have set

$$\beta \equiv \frac{\frac{\kappa_2}{\mu_2} + \frac{1}{\mu_1}}{\frac{\kappa_1}{\mu_1} + \frac{1}{\mu_2}} > 0, \quad \eta \equiv \frac{\frac{1}{\mu_1} - \frac{1}{\mu_2}}{\frac{\kappa_1}{\mu_1} + \frac{1}{\mu_2}}. \tag{4.11}$$

Hence, it remains to determine a single analytic function $\phi_2(z)$ in S_2 with the interface condition (4.10). It turns out that, different than the homogeneous imperfect interface, examined in Section 2, where the conventional power series method gives the finite form solution (3.2)–(3.6), the variable parameter $n(\theta)$, in the present case, prevents the exact solution for (4.10) when the power series method is used. In fact, this will lead to

Downloaded 04 May 2010 to 171.66.16.26. Redistribution subject to ASME license or copyright; see http://www.asme.org/terms/Terms_Use.cfm

a coupled infinite system of algebraic equations for the unknown coefficients $X_k (k = 1, 2 \ldots)$ and one cannot determine exact expressions for even the first few coefficients. To overcome this difficulty, a method is presented below that reduces (4.10) to a first-order differential equation for $\phi_2(z)$. In doing so, the finite form solution can be obtained for the general case of the circumferentially inhomogeneous sliding interface (4.3), (4.4).

4.3 The Differential Equation of $\phi_2(z)$. To derive the differential equation for $\phi_2(z)$, we note that the left-hand side of (4.10) is analytic in S_1 and approaches $(P_0 + P_1(z))$ at infinity, where $P_1(z)$ is defined by

$$P_1(z) \equiv \frac{1}{2}\sum_{k=1}^{M}\left[(b_k - ia_k)\frac{z^k}{R^k} \times \sum_{j=0}^{k}\left(\frac{1+\beta}{2}j - \beta\right)\overline{X_j}\left(\frac{R^2}{z}\right)^{j-1}\right] + \frac{1}{4}\left[\frac{B_1}{R^2} + (1-\beta)X_1\right]\sum_{k=1}^{M}(b_k - ia_k)\frac{z^k}{R^k} + \frac{1}{2}\left[\frac{\bar{B}}{2}(1+\eta) + \frac{\epsilon_2 + i\epsilon_3}{\left(\frac{\kappa_1}{\mu_1} + \frac{1}{\mu_2}\right)}\right] \times \sum_{k=3}^{M}(b_k - ia_k)\frac{z^{k-2}}{R^{k-2}} \quad (4.12)$$

and the constant P_0 is defined by

$$P_0 \equiv \frac{1}{2}\sum_{k=1}^{M}\left[(b_k - ia_k)R^k\left[\frac{1+\beta}{2}(k+1) - \beta\right]\overline{X_{k+1}}\right] + \frac{1}{2}(b_2 - ia_2)\left[\frac{\epsilon_2 + i\epsilon_3}{\left(\frac{\kappa_1}{\mu_1} + \frac{1}{\mu_2}\right)} + \frac{\bar{B}}{2}(1+\eta)\right] + \left[\frac{1}{2}(1+\beta) + (\alpha_0 - 1)\beta\right]\overline{X_1} + \frac{1}{2}(\alpha_0 - 1)(A + \beta X_1) + \frac{1}{2}\left[A + \frac{B_1}{R^2} + X_1\right] + \frac{\alpha_0}{2}\eta\left(A + \frac{B_1}{R^2} - \overline{X_1}\right). \quad (4.13)$$

Since the right of (4.10) is the conjugate complex value of the left, it is analytical in S_2 except at the origin where it has the singularities

$$\overline{P_1}\left(\frac{R^2}{z}\right). \quad (4.14)$$

According to analytic continuation principle, we conclude that the right and the left of (4.10) are identically equal to

$$P(z) \equiv P_1(z) + \overline{P_1}\left(\frac{R^2}{z}\right) + P_0 \quad (4.15)$$

inside and outside the circular inclusion, respectively. The compatibility between the resulting relations gives the second compatibility condition

$$P_0 = \overline{P_0}. \quad (4.16)$$

Hence, within the circular inclusion S_2, we have the relation

$$\phi_2'(z) + \frac{2\beta}{1+\beta}\frac{\alpha_0 - 1 - f(z)}{1+f(z)}\frac{\phi_2(z)}{z} = F(z), \quad z \in S_2 \quad (4.17)$$

where $F(z)$ is given by

$$\frac{1+\beta}{2}[1+f(z)]F(z) = P(z) - (1+f(z))\left[\frac{A + \frac{B_1}{R^2} + \overline{X_1}}{2} + \frac{z^2(\epsilon_2 - i\epsilon_3)}{R^2\left(\frac{\kappa_1}{\mu_1} + \frac{1}{\mu_2}\right)} + (1+\eta)\frac{Bz^2}{2R^2}\right] + \frac{1}{2}[f(z) + 1 - \alpha_0](A + \beta\overline{X_1}) - \frac{\alpha_0}{2}\eta\left(A + \frac{B_1}{R^2} - X_1\right), \quad z \in S_2. \quad (4.18)$$

The Eq. (4.17) can be regarded as a first-order differential equation for $\phi_2(z)$ having variable coefficients. Its general solution is given by

$$\phi_2(z) = C(z)\exp^{Q(z)},$$

$$C(z) = \int_{z_0}^{z} F(t)\exp^{-Q(t)}dt + C_0, \quad z \in S_2 \quad (4.19)$$

$$Q(z) = \frac{2\beta}{1+\beta}\int\frac{1+f(z)-\alpha_0}{z[1+f(z)]}dz \quad (4.20)$$

where C_0 is an arbitrary constant of integration and z_0 an arbitrary point within S_2.

Since the nonhomogeneous term $F(z)$ includes the $(M+1)$ unknown constants $X_k (k = 1, 2 \ldots M+1)$, in view of (2.7), any admissible solution $\phi_2(z)$ of (4.17) has to satisfy the consistency conditions

$$\frac{\phi_2^{(k)}(0)}{k!} = X_k, \quad k = 1, \ldots (M+1) \quad (4.21)$$

To verify (4.21), we assume that (4.17) has an analytic solution $\phi_2(z)$ in S_2 which admits a Taylor expansion. Substituting this expansion into (4.17) and equating the coefficients for each of all nonpositive powers of z (from z^{-M} to z^0), we obtain $(M+1)$ conditions which are turned out to be identical to (4.21), provided that $\beta \neq 1$. This implies that any analytic solution of (4.17) in S_2 will automatically satisfy (4.21) when $\beta \neq 1$. If $\beta = 1$, however, one of the aforementioned $(M+1)$ conditions, obtained by equating the coefficients of z^{-M}, becomes an identity. Consequently, when $\beta = 1$, the first one of the $(M+1)$ consistency conditions (4.21) cannot be automatically satisfied by the analytic solution of (4.17). Therefore, when $\beta = 1$, the admissible analytic solution of (4.17) will be required to satisfy an additional condition

$$\phi_2^{(1)}(0) = X_1, \quad \text{when} \quad \beta = 1. \quad (4.22)$$

On the other hand, the presence of irregular points, such as poles and/or branch points of the multivalued functions appearing in (4.17)–(4.20), implies that the solution $\phi_2(z)$, given by (4.19), is defined only in the simply connected region obtained by cutting S_2 along some appropriately chosen lines. Accordingly, $\phi_2(z)$ given by (4.19) is not, in general, analytic in the uncut region. For example, it may be discontinuous across branch cuts or/and may become unbounded at some or all iso-

Downloaded 04 May 2010 to 171.66.16.26. Redistribution subject to ASME license or copyright; see http://www.asme.org/terms/Terms_Use.cfm

lated irregular points. To ensure the analyticity of $\phi_2(z)$ in the uncut region S_2, therefore, we have to verify (i) $\phi_2(z)$ given by (4.19) is bounded at all irregular points, and (ii) $\phi_2(z)$ given by (4.19) is continuous across all branch cuts.

In summary, the solution $\phi_2(z)$ is given by (4.19) that includes the $(M + 1)$ unknown constants X_k $(k = 1, 2 \ldots M + 1)$. These constants can be determined by the analyticity requirements of $\phi_2(z)$, given by (4.19), the compatibility conditions (4.9), (4.16) and the consistency condition (4.22) (applicable only when $\beta = 1$). Once $\phi_2(z)$ is known, the other three functions $\phi_1(z)$, $\psi_1(z)$, and $\psi_2(z)$ can be found from (4.7), (2.10). In the following sections, a particular class of inhomogeneous sliding interface serves to illustrate the method.

5 A Class of Inhomogeneous Sliding Interface

For sake of illustration, we consider the class of inhomogeneous sliding interface defined by

$$f(\theta) = b_M \cos [M\theta], \quad f(z) = \frac{b_M}{2}\left(\frac{z^M}{R^M} + \frac{R^M}{z^M}\right), \qquad -1 < b_M < 1. \quad (5.1)$$

As a polynomial of degree $2M$, the equation

$$\frac{2}{b_M}\left(\frac{z}{R}\right)^M + \left(\frac{z}{R}\right)^{2M} + 1 = 0 \quad (5.2)$$

has M roots within the unit circle. Let that the M roots be denoted by

$$\rho_1, \rho_2, \ldots \rho_M$$

then they can be determined by

$$\rho^M = \rho^* \quad (5.3)$$

where ρ^* is a real number, between -1 and 1, given by

$$\rho^* = \begin{cases} \sqrt{\dfrac{1}{b_M^2} - 1} - \dfrac{1}{b_M} < 0, & \text{when} \quad b_M > 0, \\ -\sqrt{\dfrac{1}{b_M^2} - 1} - \dfrac{1}{b_M} > 0, & \text{when} \quad b_M < 0. \end{cases} \quad (5.4)$$

In particular

$$\rho^{*2} \to 1, \quad \text{when} \quad b_M^2 \to 1,$$

$$\rho^* \to -\frac{b_M}{2}, \quad \text{when} \quad b_M \to 0.$$

Note that

$$\frac{(\alpha_0 - 1) - f(z)}{\dfrac{z}{R}[1 + f(z)]} = \frac{-1}{\left(\dfrac{z}{R}\right)} - \lambda \frac{\dfrac{z^{M-1}}{R^{M-1}}}{\left(\dfrac{z^M}{R^M} - \rho^*\right)} + \lambda \frac{\dfrac{z^{M-1}}{R^{M-1}}}{\left(\dfrac{z^M}{R^M} - \frac{1}{\rho^*}\right)},$$

$$\lambda \equiv \alpha_0 \frac{(1 + \rho^{*2})}{(\rho^{*2} - 1)} < 0 \quad (5.5)$$

then the general solution (4.19) has now the form

$$\phi_2(z) = \left(\frac{z}{R}\right)^{2\beta/(1+\beta)} \left(\frac{z^M}{R^M} - \rho^*\right)^{2\beta\lambda/(1+\beta)M} \times \left(\frac{z^M}{R^M} - \frac{1}{\rho^*}\right)^{-2\beta\lambda/(1+\beta)M} \int_{R\rho_1}^{z} F(t)\left(\frac{t}{R}\right)^{-2\beta/(1+\beta)} \times \left(\frac{t^M}{R^M} - \rho^*\right)^{-2\beta\lambda/(1+\beta)M} \left(\frac{t^M}{R^M} - \frac{1}{\rho^*}\right)^{2\beta\lambda/(1+\beta)M} dt \quad (5.6)$$

where S_2 is cut along some nonintersecting straight lines, issuing from each of the irregular points in S_2, such that $\phi_2(z)$ given by (5.6) is well defined in the cut simply connected region S_2. Owing to $\lambda < 0$, the integral in (5.6) is convergent at each of the M branch points, $z = R\rho_k$ $(k = 1, \ldots M)$, and then the integration path can be taken along the edges of any one of the M branch cuts made from $z = R\rho_k$ $(k = 1, \ldots M)$ and pass through any one of the M integrable branch points. In this way, note that the multi-valued functions appearing under and outside the integral sign compensate each other, $\phi_2(z)$ given by (5.6) is continuous across each of the M branch cuts, made from $z = R\rho_k$ $(k = 1, \ldots M)$ (cf. Muskhelishvili (1963) and England (1971)). On the other hand, the boundedness of $\phi_2(z)$ at $z = R\rho_1$ and the other $(M - 1)$ branch points gives $C_0 = 0$ and

$$\int_{R\rho_1}^{R\rho_k} F(z)\left(\frac{t}{R}\right)^{-2\beta/(1+\beta)} \left(\frac{t^M}{R^M} - \rho^*\right)^{-2\beta\lambda/(1+\beta)M} \times \left(\frac{t^M}{R^M} - \frac{1}{\rho^*}\right)^{2\beta\lambda/(1+\beta)M} dt = 0, \quad k = 2, 3, \ldots M \quad (5.7)$$

respectively. To determine the $(M + 1)$ unknown complex constants X_k $(k = 1, \ldots M + 1)$, in addition to the two real compatibility conditions (4.9), (4.16) and the $(M - 1)$ complex boundedness conditions (5.7), one more complex-form condition is needed. This condition will be provided by the analyticity of $\phi_2(z)$, given by (5.6), at the remaining irregular point $z = 0$. Since its form depends on the value of β, we have to discuss three possible cases separately.

5.1 $\beta > 1$. In this case, $\phi_2(z)$ given by (5.6) vanishes as z tends to $z = 0$. To guarantee the analyticity of $\phi_2(z)$ in S_2, it remains to verify the continuity of the right of (5.6) across the straight branch cut made from the branch point $z = 0$. This requires that two limit values of the following varying-limit integral

$$\int_{R\rho_1}^{z} F(t)\left(\frac{z}{t}\right)^{2\beta/(1+\beta)} \left[\frac{\dfrac{z^M}{R^M} - \rho^*}{\dfrac{t^M}{R^M} - \rho^*}\right]^{2\beta\lambda/(1+\beta)M} \times \left[\frac{\dfrac{t^M}{R^M} - \dfrac{1}{\rho^*}}{\dfrac{z^M}{R^M} - \dfrac{1}{\rho^*}}\right]^{2\beta\lambda/(1+\beta)M} dt \quad (5.8)$$

are equal when the upper limit z approaches any point on the branch cut from both sides, respectively. Here, because the integrand in (5.8) has an unintegrable singularity at $z = 0$, the integration path cannot pass through the point $z = 0$.

Note that the integration of the integrand in (5.8) over any segment of one edge of the straight branch cut is equal to its integration over the same segment of the opposite edge, the condition (5.8) holds for all points provided that it holds for any particular point on the branch cut. Hence, the condition (5.8) can be given by

$$\int_{\Gamma^*} F(t)\left(\frac{z^*}{t}\right)^{2\beta/(1+\beta)} \left[\frac{\dfrac{z^{*M}}{R^M} - \rho^*}{\dfrac{t^M}{R^M} - \rho^*}\right]^{2\beta\lambda/(1+\beta)M} \times \left[\frac{\dfrac{t^M}{R^M} - \dfrac{1}{\rho^*}}{\dfrac{z^{*M}}{R^M} - \dfrac{1}{\rho^*}}\right]^{2\beta\lambda/(1+\beta)M} dt = 0, \quad \beta > 1 \quad (5.9)$$

where z^* is any particular point on the branch cut, and Γ^* is

Downloaded 04 May 2010 to 171.66.16.26. Redistribution subject to ASME license or copyright; see http://www.asme.org/terms/Terms_Use.cfm

an arbitrary closed curve within S_2, enclosing $z = 0$ and passing through the points $z = z^*$ and $z = R\rho_1$. In particular, in (5.9), the value of z^* jumps from one edge of the branch cut to the opposite edge when the variable of integration, t, passes through the point $z = R\rho_1$ along Γ^*. Hence, when $\beta > 1$, the additional condition is provided by (5.9) and the $(M + 1)$ constants X_k $(k = 1, 2, \ldots M + 1)$ are determined by (4.9), (4.16), (5.7), and (5.9).

5.2 $\beta < 1$. In this case, (5.6) can be written into the form

$$\frac{\phi_2}{\frac{z}{R}} = \left(\frac{z}{R}\right)^{(\beta-1)/(1+\beta)} \times \left(\frac{z^M}{R^M} - \rho^*\right)^{2\beta\lambda/(1+\beta)M} \left(\frac{z^M}{R^M} - \frac{1}{\rho^*}\right)^{-2\beta\lambda/(1+\beta)M} \times \int_{R\rho_1}^{z} F(t)\left(\frac{t}{R}\right)^{-2\beta/(1+\beta)} \left(\frac{t^M}{R^M} - \rho^*\right)^{-2\beta\lambda/(1+\beta)M} \times \left(\frac{t^M}{R^M} - \frac{1}{\rho^*}\right)^{2\beta\lambda/(1+\beta)M} dt. \quad (5.10)$$

In view of the fact that $X_0 = 0$, the left-hand side of (5.10) is analytic within S_2 and, consequently, it must be bounded at $z = 0$. Owing to $\beta < 1$, it follows that

$$\int_{R\rho_1}^{0} F(t)\left(\frac{t}{R}\right)^{-2\beta/(1+\beta)} \left(\frac{t^M}{R^M} - \rho^*\right)^{-2\beta\lambda/(1+\beta)M} \times \left(\frac{t^M}{R^M} - \frac{1}{\rho^*}\right)^{2\beta\lambda/(1+\beta)M} dt = 0, \quad \beta < 1. \quad (5.11)$$

Note that the integration path can pass through the integrable branch point $z = 0$, $\phi_2(z)$, given by (5.10), is continuous across the branch cut made from $z = 0$. Hence, when $\beta < 1$, the $(M + 1)$ constants X_k $(k = 1, \ldots M + 1)$ are determined by (4.9), (4.16), (5.7), and (5.11).

5.3 $\beta = 1$. Finally, we examine the case $\beta = 1$. In this case, $z = 0$ is not a branch point and $F(0) = 0$ (then $F(z)/z$ is not singular at $z = 0$). Hence, $\phi_2(z)$, given by (5.6), is zero at $z = 0$. On the other hand, the consistency condition (4.22), which applies when $\beta = 1$, gives

$$RX_1 = (-\rho^*)^{\lambda/M}\left(-\frac{1}{\rho^*}\right)^{-\lambda/M} \int_{R\rho_1}^{0} \frac{F(t)}{\frac{t}{R}} \times \left(\frac{t^M}{R^M} - \rho^*\right)^{-\lambda/M}\left(\frac{t^M}{R^M} - \frac{1}{\rho^*}\right)^{\lambda/M} dt \quad (5.12)$$

Thus, when $\beta = 1$, the $(M + 1)$ constants X_k $(k = 1, \ldots M + 1)$ are determined by (4.9), (4.16), (5.7), and (5.12).

In summary, for the inhomogeneous sliding interface (5.1), the solution $\phi_2(z)$ is given by (5.6) and the $(M + 1)$ unknown constants X_k $(k = 1, \ldots M + 1)$ are determined by a system of $(M + 1)$ linear algebraic equations. It turns out that the $(M + 1)$ constants X_k $(k = 1, \ldots M + 1)$ can be given in terms of the definite integrals of several known power functions and then the rigorous solution $\phi_2(z)$ can be obtained in a finite form.

6 Discussions

Here, for sake of illustrating the method, several examples are discussed in detail. To be definite, we confine ourselves to the case $\beta = 1$. In this case, $\phi_2(z)$ is given by

$$\frac{\phi_2(z)}{\left(\frac{z}{R}\right)} = \left(\frac{z^M}{R^M} - \rho^*\right)^{\lambda/M}\left(\frac{z^M}{R^M} - \frac{1}{\rho^*}\right)^{-\lambda/M} \times \int_{R\rho_1}^{z} \frac{F(t)}{\left(\frac{t}{R}\right)}\left(\frac{t^M}{R^M} - \rho^*\right)^{-\lambda/M}\left(\frac{t^M}{R^M} - \frac{1}{\rho^*}\right)^{\lambda/M} dt \quad z \in S_2 \quad (6.1)$$

and $F(z)$ is given by (4.18) that includes the $(M + 1)$ unknown constants X_k $(k = 1, \ldots M + 1)$.

6.1 Examples. First, we give the explicit results. For instance, when $M = 1$, the only two unknown constants X_1 and X_2 can be obtained from (4.9), (4.16), and (5.12), with the results

$$X_1 = A - 2\frac{\mu_1}{1 + \kappa_1}\epsilon_1 + \frac{b_1 R}{2\alpha_0(\eta - 1)}(X_2 - \overline{X_2})$$

$$X_2 R^2 \frac{\rho^*}{\lambda(1 - \rho^{*2})} = \left[(1 + \eta)\frac{B}{2} + \frac{\epsilon_2 - i\epsilon_3}{\frac{\kappa_1}{\mu_1} + \frac{1}{\mu_2}} \quad I_1\right] \quad (6.2)$$

where

$$\frac{I_1}{R} = (-\rho^*)^{\lambda}\left(-\frac{1}{\rho^*}\right)^{-\lambda} \int_{\rho^*}^{0} t(t - \rho^*)^{-\lambda}\left(t - \frac{1}{\rho^*}\right)^{\lambda} dt \quad (6.3)$$

It is verified that $X_2 = 0$ when $\rho^* = 0$. This agrees with the result obtained in Section 3 for a homogeneous imperfect interface. In this case, X_1 given by (6.2) is identical to that given by (3.3). Obviously, once X_1 and X_2 are known, $\phi_2(z)$ is given by (6.1) in a finite form. For example, when $\lambda = -1$, the explicit expression for $\phi_2(z)$ is given by

$$\phi_2(z) = z\left[A + \eta(A - \overline{X_1}) + \frac{b_1 R\overline{X_2}}{2\alpha_0}\right] - (1 + \eta)\frac{B}{2}z\left[\left(\frac{z}{R} - \frac{1}{\rho^*}\right)\left(\frac{z}{2R} + \frac{1}{\rho^*} - \frac{\rho^*}{2}\right) + \frac{(1 - \rho^{*2})\left(\frac{z}{R} - \frac{1}{\rho^*}\right)}{\rho^{*2}\left(\frac{z}{R} - \rho^*\right)} \ln\left[\frac{\left(1 - \rho^*\frac{z}{R}\right)}{(1 - \rho^{*2})}\right]\right], \quad z \in S_2 \quad (6.4)$$

and $\phi_1(z)$, $\psi_1(z)$, and $\psi_2(z)$ can be obtained immediately from (4.7), (2.10), and (2.11). Despite its elementary form, the solution (6.4) cannot be obtained by the power series method because its Taylor expansion is an infinite series.

When $M = 2$, on the other hand, the boundedness condition (5.7) at $z = R\rho_2$ implies $X_2 = 0$ and the nonzero constant X_1 and X_3 are given by

$$2X_1 = \frac{2b_2 R^2}{\alpha_0(\eta - 1)}(X_3 - \overline{X_3}) + \frac{b_2}{\alpha_0(\eta - 1)} \times \left[\frac{1 + \eta}{2}(B - \overline{B}) - \frac{2i\epsilon_3}{\frac{\kappa_1}{\mu_1} + \frac{1}{\mu_2}}\right] + 2A - 4\epsilon_1\frac{\mu_1}{1 + \kappa_1},$$

Downloaded 04 May 2010 to 171.66.16.26. Redistribution subject to ASME license or copyright; see http://www.asme.org/terms/Terms_Use.cfm

$$2X_3R^2\frac{\rho^*}{\lambda(1-\rho^{*2})}=\left[(1+\eta)\frac{B}{2}+\frac{\epsilon_2-i\epsilon_3}{\frac{\kappa_1}{\mu_1}+\frac{1}{\mu_2}}\right]\times\left(\frac{I_2}{R}-\frac{\rho^*}{\lambda(1-\rho^{*2})}\right)\quad(6.5)$$

where

$$2\frac{I_2}{R}=|\rho^*|^{\lambda}\int_{\rho^*}^{0}\left|\frac{t-\rho^*}{t-\frac{1}{\rho^*}}\right|^{-(\lambda/2)}dt.\quad(6.6)$$

Once X_1 and X_3 are known, the rigorous solution $\phi_2(z)$ is given by (6.1) and $\phi_1(z)$, $\psi_1(z)$, and $\psi_2(z)$ can be found from (4.7), (2.10), and (2.11).

6.2 The Average Stresses. The solutions given above are now used to examine the effects of the circumferential inhomogeneity of a sliding interface on local and average stresses. First, we consider the average stresses. The exact average stresses within the circular inclusion can be calculated by

$$\overline{\sigma_{xx}}+\overline{\sigma_{yy}}=2[X_1+\overline{X_1}],$$

$$\overline{\sigma_{xx}}-i\overline{\sigma_{xy}}=X_1+\overline{X_1}-2\left[\frac{\beta}{2}R^2X_3+(1+\eta)\frac{B}{2}+\frac{\epsilon_2-i\epsilon_3}{\frac{\kappa_1}{\mu_1}+\frac{1}{\mu_2}}\right]\quad(6.7)$$

where the bar "–" denotes the average value. One of the advantages of the present method is that the exact values of X_1 and X_3 can be obtained without knowledge of the complete solution. Consequently, the exact average stresses can be calculated through (6.7) without solving the full problem. To demonstrate this, let us consider the inhomogeneous interface defined by $\beta = 1$ and $M = 2$, namely

$$\frac{1}{n(\theta)}=\frac{R\left(\frac{\kappa_1}{\mu_1}+\frac{1}{\mu_2}\right)}{2\alpha_0}(1+b_2\cos[2\theta]),\qquad -1<b_2<1.\quad(6.8)$$

For sake of comparison, we also consider the corresponding homogeneous interface ($b_2 = 0$, under otherwise identical conditions)

$$\frac{1}{n(\theta)}=\frac{R\left(\frac{\kappa_1}{\mu_1}+\frac{1}{\mu_2}\right)}{2\alpha_0}.\quad(6.9)$$

Obviously, (6.9) can be regarded as the average value of (6.8). In addition, all eigenstrains are taken to be zero. Thus, the average stresses associated with the homogeneous interface (6.9) can be obtained from (3.1)–(3.6) as follows:

$$(\overline{\sigma_{xx}}+\overline{\sigma_{yy}})_0=4A,\qquad\left(\frac{\overline{\sigma_{yy}}-\overline{\sigma_{xx}}}{2}+i\overline{\sigma_{xy}}\right)_0=B(1+\eta)\frac{2\alpha_0+3}{2\alpha_0+4}\quad(6.10)$$

where the subscript "0" indicates the stresses associated with the homogeneous interface. Next, the average stresses associated with the inhomogeneous interface (6.8) are found from (6.5), (6.7) as

$$\overline{\sigma_{xx}}+\overline{\sigma_{yy}}=4A,\qquad\frac{\overline{\sigma_{yy}}-\overline{\sigma_{xx}}}{2}+i\overline{\sigma_{xy}}=(1+\eta)B\left[\frac{3}{4}-\frac{\alpha_0I_2(\rho^{*2}+1)}{4R\rho^*}\right]\quad(6.11)$$

where I_2 is given by (6.6). Thus, the average mean stress within the circular inclusion is independent of the detail of a sliding interface (this general result can be readily seen from (4.9) and (6.6)). On the other hand, the deviatoric and shear components of the average stress, associated with (6.8) and (6.9), respectively, are related by

$$\frac{\overline{\sigma_{yy}}-\overline{\sigma_{xx}}}{2}+i\overline{\sigma_{xy}}=h(\rho^*,\alpha_0)\left[\frac{\overline{\sigma_{yy}}-\overline{\sigma_{xx}}}{2}+i\overline{\sigma_{xy}}\right]_0,$$

$$h(\rho^*,\alpha_0)\equiv\frac{2\alpha_0+4}{2\alpha_0+3}\left[\frac{3}{4}-\frac{\alpha_0I_2(\rho^{*2}+1)}{4R\rho^*}\right].\quad(6.12)$$

Hence, the effect of the circumferential inhomogeneity is represented by a single function $h(\rho^*, \alpha_0)$. Somewhat surprisingly, $h(\rho^*, \alpha_0)$ is found to be very close to unity over a wide range of interface parameters α_0 and ρ^* (for instance, the error is typically less than five percent for $-0.95 < \rho^* < 0.95$ and $0.1 < \alpha_0 < 100$). Hence, the average stresses associated with the inhomogeneous interface (6.8) can be estimated, with only an ignorable error, using the homogeneous interface (6.9). This insensitivity is attributed to the symmetric character of the inhomogeneous interface (6.8) (it has two mutually orthogonal axes of symmetry) and the continuity of the normal displacement throughout the sliding interface ($m = \infty$).

6.3 The Mean Stress. Finally, we examine the effect of the circumferential inhomogeneity of a sliding interface on local stresses at the interface. Because the mean stress gives the simplest measure of stress intensity, we consider the mean stress for the special case $\beta = 1$, $M = 1$, and $\lambda = -1$. For sake of comparison, together with the inhomogeneous interface

$$\frac{1}{n(\theta)}=\frac{R\left(\frac{\kappa_1}{\mu_1}+\frac{1}{\mu_2}\right)}{2\alpha_0}(1+b_1\cos[\theta]),\qquad\alpha_0=\frac{1-\rho^{*2}}{1+\rho^{*2}},\quad -1<b_1<1\quad(6.13)$$

we also consider the corresponding homogeneous interface ($b_1 = 0$, under otherwise identical conditions)

$$\frac{1}{n(\theta)}=\frac{R\left(\frac{\kappa_1}{\mu_1}+\frac{1}{\mu_2}\right)}{2\alpha_0},\quad\alpha_0=\frac{1-\rho^{*2}}{1+\rho^{*2}}.\quad(6.14)$$

In addition, we assume that Im $[B] = 0$ (bi-axial stress state) and all eigenstrains vanish. Thus, the mean stress at the interface, associated with the homogeneous interface (6.14), is given by

$$\left(\frac{\sigma_{rr}+\sigma_{\theta\theta}}{2}\right)_0\Bigg|_{S_2\to\Gamma}=2A-\frac{3(1+\eta)(1+\rho^{*2})}{3+\rho^{*2}}B\cos[2\theta]\quad(6.15)$$

and the corresponding mean stress, associated with the inhomogeneous interface (6.13), can be found from (6.2)–(6.4) as follows:

Downloaded 04 May 2010 to 171.66.16.26. Redistribution subject to ASME license or copyright; see http://www.asme.org/terms/Terms_Use.cfm

$$\left.\frac{\sigma_{rr}+\sigma_{\theta\theta}}{2}\right|_{S_2\to\Gamma} = 2A + \frac{b_1 R X_2}{\alpha_0}$$

$$- (1+\eta)B\ \mathrm{Re}\left[\frac{3}{2}\frac{z^2}{R^2} + \left(1 - \frac{z}{R}\rho^*\right)\frac{(1-\rho^{*2})}{\rho^{*2}\left|\frac{z}{R} - \rho^*\right|^2}\right.$$

$$\left. + \frac{z}{R}\left(\frac{1}{\rho^*} - \rho^*\right) + \frac{1}{2} - \frac{1}{\rho^{*2}} + \frac{(1-\rho^{*2})}{\rho^{*2}\left|\frac{z}{R} - \rho^*\right|^2}\right.$$

$$\times \ln\left[\frac{\left(1 - \frac{z}{R}\rho^*\right)}{(1-\rho^{*2})}\right]\left[2 - \frac{z}{R}\rho^* - \frac{\bar{z}}{R\rho^*}\right.$$

$$\left.\left. + \frac{(1-\rho^{*2})}{\rho^*\left|\frac{z}{R} - \rho^*\right|^2}\left[\frac{\bar{z}}{R} - 2\rho^* + \frac{z}{R}\rho^{*2}\right]\right]\right]. \quad (6.16)$$

For example, for the uniaxial tension along the x-axis, $2A + B = 0$, and then the ratio of the mean stress (6.16) to (6.15) at the point $z = R$ gives

$$g(\eta, \rho^*) = \frac{3 + \rho^{*2}}{3 + \rho^{*2} + 3(1+\eta)(1+\rho^{*2})}$$

$$\times\left[1 + (1+\eta)\left[2 - \rho^* + \frac{2}{\rho^*} - 2\frac{(1+\rho^*)}{\rho^{*2}}\right.\right.$$

$$\times \ln[(1+\rho^*)] + \frac{1}{\rho^{*2}}\left[1 - \frac{\rho^{*2}}{2} + \frac{(1-\rho^{*2})}{\rho^{*2}}\right.$$

$$\left.\left.\left.\times \ln[(1-\rho^{*2})]\right]\right]\right]. \quad (6.17)$$

The function $g(\eta, \rho^*)$ is depicted in Fig. 2 for several different values of η. It is seen that the circumferential variation of the interface (6.13) has a significant effect on the mean stress at the interface. In the present case, replacing the inhomogeneous interface (6.13) by its average value (6.14) leads to a relative error up to 80 percent in the mean stress at the point $z = R$.

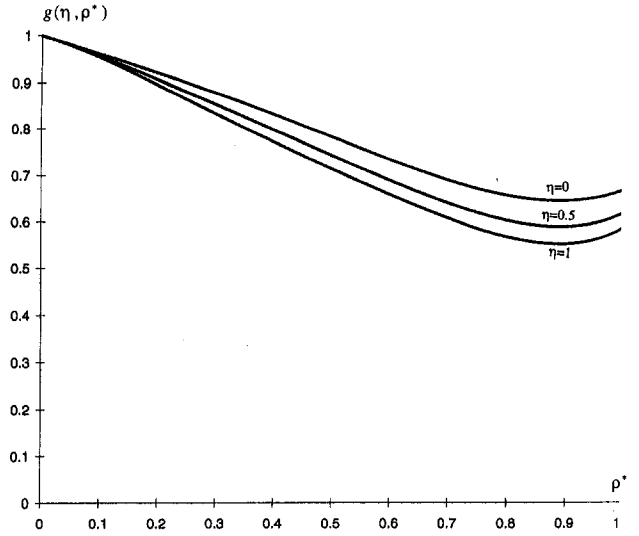

Fig. 2 The effect of the circumferential inhomogeneity of the sliding interface (6.13) on the mean stress at the point $z = R$

Acknowledgment

This work was completed when the author was a post-doctoral fellow supported by the Natural Science and Engineering Research Council of Canada through Profs. David Steigmann and Peter Schiavone in the University of Alberta. The author is greatly indebted to Schiavone and Steigmann for their useful discussions that have stimulated this research.

References

Achenbach, J. D., and Zhu, H., 1989, "Effects of interfacial zone on mechanical behaviour and failure of fibre-reinforced composites," *Journal of Mechanics and Physics of Solids,* Vol. 37, pp. 381–393.

Benveniste, Y., 1984, "On the effect of debonding on the overall behaviour of composite materials," *Mechanics of Materials,* Vol. 3, pp. 349–358.

England, A. H., 1971, *Complex Variable Method in Elasticity,* Wiley Interscience, London.

Gao, J., 1995, "A Circular Inclusion With Imperfect Interface: Eshelby's Tensor and Related Problems," ASME JOURNAL OF APPLIED MECHANICS, Vol. 62, pp. 860–866.

Hashin, Z., 1990, "Thermoelastic properties of fibre composites with imperfect interface," *Mechanics of Materials,* Vol. 8, pp. 333–348.

Hashin, Z., 1991, "The Spherical Inclusion With Imperfect Interface," ASME JOURNAL OF APPLIED MECHANICS, Vol. 58, pp. 444–449.

Jasiuk, I., and Kouider, M. W., 1993, "The effect of an inhomogeneous interphase on the elastic constants of transversely isotropic composites," *Mechanics of Materials,* Vol. 15, pp. 53–63.

Jun, S., and Jasiuk, I., 1993, "Elastic moduli of two-dimensional composites with sliding inclusions—A comparison of effective medium theories," *International Journal of Solids and Structures,* Vol. 30, pp. 2501–2523.

Karihaloo, B. L., and Viswanathan, K., 1985, "Elastic Field of a Partially Debonded Elliptic Inhomogeneity in an Elastic Matrix (Plane-Strain), ASME JOURNAL OF APPLIED MECHANICS, Vol. 52, pp. 835–840.

Muskhelishvili, N. I., 1963, *Some Basic Problems of the Mathematical Theory of Elasticity,* P. Noordhoff Ltd., Groningen, Netherlands.

Tandon, G. P., and Pagano, N. J., 1996, "Effective thermoelastic moduli of a unidirectional fiber composite containing interfacial arc microcracks," ASME JOURNAL OF APPLIED MECHANICS, Vol. 63, pp. 210–217.

Thorpe, M. F., and Jasiuk, I., 1992, "New results in the theory of elasticity for two-dimensional composites," *Proceedings of the Royal Society of London,* Vol. A438, pp. 531–544.

Downloaded 04 May 2010 to 171.66.16.26. Redistribution subject to ASME license or copyright; see http://www.asme.org/terms/Terms_Use.cfm

H. Poon
Postdoctoral Research Associate,
National Center for
Supercomputing Applications,
University of Illinois at
Urbana—Champaign,
Urbana, IL 61801

S. Mukherjee
Professor,
Department of Theoretical
and Applied Mechanics,
Cornell University,
Ithaca, NY 14853
Fellow ASME

M. Fouad Ahmad
Senior Research Scientist,
National Center for Supercomputing
Applications,
University of Illinois at
Urbana—Champaign,
Urbana, IL 61801
Mem. ASME

Use of "Simple Solutions" in Regularizing Hypersingular Boundary Integral Equations in Elastoplasticity

The subject of this paper is the use of "simple solutions" or "modes" to regularize a hypersingular boundary integral equations (HBIE) for small strain elastoplasticity. A particularly simple form of the regularized HBIE is obtained by the use of three global "modes" of deformation: rigid-body displacement, linear displacement, and a fully constrained plastic solution. The resulting regularized HBIE is used in an implicit boundary element method (BEM) scheme for solving elastoplasticity problems. Numerical results are presented for an illustrative plane-strain example.

1 Introduction

This paper is concerned with the use of "simple solutions" or "modes" for regularization of hypersingular boundary integral equations (HBIEs) in small-strain elastoplasticity. Hypersingular integrals, and their role in the boundary element method (BEM), is a subject of considerable current research interest. A recent review article by Tanaka et al. (1994) cites 350 references! An updated review of HBIEs can be found in Paulino (1995). It is fair to say that most research papers to date, that are concerned with hypersingular integrals, address linear problems. Exceptions are recent papers by Leitao et al. (1995), Huber et al. (1996), and Bonnet et al. (1998) that are concerned with elastoplasticity. The hypersingular expression in Leitao et al. (1995) is not regularized, but contains Cauchy Principal Value (CPV) and Hadamard Finite Part (HFP) integrals. In their numerical implementation, these authors employ tricks such as discontinuous domain cells, collocating at nodes away from the boundary.

Huber et al. (1996) have derived a three-dimensional hypersingular BIE for elastoplasticity and have used it to compute surface stresses. Their regularization procedure, which is an extension of the method proposed by Guiggiani et al. (1992) for linear elasticity, is quite complicated. They should, however, be commended for carrying out a three-dimensional numerical implementation. Bonnet et al. (1998) present a different approach, which transfers tangential derivatives from the singular kernels to the displacements, so that the final form is fully regularized. An implicit BEM with the consistent tangent operator (CTO) is employed in Bonnet et al. (1998), while Huber et al. (1996) do not use the CTO in their work.

A powerful method for regularization of HBIEs is the use of simple solutions or modes. In this approach, certain global solutions (e.g., rigid-body displacement, constant strain, etc.), of the boundary value problem under consideration, are used to derive identities that enable one to obtain regularized integral equations. This approach was first proposed for the regularization of HBIEs, for linear boundary value problems, by Rudolphi (see, for example, Krishnasamy et al., 1992). Lutz et al. (1992) have successfully applied this idea to three-dimensional linear elastic fracture mechanics. To the best of the author's knowledge, the present paper is the first one to use modes to regularize an HBIE that arises in the nonlinear problem of elastoplasticity. In addition to the usual constant and linear displacement modes, a fully constrained plastic mode is also employed here. The resulting regularized HBIE (Eq. (14)—the key contribution of this work) is of surprisingly simple form. Also, following Cruse and Richardson (1996) for the elastic case, Eq. (14) is valid at any boundary point (including edges or corners), provided that the stress, strain, and plastic strain are continuous at that point. (It is worth mentioning here that the regularized equations presented by Huber et al. (1996) are not valid at an edge or corner—please see the second paragraph on page 2568 of their paper.) Numerical implementation of Eq. (14), however, has only been carried out at regular boundary points in the present work.

An important issue that should be mentioned here is that, while the HBIE is employed in many papers, including the present one, to obtain boundary values of strains, the usefulness of HBIEs far exceeds this application. HBIEs, for example, have been employed in wave scattering (e.g., Krishnasamy et al., 1990), in fracture mechanics (e.g., Gray et al., 1990; Lutz et al., 1992; Paulino, 1995; Gray and Paulino, 1998), to obtain symmetric Galerkin boundary element formulations (e.g., Bonnet, 1995; Gray et al., 1995; Gray and Paulino, 1997), and in adaptive analysis (e.g., Paulino et al., 1996; Menon, 1996; Menon et al., 1998).

This paper is organized as follows. The use of modes for regularizing an HBIE in elastoplasticity is presented first. A convenient computable form of this equation, for plane strain, is derived next. A summary of an implicit solution scheme with

Contributed by the Applied Mechanics Division of THE AMERICAN SOCIETY OF MECHANICAL ENGINEERS for publication in the ASME JOURNAL OF APPLIED MECHANICS.

Discussion on the paper should be addressed to the Technical Editor, Professor Lewis T. Wheeler, Department of Mechanical Engineering, University of Houston, Houston, TX 77204-4792, and will be accepted until four months after final publication of the paper itself in the ASME JOURNAL OF APPLIED MECHANICS.

Manuscript received by the ASME Applied Mechanics Division, Feb. 4, 1997; final revision, May, 27, 1997. Associate Technical Editor: R. Becker.

 Copyright © 1998 by ASME

Downloaded 04 May 2010 to 171.66.16.26. Redistribution subject to ASME license or copyright; see http://www.asme.org/terms/Terms_Use.cfm

the CTO (Bonnet and Mukherjee, 1996; Poon et al., 1998; Bonnet et al., 1998) comes next. The final section presents numerical results for the problem of a square plate, with a circular hole, stretched under plane-strain conditions.

2 Boundary Integral Equations for Elastoplasticity

A brief summary of the BIE for elastoplasticity, from Bonnet and Mukherjee (1996), is presented in this section.

The regularized boundary integral equation (BIE) (without body forces) in the presence of plastic strain reads

$$\int_{\partial\Omega} [u_i(\mathbf{z}) - u_i(\mathbf{x})] P_i^k(\mathbf{x}, \mathbf{z}) dS_z - \int_{\partial\Omega} p_i(\mathbf{z}) U_i^k(\mathbf{x}, \mathbf{z}) dS_z = \int_{\Omega} U_{i,j}^k(\mathbf{x}, \mathbf{z}) C_{ijab} \epsilon_{ab}^p(\mathbf{z}) dV_z \quad (1)$$

where $\mathbf{x}$ is any fixed source point on the boundary $\partial\Omega$, and $\mathbf{p}$, $\mathbf{u}$, $\boldsymbol{\epsilon}^p$ denote the traction, displacement, and plastic strain, respectively. U_i^k, P_i^k are the Kelvin displacement and traction kernels. The variable field point is denoted by $\mathbf{z}$ and $_{,j} \equiv \partial/\partial \mathbf{z}_j$. The tensor C_{ijkl} is the usual Hookean elasticity tensor, which, for isotropic elasticity, has the form

$$C_{ijkl} = \frac{2G\nu}{1 - 2\nu} \delta_{ij}\delta_{kl} + G(\delta_{ik}\delta_{jl} + \delta_{il}\delta_{jk})$$

where G is the shear modulus, ν the Poisson's ratio, and $\boldsymbol{\delta}$ is the Kronecker delta.

This equation can be collocated at any point $\mathbf{x}$ on the boundary $\partial\Omega$ of the body.

Next, the displacement at an internal point is given by

$$u_k(\mathbf{x}) = \int_{\partial\Omega} \{p_i(\mathbf{z}) U_i^k(\mathbf{x}, \mathbf{z}) - u_i(\mathbf{z}) P_i^k(\mathbf{x}, \mathbf{z})\} dS_z + \int_{\Omega} U_{i,j}^k(\mathbf{x}, \mathbf{z}) C_{ijab} \epsilon_{ab}^p(\mathbf{z}) dV_z. \quad (2)$$

Differentiating Eq. (2) with respect to an internal source point $\mathbf{x}$, and regularizing the domain integral, yields

$$u_{k,l}(\mathbf{x}) = \int_{\partial\Omega} u_i(\mathbf{z}) P_{il}^k(\mathbf{x}, \mathbf{z}) dS_z - \int_{\partial\Omega} p_i(\mathbf{z}) U_{i,l}^k(\mathbf{x}, \mathbf{z}) dS_z - C_{ijab}\epsilon_{ij}^p(\mathbf{x}) \int_{\partial\Omega} n_l(\mathbf{z}) U_{a,b}^k(\mathbf{x}, \mathbf{z}) dS_z - \int_{\Omega} U_{i,jl}^k(\mathbf{x}, \mathbf{z}) C_{ijab}[\epsilon_{ab}^p(\mathbf{z}) - \epsilon_{ab}^p(\mathbf{x})] dV_z \quad (3)$$

where $P_{il}^k \equiv -P_{i,\bar{l}}^k$ with $_{,\bar{l}} \equiv \partial/\partial x_l$.

It is important to note that Eq. (3) is only partially regularized in the sense that it can only be collocated at an internal source point $\mathbf{x} \in \Omega$ which is $\notin \partial\Omega$. Equation (3) becomes hypersingular if an internal source point approaches the boundary $\partial\Omega$. The purpose of the next section of this paper is to derive a fully regularized version of Eq. (3) that can be collocated at any point $\mathbf{x} \in (\Omega \cup \partial\Omega)$ (including edges and corners) provided that the stress is continuous there.

3 Regularized Hypersingular Boundary Integral Equation

The method of using simple solutions or modes is used in this section to fully regularize the HBIE (Eq. (3)) when an internal source point $\mathbf{x}$ approaches the boundary $\partial\Omega$. Please see, for example, Krishnasamy et al. (1992) and Lutz et al. (1992) for applications of this idea in linear elasticity.

The first step is to subtract suitable terms from the first and second integrands in the right-hand side of Eq. (3), and then add them back. This results in

$$\begin{aligned} u_{k,l}(\mathbf{x}) = &\int_{\partial\Omega} P_{il}^k(\mathbf{x}, \mathbf{z})[u_i(\mathbf{z}) - u_i(\mathbf{x}) - u_{i,n}(\mathbf{x})(z_n - x_n)] dS_z \\ &- \int_{\partial\Omega} U_{i,l}^k(\mathbf{x}, \mathbf{z})[\sigma_{ij}(\mathbf{z}) - \sigma_{ij}(\mathbf{x})] n_j(\mathbf{z}) dS_z \\ &+ u_i(\mathbf{x}) \int_{\partial\Omega} P_{il}^k(\mathbf{x}, z) dS_z \\ &- \sigma_{ij}(\mathbf{x}) \int_{\partial\Omega} U_{i,l}^k(\mathbf{x}, \mathbf{z}) n_j(\mathbf{z}) dS_z \\ &+ u_{i,n}(\mathbf{x}) \int_{\partial\Omega} P_{il}^k(\mathbf{x}, \mathbf{z})(z_n - x_n) dS_z \\ &- C_{ijab}\epsilon_{ij}^p(\mathbf{x}) \int_{\partial\Omega} U_{a,b}^k(\mathbf{x}, \mathbf{z}) n_l(\mathbf{z}) dS_z \\ &- \int_{\Omega} U_{i,jl}^k(\mathbf{x}, \mathbf{z}) C_{ijab}[\epsilon_{ab}^p(\mathbf{z}) - \epsilon_{ab}^p(\mathbf{x})] dV_z. \end{aligned} \quad (4)$$

Attention is now focussed on the third, fourth, and fifth (the add back terms) as well as the sixth term on the right-hand side of Eq. (4).

Use of the rigid-body mode

$$u_i(\mathbf{z}) = u_i(\mathbf{x}), \quad \epsilon_{ij}^p = 0 \quad (5)$$

immediately leads to the conclusion

$$\int_{\partial\Omega} P_{il}^k(\mathbf{x}, \mathbf{z}) dS_z = 0 \quad (6)$$

so that the third term vanishes.

Next, use of the constitutive equation

$$\sigma_{ij}(\mathbf{x}) = C_{ijab}(u_{a,b}(\mathbf{x}) - \epsilon_{ab}^p(\mathbf{x})) \quad (7)$$

and symmetry of the Hookean elasticity tensor

$$C_{ijab} = C_{abij} \quad (8)$$

allows one to write the fourth, fifth, and sixth terms together as

$$\begin{aligned} J &= I_4 + I_5 + I_6 \\ &= C_{ijab}\epsilon_{ij}^p(\mathbf{x}) \int_{\partial\Omega} [U_{a,l}^k(\mathbf{x}, \mathbf{z}) n_b(\mathbf{z}) - U_{a,b}^k(\mathbf{x}, \mathbf{z}) n_l(\mathbf{z})] dS_z \\ &\quad + u_{i,n}(\mathbf{x}) \int_{\partial\Omega} [P_{il}^k(\mathbf{x}, \mathbf{z})(z_n - x_n) \\ &\quad - C_{amin} U_{a,l}^k(\mathbf{x}, \mathbf{z}) n_m(\mathbf{z})] dS_z \\ &\equiv J_1 + J_2. \end{aligned} \quad (9)$$

Use of the linear mode (see Krishnasamy et al. (1992) and Lutz et al. (1992) for applications in potential theory and linear elasticity)

$$\left.\begin{aligned} u_i(\mathbf{z}) &= u_{i,n}(\mathbf{x})(z_n - x_n) \\ \epsilon_{ij}^p &= 0 \\ u_{i,n}(\mathbf{z}) &= u_{i,n}(\mathbf{x}) \\ \sigma_{ij}(\mathbf{z}) &= C_{ijab} u_{a,b}(\mathbf{x}) \end{aligned}\right\} \quad (10)$$

in Eq. (4) leads to the conclusion that the second term on the right-hand side of Eq. (9)

$$J_2 = u_{k,l}(\mathbf{x}). \quad (11)$$

Finally, a fully constrained plastic mode is employed in which the complete boundary $\partial\Omega$ of the body has zero displacement but the body has undergone plastic deformation. In this case the displacements everywhere in the body vanish, although the body is stressed. This mode is

Downloaded 04 May 2010 to 171.66.16.26. Redistribution subject to ASME license or copyright; see http://www.asme.org/terms/Terms_Use.cfm

$$\left.\begin{aligned} u_i(\mathbf{z}) &= 0 \\ \epsilon^p_{ab}(\mathbf{z}) &= \epsilon^p_{ab}(\mathbf{x}) \\ \sigma_{ij}(\mathbf{z}) &= \sigma_{ij}(\mathbf{x}) = -C_{ijab}\epsilon^p_{ab}(\mathbf{x}) \end{aligned}\right\}. \quad (12)$$

Use of this mode in Eq. (4) leads to the conclusion that the first term on the right-hand side of Eq. (9)

$$J_1 = 0. \quad (13)$$

Use of Eqs. (6), (11), and (13) in Eq. (4) leads to a completely regularized HBIE for elastoplasticity. This has the very simple form

$$0 = \int_{\partial\Omega} P^k_{il}(\mathbf{x}, \mathbf{z})[u_i(\mathbf{z}) - u_i(\mathbf{x}) - u_{i,n}(\mathbf{x})(z_n - x_n)]dS_z - \int_{\partial\Omega} U^k_{i,l}(\mathbf{x}, \mathbf{z})[\sigma_{ij}(\mathbf{z}) - \sigma_{ij}(\mathbf{x})]n_j(\mathbf{z})dS_z - \int_{\Omega} U^k_{i,jl}(\mathbf{x}, \mathbf{z})C_{ijab}[\epsilon^p_{ab}(\mathbf{z}) - \epsilon^p_{ab}(\mathbf{x})]dV_z. \quad (14)$$

In three dimensions, the first and second integrands on the right-hand side of Eq. (14) are each $O(1/r)$ while the domain integrand is $O(1/r^2)$. In two dimensions, the first two integrands are regular while the third is $O(1/r)$. Thus, all the terms in Eq. (14) are, at most, weakly singular. It is therefore possible to take the limit of Eq. (14) as an internal source point approaches a boundary point. Following Cruse and Richardson (1996, for the elastic case), the regularized HBIE (Eq. (14)) is valid at any point $\mathbf{x}$ (including edges and corners), provided that the stress, displacement gradient, and plastic strain are continuous there.

It is interesting to compare the simple form of Eq. (14) with the corresponding HBIE for elastoplasticity in Huber et al. (1996), where the approach originally proposed for elasticity problems by Guiggiani et al. (1992) has been used for regularization. It is also interesting to compare Eq. (14) with Eq. (20) in Bonnet et al. (1998) where an indirect regularization approach, with an exclusion zone, has been used.

4 A Convenient Computable Form of the Regularized HBIE for Plane Strain

A convenient computable form of the HBIE (Eq. (14)) is derived in this section. The resulting regularized HBIE (Eq. (19)) is only valid for collocation at regular points on the boundary (i.e., where the boundary is locally smooth) because continuity of the normal and tangent vectors to the boundary, at a collocation point, is assumed in the analysis presented below. Also, ideally, $C^{1,\alpha}$ shape functions should be used for interpolating boundary displacements in a numerical implementation (see, for example, Martin and Rizzo (1996) and Bonnet et al. (1998)).

4.1 The First Term in Eq. (14). It can be shown that (Ghosh et al., 1986), for two-dimensional problems,

$$P^k_{il} = -\frac{\partial}{\partial s_z} W^k_{i,l}, \quad (15)$$

where, for plane strain,

$$W^k_{i,l} = \frac{1}{4\pi(1-\nu)r}[2(1-\nu)r_{,m}\gamma_{ml}\delta_{ki} - 2\gamma_{im}r_{,k}r_{,m}r_{,l} + (1-2\nu)r_{,l}\gamma_{ki} + \gamma_{im}(r_{,m}\delta_{kl} + r_{,k}\delta_{ml})] \quad (16)$$

with $\gamma_{11} = \gamma_{22} = 0$, $\gamma_{12} = -\gamma_{21} = 1$, δ_{ij} the components of the Kronecker delta, and ν the Poisson's ratio of the elastic material. Also, r is the Eucledian distance between $\mathbf{x}$ and $\mathbf{z}$.

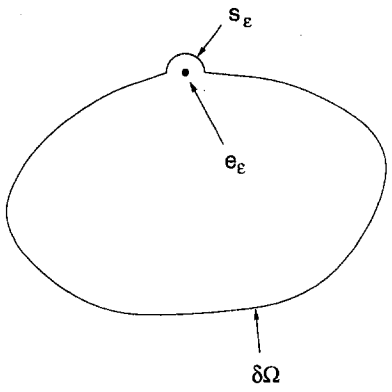

Fig. 1 Notations for inclusion zone

Integration by parts of the first integrand in Eq. (14) gives (see Fig. 1)

$$I_1 = -W^k_{i,l}(\mathbf{x}, \mathbf{z})[u_i(\mathbf{z}) - u_i(\mathbf{x}) - u_{i,n}(\mathbf{x})(z_n - x_n)]\Big|^{\mathbf{x}'}_{\mathbf{x}} + \int_{\partial\Omega - e_\epsilon} W^k_{i,l}(\mathbf{x}, \mathbf{z})[d_i(\mathbf{z}) - u_{i,n}(\mathbf{x})[t_n(\mathbf{z})t_n(\mathbf{t}) - t_n(\mathbf{x}) + t_n(\mathbf{x}) - t_n(\mathbf{x}) + t_n(\mathbf{x})]]dS_z + \int_{s_\epsilon} W^k_{i,l}(\mathbf{x}, \mathbf{z})[d_i(\mathbf{z}) - u_{i,n}(\mathbf{x})t_n(\mathbf{z})]dS_z \quad (17)$$

where $d_i = \partial u_i/\partial s$ and t_i are the components of the unit (counterclockwise) tangent vector to $\partial\Omega$ at a regular point on it. Also, $\mathbf{x}'$ is an arbitrary point on the extended boundary $(\partial\Omega - e_\epsilon) + s_\epsilon$.

The first term in Eq. (17) vanishes and so does the third, in the limit $s_\epsilon \to 0$, since its integrand is $O(1)$. Only the second survives.

4.2 The Second Term in Eq. (14). This term is written as

$$I_2 = -\int_{\partial\Omega} U^k_{i,l}(\mathbf{x}, \mathbf{z})[p_i(\mathbf{z}) - \sigma_{ij}(\mathbf{x})[n_j(\mathbf{z}) - n_j(\mathbf{x}) + n_j(\mathbf{x})]]dS_z \quad (18)$$

where n_i are the components of the unit outward normal vector to $\partial\Omega$ at a regular point on it.

4.3 The Third Term in Eq. (14). It is computationally efficient to evaluate the domain integral by integrating only over the potentially plastic zone $\Omega_P \subset \Omega$. Referring to Fig. 2, only Ω_P needs to be discretized with internal cells while its complement Ω_C, which remains elastic, is not discretized. This results in an integral over Ω_P and a boundary integral over $\partial\Omega_C$. The exact form is given in Eq. (19).

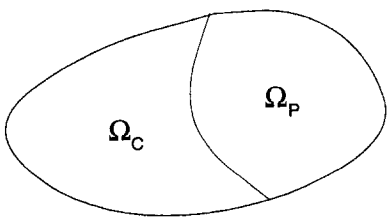

Fig. 2 Domain partitioning into a potentially plastic part and its complement

Downloaded 04 May 2010 to 171.66.16.26. Redistribution subject to ASME license or copyright; see http://www.asme.org/terms/Terms_Use.cfm

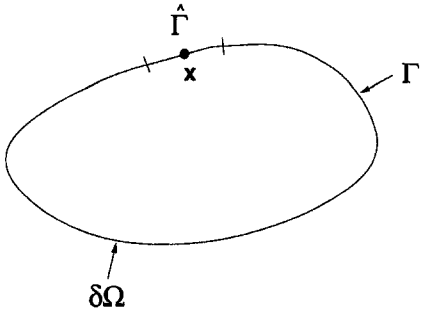

Fig. 3 Boundary partitioning into a portion adjacent to a source point and one remote from it

4.4 The Reformulated Hypersingular Boundary Integral Equations. One more operation is necessary to arrive at the final reformulated version of Eq. (14). Referring to Fig. 3, let

$$\partial\Omega = \Gamma \cup \hat{\Gamma}$$

where $\hat{\Gamma}$ is the part of $\partial\Omega$ that is adjacent to $\mathbf{x}$ (i.e., $\hat{\Gamma}$ is made up of those boundary element(s) which contain $\mathbf{x}$) and Γ is the part remote from $\mathbf{x}$. The boundary integrals (except the one over $\partial\Omega_C$ which is regular) are separated into two pieces, one over Γ, the other over $\hat{\Gamma}$. The final form of Eq. (14), which can be shown to be equivalent to Eqs. (24)–(25) in Bonnet et al. (1998), is

$$\begin{aligned}
0 = &\int_\Gamma W^k_{i,l}(\mathbf{x},\mathbf{z})d_i(\mathbf{z})dS_z + \int_{\hat{\Gamma}} W^k_{i,l}(\mathbf{x},\mathbf{z})[d_i(\mathbf{z}) \\
&- d_i(\mathbf{x})]dS_z - u_{i,n}(\mathbf{x})\left\{\int_\Gamma W^k_{i,l}(\mathbf{x},\mathbf{z})t_n(\mathbf{z})dS_z \right. \\
&\left. + \int_{\hat{\Gamma}} W^k_{i,l}(\mathbf{x},\mathbf{z})[t_n(\mathbf{z}) - t_n(\mathbf{x})]dS_z\right\} \\
&- \int_\Gamma U^k_{i,l}(\mathbf{x},\mathbf{z})p_i(\mathbf{z})dS_z - \int_{\hat{\Gamma}} U^k_{i,l}(\mathbf{x},\mathbf{z})[p_i(\mathbf{z}) \\
&- p_i(\mathbf{x})]dS_z + \sigma_{ij}(\mathbf{x})\left\{\int_\Gamma U^k_{i,l}(\mathbf{x},\mathbf{z})n_j(\mathbf{z})dS_z \right. \\
&\left. + \int_{\hat{\Gamma}} U^k_{i,l}(\mathbf{x},\mathbf{z})[n_j(\mathbf{z}) - n_j(\mathbf{x})]dS_z\right\} \\
&- \int_{\Omega_P} U^k_{i,jl}(\mathbf{x},\mathbf{z})C_{ijab}[\epsilon^p_{ab}(\mathbf{z}) - \epsilon^p_{ab}(\mathbf{x})]dV_z \\
&+ C_{ijab}\epsilon^p_{ab}(\mathbf{x})\int_{\partial\Omega_C} U^k_{i,l}(\mathbf{x},\mathbf{z})n_j(\mathbf{z})dS_z. \quad (19)
\end{aligned}$$

The above formula is suitable for a source point $\mathbf{x}$ lying on the potentially plastic part of the domain boundary, i.e., $\partial\Omega \cap \partial\Omega_P$. For the remainder of the boundary $\partial\Omega \cap \partial\Omega_C$, the last term in Eq. (19), which involves a strongly singular integral, should be dropped, since $\epsilon^p_{ab}(\mathbf{x}) = 0$.

5 Implicit Solution Scheme With the Consistent Tangent Operator

This section summarizes an implicit solution scheme that uses the consistent tangent operator (CTO). Further details are available in Bonnet and Mukherjee (1996), Poon et al. (1998) and Bonnet et al. (1998).

5.1 Discretized Equations. A discretized version of the BIE (Eq. (1)) can be written as

$$[\mathbf{H}]\{\mathbf{u}\} - [\mathbf{G}]\{\mathbf{p}\} = [\mathbf{Q}]\{\mathbf{C} : \boldsymbol{\epsilon}^p\}. \quad (20)$$

Strains at interior nodes are computed via Eq. (3), which symbolically reads

$$\{\boldsymbol{\epsilon}\} = [\mathbf{G}']\{\mathbf{p}\} - [\mathbf{H}']\{\mathbf{u}\} + [\mathbf{Q}']\{\mathbf{C} : \boldsymbol{\epsilon}^p\}. \quad (21)$$

Although not so obvious at first glance, strains on the boundary, computed via Eq. (19), also fit into the symbolic form Eq. (21). Bearing in mind that k and l are the free indices, one notices the coupling among the displacement gradient components. The pertinent components being sought (for the purpose of getting strain components) are $u_{1,1}$, $u_{2,2}$, $u_{1,2}$, and $u_{2,1}$. By ranging the free indices k, l from 1 to 2, one can form a system of four equations involving the four sought-after unknowns. The 4-by-4 system can then be easily inverted, either numerically through Gaussian elimination, or "exactly" through Cramer's rule, to recover the individual $u_{1,1}$, $u_{2,2}$, $u_{1,2}$, and $u_{2,1}$. These are then easily translated into strain components ϵ_{ij}. The other side of the equation will contain, besides the nodal tractions and plastic strains, displacement tangential derivatives over the boundary. Through shape function differentiation, the latter can be related to the boundary nodal displacements. However, standard $C^{0,\alpha}$ boundary elements lead to discontinuous tangential derivatives, violating the key continuity assumptions of the present work. Instead of using $C^{1,\alpha}$ elements, an alternative "smoothing technique," proposed by Polch et al. (1987), is employed as a remedy. In a nutshell, a new C^0 interpolation for $\mathbf{d}$ is constructed in such a way that it approximates the shape function differentiation of (the C^0 interpolation of) $\mathbf{u}$ in a least-squares sense. The details can be found in Bonnet et al. (1998) and Poon (1996). Having related the displacement tangential derivatives to the boundary nodal displacements, the end result is that the symbolic strain representation (21) is preserved.

5.2 Combination of Equations for the Implicit Scheme. Two strategies are possible for combining the discretized equations. The first involves use of both the primary BIE (Eq. (20)) and the strain Eq. (21). The second eliminates the use of Eq. (20).

Strategy One: This strategy has been employed in Bonnet et al. (1998). Separating the known $\{\mathbf{g}\}$ and unknown $\{\mathbf{y}\}$ quantities on the boundary, one rewrites Eqs. (20) and (21) as

$$[\mathbf{A}]\{\mathbf{y}\} = [\mathbf{B}]\{\mathbf{g}\} + [\mathbf{Q}]\{\mathbf{C} : \boldsymbol{\epsilon}^p\} \quad (22)$$

$$\{\boldsymbol{\epsilon}\} = -[\mathbf{A}']\{\mathbf{y}\} + [\mathbf{B}']\{\mathbf{g}\} + [\mathbf{Q}']\{\mathbf{C} : \boldsymbol{\epsilon}^p\}. \quad (23)$$

Substitution for $\{\mathbf{y}\}$ from (22) into (23) yields

$$\{\boldsymbol{\epsilon}\} = \{\mathbf{n}\} + [\mathbf{S}]\{\mathbf{C} : \boldsymbol{\epsilon}^p\} \quad (24)$$

where

$$\{\mathbf{n}\} = \{\mathbf{f}'\} - [\mathbf{A}'][\mathbf{A}]^{-1}\{\mathbf{f}\}$$

$$[\mathbf{S}] = [\mathbf{Q}'] - [\mathbf{A}'][\mathbf{A}]^{-1}[\mathbf{Q}]$$

with

$$\{\mathbf{f}\} = [\mathbf{B}]\{\mathbf{g}\} \quad \text{and} \quad \{\mathbf{f}'\} = [\mathbf{B}']\{\mathbf{g}\}.$$

Note that $\{\mathbf{n}\}$ denotes the purely elastic solution, i.e., the one obtained for the same loading but in the absence of plastic strain.

At this point, recall Hooke's law and the additive decomposition of strain:

$$\boldsymbol{\sigma} = \mathbf{C} : (\boldsymbol{\epsilon} - \boldsymbol{\epsilon}^p) \quad (25)$$

or

$$\{\mathbf{C} : \boldsymbol{\epsilon}^p\} = \{\mathbf{C} : \boldsymbol{\epsilon}\} - \{\boldsymbol{\sigma}\}$$

Downloaded 04 May 2010 to 171.66.16.26. Redistribution subject to ASME license or copyright; see http://www.asme.org/terms/Terms_Use.cfm

giving, when combined with Eq. (24),

$$\{\boldsymbol{\epsilon}\} = \{\mathbf{n}\} + [\mathbf{S}](\{\mathbf{C} : \boldsymbol{\epsilon}\} - \{\boldsymbol{\sigma}\}),$$

or

$$[\mathbf{S}]\{\boldsymbol{\sigma} - \mathbf{C}\boldsymbol{\epsilon}\} - \{\mathbf{n}\} + [\mathbf{I}]\{\boldsymbol{\epsilon}\} = \{\mathbf{0}\}, \quad (26)$$

with the corresponding incremental form

$$[\mathbf{S}]\{\Delta\boldsymbol{\sigma}_n - \mathbf{C}\Delta\boldsymbol{\epsilon}_n\} - \{\Delta n_n\} + [\mathbf{I}]\{\Delta\boldsymbol{\epsilon}_n\} = \{\mathbf{0}\}, \quad (27)$$

where $\Delta f_n = f_{n+1} - f_n$.

Strategy two: In this case, Eq. (22) is not used. However, the quantities traction, total displacement gradient, tangential displacement gradient, and plastic strain are related at a regular boundary point. An explicit relationship can be written for plane strain as (see Zhang et al. (1992) for elastoplasticity and Cruse and Vanburen (1971) and Sladek and Sladek (1986) for linear elasticity)

$$u_{i,j} = E_{ijk}p_k + F_{ijk}d_k + G_{ijkl}\epsilon^p_{kl} \quad (28)$$

where the tensors $\mathbf{E}$, $\mathbf{F}$, and $\mathbf{G}$, given in Zhang et al. (1992), are explicit functions of the material parameters and local geometry (the vectors $\mathbf{n}$ and $\mathbf{t}$) at a regular boundary point $\mathbf{x}$. Equation (28) is the basis of the "boundary shortcut" approach that has been used in Poon et al. (1998).

With, for example, $\mathbf{d}$ written in terms of $\mathbf{u}$ by differentiating $C^{1,\alpha}$ shape functions, or from the smoothing technique (see Polch et al., 1987; Bonnet et al., 1998), one can write a global version of Eq. (28) in the same form as Eq. (23), i.e.,

$$\{\boldsymbol{\epsilon}\}_b = -[\mathbf{A}'']\{\mathbf{y}\} + [\mathbf{B}'']\{\mathbf{g}\} + [\mathbf{Q}'']\{\mathbf{C} : \boldsymbol{\epsilon}^p\} \quad (29)$$

where $\{\boldsymbol{\epsilon}\}_b$ contains the boundary strains.

The vector $\{\mathbf{y}\}$ is then eliminated from Eq. (23) by using Eq. (29), and one then proceeds in a manner similar to strategy one.

5.3 The Radial Return Algorithm and the Consistent Tangent Operator. A discretized form of the elastoplastic constitutive relationship, that relates $\Delta\boldsymbol{\sigma}_n$ and $\Delta\boldsymbol{\epsilon}_n$, is needed next. This is accomplished by the Radial Return Algorithm (RRA) (Simo and Taylor, 1985). Conceptually, the RRA serves the following function:

Input: $\boldsymbol{\sigma}_n$, $\boldsymbol{\epsilon}_n$, $\bar{e}^p_n$, $\Delta\boldsymbol{\epsilon}_n$
Output: $\bar{\boldsymbol{\sigma}} = \boldsymbol{\sigma}_{n+1}$ and $\bar{e}^p_{n+1}$

The consistent tangent operator (CTO), denoted in the present paper by $\mathbf{C}_{n+1}$, comes from "differentiating" the RRA. Being a fourth-order tensor, it provides a linear mapping from an infinitesimal perturbation in the input strain increment $\delta\Delta\boldsymbol{\epsilon}_n$ to the corresponding infinitesimal change in the output stress $\delta\bar{\boldsymbol{\sigma}}$:

$$\mathbf{C}_{n+1} = \frac{\partial\bar{\boldsymbol{\sigma}}}{\partial\Delta\boldsymbol{\epsilon}_n}.$$

Both the RRA and the CTO are explained in detail in Simo and Taylor (1985) and briefly summarized in Bonnet and Mukherjee (1996).

Combining the equilibrium and constitutive equations in the form

$$\{\boldsymbol{\sigma}_n\} + \{\Delta\boldsymbol{\sigma}_n\} = \{\bar{\boldsymbol{\sigma}}\}$$

(where $\Delta\boldsymbol{\sigma}_n(\Delta\boldsymbol{\epsilon}_n, \ldots, .)$ comes from the BEM equation (e.g., (27) from strategy one), while $\bar{\boldsymbol{\sigma}}(\Delta\boldsymbol{\epsilon}_n, \ldots, .)$ (which is $\boldsymbol{\sigma}_{n+1}$) comes from the RRA), one obtains a nonlinear equation for $\Delta\boldsymbol{\epsilon}_n$ of the form

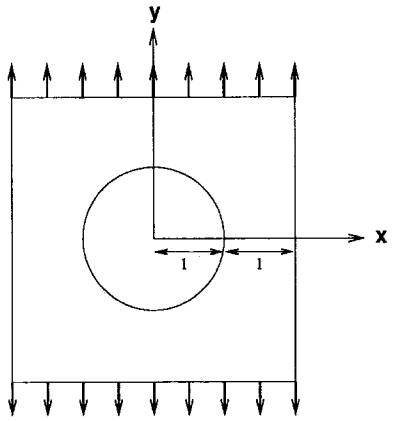

Fig. 4 Geometry, loading, and axes convention

$$\{G(\Delta\boldsymbol{\epsilon}_n)\} \equiv [\mathbf{S}]\{\bar{\boldsymbol{\sigma}}(\boldsymbol{\epsilon}_n, \boldsymbol{\sigma}_n, \bar{e}^p_n, \Delta\boldsymbol{\epsilon}_n) - \boldsymbol{\sigma}_n - \mathbf{C}\Delta\boldsymbol{\epsilon}_n\} - \{\Delta n_n\} + [\mathbf{I}]\{\Delta\boldsymbol{\epsilon}_n\} = \{\mathbf{0}\}. \quad (30)$$

The consistent tangent operator $\mathbf{C}_{n+1}$ appears upon application of Newton's method. The additive correction $\delta\boldsymbol{\epsilon}^i_n = \Delta\boldsymbol{\epsilon}^{i+1}_n - \Delta\boldsymbol{\epsilon}^i_n$ to $\Delta\boldsymbol{\epsilon}^i_n$ solves the equation

$$([\mathbf{S}][\mathbf{C} - \mathbf{C}^i_{n+1}] - [\mathbf{I}])\{\delta\boldsymbol{\epsilon}^i_n\} = \{G(\Delta\boldsymbol{\epsilon}^i_n)\}. \quad (31)$$

The quantity $([\mathbf{S}][\mathbf{C} - \mathbf{C}^i_{n+1}] - [\mathbf{I}]) = ([\mathbf{D}^i_{n+1}] - [\mathbf{I}])$ is hereafter called the global CTO (see Kleiber et al. (1994) for the FEM version). Once the nonlinear Eq. (30) is solved for $\Delta\boldsymbol{\epsilon}_n$, all the variables at time t_{n+1} are readily computed (Bonnet and Mukherjee, 1996, Poon et al., 1998).

6 Numerical Example

Using the final reformulated Eq. (19), together with strategy one for combining the discretized equations, the problem of a square plate with a circular hole, made of an elastoplastic material stretched under plane-strain conditions, is solved next.

To avoid corners (recall that the analysis in Section 4 is only valid for regular boundary points), the square plate is modeled in full, with a complete circle as the inner boundary. Each of the outer corners of the square plate is approximated by a circular arc with a finite, but negligible, radius of curvature.

In the absence of closed-form solutions, reference results are furnished by running the commercial finite element code ABAQUS on a fine mesh.

The square plate has inner radius 1 and outer side length 4. The elastic constants are $G = 1$, $\nu = 0.3$ where G is the shear modulus and ν the Poisson ratio. The material deforms plastically according to the classical J2 theory, with isotropic strain hardening of the form

$$\kappa = 2G(0.001 + 0.001(\bar{e}^p)^m)$$

where κ is the Mises yield stress and $m = 0.2$ (nonlinear strain hardening). The usual practice of nondimensionalization (e.g., dividing stresses by the shear modulus, radial distances by the inner radius, etc.) becomes unnecessary with the current choice of material and geometrical parameters.

Quadratic interpolation of nodal quantities is used in the present work. The BEM implementation uses three-noded boundary elements and six-noded triangular internal cells. Only the potentially plastic zone Ω_P (see Fig. 2) is discretized. The FEM setup (ABAQUS) employs eight-noded quadrilateral elements.

The geometry, loading, and axes convention are shown in Fig. 4. Of course, to prevent rigid-body motion, certain boundary nodes along the symmetry lines are constrained in the proper manner. For instance, the node situated at (1, 0) has

- x-direction: zero traction, unknown displacement

Downloaded 04 May 2010 to 171.66.16.26. Redistribution subject to ASME license or copyright; see http://www.asme.org/terms/Terms_Use.cfm

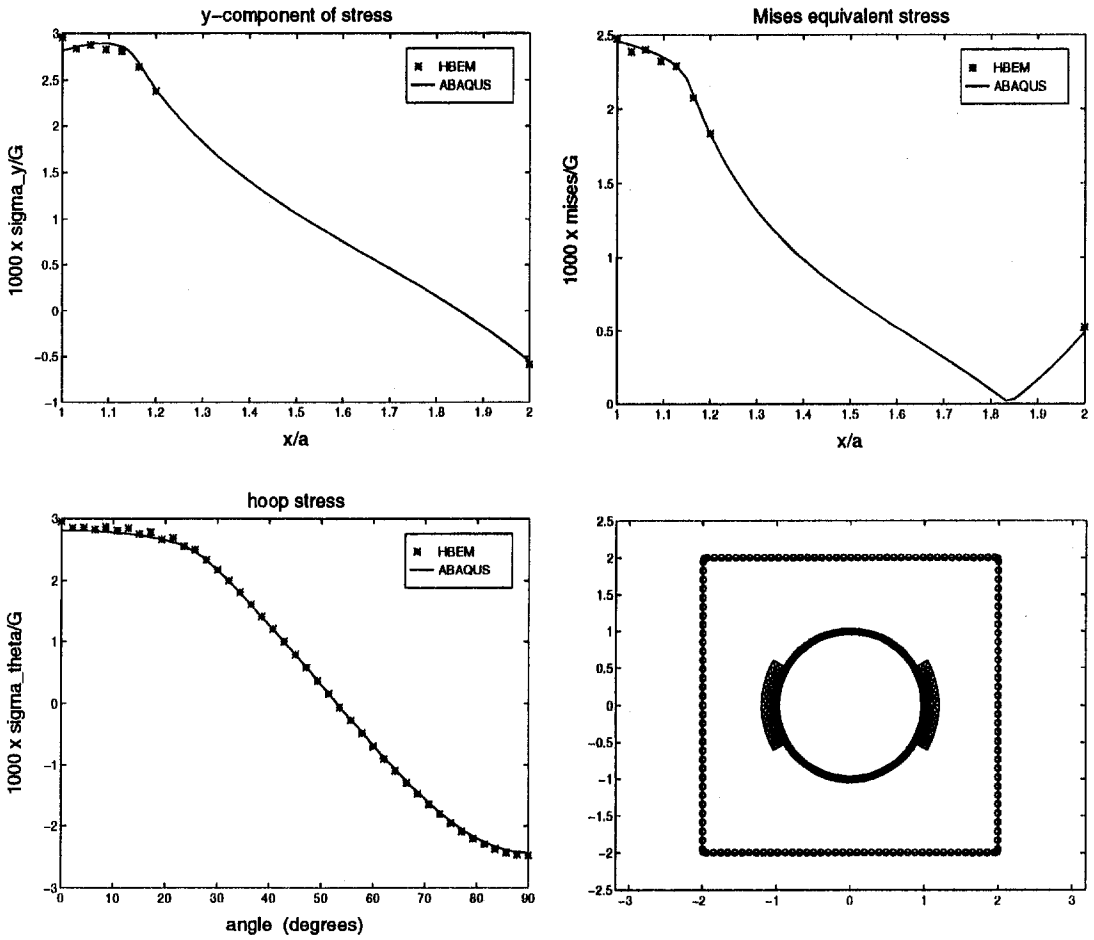

Fig. 5 Numerical results for a square plate with a hole

- y-direction: zero displacement, unknown traction (eventually symmetry forces it to be zero).

For conciseness, the results are shown in Fig. 5 as a set of four subfigures, arranged in the following manner:

- top left: σ_y at $y = 0$ as a function of x
- top right: Mises equivalent stress at $y = 0$ as a function of x
- bottom left: σ_θ at $r = 1$ as a function of θ
- bottom right: BEM mesh

In the legend boxes in Fig. 5, "HBEM" stands for hypersingular BEM.

The HBEM results are seen to agree well with the FEM ones from ABAQUS. The authors believe that the slight discrepancy between the two solutions originates from the use of the smoothing technique which is able to enforce continuity of the displacement tangential derivatives, across boundary elements, only in a "least-squares" sense. Use of C^1 boundary elements is expected to improve agreement between the two solutions even further.

Note the following pertinent remarks:

- The example is analyzed using one load step, thanks to the power of the CTO.
- The circles in the BEM mesh denote nodes of the (quadratic) boundary elements, since the boundary discretization cannot be inferred from the internal cells.
- Without showing explicitly the elastic-plastic boundary, we do give the reader a rough suggestion of the size of the plastic zone. The area that has gone plastic is first discovered by an ABAQUS run, then the BEM domain mesh is chosen to minimally capture that area, within the limitations of our rudimentary meshing scheme. In the present example, the plastic zone is found to be confined to $1 < r < 1.2$, -30 deg $< \theta < 30$ deg, and the domain meshed accordingly.
- Despite the apparent small size of the plastic zone, the degree of plastic flow is significant. At the node located at (1, 0), the equivalent plastic strain (0.0765 percent) is comparable in magnitude to the elastic strain there ($\epsilon^e_{11} = -0.0431$ percent, $\epsilon^e_{22} = 0.0984$ percent), meanwhile the radius of the yield surface has expanded by almost 25 percent from the unstressed value.
- In the interest of brevity, only one example is shown here. The current approach is fully capable of solving other problems where substantial plastic zones develop. One example is the thick hollow cylinder under internal pressure loading. The present computational formula (19), algebraically equivalent to the final formula in Bonnet et al. (1998) derived using different means (mainly integration by parts), can, in one single step of the implicit CTO scheme, solve for the state of stress when the plastic zone encompasses half the thickness of the cylinder. The interested reader is referred to Example 3 in Bonnet et al. (1998) for details.

7 Conclusion

This paper demonstrates the fact that the powerful modal method of regularizing HBIEs for linear problems is also very

Downloaded 04 May 2010 to 171.66.16.26. Redistribution subject to ASME license or copyright; see http://www.asme.org/terms/Terms_Use.cfm

effective for nonlinear ones. The simple form of the resulting regularized Eq. (14) is quite striking.

The regularized HBIE had been used in this paper for the determination of boundary strains within the context of an implicit BEM. As stated in the Introduction of this paper, various other uses of this idea are also possible. It would be very interesting, for example, to employ a slightly modified version of this approach to solve problems in elastoplastic fracture mechanics.

Acknowledgments

The computational aspect of this work was performed at the National Center for Supercomputing Applications (NCSA) of the University of Illinois at Urbana-Champaign (UIUC). The authors wish to acknowledge the support of the NCSA staff and consultants.

References

Bonnet, M., 1995, "Regularized Direct and Indirect Symmetric Variational BIE Formulations for Three-Dimensional Elasticity," *Engineering Analysis with Boundary Elements,* Vol. 15, pp. 93–102.

Bonnet, M., and Mukherjee, S., 1996, "Implicit BEM formulations for usual and sensitivity problems in elasto-plasticity using the consistent tangent operator concept," *International Journal of Solids and Structures,* Vol. 33, pp. 4461–4480.

Bonnet, M., Poon, H., and Mukherjee, S., 1998, "Hypersingular formulation for boundary strain evaluation in the context of a CTO-based implicit BEM scheme for small strain elasto-plasticity," submitted for publication.

Cruse, T. A., and Vanburen, W., 1971, "Three-Dimensional Elastic Stress Analysis of a Fracture Specimen with an Edge Crack," *International Journal of Fracture Mechanics,* Vol. 7, pp. 1–15.

Cruse, T. A., and Richardson, J. D., 1996, "Non-singular Somigliana Stress Identities in Elasticity," *International Journal of Numerical Methods in Engineering,* Vol. 39, pp. 3273–3304.

Ghosh, N., Rajiyah, H., Ghosh, S., and Mukherjee, S., 1986, "A New Boundary Element Method Formulation for Linear Elasticity," ASME JOURNAL OF APPLIED MECHANICS, Vol. 53, pp. 69–76.

Gray, L. J., Martha, L. F., and Ingraffea, A. R., 1990, "Hypersingular Integrals in Boundary Element Fracture Analysis," *International Journal of Numerical Methods in Engineering,* Vol. 29, pp. 1135–1158.

Gray, L. J., Balakrishna, C., and Kane, J. H., 1995, "Symmetric Galerkin Fracture Analysis," *Engineering Analysis with Boundary Elements,* Vol. 15, pp. 103–109.

Gray, L. J., and Paulino, G. H., 1997, "Symmetric Galerkin Boundary Integral Formulation for Interface and Multi-Zone Problems," *International Journal of Numerical Methods in Engineering,* Vol. 40, pp. 3085–3101.

Gray, L. J., and Paulino, G. H., 1998, "Crack Tip Interpolation, Revisited," *SIAM Journal on Applied Mathematics,* in press.

Guiggiani, M., Krishnasamy, K., Rudolphi, T. J., and Rizzo, F. J., 1992, "A General Algorithm for the Numerical Solution of Hypersingular Boundary Integral Equations," ASME JOURNAL OF APPLIED MECHANICS, Vol. 59, pp. 604–614.

Huber, O., Dallner, R., Partheymuller, P., and Kuhn, G., 1996, "Evaluation of the stress tensor in 3-D elastoplasticity by direct solving of hypersingular integrals," *International Journal of Numerical Methods in Engineering,* Vol. 39, pp. 2555–2573.

Kleiber, M., Hien, T. D., and Postek, E., 1994, "Incremental finite-element sensitivity analysis for non-linear mechanics applications," *International Journal of Numerical Methods in Engineering,* Vol. 37, pp. 3291–3308.

Krishnasamy, G., Schmerr, L. W., Rudolphi, T. J., and Rizzo, F. J., 1990, "Hypersingular Boundary Integral Equations: Some Applications in Acoustics and Elastic Wave Scattering," ASME JOURNAL OF APPLIED MECHANICS, Vol. 57, pp. 404–414.

Krishnasamy, G., Rizzo, F. J., and Rudolphi, T. J., 1992, "Hypersingular Boundary Integral Equations: Their Occurrence, Interpretation, Regularization and Computation," *Developments in Boundary Element Methods,* Vol. 7, P. K. Banerjee and S. Kobayashi, eds., Elsevier Applied Science, London, pp. 207–252.

Leitao, V., Aliabadi, M. H., and Rooke, D. P., 1995, "The dual boundary element formulation for elastoplastic fracture mechanics," *International Journal of Numerical Methods in Engineering,* Vol. 38, pp. 315–333.

Lutz, E. D., Ingraffea, A. R., and Gray, L. J., 1992, "Use of simple solutions for boundary integral methods in elasticity and fracture analysis," *International Journal of Numerical Methods in Engineering,* Vol. 35, pp. 1737–1751.

Martin, P. A., and Rizzo, F. J., 1996, "Hypersingular Integrals: How Smooth Must the Density Be?," *International Journal of Numerical Methods in Engineering,* Vol. 39, pp. 687–704.

Menon, G., 1996, "Hypersingular Error Estimates in Boundary Element Methods," M.S. thesis, Cornell University, Ithaca, NY.

Menon, G., Paulino, H., and Mukherjee, S., 1998, "Analysis of Hypersingular Residual Error Estimates in Boundary Element Methods for Potential Problems," *Computer Methods in Applied Mechanics and Engineering,* in press.

Paulino, G. H., 1995, "Novel Formulations of the Boundary Element Method for Fracture Mechanics and Error Estimation," Ph.D. dissertation, Cornell University, Ithaca, NY.

Paulino, G. H., Gray, L. J., and Zarkian, V., 1996, "Hypersingular Residuals—A New Approach for Error Estimation in the Boundary Element Method," *International Journal of Numerical Methods in Engineering,* Vol. 39, pp. 2005–2029.

Polch, E. Z., Cruse, T. A., and Huang, C. J., 1987, "Traction BIE solutions for flat cracks," *Computational Mechanics,* Vol. 2, pp. 253–267.

Poon, H., 1996, "Numerical Solutions of Some Problems in Elasto-Plasticity With Finite and Boundary Element Methods," Ph.D. Thesis, Cornell University, Ithaca, NY.

Poon, H., Mukherjee, S., and Bonnet, M., 1998, "Numerical implementation of a CTO-based implicit approach for the BEM solution of usual and sensitivity problems in elasto-plasticity," *Engineering Analysis With Boundary Elements,* in press.

Simo, J. C., and Taylor, R. L., 1985, "Consistent tangent operators for rate-independent elastoplasticity," *Computer Methods in Applied Mechanics and Engineering,* Vol. 48, pp. 101–118.

Sladek, J., and Sladek, V., 1986, "Computation of Stresses by BEM in 2-D Elastostatics," *Acta Technica CSAV,* Vol. 31, pp. 523–531.

Tanaka, M., Sladek, V., and Sladek, J., 1994, "Regularization Techniques Applied to Boundary Element Methods," ASME *Applied Mechanics Reviews,* Vol. 47, pp. 457–499.

Zhang, Q., Mukherjee, S., and Chandra, A., 1992, "Shape design sensitivity analysis for geometrically and materially nonlinear problems by the boundary element method," *International Journal of Solids and Structures,* Vol. 29, pp. 2503–2525.

Downloaded 04 May 2010 to 171.66.16.26. Redistribution subject to ASME license or copyright; see http://www.asme.org/terms/Terms_Use.cfm

Inflation of a Thick-Walled Shell Which Exhibits Stress Softening

J. B. Haddow
Mem. ASME.

J. L. Wegner

Department of Mechanical Engineering,
University of Victoria,
Victoria, BC V8W 3P6
Canada

The Mullins effect (Mullins, 1947), also known as stress softening, is exhibited by certain rubberlike materials and refers to changes of the mechanical properties, due to prior deformation. Johnson and Beatty (1995) have investigated the Mullins effect in equibiaxial tension by performing cycles of static inflation and deflation experiments on latex balloons. These experiments show that stress softening results in a decrease in the pressure necessary to inflate a balloon, and in addition, indicate inelastic effects of hysteresis and permanent set. The objective of this paper is to investigate the finite deformation static inflation from the virgin state, followed by quasi-static removal of the internal pressure, of a thick-walled homogeneous spherical shell composed of an incompressible isotropic rubberlike material which exhibits stress softening and permanent set. Since the initial inflation of the shell, due to application of an internal pressure, does not result in a homogeneous deformation, a state of residual stress is present after complete removal of the internal pressure. A procedure is presented for the determination of the response of the shell for the first cycle of inflation and deflation from the virgin state, and the analysis includes strain softening and the inelastic effects of hysteresis and permanent set. It is assumed that, for the initial static inflation of the shell from the virgin state, the internal pressure and stress distribution for a monotonically increasing internal or external radius are the same as for a hyperelastic shell, and also that the magnitude of the permanent set of an element of the material is related monotonically to the deformation at the end of the inflation.

1 Introduction

This paper is concerned with finite deformation static inflation, followed by quasi-static deflation, of a thick-walled homogeneous spherical shell composed of an incompressible isotropic rubberlike material. Initially the material of the shell is in the virgin state, that is it has not been subjected to prior deformation, consequently stress softening, which is the Mullins effect, has not yet occurred. The initial inflation is assumed to be governed by an elastic constitutive relation and it is further assumed that, for an element of the material, monotonic loading, followed by unloading results in a hysteresis loop and a permanent set, whose magnitude is related to the deformation at the end of loading. Since the initial inflation of the shell, due to application of an internal pressure, does not result in a homogeneous deformation, a state of residual stress and deformation is present after complete removal of the internal pressure.

If a balloon is assumed to be a spherically symmetric membrane of uniform initial thickness and material properties, the state of stress is essentially equibiaxial. It follows that the stress-deformation relations for equibiaxial stress of an incompressible rubberlike material can be investigated by considering the inflation of a balloon. Johnson and Beatty (1995) have investigated the Mullins effect in equibiaxial tension by considering the inflation of latex balloons and have presented experimental results for several inflation-deflation cycles beyond the virgin state. This paper presents a procedure for the analysis of the first cycle of inflation and deflation from the virgin state and the residual stress and deformation after deflation, of a thick-walled spherical shell composed of incompressible rubberlike material which exhibits stress softening and permanenent set. It is assumed that the inflation and deflation arise from the quasi-static application and removal of an internal pressure. A Mooney-Rivlin type model for the loading and unloading of a material element is used in order to illustrate the procedure; however, more realistic models can be devised and incorporated into the numerical procedure.

At any point of a spherically symmetric stress field the stress is equivalent to an equibiaxial Cauchy stress with a superimposed hydrostatic stress. Consequently the experimental data of Johnson and Beatty (1995) may be applicable to the present problem if it is assumed that, for an incompressible solid, the superimposed hydrostatic stress does not effect the deformation due to the equibiaxial stress.

The stress at any point of a spherically symmetric stress field is also equivalent to a uniaxial Cauchy stress with a superimposed hydrostatic stress. It follows that, if the uniaxial stress-stretch relation is not effected by a superimposed hydrostatic stress, an analysis of the deformation of an incompressible isotropic thick-walled spherical shell can be based on the the constitutive relation for uniaxial stress. For an incompressible isotropic solid, the constitutive equation for uniaxial stress can be deduced from the relations for equibiaxial stress if a superimposed hydrostatic stress does not effect the deformation due to the uniaxial stress.

2 Constitutive Assumptions

A spherical polar coordinate system (r, θ, ϕ), where r, θ and ϕ are the radial, azimuthal, and colatitude coordinates, respectively, is used in the analysis with the origin taken as the center of the shell. The state of stress for radial symmetry is equivalent to a hydrostatic stress $(\sigma_\theta, \sigma_\theta, \sigma_\theta)$ superimposed on a uniaxial stress $(\sigma_r - \sigma_\theta)$ where σ_r and $\sigma_\theta = \sigma_\phi$ are the principal components of the Cauchy stress in the usual notation. The corresponding principal stretches are denoted by λ_r, λ_θ and $\lambda_\phi = \lambda_\theta$. It follows from this and the incompressibility condition

Contributed by the Applied Mechanics Division of THE AMERICAN SOCIETY OF MECHANICAL ENGINEERS for publication in the ASME JOURNAL OF APPLIED MECHANICS.

Discussion on the paper should be addressed to the Technical Editor, Professor Lewis T. Wheeler, Department of Mechanical Engineering, University of Houston, Houston, TX 77204-4792, and will be accepted until four months after final publication of the paper itself in the ASME JOURNAL OF APPLIED MECHANICS.

Manuscript received by the ASME Applied Mechanics Division, Feb. 25, 1997; final revision, May 6, 1997. Associate Technical Editor: R. Abeyaratne.

 Copyright © 1998 by ASME

Downloaded 04 May 2010 to 171.66.16.26. Redistribution subject to ASME license or copyright; see http://www.asme.org/terms/Terms_Use.cfm

$\lambda_r\lambda_\theta^2 = 1$, that, for the analysis of a spherically symmetric problem for an incompressible solid, only the constitutive equation for uniaxial stress is required, if the uniaxial Cauchy stress-stretch relation is not influenced by a superimposed hydrostatic pressure. Since most of the experimental results for uniaxial or equibiaxial stress are presented in terms of the nominal stress a model based on the uniaxial nominal stress and stretch is proposed for loading and unloading from the natural reference state which is taken as initial undeformed virgin state. It is assumed that, for the static inflation of the shell from the reference configuration, the response for a monotonically increasing inflation is the same as that for a hyperelastic shell with an appropriate strain energy function. The analysis and results presented are for a Mooney-Rivlin type model although the procedure can be adapted to consider any admissible incompressible strain rate independent constitutive relation, for uniaxial stress loading and unloading from the virgin state. Some remarks on the suitability of the Mooney-Rivlin type model appear in Section 6.

The Mooney-Rivlin constitutive relation for uniaxial stress loading is

$$T = \mu\{\alpha(\lambda - \lambda^{-2})\} + (1 - \alpha)(1 - \lambda^{-3}), \qquad (1)$$

where T is uniaxial nominal stress, λ is the stretch, μ is the shear modulus for infinitesimal deformation from the ground state, $0 \le \alpha \le 1$. The neo-Hookean relation is the special case of (1) with $\alpha = 1$. For uniaxial stress of an incompressible solid

$$\sigma = T\lambda, \qquad (2)$$

where σ is the uniaxial Cauchy stress.

It is convenient to introduce the strain ε given by $\varepsilon = \lambda - 1$. For the material model considered, on unloading from a state of uniaxial stress, there is a hysteresis effect and a residual strain when the uniaxial stress is removed quasi statically, and reloading up to the previous maximum strain is governed by the same type of constitutive relation as for unloading. Experimental results obtained by Johnson and Beatty (1995), for balloon inflation, indicate a hysteresis effect and residual strain. It is reasonable to assume that, for the model, the magnitude of the residual strain is a monotone increasing function of the magnitude of the strain reached in the loading. It is further assumed that this function is linear so that

$$\varepsilon^{(r)} = \beta\varepsilon_m, \qquad (3)$$

where $\varepsilon^{(r)}$ and ε_m are the residual strain and the strain at the end of the monotonic application of uniaxial stress, respectively, and β is a positive constant. The value of β will depend on the particular rubberlike material modelled. For the model considered, uniaxial stress unloading follows the same stress stretch relation as reloading from the unstressed state with residual strain. A semi-analytical solution for the spherical shell problem can be obtained for a Mooney-Rivlin type constitutive relation for uniaxial stress with the infinitesimal shear modulus μ^*, for unloading/reloading, where μ^* is based on infinitesimal deformation from the residually deformed state, and $\mu^* < \mu$ in order to account for strain softening. This is assumed to be valid until the strain ε_m is attained if the reloading stress has the same sign as the original loading stress. For the numerical examples considered, it is assumed that μ^* is constant for the range of residual strain which occurs. Dependence of μ^* on $\varepsilon^{(r)}$ or ε_m can be included in the analysis; however, there seems to be no experimental results upon which to model this dependence. The stretch used in the constitutive relation for reloading is denoted by $\tilde{\lambda}$ and is based on the unstressed residually strained configuration so that the stretch λ, based on the original reference configuration, is given by

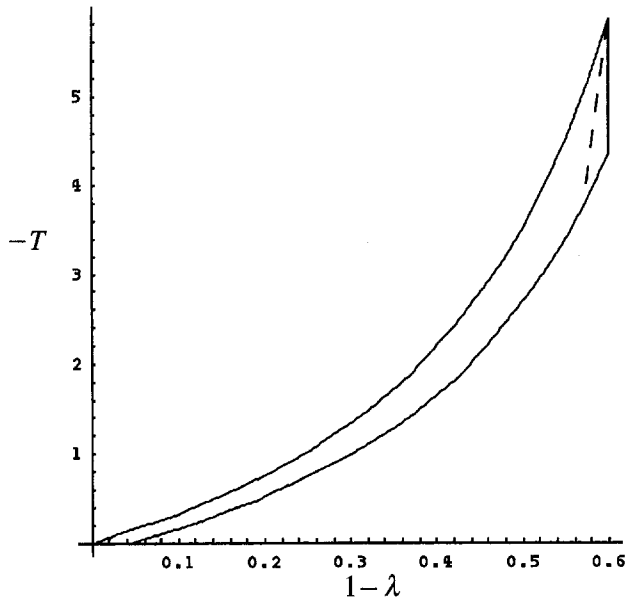

Fig. 1 Nominal stress versus stretch for uniaxial compressive loading of the Mooney-Rivlin type model with $\alpha = 0.95$, $\beta = 0.075$, $\mu^* = 0.9$

$$\lambda = \tilde{\lambda}(1 + \varepsilon^{(r)}). \qquad (4)$$

The nominal stress for reloading, referred to the original reference configuration, is then given by

$$T = \frac{\mu^*\{\alpha(\tilde{\lambda} - \tilde{\lambda}^{-2}) + (1 - \alpha)(1 - \tilde{\lambda}^{-3})\}}{1 + \varepsilon^{(r)}}, \qquad (5)$$

where the incompressibility condition has been used. It then follows from (4) that, for the reloading, (5) can be expressed in the form,

$$T = \mu^*\{\alpha[\lambda(1 + \varepsilon^{(r)})^{-2} - \lambda^{-2}(1 + \varepsilon^{(r)})] + (1 - \alpha)[(1 + \varepsilon^{(r)})^{-1} - \lambda^{-3}(1 + \varepsilon^{(r)})^2]\}. \qquad (6)$$

For the model, the stress-stretch relation for unloading is also given by (6), and at the start of the unloading process the stress T undergoes a sudden decrease in magnitude from

$$T = \mu\{\alpha[(1 + \varepsilon_m) - (1 + \varepsilon_m)^{-2}] + (1 - \alpha)[1 - (1 + \varepsilon_m)^{-3}]\}$$

to

$$T = \mu^*\{\alpha[(1 + \varepsilon_m)(1 + \varepsilon^{(r)})^{-2} - (1 + \varepsilon_m)^{-2}(1 + \varepsilon^{(r)})] + (1 - \alpha)[(1 + \varepsilon^{(r)})^{-1} - (1 + \varepsilon_m)^{-3}(1 + \varepsilon^{(r)})^2]\}.$$

The loading and unloading is shown in Fig. 1 which shows the relation between nominal uniaxial compressive stress T and stretch λ, both based on the original reference configuration.

The sudden drop in stress at the onset of unloading is an idealization since the experimental results given by Johnson and Beatty (1995) indicate that the stress-stretch relation at the start of the unloading is represented, qualitatively, by the dashed curve shown in Fig. 1. The magnitude of the residual stress, at any radius, when the inflated sphere is unloaded is very small compared with that for the inflation, consequently the assumed sudden change in stress for the material model at the onset of unloading does not effect the predicted residual stress distribution. Empirical stress-stretch relations for uniaxial stress loading and unloading could be incorporated into the analysis and, to facilitate the representation of hysteresis loops for all values of ε_m, the assumption of a sudden change of stress at the onset of unloading may be necessary and this is discussed in Section 8.

Downloaded 04 May 2010 to 171.66.16.26. Redistribution subject to ASME license or copyright; see http://www.asme.org/terms/Terms_Use.cfm

3 Formulation of the Problem

A thick walled spherical shell is composed of incompressible isotropic rubberlike material. In the initial undeformed reference configuration the material of the shell is homogeneous and has not been subjected to prior deformation so that strain softening has not occurred. The inner and outer radii in the reference configuration are A and B, respectively. An internal pressure is applied quasi-statically, with the outer surface remaining traction free, and the inner and outer radii become a_o and b_o, respectively, with $B^3 - A^3 = b_o^3 - a_o^3$. The internal pressure is then removed quasi-statically so that the shell has no surface tractions but is in a state of residual stress and deformation due to the nonuniform residual strain.

At this stage it is convenient to nondimensionalize quantities with the dimension of length and stress by dividing by A and μ, respectively. Henceforth nondimensional quantities, unless otherwise noted, are used.

It follows from the incompressibility condition that the deformation is kinematically determined, so that $B^3 - 1 = b^3 - a^3$ and

$$r(R) = (v^3B^3 - B^3 + R^3)^{1/3}, \tag{7}$$

where r and R are the radial coordinates of a material particle in a deformed and the reference configuration, respectively, $r(1) = a$, $r(B) = b$ and $v = b/B$. The stretches are given by

$$\lambda_r = dr/dR \quad \text{and} \quad \lambda_\theta = r/R, \tag{8}$$

consequently $v = \lambda_\theta(B)$. If v is prescribed then $\lambda_r(R)$ and $\lambda_\theta(R)$ are obtained from (7) and (8).

4 Initial Inflation

The problem of spherically symmetric deformation of an isotropic incompressible hyperelastic spherical shell has been extensively studied and a treatment of the problem is given by Green and Zerna (1968) who also give references to earlier work. A different treatment, which is relevant for the later determination of the residual stress on unloading, is given in this section for the Mooney-Rivlin material. This treatment can be adapted to any isotropic incompressible hyperelastic material since all that is required is the uniaxial stress-stretch constitutive relation.

Henceforth the subscript o is used to denote values for the first inflated configuration from the virgin state.

For inflation of the incompressible shell $(\sigma_{ro} - \sigma_{\theta o}) < 0$, that is compressive, and it follows from (1) and (2) that

$$(\sigma_{ro} - \sigma_{\theta o}) = \alpha(\lambda_{ro}^2 - \lambda_{ro}^{-1}) + (1 - \alpha)(\lambda_{ro} - \lambda_{ro}^{-2}), \tag{9}$$

and from (7) that

$$r_o(R) = (v_o^3B^3 - B^3 + R^3)^{1/3}. \tag{10}$$

Consequently the stretches are given by

$$r_o' = \lambda_{ro}(R) = R^2(v_o^3B^3 - B^3 + R^3)^{-2/3},$$
$$\lambda_{\theta o}(R) = (v_o^3B^3 - B^3 + R^3)^{1/3}/R, \tag{11a, b}$$

where a prime denotes differentiation with respect to R. The equilibrium equation, in terms of the Cauchy stress is

$$\frac{d\sigma_{ro}}{dr_o} + \frac{2(\sigma_{ro} - \sigma_{\theta o})}{r_o} = 0, \tag{12}$$

which can be put in the form

$$\frac{d\sigma_{ro}}{dR} = -\frac{2[\alpha(r_o'^3 - 1) + (1 - \alpha)(r_o'^2 - r_o'^{-1})]}{r_o}, \tag{13}$$

with the use of (9). The right-hand side of (13) is a function of R with r_o and r_o' given by (10) and (11a), respectively, and integration of (13) with the boundary condition $\sigma_{ro}(B) = 0$ gives

$$\sigma_{ro}(R) = -\left\{\begin{array}{l} \alpha\left[\dfrac{1 + 4v_o^3}{2v_o^4} + \dfrac{R(4B^3 - 5R^3 - 4B^3v_o^3)}{2(R^3 - B^3 + B^3v_o^3)^{4/3}}\right] + \\ (1 - \alpha)\left[\dfrac{1 - 2v_o^3}{v_o^2} + \dfrac{(R^3 - 2B^3 + 2B^3v_o^3)}{R(R^3 - B^3 + B^3v_o^3)^{2/3}}\right] \end{array}\right\}, \tag{14}$$

and $\sigma_{\theta o}(R)$ can be obtained from (14) and (9). Substitution of $R = (r_o^3 - v_o^3B^3 + B^3)^{1/3}$ in (14) gives σ_{ro} as a function of r_o. Equation (14) is used to determine the internal pressure $p_i = -\sigma_{ro}(1)$ as a function of v_o for a given value of B, however p_i is not required for the determination of the residual stresses since the inflated deformation is kinematically determined by v_o.

5 Determination of Residually Stressed State

For the unloaded spherical shell it follows from (3) there is a non uniform residual radial strain $\hat{\varepsilon}(R) = \beta(r_o' - 1)$ and the corresponding stretch is

$$\hat{\lambda}_r(R) = 1 + \beta(r_o' - 1). \tag{15}$$

The stretch distributions $\hat{\lambda}_r(R)$ and $\hat{\lambda}_\theta(R)$, where $\hat{\lambda}_\theta(R)$ is obtained from the incompressibility condition $\hat{\lambda}_r\hat{\lambda}_\theta^2 = 1$, do not satisfy the compatibility relation

$$R\frac{d\hat{\lambda}_\theta}{dR} = \hat{\lambda}_r - \hat{\lambda}_\theta, \tag{16}$$

and correspond to an incompatible intermediate state with each spherical element of infinitesimal wall thickness stress free. The unloaded state of shell is residually stressed because of the incompatibility of $\hat{\lambda}_r(R)$ and $\hat{\lambda}_\theta(R)$. Next let $(\lambda_r, \lambda_\theta)$ be the stretches in the final unloaded residually stressed state. These stretches can not be used directly in the constitutive relation relating stress and stretch. Stretches which relate the final unloaded residually stressed state to the incompatible intermediate state are required for the constitutive relation, and these stretches are denoted by $(\tilde{\lambda}_r, \tilde{\lambda}_\theta)$. Stretches $(\tilde{\lambda}_r, \tilde{\lambda}_\theta)$ also do not satisfy compatibility. Consideration of uniaxial stress shows that

$$\tilde{\lambda}_r = \frac{\lambda_r}{\hat{\lambda}_r}, \tag{17}$$

and it follows from the incompressibility condition that

$$\tilde{\lambda}_\theta = \tilde{\lambda}_r^{-1/2}. \tag{18}$$

Equations (17) and (18) give $\tilde{\lambda}_r$ and $\tilde{\lambda}_\theta$ as functions of R.

In this section the stretches and Cauchy stresses in the final state of residual stress and deformation are denoted by $(\sigma_r, \sigma_\theta)$ and $(\lambda_r, \lambda_\theta)$, respectively, and the radial coordinate of a particle by r. The residual Cauchy stresses satisfy the relations

$$(\sigma_r - \sigma_\theta) = \mu^*\{\alpha(\tilde{\lambda}_r^2 - \tilde{\lambda}_r^{-1}) + (1 - \alpha)(\tilde{\lambda}_r - \tilde{\lambda}_r^{-2})\}, \tag{19}$$

which are obtained in the same way as (9), and the equilibrium equation

$$\frac{d\sigma_r}{dr} + \frac{2(\sigma_r - \sigma_\theta)}{r} = 0. \tag{20}$$

Substituting (19) in (20) and using (17) and the result $d\sigma_r/dr = (d\sigma_r/dR)/r'$ gives

Downloaded 04 May 2010 to 171.66.16.26. Redistribution subject to ASME license or copyright; see http://www.asme.org/terms/Terms_Use.cfm

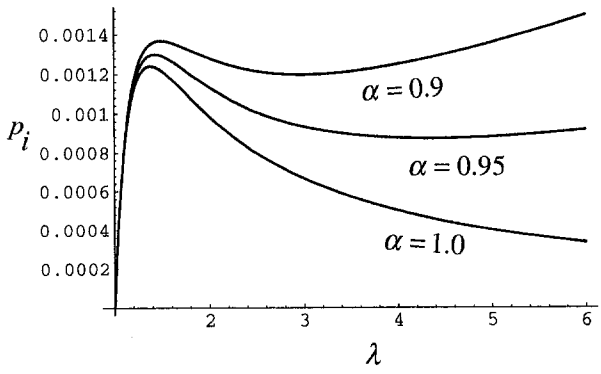

Fig. 2 Internal pressure p_i versus λ for thin-walled Mooney-Rivlin spherical shell with $B = 1.001$

$$\frac{d\sigma_r}{dR} = -\frac{2\mu^* r'}{r}\{\alpha[(r'/\hat{\lambda}_r)^2 - (r'/\hat{\lambda}_r)^{-1}] + (1-\alpha)[(r'/\hat{\lambda}_r) - (r'/\hat{\lambda}_r)^{-2}]\}, \quad (21)$$

where $\hat{\lambda}_r$ is given by (15) and r and r' by (10) and (11a), respectively, with r_o, v_o, and r'_o replaced by r, v, and r'. If μ^* is a known function of $\varepsilon_m(R)$, which can be found from the kinematically determined deformation field for the first inflation the right-hand side of (21) is a function of R and v and can be integrated with respect to R for a given value of v. However, the value of $v = v^{(r)}$, for the unloaded residually stressed state, is not known beforehand. Boundary conditions for the residual stress distribution are $\sigma_r(1) = \sigma_r(B) = 0$ and these are used to obtain $v^{(r)}$ since, along with (21), they imply that

$$\int_1^B \frac{\mu^* r'}{r}\{\alpha[(r'/\hat{\lambda}_r)^2 - (r'/\hat{\lambda}_r)^{-1}] + (1-\alpha)[(r'/\hat{\lambda}_r) - (r'/\hat{\lambda}_r)^{-2}]\}dR = 0, \quad (22)$$

which is solved numerically for $v^{(r)}$. Then $v^{(r)}$ is substituted in the expressions for r and r' which become functions of R only and it follows from (21) that $\sigma_r(R)$ is given by

$$\sigma_r(R) = 2\int_R^B \frac{\mu^* r'(\mathcal{R}, v^{(r)})}{r(\mathcal{R}, v^{(r)})} \left\{ \begin{array}{c} \alpha[(r'(\mathcal{R}, v^{(r)})/\hat{\lambda}_r(\mathcal{R}, v^{(r)}))^2 - (r'(\mathcal{R}, v^{(r)})/\hat{\lambda}_r(\mathcal{R}, v^{(r)}))^{-1}] \\ + (1-\alpha)\left[\begin{array}{c}(r'(\mathcal{R}, v^{(r)})/\hat{\lambda}_r(\mathcal{R}, v^{(r)})) \\ -(r'(\mathcal{R}, v^{(r)})/\hat{\lambda}_r(\mathcal{R}, v^{(r)}))^{-2}\end{array}\right] \end{array} \right\} d\mathcal{R} = 0 \quad (23)$$

and $\sigma_\theta(R)$ is obtained from (19). In order to obtain $\sigma_r(r)$ and $\sigma_\theta(r)$, R is replaced by $(r^3 - v^{(r)^3}B^3 + B^3)$, which follows from incompressibility.

Stress distributions for the deflation process or reinflation from the residually stressed state up to $\lambda_\theta(B) = v_o$ can also be obtained from (23) by replacing $v^{(r)}$ by v^* where v^* is the appropriate value of v in the interval $v^{(r)} < v^* < v_o$.

6 Some Remarks on Inflation From the Virgin State

The procedure described is illustrated by considering the Mooney-Rivlin model and the numerical results are for this model, consequently it desirable to comment on whether this model is appropriate for the first inflation of a balloon or a thick-walled spherical shell, even though the procedure can readily be adapted to other constitutive models.

It is well known that for the first monotonically increasing inflation of a balloon from the virgin state the applied internal pressure rises to a maximum value, decreases to a local minimum value and then increases monotonically and for some materials the balloon loses its spherical symmetry just after the maximum pressure and regains it just before the minimum pressure. This puts restrictions on possible stress-stretch relations used to model the first monotonic inflation from the virgin state. The relation between p and λ_θ for inflation of a balloon modeled as thin-walled spherical shell composed of Mooney-Rivlin material is shown graphically in Fig. 2 for various values of α. Referring to Fig. 2, the relation shown for $\alpha = 0.95$ closely resembles experimental data for inflation of a balloon but the Mooney-Rivlin material does not predict the loss of spherical symmetry. Since it is unlikely loss of spherical symmetry can occur for the thick-walled incompressible spherical shell problem, it is reasonable to assume that the Mooney-Rivlin model with $\alpha = 0.95$ is realistic for the first inflation if the equibiaxial stress-stretch relation is not influenced by superimposed hydrostatic stress.

Depending on the values of B and α a thick-walled Mooney-Rivlin shell may become unstable when the internal pressure reaches a critical value. For example for $B = 3$, the onset of instability is at $v_o = 1.118$ and $p_o = -\sigma_{ro}(1) = 1.21$ for $\alpha = 1$, and after the maximum pressure the pressure decreases monotonically as the inflation proceeds. There is a range of α for which the internal pressure during inflation has qualitatively the same behavior as observed for a balloon and this is illustrated in Fig. 3 for $\alpha = 0.95$. For $B = 3$ and $\alpha < 0.8747$ there is no instability.

7 Numerical Results

In order to obtain numerical results for the residual stresses, (22) is solved numerically for v and (23) is evaluated numerically at $R = 1 + n\Delta R$, where $\Delta R = (B-1)/q$, $q > 0$ is a positive integer and $n \in \{0, 1, \ldots, q\}$. Corresponding values of σ_θ are then obtained from (19) and the stresses as functions of r are obtained by using the incompressibility condition (7). The internal pressure, $p = -\sigma_{ro}(1)$, for the inflation is obtained from (14).

Results for two cases (a) and (b) are now given.

Case (a): $B = 3$, $\mu^* = 0.9$, $\beta = 0.075$, $\lambda_{\theta o}(B) = v_o = 1.3$, $\alpha = 0.95$.

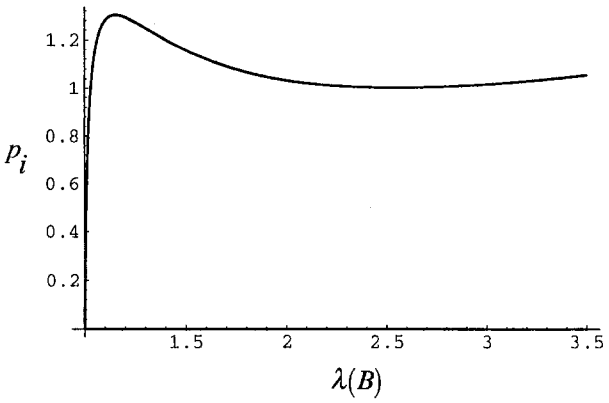

Fig. 3 Internal pressure p_i versus $\lambda(B)$ for thick-walled Mooney-Rivlin shell with $B = 3$, $\alpha = 0.95$

Downloaded 04 May 2010 to 171.66.16.26. Redistribution subject to ASME license or copyright; see http://www.asme.org/terms/Terms_Use.cfm

Case (b): $B = 1.5$, $\mu^* = 0.9$, $\beta = 0.075$, $\lambda_{\theta o}(B) = v_o = 2$, $\alpha = 0.95$.

For case (a), the inflation pressure is $p_i = 1.2495$, and the residual stretches are $\lambda_\theta(3) = 1.00392$ and $\lambda_\theta(1) = 1.0967$. The residual stress distributions are shown in Fig. 4 as functions of r. The residual stress distributions and values of $\lambda_\theta(1)$ and $\lambda_\theta(3)$ differ negligibly for different values of α and the given values of B, μ^*, β, and v_o.

For case (b), the inflation pressure is $p_i = 0.4175$, and the residual stretches are $\lambda_\theta(1.5) = 1.0171$, and $\lambda_\theta(1) = 1.0557$. The residual stress distributions are shown in Fig. 5 as functions of r.

8 Concluding Remarks

It is evident that, for an incompressible shell, the distribution of incompatible permanent set given by $\hat{\lambda}_r$ and $\hat{\lambda}_\theta$ depends only on (15) and v_o for a given value of nondimensional B, but does not depend the constitutive relation for the initial inflation. Since the residual stresses due to the incompatible distribution of $\hat{\lambda}_r$ and $\hat{\lambda}_\theta$ are relatively small, the residual stress distribution depends on μ^* but otherwise has negligible dependence on the form of the constitutive relation for unloading and reloading. This conclusion follows from numerical results obtained using the approximation of constant μ^*.

An experimentally obtained set of stress stretch relations for equibiaxial stress, or uniaxial stress, loading and unloading from the virgin state could be used to determine $\mu^*(\varepsilon_m)$ and empirical uniaxial stress-stretch relations

$$T_L = \mu F_L(\lambda), \tag{24}$$

and

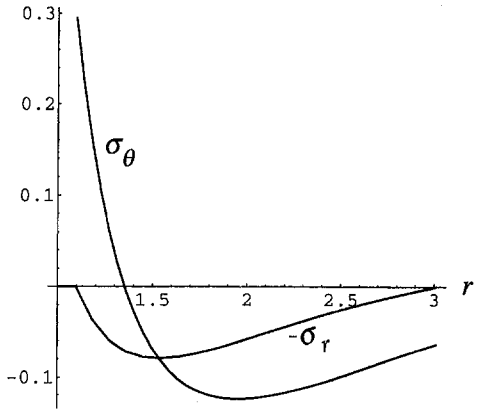

Fig. 4 Residual stress distribution for $B = 3$, $\mu^* = 0.9$, $\beta = 0.075$, $v_o = 1.3$, $\alpha = 0.95$

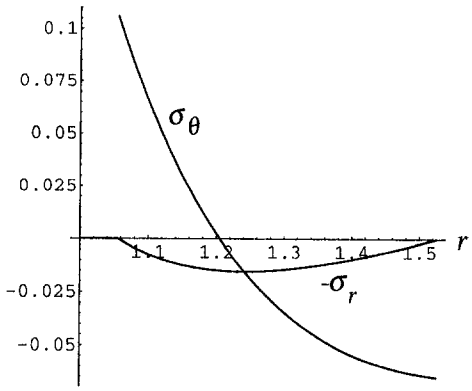

Fig. 5 Residual stress distribution for $B = 1.5$, $\mu^* = 0.9$, $\beta = 0.075$, $v_o = 2.0$, $\alpha = 0.95$

$$T_U = \frac{\mu^*(\varepsilon_m)F_U(\tilde{\lambda})}{1 + \varepsilon^{(r)}} = \frac{\mu^*(\varepsilon_m)F_U(\lambda(1 + \varepsilon^{(r)})^{-1})}{1 + \varepsilon^{(r)}}, \tag{25}$$

for loading and unloading (or reloading), respectively. It may be difficult to obtain empirical relations which satisfy $T_L(\lambda_m) = T_U(\lambda_m)$ for the whole range of λ_m, where $\lambda_m = 1 + \varepsilon_m$; however, a sudden drop in stress at the onset of unloading as for the Mooney-Rivlin based model could be introduced at the onset of unloading in order to satisfy this condition. Equations (1) and (5) are replaced by (24) and (25), respectively, and (13) and (21) by

$$\frac{d\sigma_{ro}}{dR} = -\frac{2r_o'^2 F_L(r')}{r_o}, \tag{26}$$

and

$$\frac{d\sigma_r}{dR} = -\frac{2\mu^*(\varepsilon_m)r'^2}{r\hat{\lambda}_r} F_U(r'/\hat{\lambda}_r), \tag{27}$$

respectively. The procedure for determination of the stress distributions is implemented as for the Mooney-Rivlin model. Equations (26) and (27) are in nondimensional form.

The term permanent set has been used rather loosely since it has been noted that residual deformation after unloading may decrease after several days; consequently, residual stresses in the deflated spherical shell may undergo partial relaxation after a similar time period.

References

Green, A. E., and Zerna, W., 1968, "Theoretical Elasticity, 2nd ed.," Oxford, University Press, Oxford, UK.

Johnson, M. A., and Beatty, M. F., 1995, "The Mullins Effect in Equibiaxial Extension and its Influence on the Inflation of a Balloon," *Int. J. Engng. Sci.*, Vol. 33, pp. 223–245.

Mullins, L., 1947, "Effect of Stretching on the Properties of Rubber," *J. of Rubber Res.*, Vol. 16, pp. 275–289.

Downloaded 04 May 2010 to 171.66.16.26. Redistribution subject to ASME license or copyright; see http://www.asme.org/terms/Terms_Use.cfm

Thermal Stresses in a Generally Anisotropic Body With an Elliptic Inclusion Subject to Uniform Heat Flow

C. K. Chao
Professor,
Department of Mechanical Engineering,
National Taiwan University of
Science and Technology,
Taipei, Taiwan, 106, R.O.C.

M. H. Shen
Assistant Professor,
Department of Mechanical Engineering,
Nakai Jr. College of Technology,
Nantou, Taiwan, R.O.C.

A general analytical solution for the elliptical anisotropic inclusion embedded in an infinite anisotropic matrix subjected to uniform heat flow is provided in this paper. Based upon the method of Lekhnitskii formulation, the technique of conformal mapping, the method of analytical continuation, and the concept of superposition, both the solutions of the temperature and stress functions either in the matrix or in the inclusion are expressed in complex matrix notation. Numerical results are carried out and provided in graphic form to elucidate the effect of material and geometric parameters on the interfacial stresses. Since the general solutions have not been found in the literature, comparison is made with some special cases of which the analytical solutions exist, which shows that our solutions presented here are exact and general.

1 Introduction

Determination of thermal stresses induced by elastic inclusions has been an important topic for studying the thermoelastic behavior of advanced composite materials. In particular, it is needed for strong, tough, and sufficiently stable fiber-reinforced composites that can survive in high-temperature environments. Early work by Florence and Goodier (1959, 1960) studied the thermoelastic problem for an isotropic medium containing a circular or ovaloid hole by the method of Muskhelishvili (1953). Since then a number of the hole or crack problems have received considerable interest such as Chen (1967) for orthotropic medium with an elliptic hole based upon the complex variable technique developed by Green and Zerna (1954), Atkinson and Clements (1977), for anisotropic medium with the two-dimensional Griffith crack using the equations derived by Clements (1973), Sturla and Barber (1988) for anisotropic material with a plane crack by applying a Green's function formulation, Hwu (1990) for anisotropic body with an elliptic hole based upon Stroh formalism (Stroh, 1958; Hwu and Ting, 1989), and Tarn and Wang (1993) for anisotropic materials with a hole or a rigid inclusion based upon Lekhnitskii complex potential approach (Lekhnitskii, 1968). As to thermoelastic inclusion problems, the thermal stresses induced by circular inclusions subjected to arbitrary thermal loadings were recently solved by Chao and Shen (1997) by employing Laurent series expansion and the method of analytical continuation. To the authors' knowledge, there is no general analytical solution for the elliptical anisotropic elastic inclusion embedded in an infinite anisotropic matrix subjected to thermal loadings.

In this paper, the Lekhnitskii formulation (Lekhnitskii, 1968) for anisotropic elasticity which is extended to include the thermal effect combined with the method of analytical continuation (Muskhelishvili, 1953), which is similar to the one proposed by Suo (1990), is developed to solve the present problem. A transformation function which maps the ellipse onto a unit circle is introduced and a restricted condition (Hwu and Yen, 1993) is applied to remedy the discontinuity problem which occurs when the transformation is required to be single-valued and conformal in the entire domain including the matrix and inclusion. Moreover, the concept of superposition is applied to formulate the general solutions which allows us to remove the unwelcomed terms of complex potentials in the matrix which may result in unbounded stresses at infinity. Both the temperature and stress functions either in the matrix or in the inclusion are expressed in compact matrix notation. Some special examples are also solved explicitly and are compared with existing analytical solutions such as isotropic circular inclusions (Chao and Shen, 1997), anisotropic elliptic holes or cracks (Hwu, 1990; Tarn and Wang, 1993). Note that the general solutions derived here cannot be directly reduced to degenerate materials such as isotropic materials due to the repeated eigenvalues of the elastic constants. A small perturbation of material constants will be employed to obtain distinct eigenvalues.

The plan of this paper is as follows. The general formulation for plane anisotropic thermoelasticity is provided in Section 2. The general forms of the complex potentials of the temperature and stress functions are derived in Section 3 and Section 4, respectively. Some special examples are solved in Section 5. Finally, Section 6 concludes the article.

2 Formulations for Plane Anisotropic Thermoelasticity

2.1 Basic Equations. The two-dimensional anisotropic thermoelastic field can be represented in terms of three stress functions $\phi_1(z_1)$, $\phi_2(z_2)$, $\phi_3(z_3)$, and a temperature function $g'(z_t)$, with the arguments $z_\alpha = x_1 + s_\alpha x_2$, $\alpha = 1, 2, 3, t$. The elasticity eigenvalues s_α ($\alpha = 1, 2, 3$) have been derived by Lekhnitskii (1963) which satisfy the sixth-order characteristic equation

$$l_2(s)l_4(s) - l_3^2(s) = 0 \tag{1}$$

with

$$l_2(s) = a_{44} - 2a_{45}s + a_{55}s^2$$

$$l_3(s) = -a_{24} + (a_{25} + a_{46})s - (a_{14} + a_{56})s^2 + a_{15}s^3$$

Contributed by the Applied Mechanics Division of THE AMERICAN SOCIETY OF MECHANICAL ENGINEERS for publication in the ASME JOURNAL OF APPLIED MECHANICS.

Discussion on this paper should be addressed to the Technical Editor, Professor Lewis T. Wheeler, Department of Mechanical Engineering, University of Houston, Houston, TX 77204-4792, and will be accepted until four months after final publication of the paper itself in the ASME JOURNAL OF APPLIED MECHANICS.

Manuscript received by the ASME Applied Mechanics Division, Apr. 3, 1995; final revision, Aug. 3, 1997. Associate Technical Editor: Editor: M. Taya.

 Copyright © 1998 by ASME

Downloaded 04 May 2010 to 171.66.16.26. Redistribution subject to ASME license or copyright; see http://www.asme.org/terms/Terms_Use.cfm

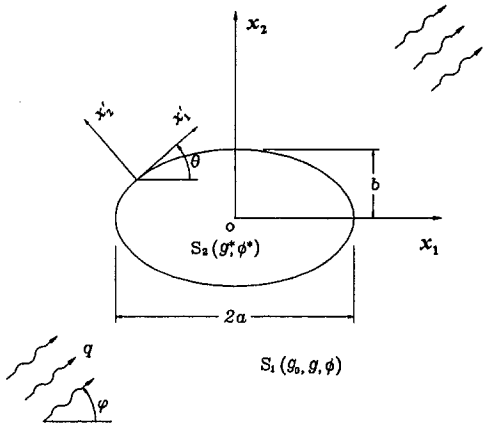

Fig. 1 Elliptic inclusion under a remote uniform heat flow

$$l_4(s) = a_{22} - 2a_{26}s + (2a_{12} + a_{66})s^2 - 2a_{16}s^3 + a_{11}s^4 \quad (2)$$

where a_{ij} $(i, j = 1, 2, \ldots, 6)$ denote the compliance tensor of an anisotropic material. The heat eigenvalue s_t is the root of the thermal characteristic equation with positive imaginary part

$$k_{22}s^2 + 2k_{12}s + k_{11} = 0 \quad (3)$$

where k_{ij} $(i, j = 1, 2)$ are the heat conductivity coefficients. The assumption of positive definiteness of the heat conductivity constants has been adopted such that the heat eigenvalue s_t cannot be a real number in Eq. (3). With stress functions $\phi_\alpha(z_\alpha)$ $(\alpha = 1, 2, 3)$ and a temperature function $g'(z_t)$, the representation for the temperature T, resultant heat flow Q, heat flux q_i, displacement u_i, resultant force p_i, and stresses σ_{ij} for uncoupled steady-state anisotropic thermoelasticity can be written as

$$T = 2\,\mathrm{Re}[g'(z_t)] \quad (4)$$

$$Q = 2\,\mathrm{Re}[i(k_{11}k_{22} - k_{12}^2)^{1/2}g'(z_t)] \quad (5)$$

$$q_i = -2\,\mathrm{Re}[(k_{i1} + s_t k_{i2})g''(z_t)] \quad (6)$$

$$u_i = 2\,\mathrm{Re}[\sum_{j=1}^{3} A_{ij}\phi_j(z_j) + c_i g(z_t)] \quad (7)$$

$$p_i = -2\,\mathrm{Re}[\sum_{j=1}^{3} L_{ij}\phi_j(z_j) + d_i g(z_t)] \quad (8)$$

$$\sigma_{2i} = 2\,\mathrm{Re}[\sum_{j=1}^{3} L_{ij}\phi_j'(z_j) + d_i g'(z_t)] \quad (9)$$

$$\sigma_{1i} = -2\,\mathrm{Re}[\sum_{j=1}^{3} L_{ij}s_j\phi_j'(z_j) + s_t d_i g'(z_t)] \quad (10)$$

with $Q = \int q_1 dx_2 - q_2 dx_1$. Here, $(')$ is designated as the derivative with respect to the associated arguments, and Re denotes the real part of a complex function. Hereafter, boldfaced symbols represent vectors or matrices. The matrices $\mathbf{L}$, $\mathbf{A}$ and the vectors $\mathbf{c}$, $\mathbf{d}$ in Eqs. (7)–(10) have been derived by Lekhnitskii (1963) and Chao and Chang (1994), respectively.

2.2 Conformal Mapping. Consider the thermoelastic problem of an anisotropic solid containing an elliptical inhomogeneity (see Fig. 1). The materials are assumed to be perfectly bonded along the common boundary. In the present problem, the regions occupied by the matrix and the inclusion are denoted by S_1 and S_2, respectively, while the starred and nonstarred quantities will be referred to the inclusion and the matrix, respectively. Now, we introduce the transformation function

$$z_\alpha = \frac{1}{2}\left\{(a - ibs_\alpha)\zeta_\alpha + (a + ibs_\alpha)\frac{1}{\zeta_\alpha}\right\} \quad (11)$$

which will transform the region outside the elliptic inclusion of the z_α-plane onto the exterior of a unit circle in the transformed ζ_α-plane and the region inside the elliptic inclusion onto the annular region between the unit circle and a circle of radius $\sqrt{m_\alpha}$ which is defined as (Hwu and Yen, 1993)

$$\sqrt{\frac{a + ibs_\alpha}{a - ibs_\alpha}} = \sqrt{m_\alpha}e^{i\theta_\alpha} \quad (12)$$

where θ_α is the argument corresponding to the modulus $\sqrt{m_\alpha}$. It has been shown that $\sqrt{m_\alpha} < 1$ if the imaginary part of s_α is set to be positive. Note that, the transformation is single valued outside the elliptic inclusion. However, it becomes double valued and nonconformal inside the elliptic inclusion. To remedy this discontinuity, the following restriction should be satisfied (Hwu and Yen, 1993):

$$f(\sqrt{m_\alpha}\sigma e^{-i\theta_\alpha}) = f(\sqrt{m_\alpha}e^{i\theta_\alpha}/\sigma) \quad (13)$$

where $\sigma = e^{i\psi}$ denotes the points located on the unit circle.

3 Uniform Heat Flow Disturbed by an Elliptic Inclusion

Consider a uniform heat flux q directed at an angle φ with respect to the positive x_1-axis is disturbed by the presence of an elliptic inclusion (see Fig. 1). In the present study, both the temperature and resultant heat flow are used to formulate the thermal boundary conditions along the interface. By applying the conformal mapping technique described above, the general solutions of the thermal field for the inclusion problem can be written as

$$\left.\begin{aligned} T &= [g_0'(\zeta) + g'(\zeta)] + [\overline{g_0'(\zeta)} + \overline{g'(\zeta)}] \\ Q &= i\beta[g_0'(\zeta) + g'(\zeta)] - i\beta[\overline{g_0'(\zeta)} + \overline{g'(\zeta)}] \end{aligned}\right\}, \quad \zeta \in S_1 \quad (14)$$

$$\left.\begin{aligned} T^* &= g'^*(\zeta) + \overline{g'^*(\zeta)} \\ Q^* &= i\beta^* g'^*(\zeta) - i\beta^*\overline{g'^*(\zeta)} \end{aligned}\right\}, \quad \zeta \in S_2 \quad (15)$$

where $\beta = (k_{11}k_{22} - k_{12}^2)^{1/2}$ and the overbar denotes the conjugate of a complex function. $g_0'(\zeta)$ represents the temperature function associated with the unperturbed field which is related to the solution of homogeneous media. $g'(\zeta)$ (or $g'^*(\zeta)$) is the temperature function corresponding to the perturbed field of matrix (or inclusion) which is holomorphic in region S_1 (or S_2) except some singular points. Note that the argument of each temperature function in (14) and (15) is written in terms of ζ instead of ζ_t. Once the solution is obtained for a given boundary value problem, a replacement of ζ_t should be made for each temperature function to calculate field quantities (Suo, 1990). Since $g'^*(\zeta)$ is holomorphic in the annular ring, it can be represented by Laurent's expansion

$$g'^*(\zeta) = \sum_{k=-\infty}^{\infty} e_k\zeta^k. \quad (16)$$

Applying (13), the constant e_k in (16) now satisfies the following condition, i.e.,

$$e_{-k} = \Gamma_k^* e_k, \quad \Gamma_k^* = \left(\frac{a + ibs_t^*}{a - ibs_t^*}\right)^k. \quad (17)$$

The solution associated with the homogeneous media subjected to remote uniform heat flux may be expressed as

Downloaded 04 May 2010 to 171.66.16.26. Redistribution subject to ASME license or copyright; see http://www.asme.org/terms/Terms_Use.cfm

$$g_0'(\zeta) = hz = h(m_{1t}\zeta + m_{2t}\zeta^{-1}) \tag{18}$$

where

$$h = \frac{q(\cos\varphi + \bar{s}_t \sin\varphi)}{i\beta(s_t - \bar{s}_t)}$$

$$m_{1t} = (a - ibs_t)/2, \quad m_{2t} = (a + ibs_t)/2. \tag{19}$$

Since the inclusion and the matrix are assumed to be perfectly bonded along the interface, both the temperature and resultant heat flow must be continuous. That is

$$T = T^*, \quad Q = Q^*, \quad \text{along the interface } \zeta = \sigma = e^{i\psi} \tag{20}$$

By using the general solutions given in (14) and (15) and the expressions given in (16)–(19), the thermal continuity conditions of (20) lead to

$$g'(\sigma) - \sum_{k=1}^{\infty} \bar{e}_k\sigma^{-k} - \sum_{k=1}^{\infty} \Gamma_k^* e_k\sigma^{-k} + (hm_{2t} + \overline{hm_{1t}})\sigma^{-1}$$
$$= -\bar{g}'\left(\frac{1}{\sigma}\right) + \sum_{k=1}^{\infty} e_k\sigma^k + \sum_{k=1}^{\infty} \bar{\Gamma}_k^* \bar{e}_k\sigma^k$$
$$- (\overline{hm_{2t}} + hm_{1t})\sigma \tag{21}$$

and

$$i\beta g'(\sigma) + i\beta^* \sum_{k=1}^{\infty} \bar{e}_k\sigma^{-k} - i\beta^* \sum_{k=1}^{\infty} \Gamma_k^* e_k\sigma^{-k}$$
$$+ (i\beta hm_{2t} - i\beta\overline{hm_{1t}})\,\sigma^{-1} = i\beta\bar{g}'\left(\frac{1}{\sigma}\right) + i\beta^* \sum_{k=1}^{\infty} e_k\sigma^k$$
$$- i\beta^* \sum_{k=1}^{\infty} \bar{\Gamma}_k^* \bar{e}_k\sigma^k + (i\beta\overline{hm_{2t}} - i\beta hm_{1t})\sigma. \tag{22}$$

Using the properties of holomorphic functions and applying the method of analytical continuation, we may introduce a new set of complex potentials $\theta_j(\zeta)$ which are holomorphic in the entire domain including the interface boundary as

$$\begin{bmatrix}\theta_1(\zeta)\\ \theta_2(\zeta)\end{bmatrix} = \begin{bmatrix}1 & -1\\ i\beta & i\beta^*\end{bmatrix}\begin{bmatrix}g'(\zeta)\\ \sum_{k=1}^{\infty} \bar{e}_k\zeta^{-k}\end{bmatrix}$$
$$- \begin{bmatrix}1\\ i\beta^*\end{bmatrix}\sum_{k=1}^{\infty} \Gamma_k^* e_k\zeta^{-k} + \begin{bmatrix}1 & 1\\ i\beta & -i\beta\end{bmatrix}\begin{bmatrix}hm_{2t}\\ \overline{hm_{1t}}\end{bmatrix}\zeta^{-1} \tag{23}$$

for $|\zeta| > 1$ and

$$\begin{bmatrix}\theta_1(\zeta)\\ \theta_2(\zeta)\end{bmatrix} = \begin{bmatrix}1 & -1\\ i\beta^* & i\beta\end{bmatrix}\begin{bmatrix}\sum_{k=1}^{\infty} e_k\zeta^k\\ \bar{g}'\left(\frac{1}{\zeta}\right)\end{bmatrix}$$
$$+ \begin{bmatrix}1\\ -i\beta^*\end{bmatrix}\sum_{k=1}^{\infty} \bar{\Gamma}_k^* \bar{e}_k\zeta^k - \begin{bmatrix}1 & 1\\ -i\beta & i\beta\end{bmatrix}\begin{bmatrix}\overline{hm_{2t}}\\ hm_{1t}\end{bmatrix}\zeta \tag{24}$$

for $|\zeta| < 1$. Since the potentials $\theta_1(\zeta), \theta_2(\zeta)$ are now holomorphic and single valued in the whole plane including the point at infinity, by Liouville's theorem we have $\theta_j(\zeta) \equiv$ constant. However, the constant functions $\theta_j(\zeta)$ can be regarded as reference temperature, we take $\theta_j(\zeta) \equiv 0$ without loss in generality. With this result, (23) and (24) lead to

$$g'(\zeta) = (-hm_{2t} + \frac{\beta - \beta^*}{\beta + \beta^*}\overline{hm_{1t}})\,\zeta^{-1}$$
$$+ \sum_{k=1}^{\infty} \frac{2\beta^*}{\beta^* + \beta} \Gamma_k^* e_k\zeta^{-k} \tag{25}$$

$$\sum_{k=1}^{\infty} e_k\zeta^k = \frac{2\beta}{\beta^* + \beta} hm_{1t}\zeta + \sum_{k=1}^{\infty} \frac{\beta^* - \beta}{\beta + \beta^*} \bar{\Gamma}_k^* \bar{e}_k\zeta^k. \tag{26}$$

By comparing the coefficients of ζ^k in (26), we obtain

$$e_1 = \frac{2\beta(\beta^* + \beta)hm_{1t} + 2\beta(\beta^* - \beta)\bar{\Gamma}_1^*\overline{hm_{1t}}}{(\beta + \beta^*)^2 - (\beta - \beta^*)^2\bar{\Gamma}_1^*\Gamma_1^*} \tag{27}$$

$$e_k = 0, \quad \text{for} \quad k \neq 1, -1. \tag{28}$$

Substitution of (27) and (28) into (16) and (25) results in

$$g'(\zeta) = (-hm_{2t} + \frac{\beta - \beta^*}{\beta + \beta^*}\overline{hm_{1t}} + \frac{2\beta^*}{\beta + \beta^*}\Gamma_1^* e_1)\,\zeta^{-1} \tag{29}$$

$$g'^*(\zeta) = e_1\zeta + \Gamma_1^* e_1\zeta^{-1}. \tag{30}$$

It is easy to verify that

$$g_0'(\zeta) + g'(\zeta) = g'^*(\zeta) = hz \tag{31}$$

for the special case of homogeneous anisotropic problem if one lets $\beta = \beta^*$ in (27) and (29).

4 Thermal Stresses Induced by an Elliptic Inclusion

Due to the linear property, the principle of superposition can be used and the solution can be represented as the sum of a homogeneous media subjected to a remote uniform heat flow and a corrective solution for which the temperature functions are $g'(\zeta)$ in the matrix and $g'^*(\zeta)$ in the inclusion. The general solutions for the inclusion problem are now be written as

$$\left.\begin{aligned}\mathbf{u} &= \mathbf{A}\phi(\zeta) + \bar{\mathbf{A}}\overline{\phi(\zeta)} + \mathbf{c}g(\zeta) + \overline{\mathbf{c}g(\zeta)}\\ \mathbf{p} &= -\mathbf{L}\phi(\zeta) - \bar{\mathbf{L}}\overline{\phi(\zeta)} - \mathbf{d}g(\zeta) - \overline{\mathbf{d}g(\zeta)}\end{aligned}\right\}, \quad \zeta \in S_1 \tag{32}$$

$$\left.\begin{aligned}\mathbf{u}^* &= \mathbf{A}^*\phi^*(\zeta) + \bar{\mathbf{A}}^*\overline{\phi^*(\zeta)} + \mathbf{c}^*g^*(\zeta)\\ &\quad + \overline{\mathbf{c}^*g^*(\zeta)} - \mathbf{c}g_0(\zeta) - \overline{\mathbf{c}g_0(\zeta)}\\ \mathbf{p}^* &= -\mathbf{L}^*\phi^*(\zeta) - \bar{\mathbf{L}}^*\overline{\phi^*(\zeta)} - \mathbf{d}^*g^*(\zeta)\\ &\quad - \overline{\mathbf{d}^*g^*(\zeta)} + \mathbf{d}g_0(\zeta) + \overline{\mathbf{d}g_0(\zeta)}\end{aligned}\right\}, \quad \zeta \in S_2. \tag{33}$$

Note that the complex functions $\mathbf{c}g_0(\zeta) + \overline{\mathbf{c}g_0(\zeta)}$ and $\mathbf{d}g_0(\zeta) + \overline{\mathbf{d}g_0(\zeta)}$ associated with the solutions of the homogeneous problem due to a uniform heat flow will not produce stress which permits us to subtract these complex functions from (7) and (8) without difficulty. Keeping in mind that, with similar reason as Suo (1990), the arguments of each complex function in (32) and (33) are written in terms ζ without referring to the associated eigenvalues s_α while a replacement of ζ_1, ζ_2, ζ_3, or ζ_t must be made for each function to calculate field quantities from (4)–(10) once the solutions of $\phi(\zeta)$ and $\phi^*(\zeta)$ are obtained. After integrating the temperature functions in (18), (29), and (30) with respect to z_t, we obtain

$$g(\zeta) = \gamma_1 \log\zeta + \gamma_2\zeta^{-2}$$
$$g^*(\zeta) = \tfrac{1}{2}e_1m_{1t}\zeta^2 + \tfrac{1}{2}\Gamma_1^* e_1m_{2t}\zeta^{-2}$$
$$g_0(\zeta) = \tfrac{1}{2}hm_{1t}^2\zeta^2 + \tfrac{1}{2}hm_{2t}^2\zeta^{-2} \tag{34}$$

where

Downloaded 04 May 2010 to 171.66.16.26. Redistribution subject to ASME license or copyright; see http://www.asme.org/terms/Terms_Use.cfm

$$\gamma_1 = \left(-hm_{2t} + \frac{\beta - \beta^*}{\beta + \beta^*}\,\overline{hm_{1t}} + \frac{2\beta^*}{\beta + \beta^*}\,\Gamma_1^* e_1 \right) m_{1t}$$

$$\gamma_2 = \frac{1}{2}\,\gamma_1 \frac{m_{2t}}{m_{1t}}. \tag{35}$$

For the condition that both the stresses and displacements are single valued either in the matrix or in the inclusion, the stress functions $\phi(\zeta)$ and $\phi^*(\zeta)$ must take the form

$$\phi(\zeta) = \mathbf{f}(\zeta) + \boldsymbol{\delta} \log \zeta \tag{36}$$

$$\phi^*(\zeta) = \sum_{-\infty}^{\infty} \boldsymbol{\lambda}_k \zeta^k \tag{37}$$

where

$$\boldsymbol{\lambda}_{-k} = \mathbf{G}_k^* \boldsymbol{\lambda}_k, \quad \mathbf{G}_k^* = \left\langle\left\langle \left(\frac{a + ibs_\alpha^*}{a - ibs_\alpha^*} \right)^k \right\rangle\right\rangle, \quad (\alpha = 1, 2, 3). \tag{38}$$

The angular bracket stands for the diagonal matrix, i.e., $\langle\langle f_\alpha \rangle\rangle = \text{diag}\,\{f_1, f_2, f_3\}$ and $\mathbf{f}(\zeta)$, $\boldsymbol{\delta}$, $\boldsymbol{\lambda}_k$ are all 3×1 matrices. The coefficient $\boldsymbol{\delta}$ in (36) satisfies the following equations:

$$\begin{aligned} \mathbf{L}\boldsymbol{\delta} - \overline{\mathbf{L}\boldsymbol{\delta}} &= -\gamma_1 \mathbf{d} + \overline{\gamma_1 \mathbf{d}} \\ \mathbf{A}\boldsymbol{\delta} - \overline{\mathbf{A}\boldsymbol{\delta}} &= -\gamma_1 \mathbf{c} + \overline{\gamma_1 \mathbf{c}}\,. \end{aligned} \tag{39}$$

Solving for (39), we obtain

$$\boldsymbol{\delta} = \mathbf{A}^{-1}(\bar{\mathbf{B}}^{-1} - \mathbf{B}^{-1})^{-1}(\gamma_1 \mathbf{d} - \overline{\gamma_1 \mathbf{d}}) + \mathbf{L}^{-1}(\bar{\mathbf{B}} - \mathbf{B})^{-1}(\gamma_1 \mathbf{c} - \overline{\gamma_1 \mathbf{c}}) \tag{40}$$

where $\mathbf{B} = \mathbf{A}\mathbf{L}^{-1}$.

Now, the remaining unknown function $\mathbf{f}(\zeta)$ in (36) and unknown constant $\boldsymbol{\lambda}_k$ in (37) will be determined from the interface continuity conditions. Since the inclusion and the matrix are assumed to be perfectly bonded along the interface, the displacements and surface tractions at the interface should be continuous. That is

$$\mathbf{u} = \mathbf{u}^*, \quad \mathbf{p} = \mathbf{p}^*, \quad \text{along the interface } \zeta = \sigma = e^{i\psi}. \tag{41}$$

By using the general solutions given in (32) and (33) and the expressions given in (34)–(38), the continuity conditions of (41) lead to

$$\begin{aligned} &\mathbf{A}\mathbf{f}(\sigma) - \bar{\mathbf{A}}^* \sum_{k=1}^{\infty} \bar{\boldsymbol{\lambda}}_k \sigma^{-k} - \mathbf{A}^* \sum_{k=1}^{\infty} \mathbf{G}_k^* \boldsymbol{\lambda}_k \sigma^{-k} \\ &+ \left[\left(\gamma_2 + \frac{h}{2} m_{2t}^2 \right) \mathbf{c} + \frac{1}{2}\,\overline{hm_{1t}^2}\,\mathbf{c} - \frac{1}{2}\,\Gamma_1^* e_1 m_{2t} \mathbf{c}^* \right. \\ &\left. - \frac{1}{2}\,\overline{e_1 m_{1t}}\,\overline{\mathbf{c}^*} \right] \sigma^{-2} = \mathbf{A}^* \sum_{k=1}^{\infty} \boldsymbol{\lambda}_k \sigma^k - \bar{\mathbf{A}}\bar{\mathbf{f}}\left(\frac{1}{\sigma} \right) \\ &+ \mathbf{A}^* \sum_{k=1}^{\infty} \bar{\mathbf{G}}_k^* \bar{\boldsymbol{\lambda}}_k \sigma^k + \left[-\left(\bar{\gamma}_2 + \frac{1}{2}\,\overline{hm_{2t}^2} \right) \bar{\mathbf{c}} \right. \\ &\left. - \frac{1}{2}\,hm_{1t}^2 \mathbf{c} + \frac{1}{2}\,\bar{\Gamma}_1^* \overline{e_1 m_{2t}}\,\overline{\mathbf{c}^*} + \frac{1}{2}\,e_1 m_{1t} \mathbf{c}^* \right] \sigma^2 \end{aligned} \tag{42}$$

and

$$\begin{aligned} &\mathbf{L}\mathbf{f}(\sigma) - \bar{\mathbf{L}}^* \sum_{k=1}^{\infty} \bar{\boldsymbol{\lambda}}_k \sigma^{-k} - \mathbf{L}^* \sum_{k=1}^{\infty} \mathbf{G}_k^* \boldsymbol{\lambda}_k \sigma^{-k} \\ &+ \left[\left(\gamma_2 + \frac{h}{2} m_{2t}^2 \right) \right] \mathbf{d} + \frac{1}{2}\,\overline{hm_{1t}^2}\,\bar{\mathbf{d}} - \frac{1}{2}\,\Gamma_1^* e_1 m_{2t} \mathbf{d}^* \\ &\left. - \frac{1}{2}\,\overline{e_1 m_{1t}}\,\bar{\mathbf{d}}^* \right] \sigma^{-2} = \mathbf{L}^* \sum_{k=1}^{\infty} \boldsymbol{\lambda}_k \sigma^k - \bar{\mathbf{L}}\bar{\mathbf{f}}\left(\frac{1}{\sigma} \right) \\ &+ \mathbf{L}^* \sum_{k=1}^{\infty} \bar{\mathbf{G}}_k^* \bar{\boldsymbol{\lambda}}_k \sigma^k + \left[-\left(\bar{\gamma}_2 + \frac{1}{2}\,\overline{hm_{2t}^2} \right) \bar{\mathbf{d}} - \frac{1}{2}\,hm_{1t}^2 \mathbf{d} \right. \\ &\left. + \frac{1}{2}\,\bar{\Gamma}_1^* \overline{e_1 m_{2t}}\,\bar{\mathbf{d}}^* + \frac{1}{2}\,e_1 m_{1t} \mathbf{d}^* \right] \sigma^2. \end{aligned} \tag{43}$$

It should be emphasized that the logarithmic terms in (42) and (43) have been removed such that one may be able to apply the method of analytical continuation. Similar to the previous approach, a new set of complex potentials $\omega_j(\zeta)$ $(j = 1, 2, \ldots, 6)$ are introduced as

$$\begin{aligned} \boldsymbol{\omega}(\zeta) = &\begin{bmatrix} \mathbf{A} & -\bar{\mathbf{A}}^* \\ \mathbf{L} & -\bar{\mathbf{L}}^* \end{bmatrix} \begin{bmatrix} \mathbf{f}(\zeta) \\ \sum_{k=1}^{\infty} \bar{\boldsymbol{\lambda}}_k \zeta^{-k} \end{bmatrix} - \begin{bmatrix} \mathbf{A}^* \\ \mathbf{L}^* \end{bmatrix} \sum_{k=1}^{\infty} \mathbf{G}_k^* \boldsymbol{\lambda}_k \zeta^{-k} \\ &+ \begin{bmatrix} \mathbf{c} & \bar{\mathbf{c}} & -\mathbf{c}^* & -\bar{\mathbf{c}}^* \\ \mathbf{d} & \bar{\mathbf{d}} & -\mathbf{d}^* & -\bar{\mathbf{d}}^* \end{bmatrix} \begin{bmatrix} \gamma_2 + \frac{h}{2} m_{2t}^2 \\ \frac{1}{2}\,\overline{hm_{1t}^2} \\ \frac{1}{2}\,\Gamma_1^* e_1 m_{2t} \\ \frac{1}{2}\,\overline{e_1 m_{1t}} \end{bmatrix} \zeta^{-2} \end{aligned} \tag{44}$$

for $\zeta \in S_1$ and

$$\begin{aligned} \boldsymbol{\omega}(\zeta) = &\begin{bmatrix} \mathbf{A}^* & -\bar{\mathbf{A}} \\ \mathbf{L}^* & -\mathbf{L} \end{bmatrix} \begin{bmatrix} \sum_{k=1}^{\infty} \boldsymbol{\lambda}_k \zeta^k \\ \mathbf{f}\left(\frac{1}{\zeta} \right) \end{bmatrix} + \begin{bmatrix} \mathbf{A}^* \\ \mathbf{L}^* \end{bmatrix} \sum_{k=1}^{\infty} \bar{\mathbf{G}}_k^* \bar{\boldsymbol{\lambda}}_k \zeta^k \\ &+ \begin{bmatrix} -\bar{\mathbf{c}} & -\mathbf{c} & \bar{\mathbf{c}}^* & \mathbf{c}^* \\ -\bar{\mathbf{d}} & -\mathbf{d} & \bar{\mathbf{d}}^* & \mathbf{d}^* \end{bmatrix} \begin{bmatrix} \bar{\gamma}_2 + \frac{1}{2}\,\overline{hm_{2t}^2} \\ \frac{h}{2} m_{1t}^2 \\ \frac{1}{2}\,\bar{\Gamma}_1^* \overline{e_1 m_{2t}} \\ \frac{1}{2}\,e_1 m_{1t} \end{bmatrix} \zeta^2 \end{aligned} \tag{45}$$

for $\zeta \in S_2$. It follows that $\boldsymbol{\omega}(\zeta)$ are holomorphic and single valued in the whole plane which will give displacements and stresses to automatically satisfy the interface condition and allow the solution of the thermoelastic interface problem to be developed conveniently in the context of analytic function theory. By Liouville's theorem we have $\omega_j(\zeta) \equiv$ const. However, the constant functions $\omega_j(\zeta)$ correspond to rigid-body motion which may be neglected, we have $\omega_j(\zeta) \equiv 0$. With this result, (44) and (45) lead to

Downloaded 04 May 2010 to 171.66.16.26. Redistribution subject to ASME license or copyright; see http://www.asme.org/terms/Terms_Use.cfm

$$\mathbf{f}(\zeta) = \sum_{k=1}^{\infty} \mathbf{H}\mathbf{G}_k^* \boldsymbol{\lambda}_k \zeta^{-k} - \left[\mathbf{a}\left(\gamma_2 + \frac{h}{2} m_{2t}^2 \right) + \mathbf{b}\,\frac{1}{2}\,\Gamma_1^* e_1 m_{2t} + \mathbf{k}\,\frac{1}{2}\,\overline{e_1 m_{1t}} + \mathbf{m}\,\frac{1}{2}\,\overline{h m_{1t}^2} \right] \zeta^{-2} \quad (46)$$

$$\sum_{k=1}^{\infty} \boldsymbol{\lambda}_k \zeta^k = -\sum_{k=1}^{\infty} \mathbf{S}\bar{\mathbf{G}}_k^* \bar{\boldsymbol{\lambda}}_k \zeta^k - \left[\mathbf{n}(\bar{\gamma}_2 + \tfrac{1}{2}\overline{h m_{2t}^2}) + \mathbf{r}\tfrac{1}{2}\bar{\Gamma}_1^* \bar{e}_1 \overline{m_{2t}} + \mathbf{v}\tfrac{1}{2} e_1 m_{1t} + \mathbf{w}\tfrac{1}{2} h m_{1t}^2 \right] \zeta^2 \quad (47)$$

where

$$H_{ij} = \sum_{k=1}^{6} M_{ik}^{-1} \bar{M}_{k(j+3)},$$

$$a_i = \sum_{k=1}^{6} M_{ik}^{-1} R_{k1}, \quad b_i = \sum_{k=1}^{6} M_{ik}^{-1} R_{k3},$$

$$k_i = \sum_{k=1}^{6} M_{ik}^{-1} R_{k4}, \quad m_i = \sum_{k=1}^{6} M_{ik}^{-1} R_{k2}, \quad (48)$$

and

$$S_{ij} = \sum_{k=1}^{6} \bar{M}_{(i+3)k}^{-1} M_{k(j+3)},$$

$$n_i = \sum_{k=1}^{6} \bar{M}_{(i+3)k}^{-1} \bar{R}_{k1}, \quad r_i = \sum_{k=1}^{6} \bar{M}_{(i+3)k}^{-1} \bar{R}_{k3},$$

$$v_i = \sum_{k=1}^{6} \bar{M}_{(i+3)k}^{-1} \bar{R}_{k4}, \quad w_i = \sum_{k=1}^{6} \bar{M}_{(i+3)k}^{-1} \bar{R}_{k2}, \quad (49)$$

in which $\mathbf{M}$ and $\mathbf{R}$ are the 6×6 matrix and 6×4 matrix in (44), respectively. Solving for (46) and (47) we obtain

$$\boldsymbol{\lambda}_2 = [\mathbf{I} - \mathbf{S}\bar{\mathbf{G}}_2^* \mathbf{S}\mathbf{G}_2^*]^{-1} \{ \mathbf{S}\bar{\mathbf{G}}_2^* [\bar{\mathbf{n}}(\gamma_2 + \tfrac{1}{2} h m_{2t}^2) + \bar{\mathbf{r}}\tfrac{1}{2}\Gamma_1^* e_1 m_{2t} + \bar{\mathbf{v}}\tfrac{1}{2}\overline{e_1 m_{1t}} + \bar{\mathbf{w}}\tfrac{1}{2}\overline{h m_{1t}^2}] - [\mathbf{n}(\bar{\gamma}_2 + \tfrac{1}{2}\overline{h m_{2t}^2}) + \mathbf{r}\tfrac{1}{2}\bar{\Gamma}_1^* \bar{e}_1 \overline{m_{2t}} + \mathbf{v}\tfrac{1}{2} e_1 m_{1t} + \mathbf{w}\tfrac{1}{2} h m_{1t}^2] \quad (50)$$

$$\boldsymbol{\lambda}_k = 0, \quad \text{for} \quad k \neq -2, 2 \quad (51)$$

and

$$\mathbf{f}(\zeta) = \left\{ \mathbf{H}\mathbf{G}_2^* \boldsymbol{\lambda}_2 - \left[\mathbf{a}\left(\gamma_2 + \frac{h}{2} m_{2t}^2 \right) + \mathbf{b}\,\frac{1}{2}\,\Gamma_1^* e_1 m_{2t} + \mathbf{k}\,\frac{1}{2}\,\overline{e_1 m_{1t}} + \mathbf{m}\,\frac{1}{2}\,\overline{h m_{1t}^2} \right] \right\} \zeta^{-2} \quad (52)$$

where $\mathbf{I}$ is an 3×3 identity matrix. Having the results of $\boldsymbol{\lambda}_k$, $\mathbf{f}(\zeta)$, the stress functions $\phi(\zeta)$, $\phi^*(\zeta)$ can now be obtained from (36) and (37), respectively, and the whole field solutions in (4)–(10) are determined accordingly with the understanding that a replacement of ζ_1, ζ_2, ζ_3, or ζ_t should be made for each component function. The stresses in the inclusion can be directly obtained by differentiating the function (37) with respect to z_α as

$$\frac{d\phi^*}{dz_\alpha} = (2\boldsymbol{\lambda}_2 \zeta - 2\boldsymbol{\lambda}_{-2}\zeta^{-3})/(m_{1\alpha} - m_{2\alpha}\zeta^{-2}) = 2(\boldsymbol{\lambda}_2 \zeta + \mathbf{G}_1^* \boldsymbol{\lambda}_2 \zeta^{-1})/m_{1\alpha} = 2\boldsymbol{\lambda}_2 z_\alpha / m_{1\alpha}^2. \quad (53)$$

Similarly, the derivative of the temperature function (30) can be expressed as

$$\frac{dg^*}{dz_t} = e_1 z_t / m_{1t}. \quad (54)$$

Upon substitution of (53) and (54) into (9) and (10), it is interesting to see that the stresses in the inclusion are always linear functions of the coordinates $z_\alpha = x_1 + s_\alpha x_2$ and $z_t = x_1 + s_t x_2$, which is basically different from the result of uniform stresses existing in the inclusion of the corresponding isothermal elastic problem. The interfacial stresses along the inclusion boundary can be performed by using the field solution of the matrix or inclusion. The stress components based upon the coordinate system (x_1', x_2') which are, respectively, the unit vectors tangent and normal to the interface boundary, are obtained as

$$\sigma_{i'j'} = e_{i'i} e_{j'j} \sigma_{ij} \quad (55)$$

where e_{ij} are the direction cosine between two coordinate systems, i.e.,

$$\mathbf{e} = \begin{bmatrix} \cos\theta & \sin\theta & 0 \\ -\sin\theta & \cos\theta & 0 \\ 0 & 0 & 1 \end{bmatrix}. \quad (56)$$

The angle θ is directed counterclockwise from the positive x_1-axis to the direction of x_1'-axis (see Fig. 1). Due to the complexity for the expressions of the stress functions, it is therefore impossible to obtain the maximum interfacial stress as a function of the material properties and the ellipticity in a general sense. In the following numerical examples, we consider both the matrix and the inclusion are orthotropic materials. The material properties of the matrix are assumed as

$$E_1 = 10 \text{ GPa}, \quad E_2 = E_3 = 5 \text{ GPa}$$

$$\nu_{12} = \nu_{13} = \nu_{23} = 0.4, \quad \alpha_{11} = \alpha_{22} = \alpha_{33} = 50 \times 10^{-6}/^\circ\text{C}$$

$$G_{12} = G_{13} = G_{23} = 1 \text{ GPa}, \quad k_{11} = k_{22} = 1 \text{ W/m°C}, \quad k_{12} = 0$$

while the material properties of the inclusion are assumed as

$$\frac{(E_i)_2}{(E_i)_1} = \frac{(G_{ij})_2}{(G_{ij})_1} = \frac{(\alpha_{ij})_2}{(\alpha_{ij})_1} = \frac{(k_{ij})_2}{(k_{ij})_1} = k, \quad \nu_{12} = \nu_{13} = \nu_{23} = 0.2$$

where k is the index of hardness. When $k > 1$ the inclusion is harder than the matrix, while $k < 1$ the inclusion is softer than the matrix. Figures 2–5 display the interfacial stresses in the matrix subject to a remote uniform heat flow approached from the negative x_2-axis with the case $b/a = 1$, $b/a = 0.6$, $k = 2$, and $k = 0.5$. It is found that, for a circular inclusion ($b/a = 1$), the maximum tangential interfacial stress in the matrix occurs at the point $x_1 = 0$, $x_2 = a$ (or $x_1 = 0$, $x_2 = -a$) for the case $k = 0.5$ (or $k = 2$). As to an elliptic inclusion ($b/a = 0.6$), the maximum tangential interfacial stress in the matrix takes place at the point $x_1 = \pm 0.8a$, $x_2 = 0.36a$ (or $x_1 = \pm 0.8a$, $x_2 = -0.36a$) for the case $k = 0.5$ (or $k = 2$). It is interesting to note that the maximum shear stress in the matrix always occurs at the ends of the major axis which would become to be infinity as b/a approaches zero.

Since the general solutions have not been found in the literature, comparisons can only be made with some special cases such as isotropic circular inclusions (Chao and Shen, 1997) and anisotropic elliptic holes or cracks (Hwu, 1990; Tarn and Wang, 1993). Note that the temperature functions given in (34)

Downloaded 04 May 2010 to 171.66.16.26. Redistribution subject to ASME license or copyright; see http://www.asme.org/terms/Terms_Use.cfm

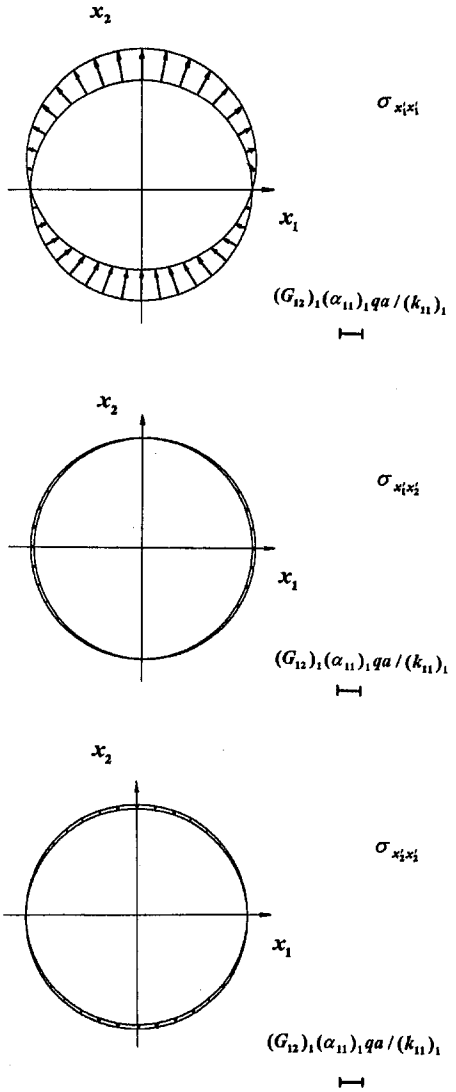

Fig. 2 Interfacial stresses in the matrix subject to a remote uniform heat flow approached from the negative x_2-axis with $b/a = 1$ and $k = 2$

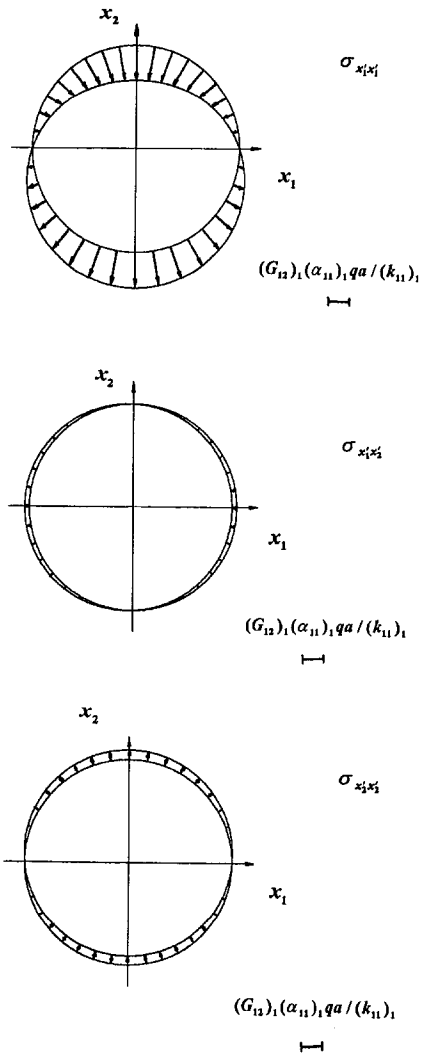

Fig. 3 Interfacial stresses in the matrix subject to a remote uniform heat flow approached from the negative x_2-axis with $b/a = 0.6$ and $k = 2$

are valid for isotropic materials if one lets $s_t = i$. However, the stress functions given in (36) and (37) cannot be directly reduced to the corresponding problem of degenerate materials due to the repeated eigenvalues of the elastic constants. In order to apply the present results to degenerate materials, a small perturbation of the material constants is employed to obtain distinct eigenvalues. By letting $a = b$ and $s_{1,2} = i \pm 10^{-6}$ in the present results, the numerical results of the interfacial stresses for isotropic circular inclusion problem are found in good agreement with the solutions given by Chao and Shen (1997).

5 Holes and Rigid Inclusions

5.1 Holes. When the inclusion is an insulated and traction-free hole, the boundary condition of $\mathbf{p} = 0$ in (32) leads to

$$\mathbf{L}\phi(\zeta) + \overline{\mathbf{L}\phi(\zeta)} = -\mathbf{d}g(\zeta) - \overline{\mathbf{d}g(\zeta)}. \quad (57)$$

The temperature function $g(\zeta)$ can be directly obtained from (34) by letting $\beta^* = 0$ as

$$g(\zeta) = \tfrac{1}{2}(-hm_{2t} + \overline{hm_{1t}})m_{2t}\zeta^{-2} - (hm_{2t} - \overline{hm_{1t}})m_{1t}\log\zeta. \quad (58)$$

Based upon the solutions of (36) and (58) and applying the method of analytic continuation, the traction-free condition (57) yields

$$\mathbf{L}\mathbf{f}(\zeta) + \tfrac{1}{2}\mathbf{d}(-hm_{2t} + \overline{hm_{1t}})m_{2t}\zeta^{-2} = 0. \quad (59)$$

Solving for (59) results in

$$\mathbf{f}(\zeta) = \tfrac{1}{2}\mathbf{L}^{-1}\mathbf{d}(hm_{2t} - \overline{hm_{1t}})m_{2t}\zeta^{-2}. \quad (60)$$

The final expression of the stress function becomes

$$\phi(\zeta) = \tfrac{1}{2}\mathbf{L}^{-1}\mathbf{d}(hm_{2t} - \overline{hm_{1t}})m_{2t}\zeta^{-2} + \boldsymbol{\delta}\log\zeta, \quad (61)$$

which is identical to the result given by Tarn and Wang (1993). The hoop stress along the hole boundary can be also obtained from the field solution in conjunction with (55) and (56).

If one lets the minor semi-axis b of the ellipse approach zero, an elliptic hole can be made into a crack of length $2a$. The solutions for the uniform heat flux obstructed by a plane crack in a general anisotropic body can be obtained by letting $b = 0$ in (58) and (61) as

$$g(\zeta) = \frac{a^2}{8}(-h + \bar{h})\zeta^{-2} + \frac{a^2}{4}(\bar{h} - h)\log\zeta \quad (62)$$

Downloaded 04 May 2010 to 171.66.16.26. Redistribution subject to ASME license or copyright; see http://www.asme.org/terms/Terms_Use.cfm

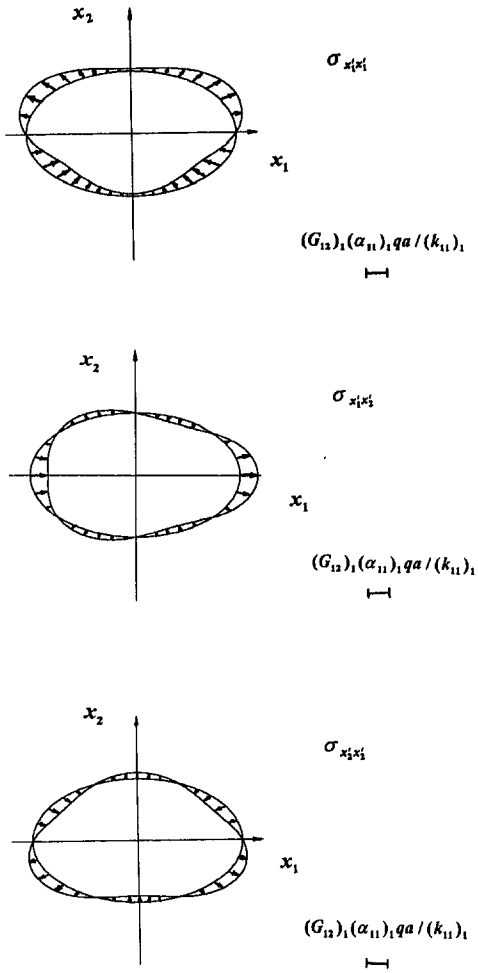

Fig. 4 Interfacial stresses in the matrix subject to a remote uniform heat flow approached from the negative x_2-axis with $b/a = 1$ and $k = 0.5$

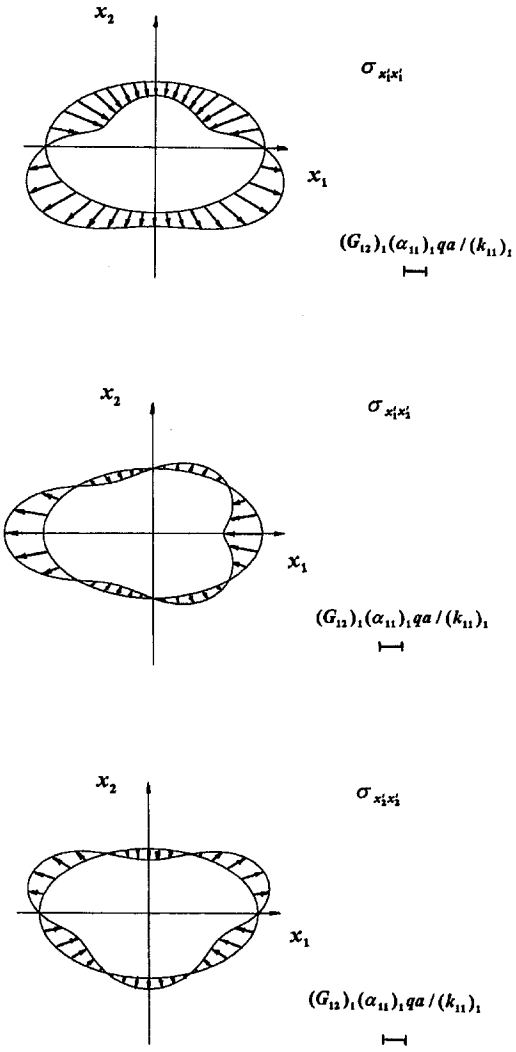

Fig. 5 Interfacial stresses in the matrix subject to a remote uniform heat flow approached from the negative x_2-axis with $b/a = 0.6$ and $k = 0.5$

and

$$\phi(\zeta) = \frac{a^2}{8}\mathbf{L}^{-1}\mathbf{d}(h - \bar{h})\zeta^{-2} + \boldsymbol{\delta}\log\zeta. \tag{63}$$

Substituting (62) and (63) into (9) and letting $x_2 = 0$, $|x_1| > a$, the stresses $\boldsymbol{\sigma}_2 = \{\sigma_{2i}\}$ ahead of the crack tip along the x_1-axis are obtained as

$$\boldsymbol{\sigma}_2 = \frac{2}{\sqrt{x_1^2 - a^2}}\,\mathrm{Re}\left[\mathbf{L}\boldsymbol{\delta} + \frac{a^2(h - \bar{h})}{4}\mathbf{d}\right]. \tag{64}$$

With the usual definition, the stress intensity factors are given by

$$\begin{Bmatrix} K_{\mathrm{II}} \\ K_{\mathrm{I}} \\ K_{\mathrm{III}} \end{Bmatrix} = \lim_{x_1 \to a}\sqrt{2\pi(x_1 - a)}\,\boldsymbol{\sigma}_2$$

$$= 2\sqrt{\frac{\pi}{a}}\,\mathrm{Re}\left\{\mathbf{L}\boldsymbol{\delta} + \frac{a^2(h - \bar{h})}{4}\mathbf{d}\right\}, \tag{65}$$

which are identical to the results given by Hwu (1990) and Tarn and Wang (1993).

5.2 Rigid Inclusions. When the inclusion is an insulated and absolutely rigid body, the boundary condition of $\mathbf{u} = 0$ in (32) leads to

$$\mathbf{A}\phi(\zeta) + \overline{\mathbf{A}\phi(\zeta)} = -\mathbf{c}g(\zeta) - \overline{\mathbf{c}g(\zeta)}. \tag{66}$$

Based upon the solutions of (36) and (58) and applying the method of analytic continuation, the boundary condition (66) yields

$$\mathbf{A}\,\mathbf{f}(\zeta) + \tfrac{1}{2}\mathbf{c}(-hm_{2t} + \overline{hm_{1t}})m_{2t}\zeta^{-2} = 0. \tag{67}$$

Solving for (67), the final expression of the stress function becomes

$$\phi(\zeta) = \tfrac{1}{2}\mathbf{A}^{-1}\mathbf{c}(hm_{2t} - \overline{hm_{1t}})m_{2t}\zeta^{-2} + \boldsymbol{\delta}\log\zeta. \tag{68}$$

Similar to the problems of elastic inclusions, the interfacial stresses can be determined from the field solution in conjunction with (55) and (56).

When an elliptic rigid inclusion becomes a rigid line inclusion of length $2a$, by a way similar to those in (62) and (63), the stresses $\boldsymbol{\sigma}_2$ ahead of the rigid line inclusion tip along the x_1-axis are obtained as

$$\boldsymbol{\sigma}_2 = \frac{2}{\sqrt{x_1^2 - a^2}}\,\mathrm{Re}\left[\mathbf{A}\boldsymbol{\delta} + \frac{a^2(h - \bar{h})}{4}\mathbf{c}\right]. \tag{69}$$

Similar to the definition of the stress intensity factors for crack problems, the stress singularity coefficients for rigid line inclusion problems are given by

Downloaded 04 May 2010 to 171.66.16.26. Redistribution subject to ASME license or copyright; see http://www.asme.org/terms/Terms_Use.cfm

$$\begin{Bmatrix} S_{II} \\ S_I \\ S_{III} \end{Bmatrix} = \lim_{x_1 \to a} \sqrt{2\pi(x_1 - a)}\boldsymbol{\sigma}_2 \tag{70}$$

$$= 2\sqrt{\frac{\pi}{a}}\,\mathrm{Re}\left\{\mathbf{A}\boldsymbol{\delta} + \frac{a^2(h - \bar{h})}{4}\mathbf{c}\right\},$$

which are the same as the results provided by Chang (1993).

6 Conclusions

The solutions presented in the literature for the thermal stresses under uniform heat flow are restricted to either anisotropic elliptic rigid inclusion and hole problems or isotropic elastic circular inclusion problems. In this paper, a general solution is given for the thermal stress field due to the obstruction of a uniform heat flow by an elliptic inclusion in a generally anisotropic body. Some special examples, such as isotropic inclusion problems, anisotropic elliptic hole and rigid inclusion problems, are also solved and compared analytically or numerically with the present results. Moreover, the stress intensity factors for crack problems and the stress singularity coefficients for rigid line inclusion problems are expressed in terms of the fundamental elasticity matrix and thermal vector.

Acknowledgment

This study was financially supported by the National Science Council, Republic of China, through grant no. NSC 86-2212-E011-006.

References

Atkinson, C., and Clements, D. L., 1977, "On Some Crack Problems in Anisotropic Thermoelasticity," *International Journal of Solids and Structures,* Vol. 13, pp. 855–864.

Chang, R. C., 1993, "Theoretical Analysis and Failure Prediction of Hygrothermoelastic Problem with an Interface Defect between Anisotropic Dissimilar Media," Ph.D. dissertation, National Taiwan Institute of Technology, Taipei, Taiwan, R. O. C.

Chao, C. K., and Chang, R. C., 1994, "Thermoelastic Problem of Dissimilar Anisotropic Solids with a Rigid Line Inclusion," ASME JOURNAL OF APPLIED MECHANICS, Vol. 61, pp. 978–980.

Chao, C. K., and Shen, M. H., 1997, "On Bonded Circular Inclusions in Plane Thermoelasticity," ASME JOURNAL OF APPLIED MECHANICS, Vol. 64, pp. 1000–1004.

Chen, W. T., 1967, "Plane Thermal Stress at an Insulated Hole Under Uniform Heat Flow in an Orthotropic Medium," ASME JOURNAL OF APPLIED MECHANICS, Vol. 34, pp. 133–136.

Clements, D. L., 1973, "Thermal Stress in an Anisotropic Elastic Half-Space," *SIAM J. Appl. Math.* Vol. 24, pp. 332–337.

Florence, A. L., and Goodier, J. N., 1959, "Thermal Stress at Spherical Cavities and Circular Holes in Uniform Heat Flow," ASME JOURNAL OF APPLIED MECHANICS, Vol. 26, pp. 293–294.

Florence, A. L., and Goodier, J. N., 1960, "Thermal Stress Due to Disturbance of Uniform Heat Flow by an Insulated Ovaloid Hole," ASME JOURNAL OF APPLIED MECHANICS, Vol. 27, pp. 635–639.

Green, A. E., and Zerna, W., 1954, *Theoretical Elasticity,* Oxford University Press, London.

Hwu, C., 1990, "Thermal Stresses in an Anisotropic Plate Disturbed by an Insulated Elliptic Hole or Crack," ASME JOURNAL OF APPLIED MECHANICS, Vol. 57, pp. 916–922.

Hwu, C., and Ting, T. C. T., 1989, "Two-Dimensional Problems of the Anisotropic Elastic Solid with an Elliptic Inclusion," *Q. J. Mech. Appl. Math.* Vol. 42, pp. 553–572.

Hwu, C., and Yen, W. J., 1993, "On the Anisotropic Elastic Inclusions in Plane Elastostatics," ASME JOURNAL OF APPLIED MECHANICS, Vol. 60, pp. 626–632.

Lekhnitskii, S. G., 1963, *Theory of Elasticity of an Anisotropic Elastic Body,* Holden-Day, San Francisco.

Muskhelishvili, N. I., 1953, *Some Basic Problems of Mathematical Theory of Elasticity,* P. Noordhoff, Groningen.

Stroh, A. N., 1958, "Dislocations and Cracks in Anisotropic Elasticity," *Phil. Mag.,* Vol. 7, pp. 625–646.

Sturla, F. A., and Barber, J. R., 1988, "Thermal Stress Due to a Plane Crack in General Anisotropic Material," ASME JOURNAL OF APPLIED MECHANICS, Vol. 55, pp. 372–376.

Suo, Z., 1990, "Singularities, Interfaces and Cracks in Dissimilar Anisotropic Media," *Proc. R. Soc. Lond.,* Vol. A427, pp. 331–358.

Tarn, J. Q., and Wang, Y. M., 1993, "Thermal Stresses in Anisotropic Bodies with a Hole or a Rigid Inclusion," *Journal of Thermal Stresses,* Vol. 16, pp. 455–471.

Downloaded 04 May 2010 to 171.66.16.26. Redistribution subject to ASME license or copyright; see http://www.asme.org/terms/Terms_Use.cfm

Toroidal Vibrations of Anisotropic Spheres With Spherical Isotropy

K. T. Chau
Department of Civil and Structural Engineering,
The Hong Kong Polytechnic University,
Hung Hom, Hong Kong
e-mail: cektchau@polyu.edu.hk
Mem. ASME

This paper derives the exact frequency equation for the toroidal mode of vibrations for a spherically isotropic elastic sphere. The vibrations of spherically isotropic solids are solved by introducing two wave potentials (Φ and Ψ) such that the general solutions for free vibrations can be classified into two independent modes of vibrations, namely the "toroidal" and "spheroidal" modes. Both of these vibration modes can be written in terms of spherical harmonics of degree n. The frequency equation for the toroidal modes is obtained analytically, and it depends on both n and β [$=(C_{11}-C_{12})/(2C_{44})$], where C_{11}, C_{12}, and C_{44} have the usual meaning of moduli and are defined in Eqs. (2)–(3); and, as expected, Lamb's (1882) classical frequency equation is recovered as the isotropic limit. Numerical results show that the normalized frequency $\omega a/C_s$ increases with both n and β, where ω is the circular frequency of vibration, a the radius of the sphere, and C_s is the shear wave speed on the spherical surfaces. The natural frequencies for spheres of transversely isotropic minerals and crystals, with β ranging from 0.3719 to 1.8897, are also tabulated. However, two coupled differential equations are obtained for the spheroidal modes, which remain to be solved.

1 Introduction

Vibrations of an isotropic elastic sphere is one of the classical problems in the mathematical theory of elasticity. The radial vibration of an elastic sphere was first considered by Poisson in 1829 (see the "Historical Introduction" by Love, 1944). Motivated by its possible implication to the rigidity of the Earth, Kelvin (1863) also considered the natural vibrations of a sphere. The first complete mathematical treatment for the vibrations of an isotropic elastic sphere was, however, given by Lamb (1882) in Cartesian coordinates and by Chree (1889) in spherical coordinates. In particular, Lamb (1882) showed that two basic types of free vibrations exist for an isotropic sphere: (1) the vibrations with zero volume change and zero radial displacement; and (2) the vibrations with zero radial component of the curl of the displacement. Lamb (1882) referred these vibrations as the "vibrations of the first and second classes", respectively. In more recent literature, the first type is normally called "torsional" or "toroidal" and the second one is called "spheroidal" or "poloidal" (e.g., see the account by Lapwood and Usami, 1981). The frequencies of free oscillations were tabulated by Sato and Usami (1962a) for the first nine roots of the characteristic equation for every spherical harmonics of degree from one to one hundred; the corresponding displacement fields were also devised by Sato and Usami (1962b). Three-dimensional diagrams for the surface displacement of the toroidal modes were presented recently by Hosseini-Hashemi and Anderson (1988).

Besides the theoretical importance, the vibrations of elastic spheres have been of considerable interest in the field of geophysics. Whenever a big earthquake strikes, the Earth is set in free vibrations for days. Numerous studies have attempted to calculate the natural frequencies of spheres and to compare them with the observed periods of oscillation of the Earth excited by earthquakes (e.g., Alsop et al., 1961; Benioff et al., 1961; Bogert, 1961; MacDonald and Ness, 1961; Ness et al., 1961; Perkeris et al., 1961; Sato and Usami, 1962a, b). We refer to Lapwood and Usami (1981) for a comprehensive list of references for such application.

More importantly, the free vibrations of a sphere is related to the determination of elastic constants of materials by using the so-called *solid resonating method* (e.g., Fraser and LeCraw, 1964; Shreiber et al., 1973; Heyliger et al., 1990; Visscher et al., 1991; Heyliger and Jilani, 1991, 1992; Chau, 1993, 1994). In particular, theoretical prediction for the natural frequencies of a specimen can be compared with the experimental measurement to give the best-fit elastic constants of the tested material. Solid sphere is one of the most commonly used shapes of specimens (e.g., Mochizuki, 1988).

However, all existing analytical solutions are for isotropic spheres, there is no exact mathematical solution for the free vibrations of anisotropic spheres. The only exception is, probably, the radial vibrations of anisotropic spheres considered by Eason (1962) and by Sur (1964). All other existing results for the free vibrations of anisotropic spheres are obtained approximately by numerical techniques (e.g., Mochizuki, 1986, 1988; Isoda et al., 1990; Heyliger and Jilani, 1991, 1992; Visscher et al., 1991).

Therefore, we consider in this paper the analytic solutions for the vibrations of spherically isotropic spheres, which is the simplest type of vibration problems for anisotropic spheres. The concept of spherical isotropy was first introduced by Saint Venant in 1865 (see p. 161 of Love, 1944). In spherically isotropic spheres, the elastic response is the same for all directions on the tangential plane on any point of a spherical surface drawn from the origin, but it differs from the elastic response along the radial direction. However, the general theory for static problems of spherically isotropic solids is not available until 90 years later (Hu, 1954). Hu's (1954) general theory for spherically isotropic solids was applied to some practical problems by Chen (1966), and the solution form was recently reconsidered by Ding and Ren (1991). To date, analytical solutions for

Contributed by the Applied Mechanics Division of THE AMERICAN SOCIETY OF MECHANICAL ENGINEERS for publication in the ASME JOURNAL OF APPLIED MECHANICS.

Discussion on this paper should be addressed to the Technical Editor, Professor Lewis T. Wheeler, Department of Mechanical Engineering, University of Houston, Houston, TX 77204-4792, and will be accepted until four months after final publication of the paper itself in the ASME JOURNAL OF APPLIED MECHANICS.

Manuscript received by the ASME Applied Mechanics Division, Aug. 9, 1995; final revision, Sept. 15, 1997. Associate Technical Editor: X. Markenscoff.

 Copyright © 1998 by ASME

Downloaded 04 May 2010 to 171.66.16.26. Redistribution subject to ASME license or copyright; see http://www.asme.org/terms/Terms_Use.cfm

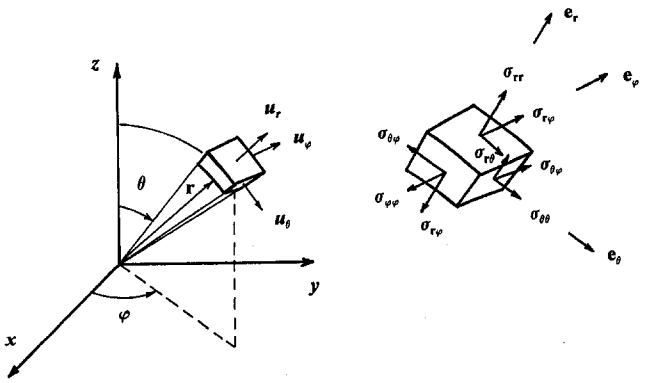

Fig. 1 A sketch for the spherical polar coordinates (r, θ, φ) together with the definitions for the displacement field (u_r, u_θ, u_φ) and the stress field (σ_{rr}, $\sigma_{\theta\theta}$, $\sigma_{\varphi\varphi}$, $\sigma_{r\theta}$, $\sigma_{r\varphi}$, $\sigma_{\theta\varphi}$)

spherically isotropic solids exist only for simple problems, such as the results by Nowinski (1959), Eason (1963), Nemish (1969), Nemish and Nemish (1976), Puro (1980), Hata (1993), and Chau (1995). There is, however, no general theory for dynamics problems of spherically isotropic materials.

Motivated by its application in material testing and geophysics, we consider here the general theory for the dynamic problems of spherically isotropic solids. In particular, by generalizing Hu's (1954) displacement potentials, we introduce two wave potentials (Φ and Ψ) such that the equations of motion are simplified to a partial differential equation for Φ, and a system of two coupled partial differential equations for Ψ and u_r, where u_r is the radial displacement of the sphere. We will show that, similar to Lamb's (1882) observation for isotropic spheres, two classes of vibrations exist. Then, the partial differential equation for Ψ is solved in terms of Bessel function of the first kind of real order, and the exact frequency equation is obtained. Numerical results for the normalized frequency of free toroidal oscillations of spherically isotropic spheres are presented in diagrams and table. Finally, we conclude the paper by posing the unsolved problem of "spheroidal vibration modes" of spherically isotropic spheres for further studies.

2 Mathematical Formulation

We consider here the general theory for the natural vibrations of spherically isotropic solids. For mathematical simplicity, only harmonic oscillations of small amplitude will be considered; and the spherical polar coordinate (r, θ, φ) being used is given in Fig. 1 together with the definitions for the displacement and stress fields. The solid is assumed to be linear elastic and the following Hooke's law for spherically isotropic solids applies:

$$\epsilon_{\theta\theta} = \frac{\sigma_{\theta\theta}}{E} - \frac{\bar{\nu}\sigma_{\varphi\varphi}}{E} - \frac{\nu'\sigma_{rr}}{E'}, \quad \epsilon_{\varphi\varphi} = -\frac{\bar{\nu}\sigma_{\theta\theta}}{E} + \frac{\sigma_{\varphi\varphi}}{E} - \frac{\nu'\sigma_{rr}}{E'},$$

$$\epsilon_{rr} = -\frac{\nu'}{E'}(\sigma_{\theta\theta} + \sigma_{\varphi\varphi}) + \frac{\sigma_{rr}}{E'}, \quad \epsilon_{\theta\varphi} = \frac{(1+\bar{\nu})}{E}\sigma_{\theta\varphi},$$

$$\epsilon_{r\alpha} = \frac{\sigma_{r\alpha}}{2G'}, \tag{1}$$

where $\alpha = \theta, \varphi$ and (r, θ, φ) are the spherical polar coordinates, $\boldsymbol{\sigma}$ is the Cauchy stress tensor, and $\boldsymbol{\epsilon}$ is the small strain tensor. Physically, E and E' are the Young's moduli governing axial deformations along directions lying in the plane of isotropy (i.e., any tangential plane on a spherical surface drawn from the origin) and along direction perpendicular to it (i.e., the radial direction), respectively; $\bar{\nu}$ and ν' are the Poisson's ratios characterizing transverse reduction in the plane of isotropy under tension in the same plane and transverse reduction in the plane of isotropy under radial tension, respectively; and G' is the shear modulus for the planes with unit normals perpendicular to the radial direction.

Alternatively, the Hooke's law given in (1) can be inverted to give

$$\sigma_{\theta\theta} = C_{11}\epsilon_{\theta\theta} + C_{12}\epsilon_{\varphi\varphi} + C_{13}\epsilon_{rr},$$

$$\sigma_{\varphi\varphi} = C_{12}\epsilon_{\theta\theta} + C_{11}\epsilon_{\varphi\varphi} + C_{13}\epsilon_{rr},$$

$$\sigma_{rr} = C_{13}(\epsilon_{\theta\theta} + \epsilon_{\varphi\varphi}) + C_{33}\epsilon_{rr}, \quad \sigma_{\theta\varphi} = (C_{11} - C_{12})\epsilon_{\theta\varphi},$$

$$\sigma_{r\alpha} = 2C_{44}\epsilon_{r\alpha}, \tag{2}$$

where the moduli $C_{11}, C_{12}, \ldots$ are obtained by comparing (1)–(2) as

$$C_{11} = -\frac{E(E' - \nu'^2 E)}{(1+\bar{\nu})\bar{E}}, \quad C_{12} = -\frac{E(\bar{\nu}E' + \nu'^2 E)}{(1+\bar{\nu})\bar{E}},$$

$$C_{13} = -\frac{\nu' E' E}{\bar{E}}, \quad C_{33} = -\frac{E'^2(1-\bar{\nu})}{\bar{E}},$$

$$C_{44} = G', \quad \bar{E} = E'(\bar{\nu} - 1) + 2\nu'^2 E. \tag{3}$$

Note that spherically isotropic materials have five material constants; and comparison of (2) with Eq. (1) of Chau (1993, 1994) shows a close resemblance between spherically and transversely isotropic materials. For spheres undergoing small deformation and small strain, the strain components can be related to the displacement field $(u_r, u_\theta, u_\varphi)$ by

$$\epsilon_{\varphi\varphi} = \frac{u_r}{r} + \frac{u_\theta}{r}\cot\theta + \frac{1}{r\sin\theta}\frac{\partial u_\varphi}{\partial\varphi},$$

$$\epsilon_{r\theta} = \frac{1}{2}\left(\frac{\partial u_\theta}{\partial r} + \frac{1}{r}\frac{\partial u_r}{\partial\theta} - \frac{u_\theta}{r}\right),$$

$$\epsilon_{r\varphi} = \frac{1}{2}\left(\frac{\partial u_\varphi}{\partial r} - \frac{u_\varphi}{r} + \frac{1}{r\sin\theta}\frac{\partial u_r}{\partial\varphi}\right), \quad \epsilon_{rr} = \frac{\partial u_r}{\partial r},$$

$$\epsilon_{\theta\theta} = \frac{u_r}{r} + \frac{1}{r}\frac{\partial u_\theta}{\partial\theta},$$

$$\epsilon_{\theta\varphi} = \frac{1}{2}\left(\frac{1}{r\sin\theta}\frac{\partial u_\theta}{\partial\varphi} + \frac{1}{r}\frac{\partial u_\varphi}{\partial\theta} - \frac{u_\varphi}{r}\cot\theta\right). \tag{4}$$

The equations of motion in spherical coordinates in terms of the stress components are (e.g., Malvern, 1969):

$$\frac{\partial\sigma_{rr}}{\partial r} + \frac{1}{r}\frac{\partial\sigma_{r\theta}}{\partial\theta} + \frac{1}{r\sin\theta}\frac{\partial\sigma_{r\varphi}}{\partial\varphi} + \frac{1}{r}(2\sigma_{rr} - \sigma_{\theta\theta} - \sigma_{\varphi\varphi} + \sigma_{r\theta}\cot\theta) = \rho\frac{\partial^2 u_r}{\partial t^2}, \tag{5}$$

$$\frac{\partial\sigma_{r\theta}}{\partial r} + \frac{1}{r}\frac{\partial\sigma_{\theta\theta}}{\partial\theta} + \frac{1}{r\sin\theta}\frac{\partial\sigma_{\theta\varphi}}{\partial\varphi} + \frac{1}{r}[3\sigma_{r\theta} + (\sigma_{\theta\theta} - \sigma_{\varphi\varphi})\cot\theta] = \rho\frac{\partial^2 u_\theta}{\partial t^2}, \tag{6}$$

$$\frac{\partial\sigma_{r\varphi}}{\partial r} + \frac{1}{r}\frac{\partial\sigma_{\theta\varphi}}{\partial\theta} + \frac{1}{r\sin\theta}\frac{\partial\sigma_{\varphi\varphi}}{\partial\varphi} + \frac{1}{r}(3\sigma_{r\varphi} + 2\sigma_{\theta\varphi}\cot\theta) = \rho\frac{\partial^2 u_\varphi}{\partial t^2}, \tag{7}$$

where ρ is the mass density of the solid. Since wave potentials will be introduced in our later analysis, it is advantageous to rewrite (5) to (7) in terms of displacements. By substitution of (2) and (4) into (5) to (7), we obtain the following equations of motion:

Downloaded 04 May 2010 to 171.66.16.26. Redistribution subject to ASME license or copyright; see http://www.asme.org/terms/Terms_Use.cfm

$$\frac{C_{11}}{r}\frac{\partial e}{\partial \theta} + (C_{11} - C_{12})\frac{1}{r\sin\theta}\frac{\partial \Omega_{\theta\varphi}}{\partial \varphi} + 2C_{44}\frac{1}{r}\frac{\partial}{\partial r}(r\Omega_{\theta r}) + (C_{13} - C_{11} + 2C_{44})\frac{1}{r}\frac{\partial^2 u_r}{\partial \theta \partial r} + (2C_{44} - C_{11} + C_{12})\left(\frac{1}{r^2}\frac{\partial u_r}{\partial \theta} - \frac{u_\theta}{r^2}\right) = \rho\frac{\partial^2 u_\theta}{\partial t^2}, \quad (8)$$

$$\frac{C_{11}}{r\sin\theta}\frac{\partial e}{\partial \varphi} + (C_{11} - C_{12})\frac{1}{r}\frac{\partial \Omega_{\varphi\theta}}{\partial \theta} + 2C_{44}\frac{1}{r}\frac{\partial}{\partial r}(r\Omega_{\varphi r}) + (C_{13} - C_{11} + 2C_{44}) \times \frac{1}{r\sin\theta}\frac{\partial^2 u_r}{\partial \varphi \partial r} + (2C_{44} - C_{11} + C_{12}) \times \left(\frac{1}{r^2\sin\theta}\frac{\partial u_r}{\partial \varphi} - \frac{u_\varphi}{r^2}\right) = \rho\frac{\partial^2 u_\varphi}{\partial t^2}, \quad (9)$$

$$(C_{13} + 2C_{44})\frac{\partial e}{\partial r} + 2\frac{C_{44}}{r\sin\theta}\left[\frac{\partial}{\partial \theta}(\sin\theta\Omega_{r\theta}) + \frac{\partial \Omega_{r\varphi}}{\partial \varphi}\right] + (C_{33} - C_{13} - 2C_{44})\frac{1}{r}\frac{\partial^2}{\partial r^2}(ru_r) + [2(C_{13} + C_{44}) - C_{11} - C_{12}]\frac{1}{r}(\epsilon_{\theta\theta} + \epsilon_{\varphi\varphi}) = \rho\frac{\partial^2 u_r}{\partial t^2}, \quad (10)$$

where $\mathbf{\Omega} = [(\nabla \mathbf{u})^T - \nabla \mathbf{u}]/2$ and $e = \nabla \cdot \mathbf{u}$ are the spin tensor and the volumetric strain, respectively. If the isotropic limit of (8) to (10) is considered, the usual form of the equations of motion for isotropic solids will be recovered. In particular, if we set $C_{11} = C_{33} = (1 - \nu)E/[(1 + \nu)(1 - 2\nu)]$, $C_{12} = C_{13} = \nu E/[(1 + \nu)(1 - 2\nu)]$ and $2C_{44} = (C_{11} - C_{12}) = E/(1 + \nu)$, Eq. (II.4.S12) on p. 672 of Malvern (1969) is recovered.

For our problem of free oscillations, if the origin of the coordinate system is located at the center of the sphere with radius a, the zero traction boundary conditions are

$$\sigma_{rr} = 0, \quad \sigma_{r\theta} = 0, \quad \sigma_{r\varphi} = 0, \quad (11)$$

on $r = a$. In principle, if the general solution for (8) to (10) is known, all dynamic problems for spherically isotropic spheres can be solved with the appropriate boundary and initial conditions. The method of solution for (8) to (10) is considered next.

3 Method of Solution

We extend in this section the general analysis of Hu (1954) to include the inertia terms (i.e., the right-hand side of (8) to (10)) by introducing the following two wave potentials:

$$u_\theta = \frac{1}{r}\frac{\partial \Phi}{\partial \theta} + \frac{1}{r\sin\theta}\frac{\partial \Psi}{\partial \varphi}, \quad u_\varphi = \frac{1}{r\sin\theta}\frac{\partial \Phi}{\partial \varphi} - \frac{1}{r}\frac{\partial \Psi}{\partial \theta}. \quad (12)$$

Substitution of (12) into the equations of motion (8) and (9) leads to the following coupled system:

$$\frac{1}{r}\frac{\partial F}{\partial \theta} + \frac{1}{r\sin\theta}\frac{\partial G}{\partial \varphi} = 0, \quad \frac{1}{r\sin\theta}\frac{\partial F}{\partial \varphi} - \frac{1}{r}\frac{\partial G}{\partial \theta} = 0, \quad (13)$$

where F and G are

$$F = C_{11}\nabla^2\Phi + C_{44}\frac{\partial^2 \Phi}{\partial r^2} - (2C_{44} - C_{11} + C_{12})\frac{\Phi}{r^2} - \rho\frac{\partial^2 \Phi}{\partial t^2} + (C_{44} + C_{13})\frac{\partial u_r}{\partial r} + (2C_{44} + C_{11} + C_{12})\frac{u_r}{r}, \quad (14)$$

$$G = \frac{1}{2}(C_{11} - C_{12})\nabla^2\Psi + C_{44}\frac{\partial^2 \Psi}{\partial r^2} - (2C_{44} - C_{11} + C_{12})\frac{\Psi}{r^2} - \rho\frac{\partial^2 \Psi}{\partial t^2}. \quad (15)$$

The Laplacian operator in the $\theta - \varphi$ plane ∇^2 is defined as

$$\nabla^2(\,) = \frac{1}{r^2\sin\theta}\frac{\partial}{\partial \theta}\left[\sin\theta\frac{\partial(\,)}{\partial \theta}\right] + \frac{1}{r^2\sin^2\theta}\frac{\partial(\,)}{\partial \varphi^2}. \quad (16)$$

Substitution of (12) into (10) leads to

$$H = (C_{13} + C_{44})\nabla^2\frac{\partial \Phi}{\partial r} - (2C_{44} + C_{11} + C_{12})\frac{1}{r}\nabla^2\Phi + 2(C_{13} - C_{11} - C_{12})\frac{u_r}{r^2} + C_{44}\nabla^2 u_r + C_{33}\frac{1}{r^2}\frac{\partial}{\partial r}\left(r^2\frac{\partial u_r}{\partial r}\right) - \rho\frac{\partial^2 u_r}{\partial t^2} = 0. \quad (17)$$

Equation (13) can further be simplified to

$$\nabla^2 F = 0, \quad \nabla^2 G = 0, \quad (18)$$

by eliminating G and F, respectively. This pair of equations implies that $F = f(r)$ and $G = g(r)$. Note, however, that u_θ and u_φ are not uniquely determined by (12) because there is a homogeneous solution for

$$\frac{1}{r}\frac{\partial \Phi_0}{\partial \theta} + \frac{1}{r\sin\theta}\frac{\partial \Psi_0}{\partial \varphi} = 0, \quad \frac{1}{r\sin\theta}\frac{\partial \Phi_0}{\partial \varphi} - \frac{1}{r}\frac{\partial \Psi_0}{\partial \theta} = 0. \quad (19)$$

Following the same procedure in obtaining (18), we have

$$\nabla^2\Phi_0 = 0, \quad \nabla^2\Psi_0 = 0. \quad (20)$$

Thus, any harmonic function of (θ, φ) plus an arbitrary function of r can be added to Φ and Ψ. Consequently, we can set $f(r) = g(r) = 0$ without loss of generality. Therefore, the solution for the equations of motion becomes the solution for

$$F = 0, \quad G = 0, \quad H = 0. \quad (21)$$

If Φ, Ψ and u_r are independent of time, the corresponding equations given by Hu (1954) are recovered. Note that $G = 0$ gives a partial differential equations for Ψ; and $F = 0$ and $H = 0$ give two coupled partial differential equations for Φ and u_r.

When $\Phi = u_r = 0$, the volumetric strain is identically zero (i.e., $e = 0$ into Eqs. (8) to (10)). For this special case, we call the solutions the toroidal modes of vibrations, following the terminology used for isotropic spheres (see Lapwood and Usami, 1981). When $\Psi = 0$, we find that $\Omega_{\theta\varphi} = 0$; thus, we term these the spheroidal modes of vibrations, again following the terminology used for isotropic spheres. Therefore, same as the conclusion by Lamb (1882) for isotropic spheres, the fundamental vibrations of spherically isotropic spheres can be classified into either toroidal modes or spheroidal modes. The characteristic equation for toroidal modes will be considered next.

4 Vibration Modes and Frequency Equation

Since all dynamical responses can theoretically be decomposed into harmonic vibrations with different magnitude, we consider here that the spherically isotropic solids are under simple harmonic motions with a period of $\omega/(2\pi)$, where ω is the circular frequency of vibration. The following vibration

Downloaded 04 May 2010 to 171.66.16.26. Redistribution subject to ASME license or copyright; see http://www.asme.org/terms/Terms_Use.cfm

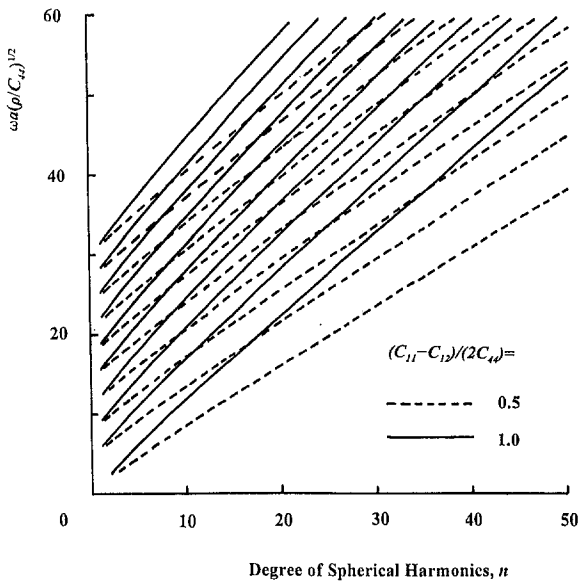

Fig. 2 Nondimensional frequency $\omega a(\rho/C_{44})^{1/2}$ versus the degree of spherical harmonics n for toroidal mode of vibrations of spherically isotropic spheres. The solid lines are for isotropic spheres (i.e., $\beta = (C_{11} - C_{12})/(2C_{44}) = 1$); the dashed lines are for $\beta = 0.5$. Only the first ten roots of the characteristic Eq. (33) are plotted.

modes for the wave potentials Φ and Ψ, and the radial displacement u_r are considered:

$$\Psi = \psi(r)P_n^m(\cos\theta)\begin{matrix}\cos(m\varphi)\\ \sin(m\varphi)\end{matrix}\exp(i\omega t), \quad (22)$$

$$\Phi = \phi(r)P_n^m(\cos\theta)\begin{matrix}\cos(m\varphi)\\ \sin(m\varphi)\end{matrix}\exp(i\omega t), \quad (23)$$

$$u_r = U(r)P_n^m(\cos\theta)\begin{matrix}\cos(m\varphi)\\ \sin(m\varphi)\end{matrix}\exp(i\omega t), \quad (24)$$

where P_n^m is the associated Legendre function of degree n and order m (Abramowitz and Stegun, 1965). The $\theta - \varphi$ dependence in (22) to (24) is called spherical harmonics of degree n (Hobson, 1955).

4.1 Toroidal Modes. Substitution of (22) into $G = 0$ gives

$$\frac{d^2\psi}{dr^2} + \left[\frac{\rho\omega^2}{C_{44}} + \frac{1/4 - \nu^2}{r^2}\right]\psi = 0, \quad (25)$$

where

$$\nu = [9/4 + (n+2)(n-1)(C_{11} - C_{12})/(2C_{44})]^{1/2}. \quad (26)$$

To find the general solution of (25), we first assume the change of variable: $\xi = i2\omega r/C_s$, where $i = (-1)^{1/2}$ the usual imaginary number and $C_s = (C_{44}/\rho)^{1/2}$ the shear wave speed on the spherical surfaces. Thus, (25) can be rewritten as a special form of Whittaker's equation (Whittaker and Watson, 1927; Abramowitz and Stegun, 1965):

$$\frac{d^2\psi}{d\xi^2} + \left[-\frac{1}{4} + \frac{1/4 - \nu^2}{\xi^2}\right]\psi = 0. \quad (27)$$

The solution of (27) can, of course, be expressed in terms of a special form of Whittaker's functions ($W_{0,\nu}$ and $M_{0,\nu}$):

$$\psi(r) = A_1 W_{0,\nu}(2i\omega r/C_s) + A_2 M_{0,\nu}(2i\omega r/C_s), \quad (28)$$

where A_1 and A_2 are constants. By combining formulas 13.1.2-3, 13.1.32-33, and 13.6 of Abramowitz and Stegun (1965), these special forms of Whittaker's functions are found in terms of Hankel function of the second kind $H_\nu^{(2)}(\zeta)$ and Bessel function of the first kind $J_\nu(\zeta)$, respectively:

$$W_{0,\nu}(2i\zeta) = \tfrac{1}{2}\pi^{1/2}(2i\zeta)^{1/2+\nu}e^{-i\pi(\nu+1/2)}(2\zeta)^{-\nu}H_\nu^{(2)}(\zeta), \quad (29)$$

$$M_{0,\nu}(2i\zeta) = \Gamma(1+\nu)(2i\zeta)^{1/2+\nu}(\tfrac{1}{2}\zeta)^{-\nu}J_\nu(\zeta), \quad (30)$$

where $\zeta = r\omega/C_s$ and $\Gamma(x)$ is the Gamma function. However, physically $\psi(r)$ must be real; therefore, we have to recast the general solution (28) into a real form. By combining (28) to (30) and noting that $H_\nu^{(2)}(\zeta)$ can be expressed in terms of Bessel functions, we propose the following solution form:

$$\psi = [\pi r\omega/(2C_s)]^{1/2}[AJ_\nu(r\omega/C_s) + BY_\nu(r\omega/C_s)], \quad (31)$$

where A and B are constants, and J_ν and Y_ν Bessel function of the first and second kinds with order ν, respectively. The validity of (31) can easily be checked by direct substitution of (31) into (25).

We now consider the frequency equation for vibrations that satisfy the zero traction boundary conditions, (11). For toroidal mode of vibrations, the first of (11) is satisfied identically, and both the second and third of (11) give the same characteristic equation:

$$\left(\frac{d\psi}{dr} - \frac{2\psi}{r}\right)_{r=a} = 0. \quad (32)$$

Substitution of (31) into (32) and considering the boundedness of solution at the center of the sphere ($r = 0$) give

$$\left(\nu - \frac{3}{2}\right)J_\nu(\eta a) - (\eta a)J_{\nu+1}(\eta a) = 0, \quad (33)$$

where $\eta = \omega/C_s$. Note that the vibration frequency is independent of the order of the spherical harmonics m. Since Bessel function is an oscillating function of argument, there is, as will be shown in Section 5, an infinite sequence of solutions to (33) for every fixed value of degree n. When the solid is isotropic (i.e., $C_{11} - C_{12} = 2C_{44}$), we have $\nu = n + \frac{1}{2}$ and (33) becomes

$$(n-1)J_{n+1/2}(\eta a) - (\eta a)J_{n+3/2}(\eta a) = 0, \quad (34)$$

which agrees with the classical result obtained by Lamb (1882). Note that although only solid spheres are considered in the present study, the present approach can also be applied to study

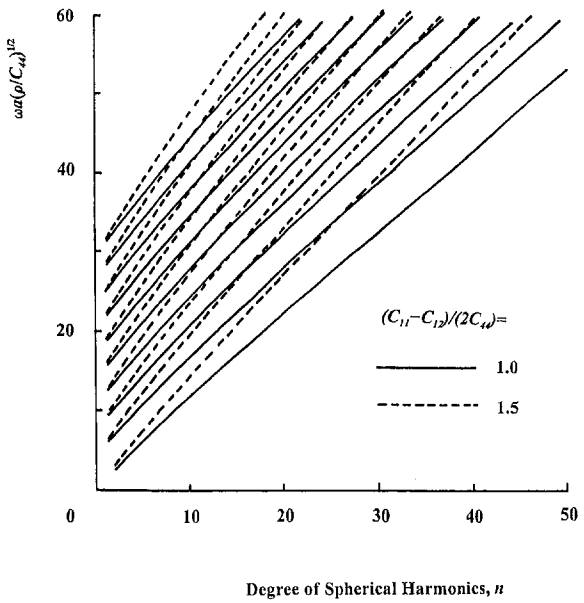

Fig. 3 Same as those for Fig. 2 except that the dashed lines are for $\beta = 1.5$

Downloaded 04 May 2010 to 171.66.16.26. Redistribution subject to ASME license or copyright; see http://www.asme.org/terms/Terms_Use.cfm

Table 1 The normalized frequencies, $\omega a/(\rho/C_{44})^{1/2}$, for spheres formed by various minerals and crystals with the first two modes of the nth degree of spherical harmonics, where $n = 2, 3, 4$ (note that $\beta = (C_{11} - C_{12})/(2C_{44})$). For $n = 1$, the natural frequency is the same for all solids, and the first four roots are 5.7635, 9.0950, 12.3229, and 15.5146 (see Hearman (1969) and Payton (1983) for the elastic constants of the minerals and crystals).

		$n = 2$		$n = 3$		$n = 4$	
Materials	β	1st	2nd	1st	2nd	1st	2nd
Thallium	0.3719	1.5308	6.3682	2.4154	7.0600	3.1966	7.7845
Titanium	0.7495	2.1778	6.8553	3.3725	7.9555	4.4497	9.0418
Beryllium	0.8188	2.2725	6.9357	3.5166	8.0973	4.6385	9.2369
Hafnium	0.9336	2.4202	7.0642	3.7414	8.3211	4.9331	9.5435
Cobalt	0.9404	2.4286	7.0716	3.7543	8.3339	4.9499	9.5611
Isotropic	1.0000	2.5011	7.1360	3.8647	8.4449	5.0946	9.7125
Yttrium	1.0016	2.5030	7.1377	3.8676	8.4479	5.0984	9.7165
Magnesium	1.0213	2.5265	7.1587	3.9033	8.4839	5.1452	9.7655
Rhenium	1.0556	2.5667	7.1948	3.9645	8.5458	5.2255	9.8498
Ice (257K)	1.1041	2.6224	7.2452	4.0493	8.6318	5.3367	9.9667
Sapphire	1.1303	2.6520	7.2721	4.0943	8.6775	5.3956	10.0288
Apatite	1.1606	2.6857	7.3029	4.1456	8.7298	5.4629	10.0997
Beryl	1.3309	2.8669	7.4707	4.4214	9.0126	5.8246	10.4821
Zinc	1.6919	3.2132	7.8005	4.9488	9.5599	6.5170	11.2183
Cadmium	1.8897	3.3860	7.9688	5.2121	9.8357	6.8630	11.5877

the natural frequencies of hollow spheres with spherical isotropy. In such case, no boundedness of the solution at the center is required (i.e., the coefficient B in (31) is not zero). Although the main concern of the present paper is the toroidal mode of vibrations, the spheroidal mode of vibrations will also be discussed briefly next.

4.2 Spheroidal Modes. Substitution of (23) and (24) into $F = 0$ and $H = 0$, we obtain two coupled linear ordinary differential equations for ϕ and U:

$$\frac{d^2\phi}{dr^2} + \left(a_1 + \frac{a_2}{r^2}\right)\phi + a_3\frac{dU}{dr} + a_4\frac{1}{r}U = 0, \quad (35)$$

$$\frac{1}{r^2}\frac{d}{dr}\left(r^2\frac{dU}{dr}\right) + \left(b_1 + \frac{b_2}{r^2}\right)U + b_3\frac{1}{r^2}\frac{d\phi}{dr} + b_4\frac{1}{r^3}\phi = 0, \quad (36)$$

where a_i and b_i $(i = 1, 2, 3, 4)$:

$$a_1 = \rho\omega^2/C_{44},$$
$$a_2 = -[2C_{44} - C_{11} + C_{12} + C_{11}n(n+1)]/C_{44},$$
$$a_3 = (C_{13} + C_{44})/C_{44},$$
$$a_4 = (2C_{44} + C_{11} + C_{12})/C_{44}, \quad b_1 = \rho\omega^2/C_{33},$$
$$b_2 = [2(C_{13} - C_{11} - C_{12}) - C_{44}n(n+1)]/C_{33},$$
$$b_3 = -n(n+1)(C_{13} + C_{44})/C_{33},$$
$$b_4 = n(n+1)(2C_{44} + C_{11} + C_{12})/C_{33}. \quad (37)$$

We can further assume the following change of variables:

$$\phi = r^{1/2}\phi^*, \quad U = r^{-1/2}U^*. \quad (38)$$

(The reason for this assumed form is that for the isotropic case u_θ and u_φ are proportional to $r^{-1/2}J_{n+1/2}(c_0 r)$ for some constant c_0.) Substitution of (38) into (35) and (36) gives the following coupled equations:

$$\frac{d^2\phi^*}{dr^2} + \left(\frac{1}{r}\frac{d\phi^*}{dr} + \frac{a_3}{r}\frac{dU^*}{dr}\right) + \left[a_1 + \frac{a_2 - 1/4}{r^2}\right]\phi^* + \frac{(a_4 - a_3/2)}{r^2}U^* = 0, \quad (39)$$

$$\frac{d^2U^*}{dr^2} + \left(\frac{1}{r}\frac{dU^*}{dr} + \frac{b_3}{r}\frac{d\phi^*}{dr}\right) + \left[b_1 + \frac{b_2 - 1/4}{r^2}\right]U^* + \frac{(b_4 + b_3/2)}{r^2}\phi^* = 0. \quad (40)$$

The general solution for (39) and (40) remains a challenging mathematical problem to be solved. Theoretically, numerical technique can be used if closed-form solutions for (39) and (40) cannot be found (e.g., Press et al., 1992). Such consideration is, however, out of the scope of the present paper.

5 Numerical Results and Discussion

The frequency equation for the toroidal mode of vibrations (33) can be solved by using standard method for solving nonlinear algebraic equation, such as Brent's method (Press et al., 1992). Figures 2 and 3 plot the nondimensional frequency $\omega a(\rho/C_{44})^{1/2}$ versus the degree of spherical harmonics n for various values of the modulus ratio $\beta = (C_{11} - C_{12})/2C_{44}$ ($\beta = 0.5$ and 1 in Fig. 2; and $\beta = 1$ and 1.5 in Fig. 3). Although $\omega a(\rho/C_{44})^{1/2}$ exists only for integer n, for easy reference we plot it as a continuous function of n, as shown in Figs. 2 and 3. As we remarked earlier, for every degree n there is an infinite sequence of roots for (33); Figs. 2 and 3 show only the first ten of them. Note that we have $\beta = 1$ for isotropic spheres (given by solid lines in both Figs. 2 and 3); and, as expected, the solid lines in both Figures are the same as those reported in Fig. 1 of Sato and Usami (1962a). For isotropic spheres, it is peculiar to see that $\omega a(\rho/C_{44})^{1/2}$ is always larger than n. However, for spherically isotropic spheres with $\beta = 0.5$, we have $\omega a(\rho/C_{44})^{1/2} < n$ for the first root to (33), independent of the values of n. Nevertheless, all natural frequencies decrease as β is reduced from 1 to 0.5. Conversely, Fig. 3 shows that all natural frequencies increase with β.

The values of β chosen in Figs. 2 and 3 should cover the typical range for most spherically isotropic solids. To see this, we assume that spherically isotropic spheres are formed by wrapping layers of transversely isotropic materials, thus the values of β can simply be found by using the usual notation of C_{11}, C_{12}, and C_{44} for transversely isotropic solids (see, for example, Hearmon, 1969; Payton, 1983). Table 1 summarizes the value of β and the corresponding first two roots of the first four spherical harmonics for various minerals and crystals. The range of β is from 0.3719 to 1.8897; and except for Thallium, Zinc and Cadmium all values of β fall into the range: $0.5 < \beta <$

Downloaded 04 May 2010 to 171.66.16.26. Redistribution subject to ASME license or copyright; see http://www.asme.org/terms/Terms_Use.cfm

1.5. This is the reason why we choose $\beta = 0.5$ and 1.5 in Figs. 2 and 3, respectively. Note that when $n = 1$, as suggested by (26), the frequency equation (33) is independent of β (i.e., independent of the material types). For this special case ($n = 1$), our numerical results for the first four roots of ηa in (33) are 1.8346π, 2.8950π, 3.9225π, and 4.9385π, which are the same as those well-known values given by Lamb (1882). As expected, the natural frequencies for isotropic materials reported in Table 1 also agree with those values given in Table 1.1 of Sato and Usami (1962a).

Figures 4 and 5 show some typical modal appearance of the toroidal vibrations by depicting the deformed meshes on the spherical surface of the sphere. The deformed meshes for the second and third spherical harmonics are shown in Fig. 4 while those for the fourth and fifth spherical harmonics are shown in Fig. 5. The first three orders for each degree of spherical harmonics (i.e., n fixed and $m = 0, 1, 2$) are plotted in both figures. Although it is evident that for a fixed n the appearance of the vibration modes are quite different for increasing order m, the natural frequencies is the same for different values of m provided that n is fixed.

6 Conclusions

In this paper, we have derived analytically the frequency equation for the toroidal mode of vibrations of spherically isotropic spheres. In particular, we introduce two wave potentials (Φ and Ψ) such that the equations of motion can be transformed into one partial differential equation for Ψ, and two coupled partial differential equations for Φ and u_r. If $\Phi = u_r = 0$, we have the so-called toroidal mode of vibrations with zero volume change and zero radial displacement. If $\Psi = 0$, we have the spheroidal mode of vibrations with zero radial component of the curl of the displacement. Therefore, as remarked by Lamb (1882) for isotropic spheres, free vibrations can be classified into either toroidal or spheroidal modes. Both of these vibration modes can be written in terms of spherical harmonics of degree n. By satisfying the zero traction boundary conditions, the frequency equation for toroidal modes is obtained analytically in terms of Bessel function of the first kind of order ν, and it is a function of the degree of spherical harmonics n and a modulus ratio β [$=(C_{11} - C_{12})/(2C_{44})$]. Lamb's (1882) classical frequency equation for isotropic spheres is recovered as a special case. Numerical results show that the natural frequency for toroidal mode of vibrations increases with both n and β. Some of the lowest natural frequencies for spheres formed by various minerals and crystals are tabulated in Table 1. However, for spheroidal mode of vibrations the solution for the two coupled ordinary differential equations for ϕ and U, (39) and (40), (where ϕ and U are the r-dependence of Φ and u_r, respectively) remains a challenging mathematical problem to be solved. Further studies are recommended.

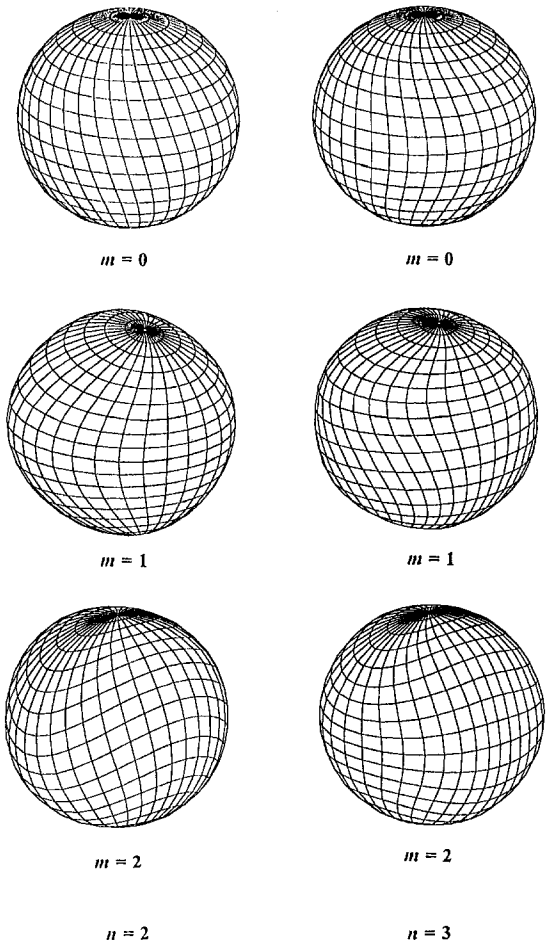

Fig. 4 Surface modal shapes of toroidal vibrations for the second and third degree of spherical harmonics ($n = 2, 3$) with various order ($m = 0, 1, 2$)

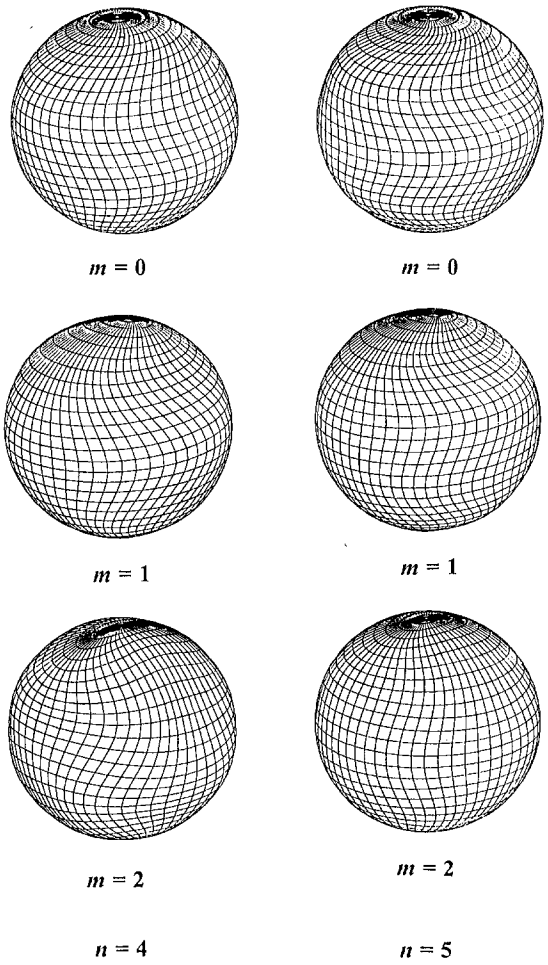

Fig. 5 Surface modal shapes of toroidal vibrations for the fourth and fifth degree of spherical harmonics ($n = 4, 5$) with various order ($m = 0, 1, 2$)

Acknowledgment

This analysis was first initiated in 1992, when I held a postdoctoral fellowship at Northwestern University offered by Prof. John Rudnicki. Most part of the analysis was, however, completed under the support of the RGC Grants and the Hong Kong

Downloaded 04 May 2010 to 171.66.16.26. Redistribution subject to ASME license or copyright; see http://www.asme.org/terms/Terms_Use.cfm

Polytechnic University Grants. Figures 4 and 5 are plotted with the help of Mr. K. C. Ho.

References

Abramowitz, M., and Stegun, I. A., 1965, *Handbook of Mathematical Functions,* Dover, New York.

Alsop, L. E., Sutton, G. H., and Ewing, M., 1961, "Free oscillations of the Earth observed on strain and pendulum seismographs," *Journal of Geophysical Research,* Vol. 66, pp. 631–641.

Benioff, H., Press, F., and Smith, S., 1961, "Excitation of the free oscillations of the Earth by earthquakes," *Journal of Geophysical Research,* Vol. 66, pp. 605–619.

Bogert, B. P., 1961, "An observation of free oscillations of the Earth," *Journal of Geophysical Research,* Vol. 66, pp. 643–646.

Chau, K. T., 1993, "Natural frequencies of finite transversely isotropic circular cylinders," *Proceedings of the Second International Conference on Vibration Problems of Mathematical Elasticity and Physics,* M. M. Banerjee and P. Biswas, eds., Vol. A, pp. 7–12.

Chau, K. T., 1994, "Vibrations of transversely isotropic finite circular cylinders," ASME JOURNAL OF APPLIED MECHANICS, Vol. 61, pp. 964–970.

Chau, K. T., 1995, "Bifurcations at a spherical cavity in a compressible solid with spherical isotropy," *International Journal for Numerical and Analytical Methods in Geomechanics,* Vol. 19, pp. 381–398.

Chen, W. T., 1966, "On some problems in spherically isotropic elastic materials," ASME JOURNAL OF APPLIED MECHANICS, Vol. 33, pp. 539–546.

Chree, C., 1889, "The equations of an isotropic elastic solid in polar and cylindrical coordinates, their solution and application," *Transactions of Cambridge Philosophical Society,* Vol. 14, pp. 250–369.

Ding, H.-J., and Ren, Y.-J., 1991, "Equilibrium problems of spherically isotropic bodies," *Applied Mathematics and Mechanics,* Vol. 12, pp. 155–162 (English Ed.).

Eason, G., 1962, "On the vibrations of anisotropic cylinders and spheres," *Applied Scientific Research,* Vol. A12, pp. 81–85.

Eason, G., 1963, "Transient thermal stresses in anisotropic bodies with spherical symmetry," *Applied Scientific Research,* Vol. A13, pp. 1–15.

Fraser, D. B., and LeCraw R. C., 1964, "Novel method of measuring elastic and anelastic properties of solids," *The Review of Scientific Instruments,* Vol. 35, pp. 1113–1115.

Hata, T., 1993, "Stress-focusing effect in a uniformly heated transversely isotropic sphere," *International of Journal of Solids and Structures,* Vol. 30, pp. 1419–1428.

Hearmon, R. F. S., 1969, "The elastic constants of non-piezoelectric crystals," *Numerical Data and Functional relationships in Science and Technology, New Series, group 3,* H. H. Landolt and R. Bornstein ed., Vol. 1, pp. 1–39.

Heyliger, P., Ledbetter, H., and Austin, M., 1990, "Resonating-orthotropic-cube method for elastic constants," *Dynamics Elastic Modulus Measurements in Materials,* ASTM STP 1045, ASTM, Philadelphia, PA, pp. 100–109.

Heyliger, P. R., and Jilani, A., 1991, "The free vibrations of elastic anisotropic cylinders and spheres," *32nd Structures, Structural Dynamics, and Materials Conference, AIAA, Part 4, Structural Dynamics II,* pp. 3039–3046.

Heyliger, P. R., and Jilani, A., 1992, "The free vibrations of inhomogeneous elastic cylinders and spheres," *International Journal of Solids and Structures,* Vol. 29, pp. 2689–2708.

Hobson, E. W., 1955, *The Theory of Spherical and Ellipsoidal Harmonics,* Chelsea Publishing Company, New York.

Hosseini-Hashemi, S., and Anderson, J. S., 1988, "Orthogonality and normalization of torsional modes of vibration of solid elastic spheres," *Journal of Sound and Vibration,* Vol. 121, pp. 511–524.

Hu, H.-C., 1954, "On the general theory of elasticity for a spherically isotropic medium," *Acta Scientia Sinica,* Vol. 3, pp. 247–260.

Isoda, S., Oda, H., Suzuki, I., and Seya, K., 1990, "Displacement distribution of a freely oscillating rutile sphere," *Tohoku Geophysical Journal,* Vol. 32, pp. 55–76.

Kelvin, Lord, 1863, "On the rigidity of the Earth," *Philosophical Transactions of the Royal Society of London,* Vol. A153, pp. 573–582.

Lamb, H., 1882, "On the vibrations of a elastic sphere," *Proceedings of the London Mathematical Society,* Vol. 13, pp. 189–212.

Lapwood, E. R., and Usami, T., 1981, *Free Oscillations of the Earth,* Cambridge University Press, Cambridge, UK.

Love, A. E. H., 1944, *A Treatise on the Mathematical Theory of Elasticity,* Dover, New York.

MacDonald, G. J. F., and Ness, N. F., 1961, "A study of the free oscillations of the Earth," *Journal of Geophysical Research,* Vol. 66, pp. 1865–1911.

Malvern, L. E., 1969, *Introduction to the Mechanics of a Continuous Medium,* Prentice-Hall, Englewood Cliffs, NJ.

Mochizuki, E., 1986, "The free oscillation of an anisotropic and heterogeneous earth," *Geophysical Journal of Royal Astronautical Society,* Vol. 86, pp. 167–176.

Mochizuki, E., 1988, "Sphere-resonance method to determine elastic constants of crystal," *Journal of Applied Physics,* Vol. 63, pp. 5668–5673.

Nemish, Yu. N., 1969, "Approximate solution of three-dimensional problems in elasticity theory for a transversely isotropic medium," *Soviet Applied Mechanics,* Vol. 5, pp. 803–810.

Nemish, Yu. N., and Nemish, V. N., 1976, "Contribution of the solution of spatial problems of the elasticity theory of a transversely isotropic medium for noncanonical regions," *Soviet Applied Mechanics,* Vol. 12, pp. 1262–1270.

Ness, N. F., Harrison, J. C., and Slichter, L. B., 1961, "Observations of the free oscillations of the Earth," *Journal of Geophysical Research,* Vol. 66, pp. 621–629.

Nowinski, J., 1959, "Note on a thermoelastic problem for a transversely isotropic hollow sphere embedded in an elastic medium," ASME JOURNAL OF APPLIED MECHANICS, Vol. 26, pp. 649–650.

Payton, R. G., 1983, *Elastic Wave Propagation in Transversely Isotropic Media,* Martinus Nijhoff, Hague.

Perkeris, C. L., Alterman, Z., and Jarosch, H., 1961, "Comparison of theoretical with observed values of the periods of free oscillation of the Earth," *Proceedings of the National Academy of Science,* Vol. 47, pp. 91–98.

Press, W. H., Teukolsky, S. A., Vetterling, W. T. and Flannery, B. P., 1992, *Numerical Recipes in FORTRAN: The Art of Scientific Computing,* 2nd ed., Cambridge University Press, Cambridge, UK.

Puro, A. E., 1980, "Variable separation in elasticity-theory equations for spherically transversely isotropic inhomogeneous bodies," *Soviet Applied Mechanics,* Vol. 16, pp. 117–121.

Sato, Y., and Usami, T., 1962a, "Basic study on the oscillation of a homogeneous elastic sphere: I. Frequency of the free oscillations," *Geophysical Magazine,* Vol. 31, pp. 15–24.

Sato, Y., and Usami, T., 1962b, "Basic study on the oscillation of a homogeneous elastic sphere: II. Distribution of displacement," *Geophysical Magazine,* Vol. 31, pp. 25–47.

Shreiber, E., Anderson, O. L., and Soga, N., 1973, *Elastic Constants and Their Measurement,* McGraw-Hill, New York.

Sur, S. P., 1964, "Vibration of inhomogeneous spherical shell of aeolotropic materials," *Indian Journal of Mechanics and Mathematics,* Vol. 2, pp. 6–9.

Visser, W. M., Migliori, A., Bell, T. M., and Reinert, R. A., 1991, "On the normal modes of free vibration of inhomogeneous and anisotropic elastic objects," *Journal of the Acoustical Society of America,* Vol. 90, pp. 2154–2162.

Whittaker, E. T., and Watson, G. N., 1927, *A Course of Modern Analysis,* 4th Ed. Cambridge University Press, Cambridge, UK.

Downloaded 04 May 2010 to 171.66.16.26. Redistribution subject to ASME license or copyright; see http://www.asme.org/terms/Terms_Use.cfm

Shankar Krishnaswamy
Assoc. Mem. ASME.

Z.-H. Jin

R. C. Batra
Fellow ASME.

Department of Engineering Science and Mechanics, Virginia Polytechnic Institute and State University, Blacksburg, VA 24061-0219

Stress Concentration in an Elastic Cosserat Plate Undergoing Extensional Deformations

We formulate and solve the boundary value problem of a linearly elastic, infinite Cosserat plate which contains a circular hole and which is loaded in tension at infinity. The effect of hole radius, plate thickness, and material parameters on the stress concentration at the hole is discussed. We also discuss the stress concentration when the plate is subjected to pure shear.

1 Introduction

The problem of stress concentration around a circular hole in the Kirchhoff-Love theory for flexural deformations of a plate was investigated by Goodier (1936). This bending theory does not consider the effect of transverse shear deformation; the paper by Reissner (1945) addresses the stress concentration problem within the context of a theory which accounts for transverse shear deformation. The corresponding problem for extensional deformations of a classical plate is well known; it is precisely the generalized plane-stress problem of linear elasticity, where the unbounded domain containing a circular hole is loaded in far-field tension (see, e.g., Sokolnikoff, 1956). However, the generalized plane stress theory does not account for transverse normal strain effects. We remark that in the context of a dynamical problem of plates, Kane and Mindlin (1956) have proposed a set of equations for extensional motions which include the effect of transverse normal strain. They have indicated the importance of this effect in the context of high-frequency extensional vibrations of plates. However, the stress concentration problem in an extensional theory of plates accounting for transverse normal strain does not appear to have been studied.

In the present work, we study the stress concentration problem using the linear theory of an elastic Cosserat plate. This theory is unified in the sense that it encompasses the set of equations for both extension as well as bending of a plate. This is in contrast to the theory of Kane and Mindlin (1956) which is specifically designed to address the high-frequency extensional behavior of plates, so much so that the value of a constant in their theory is tailored to accurately reflect three-dimensional high-frequency behavior. This is the main reason we choose the Cosserat theory to model our plate.

In Section 2, we record the basic equilibrium equations of the linear theory of a Cosserat plate. We also indicate the relationship between the extensional equations arising in this theory and those utilized by Kane and Mindlin (1956). In Section 3, we formulate and solve the stress concentration problem for the case of uniaxial tension. We also discuss in this section the stress concentration when the plate is subjected to pure shear at infinity.

Contributed by the Applied Mechanics Division of THE AMERICAN SOCIETY OF MECHANICAL ENGINEERS for publication in the ASME JOURNAL OF APPLIED MECHANICS.

Discussion on this paper should be addressed to the Technical Editor, Professor Lewis T. Wheeler, Department of Mechanical Engineering, University of Houston, Houston, TX 77204-4792, and will be accepted until four months after final publication of the paper itself in the ASME JOURNAL OF APPLIED MECHANICS.

Manuscript received by the ASME Applied Mechanics Division, Oct. 31, 1996; final revision, June 25, 1997. Associate Technical Editor: J. T. Jenkins.

2 Basic Equations for a Linearly Elastic Cosserat Plate

We recall that a Cosserat plate is an initially flat material surface embedded in a three-dimensional Euclidean space and to each point of which is attached deformable vector fields called directors. Here, we confine ourselves to the case of a single director. These models have been discussed extensively by Naghdi (1972).

The linear version of the theory of a Cosserat plate has been discussed in detail by Green and Naghdi (1967) and by Green, Naghdi, and Wenner (1971). The basic kinematic ingredients in the theory are the displacement $\mathbf{u}(x_\alpha)$ of surface particles and the director displacement $\boldsymbol{\delta}(x_\alpha)$, where x_α ($\alpha = 1, 2$) denote rectangular Cartesian coordinates on the midsurface of the plate.[1] The fundamental kinematic assumption in the theory is the following condition relating the displacement $\mathbf{u}^*(x_\alpha, x_3)$ of a particle in the three-dimensional plate-like continuum to $\mathbf{u}$ and $\boldsymbol{\delta}$:

$$\mathbf{u}^*(x_\alpha, x_3) = \mathbf{u}(x_\alpha) + x_3\boldsymbol{\delta}(x_\alpha), \tag{2.1}$$

where x_3 is the third Cartesian coordinate which is normal to the midsurface.[2] We denote the fixed orthonormal basis associated with x_i by $\{\mathbf{e}_i\}$ and write

$$\mathbf{u} = u_i\mathbf{e}_i, \quad \boldsymbol{\delta} = \delta_\alpha\mathbf{e}_\alpha + \delta\mathbf{e}_3. \tag{2.2}$$

The kinematical variables which enter the theory of a Cosserat plate are the quantities $e_{\alpha\beta}$, γ_i, and $\kappa_{i\alpha}$ defined by

$$2e_{\alpha\beta} = u_{\alpha,\beta} + u_{\beta,\alpha}, \quad \gamma_\alpha = \delta_\alpha + u_{3,\alpha},$$
$$\gamma_3 = \delta, \quad \kappa_{\alpha\beta} = \delta_{\alpha,\beta}, \quad \kappa_{3\alpha} = \delta_{,\alpha}, \tag{2.3}$$

where a comma followed by the index α denotes partial differentiation with respect to x_α. From a physical standpoint, $e_{\alpha\beta}$ represents the strain at a point on the midsurface, γ_α is the transverse shear strain, δ is the transverse normal strain, and $\kappa_{i\alpha}$ represents the variation of δ_i on the midsurface.

Relative to the basis $\{\mathbf{e}_i\}$, components of the contact force are denoted by $N_{\alpha i}$, those of the contact director couple by $M_{\alpha i}$ and those of the intrinsic director couple by k_i.[3] We assume that there are no body forces and body couples. The kinetic

[1] Greek indices range from 1 to 2 while Latin ones from 1 to 3. Also, the usual summation convention is adopted for both Greek and Latin indices.

[2] We refer to the surface defined by $x_3 = 0$ as the midsurface and take it to also be the material surface defining the Cosserat plate.

[3] The director displacement $\boldsymbol{\delta}$ is chosen here to be dimensionless and hence the quantities k_i have physical dimensions of couple per unit area. For an elaboration of this point, see p. 482 of Naghdi (1972).

 Copyright © 1998 by ASME

Downloaded 04 May 2010 to 171.66.16.26. Redistribution subject to ASME license or copyright; see http://www.asme.org/terms/Terms_Use.cfm

quantities just introduced are integrated versions of the three-dimensional stress tensor $\mathbf{T} = T_{ij}\mathbf{e}_i \otimes \mathbf{e}_j$:

$$N_{\alpha i} = \int_{-h/2}^{h/2} T_{\alpha i}\, dx_3, \quad M_{\alpha l} = \int_{-h/2}^{h/2} x_3 T_{\alpha i}\, dx_3,$$

$$k_i = \int_{-h/2}^{h/2} T_{3i}\, dx_3, \tag{2.4}$$

where h is the uniform initial thickness of the plate. The equilibrium equations governing the infinitesimal deformations of the Cosserat plate are

$$N_{\alpha\beta,\alpha} = 0, \quad M_{\alpha 3,\alpha} = k_3, \tag{2.5}$$

$$M_{\alpha\beta,\alpha} = k_\beta, \quad N_{\alpha 3,\alpha} = 0, \tag{2.6}$$

along with the restrictions

$$N_{\alpha\beta} = N_{\beta\alpha}, \quad N_{\alpha 3} = k_\alpha. \tag{2.7}$$

The basic idea behind the constitutive theory is to first define a two-dimensional complementary energy function by integrating its three-dimensional counterpart through the thickness of the plate. The constitutive equations for the plate then follow from appropriate relationships involving the two-dimensional complementary energy. We refer the reader to Green, Naghdi, and Wenner (1971) and Section 20 of Naghdi (1972) for details and simply record the following constitutive relations:

$$N_{\alpha\beta} = (1 - \nu)C\left[\frac{\nu}{1 - 2\nu}\, e_{\gamma\gamma}\delta_{\alpha\beta} + e_{\alpha\beta} + \frac{\nu}{1 - 2\nu}\, \delta_{\alpha\beta}\gamma_3\right], \tag{2.8}$$

$$M_{(\alpha\beta)} = B[\nu\delta_{\alpha\beta}\delta_{\gamma\delta} + (1 - \nu)\delta_{\alpha\gamma}\delta_{\beta\delta}]\kappa_{(\gamma\delta)}, \tag{2.9}$$

$$M_{[\alpha\beta]} = 0, \tag{2.10}$$

$$N_{\alpha 3} = \frac{5}{12}\frac{Eh}{(1 + \nu)}\, \gamma_\alpha, \tag{2.11}$$

$$M_{\alpha 3} = \frac{7}{20}(1 - \nu)B\kappa_{3\alpha}, \tag{2.12}$$

$$k_3 = \frac{1 - \nu}{1 - 2\nu}\, C[(1 - \nu)\gamma_3 + \nu e_{\alpha\alpha}], \tag{2.13}$$

where $\delta_{\alpha\beta}$ is the two-dimensional Kronecker delta, ν is Poisson's ratio, E is Young's modulus, the symbols ( ) and [ ] in (2.9) and (2.10) denote the symmetric and skew-symmetric parts of $M_{\alpha\beta}$, respectively, and

$$B = \frac{Eh^3}{12(1 - \nu^2)}, \quad C = \frac{Eh}{1 - \nu^2}. \tag{2.14}$$

Equations (2.5), (2.8), (2.12), and (2.13) are associated with extensional deformations of the plate while Eqs. (2.6), (2.9), (2.10), and (2.11) characterize flexural deformations of the plate. In the linear theory, the extensional equations are decoupled from the flexural ones. The flexural Eqs. (2.6) along with constitutive Eqs. (2.9), (2.10), and (2.11) are identical to those of Reissner's plate theory (1945).

The extensional Eqs. (2.5), (2.8), and (2.13) correspond to the static counterpart of those used by Kane and Mindlin (1956) provided δ in (2.2) is identified with $2w/h$ of their paper and the ratio of resultants in (2.4) to the corresponding ones in Kane and Mindlin's work is identified as the plate thickness. As regards (2.12), Naghdi (1972, p. 574) indicates the procedure by which the constant 7/20 is obtained and also comments on its reasonableness. Jin and Hwang (1989) have indicated that for static problems, the value of the constant κ in Kane and Mindlin's paper be taken as 1; this corresponds to a value 1/2 in (2.12) rather than 7/20. The slight difference in our final results from those gotten by utilizing the static counterpart of the Kane-Mindlin theory (see Fig. 3) can be attributed to the value of the constant in (2.12). In a recent paper, Naghdi and Rubin (1995) utilize a third procedure which results in a value 1/2 for the aforementioned constant. This indicates that the choice 1/2 in (2.12) may perhaps be more accurate. However, we shall see in Section 3 that the two choices produce almost identical results for both the stress concentration problem of uniaxial tension and pure shear. We note that $(2.5)_1$ and (2.8) are the equations of generalized plane stress or alternatively, they may be regarded as those governing extensional deformations in the classical Kirchhoff-Love plate theory.

We now obtain the equations of extensional deformations of the Cosserat plate in terms of an Airy function φ. The extensional equations for the static counterpart of the Kane-Mindlin theory have been given by Jin and Hwang (1989) in terms of an Airy function. In the Cosserat theory, the procedure is identical and we briefly describe it below. From Eq. $(2.5)_1$, it may be deduced that there exists a scalar function $\varphi(x_\alpha)$ such that

$$N_{\alpha\beta} = \nabla^2\varphi\delta_{\alpha\beta} - \varphi_{,\alpha\beta}, \tag{2.15}$$

where $\nabla^2\varphi$ denotes the two-dimensional Laplacian of φ. Now, we use the compatibility condition[4]

$$e_{11,22} + e_{22,11} - 2e_{12,12} = 0 \tag{2.16}$$

of the linear theory of a Cosserat plate and the constitutive Eqs. (2.8) and (2.13) to deduce that the Airy function φ satisfies the differential equation

$$\frac{(1 - \nu^2)}{E\nu}\nabla^4\varphi - \nabla^2\delta = 0, \tag{2.17}$$

where ∇^4 is the two-dimensional biharmonic operator. The remaining constitutive Eq. (2.12) may be used in conjunction with (2.13) to obtain

$$\frac{7}{240}\frac{h^2}{(1 + \nu)}\nabla^2\delta - \delta - \frac{\nu}{Eh}\nabla^2\varphi = 0. \tag{2.18}$$

The two differential Eqs. (2.17) and (2.18) for φ and δ may be rewritten as

$$\nabla^4\delta - G\nabla^2\delta = 0, \tag{2.19}$$

$$\nabla^2\varphi = G_1\nabla^2\delta - G_2\delta, \tag{2.20}$$

where

$$G_1 = \frac{7Eh^3}{240\nu(1 + \nu)}, \quad G_2 = \frac{Eh}{\nu}, \quad G = \frac{240}{7h^2}\frac{1}{(1 - \nu)}. \tag{2.21}$$

Once (2.19) has been solved for δ, we can solve (2.20) for φ.

3 A Boundary Value Problem

Consider an infinite plate with uniform initial thickness h. The plate contains a circular hole of radius R and is loaded in far-field tension as shown in Fig. 1. We introduce polar coordinates (r, θ) and record the boundary conditions below.

$$\text{As } r \to \infty, \quad N_{rr} = \frac{N}{2}(1 + \cos 2\theta), \quad N_{r\theta} = -\frac{N}{2}\sin 2\theta,$$

$$N_{\theta\theta} = \frac{N}{2}(1 - \cos 2\theta), \tag{3.1}$$

$$\text{At } r = R, \quad N_{rr} = 0, \quad N_{r\theta} = 0, \quad M_{r3} = 0. \tag{3.2}$$

The quantities appearing in (3.1) and (3.2) represent the physi-

[4] See Section 6 of Naghdi (1972).

Downloaded 04 May 2010 to 171.66.16.26. Redistribution subject to ASME license or copyright; see http://www.asme.org/terms/Terms_Use.cfm

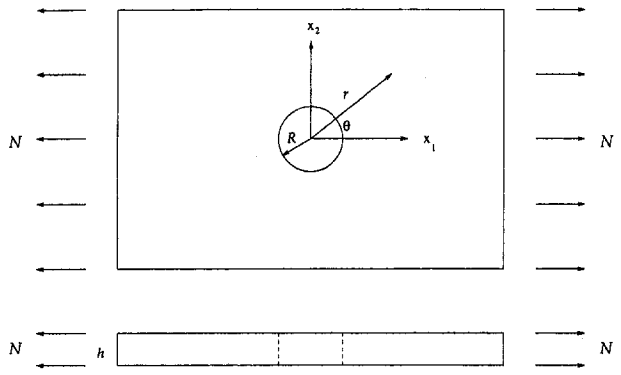

Fig. 1 Plate loaded in tension at infinity

cal components $N_{\langle\alpha\beta\rangle}$ and $M_{\langle\alpha 3\rangle}$. That the solution to the boundary value problem defined by (2.6)–(2.8) and (3.1)–(3.2) is unique (upto a rigid motion) follows from the discussion in Section 26 of Naghdi (1972).

Keeping in mind the form of the boundary conditions (3.1), we seek a solution to (2.19) of the form

$$\delta(r, \theta) = \delta_a(r) + \delta_b(r) \cos 2\theta. \tag{3.3}$$

Substitution of (3.3) into (2.19) results in a pair of ordinary differential equations for δ_a and δ_b, whose solutions involve modified Bessel functions I_0, K_0 of order zero and I_2, K_2 of order 2. The solution procedure being straightforward, we merely present the result for δ below:

$$\delta(r, \theta) = a_1 + a_2 \ln r + a_3 I_0(\sqrt{G}r) + a_4 K_0(\sqrt{G}r) + \left[b_1 r^2 + \frac{b_2}{r^2} + b_3 I_2(\sqrt{G}r) + b_4 K_2(\sqrt{G}r) \right] \cos 2\theta, \tag{3.4}$$

where a_1, a_2, a_3, a_4, b_1, b_2, b_3, and b_4 are constants to be determined from the boundary conditions. Since the director displacement δ must remain bounded at infinity, the constants a_2, a_3, b_3, and b_1 vanish so that

$$\delta(r, \theta) = a_1 + a_4 K_0(\sqrt{G}r) + \left[\frac{b_2}{r^2} + b_4 K_2(\sqrt{G}r) \right] \cos 2\theta. \tag{3.5}$$

We now substitute (3.5) into (2.20) and observe that φ satisfies the Poisson equation. The solution for φ is

$$\varphi(r, \theta) = p_1 + p_2 \ln r + \frac{\bar{a}}{4} r^2 + \frac{\bar{b}}{G} K_0(\sqrt{G}r) + \left[a_1 r^2 + \frac{q_2}{r^2} - \frac{\bar{c}}{4} + \frac{\bar{d}}{G} K_2(\sqrt{G}r) \right] \cos 2\theta, \tag{3.6}$$

where

$$\bar{a} = -a_1 G_2, \quad \bar{b} = a_4(GG_1 - G_2),$$
$$\bar{c} = -b_2 G_2, \quad \bar{d} = b_4(GG_1 - G_2), \tag{3.7}$$

and p_1, p_2, q_1, q_2 are constants to be determined from the boundary conditions. Expressions for the resultants in polar coordinates are

$$N_{rr} = \frac{1}{r}\frac{\partial \varphi}{\partial r} + \frac{1}{r^2}\frac{\partial^2 \varphi}{\partial \theta^2}, \quad N_{r\theta} = N_{\theta r} = \frac{1}{r^2}\frac{\partial \varphi}{\partial \theta} - \frac{1}{r}\frac{\partial^2 \varphi}{\partial r \partial \theta}, \tag{3.8}$$

$$N_{\theta\theta} = \frac{\partial^2 \varphi}{\partial r^2}, \quad M_{r3} = \frac{7}{20}(1 - \nu)B\frac{\partial \delta}{\partial r},$$

$$M_{\theta 3} = \frac{7}{20}(1 - \nu)B\frac{\partial \delta}{\partial \theta}. \tag{3.9}$$

Using (3.5) and (3.6) to calculate the derivatives appearing above, we record expressions for all the resultants:

$$N_{rr} = \left(\frac{p_2}{r^2} + \frac{\bar{a}}{2} - \frac{\bar{b}K_1}{\sqrt{G}r} \right) + \left[-2q_1 - \frac{6q_2}{r^4} + \frac{\bar{c}}{r^2} - \frac{\bar{d}}{G}\left(\frac{4K_1}{\sqrt{G}r^3} + \frac{\sqrt{G}K_1}{r^2} + \frac{2K_0}{r^2} - \frac{4K_2}{r^2} \right) \right] \cos 2\theta, \tag{3.10}$$

$$N_{r\theta} = \left[2q_1 - \frac{6q_2}{r^4} + \frac{\bar{c}}{2r^2} - \frac{2\bar{d}}{G}\left(\frac{4K_1}{\sqrt{G}r^3} + \frac{\sqrt{G}K_1}{r} + \frac{2K_0}{r^2} + \frac{K_2}{r^2} \right) \right] \sin 2\theta, \tag{3.11}$$

$$N_{\theta\theta} = \left(\frac{\bar{a}}{2} + \bar{b}K_0 + \frac{\bar{b}K_1}{\sqrt{G}r} - \frac{p_2}{r^2} \right) + \left[2q_1 + \frac{6q_2}{r^4} + \frac{\bar{d}}{G}\left(\frac{12K_1}{\sqrt{G}r^3} + \frac{3\sqrt{G}K_1}{r} + \frac{6K_0}{r^2} + GK_0 \right) \right] \cos 2\theta, \tag{3.12}$$

$$M_{r3} = \frac{7}{20}(1 - \nu)B\left\{ -a_4\sqrt{G}K_1 - \left[\frac{2b_2}{r^3} + \frac{4b_4K_1}{\sqrt{G}r^2} + b_4\sqrt{G}K_1 + \frac{2b_4K_0}{r} \right] \cos 2\theta \right\}, \tag{3.13}$$

$$M_{\theta 3} = -\frac{7}{20}(1 - \nu)B\left(\frac{2b_2}{r^3} + \frac{2b_4K_2}{r} \right) \sin 2\theta, \tag{3.14}$$

where the argument $\sqrt{G}r$ of the functions K_0, K_1, and K_2 has been suppressed. The boundary conditions (3.1) and (3.2) yield the following values for the constants:

$$\bar{a} = N, \quad \bar{b} = 0, \tag{3.15}$$

$$\bar{c} = \frac{-2NR^2(2K_2 + \rho K_1)}{16K_2\left(\frac{GG_1}{G_2} - 1 \right) + 12K_1\left(\frac{GG_1}{G_2} - 1 \right) + 2K_2 + \rho K_1}, \tag{3.16}$$

$$\bar{d} = \frac{-4N}{\frac{16K_2}{\rho^2} + \frac{12K_1}{\rho} + \frac{2K_2}{\left(\frac{GG_1}{G_2} - 1 \right)} + \frac{\rho K_1}{\left(\frac{GG_1}{G_2} - 1 \right)}}, \tag{3.17}$$

$$p_2 = -\frac{NR^2}{2}, \quad q_1 = -\frac{N}{4}, \tag{3.18}$$

$$q_2 = \frac{R^4}{6}\left[\frac{N}{2} + \frac{\bar{c}}{R^2} + \bar{d}\left(\frac{K_1}{\rho} - \frac{2K_2}{\rho^2} \right) \right], \tag{3.19}$$

where $\rho = \sqrt{G}R$. We note that the constant p_1 in (3.6) does not influence the value of any of the resultants and hence can have any arbitrary value.

The ratio $N_{\theta\theta}/N$ at $r = R$ is given by

Downloaded 04 May 2010 to 171.66.16.26. Redistribution subject to ASME license or copyright; see http://www.asme.org/terms/Terms_Use.cfm

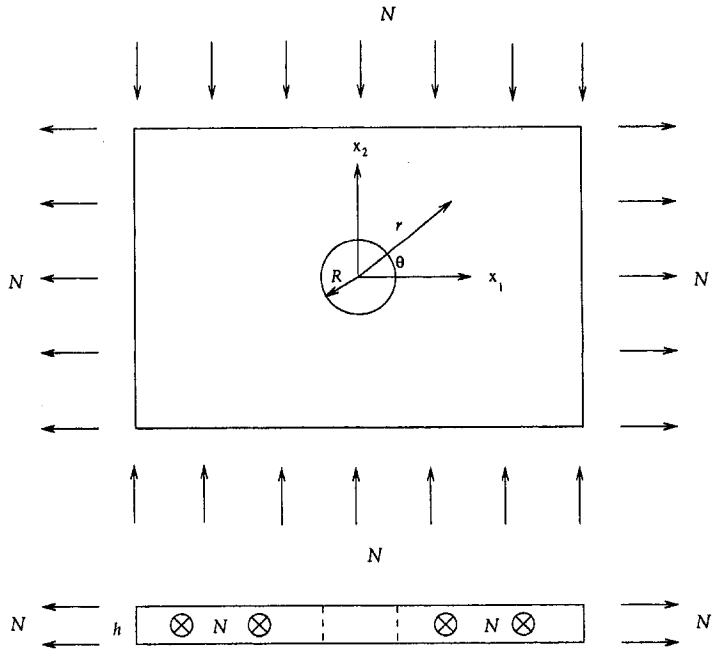

Fig. 2 Plate subjected to pure shear at infinity

$$\frac{N_{\theta\theta}(R,\theta)}{N} = 1 - \left[\frac{\bar{c}}{NR^2} + \frac{\bar{d}}{N}\left(\frac{4K_2}{\rho^2} + \frac{4K_1}{\rho} + K_0\right)\cos 2\theta\right]. \quad (3.20)$$

The stress concentration C_{ut} (the subscript ut denotes uniaxial tension) is defined as the maximum value of the expression (3.20), which occurs at both $\theta = \pi/2$ and $\theta = 3\pi/2$:

$$C_{ut} = \frac{N_{\theta\theta}(R,\pi/2)}{N} = 1 - \left[\frac{\bar{c}}{NR^2} + \frac{\bar{d}}{N}\left(\frac{4K_2}{\rho^2} + \frac{4K_1}{\rho} + K_0\right)\right]. \quad (3.21)$$

In the limit when $\rho \to \infty$, which for a given R, corresponds to a vanishingly thin plate, we expect to recover the stress concentration in the generalized plane-stress problem. Indeed, from (3.21), we have

$$\lim_{\rho\to\infty} C_{ut} = 3, \quad (3.22)$$

and the limiting value (3.22) is independent of the material parameters, hole radius and plate thickness, as it should be. The stress concentration factor C_{ut} depends on the material parameters ρ and the ratio GG_1/G_2 occurring in (3.16) and (3.17). From (3.21) and (2.21) it is clear that C_{ut} only depends on Poisson's ratio ν of the material. We plot the variation of C_{ut} as a function of R/h in Fig. 3 for $\nu = 1/3$. The result from the static counterpart of the Kane-Mindlin equations is also depicted here. It may be deduced from (3.21) that in the limit when R/h approaches zero, C_{ut} equals 2.

Finally, we discuss the stress concentration factor C_{ps} when the plate is subjected to pure shear as shown in Fig. 2. It is clear that the solution to this problem may be obtained by suitably superposing the solution for uniaxial tension in the x_1 direction and that for uniaxial compression in the x_2 direction. We do not present expressions for the resultants but note that the stress concentration factor is

$$C_{ps} = \frac{N_{\theta\theta}(R,\pi/2)}{N} = -2\left[\frac{\bar{c}}{NR^2} + \frac{\bar{d}}{N}\left(\frac{4K_2}{\rho^2} + \frac{4K_1}{\rho} + K_0\right)\right]. \quad (3.23)$$

It is clear from (3.23) that the remarks pertaining to C_{ut} apply to C_{ps} as well. In the limiting case when $\rho \to \infty$, C_{ps} equals 4, which corresponds to the generalized plane-stress value. For $\nu = 1/3$, the variation of C_{ps} with R/h is shown in Fig. 3.

The stress concentration factors C_{ut} and C_{ps} do not vary appreciably from their generalized plane stress counterparts of 3 and 4, respectively, for $R/h > 1$. Also, there is very little difference between these factors using the Cosserat versus the Kane-Mindlin theory. However, it is possible that in other equilibrium problems involving extensional deformations, the effect of transverse normal strain may be more pronounced; we mention the paper by Naghdi and Rubin (1989) who have emphasized the importance of this effect for contact problems of beams.

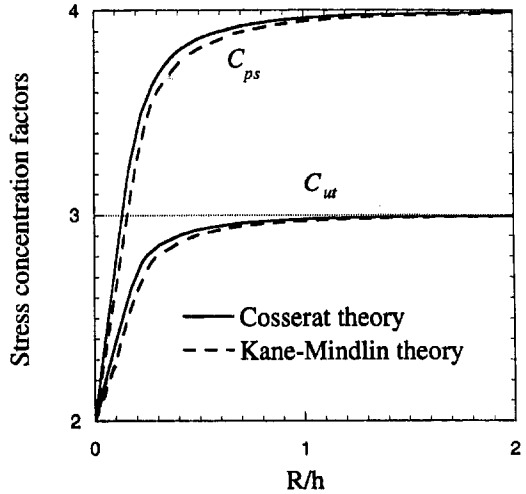

Fig. 3 Variation of stress concentration factors with R/h

Downloaded 04 May 2010 to 171.66.16.26. Redistribution subject to ASME license or copyright; see http://www.asme.org/terms/Terms_Use.cfm

The procedure outlined in Section 2 is general and may be used to solve other problems where thickness effects play an important role.

We note that for values of $R/h < 1$, the inclusion of transverse normal strain *lowers* the stress concentration factor. Although we have plotted these factors for very small R/h, we caution the reader that neither the Cosserat theory nor the Kane-Mindlin theory may be very accurate in this regime since these theories, in general, are not valid for very thick plates.

References

Goodier, J. N., 1936, "The influence of circular and elliptical holes on the transverse flexure of elastic plates," *Philosophical Magazine,* Ser. VII, Vol. 22, pp. 69–80.

Green, A. E., and Naghdi, P. M., 1967, "The linear theory of an elastic Cosserat plate," *Proceedings of the Cambridge Philosophical Society,* Vol. 63, pp. 537–550.

Green, A. E., Naghdi, P. M., and Wenner, M. L., 1971, "Linear theory of a Cosserat surface and elastic plates of variable thickness," *Proceedings of the Cambridge Philosophical Society,* Vol. 69, pp. 227–254.

Jin, Z. H., and Hwang, K. C., 1989, "An analysis of three-dimensional effects near the tip of a crack in an elastic plate," *Acta Mechanica Solida Sinica,* Vol. 2, pp. 387–401.

Kane, T. R., and Mindlin, R. D., 1956, "High-Frequency Extensional Vibrations of Plates," ASME JOURNAL OF APPLIED MECHANICS, Vol. 23, pp. 277–283.

Naghdi, P. M., 1972, *The Theory of Shells and Plates, Handbuch der Physik,* Vol. VI a/2 C. Truesdell, ed., Springer-Verlag, Berlin, pp. 425–640.

Naghdi, P. M., and Rubin, M. B., 1989, "On the significance of normal cross-sectional extension in beam theory with application to contact problems," *International Journal of Solids and Structures,* Vol. 25, pp. 249–265.

Naghdi, P. M., and Rubin, M. B., 1995, "Restrictions on nonlinear constitutive equations for elastic shells," *Journal of Elasticity,* Vol. 39, pp. 133–163.

Reissner, E., 1945, "The Effect of Transverse Shear Deformation on the Bending of Elastic Plates," ASME JOURNAL OF APPLIED MECHANICS, Vol. 12, A-69-77.

Sokolnikoff, I. S., 1956, *Mathematical Theory of Elasticity,* 2nd ed; Krieger, Malabar, FL.

Downloaded 04 May 2010 to 171.66.16.26. Redistribution subject to ASME license or copyright; see http://www.asme.org/terms/Terms_Use.cfm

Effect of the *T*-Stress in Microcrack Shielding Problems

LiGuo Zhao

YiHeng Chen

Department of Engineering Mechanics,
Xi-an Jiaotong University,
Xi-an, Shaanxi Province,
710049, P. R. China

The effect of the T-stress in microcrack shielding problems is studied by solving the interaction problem of a macrocrack with near tip microcracks applying a discrete model. The T-stress has no effect on the results for the parallel microcrack cases; however, it plays an important role for the oriented microcrack cases, especially for large values of the T-stress and large distances of the microcrack center from the macrocrack tip. In determining the shielding or amplification effect of the oriented microcracks, it is necessary to consider the effect of the T-stress. The effect of the T-stress on microcrack shielding or amplification is substantially dependent on the sign and magnitude of the T-stress as well as on the geometry of the microcrack arrangement. The contribution to the J-integral induced from the microcracks is reexamined by considering the T-stress and shown to be still in a consistent relation with those induced from the macrocrack tip and the remote stress field.

Introduction

The stress distribution in the vicinity of a crack tip was investigated by Williams (1957) and can be expressed in the cylindrical coordinates (r, θ) as

$$\begin{bmatrix} \sigma_{11} & \sigma_{12} \\ \sigma_{21} & \sigma_{22} \end{bmatrix} = \frac{K}{\sqrt{2\pi r}} \begin{bmatrix} f_{11}(\theta) & f_{12}(\theta) \\ f_{21}(\theta) & f_{22}(\theta) \end{bmatrix} + \begin{bmatrix} T & 0 \\ 0 & 0 \end{bmatrix} + O(\sqrt{r}). \quad (1)$$

The first term in the expansion is singular at the crack tip, whereas the second term is finite and bounded. In the notation of Rice (1974), the second term is denoted the *T*-stress and can be regarded as a stress acting parallel to the crack plane.

Larsson and Carlsson (1973) and Rice (1974) showed that the sign and magnitude of the *T*-stress substantially alter the size and shape of the plane-strain crack-tip plastic zone at finite load levels. The work by Bilby et al. (1986) indicated that the *T*-stress extends the range of validity of the small-scale yielding conditions at finite strains. Betegon and Hancock (1991) characterized the elastic-plastic crack tip fields by using a two-parameter law, i.e., *J*-integral and *T*-stress. Another significance of the *T*-stress in fracture analysis is that it governs the stability of a straight crack path (Cotterell and Rice, 1980; Fleck et al., 1991) under mode *I* loading conditions. Tvergaard and Hutchinson (1994) studied the effect of the *T*-stress on mode *I* crack growth resistance in a ductile solid.

There now exists experimental evidence that stress-induced microcracking near a macrocrack tip enhances the fracture toughness of brittle materials (Ruhle et al., 1987). Microcrack toughening has also been the subject of numerous modeling studies. As pointed out by Cai and Faber (1992), the two basic approaches are continuum modeling (Evans and Faber, 1981, 1984; Evans and Fu, 1985; Hutchinson, 1987; Ortiz, 1987; Ortiz and Giannakopoulos; 1989) and discrete modeling (Kachanov and Montagut, 1986; Rose, 1986; Rubinstein, 1986; Chudnovsky et al., 1987; Gong and Horii, 1989). Both approaches are associated with the release of a general residual stress field as a result of the formation of microcracks in the vicinity of a macrocrack tip, in which only the singular term corresponding to the stress intensity factor K in the expansion (1) is considered and the second term corresponding to the *T*-stress is neglected. However, the *T*-stress cannot be neglected when the microcracks are located at some distance $r = r_1$, where the *T*-stress has the same order as the stress $K/\sqrt{2\pi r}$.

What's more, during the investigation of the microcrack shielding effect, Chen (1996) and Zhao and Chen (1997) have found the following relation of the *J*-integral:

$$J_t + \Delta J = J_\infty, \quad (2)$$

where J_∞ is the contribution from the remote stress field parameterized by K_I^∞ and K_{II}^∞, J_t is the contribution from the macrocrack tip, and ΔJ is the contribution from the existing microcracks.

Relation (2) reveals that there is a wastage, i.e., ΔJ, when the remote *J*-integral, J_∞, transmits across the microcracking zone from the infinity to the macrocrack tip, which is different from the relation $J_t = J_\infty$ used in the continuum modeling (Evans and Faber, 1981, 1984; Evans and Fu, 1985; Hutchinson, 1987; Ortiz, 1987; Ortiz and Giannakopoulos, 1989). The wastage ΔJ just due to the microcracks can be used as a criterion to determine the microcrack shielding or amplification effect (Zhao and Chen, 1997).

Dividing by J_∞ on the right and left side of the relation (2), we can get a consistent relation of the *J*-integral as (see Eq. (11) given by Chen (1996) and Eq. (20) given by Zhao and Chen (1997))

$$\frac{J_t}{J_\infty} + \frac{\Delta J}{J_\infty} = 1. \quad (3)$$

The consistent relation (3) has been proved numerically by Chen (1996) in homogeneous solids and Zhao and Chen (1997) in bimaterial solids, which also excludes the effect of the *T*-stress.

The purpose of this work is to study the effect of the *T*-stress in microcrack shielding problems by adopting the discrete model requiring the consideration of the interaction of a macrocrack with microcracks. The numerical scheme has been addressed thoroughly by Chen (1996) and Zhao and Chen (1997) and can be easily extended to the current study by taking the *T*-stress into account in the remote stress field, i.e., not only the

Contributed by the Applied Mechanics Division of THE AMERICAN SOCIETY OF MECHANICAL ENGINEERS for publication in the ASME JOURNAL OF APPLIED MECHANICS.

Discussion on the paper should be addressed to the Technical Editor, Professor Lewis T. Wheeler, Department of Mechanical Engineering, University of Houston, Houston, TX 77204-4792, and will be accepted until four months after final publication of the paper itself in the ASME JOURNAL OF APPLIED MECHANICS.

Manuscript received by the ASME Applied Mechanics Division, Nov. 19, 1996; final revision, May 26, 1997. Associate Technical Editor: W. J. Drugan.

 Copyright © 1998 by ASME

Downloaded 04 May 2010 to 171.66.16.26. Redistribution subject to ASME license or copyright; see http://www.asme.org/terms/Terms_Use.cfm

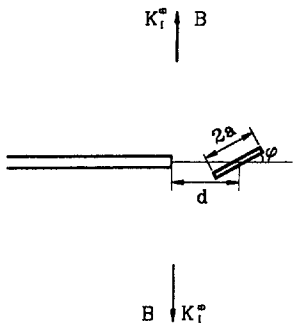

Fig. 1 A macrocrack interacting with a microcrack centered just ahead of the macrocrack tip

singular term corresponding to the stress intensity factor K but also the second term corresponding to the T-stress in the expansion (1) is considered for the release of the residual stress field as a result of the formation of microcracks in the vicinity of a macrocrack tip. The stress intensity factors of the macrocrack are determined for several numerical examples. It is shown that the T-stress has no effect on the results for the parallel microcrack; however, it plays an important role for the oriented microcrack cases. Effects of the T-stress should be considered in determining the oriented microcrack shielding or amplification effect, especially for large values of the T-stress and large distances of the microcrack center from the macrocrack tip. The effect of the T-stress on microcrack shielding or amplification effect is substantially dependent on the sign and magnitude of the T-stress as well as on the geometry of the microcrack arrangement. The consistent relation (3) of the J-integral is also re-examined when considering the T-stress and is concluded to be still valid.

Analysis

A general effective numerical solution to the interaction of a macrocrack with multiple near-tip microcracks subjected to a remote stress field parameterized by the first term of the macrocrack-tip stress field expansion corresponding to the stress intensity factors K_I^∞ and K_{II}^∞ has been fully described by Chen (1996) and Zhao and Chen (1997) using the principle of superposition and the Fredholm integral equations technique. The numerical scheme can be extended to consider the effect of the T-stress by just adding the second term of the crack-tip stress field expansion corresponding to the T-stress T^∞ to the remote stress field, i.e., not only the singular term corresponding to the stress intensity factor K but also the second term corresponding to the T-stress in the expansion (1) is considered for the release of the residual stress field as a result of the formation of microcracks in the vicinity of a macrocrack tip, which also results in a system of Fredholm integral equations and can be solved numerically. With the obtained solution, the incremental values of the stress intensity factors at the macrocrack tip, ΔK_I and ΔK_{II}, and the stress intensity factors of the right and left micro-

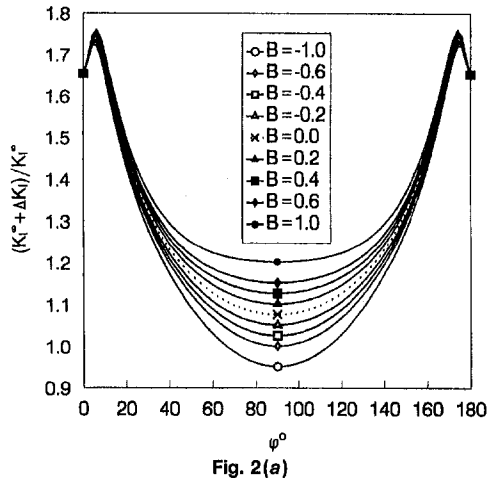

Fig. 2(a)

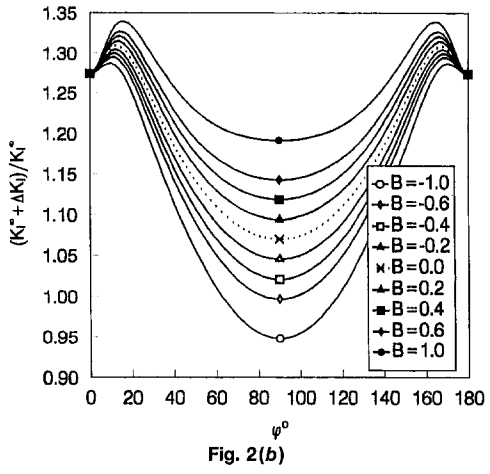

Fig. 2(b)

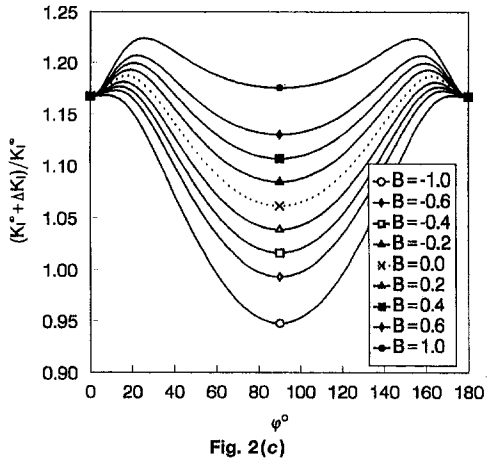

Fig. 2(c)

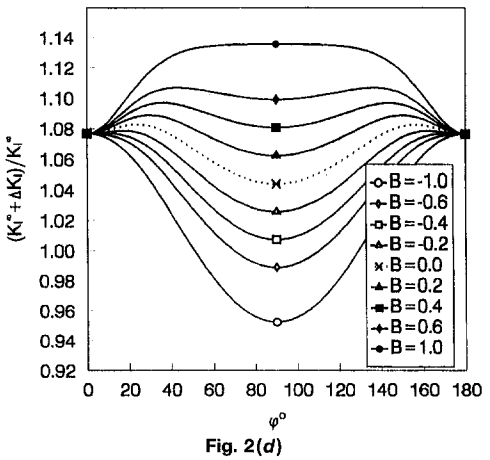

Fig. 2(d)

Fig. 2 The stress intensity factor of the macrocrack vs. the microcrack orientation angle φ; (a) d/a = 1.1, (b) d/a = 1.3, (c) d/a = 1.5, (d) d/a = 2.0

Downloaded 04 May 2010 to 171.66.16.26. Redistribution subject to ASME license or copyright; see http://www.asme.org/terms/Terms_Use.cfm

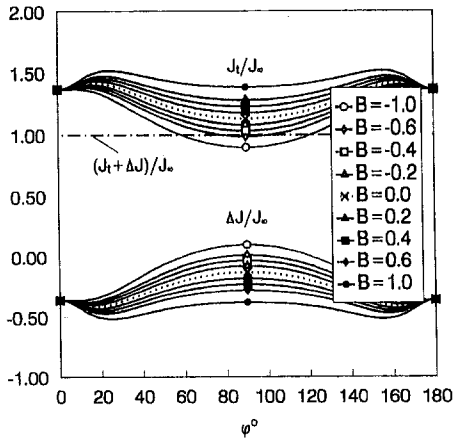

Fig. 3 The *J*-integrals versus the microcrack orientation angle φ for $d/a = 1.5$

crack tips, K^R and K^L, can be calculated easily. Then, J_∞, J_t, and ΔJ in relation (2) can be obtained by the calculated stress intensity factors and the technique developed by Zhao and Chen (1997).

In this work, the magnitude of the remote T-stress, T^∞, is defined through a biaxiality parameter B, introduced by Leevers and Radon (1983) and Betegon and Hancock (1991)

$$B = \frac{T^\infty \sqrt{\pi a}}{K_I^\infty}, \tag{4}$$

where a is half of the mean length of the N microcracks

$$a = \sum_{i=1}^{N} \frac{a_i}{N}. \tag{5}$$

For a finite crack of length $2a$ in an infinite plate, the T-stress is dependent on the applied remote loading. For example, when the plate is loaded by a stress σ normal to the crack and $R\sigma$ parallel to it, we have (Cotterell and Rice, 1980)

$$T = (R-1)\sigma, \quad K_I = \sigma\sqrt{\pi a}, \quad B = \frac{T\sqrt{\pi a}}{K_I} = R - 1. \tag{6}$$

As one can see, $-1 \le B \le 1$ for $0 \le R \le 2$, so it is appropriate to take some values of B in the interval $(-1, 1)$ in the following calculation. Also, the remote stress field is parameterized by K_I^∞ and B ($K_{II}^\infty = 0$).

Numerical Examples and Discussion

First, consider a macrocrack and a microcrack of length $2a$ just centered ahead the macrocrack tip shown in Fig. 1. The numerical results of the stress intensity factors of the macrocrack are presented in Figs. $2(a)$, (b), (c), and (d) with the variation of the microcrack orientation angle φ. It can be seen that when $\varphi = 0$ deg or 180 deg, i.e., the collinear microcrack, the T-stress has no effect on the results. However, the sign and magnitude of the T-stress alter the results for the oriented microcrack. There exist obvious differences between the results obtained with the T-stress (see the continuous lines in the figures for $B \neq 0$) and those without it (see the dotted lines in the figures for $B = 0$). As shown in the figures, the T-stress substantially influences the oriented microcrack shielding or amplification effect, especially for large values of d/a and $|B|$. The positive T-stress ($B > 0$) increases the amplification effect, whereas the negative T-stress ($B < 0$) decreases the amplification effect and, to some extent, it will cause a shielding effect. The T-stress will produce the most significant effect when $\varphi = 90$ deg. Figure 3 shows the results of the J-integrals for $d/a = 1.5$. We can see that the consistent relation (3) of the J-integral is still valid when considering the T-stress, although the T-stress influences the values of J_t and ΔJ. It should be pointed out that the omitted results for $d/a = 1.1$, 1.3, and 2.0 also prove the consistent relation (3) of the J-integral.

Then, consider a macrocrack and a microcrack of length $2a$ just centered below the macrocrack tip as shown in Fig. 4. The calculated stress intensity factors of the macrocrack are presented in Figs. $5(a)$, (b), (c), and (d) with the variation of the microcrack orientation angle φ. It is also shown that, for the parallel microcrack, i.e., $\varphi = 0$ deg or 180 deg, the results are independent of the T-stress. However, for the oriented microcrack, the results are dependent on the sign and magnitude of the T-stress as well as on the arrangement of the microcrack. The microcrack shielding or amplification effect is substantially different for different sign and magnitude of the T-stress and different microcrack orientation. The curves in each of the figures are noted to cross at a point, which hints that the results are weakly dependent on the T-stress for the specified microcrack orientation. Such specified microcrack orientation is denoted by φ_T in this paper and $\varphi_t = 87.6$ deg for $d/a = 1.1$, 84.3 deg for $d/a = 1.3$, 81.9 deg for $d/a = 1.5$ and 78.2 deg for $d/a = 2.0$. When $\varphi < \varphi_T$, the positive T-stress ($B > 0$) increases the shielding effect or decreases the amplification effect and the negative T-stress ($B < 0$) decreases the shielding effect or increases the amplification effect. When $\varphi > \varphi_T$, the positive T-stress ($B > 0$) increases the amplification effect or decreases the shielding effect and the negative T-stress ($B < 0$) decreases the amplification effect or increases the shielding effect. Significant effect of the T-stress will occur for the large values of h/a and $|B|$. Figure 6 shows the results of the J-integrals for $h/a = 1.5$. It can also be seen that the consistent relation (3) of the J-integral is still valid when considering the T-stress, although the T-stress influences the values of J_t and ΔJ. The omitted results for $h/a = 1.1$, 1.3, and 2.0 also prove the consistent relation (3) of the J-integral.

Furthermore, consider two symmetrical microcracks just centered above and below the macrocrack tip, respectively, as shown in Fig. 7. The results are given in Fig. 8 and Fig. 9 for $h/a = 1.5$. The curves in Fig. 8 are seen to cross at a point for the specified microcrack orientation $\varphi_T = 82.0$ where the results are independent of the T-stress, which is similar to the parallel microcrack arrangement. When $\varphi < \varphi_T$, the positive T-stress ($B > 0$) increases the shielding effect or decreases the amplification effect and the negative T-stress ($B < 0$) decreases the shielding effect or increases the amplification effect. When $\varphi > \varphi_T$, the positive T-stress ($B > 0$) increases the amplification effect or decreases the shielding effect and the negative T-stress

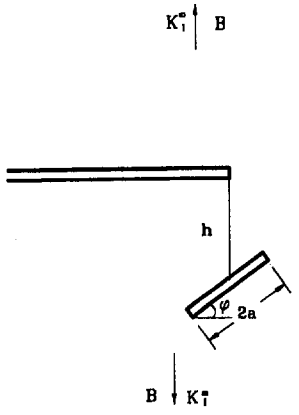

Fig. 4 A macrocrack interacting with a microcrack centered just below the macrocrack tip

Downloaded 04 May 2010 to 171.66.16.26. Redistribution subject to ASME license or copyright; see http://www.asme.org/terms/Terms_Use.cfm

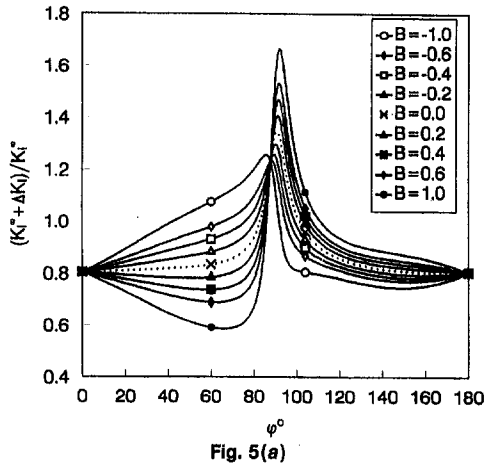

Fig. 5(a)

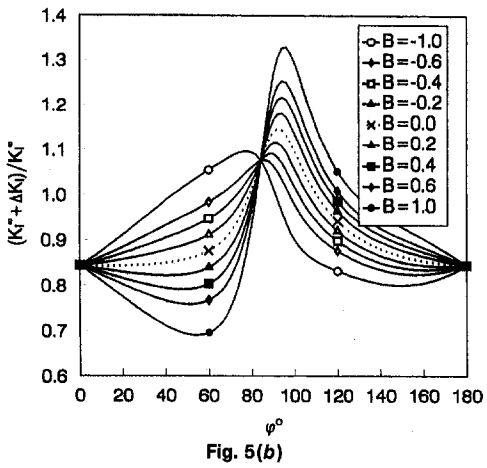

Fig. 5(b)

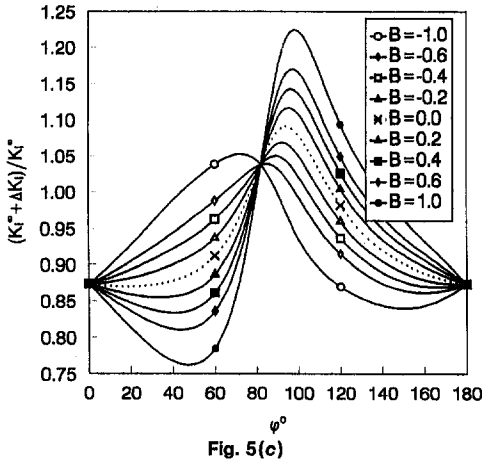

Fig. 5(c)

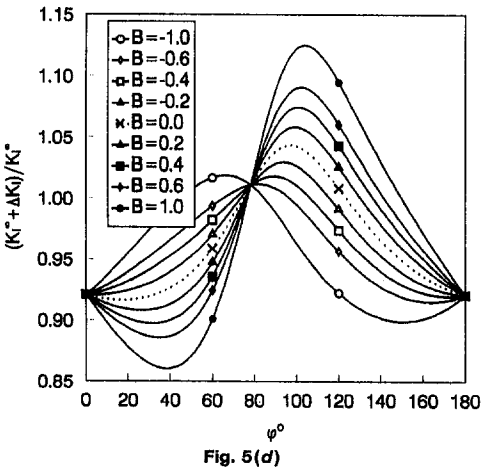

Fig. 5(d)

Fig. 5 The stress intensity factor of the macrocrack versus the microcrack orientation angle φ; (a) h/a = 1.1, (b) h/a = 1.3, (c) h/a = 1.5, (d) h/a = 2.0

($B < 0$) decreases the amplification effect or increases the shielding effect. Significant effect of the T-stress will occur for the large values of $|B|$. As shown in Fig. 9, the consistent relation (3) of the J-integral is still valid when considering the T-stress.

Summary

We have studied the effect of the T-stress in microcrack shielding problems by considering the interaction of the macrocrack with near-tip microcracks using a discrete model. The following summary can be made:

1 The T-stress has no effect on the results for the parallel microcrack cases; however, it plays an important role for the oriented microcrack cases, especially for large values of the T-stress and large distances of the microcrack center from the macrocrack tip.

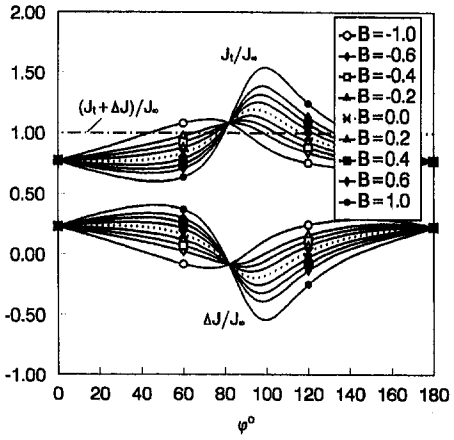

Fig. 6 The J-integrals versus the microcrack orientation angle φ for h/a = 1.5

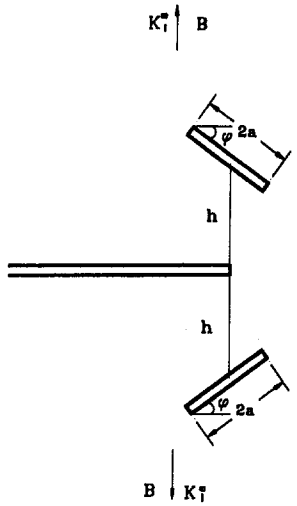

Fig. 7 A macrocrack interacting with two microcracks centered just above and below the macrocrack tip, respectively

Downloaded 04 May 2010 to 171.66.16.26. Redistribution subject to ASME license or copyright; see http://www.asme.org/terms/Terms_Use.cfm

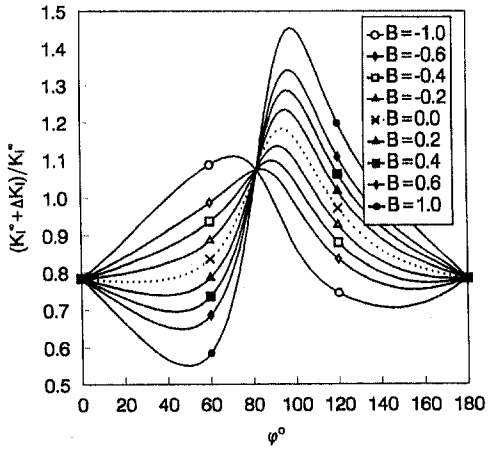

Fig. 8 The stress intensity factor of the macrocrack vs. the microcrack orientation angle φ for $h/a = 1.5$

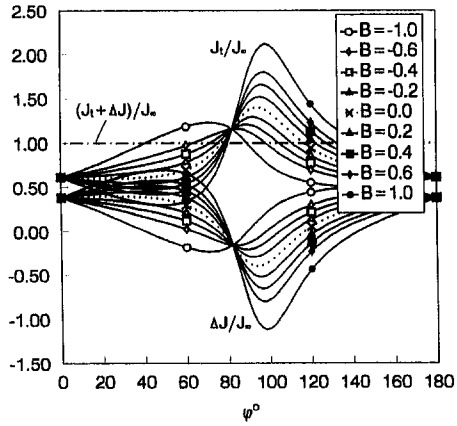

Fig. 9 The J-integrals versus the microcrack orientation angle φ for $h/a = 1.5$

2 In determining the shielding or amplification effect of the oriented microcracks, it is necessary to consider the effect of the T-stress. Effect of the T-stress on microcrack shielding or amplification effect is substantially dependent on the sign and magnitude of the T-stress as well as on the geometry of the microcrack arrangement.

3 Although the T-stress influences the contributions to the J-integral induced from the microcracks (ΔJ) and the macrocrack tip (J_t) when considering the T-stress, the consistent relation (3) of the J-integral is still valid.

Acknowledgment

This work was supported by the Chinese National Natural Science Foundation.

References

Betegon, C., and Hancock, J. W., 1991, "Two-Parameter Characterization of Elastic Plastic Crack-Tip Fields," ASME JOURNAL OF APPLIED MECHANICS, Vol. 58, pp. 104–110.

Bilby, B. A., Cardew, G. E., Goldthorpe, M. R., and Howard, I. C., 1986, "A Finite Element Investigation of the Effect of Specimen Geometry on the Fields of Stress and Strain at the Tips of Stationary Cracks," *Size Effects in Fracture,* Mechanical Engineering Publications, Ltd., London, pp. 37–46.

Cai, H., and Faber, K. T., 1992, "On the Use of Approximation Methods for Microcrack Shielding Problems," ASME JOURNAL OF APPLIED MECHANICS, Vol. 59, pp. 497–501.

Chen, Y. H., 1996, "On the Contribution of Discontinuities in a Near-Tip Stress Field to the J-Integral," *Int. J. Engng Sci.,* Vol. 34, pp. 819–829.

Chudnovsky, A., Dolgopolsky, A., and Kachanov, M., 1987, "Elastic Interaction of a Crack with a Microcrack Array," *Int. J. Solids Struct.,* Vol. 23, pp. 1–21.

Cotterell, B., and Rice, J. R., 1980, "Slightly Curved or Kinked Cracks," *Int. J. Fract.,* Vol. 16, pp. 155–169.

Evans, A. G., and Faber, K. T., 1981, "Toughening of Ceramics by Circumferential Microcracking," *J. Am. Ceram. Soc.,* Vol. 64, pp. 394–398.

Evans, A. G., and Faber, K. T., 1984, "Crack-Growth Resistance of Microcracking Brittle Materials," *J. Am. Ceram. Soc.,* Vol. 67, pp. 255–260.

Evans, A. G., and Fu, Y., 1985, "Some Effects of Microcracks on the Mechanical Properties of Brittle Materials—II. Microcrack Toughening," *Acta Metall.,* Vol. 33, pp. 1525–1530.

Fleck, N. A., Hutchinson, J. W., and Suo, Z., 1991, "Crack Path Selection in a Brittle Adhesive Layer," *Int. J. Solids Struct.,* Vol. 27, pp. 1683–1703.

Gong, S. X., and Horii, H., 1989, "General Solution to the Problem of Microcracks Near the Tip of a Main Crack," *J. Mech. Phys. Solids,* Vol. 37, pp. 27–46.

Hutchinson, J. W., 1987, "Crack Tip Shielding by Micro-Cracking in Brittle Solids," *Acta Metall.,* Vol. 35, pp. 1605–1619.

Kachanov, M., and Montagut, E., 1986, "Interaction of a Crack with Certain Microcrack Arrays," *Engng Fract. Mech.,* Vol. 25, pp. 625–636.

Larsson, S. G., and Carlsson, A. J., 1973, "Influence of Non-Singular Stress Terms and Specimen Geometry on Small-Scale Yielding at Crack Tips in Elastic-Plastic Materials," *J. Mech. Phys. Solids,* Vol. 21, pp. 263–277.

Leevers, P. S., and Radon, J. C., 1983, "Inherent Stress Biaxiality in Various Fracture Specimen Geometries," *Int. J. Fract.,* Vol. 19, pp. 311–325.

Ortiz, M., 1987, "A Continuum Theory of Crack Shielding in Ceramics," ASME JOURNAL OF APPLIED MECHANICS, Vol. 54, pp. 54–58.

Ortiz, M., and Giannakopoulos, A. E., 1989, "Maximal Crack Tip Shielding by Microcracking," ASME JOURNAL OF APPLIED MECHANICS, Vol. 56, pp. 279–283.

Rice, J. R., 1968, "A Path-Independent Integral and the Approximate Analysis of Strain Concentration by Notches and Cracks," ASME JOURNAL OF APPLIED MECHANICS, Vol. 35, pp. 379–386.

Rice, J. R., 1974, "Limitations to the Small Scale Yielding Approximation for Crack Tip Plasticity," *J. Mech. Phys. Solids,* Vol. 22, pp. 17–26.

Rose, L. R. F., 1986, "Microcrack Interaction with a Main Crack," *Int. J. Fract.,* Vol. 31, pp. 233–242.

Rubinstein, A. A., 1986, "Macrocrack-Microdefect Interaction," ASME JOURNAL OF APPLIED MECHANICS, Vol. 53, pp. 505–510.

Ruhle, M., Evans, A. G., McMeeking, R. M., Charalambides, P. G., and Hutchinson, J. W., 1987, "Microcrack Toughening in Alumina/Zirconia," *Acta Metall.,* Vol. 35, pp. 2701–2710.

Tvergaard, V., and Hutchinson, J. W., 1994, "Effect of T-Stress on Mode I Crack Growth Resistance in a Ductile Solid," *Int. J. Solids Struct.,* Vol. 31, pp. 823–833.

Williams, M. L., 1957, "On the Stress Distribution at the Base of a Stationary Crack," ASME JOURNAL OF APPLIED MECHANICS, Vol. 24, pp. 111–114.

Zhao, L. G., and Chen, Y. H., 1997, "On the Contribution of Subinterface Microcracks Near the Tip of an Interface Macrocrack to the J Integral in Bimaterial Solids," *Int. J. Engng Sci.,* Vol. 35, pp. 387–407.

Downloaded 04 May 2010 to 171.66.16.26. Redistribution subject to ASME license or copyright; see http://www.asme.org/terms/Terms_Use.cfm

Analysis of Conducting Rigid Inclusion at the Interface of Two Dissimilar Piezoelectric Materials

Wei Deng

S. A. Meguid
Mem. ASME.

Engineering Mechanics and Design Laboratory, Department of Mechanical and Industrial Engineering, University of Toronto, 5 King's College Road, Toronto, Ontario M5S 3G8 Canada

This paper is concerned with the electro-elastic analysis of a conducting rigid line inclusion at the interface of two bonded piezoelectric materials. By combining the analytic function theory and the Stroh formalism, we were able to obtain closed-form expressions for the field variables. Both the mechanical stresses and the electric displacement are shown to have at least one of the following behaviors: (i) traditional square root singularity; (ii) nonsquare root singularity; and (iii) oscillatory singularity, which depend upon the electro-elastic mismatch at the interface. By using the static equilibrium conditions, the rigid rotation vector of the inclusion is determined and the extended stress singularity factors (ESSF) are evaluated.

1 Introduction

Piezoelectric materials are widely used as sensors and actuators in the technologies of smart material. Significant progress has recently been made in the development of these materials as a result of the extensive research efforts of the scientific and industrial communities. The main difficulties with this class of materials, however, arise as a result of the presence of microdefects and inhomogeneities.

A number of contributions concerning the crack models in isotropic or transversely isotropic piezoelectric materials have appeared in the literature. Some important solutions have been derived by Parton (1976), Deeg (1980), McMeeking (1987), Pak (1990), Sosa and Pak (1990), Zhang and Tong (1996), Zhong and Meguid (1997), among others. Because of the anisotropic nature of piezoelectric materials and the coupling of an additional field variable in the governing equations, however, piezoelectric boundary value problems generally pose serious mathematical difficulty and thus require special treatments. By extending the six-dimensional Stroh formalism (Stroh, 1962) in anisotropic elasticity to an eight-dimensional formalism, Lothe and Barnett (1976) studied the surface waves in anisotropic piezoelectric crystals. With this powerful formalism, Kuo and Barnett (1991) and Suo et al. (1992) further studied the singularities of cracks in a homogeneous anisotropic piezoelectric material and those of interfacial cracks in bonded anisotropic piezoelectric media.

Efforts have also been made to develop inclusion models in a homogeneous piezoelectric material. Deeg (1980) theoretically addressed the problem of defects other than cracks; Wang (1992) and Chen (1993) analysed the inclusion problem in a piezoelectric matrix by means of Green's function and Fourier transformation techniques. Liang et al. (1995) and Chung and Ting (1996) developed a general solution for an infinite anisotropic piezoelectric medium with elliptic inclusion. More recently, Zhong and Meguid (1997) studied the partially debonded circular inhomogeneity problem in piezoelectric material under antiplane shear and in-plane electric field, while Meguid and Deng (1997) discussed the electro-elastic interaction between a screw dislocation and an elliptical inhomogeneity in piezoelectric media. In all of these papers, however, the inclusion is assumed to be embedded in a homogeneous piezoelectric matrix.

Although the significance of the interaction problems of various defects with the interface between two dissimilar piezoelectric media has been addressed and the corresponding crack problems have been solved by McMeeking (1987) and Suo et al. (1992), a number of problems, such as those of interfacial inclusions which result during electric packaging and manufacturing of intelligent composites, remain unsolved. These practical problems have motivated work in this important area of research (Sosa and Khutoryansky, 1996). In addition, the extended eight-dimensional Stroh formalism, compared with its six-dimensional counterpart, has a number of new and interesting properties, and thus needs further examination.

It is therefore the objective of this study to treat the problem of a conducting rigid line inclusion at the interface between two bonded half-infinite piezoelectric media. The inclusion can be used to model a flat conducting defect, such as a metal precipitate. By combining the Stroh formalism and analytic function theory used by Suo et al. (1992) and Asundi and Deng (1995), the full-field closed-form solutions and the formulations for calculating the extended stress singularity factors are obtained. In Section 2 some basic equations and the eight-dimensional Stroh formalism are outlined. The boundary value problem and related field expressions are given in Section 3. The field solutions and the singularities for all possible combinations of two bimaterial parameters representing the interfacial electro-elastic mismatch are discussed in details in Sections 4 and 5. As illustrations, two examples are given and some discussions are made in Section 6. Finally, the paper is concluded in Section 7.

2 Basic Equations and Extended Stroh Formalism

In a linear piezoelectric medium, the elastic and electric field equations can be written as

$$\sigma_{ij} = c_{ijkl}u_{k,l} + e_{lij}\phi_{,l}, \quad D_i = e_{ikl}u_{k,l} - \epsilon_{il}\phi_{,l} \tag{1}$$

$$\sigma_{ij,j} = 0, \quad D_{i,i} = 0, \quad E_i = -\phi_{,i} \tag{2}$$

Contributed by the Applied Mechanics Division of THE AMERICAN SOCIETY OF MECHANICAL ENGINEERS for publication in the ASME JOURNAL OF APPLIED MECHANICS.

Discussion on this paper should be addressed to the Technical Editor, Professor Lewis T. Wheeler, Department of Mechancial Engineering, University of Houston, Houston, TX 77204-4792, and will be accepted until four months after final publication of the paper itself in the ASME JOURNAL OF APPLIED MECHANICS.

Manuscript received by the ASME Applied Mechanics Division, Nov. 18, 1996; final revision, Sept. 3, 1997. Associate Technical Editor: M. Taya.

 Copyright © 1998 by ASME

Downloaded 04 May 2010 to 171.66.16.26. Redistribution subject to ASME license or copyright; see http://www.asme.org/terms/Terms_Use.cfm

where σ_{ij}, u_i, D_i, E_i, and ϕ are stress, displacement, electric displacement, electric fields and electric potential, respectively. c_{ijkl}, e_{ijk}, and ϵ_{ij} are the corresponding elastic, piezoelectric, and dielectric constants, which satisfy the following symmetry relations:

$$c_{ijkl} = c_{jikl} = c_{ijlk} = c_{klij}, \quad e_{ijk} = e_{ikj}, \quad \epsilon_{ij} = \epsilon_{ji}.$$

Following the method by Eshelby et al. (1953) in treating generalized anisotropic elastic media, in which the displacements and stresses depend only on x_1 and x_2, a general solution for (1) and (2) can be expressed as

$$u_k = a_k h(z), \quad \phi = u_4 = a_4 h(z), \quad k = 1, 2, 3 \tag{3}$$

where $z = x_1 + px_2$, $h(z)$ is a function of z, a_α ($\alpha = 1, 2, 3, 4$) and p are constants to be determined. By substituting (3) into (1) and (2), we obtain the homogeneous equations

$$\left.\begin{aligned} &[c_{i1k1} + p(c_{i1k2} + c_{i2k1}) + p^2 c_{i2k2}]a_k \\ &\quad + [e_{1i1} + p(e_{1i2} + e_{2i1}) + p^2 e_{2i2}]a_4 = 0 \\ &[e_{1k1} + p(e_{1k2} + e_{2k1}) + p^2 e_{2k2}]a_k \\ &\quad - [\epsilon_{11} + p(\epsilon_{12} + \epsilon_{21}) + p^2 \epsilon_{22}]a_4 = 0 \end{aligned}\right\} \tag{4a}$$

or

$$\{\mathbf{Q} + p(\mathbf{R} + \mathbf{R}^{\mathrm{T}}) + p^2\mathbf{T}\}\,\mathbf{a} = \mathbf{0} \tag{4b}$$

where $\mathbf{a} = (a_1, a_2, a_3, a_4)^T$, and $\mathbf{Q}$, $\mathbf{R}$ and $\mathbf{T}$ are 4×4 matrices defined as

$$\mathbf{Q} = \begin{bmatrix} c_{i1k1} & e_{1i1} \\ e^T_{1k1} & -\epsilon_{11} \end{bmatrix}, \quad \mathbf{R} = \begin{bmatrix} c_{i1k2} & e_{2i1} \\ e^T_{1k2} & -\epsilon_{12} \end{bmatrix},$$

$$\mathbf{T} = \begin{bmatrix} c_{i2k2} & e_{2i2} \\ e^T_{2k2} & -\epsilon_{22} \end{bmatrix}.$$

It is apparent from the symmetry relations that $\mathbf{Q}$ and $\mathbf{T}$ are both symmetric.

In order to obtain a nontrivial solution for (4b), it is required that

$$\|\mathbf{Q} + p(\mathbf{R} + \mathbf{R}^{\mathrm{T}}) + p^2\mathbf{T}\| = 0. \tag{5}$$

The left-hand side of Eq. (5) is an eighth-degree polynomial in p. Suo et al. (1992) showed that (5) has no real roots. Hence the eight eigenvalues form four conjugate pairs p_α and $\bar{p}_\alpha$ ($p_{\alpha+4} = \bar{p}_\alpha$, $\alpha = 1, 2, 3, 4$), where p_α ($\alpha = 1, 2, 3, 4$) is assumed to have positive imaginary part. Corresponding to each root, p_α or $\bar{p}_\alpha$, there is a complex eigenvector $\mathbf{a}_\alpha$ and $\bar{\mathbf{a}}_\alpha$ ($\mathbf{a}_{\alpha+4} = \bar{\mathbf{a}}_\alpha$, $\alpha = 1, 2, 3, 4$). With an auxiliary vector $\mathbf{b}$ introduced by Stroh (1962) defined as

$$\mathbf{b} = (\mathbf{R}^{\mathrm{T}} + p\mathbf{T})\mathbf{a} = -\frac{1}{p}(\mathbf{Q} + p\mathbf{R})\mathbf{a} \tag{6}$$

we obtain two 4×4 nonsingular material matrices $\mathbf{A}$ and $\mathbf{L}$, as follows:

$$\mathbf{A} = [\mathbf{a}_1, \mathbf{a}_2, \mathbf{a}_3, \mathbf{a}_4], \quad \mathbf{L} = [\mathbf{b}_1, \mathbf{b}_2, \mathbf{b}_3, \mathbf{b}_4]. \tag{7}$$

Applying a similar procedure to that of Ting (1986), one can construct the important relations between $\mathbf{A}$ and $\mathbf{L}$

$$\left.\begin{aligned} &\mathbf{A}^{\mathrm{T}}\mathbf{L} + \mathbf{L}^{\mathrm{T}}\mathbf{A} = \mathbf{I} = \bar{\mathbf{A}}^{\mathrm{T}}\bar{\mathbf{L}} + \bar{\mathbf{L}}^{\mathrm{T}}\bar{\mathbf{A}}, \\ &\mathbf{A}^{\mathrm{T}}\bar{\mathbf{L}} + \mathbf{L}^{\mathrm{T}}\bar{\mathbf{A}} = \mathbf{0} = \bar{\mathbf{L}}^{\mathrm{T}}\mathbf{A} + \bar{\mathbf{A}}^{\mathrm{T}}\mathbf{L} \\ &\mathbf{L}\mathbf{A}^{\mathrm{T}} + \overline{\mathbf{L}\mathbf{A}}^{\mathrm{T}} = \mathbf{I} = \mathbf{A}\mathbf{L}^{\mathrm{T}} + \overline{\mathbf{A}\mathbf{L}}^{\mathrm{T}}, \\ &\mathbf{A}\mathbf{A}^{\mathrm{T}} + \overline{\mathbf{A}\mathbf{A}}^{\mathrm{T}} = \mathbf{0} = \mathbf{L}\mathbf{L}^{\mathrm{T}} + \overline{\mathbf{L}\mathbf{L}}^{\mathrm{T}}. \end{aligned}\right\} \tag{8}$$

It can be readily seen from the above relations that $\mathbf{L}^{\mathrm{T}}\bar{\mathbf{A}}$ and $\mathbf{L}\mathbf{A}^{-1}$ are skew-Hermitian matrices, while $\mathbf{A}\mathbf{A}^{\mathrm{T}}$ and $\mathbf{L}\mathbf{L}^{\mathrm{T}}$ are purely imaginary matrices. Now let

$$\mathbf{A}\mathbf{A}^{\mathrm{T}} = -\tfrac{1}{2}i\mathbf{E}, \quad \mathbf{L}\mathbf{L}^{\mathrm{T}} = \tfrac{1}{2}i\mathbf{F}, \quad \mathbf{A}\mathbf{L}^{\mathrm{T}} = \tfrac{1}{2}(\mathbf{I} - i\mathbf{G}) \tag{9}$$

where $\mathbf{E}$ and $\mathbf{F}$ are 4×4 real symmetric non-singular matrices with three positive eigenvalues and one negative eigenvalue (Lothe and Barnett, 1976), $\mathbf{I}$ is a 4×4 unit matrix and $\mathbf{G}$ is a 4×4 matrix, then we have

$$\begin{aligned} \mathbf{A}\mathbf{L}^{-1} &= -(\mathbf{G} + i\mathbf{I})\mathbf{F}^{-1} = \mathbf{F}^{-1}(\mathbf{G}^{\mathrm{T}} - i\mathbf{I}), \\ \mathbf{L}\mathbf{A}^{-1} &= (\mathbf{G}^{\mathrm{T}} + i\mathbf{I})\mathbf{E}^{-1} = -\mathbf{E}^{-1}(\mathbf{G} - i\mathbf{I}). \end{aligned} \tag{10}$$

The general solution contains four analytic functions, each depending on its own complex variable. For convenience, Suo et al. (1992) introduced a function vector $\mathbf{h}(z)$ defined as

$$\mathbf{h}(z) = [h_1(z), h_2(z), h_3(z), h_4(z)]^T \tag{11}$$

where, for simplicity, each function component is considered as a function of one complex variable z instead of $z_\alpha = x_1 + p_\alpha x_2$. However, when calculating the αth component of the function, z should be replaced by z_α. With (7) and (11), the general forms of the extended displacements (mechanical displacement and electric potential) and the extended stresses (mechanical stresses and electric displacement) can be expressed as

$$\mathbf{u} = \{u_1, u_2, u_3, \phi\}^T = \mathbf{A}\mathbf{h}(z) + \bar{\mathbf{A}}\overline{\mathbf{h}(z)} \tag{12a}$$

$$\mathbf{t} = \{\sigma_{21}, \sigma_{22}, \sigma_{23}, D_2\}^T = \mathbf{L}\mathbf{h}'(z) + \bar{\mathbf{L}}\overline{\mathbf{h}'(z)} \tag{12b}$$

$$\mathbf{s} = \{\sigma_{11}, \sigma_{12}, \sigma_{13}, D_1\}^T = -\mathbf{L}\mathbf{P}\mathbf{h}'(z) - \overline{\mathbf{L}\mathbf{P}\mathbf{h}'(z)} \tag{12c}$$

where primes represent the derivative with respect to the variable of the associated function. $\mathbf{P}$ is a diagonal matrix

$$\mathbf{P} = \mathrm{diag}\,\{p_1, p_2, p_3, p_4\}^T. \tag{13}$$

Representation (12) is known as extended Stroh formalism.

3 Field Expressions and Boundary Conditions

Consider two bonded half-infinite piezoelectric materials which contain a conducting rigid line inclusion of length $2a$ at the interface subject to external mechanical and electric loads at infinity, as shown in Fig. 1. The solution consists of two parts: the homogeneous solution which excludes the inclusion, and the disturbed solution which includes the inclusion. In our problem, only the disturbed solution is associated with the singularities of the stresses and thus will be our main concern. For convenience, we shall attach the subscripts 1 and 2 to the upper

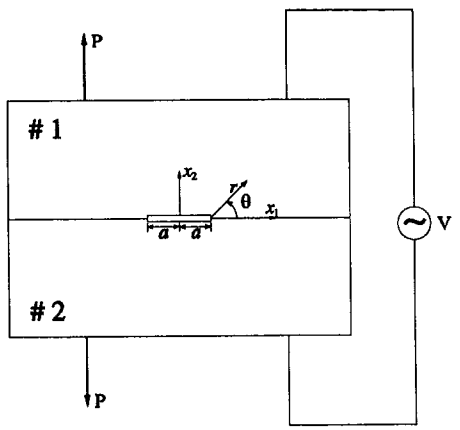

Fig. 1 A conducting rigid line inclusion on the interface between two bonded piezoelectric materials

Downloaded 04 May 2010 to 171.66.16.26. Redistribution subject to ASME license or copyright; see http://www.asme.org/terms/Terms_Use.cfm

and the lower half-planes of the piezoelectric bimaterial, respectively.

Note that a conductor is a equipotential body and thus when the conducting inclusion and the two piezoelectric materials are perfectly bonded, both the electric potential and mechanical displacements will be continuous across the entire interface. Assume now that the extended displacements for the homogeneous problem are specified and given by $\mathbf{u}_0(x_1)$ along the interface, then the extended displacements for the disturbed problem should satisfy (Asundi and Deng, 1995)

$$\mathbf{u}'(x_1) = \mathbf{q} - \mathbf{u}_0'(x_1) \quad |x_1| < a \tag{14}$$

with

$$\mathbf{q} = (0, q_2, 0, 0)^T \tag{15}$$

where q_2 is a quantity expressing the rigid rotation of the inclusion around x_3 and can be determined from the equilibrium conditions of the inclusion. The continuity of the extended displacement across the whole real axis requires from (12a) that

$$\mathbf{A}_1\mathbf{h}_1(x_1) + \bar{\mathbf{A}}_1\bar{\mathbf{h}}_1(x_1) = \mathbf{A}_2\mathbf{h}_2(x_1) + \bar{\mathbf{A}}_2\bar{\mathbf{h}}_2(x_1) \tag{16a}$$

or

$$\mathbf{A}_1\mathbf{h}_1'(x_1) - \bar{\mathbf{A}}_2\bar{\mathbf{h}}_2'(x_1) = \mathbf{A}_2\mathbf{h}_2'(x_1) - \bar{\mathbf{A}}_1\bar{\mathbf{h}}_1'(x_1). \tag{16b}$$

The two sides of (16b) represent the boundary values of two holomorphic functions in the respective two half-planes. Hence, both functions can be analytically extended into the entire plane. Noting that the extended stress components defined in (12b) and (12c) vanish at infinity, we have

$$\begin{cases} \mathbf{A}_1\mathbf{h}_1'(z) = \bar{\mathbf{A}}_2\bar{\mathbf{h}}_2'(z) & z \in 1 \\ \mathbf{A}_2\mathbf{h}_2'(z) = \bar{\mathbf{A}}_1\bar{\mathbf{h}}_1'(z) & z \in 2. \end{cases} \tag{17}$$

Substituting (17) into (12) yields

$$\begin{cases} \mathbf{u}'(x_1) = \mathbf{A}_1\mathbf{h}_1'(x_1) + \mathbf{A}_2\mathbf{h}_2'(x_1) \\ \mathbf{t}_1(x_1) = \mathbf{L}_1\mathbf{h}_1'(x_1) + \bar{\mathbf{L}}_1\bar{\mathbf{A}}_1^{-1}\mathbf{A}_2\mathbf{h}_2'(x_1) \\ \mathbf{t}_2(x_1) = \mathbf{L}_2\mathbf{h}_2'(x_1) + \bar{\mathbf{L}}_2\bar{\mathbf{A}}_2^{-1}\mathbf{A}_1\mathbf{h}_1'(x_1). \end{cases} \tag{18}$$

Let us define the traction jump as being

$$\Delta\mathbf{t}(x_1) = \mathbf{t}_1(x_1) - \mathbf{t}_2(x_1) = (\mathbf{W}' + i\mathbf{D}')\mathbf{A}_1\mathbf{h}_1'(x_1) + (\mathbf{W}' - i\mathbf{D}')\mathbf{A}_2\mathbf{h}_2'(x_1) \tag{19}$$

where $\mathbf{W}'$ and $\mathbf{D}'$ are 4×4 real bimaterial matrices given by

$$(\mathbf{W}' + i\mathbf{D}') = \mathbf{L}_1\mathbf{A}_1^{-1} - \bar{\mathbf{L}}_2\bar{\mathbf{A}}_2^{-1} = (\mathbf{G}_1^T\mathbf{E}_1^{-1} - \mathbf{G}_2^T\mathbf{E}_2^{-1}) + i(\mathbf{E}_1^{-1} + \mathbf{E}_2^{-1}). \tag{20}$$

Noting that the sum of two positive definite matrices is positive and that the 3×3 submatrix on the upper left corner of $\mathbf{D}'$ from (10) is positive, while $D_{44}' < 0$, one can show (Ting, 1996) that the three eigenvalues of $\mathbf{D}'$ are positive and nonzero. In addition, the fourth eigenvalue is negative and nonzero. Thus, $\mathbf{D}'$ is a nonsingular symmetric matrix. Furthermore, it is obvious from (10) that $\mathbf{W}'$ is a skew symmetric matrix which reflects the electro-elastic mismatch at the interface, and is thus called the mismatch matrix. Since there are no external tractions and electric charges at the bonded interface, then

$$\Delta\mathbf{t}(x_1) = \mathbf{0} \quad |x_1| > a. \tag{21}$$

Hence from (19) and (21), the function $\mathbf{A}_1\mathbf{h}_1'(z)$ and $\mathbf{A}_2\mathbf{h}_2'(z)$ can be analytically extended into the whole plane except on the inclusion in such a way that

$$(\mathbf{W}' + i\mathbf{D}')\mathbf{A}_1\mathbf{h}_1'(z) = -(\mathbf{W}' - i\mathbf{D}')\mathbf{A}_2\mathbf{h}_2'(z) \qquad z \neq x_1 \quad \text{when} \quad |x_1| \leq a. \tag{22}$$

Using (19) and (22), Eq. (18) can be written as

$$\mathbf{u}'(x_1) = \mathbf{A}_1\mathbf{h}_1'^{+}(x_1) - (\mathbf{W}' - i\mathbf{D}')^{-1}(\mathbf{W}' + i\mathbf{D}')\mathbf{A}_1\mathbf{h}_1'^{-}(x_1) \qquad |x_1| < a \tag{23a}$$

$$\mathbf{t}(x_1) = \mathbf{L}_1\mathbf{h}_1'(x_1) - \bar{\mathbf{L}}_1\bar{\mathbf{A}}_1^{-1}(\mathbf{W}' - i\mathbf{D}')^{-1} \times (\mathbf{W}' + i\mathbf{D}')\mathbf{A}_1\mathbf{h}_1'(x_1) \quad |x_1| > a \tag{23b}$$

$$\Delta\mathbf{t}(x_1) = (\mathbf{W}' + i\mathbf{D}')\mathbf{A}_1[\mathbf{h}_1'^{+}(x_1) - \mathbf{h}_1'^{-}(x_1)] \qquad |x_1| < a \tag{23c}$$

where the superscripts "+" and "−" denote the upper and lower surfaces of the inclusion, respectively.

The static and electric equilibrium equations of the inclusion are given by

$$\int_{-a}^{a} \Delta\mathbf{t}(x_1)dx_1 = 0, \quad \int_{-a}^{a} \Delta t_2(x_1)x_1 dx_1 = 0 \tag{24}$$

where $\Delta t_2(x_1) = \sigma_{22}^{+}(x_1) - \sigma_{22}^{-}(x_1)$ is the second component of $\Delta\mathbf{t}(x_1)$. In the following, the boundary value problem for various kinds of singularity fields will be treated separately.

4 Field Solutions With Vanishing Mismatch Matrix W'

In this section, we will consider a special case when a piezoelectric bimaterial has sufficient symmetry such that $\mathbf{G}_1^T\mathbf{E}_1^{-1} = \mathbf{G}_2^T\mathbf{E}_2^{-1}$. Accordingly, the skew symmetric mismatch matrix $\mathbf{W}'$ vanishes. In this case, we have from (14) and (23a) the nonhomogeneous Hilbert problem

$$\mathbf{A}_1\mathbf{h}_1'^{+}(x_1) + \mathbf{A}_1\mathbf{h}_1'^{-}(x_1) = \mathbf{q} - \mathbf{u}_0'(x_1) \quad |x_1| < a. \tag{25}$$

The above equation, which includes four unknown functions, can be decoupled by simply premultiplying the two sides by $\mathbf{A}_1^{-1}$. The solution can thus be easily obtained from the analytic function method of Muskhelishvili (1975) as

$$\mathbf{A}_1\mathbf{h}_1'(z) = \frac{1}{2\pi i}\int_{-a}^{a} \mathbf{A}_1\left\langle \frac{\chi_0(z)}{\chi_0^{+}(\xi)(\xi - z)}\right\rangle \mathbf{A}_1^{-1}[\mathbf{q} - \mathbf{u}_0'(\xi)]d\xi \tag{26}$$

where the bracket $\langle \ldots \rangle$ indicates that

$$\langle\varphi(z)\rangle = \text{diag}\,[\varphi(z_1), \varphi(z_2), \varphi(z_3), \varphi(z_4)]$$

and $\chi_0(z)$ is a function of z given by

$$\chi_0(z) = (z - a)^{-(1/2)}(z + a)^{-(1/2)} \tag{27}$$

with the branch cut being chosen along the inclusion.

Following a similar procedure to that adopted by Asundi and Deng (1995), the non-trivial component of the rigid rotation $\mathbf{q}$ in (15) can be determined by

$$q_2 = \frac{2}{i\pi a^2 D_{22}'}\int_{-a}^{a} \frac{[\mathbf{D}'\mathbf{u}_0'(\xi)]_2}{\chi_0^{+}(\xi)}\,d\xi \tag{28}$$

In obtaining (26) and (28), use was made of the equilibrium condition (24). The extended displacements and stresses can then be derived by inserting (26) into (12) with $\mathbf{q}$ being given

Downloaded 04 May 2010 to 171.66.16.26. Redistribution subject to ASME license or copyright; see http://www.asme.org/terms/Terms_Use.cfm

by (28). At the bonded part of the interface, the extended stresses are

$$\mathbf{t}(x_1) = \pm \frac{\mathbf{G}_1^T\mathbf{E}_1^{-1}}{\pi(x_1^2 - a^2)^{1/2}} \int_{-a}^{a} \frac{(a^2 - \xi^2)^{1/2}}{\xi - x_1} [\mathbf{q} - \mathbf{u}_0'(\xi)] d\xi \qquad |x_1| > a \quad (29)$$

where the plus sign is for $x_1 > a$ and the minus sign is for $x_1 < -a$.

At the ends of the line inclusion, both the stresses and electric displacements show square root singularities. The degree of that singularity can be described by four real constants, known as extended stress singularity factors (ESSF) K_{I}, K_{II}, K_{III}, and K_{IV}. At the right end of the inclusion, the four factors are evaluated by

$$\mathbf{K} = (K_{\mathrm{II}}, K_{\mathrm{I}}, K_{\mathrm{III}}, K_{\mathrm{IV}})^T = \lim_{x_1 \to a^+} \{[2\pi(x_1 - a)]^{1/2}\mathbf{t}(x_1)\}$$

$$= -\frac{\mathbf{G}_1^T\mathbf{E}_1^{-1}}{\sqrt{\pi a}} \int_{-a}^{a} \sqrt{\frac{a + \xi}{a - \xi}} [\mathbf{q} - \mathbf{u}_0'(\xi)] d\xi. \quad (30)$$

With (30), the extended traction at the interface a distance r ahead of the crack tip can be given by

$$\mathbf{t}(r) = (2\pi r)^{-1/2}\mathbf{K}. \quad (31)$$

It should be pointed out that all the results in this section apply to the corresponding problem of a conducting rigid line inclusion in a homogeneous piezoelectric material, which is a special case of $\mathbf{W}' = \mathbf{0}$.

5 Field Solutions With Nonvanishing Mismatch Matrix W'

In this section, we will discuss the field solutions for the general case when $\mathbf{W}'$ exists. In this case, we have from (14) and (23a) that

$$\mathbf{A}_1\mathbf{h}_1'^{+}(x_1) - (\mathbf{W}' - i\mathbf{D}')^{-1}(\mathbf{W}' + i\mathbf{D}')\mathbf{A}_1\mathbf{h}_1'^{-}(x_1) = \mathbf{q} - \mathbf{u}_0'(x_1) \quad |x_1| < a. \quad (32)$$

Equation (32) is a coupled nonhomogeneous Hilbert problem. The corresponding homogeneous equation is

$$(\mathbf{W}' - i\mathbf{D}')\mathbf{A}_1\mathbf{h}_1'^{+}(x_1) - (\mathbf{W}' + i\mathbf{D}')\mathbf{A}_1\mathbf{h}_1'^{-}(x_1) = \mathbf{0} \qquad |x_1| < a. \quad (33)$$

A solution of (33) allowing for singularities leads to

$$\mathbf{h}_1'(z) = (z - a)^{\delta}(z + a)^{-\delta-1}\mathbf{A}_1^{-1}\mathbf{k} \qquad (-1 < \mathrm{Re}\delta < 1) \quad (34)$$

where the branch cut is along the inclusion. Substitution of (34) into (33) yields the following characteristic equation

$$(\mathbf{W}' + i\lambda\mathbf{D}')\mathbf{k} = \mathbf{0}, \quad \|\mathbf{W}' + i\lambda\mathbf{D}'\| = 0 \quad (35)$$

in which

$$\lambda = \frac{1 + e^{2\pi\delta i}}{1 - e^{2\pi\delta i}} = -\tanh(\pi\delta i + \pi\delta/2). \quad (36)$$

The four eigenvalues of (35) can be obtained in a manner similar to that adopted by Kuo and Barnett (1991) such that

$$\lambda_{1,2} = \pm\beta_1, \quad \lambda_{3,4} = \pm i\beta_2 \quad (37)$$

where the bimaterial parameters β_1 and β_2 are non-negative real numbers given by

$$\left.\begin{aligned} \beta_1 &= \tfrac{1}{2}\sqrt{2\sqrt{I_2^2 - 4I_4} + 2I_2}, \quad \beta_2 = \tfrac{1}{2}\sqrt{2\sqrt{I_2^2 - 4I_4} - 2I_2} \\ I_2 &= -\tfrac{1}{2}\,\mathrm{tr}(\mathbf{W}'\mathbf{D}'^{-1})^2, \qquad I_4 = \|\mathbf{W}'\mathbf{D}'^{-1}\| \le 0 \end{aligned}\right\}. \quad (38)$$

From (38) we see that the parameters β_1 and β_2 depend on the mismatch matrix $\mathbf{W}'$ and can thus be called mismatch parameters. It follows from (36) and (37) that

$$\delta_{1,2} = -\tfrac{1}{2} \pm i\epsilon, \quad \text{and} \quad \delta_{3,4} = -\tfrac{1}{2} \pm \kappa \quad (39)$$

where

$$\epsilon = \frac{1}{2\pi}\ln\frac{1 + \beta_1}{1 - \beta_1}, \quad \text{and} \quad \kappa = \frac{1}{\pi}\tan^{-1}\beta_2. \quad (40)$$

In general, there are four linearly independent eigenvectors $\mathbf{k}_j$ ($j = 1, 2, 3, 4$). In the case of repeated eigenvalues, however, the number of the eigenvectors may be less than four. Without loss of generality, the general solution for (33) can be written as

$$\mathbf{h}_1'(z) = K_1\chi_1(z)\mathbf{A}_1^{-1}\mathbf{k}_1 + K_2\chi_2(z)\mathbf{A}_1^{-1}\mathbf{k}_2 + K_3\chi_3(z)\mathbf{A}_1^{-1}\mathbf{k}_3 + K_4\chi_4(z)\mathbf{A}_1^{-1}\mathbf{k}_4 \quad (41)$$

where K_j ($j = 1, 2, 3, 4$) are complex or real constants, and $\chi_j(z)$ ($j = 1, 2, 3, 4$) are given as

$$\left.\begin{aligned} \chi_1(z) = \bar{\chi}_2(z) &= (z - a)^{-1/2+i\epsilon}(z + a)^{-1/2-i\epsilon} \\ \chi_3(z) &= (z - a)^{-1/2-\kappa}(z + a)^{-1/2+\kappa} \\ \chi_4(z) &= (z - a)^{-1/2+\kappa}(z + a)^{-1/2-\kappa} \end{aligned}\right\} \quad (42)$$

With (23b) and (41), the asymptotic extended traction is

$$\mathbf{t}(x_1) = 2\,\mathrm{Re}\{K_1\chi_1(x_1)\mathbf{L}_1\mathbf{A}_1^{-1}\mathbf{k}_1 + K_2\chi_2(x_1)\mathbf{L}_1\mathbf{A}_1^{-1}\mathbf{k}_2 + K_3\chi_3(x_1)\mathbf{L}_1\mathbf{A}_1^{-1}\mathbf{k}_3 + K_4\chi_4(x_1)\mathbf{L}_1\mathbf{A}_1^{-1}\mathbf{k}_4\}. \quad (43)$$

It can be easily found from (41)–(43) that the singularity behavior of $\mathbf{h}_1'(z)$ and the extended stresses depends on the two mismatch parameters β_1 and β_2 (or ϵ and κ). When β_1 (or β_2) does not vanish, the extended stresses have the oscillatory (or nonsquare root) singularities. Only when both β_1 and β_2 vanish simultaneously, the extended stresses show traditional square root singularities. The degrees of these singularities are described by the constants K_j ($j = 1, 2, 3, 4$). In this sense, K_j can also be called "extended stress singularity factors," as mentioned in Section 4.

In the remainder of this section, the solutions for various combinations of the mismatch parameters β_1 and β_2, which correspond to different singular behaviors, will be given. The orthogonal relations among the eigenvectors used in this section can be found in Appendix A.

5.1 Case 1: Nonvanishing Mismatch Parameters β_1 and β_2 ($I_4 \neq 0$). Generally, both β_1 and β_2 exist, the solution for the nonhomogeneous Hilbert problem (32) can be expressed as

$$\mathbf{A}_1\mathbf{h}_1'(z) = \mathbf{A}_1 < \eta_1(z) > \mathbf{A}_1^{-1}\mathbf{k}_1 + \mathbf{A}_1 < \eta_2(z) > \mathbf{A}_1^{-1}\bar{\mathbf{k}}_1 + \mathbf{A}_1 < \eta_3(z) > \mathbf{A}_1^{-1}\mathbf{k}_3 + \mathbf{A}_1 < \eta_4(z) > \mathbf{A}_1^{-1}\mathbf{k}_4 \quad (44)$$

where $\eta_j(z)$ ($j = 1, 2, 3, 4$) are functions of z to be determined. $\mathbf{k}_1$ is a complex eigenvector while $\mathbf{k}_3$ and $\mathbf{k}_4$ are real eigenvectors. They satisfy the orthogonal relation (A9). It follows from (44) that

$$\mathbf{A}_1\mathbf{h}_1'(x_1) = \mathbf{K}_M\boldsymbol{\eta}(x_1) \quad (45)$$

Downloaded 04 May 2010 to 171.66.16.26. Redistribution subject to ASME license or copyright; see http://www.asme.org/terms/Terms_Use.cfm

where the 4×4 nonsingular matrix $\mathbf{K_M}$ has been defined in $(A.10)_1$ and $\eta(x_1)$ is a function vector, such that

$$\boldsymbol{\eta}(x_1) = [\eta_1(x_1), \eta_2(x_1), \eta_3(x_1), \eta_4(x_1)]^T. \quad (46)$$

By putting (45) into (32), one obtains

$$\mathbf{K_M}\boldsymbol{\eta}^+(x_1) - (\mathbf{W}' - i\mathbf{D}')^{-1}(\mathbf{W}' + i\mathbf{D}')\mathbf{K_M}\boldsymbol{\eta}^-(x_1) = \mathbf{q} - \mathbf{u}_0'(x_1) \quad |x_1| < a. \quad (47)$$

Noting that

$$(\mathbf{W}' - i\mathbf{D}')^{-1}(\mathbf{W}' + i\mathbf{D}')\mathbf{K_M} = -\mathbf{K_M}\,\mathrm{diag}\left(\frac{1-\beta_1}{1+\beta_1}, \frac{1+\beta_1}{1-\beta_1}, \frac{1-i\beta_2}{1+i\beta_2}, \frac{1+i\beta_2}{1-i\beta_2}\right) \quad (48)$$

and premultiplying the two sides of (47) by $\mathbf{K_M^{-T}}$, we get

$$\eta_j^+(x_1) - \gamma_j\eta_j^-(x_1) = v_j(x_1) \quad (j = 1, 2, 3, 4) \quad |x_1| < a \quad (49)$$

where

$$\gamma_1 = -e^{-2\pi\epsilon}, \quad \gamma_2 = -e^{2\pi\epsilon}, \quad \gamma_3 = -e^{-2\pi\kappa i}, \quad \gamma_4 = -e^{2\pi\kappa i}$$

$$\nu_1(x_1) = \bar{\mathbf{k}}_1^{\mathrm{T}}\mathbf{D}'[\mathbf{q} - \mathbf{u}_0'(x_1)]/e_1,$$

$$\nu_2(x_1) = \mathbf{k}_1^{\mathrm{T}}\mathbf{D}'[\mathbf{q} - \mathbf{u}_0'(x_1)]/e_1$$

$$\nu_3(x_1) = \mathbf{k}_4^{\mathrm{T}}\mathbf{D}'[\mathbf{q} - \mathbf{u}_0'(x_1)]/e_2,$$

$$\nu_4(x_1) = \mathbf{k}_3^{\mathrm{T}}\mathbf{D}'[\mathbf{q} - \mathbf{u}_0'(x_1)]/e_2 \quad (50)$$

in which e_1 and e_2 are given in (A12). Equation (49) contains four decoupled nonhomogeneous Hilbert problems, the solution of which are (Muskhelishvili, 1975)

$$\eta_j(z) = \frac{\chi_j(z)}{2\pi i}\int_{-a}^{a}\frac{\nu_j(\xi)d\xi}{\chi_j^+(\xi)(\xi - z)} \quad (j = 1, 2, 3, 4)$$

$$q_2 = \frac{1}{\Lambda_{22}}\int_{-a}^{a}\left\{(\mathbf{W}' + i\mathbf{D}')\mathbf{K_M}\,\mathrm{diag}\left(\frac{1}{\chi_1^+(x_1)}, \frac{1}{\chi_2^+(x_1)}, \frac{1}{\chi_3^+(x_1)}, \frac{1}{\chi_4^+(x_1)}\right)\mathbf{K_M^{-1}}\mathbf{u}_0'(x_1)\right\}_2 dx_1 \quad (51)$$

where $\chi_j(z)$ $(j = 1, 2, 3, 4)$ has been defined in (42), Λ_{22} is an element of the following matrix

$$\boldsymbol{\Lambda} = i\pi a^2(\mathbf{W}' + i\mathbf{D}')\mathbf{K_M}\,\mathrm{diag}\left(\frac{(1+4\epsilon^2)e^{\pi\epsilon}}{2\cosh\pi\epsilon}, \frac{(1+4\epsilon^2)e^{-\pi\epsilon}}{2\cosh\pi\epsilon}, \frac{(1-4\kappa^2)e^{\pi\kappa i}}{2\cos\pi\kappa}, \frac{(1-4\kappa^2)e^{-\pi\kappa i}}{2\cos\pi\kappa}\right)\mathbf{K_M^{-1}}. \quad (52)$$

In obtaining (51), we have made use of the equilibrium conditions (24) and the following relations:

$$\frac{1}{2\pi i}\int_{-a}^{a}\frac{\chi_j^+(x_1)}{x_1 - \xi}dx_1 = \frac{\gamma_j + 1}{2(\gamma_j - 1)}\chi_j^+(\xi) \quad (j = 1, 2, 3, 4) \quad |\xi| < a$$

$$\int_{-a}^{a}x_1[\eta_j^+(x_1) - \eta_j^-(x_1)]dx_1 = \int_{-a}^{a}\frac{v_j(x_1)}{\chi_j^+(x_1)}dx_1 \quad (j = 1, 2, 3, 4)$$

$$\int_{-a}^{a}\frac{dx_1}{\chi_j^+(x_1)} = \begin{cases} i\pi a^2(1+4\epsilon^2)e^{\pi\epsilon}/2\cosh\pi\epsilon & j = 1 \\ i\pi a^2(1+4\epsilon^2)e^{-\pi\epsilon}/2\cosh\pi\epsilon & j = 2 \\ i\pi a^2(1-4\kappa^2)e^{\pi\kappa i}/2\cos\pi\kappa & j = 3 \\ i\pi a^2(1-4\kappa^2)e^{-\pi\kappa i}/2\cos\pi\kappa & j = 4. \end{cases} \quad (53)$$

Substituting of (51) into (44) gives the solution of the field potential from which the extended displacement and stress components in (12) can be obtained. Among these components is the traction $\mathbf{t}(x_1)$ on the bonded surface. It follows from $(12b)$ and (45) that

$$\mathbf{t}(x_1) = 2\,\mathrm{Re}\{\eta_1(x_1)\mathbf{L_1}\mathbf{A_1^{-1}}\mathbf{k}_1 + \eta_2(x_1)\mathbf{L_1}\mathbf{A_1^{-1}}\bar{\mathbf{k}}_1 + \eta_3(x_1)\mathbf{L_1}\mathbf{A_1^{-1}}\mathbf{k}_3 + \eta_4(x_1)\mathbf{L_1}\mathbf{A_1^{-1}}\mathbf{k}_4\} \quad |x_1| > a \quad (54)$$

It is apparent from (54) and (51) that the stresses have both oscillatory singularities and nonsquare root singularities. The extended stress singularity factors (ESSF) K_j $(j = 1, 2, 3, 4)$ in the asymptotic field (43) can now be determined by comparing (43) with (54). For the right end of the inclusion, it is readily found that

$$K_j = \lim_{x_1 \to a^+}\frac{\eta_j(x_1)}{\chi_j(x_1)} = \frac{1}{2\pi i}\int_{-a}^{a}\frac{\nu_j(\xi)d\xi}{\chi_j^+(\xi)(\xi - a)} \quad (j = 1, 2, 3, 4) \quad (55a)$$

or

$$\begin{cases} K_1 = -\dfrac{e^{\pi\epsilon}}{2\pi e_1}\displaystyle\int_{-a}^{a}\left(\frac{a+\xi}{a-\xi}\right)^{1/2+i\epsilon}\bar{\mathbf{k}}_1^{\mathrm{T}}\mathbf{D}'[\mathbf{q} - \mathbf{u}_0'(\xi)]d\xi \\ K_2 = -\dfrac{e^{-\pi\epsilon}}{2\pi e_1}\displaystyle\int_{-a}^{a}\left(\frac{a+\xi}{a-\xi}\right)^{1/2-i\epsilon}\mathbf{k}_1^{\mathrm{T}}\mathbf{D}'[\mathbf{q} - \mathbf{u}_0'(\xi)]d\xi \\ K_3 = -\dfrac{e^{\pi\kappa i}}{2\pi e_2}\displaystyle\int_{-a}^{a}\left(\frac{a+\xi}{a-\xi}\right)^{1/2-\kappa}\mathbf{k}_4^{\mathrm{T}}\mathbf{D}'[\mathbf{q} - \mathbf{u}_0'(\xi)]d\xi \\ K_4 = -\dfrac{e^{-\pi\kappa i}}{2\pi e_2}\displaystyle\int_{-a}^{a}\left(\frac{a+\xi}{a-\xi}\right)^{1/2+\kappa}\mathbf{k}_3^{\mathrm{T}}\mathbf{D}'[\mathbf{q} - \mathbf{u}_0'(\xi)]d\xi. \end{cases} \quad (55b)$$

The factors K_j $(j = 1, 2, 3, 4)$ for the left end can be obtained by replacing ξ in $(55a)$ or $(55b)$ by $-\xi$. When $\mathbf{u}_0'(x_1)$ is an even vector function of x_1, the coefficients for the two ends are identical.

5.2 Case 2: Vanishing Mismatch Parameters β_1 and β_2 ($I_2 = I_4 = 0$). For this combination, the rank r of the matrix $\mathbf{W}'$ satisfies $2 \le r \le 3$ (See, Appendix A). Thus, there are at most two linearly independent eigenvectors, say $\mathbf{k}_1$ and $\mathbf{k}_2$, for (35). The general solution for (32) is

$$\mathbf{A_1}\mathbf{h}_1'(z) = \mathbf{A_1} < \eta_1(z) > \mathbf{A_1^{-1}}\mathbf{k}_1 + \mathbf{A_1} < \eta_2(z) > \mathbf{A_1^{-1}}\mathbf{k}_2 \quad (56)$$

where $\eta_j(z)$ $(j = 1, 2)$ are functions of z which are to be determined. Along the real axis, the field potential becomes

$$\mathbf{A_1}\mathbf{h}_1'(x_1) = \mathbf{K_M}\boldsymbol{\eta}(x_1) \quad (57)$$

where $\mathbf{K_M}$ is a matrix defined in (A15a) or (A15b), and

$$\boldsymbol{\eta}(x_1) = [\eta_1(x_1), \eta_2(x_1)]^T. \quad (58)$$

Substituting (57) into (32) and making use of (A16), we have

$$\boldsymbol{\eta}^+(x_1) + \boldsymbol{\eta}^-(x_1) = \mathbf{C}^{-1}\mathbf{K_M^T}\mathbf{D}'[\mathbf{q} - \mathbf{u}_0'(x_1)] \quad |x_1| < a \quad (59)$$

Downloaded 04 May 2010 to 171.66.16.26. Redistribution subject to ASME license or copyright; see http://www.asme.org/terms/Terms_Use.cfm

where $\mathbf{C}$ is a nonsingular matrix defined by

$$\mathbf{C} = \mathbf{K}_M^T \mathbf{D}' \mathbf{K}_M. \tag{60}$$

The solution of (59) is

$$\boldsymbol{\eta}(z) = \begin{Bmatrix} \eta_1(z) \\ \eta_2(z) \end{Bmatrix} = \frac{\chi_0(z)}{2\pi i} \int_{-a}^{a} \frac{\mathbf{C}^{-1}\mathbf{K}_M^T \mathbf{D}' [\mathbf{q} - \mathbf{u}_0'(\xi)] d\xi}{\chi_j^+(\xi)(\xi - z)} \tag{61}$$

$$q_2 = \frac{1}{\Lambda_{22}} \left\{ \mathbf{D}' \mathbf{K}_M \mathbf{C}^{-1} \mathbf{K}_M^T \mathbf{D}' \int_{-a}^{a} \frac{\mathbf{u}_0'(\xi)}{\chi_j^+(\xi)} d\xi \right\}_2 \tag{62}$$

with

$$\boldsymbol{\Lambda} = \frac{i\pi a^2}{2} \mathbf{D}' \mathbf{K}_M \mathbf{C}^{-1} \mathbf{K}_M^T \mathbf{D}'. \tag{63}$$

Further, we have on the bonded interface

$$\mathbf{t}(x_1) = 2\,\mathrm{Re}\{\, \eta_1(x_1)\mathbf{L}_1\mathbf{A}_1^{-1}\mathbf{k}_1 + \eta_2(x_1)\mathbf{L}_1\mathbf{A}_1^{-1}\mathbf{k}_2 \,\} \qquad |x_1| < a \tag{64}$$

and the ESSF are given as

$$\begin{Bmatrix} K_1 \\ K_2 \end{Bmatrix} = -\frac{1}{2\pi} \int_{-a}^{a} \left(\frac{a+\xi}{a-\xi} \right)^{1/2} \mathbf{C}^{-1}\mathbf{K}_M^T \mathbf{D}' [\mathbf{q} - \mathbf{u}_0'(\xi)] d\xi. \tag{65}$$

From (64) and (61) we know that the stress fields exhibit the traditional square root singularities.

5.3 Case 3: Vanishing Mismatch Parameter β_1 and Nonvanishing Mismatch Parameter β_2($I_2 < 0$, $I_4 = 0$). In this case, the general solution for (32) is

$$\mathbf{A}_1\mathbf{h}_1'(z) = \mathbf{A}_1 < \eta_1(z) > \mathbf{A}_1^{-1}\mathbf{k}_1 + \mathbf{A}_1 < \eta_2(z) > \mathbf{A}_1^{-1}\mathbf{k}_2 + \mathbf{A}_1 < \eta_3(z) > \mathbf{A}_1^{-1}\mathbf{k}_3 + \mathbf{A}_1 < \eta_4(z) > \mathbf{A}_1^{-1}\mathbf{k}_4 \tag{66}$$

where the four real eigenvectors satisfy the orthogonal relations (A18) and form two nonsingular matrices $\mathbf{K}_M$ and $\mathbf{K}_N$ defined in (A19). Following a similar procedure to that adopted in Section 5.1 and using (48), we obtain the following uncoupled Hilbert problem:

$$\eta_j^+(x_1) - \gamma_j \eta_j^-(x_1) = v_j(x_1) \quad (j = 1, 2, 3, 4) \quad |x_1| < a \tag{67}$$

where

$$\gamma_1 = -1, \quad \gamma_2 = -1, \quad \gamma_3 = -e^{-2\pi\kappa i}, \quad \gamma_4 = -e^{2\pi\kappa i}$$

$$\nu_1(x_1) = \mathbf{k}_1^T \mathbf{D}' [\mathbf{q} - \mathbf{u}_0'(x_1)]/e_1,$$

$$\nu_2(x_1) = \mathbf{k}_2^T \mathbf{D}' [\mathbf{q} - \mathbf{u}_0'(x_1)]/e_2$$

$$\nu_3(x_1) = \mathbf{k}_4^T \mathbf{D}' [\mathbf{q} - \mathbf{u}_0'(x_1)]/e_3,$$

$$\nu_4(x_1) = \mathbf{k}_3^T \mathbf{D}' [\mathbf{q} - \mathbf{u}_0'(x_1)]/e_3 \tag{68}$$

with e_1 and e_2 being given in (A21).

The solution for (67) can be given by (51), except that ϵ should be set to zero in the related expressions. Furthermore, the ESSF for the right end of the inclusion can be calculated as

$$\begin{cases} K_1 = -\dfrac{1}{2\pi e_1} \displaystyle\int_{-a}^{a} \left(\frac{a+\xi}{a-\xi} \right)^{1/2} \mathbf{k}_1^T \mathbf{D}' [\mathbf{q} - \mathbf{u}_0'(\xi)] d\xi \\ K_2 = -\dfrac{1}{2\pi e_2} \displaystyle\int_{-a}^{a} \left(\frac{a+\xi}{a-\xi} \right)^{1/2} \mathbf{k}_2^T \mathbf{D}' [\mathbf{q} - \mathbf{u}_0'(\xi)] d\xi \\ K_3 = -\dfrac{e^{\pi\kappa i}}{2\pi e_3} \displaystyle\int_{-a}^{a} \left(\frac{a+\xi}{a-\xi} \right)^{1/2-\kappa} \mathbf{k}_4^T \mathbf{D}' [\mathbf{q} - \mathbf{u}_0'(\xi)] d\xi \\ K_4 = -\dfrac{e^{-\pi\kappa i}}{2\pi e_3} \displaystyle\int_{-a}^{a} \left(\frac{a+\xi}{a-\xi} \right)^{1/2+\kappa} \mathbf{k}_3^T \mathbf{D}' [\mathbf{q} - \mathbf{u}_0'(\xi)] d\xi. \end{cases} \tag{69}$$

It is easily seen from (51) that the extended stresses have both the square root and nonsquare root singularities when $\epsilon = 0$.

5.4 Case 4: Nonvanishing Mismatch Parameter β_1 and Vanishing Mismatch Parameter β_2($I_2 > 0$, $I_4 = 0$). The general solution for field potential (32) is

$$\mathbf{A}_1\mathbf{h}_1'(z) = \mathbf{A}_1 < \eta_1(z) > \mathbf{A}_1^{-1}\mathbf{k}_1 + \mathbf{A}_1 < \eta_2(z) > \mathbf{A}_1^{-1}\bar{\mathbf{k}}_1 + \mathbf{A}_1 < \eta_3(z) > \mathbf{A}_1^{-1}\mathbf{k}_3 + \mathbf{A}_1 < \eta_4(z) > \mathbf{A}_1^{-1}\mathbf{k}_4 \tag{70}$$

where $\mathbf{k}_1$ is a complex eigenvector while $\mathbf{k}_3$ and $\mathbf{k}_4$ are real eigenvectors. These eigenvectors should satisfy the orthogonal relations (A23). By substituting (70) into (32) and making use of (48), we have

$$\eta_j^+(x_1) - \gamma_j \eta_j^-(x_1) = v_j(x_1) \quad (j = 1, 2, 3, 4) \quad |x_1| < a \tag{71}$$

where

$$\gamma_1 = -e^{-2\pi\epsilon}, \quad \gamma_2 = -e^{2\pi\epsilon}, \quad \gamma_3 = -1, \quad \gamma_4 = -1$$

$$\nu_1(x_1) = \bar{\mathbf{k}}_1^T \mathbf{D}' [\mathbf{q} - \mathbf{u}_0'(x_1)]/e_1,$$

$$\nu_2(x_1) = \mathbf{k}_1^T \mathbf{D}' [\mathbf{q} - \mathbf{u}_0'(x_1)]/e_1$$

$$\nu_3(x_1) = \mathbf{k}_3^T \mathbf{D}' [\mathbf{q} - \mathbf{u}_0'(x_1)]/e_2,$$

$$\nu_4(x_1) = \mathbf{k}_4^T \mathbf{D}' [\mathbf{q} - \mathbf{u}_0'(x_1)]/e_3 \tag{72}$$

with e_1, e_2, and e_3 being given in (A26). The solution for (71) can still be given by (51), except that κ should be set to zero in the corresponding expressions.

The extended stress fields have both oscillatory singularities and square root singularities and the ESSF for the right end of the inclusion can be calculated by

$$\begin{cases} K_1 = -\dfrac{e^{\pi\epsilon}}{2\pi e_1} \displaystyle\int_{-a}^{a} \left(\frac{a+\xi}{a-\xi} \right)^{1/2+i\epsilon} \bar{\mathbf{k}}_1^T \mathbf{D}' [\mathbf{q} - \mathbf{u}_0'(\xi)] d\xi \\ K_2 = -\dfrac{e^{-\pi\epsilon}}{2\pi e_2} \displaystyle\int_{-a}^{a} \left(\frac{a+\xi}{a-\xi} \right)^{1/2-i\epsilon} \mathbf{k}_1^T \mathbf{D}' [\mathbf{q} - \mathbf{u}_0'(\xi)] d\xi \\ K_3 = -\dfrac{1}{2\pi e_3} \displaystyle\int_{-a}^{a} \left(\frac{a+\xi}{a-\xi} \right)^{1/2} \mathbf{k}_3^T \mathbf{D}' [\mathbf{q} - \mathbf{u}_0'(\xi)] d\xi \\ K_4 = -\dfrac{1}{2\pi e_3} \displaystyle\int_{-a}^{a} \left(\frac{a+\xi}{a-\xi} \right)^{1/2} \mathbf{k}_4^T \mathbf{D}' [\mathbf{q} - \mathbf{u}_0'(\xi)] d\xi \end{cases} \tag{73}$$

Downloaded 04 May 2010 to 171.66.16.26. Redistribution subject to ASME license or copyright; see http://www.asme.org/terms/Terms_Use.cfm

Again, if $\mathbf{u}_0'(x_1)$ is an even vector function of x_1, the ESSF for the left end are identical to those for the right end.

6 Examples and Discussions

Let us consider the asymptotic field solutions when $\mathbf{u}_0'(x_1) = \mathbf{u}_0' = (u_{01}', u_{02}', u_{03}', \phi_0')^T$ is a constant vector.

In the special case when $\mathbf{W}' = \mathbf{0}$, we have from (28), (30), and (31) that

$$\mathbf{t}(r) = (2\pi r)^{-1/2}\mathbf{K} \quad r = x_1 - a > 0 \tag{74}$$

$$\mathbf{K} = (K_{\mathrm{II}}, K_{\mathrm{I}}, K_{\mathrm{III}}, K_{\mathrm{IV}})^T = -\sqrt{\pi}\mathbf{G}_1^T\mathbf{E}_1^{-1}(\mathbf{q} - \mathbf{u}_0') \tag{75}$$

$$q_2 = \frac{D_{21}'u_{01}' + D_{22}'u_{02}' + D_{23}'u_{03}' + D_{24}'\phi_0'}{D_{22}'}. \tag{76}$$

The asymptotic extended stress fields exhibit square root singularity as if the conducting rigid inclusion was embedded in a homogeneous piezoelectric material. In the absence of the electric field, the extended stress singularity factors (ESSF) $\mathbf{K}$ and the rigid rotation $\mathbf{q}$ reduce to those for pure elastic problem obtained by Li and Ting (1989) and Asundi and Deng (1995).

In the general case when $\beta_1 \neq 0$ and $\beta_2 \neq 0$, it follows from (43), (51), (52), and (55) that

$$\mathbf{t}(r) = 2(2ar)^{-1/2}\,\mathrm{Re}\left\{\left(\frac{r}{2a}\right)^{i\epsilon}K_1\mathbf{L}_1\mathbf{A}_1^{-1}\mathbf{k}_1 + \left(\frac{r}{2a}\right)^{-i\epsilon}K_2\mathbf{L}_1\mathbf{A}_1^{-1}\mathbf{k}_2 + \left(\frac{r}{2a}\right)^{-\kappa}K_3\mathbf{L}_1\mathbf{A}_1^{-1}\mathbf{k}_3 + \left(\frac{r}{2a}\right)^{\kappa}K_4\mathbf{L}_1\mathbf{A}_1^{-1}\mathbf{k}_4\right\} \quad r = x_1 - a > 0 \tag{77}$$

$$\left.\begin{aligned} K_1 &= -\frac{(1 + 2i\epsilon)ae^{\pi\epsilon}}{2e_1\cosh\pi\epsilon}\bar{\mathbf{k}}_1^T\mathbf{D}'(\mathbf{q} - \mathbf{u}_0'),\\ K_2 &= -\frac{(1 - 2i\epsilon)ae^{-\pi\epsilon}}{2e_1\cosh\pi\epsilon}\mathbf{k}_1^T\mathbf{D}'(\mathbf{q} - \mathbf{u}_0')\\ K_3 &= -\frac{(1 - 2\kappa)ae^{\pi\epsilon i}}{2e_2\cos\pi\kappa}\mathbf{k}_4^T\mathbf{D}'(\mathbf{q} - \mathbf{u}_0'),\\ K_4 &= -\frac{(1 + 2\kappa)ae^{-\pi\kappa i}}{2e_2\cos\pi\kappa}\mathbf{k}_3^T\mathbf{D}'(\mathbf{q} - \mathbf{u}_0') \end{aligned}\right\} \tag{78}$$

$$q_2 = \frac{\Lambda_{21}u_{01}' + \Lambda_{22}u_{02}' + \Lambda_{23}u_{03}' + \Lambda_{24}\phi_0'}{\Lambda_{22}} \tag{79}$$

where Λ_{ij} $(i = 2, j = 1, 2, 3, 4)$ are elements of the 4×4 matrix Λ defined in (52), and e_1 and e_2 are given in (A12). Due to the existence of ϵ and κ, the extended stress fields have both oscillatory and nonsquare root singularities. In the absence of the electric field, the eight-dimensional Stroh formalism becomes the classical six-dimensional one, hence $\kappa = 0$ and $\mathbf{k}_3 = \mathbf{k}_4$. The solutions given in (77)–(79) reduce to those obtained by Asundi and Deng (1995) for anisotropic elasticity.

The results developed in this paper can also be extended to the collinear conducting rigid inclusion problem. Assume the number of the rigid inclusion is n, the field solution (26) and $(51)_1$ will be replaced by

$$\mathbf{A}_1\mathbf{h}_1'(z) = \frac{1}{2\pi i}\sum_{r=1}^{n}\int_{a_r}^{b_r}\mathbf{A}_1\left\langle\frac{\chi_0(z)}{\chi_0^+(\xi)(\xi - z)}\right\rangle \times \mathbf{A}_1^{-1}[\mathbf{q}_r - \mathbf{u}_0'(\xi)]d\xi + \mathbf{A}_1\langle\chi_0(z)\rangle\mathbf{y}(z) \tag{80}$$

and

$$\eta_j(z) = \frac{\chi_j(z)}{2\pi i}\sum_{r=1}^{n}\int_{a_r}^{b_r}\frac{\nu_{jr}(\xi)d\xi}{\chi_j^+(\xi)(\xi - z)} + \chi_j(z)y_j(z) \quad (j = 1, 2, 3, 4) \tag{81}$$

where a_r and b_r $(r = 1, 2, \ldots, n)$ are ends of the rth rigid line inclusion, $\mathbf{y}(z)$ are function vector defined as

$$\mathbf{y}(z) = [y_1(z_1), y_2(z_2), y_3(z_3), y_4(z_4)]^T \tag{82}$$

where $y_\alpha(z_\alpha)$ $(\alpha = 1, 2, 3, 4)$ is a polynomial of z_α the degree of which does not exceed $(n - 1)$, while $\chi_j(z)$ and $\nu_{jr}(x_1)$ are given by

$$\left.\begin{aligned} \chi_0(z) &= \prod_{r=1}^{n}(z - a_r)^{-1/2}(z - b_r)^{-1/2}\\ \chi_1(z) = \bar{\chi}_2(z) &= \prod_{r=1}^{n}(z - a_r)^{-1/2+i\epsilon}(z - b_r)^{-1/2-i\epsilon}\\ \chi_3(z) &= \prod_{r=1}^{n}(z - a_r)^{-1/2-\kappa}(z - b_r)^{-1/2+\kappa}\\ \chi_4(z) &= \prod_{r=1}^{n}(z - a_r)^{-1/2+\kappa}(z - b_r)^{-1/2-\kappa} \end{aligned}\right\} \tag{83}$$

and

$$\left.\begin{aligned} \nu_{1r}(x_1) &= \bar{\mathbf{k}}_1^T\mathbf{D}'[\mathbf{q}_r - \mathbf{u}_0'(x_1)]/e_1,\\ \nu_{2r}(x_1) &= \mathbf{k}_1^T\mathbf{D}'[\mathbf{q}_r - \mathbf{u}_0'(x_1)]/e_1\\ \nu_{3r}(x_1) &= \mathbf{k}_4^T\mathbf{D}'[\mathbf{q}_r - \mathbf{u}_0'(x_1)]/e_2,\\ \nu_{4r}(x_1) &= \mathbf{k}_3^T\mathbf{D}'[\mathbf{q}_r - \mathbf{u}_0'(x_1)]/e_2, \end{aligned}\right\} \tag{84}$$

respectively.

To completely determine the n unknown vectors $\mathbf{q}_r$ $(r = 1, 2, \ldots n)$ and the four polynomials in (80) or (81), the equilibrium conditions for each of the n inclusions should be used.

7 Conclusions

The Stroh formalism in anisotropic elasticity is utilized to study the problem of a conducting rigid line inclusion at the interface of two bonded half-infinite piezoelectric materials. The explicit expressions for the coupled electric and elastic fields are obtained. The conditions needed for the development of singularities in the stress and electric displacement fields are identified and discussed. The formulations for calculating the stress singularities factors are given. It is found that the singularities are dependent on the combinations of the two parameters representing the electro-elastic mismatch at the interface of the piezoelectric bimaterial.

Acknowledgments

The authors wish to acknowledge the support provided by Ontario Centres of Excellence: MRCO, OCMR of Canada, and ALCOA and ALCOA Foundation of the USA.

References

Asundi, A., and Deng, W., 1995, "Rigid Inclusions on the Interface Between Two Bonded Anisotropic Media," *J. Mech. Phys. Solids*, Vol. 43, pp. 1045–1058.

Chen, T., 1993, "The Rotation of a Rigid Ellipsoidal Inclusion Embedded in an Anisotropic Piezoelectric Medium," *Int. J. Solids Structures*, Vol. 30, pp. 1983–1995.

Chung, M. Y., and Ting, T. C. T., 1996, "Piezoelectric Solid with an Elliptical Inclusion or Hole," *Int. J. Solids Structures*, Vol. 33, pp. 3343–3361.

Deeg, W. F., 1980, "The Analysis of Dislocation, Crack, and Inclusion Problems in Piezoelectric Solids," Ph.D. thesis, Stanford University, Stanford, CA.

Eshelby, J. D., Read, W. T., and Shockley, W., 1953, "Anisotropic Elasticity with Applications to Dislocation Theory," *Acta Metall.*, Vol. 1, pp. 252–259.

Downloaded 04 May 2010 to 171.66.16.26. Redistribution subject to ASME license or copyright; see http://www.asme.org/terms/Terms_Use.cfm

Kuo, C.-M., and Barnett, D. M., 1991, In: *Modern Theory of Anisotropic Elasticity and Applications* J. J. Wu, T. C. T. Ting, and D. M. Barnett, eds, SIAM Proceedings, pp. 35–50.

Li, Q. Q., and Ting, T. C. T., 1989, "Line Inclusions in Anisotropic Elastic Solids," ASME JOURNAL OF APPLIED MECHANICS, Vol. 56, pp. 556–563.

Liang, J., Han, J.-C., Wang, B., and Du, S., 1995, "Electroelastic Modelling of Anisotropic Piezoelectric Materials with an Elliptic Inclusion," *Int. J. Solids Structures,* Vol. 32, pp. 2989–3000.

Lothe, J., and Barnett, D. M., 1976, "Integral Formalism for Surface Waves in Piezoelectric Crystal. Existence Consideration," *J. Appl. Phys.,* Vol. 47, pp. 1799–1807.

McMeeking, R. M., 1987, "On Mechanical Stresses at Cracks in Dielectrics with Application to Dielectric Breakdown," *J. Appl. Phys.,* Vol. 62, pp. 3116–3122.

Meguid, S. A., and Deng, W., 1997, "Electro-Elastic Interaction Between a Screw Dislocation and an Elliptical Inhomogeneity in Piezoelectric Materials," *Int. J. Solids Structures* in press.

Muskhelishvili, N. I., 1975, *Some Basic Problems of the Mathematical Theory of Elasticity,* Noordhoff, Leyden.

Pak, Y. E., 1990, "Crack Extension Force in a Piezoelectric Material," ASME JOURNAL OF APPLIED MECHANICS, Vol. 57, pp. 79–100.

Parton, V. Z., 1976, "Fracture Mechanics of Piezoelectric Materials," *Acta Astronaut,* Vol. 3, pp. 671–683.

Sosa, H., and Khutoryansky, N., 1996, "New Developments Concerning Piezoelectric Materials with Defects," *Int. J. Solids Structures,* Vol. 33, pp. 3399–3414.

Sosa, H. A., and Pak, Y. E., 1990, "Three-Dimensional Eigenfunction Analysis of a Crack in a Piezoelectric Material," *Int. J. Solids Structures,* Vol. 26, pp. 1–15.

Stroh, A. H., 1962, "Steady Static Problems in Anisotropic Elasticity," *J. Math. Phys.,* Vol. 41, pp. 77–103.

Suo, Z., Kuo, C.-M., Barnett, D. M., and Willis, J. R., 1992, "Fracture Mechanics for Piezoelectric Ceramics," *J. Mech. Phys. Solids,* Vol. 40, pp. 739–765.

Ting, T. C. T., 1986, "Explicit Solution and Invariance of the Singularities at an Interface Crack in Anisotropic Composites," *Int. J. Solids Structures,* Vol. 22, pp. 965–983.

Ting, T. C. T., 1996, *Anisotropic Elasticity: Theory and Applications,* Oxford University Press, Oxford, UK.

Wang, B., 1992, "Three-Dimensional Analysis of an Ellipsoidal Inclusion in Piezoelectric Material," *Int. J. Solids Structures,* Vol. 29, pp. 293–308.

Zhang, T.-Y., and Tong, P., 1996, "Fracture Mechanics for a Mode II Crack in a Piezoelectric Material," *Int. J. Solids Structures,* Vol. 33, pp. 343–359.

Zhong, Z., and Meguid, S. A., 1997, "Interfacial Debonding of a Circular Inhomogeneity in Piezoelectric Materials," *Int. J. Solids Structures,* Vol. 34, pp. 1965–1984.

APPENDIX

Orthogonal Relations Among Eigenvectors

In this appendix, the orthogonal relations among the eigenvectors of characteristic Eq. (35) will be given under the assumption that $\mathbf{W}' \neq \mathbf{0}$. These relations have been utilized in section 5 for different cases.

Case 1: Nonvanishing β_1 and β_2 ($I_4 \neq 0$). In this case, both ϵ and κ do not vanish. We have four distinct roots λ_j ($j = 1, 2, 3, 4$). Assume $\mathbf{k}_j$ is the eigenvector corresponding to λ_j, it follows from $(35)_1$ that

$$\mathbf{k}_j^T \mathbf{W}' \mathbf{k}_j + i\lambda_j \mathbf{k}_j^T \mathbf{D}' \mathbf{k}_j = 0. \tag{A1}$$

Taking transpose and noting that $\mathbf{W}'^T = -\mathbf{W}'$, $\mathbf{D}'^T = \mathbf{D}'$, Eq. (A1) becomes

$$-\mathbf{k}_j^T \mathbf{W}' \mathbf{k}_j + i\lambda_j \mathbf{k}_j^T \mathbf{D}' \mathbf{k}_j = 0. \tag{A2}$$

Adding (A1) and (A2) yields

$$\mathbf{k}_j^T \mathbf{D}' \mathbf{k}_j = 0, \quad \text{and} \quad \mathbf{k}_j^T \mathbf{W}' \mathbf{k}_j = 0 \quad (j = 1, 2, 3, 4). \tag{A3}$$

Now, assume $\mathbf{k}_j$ and $\mathbf{k}_m$ are eigenvectors corresponding to λ_j and λ_m ($j \neq m$), respectively. Then from $(35)_1$, we get

$$\mathbf{k}_m^T \mathbf{W}' \mathbf{k}_j + i\lambda_j \mathbf{k}_m^T \mathbf{D}' \mathbf{k}_j = 0 \tag{A4}$$

$$\mathbf{k}_j^T \mathbf{W}' \mathbf{k}_m + i\lambda_m \mathbf{k}_j^T \mathbf{D}' \mathbf{k}_m = 0. \tag{A5}$$

By taking transpose, Eq. (A5) can be written as

$$-\mathbf{k}_m^T \mathbf{W}' \mathbf{k}_j + i\lambda_m \mathbf{k}_m^T \mathbf{D}' \mathbf{k}_j = 0. \tag{A6}$$

A summation of (A4) and (A6) produces

$$i(\lambda_j + \lambda_m) \mathbf{k}_m^T \mathbf{D}' \mathbf{k}_j = 0 \tag{A7}$$

thus

$$\mathbf{k}_m^T \mathbf{D}' \mathbf{k}_j = 0, \quad \mathbf{k}_m^T \mathbf{W}' \mathbf{k}_j = 0, \quad (m \neq j, \lambda_j + \lambda_m \neq 0). \tag{A8}$$

Further, it is seen from $(35)_1$ that if $\lambda_j \neq -\bar{\lambda}_j$, then λ_j and $-\bar{\lambda}_j$ are two distinct eigenvalues, while $\mathbf{k}_j$ and $\bar{\mathbf{k}}_j$ are their corresponding eigenvectors, respectively. Obviously this is the case of $\lambda_{1,2} = \pm\beta_1$. If $\lambda_j = -\bar{\lambda}_j$, the corresponding eigenvectors can be chosen as two distinct real vectors. This corresponds to the case of $\lambda_{3,4} = \pm i\beta_2$. Thus, we know that the eigenvectors of (35) consist of a pair of conjugated complex vectors $\mathbf{k}_1$, $\bar{\mathbf{k}}_1$ and two real vectors $\mathbf{k}_3$ and $\mathbf{k}_4$ which satisfy the following orthogonal relations:

$$\left.\begin{aligned} \mathbf{k}_1^T \mathbf{D}' \mathbf{k}_1 = \bar{\mathbf{k}}_1^T \mathbf{D}' \bar{\mathbf{k}}_1 = \mathbf{k}_3^T \mathbf{D}' \mathbf{k}_3 = \mathbf{k}_4^T \mathbf{D}' \mathbf{k}_4 = 0 \\ \mathbf{k}_1^T \mathbf{D}' \mathbf{k}_3 = \mathbf{k}_1^T \mathbf{D}' \mathbf{k}_4 = \bar{\mathbf{k}}_1^T \mathbf{D}' \mathbf{k}_3 = \bar{\mathbf{k}}_1^T \mathbf{D}' \mathbf{k}_4 = 0 \end{aligned}\right\}. \tag{A9}$$

Assume the four eigenvectors are linearly independent. By introducing two 4×4 nonsingular matrices $\mathbf{K_M}$ and $\mathbf{K_N}$ defined as

$$\mathbf{K_M} = [\mathbf{k}_1 \quad \bar{\mathbf{k}}_1 \quad \mathbf{k}_3 \quad \mathbf{k}_4], \quad \mathbf{K_N} = [\bar{\mathbf{k}}_1 \quad \mathbf{k}_1 \quad \mathbf{k}_4 \quad \mathbf{k}_3] \tag{A10}$$

it follows from (A9) and (A10) that

$$\left.\begin{aligned} \mathbf{K_N}^T \mathbf{D}' \mathbf{K_M} = \text{diag}\,(e_1, e_1, e_2, e_2) \\ \mathbf{K_N}^T \mathbf{W}' \mathbf{K_M} = \text{diag}\,(-i\beta_1 e_1, i\beta_1 e_1, \beta_2 e_2, -\beta_2 e_2) \end{aligned}\right\} \tag{A11}$$

where

$$e_1 = \bar{\mathbf{k}}_1^T \mathbf{D}' \mathbf{k}_1 = \mathbf{k}_1^T \mathbf{D}' \bar{\mathbf{k}}_1 \neq 0,$$

$$e_2 = \mathbf{k}_4^T \mathbf{D}' \mathbf{k}_3 = \mathbf{k}_3^T \mathbf{D}' \mathbf{k}_4 \neq 0. \tag{A12}$$

Case 2: Vanishing β_1 and β_2 ($I_2 = I_4 = 0$). In this case, $\epsilon = 0$ and $\kappa = 0$. $\lambda = 0$ is a repeated root of order four. Equation $(35)_1$ becomes

$$\mathbf{W}' \mathbf{k}_j = \mathbf{0}. \tag{A13}$$

Since $\mathbf{W}' \neq 0$ but $\|\mathbf{W}'\| = 0$, we know the rank r of the skew symmetric matrix $\mathbf{W}'$ must satisfy the relation $2 \leq r \leq 3$. Therefore, there exist $d = 4 - r$ ($1 \leq d \leq 2$) linearly independent vectors. Assume $d = 2$, then the two eigenvectors $\mathbf{k}_1$ and $\mathbf{k}_2$ satisfy

$$\mathbf{W}' \mathbf{k}_1 = \mathbf{0}, \quad \mathbf{W}' \mathbf{k}_2 = \mathbf{0}. \tag{A14}$$

Let us define a 4×2 matrix $\mathbf{K_M}$ composed of $\mathbf{k}_1$ and $\mathbf{k}_2$ as being

$$\mathbf{K_M} = [\mathbf{k}_1 \quad \mathbf{k}_2]. \tag{A15a}$$

Then, from (A14)

$$\mathbf{W}' \mathbf{K_M} = \mathbf{0}. \tag{A16}$$

If $d = 1$, $\mathbf{K_M}$ becomes a 4×1 matrix given by

$$\mathbf{K_M} = \mathbf{k}_1. \tag{A15b}$$

Case 3: Vanishing β_1 and Nonvanishing β_2 ($I_2 < 0$, $I_4 = 0$). In this case, ϵ vanishes but κ does not. $\lambda_{1,2} = 0$ is a repeated root of order two. As the rank r of the matrix $\mathbf{W}'$ still satisfies $2 \leq r \leq 3$ ($1 \leq d \leq 2$), we can assume there are two real linearly independent vectors $\mathbf{k}_1$ and $\mathbf{k}_2$, which correspond to the repeated root and have been orthogonalized by performing the Schmidt orthogonalization procedure such that

$$\mathbf{k}_1^T \mathbf{D}' \mathbf{k}_2 = 0. \tag{A17}$$

Downloaded 04 May 2010 to 171.66.16.26. Redistribution subject to ASME license or copyright; see http://www.asme.org/terms/Terms_Use.cfm

The two other eigenvectors corresponding to $\lambda_{3,4} = \pm i\beta_2$ are also chosen as real vectors $\mathbf{k}_3$ and $\mathbf{k}_4$. According to the previous discussions, we have

$$\left.\begin{aligned} \mathbf{W}'\mathbf{k}_1 = \mathbf{0}, \quad \mathbf{W}'\mathbf{k}_2 = \mathbf{0}, \quad \mathbf{k}_3^T\mathbf{D}'\mathbf{k}_3 = \mathbf{k}_4^T\mathbf{D}'\mathbf{k}_4 = 0 \\ \mathbf{k}_1^T\mathbf{D}'\mathbf{k}_2 = \mathbf{k}_1^T\mathbf{D}'\mathbf{k}_3 = \mathbf{k}_1^T\mathbf{D}'\mathbf{k}_4 = \mathbf{k}_2^T\mathbf{D}'\mathbf{k}_3 = \mathbf{k}_2^T\mathbf{D}'\mathbf{k}_4 = 0 \end{aligned}\right\}. \tag{A18}$$

If $\mathbf{k}_1$, $\mathbf{k}_2$, $\mathbf{k}_3$, and $\mathbf{k}_4$ are linearly independent, let

$$\mathbf{K}_M = [\mathbf{k}_1 \quad \mathbf{k}_2 \quad \mathbf{k}_3 \quad \mathbf{k}_4], \quad \mathbf{K}_N = [\mathbf{k}_1 \quad \mathbf{k}_2 \quad \mathbf{k}_4 \quad \mathbf{k}_3] \tag{A19}$$

then we have

$$\left.\begin{aligned} \mathbf{K}_N^T\mathbf{D}'\mathbf{K}_M = \text{diag}\,(e_1, e_2, e_3, e_3) \\ \mathbf{K}_N^T\mathbf{W}'\mathbf{K}_M = \text{diag}\,(0, 0, \beta_2 e_3, -\beta_2 e_3) \end{aligned}\right\} \tag{A20}$$

where

$$e_1 = \mathbf{k}_1^T\mathbf{D}'\mathbf{k}_1 \neq 0, \quad e_2 = \mathbf{k}_2^T\mathbf{D}'\mathbf{k}_2 \neq 0,$$
$$e_3 = \mathbf{k}_4^T\mathbf{D}'\mathbf{k}_3 = \mathbf{k}_3^T\mathbf{D}'\mathbf{k}_4 \neq 0. \tag{A21}$$

Case 4: Nonvanishing β_1 and Vanishing β_2 ($I_2 > 0$, $I_4 = 0$). In this case, ϵ does not vanish but κ vanishes. $\lambda_{3,4} = 0$ is a repeated root of order two. Then $\mathbf{k}_3$ and $\mathbf{k}_4$ are two linearly independent eigenvectors which satisfy the orthogonal relation

$$\mathbf{k}_3^T\mathbf{D}'\mathbf{k}_4 = 0. \tag{A22}$$

The two eigenvectors corresponding to $\lambda_{1,2} = \pm\beta_1$ are still a pair of conjugated complex vectors $\mathbf{k}_1$ and $\bar{\mathbf{k}}_1$. The following relations hold true:

$$\left.\begin{aligned} \mathbf{k}_1^T\mathbf{D}'\mathbf{k}_1 = \bar{\mathbf{k}}_1^T\mathbf{D}'\bar{\mathbf{k}}_1 = 0, \quad \mathbf{W}'\mathbf{k}_3 = \mathbf{0}, \quad \mathbf{W}'\mathbf{k}_4 = \mathbf{0} \\ \mathbf{k}_1^T\mathbf{D}'\mathbf{k}_3 = \mathbf{k}_1^T\mathbf{D}'\mathbf{k}_4 = \bar{\mathbf{k}}_1^T\mathbf{D}'\mathbf{k}_3 = \bar{\mathbf{k}}_1^T\mathbf{D}'\mathbf{k}_4 = \mathbf{k}_3^T\mathbf{D}'\mathbf{k}_4 = \mathbf{0} \end{aligned}\right\}. \tag{A23}$$

Let

$$\mathbf{K}_M = [\mathbf{k}_1 \quad \bar{\mathbf{k}}_1 \quad \mathbf{k}_3 \quad \mathbf{k}_4], \quad \mathbf{K}_N = [\bar{\mathbf{k}}_1 \quad \mathbf{k}_1 \quad \mathbf{k}_3 \quad \mathbf{k}_4] \tag{A24}$$

then

$$\left.\begin{aligned} \mathbf{K}_N^T\mathbf{D}'\mathbf{K}_M = \text{diag}\,(e_1, e_1, e_2, e_3) \\ \mathbf{K}_N^T\mathbf{W}'\mathbf{K}_M = \text{diag}\,(-i\beta_1 e_1, i\beta_1 e_1, 0, 0) \end{aligned}\right\} \tag{A25}$$

where

$$e_1 = \bar{\mathbf{k}}_1^T\mathbf{D}'\mathbf{k}_1 \neq 0, \quad e_2 = \mathbf{k}_3^T\mathbf{D}'\mathbf{k}_3 \neq 0,$$
$$e_3 = \mathbf{k}_4^T\mathbf{D}'\mathbf{k}_4 \neq 0. \tag{A26}$$

Downloaded 04 May 2010 to 171.66.16.26. Redistribution subject to ASME license or copyright; see http://www.asme.org/terms/Terms_Use.cfm

The Energy Release Rate in the General Delamination Problem of Anisotropic Laminates Under Thermomechanical Loads

Wan-Lee Yin
Professor,
School of Civil and
Environmental Engineering,
Georgia Institute of Technology,
Atlanta, GA 30332-0355

A simple formulation, directly in terms of the local variables of the laminated plate theory, is used to derive the general expression of the energy release rate at a boundary point of an arbitrarily shaped delamination in a multilayered anisotropic laminate under combined mechanical and temperature loads. The intact and debonded sublaminates are modeled using the first-order shear deformation theory. If the thermoelastic constitutive equations of the sublaminates are linear and uncoupled, then the expression of the energy release rate may be reduced to a simple form depending only on the sublaminate stiffness coefficients and the local values of the midplane strains and curvatures. The expression does not explicitly involve the temperature load, and is also independent of the strain and curvature parameters tangential to the delamination front. The corresponding expression for delamination in classical laminated plates is also given. The results are applied to the problem of a laminated strip with a fully developed edge delamination loaded under axial extension, bending, and twisting.

1 Introduction

Due to the heterogeneity and anisotropy of composite laminates and geometrical nonlinearity associated with post-buckling deformation, the study of the general delamination problem of multilayered structures presents serious analytical and computational challenges. From its beginning the delamination problem has been investigated largely by using homogeneous or laminated plate analysis (Kachanov, 1975; Chai et al., 1981; Bottega, 1983; Yin et al., 1986; Storakers and Andersson, 1988). Even with this simplified approach, accurate solutions for the force and moment variables in the nonlinear theory of anisotropic laminates, which are needed for assessing the load response and residual strength of delaminated structures, may require a large number of coefficients in a Rayleigh-Ritz analysis and very significant computational effort (Yin and Jane, 1992).

An important issue in the delamination analysis is the prediction of the geometrical and stability characteristics of delamination growth, which requires the evaluation of fracture parameters. In one-dimensional problems involving separation of layers from a cylinder or a beam, the change of the total potential energy associated with crack extension gives the energy available for crack growth (Kachanov, 1975; Chai et al., 1981). This simple concept cannot be used in two-dimensional delamination problems where the crack growth behavior must be determined from the local states that vary along the delamination front.

Using a variational integral with an arbitrarily shaped moving boundary, Bottega (1983) obtained an analytical expression of the pointwise values of the energy release rate associated with the debonding growth of a thin layer from a base laminate with prescribed deformation. The analysis considered only the work and energy associated with the thin layer and, therefore, is applicable to thin-film delaminations and to symmetric laminates with a midplane delamination. For general models allowing energy transfer among the intact and debonded sublaminates, an algebraic expression for the energy release rate was derived for plane-strain deformation of delaminated beam-plates by Yin and Wang (1984) using the J-integral method. The formula was extended and applied to two-dimensional delamination problems, and pointwise values of the energy release rate were calculated for cross-ply and angle-ply composite laminates along the boundary of an elliptical delamination (Jane, 1989). Explicit expressions of the energy release rate for the general delamination problem were obtained first by Storakers and Anderson (1988) and, in alternative forms, by Nilsson and Storakers (1992) using the variational method and the kinematical assumptions of the classical (Kirchhoff) plate theory.

Composite laminates generally have relatively low transverse shear stiffness so that the out-of-plane shear deformation may become significant when the laminate transmits shear loads. For the plane-strain deformation of delaminated beam-plates, expressions of the energy release rate accounting for the transverse shear effect were obtained by Kardomateas and Schmueser (1988) and Chen (1991), respectively, using the J-integral method and the variational method. The former expression was based on an approximate relation between the transverse shear force and the longitudinal force (which effectively defines the transverse shear response of the beam) and, therefore, differs from Chen's expression using the standard first-order shear deformation theory of laminated beams. For the general delamination problem in composite laminates, an expression of the energy release rate including both in-plane and out-plane shear deformation and biaxial bending and twisting effects has not been found in the existing literature. Results are also lacking, until recently (Yin, 1995), in the important case when the delaminated plate is subjected to thermal loads.

In this paper, a simple derivation of the energy release rate G is shown for the general delamination problem of multilayered

Contributed by the Applied Mechanics Division of THE AMERICAN SOCIETY OF MECHANICAL ENGINEERS for publication in the ASME JOURNAL OF APPLIED MECHANICS.

Discussion on this paper should be addressed to the Technical Editor, Professor Lewis T. Wheeler, Department of Mechanical Engineering, University of Houston, Houston, TX 77204-4792, and will be accepted until four months after final publication of the paper itself in the ASME JOURNAL OF APPLIED MECHANICS.

Manuscript received by the ASME Applied Mechanics Division, Jan. 6, 1997; final revision, June 30, 1997. Associate Technical Editor: W. J. Drugan.

 Copyright © 1998 by ASME

Downloaded 04 May 2010 to 171.66.16.26. Redistribution subject to ASME license or copyright; see http://www.asme.org/terms/Terms_Use.cfm

anisotropic laminates subjected to combined mechanical and thermal loads. Reduced algebraic expressions of G are obtained by modeling the intact and debonded sublaminates using the first-order shear deformation theory. The derivation is similar in concept to the proof of the equivalence of the J-integral to the energy release rate in the elasticity theory, and the validity of the result may be extended to nonlinearly elastic anisotropic laminates undergoing large deflection. However, the present analysis involves the kinetic and kinematical variables of the laminated plate theory directly, rather than through integration of three-dimensional variables across the thickness of the sublaminates. By using only algebraic operations in terms of the sublaminate variables at a particular point of the delamination front, the analysis shows that, within the context of classical and improved theories of laminated plates, the evaluation of G is purely algebraic in nature, and the value of G at any point is independent of the evolution of the shape of delamination.

For linearly thermoelastic laminates, an exceedingly simple expression of G may be given as a quadratic function of the midplane strains and curvatures of the intact and debonded sublaminates. The coefficients of the expression involve only the thicknesses of the sublaminates and their stiffness matrices (referred to the local normal and tangential directions of the crack boundary). A remarkable feature is that the expression does *not* explicitly contain the temperature field or the thermal expansion coefficients of the various layers. Furthermore, it does not depend on the strain and curvature along the tangential direction of the crack boundary. When the sublaminates do not allow transverse shear deformation (classical laminate theory), the expression is also unaffected by the local twisting curvature. These important features are shown by superimposing auxiliary solutions with no stress singularity upon the actual deformation of the delaminated plate.

For composite laminates with a strip delamination undergoing generalized plane deformation, the differential equations governing the post-buckling deformation reduce to algebraic equations for a set of deformation parameters, so that G may be readily evaluated in terms of the solutions of the algebraic equations (see Yin (1986 and 1995, respectively) for the mechanical and thermomechanical load cases; see also Chen (1991) for purely mechanical solutions including the transverse shear effect). Another type of delamination problems that yields closed-form exact solutions concerns laminated strips with edge delaminations of constant width, when the strip is subjected to axial extension, bending, and twisting loads and to a temperature load that may vary arbitrarily in the thickness direction. The solutions are obtained in the final section of this paper, along with the energy release rate. Aside from the terms associated with the transverse shear effect, the expression of G for the shear-deformation theory differs from that of the classical theory by additional terms involving the effect of twisting. Such terms vanish in the classical theory but not in the improved theory due to the differences in the kinematical assumptions. These differences have significant implications on the type of continuity conditions for the sublaminate variables across the front of delamination.

2 Delamination in a Shear-Deformable Composite Laminate With Thermal Strain

We consider an arbitrarily shaped interfacial crack in a multilayered composite laminate with the crack front Γ. At a generic point of Γ, let $\mathbf{n}$ denote the local outward unit normal vector and let $\mathbf{s}$ and $\mathbf{k}$ denote, respectively, the unit vectors in the tangential and thickness directions. An element of the delaminated plate containing a short segment of Γ is shown in Fig. 1. This element contains portions of the two delaminated sublaminates (with thicknesses h and H) and a portion of the intact sublaminate (with the thickness $t = h + H$). It is assumed that, in the vicinity of the crack front, the midplane

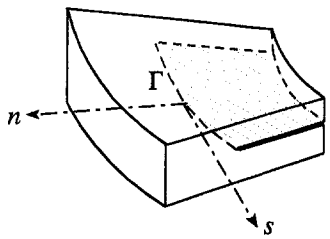

Fig. 1 An element of the debonded composite laminate

displacements and the stress and moment resultants of the sublaminates have been determined by a thermoelastic laminated plate analysis.

The various laminate theories that account for shear deformation use different kinematical and constitutive assumptions (including the use of the "shear correction factor" which, for anisotropic laminates, is not a single scalar factor but a set of factors depending on the ply configuration and anisotropic elasticity) and, therefore, may lead to different resulting expressions for the energy release rate. In the following, we assume that first-order shear deformation theory may be applied to the intact and debonded sublaminates. In this theory, it is commonly assumed that the elastic anisotropy of the sublaminates shows no coupling between the in-plane and out-of-plane responses. For simplicity, we also assume that the thermal strain components e^*_{3n} and e^*_{3s} vanish. These features are valid for composite laminates made of unidirectional plies where the fiber direction varies from layer to layer but remains parallel to the layers.

Referred to the axes $\{\mathbf{n}, \mathbf{s}\}$, the in-plane components of the stress and strain fields will be denoted by

$$\{e_1, e_2, e_6\} = \{e_n, e_s, 2e_{ns}\},$$
$$\{\sigma_1, \sigma_2, \sigma_6\} = \{\sigma_n, \sigma_s, \tau_{ns}\}. \quad (1)$$

Assume linearity of material response for the moment, the anisotropic thermoelastic properties of each layer in the laminate is given by

$$\sigma_\alpha = C_{\alpha\beta}(e_\beta - e^*_\beta), \quad (\alpha = 1, 2, 6) \quad (2)$$

where $e^*_\beta = \alpha_\beta T\,(\beta = 1, 2, 6)$ denotes the thermal strain caused by a temperature load T. In anisotropic composite laminates the elasticity constants and the thermal expansion coefficients, when referred to intrinsic material axes, generally vary from layer to layer but are constant in each layer. However, since $C_{\alpha\beta}$ and α_β are referred to the variable directions $\mathbf{n}$ and $\mathbf{s}$, they are also dependent upon the position along the curved delamination boundary. The temperature field T may vary arbitrarily in the thickness direction.

In the first-order shear deformation theory, the in-plane displacement functions in the kth sublaminate (where $k = 0$ for the intact sublaminate and $k = 1$ and 2, respectively, for the lower and upper debonded sublaminates) differ from their values on the midplane of the sublaminate, $u_p^{(k)}$, by amounts $-z^{(k)}\psi_p (p = 1, 2)$, where ψ_1 and ψ_2 denote the rotations of the sublaminate cross sections in the $\mathbf{n}$ and $\mathbf{s}$ directions, respectively, and $z^{(k)}$ is the thickness coordinate originating from the midplane. The relations among the thickness coordinates of the three sublaminates are given by

$$z^{(1)} \equiv z^{(0)} + h/2, \quad z^{(2)} \equiv z^{(0)} - H/2. \quad (3)$$

Referred to the midplane of the intact sublaminate, the positions of the midplanes of the lower and upper debonded sublaminates are, respectively,

Downloaded 04 May 2010 to 171.66.16.26. Redistribution subject to ASME license or copyright; see http://www.asme.org/terms/Terms_Use.cfm

$$\bar{z}^{(1)} = -h/2 \quad \text{and} \quad \bar{z}^{(2)} = H/2. \tag{4}$$

The tangential strains e_α in the sublaminates may be expressed in terms of the midplane strains $\epsilon_\alpha^{(k)}$ and the curvatures $\kappa_\alpha^{(k)}$ as follows:

$$e_\alpha = \epsilon_\alpha^{(k)} - z^{(k)}\kappa_\alpha^{(k)}, \quad (\alpha = 1, 2, 6 \text{ and } k = 0, 1, 2) \tag{5}$$

where

$$\kappa_1^{(k)} \equiv \kappa_n^{(k)} \equiv \partial\psi_1/\partial x_1, \quad \kappa_2^{(k)} \equiv \kappa_s^{(k)} \equiv \partial\psi_2/\partial x_2,$$
$$\kappa_6^{(k)} \equiv \kappa_{ns}^{(k)} \equiv \partial\psi_1/\partial x_2 + \partial\psi_2/\partial x_1, \tag{6}$$

and $\{x_1, x_2, z^{(k)}\}$ is a local rectangular coordinate system with the base vectors along the $\mathbf{n}$, $\mathbf{s}$, and $\mathbf{k}$ directions. In the following, we shall, for simplicity, use the symbols z and κ_α instead of $z^{(0)}$ and $\kappa_\alpha^{(0)}$, respectively, in the intact sublaminate. The transverse shear strains, $\gamma_{3p}^{(k)}$, are defined by

$$\gamma_{3p}^{(k)} \equiv -\psi_p + \partial u_z/\partial x_p, \quad (p = 1, 2 \text{ and } k = 0, 1, 2). \tag{7}$$

The midplane tangential displacements $u_1^{(k)}$ and $u_2^{(k)}$ are related as follows among the three sublaminates

$$u_p^{(1)} = u_p^{(0)} + (h/2)\psi_p, \quad u_p^{(2)} = u_p^{(0)} - (H/2)\psi_p \quad (p = 1, 2).$$

The rotations ψ_1 and ψ_2 may be set to zero at the point $(x_1, x_2) = (0, 0)$, by superimposing, if necessary, a rigid-body rotation of the whole laminate. Then, at the point of delamination front under consideration, $u_p^{(0)} = u_p^{(1)} = u_p^{(2)}$ and Eq. (7) reduces to

$$\gamma_{3p}^{(k)} = \partial u_z/\partial x_p \quad (p = 1, 2). \tag{8}$$

Across the delamination front, the tangential derivatives of the displacements and rotations are continuous but the normal derivative are generally not. This yields the continuity of $\gamma_{3s}^{(k)}$ and the curvature $\kappa_s^{(k)}$ but not of $\gamma_{3n}^{(k)}$, $\kappa_n^{(k)}$, and $\kappa_{ns}^{(k)}$, because $\partial u_z/\partial x_1$ and $\partial\psi_2/\partial x_1$ are generally not continuous. Hence the following equalities hold along the crack front

$$\kappa_s^{(1)} = \kappa_s^{(2)} = \kappa_s, \quad \gamma_{3s}^{(1)} = \gamma_{3s}^{(2)} = \gamma_{3s}^{(0)} \equiv \gamma_{3s}, \quad (9a, b)$$
$$\epsilon_s^{(1)} = \epsilon_s^{(0)} + (h/2)\kappa_s, \; \epsilon_s^{(2)} = \epsilon_s^{(0)} - (H/2)\kappa_s. \quad (9c, d)$$

We note that, when transverse shear strains are permitted, $\partial u_z/\partial x_1$ and $\partial u_2/\partial x_1$ have comparable continuity properties from a kinematical viewpoint and, just as $\partial u_2/\partial x_1$ and γ_{ns} are discontinuous across the crack front, there is no a priori reason to assume the continuity of $\partial u_z/\partial x_1$ and $\gamma_{3s}^{(k)}$.

3 Constitutive Equations of the Sublaminates and Crack-Front Balance Conditions

The membrane forces and the bending and twisting moments in the three sublaminates are defined as follows:

$$N_\alpha^{(k)} = \int \sigma_\alpha dz^{(k)}, \quad M_\alpha^{(k)} = -\int \sigma_\alpha z^{(k)} dz^{(k)},$$
$$(\alpha = 1, 2, 6) \tag{10}$$

where the range of integration extends across all layers of the kth sublaminate ($k = 0, 1, 2$). At the crack front, these stress and moment resultants satisfy the balance conditions:

$$[\![N_n]\!] = [\![N_{ns}]\!] = 0,$$
$$[\![M_n]\!] + \langle N_n \rangle = [\![M_{ns}]\!] + \langle N_{ns} \rangle = 0, \tag{11a, b}$$

where the symbols $[\![N_\alpha]\!]$ and $\langle N_\alpha \rangle$ have the definitions

$$[\![N_\alpha]\!] \equiv N_\alpha^{(0)} - N_\alpha^{(1)} - N_\alpha^{(2)}, \tag{12a}$$
$$\langle N_\alpha \rangle \equiv -(h/2)N_\alpha^{(1)} + (H/2)N_\alpha^{(2)} = \bar{z}^{(1)}N_\alpha^{(1)} + \bar{z}^{(2)}N_\alpha^{(2)}. \tag{12b}$$

Clearly, $-\langle N_\alpha \rangle$ is the sum of the moments of $N_\alpha^{(1)}$ and $N_\alpha^{(2)}$ with respect to an axis in the plane $z = 0$.

If the thermoelastic properties of the constituent layers are linear, it is convenient to introduce the sublaminate "thermal forces" and "thermal moments" as defined by

$$N_\alpha^{*(k)} = -\int C_{\alpha\beta} e_\beta^* dz^{(k)}, \quad M_\alpha^{*(k)} = \int C_{\alpha\beta} e_\beta^* z^{(k)} dz^{(k)},$$
$$(\alpha = 1, 2, 6 \text{ and } k = 0, 1, 2). \tag{13}$$

These are fictitious forces and moments calculated from the reaction stress to the temperature load when all material elements are not allowed any deformation. Provided that the temperature field and hence the associated thermal strains ϵ_β^* are continuous across the crack front, Eq. (3) implies the following relations (Yin, 1993):

$$[\![N_\alpha^*]\!] = 0, \quad [\![M_\alpha^*]\!] + \langle N_\alpha^* \rangle = 0. \quad (\alpha = 1, 2, 6). \tag{14}$$

Notice that $[\![N_s^*]\!]$ and $[\![M_s^*]\!] + \langle N_s^* \rangle$ vanish whereas $[\![N_s]\!]$ and $[\![M_s]\!] + \langle N_s \rangle$ do *not*.

We define the sublaminate stiffness matrices

$$A_{\alpha\beta}^{(k)} = \int C_{\alpha\beta} dz^{(k)}, \quad B_{\alpha\beta}^{(k)} = -\int C_{\alpha\beta} z^{(k)} dz^{(k)},$$
$$D_{\alpha\beta}^{(k)} = \int C_{\alpha\beta} (z^{(k)})^2 dz^{(k)}. \tag{15}$$

The following relations are easily established by virtue of Eq. (3):

$$[\![A_{\alpha\beta}]\!] = 0, \quad [\![B_{\alpha\beta}]\!] + \langle A_{\alpha\beta} \rangle = 0,$$
$$[\![D_{\alpha\beta}]\!] + 2\langle B_{\alpha\beta} \rangle - \langle\langle A_{\alpha\beta} \rangle\rangle = 0, \tag{16}$$

where

$$\langle\langle A_{\alpha\beta} \rangle\rangle \equiv A_{\alpha\beta}^{(1)} h^2/4 + A_{\alpha\beta}^{(2)} H^2/4. \tag{17}$$

By integrating Eq. (2) and summing the results over the layers of each sublaminate, the following sublaminate thermoelastic constitutive equations may be obtained from the defining Eqs. (10) and (13):

$$N_\alpha^{(k)} - N_\alpha^{*(k)} = A_{\alpha\beta}^{(k)} \epsilon_\beta^{(k)} + B_{\alpha\beta}^{(k)} \kappa_\beta^{(k)},$$
$$M_\alpha^{(k)} - M_\alpha^{*(k)} = B_{\alpha\beta}^{(k)} \epsilon_\beta^{(k)} + D_{\alpha\beta}^{(k)} \kappa_\beta^{(k)},$$
$$(k = 0, 1, 2 \text{ and } \alpha = 1, 2, 6). \tag{18a, b}$$

These equations are supplemented by the equations for the transverse shearing forces $\{Q_1^{(k)}, Q_2^{(k)}\} = \{Q_n^{(k)}, Q_s^{(k)}\}$:

$$Q_p^{(k)} = E_{pq}^{(k)} \gamma_{3q}^{(k)}, \quad (p = 1, 2) \tag{18c}$$

where the index q is summed over the range 1 and 2 and $E_{pq}^{(k)}$ characterizes the transverse shear stiffness of the kth sublaminate. Shear correction factors may be included in the stiffness coefficients $E_{pq}^{(k)}$. Since the shear correction effect may depend on the ply configuration of the sublaminates, the relations

$$[\![E_{pq}]\!] = 0, \quad (p = 1, 2; q = 1, 2) \tag{19}$$

are generally *not* satisfied exactly by $E_{pq}^{(k)}$. However, they are assumed to be valid approximately. Then the following balance condition of the normal shearing force $Q_n^{(k)}$ at the crack front

$$[\![Q_n]\!] = 0 \tag{20}$$

yields an approximate relation $E_{11}^{(1)}\{\gamma_{3n}^{(1)} - \gamma_{3n}^{(0)}\} + E_{11}^{(2)}\{\gamma_{3n}^{(2)} - \gamma_{3n}^{(0)}\} = 0$, which is still insufficient to ensure the continuity of $\gamma_{3n}^{(k)}$ and $\partial u_z/\partial x_1$.

The strain energy per unit area of the sublaminate, U_0, is obtained by integrating $(\frac{1}{2})\sigma_\alpha(e_\alpha - e_\alpha^*)$ across the thickness and combining the result with $(1/2)Q_p^{(k)}\gamma_{3p}^{(k)}$. Since

Downloaded 04 May 2010 to 171.66.16.26. Redistribution subject to ASME license or copyright; see http://www.asme.org/terms/Terms_Use.cfm

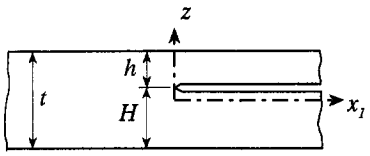

Fig. 2(*a*)

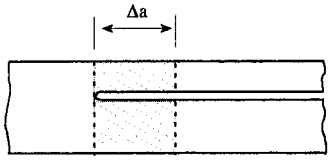

Fig. 2(*b*)

Fig. 2 Growth of the interface crack

$$\int (1/2)\sigma_\alpha(e_\alpha - e_\alpha^*)dz$$
$$= (1/2)\int \sigma_\alpha(\epsilon_\alpha^{(k)} - z^{(k)}\kappa_\alpha^{(k)} - e_\alpha^*)dz^{(k)}$$
$$= (1/2)(N_\alpha^{(k)}\epsilon_\alpha^{(k)} + M_\alpha^{(k)}\kappa_\alpha^{(k)}) + (1/2)\int C_{\alpha\beta}(\epsilon_\beta^{(k)} - z^{(k)}\kappa_\beta^{(k)} - e_\beta^*)e_\alpha^* dz,$$

we obtain

$$U_0 = (1/2)\left\{ Q_p^{(k)}\gamma_{3p}^{(k)} + (N_\alpha^{(k)} + N_\alpha^{*(k)})\epsilon_\alpha^{(k)} + (M_\alpha^{(k)} + M_\alpha^{*(k)})\kappa_\alpha^{(k)} + \int C_{\alpha\beta}e_\alpha^* e_\beta^* dz \right\}. \quad (21)$$

4 The Energy Release Rate

The energy release rate G at a point of the delamination front depends only on the asymptotic stress state in the immediate vicinity of the point. When the intact and debonded sublaminates deform according to the kinematical assumptions of the first-order shear deformable theory, G depends only on the sublaminate forces, moments, midplane strains, curvatures, transverse shear strains, and the temperature in the immediate vicinity of the crack front, i.e., $N_\alpha^{(k)}$, $M_\alpha^{(k)}$, $Q_p^{(k)}$, $\epsilon_\alpha^{(k)}$, $\kappa_\alpha^{(k)}$, γ_{3p}, and $T(z)$.

In the *fixed* rectangular coordinate system $\{x_1, x_2, x_3\}$, let $u_i^{(k)}(x_j)$ and $\psi_p(x_j)$ denote the midplane displacements and the rotations of the kth sublaminate when the crack front momentarily occupies the position $x = 0$. After the delamination crack extends in the negative x_1-direction by a small amount Δa, the displacements at the fixed position x_j change to $u_i(x_j + \Delta a) = u_i(x_j) + \Delta a(\partial u_i/\partial x_1)$, and so do the rotations ψ_p. On the left face of the cracked rectangular region shown in Figs. 2(*a*) and 2(*b*), the combined work of the normal and shearing forces $-N_n^{(0)}$ and $-N_{ns}^{(0)}$ through the respective incremental displacements $\Delta a(\partial u_1^{(0)}/\partial x_1)$ and $\Delta a(\partial u_2^{(0)}/\partial x_1)$ is

$$-N_n^{(0)}\Delta a(\partial u_1^{(0)}/\partial x_1) - N_{ns}^{(0)}\Delta a(\partial u_2^{(0)}/\partial x_1)$$
$$= -\Delta a[N_n^{(0)}\{\epsilon_n^{(0)} - (1/2)(\partial u_z/\partial x_1)^2\} + N_{ns}^{(0)}\{\gamma_{ns}^{(0)} - (\partial u_z/\partial x_1)(\partial u_z/\partial x_2)\} - N_{ns}^{(0)}(\partial u_1^{(0)}/\partial x_2)]$$
$$= -\Delta a[N_n^{(0)}\{\epsilon_n^{(0)} - (1/2)(\gamma_{3n}^{(0)})^2\} + N_{ns}^{(0)}(\gamma_{ns}^{(0)} - \gamma_{3n}^{(0)}\gamma_{3s}^{(0)}) - N_{ns}^{(0)}(\partial u_1^{(0)}/\partial x_2)]. \quad (22a)$$

Notice that, in addition to Eq. (8), the nonlinear strain-displacement relations of the von Karman plate theory have been used to account for the effect of large rotation in post-buckling deformation of the sublaminates. On the right faces of the debonded sublaminates in the same figures, the forces $N_n^{(k)}$ and $N_{ns}^{(k)}$ $(k = 1, 2)$ perform the incremental work

$$\Delta a[N_n^{(k)}\{\epsilon_n^{(k)} - (1/2)(\gamma_{3n}^{(k)})^2\} + N_{ns}^{(k)}(\gamma_{ns}^{(k)} - \gamma_{3n}^{(k)}\gamma_{3s}^{(k)}) - N_{ns}^{(k)}(\partial u_1^{(k)}/\partial x_2)]. \quad (22b)$$

In consistency with the first-order shear deformation theory, we have

$$\partial u_1^{(k)}/\partial x_2 - \partial u_1^{(0)}/\partial x_2 = \bar{z}^{(k)}\partial^2 u_1^{(k)}/\partial x_2\partial x_3 = -\bar{z}^{(k)}\partial\psi_1/\partial x_2. \quad (23)$$

By substituting Eq. (23) into (22*b*) and combining the result with (22*a*), we obtain the work of the in-plane forces from all three sublaminates

$$\Delta a\{-[\![N_n\epsilon_n]\!] - [\![N_{ns}\gamma_{ns}]\!] + (\partial\psi_1/\partial x_2)\langle N_{ns}\rangle + [\![\gamma_{3n}^2 N_n/2]\!] + [\![\gamma_{3n}\gamma_{3s}N_{ns}]\!]\}. \quad (24)$$

The incremental work contributed by the sublaminate normal bending and twisting moments is easily found to be

$$-\Delta a\{[\![M_n\kappa_n]\!] + [\![M_{ns}(\kappa_{ns} - \partial\psi_1/\partial x_2)]\!]\}. \quad (25)$$

Furthermore, the combined work of the shearing forces $Q_n^{(k)}$ is

$$-\Delta a[\![Q_n\gamma_{3n}]\!]. \quad (26)$$

As the crack extends by the amount $\Delta a = 1$, the strain energy of the shaded region in Fig. 2(*b*) decreases from the expression of Eq. (21) with $k = 0$ to the sum of the same expressions with $k = 1$ and 2. The amount of the decrement is

$$[\![U_0]\!] = (1/2)[\![(N_\alpha + N_\alpha^*)\epsilon_\alpha + (M_\alpha + M_\alpha^*)\kappa_\alpha + Q_p\gamma_{3p}]\!], \quad (27)$$

because $[\![\int C_{\alpha\beta}e_\alpha^* e_\beta^* dz]\!]$ vanishes by virtue of the assumed continuity of the thermal strain across the delamination front. Combining the decrement of the strain energy with the work of the sublaminate forces and moments shown in Eqs. (24)–(26), and making use of Eq. (8), we obtain the following expression for the energy supply to the crack tip:

$$G = (1/2)[\![(N_\alpha + N_\alpha^*)\epsilon_\alpha + (M_\alpha + M_\alpha^*)\kappa_\alpha + Q_p\gamma_{3p}]\!] - [\![N_n\epsilon_n + N_{ns}\gamma_{ns} + M_n\kappa_n + M_{ns}\kappa_{ns} + Q_n\gamma_{3n}]\!] + [\![(1/2)\gamma_{3n}^2 N_n]\!] + [\![\gamma_{3n}\gamma_{3s}N_{ns}]\!]. \quad (28)$$

It is clear that the terms in the last line of the preceding expression are of higher order in smallness and should be discarded in consistency with the assumptions of the first-order theory. Furthermore, by using Eqs. (9), (11), and (14), the last expression reduces to

$$2G = -[\![(N_n - N_n^*)\epsilon_n + (N_{ns} - N_{ns}^*)\gamma_{ns} + (M_n - M_n^*)\kappa_n + (M_{ns} - M_{ns}^*)\kappa_{ns}]\!] + [\![(N_s - N_s^*)\epsilon_s + (M_s - M_s^*)\kappa_s]\!] - [\![Q_n\gamma_{3n}]\!] + [\![Q_s\gamma_{3s}]\!]. \quad (29)$$

In the preceding expression, all stress and moment resultants appear in combination with the corresponding negative thermal forces and moments (there are no thermal forces associated with Q_n and Q_s because of the assumption $e_{3n}^* = e_{3s}^* = 0$). Hence the sublaminate constitutive equations may be used to express G in terms of only the *actual* midplane strains and curvatures of the sublaminates. Alternatively, G can be expressed in terms of the local values of $N_\alpha^{(k)} - N_\alpha^{*(k)}$, $M_\alpha^{(k)} - M_\alpha^{*(k)}$ and Q_p only.

The derivation of the work contributions of Eqs. (24)–(26) made no use of the thermoelastic constitutive equations of the sublaminates and, therefore, is valid also for materially nonlinear sublaminates. An expression of G for delamination in non-

Downloaded 04 May 2010 to 171.66.16.26. Redistribution subject to ASME license or copyright; see http://www.asme.org/terms/Terms_Use.cfm

linearly thermoelastic laminates may be obtained by using a general form of the free energy function appropriate to the sublaminates (instead of Eq. (21)) and by combining the result with Eqs. (24)–(26).

5 Superposition of a Nonsingular Auxiliary Solution and a Reduced Form of G

We consider an auxiliary state of deformation of the delaminated plate in which the midplane strains of the intact sublaminate have the values $-\epsilon_\alpha^{(0)}$ and those of the debonded sublaminates have the values $-\epsilon_\alpha^{(0)} + \bar{z}^{(k)}\kappa_\alpha (k = 1, 2)$. Simultaneously, all three sublaminates are subjected to the same constant curvature loads $-\kappa_\alpha$ and to the temperature load $-T(z)$ with resulting thermal strains $-e_\alpha^*$ ($\alpha = 1, 2, 6$). It is clear that this state of deformation causes no interlaminar stresses and, therefore, produces no singularity at the crack tip. Hence the stress intensity factors vanish and so does the energy release rate.

When this nonsingular state of deformation (including the thermal strains $-e_\alpha^*$ due to the temperature field $-T(z)$) is superimposed upon the actual deformation of the delaminated plate, we obtain a combined state (with zero temperature load and hence vanishing thermal strain) in which the intact sublaminate is free from strain and stress at the delamination front, whereas the two debonded sublaminates have the midplane strains $\Delta\epsilon_\alpha^{(k)} = \epsilon_\alpha^{(k)} - \epsilon_\alpha^{(0)} + \bar{z}^{(k)}\kappa_\alpha$ and curvatures $\Delta\kappa_\alpha^{(k)} = \kappa_\alpha^{(k)} - \kappa_\alpha$. For a linearly thermoelastic laminate, superimposing the nonsingular solution does not change the stress intensity factors and the energy release rate. For the combined deformation, the thermal strains and the thermal forces and moments vanish in all three sublaminates.

According to Eqs. ($9a$, c, d), the combined state of deformation has vanishing transverse strain $\Delta\epsilon_s^{(k)}$ and curvature $\Delta\kappa_s^{(k)}$ in all three sublaminates. Furthermore, all membrane forces and bending and twisting moments in the intact sublaminate, $\Delta N_\alpha^{(0)}$ and $\Delta M_\alpha^{(0)}$, vanish at the crack front. Hence, for the combined deformation, Eq. (29) reduces to

$$2G = \Delta N_n^{(1)}\Delta\epsilon_n^{(1)} + \Delta N_{ns}^{(1)}\Delta\gamma_{ns}^{(1)} + \Delta M_n^{(1)}\Delta\kappa_n^{(1)} + \Delta M_{ns}^{(1)}\Delta\kappa_{ns}^{(1)} + \Delta N_n^{(2)}\Delta\epsilon_n^{(2)} + \Delta N_{ns}^{(2)}\Delta\gamma_{ns}^{(2)} + \Delta M_n^{(2)}\Delta\kappa_n^{(2)} + \Delta M_{ns}^{(2)}\Delta\kappa_{ns}^{(2)} - [\![Q_n\gamma_{3n}]\!] + [\![Q_s\gamma_{3s}]\!].$$

By using Eqs. (18), (19), and (20), the following expression is obtained:

$$G = (1/2)\{\Delta\epsilon_n^{(1)}, \Delta\gamma_{ns}^{(1)}, \Delta\kappa_n^{(1)}, \Delta\kappa_{ns}^{(1)}\} \times [H^{(1)}]\{\Delta\epsilon_n^{(1)}, \Delta\gamma_{ns}^{(1)}, \Delta\kappa_n^{(1)}, \Delta\kappa_{ns}^{(1)}\}^T + (1/2)\{\Delta\epsilon_n^{(2)}, \Delta\gamma_{ns}^{(2)}, \Delta\kappa_n^{(2)}, \Delta\kappa_{ns}^{(2)}\} \times [H^{(2)}]\{\Delta\epsilon_n^{(2)}, \Delta\gamma_{ns}^{(2)}, \Delta\kappa_n^{(2)}, \Delta\kappa_{ns}^{(2)}\}^T + (1/2)E_{11}^{(1)}(\Delta\gamma_{3n}^{(1)})^2 + (1/2)E_{11}^{(2)}(\Delta\gamma_{3n}^{(2)})^2, \quad (30)$$

where

$$\Delta\epsilon_n^{(k)} = \epsilon_n^{(k)} - \epsilon_n^{(0)} + \bar{z}^{(k)}\kappa_n, \quad \Delta\gamma_{ns}^{(k)} = \gamma_{ns}^{(k)} - \gamma_{ns}^{(k)} + \bar{z}^{(k)}\kappa_{ns},$$
$$\Delta\kappa_n^{(k)} = \kappa_n^{(k)} - \kappa_n, \quad \Delta\kappa_{ns}^{(k)} = \kappa_{ns}^{(k)} - \kappa_{ns},$$
$$\Delta\gamma_{3n}^{(k)} = \gamma_{3n}^{(k)} - \gamma_{3n}^{(0)},$$

and the matrices $[H^{(k)}]$ are defined in terms of the elements of the stiffness matrices of the debonded sublaminates

$$[H^{(k)}] \equiv \begin{bmatrix} A_{11}^{(k)} & A_{16}^{(k)} & B_{11}^{(k)} & B_{16}^{(k)} \\ A_{16}^{(k)} & A_{66}^{(k)} & B_{16}^{(k)} & B_{66}^{(k)} \\ B_{11}^{(k)} & B_{16}^{(k)} & D_{11}^{(k)} & D_{16}^{(k)} \\ B_{16}^{(k)} & B_{66}^{(k)} & D_{16}^{(k)} & D_{66}^{(k)} \end{bmatrix} \quad (k = 1, 2). \quad (31)$$

This result is significant because the form of the expression is *not* affected by the temperature load and the associated thermal strain. It is also independent on the tangential midplane strains $\epsilon_s^{(k)}$ and the curvature κ_s. Furthermore, only $E_{11}^{(k)}$ and those stiffness coefficients of the debonded sublaminates which occur in the matrices $[H^{(k)}]$ are required for evaluating the energy release rate in terms of the sublaminate strains and curvatures. These features are not shared by the previous expression of Eq. (29), which requires the data of the thermal strains (through $N_\alpha^{*(k)}$ and $M_\alpha^{*(k)}$) and the deformation parameters $\epsilon_s^{(k)}$ and κ_s.

If the first-order shear deformation theory is replaced by the classical laminated plate theory, then the terms $\frac{1}{2}E_{11}^{(k)}(\Delta\gamma_{3n}^{(k)})^2$ in Eq. (30) vanish. Furthermore, the kinematical assumptions of the classical plate theory require, in addition, that $\kappa_{ns} = \partial^2 u_z/\partial x_1\partial x_2$ should be continuous across the delamination front. Hence $\Delta\kappa_{ns}^{(k)} = \kappa_{ns}^{(k)} - \kappa_{ns}$ vanishes at the delamination front in each sublaminate, and Eq. (30) reduces to a simpler expression

$$G = (1/2)\{\Delta\epsilon_n^{(1)}, \Delta\gamma_{ns}^{(1)}, \Delta\kappa_n^{(1)}\} \times [K^{(1)}]\{\Delta\epsilon_n^{(1)}, \Delta\gamma_{ns}^{(1)}, \Delta\kappa_n^{(1)}\}^T + (1/2)\{\Delta\epsilon_n^{(2)}, \Delta\gamma_{ns}^{(2)}, \Delta\kappa_n^{(2)}\} \times [K^{(2)}]\{\Delta\epsilon_n^{(2)}, \Delta\gamma_{ns}^{(2)}, \Delta\kappa_n^{(2)}\}^T, \quad (32)$$

where, for each debonded sublaminate, the matrix $[K^{(k)}]$ may be obtained from $[H^{(k)}]$ by deleting the last row and the last column.

The idea of superimposing an auxiliary equilibrium solution with a nonsingular stress field to reduce the expression of G to simple forms was used by Yin and Wang (1984) for a delaminated homogeneous beam-plate in conjunction with the J-integral method (see also Yin (1985) for a similar reduction in the evaluation of G for a circular delamination using the M-integral). The expression for an anisotropic delaminated classical beam-plate, given in terms of the sublaminate strains and curvatures (Yin, 1986), is formally identical to the present result for the general delamination model, and was used subsequently in evaluating G along the boundary of an elliptical delamination in cross-ply and angle-ply laminates (Jane and Yin, 1992). Equation (32) has been used in the post-buckling analysis of strip delamination models subjected to thermomechanical loads (Yin, 1995). In the absence of the temperature load, general and reduced expressions of G for arbitrarily shaped delaminations in classical laminated plates were given by Storakers and Andersson (1988) and by Nilsson and Storakers (1992) in terms of both kinetic and kinematical variables of the sublaminates.

In the special case of plane-strain deformation of a delaminated composite beam under mechanical loading, Chen (1991) obtained an expression of G in the first-order shear deformation theory by using the variational method. His expression (Eq. (21) in his paper) does not contain the terms involving in-plane shear and twisting because of the plane-strain assumption; it contains terms equivalent to

$$\tfrac{1}{2}\{(Q_n^{(0)})^2/E_{11}^{(0)} - (Q_n^{(1)})^2/E_{11}^{(1)} - (Q_n^{(2)})^2/E_{11}^{(2)}\} + \tfrac{1}{2}\{N_n^{(0)}(\partial u_z^{(0)}/\partial x_1)^2 - N_n^{(1)}(\partial u_z^{(1)}/\partial x_1)^2 - N_n^{(2)}(\partial u_z^{(2)}/\partial x_1)^2\}$$

in the present notation. The second group of terms are equal to the higher order terms in the present Eq. (28) and should be discarded in consistency with the first-order theory. The first group of terms are equal in magnitude but opposite in sign to the terms in Eq. (30) involving transverse shear strain. This apparent sign error yields incorrect results for the following reason. Suppose a symmetric double cantilever beam is subjected only to a pair of equal and opposite forces $-Q_n^{(1)} = Q_n^{(2)} > 0$ and the two debonded sublaminates are so short that $-M_n^{(1)} = M_n^{(2)}$ is negligibly small at the crack front. Then Eq. (21) in Chen's paper gives a negative value for G.

Downloaded 04 May 2010 to 171.66.16.26. Redistribution subject to ASME license or copyright; see http://www.asme.org/terms/Terms_Use.cfm

6 Comparison With Elasticity Solutions

The accuracy of an expression of the energy release rate based on the deformation variables of anisotropic sublaminates depends on how closely the kinematical assumptions of the classical or first-order shear deformation theory are realized in a specific situation. In the context of laminated plate analysis, the energy release rate at any specific point of the delamination front is a *local* quantity depending only on the *local* values of $N_{\alpha\beta}^{(k)}$, $M_{\alpha\beta}^{(k)}$, and $Q_{\alpha}^{(k)}$, and the associated thermal forces and thermal moments. Therefore, the accuracy of the expression of the energy release rate will be assessed by comparison with a generalized two-dimensional elasticity solution where all stress and strain variables depend only on two rectangular coordinates x and z, where x is the local in-plane normal direction to the delamination front and z is the thickness direction of the laminate.

We first consider a symmetric double cantilever beam of thickness $2h$, length $a + b$, which is split on the middle plane from $x = -a$ to $x = 0$, while the remaining portion of the middle plane remain bonded. The two debonded sublaminates are subjected to equal and opposite pure bending moments of magnitude 1. The double cantilever beam is made of a unidirectional graphite-epoxy composite with the orthotropic elastic moduli (Tsai and Hahn, 1980)

$$E_1 = 181 \text{ GPa}, \quad E_2 = E_3 = 10.3 \text{ GPa},$$

$$G_{12} = G_{13} = 7.17 \text{ GPa},$$

$$\nu_{12} = \nu_{13} = \nu_{23} = 0.28,$$

and thermal expansion coefficients $\alpha_1 = 0.02 \times 10^{-6}/°\text{C}$ and $\alpha_2 = \alpha_3 = 22.5 \times 10^{-6}/°\text{C}$, where the subscript 1 denotes the fiber direction (along the axis of the double cantilever beam). For $h = 1$, and under the plane-strain condition, Eq. (29) yields $G = 3.142$ MPa, regardless of the lengths a and b. However, the elasticity solution of the model depends on a and b. When plane-strain finite element analysis is used to determined the stress and deformation fields in the region away from the singularity, and when the J-integral method is subsequently used to evaluate the energy release rate, one obtains the following results: $J = 3.142$ for $a = 6$ and $b = 12$; $J = 3.142$ for $a = 2$ and $b = 4$; and $J = 3.975$ for $a = 1.5$ and $b = 3$. Thus the present expression for G in terms of the laminate deformation variables yields nearly exact results when the sublaminates are subjected to pure bending moments and when the length-to-thickness ratio of the sublaminates is larger than 2.

If the preceding homogeneous double cantilever beam is replaced by a two-layer cross-ply beam by changing the fiber orientation of the upper sublaminate from the x-direction to the y-direction, then the split beam is no longer symmetric with respect to the middle plane and mixed-mode behavior occurs under any type of external loading. When the two debonded sublaminates of this beam are subjected to equal and opposite opening moments $M = 1$, a complex, oscillatory pattern of interfacial stresses occurs near the crack tip. An anisotropic elasticity solution based on eigensolution expansions and the boundary collocation method has been given for $a/h = 4$ and $b/h = 8$ (Yin, 1997). The solution yields the complex stress intensity factor $K = 20.24 - 11.42i$ and the energy release rate $G = 29.35$. Equation (28), based on the laminated plate theory, yields the result $G = 29.27$. The discrepancy is smaller than one percent. A similar comparison was shown for a different type of loading on the model, when the two debonded sublaminates are subjected to equal upward bending moments $M = 0.5$ and, additionally, to equal and opposite axial forces that result in global equilibrium of moments.

Next consider the same half-split bilayer beam, but with the length to thickness ratios $a/h = b/h = 2$. The beam is subjected to a uniform temperature load $\Delta T = 1°\text{C}$ under the plane-strain condition (i.e., no contraction is allowed in the y-direction). A laminated plate analysis yields the thermal expansion strains $\epsilon_x = -0.739 \times 10^{-6}$ and $+12.99 \times 10^{-6}$, respectively, in the lower and upper debonded sublaminates. The unsplit segment of the bilayer beam has the thermal expansion strain $\epsilon_x = 5.315 \times 10^{-6}$ and curvature $\kappa_x = -8.395 \times 10^{-6}/h$. However, these thermal strains and curvatures cannot be exactly realized unless the sublaminates have infinite length. Since the unsplit sublaminate has a small length-to-thickness ratio, i.e., $b/(2h) = 1$, the deviation of the true axial strain and curvature from the preceding nominal values may be significant. Using the preceding nominal values, one obtains from Eq. (30) the energy release rate $G = 1.487$ MPa. A thermoelasticity solution of the model has been obtained recently (Yin et al., 1997) based on complex eigensolution expansions and the collocation method. The solution yields the complex stress intensity factor $K = 0.0589 + 0.1646i$ and the energy release rate $G = 1.660$ MPa. Thus Eq. (30) underestimates G by 10.4 percent. This significant error is caused by the small length-to-thickness ratio of the unsplit segment, $b/(2h) = 1$.

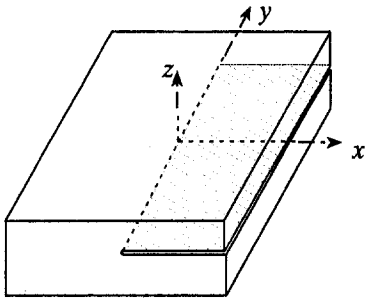

Fig. 3 A laminated strip with an edge delamination

In all preceding examples the sublaminates carry no shearing force in the thickness direction, so that there is no difference between the predictions of the classical laminate theory and the first-order shear deformation theory. An estimate of the discrepancy between the two theories may be given for the homogeneous unidirectional double cantilever beam considered at the beginning of this section. When the lower and upper debonded sublaminates of the split beam are subjected to downward and upward unit shearing forces at their left ends $x = -a$, the bending moments in the debonded sublaminates are $M = -a$ and a, respectively, across the cross section at $x = 0$. Using the classical laminate theory, Eq. (29) yields the energy release rate

$$G = (1/h)\{0.0330(a/h)^2 + 0.0697/k\},$$

where k is the shear correction factor and is taken to be 0.86. Setting $h = 1$, the shear deformation effect contributes an additional amount 0.0811 GPa to the energy release rate of the classical laminate theory, i.e., $0.033\,(a/h)^2$. The additional contribution to G due to the thickness shear effect is 15 percent if $a/h = 4$ and 61 percent if $a/h = 2$.

7 Laminated Strips With Fully Developed Edge Delaminations

We consider a laminated strip with an edge delamination, as shown in Fig. 3 with reference to a global rectangular coordinate system $\{x, y, z\}$. The geometry of the model is constant in the y-direction, and constant midplane strain and curvature loads ϵ_y and κ_y are applied to the strip. In addition, a constant transverse shear strain γ_{yz} is imposed. The delamination is assumed to be fully developed in the sense that the width of the delamination is sufficiently large to warrant the use of the laminated plate theory to the two debonded sublaminates. All three sublaminates carry vanishing $N_x^{(k)}$, $N_{xy}^{(k)}$, $M_x^{(k)}$, and $M_{xy}^{(k)}$ ($k = 0, 1, 2$). Using the sublaminate constitutive Eqs. (18a, b), the

Downloaded 04 May 2010 to 171.66.16.26. Redistribution subject to ASME license or copyright; see http://www.asme.org/terms/Terms_Use.cfm

midplane strains $\epsilon_x^{(k)}$ and $\gamma_{xy}^{(k)}$ and the curvatures $\kappa_x^{(k)}$ and $\kappa_{xy}^{(k)}$ are obtained as follows:

$$\{\epsilon_x^{(k)}, \gamma_{xy}^{(k)}, \kappa_x^{(k)}, \kappa_{xy}^{(k)}\}^T = [H^{(k)}]^{-1}(\{N_x^{*(k)}, N_{xy}^{*(k)}, M_x^{*(k)}, M_{xy}^{*(k)}\}^T - [L^{(k)}]\{\epsilon_y - \bar{z}^{(k)}\kappa_y, \kappa_y\}^T), \quad (k = 0, 1, 2) \quad (33)$$

where $[H^{(k)}]^{-1}$ is the inverse of the matrix in Eq. (31) and where

$$[L^{(k)}] \equiv \begin{bmatrix} A_{12}^{(k)} & B_{12}^{(k)} \\ A_{26}^{(k)} & B_{26}^{(k)} \\ B_{12}^{(k)} & D_{12}^{(k)} \\ B_{26}^{(k)} & D_{26}^{(k)} \end{bmatrix}.$$

The thermal forces and the thermal moments are as defined by Eq. (13). The transverse shear strains $\gamma_{xz}^{(k)}$ are given by

$$\gamma_{xz}^{(k)} = -(E_{12}^{(k)}/E_{11}^{(k)})\gamma_{yz}. \quad (34)$$

The energy release rate is obtained by substituting (33) and (34) into Eq. (30). It is clear that Eqs. (33) and (34) generally yield unequal twisting curvatures $\kappa_{xy}^{(k)}$ and transverse shear strains $\gamma_{xz}^{(k)}$ in the three sublaminates. It may also be mentioned that, although Eq. (30) does not involve *explicitly* the strain load ϵ_y, the curvature κ_y and the temperature load, G is determined implicitly by these load parameters through Eq. (33).

If the sublaminates are modeled as classical laminated plates, then $\partial u_z/\partial x_1$ and the twisting curvature $\kappa_{xy} = \partial^2 u_z/\partial x_1 \partial x_2$ are continuous across the crack front and the latter may be imposed as an additional load parameter. We then obtain the following solutions from the conditions $N_x^{(k)} = N_{xy}^{(k)} = M_x^{(k)} = 0$ and Eqs. (18*a*, *b*):

$$\{\epsilon_x^{(k)}, \gamma_{xy}^{(k)}, \kappa_x^{(k)}\}^T = [K^{(k)}]^{-1}(\{N_x^{*(k)}, N_{xy}^{*(k)}, M_x^{*(k)}\}^T - [R^{(k)}]\{\epsilon_y - \bar{z}^{(k)}\kappa_y, \kappa_y, \kappa_{xy}\}^T), \quad (k = 0, 1, 2) \quad (35)$$

where the matrix $[R^{(k)}]$ is defined by

$$[R^{(k)}] \equiv \begin{bmatrix} A_{12}^{(k)} & B_{12}^{(k)} & B_{16}^{(k)} \\ A_{26}^{(k)} & B_{26}^{(k)} & B_{66}^{(k)} \\ B_{12}^{(k)} & D_{12}^{(k)} & D_{16}^{(k)} \end{bmatrix}.$$

The solution generally does not satisfy the free-edge conditions $M_{xy}^{(k)} = 0$, so that edge twisting moments and transverse corner forces $P^{(k)} = 2M_{xy}^{(k)}$ may be required to maintain equilibrium. This is consistent with the fact that, in addition to $N_x = N_{xy} = M_x = 0$, only one more edge condition,

$$Q_x + \partial M_{xy}/\partial y = 0,$$

may be specified for a classical laminate. Hence $Q_x^{(k)} = 0$ yield constant but generally nonvanishing boundary values of $M_{xy}^{(k)}$. The energy release rate is obtained by substituting (35) into Eq. (32). Special results of this case under restricted types of loading (without twisting and the temperature load) were obtained by O'Brien (1984). For cross-ply laminates with edge delaminations, Davidson (1994) obtained an expression of the energy release rate under uniform temperature loads and strain and curvature loads along a direction parallel to the front of the edge delamination. In such cases the classical laminate solution is also an exact elasticity solution for a delaminated laminate with infinite dimensions in both in-plane directions (Yin, 1993). Hence Eq. (28) yields results identical to Eq. (11) of Davidson (1994).

8 Concluding Remarks

The issues of delamination initiation and growth are important for assessing the residual strength of a damaged composite laminate, particularly when the laminate is subjected to bending and in-plane compression loads which may cause local buckling of debonded sublaminates. A three-dimensional buckling and post-buckling analysis of the general delamination problem is extremely difficult and requires tremendous computational effort. In practice one is forced to apply laminated plate analysis to the debonded and intact sublaminates in the delamination model, and numerical methods such as the Rayleigh-Ritz scheme have to be used to obtain approximate solutions of the von Karman plate equations. As was already mentioned in the Introduction, even for a relatively simple case of a thin-film elliptical delamination (where only the deformation of the one debonded sublaminate is to be obtained), the Rayleigh-Ritz solutions of the postbuckling problem require a very large number of undetermined coefficients to obtain reasonably accurate results for the stress and moment resultants, which are necessary for accurate evaluation of the energy release rate.

Within the context of the laminated plate theory, the energy release rate at each point of the delamination front is a local quantity depending only on the local values of the sublaminate midplane strains and curvatures, $\epsilon_{\alpha\beta}$ and $\kappa_{\alpha\beta}$ (with the addition of $\gamma_{3\alpha}$ for the sublaminates of the first-order shear deformation theory), and of the stress and moment resultants, $N_{\alpha\beta}$ and $M_{\alpha\beta}$ (with the addition of Q_α when appropriate) and the corresponding thermal forces and moments, $N_{\alpha\beta}^*$ and $M_{\alpha\beta}^*$. A simple procedure for deriving the algebraic form of the pointwise energy release rate in terms of the local laminate variables is shown in this paper. This procedure is applicable to various types of sublaminates defined by different kinematical assumptions, including classical laminates and shear deformable laminates. As mention toward the end of Section 4, the procedure is also applicable to materially nonlinear sublaminates through the use of a more general form of the free-energy function appropriate to the sublaminates. For the sublaminates with linear thermoelastic constitutive equations, a mixed form of the expression is given in Eq. (29). By using the sublaminate constitutive equations and various balance conditions, this simple expression is further reduced to Eq. (30), which involves only the local values of the sublaminate midplane strains and curvatures, and does *not* involve the theraml strains. Such an expression is useful when the energy release rate is to be evaluated directly from experimentally measured deformation field.

The results from the present expressions have been compared with the results based on analytical and numerical (finite element) elasticity solutions in two different ways. One is to obtain the elasticity solution of the delamination model by using the finite element method, and then use the J-integral to evaluate the energy release rate based on the computed stress and deformation fields along a path away from the singularity. The other way is to solve the elasticity problem of the bimaterial wedge around the singularity in terms of eigensolutions, with the coefficients of the expansion determined by boundary collocation. This yields the asymptotic solution (i.e., the dominant eigensolution) and the associated complex stress intensity factor, whose magnitude is directly related to the energy release rate. Comparisons made for several homogeneous and bimaterial delamination models yield close agreement between the results of the elasticity solutions and the results based on Eqs. (29) and (30), provided that the length-to-thickness ratio of the sublaminate is not too small.

It is well known that for composites with very stiff fibers the shear deformation effect may become prominent. Current analysis of composite laminates in the aerospace industry is seldom based on classical laminated plate theory and usually takes into account the shear deformation effect in an appropriate manner. Using a simple example, we point out in Section 6 that the thickness shear deformation may contribute very significantly to the energy release rate when the sublaminate length-to-thickness ratio is at a level such that the formulae of the energy release rate based on laminated plate theory would still

Downloaded 04 May 2010 to 171.66.16.26. Redistribution subject to ASME license or copyright; see http://www.asme.org/terms/Terms_Use.cfm

yield accurate results if the shearing forces were absent. While certain expressions of the energy release rate involving the shear deformation effect were given previously for the special case of one-dimensional delamination models under mechanical loads (Kardomateas and Schmueser (1988) and Chen (1991)), we present in this work general analytical expressions of G that are valid for an arbitrarily shaped delamination under thermomechanical loads.

It is well known that, for interface fracture between dissimilar materials, the crack-tip asymptotic stress field of the elasticity solution generally shows oscillatory behavior characterized by a complex stress intensity factor. The peeling and shearing actions are intrinsically coupled and no pure mode behavior may occur under any state of loading. The crack closure integrals associated with peeling and shearing actions do not converge separately, and partition of the energy release rate into distinct mode contributions is not possible. Attempts have been made, however, to obtain the phase of the stress intensity factor (i.e., the mode mixity) in terms of the local solutions of sublaminate variables at the delamination front. Such attempts are doomed to fail because the phase of the complex stress intensity factor is dependent on the anisotropic elasticity of the two layers adjacent to the debonded interface, and the constitutive equations of the sublaminates do not contain such detailed information of individual constituent layers. Therefore, unlike the magnitude of the complex stress intensity factor (which is a global quantity related to a path-independent integral), it cannot be determined at the level of laminated plate analysis. An elasticity analysis of the bimaterial region surrounding the interface crack yields a sequence of eigensolutions in terms of complex variables. These eigensolutions may be combined with appropriate coefficients so that the resulting stress field satisfies the traction boundary conditions of the bimaterial region resulting from the sublaminate forces and moments. A general procedure of singularity analysis involving interface cracks and other types of multimaterial wedges may be found in Yin (1997).

References

Bottega, W. J., 1983, "A growth law for propagation of arbitrary shaped delamination in layered plates," *Int. J. Solids Struc.,* Vol. 19, pp. 1009–1017.

Chai, H., Babcock, C. D., and Knauss, W. G., 1981, "One-dimensional modeling of failure in laminated plates by delamination buckling," *Int. J. Solids Struc.,* Vol. 17, pp. 1069–1083.

Chen, H. P., 1991, "Shear deformation theory for compressive delamination buckling and growth," *AIAA J.,* Vol. 29, pp. 813–819.

Davidson, B. D., 1994, "Energy release rate determination for edge delamination under combined in-plane, bending and hygrothermal loading. Part I—Delamination at a single interface," *J. Composite Materials,* Vol. 28, pp. 1009–1031.

Jane, K. C., 1989, "Buckling, Postbuckling Deformation and Vibration of a Delaminated Plate," Ph.D. dissertation, Georgia Institute of Technology, Atlanta, GA.

Jane, K. C., and Yin, W.-L., 1992, "Refined buckling and postbuckling analysis of two-dimensional delaminations—II. Results for anisotropic laminates and conclusion," *Int. J. Solids Struc.,* Vol. 29, pp. 611–639.

Kachanov, L. M. 1976, "Separation failure of composite materials," *Poly. Mech.,* Vol. 12, pp. 811–815.

Kardomateas, G. A., and Schmueser, D. W., 1988, "Buckling and postbuckling of delaminated composites under compressive loads including transverse shear effects," *AIAA J.,* Vol. 26, pp. 337–343.

O'Brien, T. K., 1984, "Mixed-mode strain-energy-release-rate effects on edge delamination of composites," *Effects of Defects in Composite Materials,* ASTM STP 836, American Society for Testing of Materials, Philadelphia, PA, pp. 125–142.

Storakers, B., and Anderson, B., 1988, "Nonlinear plate theory applied to delamination in composites," *J. Mech. Phys. Solids,* Vol. 36, pp. 689–718.

Nilsson, K.-F., and Storakers, B., 1992, "On Interface Crack Growth in Composite Plates," ASME JOURNAL OF APPLIED MECHANICS, Vol. 59, pp. 530–538.

Yin, W.-L., 1985, "Axisymmetric buckling and growth of a circular delamination in a compressed laminate," *Int. J. Solids Struc.,* Vol. 21, pp. 503–514.

Yin, W.-L., 1986, "Cylindrical buckling of laminated and delaminated plates," *Proc. AIAA/ASME/ASCE/AHS 27th SDM Conference,* San Antonio, TX, pp. 165–179.

Yin, W.-L., 1993, "Thermal stresses in anisotropic multilayered structures," *Thermal Stress and Strain in Microelectronics Packaging,* J. H. Lau, ed., van Nostrand Reinhold, New York, pp. 95–138.

Yin, W.-L., 1995, "Thermal buckling of composite plates with a strip delamination," *Proc. AIAA/ASME/ASCE/AHS/ASC 36th SDM Conference,* Apr., 10–13, New Orleans, LA, pp. 1389–1397, revised version to appear in *Int. J. Solids Struc.*

Yin, W.-L., 1997, "A general analysis method for singularities in composite structures," *Proc. AIAA/ASME/ASCE/AHS/ASC 38th SDM Conference,* Orlando, FL, pp. 2238–2245.

Yin, W.-L., and Jane, K. C., 1992, "Refined buckling and postbuckling analysis of two-dimensional delaminations—I. Analysis and validation," *Int. J. Solids Struc.,* Vol. 29, pp. 591–610.

Yin, W.-L., and Wang, J. T. S., 1984, "The Energy Release Rate in the Growth of a One-Dimensional Delamination," ASME JOURNAL OF APPLIED MECHANICS, Vol. 51, pp. 939–941.

Yin, W.-L., Sallam, S. N., and Simitses, G. J., 1986, "Ultimate axial load capacity of a delaminated beam-plate," *AIAA J.,* Vol. 23, pp. 1437–1444.

Yin, W.-L., Jane, K.-C., and Lin, C.-C., 1997, "Singular solutions of multimaterial wedges under thermomechanical loading," *Analysis and Design Issues for Modern Aerospace Vehicles—1977,* G. J. Simitses, ed., ASME, New York, pp. 159–166.

Downloaded 04 May 2010 to 171.66.16.26. Redistribution subject to ASME license or copyright; see http://www.asme.org/terms/Terms_Use.cfm

Kinematic Description of Damage

Taehyo Park
Department of Civil Engineering,
Korea Maritime University,
Youngdo, Pusan 606-791,
Korea
Mem. ASME.

G. Z. Voyiadjis
Department of Civil and
Environmental Engineering,
Louisiana State University,
Baton Rouge, LA 70803
Mem. ASME.

In this paper the kinematics of damage for finite elastic deformations is introduced using the fourth-order damage effect tensor through the concept of the effective stress within the framework of continuum damage mechanics. However, the absence of the kinematic description of damage deformation leads one to adopt one of the following two different hypotheses. One uses either the hypothesis of strain equivalence or the hypothesis of energy equivalence in order to characterize the damage of the material. The proposed approach in this work provides a relation between the effective strain and the damage elastic strain that is also applicable to finite strains. This is accomplished in this work by directly considering the kinematics of the deformation field and furthermore it is not confined to small strains as in the case of the strain equivalence or the strain energy equivalence approaches. The proposed approach shows that it is equivalent to the hypothesis of energy equivalence for finite strains. In this work, the damage is described kinematically in the elastic domain using the fourth-order damage effect tensor which is a function of the second-order damage tensor. The damage effect tensor is explicitly characterized in terms of a kinematic measure of damage through a second-order damage tensor. The constitutive equations of the elastic-damage behavior are derived through the kinematics of damage using the simple mapping instead of the other two hypotheses.

Introduction

In 1958, Kachanov (1958) introduced the concept of effective stress in damaged materials. This pioneering work started the subject that is now known as continuum damage mechanics. Research in this area has steadily grown and reached a stage that warrants its use in today's engineering applications. Continuum damage mechanics is now widely used in different areas including brittle failure (Krajcinovic, 1983, 1985; Krajcinovic and Foneska, 1981; Lubarda et al., 1994; Ju and Lee, 1991; Lee and Ju, 1991; Ju and Chen, 1994a, b), ductile failure (Lemaitre, 1985, 1986; Chaboche, 1979, 1981, 1988a, b; Chow and Wang, 1987), composite materials (Allen et al., 1987; Boyd et al., 1983; Voyiadjis and Kattan, 1993; Voyiadjis and Park, 1995a, b), and fatigue (Chow and Wei 1991). In this theory, a continuous damage variable is defined and used to represent degradation of the material which reflects various types of damage at the microscale level like nucleation and growth of voids, cavities, microcrack, and other microscopic defects.

In continuum damage mechanics, the effective stress tensor is usually not symmetric. This leads to a complicated theory of damage mechanics involving micropolar media and the Cosserat continuum. Therefore, to avoid such a theory, symmetrization of the effective stress tensor is used to formulate a continuum damage theory in the classical sense (Lee et al., 1986; Sidoroff, 1979; Cordebois and Sidoroff, 1982; Murakami and Ohno, 1980; Betten, 1983; Lu and Chow, 1990). A linear transformation tensor, defined as a fourth-order damage effect tensor is used to symmetrize the effective stress tensor.

The kinetics of damage is well defined presently through the effective stress concept. However, the kinematics of the deformation with damage is only considered indirectly and is only limited to the small strain theory based on the hypothesis of the strain equivalence (Lemaitre and Chaboche, 1978) or energy equivalence (Sideroff, 1980). The finite deformation damage models by Ju (1989) and Zbib (1993) emphasize that "added flexibility" due to the existence of microcracks or microvoids is already embedded in the deformation gradient implicity. Murakami (1988) presented the kinematics of damage deformation using the second-order damage tensor. However, the lack of an explicit formulation for the kinematics of finite deformation with damage leads to the failure in obtaining an explicit derivation of the kinematics that directly consider the damage deformation.

The kinematics of damage is described here explicitly by considering damage directly in the kinematic field using the second-order damage tensor. The deformation gradient of damage is defined using the second-order damage tensor based on the geometically symmetrized effective stress concept (using a fourth-order tensor). The Green deformation tensor of the elastic damage deformation is also derived.

For a detailed review of the principles of continuum damage mechanics as used in this work, the reader is referred to the works of Kachanov (1958), Lemaitre (1985, 1986), Krajcinovic (1985), Lubarda and Krajcinovic (1995), Chaboche (1981, 1988a, b), Murakami (1988), Sidoroff (1979, 1980), and Voyiadjis and Kattan (1992).

Theoretical Preliminaries

Referring to Fig. 1, the initial undeformed configuration of the body is denoted by C_0, while the elastic damage deformed configuration after the body is subjected to a set of external agencies is denoted by C. The body in configuration C_0 undergoes a sequence of deformations starting with an elastic deformation without damage, followed by a damage deformation. This is indicated by path I in Fig. 1. The configuration denoted by C^e implies the elastic deformed configuration. The initial undeformed body may have a pre-existing damage state. A fictitious effective configuration for the body denoted by $\bar{C}$ is assumed that is obtained from C by fictitiously removing all the damage that the body has undergone. This is the fictitious effective configuration which is based on the effective stress

Contributed by the Applied Mechanics Division of THE AMERICAN SOCIETY OF MECHANICAL ENGINEERS for publication in the ASME JOURNAL OF APPLIED MECHANICS.

Discussion on the paper should be addressed to the Technical Editor, Professor Lewis T. Wheeler, Department of Mechanical Engineering, University of Houston, Houston, TX 77204-4792, and will be accepted until four months after final publication of the paper itself in the ASME JOURNAL OF APPLIED MECHANICS.

Manuscript received by the ASME Applied Mechanics Division, Sept. 24, 1996; final revision, Apr. 15, 1997. Associate Technical Editor: J. W. Ju.

 Copyright © 1998 by ASME

Downloaded 04 May 2010 to 171.66.16.26. Redistribution subject to ASME license or copyright; see http://www.asme.org/terms/Terms_Use.cfm

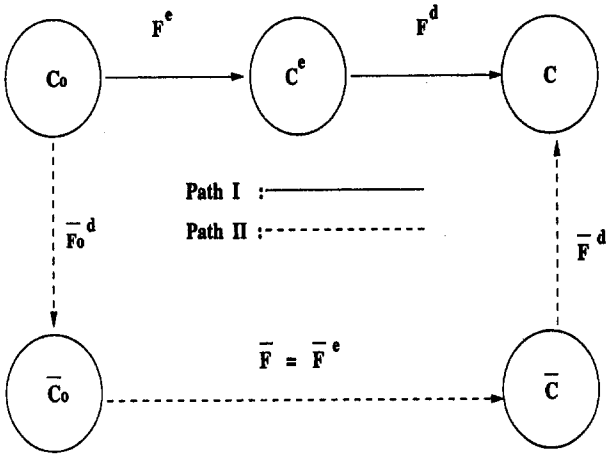

Fig. 1 Schematic representation of elastic damage deformation configurations

concept. In this configuration, the body has only deformed elastically without damage. In addition to the fictitious effective configuration $\bar{C}$, the initial fictitious effective configuration denoted by $\bar{C}_0$ is defined by removing the initial damage from the initial undeformed configuration of the body. In the case of no initial damage existing in the undeformed body, the initial fictitious effective configuration is identical to the initial undeformed configuration. This work is limited to elastic strains with damage. The finite strain problem with both plastic deformation and damage will be considered in a forthcoming paper.

Description of Damage State

The damage state can be described using an even-order tensor (Leckie, 1993; Onat, 1986; Betten, 1986). Ju (1990) pointed out that even for isotropic damage one should employ a damage tensor (not a scalar damage variable) to characterize the state of damage in materials. However, the damage generally is anisotropic due to the external agency condition or the material nature itself. Although the fourth-order damage tensor can be used directly as a linear transformation tensor to define the effective stress tensor, it is not easy to characterize physically the fourth-order damage tensor compared to the second-order damage tensor. In this work, the damage is considered as a symmetric second-order tensor. The second-order damage tensor is given by (Murakami, 1983) as follows:

$$\phi_{ij} = \sum_{k=1}^{3} \hat{\phi}_k \hat{n}_i^k \hat{n}_j^k \quad \text{(no sum in } k\text{)} \tag{1}$$

or

$$\phi_{ij} = b_{ir} b_{js} \hat{\phi}_{rs} \tag{2}$$

where $\hat{\mathbf{n}}^k$ is an eigenvector corresponding to the eigenvalue, $\hat{\phi}_k$, of the damage tensor, $\boldsymbol{\phi}$. The damage tensor in the coordinate system that coincides with the three orthogonal principal directions of the damage tensor, $\hat{\phi}_{rs}$, in Eq. (2) is of diagonal form and is given by

$$\hat{\phi}_{ij} = \begin{bmatrix} \hat{\phi}_1 & 0 & 0 \\ 0 & \hat{\phi}_2 & 0 \\ 0 & 0 & \hat{\phi}_3 \end{bmatrix} \tag{3}$$

and the second-order transformation tensor $\mathbf{b}$ is given by

$$b_{ir} = \begin{bmatrix} n_1^1 & n_2^1 & n_3^1 \\ n_1^2 & n_2^2 & n_3^2 \\ n_1^3 & n_2^3 & n_3^3 \end{bmatrix}. \tag{4}$$

This proper orthogonal transformation tensor requires that

$$b_{ij} b_{kj} = \delta_{ik} \tag{5}$$

where δ_{ik} is a kronecker delta and the determinant of the matrix $[b]$ is given by

$$|[b]| = 1. \tag{6}$$

Voyiadjis and Venson (1995) quantified the physical values of the eigenvalues $\hat{\phi}_k$ ($k = 1, 2, 3$) and the second-order damage tensor $\boldsymbol{\phi}$ for the unidirectional fibrous composite by measuring the crack density with the assumption that one of the eigendirections of the damage tensor coincides with the fiber direction provided the load is applied uniformly along the fiber direction. This introduces a distinct kinematic measure of damage which is complimentary to the deformation kinematic measure of strain. A thermodynamically consistent evolution equation for the damage tensor $\boldsymbol{\phi}$ together with a generalized thermodynamic force (Chaboche, 1977) conjugate to the damage tensor is presented in the paper by Voyiadjis and Park (1995a, b).

Fourth-Order Anisotropic Damage Effect Tensor

In a general state of deformation and damage, the effective stress tensor $\bar{\boldsymbol{\sigma}}$ is related to the stress tensor $\boldsymbol{\sigma}$ by the following linear transformation (Murakami and Ohno, 1980):

$$\bar{\sigma}_{ij} = M_{ijkl} \sigma_{kl} \tag{7}$$

or

$$\bar{\boldsymbol{\sigma}} = \mathbf{M}\boldsymbol{\sigma} \tag{8}$$

where $\boldsymbol{\sigma}$ is the Cauchy stress tensor and $\mathbf{M}$ is a fourth-order linear transformation operator called the damage effect tensor. Depending on the form used for $\mathbf{M}$, it is very clear from Eq. (8) that the effective stress tensor $\bar{\boldsymbol{\sigma}}$ is generally not symmetric. Using a nonsymmetric effective stress tensor as given by Eq. (8) to formulate a constitutive model will result in the introduction of the Cosserat and a micropolar continua. However, the use of such complicated mechanics can be easily avoided if the proper fourth-order linear transformation tensor is formulated in order to symmetrize the effective stress tensor. Such a linear transformation tensor called the damage effect tensor is obtained in the literature (Lee et al., 1986; Sidoroff, 1979) using symmetrization methods. The effective stress tensor is symmetrized using the following expressions by Cordebois and Sidoroff (1979) and Lee et al. (1986).

$$\bar{\sigma}_{ij} = (\delta_{ik} - \phi_{ik})^{-1/2} \sigma_{kl} (\delta_{jl} - \phi_{jl})^{-1/2} \tag{9}$$

$$\bar{\sigma}_{ij} = \tfrac{1}{2}[(\delta_{ik} - \phi_{ik})^{-1} \sigma_{kl} \delta_{jl} + \delta_{ik} \sigma_{kl} (\delta_{jl} - \phi_{jl})^{-1}] \tag{10}$$

$$\sigma_{ij} = \tfrac{1}{2}[(\delta_{ik} - \phi_{ik}) \bar{\sigma}_{kl} \delta_{jl} + \delta_{ik} \bar{\sigma}_{kl} (\delta_{jl} - \phi_{jl})] \tag{11}$$

The fourth-order damage effect tensors corresponding to Eqs. (9), (10), and (11) are defined such as

$$M_{ikjl} = (\delta_{ik} - \phi_{ik})^{-1/2} (\delta_{jl} - \phi_{jl})^{-1/2} \tag{12}$$

$$M_{ikjl} = \tfrac{1}{2}[(\delta_{ik} - \phi_{ik})^{-1} \delta_{jl} + \delta_{ik} (\delta_{jl} - \phi_{jl})^{-1}] \tag{13}$$

$$M_{ikjl} = 2[(\delta_{ik} - \phi_{ik}) \delta_{jl} + \delta_{ik} (\delta_{jl} - \phi_{jl})]^{-1}. \tag{14}$$

Another approach is that of the damage effect tensor using the fourth-order damage tensor $\boldsymbol{\psi}$ as defined by Chaboche (1979)

$$M_{ikjl} = (I_{ikjl} - \psi_{ikjl})^{-1} \tag{15}$$

where I_{ikjl} is a fourth-order identity tensor and is given by

$$I_{ikjl} = \tfrac{1}{2}(\delta_{ij} \delta_{kl} + \delta_{il} \delta_{kj}). \tag{16}$$

Downloaded 04 May 2010 to 171.66.16.26. Redistribution subject to ASME license or copyright; see http://www.asme.org/terms/Terms_Use.cfm

However, it is not easy to characterize physically the fourth-order damage tensor ψ_{ijkl} as opposed to the second-order damage tensor ϕ_{ij}. For the case of isotropic damage, the fourth-order damage tensor is defined by Ju (1990) as follows:

$$\psi_{ikjl} = d_1\delta_{ik}\delta_{jl} + d_2 I_{ikjl} \tag{17}$$

where d_1 and d_2 are scalars (dependent or independent) damage variables.

In order to describe the kinematics of damage, the physical meaning of the fourth-order damage effect tensor should be interpreted and not merely given as the symmetrization of the effective stress. In this work, the fourth-order damage effect tensor given by Eq. (12) will be used because of its geometrical symmetrization of the effective stress (Cordebois and Sidoroff, 1979). However, it is very difficult to obtain the explicit representation of $(\delta_{ik} - \phi_{ik})^{-1/2}$. The explicit representation of the fourth-order damage effect tensor $\mathbf{M}$ using the second-order damage tensor $\boldsymbol{\phi}$ is of particular importance in the implementation of the constitutive modeling of damage mechanics. Therefore, the damage effect tensor $\mathbf{M}$ of Eq. (12) should be obtained using the coordinate transformation of the principal damage direction coordinate system. Thus the fourth-order damage effect tensor given by Eq. (12) can be written as

$$M_{ikjl} = b_{mi}b_{nj}b_{pk}b_{ql}\hat{M}_{mnpq} \tag{18}$$

where $\hat{\mathbf{M}}$ is a fourth-order damage effect tensor with reference to the principal damage direction coordinate system. The fourth-order damage effect tensor $\hat{\mathbf{M}}$ can be written as follows:

$$\hat{M}_{mpnq} = \hat{a}_{mp}\hat{a}_{nq} \tag{19}$$

where the second-order tensor $\mathbf{a}$ of the principal damage direction coordinate system is given by

$$\hat{a}_{mp} = [\delta_{mp} - \hat{\phi}_{mp}]^{-1/2} = \begin{bmatrix} \frac{1}{\sqrt{1-\hat{\phi}_1}} & 0 & 0 \\ 0 & \frac{1}{\sqrt{1-\hat{\phi}_2}} & 0 \\ 0 & 0 & \frac{1}{\sqrt{1-\hat{\phi}_3}} \end{bmatrix}. \tag{20}$$

Substituting Eq. (19) into Eq. (18), one obtains the following relation:

$$M_{ikjl} = b_{mi}b_{nj}b_{pk}b_{ql}\hat{a}_{mp}\hat{a}_{nq} = a_{ik}a_{jl}. \tag{21}$$

Using Eq. (21), a second-order tensor $\mathbf{a}$ is defined as follows:

$$a_{ik} = b_{mi}b_{pk}\hat{a}_{mp}. \tag{22}$$

The matrix form of Eq. (22) is as follows:

$$[a] = [b]^T[\hat{a}][b] = \begin{bmatrix} \frac{b_{11}b_{11}}{\sqrt{1-\hat{\phi}_1}} + \frac{b_{21}b_{21}}{\sqrt{1-\hat{\phi}_2}} + \frac{b_{31}b_{31}}{\sqrt{1-\hat{\phi}_3}} & \frac{b_{11}b_{12}}{\sqrt{1-\hat{\phi}_1}} + \frac{b_{21}b_{22}}{\sqrt{1-\hat{\phi}_2}} + \frac{b_{31}b_{32}}{\sqrt{1-\hat{\phi}_3}} & \frac{b_{11}b_{13}}{\sqrt{1-\hat{\phi}_1}} + \frac{b_{21}b_{23}}{\sqrt{1-\hat{\phi}_2}} + \frac{b_{31}b_{33}}{\sqrt{1-\hat{\phi}_3}} \\ \frac{b_{12}b_{11}}{\sqrt{1-\hat{\phi}_1}} + \frac{b_{22}b_{21}}{\sqrt{1-\hat{\phi}_2}} + \frac{b_{32}b_{31}}{\sqrt{1-\hat{\phi}_3}} & \frac{b_{12}b_{12}}{\sqrt{1-\hat{\phi}_1}} + \frac{b_{22}b_{22}}{\sqrt{1-\hat{\phi}_2}} + \frac{b_{32}b_{32}}{\sqrt{1-\hat{\phi}_3}} & \frac{b_{12}b_{13}}{\sqrt{1-\hat{\phi}_1}} + \frac{b_{22}b_{23}}{\sqrt{1-\hat{\phi}_2}} + \frac{b_{32}b_{33}}{\sqrt{1-\hat{\phi}_3}} \\ \frac{b_{13}b_{11}}{\sqrt{1-\hat{\phi}_1}} + \frac{b_{23}b_{21}}{\sqrt{1-\hat{\phi}_2}} + \frac{b_{33}b_{31}}{\sqrt{1-\hat{\phi}_3}} & \frac{b_{13}b_{12}}{\sqrt{1-\hat{\phi}_1}} + \frac{b_{23}b_{22}}{\sqrt{1-\hat{\phi}_2}} + \frac{b_{33}b_{32}}{\sqrt{1-\hat{\phi}_3}} & \frac{b_{13}b_{13}}{\sqrt{1-\hat{\phi}_1}} + \frac{b_{23}b_{23}}{\sqrt{1-\hat{\phi}_2}} + \frac{b_{33}b_{33}}{\sqrt{1-\hat{\phi}_3}} \end{bmatrix}. \tag{23}$$

Kinematic Description of Elastic-Damage Deformation

A schematic drawing representing the kinematics of finite elastic deformation and damage is shown in Fig. 1. C_0 is the initial undeformed configuration of the body which may have initial damage in the material. C represents the final elastically deformed and damaged configuration of the body. The configuration $\bar{C}_0$ represents the initial configuration of the body that is obtained by fictitiously removing the initial damage from the C_0 configuration. If the initial configuration is undamaged consequently there is no difference between configurations C_0 and $\bar{C}_0$. Configuration $\bar{C}$ is obtained by fictitiously removing the damage from configuration C. Considering path I the deformation gradient referred to the undeformed configuration, C_0, denoted by $\mathbf{F}$ is polarly decomposed into the elastic deformation gradient denoted by $\mathbf{F}^e$ and the damage deformation gradient denoted by $\mathbf{F}^d$ such that

$$\mathbf{F} = \mathbf{F}^e\mathbf{F}^d. \tag{24}$$

The Green deformation tensor of the elastic damage deformation can be obtained through either path I or path II as shown in Fig. 1. Path I gives the Green deformation tensor as follows:

$$\mathbf{G} = \mathbf{F}^T\mathbf{F} = \mathbf{F}^{d^T}\mathbf{F}^{e^T}\mathbf{F}^e\mathbf{F}^d. \tag{25}$$

Considering path II the fictious initial damage Green deformation tensor, $\bar{\mathbf{G}}_0^d$, and the fictitious damage Green deformation tensor, $\bar{\mathbf{G}}^d$, are defined as follows:

$$\bar{\mathbf{G}}_0^d = \bar{\mathbf{F}}_0^{d^T}\bar{\mathbf{F}}_0^d \tag{26}$$

and

$$\bar{\mathbf{G}}^d = \bar{\mathbf{F}}^{d^T}\bar{\mathbf{F}}^d, \tag{27}$$

respectively. $\bar{\mathbf{F}}_0^d$ and $\bar{\mathbf{F}}^d$ are the fictitious effective initial damage deformation and the fictitious effective damage deformation gradients, respectively. The deformation gradient and the Green deformation tensor used in following path II may appear initially to be of the following forms:

$$\mathbf{F} = \bar{\mathbf{F}}_0^d\bar{\mathbf{F}}^e\bar{\mathbf{F}}^d \tag{28}$$

and

$$\mathbf{G} = \bar{\mathbf{F}}^{d^T}\bar{\mathbf{F}}^{e^T}\bar{\mathbf{F}}_0^{d^T}\bar{\mathbf{F}}_0^d\bar{\mathbf{F}}^e\bar{\mathbf{F}}^d, \tag{29}$$

respectively. However, due to the fictitious removal of damage from configurations C_0 and C, the deformation gradient and the Green deformation tensor cannot be expressed by Eqs. (28) and (29). Since the two effective configurations, $\bar{C}_0$ and $\bar{C}$, are obtained by fictitiously removing damage from the real configurations, therefore the difference between the two fictitious damage deformation tensors needs to be subtracted from the Green deformation tensor given by Eq. (29). Thus the re-

Downloaded 04 May 2010 to 171.66.16.26. Redistribution subject to ASME license or copyright; see http://www.asme.org/terms/Terms_Use.cfm

sulting Green deformation tensor in considering path II is given by

$$\mathbf{G} = \bar{\mathbf{F}}^{d^T}\bar{\mathbf{F}}^{e^T}\bar{\mathbf{F}}_0^{d^T}\bar{\mathbf{F}}_0^{d}\bar{\mathbf{F}}^{e}\bar{\mathbf{F}}^{d} - (\bar{\mathbf{G}}^{d} - \bar{\mathbf{G}}_0^{d})$$
$$= \bar{\mathbf{F}}^{d^T}\bar{\mathbf{F}}^{e^T}\bar{\mathbf{F}}_0^{d^T}\bar{\mathbf{F}}_0^{d}\bar{\mathbf{F}}^{e}\bar{\mathbf{F}}^{d} - (\bar{\mathbf{F}}^{d^T}\bar{\mathbf{F}}^{d} - \bar{\mathbf{F}}_0^{d^T}\bar{\mathbf{F}}_0^{d}). \quad (30)$$

It should be noted that the deformation gradients following paths I and II are not related directly. However, the Green deformation tensors may be obtained following paths I or II. This is clearly indicated in Eq. (30) where one needs to remove $(\bar{\mathbf{F}}^{d^T}\bar{\mathbf{F}}^{d})$ due to the fictitious removal of damage from the material. However, one needs to add the initial fictitiously removed deformation due to damage. Both Eqs. (25) and (30) show that the Green deformation tensor can be expressed by either path I or path II, respectively. In addition, the effective Green deformation tensor of path II is the counterpart of the effective stress field and is defined as follows:

$$\bar{\mathbf{G}} = \bar{\mathbf{F}}^{e^T}\bar{\mathbf{F}}^{e}. \quad (31)$$

For simplicity, one assumes that no initial damage exists in the initial undeformed body. Consequently one obtains the following relation, such that

$$\bar{\mathbf{F}}_0^{d^T}\bar{\mathbf{F}}_0^{d} = \mathbf{I} \quad (32)$$

$$\bar{\mathbf{F}}^{e} = \mathbf{F}^{e}, \quad (33)$$

where $\mathbf{I}$ is a second-order identity tensor. Using Eqs. (31), (32), (33), one obtains the Green deformation tensor relating paths I and II as follows:

$$\mathbf{G} = \mathbf{F}^{d^T}\bar{\mathbf{G}}\mathbf{F}^{d} \quad (34)$$

or

$$\mathbf{G} = \bar{\mathbf{F}}^{d^T}\bar{\mathbf{G}}\bar{\mathbf{F}}^{d} - (\bar{\mathbf{F}}^{d^T}\bar{\mathbf{F}}^{d} - \mathbf{I}) \quad (35)$$

From Eq. (35), one obtains the effective Green deformation tensor as follows:

$$\bar{\mathbf{G}} = \bar{\mathbf{F}}^{d^{-T}}[\mathbf{G} + (\bar{\mathbf{F}}^{d^T}\bar{\mathbf{F}}^{d} - \mathbf{I})]\bar{\mathbf{F}}^{d^{-1}}$$
$$= \bar{\mathbf{F}}^{d^{-T}}\mathbf{G}\bar{\mathbf{F}}^{d^{-1}} - \bar{\mathbf{F}}^{d^{-T}}\bar{\mathbf{F}}^{d^{-1}} + \mathbf{I}. \quad (36)$$

Equating Eqs. (34) and (35), one obtains the following relationship:

$$\mathbf{F}^{d^T}\bar{\mathbf{G}}\mathbf{F}^{d} = \bar{\mathbf{F}}^{d^T}\bar{\mathbf{G}}\bar{\mathbf{F}}^{d} - \bar{\mathbf{F}}^{d^T}\bar{\mathbf{F}}^{d} + \mathbf{I}. \quad (37)$$

The Green-Saint-Venant strain tensor termed here the strain tensor is defined as follows:

$$\boldsymbol{\epsilon} = \tfrac{1}{2}(\mathbf{G} - \mathbf{I}). \quad (38)$$

The corresponding effective strain tensor of the counterpart of the effective stress is defined such that

$$\bar{\boldsymbol{\epsilon}} = \tfrac{1}{2}(\bar{\mathbf{G}} - \mathbf{I}). \quad (39)$$

Substituting Equation (36) into Eq. (39), one obtains the effective strain tensor in terms of the elastic-damage Green tensor and the fictitious effective damage gradient such that

$$\bar{\boldsymbol{\epsilon}} = \tfrac{1}{2}\bar{\mathbf{F}}^{d^{-T}}(\mathbf{G} - \mathbf{I})\bar{\mathbf{F}}^{d^{-1}}. \quad (40)$$

Finally one obtains the relation between $\bar{\boldsymbol{\epsilon}}$ and $\boldsymbol{\epsilon}$ using Eqs. (38) and (40) such that

$$\bar{\boldsymbol{\epsilon}} = \bar{\mathbf{F}}^{d^{-T}}\boldsymbol{\epsilon}\bar{\mathbf{F}}^{d^{-1}}. \quad (41)$$

Alternatively, the strain tensor is given by

$$\boldsymbol{\epsilon} = \bar{\mathbf{F}}^{d^T}\bar{\boldsymbol{\epsilon}}\bar{\mathbf{F}}^{d}. \quad (42)$$

The proposed approach provides a relation between the effective strain and the damage elastic strain applicable also to finite strains and is not confined to small strains as in the case of the strain equivalence or the strain energy equivalence approach. Since the fictitious effective deformed configuration denoted by $\bar{C}$, is obtained by removing the damage from the real deformed configuration denoted by C, the fictitious effective deformed volume denoted by $\bar{\Omega}$ is similarly obtained as follows:

$$\bar{\Omega} = \Omega - \Omega^{d}$$
$$= \sqrt{(1-\hat{\phi}_1)(1-\hat{\phi}_2)(1-\hat{\phi}_3)}\,\Omega \quad (43)$$

or

$$\Omega = \bar{J}^{d}\bar{\Omega} \quad (44)$$

where Ω is the deformed volume, Ω^{d} is the damage volume, and $\bar{J}^{d}$ is the Jacobian of the damage deformation. The Jacobian of the damage deformation is given by

$$\bar{J}^{d} = \frac{1}{\sqrt{(1-\hat{\phi}_1)(1-\hat{\phi}_2)(1-\hat{\phi}_3)}}. \quad (45)$$

However, the Jacobian of the damage is defined such that

$$\bar{J}^{d} = \sqrt{|\bar{\mathbf{G}}^{d}|}$$
$$= \sqrt{|\bar{\mathbf{F}}^{d^T}\bar{\mathbf{F}}^{d}|}$$
$$= \sqrt{|\bar{\mathbf{F}}^{d^T}||\bar{\mathbf{F}}^{d}|}. \quad (46)$$

The determinant of the matrix $[a]$ in Eq. (27) is given by

$$|[a]| = |[b]^T||[\hat{a}]||[b]|$$
$$= |[\hat{a}]|$$
$$= \frac{1}{\sqrt{(1-\hat{\phi}_1)(1-\hat{\phi}_2)(1-\hat{\phi}_3)}}. \quad (47)$$

Thus one assumes the following relation similar to Eq. (7) without loss of generality

$$\hat{\bar{\sigma}}_{ij} = \hat{M}_{ikjl}\hat{\sigma}_{kl}$$
$$= \hat{a}_{ik}\hat{a}_{jl}\hat{\sigma}_{kl}$$
$$= \hat{\bar{F}}^{d}_{ik}\hat{\bar{F}}^{d}_{jl}\hat{\sigma}_{kl} \quad (48)$$

for stresses coinciding with the principal directions of damage. Consequently one obtains

$$\hat{\bar{F}}^{d}_{ij} = \hat{a}_{ij} \quad (49)$$

and

$$\bar{F}^{d}_{ij} = a_{ij}. \quad (50)$$

Although the identity is established between $\bar{J}^{d}$ and $|a|$, this is not sufficient to demonstrate the validity of Eq. (49). Equation (49) is assumed here based on the physics of the geometrically symmetrized effective stress concept (Cordebois and Sidoroff, 1979; Voyiadjis and Park, 1996). Equation (41) may now be expressed as follows:

$$\bar{\epsilon}_{ij} = a^{-1}_{ik}a^{-1}_{jl}\epsilon_{kl}$$
$$= M^{-1}_{ikjl}\epsilon_{kl}. \quad (51)$$

Similarly, Eq. (42) can be written as follows:

$$\epsilon_{ij} = a_{ik}a_{jl}\bar{\epsilon}_{kl}$$
$$= M_{ikjl}\bar{\epsilon}_{kl}. \quad (52)$$

The relations combining the strain of the elastic damage deformation and the effective strain in Eqs. (51) and (52) indicate that these relationships are equivalent to those obtained using the hypothesis of energy equivalence (Cordebois and Sidoroff, 1982).

Downloaded 04 May 2010 to 171.66.16.26. Redistribution subject to ASME license or copyright; see http://www.asme.org/terms/Terms_Use.cfm

Constitutive Equation of Elastic-Damage Behavior

The constitutive equation of the elastic-damage behavior is obtained by simple mapping rather than using the energy equivalence hypothesis. The constitutive equation in the effective configuration is given by

$$\bar{\sigma}_{ij} = \bar{E}_{ijkl}\bar{\epsilon}_{kl}. \tag{53}$$

$\bar{\mathbf{E}}$ is the elastic stiffness tensor of the material in the absence of damage. Substituting Eqs. (7) and (51) into Eq. (53), the elastic-damage constitutive equation is obtained as follows:

$$\begin{aligned}\sigma_{ij} &= N_{ikjl}\bar{E}_{klpq}N_{prqs}\epsilon_{rs} \\ &= E_{ijrs}\epsilon_{rs}.\end{aligned} \tag{54}$$

The elastic damage stiffness is given as follows:

$$E_{ijrs} = N_{ikjl}\bar{E}_{klpq}N_{prqs} \tag{55}$$

where

$$\begin{aligned}N_{ikjl} &= M^{-1}_{ikjl} \\ &= a^{-1}_{ik}a^{-1}_{jl}.\end{aligned} \tag{56}$$

The elastic damage stiffness given by Eq. (55) is symmetric. This is in line with the classic (nonpolar) sense of continuum mechanics which is violated by using the hypothesis of strain equivalence. The damaged elastic stiffness is re-examined here using the fourth-order damage effective tensor $\mathbf{M}$ which is a function of the second-order damage tensor $\boldsymbol{\phi}$. The example of parallel cracks normal to the axis "1" is considered here. In this example the nonvanishing damage variables are the following:

$$\phi_{11} = \hat{\phi}_1 \tag{57}$$

$$\phi_{22} = \hat{\phi}_2 \tag{58}$$

$$\phi_{33} = \hat{\phi}_3. \tag{59}$$

Since $\hat{\phi}_2 = \hat{\phi}_3 \ll \hat{\phi}_1$, one may assume for simplicity that $\phi_{22} = \phi_{33} = 0$. However, nonzeros for $\hat{\phi}_2$ and $\hat{\phi}_3$ are used here. The matrix form of the damaged elastic stiffness $\mathbf{E}$ is as follows:

$$[E] = \begin{bmatrix} \hat{\psi}_1\hat{\psi}_1\bar{E}_{1111} & \hat{\psi}_1\hat{\psi}_2\bar{E}_{1122} & \hat{\psi}_1\hat{\psi}_3\bar{E}_{1133} & 0 & 0 & 0 \\ \hat{\psi}_1\hat{\psi}_2\bar{E}_{1122} & \hat{\psi}_2\hat{\psi}_2\bar{E}_{2222} & \hat{\psi}_2\hat{\psi}_3\bar{E}_{2233} & 0 & 0 & 0 \\ \hat{\psi}_1\hat{\psi}_3\bar{E}_{1133} & \hat{\psi}_2\hat{\psi}_3\bar{E}_{2233} & \hat{\psi}_3\hat{\psi}_3\bar{E}_{3333} & 0 & 0 & 0 \\ 0 & 0 & 0 & \hat{\psi}_1\hat{\psi}_2\bar{E}_{1212} & 0 & 0 \\ 0 & 0 & 0 & 0 & \hat{\psi}_2\hat{\psi}_3\bar{E}_{2323} & 0 \\ 0 & 0 & 0 & 0 & 0 & \hat{\psi}_1\hat{\psi}_3\bar{E}_{1313} \end{bmatrix} \tag{60}$$

where $\hat{\psi}_i = (1 - \hat{\phi}_i)$. Alternatively, the matrix form of the damaged elastic compliance tensor $\mathbf{S}$ which is initially isotropic is given by

$$[S] = \begin{bmatrix} \frac{1}{\hat{\psi}_1\hat{\psi}_1\bar{E}} & \frac{-\bar{\nu}}{\hat{\psi}_1\hat{\psi}_2\bar{E}} & \frac{-\bar{\nu}}{\hat{\psi}_1\hat{\psi}_3\bar{E}} & 0 & 0 & 0 \\ \frac{-\bar{\nu}}{\hat{\psi}_1\hat{\psi}_2\bar{E}} & \frac{1}{\hat{\psi}_2\hat{\psi}_2\bar{E}} & \frac{-\bar{\nu}}{\hat{\psi}_2\hat{\psi}_3\bar{E}} & 0 & 0 & 0 \\ \frac{-\bar{\nu}}{\hat{\psi}_1\hat{\psi}_3\bar{E}} & \frac{-\bar{\nu}}{\hat{\psi}_2\hat{\psi}_3\bar{E}} & \frac{1}{\hat{\psi}_3\hat{\psi}_3\bar{E}} & 0 & 0 & 0 \\ 0 & 0 & 0 & \frac{1}{\hat{\psi}_1\hat{\psi}_2\bar{G}} & 0 & 0 \\ 0 & 0 & 0 & 0 & \frac{1}{\hat{\psi}_2\hat{\psi}_3\bar{G}} & 0 \\ 0 & 0 & 0 & 0 & 0 & \frac{1}{\hat{\psi}_1\hat{\psi}_3\bar{G}} \end{bmatrix} \tag{61}$$

where $\bar{\nu}$, $\bar{E}$, and $\bar{G}$ are the Poisson ratio, elastic, and shear modulii, respectively. Obviously, the damaged stiffness or compliance tensor shown is for transversely isotropic material. The damaged material is limited to orthotropic behavior using the second-order damage tensor $\boldsymbol{\phi}$. However, the damaged material exhibits general orthotropy when the principal damage directions are not coincident with the current coordinates. In this case, all components are not zero. More detailed examples of damaged compliance for microcrack distribution using scalar, second-order, fourth-order, and sixth-order damage tensors are available in the recent work by Krajcinovic and Mastilovic (1995).

Conclusion

The fourth-order anisotropic damage effect tensor, $\mathbf{M}$, using the kinematic measure for damage expressed through the second-order damage tensor $\boldsymbol{\phi}$, is reviewed here in reference to the symmetrization of the effective stress tensor. This introduces a distinct kinematic measure of damage which is complimentary to the deformation kinematic measure of strain. A thermodynamically consistent evolution equation for the damage tensor, $\boldsymbol{\phi}$ together with a generalized thermodynamic force conjugate to the damage tensor is presented in the paper by Voyiadjis and Park (1995a, b). Voyiadjis and Venson (1995) quantified the physical values of the eigenvalues, $\hat{\phi}_k$ ($k = 1, 2, 3$), and the second-order damage tensor, $\boldsymbol{\phi}$, for the unidirectional fibrous composite by measuring the crack densities with the assumption that one of the eigendirections of the damage tensor coincides with the fiber direction.

The fourth-order anisotropic damage effect tensor used here is obtained through the geometrical symmetrization of the effective stress (Cordebois and Sidoroff, 1979; Voyiadjis and Park, 1996). This tensor is used here for the kinematic description of damage. The explicit representation of the fourth-order damage effect tensor is obtained with reference to the principal damage direction coordinate system.

The elastic-damage deformation for finite strain is also described here using the kinematics of damage. The kinematics of elastic-damage behavior proposed here allows one to obtain the strain tensor of the elastic-damage deformation without the use of either the hypotheses of energy equivalence or strain equivalence. The proposed approach provides a relation between the effective strain and the damage elastic strain applicable to finite strains and is not confined to small strains as in the case of the strain equivalence or strain energy equivalence approaches. This leads to a simpler derivation of the elastic-damage constitutive equation for the elastic-damage behavior without the use of the hypothesis of energy equivalence.

Acknowledgment

The research described in this paper was sponsored by the Air Force Office of Scientific Research under Grants F49620-93-1-0097DEf and F49620-92-J-0463.

References

Allen, D. H., Harris, C. E., Groves, S. E., 1987, "A Thermomechanical Constitutive Theory for Elastic Composites With Distributed Damage, I. Theoretical Development," *International Journal of Solids and Structures*, Vol. 23, No. 9, pp. 1301–1318.

Downloaded 04 May 2010 to 171.66.16.26. Redistribution subject to ASME license or copyright; see http://www.asme.org/terms/Terms_Use.cfm

Betten, J., 1983, "Damage Tensors in Continuum Mechanics," *Journal de Mécanique Théorique et Appliquée,* Vol. 2, No. 1, pp. 13–32.

Betten, J., 1986, "Applications of Tensor Functions to the Formulation of Constitutive Equations Involving Damage and Initial Anisotrophy," *Engineering Fracture Mechanics,* Vol. 25, No. 5–6, pp. 573–584.

Boyd, J. G., Costanzo, F., and Allen, D. H., 1983, "A Micromechanics Approach for Constructing Locally Averaged Damage Dependent Constitutive Equations in Inelastic Composites," *International Journal of Damage Mechanics,* Vol. 2, pp. 209–228.

Chaboche, J. L., 1977, "Sur l'utilisation des variables d'état interne pour la description du comportement viscoplastique et de la rupture par endommagement," *Symposium France-polonais de Rhéologie et Mécanique,* Cracovie.

Chaboche, J. L., 1979, "Le concept de contrainte effective appliqué à l'élasticité et à la viscoplasticité en presénce d'un endommagement anisotrope," *Colloque Euromech 115,* Villard-de-Lans, June.

Chaboche, J. L., 1981, "Continuous Damage Mechanics: A Tool to Describe Phenomena Before Crack Initiation," *Nuclear Engineering and Design,* Vol. 64, pp. 233–247.

Chaboche, J. L., 1988a, "Continuum Damage Mechanics, Part I: General Concepts," ASME JOURNAL OF APPLIED MECHANICS, Vol. 55, pp. 59–64.

Chaboche, J. L., 1988b, "Continuum Damage Mechanics, Part II: Damage Growth, Crack Initiation, and Crack Growth," ASME JOURNAL OF APPLIED MECHANICS, Vol. 55, pp. 65–72.

Chow, C. L., and Wang, J., 1987, "An Anisotropic Theory of Continuum Damage Mechanics for Ductile Fracture," *Engineering Fracture Mechanics,* Vol. 27, pp. 547–588.

Chow, C. L., and Wei, Y., 1991, "A Damage Mechanics Model of Fatigue Crack Initiation in Notched Plates," *Theoretical and Applied Fracture Mechanics,* Vol. 16, pp. 123–133.

Cordebois, J. P., and Sidoroff, F., 1979, "Damage Induced Elastic Anisotrophy," *Mechanical Behavior of Anisotropic Solids, Colloque Euromech 115,* J. P. Boehler, ed., Villard-de-Lans, June 19–22, Martinus Nijhoff, Dordrecht, The Netherlands, pp. 761–774.

Cordebois, J. P., and Sidoroff, F., 1982, "Anisotropic Damage in Elasticity and Plasticity," *Journal de Mécanique Théorique et Appliquée,* Numéro Spécial, pp. 45–60.

Ju, J. W., 1989, "Energy-Based Coupled Elastoplastic Damage Models at Finite Strains," *Journal of Engineering Mechanics,* Vol. 115, No. 11, pp. 2507–2525.

Ju, J. W., 1990, "Isotropic and Anisotropic Damage Variables in Continuum Damage Mechanics," *Journal of Engineering Mechanics,* Vol. 116, No. 12, pp. 2764–2770.

Ju, J. W., and Chen, Tsung-Muh, 1994a, "Effective Elastic Moduli of Two-Dimensional Brittle Solids With Interacting Microcracks, Part I: Basic Formulations," ASME JOURNAL OF APPLIED MECHANICS, Vol. 61, pp. 349–357.

Ju, J. W., and Chen, Tsung-Muh, 1994b, "Effective Elastic Moduli of Two-Dimensional Brittle Solids With Interacting Microcracks, Part II: Evolutionary Damage Models," ASME JOURNAL OF APPLIED MECHANICS, Vol. 61, pp. 358–366.

Ju, J. W., and Lee, X., 1991, "Micromechanical Damage Models for Brittle Solids, I: Tensile Loadings," *Journal of Engineering Mechanics,* Vol. 117, No. 7, pp. 1495–1514.

Kachanov, L. M., 1958, "On the Creep Fracture Time," *Izv. Akad. Nauk. USSR Otd. Tekh.,* Vol. 8, pp. 26–31.

Krajcinovic, D., 1983, "Constitutive Equations for Damaging Materials," ASME JOURNAL OF APPLIED MECHANICS, Vol. 50, pp. 335–360.

Krajcinovic, D., 1985, "Continuous Damage Mechanics Revisited Basic Concepts and Definitions," ASME JOURNAL OF APPLIED MECHANICS, Vol. 52, pp. 829–834.

Krajcinovic, D., and Fonseka, G. U., 1981, "The Continuum Damage Theory for Brittle Materials," ASME JOURNAL OF APPLIED MECHANICS, Vol. 48, pp. 809–824.

Krajcinovic, D., and Mastilovic, S., "Some Fundamental Issues of Damage Mechanics," *Mechanics of Materials,* Vol. 21, pp. 217–230.

Leckie, F. A., 1993, "Tensorial Nature of Damage Measuring Internal Variables," *International Journal of Solids and Structures,* Vol. 30, No. 1, pp. 19–36.

Lee, H., Li, G., and Lee, S., 1986, "The Influence of Anisotropic Damage on the Elastic Behavior of Materials," *International Seminar on Local Approach of Fracture,* Moret-sur-Loing, France, June, pp. 79–90.

Lee, X., and Ju, J. W., 1991, "Micromechanical Damage Models for Brittle Solids, II: Compressive Loadings," *Journal of Engineering Mechanics,* Vol. 117, No. 7, pp. 1515–1536.

Lemaitre, J., 1985, "A Continuous Damage Mechanics, Model of Ductile Fracture," *Journal of Engineering Materials and Technology,* Vol. 107, No. 42, pp. 83–89.

Lemaitre, J., 1986, "Local Approach of Fracture," *Engineering Fracture Mechanics,* Vol. 25, No. 5–6, pp. 523–537.

Lemaitre, J., and Chaboche, J. L., 1978, "Aspects Phénoménologique de la Rupture par Endommagement," *Journal of Mecanique Théorique et Appliquée,* pp. 317–365.

Lu, T. J., and Chow, C. L., 1990, "On Constitutive Equations of Inelastic Solids With Anisotropic Damage," *Theoretical and Applied Fracture Mechanics,* Vol. 14, pp. 187–218.

Lubarda, V. A., and Krajcinovic, D., 1995, "Some Fundamental Issues in Rate Theory of Damage-Elastoplasticity," *International Journal of Plasticity,* Vol. 11, No. 7, pp. 763–797.

Lubarda, V. A., Krajcinovic, D., and Mastilovic, S., 1994, "Damage Model for Brittle Elastic Solids With Unequal Tensile and Compressive Strengths," *Engineering Fracture Mechanics,* Vol. 49, No. 5, pp. 681–697.

Murakami, S., 1983, "Notion of Continuum Damage Mechanics and its Application to Anisotropic Creep Damage Theory," *Journal of Engineering Materials and Technology,* Vol. 105, pp. 99–105.

Murakami, S., 1988, "Mechanical Modelling of Material Damage," ASME JOURNAL OF APPLIED MECHANICS, Vol. 55, pp. 280–286.

Murakami, S., and Ohno, N., 1980, "A Continuum Theory of Creep and Creep Damage," *Creep in Structures,* A. R. S. Ponter and D. R. Hayhurst, eds., IUTAM 3rd Symposium, Leicester, U. K., Sept. 8–12, Springer-Verlag, New York, pp. 422–443.

Onat, E. T., 1986, "Representation of Mechanical Behavior in the Presence of Internal Damage," *Engineering Fracture Mechanics,* Vol. 25, No. 5–6, pp. 605–614.

Sidoroff, F., 1979, "Description of Anisotropic Damage Application to Elasticity," *Mechanical Behavior of Anisotropic Solids,* Jean-Paul Boehler, ed., Proceedings of the Euromech Colloqium 115, No. 295, Villard-de-Lans, France, June 19–22.

Sidoroff, F., 1980, "Description of Anisotrtopic Damage Application to Elasticity," *Physical Non-Linearities in Structural Analysis,* J. Hult and J. Lemaitre, eds., IUTAM Series, Springer-Verlag, New York, pp. 237–244.

Voyiadjis, G. Z., and Kattan, P. I., 1992, "A Plasticity-Damage Theory for Large Deformation of Solids, I: Theoretical Formulation," *International Journal of Engineering Science,* Vol. 30, No. 9, pp. 1089–1108.

Voyiadjis, G. Z., and Kattan, P. I., 1993, "Damage of Fiber-Reinforced Composite Materials With Micromechanical Characterization," *International Journal of Solids and Structures,* Vol. 30, No. 20, pp. 2757–2778.

Voyiadjis, G. Z., and Park, T., 1995a, "Anisotropic Damage of Fiber Reinforced MMC Using an Overall Damage Analysis," *Journal of Engineering Mechanics,* Vol. 121, No. 11, pp. 1209–1217.

Voyiadjis, G. Z., and Park, T., 1995b, "Local and Interfacial Damage Analysis of Metal Matrix Composites," *International Journal of Engineering Science,* Vol. 33, No. 11, pp. 1595–1621.

Voyiadjis, G. Z., and Park, T., 1996, "Anisotropic Damage Effect Tensors for the Symmetrization of the Effective Stress Tensor," ASME JOURNAL OF APPLIED MECHANICS, Vol. 64, No. 1, pp. 107–110.

Voyiadjis, G. Z., and Venson, A. R., 1995, "Experimental Damage Investigation of a SiC-TI Aluminide Metal Matrix Composite," International Journal of Damage Mechanics, Vol. 4, No. 4, pp. 338–361.

Zbib, H. M., 1993, "On the Mechanics of Large Inelastic Deformations: Kinematics and Constitutive Modeling," *ACTA Mechanica,* Vol. 96, pp. 119–138.

Downloaded 04 May 2010 to 171.66.16.26. Redistribution subject to ASME license or copyright; see http://www.asme.org/terms/Terms_Use.cfm

The Axisymmetric Deformation of Linearly and Nonlinearly Elastic Spinning Tubes Under End Thrusts and Torques

T. J. McDevitt
Department of Mathematics,
Millersville University,
Millersville, PA 17551

J. G. Simmonds
Institute of Applied Mathematics
and Mechanics,
University of Virginia,
Charlottesville, VA 22903
Fellow ASME

We consider the steady-state deformations of elastic tubes spinning steadily and attached in various ways to rigid end plates to which end thrusts and torques are applied. We assume that the tubes are made of homogeneous linearly or nonlinearly anisotropic material and use Simmonds' (1996) simplified dynamic displacement-rotation equations for shells of revolution undergoing large-strain large-rotation axisymmetric bending and torsion. To exploit analytical methods, we confine attention to the nonlinear theory of membranes undergoing small or large strains and the theory of strongly anisotropic tubes suffering small strains. Of particular interest are the boundary layers that appear at each end of the tube, their membrane and bending components, and the penetration of these layers into the tube which, for certain anisotropic materials, may be considerably different from isotropic materials. Remarkably, we find that the behavior of a tube made of a linearly elastic, anisotropic material (having nine elastic parameters) can be described, to a first approximation, by just two *combined parameters. The results of the present paper lay the necessary groundwork for a subsequent analysis of the* whirling *of spinning elastic tubes under end thrusts and torques.*

Introduction

For an elastic shell of revolution undergoing simultaneous dynamic bending and torsion in which the strain-energy density depends only on (arbitrarily large) extensional and bending strains, Simmonds (1996) has obtained a set of governing equations in terms of two displacements u and w and an angle of twist ψ. A simplifying feature of these equations is that the various strains are, at most, quadratic in u, w, and ψ and their derivatives. For a tube (i.e., a circular cylindrical shell) with reference surface $\mathcal{T}$ of radius R and of constant thickness $R\epsilon$, spinning at a constant frequency Ω (Fig. 1), the governing equations can be reduced to *four* first-order differential equations and *two* algebraic equations. Further, as we shall show, we can use asymptotic methods to construct accurate approximate solutions for a variety of strain-energy densities, external loads, and boundary conditions. The details are as follows.

The Field Equations

Let $\{\mathbf{e}_x, \mathbf{e}_y, \mathbf{e}_z\}$ denote the standard orthonormal basis in a fixed, dextral Cartesian reference frame and let $\{\mathbf{e}_r, \mathbf{e}_\theta, \mathbf{e}_z\}$ denote the standard basis associated with a set of circular cylindrical coordinates (r, θ, z), where

$$\mathbf{e}_r = \cos\theta\mathbf{e}_x + \sin\theta\mathbf{e}_y, \quad \mathbf{e}_\theta = -\sin\theta\mathbf{e}_x + \cos\theta\mathbf{e}_y. \quad (1)$$

Then the reference surface $\mathcal{T}$ of the undeformed tube may be expressed as

$$\mathcal{T}: \mathbf{y} = R[\mathbf{e}_r(\theta + \Omega t) + z\mathbf{e}_z], \quad 0 \le z \le \lambda, \quad 0 \le \theta < 2\pi, \quad (2)$$

where z is a *dimensionless* axial coordinate.

We assume that the loading and material properties of the tube are such that in the rotating, twisted reference frame $\{\bar{\mathbf{e}}_r, \bar{\mathbf{e}}_\theta, \mathbf{e}_z\}$, where

$$\bar{\mathbf{e}}_r \equiv \mathbf{e}_r(\theta + \psi(z) + \Omega t), \quad \bar{\mathbf{e}}_\theta \equiv \mathbf{e}_\theta(\theta + \psi(z) + \Omega t), \quad (3)$$

the deformed reference surface has the representation

$$\bar{\mathcal{T}}: \bar{\mathbf{y}} = R[\bar{r}(z)\bar{\mathbf{e}}_r(z, \theta, t) + \bar{z}(z)\mathbf{e}_z]$$
$$= R\{[1 + w(z)]\bar{\mathbf{e}}_r(z, \theta, t) + [z + u(z)]\mathbf{e}_z\}. \quad (4)$$

Here, Simmonds' (1996) angular variable ψ has been set equal to $\Omega t + \psi$ and his symbols for the axial and radial components of displacement of a general shell of revolution have been reversed, in accordance with the usual notation for cylindrical shells. Computing the acceleration of a point on $\bar{\mathcal{T}}$, we have, by (1), (3), and (4),

$$\ddot{\bar{\mathbf{y}}} = -R(1 + w)\Omega^2\bar{\mathbf{e}}_r. \quad (5)$$

Thus, the equations of motion (55), (56), and (57) of Simmonds (1996) reduce to

$$N_\theta = H' + mR^2(1 + w)\Omega^2, \quad V = P, \quad (1 + w)S = T, \quad (6)$$

where N_θ, V, and S are, respectively, hoop, axial, and shear stress resultants, measured per unit *undeformed* length, and $2\pi R(P, T)$ are, respectively, the (constant) net axial tension and torque applied to the tube.

To complete the field equations, we add the stress-strain relations given by Eqs. (47)–(49) of Simmonds (1996). For our tube, these reduce to

$$H = (\Phi_{,e_z} + 2\Lambda_z^{-2}k_z\Phi_{,k_z})w' + \Lambda_z^{-2}(\Lambda_z^2\Phi_{,k_z})'(1 + u') \quad (7)$$

$$V = (\Phi_{,e_z} + 2\Lambda_z^{-2}k_z\Phi_{,k_z})(1 + u') + \Phi_{,k_\theta}$$
$$- \Lambda_z^{-2}(\Lambda_z^2\Phi_{,k_z})'w' \quad (8)$$

Contributed by the Applied Mechanics Division of THE AMERICAN SOCIETY OF MECHANICAL ENGINEERS for publication in the ASME JOURNAL OF APPLIED MECHANICS.

Discussion on this paper should be addressed to the Technical Editor, Professor Lewis T. Wheeler, Department of Mechanical Engineering, University of Houston, Houston, TX 77204-4792, and will be accepted until four months after final publication of the paper itself in the ASME JOURNAL OF APPLIED MECHANICS.

Manuscript received by the ASME Applied Mechanics Division, Jan. 30, 1997; final revision, May 6, 1997. Associate Technical Editor: R. Abeyaratne.

 Copyright © 1998 by ASME

Downloaded 04 May 2010 to 171.66.16.26. Redistribution subject to ASME license or copyright; see http://www.asme.org/terms/Terms_Use.cfm

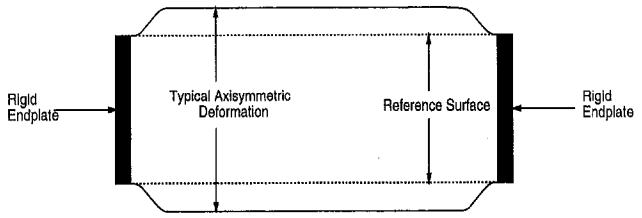

Fig. 1 A steadily spinning elastic tube fixed to rigid end plates

$$S = \Phi_{,\gamma}, \quad N \equiv N_\theta - \psi' S = \Phi_{,e_\theta}. \tag{9}$$

Here, H is a radial stress resultant per unit undeformed length, $\Phi = \Phi(e_z, e_\theta, \gamma, k_z, k_\theta)$ is the strain-energy density, and

$$\Lambda_z = \sqrt{1 + 2e_z} \tag{10}$$

is the *axial stretch.* The extensional and (dimensionless) bending strains follow from Eqs. (7)–(9) and (37) of Simmonds (1996) as

$$e_z = u' + \tfrac{1}{2}(w'^2 + u'^2), \quad e_\theta = w, \quad \gamma = (1 + w)\psi' \tag{11}$$

and

$$k_z \equiv R\kappa_s = w'u'' - (1 + u')w'', \quad k_\theta \equiv R\kappa_\theta = u'. \tag{12}$$

We recall that one feature of Simmonds' (1996) field equations is that the torsional bending strain can be expressed in terms of the two bending strains k_z and k_θ and the extensional strains; hence, the strain-energy density is a function of *five* strain measures only.

If we introduce the change in meridional angle

$$\beta \equiv \tan^{-1}\left(\frac{w'}{1 + u'}\right), \tag{13}$$[1]

a meridional stress resultant

$$N_z \equiv \Phi_{,e_z} = \Lambda_z^{-1}\Phi_{,\Lambda_z}, \tag{14}$$

and set $V = P$, then we may form the following trigonometric combinations of (7) and (8):

$$H \cos\beta = P \sin\beta + \Lambda_z^{-1}(\Lambda_z^2\Phi_{,k_z})' - \Phi_{,k_\theta}\sin\beta \tag{15}$$

$$\Lambda_z N_z = P\cos\beta + H\sin\beta + 2\beta'\Lambda_z\Phi_{,k_z} - \Phi_{,k_\theta}\cos\beta. \tag{16}$$

Furthermore, from Eqs. (36) of Simmonds (1996), the bending strains may be expressed as

$$k_z = -\Lambda_z^2\beta',$$

$$k_\theta = \Lambda_z\cos\beta - 1 = -2\Lambda_z\sin^2(\beta/2) + (\Lambda_z - 1). \tag{17}$$

These expressions will prove useful.

Finally, we note the compatibility condition

$$\Lambda_\theta' = \Lambda_z \sin\beta \tag{18}$$

that follows from (10), (11), and (12) upon setting

$$\Lambda_\theta = 1 + e_\theta = 1 + w. \tag{19}$$

Boundary Conditions

We consider three types. At $z = 0$ and $z = \lambda$:

(i) Free ends (no local end moment or transverse shear stress resultant)

$$\Phi_{,k_z} = H = 0. \tag{20}$$

(ii) Hinged ends

$$\Phi_{,k_z} = w = 0. \tag{21}$$

(iii) Clamped ends

$$w = w' = 0. \tag{22}$$

A First Integral

Our field equations and those boundary conditions (20)–(22) which are *natural* may be obtained by rendering the dimensionless energy functional

$$\Pi[u, w, \psi] \equiv \int_0^\lambda [\phi(e_z, e_\theta, \gamma, k_z, k_\theta) - \omega^2(w + \tfrac{1}{2}w^2)]dz - pu(\lambda) - \tau\psi(\lambda) \tag{23}$$

stationary over all admissible displacement-rotation fields $\{u(z), w(z), \psi(z)\}$, that is, over all sufficiently smooth displacement-rotation fields such that

$$u(0) = w(0) = \phi(0) = w(\lambda) = 0$$

$$\text{and if clamped} \quad w'(0) = w'(\lambda) = 0. \tag{24}$$

In (23) and what follows,

$$(\Phi, mR^2\Omega^2, H, N_\theta, P, T) = ER\epsilon(\phi, \omega^2, h, n_\theta, p, \tau), \tag{25}$$

and the strains are to be expressed in terms of u, w, ϕ, and their derivatives by (11) and (12).

Because the integrand in (23) involves neither u, ψ nor the independent variable z, the Euler (field) equations implied by $\delta\Pi = 0$ admit three first integrals. The first two of these, whose mechanical meaning is clear, are just $(6)_2$ and $(6)_3$. The first integral associated with the absence an explicit dependence on z is new and has no immediate mechanical interpretation. To display its most useful form, we modify (23) by: (1) using (10), $(11)_3$, (17), and (19) to express ϕ in terms of Λ_z, Λ_θ, γ, β, and β'; (2) enforcing the compatibility condition (18) by means of a Lagrange multiplier (that turns out to be $h = H/ER\epsilon$); and (3) using $(11)_3$, $(12)_3$, $(17)_2$, (18), and (24) to set

$$u(\lambda) = \int_0^\lambda u'dz = \int_0^\lambda (\Lambda_z\cos\beta - 1)dz \quad \text{and}$$

$$\psi(\lambda) = \int_0^\lambda \psi' dz = \int_0^\lambda (\gamma/\Lambda_\theta)dz. \tag{26}$$

Altogether, our modified functional has the form

$$\Pi^*[\Lambda_z, \Lambda_\theta, \gamma, \beta] = \int_0^\lambda g(\Lambda_z, \Lambda_\theta, \Lambda_\theta', \gamma, \beta, \beta')dz, \tag{27}$$

where

$$g = \phi(\Lambda_z, \Lambda_\theta, \gamma, \beta, \beta') - \tfrac{1}{2}\omega^2(\Lambda_\theta^2 - 1) + h(\Lambda_\theta' - \Lambda_z\sin\beta) + p(1 - \Lambda_z\cos\beta) - \tau(\gamma/\Lambda_\theta). \tag{28}$$

By a well-known procedure in the Calculus of Variations (e.g., Gelfand and Fomin, 1963, p. 70), it follows that the Euler equations implied by $\delta\Pi^* = 0$ have the first integral

$$g - \left(\frac{\partial g}{\partial \Lambda_\theta'}\right)\Lambda_\theta' - \left(\frac{\partial g}{\partial \beta'}\right)\beta' = C, \quad \text{a constant.} \tag{29}$$

[1] Equal to $\frac{1}{2}\pi - \bar{\alpha}$ in Simmonds' (1996) notation.

Downloaded 04 May 2010 to 171.66.16.26. Redistribution subject to ASME license or copyright; see http://www.asme.org/terms/Terms_Use.cfm

That is, from (28),

$$\phi(\Lambda_z, \Lambda_\theta, \gamma, \beta, \beta') - \tfrac{1}{2}\omega^2\Lambda_\theta^2 - h\Lambda_z \sin\beta - \phi_{,\beta'}\beta'$$

$$- p\Lambda_z \cos\beta - \tau(\gamma/\Lambda_\theta) = C - \tfrac{1}{2}\omega^2 - p \equiv C^*. \quad (30)$$

Strain-Energy Densities

To make headway analytically, we shall consider only two types, one for shells (i) and one for membranes (ii):

(i) Anisotropic, uncoupled, homogeneous, quadratic

$$\Phi = \tfrac{1}{2}ER\epsilon(A_{\alpha\beta\gamma\delta}e_{\alpha\beta}e_{\gamma\delta} + \epsilon^2 C_{\alpha\beta}k_\alpha k_\beta), \quad (31)$$

where E is some convenient nondimensionalizing elastic modulus, $\{e_{11}, 2e_{12}, e_{22}\} = \{e_\theta, \gamma, e_z\}$, $\{k_1, k_2\} = \{k_\theta, k_z\}$, and we sum from 1 to 2 over a repeated Greek subscript.

(ii) Membrane-like, homogeneous

$$\Phi = ER\epsilon f(\Lambda_z, \Lambda_\theta, \gamma). \quad (32)$$

The next section will be devoted to strain-energy densities of type (i).

In what follows it is useful to refer to the *norm* of the extensional and bending strains—the latter referring to the extensional strains in the outer fibers of the tube—which we define, respectively, by

$$e_E \equiv \sqrt{e_{\alpha\beta}e_{\alpha\beta}} = \sqrt{e_z^2 + e_\theta^2 + \tfrac{1}{2}\gamma^2} \quad (33)$$

and

$$e_B \equiv \epsilon\sqrt{k_\alpha k_\alpha} = \epsilon\sqrt{k_z^2 + k_\theta^2}. \quad (34)$$

The norm of the total strain field is defined by

$$e \equiv \sqrt{e_E^2 + e_B^2}. \quad (35)$$

Quadratic Strain-Energy Densities

When Φ is quadratic, it is simpler and leads to more symmetric (and better conditioned) equations to take as unknowns the dimensionless horizontal stress resultant h and the change in meridional angle β and to work with the *mixed-energy density*

$$\Psi \equiv \Phi - N_z e_z - N e_\theta - S\gamma, \quad (36)$$

where N is defined in $(9)_2$. Thus, solving the linear relations (9) and (14) for e_z, e_θ, and γ in terms of N_z, N, and S, we have

$$\Psi = \tfrac{1}{2}[ER\epsilon^3 C_{\alpha\beta}k_\alpha k_\beta - (ER\epsilon)^{-1}B_{\alpha\beta\gamma\delta}N_{\alpha\beta}N_{\gamma\delta}]$$

$$= \Psi(N_z, N, S, k_z, k_\theta), \quad (37)$$

where $\{N_{11}, N_{22}, N_{12}\} = \{N, N_z, S\}$ and the $B_{\alpha\beta\gamma\delta}$ are dimensionless compliances having the usual symmetries ($B_{1112} = B_{1121}$, $B_{1212} = B_{2121}$, etc.). Thus,

$$e_z = -\Psi_{,N_z}, \quad e_\theta = -\Psi_{,N}, \quad \gamma = -\Psi_{,S}. \quad (38)$$

Our basic field equations are the moment equilibrium condition (15) and the compatibility condition (18).

To further reduce (15) and (18), we first note that

$$\Phi_{,k_\theta} = \Psi_{,k_\theta} = ER\epsilon^3(C_{11}k_\theta + C_{12}k_z),$$

$$\Phi_{,k_z} = \Psi_{,k_z} = ER\epsilon^3(C_{22}k_z + C_{12}k_\theta) \quad (39)$$

$$ER\epsilon e_\theta = B_{1111}N + B_{1122}N_z + B_{1112}S \quad (40)$$

$$ER\epsilon e_z = B_{2222}N_z + B_{2211}N + B_{2212}S, \quad ER\epsilon\gamma = 2B_{1212}S. \quad (41)$$

Next—and this is our most important simplification—because any quadratic strain-energy density is, essentially, an approximation in which terms cubic in strains have been neglected, i.e., terms of the *relative* order e, then in any term involving Φ, we may ignore strains compared to 1. Thus, substituting (17) into (39), the resulting expressions into (15), setting $\Lambda_z \approx 1$, and noting (25), we obtain

$$h\cos\beta = p\sin\beta$$

$$- \epsilon^2[C_{22}\beta'' - 4C_{11}\sin^3(\beta/2)\cos(\beta/2)]. \quad (42)$$

Turning to (18), we take e_θ from (40), but, consistent with our small strain approximation, we set $N \approx N_\theta$. Then, we replace N_θ by the right side of $(6)_1$ with $1 + w = 1 + e_\theta \approx 1$. To replace N_z, we use (16) with $\Lambda_z \approx 1$. At the same time we make another major simplification by noting that in working with (31) we are ignoring coupling terms of the form $\frac{1}{2}ER\epsilon^3 D_{\alpha\beta\gamma}e_{\alpha\beta}k_\gamma$ which, by Cauchy's inequality, are $O(ER\epsilon^2 e^2)$. See Koiter (1960). This implies that in the stress-strain relation (14) we may neglect terms of the form $ER\epsilon^3(D_{221}k_\theta + D_{222}k_z)$, and thus the last two terms in (16) involving Φ. Finally, we use $(6)_3$ and the small strain approximation to set $S \approx T$. Altogether, we have

$$e_\theta = B_{1111}(h' + \omega^2)$$

$$+ B_{1122}(p\cos\beta + h\sin\beta) + B_{1112}\tau. \quad (43)$$

Substituting this expression into (18), differentiating, and again setting $\Lambda_z \approx 1$, we obtain

$$B_{1111}h'' + B_{1122}(p\cos\beta + h\sin\beta)' = \sin\beta. \quad (44)$$

We now carry out the differentiation in the second term on the left of (44) and use (42) to replace part of the resulting expression. The remaining part, when combined with the right side of (44), contains the factor $(1 - B_{1122}h')$. But, by (43), h' is of the order of magnitude of the strains, and hence may be neglected compared to 1. Re-introducing the bending strains from (17), we find that (44) can be rewritten as

$$[B_{1111}h' - \tfrac{1}{2}\epsilon^2 B_{1122}(C_{22}k_z^2 - C_{11}k_\theta^2)]' = \sin\beta. \quad (45)$$

But the first term in brackets on the left is $O(e_E)$ while the second, by (34), is $O(e_B^2)$ and hence negligible, leaving us with the (much simplified) field equation

$$B_{1111}h'' = \sin\beta. \quad (46)$$

A Simplified First Integral. If we multiply (42) by β', (46) by h' and add the resulting expressions, we obtain a perfect differential which, when integrated, yields

$$h\sin\beta + p\cos\beta - \tfrac{1}{2}\{B_{1111}h'^2$$

$$+ \epsilon^2[4C_{11}\sin^4(\beta/2) - C_{22}\beta'^2]\} = \bar{C}, \quad (47)$$

a constant. This is a simplified form of (30). Because we impose the same boundary conditions at each end of the tube, $\beta(\lambda/2) = h(\lambda/2) = 0$ at the center. Moreover, if we assume that bending effects are confined to narrow end zones, then we may set $\bar{C} = P$ in which case (47) takes the form

$$h\sin\beta - 2p\sin^2(\beta/2)$$

$$= \tfrac{1}{2}\{B_{1111}h'^2 + \epsilon^2[4C_{11}\sin^4(\beta/2) - C_{22}\beta'^2]\}. \quad (48)$$

Note that the first term on the right is $O(e_E^2)$ while the second is $O(e_B^2)$; hence nothing further can be neglected. However, we can use (17) and (48) to express (43) as

$$e_\theta = B_{1111}[h'(1 + \underline{h'}) + \omega^2]$$

$$+ B_{1122}[p + \underline{\tfrac{1}{2}\epsilon^2(C_{11}k_\theta^2 - C_{22}k_z^2)}] + B_{1122}\tau. \quad (49)$$

But the underlined terms are of relative $O(e)$ and hence negligible. Thus, we may approximate the hoop strain by

$$e_\theta = B_{1111}(h' + \omega^2) + B_{1122}p + B_{1112}\tau. \quad (50)$$

Downloaded 04 May 2010 to 171.66.16.26. Redistribution subject to ASME license or copyright; see http://www.asme.org/terms/Terms_Use.cfm

Boundary Conditions. From (17), (20)–(22), (39), and (50), these may be summarized in terms of our two basic unknowns h and β as follows: at $z = 0$ and $z = \lambda$,

free: $h = 0.$ (51)

free or hinged: $\epsilon^2[C_{22}\beta' + 2C_{12}\sin^2(\beta/2)] = 0.$ (52)

hinged or clamped:

$$B_{1111}(h' + \omega^2) + B_{1122}p + B_{1112}\tau = 0. \quad (53)$$

clamped: $\beta = 0.$ (54)

Exact Solution for Free Ends. As we may verify immediately,

$$h = \beta = 0 \quad (55)$$

satisfies the field Eqs. (42) and (46) and the boundary conditions (51) and (52). Then $(11)_2$ and (50) yield

$$w = e_\theta = B_{1111}\omega^2 + B_{1122}p + B_{1112}\tau. \quad (56)$$

Linearization. We can gain much insight into the effects of anisotropy on rotating tubes subject to hinged or clamped boundary conditions by linearizing our governing equations. Thus, the field Eqs. (42) and (46) reduce to

$$h = p\beta - \epsilon^2 C_{22}\beta'' \quad (57)$$

$$B_{1111}h'' = \beta, \quad (58)$$

while the boundary conditions (52)–(54) take the form: at $z = 0$ and $z = \lambda$,

hinged: $\beta' = 0.$ (59)

hinged or clamped:

$$B_{1111}(h' + \omega^2) + B_{1122}p + B_{1112}\tau = 0. \quad (60)$$

clamped: $\beta = 0.$ (61)

Introducing the change of variables and parameters

$$z = \delta\zeta, \quad (h, p) = \epsilon\sqrt{C_{22}/B_{1111}}(\eta, \rho),$$
$$\delta = \epsilon^{1/2}(B_{1111}C_{22})^{1/4}\zeta \quad (62)$$

(where δ and η will be used later) and eliminating h between (57) and (58), we obtain the differential equation

$$\beta'''' - \rho\beta'' + \beta = 0, \quad \beta' = d\beta/d\zeta. \quad (63)$$

This equation has solutions of the form

$$\beta = Ce^{a\zeta}, \quad a, C = \text{constants}, \quad (64)$$

where a satisfied the characteristic equation

$$a^4 - \rho a^2 + 1 = 0. \quad (65)$$

This is precisely the equation discussed by Libai and Simmonds (1988) on pp. 215–216 where the *critical* (*dimensionless*) *axial load,* i.e., the *buckling load,* is defined as the smallest value of ρ, namely $\rho_{cr} = -2$, at which a becomes purely imaginary (thus yielding solutions which are purely oscillatory). Henceforth, we assume that $\rho > -2$. In terms of the dimensionless *transition number*

$$\sigma = \frac{B_{1111}\omega^2 + B_{1122}p + B_{1112}\tau}{\epsilon^{1/2}(B_{1111}C_{22})^{1/4}} \equiv \frac{\nu}{\delta} \quad (66)$$

—the terminology will be explained later—the boundary condition (52) reads: at $z = 0$ and $z = \lambda$,

hinged or clamped: $\beta'''' - \rho\beta' = \sigma.$ (67)

Returning to dimensional variables for a moment, we infer from (62), (64), and (65) that, at the ends of the tube, there are boundary layers whose widths are of the order of magnitude

$$\sqrt{\epsilon R^2}(B_{1111}C_{22})^{1/4}\begin{cases} 1 & \text{if } \rho = O(1) \\ \rho^{\pm 1/2} & \text{if } \rho \gg 1 \end{cases}. \quad (68)$$

The first factor in (68) is the width of the well-known bending boundary layer in *isotropic* shell theory. Remarkably, the effects of general anisotropy are manifested only through the *single* dimensionless parameter, $(B_{1111}C_{22})^{1/4}$. For example, a symmetrically laminated carbon-epoxy tube can have a hoop modulus 15 times that in the axial direction which implies a boundary layer width $15^{-1/4} \approx \frac{1}{2}$ that of an isotropic tube.

To complete our solution, we apply the boundary conditions (59), (61), and (67). With

$$\gamma_1 = \tfrac{1}{2}\sqrt{2 + \rho}, \quad \gamma_2 = \tfrac{1}{2}\sqrt{2 - \rho}, \quad \bar{\zeta} = \lambda/\delta, \quad (69)$$

and $-2 < \rho < 2$, we find that for clamped ends

$$\beta = \frac{\sigma}{\gamma_2 \sinh \gamma_1\bar{\zeta} - \gamma_1 \sin \gamma_2\bar{\zeta}}[\sin \gamma_2\zeta \sinh \gamma_1(\zeta - \bar{\zeta}) - \sin \gamma_2(\zeta - \bar{\zeta}) \sinh \gamma_1\zeta] \quad (70)$$

while for hinged ends

$$\beta = -\frac{\sigma}{2\gamma_1\gamma_2(\sinh \gamma_1\bar{\zeta} + \cos \gamma_2\bar{\zeta}) \sin \gamma_2\bar{\zeta}} \times \{\gamma_1 \sin \gamma_2\bar{\zeta}[\sinh \gamma_1\zeta \sin \gamma_2(\zeta - \bar{\zeta}) - \sinh \gamma_1(\zeta - \bar{\zeta}) \sin \gamma_2\zeta] + \gamma_2[\cosh \gamma_1\zeta \sin \gamma_2\zeta + \cosh \gamma_1(\zeta - \bar{\zeta}) \sin \gamma_2(\zeta - \bar{\zeta})] + \gamma_2 \cos \gamma_2\bar{\zeta}[\cosh \gamma_1\zeta + \sin \gamma_2(\zeta - \bar{\zeta}) + \cosh \gamma_1(\zeta - \bar{\zeta}) \sin \gamma_2\zeta]\}. \quad (71)$$

If $\rho > 2$, we merely replace γ_2 by $\gamma_3 \equiv \frac{1}{2}\sqrt{\rho - 2}$ and $\sin \gamma_2 \ldots$ by $\sinh \gamma_3 \ldots$. Solutions for $\rho = 2$ may be obtained from (70) and (71) by taking the limit as $\rho \to 2-$.

Nonlinear Membrane Theory. This theory is obtained by setting $\epsilon = 0$ in the field Eqs. (42) and (48) and in the boundary condition (52). If we introduce a new dimensionless load parameter

$$q \equiv \frac{2\rho}{\sigma^2} = \frac{2B_{1111}p}{(B_{1111}\omega^2 + B_{1122}p + 2B_{1112}\tau)^2} \quad (72)$$

and the change of variables

$$x = z/\nu \quad \text{and} \quad y = q \tan \beta, \quad (73)$$

then (42), (62), and (66) yield

$$h = \tfrac{1}{2}(\nu^2/B_{1111})y \quad \text{or} \quad \eta = \tfrac{1}{2}\sigma^2 y, \quad (74)$$

while (48) (with $\epsilon = 0$) and (53) reduce to

$$(1/4)(dy/dx)^2 = \sqrt{q^2 + y^2} - q, \quad 0 < x < \lambda/\nu \quad (75)$$

and

$$dy/dx = -2 \quad \text{at} \quad x = 0, \quad \lambda/\nu. \quad (76)$$

If we assume that (75) holds at the ends of the shell as well, then we can replace (76) by the condition

$$y = \sqrt{1 + 2q} \quad \text{at} \quad x = 0, \quad \lambda/\nu, \quad (77)$$

Downloaded 04 May 2010 to 171.66.16.26. Redistribution subject to ASME license or copyright; see http://www.asme.org/terms/Terms_Use.cfm

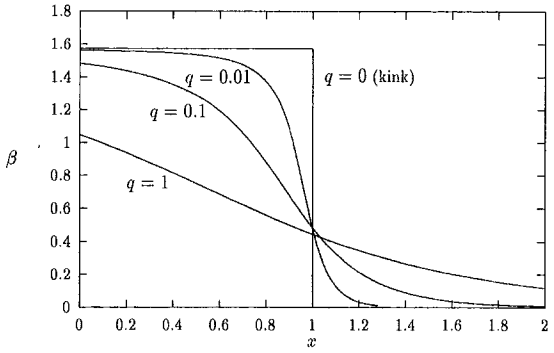

Fig. 2 Meridional angle of rotation β versus scaled axial distance $x = z/\nu$ for several values of the combined axial load parameter q. See (66) and (72) for definitions of ν and q, respectively.

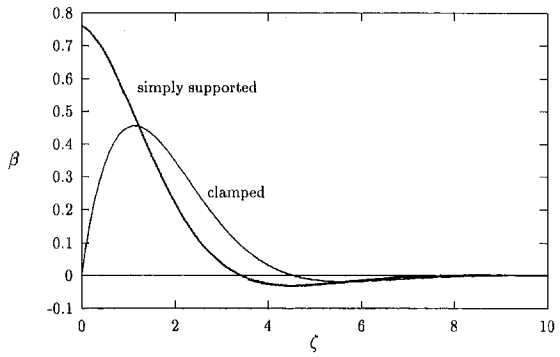

Fig. 4 Meridional angle of rotation β versus scaled axial distance $\zeta = z/\delta$ for the transition number $\sigma = 1$ and no axial load. See $(62)_3$ and (66) for definitions of δ and σ, respectively.

which serves as an *initial condition* for (75). Moreover, From $(6)_1$, (25), (66), (73), (74), and (76), we find that

$$B_{1111}n_\theta = (\nu/2)(dy/dx) + B_{1111}\omega^2 = \begin{cases} -(B_{1122}p + 2B_{1112}\tau) & \text{at} \quad x = 0 \\ B_{1111}\omega^2 > 0 & \text{at} \quad x = \lambda/2\nu \end{cases}. \tag{78}$$

Thus, if $B_{1122}p > B_{1112}\tau$, *there is wrinkling near the ends of the tube,* but we do not analyze this phenomenon further.

Of particular interest is the behavior of y as the axial tension P, and hence q, approaches zero. Concentrating on the left half of the tube where $dy/dx \leq 0$ and denoting this limiting solution by Y, we have, from (75),

$$dY/dx = -2\sqrt{Y} \tag{79}$$

which is subject to symmetry conditions $Y = dY/dx = 0$ at the center of the tube and the limiting form of (77), namely,

$$Y = 1 \quad \text{at} \quad x = 0, \quad \lambda/\nu. \tag{80}$$

One easily verifies that the only smooth solution of (79) satisfying these conditions is

$$Y = \begin{cases} (1 - x)^2, & 0 \leq x \leq 1 \\ 0, & 1 < x \leq \frac{1}{2}x^*, \end{cases} \tag{81}$$

where, from $(73)_1$,

$$x^* = \lambda/2\nu. \tag{82}$$

This limit solution has interesting implications. From $(73)_2$ and (81),

$$\lim_{q\to 0} \beta(x, q) = \begin{cases} \pi/2, & 0 \leq x \leq 1 \\ 0, & 1 < x \leq \frac{1}{2}x^*. \end{cases} \tag{83}$$

Thus, in the membrane limit, a right-angle *kink* develops at a finite distance $R\nu = O(Re_E)$ from each end. (The occurrence of such flanges in circular cylindrical membranes under other types of loading is discussed in Libai and Simmonds (1988).)

For $q > 0$, i.e., when there is a tensile load on the spinning tube, we may solve (75) exactly (although implicitly) by first taking the negative square root of the right side and then separating variables to obtain

$$\frac{dy}{\sqrt{\sqrt{q^2 + y^2} - q}} = -2dx. \tag{84}$$

Integrating both sides of (84) from 0 to x and incorporating the initial condition (77), we find that

$$x = g_0 - g + \frac{\sqrt{2q}}{4} \ln\left[\frac{(g_0 - \sqrt{2q})(g + \sqrt{2q})}{(g_0 + \sqrt{2q})(g - \sqrt{2q})}\right], \tag{85}$$

where

$$g = \sqrt{\sqrt{q^2 + y^2} + q} \tag{86}$$

and, from (77),

$$g_0 = \sqrt{1 + 2q}. \tag{87}$$

Figures 2 and 3 are, respectively, graphs of β and y versus x for several values of q.

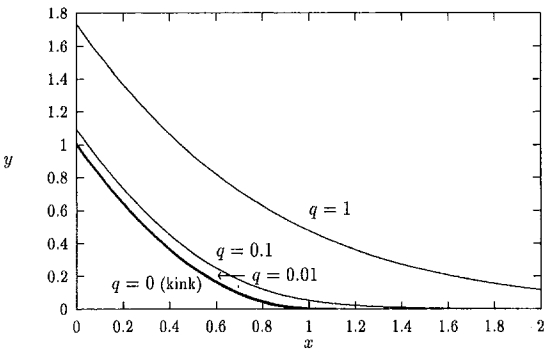

Fig. 3 Dimensionless radial stress resultant y versus scaled axial distance $x = z/\nu$ for several values of the combined axial load parameter q. See (66), (72), and $(74)_1$ for definitions of ν, q, and y, respectively.

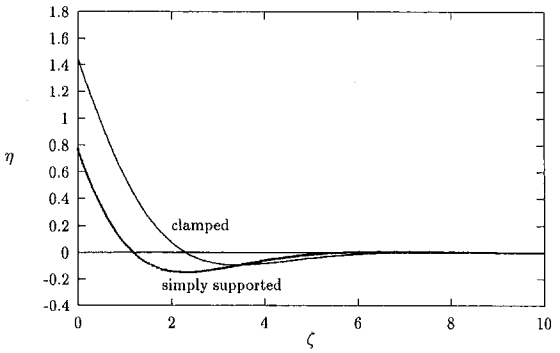

Fig. 5 Dimensionless radial stress resultant η versus the scaled axial distance $\zeta = z/\delta$ for the transition number $\sigma = 1$ and no axial load. See $(62)_{2,3}$ and (66) for definitions of η, δ, and σ, respectively.

Downloaded 04 May 2010 to 171.66.16.26. Redistribution subject to ASME license or copyright; see http://www.asme.org/terms/Terms_Use.cfm

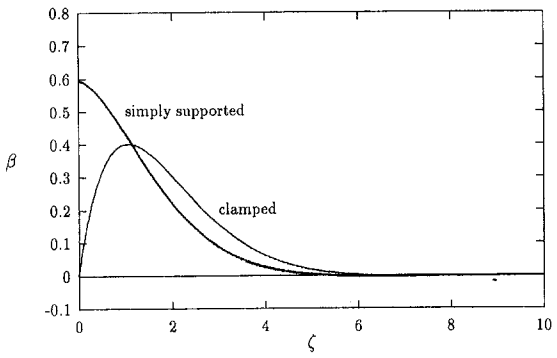

Fig. 6 Meridional angle of rotation β versus scaled axial distance $\zeta = z/\delta$ for the transition number $\sigma = 1$ and the dimensionless axial parameter $\rho = 1$. See $(62)_{2,3}$ and (66) for definitions of ρ, δ, and σ, respectively.

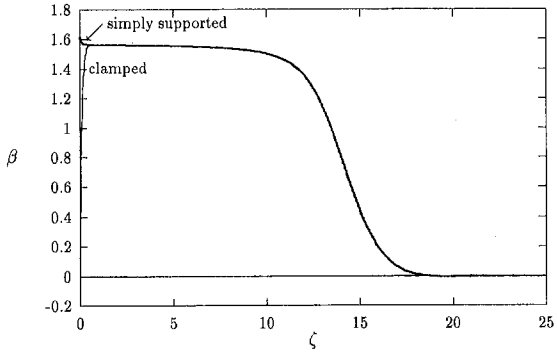

Fig. 8 Meridional angle of rotation β versus scaled axial distance $\zeta = z/\delta$ for the transition number $\sigma = 1$ and no axial load. See $(62)_3$ and (66) for definitions of δ, and σ, respectively.

The Full Nonlinear Bending Theory. In the linear theory, we found that there was a boundary layer at the ends of dimensionless width $O(\delta)$, whereas in the nonlinear membrane theory, the change of independent variable $(73)_1$ and the subsequent smooth behavior of the scaled equations showed the existence of a boundary layer of dimensionless width $O(\nu)$, where δ and ν are defined in (66).

If we introduce the change of variables and parameters (62) used in studying the linearized version of our equations and, as before, set $d/d\zeta = {}^{\cdot}$, then our field equations (46) and (48) can be written as the system of first-order differential equations

$$\eta^{\cdot} = v, \quad v^{\cdot} = \sin\beta \tag{88}$$

$$\beta^{\cdot} = \pm\sqrt{v^2 - 2\eta\sin\beta + 4\rho\sin^2(\beta/2) + 4\epsilon C_1\sin^4(\beta/2)}, \tag{89}$$

while the boundary conditions (52)–(54) assume the form: at $\zeta = 0$ and $\zeta = \bar{\zeta} = \lambda/\delta$,

$$\text{hinged:} \quad \beta^{\cdot} + 2\sqrt{\epsilon}C_2\sin^2(\beta/2) = 0. \tag{90}$$

$$\text{hinged or clamped:} \quad v + \sigma = 0. \tag{91}$$

$$\text{clamped:} \quad \beta = 0. \tag{92}$$

Here,

$$C_1 \equiv C_{11}\sqrt{B_{1111}/C_{22}} \quad \text{and} \quad C_2 = C_{12}B_{1111}^{1/4}/C_{22}^{3/4}. \tag{93}$$

Due to symmetry, we need only solve these equations on the interval $0 \le \zeta \le \bar{\zeta}/2$.

The *qualitative* picture of the solutions of these equations is as follows: (i) if $\sigma \ll 1$, linear theory holds with $\beta, \eta = O(\sigma)$; (ii) if $\sigma = O(1)$ all terms in our system may be important; (iii) if $\sigma \gg 1$, there are (relatively narrow) bending boundary layers at $\zeta = 0$ and at $\zeta = O(\sigma)$ (i.e., near $x = 1$ where nonlinear membrane theory predicts a kink). Nonlinear membrane theory holds sway between the first two layers and the trivial free-edge solution holds sway in the interior.

The solution in case (i) has been given in the subsection entitled **Linearization**; the solution in case (ii) was obtained numerically using a using a straightforward shooting technique and is displayed in Figs. 4–7 for $\sigma = 1$ and $\rho = 0$ (no axial load) and $\rho = 1$ (axial tension). So long as C_1 and C_2 are $O(1)$, their influence is, at most, $O(\sqrt{\epsilon})$ and so their influence in these figures is, to a first approximation, negligible.

In case (iii), the following scaling is necessary as $\sigma \to \infty$ to obtain a well-posed problem for the very narrow bending boundary layer at $\zeta = 0$:

$$\eta = \sigma^2 U_\infty, \quad v = -\sigma V_\infty, \quad \zeta = t/\sigma. \tag{94}$$

Thus, the field Eqs. (88) and (89) reduce to

$$\frac{dU_\infty}{dt} = 0, \quad \frac{dV_\infty}{dt} = 0, \quad \frac{d\beta_\infty}{dt} = \pm\sqrt{V_\infty^2 - 2U_\infty\sin\beta_\infty} \tag{95}$$

while the boundary conditions (90)–(92) may be summarized as: at $t = 0$ and $t = \sigma\bar{\zeta} = (\nu/\delta^2)\lambda$,

$$\text{hinged:} \quad \frac{d\beta_\infty}{dt} = 0;$$

$$\text{hinged or clamped:} \quad V_\infty = 1;$$

$$\text{clamped:} \quad \beta_\infty = 0. \tag{96}$$

Further, by $(62)_1$, (66), and $(73)_1$, the independent variables in the linear bending and nonlinear membrane theories are related by $\zeta = \sigma x$. Hence, as $\sigma \to \infty$ for ζ fixed, $t \to \infty$ and $x \to$

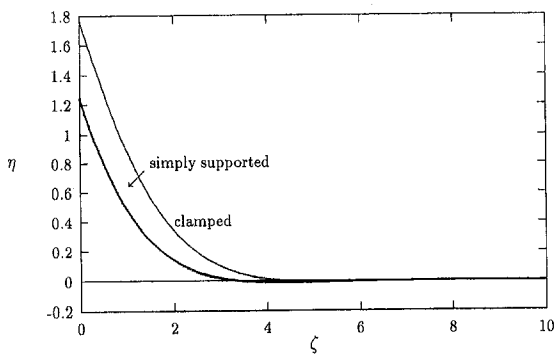

Fig. 7 Dimensionless radial stress resultant η versus the scaled axial distance $\zeta = z/\delta$ for the transition number $\sigma = 1$ and the dimensionless axial load $\rho = 1$. See $(62)_{2,3}$ and (66) for definitions of η, ρ, δ, and σ, respectively.

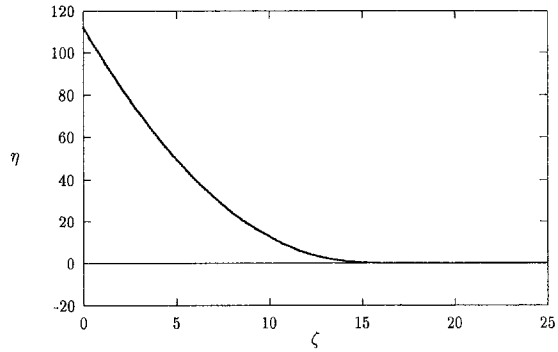

Fig. 9 Dimensionless radial stress resultant η versus the scaled axial distance $\zeta = z/\delta$ for the transition number $\sigma = 1$ and no axial load. See $(62)_{2,3}$ and (66) for definitions of η, δ, and σ, respectively.

Downloaded 04 May 2010 to 171.66.16.26. Redistribution subject to ASME license or copyright; see http://www.asme.org/terms/Terms_Use.cfm

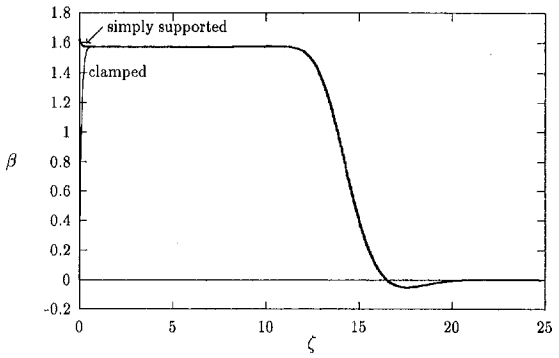

Fig. 10 Meridional angle of rotation β versus scaled axial distance $\zeta = z/\delta$ for the transition number $\sigma = 15$ and the dimensionless axial load $\rho = 1$. See $(62)_{2,3}$ and (66) for definitions of ρ, δ, and σ, respectively.

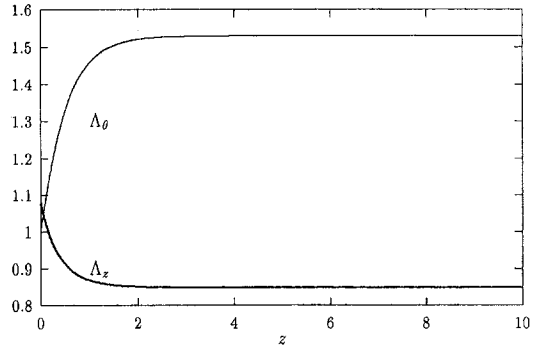

Fig. 12 Radial and axial stretches Λ_θ and Λ_z versus dimensionless axial distance z for $\omega = 0.5$, $p = 0.05$ and $\tau = 0.05$. See (25) for definitions of ω, p, and τ, respectively.

0 so that, from $(62)_2$, (72), (74), (77), (94), and (95), $U_\infty(t) = \frac{1}{2}$ and $V_\infty(t) = 1$. Thus, (95) and (96) yield

$$\beta_\infty = \begin{cases} \pi/2 & \text{(hinged)} \\ \pi/2 - 4\tan^{-1}\left[e^{-t/\sqrt{2}}\tan(\pi/8)\right] & \text{(clamped)} \end{cases}. \quad (97)$$

For the other (very narrow) boundary layer that develops near $\zeta = \sigma$ for $\sigma \gg 1$, we must use the unsimplified system of differential Eqs. (88) and (89). If we introduce a translated independent variable by setting $\zeta = \sigma + \xi$, so that the second boundary layer occurs around $\xi = 0$, then (88) and (89) are unchanged in form. However, as $\sigma \to \infty$, their solutions η, v, β are subject to the condition that as $\xi \to -\infty$, they must approach the nonlinear membrane solutions as $x \to 1+$, and that as $\xi \to +\infty$, these solutions must all approach zero. Numerical solutions for β for $\sigma = 15$, $\rho = 0$ (no axial load), and $\rho = 1$ are given in Figs. 8–11.

A Remarkable Simplification. Although our fully anisotropic, quadratic mixed strain-energy density ψ given by (37) depends on *nine* (dimensionless) elastic parameters, none of these parameters appears explicitly in our final solutions to a first approximation—that is, to within a relative error of $O(\sqrt{\epsilon})$. Rather they appear in "disguised" form in the combined load parameters ρ and σ, defined in $(62)_2$ and (66), and in the scaled independent variable ζ, defined in $(62)_1$. A glance at (89) and (90) shows why: the combined elastic parameters C_1 and C_2, defined in (93), are multiplied, respectively, by ϵ and $\sqrt{\epsilon}$. The practical implications of these observations are obvious: *In a design study of a fully anisotropic spinning tube subject to axial tension and torque only two (combined) parameters, ρ and σ, are of prime importance.*

Large-Strain Membrane Theory

Using $(11)_1$, (19), (25), and (32), we obtain from $(6)_1$, $(6)_3$, and (9) one algebraic and one differential equation:

$$\Lambda_\theta f_{,\gamma} = \tau \quad (98)$$

and

$$h' = f_{,\Lambda_\theta} + (\gamma/\Lambda_\theta^2)\tau - \Lambda_\theta\omega^2. \quad (99)$$

From (15) follows

$$\sin\beta = \frac{h}{\sqrt{p^2 + h^2}}, \quad \cos\beta = \frac{p}{\sqrt{p^2 + h^2}}. \quad (100)$$

Thus, by (14), (32), and (100), (16) and (18) take the form

$$f_{,\Lambda_z} = \sqrt{p^2 + h^2} \quad \text{and} \quad \Lambda_\theta' = \Lambda_z h/\sqrt{p^2 + h^2}. \quad (101)$$

Our final field equation is algebraic and follows upon substituting (100) and the strain-energy density (32) into the first integral (30):

$$f(\Lambda_z, \Lambda_\theta, \gamma) - (1/2)\omega^2\Lambda_\theta - \Lambda_z\sqrt{p^2 + h^2} - \tau(\gamma/\Lambda_\theta) = C^*. \quad (102)$$

The boundary conditions are

$$\Lambda_\theta(0) = 1, \quad h(\lambda/2) = 0. \quad (103)$$

Neo-Hookean Strain-Energy Density. For a membrane, the three-dimensional strain-energy density reduces to the well-known expression

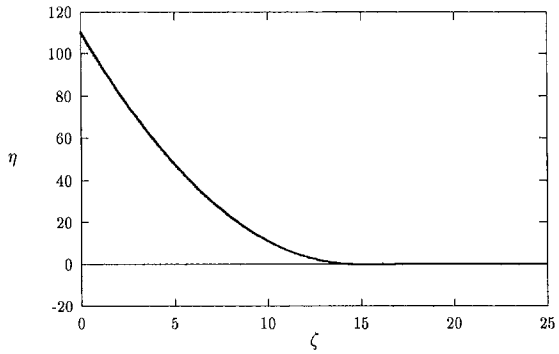

Fig. 11 Dimensionless radial stress resultant η versus the scaled axial distance $\zeta = z/\delta$ for the transition number $\sigma = 15$ and the dimensionless axial load $\rho = 1$. See $(62)_{2,3}$ and (66) for definitions of η, ρ, δ, and σ, respectively.

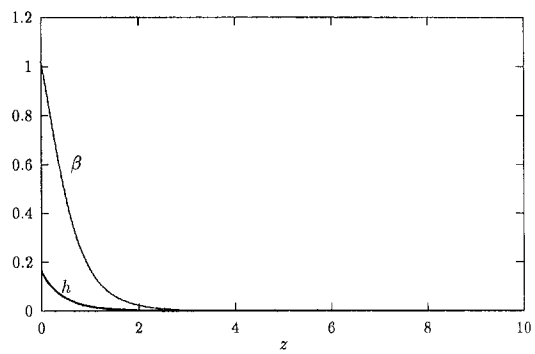

Fig. 13 Meridional angle of rotation β and dimensionless radial stress resultant h versus axial distance z for $\omega = 0.5$, $p = 0.05$, and $\tau = 0.05$. See (25) for definitions of ω, p, and τ, respectively.

Downloaded 04 May 2010 to 171.66.16.26. Redistribution subject to ASME license or copyright; see http://www.asme.org/terms/Terms_Use.cfm

$$f = \frac{1}{6}\left(\lambda_z^2 + \lambda_\theta^2 + \frac{1}{\lambda_z^2\lambda_\theta^2} - 3\right), \tag{104}$$

where λ_z^2 and λ_θ^2 are the eigenvalues of the two-dimensional right Cauchy-Green deformation tensor $\mathbf{G}$ and where the factor of $\frac{1}{6}$ arises because we have have set the shear modulus for an incompressible material equal to $E/3$. From (4), (10), (11), and (19),

$$d\bar{\mathbf{y}}\cdot d\bar{\mathbf{y}} = d\mathbf{y}\cdot\mathbf{G}\cdot d\mathbf{y} = R^2[(\Lambda_z^2 + \gamma^2)dz^2 + 2\Lambda_\theta\gamma dz d\theta + \Lambda_\theta^2 d\theta^2]. \tag{105}$$

Hence,

$$\text{trace}\,\mathbf{G} = \Lambda_z^2 + \Lambda_\theta^2 + \gamma^2 \quad \text{and} \quad \det\mathbf{G} = \Lambda_z^2\Lambda_\theta^2 \tag{106}$$

from which we conclude that

$$\begin{Bmatrix}\lambda_z^2\\ \lambda_\theta^2\end{Bmatrix} = (1/2)[\Lambda_z^2 + \Lambda_\theta^2 + \gamma^2 \pm \sqrt{(\Lambda_z^2 - \Lambda_\theta^2)^2 + \gamma^2(\gamma^2 + 2\Lambda_z^2 + 2\Lambda_\theta^2)}]. \tag{107}$$

Thus, (104) takes the form

$$f = \frac{1}{6}\left(\Lambda_z^2 + \Lambda_\theta^2 + \gamma^2 + \frac{1}{\Lambda_z^2\Lambda_\theta^2} - 3\right). \tag{108}$$

(It is interesting to note that the shear strain γ enters this expression *quadratically,* just as it does in the linear theory of elasticity based on a quadratic strain-energy density.)

Our field equations now reduce as follows: from (98) and (108),

$$\gamma = 3\tau/\Lambda_\theta \tag{109}$$

which when substituted into (99), (101), and (102), along with (109) yields the four field equations (two differential and two algebraic)

$$h' = \frac{1}{3}\left(\Lambda_\theta - \frac{1}{\Lambda_z^2\Lambda_\theta^3}\right) + \frac{3\tau^2}{\Lambda_\theta^3} - \Lambda_\theta\omega^2 \tag{110}$$

$$\Lambda_\theta' = \Lambda_z h/\sqrt{p^2 + h^2} \tag{111}$$

$$\frac{1}{3}\left(\Lambda_z - \frac{1}{\Lambda_z^3\Lambda_\theta^2}\right) = \sqrt{p^2 + h^2} \tag{112}$$

$$\frac{1}{6}\left(\Lambda_z^2 + \Lambda_\theta^2 + \frac{1}{\Lambda_z^2\Lambda_\theta^2} - 3\right) - (1/2)\omega^2 - \Lambda_z\sqrt{p^2 + h^2} - \frac{3\tau^2}{2\Lambda_\theta^2} = C^*. \tag{113}$$

The boundary conditions (103) remain unchanged.

We solved these equations numerically by first solving the governing equations for free ends. In this case, nothing depends on z, $h \equiv 0$, and (110) and (112) are easily solved for Λ_θ and Λ_z for any values of the dimensionless axial force and torque, p and τ. Next, the boundary condition $(103)_1$ of no radial displacement at the ends was replaced by the condition

$$\Lambda_\theta(0) = 1 + \Lambda. \tag{114}$$

We then did a continuation on the parameter Λ, from its known value for free ends to its value of zero for fixed ends. As is well known with this method, differentiation of all unknowns with respect to the continuation parameter Λ leads to a sequence of easily solved *linear* boundary value problems together with first-order differential equations in Λ. In Figs. 12 and 13, we have plotted the stretches Λ_θ and Λ_z, the meridional angle of rotation β, and the dimensionless radial stress resultant h versus the dimensionless axial length z for $\omega = 0.5$ and $p = \tau = 0.05$.

Acknowledgments

This research was supported by the U.S. Army Research Office under grant DAAH04-94-G-0189 and by the National Aeronautics and Space Administration under grant NAG-1-1854.

References

Gelfand, I. M., and Fomin, S. V., 1963, *Calculus of Variations,* Prentice-Hall, Englewood Cliffs, NJ.

Koiter, W. T., 1960, "A Consistent first Approximation in the General Theory of Thin Elastic Shells," *The Theory of Thin Elastic Shells* (W. T. Koiter, ed.,), North-Holland, Amsterdam, pp. 12–33.

Libai, A., and Simmonds, J. G., 1988, *The Nonlinear Theory of Elastic Shells: One Spatial Dimension,* Academic Press, Boston.

Simmonds, J. G., 1996, "A Simplified Displacement-Rotation Form for the Equations of Motion of Nonlinearly Elastic Shells of Revolution Undergoing Combined Bending and Torsion," ASME JOURNAL OF APPLIED MECHANICS, Vol. 63, pp. 539–542.

Downloaded 04 May 2010 to 171.66.16.26. Redistribution subject to ASME license or copyright; see http://www.asme.org/terms/Terms_Use.cfm

M. Sheplak[1]
Microsystems Technology Laboratories,
Room 39-561,
Mem. ASME

J. Dugundji
Technology Laboratory for
Advanced Composites,
Department of Aeronautics
and Astronautics,
Room 9-468

Massachusetts Institute of Technology,
77 Massachusetts Avenue,
Cambridge, MA 02139

Large Deflections of Clamped Circular Plates Under Initial Tension and Transitions to Membrane Behavior

The large deflections of a clamped circular plate are investigated over a wide range of transverse loadings and initial in-plane tension loads. The continuous transition from plate behavior to membrane behavior is described in detail, along with the development of the accompanying edge zone region where properties change rapidly. We give a simple approximation of this edge zone and its properties, provide limits for the validity of small deflection, linear theory, and note the similar effects of large in-plane tension and large transverse loading. The values and trends are presented in general nondimensional form, and should prove useful for the design of thin circular disks for microsensing applications.

1 Introduction

Recently, there has been considerable interest in using thin films of silicon-based materials in miniature mechanical devices and components (for example, Sze, 1994). Silicon micromachining processes, prevalent in the microelectronics industry, permit the miniaturization of sensors for the measurement of pressure, temperature, and other physical, electrical, and chemical quantities (Sze, 1994). One such application deals with the development of very small silicon pressure sensors for measuring both static and dynamic pressure (Clark and Wise, 1979; Schellin and Hess, 1992). Often these devices involve small, very thin films ($\approx$3000 Å) under initial membrane tension (Löfdahl et al., 1994). The tension present in these films can be as large as 1 GPa (Cho et al., 1992). Unfortunately, scaling arguments indicate that the deflection-based pressure sensitivity of such films is expected to degrade significantly (Chau and Wise, 1987). These arguments, however, were made without study of how initial tension affects the onset of nonlinearity. Furthermore, little is known concerning the relationship between initial tension and the characteristic stress and strain fields, which determine the performance of piezoresistive-based transducers (i.e., strain-gauge pressure sensors). Therefore, it is desirable to examine carefully the effects of internal stress on the structural behavior and linearity of these devices.

Several authors, including Nádai (1925) and Way (1934), examined the large deflection behavior for the pure plate case (discussed by Timoshenko and Woinowsky-Krieger (1959)). Zheng and Zhou (1990) extended the work of Way by providing the general analytical formulas for axisymmetric plates subjected to compliant boundary conditions. Way (1934) and, also, McPherson et al. (1942) have conducted some experimental measurements on large metal plates. More recently, Voorthuyzen and Bergveld (1984) used a finite-difference model to investigate the large-deflection characteristics of circular plates subjected to in-plane loading over a limited dimensional domain. Allen (1986) investigated the effects of in-plane loads on the center deflection characteristics by employing energy methods. None of these studies, however, investigated the combined effects of nonlinear loading and in-plane tension on the stress and strain fields. The present investigation deals specifically with the nonlinear deflection field of a clamped, circular plate with an initial in-plane tension load[2], subjected to a uniform pressure load over its surface. In particular, the effects of varying the initial tensile load from zero (pure plate case) to very large values (pure membrane case) are explored. In the following section, the governing equations are developed and the appropriate nondimensional scaling parameters identified. The small deflection characteristics and the transitions from pure plate to pure membrane behavior are detailed in Section 3. Section 4 contains the large deflection behavior and equivalent effects of initial tension and large loading, and the conclusions are presented in Section 5.

2 Basic Equations

Figure 1 shows a circular plate of radius a and thickness h, under an initial in-plane tension load, $N_r = N_0$, and a uniform transverse load, $p_z = p_0$. The equilibrium equations for the symmetrical bending of this plate are

$$\frac{dN_r}{dr} + \frac{N_r - N_\theta}{r} = 0, \tag{1}$$

$$\frac{d}{dr}(rQ_r) + \frac{d}{dr}\left(rN_r\frac{dw}{dr}\right) + rp_0 = 0, \tag{2}$$

and

$$Q_r = \frac{dM_r}{dr} + \frac{M_r - M_\theta}{r}, \tag{3}$$

where N_r, N_θ are the lateral loads, Q_r is the shear force, M_r, M_θ are the bending moments per unit length, and w is the deflection of the plate in the z-direction. The radial and tangential midplane

[1] Present address: Department of Aerospace Engineering, Mechanics & Engineering Science, 231 Aerospace Building, University of Florida, P.O. Box 116250, Gainesville, FL 32611-6250.

Contributed by the Applied Mechanics Division of THE AMERICAN SOCIETY OF MECHANICAL ENGINEERS for publication in the ASME JOURNAL OF APPLIED MECHANICS.

Discussion on the paper should be addressed to the Technical Editor, Professor Lewis T. Wheeler, Department of Mechanical Engineering, University of Houston, Houston, TX 77204-4792, and will be accepted until four months after final publication of the paper itself in the ASME JOURNAL OF APPLIED MECHANICS.

Manuscript received by the ASME Applied Mechanics Division, Feb. 3, 1997; final revision, May 14, 1997. Associate Technical Editor: W. K. Liu.

[2] For an introduction to the alternate problem of in-plane compression, the "buckling problem," see Timoshenko and Woinowsky-Krieger (1959).

 Copyright © 1998 by ASME

Downloaded 04 May 2010 to 171.66.16.26. Redistribution subject to ASME license or copyright; see http://www.asme.org/terms/Terms_Use.cfm

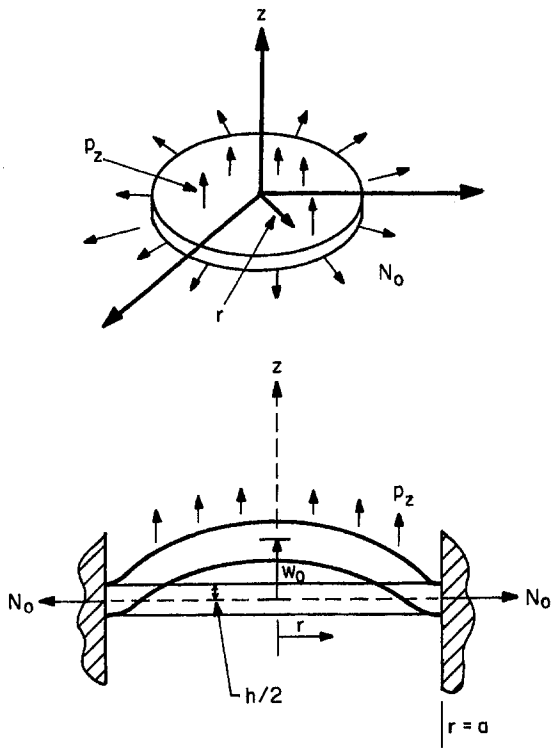

Fig. 1 Schematic of clamped circular disk with initial in-plane tension

strains assuming von Kármán plate theory for large plate deflections are

$$\epsilon_r = \frac{du}{dr} + \frac{1}{2}\left(\frac{dw}{dr}\right)^2 \quad \text{and} \quad \epsilon_\theta = \frac{u}{r}, \tag{4}$$

where u is the radial displacement, while the radial and tangential curvatures are

$$\mathcal{K}_r = -\frac{d^2w}{dr^2} \quad \text{and} \quad \mathcal{K}_\theta = -\frac{1}{r}\frac{dw}{dr}. \tag{5}$$

The lateral loads and moments per unit length for large plate deflections are

$$N_r = A(\epsilon_r + \nu\epsilon_\theta), \quad N_\theta = A(\epsilon_\theta + \nu\epsilon_r), \tag{6}$$

and

$$M_r = D(\mathcal{K}_r + \nu\mathcal{K}_\theta), \quad M_\theta = D(\mathcal{K}_\theta + \nu\mathcal{K}_r), \tag{7}$$

where $A = Eh/(1-\nu^2)$ and $D = Eh^3/12(1-\nu^2)$ are the plate extensional and bending stiffnesses respectively, ν is Poisson's ratio, and E is the modulus of elasticity. Shearing deformations are neglected for the thin plates considered here ($h/a < 1/25$, Timoshenko and Woinowsky-Krieger (1959)).

These equations are reduced by first integrating (2),

$$Q_r + N_r\frac{dw}{dr} + \frac{p_0 r}{2} = 0, \tag{8}$$

and rewriting (4) in compatibility form,

$$r\frac{d\epsilon_\theta}{dr} + \epsilon_\theta - \epsilon_r + \frac{1}{2}\left(\frac{dw}{dr}\right)^2 = 0. \tag{9}$$

Substituting (5) into (7) and then into the moment equilibrium relation (3) gives

$$M_r = -D\left(\frac{d^2w}{dr^2} + \frac{\nu}{r}\frac{dw}{dr}\right), \tag{10}$$

$$M_\theta = -D\left(\frac{1}{r}\frac{dw}{dr} + \nu\frac{d^2w}{dr^2}\right), \tag{11}$$

and

$$Q_r = -D\left(\frac{d^3w}{dr^3} + \frac{1}{r}\frac{d^2w}{dr^2} - \frac{1}{r^2}\frac{dw}{dr}\right). \tag{12}$$

Placing (10)–(12) into (8) produces

$$\frac{d^3w}{dr^3} + \frac{1}{r}\frac{d^2w}{dr^2} - \frac{1}{r^2}\frac{dw}{dr} - \frac{N_r}{D}\frac{dw}{dr} = \frac{p_0 r}{2D}. \tag{13}$$

The inversion of (6) yields

$$\epsilon_r = \frac{1}{Eh}(N_r - \nu N_\theta) \quad \text{and} \quad \epsilon_\theta = \frac{1}{Eh}(N_\theta - \nu N_r). \tag{14}$$

Substituting (14) into the compatibility relation (9) yields

$$\frac{dN_\theta}{dr} + \frac{dN_r}{dr} + \frac{Eh}{2r}\left(\frac{dw}{dr}\right)^2 = 0. \tag{15}$$

Further manipulation of (15) by introducing (1) produces

$$\frac{dN_\theta}{dr} - \frac{N_r - N_\theta}{r} + \frac{Eh}{2r}\left(\frac{dw}{dr}\right)^2 = 0. \tag{16}$$

Equations (1), (13), and (16) represent three nonlinear equations in the three unknowns dw/dr, N_r, and N_0. The nonlinearity appears in the $N_r dw/dr$ term in (13) and the $(dw/dr)^2$ term in (16).

For the problem in Fig. 1, the circular plate is first stretched by an in-plane tension load $N_r = N_\theta$ around its circumference and then subjected to a uniform load, p_0. The solution of the initial in-plane tension problem is obtained from the general equations (1)–(7) by setting $w = 0$ and $p_0 = 0$. This yields the following results:

$$N_r = N_\theta = N_0 \quad \text{and} \quad u = \frac{N_0}{Eh}(1-\nu)r, \tag{17}$$

which also satisfy the boundary condition, $N_r = N_0$ at $r = a$. Since $N_r = \sigma_r h$, where σ_r is the radial stress, the quantity $N_0/Eh = \sigma_r/E = \epsilon_0$ can be interpreted as the uniaxial strain in the material.

After being initially stretched by the load N_0, the plate is then subjected to the vertical load, p_0. For this case, the lateral loads are decomposed as follows:

$$N_r = N_0 + \tilde{N}_r \quad \text{and} \quad N_\theta = N_0 + \tilde{N}_\theta \tag{18}$$

where $\tilde{N}_r$ and $\tilde{N}_\theta$ are incremental changes from N_0 and are functions of r. The placement of these expressions into (13), (1), (16) yields

$$\frac{d^3w}{dr^3} + \frac{1}{r}\frac{d^2w}{dr^2} - \frac{1}{r^2}\frac{dw}{dr} - \frac{N_0}{D}\frac{dw}{dr} - \frac{\tilde{N}_r}{D}\frac{dw}{dr} = \frac{p_0 r}{2D}, \tag{19}$$

$$\frac{d\tilde{N}_r}{dr} + \frac{\tilde{N}_r - \tilde{N}_\theta}{r} = 0, \tag{20}$$

and

Downloaded 04 May 2010 to 171.66.16.26. Redistribution subject to ASME license or copyright; see http://www.asme.org/terms/Terms_Use.cfm

$$\frac{d\tilde{N}_\theta}{dr} - \frac{\tilde{N}_r - \tilde{N}_\theta}{r} + \frac{Eh}{2r}\left(\frac{dw}{dr}\right)^2 = 0. \quad (21)$$

It is convenient to nondimensionalize these equations as follows:

$$\xi = \frac{r}{a}, \quad (\ )' = \frac{d}{d\xi}, \quad W = \frac{w}{h}, \quad U = \frac{u}{h}$$

$$\theta = \frac{dW}{d\xi} = \frac{a}{h}\frac{dw}{dr}, \quad \Psi = \frac{d\theta}{d\xi} = \frac{a^2}{h}\frac{d^2w}{dr^2},$$

$$S_r = \frac{\tilde{N}_r a^2}{Eh^3}, \quad S_\theta = \frac{\tilde{N}_\theta a^2}{Eh^3}. \quad (22)$$

The nondimensional forms of (19)–(21) are

$$\theta'' + \frac{\theta'}{\xi} - \left(k^2 + \frac{1}{\xi^2}\right)\theta - 12(1-\nu^2)S_r\theta = 6(1-\nu^2)P\xi, \quad (23)$$

$$S_r' + \frac{S_r - S_\theta}{\xi} = 0, \quad (24)$$

and

$$S_\theta' - \frac{S_r - S_\theta}{\xi} = -\frac{1}{2\xi}\theta^2, \quad (25)$$

where a nondimensional tension parameter k, and a loading parameter P, have been introduced as

$$k = \sqrt{\frac{N_0 a^2}{D}} = \frac{a}{h}\sqrt{\frac{12(1-\nu^2)N_0}{Eh}} \quad \text{and} \quad P = \frac{p_0 a^4}{Eh^4}. \quad (26)$$

The corresponding nondimensional in-plane displacement U as obtained from (4) and (14) and the vertical displacement W as obtained by integration, are then

$$U = \frac{u}{h} = \frac{h}{a}(S_\theta - \nu S_r)\xi \quad (27)$$

and

$$W = \frac{w}{h} = \int \theta d\xi. \quad (28)$$

Equations (23)–(25) are subject to the following boundary conditions:

$$@\xi = 0: \quad \theta = 0, \quad S_r = S_\theta \quad (29)$$

and

$$@\xi = 1: \quad \theta = 0, \quad U = \frac{h}{a}(S_\theta - \nu S_r) = 0 \quad (30)$$

which represent symmetry conditions at the center and clamped conditions at the edge of the plate.

The corresponding radial stress field in the plate is found from the definitions of the stress resultants,

$$\sigma_r = \frac{N_r}{h} + \frac{12M_r z}{h^3}, \quad (31)$$

where the extrema occur at the top and bottom surfaces, $z = \pm h/2$. The nondimensional form is obtained by making use of (10) and (18),

$$\sigma_r = \frac{N_0}{h} + \frac{Eh^2}{a^2}\left[S_r - \frac{z}{h(1-\nu^2)}\left(\Psi + \frac{\nu\theta}{\xi}\right)\right]. \quad (32)$$

The first term represents the initial stress, the second the membrane stress, and the third the bending stress. The corresponding strain ϵ_r in the plate is obtained from (14) and (18),

$$\epsilon_r = \frac{1}{Eh}(N_r + \nu N_\theta) + z\mathcal{K}_r. \quad (33)$$

The nondimensional form is obtained by making use of (5),

$$\epsilon_r = (1-\nu)\frac{N_0}{Eh} + \left(\frac{h}{a}\right)^2\left[S_r - \nu S_\theta - \frac{z}{h}\Psi\right]. \quad (34)$$

The corresponding tangential stress (σ_θ) and strain (ϵ_θ) fields can be obtained through similar manipulations.

3 Linear Theory

Before investigating the nonlinear behavior (23)–(25), it is informative to look at the small deflection, linear behavior of these equations as the tension parameter k varies from 0 to ∞. For small deflections, the midplane load S_r is assumed small, so that the nonlinear $S_r\theta$ term in (23) can be neglected. Multiplying (23) by ξ^2 then leads to the linear equation[3],

$$\xi^2\theta'' + \xi\theta' - (1 + k^2\xi^2)\theta = 5.56P\xi^3, \quad (35)$$

which is a modified Bessel equation possessing the general solution,

$$\theta(\xi) = C_1 I_1(k\xi) + C_2 K_1(k\xi) - \frac{5.56P\xi}{k^2}, \quad (36)$$

where $I_1(k\xi)$ and $K_1(k\xi)$ are modified Bessel functions of the first kind and second kind, respectively (Abramowitz and Stegun, 1972). The requirement of a bounded solution at $\xi = 0$ and implementation the boundary conditions (29)–(30) yields,

$$\theta(\xi) = 5.56P\left[\frac{I_1(k\xi)}{k^2 I_1(k)} - \frac{\xi}{k^2}\right]. \quad (37)$$

The corresponding deflection is obtained by integrating (37),

$$W(\xi) = 2.78P\left[\frac{2(I_0(k\xi) - I_0(k))}{k^3 I_1(k)} + \frac{1-\xi^2}{k^2}\right]. \quad (38)$$

Two limiting cases are of interest here. For the case of a pure plate ($k = 0$), (35) becomes an equidimensional ordinary differential equation possessing the following solutions:

$$\theta(\xi) = -0.695P\xi(1-\xi^2) \quad (39)$$

and

$$W(\xi) = 0.174P(1-\xi^2)^2. \quad (40)$$

For the other case of a pure membrane, $k \to \infty$, only the $k^2\xi^2\theta$ term remains on the left-hand side of Eq. (35). The resulting equation is integrated to yield

$$\theta(\xi) = -\frac{5.56P\xi}{k^2} \quad (41)$$

and

[3] In this and all subsequent equations, the Poisson ratio is taken as $\nu = 0.27$, which is typical of silicon nitride. Small modifications can be made for other values of ν.

Downloaded 04 May 2010 to 171.66.16.26. Redistribution subject to ASME license or copyright; see http://www.asme.org/terms/Terms_Use.cfm

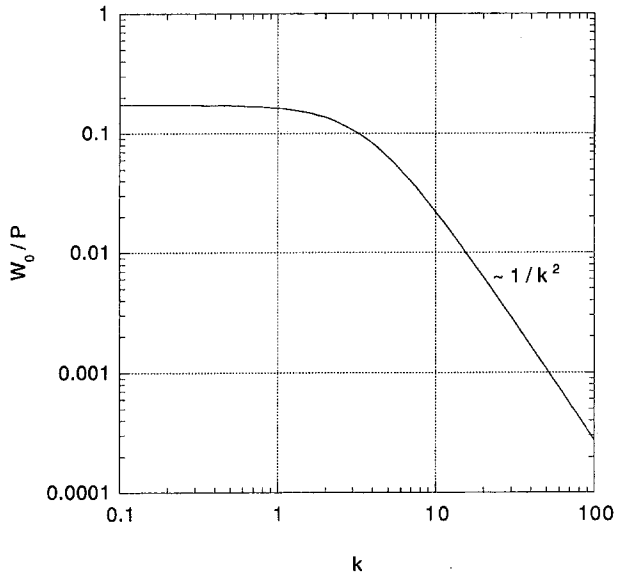

Fig. 2 Center deflection normalized by loading as a function of in-plane tension

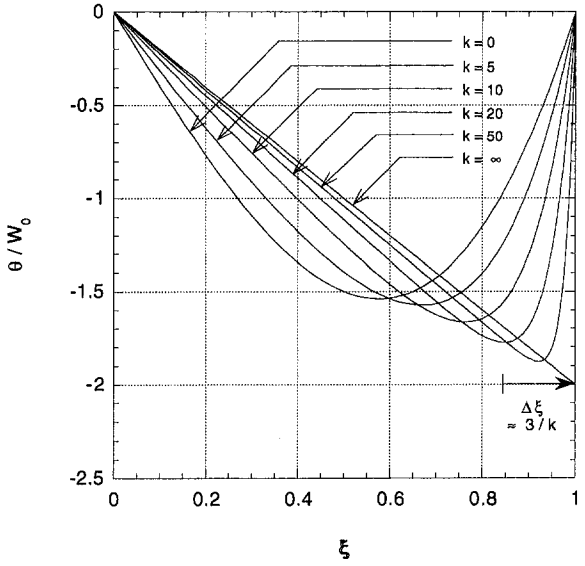

Fig. 4 Normalized deflection slope as a function of radial distance for several values of *k*

$$W(\xi) = \frac{2.78P}{k^2}(1 - \xi^2). \tag{42}$$

Equations (39) – (42) can also be obtained by taking the small and large argument limit of the modified Bessel solutions (37) – (38).

The effect of initial in-plane tension is shown by plotting the center deflection, W_0, as a function of tension parameter (see Fig. 2). In this figure, Eqs. (40) and (42) form two asymptotes to the deflections obtained from (38). There appears to be a transition from plate behavior to membrane behavior in the region from $k \approx 1$ to $k \approx 20$. The corresponding change in deflection shape is shown in Fig. 3. As the tension parameter increases, one notes the sharp change in curvature near the edge, $\xi \approx 1$, in order to accommodate the zero slope boundary condition there.

A better understanding of the transition to membrane behavior is gained by introducing the large value approximation for the modified Bessel functions, namely (Abramowitz and Stegun, 1972)

$$\lim_{z\to\infty} I_\nu(z) \approx \frac{e^z}{\sqrt{2\pi z}}, \quad \forall\ \nu. \tag{43}$$

The placement of this approximation into (37) and (38) produces for large k

$$\theta(\xi) \approx \frac{-5.56P}{k^2}\left[\xi - \frac{e^{-k(1-\xi)}}{\sqrt{\xi}}\right] \tag{44}$$

and

$$W(\xi) \approx \frac{2.78P}{k^2}\left[1 - \xi^2 - \frac{2}{k}\left(1 - \frac{e^{-k(1-\xi)}}{\sqrt{\xi}}\right)\right]. \tag{45}$$

These equations indicate small exponential edge-zone corrections to the pure membrane case (41) and (42), to accommodate the zero slope condition at $\xi = 1$. Figure 4 shows the slope θ plotted versus nondimensional radius ξ for increasing values of k. The extent of this edge zone[4], $\Delta\xi$, gets smaller as k increases and is estimated by assuming that the exponential decays to five percent of its maximum value,

$$\Delta\xi \approx \frac{3}{k}. \tag{46}$$

Furthermore, the change in center deflection, W_0, from the pure membrane case is approximated from (45) as

$$W_0 \approx \left[1 - \frac{2}{k}\right](W_0)_{\text{mem}}. \tag{47}$$

The corresponding stresses σ_r and strains ϵ_r in the plate are found from (32) and (34). For linear theory, the main contributions to the stress and strain fields come from the initial stress and the bending forces, the later of which are dominated by the curvature term Ψ, namely

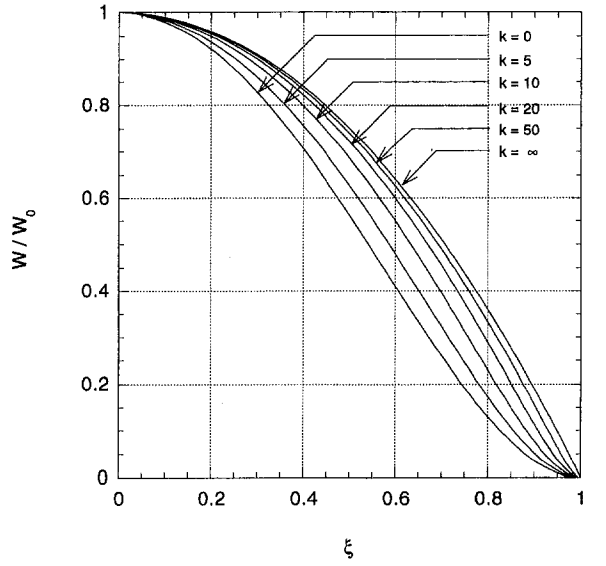

Fig. 3 Normalized deflection as a function of radial distance for several values of *k*

[4] Friedrichs (1949) first noted the development of an edge zone region with rapidly changing properties in his study of plate deflections.

Downloaded 04 May 2010 to 171.66.16.26. Redistribution subject to ASME license or copyright; see http://www.asme.org/terms/Terms_Use.cfm

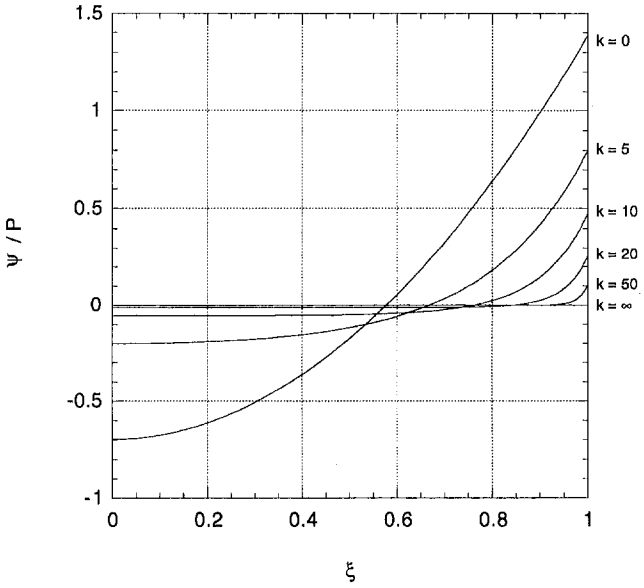

Fig. 5 Normalized deflection curvature as a function of radial distance for several values of in-plane tension

$$\Psi = 5.56P\left[\frac{I_0(k\xi)}{kI_1(k)} - \frac{1}{k^2\xi}\frac{I_1(k\xi)}{I_1(k)} - \frac{1}{k^2}\right]. \quad (48)$$

The large k approximation of (48) is

$$\Psi \approx \frac{5.56P}{k^2}\left[-1 + \frac{k\xi - 1}{\xi^{3/2}}\, e^{-k(1-\xi)}\right], \quad (49)$$

which represents the membrane solution plus a small exponential edge zone correction. Figure 5 shows the curvature term plotted versus radius for different values of the tension parameter. For large k, the maximum curvature term at the edge is

$$\Psi \approx \frac{5.56P}{k}, \quad (50)$$

which is considerably greater than the membrane curvature, $\Psi = -5.56P/k^2$ occurring at the center and over most of the remaining portion of the plate. Physically, this indicates the presence of a stress concentration near the clamped plate boundary (for example, Eq. (32)).

4 Nonlinear Theory

For large deflections ($W \gg 1$), nonlinear behavior arises when the incremental midplane forces, $\tilde{N}_r$, $\tilde{N}_\theta$, are no longer negligible. This behavior is manifested by the θ^2 term in (25) changing the midplane force S_r, which in turn affects the deflection equations through the nonlinear $S_r\theta$ term in (23).

A convenient way of numerically solving this nonlinear system is to combine (24)–(25) and recast (23)–(25) as two coupled, second-order equations in the variables θ and S_r (Voorthuyzen and Bergveld, 1984),

$$\xi^2\theta'' + \xi\theta' - [1 + \xi^2(k^2 + 11.12S_r)]\theta = 5.56P\xi^3, \quad (51)$$

$$\xi^2 S_r'' + 3\xi S_r' = -\frac{\theta^2}{2}. \quad (52)$$

The corresponding boundary conditions from (29) and (30) now become

$$@\xi = 0: \quad \theta = 0, \quad S_r' = 0, \quad (53)$$

$$@\xi = 1: \quad \theta = 0, \quad S_r' + 0.73S_r = 0. \quad (54)$$

Prior to discretizing (51)–(54), the following coordinate transform pair was used to refine the mesh in the edge zone region (46),

$$\xi = 1 - \frac{(\beta + 1) - (\beta - 1)\left[\dfrac{\beta + 1}{\beta - 1}\right]^{\bar{\xi}}}{\left[\dfrac{\beta + 1}{\beta - 1}\right]^{\bar{\xi}} + 1} \quad \text{and}$$

$$\bar{\xi} = -\frac{\ln\dfrac{\beta - \xi}{\beta + \xi}}{\ln\dfrac{\beta + 1}{\beta - 1}}, \quad (55)$$

where ξ is the physical plane with grid points clustered near $\xi = 1$, $\bar{\xi}$ is the uniformly spaced computational plane, and β is the stretching parameter (Roberts, 1971). This stretching transform clusters more points near $\xi = 1$ as β approaches 1. In the present study, a value of $\beta = 1.05$ was used to capture the physics of the edge-zone by clustering 30 percent of the grid points in the region $0.9 < \xi < 1.0$. The transformed versions of (51)–(54) are

$$\xi(\bar{\xi})^2\left(\frac{d\bar{\xi}}{d\xi}\right)^2\frac{d^2\theta}{d\bar{\xi}^2} + \left[\xi(\bar{\xi})\frac{d\bar{\xi}}{d\xi} + \xi(\bar{\xi})^2\left(\frac{d^2\bar{\xi}}{d\xi^2}\right)\right]\frac{d\theta}{d\bar{\xi}}$$

$$- [1 + \xi(\bar{\xi})^2(k^2 + 11.12S_r(\bar{\xi}))]\theta(\bar{\xi}) = 5.56P\xi(\bar{\xi})^3, \quad (56)$$

$$\xi(\bar{\xi})^2\left(\frac{d\bar{\xi}}{d\xi}\right)^2\frac{d^2S_r}{d\bar{\xi}^2} + \left[3\xi(\bar{\xi})\frac{d\bar{\xi}}{d\xi} + \frac{d^2\bar{\xi}}{d\xi^2}\right]\frac{dS_r}{d\bar{\xi}} = -\frac{\theta(\bar{\xi})^2}{2}, \quad (57)$$

and

$$@\bar{\xi} = 0: \quad \theta = 0, \quad \frac{d\bar{\xi}}{d\xi}\frac{dS_r}{d\bar{\xi}} = 0, \quad (58)$$

$$@\bar{\xi} = 1: \quad \theta = 0, \quad \frac{d\bar{\xi}}{d\xi}\frac{dS_r}{d\bar{\xi}} + 0.73S_r = 0. \quad (59)$$

Equations (56) and (57) were then discretized using second-order accurate central-difference schemes, while the derivative and mixed boundary conditions were implemented by using second-order accurate forward and backward-differencing schemes, respectively (for example, Anderson et al., 1984). The computational domain consisted of a radial mesh containing 101 points to provide adequate resolution in the edge zone. In matrix form, (56) and (57) are represented as

$$[\mathcal{A}(S_r)]\Theta = C, \quad (60)$$

$$[\mathcal{B}]S_r = \tfrac{1}{2}\Theta^2, \quad (61)$$

where $[\mathcal{A}(S_r)]$ and $[\mathcal{B}]$ are square matrices in tridiagonal form. This nonlinear system was then solved using an implicit iteration technique similar to that used by Voorthuyzen and Bergveld (1984). For a given k, (61) can be readily solved by direct inversion provided Θ is known, since $[\mathcal{B}]$ is in modified tridiagonal form. In the present study, the linear solution was used as an initial guess (see (37)). Once determined, S_r was then substituted into (60) and was again inverted to produce an updated Θ. The updated Θ was first corrected by employing an under-relaxation technique (see, for example, Anderson et al., 1984) and then substituted into (61) producing a new S_r. In this study, an under-relaxation parameter of 0.2 was used to accelerate convergence. This iterative process was repeated until the solution converged to within a tolerance of 0.5 percent. Finally, the variables W, Ψ, S_θ, and U were then determined

Downloaded 04 May 2010 to 171.66.16.26. Redistribution subject to ASME license or copyright; see http://www.asme.org/terms/Terms_Use.cfm

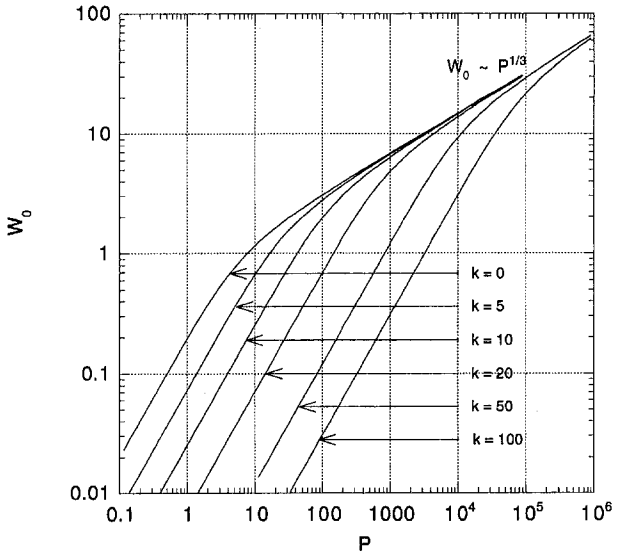

Fig. 6 Center deflection as a function of loading for several values of in-plane tension

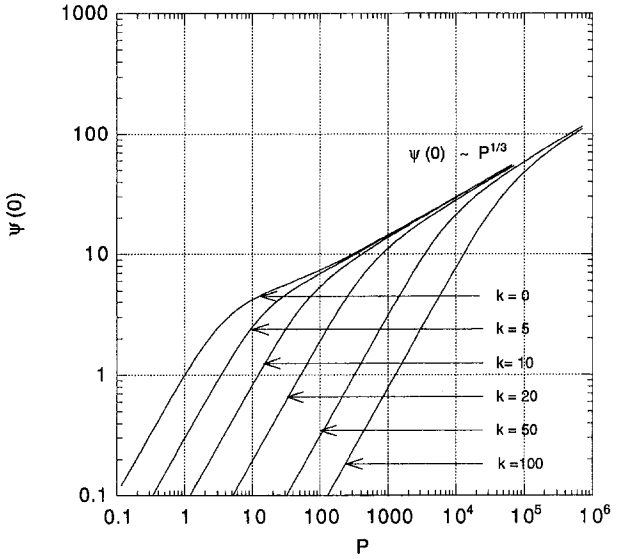

Fig. 8 Center deflection curvature as a function of loading for several values of in-plane tension

by employing second-order accurate differencing schemes for the differentiation and integration operators.

Results of the nonlinear calculations for the deflection, deflection curvature, and in-plane load at the center of the plate are given in Figs. 6 to 9. Figure 6 shows the variation of the center deflection with loading. For the zero initial tension case, $k = 0$, the deflection scaling changes from the linear $W_0 \sim P$ at low loading levels to $W_0 \sim P^{1/3}$ at high loading. The numerical results for center-deflection characteristics agree very well with those given by Nádai (1925) for $k = 0$ and with Voorthuyzen and Bergveld (1984) and Allen (1986) for $k > 0$. For the cases with $k > 0$, the curves start from their respective linear values and become asymptotic to the $k = 0$ case. In addition, the onset of nonlinearity is delayed with increasing k. This effect is better illustrated by plotting the maximum loading, P_{max}, that will produce a five percent departure from linearity in the center deflection, as a function of k (see Fig. 7). The delay of the onset of nonlinear behavior with increasing k scales according to $P_{max} \sim k^3$. Figure 8 shows the variation of the curvature at the plate center, Ψ_0, with loading. Again, for the $k = 0$ case, the curvature scaling changes from $\Psi_0 \sim P$ at low loads to $\Psi_0 \sim P^{1/3}$ at high loads, but there appears a small bump in the transition. The $k > 0$ cases again merge asymptotically into the $k = 0$ case. Figure 9 shows the variation of the in-plane load at the plate center with loading. For the $k = 0$ case, the in-plane load developed in the plate is always nonlinear and changes from $S_r \sim P^2$ at low loadings to $S_r \sim P^{2/3}$ at higher loadings. This behavior is attributed to the Θ^2 term present in (57) which determines S_r. The cases with initial tension also merge asymptotically into the $k = 0$ case.

The distribution of the deflection, slope, and curvature in the plate for the $k = 0$ case are given in Figs. 10 to 12. Figure 10 shows the deflection distributions in the plate at different values of loading. The $P = 1$ case represents the linear bending behavior (see Fig. 7), while for higher loadings, large in-plane loads develop and the deflections tend to exhibit membrane behavior shown earlier in Fig. 3. Similar trends with loading are apparent for the nonlinear slope and curvature distributions given in Figs. 11 and 12. These trends in Figs. 11 and 12 are similar to those

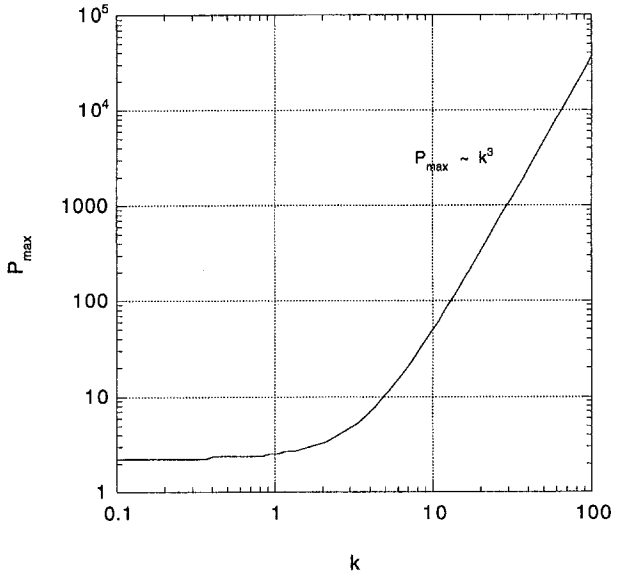

Fig. 7 Maximum linear loading as a function of in-plane tension

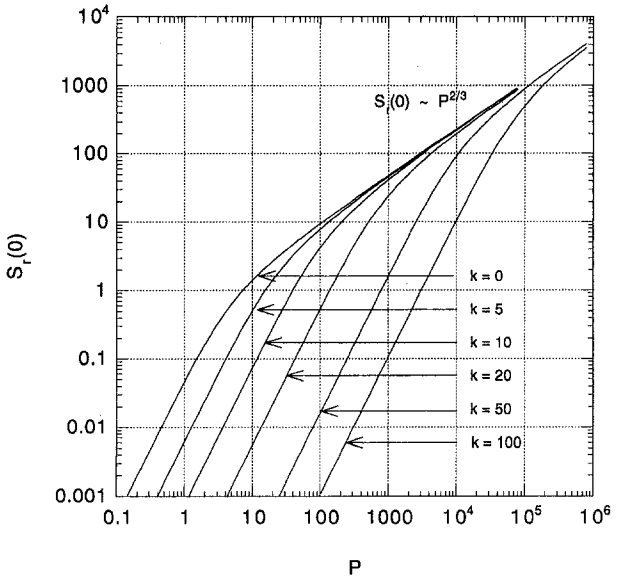

Fig. 9 Center in-plane stress as a function of loading for several values of in-plane tension

Downloaded 04 May 2010 to 171.66.16.26. Redistribution subject to ASME license or copyright; see http://www.asme.org/terms/Terms_Use.cfm

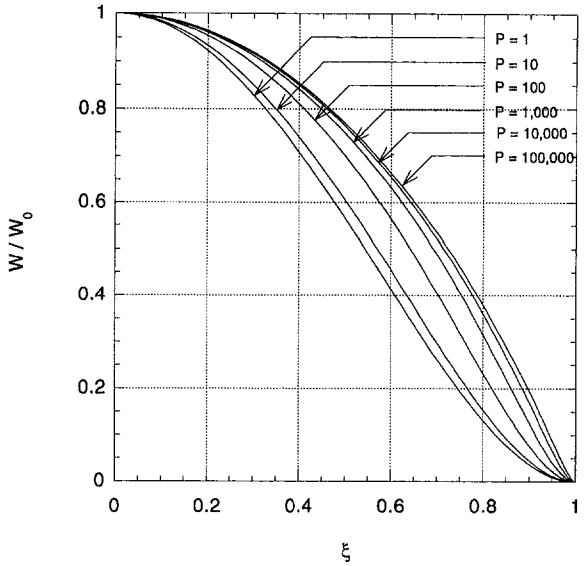

Fig. 10 Normalized deflection as a function of radial distance for several values of loading ($k = 0$)

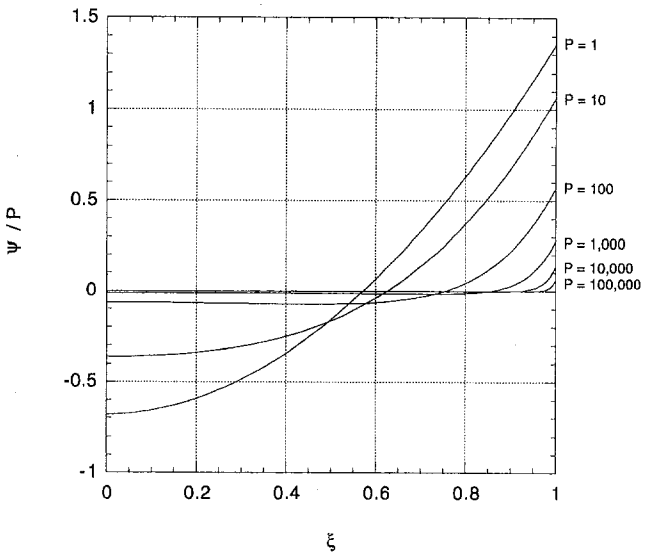

Fig. 12 Normalized deflection curvature as a function of radial distance for several values of loading ($k = 0$)

found in Figs. 4 and 5. The corresponding distribution of in-plane loads and in-plane deflection for the $k = 0$ case are shown in Figs. 13 to 15. The in-plane loads plotted in Figs. 13 and 14 become more uniform at the higher loads, although never quite constant. Interestingly, Fig. 15 demonstrates that the in-plane deflection becomes negative near the edge of the plate.

The similar influences of large P and large k discussed above can be traced to the $(k^2 + 11.12S_r)$ term in (56). Therefore, an equivalent linear tension parameter, k_E, is defined as

$$k_E = \sqrt{k^2 + 11.12S_r}, \tag{62}$$

where S_r is taken as $S_r \approx S_r(0)$ and k_E is now only a function of P and k (see Fig. 9). The equivalent tension parameter k_E is plotted as a function of loading in Fig. 16. For any given P and k combination, Fig. 16 determines the equivalent tension parameter, k_E, which in turn identifies the appropriate deflection, slope, and curvature distribution characteristics from the basic linear theory, ((37), (38), and (48)) or Figs. 3–5. Also, k_E can be used in the convenient approximations of (46), (47), and (50). Alternatively, by moving the given (P, k) point on Fig. 16 horizontally to the right to the $k = 0$ case, one obtains the loading P which identifies the appropriate distribution characteristics from the previous $k = 0$ nonlinear theory, Figs. 10–15. The basic values of W_0, Ψ_0, and $S_r(0)$ for a given (P, k) are obtained from Figs. 6, 8, and 9.

Figure 16 shows that the nonlinear $P = 1$, 10, 100, 1000, 10,000, 100,000 cases for $k = 0$ calculated here (Figs. 10–15) correspond approximately to the linear $k = 1$, 5, 10, 20, 50, 100 cases[5] (Figs. 3–5). They have similar distribution behavior, particularly with regards to the extent of the edge zone. The slight variation in Θ/W_0 arises from S_r varying slightly across the plate instead of remaining constant at S_0. Figure 16 also displays a dotted line which indicates the extent of the linear region, mentioned previously (see Fig. 7). For a given value of k, points to the right of the dotted line indicate a departure from linearity greater than five percent for the center deflections.

[5] The $k = 1$ case is essentially identical to the $k = 0$ case (see Fig. 2).

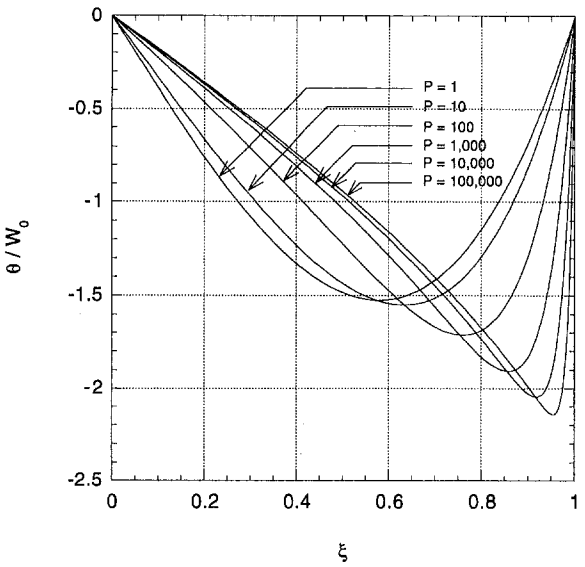

Fig. 11 Normalized deflection slope as a function of radial distance for several values of loading ($k = 0$)

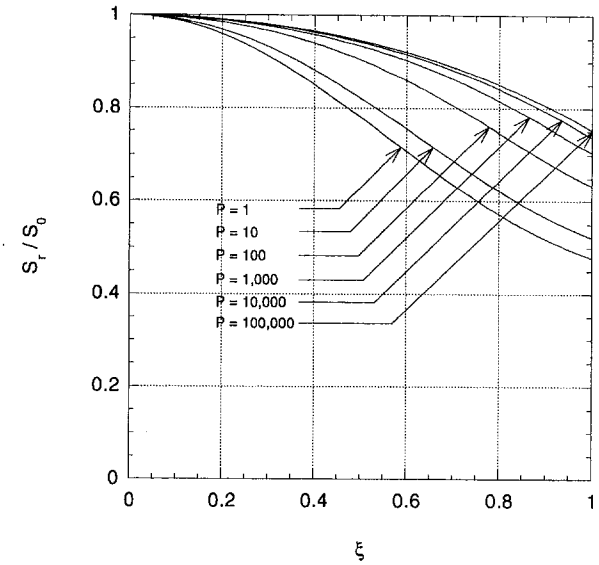

Fig. 13 Normalized in-plane radial stress as a function of radial distance for several values of loading ($k = 0$)

Downloaded 04 May 2010 to 171.66.16.26. Redistribution subject to ASME license or copyright; see http://www.asme.org/terms/Terms_Use.cfm

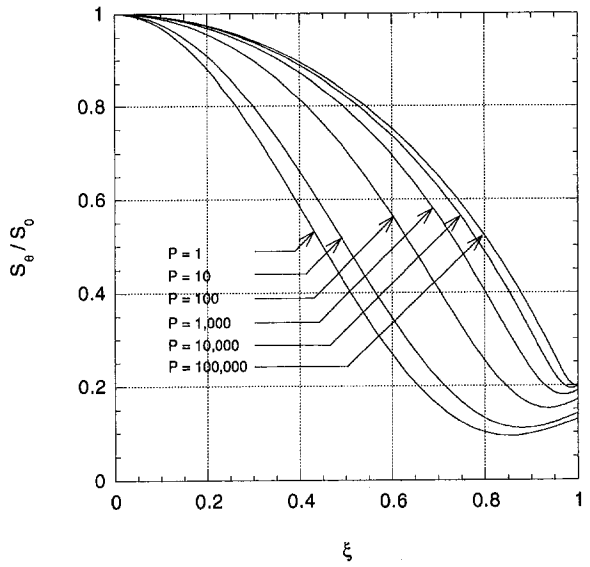

Fig. 14 Normalized in-plane tangential stress as a function of radial distance for several values of loading ($k = 0$)

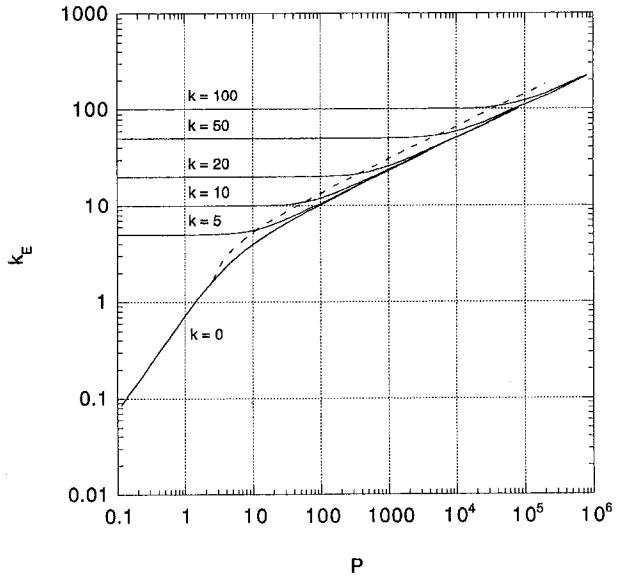

Fig. 16 Equivalent tension parameter as a function of loading

All points to the left of the dotted line indicate linear theory is valid.

5 Conclusions

The large deflections of a clamped circular plate have been investigated over a wide range of transverse loadings and initial in-plane tension loads. The transition from plate behavior to membrane behavior for small deflections is a function of the initial tension parameter, k. This transition occurs over the range $1 < k < 20$, with plate behavior dominating for $k < 1$. For $k > 20$, membrane behavior dominates the majority of the clamped plate, however, a narrow edge-zone region develops near $\xi = 1$ to meet the zero-slope boundary condition. Simple estimates of this edge zone and its properties are given. In addition, the loading limits for the validity of small deflection, linear theory are presented as a function of the initial tension parameter. The similar effects of large initial in-plane tension k and large loadings P are combined into a single equivalent tension parameter, k_E, which conveniently characterizes the plate behavior. The equivalent tension parameter permits the use of the closed-form linear solutions to characterize the nonlinear behavior of the plate.

The values and trends presented in this study are useful aids for the design of thin circular disks often found in microelectromechanical systems. For example, the results in Section 3 imply that the nondimensional sensitivity of deflection-based pressure sensors ($W_0/P \sim 1/k^2$) and the sensitivity piezoresistive-based pressure sensors ($\Psi_{\xi=1}/P \sim 1/k$) scale differently with initial tension. In addition, for piezoresistive transducers the edge-zone scaling indicates the extent of the stress concentration region and thus dictates the placement and size of the piezoresistors. Finally, the scaling law regarding limits of linear theory with increasing initial tension indicate that the loss of sensitivity with increasing dimensional tension can be offset by a subsequent increase in thickness ratio.

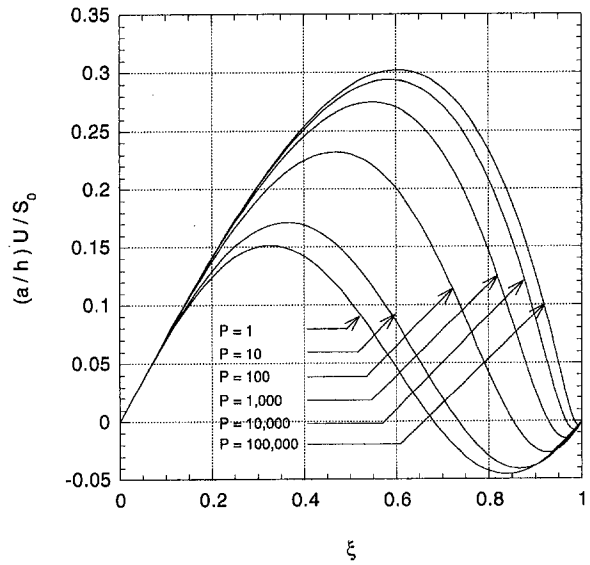

Fig. 15 Normalized radial displacement as a function of radial distance for several values of loading ($k = 0$)

Acknowledgments

This work has been sponsored by NASA-Langley Research Center under grant NAG-1-1785, (monitored by John M. Seiner). The authors would like to thank Lalitha Parameswaran, Kenneth S. Breuer, Stephen D. Senturia, and Martin A. Schmidt for their helpful comments.

References

Allen, M. G., 1986, "Measurement of Mechanical Properties and Adhesion of Thin Polyimide Films," M.S. thesis, MIT, Cambridge, MA.

Abramowitz, M., and Stegun, I. A., 1972, *Handbook of Mathematical Functions,* 9th Ed., Dover, New York.

Anderson, D. A., Tannehill, J. C., and Pletcher, R. H., 1984, *Computational Fluid Mechanics and Heat Transfer,* Hemisphere, New York.

Chau, H.-L. and Wise, K. D., 1987, "Scaling Limits in Batch-Fabricated Silicon Pressure Sensors," *IEEE Transaction of Electron Devices,* Vol. ED-34, pp. 850–858.

Cho, S. T., Najafi, K., and Wise, K. D., 1992, "Internal Stress Compensation and Scaling in Ultra-sensitive Silicon Pressure Sensors," *IEEE Transaction of Electron Devices,* Vol. 39, No. 4, pp. 836–842.

Clark, S. K., and Wise, K. D., 1979, "Pressure Sensitivity in Anisotropically Etched Thin-Diaphragm Pressure Sensors," *IEEE Transaction of Electron Devices,* Vol. ED-26, No. 12, pp. 1887–1896.

Friedrichs, K. O., 1949, "The Edge Effect In Bending and Buckling with Large Deflections," *Proceedings of Symposia in Applied Mathematics,* Vol. 1 (Non-Linear Problems in Mechanics of Continua), American Mathematical Society, New York, pp. 188–193.

Löfdahl, L., Kälvesten, E., and Stemme, G., 1994, "Small Silicon Based Pressure Transducers for Measurements in Turbulent Boundary Layers," *Experiments in Fluids,* Vol. 17, pp. 24–31.

Downloaded 04 May 2010 to 171.66.16.26. Redistribution subject to ASME license or copyright; see http://www.asme.org/terms/Terms_Use.cfm

McPherson, A., Ramberg, W., and Levy, S., 1942, "Normal-Pressure Tests of Circular Plates with Clamped Edge," NACA Technical Report 744.

Nádai, A., 1925, *Elastisclie Platten,* Julius Springer, Berlin, p. 288.

Roberts, G. O., 1971, "Computational Meshes for Boundary Layer Problems," *Lecture Notes in Physics,* Vol. 8, Springer-Verlag, New York, pp. 171–177.

Schellin, R., and Hess, G., 1992, "A Silicon Subminiature Microphone Based on Piezoresistive Polysilicon Strain Gauges," *Sensors and Actuators A,* Vol. 32, pp. 555–559.

Sze, S. M., 1994, *Semiconductor Sensors,* John Wiley and Sons, New York.

Timoshenko, S. P., and Woinowsky-Krieger, S., 1959, *Theory of Plates and Shells,* 2nd Ed., McGraw-Hill, New York.

Voorthuyzen, J. A., and Bergveld, P., 1984, "The Influence of Tensile Forces on the Deflection of Circular Diaphragms in Pressure Sensors," *Sensors and Actuators A,* Vol. 6, pp. 201–213.

Way, S., 1934, "Bending of Circular Plates with Large Deflection," *Transactions of the ASME,* Vol. 56, pp. 627–636.

Zhen, X., and Zhou, Y., 1990, "Analytical Formulas of Solutions of Geometrically Nonlinear Equations of Axisymmetric Plates and Shallow Shells," *Acta Mechanica Sinca,* Vol. 6, No. 1.

Downloaded 04 May 2010 to 171.66.16.26. Redistribution subject to ASME license or copyright; see http://www.asme.org/terms/Terms_Use.cfm

Critical Speed for Floppy Disks

A. A. Renshaw
Department of Mechanical Engineering,
Columbia University,
New York, NY 10027
Mem. ASME.

This paper uses Lyapunov's method to determine the critical speed of a flexible spinning disk enclosed in a housing that hydrodynamically couples the transverse motion of the disk to the motion of the thin films of air surrounding the disk. Depending on the clamping ratio, this critical speed is three to ten times higher than the critical speed in the absence of hydrodynamic coupling and does not depend on the strength of the hydrodynamic coupling. Despite the nonlinearity of the underlying model, the critical speed problem is linear and tractable. The linearized free-vibration problem is also computed to verify the stability prediction and to examine linearized damping and stiffness as possible design criteria. The results are relevant to the design of both conventional computer floppy disks and the emerging generation of 100+ MB floppies.

1 Introduction

The underlying phenomena governing the stability of spinning disks with small or negligible coupling to the surrounding air such as industrial circular saws and computer hard disk drives have been studied extensively during the past four decades and are well understood. In the absence of hydrodynamic coupling, the maximum rotation speed for these systems is the lowest speed at which the propagation speed of a backward traveling, circumferential wave equals the disk rotation speed (Tobias and Arnold, 1957). Although the spinning disk is stable at this speed (Renshaw and Mote, 1996), stationary, constant, transverse forces cause resonant vibration of the disk which degrades sawing accuracy and magnetic recording fidelity (Mote, 1970; Iwan and Moeller, 1976; Benson and Bogy, 1978). Circular saws presently operate at 80 percent of the uncoupled critical speed while hard disk drives operate at 15–20 percent.

The dynamic stability of spinning disks with significant hydrodynamic coupling such as computer floppy disks is less well understood. It is known that the uncoupled critical speed is not a limiting parameter because early floppy disks operated above the uncoupled critical speed (Benson and Bogy, 1978). Current 3.5-in. floppies operate at 30–50 percent of the uncoupled critical speed, but Iomega's Zip Drive operates at 400 percent of the uncoupled critical speed. As with hard disk drives, transverse vibration of floppy disks is deleterious to recording fidelity and needs to be controlled. An understanding of the speeds over which a hydrodynamically coupled spinning disk system is stable would be useful in this respect.

The primary difficulty in the coupled stability analysis is the nonlinearity of the underlying model. Previous researchers have determined axisymmetric steady-state equilibria without addressing the question of stability (Pelech and Shapiro, 1964; Carpino and Domoto, 1988), while others determined the stability of idealized equilibrium configurations (Chonan et al., 1992; Huang and Mote, 1995; Huang and Mote, 1996). These stability analyses confirmed that hydrodynamically coupled spinning disks can be stable above the uncoupled critical speed, but no general speed limit was proposed. Some studies have modeled the hydrodynamic coupling as a linear elastic foundation (e.g., Adams, 1987; Chonan et al., 1992).

This paper introduces a Lyapunov functional for the hydrodynamically coupled spinning disk that determines its maximum stable rotation speed. As expected, this coupled critical speed is three to ten times higher than the uncoupled critical speed, depending on the clamping ratio. Surprisingly, the coupled critical speed is independent of the strength of hydrodynamic coupling. Despite the nonlinearity of the underlying model, the critical speed problem is linear and tractable. The linearized free-vibration problem is also computed to verify the stability prediction and to examine linearized damping and stiffness as possible design criteria. These results are relevant to the design of both conventional computer floppy disks and the emerging generation of 100+ MB floppies.

2 Modeling

A thin axisymmetric circular disk spins about its axis of symmetry at constant angular speed Ω^*. Polar coordinates (R, θ) are fixed in the stationary frame of reference with the center of the disk at the origin. The disk is clamped at inner radius R_i, free at outer radius R_0, and has uniform thickness Δ, density ρ (mass per unit volume), flexural rigidity D, and Poisson's ratio ν. The in-plane, axisymmetric stresses σ_r^* and σ_θ^* are induced in the disk by the rotation, and the transverse displacement of the disk is $W(T, R, \theta)$ where T is time.

The disk spins in the narrow rigid annular enclosure shown in Fig. 1. The upper and lower surfaces of the undeflected disk are each separated from rigid walls by clearance C, and these upper and lower walls are rigidly joined with an air-tight seal to a third circular wall beyond the outer periphery of the disk. The enclosure is filled with air of constant density and viscosity μ which can only enter the enclosure through the two annular openings located at $R = R_i$, one below the disk, the other above. $H_L = C + W$ and $H_U = C - W$ are the thicknesses of the lower and upper air films, respectively, while P_L and P_U are the air pressures below and above the disk.

Dimensionless variables describing the disk and fluid films (omitting subscripts r and θ on σ and σ^* and L and U on h, H, p, and P) are

$$r = R/R_0 \quad w = W/C \quad t = T/\sqrt{\rho\Delta R_0^4/D}$$

$$\sigma = \sigma^*\Delta R_0^2/D \quad h = H/C \quad p = P(C^2/\mu)\sqrt{\rho\Delta/D}. \quad (1)$$

The transverse motion of the disk is modeled using classical Kirchhoff plate theory with in-plane stresses (Nowinski, 1964; Iwan and Moeller, 1976).

$$w_{,tt} + 2\Omega w_{,t\theta} + \Omega^2 w_{,\theta\theta} = \Lambda(p_L - p_U) - \nabla^4 w + (r\sigma_r w_{,r})_{,r}/r + \sigma_\theta w_{,\theta\theta}/r^2 \quad (2)$$

Contributed by the Applied Mechanics Division of THE AMERICAN SOCIETY OF MECHANICAL ENGINEERS for publication in the ASME JOURNAL OF APPLIED MECHANICS.

Discussion on this paper should be addressed to the Technical Editor, Professor Lewis T. Wheeler, Department of Mechanical Engineering, University of Houston, Houston, TX 77204-4792, and will be accepted until four months after final publication of the paper itself in the ASME JOURNAL OF APPLIED MECHANICS.

Manuscript received by the ASME Applied Mechanics Division, Jan. 30, 1997; final revision, July 6, 1997. Associate Technical Editor: N. C. Perkins.

 Copyright © 1998 by ASME

Downloaded 04 May 2010 to 171.66.16.26. Redistribution subject to ASME license or copyright; see http://www.asme.org/terms/Terms_Use.cfm

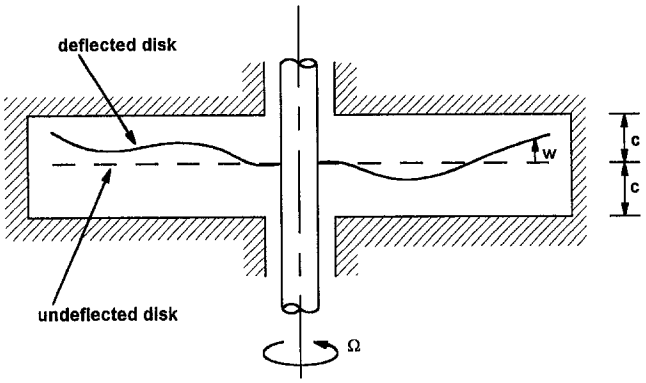

Fig. 1 Cross-sectional schematic of the annular disk spinning inside the rigid enclosure

∇^4 is the biharmonic operator and a comma indicates partial differentiation. Two dimensionless parameters appear in (2):

$$\Omega = \Omega^*\sqrt{\rho \Delta R_0^4/D}, \tag{3}$$

the dimensionless rotation speed; and

$$\Lambda = \mu R_0^4/[C^3\sqrt{\rho \Delta D}], \tag{4}$$

the hydrodynamic coupling strength. The clamping ratio is $\kappa = R_i/R_0$. w satisfies clamped-free boundary conditions

$$w = w_{,r} = 0 \quad \text{at} \quad r = \kappa \tag{5}$$

$$w_{,rr} + \nu(w_{,r}/r + w_{,\theta\theta}/r^2) = (\nabla^2 w)_{,r}$$

$$+ (1 - \nu)(w_{,r\theta\theta}/r^2 - w_{,\theta\theta}/r^3) = 0 \quad \text{at} \quad r = 1. \tag{6}$$

∇^2 is the Laplacian operator. The axisymmetric solutions of the generalized plane stress equations of linear elasticity with a centripetal body force, single-valued displacements, zero displacement at $r = \kappa$ and zero traction at $r = 1$ are (Sokolnikoff, 1956)

$$\sigma_r = \Omega^2[c_1/r^2 + c_2 + c_3 r^2]$$

$$\sigma_\theta = \Omega^2[-c_1/r^2 + c_2 + c_4 r^2] \tag{7}$$

where

$$c_1 = \frac{\kappa^2(1 - \nu)[3 + \nu - (1 + \nu)\kappa^2]}{8[1 + \nu + (1 - \nu)\kappa^2]}$$

$$c_2 = \frac{(1 + \nu)[3 + \nu + (1 - \nu)\kappa^4]}{8[1 + \nu + (1 - \nu)\kappa^2]}$$

$$c_3 = -(3 + \nu)/8 \quad c_4 = -(1 + 3\nu)/8. \tag{8}$$

The pressure variations in the films are modeled using the incompressible Reynolds' equation (Szeri, 1980).

$$(rh^3 p_{,r})_{,r}/r + (h^3 p_{,\theta})_{,\theta}/r^2 = 12h_{,t} + 6\Omega h_{,\theta}. \tag{9}$$

Equation (9) represents two distinct equations: for the fluid below the disk $p = p_L$ and $h = h_L = 1 + w$, while for the fluid above the disk $p = p_U$ and $h = h_U = 1 - w$. The normalized pressure distributions satisfy pressure boundary conditions

$$p_L = p_U = 0 \quad \text{at} \quad r = \kappa \tag{10}$$

$$p_L = p_U \quad \text{at} \quad r = 1. \tag{11}$$

In addition, continuity at the outer edge of the disk requires

$$h_L^3 p_{L,r} + h_U^3 p_{U,r} = 0 \quad \text{at} \quad r = 1. \tag{12}$$

3 Representative Parameter Values

Table 1 list the geometrical properties of three prototypical polymer, computer memory disks: the 5.25 and 3.5-in. floppy disks and Iomega's Zip drive. These numbers define the relevant values of Ω and Λ. Ω varies from 2.6 to 26, indicating a broad range of possible operational speeds. Λ ranges from 40 to 80 for the clearances shown. The speeds and clearances given in the table are approximate. For example, there are 3.5-in. floppy disks that rotate at 300 and 720 rpm, and the exact clearances of 5.25 and 3.5-in. floppy disks are not well defined due to the flexibility of the housing and the layers of gauze filling the clearance. The table also does not include floppy disk designs from the 1970s which operated at speeds as high as $\Omega = 50$ (Benson and Bogy, 1978).

4 Critical Speed

The model in Section 2 has two distinct speeds, herein denoted critical speeds, related to the flatness of the spinning disk: (1) the uncoupled critical speed, which is the maximum rotation speed that avoids stationary load resonance when $\Lambda = 0$; and (2) the coupled critical speed, which defines the maximum stable rotation speed for $\Lambda \neq 0$. In the latter case, stability refers to the stability of the trivial equilibrium $w = p_L = p_U = 0$.

When $\Lambda = 0$, the uncoupled critical speeds can be found from the Jacobi integral

$$J[w] = U[w] + \tfrac{1}{2}\int w_{,t}^2 - \Omega^2 w_{,\theta}^2 dA \tag{13}$$

where $dA = rdrd\theta$ is the planar area of the disk (Pars, 1979; Renshaw et al., 1996). U is the potential energy of the spinning disk

$$U[w] = \tfrac{1}{2}\int (\nabla^2 w)^2 - 2(1 - \nu)\{w_{,rr}(w_{,r}/r + w_{,\theta\theta}/r^2)$$

$$- [(w_{,\theta}/r)_{,r}]^2\} + \sigma_r w_{,r}^2 + \sigma_\theta w_{,\theta}^2/r^2 dA. \tag{14}$$

Direct computation shows that J is conserved, i.e.,

$$J_{,t} = 0 \quad \text{for} \quad \Lambda = 0. \tag{15}$$

Consequently, the uncoupled disk motion is stable by Lyapunov's method for all speeds for which J is positive definite (Movchan, 1959; Hahn, 1967). This positive definiteness calculation gives the uncoupled critical speed as the solution of a linear time-independent eigenvalue problem. (Lyapunov's method is sufficient but not necessary to show stability. A similar calculation shows that the total energy of the disk is also conserved. Since energy is positive definite at all speeds, it also qualifies as a Lyapunov functional and demonstrates that the uncoupled disk is stable at all speeds. Strictly speaking, the uncoupled critical speed defines a resonance not an instability. See, for example, Renshaw et al. (1996).)

For $\Lambda \neq 0$, the functional

$$S[w] = U[w] + \tfrac{1}{2}\int (w_{,t} + \Omega w_{,\theta}/2)^2 - \Omega^2 w_{,\theta}^2/4 dA \tag{16}$$

has the time derivative

Table 1 Design specifications for polymer computer memory disks

Device	R_o (mm)	R_i (mm)	Δ (mm)	C (mm)	Ω^* (rpm)	κ	Ω	Λ
5.25" Floppy	65.0	14.3	0.08	0.1	360	0.22	3.75	81
3.5" Floppy	43.0	12.5	0.05	0.1	360	0.29	2.63	40
Iomega Zip Drive	43.0	12.5	0.05	0.1	3600	0.29	26.3	40

In all cases, $\rho = 1300$ kg/m^3, E = 4 GPa, $\nu = 0.3$, and $\mu = 2 \times 10^{-5}$ Kg/s/m.

Downloaded 04 May 2010 to 171.66.16.26. Redistribution subject to ASME license or copyright; see http://www.asme.org/terms/Terms_Use.cfm

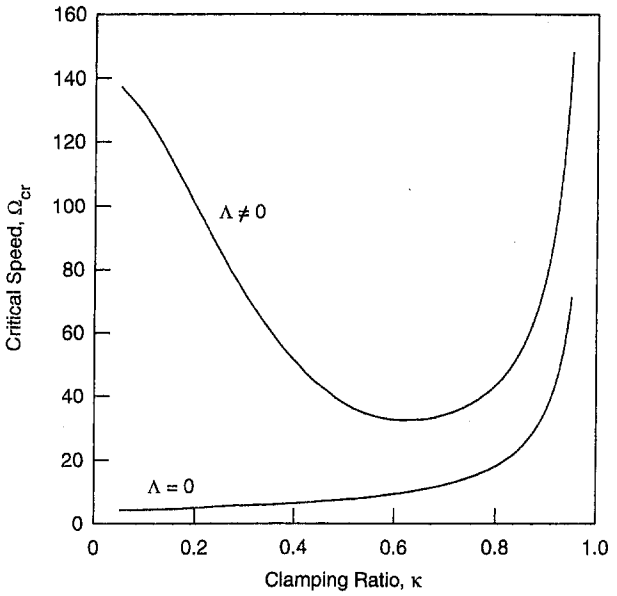

Fig. 2 The uncoupled ($\Lambda = 0$) and coupled ($\Lambda \neq 0$) critical speeds defined by the positive definiteness of J and S as functions of κ

$$S_{,t} = -\frac{\Lambda}{12}\int h_L^3(p_{L,r})^2 + h_L^3(p_{L,\theta})^2/r^2 + h_U^3(p_{U,r})^2 + h_U^3(p_{U,\theta})^2/r^2 dA. \quad (17)$$

Since h_L and h_U are always positive, S is a nonincreasing function in time and the trivial equilibrium is stable whenever S is positive definite. The positive definiteness of S and, consequently, the stability of the fluid-disk system are independent of Λ. This positive definiteness calculation gives the coupled critical speed.

Figure 2 shows the two critical speeds defining the positive definite boundaries of J and S as functions of κ. These boundaries were computed with Galerkin's method using the separable substitution

$$w(t, r, \theta) = u(r)e^{in\theta} \quad (18)$$

which is valid at any instant of time (Dym, 1974; Wickert and Mote, 1990). The number of nodal diameters, n, of the function (18) and the number of nodal circles in the solution that is first nonpositive definite are shown in Fig. 3. Thirteen orthonormal Chebyshev polynomials were used to define $u(r)$. As few as three polynomials were sufficient to give one percent accuracy for the uncoupled critical speeds. Ten polynomials were required for comparable accuracy for the coupled critical speed calculation.

As expected from the performance of devices such as Iomega's Zip Drive and the early floppy disk designs, the coupled critical speed is substantially larger than the uncoupled critical speed. The critical coupled eigenfunction also has many more nodal diameters than the critical uncoupled eigenfunction, and for $\kappa < 0.25$ one nodal circle.

Any motion of the disk for which $12w_{,t} + 6\Omega w_{,\theta} = 0$ generates no pressure in the air films and corresponds to undamped vibration of the disk. Such motions take the form $w(t, r, \theta) = u(r)e^{\lambda t + in\theta}$ where $\lambda = -in\Omega/2$ and correspond to a forward-traveling circumferential wave with n nodal diameters traveling at one-half the rotation speed of the disk. The eigenvalue calculation for such a λ is identical to the calculation of the positive definiteness boundary of S. These undamped modes therefore define the coupled critical speed. Since any other motion of the disk generates a nonzero pressure field, $S_{,t}$ is negative definite for speeds below the coupled critical speed, and the trivial equilibrium is asymptotically stable below the coupled critical speed.

5 Linearized Free Vibration

The strength of the hydrodynamic stiffness and damping at arbitrary speeds can be evaluated by linearizing the governing equations and boundary conditions about the equilibrium $w = p_L = p_U = 0$ and solving the free-response eigenvalue problem. After linearization, boundary condition (12) becomes

$$p_{L,r} + p_{U,r} = 0 \quad \text{at} \quad r = 1 \quad (19)$$

and (9) becomes

$$\nabla^2 p = \pm 12 w_{,t} \pm 6 w_{,\theta} \quad (20)$$

where the + sign is used for $p = p_L$ and the minus sign is used for $p = p_U$. The antisymmetry of (19) and (20) imply that $p_U = -p_L$ throughout the disk and $p_U = p_L = 0$ at $r = 1$. Consequently (20) need only be solved for $p = p_L$ and the term $(p_L - p_U)$ in (2) can be replaced by $2p_L$. For an arbitrary function $f(r)e^{in\theta}$, the equation

$$\nabla^2 p = f e^{in\theta} \quad (21)$$

with vanishing pressure at $r = \kappa$ and $r = 1$ has the solution

$$p = e^{in\theta} G_n[f] = e^{in\theta}\left\{\int_\kappa^r G_{n1}(z, r)f(z)dz + \int_r^1 G_{n2}(z, r)f(z)dz\right\} \quad (22)$$

where

$$G_{n1} = \begin{cases} -\log(r)z\log(z/\kappa)/\log(\kappa) & n = 0 \\ (r^n - r^{-n})z(z^n - \kappa^{2n}z^{-n})/[2n(1-\kappa^{2n})] & n \neq 0 \end{cases} \quad (23)$$

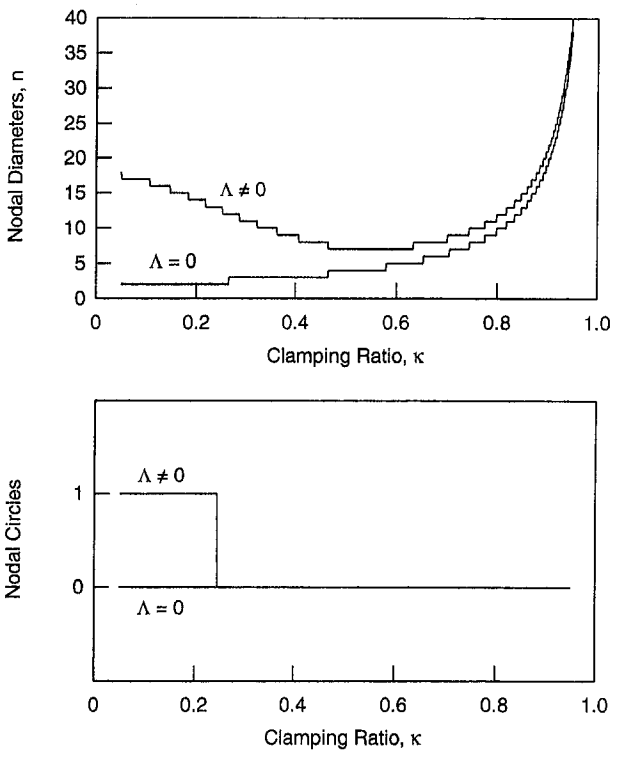

Fig. 3 The number of nodal diameters and nodal circles in the uncoupled and coupled critical speed solutions

Downloaded 04 May 2010 to 171.66.16.26. Redistribution subject to ASME license or copyright; see http://www.asme.org/terms/Terms_Use.cfm

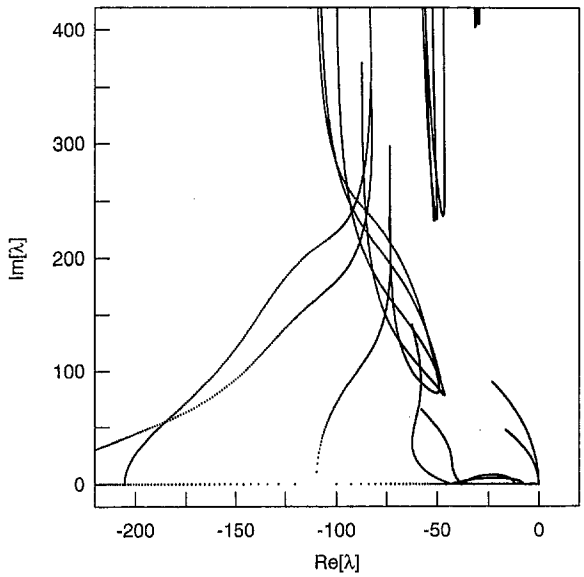

Fig. 4 Roots locus of the free vibration eigenvalues with $n = 0, \pm 1$, and ± 2 as Ω varies from 0 to 100 in increments of 0.25. As the eigensolutions come in conjugate pairs, only Im[λ] ≥ 0 are shown.

$$G_{n2} = \begin{cases} -\log(r/\kappa) z \log(z)/\log(\kappa) & n \neq 0 \\ (z^n - z^{-n}) z (r^n - \kappa^{2n} r^{-n})/[2n(1 - \kappa^{2n})] & n \neq 0. \end{cases} \tag{24}$$

Consequently, under the assumption

$$w(t, r, \theta) = u(r) e^{\lambda t + in\theta}, \tag{25}$$

the free-response problem takes the form

$$(\lambda^2 + 2\Omega i n\lambda - n^2\Omega^2)u = (24\Lambda\lambda + 12 i n \Omega \Lambda) G_n[u] - \nabla_n^4 u + (r\sigma_r u_{,r})_{,r}/r - n^2 \sigma_\theta u / r^2, \tag{26}$$

where ∇_n^4 is the biharmonic operator associated with n nodal diameters.

Figures 4, 5, and 6 shows the root loci of the eigenvalues, λ, for Ω ranging from 0 to 100 in increments of 0.25 for κ = 0.3 and Λ = 1000. Figure 4 shows the loci for $n = 0, \pm 1$, and ± 2; Fig. 5 shows the loci for $n = \pm 11$, the eigensolution for this κ that becomes unstable at $\Omega = 72.27$; and Fig. 6 shows the loci for $n = \pm 31$. Since the eigensolutions come in complex conjugate pairs, only the positive imaginary loci are shown. The same 13 orthonormal Chebyshev polynomials as in the previous section were used to define $u(r)$.

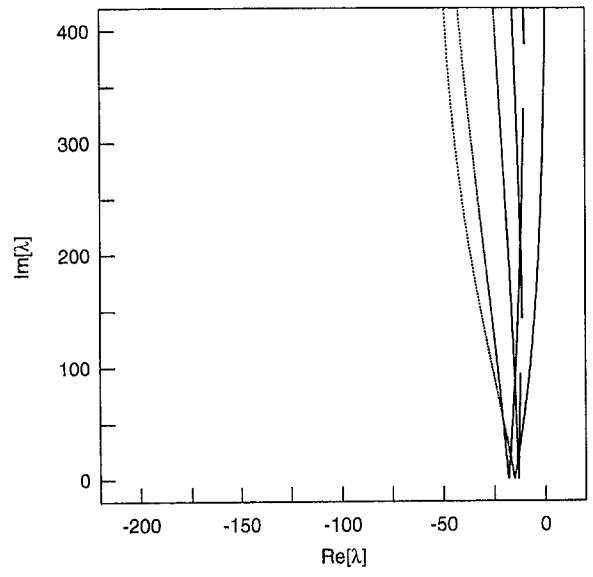

Fig. 5 Same as Fig. 4 except $n = 11$. The coupled critical speed solutions crosses the imaginary axis at Im[λ] = 397 when Ω = 72.27.

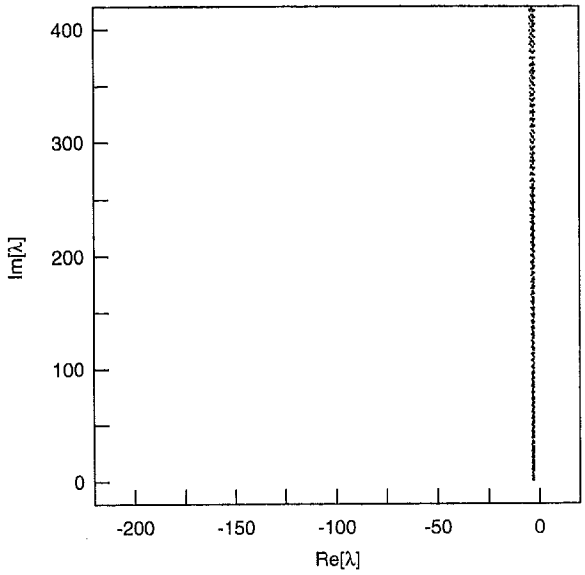

Fig. 6 Same as Fig. 4 except $n = 31$

The results confirm the stability prediction of Section 4 and show that the disk is unstable above the stability boundary. The first eigensolution with Re[λ] > 0 is the $n = 11$ solution occurring at $\Omega = 72.27$. Although several of the frequencies in Fig. 4 are close to the origin, they all have a small negative real part. There is no obvious pattern to the trajectories of the root loci as Ω increases. Branches corresponding to forward traveling waves move up along the positive imaginary axis while those associated with backward traveling waves approach the origin. The unstable locus crosses the imaginary axis at Im[λ] = $n\Omega/2 = 397$. As the number of nodal diameters n gets large, the root loci approach the imaginary axis, as illustrated in Figs. 5 and 6. Hence, the influence of hydrodynamic coupling decreases as n increases. Since stable eigensolutions exist in which either Re[λ] is negative but arbitrarily small or Im[λ] = 0, it is difficult to use λ as a design parameter measuring either linear stiffness or damping. These numerical observations are supported by empirical observations (Benson and Bogy, 1978).

5 Discussion

The time rate of change of S is dependent upon the displacement and pressure boundary conditions, and the problem considered has been posed so that (1) the entire disk (as opposed to a sector, for example) is coupled to the hydrodynamic lubrication and (2) the pressure boundary conditions are homogenous. If either of these is not true, then S no longer qualifies as a Lyapunov function and cannot be used to determine the stability of the system. For example, in many spinning disk studies, the outer shroud is not included and the rotation of the disk creates a significant radial air flow which in turn leads to non-homogenous pressure boundary conditions (Pelech and Shapiro, 1964; Chonan et al., 1992; Huang and Mote, 1995). These nonhomogenous boundary conditions disqualify S as a Lyapunov functional. While the absence of a Lyapunov functional does not imply that "shroudless" configurations are less stable, experimental evidence indicates that external shrouds significantly reduce disk vibration, even when hydrodynamic coupling is slight (Harrison et al., 1991).

Downloaded 04 May 2010 to 171.66.16.26. Redistribution subject to ASME license or copyright; see http://www.asme.org/terms/Terms_Use.cfm

Although there are many similarities between the spinning floppy disk problem and the longitudinal magnetic recording tape or "foil-bearing" problem (Wickert, 1993), the lack of periodic boundary conditions disqualifies the corresponding functional for the magnetic tape problem as a Lyapunov functional.

The specific form of S is determined by the coefficients 12 and 6 on the right-hand side of Reynolds' Eq. (9). If circumstances are arranged so that those two coefficients are equal, then a different Lyapunov functional can be constructed which is stable at all speeds. For example, if the fixed upper and lower surfaces of the floppy disk enclosure were to rotate at the same speed and in the same direction as the floppy disk itself, the coefficients in Reynolds' equation would both be 12. Or if these surfaces could deflect transversely at half the normal velocity of the floppy disk, both coefficients would be 6. These scenarios are reminiscent of the stacked flexible disk drive configuration proposed by Bogy and Talke (1978) which may possess interesting stability properties.

6 Conclusions

1 The stability of flexible rotating disks coupled to incompressible hydrodynamic lubrication can be analyzed using Lyapunov's method. This analysis shows that these systems are asymptotically stable for rotation speeds below a hydrodynamically coupled critical speed.

2 The hydrodynamically coupled critical speed is three to ten times higher than the uncoupled critical speed.

3 The stable speed range is independent of the strength of hydrodynamic coupling.

4 The Lyapunov stability result is corroborated by linear free-vibration analysis.

5 The validity of the Lyapunov functional is dependent on hydrodynamic coupling over the entire disk and homogenous pressure boundary conditions. The stability of floppy disk designs which permit significant radial flow, or which involve hydrodynamic lubrication over only a sector of the disk, cannot be analyzed using the Lyapunov functional given here.

References

Adams, G. G., 1987, "Critical Speeds for a Flexible Spinning Disk," *International Journal of Mechanical Sciences,* Vol. 29, pp. 525–531.

Benson, R. C., and Bogy, D. B., 1978, "Deflection of a Very Flexible Spinning Disk Due to a Stationary Transverse Load," ASME JOURNAL OF APPLIED MECHANICS, Vol. 45, pp. 636–642.

Bogy, D. B., and Talke, F. E., 1978, "Steady Axisymmetric Solutions for Pressurized Rotating Flexible Disk Packs," *IBM Journal of Research and Development,* Vol. 22, No. 2, pp. 179–184.

Carpino, M., and Domoto, G. A., 1988, "Axisymmetric Solution of a Flexible Disk Rotating Near a Rigid Surface," ASME *Journal of Tribology,* Vol. 110, pp. 674–677.

Chonan, S., Jiang, Z. W., and Shyu, Y. J., 1992, "Stability Analysis of a 2 Inch Floppy Disk Drive System and the Optimum Design of the Disk Stabilizer," *Journal of Vibration and Acoustics,* Vol. 114, pp. 283–286.

Dym, C. L., 1974, *Stability Theory and Its Applications to Structural Mechanics,* Noordhoff International, Leyden.

Hahn, W., 1967, *Stability of Motion,* Springer-Verlag, New York.

Harrison, J. C., Miller, C. W., and Talke, F. E., 1991, "Disk Surface Acceleration Effects Due to Air Flow Induced by the Rotation," *Advances in Information Storage Systems,* Vol. 1, pp. 155–169.

Huang, F. Y., and Mote, Jr., C. D., 1995, "On the Instability Mechanisms of a Disk Rotating Close to a Rigid Surface," ASME JOURNAL OF APPLIED MECHANICS, Vol. 62, pp. 764–771.

Huang, F. Y., and Mote, Jr., C. D., 1996, "Mathematical Analysis of Stability of a Spinning Disk Under Rotating, Arbitrarily Large Damping Forces," *Journal of Vibration and Acoustics,* Vol. 118, pp. 657–662.

Iwan, W. D., and Moeller, T. L., 1976, "The Stability of a Spinning Elastic Disk with a Transverse Load System," ASME JOURNAL OF APPLIED MECHANICS, Vol. 43, pp. 485–490.

Mote, Jr., C. D., 1970, "Stability of Circular Plates Subjected to Moving Loads," *Journal of the Franklin Institute,* Vol. 290, No. 4, pp. 329–344.

Movchan, A. A., 1959, "The Direct Method of Liapunov in Stability Problems of Elastic Systems," *Journal of Applied Mathematics and Mechanics,* Vol. 23, No. 1, pp. 686–700.

Nowinski, J. L., 1964, "Nonlinear Transverse Vibrations of a Spinning Disk," ASME JOURNAL OF APPLIED MECHANICS, Vol. 31, pp. 72–78.

Pars, L. A., 1979, *A Treatise on Analytical Dynamics,* Ox Bow Press, Woodbridge, CT.

Pelech, I., and Shapiro, A. H., 1964, "Flexible Disk Rotating on a Gas Film Next to a Wall," ASME JOURNAL OF APPLIED MECHANICS, Vol. 31, pp. 577–584.

Renshaw, A. A., and Mote, Jr., C. D., 1996, "Local Stability of Gyroscopic Systems Near Vanishing Eigenvalues," ASME JOURNAL OF APPLIED MECHANICS, Vol. 63, pp. 116–120.

Renshaw, A. A., Rahn, C. D., Wickert, J. A., Mote, Jr., C. D., 1996, "Energy and Conserved Functionals for Axially Moving Materials," *Journal of Vibration and Acoustics,* to appear.

Szeri, A. Z., ed., 1980, *Tribology: Friction, Lubrication, and Wear,* McGraw-Hill, New York.

Sokolnikoff, I. S., 1956, *Mathematical Theory of Elasticity,* 2nd ed, McGraw-Hill, New York.

Tobias, S. A., and Arnold, R. N., 1957, "The Influence of Dynamical Imperfection on the Vibration of Rotating Disks," *Proceedings of the Institute of Mechanical Engineers,* Vol. 171, pp. 669–690.

Wickert, J. A., 1993, "Free Linear Vibration of Self-Pressurized Foil Bearings," *Journal of Vibration and Acoustics,* Vol. 115, pp. 145–151.

Wickert, J. A., and Mote, Jr., C. D., 1990, "Classical Vibration Analysis of Axially Moving Continua," ASME JOURNAL OF APPLIED MECHANICS, Vol. 57, pp. 738–744.

Downloaded 04 May 2010 to 171.66.16.26. Redistribution subject to ASME license or copyright; see http://www.asme.org/terms/Terms_Use.cfm

A Theoretical Prediction of Natural Frequency of a Ferromagnetic Beam Plate With Low Susceptibility in an In-Plane Magnetic Field

You-He Zhou
Professor,
Department of Mechanics,
Lanzhou University,
Lanzhou, Gansu 730000, P. R. China
e-mail: zhouyh@lzu.edu.cn

Kenzo Miya
Professor,
Nuclear Engineering Research Laboratory,
The University of Tokyo,
Tokyo, Japan

In order to simulate the experimental phenomenon of increase of natural frequency to a cantilevered ferromagnetic beam plate in in-plane magnetic fields, a theoretical model for behaving the magnetoelastic interaction is proposed in this paper based on the variational principle of energy functional of the system. It is found that the expression of magnetic force is distinctly different from those of the existing theoretical models in publications, and the experimental phenomenon is successfully simulated by this theoretical model. After the increase of natural frequency is quantitatively considered in the predictions of magnetic damping, the theoretical predictions of magnetic damping ratio are agreement with the corresponding experimental data well.

1 Introduction

The research for behaving magnetoelastic interaction of ferromagnetic structures can be traced to the 1960s (Panovko and Gubanova, 1965; Moon and Pao, 1968). Moon and Pao (1968) were the first to conduct experiments of magnetoelastic buckling to a ferromagnetic cantilevered plate in transverse magnetic fields, which shows the buckling magnetic field varying with $-\frac{3}{2}$ power of the ratio of length to thickness. At the same time, they proposed a theoretical model for predicting the experimental phenomenon. Since there is, sometimes, a big discrepancy between the theoretical predictions and the experimental data of critical magnetic field, many researchers devote their attention to finding an explanation for why this is so (Popeler, 1972; Wallerstain and Peach, 1972; Dalrymple et al., 1974; Miya et al., 1978, 1980; Peach et al., 1988 etc.). On the other hand, there are a number of monographs which discuss the general theory of magnetoelastic interaction for ferromagnetic solids on the basis of the axiomatic method or variational principle of the coupled system of electromagnetic theory and continuum solid mechanics in which the magnetic force exterted on the magnetic body is prechosen as a Maxwell stress tensor (e.g., Brown, 1966; Pao and Yeh, 1973; and van Lieshout et al., 1987; etc.). It is found that these theoretical models can simulate the experimental phenomenon of magnetoelastic interaction of ferromagnetic plate structures. However, the discrepancy has not been disappeared. Recently, Zhou et al. (1995) and Zhou and Zheng (1996) proposed a new theoretical model for the magnetoelastic buckling and bending of ferromagnetic plate in a transverse and/or oblique magnetic field. It is exhabited in this new model that magnetic force system on magnetic body consists of the body force only. The obtained results show that the predictions from this model are much lower than those of Moon-Pao's formula and, some of them, a little higher than experimental data. From the magnetoelastic bending of the plate in oblique magnetic fields, the discrepancy can be explained well.

As the ferromagnetic structure with low susceptibility was suggested as a candidate of the first wall in fusion reactors, such as a ferritic steel (8% Cr – 2% W – 0.2% V – 0.04% Ta-Fe, which is abbreviated as F-82H), the research on the behavior of the interaction between the magnetic field and mechanical deformation for the structures, which are made of the F-82H materials, attracted the attention of researchers and engineers (Yamanouchi et al., 1992; Tagaki et al., 1993). An interesting experiment for the ferromagnetic plate in an in-plane applied magnetic field was conducted by Tagaki et al. (1993). The experimental results show that the natural frequency of the structure increases with the applied magnetic field. This experimental phenomenon is indeed a challenge to all existing models mentioned above since they cannot describe it. That is, when we use them to predict the experiment of an increase of natural frequency, the decrease of natural frequency will be obtained. In this case, there is a necessity for us to find a way of predicting the experimental phenomenon by accounting for the characteristics of the magnetoelastic interaction for the ferromagnetic structures.

Based on the variational principle of a total energy functional of the magnetic and mechanical systems, a new theory for the ferromagnetic beam plate with low susceptibility in an in-plane magnetic field is established so that the experimental phenomenon of an increase of natural frequency with an applied magnetic field can be explained theoretically. After the change of natural frequency of the plate is considered, the predictions of the magnetic damping ratio are in good agreement with the experimental data.

2 Variational Principle

For the reason of simplicity, here we will neglect the effect of an eddy current on the natural frequency in the derivation of an expression of magnetic force for the problem considered in this paper. For a stationary magnetic field without an electric field, charge distribution, and conduction current on and in the

Contributed by the Applied Mechanics Division of THE AMERICAN SOCIETY OF MECHANICAL ENGINEERS for publication in the ASME JOURNAL OF APPLIED MECHANICS.

Discussion on this paper should be addressed to the Technical Editor, Professor Lewis T. Wheeler, Department of Mechanical Engineering, University of Houston, Houston, TX 77204-4792, and will be accepted until four months after final publication of the paper itself in the ASME JOURNAL OF APPLIED MECHANICS.

Manuscript received by the ASME Applied Mechanics Division, Oct. 31, 1994; final revision, Aug. 3, 1997. Associate Technical Editor: M. Taya.

 Copyright © 1998 by ASME

Downloaded 04 May 2010 to 171.66.16.26. Redistribution subject to ASME license or copyright; see http://www.asme.org/terms/Terms_Use.cfm

magnetoelastic medium from the Maxwell equations of electromagnetism, we can introduce a scalar potential function ϕ, that is,

$$-\nabla\phi = \mathbf{H}. \tag{1}$$

After taking a closed surface which incloses and is far away from the ferromagnetic medium, and denoting it as S_0, we can write the magnetic energy of the form (Zhou et al., 1995)

$$\Pi_1\{\phi, \mathbf{U}\} = \frac{1}{2}\int_{\Omega^-(\mathbf{U})} \mu_0(\nabla\phi^-)^2 dv + \frac{1}{2}\int_{\Omega^+(\mathbf{U})} \mu_0\mu_r(\nabla\phi^+)^2 dv + \int_{S_0} \mathbf{n}\cdot\mathbf{B}_0\phi^- ds. \tag{2}$$

The last term in the above formula is the external work by the applied magnetic field. For a linear magnetic relation between the magnetic field vector $\mathbf{H}$ and magnetization $\mathbf{M}$ or magnetic induction $\mathbf{B}$, we can write

$$\mathbf{M}^+ = \chi\mathbf{H}^+ \quad \text{in} \quad \Omega^+ \tag{3a}$$

$$\mathbf{M}^- = \mathbf{0} \quad \text{in} \quad \Omega^- \tag{3b}$$

or

$$\mathbf{B}^+ = \mu_0\mu_r\mathbf{H}^+ \quad \text{in} \quad \Omega^+ \tag{4}$$

$$\mathbf{B}^- = \mu_0\mathbf{H}^- \quad \text{in} \quad \Omega^-. \tag{5}$$

Here, Ω^+ and Ω^- represent the inside and outside regions of a deformed ferromagnetic medium, respectively; S denotes the surface of the ferromagnetic medium; $\mathbf{B}_0$ is an applied magnetic field; $\mathbf{n}$ is a unit vector outward normal to S or S_0; χ is susceptibility of the soft ferromagnetic medium; μ_0 and μ_r are the magnetic permeability of a vacuum and the relative permeability of the ferromagnetic medium, respectively; and the following formula

$$\mu_r = \chi + 1 \tag{6}$$

is held for the soft ferromagnetic material.

The mechanical strain energy in Ω^+ and the external work on S_t can be written as follows:

$$\Pi_2\{\phi, \mathbf{U}\} = \frac{1}{2}\int_{\Omega^+} \boldsymbol{\sigma} : \boldsymbol{\epsilon} dv - \int_{S_t} \mathbf{F}^*\cdot\mathbf{U} ds. \tag{7}$$

For linear elasticity of both material and geometry, we can write

$$\boldsymbol{\sigma} = \mathbf{Y} : \boldsymbol{\epsilon} \quad \text{in} \quad \Omega^+ \tag{8}$$

for constitutive equations of elasticity, and

$$\boldsymbol{\epsilon} = (\nabla\mathbf{U} + (\nabla\mathbf{U})^T)/2 \quad \text{in} \quad \Omega^+ \tag{9}$$

for geometrical relations. Here, $\boldsymbol{\sigma}$ and $\boldsymbol{\epsilon}$ represent stress and strain tensors, respectively; $\mathbf{Y}$ is a fourth-order tensor of elastic constants of the material; $\mathbf{U}$ denotes a displacement vector; $\mathbf{F}^*$ is a specific external force on S_t of the force boundary of surface S; and the superscript "T" represents the transpose of a tensor or matrix.

Thus the total energy of the system can be obtained by adding Π_1 and Π_2. That is

$$\Pi\{\phi, \mathbf{U}\} = \Pi_1\{\phi, \mathbf{U}\} + \Pi_2\{\phi, \mathbf{U}\} = \frac{1}{2}\int_{\Omega^-(\mathbf{U})} \mu_0(\nabla\phi^-)^2 dv + \frac{1}{2}\int_{\Omega^+(\mathbf{U})} \mu_0\mu_r(\nabla\phi^+)^2 dv + \int_{S_0} \mathbf{n}\cdot\mathbf{B}_0\phi^- ds + \frac{1}{2}\int_{\Omega^+} \boldsymbol{\sigma} : \boldsymbol{\epsilon} dv - \int_{S_t} \mathbf{F}^*\cdot\mathbf{U} ds. \tag{10}$$

It should be noted that the displacement $\mathbf{U}$ does not explicitly appear in ϕ; and the effect of displacement on the region Ω^+ in the integral of strain energy will be neglected for a small deformation. Let $\delta\mathbf{U}$ and $\delta\phi$ be the admissible variations of displacement and the magnetic potential function of the system, respectively. Then we have

$$\delta\mathbf{U} = \mathbf{0} \quad \text{on} \quad S_u \tag{11}$$

and

$$\delta\phi^+ = \delta\phi^- = \delta\phi \quad \text{on} \quad S \tag{12}$$

and the compatibility conditions for $\delta\mathbf{U}$ should be satisfied. Here, S_u represents the displacement boundary surface of S. Considering that the variations of ϕ and $\mathbf{U}$ are independent of each other, according to the arithmetic of variation, we can get (Zhou et al., 1995):

$$\delta\Pi\{\phi, \mathbf{U}\} = -\int_{\Omega^+(\mathbf{U})} \mu_0\mu_r(\nabla^2\phi^+)\delta\phi^+ dv - \int_{\Omega^-(\mathbf{U})} \mu_0(\nabla^2\phi^-)\delta\phi^- dv + \oint_S \boldsymbol{\mu}_0\left\{\mu_r\frac{\partial\phi^+}{\partial n} - \frac{\partial\phi^-}{\partial n}\right\}\delta\phi ds + \int_{S_0} \mathbf{n}\cdot\{\mu_0\nabla\phi^- + \mathbf{B}_0\}\delta\phi^- ds + \oint_S T(x, y, z)\mathbf{n}\cdot\delta\mathbf{U} ds - \int_{\Omega^+} \nabla\cdot\boldsymbol{\sigma}\cdot\delta\mathbf{U} dv + \int_{S_t} \{\mathbf{n}\cdot\boldsymbol{\sigma} - \mathbf{F}^*\}\cdot\delta\mathbf{U} ds + \int_{S_U} \mathbf{n}\cdot\boldsymbol{\sigma}\cdot\delta\mathbf{U} ds \tag{13}$$

in which

$$T = -\frac{\mu_0\mu_r\chi}{2}(H_n^+)^2 + \frac{\mu_0\chi}{2}(H_\tau^+)^2 \quad \text{on} \quad S \tag{14}$$

is the change of density of magnetic energy between the two sides on surface S. Thus, its integration on the surface S represents the flux of magnetic energy flowing out the region Ω^+ when a set of admissible variation of displacement, $\delta\mathbf{U}$, is given. Here, the subscripts "n" and "τ" are used to represent the normal and tangential components of the quantities.

For a thin ferromagnetic beam plate in an in-plane applied magnetic field as shown in Fig. 1, we introduce two assumptions:

$$\nabla\cdot\delta\mathbf{U} \approx 0 \quad \text{in} \quad \Omega^+ \tag{15}$$

$$\frac{\mu_0\chi}{2}(H^+)^2 \gg \frac{\mu_0\chi(\mu_r + 1)}{2}(H_n^+)^2 \quad \text{on} \quad S. \tag{16}$$

In the next section we will give some numerical valuations to show the reasonability of these two assumptions for the thin beam plate with low susceptibility when the plate is placed in

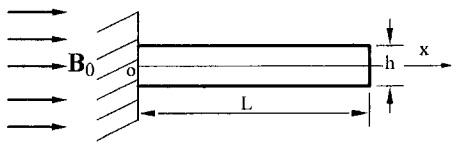

Fig. 1 Schematic drawing of a ferromagnetic cantilevered beam plate in an in-plane magnetic field

Downloaded 04 May 2010 to 171.66.16.26. Redistribution subject to ASME license or copyright; see http://www.asme.org/terms/Terms_Use.cfm

an in-plane applied magnetic field. Under these assumptions we can get

$$\oint_S T(x, y, z)\mathbf{n}\cdot\delta\mathbf{U}ds \approx \frac{\mu_0\chi}{2}\int_{\Omega^+}\{\nabla(H^+)^2\}\cdot\delta\mathbf{U}dv. \quad (17)$$

Substituting Eq. (17) into Eq. (13), we have

$$\begin{aligned}\delta\Pi\{\phi, \mathbf{U}\} = &-\int_{\Omega^+(\mathbf{U})}\mu_0\mu_r(\nabla^2\phi^+)\delta\phi^+dv\\ &-\int_{\Omega^-(\mathbf{U})}\mu_0(\nabla^2\phi^-)\delta\phi^-dv\\ &+\oint_S\mu_0\left\{\mu_r\frac{\partial\phi^+}{\partial n}-\frac{\partial\phi^-}{\partial n}\right\}\delta\phi ds\\ &+\int_{S_0}\mathbf{n}\cdot\{\mu_0\nabla\phi^- + \mathbf{B}_0\}\delta\phi^-ds\\ &-\int_{\Omega^+}\left\{\nabla\cdot\boldsymbol{\sigma}-\frac{\mu_0\chi}{2}\nabla(H^+)^2\right\}\cdot\delta\mathbf{U}dv\\ &+\int_{S_t}\{\mathbf{n}\cdot\boldsymbol{\sigma}-\mathbf{F}^*\}\cdot\delta\mathbf{U}ds\\ &+\int_{S_U}\mathbf{n}\cdot\boldsymbol{\sigma}\cdot\delta\mathbf{U}ds. \quad (18)\end{aligned}$$

Let $\delta\Pi\{\phi, \mathbf{U}\} = 0$. According to arbitrariness and independence of $\delta\phi$ and $\delta\mathbf{U}$, there is no difficulty for one to obtain all governing equations and boundary conditions of a theoretical model for characterizing the magnetoelastic interaction as follows.

Governing Equations for Magnetic fields.

$$\nabla^2\phi^+ = 0 \quad \text{in} \quad \Omega^+, \quad (19)$$

$$\nabla^2\phi^- = 0 \quad \text{in} \quad \Omega^-, \quad (20)$$

with the connected conditions

$$\phi^+ = \phi^- \quad \text{on} \quad S, \quad (21)$$

$$\mu_r\frac{\partial\phi^+}{\partial n} = \frac{\partial\phi^-}{\partial n} \quad \text{on} \quad S \quad (22)$$

and the boundary conditions on S_0

$$-\nabla\phi^- = \frac{1}{\mu_0}\mathbf{B}_0 \quad \text{at} \quad \infty \quad \text{or} \quad \text{on} \quad S_0. \quad (23)$$

Mechanical Equilibrium Equations.

$$\nabla\cdot\boldsymbol{\sigma} + \mathbf{f}^{em} = \mathbf{0} \quad \text{in} \quad \Omega^+ \quad (24)$$

with the boundary equations

$$\mathbf{U} = \mathbf{U}^* \quad \text{on} \quad S_u \quad (25)$$

$$\mathbf{n}\cdot\boldsymbol{\sigma} = \mathbf{F}^* \quad \text{on} \quad S_t \quad (26)$$

where $\mathbf{U}^*$ is a specific displacement vector on S_u; and the magnetic body force exerted on the ferromagnetic plate is formulated by

$$\mathbf{f}^{em} = -\frac{\mu_0\chi}{2}\nabla(\mathbf{H}^+)^2 \quad \text{in} \quad \Omega^+. \quad (27)$$

It is obvious that this expression of magnetic force is totally different from those which appeared in the existing theoretical models for the magnetoelastic interaction of a ferromagnetic medium in an applied magnetic field. For example, Zhou et al. (1995) and Zhou and Zheng (1996) gave the formula of magnetic force for the magnetoelastic buckling of ferromagnetic plates in a transverse magnetic field with the form

$$\mathbf{f}^{em} = \frac{\mu_0\chi\mu_r}{2}\nabla(\mathbf{H}^+)^2 \quad \text{in} \quad \Omega^+.$$

We will see later that the theoretical model associated with the magnetic force of Eq. (27) can simulate the experimental phenomenon in Tagaki et al. (1993).

3 Applicability Region of the Theoretical Model

From Section 2 we can find that the theoretical model associated with the expression of the magnetic force of Eq. (27) obtained in the previous section is dependent on the two assumptions we introduced. When the plate is thin, the variation of volume strain, $\nabla\cdot\delta\mathbf{U}$, in the region Ω^+ is so small that we can neglect it. Hence, the first assumption is reasonable and acceptable for the case of thin plates. The next is to show when the second assumption is held. Let

$$T_n^* = \frac{\mu_0\chi(\mu_r+1)}{2}(H_n^+)^2|_{z=\pm h/2},$$

$$T_\tau^* = \frac{\mu_0\chi}{2}(H^+)^2|_{z=\pm h/2}. \quad (28)$$

Some numerical tests are conducted to show the distributions of T_n^* and T_τ^* for the case of ferromagnetic beam plates placed in a uniformly distributed in-plane magnetic field. The distributions of T_n^* and T_τ^* on the top or bottom surface of the plate are plotted in Fig. 2 for the ratio of length to thickness, $L/h = 100$, and $\chi = 14$. In this figure, the solid and dot dash lines respectively represent the distributions of T_τ^* and T_n^* on the top or bottom surface of the beam plate along the axial direction. From this figure it shows that the magnitude of T_n^* is much smaller than the value of T_τ^* in almost the whole region except for the small regions near the end points of the plate. As the susceptibility increases, the value of T_n^* increases while T_τ^* decreases for a fixed ratio L/h. When χ is greater than the value χ_0, the former will not become small in comparison with the value of the latter. In this case, the condition of the second assumption of Eq. (16) is violated; thus the obtained expression of the magnetic force of Eq. (27) cannot be used in the cases of the plates with large value of susceptibility χ, which is over the critical value χ_0. The numerical valuations show that the critical value χ_0 is dependent upon the ratio of length to thickness of the plate. The larger the ratio, the larger the value of χ_0. Since it is dependent on the comparison of values of T_n^* and T_τ^*, in practice, it is not easy for us to exactly give the critical value χ_0. A rough confirmation for this value from the numerical tests is carried out here. Three cases of the ratio of

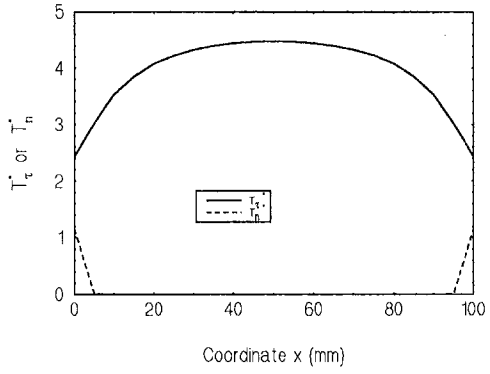

Fig. 2 The distribution of T_τ^* and T_n^* on the top and bottom surface of the beam plate in an in-plane magnetic field (B_0 = 17; L/h = 100; χ = 14.0)

Downloaded 04 May 2010 to 171.66.16.26. Redistribution subject to ASME license or copyright; see http://www.asme.org/terms/Terms_Use.cfm

100, 200, and 333.3 for the critical value χ_0 are listed in Table 1. From Table 1 we can find the region of susceptibility for the applications of the theoretical model of Eqs. (19)–(27), and that the value of χ of the ferromagnetic material employed in the experiments of increase of natural frequency is in the applicability region of susceptibility. Hence, the new model of Eqs. (19)–(26) associated with the magnetic force formula of Eq. (27) can be applied to simulating the experimental phenomenon of increase of natural frequency (Tagaki et al., 1993, 1995).

4 Galerkin Method for Natural Frequency

Take a rectangular coordinate system xoz as shown Fig. 1 in which the x and z-axes are along the axial direction and the transverse direction of the beam plate, respectively. For the unit width of the plate after the magnetic forces are transformed to the middle plane of the plate, the dynamic governing equations for the cantilevered beam plate subjected to both transverse and axial magnetic forces is expressed by the form

$$D\frac{\partial^4 w}{\partial x^4} - N_x\frac{\partial^2 w}{\partial x^2} - \frac{\partial N_x}{\partial x}\frac{\partial w}{\partial x} = -\rho h\frac{\partial^2 w}{\partial t^2} + q_z^{em}(x) \qquad 0 < x < L \quad (29)$$

with the boundary conditions

$$x = 0 : w = 0; \quad \frac{\partial w}{\partial x} = 0; \qquad (30a,b)$$

$$x = L : \frac{\partial^2 w}{\partial x^2} = 0; \quad \frac{\partial^3 w}{\partial x^3} = 0. \qquad (31a,b)$$

Here the transverse magnetic force exerted on the plate is given by

$$q_z^{em}(x) = \int_{-h/2}^{h/2} f_z^{em}(x, z)dz. \qquad (32)$$

From the equilibrium equation in the x-direction one can write

$$N_x(x) = -\int_x^L \int_{-h/2}^{h/2} f_x^{em}(x, z)dzdx. \qquad (33)$$

Substitution of Eq. (27) into Eqs. (32) and (33) leads to

$$q_z^{em}(x) = -\frac{\mu_0\chi}{2}\{[H^+(x, h/2)]^2 - [H^+(x, -h/2)]^2\} \quad (34)$$

$$N_x(x) = \frac{\mu_0\chi}{2}\int_{-h/2}^{h/2}\{[H^+(x, z)]^2 - [H^+(L, z)]^2\}dz \approx \frac{\mu_0\chi h}{2}\{[H^+(x, 0)]^2 - [H^+(L, 0)]^2\}. \qquad (35)$$

Here D is the flexural rigidity of the plate; h is the thickness of the plate; L is the length of the plate; w is the deflection in the transverse direction; N_x is the internal force in the axial direction; ρ is the density of mass of the plate; t is the time variable; and f_x^{em} and f_z^{em} represent the components of the magnetic force $\mathbf{f}^{em}$ in the x and z-directions, respectively.

Let $\bar{w}(x)$ be a normalized eigenfunction of the dynamic problem and

Table 1 The applicability region of susceptibility of the theoretical model proposed in this paper: $\chi \leq \chi_0$

L/h	χ_0
100	500
200	2000
333.3	10000

$$w(x, t) = \alpha\bar{w}(x)e^{i\omega t} \qquad (36)$$

in which α is a small positive number and ω refers to a natural frequency of the loaded plate. When the deflection is small we can expand the magnetic field vector $\mathbf{H}^+(x, \bar{z})$ in the case of a deformed state of a plate by the magnetic field $\mathbf{H}_0^+(x, z)$ in the case of an undeformed state of the plate. Denoting the coordinate z for the undeformed state and the coordinate $\bar{z}$ for the deformed state of the plate, we have

$$\bar{z} = z + \alpha\bar{w}e^{i\omega t} \qquad (37)$$

$$\mathbf{H}^+(x, \bar{z}) = \mathbf{H}_0^+(x, z) + \alpha\bar{w}(x)\frac{\partial\mathbf{H}_0^+(x, z)}{\partial z}e^{i\omega t} + \ldots. \qquad (38)$$

Considering the symmetric property of $\mathbf{H}_0^+(x, z)$ as in Zhou et al. (1995), and substituting Eq. (38) into Eq. (34), then neglecting the terms of order 2 and higher than order 2 of α, one can obtain the linear expression of the equivalent transverse magnetic force

$$q_z^{em}(x, t) = \alpha\bar{q}_z^{em}(x)e^{i\omega t} \qquad (39)$$

where

$$\bar{q}^{em}(x) = -2\mu_0\chi\mathbf{H}_0^+(x, h/2)\cdot\frac{\partial\mathbf{H}_0^+(x, h/2)}{\partial z}\bar{w}(x). \quad (40)$$

Substituting Eqs. (36) and (39) into Eqs. (29)–(31), we get the eigenvalue equations of $\bar{w}(x)$ as follows:

$$D\frac{d^4\bar{w}}{dx^4} - N_x\frac{d^2\bar{w}}{dx^2} - \frac{dN_x}{dx}\frac{d\bar{w}}{dx} = \rho h\omega^2\bar{w}(x) + \bar{q}_z^{em}(x) \qquad 0 < x < L \quad (41)$$

with the boundary conditions

$$x = 0 : \bar{w} = 0; \quad \frac{d\bar{w}}{dx} = 0; \qquad (42a,b)$$

$$x = L : \frac{d^2\bar{w}}{dx^2} = 0; \quad \frac{d^3\bar{w}}{dx^3} = 0. \qquad (43a,b)$$

In the following, we will choose the eigenfunction of the cantilevered beam plate without applied loads as an admissible function of the Galerkin method to approximately calculate the natural frequency of the ferromagnetic structure. From the textbook we have (Meirovitch, 1967, pp. 161–166),

$$\bar{w}(x) = \bar{w}^*(x) = [(\sin\beta L - \sinh\beta L)(\sin\beta x - \sinh\beta x) + (\cos\beta L + \cosh\beta L)(\cos\beta x - \cosh\beta x)]/(\sin\beta L - \sinh\beta L) \quad (44)$$

which satisfies all boundary conditions of Eqs. (42)–(43). By applying the Galerkin method to Eq. (41), we get

$$\omega^2 = \omega_1^2 + \frac{1}{\Delta}\int_0^L N_x(x)\left[\frac{d\bar{w}^*}{dx}\right]^2 dx - \frac{1}{\Delta}\int_0^L \bar{q}_z^{em}(x)\bar{w}^*(x)dx \quad (45)$$

Downloaded 04 May 2010 to 171.66.16.26. Redistribution subject to ASME license or copyright; see http://www.asme.org/terms/Terms_Use.cfm

in which

$$\Delta = \rho h \int_0^L [\bar{w}^*(x)]^2 dx \tag{46}$$

$$\omega_1^2 = \frac{1}{\Delta} \int_0^L D \frac{d^4 \bar{w}^*(x)}{dx^4} \bar{w}^*(x) dx \tag{47}$$

where ω_1 is a natural frequency of the cantilevered beam plate under no applied load. From Eq. (45) we find that the last two terms on the right-hand side of the equation are the effect of the axial extension force and the equivalent transverse magnetic force on the natural frequency of the plate, respectively.

5 Numerical Results and Analysis

According to the analysis in the previous sections, a numerical program is carried out by computer for predicting the natural frequency of free vibration of the first mode of the cantilevered beam plate in a uniform in-plane applied magnetic field. Here, the distribution of magnetic fields are analyzed by the finite element method (Zhou and Zheng, 1994; Zhou et al., 1995). From the eigenfunction of vibration of the first mode to a cantilevered plate under no applied load (Eq. (44)), we know that $\beta L = 1.875$ (Meirovitch, 1967, pp. 161–166). In order to make a comparison with the experimental data, the parameters of the apparatus, which are listed in Table 2, are taken as the same as those given in Tagaki et al. (1995). Let

$$a_1 = \frac{1}{\Delta} \int_0^L N_x(x) \left[\frac{d\bar{w}^*(x)}{dx} \right]^2 dx \tag{48}$$

$$a_2 = -\frac{1}{\Delta} \int_0^L \bar{q}_z^{em}(x) \bar{w}^*(x) dx. \tag{49}$$

From the output values of a_1 and a_2, we find that both a_1 and a_2 are greater than zero, and a_2 is much greater than a_1. These results tell us that the change of natural frequency is mainly generated from the equivalent transverse magnetic force, $q_z^{em}(x)$. The change of natural frequency with the in-plane applied magnetic field is shown in Fig. 3(a) for $L/h = 100/0.29$ and Fig. 3(b) for $L/h = 100/0.5$, where $\chi = 7 \sim 15$ corresponds to the region of the parameter used in the experiments (Tagaki et al., 1995). From them one can find that the natural frequency of the plate increases with the applied magnetic field, and there is an obvious effect of susceptibility χ on the change of frequency. The larger the susceptibility of the ferromagnetic plate the larger the change.

Comparison of the theoretical predictions with the experimental data of the increase of natural frequency is shown in Fig. 3. It is found that this model successfully predicts the increase of natural frequency with the applied magnetic field, but there is some difference between the theoretical predictions and the experimental data. That is, the experimental curves of natural frequency with the applied magnetic field convexly increase while the theoretical predictions concavely increase. Since the interaction between the magnetic field and deformation is sensitive to the nonlinear coupling interaction of magnetoelasticity as pointed out in Zhou et al. (1995), and there is the effect of the nonlinearly magnetic constitutive relation on

Table 2 Parameters of apparatus of ferromagnetic material F-82H (taken from Tagaki et al., 1995)

Density of mass, ρ	7.8×10^3 (Kg/m^3)
Young modulus, E	2.0×10^{11} (Pa)
Poisson's ratio, ν	0.30
Thickness of plate, h	0.29 and 0.50 (mm)
Length of plate, L	100 (mm)
Magnetic permeability, μ	$1-2 \times 10^{-5}$
Conductivity, σ,	2.3×10^6 (S/m)

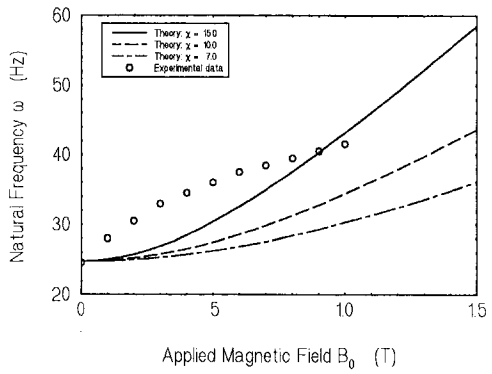

Fig. 3(a)

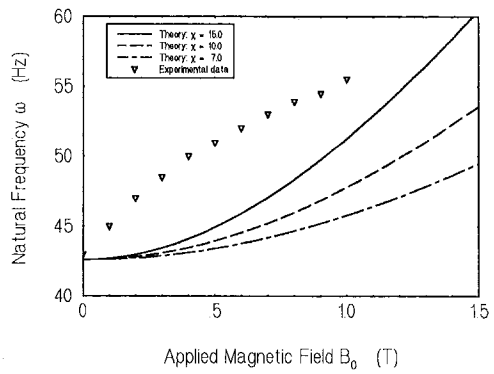

Fig. 3(b)

Fig. 3 Change of natural frequency with a magnetic field for an F-82H ferromagnetic cantilevered beam plate in an in-plane magnetic field (L = 100 mm)

vibration frequency in the experiments, the theoretical predictions should be revised on the basis of the nonlinear theory. After these influences are considered, it is possible that the theoretical predictions would become closer to the experimental data.

By the way, there is no difficulty in giving a revision to the theoretical prediction of magnetic damping based on the method of Tagaki et al. (1993) after the change of natural frequency is considered. According to the Faraday's law of Maxwell equations, and Ohm's law, it is reasonable to assume that the density of an eddy current in the structure is proportional to the vibration frequency of a magnetic field, further, to the natural frequency of the structure. Under this assumption, from Eqs. (8) and (9) in Tagaki et al. (1993) for the calculations of magnetic damping, we can find that the equivalent magnetic viscous damping coefficient c_j would be independent of the natural frequency ω_j. Let ξ_j^* be the theoretical prediction, given by Tagaki et al. (1993), of the magnetic damping ratio which has the relation

$$\xi_j^* = \frac{c_j}{2\omega_j^*} \tag{50}$$

in which ω_j^* is a natural frequency of the structure when the applied magnetic field is equal to zero (see Tagaki et al., 1993; p. 85). Since the natural frequency is changed with the applied magnetic field, the natural frequency should be ω rather than ω_j^*. Hence, Eq. (50) should be revised by the replacement of ω_j^* with ω, denoted by

$$\alpha = \frac{\omega_j^*}{\omega}. \tag{51}$$

Downloaded 04 May 2010 to 171.66.16.26. Redistribution subject to ASME license or copyright; see http://www.asme.org/terms/Terms_Use.cfm

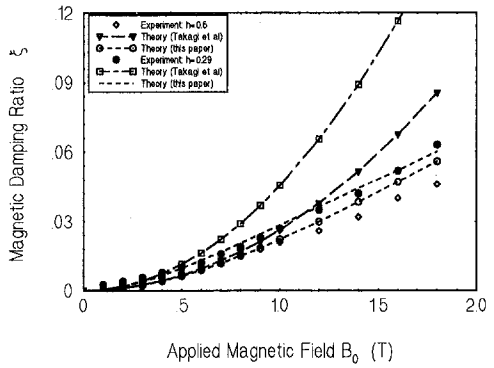

Fig. 4 Comparison of theoretical predictions and experimental data of a magnetic damping ratio versus an applied magnetic field ($\chi = 14$)

Then the revised magnetic damping ratio is

$$\xi = \alpha\xi_f^*. \tag{52}$$

According to Fig. 8 in Tagaki et al. (1993), we can get the values of ξ_f^*. Then from Eq. (52) the revised theoretical prediction of magnetic damping ratio ξ can be obtained. Figure 4 exhibits the theoretical and experimental data of the magnetic damping ratio ξ for the ferromagnetic plates of the material F-82H of $\chi = 14$ with $L/h = 100/0.29$ and $L/h = 100/0.5$. It is clearly found that the theoretical predictions of the magnetic damping ratio, after it is revised by considering the change of natural frequency which is predicted in this paper, is close to the experimental data for the first case when $B_0 < 1.60\ T$ and for the second case when $B_0 < 1.20\ T$.

6 Conclusions

A new theoretical model for characterizing the magnetoelastic interaction of a ferromagnetic plate with low susceptibility, when it is placed in an in-plane applied magnetic field, is obtained by means of the variational principle. The applicability region of the model to a cantilevered beam plate in in-plane magnetic fields is discussed numerically. It is this model that the experimental phenomenon of increase of natural frequency with the applied magnetic fields is first simulated in theory. After the increase of natural frequency with an applied magnetic field is predicted, the predictions of the magnetic damping ratio are revised by considering the change of natural frequency, making the theoretical predictions of the magnetic damping ratio closer to the experimental data.

Acknowledgment

The first author of this paper would like to acknowledge support of this subject in part by a grant from the National Natural Science Foundation of China, and the Science Foundation of the National Education Committee of China for the Scholars Returned from Abroad and for the Outstanding Young Researchers in Universities. And the authors sincerely appreciate Professor Tagaki's efforts in supplying the experimental data and parameters of the experiment.

References

Brown, W. F., 1966, "Magnetoelastic interaction", *Tracts in Natural Philosophy,* No. 9, Springer, Berlin.

Dalrymple, J. M., Peach, M. O., and Viegelaha, G. L., 1974, "Magnetoelastic Buckling of Thin Magnetically Soft Plate in Cylindrical Model," ASME JOURNAL OF APPLIED MECHANICS, Vol. 41, pp. 145–150.

Meirovitch, L., 1967, *Analytical methods in vibrations,* Macmillan, New York, pp. 161–166.

Miya, K., Hara, K., and Someya, K., 1978, "Experimental and Theoretical Study on Magnetoelastic Buckling of a Ferromagnetic Cantilevered Beam-Plate," ASME JOURNAL OF APPLIED MECHANICS, Vol. 45, pp. 355–360.

Miya, K., Tagaki, T., and Ando, Y., 1980, "Finite Element Analysis of Magnetoelastic Buckling of a Ferromagnetic Beam-Plate," ASME JOURNAL OF APPLIED MECHANICS, Vol. 47, pp. 377–382.

Moon, F. C., and Pao, Y. H., 1968, "Magnetoelastic Buckling of a Thin Plate," ASME JOURNAL OF APPLIED MECHANICS, Vol. 35, pp. 53–58.

Moon, F. C., 1984, *Magneto-solid mechanics,* John Wiley and Sons, New York.

Panovko, Y. G., and Gubanova, I. I., 1965, "Stability and Oscillations of Elastic Systems," *Consulation Bureau,* New York, p. 17 (English translation of Russian).

Pao, Y. H., and Yeh, C. S., 1973, "A Linear Theory for Soft Ferromagnetic Elastic Solids," *Int. J. Engng. Sci.,* Vol. 11, pp. 415–436.

Peach, M. O., Christopherson, N. S., Dalrymple, J. M., and Viegelahn, G. L., 1988, "Magnetoelastic Buckling: Why Theory and Experiment Disagree," *Experimental Mechanics,* Vol. 28, pp. 65–69.

Popelar, C. H., 1972, "Postbuckling Analysis of a Magnetoelastic Beam," ASME JOURNAL OF APPLIED MECHANICS, Vol. 39, pp. 207–211.

Tagaki, T., Tani, J., Matsubara, Y., and Mogi, I., 1993, "Electromagneomechanical Coupling Effects for Non-ferromagnetic and Ferromagnetic Structures," *Proc. 2nd Int. Workshop on Electromagnetic Forces and Related effects on Blankets and Other Structures Surrounding the Fission Plasma Torus,* K. Miya, ed., Tokai, Japan, Sept. 15–17, pp. 81–90.

Tagaki, T., Tani, J., Matsubara, Y., and Mogi, I., 1995, "Dynamic Behavior of Fusion Structural Components Under Strong Magnetic Fields," *Fusion Eng. and Design,* Vol. 27, pp. 481–489.

van Lieshout, P. H., Rongen, P. M. J., and van de Ven, A. A. F., 1987, "A Variational Principle for Magneto-elastic Buckling," *J. Eng. Math.,* Vol. 21, pp. 227–252.

Wallerstein, D. V., and Peach, M. O., 1972, "Magnetoelastic Buckling of Beams and Thin Plates of Magnetically Soft Materials," ASME JOURNAL OF APPLIED MECHANICS, Vol. 39, pp. 451–455.

Yamanouchi, N., Tamura, M., Hayakawa, H., Hishinuma, A., and Kondo, T., 1992, "Accumulation of Engineering Data for Practical use of Reduced Activation Ferritic Steel: 8% Cr – 2% W – 0.2% V – 0.04% Ta – Fe," *J. Nucl. Mater.,* Vol. 191–194, pp. 822–826.

Zhou, Y. H., and Zheng, X. J., 1994, "Finite Element and Finite Difference Analyses of Bending and Snapping of a Ferromagnetic cantilevered beam-plate," *Proc. IACM Third World Congr. Comput. Mech.,* Tokyo, Japan, Aug.

Zhou, Y. H., and Zheng, X. J., 1996, "A Theoretical Model for Magnetoelastic Buckling of Ferromagnetic Beam-Plate," *Acta Mechanica Sinica,* Vol. 12, pp. 213–224 (English Edition).

Zhou, Y. H., Zheng, X. J., and Miya, K., 1995, "Magnetoelastic Bending and Snapping of Ferromagnetic Plates in Oblique Magnetic Field," *Fusion Engineering and Design,* Vol. 30, pp. 325–337.

Downloaded 04 May 2010 to 171.66.16.26. Redistribution subject to ASME license or copyright; see http://www.asme.org/terms/Terms_Use.cfm

Property Distribution Determination for Nonuniform Composite Beams From Vibration Response Measurements and Galerkin's Method

Wei-Hung Chen[1]
Graduate Research Assistant.

R. F. Gibson[2]
Professor,
Fellow ASME.

Mechanical Engineering Department,
Advanced Composites Research Laboratory,
Wayne State University,
Detroit, MI 48202

This paper presents initial results from a program to develop a "rapid screening test" for determining the in-plane fiber distributions in unidirectionally reinforced composite structures by the use of the vibration response measurements and Galerkin's method. Theoretical models and experimental data are generated on the basis of two methods: (1) the "shifting method," in which the effective length of the beam is changed, and (2) the "added mass method," in which the mass distribution of the beam is changed. The elastic constants and the density are all assumed to be functions of fiber volume fraction, while the spatial distribution of the fiber volume fraction is assumed to be given by a polynomial function. The concept of an effective density is employed to obtain the appropriate solution to the coefficients of the polynomial function. Results show that the fundamental mode gives rise to better predictions of physical properties than the higher modes do. An error analysis includes discussion of the errors due to the influences of the mode number, the assumed order of the polynomial in the fiber volume fraction distribution, and the bending-extension coupling effect caused by the unsymmetrical distribution of properties about the beam middle surface.

Introduction

Uniformity of physical property distributions in manufactured parts is a very important issue in many industries. This is particularly true for high volume manufacturing of fiber-reinforced composites parts where reinforcing fibers may be nonuniformly distributed within the matrix material. Resin transfer molding, thermostamping, structural reaction molding, and sheet molding compound processing are often used for such high-volume manufacture of composite parts, and all of these processes have the potential for nonuniform fiber distributions.

Physical property data for specimens cut from a composite panel often exhibit considerable experimental scatter because of nonuniform fiber distributions. For example, Stokes (1990) observed that, in thermostamped glass fiber reinforced polymer composite panels, the modulus of elasticity varied by as much as a factor of three over a 152.4 mm × 304.8 mm (6 in. × 12 in.) area because of the redistribution of fibers induced by lateral resin flow during the thermostamping process. Tung (1982) has shown that, in composites made from sheet molding compounds, such scatter in property data may be large enough to mask out any effects of changes in processing variables.

Characterization of the elastic properties of a machine or structural part by employing fast, inexpensive dynamic measurements has been one of the most challenging topics in nondestructive testing in recent years. This kind of engineering problem can be classified as an "inverse problem," and could be of great practical importance because of its potential applications in quality control, damage detection, and optimal design. The impulse-frequency response technique is a widely used experimental method for measuring the required vibration response data, and has been adopted for the determination of the globally averaged properties of orthotropic composite panels in conjunction with certain theoretical models such as Galerkin's method (DeWilde, 1984), the Rayleigh-Ritz method (Deobald and Gibson, 1988), the Rayleigh method (Ayorinde and Gibson, 1993), and the finite element method (Nelson and Wolf, 1993). These previous studies did not address the problem of nonuniform mechanical property distributions, however, and only a single measured frequency spectrum with the required number of modal frequencies was needed.

The inverse problem for the vibration of a nonuniform isotropic, homogeneous beam appears to have been first investigated by Barcilon (1976, 1982). Gladwell (1986, 1987) extended this work and established the necessary and sufficient conditions for a unique solution. According to these analyses, three sets of distinct frequency spectra corresponding to three different end conditions were required to reconstruct the flexural rigidity and density of a nonuniform, isotropic and homogeneous beam, and these spectra must satisfy a certain inequality condition and asymptotic trend which involves the interlacing of eigenvalues.

The present work is concerned with the development of a "rapid screening test" for determination of in-plane fiber distri-

[1] Currently, Engineer, Ford Lio Ho, Taiwan.

[2] To whom correspondence should be sent.

Contributed by the Applied Mechanics Division of THE AMERICAN SOCIETY OF MECHANICAL ENGINEERS for publication in the ASME JOURNAL OF APPLIED MECHANICS.

Discussion on this paper should be addressed to the Technical Editor, Professor Lewis T. Wheeler, Department of Mechanical Engineering, University of Houston, Houston, TX 77204-4792, and will be accepted until four months after final publication of the paper itself in the ASME JOURNAL OF APPLIED MECHANICS.

Manuscript received by the ASME Applied Mechanics Division, Mar. 10, 1995; final revision, July 22, 1997. Associate Technical Editor: I. M. Daniel.

 Copyright © 1998 by ASME

Downloaded 04 May 2010 to 171.66.16.26. Redistribution subject to ASME license or copyright; see http://www.asme.org/terms/Terms_Use.cfm

butions in heterogeneous, anisotropic composite beams from a set of measured transverse vibration frequency spectra. Through-the-thickness fiber distributions are not included in the present work due to complications introduced by the resulting coupling effects in the equations of motion. In order to obtain the required set of distinct frequency spectra for the nonuniform isotropic beam, Barcilon (1976, 1982) and Gladwell (1986, 1987) changed the end conditions at the free end of a cantilever beam. The other two configurations in addition to clamped-free were clamped-pinned and clamped-sliding. This procedure is not only time consuming but is also difficult to conduct experimentally. In the present work, we investigate two different methods for determining the required spectra. The first one is called the "shifting method," in which the effective length of the beam is changed. The second method is called the "added mass method," in which the mass distribution of the beam is changed. Analytical models are derived from the Bernoulli-Euler beam theory and Galerkin's method. In our previous related work (Gibson, Hwang, and Chen, 1992), we used an "effective modulus" approach to derive the analytical model, but Galerkin's method was selected for the present work because it is more readily adapted to more complex problems and to eventual finite element implementation. Composite modulus and density are expressed in terms of the fiber volume fraction based on the micromechanics of composite materials, and the spatial distribution of fiber volume fraction is assumed to be given by a polynomial function. The coefficients of the polynomial function are obtained by solving a set of simultaneous equations which could be linear or nonlinear. The appropriate solution is then found by employing the concept of an "effective density."

Galerkin's Method

The Bernoulli-Euler equation of motion for the flexural vibration of a composite beam with constant cross-sectional area and nonuniform property distribution along its length is

$$\frac{\partial^2}{\partial x^2}\left[E_c(x)I\frac{\partial^2 w(x,t)}{\partial x^2}\right]+\rho_c(x)A\frac{\partial^2 w(x,t)}{\partial t^2}=0 \quad (1)$$

where the x direction is along the length of the beam; $E_c(x)$ and $\rho_c(x)$ are the local composite modulus and the local composite density, respectively; $w(x, t)$ is the transverse displacement of beam; I refers to the area moment of inertia of beam cross section about neutral axis; and A is the beam cross-sectional area. The test method described later involves measurement of modal frequencies associated with transverse vibrations of composite beams which have nonuniform fiber distributions along their lengths. As shown later in the error analysis, if the bending-extension coupling due to nonuniform distribution of properties through the thickness of the beam is also included in the analysis, a set of coupled equations in both transverse and longitudinal in-plane displacements result, and the measurement of in-plane vibration response becomes necessary. As explained later, such measurements were beyond the scope of the current research. The effects of this and other limitations of this equation in this application are discussed later in the error analysis. The assumption of constant cross-sectional area is based on the fact that thickness of composite parts is usually with controlled acceptable precision by the mold used. The local longitudinal modulus and density of a unidirectional fiber-reinforced laminated beam with nonuniformly distributed fiber volume fraction along the length can be expressed by the well-known rule of mixtures relationships as

$$E_c(x)=E_f v_f(x)+E_m v_m(x)=v_f(x)(E_f-E_m)+E_m \quad (2a)$$

$$\rho_c(x)=\rho_f v_f(x)+\rho_m v_m(x)=v_f(x)(\rho_f-\rho_m)+\rho_m \quad (2b)$$

where the subscripts c, f, and m refer to composite, fiber, and matrix, respectively, and $v_f(x)$ is the local fiber volume fraction. It is assumed that fiber and matrix materials are isotropic, and that $v_f(x)+v_m(x)=1$. For free harmonic vibration at natural frequency, ω, the transverse displacement is separable in time and space as

$$w(x,t)=W(x)e^{i\omega t} \quad (3)$$

where

$$W(x)=\sum_{i=1}^{N} C_i\phi_i(x) \quad (4)$$

and

$\phi_i(x)$ = the ith mode shape function
C_i = the ith magnitude which indicates the contribution of the ith mode.

Substitution of Eq. (3) into Eq. (1) gives the characteristic equation

$$\frac{d^2}{dx^2}\left[E_c(x)I\frac{d^2W(x)}{dx^2}\right]-\rho_c(x)A\omega^2W(x)=0 \quad (5)$$

and from Galerkin's method, Eq. (5) becomes

$$\int_0^L \frac{d^2}{dx^2}\left[E_c(x)I\frac{d^2W(x)}{dx^2}\right]\phi(x)dx - \omega^2\int_0^L \rho_c(x)AW(x)\phi(x)dx=0 \quad (6)$$

where L = beam length. The trial function $\phi(x)$ has the same form as that of the displacement $W(x)$. Substituting Equation (4) into Equation (6), we have

$$\sum_{i,j=1}^{N} C_i\left\{\int_0^L \frac{d^2}{dx^2}\left[E_c(x)I\frac{d^2\phi_i(x)}{dx^2}\right]\phi_j(x)dx - \omega_i^2\int_0^L \rho_c(x)A\phi_i(x)\phi_j(x)dx\right\}=0 \quad (7)$$

which can be expressed in matrix form as

$$[k_{ij}-\omega_i^2 m_{ij}]\{C_i\}=0 \quad (8)$$

k_{ij} and m_{ij} are the components of $N\times N$ symmetric stiffness and mass matrices, respectively, and have the following forms:

$$k_{ij}=\int_0^L \frac{d^2}{dx^2}\left[E_c(x)I\frac{d^2\phi_i(x)}{dx^2}\right]\phi_j(x)dx \quad (9)$$

$$m_{ij}=\int_0^L \rho_c(x)A\phi_i(x)\phi_j(x)dx. \quad (10)$$

Equation (8) represents the eigenvalue problem for an N-degree-of-freedom discrete system. For nontrivial solution of eigenvector $\{C_i\}$, the determinant of coefficient matrix in Eq. (8) should be equal to zero, i.e.,

$$|k_{ij}-\omega_i^2 m_{ij}|=0. \quad (11)$$

The objective of this research is to find the physical properties k_{ij} and m_{ij} in terms of fiber volume fraction from the measured vibration frequencies ω_i on the basis of Eq. (11).

Downloaded 04 May 2010 to 171.66.16.26. Redistribution subject to ASME license or copyright; see http://www.asme.org/terms/Terms_Use.cfm

Equation (9) can be integrated by parts over the domain $0 < x < L$ as

$$\int_0^L \frac{d^2}{dx^2}\left[E_c(x)I\frac{d^2\phi_i(x)}{dx^2}\right]\phi_j(x)dx$$

$$= \left\{\phi_j(x)\frac{d}{dx}\left[E_c(x)I\frac{d^2\phi_i(x)}{dx^2}\right]\right\}\Bigg|_0^L$$

$$- \left[\frac{d\phi_j(x)}{dx}E_c(x)I\frac{d^2\phi_i(x)}{dx^2}\right]\Bigg|_0^L$$

$$+ \int_0^L E_c(x)I\frac{d^2\phi_i(x)}{dx^2}\frac{d^2\phi_j(x)}{dx^2}dx. \quad (12)$$

In this case, the first two terms on the right-hand side of Eq. (12) are determined from two different types of specified boundary conditions as shown below.

Shifting Method

The distinct frequency spectra in this method are generated by using the clamped-free beam configuration and shifting the clamping locations along the beam. As shown in Fig. 1(*a*), the shift parameter c is the distance between the new and original clamping locations, and hence, the effective free length of the beam is represented by $L - c$. The distribution of fiber volume fraction is assumed to be given by a polynomial function as

$$v_f(x) = \sum_{n=0}^{K} v_n(x + c)^n \quad (13)$$

where K is the assumed order of the polynomial and v_n are the coefficients to be determined. The corresponding boundary conditions are

$$\phi_i(0) = \frac{d\phi_i(0)}{dx} = 0$$

$$E_c(L - c)I\frac{d^2\phi_i(L - c)}{dx^2}$$

$$= \frac{d}{dx}\left[E_c(L - c)I\frac{d^2\phi_i(L - c)}{dx^2}\right] = 0. \quad (14)$$

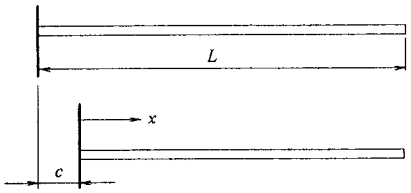

(a)

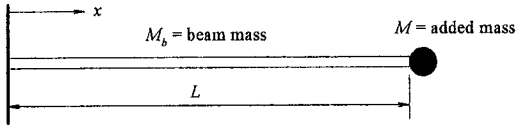

(b)

Fig. 1 Beam configurations: (*a*) clamped-free, (*b*) clamped-mass

The first two terms in Eq. (12) vanish with these boundary conditions. The stiffness and mass matrices become

$$k_{ij} = \int_0^{L-c} E_c(x)I\phi_i''(x)\phi_j''(x)dx \quad (15)$$

$$m_{ij} = \int_0^{L-c} \rho_c(x)A\phi_i(x)\phi_j(x)dx \quad (16)$$

where $(')$ refers to $d^2(\ )/dx^2$. By substituting Eq. (13) into Eqs. (2*a*), (2*b*), (15), and (16), Eq. (11) now reads

$$\left|\int_0^{L-c}\left[\sum_{n=0}^{K} v_n(x + c)^n(E_f - E_m) + E_m\right]I\phi_i''(x)\phi_j''(x)dx\right.$$

$$- \omega_i^2\int_0^{L-c}\left[\sum_{n=0}^{K} v_n(x + c)^n(\rho_f - \rho_m)\right.$$

$$\left.\left. + \rho_m\right]A\phi_i(x)\phi_j(x)dx\right| = 0. \quad (17)$$

Accordingly, a set of $K + 1$ homogeneous algebraic equations in terms of coefficients $\{v_n\}$ will be created. Generally, $K + 1$ distinct frequencies generated from $K + 1$ different beam structures are required to solve the coefficients uniquely. Each value of shift parameter c will generate a frequency spectrum. The local modulus and density are then computed from the calculated coefficients $\{v_n\}$ by virtue of Eqs. (2*a*) and (2*b*).

The mode shape functions used in the theoretical model are those for a cantilever beam with uniformly distributed properties. The nonuniform property distributions are assumed to have little or no effect on the mode shapes at this point. As shown later, the experimental measurements verify the validity of this assumption for this specific situation. For the ith mode, the mode shape function is (Blevins, 1979)

$$\phi_i(x) = \cosh\frac{\lambda_i x}{L - c} - \cos\frac{\lambda_i x}{L - c}$$

$$- \sigma_i\left(\sinh\frac{\lambda_i x}{L - c} - \sin\frac{\lambda_i x}{L - c}\right) \quad (18)$$

where σ_i is a constant and λ_i is the corresponding eigenvalue.

Added Mass Method

In this method, the vibration measurements are obtained from the clamped-mass beam configuration. As shown in Fig. 1(*b*), beam structures are built by clamping one end of the beam and adding different masses at the free end. The distribution of fiber volume fraction is assumed to be given by

$$v_f(x) = \sum_{n=0}^{K} v_n x^n. \quad (19)$$

For the clamped-mass configuration, the boundary conditions are

$$\phi_i(0) = \frac{d\phi_i(0)}{dx} = 0$$

$$E_c(L)I\frac{d^2\phi_i(L)}{dx^2} = 0$$

$$\frac{d}{dx}\left[E_c(L)I\frac{d^2\phi_i(L)}{dx^2}\right] = M\frac{d^2\phi_i(L)}{dt^2} = -M\omega_i^2\phi_i(L) \quad (20)$$

where M is the added mass. The added masses are small and light in comparison with the beam itself in order to avoid the rotatory inertia effect, and are cylindrical for the purpose of simulating a concentrated load exerted across the beam width.

Downloaded 04 May 2010 to 171.66.16.26. Redistribution subject to ASME license or copyright; see http://www.asme.org/terms/Terms_Use.cfm

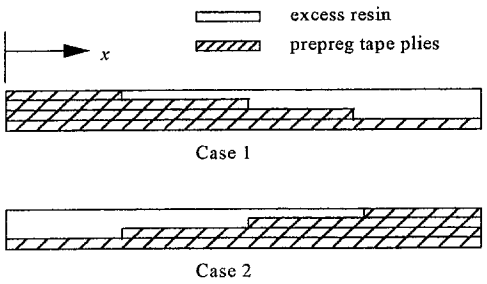

Fig. 2 Fabrication of beam specimens

After substitution of these boundary conditions into Eq. (12), the stiffness and mass matrices become

$$k_{ij} = \int_0^L E_c(x) I \phi_i''(x) \phi_j''(x) dx \tag{21}$$

$$m_{ij} = \int_0^L \rho_c(x) A \phi_i(x) \phi_j(x) dx + M \phi_i(L) \phi_j(L). \tag{22}$$

With the substitution of Eq. (19) into Eqs. (2*a*), (2*b*), (21), and (22), Eq. (11) turns out to be

$$\left| \int_0^L [\sum_{n=0}^{K} v_n x^n (E_f - E_m) + E_m] I \phi_i''(x) \phi_j''(x) dx - \omega_i^2 \left\{ \int_0^L [\sum_{n=0}^{K} v_n x^n (\rho_f - \rho_m) + \rho_m] A \phi_i(x) \phi_j(x) dx + M \phi_i(L) \phi_j(L) \right\} \right| = 0. \tag{23}$$

The $K + 1$ coefficients $\{v_n\}$ are again solved by $K + 1$ distinct frequencies. Each value of mass M gives a different frequency spectrum.

The mode shape functions which were presented by Laura et al. (1974) are employed for this beam configuration. These exact functions were established for different mass ratios (added mass/beam mass) and for beams with uniformly distributed properties. For the ith mode, the eigenvalue is calculated by the following transcendental equation:

$$\frac{1}{\lambda_i} \frac{1 + \cos \lambda_i \cosh \lambda_i}{\sin \lambda_i \cosh \lambda_i - \cos \lambda_i \sinh \lambda_i} = \frac{M}{M_b}. \tag{24}$$

For different mass ratios (M/M_b), the eigenvalues are different. The corresponding mode shape function for mode i is

$$\phi_i(x) = \cosh \frac{\lambda_i x}{L} - \cos \frac{\lambda_i x}{L} - \left(\frac{\cosh \lambda_i + \cos \lambda_i}{\sinh \lambda_i + \sin \lambda_i} \right) \left(\sinh \frac{\lambda_i x}{L} - \sin \frac{\lambda_i x}{L} \right). \tag{25}$$

Again, the mode shapes are assumed to be insensitive to the nonuniform property distributions for this specific case, and this assumption will be justified by experimental measurements later. The physical eigenvalues in this research were calculated by Newton-Gregory backward interpolation of order 4 from Laura's eigenvalue table. When the mass ratio is equal to zero, Eq. (25) becomes $1 + \cosh \lambda_i \cos \lambda_i = 0$, which is the characteristic equation for a cantilever beam in flexural vibration. This implies that the clamped-free configuration can be regarded as a special case of clamped-mass configuration.

Experiments

Specimens. The two types of composite beam arrangements investigated in this work are shown schematically in Fig. 2. Case 1 stands for the beams having fiber volume fraction distribution decreasing along the length in a stepwise linear fashion, while Case 2 represents the beams with fiber volume fraction increasing along the length in a similar fashion. There were two specimens in each case. These laminated beams were made of 10 plies of 3M Scotchply 1003 unidirectional glass/epoxy prepreg tape by using an autoclave-style press cure. The fiber and matrix properties for use in Eqs. (2*a*) and (2*b*) are tabulated elsewhere (Chen, 1995). Specimen dimensions, for both cases, were

length L = 9 in. (228.6 mm)
width = 0.6 ± 0.005 in. (15.24 ± 0.127 mm)
thickness = 0.082 ± 0.0015 in. (2.0828 ± 0.0381 mm)

Impulse-Frequency Response Measurements. Natural frequencies and physical mode shapes were measured by using the impulse-frequency response technique, which has been described in detail elsewhere (Suarez and Gibson, 1987). The flexural vibration apparatus for testing cantilever beam specimens with this technique is shown in Fig. 3.

Recall that in the discussion leading to Eqs. (18) and (25), it was assumed that the mode shapes were not affected significantly by nonuniform property distributions. The validity of this assumption was assessed by using the impulse-frequency response method to measure mode shapes for nonuniform beams and then comparing with theoretical mode shapes for uniform beams. Mode shapes were measured by making transfer function measurements at multiple locations along the beam (Chen, 1995). Figure 4 shows the first three mode shapes of a uniform beam (theoretical) and a nonuniform composite beam (experimental) under the clamped-free configuration for Case 1. The experimental data were obtained by testing a single specimen in each case. Excellent agreement between the theoretical and experimental data for both Case 1 and Case 2 (Chen, 1995). This observation can be extended to the clamped-mass configuration since the clamped-free configuration can be considered as a special case of the clamped-mass configuration. Hence, we may conclude that the nonuniform property distributions have negligible influence on the mode shapes for these specific cases.

Burn-Out Test. The true physical fiber volume fraction distributions were obtained by using a burn-out test. In this test, small samples were cut from different positions along the beam specimens and the matrix resin was burned away in a furnace at a temperature of 1050°F (565°C) for one hour. From the weight differences of these small pieces before and after the test, the in situ fiber volume fractions were computed.

Results and Discussion

Since the specimens were fabricated with fiber contents varying as shown in Fig. 2, we selected the order of the polynomial function, K, as 1, so that

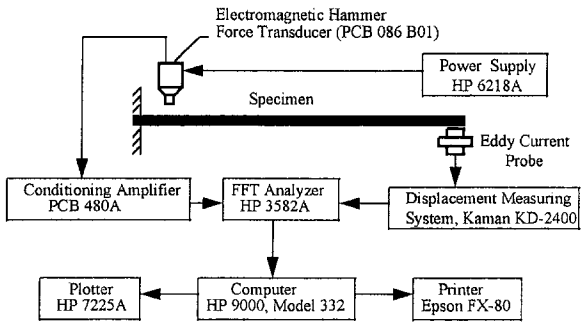

Fig. 3 Flexural vibration apparatus for beam specimens

Downloaded 04 May 2010 to 171.66.16.26. Redistribution subject to ASME license or copyright; see http://www.asme.org/terms/Terms_Use.cfm

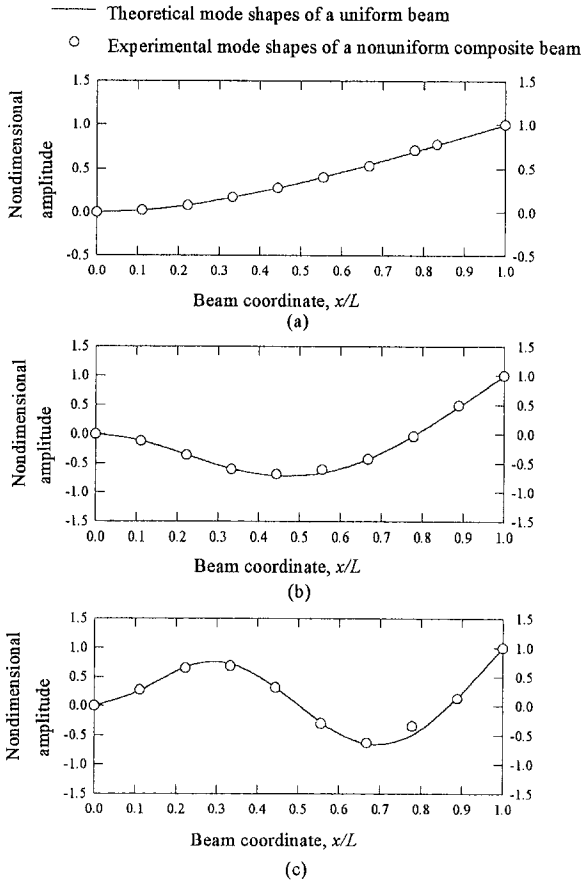

Fig. 4 Mode shapes for clamped-free beam configuration in Case 1: (*a*) first mode, (*b*) second mode, (*c*) third mode

$$v_f = v_0 + v_1(x + c) \quad \text{for shifting method} \tag{26}$$

$$v_f = v_0 + v_1 x \quad \text{for added mass method.} \tag{27}$$

Two distinct natural frequencies generated from two different structures are needed to compute the coefficients v_0 and v_1 for both methods. Each combination of two different shift parameters c (shifting method) or added masses M (added mass method) will give rise to a solution. The concept of an "effective density" is then employed for the appropriate selection of the coefficients. The effective density of an equivalent homogeneous beam with a constant cross-sectional area is defined as

$$\rho_{c,\text{eff}} = \frac{\int_0^L \rho_c(x)dx}{\int_0^L dx} \tag{28}$$

where $\rho_c(x)$ is the local composite density defined in Eq. (2*b*). The actual specimen densities are easily measured. The best solution for v_0 and v_1 is therefore the one which yields the least difference between the measured and calculated effective densities.

Solutions from several combinations of the shift parameters (in shifting method) and the added masses (in added mass method) were found for both cases of beams. Figures 5 and 6 show the best results for the measured and predicted fiber volume fraction distributions in Case 1 and Case 2, respectively. In the shifting method, the structures were tested with shift parameters c/L of zero and 0.11 for Case 1, then zero and 0.22 for Case 2. In the added mass method, the structures were tested with mass ratios of zero and 0.1234 for Case 1, then zero and 0.1205 for Case 2. It is seen that the agreement in Case 1 for

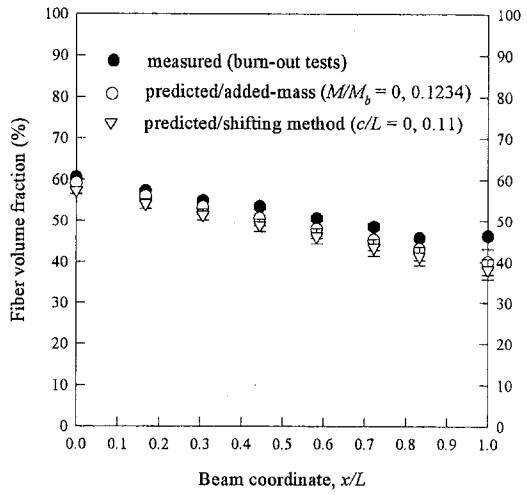

Fig. 5 Comparison between the measured and predicted fiber volume fraction distributions in Case 1

both methods is very good. For Case 2, the differences between the predictions and measured data are larger than those in Case 1. With the same beam structures, the averaged differences between the measured and predicted fiber volume fractions for different modes are listed in Tables 1(*a*) and 1(*b*). The difference in fiber volume fraction is defined as the average of the absolute values of the differences between the measured, v_{fm}, and predicted, v_{fp}, fiber volume fractions at eight different locations mentioned previously and can be expressed as

$$\frac{1}{8}\sum_{j=1}^{8} \frac{|v_{fm}^{(j)} - v_{fp}^{(j)}|}{v_{fm}^{(j)}} \times 100 \tag{29}$$

where j refers to the jth location. These two tables show that the fundamental mode gives rise to better prediction of fiber volume fraction distribution than the higher modes do based on the clamped-free and clamped-mass configurations. The errors and the likely explanations for them will be discussed in the next section.

Error Analysis

The differences between measured and predicted volume fractions in the previous section will now be analyzed from several points of view.

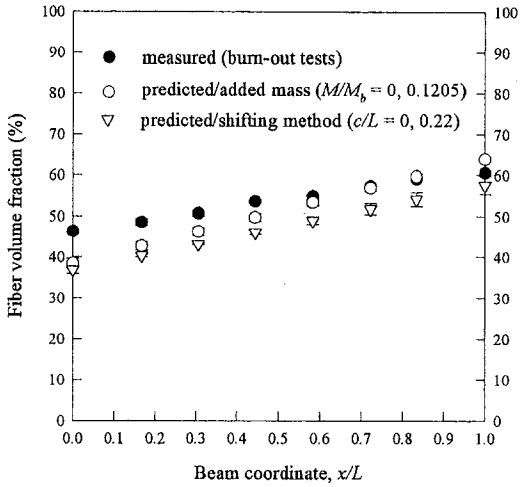

Fig. 6 Comparison between the measured and predicted fiber volume fraction distributions in Case 2

Downloaded 04 May 2010 to 171.66.16.26. Redistribution subject to ASME license or copyright; see http://www.asme.org/terms/Terms_Use.cfm

Table 1 Averaged (percent) differences between the measured and predicted fiber volume fractions for different modes in (*a*) the shifting method; (*b*) the added mass method

	First mode	Second mode	Third mode
Case 1	8.81 ± 2.38	11.77 ± 0.72	13.49 ± 2.28
Case 2	12.54 ± 0.82	12.85 ± 0.46	13.29 ± 2.49

(*a*)

Case 1	4.97 ± 2.85	11.88 ± 0.82	13.17 ± 2.57
Case 2	6.62 ± 0.65	9.79 ± 0.85	10.53 ± 2.38

(*b*)

"Ill-Condition" Analysis. The systems of simultaneous equations resulting from inverse problems of this type are often ill-conditioned. For a system of the form (Hensel, 1991)

$$[D]\{X\} = \{B\} \tag{30a}$$

or

$$\{X\} = [D]^{-1}\{B\} \tag{30b}$$

the nonsingular matrix $[D]$ is said to be ill-conditioned for inversion when the output solution vector $\{X\}$ is overly sensitive to small errors in the input vector $\{B\}$. The condition number, $Q(D)$, of the coefficient matrix $[D]$ is used to quantify the degree of ill-conditioning,

$$Q(D) = \|D\|\|D^{-1}\| \tag{31}$$

where $\|D\|$ is defined as the norm of an $N \times N$ matrix $[D]$, and $\|D^{-1}\|$ is the norm of the inverse matrix $[D^{-1}]$. If $Q(D) \leq 1$, the system is said to be well-conditioned. If $Q(D) > 1$, the system is ill-conditioned. The greater the condition number, the worse the ill-conditioning.

Notice that this ill-condition analysis is applicable only to the linear equations in Eqs. (17) and (23), which can be rearranged in the form of Eq. (30*a*) or (30*b*). The equations defining the $[B]$, $[D]$ and $\{X\}$ matrices are too long to present here (Chen, 1995). In this work, these equations are linear in coefficients v_0 and v_1 when only first mode is to be considered, and are nonlinear when higher modes are to be investigated even when the order of polynomial $K = 1$. It is necessary to linearize the nonlinear equations in order to conduct the test for ill-conditioning. Equations (17) and (23) are linearized by Taylor series expansion about an equilibrium solution and only the first-order terms are considered. The forms of $[D]$ and $\{X\}$ are the same, but $\{B\}$ is different for the clamped-free and clamped-mass configurations (Chen, 1995).

The condition numbers for different modes and for different orders of the polynomial function assumptions are listed in Tables 2 and 3. It is shown in Table 2(*a*) that in the clamped-free configuration for both cases, there are no pronounced differences in condition numbers for different vibration modes and this explains why the differences between the measured and predicted fiber volume fractions (Table 1) for different modes are small. As shown in Table 3(*a*), the condition numbers for higher modes in the clamped-mass configuration are larger than those for the fundamental mode, which implies that the higher modes give rise to worse ill-conditioning than the fundamental mode does. It was also found that for $K = 1$, the condition numbers for different shift parameters and mass ratios are small (order of 0) for the first mode. For $K > 1$, as shown in Tables 2(*b*) and 3(*b*), the condition numbers are very large, and a small amount of error in the measured frequencies would cause large errors in the solution. In fact, the results we obtained in this case were very unsatisfactory. Due to the limitation of our test fixture, we were not able to obtain precise enough frequency measurements for a satisfactory solution when the order of the polynomial function was higher than one.

Limitations of Bernoulli-Euler Beam Theory. It is known that the transverse shear deformation and rotatory inertia effects are more pronounced in higher modes. These effects are not included in the Bernoulli-Euler beam theory. This is one reason why the fundamental mode gave better results than the higher modes in the previously described experiments.

Coupling Effect. The previous theoretical models are derived based on the classical beam theory. In addition to the ignored shear deformation and rotatory inertia effects, the coupling effect between the in-plane and out-of-plane deformation is also neglected. However, when the properties are not symmetric about the middle plane of the beam, the bending-extension coupling effect will reduce the natural frequencies. It can be shown (Chen, 1995) that the equations governing in-plane longitudinal midplane displacement, u^0, and transverse displacement, w, in a specially orthotropic, nonsymmetric beam are

$$A_{11}\frac{\partial^2 u^0}{\partial x^2} - B_{11}\frac{\partial^3 w}{\partial x^3} = 0$$

$$-B_{11}\frac{\partial^3 u^0}{\partial x^3} + D_{11}\frac{\partial^4 w}{\partial x^4} = -\rho\frac{\partial^2 w}{\partial t^2} \tag{32}$$

where A_{11} = extensional stiffness, B_{11} = coupling stiffness, and D_{11} = bending stiffness. Although these equations can not be solved in closed form for the clamped-free boundary condition, such a solution is possible for the simply supported beam for comparison. If the in-plane vibration is assumed to occur at the

Table 2 Condition numbers for clamped-free configuration; (*a*) different modes and $K = 1$, and (*b*) first modes and $K = 1, 2$

Mode number	Case 1	Case 2
1	6.40 ± 0.30	3.48 ± 0.05
2	6.29 ± 1.89	11.75 ± 0.25
3	24.99 ± 0.54	6.09 ± 0.07

(*a*)

K	Case 1	Case 2
1	6.40 ± 0.30	3.48 ± 0.05
2	669.30 ± 49.96	776.39 ± 34.17

(*b*)

Table 3 Condition numbers for clamped-mass configuration; (*a*) different modes and $K = 1$, and (*b*) first modes and $K = 1, 2$

Mode number	Case 1	Case 2
1	4.82 ± 0.12	3.29 ± 0.02
2	78.67 ± 1.34	93.06 ± 2.70
3	262.42 ± 0.34	218.83 ± 41.33

(*a*)

K	Case 1	Case 2
1	4.82 ± 0.12	3.29 ± 0.02
2	18906 ± 1058	10704 ± 203

(*b*)

Downloaded 04 May 2010 to 171.66.16.26. Redistribution subject to ASME license or copyright; see http://www.asme.org/terms/Terms_Use.cfm

same frequency as the transverse vibration, the corresponding frequency equation is (Chen, 1995)

$$\omega^2 = \frac{\pi^4}{\rho}\left(\frac{m}{L}\right)^4\left(D_{11} - \frac{B_{11}^2}{A_{11}}\right). \quad (33)$$

For the specially orthotropic, nonsymmetric laminate, it can be shown that $A_{11} > 0$ and $B_{11} > 0$, so that the natural frequencies are lower than those of the symmetric beam with the same bending stiffness D_{11} and density ρ. In other words, the bending-extension coupling term B_{11} due to the nonsymmetry about the middle plane of the beam reduces the natural frequency. This general conclusion can be extended to other types of boundary conditions such as the clamped-free and clamped-mass configurations used in this work, although exact solutions are not possible for these cases.

As mentioned earlier, the differences between the measured and predicted fiber volume fractions for Case 2 are larger than those for Case 1. The reason is believed to be the fact that the bending-extension coupling has a more pronounced effect in Case 2 than in Case 1. For Case 2, the nonsymmetric condition which leads to the coupling effect is more pronounced toward the clamped end where the maximum bending moment occurs, while for Case 1, the coupling is more pronounced near the free end where the bending moment has the least value.

Finally, even if the coupled Eqs. (32) are solved in numerical form, the use of such equations as part of a test methodology would mean that the modal frequencies associated with both w and u^0 would have to be measured, and it is believed that the amplitudes of the longitudinal modes would be too small to measure with the existing transducers. In manufacturing of typical thin composite structures, the in-plane nonuniformities are believed to be more important than the through-the-thickness nonuniformities, so from the point of view of a rapid screening test methodology, the measurement of transverse vibrations should be all that is needed.

Conclusions

Analytical models based on measured frequency spectra for transverse vibrations and Galerkin's method have been developed for the clamped-free and clamped-mass beam configurations in order to determine the fiber volume fraction distributions along the length of nonuniform composite beams. An error analysis leads to the conclusion that the fundamental mode is better than the higher modes in the predictions of physical properties, and that the errors due to bending-extension coupling are less pronounced in Case 1 than in Case 2. It is more important that this coupling effect be taken into consideration when solving the inverse problem of specimens with properties distributed in the same fashion as in Case 2. An ill-condition analysis verifies the infeasibility of the present methodology when the order of the polynomial for the distribution of fiber volume fractions is higher than 1. This means that one would likely obtain an incorrect solution to the inverse problem by solving the resulting set of simultaneous linear equations directly for higher order polynomial distribution functions. An optimization scheme to minimize the discrepancy between the measured and predicted responses would be a possible solution to these problems. Discretization of the model on the basis of Galerkin's method and the use of an optimization procedure appears to be a feasible approach, and we plan to report on this approach in future papers.

Acknowledgments

The authors gratefully acknowledge a graduate assistantship funded by the Institute for Manufacturing Research at Wayne State University. Additional support from a grant from Ford Motor Company is also greatly appreciated.

References

Ayorinde, E. O., and Gibson, R. F., 1993, "Elastic Constants of Orthotropic Composite Materials Using Plate Resonant Frequencies, Classical Lamination Theory and an Optimized Three-Mode Rayleigh Formulation," *Composites Engineering,* Vol. 3, No. 5, pp. 395–407.

Barcilon, V., 1976, "Inverse Problem for a Vibrating Beam," *Journal of Applied Mathematics and Physics (ZAMP),* Vol. 27, pp. 347–357.

Barcilon, V., 1982, "Inverse Problem for the Vibrating Beam in the Free-Clamped Configuration," *Royal Society of London, Philosophical Transactions,* Vol. A304, pp. 211–251.

Blevins, R. D., 1979, *Formulas for Natural Frequency and Mode Shape,* Van Nostrand Reinhold, New York.

Chen, W. H., 1995, "Determination of Property Distributions of Nonuniform Composites by the Use of Vibration Measurements," Ph.D. dissertation, Wayne State University, Detroit, MI.

Deobald, L. R., and Gibson, R. F., 1988, "Determination of Elastic Constants of Orthotropic Plates by a Modal Analysis/Rayleigh-Ritz Technique," *Journal of Sound and Vibration,* Vol. 124, No. 2, pp. 269–283.

DeWilde, W. P., 1984, "Determination of the Material Constants of an Anisotropic Lamina by Free Vibration Analysis," *Proceedings of the 2nd International Modal Analysis Conference,* Orlando, FL, I, pp. 44–49.

Gibson, R. F., Hwang, S. J., and Chen, W. H., 1992, "Vibration Response Measurements for Determination of Physical Property Distributions in Laminated Composite Beams," *Proceedings of the 8th ASM/ESD Advanced Composites Conference,* Chicago, IL, Nov. 2–5, ASM International Materials, Park, OH, pp. 317–326.

Gladwell, G. M. L., 1986, *Inverse Problems in Vibration,* Martinus Nijhoff, Dordrecht, The Netherlands.

Gladwell, G. M. L., 1987, "Examples of Reconstruction of an Euler-Bernoulli Beam from Spectral Data," *Journal of Sound and Vibration,* Vol. 119, No. 1, pp. 81–94.

Hensel, E., 1991, *Inverse Theory and Applications for Engineers,* Prentice-Hall, Englewood Cliffs, NJ.

Laura, P. A. A., Pombo, J. L., and Susemihl, E. A., 1974, "A Note on the Vibrations of a Clamped-Free Beam with a Mass at the Free End," *Journal of Sound and Vibration,* Vol. 37, No. 2, pp. 161–168.

Nelson, M. F., and Wolf, J. A., 1992, "A Nondestructive Technique for Determining the Elastic Constants of Advanced Composites," *Vibro-Acoustic Characterization of Materials and Structures,* ASME, P. K. Raju, ed., ASME, New York, pp. 227–233.

Stokes, V. K., 1990, "Random Glass Mat Reinforced Thermoplastic Composites, Part I: Phenomenology of Tensile Modulus Variations," *Polymer Composites,* Vol. 11, pp. 32–44.

Suarez, S. A., and Gibson, R. F., 1987, "Improved Impulse-Frequency Response Techniques for Measurement of Dynamic Mechanical Properties of Composite Materials," *Journal of Testing and Evaluation,* Vol. 15, No. 2, pp. 114–121.

Tung, R. W., 1987, "Effect of Processing Variables on the Mechanical and Thermal Properties of Sheet Molding Compound," *Short Fiber Reinforced Composite Materials,* ASTM STP 772, B. A. Sanders, ed., American Society for Testing and Materials, Philadelphia, PA, pp. 51–63.

Downloaded 04 May 2010 to 171.66.16.26. Redistribution subject to ASME license or copyright; see http://www.asme.org/terms/Terms_Use.cfm

On the Eigenvalues and Critical Speed Stability of Gyroscopic Continua

R. G. Parker
Department of Mechanical Engineering,
Ohio State University,
206 W. 18th Avenue,
Columbus, OH 43210-1107
parker.242@osu.edu
Mem. ASME

In order to provide analytical eigenvalue estimates for general continuous gyroscopic systems, this paper presents a perturbation analysis to determine approximate eigenvalue loci and stability conclusions in the vicinity of critical speeds and zero speed. The perturbation analysis relies on a formulation of the general continuous gyroscopic system eigenvalue problem in terms of matrix differential operators and vector eigenfunctions. The eigenvalue λ appears only as λ^2 in the formulation, and the smoothness of λ^2 at the critical speeds and zero speed is the essential feature. First-order eigenvalue perturbations are determined at the critical speeds and zero speed. The derived eigenvalue perturbations are simple expressions in terms of the original mass, gyroscopic, and stiffness operators and the critical-speed/zero-speed eigenfunctions. Prediction of whether an eigenvalue passes to or from a region of divergence instability at the critical speed is determined by the sign of the eigenvalue perturbation. Additionally, eigenvalue perturbation at the critical speeds and zero speed yields approximations for the eigenvalue loci over a range of speeds. The results are limited to systems having one independent eigenfunction associated with each critical speed and each stationary system eigenvalue. Examples are presented for an axially moving tensioned beam, an axially moving string on an elastic foundation, and a rotating rigid body. The eigenvalue perturbations agree identically with exact solutions for the moving string and rotating rigid body.

Introduction

Rotating bodies, axially moving materials, and fluid-conveying pipes are examples of gyroscopic systems. These systems exhibit rich eigenvalue and stability behavior including critical speeds (zero eigenvalues), divergence, and flutter. For continuous (distributed-parameter) systems, the presence of the skew-symmetric gyroscopic operator in the governing equations limits analytical determination of the eigenvalues to simple systems such as uniform rotating disks and axially moving strings. Complicating effects such as coupling between components, asymmetries, bearing interactions, and aerodynamic influences, which can dramatically impact system behavior, normally prevent analytical eigenvalue solutions. With the goal of obtaining closed-form eigenvalue loci and stability estimates from the continuous system equations of motion, this paper presents a formulation of the gyroscopic system eigenvalue problem that is suitable for perturbation analysis. Closed-form perturbations of the critical speed and stationary system eigenvalues are determined in terms of the critical speed and stationary system eigenfunctions. In particular, system stability near critical speeds is predicted. The results yield piecewise-linear approximations for the eigenvalues of complicated gyroscopic systems provided the critical-speed and zero-speed eigensolutions can be determined. This provision is not a strong restriction because the critical-speed and zero-speed eigenvalue problems are self-adjoint and independent of the gyroscopic operator.

The perturbation results allow investigation of the complicating effects noted above without the effort associated with discretization. Discretization introduces approximation, requires admissible functions that may be difficult to find, and, if speed-dependent admissible functions are not used, may lead to poor convergence (Wickert and Mote, 1991). Despite the emphasis on continuous system models, the developed techniques apply to discrete gyroscopic systems.

A key element of this paper is the investigation of continuous gyroscopic system stability in the vicinity of critical speeds. We seek a simple analytical method to predict which of two distinct critical-speed stability behaviors (described below) occurs. The approach depends on a reformulation of the continuous gyroscopic system eigenvalue problem in terms of λ^2, where λ is the eigenvalue. This idea was introduced by Huseyin and Plaut for discrete gyroscopic systems (Huseyin, 1976; Huseyin and Plaut, 1974–1975; Plaut, 1976). They exploited a formulation of the discrete system eigenvalue problem in terms of λ^2 and ν^2, where ν is the gyroscopic speed parameter, to examine stability boundaries, eigenvalue loci convexity, and flutter instability. The essential feature of this formulation in the current work is that λ^2 is differentiable at a critical speed whereas λ is not. This contrasting behavior is evident in Fig. 1 which depicts the eigenvalues near a critical speed of the two-degree-of-freedom rotor of Fig. 2. Smoothness of λ^2 admits a regular perturbation analysis for λ^2 in the vicinity of a critical speed. In contrast, standard perturbation (Appendix) and eigenvalue differentiation (Friswell, 1996; Plaut and Huseyin, 1973; Rogers, 1970; Tang et al., 1996) of λ fail because λ is not differentiable at a critical speed.

The two possible stability pictures near critical speeds are strikingly different. In one case, the system eigenvalues are imaginary in the neighborhood of a critical speed and the system remains stable. This behavior occurs in axisymmetric Jeffcott rotors (Huseyin and Plaut, 1974–1975), rotating beams, and rotating disks (Mote, 1970) as well as translating strings (Perkins, 1990). Alternatively, an eigenvalue of positive real part can occur in a neighborhood of the critical speed and divergence instability results. Asymmetric Jeffcott rotors, rotating beams,

Contributed by the Applied Mechanics Division of THE AMERICAN SOCIETY OF MECHANICAL ENGINEERS for publication in the ASME JOURNAL OF APPLIED MECHANICS.

Discussion on the paper should be addressed to the Technical Editor, Professor Lewis T. Wheeler, Department of Mechanical Engineering, University of Houston, Houston, TX 77204-4792, and will be accepted until four months after final publication of the paper itself in the ASME JOURNAL OF APPLIED MECHANICS.

Manuscript received by the ASME Applied Mechanics Division, Aug. 6, 1996; final revision, June 23, 1997. Associate Technical Editor: N. C. Perkins.

 Copyright © 1998 by ASME

Downloaded 04 May 2010 to 171.66.16.26. Redistribution subject to ASME license or copyright; see http://www.asme.org/terms/Terms_Use.cfm

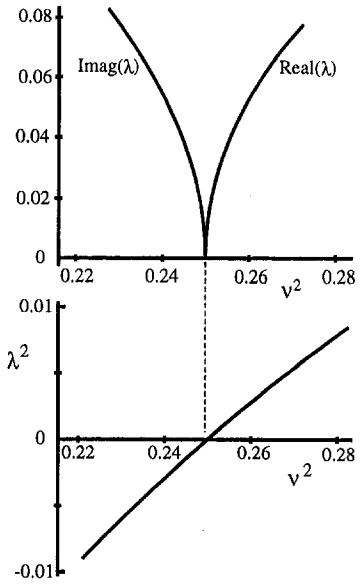

Fig. 1 Eigenvalues of the rotating rigid body of Fig. 2 in the vicinity of a critical speed. The upper figure depicts the real and imaginary components, and the lower figure depicts the square of the eigenvalue, which is real both above and below the critical speed.

and rotating disks as well as translating beams (Wickert and Mote, 1990) exhibit such behavior. The perturbation analysis presented herein predicts which of these critical speed eigenvalue behaviors occurs by the sign of the eigenvalue perturbation. Based on an insightful examination of the critical speed eigenfunctions, Renshaw and Mote (1996) give a conjecture for predicting qualitative eigenvalue behavior in the vicinity of critical speeds. The conjecture is shown to work for several examples. Their results do not provide quantitative eigenvalue predictions. The perturbation analysis herein provides mathematical justification for the conjecture and gives quantitative eigenvalue predictions. The present work is restricted to critical speeds having only one associated eigenfunction. Extension of the current method to degenerate eigenvalue perturbation is necessary to treat the important class of systems having multiple eigenfunctions at a critical speed.

The results are demonstrated for three example problems: an axially moving tensioned beam, an axially moving string on an elastic foundation, and a two-degree-of-freedom rotor. Closed-form solutions for the last two of these examples confirm the perturbation predictions.

Gyroscopic System Eigenvalue Problem

The canonical equation of motion for gyroscopic continua is

$$Mu_{tt} + \nu Gu_t + (K - \nu^2 \check{K})u = 0 \quad P \quad B_i u = 0 \quad \partial P \qquad (1)$$

where P and ∂P denote the domain and its boundary, respectively. M, G, K, $\check{K}$, and B_i represent linear time-independent operators. ν is the gyroscopic parameter (e.g., rotation/translation speed) and all operators are independent of ν. With the inner product $(v, w) = \int_P v\bar{w}dP$, where the overbar denotes complex conjugate, the following symmetries are specified for comparison functions $v(P)$ and $w(P)$:

$$(Mv, w) = (v, Mw) \quad (Gv, w) = -(v, Gw)$$
$$(Kv, w) = (v, Kw) \quad (\check{K}v, w) = (v, \check{K}w). \qquad (2)$$

The inertia operator M is positive-definite. The eigenvalue problem is obtained from the separable solution $u(P, t) = \mathrm{Re}\{\psi(P)e^{\lambda t}\}$.

$$\lambda^2 M\psi + \lambda\nu G\psi + (K - \nu^2\check{K})\psi = 0$$
$$B_i\psi = 0 \qquad (3)$$

The solution of (3) with $\lambda = 0$ yields the critical speeds ν_c and critical speed eigenfunctions ψ_c. This critical speed eigenvalue problem is frequently straightforward analytically as it depends only on the self-adjoint stiffness operators. The critical speed eigensolutions are assumed calculable. Taking $\nu = 0$, a similarly straightforward eigenvalue problem results for the stationary system eigensolutions λ_0, ψ_0. Although the ψ are complex in general, the ψ_c and ψ_0 are real solutions of self-adjoint eigenvalue problems. The eigenspaces at the critical speeds and zero speed are assumed to be one dimensional.

A formulation of the equations of motion in terms of λ^2 and ν^2 is essential for subsequent perturbation analysis. One necessary equation is obtained by differentiation of (1) and the second is obtained by multiplication of (1) by ν. The results yield equations of motion for free response in terms of matrix differential operators

$$\mathbf{C}\tau_{tt} - \nu^2\mathbf{D}\tau + \mathbf{E}\tau = \mathbf{0} \quad B_i\tau_1 = B_i\tau_2 = 0 \qquad (4)$$

$$\mathbf{C} = \begin{bmatrix} M & G \\ 0 & M \end{bmatrix} \quad \mathbf{D} = \begin{bmatrix} \check{K} & 0 \\ -G & \check{K} \end{bmatrix}$$

$$\mathbf{E} = \begin{bmatrix} K & 0 \\ 0 & K \end{bmatrix} \quad \tau = \begin{Bmatrix} u_t \\ \nu u \end{Bmatrix} = \begin{Bmatrix} \tau_1 \\ \tau_2 \end{Bmatrix} \qquad (5)$$

The eigenvalue problem governing stability of the trivial solution results from the separable solution $\tau(P, t) = \mathrm{Re}\{\mathbf{z}(P)e^{\lambda t}\}$ where $\mathbf{z}(P) = (z_1\ z_2)^T$ is a vector of complex functions of coordinates

$$\lambda^2\mathbf{C}\mathbf{z} - \nu^2\mathbf{D}\mathbf{z} + \mathbf{E}\mathbf{z} = \mathbf{0} \quad B_i z_1 = B_i z_2 = 0. \qquad (6)$$

The inner product for arbitrary vectors $\mathbf{v}$, $\mathbf{w}$ having the form of $\mathbf{z}$ is defined as $\langle \mathbf{v}, \mathbf{w}\rangle = (v_1, w_1) + (v_2, w_2)$. The adjoint operators $\mathbf{C}^*$, $\mathbf{D}^*$, and $\mathbf{E}^*$, defined by $\langle \mathbf{C}\mathbf{u}, \mathbf{v}\rangle = \langle \mathbf{u}, \mathbf{C}^*\mathbf{v}\rangle$ and similar relationships, and the eigenvalue problem adjoint to (6) are

$$\bar{\lambda}^2\mathbf{C}^*\mathbf{a} - \nu^2\mathbf{D}^*\mathbf{a} + \mathbf{E}\mathbf{a} = \mathbf{0} \quad B_i a_1 = B_i a_2 = 0$$

$$\mathbf{C}^* = \begin{bmatrix} M & 0 \\ -G & M \end{bmatrix} \quad \mathbf{D}^* = \begin{bmatrix} \check{K} & G \\ 0 & \check{K} \end{bmatrix} \quad \mathbf{E}^* = \begin{bmatrix} K & 0 \\ 0 & K \end{bmatrix}. \qquad (7)$$

The key feature of the formulation (4) is that the associated eigenvalue problem (6) is cast in terms of λ^2 and ν^2.

The quantity ψ in (3) may represent a vector (as in finite degree-of-freedom systems or certain formulations of continuous systems). In recognition of the vector formulation of $\mathbf{z}$,

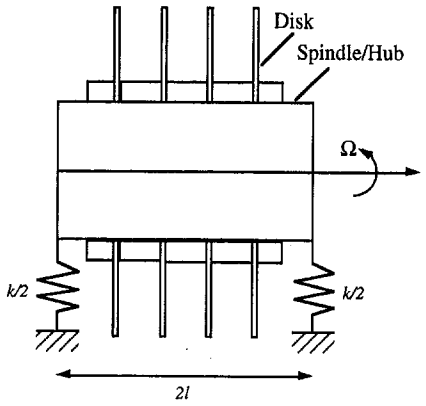

Fig. 2 Rigid body rotating with constant angular velocity about an axis fixed in space

Downloaded 04 May 2010 to 171.66.16.26. Redistribution subject to ASME license or copyright; see http://www.asme.org/terms/Terms_Use.cfm

however, the eigenfunctions of (3) and (6) will be referred to as scalar and vector eigenfunctions, respectively.

Perturbation About Critical Speeds

To examine eigenvalue behavior in the vicinity of a critical speed, a small parameter ε representing the speed perturbation about a critical speed is introduced as $\nu^2 = \nu_c^2 + \varepsilon$. The eigensolutions of (6) are represented as

$$\lambda^2 = \lambda_c^2 + \varepsilon\mu = \varepsilon\mu \quad \mathbf{z} = \mathbf{x} + \varepsilon\mathbf{y} \tag{8}$$

where the vanishing of the critical speed eigenvalue is incorporated in (8a). The eigenvalue perturbation μ is the critical parameter in predicting stability behavior near a critical speed. If λ^2 is negative (λ is imaginary) in speed neighborhoods both above and below a critical speed, then $\lambda^2 = 0$ is a local maximum at the critical speed and $\mu = 0$. Similarly, if λ^2 is positive in both of these neighborhoods (λ is real), $\lambda^2 = 0$ is a local minimum at the critical speed and $\mu = 0$. If a stability change occurs at the critical speed, λ^2 changes sign across the critical speed, λ changes from imaginary to real or vice versa, and $\mu \neq 0$. $\mu > 0$ predicts a change from stability to a region of divergence instability above the critical speed; $\mu < 0$ predicts a change from divergence to stability. For example, the eigenvalue in Fig. 1 loses stability above the critical speed ($\mu > 0$). Substitution of $\nu^2 = \nu_c^2 + \varepsilon$ and (8) into (6) yields the perturbation problems

$$-\nu_c^2\mathbf{Dx} + \mathbf{Ex} = \mathbf{0} \quad B_i x_1 = B_i x_2 = 0 \tag{9}$$

$$-\nu_c^2\mathbf{Dy} + \mathbf{Ey} = -\mu\mathbf{Cx} + \mathbf{Dx} \quad B_i y_1 = B_i y_2 = 0. \tag{10}$$

The subscript c denoting a critical speed will be omitted subsequently. The component equations of the unperturbed problem (9) are

$$(K - \nu^2\tilde{K})x_1 = 0 \quad B_i x_1 = 0$$

$$(K - \nu^2\tilde{K})x_2 = -\nu^2 G x_1 \quad B_i x_2 = 0. \tag{11}$$

Solutions of (11a) are the scalar critical speed eigenfunctions of (3), i.e., $x_1 = \psi_c$. The solvability condition for (11b) is $(G\psi_c, \psi_c) = 0$, which is satisfied because G is skew-symmetric and ψ_c is real. The solution of (11b) is $x_2 = c\psi_c + \hat{x}_2$, where the first term is associated with the nontrivial solution of the homogeneous form of (11b), c is an undetermined constant, and $(\hat{x}_2, \psi_c) = 0$ is specified. The solution of (9), which is also the vector critical speed eigenfunction of (6), is

$$\mathbf{x} = \begin{Bmatrix} \psi_c \\ c\psi_c + \hat{x}_2 \end{Bmatrix}. \tag{12}$$

The solvability condition for (10) requires that the right-hand side be orthogonal to the solution of the homogeneous adjoint problem (7). Thus,

$$\langle -\mu\mathbf{Cx} + \mathbf{Dx}, \mathbf{a}\rangle = 0 \Rightarrow \mu = \frac{\langle \mathbf{Dx}, \mathbf{a}\rangle}{\langle \mathbf{Cx}, \mathbf{a}\rangle}. \tag{13}$$

The component equations of (7) with $\lambda = 0$ are

$$(K - \nu^2\tilde{K})a_1 = \nu^2 G a_2 \quad B_i a_1 = 0$$

$$(K - \nu^2\tilde{K})a_2 = 0 \quad B_i a_2 = 0. \tag{14}$$

Equation (14b) is identical to (11a) with the solution $a_2 = \psi_c$. Comparison of (14a) and (11b) reveals that $a_1 = d\psi_c - \hat{x}_2$, where d is an undetermined coefficient. The adjoint vector eigenfunction is

$$\mathbf{a} = \begin{Bmatrix} d\psi_c - \hat{x}_2 \\ \psi_c \end{Bmatrix}. \tag{15}$$

Evaluation of (13) using (5), (12), and (15) gives

$$\langle \mathbf{Dx}, \mathbf{a}\rangle = (c + \bar{d})(\tilde{K}\psi_c, \psi_c)$$

$$\langle \mathbf{Cx}, \mathbf{a}\rangle = (c + \bar{d})[(M\psi_c, \psi_c) - (G\psi_c, \hat{x}_2)] \tag{16}$$

$$\mu = \frac{(\tilde{K}\psi_c, \psi_c)}{(M\psi_c, \psi_c) - (G\psi_c, \hat{x}_2)}. \tag{17}$$

The result (17) applies for general gyroscopic systems. Only the original system operators and the scalar critical speed eigenfunctions are needed to evaluate μ. Thus, although the matrix differential operator formulation is used to derive (17), the formulation is not necessary for applying the result to specific problems. The operator $\tilde{K}$ is positive-definite for many gyroscopic systems of practical importance. For all such systems, $\mu \neq 0$ and a λ^2 locus crosses the ν^2-axis at *every* critical speed having only one independent eigenfunction. Consequently, a neighborhood of divergence instability exists either above or below each critical speed. For positive-definite $\tilde{K}$ the denominator of (17) governs the sign of μ and thus whether an eigenvalue gains or loses stability as ν^2 crosses a critical speed. Although the constants c and d arising from the indeterminacy of (12) and (15) are not required in the evaluation of (17), their inclusion is essential as seen in (16).

As an alternate approach, the eigenvalue perturbation (17) can be derived directly from perturbation of (3) using fractional power eigensolution expansions. This procedure and its equivalence to that given above are presented in the Appendix.

Perturbation About Stationary System Eigenvalues

A development analogous to the above can be carried out for perturbation of the stationary system eigenvalues. In this case, the speed perturbation and eigensolution representations are

$$\nu^2 = \varepsilon \quad \lambda^2 = \lambda_0^2 + \varepsilon\mu \quad \mathbf{z} = \mathbf{x} + \varepsilon\mathbf{y} \tag{18}$$

where λ_0^2 denotes a stationary system eigenvalue. Substitution of (18) into (6) yields

$$\lambda_0^2\mathbf{Cx} + \mathbf{Ex} = \mathbf{0} \quad B_i x_1 = B_i x_2 = 0 \tag{19}$$

$$\lambda_0^2\mathbf{Dy} + \mathbf{Ey} = -\mu\mathbf{Cx} + \mathbf{Dx} \quad B_i y_1 = B_i y_2 = 0. \tag{20}$$

The subscript 0 will be omitted subsequently. The component equations of (19) are

$$(\lambda^2 M + K)x_1 = -\lambda^2 G x_2 \quad B_i x_1 = 0$$

$$(\lambda^2 M + K)x_2 = 0 \quad B_i x_2 = 0. \tag{21}$$

Equation (21b) is the eigenvalue problem for the scalar stationary system eigensolutions. Thus, $x_2 = \psi_0$. Using notation for c and $\hat{x}_1$ analogous to (12), the solution of (21a) is $x_1 = c\psi_0 + \hat{x}_1$ where $(\hat{x}_1, \psi_0) = 0$. The stationary system vector eigenfunction is $\mathbf{x} = \begin{Bmatrix} c\psi_0 + \hat{x}_1 \\ \psi_0 \end{Bmatrix}$. The adjoint eigenfunction $\mathbf{a}$ is the solution of (7) with $\nu^2 = 0$. A development analogous to that for critical speed perturbation yields $\mathbf{a} = \begin{Bmatrix} \psi_0 \\ d\psi_0 - \hat{x}_1 \end{Bmatrix}$. The solvability condition for (20) gives

$$\mu = \frac{(\tilde{K}\psi_0, \psi_0) + (G\psi_0, \hat{x}_1)}{(M\psi_0, \psi_0)}. \tag{22}$$

Again the eigenvalue perturbation depends only on the scalar stationary system eigenfunction ψ_0 and the original system operators; the matrix differential operator formulation is *not* required in the application of (22). μ is finite because M is positive-definite, and the λ^2 versus ν^2 loci cannot be vertical at $\nu^2 = 0$.

Downloaded 04 May 2010 to 171.66.16.26. Redistribution subject to ASME license or copyright; see http://www.asme.org/terms/Terms_Use.cfm

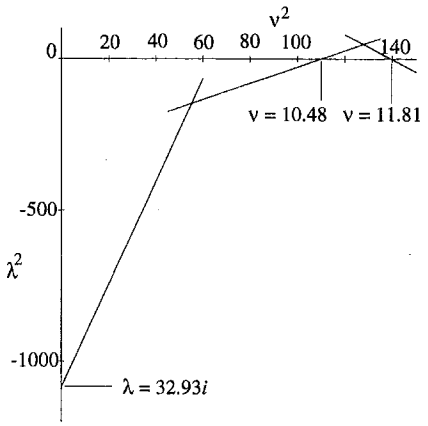

Fig. 3 Piecewise-linear perturbation approximation of the fundamental eigenvalue λ^2 versus transport speed ν^2 for an axially moving tensioned beam. The tensioning is $\kappa^2 = 100$.

The operators $\tilde{K}$ and G derive from the motion of the system. It is appropriate that when the scalar critical speed eigenfunctions ψ_c and stationary system eigenfunctions ψ_0 are normalized to unit generalized mass, the eigenvalue perturbations (17) and (22) are a balance of the actions of these operators on the unperturbed eigenfunctions.

Piecewise-Linear Eigenvalue Approximation

The preceding analysis yields the slopes of the λ^2 versus ν^2 loci at the critical speed and stationary system eigenvalues. A piecewise-linear approximation for the eigenvalue loci is readily constructed by connecting the linear approximations generated at each stationary system eigenvalue and at each critical speed. Figure 3 is an example for an axially moving tensioned beam. Figure 5 shows both the exact and approximate eigenvalue loci for the system of Fig. 2. Closed-form solution of gyroscopic system eigenvalue problems is difficult to achieve in general, and numerical discretization is frequently necessary. As demonstrated by Wickert and Mote (1991), however, discretization can lead to errors if complex speed-dependent admissible functions capturing the spatial phase distribution of the gyroscopic eigenfunctions are not used. The piecewise-linear perturbation approximation yields an analytical estimate for the eigenvalue loci using only the eigenfunctions of the self-adjoint critical-speed and zero-speed eigenvalue problems.

Example 1: Axially Moving Tensioned Beam

An axially moving tensioned Euler-Bernoulli beam is commonly used to model band saws, belts, magnetic tapes, and textiles. The dimensionless equation of motion for free response is

$$u_{tt} + 2\nu u_{xt} + u_{xxxx} + (\nu^2 - \kappa^2)u_{xx} = 0 \qquad (23)$$

where ν and κ represent the transport speed and axial tension, respectively. The operators in (1) are

$$M = I \quad G = 2\frac{\partial}{\partial x} \quad K = \frac{\partial^4}{\partial x^4} - \kappa^2\frac{\partial^2}{\partial x^2} \quad \tilde{K} = -\frac{\partial^2}{\partial x^2}. \qquad (24)$$

Simply supported boundary conditions are specified.

Critical Speed Perturbation: Equation (3) and $\lambda = 0$ yield the eigenvalue problem associated with buckling of a thin column. The critical speeds and scalar critical speed eigenfunctions are

$$\nu_c^2 = \kappa^2 + n^2\pi^2 \qquad \psi_c(x) = \sin n\pi x \qquad n = 1, 2, \ldots. \qquad (25)$$

These are also the solutions of (11a). Solution of (11b) with $x_1 = \psi_c$ yields (12) where

$$\hat{x}_2 = A_1 \sin n\pi x + A_2 \cos n\pi x + A_3 x + A_4 + \frac{\nu_c^2}{n^2\pi^2} x \sin n\pi x. \qquad (26)$$

The last term is a particular solution of (11b), and the A_i are determined from simply supported boundary conditions and $(\hat{x}_2, \psi_c) = 0$. The eigenvalue perturbation μ is evaluated from (17).

For the dimensionless axial tension $\kappa^2 = 100$, the first two critical speeds and the eigenvalue perturbations are

$$\nu_c^2 = 109.9 \rightarrow \nu_c = 10.48 \quad \mu = 2.670$$
$$\nu_c^2 = 139.5 \rightarrow \nu_c = 11.81 \quad \mu = -4.113. \qquad (27)$$

The positive μ at the first critical speed predicts a change in λ^2 from negative to positive, or, equivalently, a change in λ from imaginary to real, as the speed increases past the first critical speed (Fig. 3). The eigenvalue is stable below the first critical speed, but divergence instability exists in a neighborhood of speeds above the first critical speed. The negative μ at the second critical speed predicts a change in λ from real to imaginary as the speed increases past this speed; the system is stable in a speed neighborhood above the second critical speed. This stability region exists even though the stiffness operator $\hat{K} = K - \nu^2\tilde{K}$ ceases to be positive-definite above the first critical speed. These stability predictions match those found numerically by Wickert and Mote (1990).

Stationary System Perturbation: Equation (3) with $\nu = 0$ yields the eigenvalue problem for free vibration of an axially loaded beam. The eigensolutions are

$$\lambda_0^2 = -n^2\pi^2(\kappa^2 + n^2\pi^2) \qquad \psi_0(x) = \sin n\pi x \qquad n = 1, 2, \ldots \qquad (28)$$

The solution of (21a) with $x_2 = \psi_0$ is $x_1 = c\psi_0 + \hat{x}_1$ where

$$\hat{x}_1 = A_1 \sin n\pi x + A_2 \cos n\pi x + A_3 \sinh \beta x + A_4 \cosh \beta x + \frac{\lambda^2}{\kappa^2 + 2n^2\pi^2} x \sin n\pi x$$

$$\beta^2 = (1/2)[\kappa^2 + \sqrt{\kappa^4 + 4n^2\pi^2(\kappa^2 + n^2\pi^2)}]. \qquad (29)$$

Simply supported boundary conditions and $(\hat{x}_1, \psi_0) = 0$ fix the A_i. μ is evaluated from (22).

For axial tensioning $\kappa^2 = 100$, the results for the two lowest stationary beam eigenvalues are

$$\lambda_1^2 = -1084. \rightarrow \lambda_1 = 32.93i \quad \mu = 16.99$$
$$\lambda_2^2 = -5506. \rightarrow \lambda_2 = 74.21i \quad \mu = 50.50. \qquad (30)$$

Each of the λ^2 increases (i.e., natural frequency decreases) as translation is introduced into the stationary system. The rate of increase is more pronounced for higher eigenvalues. Figure 3 shows a piecewise-linear approximation of the lowest eigenvalue locus constructed from (27) and (30). Higher eigenvalues are similarly approximated.

Example 2: Axially Moving String on an Elastic Foundation

We can compare the perturbation results to an exact, continuous system solution for an axially moving string on an elastic foundation. The dimensionless governing equation for transport speed ν and foundation stiffness k is

Downloaded 04 May 2010 to 171.66.16.26. Redistribution subject to ASME license or copyright; see http://www.asme.org/terms/Terms_Use.cfm

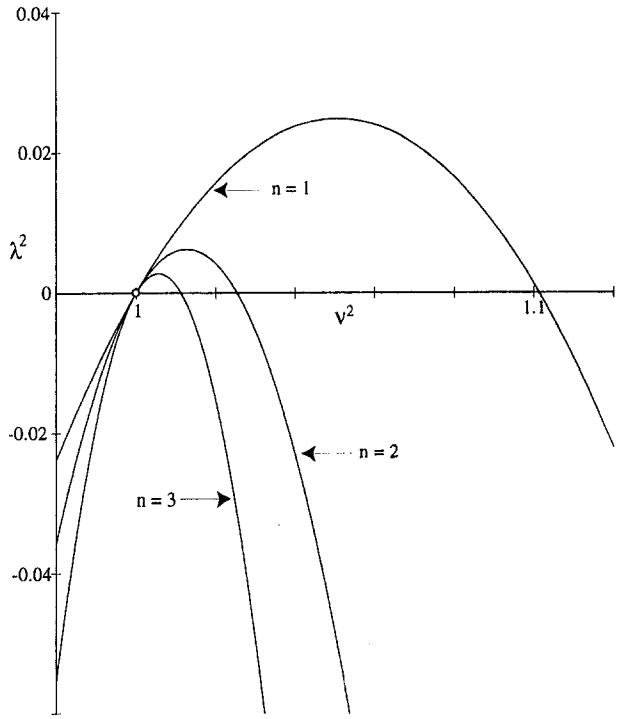

Fig. 4 Lowest three eigenvalues λ^2 versus transport speed ν^2 for an axially moving string on an elastic foundation of stiffness $k = 1$. $\lambda^2 = 0$ is *not* an eigenvalue at $\nu^2 = 1$.

$$u_{tt} + 2\nu u_{xt} - (1 - \nu^2)u_{xx} + ku = 0. \tag{31}$$

We consider fixed boundary conditions at $x = 0$ and 1. Perturbation about the critical speeds yields

$$\nu_c^2 = 1 + k/(n^2\pi^2) \quad \psi_c(x) = \sin n\pi x$$

$$\hat{x}_2 = -[1 + n^2\pi^2/k]x \sin n\pi x \quad \mu = -k$$

$$n = 1, 2, \ldots. \tag{32}$$

Notice that μ is independent of n. Perturbation about the stationary system eigensolutions gives

$$\lambda_0^2 = -k - n^2\pi^2 \quad \psi_0(x) = \sin n\pi x$$

$$\hat{x}_1 = (k + n^2\pi^2)(x - 1/2) \sin n\pi x \quad \mu = k + 2n^2\pi^2$$

$$n = 1, 2, \ldots. \tag{33}$$

The exact eigenvalue solution is $\lambda^2 = -(1 - \nu^2)[k + n^2\pi^2(1 - \nu^2)]$ (Perkins, 1990). Differentiation of the exact solution at the critical speeds and zero speed yields

$$\partial(\lambda^2)/\partial(\nu^2)|_{\nu^2=\nu_c^2} = -k$$

$$\partial(\lambda^2)/\partial(\nu^2)|_{\nu^2=0} = k + 2n^2\pi^2 \tag{34}$$

which confirm the perturbation results. Figure 4 shows the lowest three eigenvalues for the string. That the critical eigenvalues all pass from unstable to stable at a critical speed is predicted by perturbation because $\mu < 0$. Note that $\lambda^2 = 0$ is not an eigenvalue at $\nu^2 = 1$.

Example 3: Spinning Body in Flexible Bearings

The perturbation results can be compared with another exact solution by considering a rigid body having a constant angular speed Ω about a fixed axis coinciding with the undeflected configuration. This system is a possible model for a disk drive rotating in finite stiffness bearings (Fig. 2). The principal moment of inertia about the body-fixed axis initially aligned with the rotation axis is J_3, and the other two principal moments of inertia are $J_{1,2}$. The isotropic bearings have stiffness $k/2$, and the center of mass is a distance l from each bearing. Denoting the Euler rotations of the body as η and ξ, the dimensionless equations of motion are

$$\mathbf{M}\ddot{\mathbf{u}} + \nu\mathbf{G}\dot{\mathbf{u}} + (\mathbf{K} - \nu^2\tilde{\mathbf{K}})\mathbf{u} = \mathbf{0} \quad \mathbf{u} = \begin{Bmatrix}\eta\\ \xi\end{Bmatrix}$$

$$\mathbf{M} = \begin{bmatrix}\beta & 0\\ 0 & \alpha\end{bmatrix} \quad \mathbf{G} = \begin{bmatrix}0 & -Q\\ Q & 0\end{bmatrix}$$

$$\mathbf{K} = \begin{bmatrix}1 & 0\\ 0 & 1\end{bmatrix} \quad \tilde{\mathbf{K}} = \begin{bmatrix}\alpha - 1 & 0\\ 0 & \beta - 1\end{bmatrix} \tag{35}$$

$$\alpha = \frac{J_1}{J_3} \quad \beta = \frac{J_2}{J_3} \le \alpha \quad t = \sqrt{\frac{kl^2}{J_3}}\,T$$

$$\nu = \sqrt{\frac{J_3}{kl^2}}\,\Omega \quad Q = \alpha + \beta - 1 > 0. \tag{36}$$

The critical speeds, which exist if and only if $\alpha > 1$ and/or $\beta > 1$, are

$$\nu_1^2 = 1/(\alpha - 1) \quad \nu_2^2 = 1/(\beta - 1) \ge \nu_1^2. \tag{37}$$

Considering the case $\alpha > \beta > 1$, perturbation yields

$$\nu_1^2 = \frac{1}{\alpha - 1} \quad x_1 = \begin{Bmatrix}1\\ 0\end{Bmatrix} \quad \hat{x}_2 = \begin{Bmatrix}0\\ -\dfrac{Q}{\alpha - \beta}\end{Bmatrix}$$

$$\mu = \frac{(\alpha - \beta)(\alpha - 1)}{\beta(\alpha - \beta) + Q^2} > 0$$

$$\nu_2^2 = \frac{1}{\beta - 1} \quad x_1 = \begin{Bmatrix}0\\ -\dfrac{\alpha - \beta}{Q}\end{Bmatrix}$$

$$\hat{x}_2 = \begin{Bmatrix}1\\ 0\end{Bmatrix} \quad \mu = \frac{(\alpha - \beta)(\alpha - 1)}{\alpha(2 - 3\beta) - (\beta - 1)^2} < 0. \tag{38}$$

Stability is lost at $\nu^2 = 1/(\alpha - 1)$ where $\mu > 0$, and stability is regained at $\nu^2 = 1/(\beta - 1)$ where $\mu < 0$ (Fig. 5(*a*)). For the case $\alpha > 1 > \beta$, only the critical speed ν_1^2 exists. The first result of (38) remains valid; divergence instability exists for

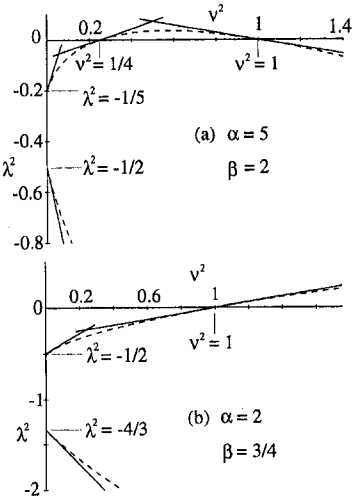

Fig. 5 Eigenvalues λ^2 for the rigid-body system of Fig. 2 for the cases $\alpha = 5$, $\beta = 2$ and $\alpha = 2$, $\beta = \frac{3}{4}$. ν^2 is the square of the dimensionless rotation speed. The solid curves are piecewise-linear perturbation approximations to the exact solutions (dashed curves).

Downloaded 04 May 2010 to 171.66.16.26. Redistribution subject to ASME license or copyright; see http://www.asme.org/terms/Terms_Use.cfm

all speeds above the first critical speed (Fig. 5(*b*)). For $1 > \alpha \geq \beta$, there are no critical speeds. The stationary system eigenvalues are $\lambda_1^2 = -1/\alpha$ and $\lambda_2^2 = -1/\beta$. Perturbation about these eigenvalues yields

$$\lambda_1^2 = -\frac{1}{\alpha} \quad \mu = \frac{\alpha^2 + (3\alpha - 1)(\beta - 1)}{\alpha(\alpha - \beta)}$$

$$\lambda_2^2 = -\frac{1}{\beta} \quad \mu = -\frac{\beta^2 + (\alpha - 1)(3\beta - 1)}{\beta(\alpha - \beta)}. \qquad (39)$$

The sign of μ is indefinite at both stationary system eigenvalues. As expected, the μ in (38) and (39) are identical to $\partial(\lambda^2)/\partial(\nu^2)$ evaluated at the critical speeds and zero speed using the exact characteristic equation derived from (35). Figure 5 compares the exact eigenvalue loci and the piecewise-linear perturbation approximations for the cases $\alpha > \beta > 1$ and $\alpha > 1 > \beta$.

Discussion

For systems having only one independent scalar eigenfunction at their critical speeds and sign-definite $\tilde{K}$, μ in (17) is nonzero and a region of divergence instability exists in a local neighborhood either above or below (but not both) *every* critical speed. When $\tilde{K}$ is sign-indefinite, such a general conclusion cannot be drawn, although evaluation of (17) reveals the behavior at a chosen critical speed. Renshaw and Mote (1996) examined a first-order formulation of the equations of motion in terms of matrix differential operators to conjecture when regions of instability exist near a critical speed. This conjecture, based on the action of G on the critical speed eigenfunctions, was not proven, but it was shown to be correct for several physical systems. For the case of a single eigenfunction ψ_c at a critical speed as considered herein, $(G\psi_c, \psi_c) = 0$. In this case, Renshaw and Mote's conjecture concludes that a region of divergence instability occurs in the neighborhood of every critical speed. Their conclusion is confirmed by the perturbation analysis *provided* $\tilde{K}$ is sign-definite. If $\tilde{K}$ is sign-indefinite, the first-order eigenvalue perturbation might vanish at a critical speed and the eigenvalue may not change stability across the critical speed. Such a case would contradict the conjecture.

Some distinctions between Renshaw and Mote's work and the stability conclusions herein can be identified. Renshaw and Mote's result is slightly simpler to apply and addresses systems with multiple eigenfunctions at a critical speed. It is, however, a conjecture, and it does not provide any quantitative information. The current work has the mathematical justification of the perturbation analysis. Equally important is that it provides quantitative eigenvalue estimates. Additionally, it offers the potential for higher-order approximations and addresses zero-speed eigenvalues. It is limited, however, to cases having a single critical speed eigenfunction. This restriction is substantial because it excludes several systems of importance, e.g., axisymmetric rotating disks, beams, and rotors. Expansion of the current perturbation to include these cases could provide additional critical speed stability rules.

The separable scalar solution $u(P, t) = \mathrm{Re}\{\psi(P)e^{\lambda t}\}$ used to generate (3) suggests that the vector eigenfunctions of (6) have the form $\mathbf{z} = \begin{Bmatrix} \lambda\psi \\ \nu\psi \end{Bmatrix}$. The derived vector eigensolutions (e.g., (12)) are not of this form, however, and a priori imposition of this form leads to erroneous perturbation results. Instead, the separable vector solution $\tau(P, t) = \mathrm{Re}\{\mathbf{z}(P)e^{\lambda t}\}$ where no conditions are placed on components of $\mathbf{z}$ is required.

Extension to higher orders of perturbation is possible provided the solutions of (10) and (20) are obtained. Such solution is likely achievable in many cases. The component equations of (10) and (20) are self-adjoint, and the inhomogeneous right-hand sides depend on the action of the system operators on the unperturbed eigenfunctions. For regularly shaped domains, these inhomogeneities are well-known functions for which the necessary particular solutions are readily derived. Higher-order perturbations would generate improved piecewise-polynomial eigenvalue loci estimates.

At flutter instability, the coalescing eigenvalues are not smooth functions of the gyroscopic parameter ν. When viewed in the λ^2–ν^2 plane, however, flutter is manifest as a smooth coalescence of two eigenvalue loci at a vertical slope (Huseyin and Plaut, 1974–1975). This smoothness offers the possibility to estimate flutter speeds using perturbation of the continuous system formulation (6).

Although the eigenvalue problem formulation (6) is natural for eigenvalue analysis, it is not optimal for response analyses because the operators lack symmetry and definiteness. The vector eigenfunction modal analysis introduced by Meirovitch (1975) and used by Wickert and Mote (1990) is more efficient for response calculations.

Conclusions

1 For general continuous and discrete gyroscopic systems, the equations of motion are cast such that the associated eigenvalue problem (6) involves only the square of the eigenvalue and the gyroscopic parameter ν (i.e., speed) appears only as ν^2. This formulation involves matrix differential operators acting on a vector eigenfunction. The formulation admits a critical-speed (zero eigenvalue) and zero-speed eigenvalue perturbation solution that takes advantage of the differentiability of λ^2 at these speeds. Although the vector eigenfunction formulation is used to derive the eigenvalue perturbations, the final results depend only on quantities associated with the standard formulation.

2 The eigenvalue perturbations are evaluated from simple inner products involving the original continuous system operators and solutions of self-adjoint eigenvalue problems independent of the gyroscopic operator. The results yield qualitative and quantitative stability predictions in the vicinity of critical speeds. The sign of the first-order eigenvalue perturbation predicts whether the critical eigenvalue passes to or from a region of divergence instability at the critical speed. For systems with one independent critical speed eigenfunction and positive-definite gyroscopic stiffness $\tilde{K}$, a stability change occurs at every critical speed. In contrast, systems having more than one critical speed eigenfunction do not necessarily change stability at a critical speed; analysis of such systems requires extension of the current work.

3 The combination of critical speed and stationary system eigenvalue perturbations provides a piecewise-linear approximation for the eigenvalue loci. These approximations are derivable for gyroscopic systems involving complexities that preclude analytical eigensolution. Higher-order perturbations that would improve these approximations seem achievable.

Acknowledgments

The author thanks A. A. Renshaw for pointing out the applicability of the fractional power perturbation expansions used in the Appendix.

References

Friswell, M. I., 1996, "The Derivatives of Repeated Eigenvalues and Their Associated Eigenvectors," ASME *Journal of Vibration and Acoustics,* Vol. 118, pp. 390–397.

Huseyin, K., 1976, "Standard Forms of the Eigenvalue Problems Associated with Gyroscopic Systems," *Journal of Sound and Vibration,* Vol. 45, pp. 29–37.

Huseyin, K., and Plaut, R. H., 1974–1975, "Transverse Vibrations and Stability of Systems with Gyroscopic Forces," *Journal of Struct. Mech.,* Vol. 3, No. 2, pp. 163–177.

Meirovitch, L., 1975, "A Modal Analysis for the Response of Linear Gyroscopic Systems," ASME JOURNAL OF APPLIED MECHANICS, Vol. 42, pp. 446–450.

Downloaded 04 May 2010 to 171.66.16.26. Redistribution subject to ASME license or copyright; see http://www.asme.org/terms/Terms_Use.cfm

Mote, C. D., Jr., 1970, "Stability of Circular Plates Subjected to Moving Loads," *Journal of the Franklin Institute,* Vol. 290, No. 4, pp. 329–344.

Perkins, N. C., 1990, "Linear Dynamics of a Translating String on an Elastic Foundation," ASME *Journal of Vibration and Acoustics,* Vol. 112, pp. 2–7.

Plaut, R. H., 1976, "Alternative Formulations for Discrete Gyroscopic Eigenvalue Problems," *AIAA Journal,* Vol. 14, No. 4, pp. 431–435.

Plaut, R. H., and Huseyin, K., 1973, "Derivatives of Eigenvalues and Eigenvectors in Non-Self-Adjoint Systems," *AIAA Journal,* Vol. 11, pp. 250–251.

Rogers, L. C., 1970, "Derivatives of Eigenvalues and Eigenvectors," *AIAA Journal,* Vol. 8, pp. 943–944.

Seyranian, A. P., 1993, "Sensitivity Analysis of Multiple Eigenvalues," *Mech. Struct. & Mach.,* Vol. 21, pp. 261–284.

Tang, J., Ni, W.-M., and Wang, W.-L., 1996, "Eigensolutions Sensitivity for Quadratic Eigenproblems," *Journal of Sound and Vibration,* Vol. 196, pp. 179–188.

Vishik, M. I., and Lyusternik, L. A., 1960, "Solution of Some Perturbation Problems in the Case of Matrices and Selfadjoint or Non-selfadjoint Equations," *Russian Math. Surveys,* Vol. 15, pp. 1–73.

Wickert, J. A., and Mote, C. D., Jr., 1990, "Classical Vibration Analysis of Axially Moving Continua," ASME JOURNAL OF APPLIED MECHANICS, Vol. 57, pp. 738–744.

Wickert, J. A., and Mote, C. D., Jr., 1991, "Response and Discretization Methods for Axially Moving Materials," ASME *Applied Mechanics Rev,* Vol. 44, pp. S279–S284.

APPENDIX

As an alternative to perturbation of the vector representation (6), the result (17) can be obtained directly from perturbation of (3). The unique feature is that the perturbation expansions must be in terms of fractional powers of the small speed perturbation about critical speed. Before presenting this method, consider the standard critical speed perturbation of (3) with $\beta \ll \nu_c$

$$\nu = \nu_c + \beta \quad \lambda = \lambda_c + \beta\lambda_1 = \beta\lambda_1 \quad \psi = \psi_c + \beta\psi_1. \tag{40}$$

The first-order perturbation problem is $K\psi_1 - \nu_c^2\tilde{K}\psi_1 = -\lambda_1\nu_c G\psi_c + 2\nu_c\tilde{K}\psi_c$. This problem is not solvable for the common case of positive-definite $\tilde{K}$ and the perturbation fails. We now approach the problem using the fractional power expansions (Seyranian, 1993; Vishik and Lyusternik, 1960).

$$\nu = \nu_c + \beta \quad \lambda = \lambda_c + \beta^{1/2}\lambda_1 + \beta\lambda_2 = \beta^{1/2}\lambda_1 + \beta\lambda_2$$
$$\psi = \psi_c + \beta^{1/2}\psi_1 + \beta\psi_2 \tag{41}$$

The perturbation problems are

$$K\psi_1 - \nu_c^2\tilde{K}\psi_1 = -\lambda_1\nu_c G\psi_c \tag{42}$$

$$K\psi_2 - \nu_c^2\tilde{K}\psi_2 = -\lambda_1^2 M\psi_c + 2\nu_c\tilde{K}\psi_c - \lambda_1\nu_c G\psi_1 - \lambda_2\nu_c G\psi_c. \tag{43}$$

Homogeneous boundary conditions as in (3) are appended to each problem. Solvability of (42) is assured because $(G\psi_c, \psi_c) = 0$. The solvability condition for (43) is

$$-\lambda_1^2(M\psi_c, \psi_c) + 2\nu_c(\tilde{K}\psi_c, \psi_c) - \lambda_1\nu_c(G\psi_1, \psi_c) = 0. \tag{44}$$

The auxiliary problem $K\hat{x}_2 - \nu_c^2\tilde{K}\hat{x}_2 = -\nu_c^2 G\psi_c$ (see (11*b*)) is solvable and $\psi_1 = (\lambda_1/\nu_c)\hat{x}_2$. Reduction of (44) then yields

$$\lambda_1^2 = \frac{2\nu_c(\tilde{K}\psi_c, \psi_c)}{(M\psi_c, \psi_c) - (G\psi_c, \hat{x}_2)} \Rightarrow$$

$$\lambda^2 = \beta\lambda_1^2 = 2\nu_c\beta\,\frac{(\tilde{K}\psi_c, \psi_c)}{(M\psi_c, \psi_c) - (G\psi_c, \hat{x}_2)}. \tag{45}$$

With the association $\varepsilon = 2\nu_c\beta$, (45) is equivalent to (17).

Downloaded 04 May 2010 to 171.66.16.26. Redistribution subject to ASME license or copyright; see http://www.asme.org/terms/Terms_Use.cfm

Nonlinear Waves in Strings: The Barrage Balloon Problem

J. F. Hall
Department of Civil Engineering, Division of Engineering and Applied Science, California Institute of Technology, Mail Code 104-44, Pasadena, CA 91125

This paper develops a theory for geometrically nonlinear waves in strings and presents analytical solutions for a traveling kink, generation of a geometric wave with its accompanying P wave, reflection of a kink at a fixed support and at a smooth sliding support, and interaction of a P wave and a kink. Conditions that must be satisfied for linear wave theory to hold are derived. The nonlinear theory is demonstrated by extending an historically important solution of the barrage balloon problem that was obtained during World War II.

Introduction

The linear theory for lateral vibration of an initially stretched string as described by the wave equation is well known. This theory is valid under conditions that include changes in slope of the string remaining small (geometric linearity) and the string staying in the linearly elastic range (material linearity). In this paper, the case where geometric linearity does not hold is examined. An early example of such a consideration occurred during World War II when an analyst with the Fifteenth Air Force of the United States solved the problem of an aircraft wing striking a barrage balloon cable. Because this solution obtained is elegant and because the circumstances of the time required an urgent assessment of the hazard posed by barrage balloon cables, the solution must be regarded as one of the classical applications of mechanics. One purpose of this paper is to present a detailed description of the barrage balloon problem for which up until now only a brief account has been published (Irvine, 1981).

The other purpose of this paper is to generalize the solution of the barrage balloon problem into a theory for geometrically-nonlinear motion of strings. The fundamental element of the theory is a traveling kink that acts as a wave front for a geometric wave of non-small slope. Solutions for reflections of a geometric wave at various types of supports as well as interaction between a geometric wave and an axial wave (P wave) are obtained. To demonstrate the theory, the barrage balloon problem is revisited and a solution valid for a duration longer than that of the earlier solution is obtained. The treatment gives considerable insight into string dynamics in the geometrically nonlinear range, and the theory may find application in such areas as the dynamics of musical string instruments, weaving machines, belt drives and tethered objects.

Basic Considerations

The theory presented here applies to a string with the following properties: initially constant cross-sectional area A and material density ρ, zero bending rigidity, small axial strains, and linear stress-strain relation ($T/AE = \epsilon$, where T = axial force, ϵ = axial strain and E = Young's modulus). The small-strain condition means that A and ρ, and hence the density per unit length ρA, can be taken as constant. Motions of the string are not limited to small slopes or velocities.

Consider the situation of Fig. 1 where a string is sliding through a stationary, frictionless and arbitrarily curved tube, entering at A and exiting at B. Every particle in the string is stretched to a constant tension $T = EA\epsilon$ and moves with constant velocity V relative to the tube in the direction tangent to the tube. If V is related to T or ϵ by

$$V = \sqrt{T/\rho A} = C\sqrt{\epsilon}, \tag{1}$$

where $C = \sqrt{E/\rho}$ = axial wave (P wave) speed in the string, then the reaction forces provided by the tube on the string are zero and, theoretically, the moving string could maintain its profile even if the tube were removed.[1] This "standing wave" exists because the vectors of resultant string force and time rate of change of momentum equal each other for every differential segment. With reference to the inset in Fig. 1,

$$2T \sin \frac{d\theta}{2} = 2V \sin \frac{d\theta}{2} V\rho A \tag{2}$$

in the normal direction, which gives Eq. (1). Note that Eq. (2) does not involve a curvature parameter. Also, if the string segments feeding in through A and exiting through B are colinear and horizontal, and if the viewer is moving to the right at velocity V, the situation becomes a traveling wave to the left at velocity V in a string that is initially stationary and stretched to a tensile strain ϵ. Note that the speed of this wave, which is given by Eq. (1), is the same as that from linear theory. Note also that this wave does not change the string tension.

The preceding applies even when sharp kinks are present in the string profile. Because kinks are simple to deal with mathematically, because any wave profile can be approximated by straight segments and kinks, and because kinks exist in their own right, the equations governing a kink in a moving string are now presented. The kink exists in a region of constant tensile strain ϵ with a straight segment on the left whose particles have constant velocity $\langle V_{LX}, V_{LY}\rangle$ and a straight segment on the right whose particles have constant velocity $\langle V_{RX}, V_{RY}\rangle$ (Fig. 2). The string particles move through the kink whose location is designated by G and whose velocity is $\langle V_{GX}, V_{GY}\rangle$ (not a particle velocity). With V from Eq. (1) denoting the relative particle velocity through the kink, the mass flux M_G through the kink (mass per time) is

$$M_G = \rho AV = \pm\sqrt{\rho AT} = \pm\rho AC\sqrt{\epsilon}, \tag{3}$$

which does not depend on the kink angle. The mass flux can be either positive (from left segment to right) or negative (right to left).

Contributed by the Applied Mechanics Division of THE AMERICAN SOCIETY OF MECHANICAL ENGINEERS for publication in the ASME JOURNAL OF APPLIED MECHANICS.

Discussion on this paper should be addressed to the Technical Editor, Professor Lewis T. Wheeler, Department of Mechanical Engineering, University of Houston, Houston, TX 77204-4792, and will be accepted until four months after final publication of the paper itself in the ASME JOURNAL OF APPLIED MECHANICS.

Manuscript received by the ASME Applied Mechanics Division, Sept. 4, 1996; final revision, Sept. 29, 1997. Associate Technical Editor: J. N. Reddy.

[1] This holds under ideal conditions and no gravity. The issue of whether a profile is stable or not is not addressed here.

 Copyright © 1998 by ASME

Downloaded 04 May 2010 to 171.66.16.26. Redistribution subject to ASME license or copyright; see http://www.asme.org/terms/Terms_Use.cfm

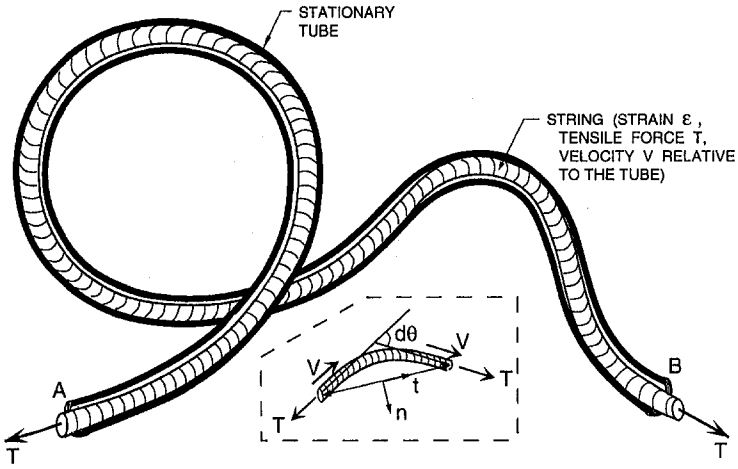

Fig. 1 Cut-away view of a string sliding through a stationary, frictionless, and arbitrarily curved tube. Inset shows a differential length of the string with the tube removed.

The mass flux M_G can be related to the velocities and to the unchanging slope angles (denoted by θ_L and θ_R) by

$$M_G = \rho A(V_{LX} \cos \theta_L + V_{LY} \sin \theta_L - V_{GX} \cos \theta_L - V_{GY} \sin \theta_L) \quad (4a)$$

$$= \rho A(V_{RX} \cos \theta_R + V_{RY} \sin \theta_R - V_{GX} \cos \theta_R - V_{GY} \sin \theta_R). \quad (4b)$$

Equation (4a) gives the mass flux into the kink from the left segment and Eq. (4b) gives the mass flux out of the kink into the right segment. Since the kink is the intersection of the two moving segments, its velocity $\langle V_{GX}, V_{GY} \rangle$ can be expressed from geometric considerations as

$$V_{GX} = (V_{RX} \tan \theta_R - V_{RY} - V_{LX} \tan \theta_L + V_{LY})/(\tan \theta_R - \tan \theta_L) \quad (5a)$$

$$V_{GY} = (V_{RX} \tan \theta_R \tan \theta_L - V_{RY} \tan \theta_L - V_{LX} \tan \theta_R \tan \theta_L + V_{LY} \tan \theta_R)/(\tan \theta_R - \tan \theta_L). \quad (5b)$$

Equations (4) and (5) can be combined to eliminate V_{GX} and V_{GY} with the following result:

$$M_G = \rho A(V_{RX} - V_{LX})/(\cos \theta_R - \cos \theta_L) \quad (6a)$$

$$= \rho A(V_{RY} - V_{LY})/(\sin \theta_R - \sin \theta_L). \quad (6b)$$

Equations (3) and (6) are three expressions relating the eight variables M_G, ϵ, V_{LX}, V_{LY}, θ_L, V_{RX}, V_{RY}, and θ_R. Example analyses using Eqs. (3) and (6) will be presented later.

Next, a situation involving two kinks (denoted by $G1$ and $G2$) will be used to illustrate a different type of solution in which the wave profile changes (Fig. 3). Again, the tensile strain ϵ is constant. Equation (3) applies for the mass flux at both $G1$ and $G2$, so

$$|M_{G1}| = |M_{G2}| = \rho AC\sqrt{\epsilon}. \quad (7)$$

When $M_{G1} = M_{G2}$, the segment between kinks $G1$ and $G2$ maintains its length, and this solution is of the type discussed earlier. However, when $M_{G1} = -M_{G2}$, then the segment either gets longer ($M_{G1} > 0$, $M_{G2} < 0$) or shorter ($M_{G1} < 0$, $M_{G2} > 0$); in either case, the wave profile changes.

Axial waves (P waves) can also travel along the string. In the aforementioned cases, the tension was constant in the lengths considered, and thus no P waves were present. In the case of a P wave impinging on a kink (presented later), the P wave is partially reflected by the kink and partially transmitted past it. The P wave causes the kink to divide into two kinks which move apart, similar to the situation of Fig. 3 where the middle segment is expanding.

In the derivations of this paper, all root operations designate the positive root.

Semi-Infinite String With Specified End Velocity

The problem is shown in Fig. 4 where a semi-infinite string that is initially stationary, horizontal, and stretched to a strain ϵ_0 has its right end moved at constant velocity $\langle V_{RX}, V_{RY} \rangle$. The solution consists of a straight geometric wave at slope angle θ_R that travels to the left with a kink at its front, preceded by a P wave traveling to the left at velocity C. The tensile strain between the P-wave front and the right end is constant at ϵ. Note that $\theta_L = 0$, $V_{GY} = 0$ and all points in the geometric wave have the same velocity as the right end. Also, $V_{LY} = 0$ and V_{LX} is caused entirely by the P wave, so

$$V_{LX} = C \cdot (\epsilon - \epsilon_0) \quad (8)$$

since the strain amplitude of the P wave is $\epsilon - \epsilon_0$. The four

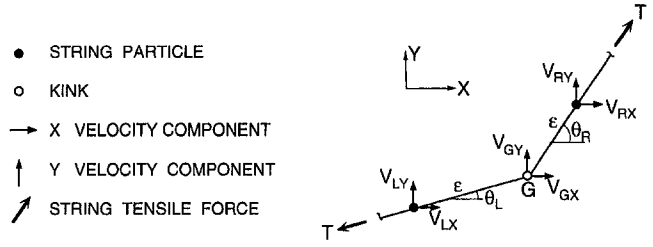

Fig. 2 Kink G traveling in a string of constant tension

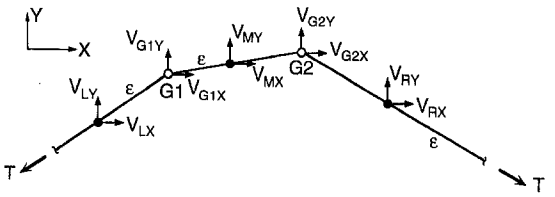

Fig. 3 Two kinks $G1$ and $G2$ traveling in a string of constant tension

Downloaded 04 May 2010 to 171.66.16.26. Redistribution subject to ASME license or copyright; see http://www.asme.org/terms/Terms_Use.cfm

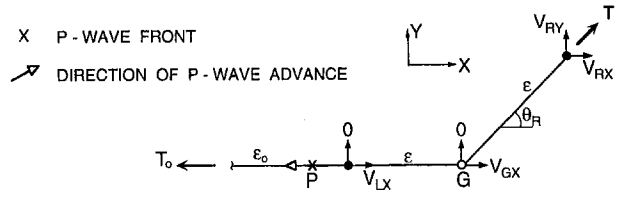

Fig. 4 Semi-infinite string with right end forced to move at constant velocity. The kink *G* travels to the left.

unknowns (M_G, ϵ, θ_R, and V_{LX}) are found from Eqs. (3), (6*a*), (6*b*), and (8). These equations can be combined to give

$$\sqrt{\epsilon} = \epsilon - \epsilon_0 - \frac{V_{RX}}{C} + \left(\epsilon - \left(\frac{V_{RY}}{C}\right)^2\right)^{1/2}, \tag{9}$$

and the mass flux through the kink is positive (+ in Eq. (3)). Since V_{RX}, V_{RY}, and ϵ_0 are specified, ϵ can be determined from Eq. (9). Equation (6*b*) yields θ_R as

$$\theta_R = \sin^{-1}\left(\frac{V_{RY}}{C\sqrt{\epsilon}}\right) \tag{10}$$

and Eq. (5*a*) yields V_{GX} as, after some manipulation,

$$V_{GX} = C\cdot(\epsilon - \epsilon_0) - C\sqrt{\epsilon}, \tag{11}$$

which is negative.

Several special cases are of interest. First, the case $V_{RX} = 0$ is useful for quantifying the "incidental" changes in string tension that occur when the string is forced to move laterally. From Eqs. (9) and (10), the relative change in string tension is

$$\frac{\epsilon - \epsilon_0}{\epsilon_0} = \frac{\sqrt{\epsilon}\cdot(1 - \cos\theta_R)}{\epsilon_0} = \frac{1}{\epsilon_0\cdot(2\sqrt{\epsilon} - \epsilon + \epsilon_0)}\left(\frac{V_{RY}}{C}\right)^2, \tag{12}$$

which is plotted in Fig. 5 versus θ_R for initial tensile strains ϵ_0 = 0.01 percent, 0.03 percent, 0.10 percent, 0.30 percent, and 1.00 percent. As seen, the tension changes can be quite large, even when the string slope angle is not. For example, for ϵ_0 = 0.10 percent and θ_R = 10 deg, the increase in tensile strain is about 60 percent. Such a large increase in tension is a nonlinear effect; the linear theory (i.e., the linear wave equation) applies only when $((\epsilon - \epsilon_0)/\epsilon_0) \ll 1$. Under close-to-linear conditions, $\epsilon \approx \epsilon_0$ and θ_R is small, so a test for linearity can be constructed from Eq. (12) as

$$\left(\frac{\theta_R^2}{2\sqrt{\epsilon_0}} \quad \text{OR} \quad \frac{1}{2\epsilon_0\sqrt{\epsilon_0}}\left(\frac{V_{RY}}{C}\right)^2\right) \ll 1. \tag{13}$$

So linearity requires that not only the string lateral motion (θ_R or V_{RY}) be small enough, but also that the initial tension be large enough.

Another special case is when V_{RX} is negative and when it and V_{RY} satisfy

$$V_{RX}^2 + V_{RY}^2 = -2C\sqrt{\epsilon_0}\, V_{RX} \tag{14}$$

which makes $\epsilon = \epsilon_0$ (as deduced from Eq. (9)) and $V_{LX} = 0$. This eliminates the *P*-wave part of the solution. It can also be shown from Eq. (6) that

$$\tan\theta_R = \frac{2V_{RX}V_{RY}}{V_{RX}^2 - V_{RY}^2}. \tag{15}$$

Equation (11) gives the velocity of the geometric wave as $V_{GX} = -C\sqrt{\epsilon_0}$, which is the wave speed from linear theory. The fact that the initial tension ϵ_0 does not change when the geometric wave is generated and that this wave travels at speed $C\sqrt{\epsilon_0}$ does not mean that this solution is linear. Superposition will not hold unless a condition like that in Eq. (13) is satisfied.

A third case is when the initial tension ϵ_0 is zero. If V_{RX} is also zero, then, from Eq. (9), a simple relation exists between V_{RY} and ϵ:

$$\left(\frac{V_{RY}}{C}\right)^2 = 2\epsilon\sqrt{\epsilon} - \epsilon^2. \tag{16}$$

Further, if the strains are small enough so that ϵ^2 can be neglected compared to $2\epsilon\sqrt{\epsilon}$, an explicit expression for ϵ is possible:

$$\epsilon = \left(\frac{V_{RY}}{\sqrt{2}C}\right)^{4/3}. \tag{17}$$

Equations (16) and (17) were originally obtained by Housner (n.d.) for the barrage balloon problem, and his solution is pub-

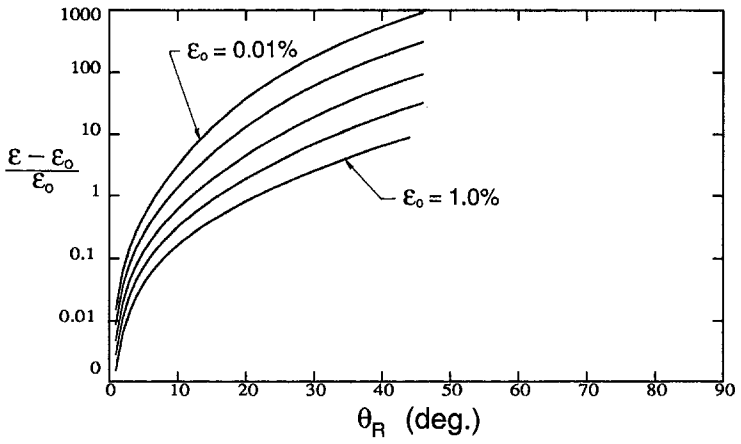

Fig. 5 Relative change in tensile strain $(\epsilon - \epsilon_0)/\epsilon_0$ when the right end of a semi-infinite string is forced to move at velocity V_{RY} (V_{RX} = 0) so as to produce slope θ_R (problem of Fig. 4). Values of initial tensile strain are ϵ_0 = 0.01 percent, 0.03 percent, 0.1 percent, 0.3 percent, and 1.0 percent. Curves are plotted for $\epsilon < 10$ percent.

Downloaded 04 May 2010 to 171.66.16.26. Redistribution subject to ASME license or copyright; see http://www.asme.org/terms/Terms_Use.cfm

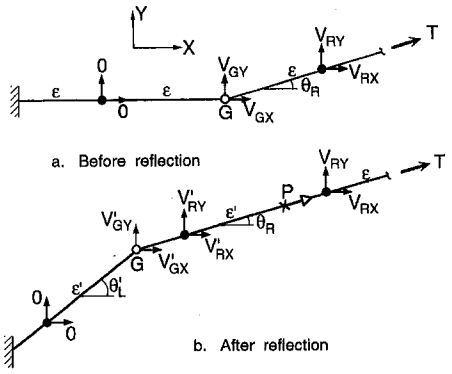

Fig. 6 Reflection of a kink at a fixed support. The kink *G* travels toward the support in part *a* and away from the support in part *b*.

lished in Irvine (1981). Another relation for ϵ_0 and V_{RX} equal to zero, one that does not require that ϵ^2 be small compared to $2\epsilon\sqrt{\epsilon}$, is

$$\epsilon = \frac{V_{RY}}{C} \tan \frac{\theta_R}{2}. \tag{18}$$

Reflection of a Kink at a Fixed End

The string in Fig. 6(a) has uniform tensile strain ϵ and contains a geometric wave propagating to the left toward a fixed end. The left segment is stationary because of the fixed end ($V_{LX} = V_{LY} = 0$), and it is taken to have zero slope ($\theta_L = 0$). Particle velocity in the right segment is related to ϵ by Eqs. (3) and (6) as

$$\sqrt{\epsilon} = \frac{-V_{RX}}{C} \Big/ (1 - \cos \theta_R) \tag{19a}$$

$$= \frac{V_{RY}}{C} \Big/ \sin \theta_R. \tag{19b}$$

Equation (14), with ϵ_0 replaced by ϵ, and Eq. (15) also apply.

Arrival of the kink at the fixed end produces a P wave (Fig. 6(b)) which travels back up the advancing right segment, changing the tensile strain to ϵ' and changing the particle velocities to $\langle V'_{RX}, V'_{RY} \rangle$ according to

$$V'_{RX} = V_{RX} - C(\epsilon' - \epsilon) \cos \theta_R \tag{20a}$$

$$V'_{RY} = V_{RY} - C(\epsilon' - \epsilon) \sin \theta_R. \tag{20b}$$

The new left segment that emerges behind the kink has zero velocity, again because of the fixed end, and nonzero slope angle θ'_L (Fig. 6(b)). Mass flux M'_G through the reflected kink is

$$M'_G = -\rho A C \sqrt{\epsilon'} \tag{21}$$

where the negative sign indicates that the mass flux is from the right segment to the left. Combining Eqs. (6) and (21) yields

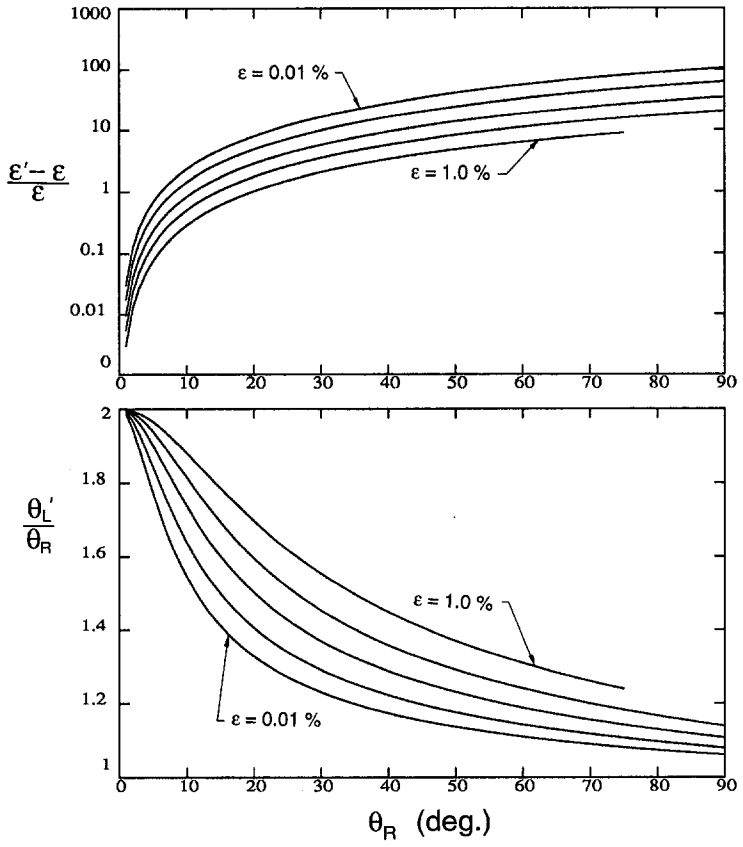

Fig. 7 Tensile-strain reflection ratio $(\epsilon' - \epsilon)/\epsilon$ and slope reflection ratio θ'_L/θ_R for a kink striking a fixed end (problem of Fig. 6). Values of initial tensile strain are ϵ = 0.01 percent, 0.03 percent, 0.1 percent, 0.3 percent, and 1.0 percent. Curves are plotted for $\epsilon' < 10$ percent.

Downloaded 04 May 2010 to 171.66.16.26. Redistribution subject to ASME license or copyright; see http://www.asme.org/terms/Terms_Use.cfm

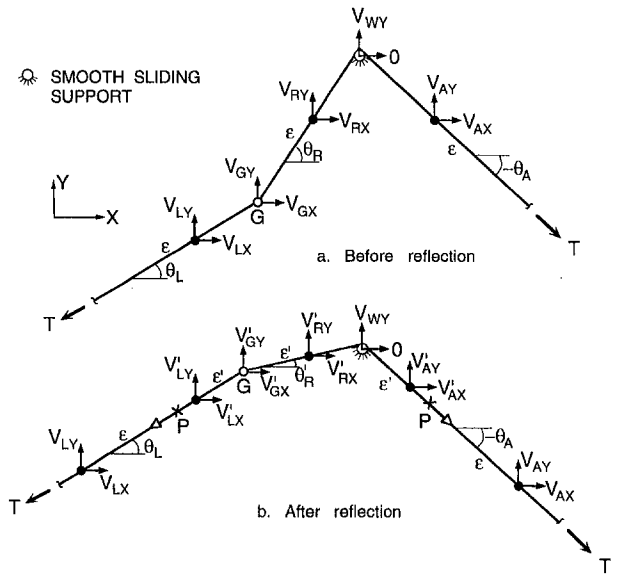

Fig. 8 Reflection of a kink at a smooth sliding support. The kink *G* travels toward the support in part *a* and away from the support in part *b*.

$$-\sqrt{\epsilon'} = \frac{V'_{RX}}{C} \Big/ (\cos\theta_R - \cos\theta'_L) \tag{22a}$$

$$= \frac{V'_{RY}}{C} \Big/ (\sin\theta_R - \sin\theta'_L) \tag{22b}$$

for the reflected kink.

Elimination of ϵ' and the velocity terms in Eqs. (19), (20), and (22) leads to

$$\sqrt{\epsilon} \cdot \left(\frac{\sin^2\theta_R - \sin^2(\theta'_L - \theta_R)}{\sin(\theta'_L - \theta_R)} \right)$$

$$= (\sin(\theta'_L - \theta_R) - \sin\theta'_L + \sin\theta_R) \tag{23}$$

from which θ'_L can be determined. The strain ϵ' is then given by

$$\epsilon' = \epsilon \frac{\sin^2\theta_R}{\sin^2(\theta'_L - \theta_R)}. \tag{24}$$

The relative change in string tension $(\epsilon' - \epsilon)/\epsilon$ versus θ_R is plotted in Fig. 7 (top) for values of $\epsilon = 0.01$ percent, 0.03 percent, 0.10 percent, 0.30 percent, and 1.00 percent, and θ'_L/θ_R versus θ_R is plotted in Fig. 7 (bottom) for the same values of ϵ. For linear behavior, $\epsilon' = \epsilon$ and $\theta'_L = 2\theta_R$, and from Fig. 7, this occurs only when ϵ is large enough and θ_R is small enough. Effects of nonlinearity are an increase in string tension when the geometric wave reflects and a less than doubling of the incident angle θ_R.

Reflection of a Kink at a Smooth Support

In this situation (Fig. 8), the string maintains contact with and slides past a support that itself has constant velocity $\langle 0, V_{WY} \rangle$. The coefficient of sliding friction between the string and support is taken to be zero. The string has a kink advancing rightward toward the support, and the slope angles are θ_L to the left of the kink, θ_R between the kink and support, and θ_A to the right of the support. In all three segments, the tensile strain is ϵ. When the kink impacts the support, equal P waves are produced which travel out on both sides of the support, changing the tensile strain to ϵ'. A reflected kink occurs to the left of the support only, and the slope of the reborn segment between the reflected kink and the support is denoted by θ'_R. To the right of the support, the slope remains at θ_A.

Before reflection of the kink, the quantities ϵ, M_G, V_{LX}, V_{LY}, θ_L, V_{RX}, V_{RY}, θ_R to the left of the support are related by Eqs. (3) and (6) and by

$$V_{RY} - V_{WY} = V_{RX} \tan\theta_R. \tag{25}$$

After reflection, the mass flux M'_G through the kink is

$$M'_G = \pm\rho AC\sqrt{\epsilon'} \tag{26}$$

which can be either positive or negative. Equation (6) for the reflected kink becomes

$$M'_G = \rho A(V'_{RX} - V'_{LX})/(\cos\theta'_R - \cos\theta_L) \tag{27a}$$

$$= \rho A(V'_{RY} - V'_{LY})/(\sin\theta'_R - \sin\theta_L). \tag{27b}$$

Particle velocities to the left of the kink are changed by the left-traveling P wave to

$$V'_{LX} = V_{LX} + C(\epsilon' - \epsilon)\cos\theta_L \tag{28a}$$

$$V'_{LY} = V_{LY} + C(\epsilon' - \epsilon)\sin\theta_L. \tag{28b}$$

The corresponding expressions for the particle velocities between the kink and the support are

$$\frac{V'_{RX}}{\cos\theta'_R} = \frac{V_{RX}}{\cos\theta_R} - C(\epsilon' - \epsilon) \tag{29a}$$

$$\frac{V'_{RY} - V_{WY}}{\sin\theta'_R} = \frac{V_{RY} - V_{WY}}{\sin\theta_R} - C(\epsilon' - \epsilon) \tag{29b}$$

and it is also true that

$$V'_{RY} - V_{WY} = V'_{RX} \tan\theta'_R. \tag{30}$$

Equation (29) is independent of the slope angle θ_A to the right of the support.

Combining the equations leads to

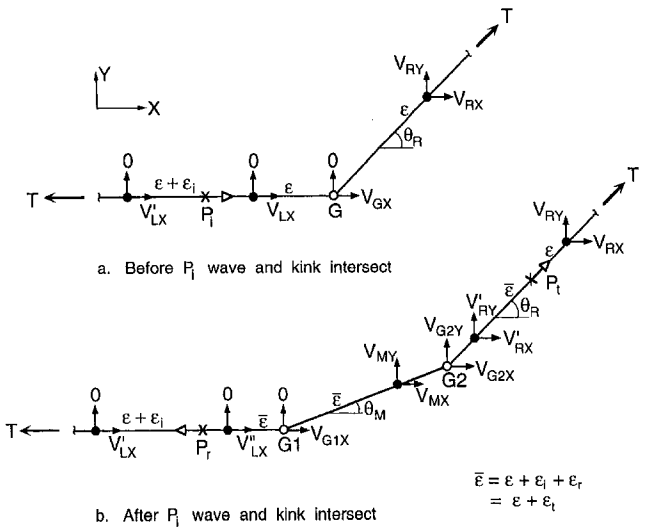

Fig. 9 Interaction of a *P* wave and a kink. In part *a*, the kink *G* could be traveling to the left or to the right. In part *b*, kinks *G1* and *G2* are moving away from each other.

Downloaded 04 May 2010 to 171.66.16.26. Redistribution subject to ASME license or copyright; see http://www.asme.org/terms/Terms_Use.cfm

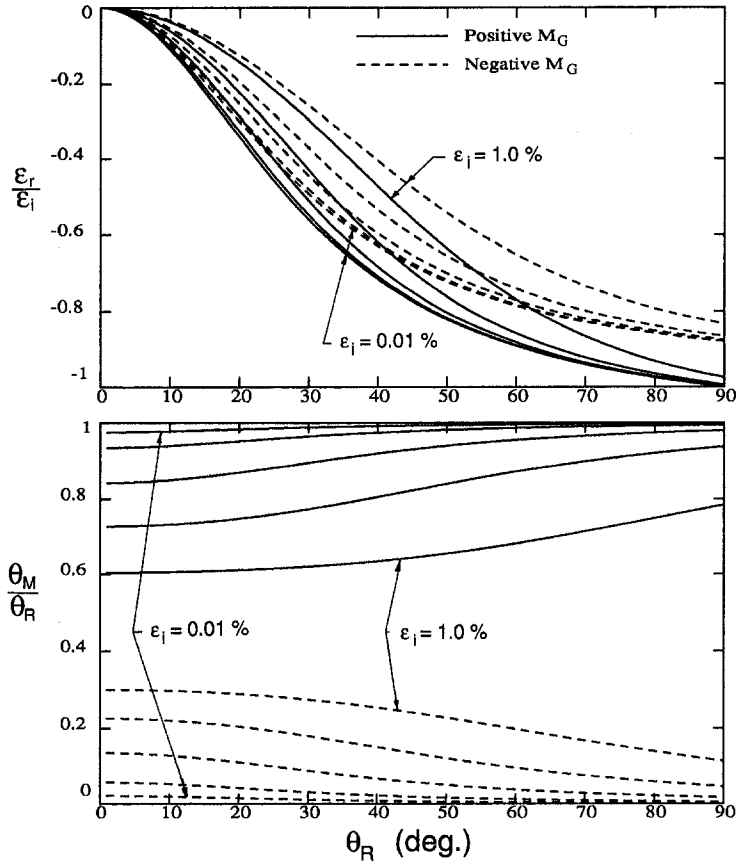

Fig. 10 Tensile strain reflection ratio ϵ_r/ϵ_i and slope ratio θ_M/θ_R for a *P* wave striking a kink (problem of Fig. 9). Values of incident *P*-wave strain are ϵ_i = 0.01 percent, 0.03 percent, 0.1 percent, 0.3 percent, and 1.0 percent; and the initial tensile strain ϵ is 0.1 percent.

$$\tan \theta_R' = \frac{-M_G' \sin \theta_L + \rho A(V_{LY}' - V_{WY})}{\rho A V_{LX}' - M_G' \cos \theta_L} \tag{31}$$

whose explicit form for θ_R' is convenient. In an iterative solution, ϵ' is adjusted until either Eq. (27*a*) or (27*b*) is satisfied, the value of θ_R' being computed from Eq. (31). Equations (26), (28), and (29) give the other terms. An example is given later as part of the solution to the barrage balloon problem where the aircraft wing is the support over which the cable slides.

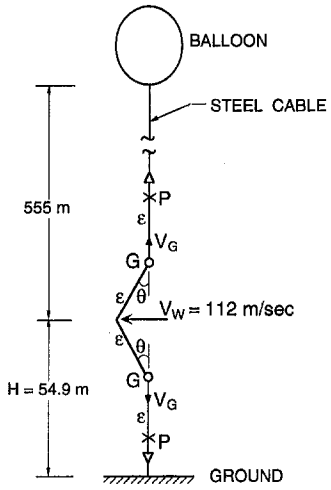

Fig. 11 Barrage balloon problem in which a vertically positioned steel cable is struck by an aircraft wing at time = 0

P-Wave Reflections at Smooth Supports and at Kinks

A *P*-wave incident to a frictionless sliding support of the type discussed in the previous section passes over the support and beyond just as if the string were straight; i.e., it is fully transmitted with no reflection. The force between the support and string does change, and it is related to the change in tension and sliding velocity of the string.

The situation of a *P*-wave incident to a kink is more complicated. Consider a kink traveling in a string of constant tensile strain ϵ (Fig. 9(*a*)). The string to the left of the kink is taken to be horizontal with only horizontal velocity. Equations (3) and (6) apply ($\theta_L = 0$, $V_{LY} = 0$). Incident to the kink from the left is a *P* wave that increases the tensile strain by an amount ϵ_i and changes the particle velocity to

$$V_{LX}' = V_{LX} - C\epsilon_i. \tag{32}$$

After the *P* wave strikes the kink (Fig. 9(*b*)), a reflected *P* wave of strain ϵ_r is sent back to the left, changing the strain to $\epsilon + \epsilon_i + \epsilon_r$ and the particle velocity to

$$V_{LX}'' = V_{LX}' + C\epsilon_r = V_{LX} - C(\epsilon_i - \epsilon_r). \tag{33}$$

A transmitted *P* wave of strain ϵ_t proceeds ahead past the kink changing the strain to $\epsilon + \epsilon_t$ and the velocity to

$$V_{RX}' = V_{RX} - C\epsilon_t \cos \theta_R \tag{34a}$$

$$V_{RY}' = V_{RY} - C\,\epsilon_t \sin \theta_R. \tag{34b}$$

Furthermore, as shown in Fig. 9(*b*), the kink splits into two kinks: *G*1 on the left and *G*2 on the right with mass fluxes M_{G1}

Downloaded 04 May 2010 to 171.66.16.26. Redistribution subject to ASME license or copyright; see http://www.asme.org/terms/Terms_Use.cfm

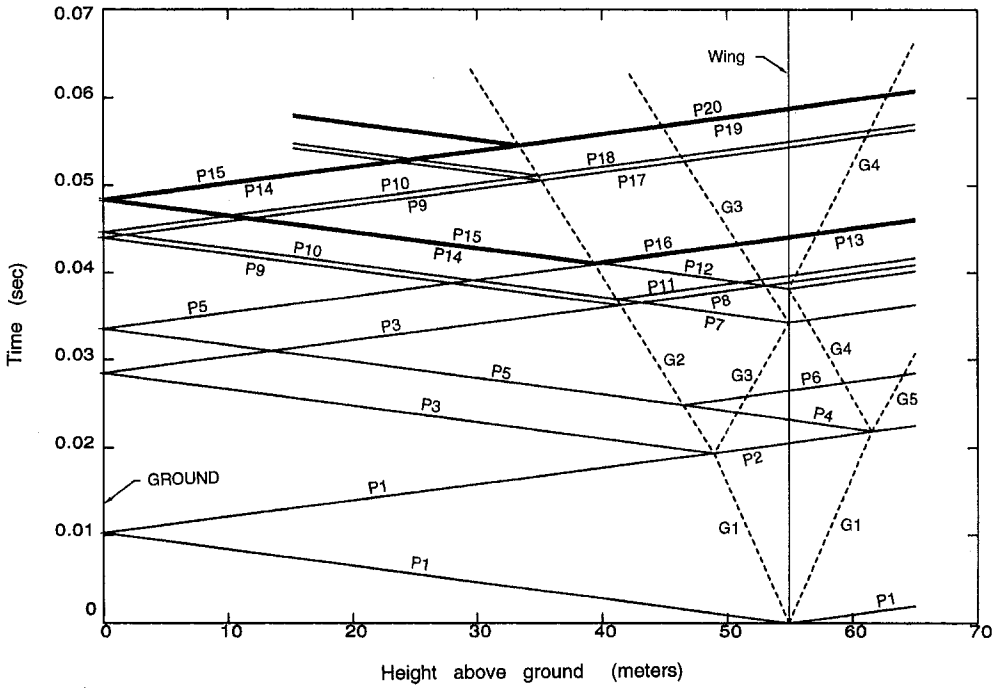

Fig. 12 Timeline for *P*-wave fronts (solid lines) and kinks (dashed lines)

and M_{G2}, respectively. The emerging middle segment between the two kinks has slope θ_M and particle velocity $\langle V_{MX}, V_{MY}\rangle$.

Since the tension must be constant within the portion of the string traversed by the two outward propagating P waves, $\epsilon_t = \epsilon_i + \epsilon_r$ and $M_{G2} = -M_{G1}$. Of the two mass fluxes, M_{G1} is the positive one. Applicable equations are Eqs. (3) and (6) written for the subject parameters at kinks $G1$ and $G2$:

$$M_{G1} = \rho AC\cdot\sqrt{\epsilon + \epsilon_i + \epsilon_r} \tag{35}$$

$$M_{G1} = \rho A(V_{MX} - V''_{LX})/(\cos\theta_M - 1) \tag{36a}$$

$$= \rho A V_{MY}/\sin\theta_M \tag{36b}$$

$$-M_{G1} = \rho A(V'_{RX} - V_{MX})/(\cos\theta_R - \cos\theta_M) \tag{37a}$$

$$= \rho A(V'_{RY} - V_{MY})/(\sin\theta_R - \sin\theta_M). \tag{37b}$$

Substitution for V''_{LX}, V'_{RX}, and V'_{RY} from Eqs. (33) and (34), then substitution for V_{LX}, V_{RX}, and V_{RY} in terms of M_G using Eq. (6), and then elimination of V_{MX} and V_{MY} results in

$$\epsilon_i = \frac{M_{G1}}{\rho AC}(\sin(\theta_R - \theta_M) - \sin\theta_M)/\sin\theta_R + \frac{M_G}{\rho AC} \tag{38a}$$

$$\epsilon_r = \frac{M_{G1}}{\rho AC}(-\sin(\theta_R - \theta_M) + \sin\theta_R - \sin\theta_M)/\sin\theta_R. \tag{38b}$$

Solution is obtained iteratively: assume θ_M; compute M_{G1} from Eq. (38a); compute ϵ_r from Eq. (38b); check Eq. (35); refine the estimate for θ_M until Eq. (35) is satisfied. Since M_{G1} is positive, Eq. (38a) requires that $\theta_M/\theta_R < \frac{1}{2}$ when $\epsilon_i - (M_G/\rho AC)$ is positive and that $\theta_M/\theta_R > \frac{1}{2}$ when $\epsilon_i - (M_G/\rho AC)$ is negative.

Example results are shown in Fig. 10: the reflection ratio ϵ_r/ϵ_i versus θ_R and the slope angle ratio θ_M/θ_R versus θ_R for initial tensile strain $\epsilon = 0.10$ percent and incident P-wave strains $\epsilon_i = 0.01$ percent, 0.03 percent, 0.10 percent, 0.30 percent, and 1.00 percent. The initial mass flux M_G, computed from Eq. (3), is taken as positive and negative. The reflected wave is negative, and the reflection ratio varies from zero at $\theta_R = 0$ to near -1

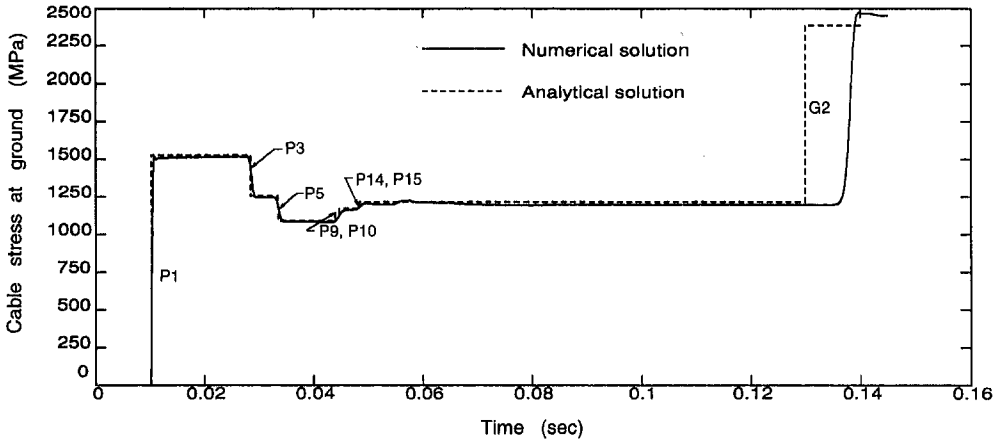

Fig. 13 Cable tensile stress at the ground as a function of time computed numerically and analytically. *P*-wave and kink arrival labels are defined in Fig. 12.

Downloaded 04 May 2010 to 171.66.16.26. Redistribution subject to ASME license or copyright; see http://www.asme.org/terms/Terms_Use.cfm

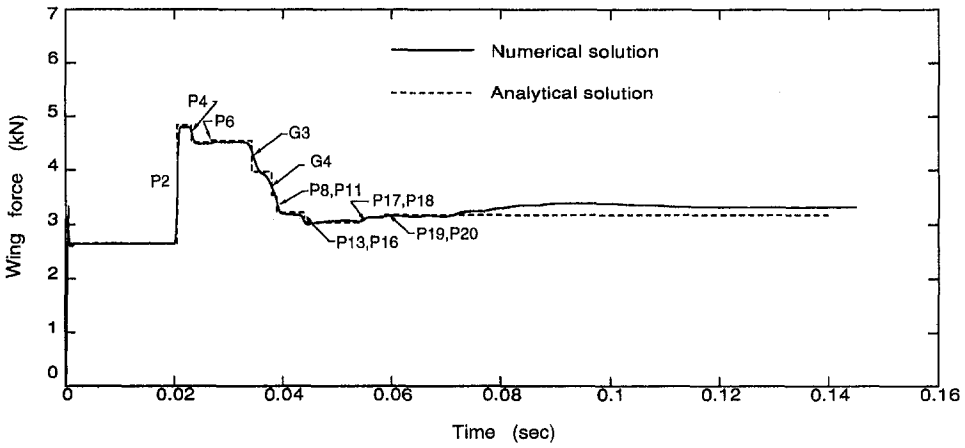

Fig. 14 Horizontal component of cable force on the wing as a function of time computed numerically and analytically. *P*-wave and kink arrival labels are defined in Fig. 12.

(complete reflection) at $\theta_R = 90$ deg. The reflection is more complete for lower values of ϵ_i and when M_G is positive. As ϵ_i tends toward zero, θ_M tends toward θ_R when M_G is positive and toward zero when M_G is negative.

The Barrage Balloon Problem

During World War II, barrage balloons were used at some facilities to deter aerial bombardment. The balloons held steel cables, suspended vertically and anchored at the ground, that could impact wings of aircraft. One early use of barrage balloons occurred in 1943 at the Ploesti Oil Refinery in Hungary. The cables were typically 610 m (2000 ft) long, 2.54 mm (0.1 in.) in diameter, and had a breaking strength of about 1379 MPa (200,000 psi). In preparing for a bombing attack on the refinery, the Fifteenth Air Force sought the advice of their Operations Analysis Section whose chief analyst was George W. Housner, who later became Professor of Civil Engineering and Applied Mechanics at Caltech.

In his analysis, Housner assumed that the cable was initially vertical with a tension of zero and that a point on the cable a distance H above the ground (the wing elevation) is given a sudden and constant horizontal velocity V_W (the plane velocity), as shown in Fig. 11. These conditions, together with the initial symmetry of the problem about the impact point, led Housner to Eq. (16), from which the cable tensile strain ϵ can be computed from the plane velocity V_W (V_{RY} in Eq. (16)). Taking $C = 5358$ m/sec (17,580 ft/sec) for steel and $V_W = 112$ m/sec (250 miles per hour), $\epsilon = .003691$ which gives a tensile stress $\sigma = 764$ MPa (110,700 psi). The geometric wave travels out at speed $V_G = 306$ m/sec (1003 ft/sec) with slope angle $\theta = 20.08$ deg. The force exerted by the cable on the wing equals $2T \sin\theta = 2.66$ kN (597.1 lbs), acting horizontally to oppose the plane's velocity. The P wave travels at speed C, and taking $H = 54.9$ m (180 feet),[2] reaches the ground in 0.01024 seconds. With a rigid ground anchor, the tension doubles in the reflection to 1527 MPa (221,500 psi). This slightly exceeds the cable's strength and so breakage could occur at this time. Breakage creates a negative P wave which travels up the cable and relieves the tension. Thus, the 2.66 kN retarding force on the plane would last about $0.01024 \times 2 = 0.02048$ sec. Taking into account the pertinent properties of a bomber, Housner (n.d.) concluded that this force amplitude and duration would be insufficient to destabilize the plane. Indeed, when the bombers returned from the mission to the Ploesti Oil Refinery, seven had evidence of cable impact on their wings in the form of cuts through the leading edge of the wing to the main spar. Of the 120 aircraft that reached the target, about a third did not return (G. W. Housner, 1997). However, the likely cause of the downed planes was antiaircraft fire, not barrage balloon cables.

If the cable does not break when the P wave reaches the ground, it would do so when the geometric wave arrives there because that would produce a large increase in cable tension. The time for the geometric wave to reach the ground can be estimated as $H/V_G = 0.179$ sec. This additional duration, as well as the possible doubling of the retarding force on the plane when the ground-reflected P wave arrives at the wing, were also judged not to be enough to impair a plane's flight.

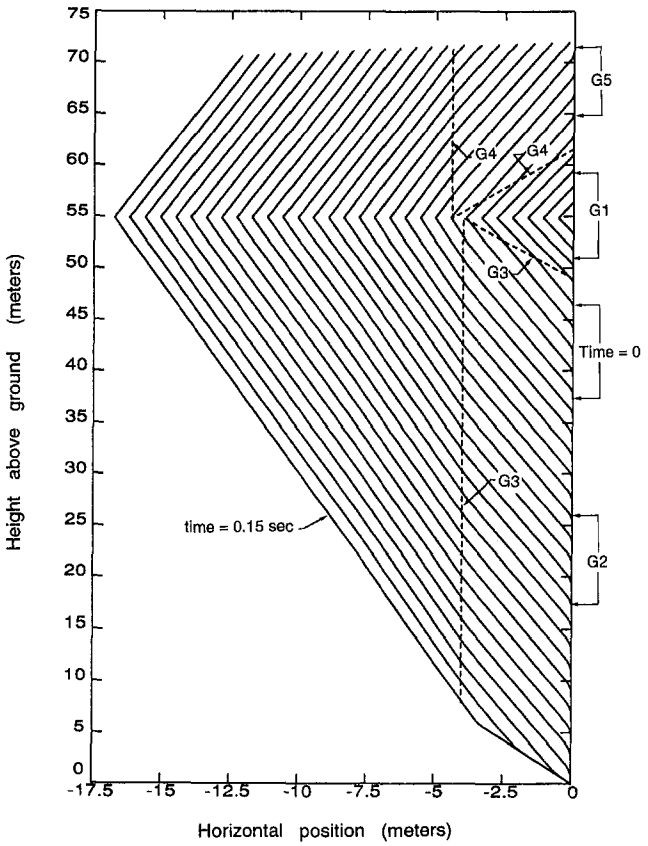

Fig. 15 Profile of cable (solid lines) at 0.005-sec intervals from time = 0 to time = 0.15 seconds computed in the numerical solution. Only the bottom 73 m of the cable are shown. Dotted lines and the right border are trajectories of the kinks included in and plotted from the analytical solution.

[2] Low-altitude raids were used to increase the bombing accuracy.

Downloaded 04 May 2010 to 171.66.16.26. Redistribution subject to ASME license or copyright; see http://www.asme.org/terms/Terms_Use.cfm

Although all of the critical aspects of the barrage balloon problem were revealed by Housner, the extended solution for the case where the P wave does not break after it strikes the ground has some interesting features, and so it will be used as a demonstration problem for the solutions presented in the previous sections. This will now be attempted.

Figure 12 shows a timeline for P-wave fronts and kinks as they travel along the cable. Impact of the wing at time = 0 generates kinks $G1$ and P waves $P1$ above and below the wing as discussed above. The downward propagating $P1$ returns and strikes kink $G1$, causing it to divide into kinks $G2$ and $G3$; $P1$ transmits as $P2$ and reflects as $P3$. Wave $P2$ continues past the wing and strikes the other $G1$, splitting it into $G4$ and $G5$; the reflected P wave is $P4$. The situation now becomes complicated as the number of P waves and kinks grows rapidly. However, certain elements of the solution can be neglected for an approximate treatment. Calculations show that it is reasonable to (1) neglect any interaction between kinks $G3$, $G4$, and $G5$ and any intersecting P waves, and (2) consider reflection and partial transmission of P waves intersecting $G2$, but neglect any effects on this kink. For example, $G3$ and $G4$ have small kink angles and so P-wave transmission occurs nearly completely.

Figure 12 incorporates these simplifications and labels all included P waves and kinks for reference in Figs. 13 and 14 where the computed cable tension at the ground and the computed horizontal force on the wing are plotted (dashed line in both figures, referred to as the analytical solution). Computations utilized the formulas presented earlier. Decreases in the cable tension at ground level occur with the arrivals of $P3$ and $P5$ (Fig. 13) because these P waves are negative. The arrival of $P2$ (Fig. 14) at the wing, at which point the cable begins to slide across the wing, produces a large increase in the force on the wing. This sawing action could have facilitated the cutting of the wings of the seven planes. Arrivals of $G3$ and $G4$ at the wing decrease the wing force (Fig. 14) because, even though the cable tension increases, the angle θ decreases.

The responses (dashed lines) in Figs. 13 and 14 are shown up to time = 0.145 sec and include the reflection of kink $G2$ at the ground, nearly doubling the cable tension (Fig. 13) which would certainly break the cable. Arrivals of the first P wave reflections from the balloon occur after time = 0.17 sec, and so no such reflection enters the calculations.

An independent solution of the barrage balloon problem was made through a numerical simulation in which the cable was discretized into springs and nodal masses and the equations of motion integrated on the computer. Features of the simulation include: 5-cm-long (2 in.) spring elements for an accurate wavefront definition, explicit time integration (central difference method), updated mesh geometry at each time step, a special scheme to allow nodes to slide past the wing, and a P-wave transmitting boundary to replace the upper $\frac{3}{4}$ of the cable. Results are shown as solid lines in Figs. 13 and 14 (referred to as the numerical solution), and the agreement with the analytical calculations (dashed lines) is quite good. The largest discrepancy is in the arrival time of kink $G2$ at the ground (Fig. 13), and this is due to neglecting the effects of intersecting P waves on $G2$, including changes in its speed. A small amount of viscous damping was used in the numerical simulation to control start-up oscillations in the solution (see Fig. 14).

The cable profile, as computed in the numerical solution over the first 0.15 sec, is shown in Fig. 15. Trajectories of kinks $G1$ through $G5$ are included. After time = 0.05 sec and up until kink $G2$ hits the ground, during which time the tension in the cable between the ground and plane remains nearly constant (see Figs. 13 and 14), this part of the cable maintains a trilinear profile and the length of the middle segment between kinks $G2$ and $G3$ does not change. Existence of such a solution was noted earlier in the section on basic considerations. Also, it is seen that a kink loses its sharpness over time. This is not a numerical artifice but rather an effect of multiple interactions with P waves.

References

Housner, G. W., "Barrage Balloon Cable Impacted by an Aircraft," undated notes.

Housner, G. W., 1997, personal communication.

Irvine, H. M., 1981, *Cable Structures,* The MIT Press, Cambridge, MA.

Downloaded 04 May 2010 to 171.66.16.26. Redistribution subject to ASME license or copyright; see http://www.asme.org/terms/Terms_Use.cfm

Chaotic Motions of a Dual-Spin Body

A. C. Or[1]
Department of Mechanical and Aerospace Engineering, University of California, Los Angeles, CA 90095-1597

The dynamics of a dual-spinner subject to the action of an internal oscillatory torque and Coulomb friction between the two linked bodies is investigated. The conditions for existence of transverse homoclinic points and homoclinic tangency of chaotic motions are obtained using Melnikov's method. Through long-term numerical integration of the equations of motion, steady-state chaotic attractors are also found and studied numerically by varying the forcing amplitude.

1 Introduction

The older topics on gyroscopic dynamics of rigid bodies are often found in association with motions of celestrial bodies (see Danby, 1962). More recent applications of the subject have to do with the dynamical behavior and control of attitude pointing of artificial spacecraft (Hughes, 1986). The earliest account on the dynamics of two linked bodies appeared to be by Masaitis (1961). Scher and Farrenkopf (1974) identified certain "anomalous" equilibrium states in actual flight simulations on the motions of spacecraft. A more recent study by Hall and Rand (1994) focused on the nonlinear dynamics.

In this paper, we examine a certain chaotic behavior of the dual spinner under the action of an oscillating motor torque and friction. For transitions to complex prechaotic motions for simpler oscillators with single degree-of-freedom, Huberman and Crutchfield (1979) and Moon and Holmes (1979), for example, demonstrated the usefulness of Melnikov's method. For an account of Melnikov's theory, we refer readers to Lichtenberg and Lieberman (1983), or Guckenheimer and Holmes (1983). In Section 2, we develop the mathematical equations and derive the Melnikov function using the residue theory described in the Appendix. In Section 3, we obtain the conditions for the existence of transverse homoclinic points and discuss the bifurcation to Smale's Horseshoe. In Section 4, we turn to the chaotic attractors which are studied numerically. In Section 5, we conclude with a few remarks.

2 Mathematical Formulation

2.1 Model Equations. Consider a rod-shaped dual spinner as shown in Fig. 1. The spinner consists of two linked bodies, hinged by a bearing unit. The rotor, $\mathcal{R}$, is spun to stabilize the pointing. The platform, $\mathcal{P}$, is mounted with antennae and maintains stationary position for radio communication. Both bodies $\mathcal{R}$ and $\mathcal{P}$ have their centers of mass located on the z-axis. The principal axes of moments of inertia coincide with the geometric axes. The Cartesian frame is rigidly attached at the center of mass of $\mathcal{R}$. With this arrangement the dimensional Euler equations are

$$I_1\dot{\omega}_1 + (H_3 - I_2\omega_r)\omega_2 = 0, \tag{1a}$$

$$I_2\dot{\omega}_2 - (H_3 - I_1\omega_r)\omega_1 = 0, \tag{1b}$$

$$I_r\dot{\omega}_r + (I_2 - I_1)\omega_1\omega_2 = T_m \cos pt - (T_c + T_d(\omega_r - \omega_p)), \tag{1c}$$

$$I_p\dot{\omega}_p = -T_m \cos pt + (T_c + T_d(\omega_r - \omega_p)). \tag{1d}$$

The total axial angular momentum H_3 is given by $H_3 = I_r\omega_r + I_p\omega_p$. The motions are described by four states: ω_1, ω_2, ω_r, and ω_p. These are, respectively, two transverse and two axial angular rates. The total transverse moments of inertia are I_1 and I_2 and the axial moments of inertia for $\mathcal{R}$ and $\mathcal{P}$ are, respectively, I_r and I_p. The forcings are the applied motor torque, T_m, and the Coulomb-friction torque, T_c. The viscous-friction torque T_d is included in the equations but $T_d = 0$ will be assumed throughout the study. The Coulomb torque T_c depends on the sign of the relative spin rate between two bodies. The frictionless motions are Hamiltonian and therefore phase-volume preserving. In this case both kinetic energy, T, and total angular momentum, h, are conserved and are determined by initial conditions. In terms of the states of motions, the two constants of motions are given by

$$2T = (I_1\omega_1^2 + I_2\omega_2^2 + I_r\omega_r^2 + I_p\omega_p^2), \tag{2a}$$

$$h^2 = (I_1\omega_1)^2 + (I_2\omega_2)^2 + (I_r\omega_r + I_p\omega_p)^2. \tag{2b}$$

In terms of the T and h, the solution can be expressed in closed form. In this paper, we examine the dynamics in the parameter space near a pitchfork bifurcation and a phase region where multiple equilibria are found. To proceed deriving the expressions for the homoclinic connection, we obtain two expressions for ω_1 and ω_2 from Eqs. (2*a*, *b*),

$$\omega_i^2 = \frac{I_r(I_j - I_r)}{I_i(I_i - I_j)}\omega_r^2 - 2\frac{I_p\omega_p I_r}{I_i(I_i - I_j)}\omega_r + \frac{h^2 - 2TI_j + I_p(I_j - I_p)\omega_p^2}{I_i(I_i - I_j)}, \tag{3}$$

where $i = 1, j = 2$ and $i = 2, j = 1$. The above expression is quadratic in ω_r. It depends on three external parameters h^2, T, and ω_p and the moments of inertia. The expression can be reordered as

$$\omega_1^2 = a_1\omega_r^2 + b_1\omega_r + c_1, \quad \omega_2^2 = a_2\omega_r^2 + b_2\omega_r + c_2. \tag{4a}$$

Upon factorization, we have

$$\omega_1^2 = a_1(\omega_r - r_1)(\omega_r - r_2),$$

$$\omega_2^2 = a_2(\omega_r - r_3)(\omega_r - r_4). \tag{4b}$$

[1] Also, Institute of Geophysics and Planetary, Physics, University of California, Los Angeles, CA 90095.

Contributed by the Applied Mechanics Division of THE AMERICAN SOCIETY OF MECHANICAL ENGINEERS for publication in the ASME JOURNAL OF APPLIED MECHANICS.

Discussion on the paper should be addressed to the Technical Editor, Professor Lewis T. Wheeler, Department of Mechanical Engineering, University of Houston, Houston, TX 77204-4792, and will be accepted until four months after final publication of the paper itself in the ASME JOURNAL OF APPLIED MECHANICS.

Manuscript received by the ASME Applied Mechanics Division, Aug. 31, 1995; final revision, Jan. 10, 1997. Associate Technical Editor: S. W. Shaw.

 Copyright © 1998 by ASME

Downloaded 04 May 2010 to 171.66.16.26. Redistribution subject to ASME license or copyright; see http://www.asme.org/terms/Terms_Use.cfm

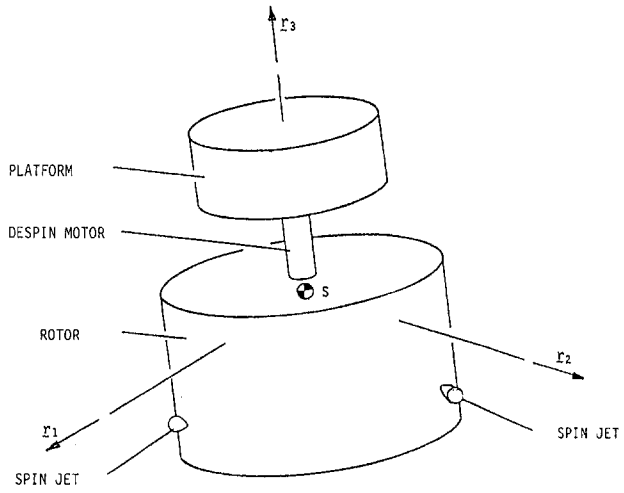

Fig. 1 Geometric configuration of the dual-spin body

The expressions for r_1 to r_4 can be readily computed as

$$r_{1,2} = -\frac{b_1}{2a_1} \pm \left(\left(\frac{b_1}{2a_1}\right)^2 - c_1\right)^{1/2},$$

$$r_{3,4} = -\frac{b_2}{2a_2} \pm \left(\left(\frac{b_2}{2a_2}\right)^2 - c_2\right)^{1/2}. \quad (4c)$$

After substituting $\omega_{1,2}$ into Eq. (1c), we obtain a single equation governing ω_r,

$$\dot{\omega}_r = \pm \frac{(I_2 - I_1)}{I_r} (a_1 a_2 (\omega_r - r_1)(\omega_r - r_2) \times (\omega_r - r_3)(\omega_r - r_4))^{1/2}. \quad (4d)$$

The above equation was solved in quadrature by Masaitis (1961). We now restrict our attention to the particular solution about the homoclinic loops. For a homoclinic loop, Masaitis gave the closed-form expression for ω_r,

$$\omega_r = \frac{r_1 \tanh^2 \lambda(t - t_0) + kr_3}{\tanh^2 \lambda(t - t_0) + k}, \quad k = \frac{r_2 - r_1}{r_3 - r_2}, \quad (5)$$

where λ is given by

$$\lambda = \frac{I_1 - I_2}{2I_r} (-a_1 a_2 (r_2 - r_3)(r_1 - r_2))^{1/2}.$$

The expressions for the transverse angular velocities of the homoclinic connection are obtained by substituting (5) into (4b), which gives

$$\omega_1 = \frac{A \operatorname{sech} \lambda(t - t_0)}{\tanh^2 \lambda(t - t_0) + k}, \quad (6a)$$

$$\omega_2 = \frac{B \tanh \lambda(t - t_0) \operatorname{sech} \lambda(t - t_0)}{\tanh^2 \lambda(t - t_0) + k}, \quad (6b)$$

where

$$A = k(a_1(r_3 - r_1)(r_3 - r_2))^{1/2},$$

$$B = (ka_2(r_1 - r_3)(r_3 - r_2))^{1/2}.$$

We assume, without loss of generality, $I_1 \geq I_2 \geq I_r$. It can be easily shown that, if the following condition is met,

$$\frac{I_p \omega_p}{I_2 - I_r} \geq \omega_r \geq \frac{I_p \omega_p}{I_1 - I_r}, \quad (7)$$

then in Eqs. (1a, b), the term $(H_3 - I_2\omega_r)$ and the term $-(H_3 - I_1\omega_r)$ will have opposite signs. In this case we expect the origin $\omega_1 = \omega_2 = 0$ to be a saddle point. Expressions (5), (6a), (6b) represent the right one of the two homoclinic loops. The left loop is its mirror reflection about the y-axis. As long as the axial angular velocities satisfy condition (7), the pair of homoclinic loops will exist. In the expressions of the angular velocities given above, the initial time $t = t_0$ starts at the saddle point.

2.2 The Melnikov Method. Equations (1a–c) can be cast into a standard nondimensional form $\dot{\mathbf{x}} = \mathbf{f}(\mathbf{x}) + \epsilon_m \mathbf{g}(\mathbf{x}, t)$. We consider $\mathbf{x}$ to be in a three-dimensional phase space, defined by $\mathbf{x} = (\omega_1, \omega_2, \omega_r)^T$ (T denotes transpose). We introduce three small parameters: $\epsilon_m = T_m/I_r\alpha_s$, $\epsilon_c = T_c/I_r\alpha_s$ and $\epsilon_d = T_d/I_r\alpha_s$ where α_s is a scale for the angular acceleration introduced for the purpose of nondimensionalization. The three components of $\mathbf{f}(\mathbf{x})$, as given by Eqs. (1a–c), are

$$f_1 = \frac{(I_2\omega_r - H_3)}{I_1} \omega_2, \quad f_2 = \frac{(H_3 - I_1\omega_r)}{I_2} \omega_1,$$

$$f_3 = \frac{(I_2 - I_1)}{I_r} \omega_1\omega_2. \quad (8)$$

For $\epsilon_m = 0$, equation $\dot{\mathbf{x}} = \mathbf{f}(\mathbf{x})$ gives the zero-order solution $\mathbf{x}^0(t - t_0)$ which corresponds to Eqs. (5), (6a), (6b). By expressing $\omega_p = \omega_p^0 + \epsilon_m\tilde{\omega}_p$, the three components of $\mathbf{g}$ are written as

$$g_1 = -\frac{I_p}{I_1} \omega_2\tilde{\omega}_p, \; g_2 = \frac{I_p}{I_2} \omega_1\tilde{\omega}_p,$$

$$g_3 = \cos pt - \left(\frac{\epsilon_c}{\epsilon_m} + \frac{\epsilon_d}{\epsilon_m} (\omega_r^0 - \omega_p^0)\right). \quad (9)$$

The Melnikov function $\mathbf{M}(t_0)$ is defined as

$$\mathbf{M}(t_0) = \int_{-\infty}^{\infty} \mathbf{f}(\mathbf{x}^0) \times \mathbf{g}(\mathbf{x}^0, t + t_0)dt, \quad (10)$$

where t now denotes $t - t_0$. Upon substituting for the expressions of the angular variables, the component of $\mathbf{M}(t_0)$ on the $\omega_1 - \omega_2$ plane, given by the integral $\int_{-\infty}^{\infty} (f_1g_2 - f_2g_1)dt$, is

$$M_3(t_0) = \int_{-\infty}^{\infty} -\frac{K_p}{\lambda} \omega_1^0(t)\omega_2^0(t)\omega_r^0(t)\tilde{\omega}_p(t + t_0)dt, \quad (11)$$

where $K_p = I_p(I_1 - I_2)/I_1I_2$. Without change of notation, t in the integral actually replaces $\lambda(t - t_0)$; since λ is a factor associated with ω_1^0 and ω_2^0 (see Eqs. (6a, b). An explicit evaluation of the Melnikov integral is quite restricted by the algebraic complexity involved. Now we consider only Coulomb damping, with $\epsilon_d = 0$. Even so our focus will be restricted to the case when $(\omega_r - \omega_p)$ does not change sign along the homoclinic loop. The reason is that the Coulomb torque depends on the sign of $\omega_r - \omega_p$. Sign changes in the integrand about the path of integration will typically render the integrand nonanalytic. The residue theory therefore cannot apply. Despite the restrictions, the Melnikov method still provides valuable information on the complex behavior for a wide range of initial conditions.

We follow the method described in the Appendix and obtain the explicit expression of M_{3a} (at $\epsilon_d = 0$), as

Downloaded 04 May 2010 to 171.66.16.26. Redistribution subject to ASME license or copyright; see http://www.asme.org/terms/Terms_Use.cfm

$$M_{3a} = -\frac{\pi K_r AB\left\{\left(\frac{F_s}{\sqrt{k}}(1-c) - \frac{pF_c}{\lambda}s\right)\sinh\frac{p\alpha}{\lambda} - \left(\frac{pF_c}{\lambda}(1-c) - \frac{F_s}{\sqrt{k}}s\right)\cosh\frac{p\alpha}{\lambda}\right\}}{64p\lambda k\sqrt{k}(1+k)^3(\cos^4\alpha)(1-c)}, \quad (12)$$

where

$$c = \cosh\frac{p\pi}{\lambda}, \quad s = \sinh\frac{p\pi}{\lambda}, \quad \alpha = \text{Imag}(a),$$

where a is defined in the Appendix and $F_{c,s}$ are given by

$$F_s = 2\left(\frac{p}{\lambda}\right)^2(2k(1-k)n_4\cos^2\alpha + kn_2),$$

$$F_c = 4((1-k)^2 + 8k)n_4\cos^2\alpha + 2(1-k)n_2,$$

and the explicit expression for M_{3c} as

$$M_{3c} = \frac{K_r AB(C_{4s}n_4\sin 4\alpha + C_{4c}n_4\cos 4\alpha + C_{2s}n_2\sin 2\alpha + C_{2c}n_2\cos 2\alpha)}{64\lambda^2 k\sqrt{k}(1+k)^3\cos^6\alpha}, \quad (13)$$

where the coefficients are given as

$$C_{4s} = p(k)\alpha(\pi-\alpha) - q(k)(\pi-2\alpha) + 2(8\alpha^2 - 8\pi\alpha - 1),$$

$$C_{2s} = p(k)\alpha(\pi-\alpha) - q(k)(\pi-2\alpha) + 2(2\alpha^2 - 2\pi\alpha - 1),$$

$$C_{4c} = q(k)4\alpha(\alpha-\pi) + 8(\pi-2\alpha),$$

$$C_{2c} = q(k)2\alpha(\alpha-\pi) + 4(\pi-2\alpha),$$

with $p(k) = (3(1-k)^2 + 4k)/k$ and $q(k) = 3(1-k)/\sqrt{k}$. Both expressions (12), (13) have been independently validated against a direct numerical integration of the infinite integrals (19), (20) of the Appendix. We consider two cases: (i) $\epsilon_c = 0$ for the undamped motions; and (ii) the dissipative motions. For $\epsilon_c = 0$, $M_3(t_0)$ has an infinite number of real roots at $t_0 = (n + \frac{1}{2})\pi\lambda/p$ (for arbitrary integer n). For $\epsilon_c \neq 0$, $M_3(t_0)$ has an infinite set so long as

$$-1 \leq \left(\frac{\epsilon_c}{\epsilon_m}\right)\frac{M_{3c}}{M_{3a}} \leq 1$$

provided $M_{3a} \neq 0$. Then the infinite set will be given by $pt_0/\lambda = 2n\pi + \cos^{-1}(-\epsilon_c M_{3c}/\epsilon_m M_{3a})$.

As for the condition of homoclinic tangency of the inset and outset curves, we differentiate M_3 with respect to t_0 and obtain $M_3'(t_0) = -(p/\lambda)M_{3a}\sin p/\lambda t_0$. Homoclinic tangency therefore occurs at a different infinite set of points, namely, $t_0 = n\pi\lambda/p$, at which $M_3'(t_0) = 0$, provided at such t_0 we also have

$$M_3 = (-1)^n M_{3a} + \frac{\epsilon_c}{\epsilon_m}M_{3c} = 0, \quad (14)$$

and the condition $M''(t_0) \neq 0$. The latter condition is met if $M_{3a} \neq 0$. When the tangency condition is satisfied, Eq. (14) defines a bifurcation surface in the parameter space. In the next section, we provide some results.

3 Results Based on Melnikov's Method

We start by examining the case with $\epsilon_c = 0$. Consider an example with $I_1 = 1.5$, $I_1 = 1.2$, $I_r = 1.0$, $I_p = 0.8$. The initial conditions at $t = 0$ are $\omega_r(0) = 1.5$ and $\omega_p = 0.7$, with $\omega_1 \approx \omega_2 \approx 0$. For $\epsilon_m = 0.01$, the top-left and right panels of Fig. 2 show, respectively, the degree of irregularity of the trajectory from a low p and a high p. Both simulations have 8×10^4 steps with a step size 0.01. Stronger chaotic behavior occurs at lower frequency corresponding to larger value of M_{3a}. The bottom panel shows M_{3a} versus p. The function $M_{3a}(p)$ changes sign at $p = 0.9163$ (see insert). At the cross frequency, we have $M_{3a} = 0$. At this frequency the homoclinic loop is unperturbed by the forcing if ϵ_m is sufficiently small.

When Coulomb friction is included, Eq. (14) gives the condition of homoclinic tangency. In Fig. 3, we show the bifurcation curves for two cases: (i) $I_2 = 1.1$ (solid line) and (ii) $I_2 = 1.4$ (dashed line). For both cases we let $\omega_r(0) = 5.0$ so that $(\omega_r - \omega_p)$ does not change sign in the homoclinic loop. All the other physical parameters remain unchanged from Fig. 2. The curves show the damping-to-forcing ratio (ϵ_c/ϵ_m) versus p. The curves are mirror-symmetric about the vertical axis $p = 0$. In both cases, we have $M_{3a} < 0$ and $M_{3c} > 0$ and n is even. The curve divides the parameter plane into two regions. Above the curve the motions are regular but below it the motion can exhibit homoclinic tangles. Strong damping and high-frequency forcing both promote regularity of motions.

Figure 4 provides a bifurcation diagram for the multiple equilibrium regimes. In the diagram with h versus ω_p, the two thin solid straight lines are given by

$$h = \frac{I_2 I_p \omega_p}{I_2 - I_r}, \quad \text{and} \quad h = \frac{I_1 I_p \omega_p}{I_1 - I_r}. \quad (15)$$

These are bifurcation curves for the unforced and undamped

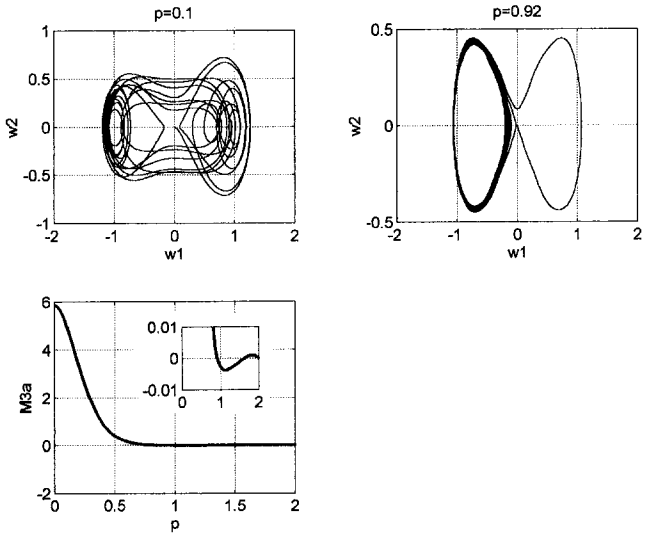

Fig. 2 Phase portraits at a low and a high forcing frequency; Melnikov's function M_{3a}

Downloaded 04 May 2010 to 171.66.16.26. Redistribution subject to ASME license or copyright; see http://www.asme.org/terms/Terms_Use.cfm

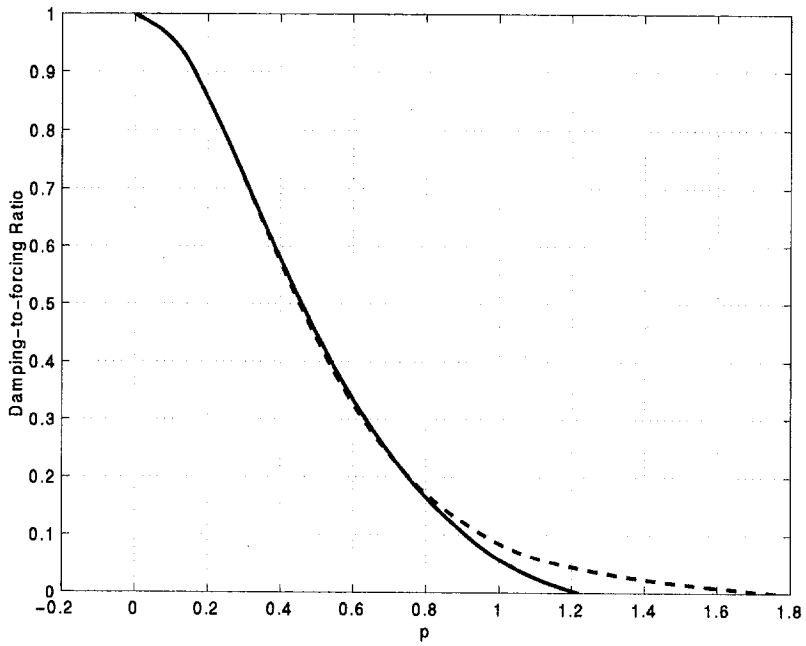

Fig. 3 Bifurcation diagram for the homoclinic tangency showing the damping-to-forcing amplitude ratio versus the forcing frequency

motions. Here ω_p is a prescribed parameter. The two lines divide the plane into three distinct regions. The lower (I), middle (II) and upper (III) regions have 1, 3, and 5 equilibria, respectively. The inserted sketches show the trajectory characteristics. The lower region corresponds to a center. The middle region corresponds to the double homoclinic loops whereas the upper region a heteroclinic loop with two homoclinic loops on its two sides. The Melnikov analysis applies only to region II. With no friction transverse homoclinic points exist on an entire region II.

We now show the bifurcation curve for homoclinic tangency (the heavy solid curve). This curve corresponds to $p = 0.3$ and $\epsilon_c/\epsilon_m = 0.3$ and $I_2 = 1.1$. Again all other parameters remain unchanged. With damping, even though h remains constant, both T and ω_p will change with time. In Fig. 4 ω_p is the initial value of $\omega_p(t)$. To the right of this bifurcation curve, transverse homoclinic points can occur. The upper branch of the heavy solid curve appears to approach the thin solid line asympotically as ω_p increases. Increase in either forcing frequency, p, or damping-to-forcing ratio, ϵ_c/ϵ_m, has the effect of shifting the heavy curve to the right. As the damping-to-forcing ratio tends to zero, we expect the heavy curve to tend to the two thin solid straight lines. The lower branch of the heavy curve is dashed because it may be invalidated by the sign changes of $\omega_r - \omega_p$ inside the homoclinic loops. The two thin dashed lines (almost straight lines) divide region II into three subregions: A, B, and C. In subregions A and C, $\omega_r - \omega_p$ does not change sign in the homoclinic loop, whereas in subregion B sign changes occur.

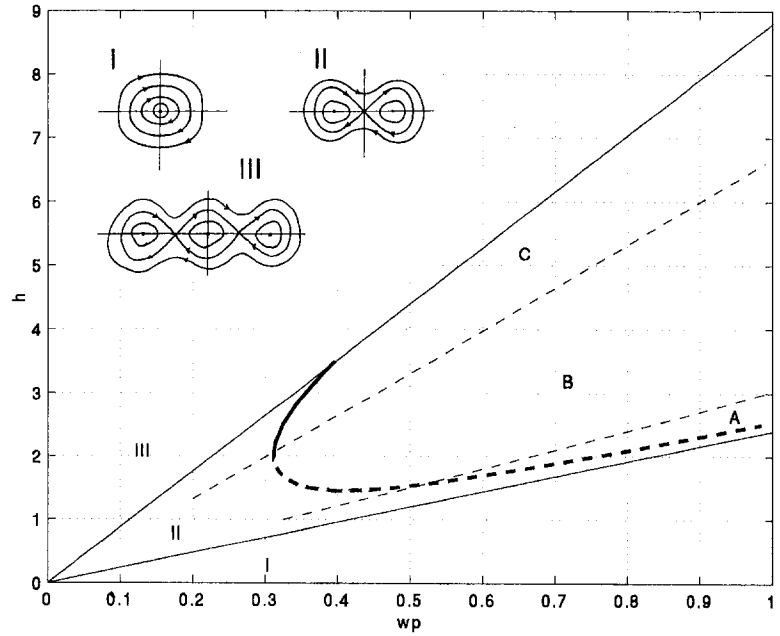

Fig. 4 Bifurcation diagram showing the multiple regimes and solution characteristics

Downloaded 04 May 2010 to 171.66.16.26. Redistribution subject to ASME license or copyright; see http://www.asme.org/terms/Terms_Use.cfm

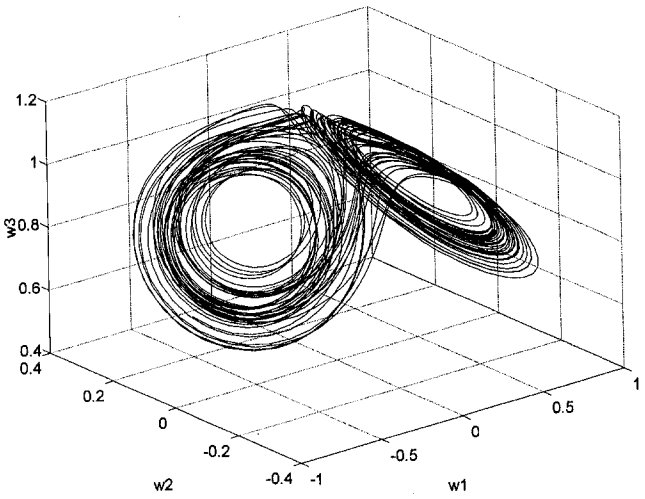

Fig. 5 A three-dimensional phase portrait showing the random motions about the two homoclinic loops

Therefore, the expression for M_{3c} is only valid in subregion A and C but not in subregion B.

Since Melnikov's method does not in general account for the steady-state behavior, here the steady-state behavior can only be studied through direct integration of the Euler's equations. This will be done by integrating Eqs. ($1a$–d) forward in time by using a fourth-order Runge-Kutta scheme.

4 Numerical Solutions

4.1 Motions Without Friction. Starting at a point inside one of the homoclinic loops, we obtain chaotic motions if the forcing amplitude is sufficiently large. The trajectory appears most irregular when the forcing is tuned to the natural frequency of the unforced motion. Subharmonic forcing also produces a strong effect but will not be considered separately. For a trajectory starting at a point outside the homoclinic loops, it tends to remain regular despite the forcing. Since the phase volume of a trajectory remains unchanged for this case, the chaotic pattern is stationary in time. But this type of motion is structurally unstable because damping, however small, will eventually change the motion characteristics by dissipating the energy. In Fig. 5 we give an illustration. The moments of inertia are $I_1 = 1.5$, $I_2 = 1.2$, $I_r = 1.0$, and $I_p = 0.8$. We now arbitrarily pick a phase point inside the right homoclinic loop, with initial condition $\omega_1 = 0.5$, $\omega_2 = 0.03$, $\omega_r = 1.4$, and $\omega_p = 0.6$. The forcing frequency is chosen to be close to the period of the unforced trajectory, which is at $p = 0.2738$. The forcing amplitude is set at $T_m = 2.0 \times 10^{-3}$. The motion just turns irregular at a slightly smaller T_m. The subsequent motion is extremely sensitive to the initial condition and becomes unpredictable. The phase point seems to lose "memory" after a certain amount of time. Although this case does not correspond to an strange attractor, many characteristics of the randomness appear similar to the well-known Lorenz attractor (Lorenz, 1963).

The two centers of the homoclinic loops represent two stable equilibria, which arise following a pitchfork bifurcation at ω_p when a gyroscopic term of the governing equations crosses zero. The irregular motions about the double loop in the phase space will translate to the inertial observer in physical space as the dual-spin body's random coning motions about two symmetrically tilted axes about the vertical. Each of the two tilted axes represents a direction about which the dual spinner can achieve spin equilibrium. At $T_m = 1.5 \times 10^{-3}$, the trajectory is almost periodic. Figure 5 shows the Poincaré section corresponding to the right limb of the right loop of the chaotic portrait on the plane $\omega_2 = 0$. A phase point in the map moves clockwise and shifts its location slightly during each cycle. There is no sensitivity to any perturbations of the initial conditions. But with a slight increase in T_m, to 1.78×10^{-3}, a phase point is now sensitive to initial conditions. In Fig. 6, there are altogether 1743 points in the map. We start with two very closely located points, labelled (1619, 1620) (mark "x") and (1537, 1538) (mark "o"). After 40 iterations the two points are still close together. But after 80 iterations, however, the two points become well separated. By 110 iterations, the "x" point is still seen, but the "o" point has escaped from the panel (at a phase coordinates (1.174, 1.194)). The sensitivity to initial conditions is a major characteristic of all chaotic behaviors. In the inserted panel, we display the entire map, for which Fig. 6 shows the top-right corner of the inserted panel. The map displays "islands" which are a result of resonances—a feature in all near-integrable systems (see Lichtenberg and Lieberman, 1983).

4.2 Attractors of the Motions. Internal friction, however small, will eventually render the two axial angular velocity components equal approximately. The motions which give rise to Smale's horseshoe cannot be considered a steady-state behavior unless the homoclinic connections occur with the initial condition $\omega_r \approx \omega_p$. Unfortunately, we noted earlier that a closed-form expression for the Melnikov function M_{3c} cannot be derived for this case because of the sign changes of Coulomb friction in the loops.

In the presence of damping, the phase volume of trajectories will continue to contract, a trajectory in transience will eventually shrink to a point or a limit cycle, or a certain fractal structure such as the strange attractor.

Consider an example with $I_1 = 1.5$, $I_2 = 1.1$, $I_r = 1.0$, and $I_p = 0.8$. The dual-spin body is forced sinusoidally by an internal motor torque. The forcing amplitude, T_m, is allowed to vary, but the frequency is fixed at $p = 0.1$. The Coulomb friction is set at $T_c = 0.002$. With damping, the results suggest that the initial conditions have little significance on the final motions. In our the numerical integrations, each run uses 3×10^5 steps at step size of 0.02. The time series is sampled and stored at a regular interval of 30 steps. Each portrait presented in the figure corresponds to the final behavior after four to five consecutive runs to ensure that it attains a steady-state characteristics. Each following run uses the end point of the previous for initialization. The shapes of the attractors are presented in Fig. 7.

At $T_m = 0.0005$, the attractor is a limit cycle. Using the same Poincaré map which iterates on the right limb ($\omega_1 > 0$) on the plane $\omega_2 = 0$, we obtain a single point (not shown). This point is located at $\omega_1 = 0.1277$. The frequency of the limit cycle is at 0.037, approximately. As T_m increases, at $T_m = 0.002$ (top-

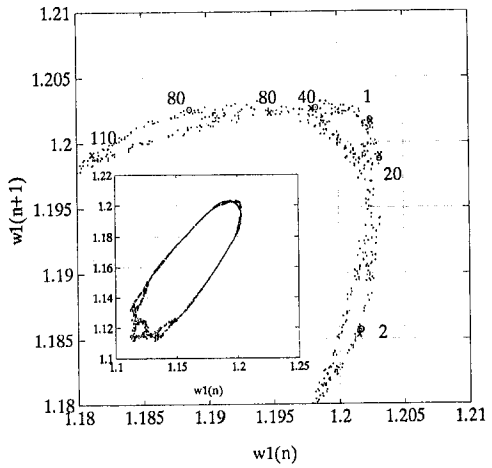

Fig. 6 Poincaré map showing the sensitivity to initial conditions for the frictionless motions

Downloaded 04 May 2010 to 171.66.16.26. Redistribution subject to ASME license or copyright; see http://www.asme.org/terms/Terms_Use.cfm

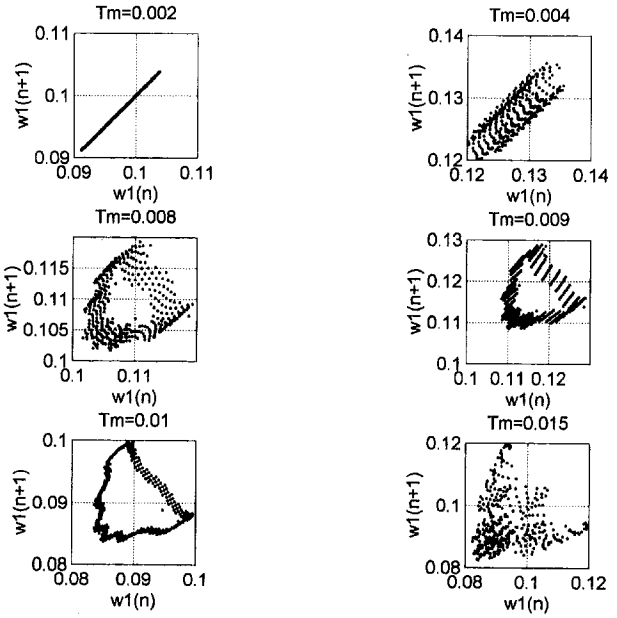

Fig. 7 A sequence of Poincaré maps illustrating the different attractors encountered as T_m varies

left panel), the map shows almost a straight line, suggesting the motion turns quasi-periodic. A second frequency emerges near 0.132. The power spectrum of the kinetic energy (not shown) displays peaks of the harmonics of the two principal frequencies as well as peaks resulting from the interactions of the two modes. The quasi-periodic cycle becomes chaotic (top-right panel) at $T_m = 0.004$. When the forcing is further increased, to $T_m = 0.008$ (middle-left panel), the chaotic map starts to show a reversed trend—reverting to regularity. An energetic peak also emerges at a frequency near 0.03 in the power spectrum. Less energetic peaks subside. At $T_m = 0.009$, the Poincaré map (middle-right panel) displays a certain mode-locking characteristics. The single energetic peak at frequency about 0.03 now dominates and other subsided peaks become the background noises. The time series of the state variables also display a short-interval intermittant behavior. Typically, it shows three short cycles separated by a long one. At $T_m = 0.01$, the Poincaré map (bottom-left panel) turns reasonably regular. But at $T_m = 0.015$ (bottom-right panel), the regularity disintegrates and the attractor becomes chaotic again. Although the regular behavior turns irregular again quite abruptly somewhere between $T_m = 0.01$ and 0.015, the two power spectra for this two cases show no noticeable difference. This again suggests a certain subtle sensitivity in the states. One last note: from the perturbation results using the Melnikov method it appears that damping has a stabilizing effects on chaotic behavior. But in fact damping promotes chaos as well. For example, for the case of the bottom-right panel, if we let $T_c = 0$, the chaotic attractor will disappear and be replaced a regular quasi-periodic cycle. This case corresponds to Region I of Fig. 4, which is prehomoclinic. When $\omega_r(0) \approx \omega_p(0)$, both motions with and without friction behave more similarly.

5 Concluding Remarks

We studied the motions of a dual spinner subject to both an internal oscillatory torque and Coulomb friction. The initial state is near a homoclinic connection. The Melnikov function is derived in an explicit form. Like those of oscillators with single degree-of-freedom, this function suggests the presence of complex prechaotic transient behavior. For the dual spinner, $\omega_r - \omega_p$ will eventually be driven close to zero by friction effect. Thus, the steady-state behavior may occur in regions not in the proximity of the homoclinic loops. To study the steady state, we turn to long-term integrations of the full equations. For the case of low forcing frequency, the attractor goes through a series of structures: limit cycle, quasi-periodic cycle, chaos, mode locking, and intermittancy, and chaos again, as the forcing amplitude increases.

References

Danby, J. M., 1962, *Fundamentals of celestial mechanics,* Macmillan, New York.

Guckenheimer, J., and Holmes, P., 1983, *Nonlinear oscillations, dynamical systems, and bifurcations of vector fields,* Springer-Verlag, New York.

Hall, C. D., and Rand, R. H., 1994, "Spinup Dynamics of Axial Dual-Spin Spacecraft," *J Guidance, Control, and Dynamics,* Vol. 17, No. 1, pp. 30–37.

Holmes, P. J., and Whitley, D. C., 1983, "On the Attracting Set for Duffing's Equation, II. A Geometrical Model for Moderate Force and Damping," *Physica,* Vol. 7D, pp. 111–123.

Huberman, B. A., and Crutchfield, J. P., 1979, "Chaotic States of Anharmonic Systems in Periodic Fields," *Phys. Rev. Lett.,* Vol. 43, pp. 1743–1747.

Hughes, P. C., 1986, *Spacecraft Attitude Dynamics,* John Wiley and Sons, New York.

Lichtenberg, A. J., and Lieberman, M. A., 1983, *Regular and stochastic motion,* Springer-Verlag, New York.

Lorenz, E. N., 1963, "Deterministic Nonperiodic Flow," *J. Atmos. Sci.,* Vol. 20, pp. 130–141.

Masaitis, C., 1961, "On the Motion of Two Linked Bodies," *Archive for Rational Mechanics and Analysis,* Vol. 8, No. 1, pp. 23–35.

Moon, F. C., and Holmes, P. J., 1979, "A Magnetoelastic Strange Attractor," *J. Sound Vib.,* Vol. 65, No. 2, pp. 285–296.

Scher, M. P., and Farrenkopf, R. L., 1974, "Dynamic Trap States of Dual Spin Spacecraft," *AIAA Journal,* Vol. 12, No. 12, pp. 1721–1725.

Ueda, Y., 1980, "Explosion of strange attractors exibitited by Duffing's Equation," *Nonlinear Dynamics,* R. H. G. Helleman, ed., New York Academy of Sciences, New York, pp. 422–434.

APPENDIX

Evaluation of Melnikov Integral

Let $f(z)$ be defined in the region enclosed by and on a simple connected circuit C; $f(z)$ is analytic except at a countable number of known singular points $a, b, c \ldots$ in the region. These are poles of $f(z)$. By the residue theorem we have

$$\oint_C f(z)dz = 2\pi i(a_1 + b_1 + c_1 \ldots), \tag{16}$$

where a_1, b_1, and c_1, etc., are residues associated with poles a, b, and c, etc. In the integral (11), ω_1^0, ω_2^0, and ω_r^0 are given, respectively, by Eqs. (5), (6*a*), (6*b*). Now, $\tilde{\omega}_p(t)$ can be obtained to first-order accuracy by integrating Eq. (1*d*), which gives

$$\tilde{\omega}_p(t) - \tilde{\omega}_p(t_0) = \left(\frac{I_r}{I_p}\right)\left(-\frac{1}{p}(\sin pt - \sin pt_0)\right.$$

$$\left. + \left(\frac{\epsilon_c}{\epsilon_m}\right)(t - t_0) + \left(\frac{\epsilon_d}{\epsilon_m}\right)\int_{t_0}^{t}(\omega_r^0 - \omega_p^0)dt\right). \tag{17}$$

The ratios of the small parameters are of order one. Only the terms with odd parity in the above expression actually contribute. We note that both ω_1^0 and ω_r^0 are even in t and ω_2^0 is odd. Here we consider only the case with $\epsilon_d = 0$. For convenience, we split M_3 in two components, such that

$$M_3(t_0) = M_{3a}\cos\frac{p}{\lambda}t_0 + \left(\frac{\epsilon_c}{\epsilon_m}\right)M_{3c}. \tag{18}$$

The applied-torque component M_{3a} has a form

$$M_{3a}(t_0) = \int_{-\infty}^{\infty}\frac{K_r}{p\lambda}\omega_1(t)\omega_2(t)\omega_r(t)\sin\frac{p}{\lambda}tdt. \tag{19}$$

The Coulomb component M_{3c} is

Downloaded 04 May 2010 to 171.66.16.26. Redistribution subject to ASME license or copyright; see http://www.asme.org/terms/Terms_Use.cfm

$$M_{3c} = \int_{-\infty}^{\infty} -\frac{K_r}{\lambda^2}\,\omega_1(t)\omega_2(t)\omega_r(t)tdt. \tag{20}$$

The factor K_r is defined by $K_r = I_r(I_1 - I_2)/I_1I_2$. After substituting for the expressions for ω_1^0, ω_2^0, and ω_r^0 from Eqs. (6*a*, *b*) and (5), we obtain

$$\omega_1^0\omega_2^0\omega_r^0 = \frac{AB}{8}(n_4 \sinh 4\lambda t + n_2 \sinh 2\lambda t), \tag{21}$$

where $n_2 = -2(r_1 - kr_3)$ and $n_4 = (r_1 + kr_3)$. We can then cast the above integrals in a form

$$M_{3a} = \int_{-\infty}^{\infty} \frac{g_a(z)}{h(z)}\,dz, \quad M_{3c} = \int_{-\infty}^{\infty} \frac{g_c(z)}{h(z)}\,dz. \tag{22}$$

Both integrals have the same $h(z)$, given by

$$h(z) = (\sinh^2 z + k\cosh^2 z)^3. \tag{23}$$

The expressions for g_a and g_c are, respectively,

$$g_a(z) = \frac{K_rAB}{8p\lambda}(n_4 \sinh 4z + n_2 \sinh 2z)\sin\frac{p}{\lambda}z, \tag{24}$$

and

$$g_c(z) = -\frac{K_rAB}{8\lambda^2}(n_4 \sinh 4z + n_2 \sinh 2z)z. \tag{25}$$

Both integrands $g_{a,c}(z)/h(z)$ tend to zero as z goes to infinity. Examining $h(z)$, we found that there are two poles, each of third-order for the integrand. The first one, $z = a$, is given by

$$\sinh a - i\sqrt{k}\cosh a = 0, \tag{26}$$

where a is purely imaginary with value between zero and $i\pi$. Pole $z = a$ has a mirror image about x-axis in the lower-half plane. But because a mirror reflection of a pole followed by a translation by a multiple of $i\pi$ is another pole, we obtain a second distinct pole at $z = b = i\pi - a$, which satisfies

$$\sinh b + i\sqrt{k}\cosh b = 0. \tag{27}$$

Having identified the two poles, we then construct a closed circuit enclosing the two poles $z = a$ and $z = b$. The circuit C chosen has the shape of a rectangular strip on the upper half complex plane. It runs counterclockwise from $z = -R$ to $z = R$, to $z = R + i\pi$, then to $z = -R + i\pi$, and back to $z = -R$. By allowing $R \to \infty$ and applying the residue theorem to Eq. (19), we obtain

$$M_{3a} = \int_{-\infty}^{\infty} \frac{g_a(z)}{h(z)}\,dz = 2\pi i\,\frac{(a_1 + b_1)}{1 - \cosh\frac{p}{\lambda}\pi}. \tag{28}$$

From the theory of complex variables, if $g(z)/h(z)$ has a k-order pole at $z = a$, the residue a_1 is given by

$$a_1 = \lim_{z\to a}\frac{1}{k-1}\frac{d^{k-1}}{dz^{k-1}}\left((z-a)^k\frac{g_a(z)}{h(z)}\right). \tag{29}$$

Furthermore, if $g(z)$ and $h(z)$ are Taylor expanded, such that

$$g(z) = g_0 + g_1(z-a) + \tfrac{1}{2}g_2(z-a)^2 + \ldots,$$

$$h(z) = \tfrac{1}{6}h_3(z-a)^3 + \tfrac{1}{24}h_4(z-a)^4 + \tfrac{1}{120}h_5(z-a)^5 + \ldots,$$

then the residue of $g(z)/h(z)$ can be shown to be

$$a_1 = \frac{3}{h_3}\left(g_2 - \frac{1}{2}\frac{g_1h_4}{h_3} - \frac{1}{10}\frac{g_0h_5}{h_3}\right). \tag{30}$$

This formula is applied twice, to the two poles $z = a$ and $z = b$ to obtain the two residues a_1 and b_1. In our case we express $h(z) = u(z)v(z)$, so that for pole $z = a$, we choose

$$u(z) = (\sinh z - i\sqrt{k}\cosh z)^3,$$

$$v(z) = (\sinh z + i\sqrt{k}\cosh z)^3. \tag{31}$$

and for pole $z = i\pi - a$, we flip u and v. For the numerical implementation, we have the following expression for residue:

$$a_1 = \frac{3}{u_3v_0}\left\{g_2 - \frac{g_1}{u_3v_0}(u_4v_0 + 4v_1u_3) - \frac{g}{10u_3v_0}\left(u_5v_0 + 10u_3v_2 - 5u_4v_1 - 20\frac{u_3v_1^2}{v_0}\right)\right\}. \tag{32}$$

The indices used are such that u_k represents the kth derivative of u evaluated at a pole. To obtain expression (12), significant algebraic manipulations are required.

The Coulomb component, M_{3c} can be evaluated by a similar procedure. Since the integrand for this case has the same demoninator. However, we notice that the line integral over the same circuit C will vanish identically because the two residues of the two poles cancel each other. After some careful consideration, we use a different integrand. The following identity is established:

$$\frac{1}{2\pi}\oint_C \frac{(iz^2 + \pi z)(n_4e^{4z} + n_2e^{2z})}{(\sinh^2 z + k\cosh^2 z)^3}\,dz = \int_{-\infty}^{\infty}\frac{(n_4e^{4t} + n_2e^{2t})t}{(\sinh^2 t + k\cosh^2 t)^3}\,dt. \tag{33}$$

To obtain the desired right integral, we evaluate the left integral by the residue method. The same expression (32) is used. Both u_i and v_j remain the same as before but g_k are different. A similar procedure will yield the expression (13).

Downloaded 04 May 2010 to 171.66.16.26. Redistribution subject to ASME license or copyright; see http://www.asme.org/terms/Terms_Use.cfm

A Parametric Study on the Free Vibration of Noncylindrical Helical Springs

V. Yıldırım
Associate Professor,
Department of Mechanical Engineering,
University of Çukurova,
01330 Balcalı,
Adana, Turkey

In the work based on the stiffness method reported in this paper, considering the rotary inertia, the axial and shear deformation terms, the natural frequencies of conical, barrel, and hyperboloidal-type helical springs fixed at both ends are calculated. The results are presented in dimensionless graphical forms for the six lowest natural frequencies of all types of noncylindrical helices for a wide range of vibrational parameters which influence the natural frequencies. A discussion about the effects of vibrational parameters on the natural frequencies is also presented.

1 Introduction

Although the free vibration of cylindrical helical springs has been the subject of numerous investigations, only a limited number of papers have been reported on the free vibration of noncylindrical helical springs. In his pioneering study, Epstein (1947) determined theoretically the fundamental frequency of conical coil springs. Nagaya et al. (1986) studied both numerically and experimentally the free vibration of hyperboloidal and barrel-type helical springs. Using the Myklestad's method for the theoretical analysis, the authors have obtained the overall dynamic transfer matrix using both the point mass matrices and the static element transfer matrices in closed form. They have taken into consideration only the axial deformation for circular cross sections. Neglecting both the rotary inertia and shear deformation effects, they have presented the first four frequencies in graphical forms. They have also investigated some parameters that affect the free-vibration frequencies in a limited manner. Recently Yıldırım (1996a) has also studied the free-vibration problem of the noncylindrical coil springs by the method of Myklestad. The effects of the rotary inertia, the axial, and shear deformations all have been taken into consideration for the computation of natural frequencies of conical, barrel, and hyperboloidal-type helical springs having different shapes of cross section. In Yıldırım's study the numerical algorithm developed by Yıldırım (1995, 1996b, 1997a), has been used for determining the static element transfer matrix. Yıldırım's study (1996a) showed that Nagaya et al. (1986) had missed some frequencies of barrel type springs. It was understood from Yıldırım's studies (1996a, 1997b) that shear deformations are of relatively greater importance for noncylindrical coil springs than cylindrical ones. Finally, considering the rotary inertia effects, the axial and shear deformations and cross sections of different shapes having double symmetry, Yıldırım (1997c) has investigated free-vibration analysis of noncylindrical coil springs by combined use of the transfer matrix and the complementary functions methods. She has obtained the overall transfer matrix by numerical integration of the differential equations and presented exact natural frequencies.

The objective of the study reported here is to develop information which may be used to estimate rapidly the natural frequencies of noncylindrical helices. In this study, the stiffness method was used in the analysis. The cylindrical helical element stiffness matrix is obtained by the transfer matrix method. The consistent spatial straight beam mass matrix is also employed. The subspace iteration method is applied to the solution of the large-scale eigenvalue problem. After verifying the results which are obtained in this study with the numerical and experimental data available in the literature, the first six natural frequencies have been presented for all types of helices. The effects of the helix pitch angle, the number of active turns, and the ratio of diameters of minimum cylinder to maximum cylinder have also been investigated.

2 Formulation

Applying the usual assumptions of the free-vibration analysis of a linear system, the governing equation

$$([K] - \omega^2[M])\{a\} = \{0\} \tag{1}$$

is obtained in which $[K]$ and $[M]$ are the square matrices containing the stiffness and mass descriptions for the helical spring; $\{a\}$ is a vector of nodal displacements; and ω is the circular frequency (rad/s) of the free undamped vibration.

The calculation of eigenvalues and eigenvectors is fundamental to the study of structural vibrations. Various methods have been developed for the solution of a large-scale eigenvalue problems (Bathe and Wilson, 1976; Wilson and Itoh, 1983; Omid et al., 1983; Weingarten et al., 1983; Nguyen and Arora, 1986). Among these, the subspace iteration method suggested by Bathe and Wilson (1976) is employed in the present analysis.

In this study, the element stiffness matrix of a typical helical element has been obtained numerically based on the transfer matrix method (Haktanır and Kıral, 1993; Yıldırım, 1995). Element equation is written as

$$\{p\} = [k]\{d\} \tag{2}$$

where $\{p\}$ and $\{d\}$ are the element vectors containing the end forces and the end displacements, respectively. $[k]$ is the element stiffness matrix. A helical node considered here has the six degrees-of-freedom shown in Fig. 1. Denoting the ends of the element by subscripts i and j, the end quantities of an element are written in open form as

$$\{p\} = \{p_1 \quad p_2 \quad p_3 \quad \dots \quad p_{12}\}^T = \{\{p\}_i \quad \{p\}_j\}^T \tag{3a}$$

$$\{d\} = \{d_1 \quad d_2 \quad d_3 \quad \dots \quad d_{12}\}^T = \{\{d\}_i \quad \{d\}_j\}^T. \tag{3b}$$

The subscripts 1, 2, 3 and 7, 8, 9 correspond to the end forces in (3a) and the translational displacements in (3b). The subscripts 4, 5, 6 and 10, 11, 12 represent the end moments in

Contributed by the Applied Mechanics Division of THE AMERICAN SOCIETY OF MECHANICAL ENGINEERS for publication in the ASME JOURNAL OF APPLIED MECHANICS.

Discussion on this paper should be addressed to the Technical Editor, Professor Lewis T. Wheeler, Department of Mechanical Engineering, University of Houston, Houston, TX 77204-4792, and will be accepted until four months after final publication of the paper itself in the ASME JOURNAL OF APPLIED MECHANICS.

Manuscript received by the ASME Applied Mechanics Division, Sept. 20, 1996; final revision, Oct. 30, 1997. Associate Technical Editor: V. K. Kinra.

 Copyright © 1998 by ASME

Downloaded 04 May 2010 to 171.66.16.26. Redistribution subject to ASME license or copyright; see http://www.asme.org/terms/Terms_Use.cfm

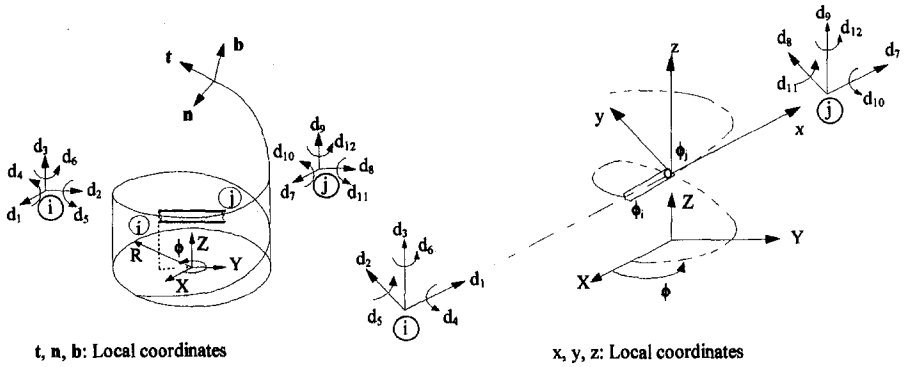

t, n, b: Local coordinates
X, Y, Z: Global coordinates
(a)Helical element

x, y, z: Local coordinates
X, Y, Z: Global coordinates
(b)Straight element

Fig. 1 Degrees-of-freedom of an element and coordinates

$(3a)$ and the rotations of cross section in $(3b)$. The end force and displacement vectors are related by the element transfer matrix, $[F]$, in the form of

$$\begin{bmatrix} \{d\}_j \\ \{p\}_j \end{bmatrix} = [F]_{(j-i)} \begin{bmatrix} \{d\}_i \\ -\{p\}_i \end{bmatrix}. \tag{4}$$

For the determination of the components of the element stiffness matrix, Eq. (4) should be solved 12 times for 12 boundary conditions which are determined by considering the definition of $[k]$. For example, since the transfer matrix method gives the solution for only positive sections, the elements $k_{1,m}$ $(m = 1, 2, \ldots, 6)$ are obtained by reversing the sign of $\{p\}_i$ $(i = 1, 2, \ldots, 6)$ which are evaluated by Eq. (5).

$$\begin{bmatrix} 0 \\ 0 \\ 0 \\ 0 \\ 0 \\ 0 \end{bmatrix} = [F_1]_{(j-i)} \begin{bmatrix} 1 \\ 0 \\ 0 \\ 0 \\ 0 \\ 0 \end{bmatrix} + [F_2]_{(j-i)} \begin{bmatrix} p_1 \\ p_2 \\ p_3 \\ p_4 \\ p_5 \\ p_6 \end{bmatrix} \tag{5}$$

Substituting the end forces at the end i in Eq. (4), the elements $k_{1,n}$ $(n = 6, 7, \ldots, 12)$ can be obtained from the following equation:

$$\begin{bmatrix} p_7 \\ p_8 \\ p_9 \\ p_{10} \\ p_{11} \\ p_{12} \end{bmatrix} = [F_3]_{(j-i)} \begin{bmatrix} 1 \\ 0 \\ 0 \\ 0 \\ 0 \\ 0 \end{bmatrix} + [F_4]_{(j-i)} \begin{bmatrix} p_1 \\ p_2 \\ p_3 \\ p_4 \\ p_5 \\ p_6 \end{bmatrix}. \tag{6}$$

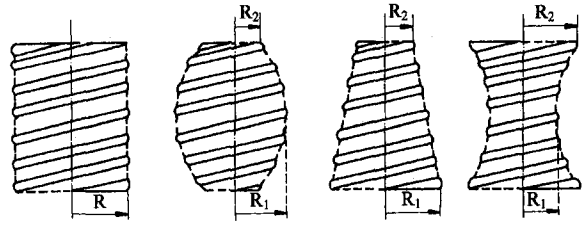

Fig. 2 Types of helical springs (*a*) $R_{max} = R$, (*b*) $R_{max} = R_1$, (*c*) $R_{max} = R_1$, (*d*) $R_{max} = R_2$

Table 1 Natural frequencies (in Hz) of hyperboloidal-type spring with circular section

	R_1/R_2	Modes					
		1	2	3	4	5	6
ANSYS (100 elements)	0.2	124.20	159.93	176.75	260.51	270.07	322.06
	0.4	94.74	119.48	129.22	167.72	199.58	231.70
	0.6	73.18	89.53	95.94	110.06	152.14	162.96
	0.8	57.12	66.96	72.62	76.69	115.68	120.54
Yıldırım (1996a)(50 elements)	0.2	121.3	157.5	171.6	248.5	276.6	299.4
	0.4	92.6	117.5	126.3	164.2	197.3	223.6
	0.6	71.6	88.0	94.2	108.1	149.2	159.5
	0.8	55.9	65.7	71.4	75.4	113.2	118.1
Present study (100 elements)	0.2	121.77	160.08	172.42	259.21	273.01	312.52
	0.4	92.83	118.73	126.77	167.42	198.91	227.57
	0.6	71.68	88.70	94.41	109.54	150.51	160.35
	0.8	55.91	66.37	71.55	76.01	113.51	119.11

Table 2 Natural frequencies (in Hz) of barrel-type spring with circular section

	R_2/R_1	Modes					
		1	2	3	4	5	6
Yıldırım (1997b) (exact)	0.2	71.86	81.19	99.95	99.96	143.88	—
	0.4	65.53	71.52	86.94	87.01	129.60	—
	0.6	59.62	61.78	75.08	75.09	114.01	—
	0.8	52.11	54.57	64.46	64.77	99.15	—
Yıldırım (1996a) (50 elements)	0.2	71.95	81.3	100.07	100.09	144.1	145.2
	0.4	65.6	71.6	87.03	87.1	129.7	135.1
	0.6	59.7	61.8	75.1	75.2	114.1	120.9
	0.8	52.1	54.6	64.5	64.8	99.2	106.0
	1.0	44.1	49.0	55.3	56.3	86.1	91.4
Nagaya et. al. (1986) (78 elements)*	0.2	71.0	81.0	—	—	143.0	150.0
	0.4	64.0	71.0	—	—	129.0	134.0
	0.6	59.0	60.0	—	—	113.0	120.0
	0.8	52.0	53.0	—	—	99.0	104.0
	1.0	43.0	48.0	—	—	85.0	90.0
Nagaya et. al. (1986) (experimental)**	0.4	66.0	72.0	—	—	129.0	136.0
	0.6	60.0	62.0	—	—	108.0	116.0
	0.8	52.0	55.0	—	—	100.0	108.0
	1.0	44.0	50.0	—	—	87.0	91.0
Present study (100 elements)	0.2	72.96	81.24	100.15	100.16	144.65	147.06
	0.4	65.53	71.57	87.10	87.17	129.96	136.69
	0.6	60.37	61.97	75.20	75.22	114.18	122.35
	0.8	52.16	55.33	64.55	64.91	99.26	107.16
	1.0	44.10	49.68	55.34	56.49	86.25	92.34
ANSYS (100 elements)	0.2	73.51	83.55	101.76	101.83	147.88	150.04
	0.4	67.07	73.46	88.50	88.57	133.04	138.64
	0.6	60.99	63.34	76.36	76.40	116.87	123.78
	0.8	53.34	55.77	65.51	65.86	101.50	108.41
	1.0	45.09	50.05	56.15	57.21	88.10	93.41

Note:* and ** are obtained approximately from the graphics given by Nagaya et. al. (1986).

Downloaded 04 May 2010 to 171.66.16.26. Redistribution subject to ASME license or copyright; see http://www.asme.org/terms/Terms_Use.cfm

Table 3 Natural frequencies (in Hz) of conical-type spring with circular section

	R_2/R_1	Modes					
		1	2	3	4	5	6
ANSYS (100 elements)	0.2	110.51	115.07	135.60	143.33	197.04	204.46
	0.4	89.35	92.31	107.88	111.86	164.09	172.03
	0.6	70.07	75.26	85.94	88.15	133.66	140.33
	0.8	55.63	61.30	69.06	70.46	108.14	114.37
Yıldırım (1996a) (50 elements)	0.2	111.8	116.4	137.4	145.4	198.9	206.4
	0.4	89.5	92.5	108.4	112.4	164.3	172.3
	0.6	69.5	74.8	85.7	87.9	132.6	139.4
	0.8	54.8	60.5	68.4	69.7	106.5	112.7
Present study (100 elements)	0.2	110.56	114.21	134.72	142.49	196.01	204.51
	0.4	88.30	92.14	106.89	110.94	162.50	171.14
	0.6	68.90	75.03	84.97	87.28	131.62	139.32
	0.8	54.53	60.97	68.16	69.67	106.12	113.30

In (5) and (6), $[F_m]$ $(m = 1, 2, 3, 4)$ are the submatrices of the element transfer matrix.

In the method for the determination of the element stiffness matrix based on the transfer matrix method, which is outlined above, the crucial step is the computation of the element transfer matrix in an accurate manner. In this study considering the axial and shear deformation effects, the element transfer matrix is obtained numerically up to any desired accuracy by the numerical algorithm devised by Yıldırım (1995, 1996a–b, 1997a). It is assumed that the centroid of the cross-section coincides with its shear center, normal, and binormal axes are the principal axes, warping is neglected and, further, the bar is made of a linear elastic, homogeneous, and isotropic material. The numerical algorithm is given in the Appendix.

The transformation of the element transfer matrix between the local and global coordinates is in the form of (Fig. 1).

$$[F(\phi_j - \phi_i)]_{XYZ} = [T(\phi_j)]^{-1}[F(\phi_j - \phi_i)]_{mb}[T(\phi_i)] \quad (7)$$

where the transformation matrix $[T]$ consists of four submatrices $[A]$.

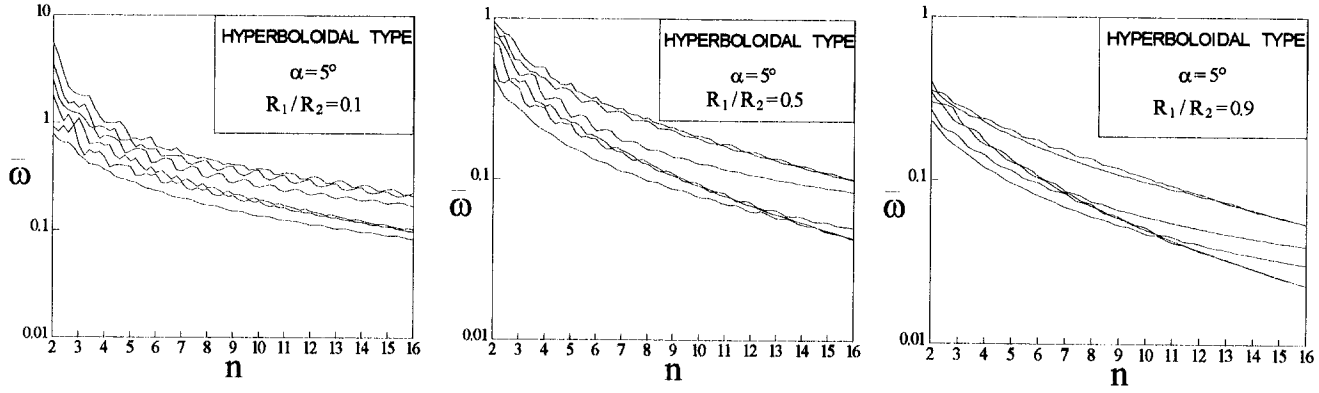

Fig. 3(*a*)

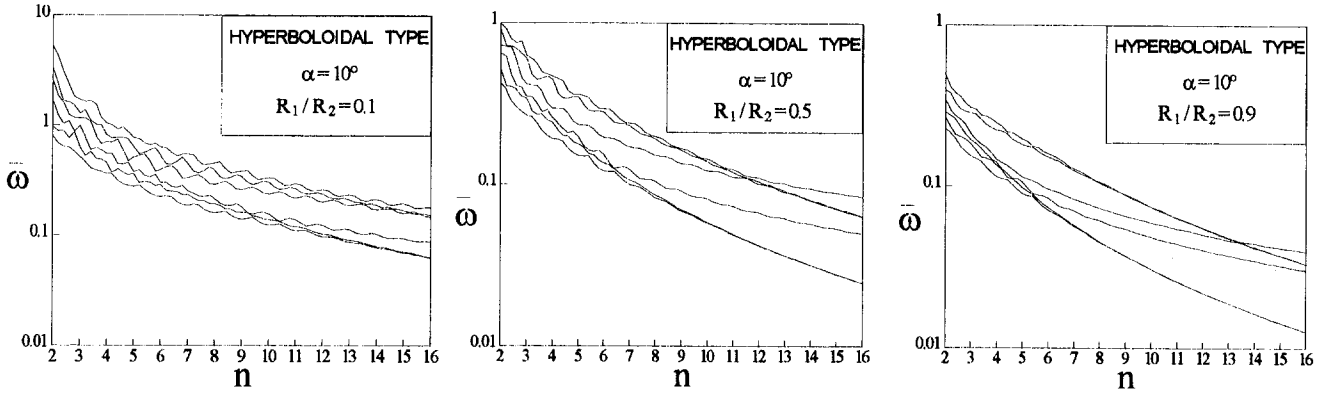

Fig. 3(*b*)

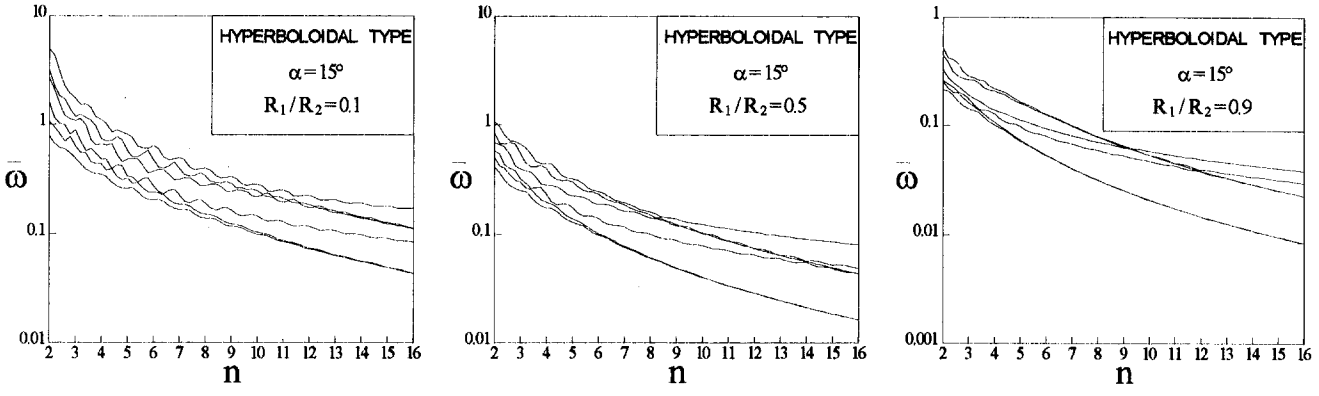

Fig. 3(*c*)

Fig. 3 The six lowest dimensionless frequencies of hyperboloidal spring fixed at both ends (*n* is the number of turns)

Downloaded 04 May 2010 to 171.66.16.26. Redistribution subject to ASME license or copyright; see http://www.asme.org/terms/Terms_Use.cfm

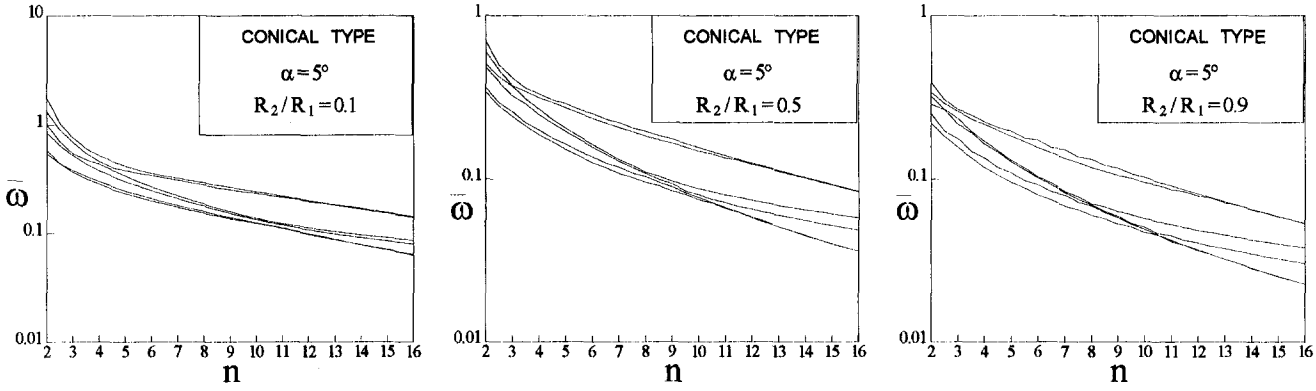

Fig. 4(*a*)

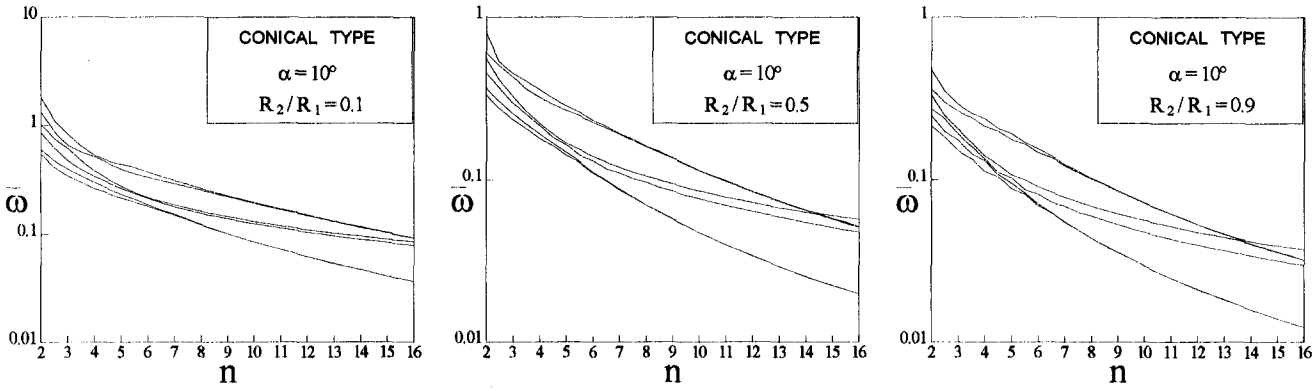

Fig. 4(*b*)

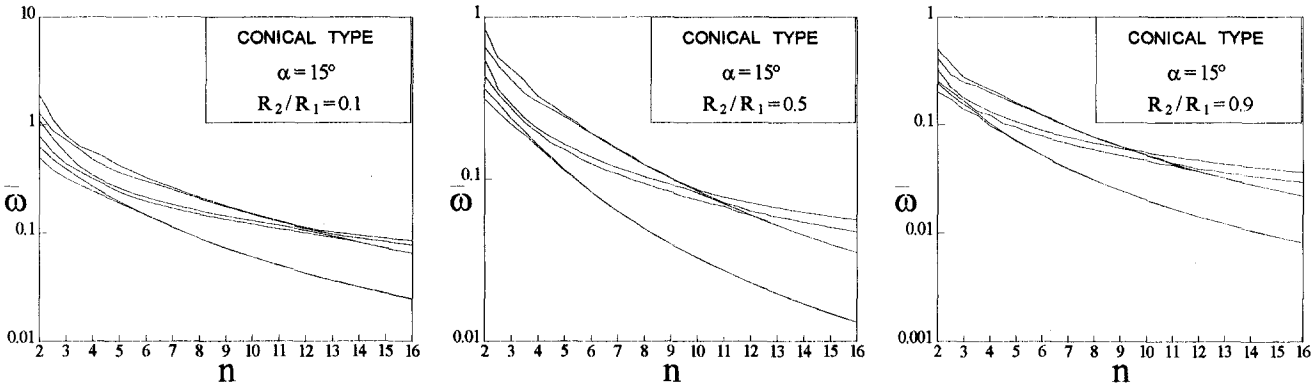

Fig. 4(*c*)

Fig. 4 The six lowest dimensionless frequencies of conical spring fixed at both ends (*n* is the number of turns)

$$[T] = \begin{bmatrix} [A] & [0] & [0] & [0] \\ [0] & [A] & [0] & [0] \\ [0] & [0] & [A] & [0] \\ [0] & [0] & [0] & [A] \end{bmatrix} \tag{8}$$

The elements of the submatrix $[A]$ are obtained as

$$[A] = \begin{bmatrix} -\cos\alpha \sin\phi & \cos\alpha \cos\phi & \sin\alpha \\ -\cos\phi & -\sin\phi & 0 \\ \sin\alpha \sin\phi & -\sin\alpha \sin\phi & \cos\alpha \end{bmatrix} \tag{9}$$

where α is the helix pitch angle. The angle ϕ is measured from the X-axis in horizontal plane (Fig. 1).

Mottershead (1980) has given the consistent cylindrical helical element mass matrix in semi-open form, which has been obtained by the finite element method. For the reason of simplicity, the consistent spatial straight element mass matrix given by Craig (1981) is employed in this study (Fig. 1(*b*)). In the computation of the element mass matrix, the total length of the element L is determined approximately as

$$L = \frac{R(\phi_j)}{\cos\alpha}(\phi_j - \phi_i) \tag{10}$$

where R is the horizontal radius of the helix.

The radius R of any point that lies on the axis of the bar varies along the axis for noncylindrical helical springs. This radius is given for a barrel and hyperboloidal-type helix by Eq. (11) and for a conical spring by Eq. (12) (Fig. 2).

$$R = R_1 + (R_2 - R_1)\left(1 - \frac{\phi}{\pi n}\right)^2 \tag{11}$$

$$R = R_1 + (R_2 - R_1)\frac{\phi}{2\pi n} \tag{12}$$

In (11) and (12), n is the number of active coils. The para-

Downloaded 04 May 2010 to 171.66.16.26. Redistribution subject to ASME license or copyright; see http://www.asme.org/terms/Terms_Use.cfm

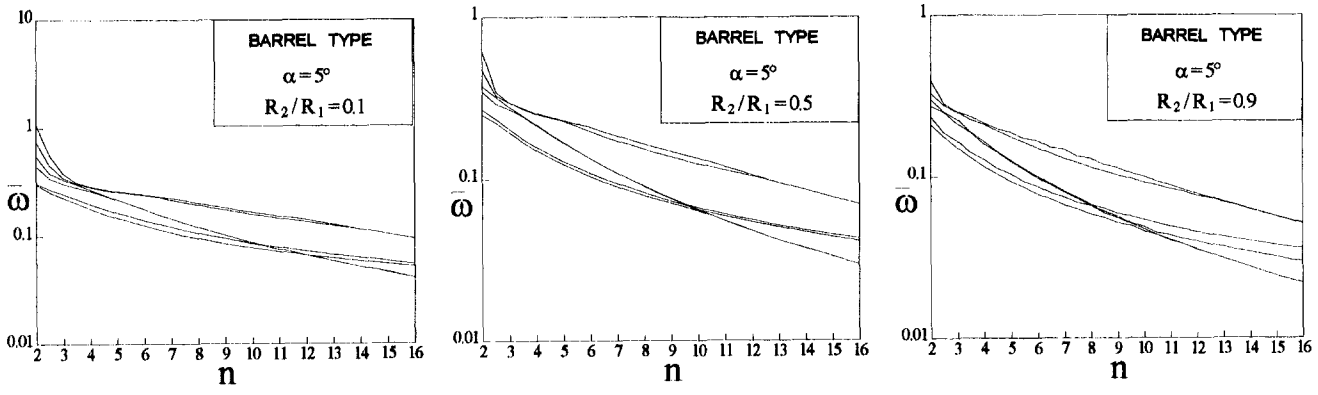

Fig. 5(*a*)

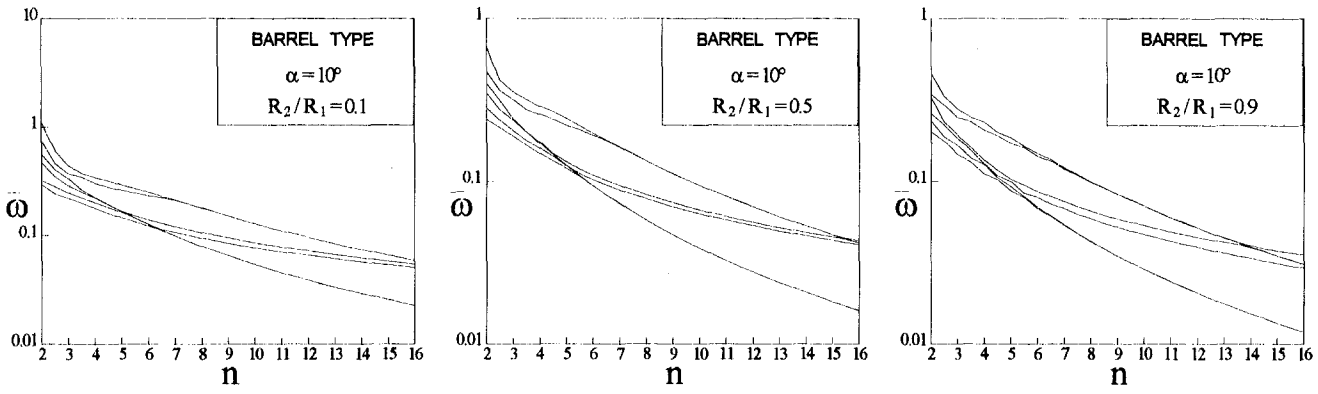

Fig. 5(*b*)

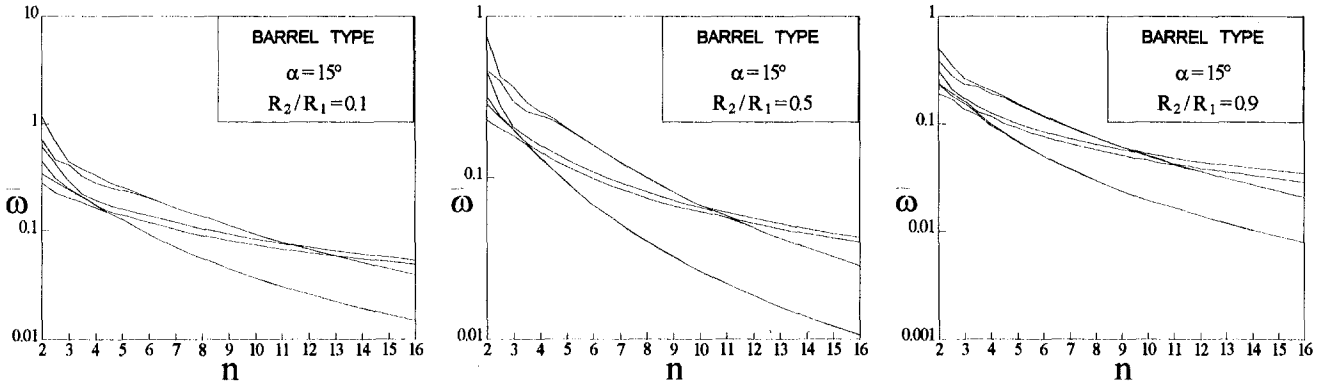

Fig. 5(*c*)

Fig. 5 The six lowest dimensionless frequencies of barrel spring fixed at both ends (*n* is the number of turns)

metric equation of noncylindrical helices in the global coordinates can be defined as

$$X = R(\phi)\cos\phi$$

$$Y = R(\phi)\sin\phi$$

$$Z = \sum \Delta Z\,(\Delta Z = R(\phi)\tan\alpha(\phi_j - \phi_i)). \qquad (13)$$

The element mass matrix in the global coordinates is in the form of

$$[m]_{XYZ} = [T]^T[m]_{xyz}[T]. \qquad (14)$$

In this study the average value of the angle ϕ, $\{= (\phi_i + \phi_j)/2\}$, is used in Eq. (14).

3 Applications

In order to verify the soundness of the results obtained, three springs fixed at both ends are considered. The helical axis is constituted by 100 elements. The boundary conditions are determined for the first element as $\{d\}_i = 0$ (at $\phi = 0$) and for the last element as $\{d\}_j = 0$ (at $\phi = 2n\pi$). As a first example a hyperboloidal-type spring is chosen (modulus of elasticity $E = 2.1\ 10^{11}$ N/m^2, Poisson's ratio $\nu = 0.3$, the mass density $\rho = 7850$ kg/m^3, $\alpha = 4.8$ deg, $n = 6.5$, $R_{max} = 25$ mm, diameter of circular section $d = 2$ mm). Typical results are shown in Table 1. A good agreement among the results of the ANSYS, the Myklestad's, and the stiffness method can be observed in the table. As can be seen from Table 1, the natural frequencies are calculated with a good approximation in this study.

As a second example a barrel-type spring having the same properties of previous example is considered. Comparison is made between the theoretical and experimental results available in the relevant literature in Table 2. As observed from the table, the barrel-type spring has very close natural frequencies. Determining these frequencies can be difficult both theoretically and experimentally. Nagaya et al. (1986) had missed the third and forth frequencies.

Downloaded 04 May 2010 to 171.66.16.26. Redistribution subject to ASME license or copyright; see http://www.asme.org/terms/Terms_Use.cfm

As in the last example a conical spring having the same geometrical and material properties given in the first example is studied. The results are presented in Table 3. A good agreement is observed among the results of the present study, the ANSYS and Yıldırım's study (1996a).

After verifying the soundness of the frequencies obtained in this study, effects of vibrational parameters which are chosen as the helix pitch angle (α = 5 deg, 10 deg, and 15 deg), the number of turns ($n = 2 - 16$) and the ratio of radii of minimum cylinder to maximum cylinder ($R_{\min}/R_{\max}$ = 0.1, 0.5, and 0.9) on the natural frequencies are studied. The results are presented in Figs. 3–5 in dimensionless graphical forms. The dimensionless frequency is determined for all types of helices with circular section as

$$\bar{\omega}^2 = \omega^2 \frac{\rho A R_{\max}^4}{E I_n} \tag{15}$$

where A is the cross-sectional area and I_n is the inertia moment of the cross section about the normal axis.

4 Conclusions

To the knowledge of the author, this is the first free-vibration analysis of noncylindrical helical springs performed by the stiffness method. To show the accuracy of the present theoretical results, numerical calculations have been carried out for all types of helices. It is shown that the present results given in tabular form are in close proximity of the previously published ones both experimental and theoretical. A parametric study shows the effects of the helix pitch angle, the number of coils and the ratio of radii of minimum cylinder to maximum cylinder on the natural frequencies. The dimensionless frequencies of all types of helices with circular section versus the number of coils are presented in graphical forms for the ratio $D_{\max}/d$ = 10 and the values of the helix pitch angle (α = 5 deg, 10 deg, 15 deg). These graphics can also be used for predicting the free-vibration frequencies.

The concise results can be outlined as (i) the hyperboloidal spring has the most rigidity compared to other types of springs which have the same maximum diameter. The conical spring follows the hyperboloidal types with respect to rigidity; (ii) in general, the dimensionless frequencies decrease with increasing the number of coils. Similarly, the natural frequencies decrease with increasing the ratio of $R_{\min}/R_{\max}$; (iii) as both the ratio of $R_{\min}/R_{\max}$ and the number of coils decrease, the higher frequencies have a peak either minimum or maximum for hyperboloidal types. This feature becomes unimportant for the fundamental frequency; (iv) a barrel-type spring has very close natural frequencies compared to other types; (v) frequencies associated with the three and upper modes of both the conical and barrel types diverge from the first two frequencies as both the n and α increase; (vi) the higher frequencies for all types of helices are close together for some values of the number of active coils.

Close natural frequencies, which are the most important features of the helical springs, could have been effectively computed in this study by means of the exact numerical cylindrical helical element stiffness matrix (Haktanır and Kıral, 1993), the subspace iteration method, the method of Jacobi's, and of the Stürm sequence method (Bathe and Wilson, 1976).

References

Bathe, K. J., and Wilson, E. L., 1976, *Numerical Methods in Finite Element Analysis,* Prentice-Hall Englewood Cliffs, NJ.

Craig, R. R., 1981, *Structural Dynamics—An Introduction to Computer Methods,* John Wiley and Sons, New York.

Epstein, I., 1947, "The Motion of A Conical Coil Spring," *Journal of Applied Physics,* Vol. 18, pp. 368–374.

Haktanır, V., and Kıral, E., 1993, "Statical Analysis of Elastically and Continuously Supported Helicoidal Structures by the Transfer and Stiffness Matrix Methods," *Comput. Struct.,* Vol. 49, pp. 663–677.

Nagaya, K., Takeda, S., and Nakata, Y., 1986, "Free Vibration of Coil Spring of Arbitrary Shape," *Int. J. Numer. Meth. Engng.,* Vol. 23, pp. 1081–1099.

Nguyen, D. T., and Arora, J. S., 1986, "An Algorithm for Solution of Large Eigenvalue Problems," *Comput. Struct.,* Vol. 24, No. 4, pp. 645–650.

Mottershead, J. E., 1980, "Finite Elements for Dynamical Analysis of Helical Rods," *Int. J. Mech. Sci.,* Vol. 22, pp. 267–283.

Omid, B. N., Parlett, B. N., and Taylor, R. L., 1983, "Lanczos versus Subspace Iteration for Solution of Eigenvalue Problems," *Int. J. Numer. Meth. Engng.,* Vol. 19, pp. 859–871.

Pestel, E. C., and Leckie, F. A., 1963, *Matrix Methods in Elastomechanics,* McGraw-Hill, New York.

Weingarten, V. I., Ramanathan, R. K., and Chen, C. N., 1983, "Lanczos Eigenvalue Algorithm for Large Structures on a Minicomputer," *Comput. Struct.,* Vol. 16, pp. 253–257.

Wilson, E. L., and Itoh, T., 1983, "An Eigen Solution Strategy for Large Systems," *Comput. Struct.,* Vol. 16, pp. 259–265.

Yıldırım, V., 1995, "Investigation of Free Vibration of Helical Springs by the Stiffness Matrix Method," *Turkish Journal of Engineering and Environmental Sciences,* Vol. 19, No. 4, pp. 343–356 (in Turkish).

Yıldırım, V., 1996a, "The Myklestad's Method for the Free Vibration of Non-Cylindrical Helical Springs," *Turkish Journal of Engineering and Environmental Sciences,* Vol. 20, No. 2, pp. 121–128 (in Turkish).

Yıldırım, V., 1996b, "Investigation of Parameters Affecting Free Vibration Frequency of Helical Springs," *Int. J. Numer. Methods Eng.,* Vol. 39, No. 1, pp. 99–114.

Yıldırım, V., 1997a, "A Computer Program for the Free Vibration Analysis of Elastic Arcs," *Comput. Struct.,* Vol. 62, No. 3, pp. 475–485.

Yıldırım, V., and İnce, N., 1997b, "Natural Frequencies of Helical Springs of Arbitrary Shape," *Journal of Sound and Vibration,* Vol. 204, No. 2, pp. 311–329.

Yıldırım, V., 1997c, "Free Vibration Analysis of Non-Cylindrical Coil Springs by Combined Use of the Transfer Matrix and the Complementary Functions Methods," *Communications in Numerical Methods in Engineering,* Vol. 13, pp. 487–494.

APPENDIX

A Numerical Algorithm for the Computation of the Cylindrical Helical Element Transfer Matrix

The statical equations of helical bars in canonical form can be expressed in the form of (Pestel and Leckie, 1963)

$$d\{S(\phi)\}/d\phi = [D]\{S(\phi)\} \tag{a}$$

where $\{S\}$ is the state vector and $[D]$ is the differential matrix. The components of the state vector in Frenet coordinates are

$$\{S(\phi)\} = \{U_t \quad U_n \quad U_b \quad \Omega_t \quad \Omega_n \quad \Omega_b \quad T_t \quad T_n \quad T_b \quad M_t \quad M_n \quad M_b\} \tag{b}$$

where T_t, T_n, and T_b are the components of the internal forces on the cross section in the **t**, **n**, and **b** directions and M_t, M_n, M_b are the components of the internal moments on this section on the **t**, **n**, and **b** directions, respectively. U_t, U_n, U_b and Ω_t, Ω_n, Ω_b are the Frenet components of the displacement and rotational vectors, respectively.

Let the components of the state vector introduce the following dimensionless group:

$$\bar{T}_i = (c^2/EI_n)T_i \quad \bar{U}_i = (1/c)U_i \quad i = t, n, b$$
$$\bar{M}_i = (c/EI_n)M_i \quad \bar{\Omega}_i = \Omega_i \tag{c}$$

where E is the Young's modulus, I_n is the moment of inertia about the normal axis **n**, and $c = R/\cos\alpha$.

The nonzero elements of $[D]$ in dimensionless form for the helical bar made of an elastic, homogeneous, and isotropic material can be obtained as

$$\bar{D}_{1,2} = -\bar{D}_{2,1} = \bar{D}_{4,5} = -\bar{D}_{5,4} = \bar{D}_{7,8} = -\bar{D}_{8,7} = \bar{D}_{10,11} = -\bar{D}_{11,10} = \cos\alpha$$
$$\bar{D}_{1,7} = I_n/(Ac^2)$$
$$\bar{D}_{2,3} = -\bar{D}_{3,2} = \bar{D}_{5,6} = -\bar{D}_{6,5} = \bar{D}_{8,9} = -\bar{D}_{9,8} = \bar{D}_{11,12} = -\bar{D}_{12,11} = \sin\alpha$$
$$\bar{D}_{2,6} = -\bar{D}_{3,5} = \bar{D}_{5,11} = \bar{D}_{11,9} = \bar{D}_{12,8} = 1$$

Downloaded 04 May 2010 to 171.66.16.26. Redistribution subject to ASME license or copyright; see http://www.asme.org/terms/Terms_Use.cfm

$$\bar{D}_{2,8} = \alpha_n EI_n/(GAc^2)$$

$$\bar{D}_{3,9} = \alpha_b EI_n/(GAc^2)$$

$$\bar{D}_{4,10} = EI_n/(GJ)$$

$$\bar{D}_{6,12} = I_n/I_b$$

where G is the shear modulus, I_b is the area moment of inertia about the binormal axis $\mathbf{b}$, and J is the torsional area inertia moment. The Timoshenko's coefficients are represented by α_n and α_b.

The state vectors at the ends of the element are related by the transfer matrix, $[F]$ as

$$\{S(\phi_j)\} = [F(\phi_j - \phi_i)]\{S(\phi_i)\}. \qquad (d)$$

The element transfer matrix can be obtained effectively using the following fundamental expression (Pestel and Leckie, 1963; Yıldırım, 1996b, 1997a–b)

$$[F(\phi)] = \sum_{k=0}^{11} \Phi_k(\phi)[D]^k \qquad (e)$$

where each $\Phi_i(\phi)$, $(k = 0, 1, \ldots, 11)$ is a function of scalar infinite series in ϕ and it can be written in the form of

$$\Phi_k(\phi) = \frac{\phi^k}{k!} + \sum_{i=0}^{\infty} T_{k+1}^{(i)} \quad [k = 0, 1, \ldots, 11]. \qquad (f)$$

Each element $T_k^{(i)}$ in the series (f) is related to the previous element $T_k^{(i-1)}$ by (Yıldırım, 1995, 1996a–b, 1997a)

$$T_{2k+1}^{(i)} = \frac{\phi^2\{T_{11}^{(i-1)}a_{6-k} + T_{2k-1}^{(i-1)}\}}{(11 + 2i)(12 + 2i)} \quad \text{for} \quad k = 0, 1, \ldots, 5$$

$$T_{2k}^{(i)} = \frac{\phi^2\{T_{12}^{(i-1)}a_{7-k} + T_{2k-2}^{(i-1)}\}}{(12 + 2i)(13 + 2i)} \quad \text{for} \quad k = 1, 2, \ldots, 6. \qquad (g)$$

When $k \leq 0$ for any i, $T_k^{(i)} = 0$. In the above algorithm,

$$a = p_{2i} \text{ and } p_{2i-1} = 0 \quad \text{for} \quad i = 1, \ldots, 6 \qquad (h)$$

and p is the coefficients of the characteristics determinant $|[D] - \lambda[I]|$ of the differential matrix ($[I]$ = unit matrix, λ = characteristic root).

The first terms of $T_k^{(i)}$ in the series are defined by

$$T_{2k+1}^{(0)} = (\phi^{12}/12!)a_{6-k} \quad \text{for} \quad k = 0, 1, \ldots, 5$$

$$T_{2k}^{(0)} = (\phi^{13}/13!)a_{7-k} \quad \text{for} \quad k = 1, 2, \ldots, 6. \qquad (i)$$

When the coefficients a_k of the characteristic polynomial given by (j) are available, $T_k^{(i)}$'s are computed recursively by (g), then using Eqs. (e) and (f) the transfer matrix $[F(\phi)]$ is obtained.

$$\lambda^{12} - a_1\lambda^{10} - a_2\lambda^8 - a_3\lambda^6 - a_4\lambda^4 - a_5\lambda^2 - a_6 = 0 \quad (j)$$

Downloaded 04 May 2010 to 171.66.16.26. Redistribution subject to ASME license or copyright; see http://www.asme.org/terms/Terms_Use.cfm

Numerical Study of Unsteady Flow Around Airfoil With Spoiler

Cheng Xu
National Measurement Centre,
Mechanical Metrology,
Singapore Productivity & Standards Board,
One Science Park Drive
Singapore 118221

W. W. H. Yeung
School of Mechanical and
Production Engineering,
Nanyang Technological University,
Singapore 639798

A discrete vortex model based on the panel method has been developed to simulate the two-dimensional unsteady separated flow generated by the rapid deployment of a spoiler on the upper surface of an airfoil. This method represents the boundary surfaces by distributing piecewise linear-vortex and constant source singularities on discrete panels. The wake of the spoiler and airfoil is represented by discrete vortices. At each sharp edge, a vortex sheet is used to feed discrete vortices at every time-step to form the downstream wake. The length and strength of each shed vortex sheet are determined by the continuity equation and a condition such that the flow, the net force, and the pressure difference across the vortex sheet are zero. The flow patterns behind the spoiler at different time-steps are presented. The pressure distributions on the airfoil based on the unsteady Bernoulli's equation are compared, where possible, with the experimental results and other computational results. The adverse lift effects have been obtained, and similar effects have been measured in experiments.

1 Introduction

Spoilers for aeronautical applications are conventionally located on the upper surface of the wing or airfoil near the trailing edge, and when deployed have the long-term effect of increasing drag and decreasing lift, thus controlling symmetric and asymmetric lift. One advantage of spoilers is that they can be used in roll control in the presence of high lift systems. An interesting question is how far spoilers can be used as fast aerodynamic devices in active control technology applications to improve the efficiency and cost-effectiveness of military and civil aircraft. In order to use spoilers for rapid maneuver control or gust alleviation, high rates of deployment are required. At such high rates of deployment, the spoiler effects are aerodynamically unsteady. Experimental studies by Consigny et al. (1984) reported that a period of adverse lift is induced on the airfoil before the intended reduction take place. The cause of the adverse lift is the formation of a very strong vortex behind the spoiler which induces a large suction on the rear upper surface of the airfoil. Eventually, the vortex is convected away by the stream leaving a fluctuating region of reduced total pressure behind the spoiler and a reduction in overall circulation. This is rather similar to the vortex build up and shedding which occurs during dynamic stall of a rapidly pitching airfoil. This phenomenon is strongly two-dimensional and a two-dimensional calculation method which models the vortex sheet evolution can be expected to give useful predictions for the initial phase of the flow. Although spoilers have been used extensively over years, there has been little theoretical information available on their performance characteristics, particularly transient behavior.

The vortex model is a powerful method for simulating high Reynolds number separated flows of unsteady nature in two and three dimensions. This method is incompressible but relatively inexpensive to compute, and because of its Lagrangian basis gives a much better delineation of the structure of a rolled-up vortex sheet at high Reynolds numbers than finite difference or element methods. The restriction to incompressible flow is not considered to be serious for the present purposes since adverse lift occurs over a range of Mach numbers and the qualitative development of the phenomenon is the same. Recently, Tou and Hancock (1987) have incorporated the point vortex method into their model of vortex sheet elements to study the flow around a rapidly deployed spoiler on an airfoil. They introduced a Kutta pressure difference condition at each separation point which relies on estimating the time-dependent unsteady surface pressure distribution in the base pressure region. However, the way of estimating total head change was crude. Computed results about lift variation with time are highly irregular when the angle of spoiler deployment is small (e.g., a spoiler deployment 0 deg → 20 deg as seen in Fig. 1) mainly because the method cannot satisfactorily deal with reattached flow behind the spoiler. Bearman et al. (1989) reported the studies on the effects of rapid spoiler deployment on the transient forces on an airfoil using the point vortex method based on a multistage analytical transformation. However, the conformal mapping is difficult to be extended to three-dimensional flow analysis and in addition the spoiler could not be continuously modeled down to the fully closed position because of the implied curvature of the spoiler resulting from the transformation. These two methods could not employ the initial condition based on the deployed velocity which is very important to the rapid deployment of spoiler. In this paper, a more realistic initial condition is presented.

In order to apply the vortex method in real viscous flow problems, viscous effects should be incorporated into the numerical scheme. There are two ways to consider the viscous flows using the discrete vortex method (Sarpkaya, 1989). One is the random vortex approach (Slaouti and Stansby, 1992). It is based on the fact that the location of a particle moving at random is determined by the diffusion equation. The method reproduces the viscous diffusion in a statistical sense. Spalart et al. (1983) noted that this method requires a huge number of vortices and extremely accurate integration of the transport term, so that the scattering it creates does not dominate random walk. Another approach is the core spreading vortex method (Sarpkaya, 1989; Maixner, 1996). In this method, each vortex blob has a vortex core expressed by the fundamental solution of the two-dimensional diffusion equation and the core-shape of the vortex spreads with time. This method allows all the vortices introduced to be distorted and diffused when encountering either a real vortex or near a solid boundary. The vortex blob method is used here to regularize the roll-up of the free

Contributed by the Applied Mechanics Division of THE AMERICAN SOCIETY OF MECHANICAL ENGINEERS for publication in the ASME JOURNAL OF APPLIED MECHANICS.

Discussion on this paper should be addressed to the Technical Editor, Professor Lewis T. Wheeler, Department of Mechanical Engineering, University of Houston, Houston, TX 77204-4792, and will be accepted until four months after final publication of the paper itself in the ASME JOURNAL OF APPLIED MECHANICS.

Manuscript received by the ASME Applied Mechanics Division, Sept. 30, 1996; final revision, July 24, 1997. Associate Technical Editor: S. A. Berger.

 Copyright © 1998 by ASME

Downloaded 04 May 2010 to 171.66.16.26. Redistribution subject to ASME license or copyright; see http://www.asme.org/terms/Terms_Use.cfm

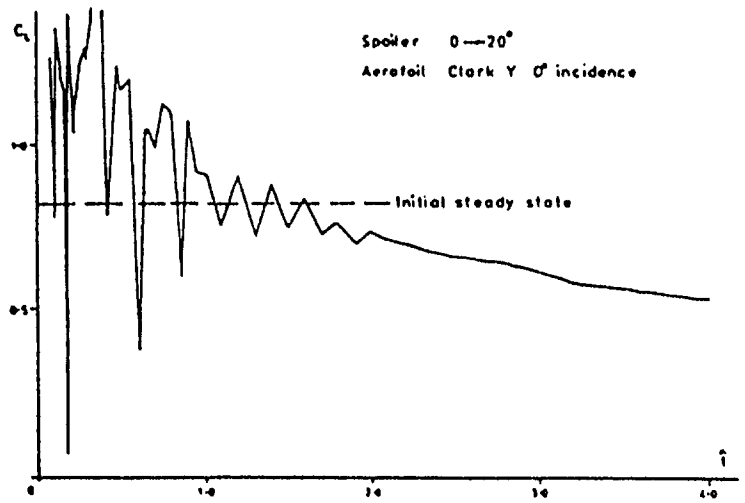

Fig. 1 The variation of the lift with time (by Tou and Hancock, 1987)

vortex (Chorin, 1973). This method inserts an artificial smoothing parameter r_0 into the equation governing the vortex motion. Convergence studies indicate that the vortex blob method is capable of resolving spiral roll-up in two-dimensional flow (Anderson and Greengard, 1991). Aside from roll-up of the vortex, another difficult aspect of the problem is separation at a sharp edge. In the present analysis, a new procedure is established for simulation of the vortex shedding process. Although the vortex method has its limitations (Anderson and Greengard, 1991), it is still widely used (Maixner, 1996; Lee et al., 1993).

The vortex model has been used extensively to compute separating flow past a sharp edge (Sarpkaya, 1989). Such computations employ a time-stepping procedure in which discrete vortex elements of suitable strength are released from the edge at regular time intervals. The computational method presented here involves four stages. The first stage is the potential flow calculation, in which the surfaces of the airfoil and spoiler are discretized into panels. Every panel is represented by a linear vortex and a constant source with their strengths determined by satisfying the normal flow condition at the control point. The unsteady separated flow associated with an airfoil and a rapidly extended spoiler is calculated by using the discrete vortex method involving the other three stages; namely, vortex shedding, convection, and diffusion. Attempts are made in this work to introduce a realistic unsteady Kutta condition at the separation points and a more realistic initial condition. In this paper, an 11 percent thick Joukowsky airfoil fitted with a spoiler of 10 percent c (c is the chord of the airfoil) in length above the airfoil surface and hinged at 70 percent c measured from the leading edge of airfoil is considered. The spoiler is deployed rapidly from 0 deg to a steady angle δ within a nondimensional time $U_\infty t_0/c$. The adverse lift effects which have been obtained are similar to the measurements in the experiment of Consigney et al. (1984). The irregular behavior of the lift with time in the present calculations is found to be less than that reported by Tou and Hancock (1987).

2 Method of Calculation

2.1 Mathematical Model. Consider a two-dimensional system configuration consisting of an airfoil with a spoiler in an incompressible flow. The flow field can be represented by a total scalar velocity potential Φ such that

$$\nabla\Phi = \nabla\phi + \nabla\phi_\infty = \mathbf{V} + \mathbf{V}_\infty \tag{1}$$

where $\nabla\phi = \nabla\phi_b + \nabla\phi_w = \mathbf{V} = \mathbf{V}_b + \mathbf{V}_w$. While ϕ_∞ and $\mathbf{V}_\infty$ represent the velocity potential of the incoming flow and its velocity at infinity, ϕ_b, ϕ_w and $\mathbf{V}_b$, $\mathbf{V}_w$ respectively represent the disturbance velocity potentials and velocity vectors due to the solid bodies (''b'') and the wake (''w''). Both the total and disturbance velocity potentials satisfy Laplace's equation

$$\nabla^2\Phi = \nabla^2\phi = 0. \tag{2}$$

Using the Green's function approach and Morino's formulation (Morino and Tseng, 1978) in the global coordinate system, Eqs. (1) and (2) are transformed into an integral equation

$$\phi(p) = \frac{1}{2\pi}\int_w \phi_w(q)\frac{\partial G(p,q)}{\partial n_w}\,ds + \frac{1}{2\pi}\int_b \left[\phi(q)\frac{\partial G(p,q)}{\partial n} - G(p,q)\frac{\partial\phi(q)}{\partial n}\right]ds \tag{3}$$

where p represents a field point and q is the running index over all panels. $\mathbf{n}$ and $\mathbf{n}_w$ are the unit outward vectors normal to the body and vortex sheets in the wake. The Green's function is given by $G = \ln(1/r)$, where r is the distance between p and q. Equation (3) provides the value of $\phi(p)$ at any point in the flow field in terms of $\phi_w(q)$, $\phi(q)$, and $\partial\phi(q)/\partial n$.

The boundary condition on the surface requires that the velocity component normal to the solid surface must be zero:

$$\nabla\Phi\cdot\mathbf{n} = (\nabla\phi_\infty + \nabla\phi_b + \nabla\phi_w)\cdot\mathbf{n} = 0. \tag{4}$$

The calculation of the pressure on the airfoil surface is based on the unsteady Bernoulli's equation. The pressure coefficients on the elements which are outside of the wake can be evaluated from

$$C_p = 1 - \frac{V^2}{U_\infty} - \frac{2}{U_\infty}\frac{\partial\Phi}{\partial t} \tag{5}$$

where V is the total velocity. Calculation of the unsteady pressure coefficient, $\partial\Phi/\partial t$, is found by the backward difference

$$\left(\frac{\partial\Phi}{\partial t}\right)_k = (\phi_k - \phi_{k-1})/(t_k - t_{k-1}). \tag{6}$$

For those elements lying inside the wake

$$C_p = C_{\text{pref}} - \left(\frac{V^2}{U_\infty^2} - \frac{V_{\text{ref}}^2}{U_\infty^2}\right) - \frac{2}{U_\infty^2}\int_{\text{ref}}\frac{\partial V}{\partial t}\,ds + \frac{\Delta H}{0.5\rho U_\infty^2}, \tag{7}$$

where ΔH is related to any total head change along the contour, C_{pref} is either the pressure coefficient at the spoiler tip or the

Downloaded 04 May 2010 to 171.66.16.26. Redistribution subject to ASME license or copyright; see http://www.asme.org/terms/Terms_Use.cfm

airfoil trailing edge either inside or outside of the wake since there should be continuity of static pressure. The lift force can be determined by integration of the pressure distribution around the airfoil and spoiler.

The boundary surface can be discretized into small straight segments. The control point for each segment is located at the segment center. The normal to the surface is approximated by the perpendicular to the straight segment. The distributions of the vortex and source on each segment are assumed to be linear and constant, respectively. The velocity potential at a field point P (ξ_P, η_P) due to a line segment (from point $(\xi_{q+1}, 0)$ to $(\xi_q, 0)$) of length $(\xi_{q+1} - \xi_q)$ with a constant strength source (σ) in a local straight-segment coordinate (ξ, η) is

$$\phi_\sigma = \frac{\sigma}{4\pi}\left[(\xi_p - \xi_q)\ln r_q^2 - (\xi_p - \xi_{q+1})\ln r_{q+1}^2 + 2\eta_p(\theta_{q+1} - \theta_q)\right] \quad (8)$$

where

$$\theta_k = \arctan\frac{\eta_p}{\xi_p - \xi_k}, \quad k = q, q+1$$

$$r_k^2 = (\xi_p - \xi_k)^2 + \eta_p^2, \quad k = q, q+1.$$

The velocity potential corresponding to a linearly distributed vortex sheet is

$$\phi_\gamma = -\frac{\gamma_q}{2\pi}\left[(\xi_p - \xi_q)\theta_q - (\xi_p - \xi_{q+1})\theta_{q+1} + \eta_p \ln\frac{r_q}{r_{q+1}}\right] - \frac{\gamma_{q+1} - \gamma_q}{4\pi(\xi_{q+1} - \xi_q)}\left[(\xi_p^2 - \eta_p^2 - \xi_q^2)\theta_q - (\xi_p^2 - \eta_p^2 - \xi_{q+1}^2)\theta_{q+1} + 2\xi_p\eta_p \ln\frac{r_q}{r_{q+1}} + \eta_p(\xi_q - \xi_{q+1})\right]. \quad (9)$$

By substituting singularity Eqs. (8) and (9) into Eq. (3) and by using the boundary conditions (4), a set of linear algebraic equations for the boundary vortices, source, and shedding vortices are obtained in the following form:

$$\sum_{q=1}^{N+Nw} A_{pq}\gamma_q + \sigma\sum_{q=1}^{N} B_{pq} = -[U(t) + u_w, V(t) + v_w]\cdot n_p. \quad (10)$$

A_{pq} and B_{pq} are influence coefficients. N is the number of the bound elements of the airfoil-spoiler configuration, and Nw is the number of the wake sheet elements. u_w and v_w can be calculated by

$$u_w = \sum_{m=1}^{Nsv} u_{pm}, \quad v_w = \sum_{m=1}^{Nsv} v_{pm} \quad (m = 1, \ldots, N_{sv})$$

$$u_{pm} = \Gamma_m \frac{1}{2\pi}\left[\frac{y_p - y_m}{(x_p - x_m)^2 + (y_p - y_m)^2}\right]$$

$$v_{pm} = -\Gamma_m \frac{1}{2\pi}\left[\frac{x_p - x_m}{(x_p - x_m)^2 + (y_p - y_m)^2}\right] \quad (11)$$

and where N_{sv} is the number of the shedding vortices. $(U(t), V(t))$ here includes the freestream velocity and the boundary velocity due to the motion of the boundary.

The discrete vortex method may cause a certain amount of leakage into the body. This leakage is a source of error. In the present calculation, the vortices shed from the trailing edge and the tip of the spoiler may have interactions between the vortices and the body. Therefore, attention must be paid to the treatment of vortices when they come close to the body. A barrier near the solid surface of thickness r_0 is introduced to prevent vortices drawing too near to the surface. When the vortices move into the barrier they are removed from the calculation.

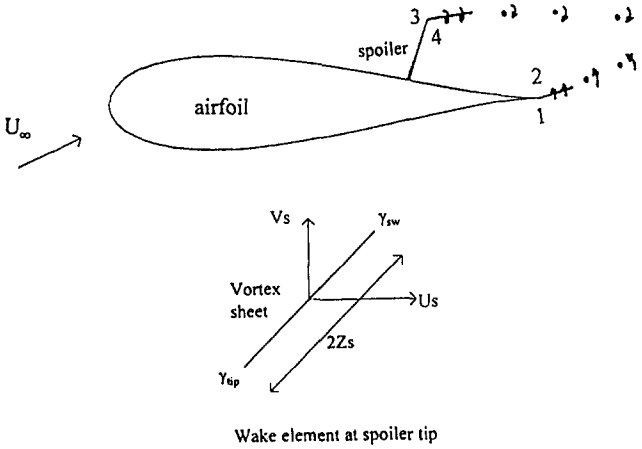

Fig. 2 The flow around an airfoil with aspoiler

2.2 Basic Equations. The flow, which is assumed to be two-dimensional separates at the spoiler tip and the trailing edge of the airfoil as shown in Fig. 2. The bound vorticity field is represented by linear piecewise vorticity and constant source along each panel element. To ensure continuity the vorticity at the spoiler hinge on the airfoil inside the wake region is taken to be zero; similarly, the vorticity at airfoil trailing edge inside the wake region is zero. The vorticity at the spoiler tip and airfoil trailing edge continues linearly along the two wake elements. The solution for the flow about an airfoil-spoiler configuration with sudden deployment of spoiler is calculated at successive intervals of time, t_k $(t_1 = t_0, k = 2, 3, 4, \ldots)$. The velocity field is calculated at the locations of each vortex as a sum of attached potential flow around the body and a velocity field calculated by the Biot-Savart law due to all the vortices in the flow.

It is assumed that during the time interval 0 to t_0, the spoiler angle increases from 0 deg to δ. At time-step $t_k(k = 2, 3, 4, \ldots)$, the airfoil is divided into $N_f - 1$ straight elements while the spoiler is divided into $N_s - 1$ elements. In the present calculation, $N_f = 57$ and $N_s = 5$. At time t_k, the variables are

(i) the vortex strength of the airfoil bound vortices $\gamma_A(i)$ at airfoil nodes, $I = 1, N_f$;
(ii) the vortex strength of spoiler bound vortices $\gamma_s(i)$ at spoiler nodes, $I = 1, N_s$;
(iii) the length of the spoiler tip wake element $2Z_s$, the vortex strength of the wake element γ_{sw} and the angle of the wake element φ_s;
(iv) the length of the airfoil trailing edge wake element $2Z$, the vortex strength of the wake element γ_w and the angle of the wake element φ; and
(v) the uniform source σ on the airfoil.

The solution at the initial time-step needs to be considered as a special case as discussed in Section 4. The number of unknowns at time t_k are $(N_f + N_s + 5)$, i.e.,

(i) $\gamma_A(i)$ on airfoil $I = 1, N_f - 1$;
(ii) $\gamma_s(i)$ on spoiler $I = 2, N_s$;
(iii) γ_{sw}, φ_s, and $(2Z_s)_k$ at the spoiler tip wake element;
(iv) γ_w, φ, and $(2Z)_k$ at the airfoil trailing edge wake element; and
(v) σ the uniform source along the airfoil.

Downloaded 04 May 2010 to 171.66.16.26. Redistribution subject to ASME license or copyright; see http://www.asme.org/terms/Terms_Use.cfm

The basic equations to be satisfied are

(i) $(N_f + N_s - 2)$ equations of normal flow condition on airfoil-spoiler elements;

(ii) conservation of circulation; The sum of circulation around the wake and body is kept constant. Hence

$$\sum_{q=1}^{2N+Nw} \Gamma_q + \sum_{m=1}^{Ns} \Gamma_m = \Gamma_0 \qquad (12)$$

where the first term on the left-hand side is circulation around a fluid curve enclosing the airfoil-spoiler system, Γ_m is circulation of each shed vortex, and Γ_0 is circulation of the system before the spoiler deployment.

(iii) unsteady Kutta condition. (This part is explained in Section 3).

2.3 Diffusion of Vorticity. The vortex method is based on Prandtl's premise that the fluid motion can be decomposed into a viscous inner flow and an inviscid outer flow. The method is meant to approximate the outer flow, and it neglects viscous effects such as energy dissipation and flow displacement due to boundary layers. Nevertheless, a recurring theme in fluid dynamics is that the vortex method provides an asymptotic approximation for slightly viscous flow (Chorin, 1973). The issue is somewhat complicated by the fact that the vortex motion is inferred from vortex blob computations with $r_0 > 0$. However, the work of Nagano et al. (1982) and Kiya et al. (1982) supports this approach. The present work seeks to extend this conclusion to unsteady flow around airfoil-spoiler problems. It is noted that a potential vortex induces the velocity whose magnitude is in inverse proportion to the distance from its center. The velocity V induced by a vortex in a viscous fluid at rest is given by (Nagano et al., 1982).

$$V = \frac{\Gamma_{mo}}{2\pi r}\left\{1 - \exp\left(-\frac{r^2}{4\nu t}\right)\right\} \qquad (13)$$

where ν is the kinematic viscosity of the fluid, t the time, and r the distance from the center of the vortex. Velocity V increases with r from zero to a maximum (at $r = r_0$) and then falls asymptotically to zero. The distance r_0 is a function of time and viscosity. If the vortex is concentrated at a point at $t = 0$, the viscous core radius r_0 is given by $r_0 = 2.242\sqrt{\nu t}$. Here t is the time required for the formation of shed vortices. The difference in the velocities induced by a potential and viscous vortex is small when r is larger than r_0, but it becomes larger as r becomes smaller than r_0. It seems reasonable to assume that each of the point vortices has a characteristic radius r_0 which varies with the kinematic viscosity of the fluid and the time elapsed after the shedding of the vortices.

3 Unsteady Kutta Condition

Flow separates at sharp edges because of the surface discontinuity. To simulate this phenomenon, the discrete vortex method creates a point vortex or a vortex sheet near the tip of a sharp edge and sheds it into the flow field at each incremental time-step. The strength and location of each vortex introduced in the flow have to be determined. The usual assumption (Brown and Michael, 1955; Rott, 1956) is that no pressure difference can be sustained across a sharp edge such as the trailing edge of an airfoil and its wake. As a result, the vortex sheet feeding discrete vortices is force free. In the present method, vortices are created by a vortex sheet extending from a sharp edge (e.g., the trailing edge of the airfoil) as shown in Fig. 3.

We adopt a model in which the vorticity shed is presented in the vortex sheet at the spoiler tip whose circulation Γ_{ms} is allowed to change with time (Fig. 2). This requires feeding of vorticity and results in a nonvanishing pressure across a vortex sheet of the unsteady potential. In order to satisfy momentum conservation approximately, the sum of forces on the vortex sheet must be zero (Edwards and Cheng, 1982). If the length of the spoiler wake vortex sheet is $2Zs$, the force on the vortex sheet is given by

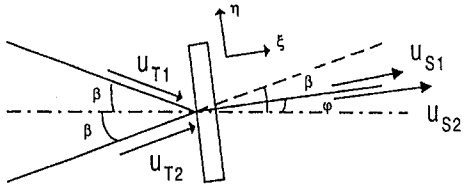

Fig. 3 Kutta conditions

$$F = -\rho \frac{d\Gamma_{ms}}{dt} Z_s + \rho V^* \Gamma_{ms} = 0 \qquad (14)$$

where V^* is the velocity of the local flow at the midpoint of the vortex sheet. From Eq. (14),

$$\left[\frac{d(\gamma_{tip} + \gamma_{sw})}{dt} Z_s + (\gamma_{tip} + \gamma_{sw}) \frac{dZ_s}{dt}\right] = (\gamma_{tip} + \gamma_{sw}) V^* \qquad (15)$$

where γ_{tip} and γ_{sw} are the vortex strength at both ends of the wake element at the spoiler tip.

At any time step, it is necessary to invoke a pressure Kutta condition linking the pressures at the spoiler tip and the trailing edge. The outside and inside of the wake element at the airfoil trailing edge are numbered as 1 and 2, respectively, whereas 3 and 4 are for those at the spoiler tip (Fig. 2). From the unsteady Bernoulli's equation

$$p_1 + \frac{1}{2}\rho V_1^2 + \rho \frac{\partial \Phi_1}{\partial t} = p_3 + \frac{1}{2}\rho V_3^2 + \rho \frac{\partial \Phi_3}{\partial t}. \qquad (16)$$

Hence

$$p_3 - p_1 = -\rho\left\{\frac{(V_3 + V_1)}{2}(V_3 - V_1) + \frac{\partial(\Phi_3 - \Phi_1)}{\partial t}\right\}. \qquad (17)$$

Applying the Bernoulli's equation along the surface "4" to "2,"

$$p_4 - p_2 = -\rho\left(\frac{(V_4 + V_2)(V_4 - V_2)}{2} + \int_4^2 \frac{\partial V}{\partial t}\, dt\right). \qquad (18)$$

The Kutta pressure difference condition is

$$p_3 - p_1 = p_4 - p_2. \qquad (19)$$

Equation (19) is nonlinear in γ and is solved using the Newton-Raphson scheme. Equations (15) and (19) permit the strengths of the nascent vortices to be determined.

In order to determine the position of the nascent vortices, the flow direction and velocity of the vortex sheet at the sharp edge should be found. Assume that the flow separates at the trailing edge as shown in Fig. 3, and the boundary layers of finite thickness are represented by a vortex sheet of zero thickness. In order to reduce the number of unknown variables, at the time step t_k, it is assumed that the inclination φ of the vortex sheet element can be found from the velocity associated with the wake element at the earlier time step t_{k-1}, i.e.,

$$\tan(\varphi)_k = [\tan\beta + (V_f)_{k-1}/(U_f)_{k-1}]/2 \qquad (20)$$

where V_f and U_f are the velocity components of the trailing edge

Downloaded 04 May 2010 to 171.66.16.26. Redistribution subject to ASME license or copyright; see http://www.asme.org/terms/Terms_Use.cfm

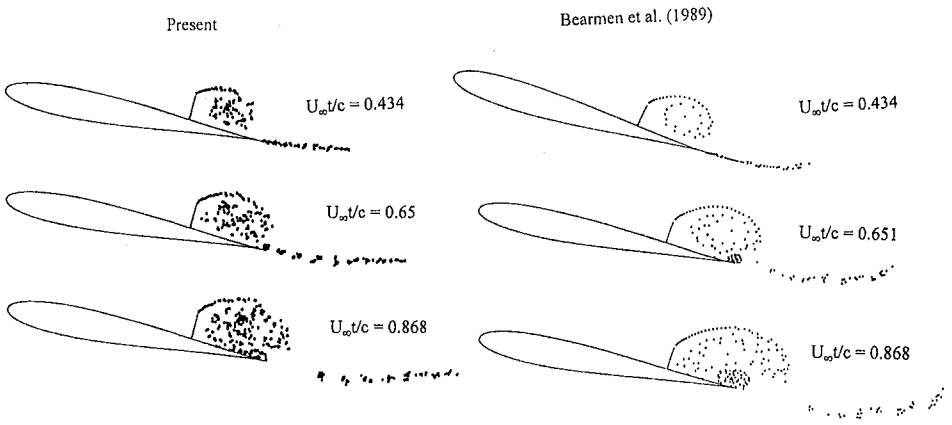

Fig. 4 The unsteady flow pattern during spoiler deployment (α = 12 deg, δ = 90 deg)

wake sheet in a global coordinate system and 2β is the trailing edge angle.

The continuity equation is applied to an infinitesimal control volume at the trailing edge. For a sufficiently small control volume (as shown in the Fig. 3), the equation can be written as

$$\int_s \rho V ds = 0 \tag{21}$$

where V is the velocity and s is the control surface. Equation (21) yields

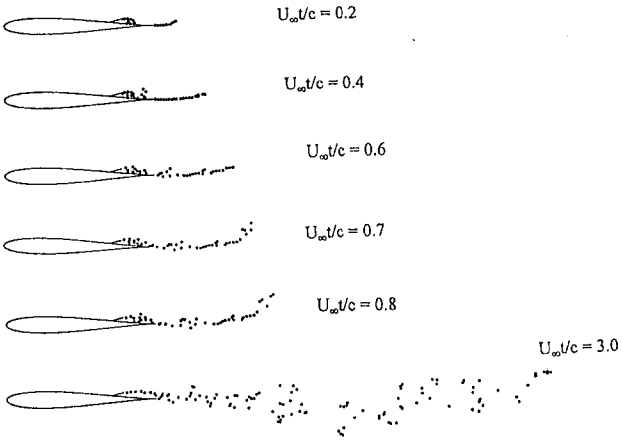

Fig. 5 The unsteady flow pattern during spoiler deployment (α = 0 deg, δ = 20 deg)

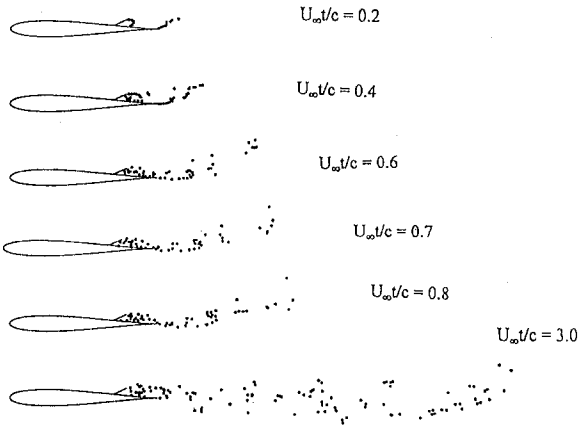

Fig. 6 The unsteady flow pattern during spoiler deployment (α = 0 deg, δ = 30 deg)

$$u_{S1} + u_{S2} = u_{T1} \cos(\beta + \varphi) + u_{T2} \cos(\beta - \varphi). \tag{22}$$

Since tangential velocities can be expressed as a function of vortex sheet strength, one has

$$u_{T1} = \frac{\gamma_{N-1} + \gamma_N}{2} \tag{23}$$

$$u_{T2} = \frac{\gamma_1 + \gamma_2}{2} \tag{24}$$

where γ_N, and γ_{N-1} are the vortex strengths at both ends of the upper surface element near the trailing edge, whereas γ_1 and γ_2 are for those at the lower surface element near the trailing edge.

With the fact that the vortex sheet moves with the local velocity of the shear layer, the length of the vortex sheet can be written as

$$\begin{aligned}(2Z)_k &= [(U_f)_k^2 + (V_f)_k^2]^{0.5}(t_k - t_{k-1}) \\ &= (u_{S1} + u_{S2}) \times (t_k - t_{k-1})/2.\end{aligned} \tag{25}$$

In the present model, the location and the strength of the wake vortex sheet are determined separately. The usual difficulty that the strength of the nascent vortex is oversensitive to its location is thus eliminated.

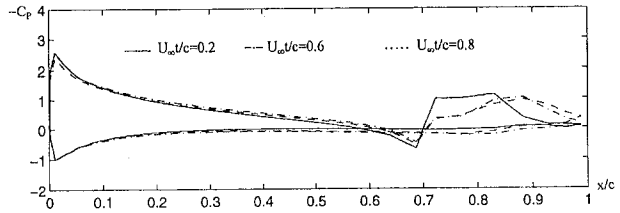

Fig. 7 The instantaneous pressure distribution on the airfoil (α = 6 deg, δ = 30 deg)

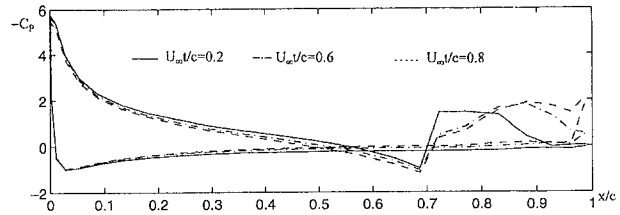

Fig. 8 The instantaneous pressure distribution on the airfoil (α = 12 deg, δ = 60 deg)

Downloaded 04 May 2010 to 171.66.16.26. Redistribution subject to ASME license or copyright; see http://www.asme.org/terms/Terms_Use.cfm

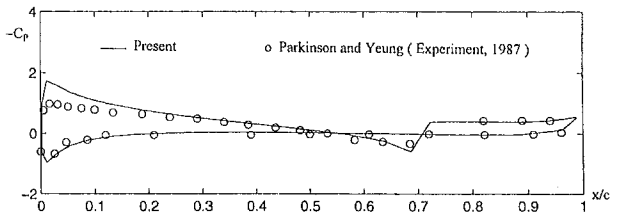

Fig. 9 Long-term pressure on the airfoil with time (α = 6 deg, δ = 30 deg)

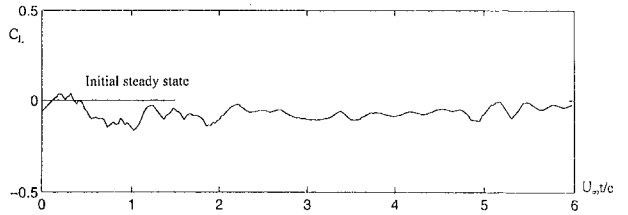

Fig. 11 The variation of the lift with time (α = 0 deg, δ = 20 deg)

4 Initial Conditions

Conditions at the initial time need to be established in order to calculate the wake element lengths and inclinations. During the first step of the calculation, another assumption needs to be taken into consideration since the unsteady Kutta condition cannot be invoked. It is assumed that the spoiler angle is increased from 0 deg to δ at a angular speed ω during the time interval t_0. The first vortex is introduced near the spoiler tip such that its circulation Γ_{ms0}, as suggested by Sarpkaya (1989), is given by

$$\Gamma_{ms0} = 0.5V^2 t_0 \tag{26}$$

where V is the velocity at the outer edge of the shear layer emanating from the spoiler tip, and the time increment is $t_0 = \delta/\omega$. Similarly, another vortex near the trailing edge is introduced, but with the velocity updated. When the spoiler is rapidly deployed with the time increment t_0, the circulation of the airfoil-spoiler configuration is kept as the same value as that of the airfoil without the spoiler. After the first step, the unsteady Kutta condition is invoked and an iterative process is required until the wake elements converge.

The time taken, t_0, for the spoiler to open from its fully retracted position to a certain angle, δ, depends on the spoiler deployment velocity. To compare with another computational work (Bearman et al., 1989), the initial time is chosen as $U_\infty t_0/c = 0.002$ for the case of the spoiler deployed instantaneously from δ = 0 deg to 90 deg, α = 12 deg (α is the incidence of the airfoil). This rate corresponds to the order of 40,000 deg/sec when the aircraft is at subsonic speeds. For other cases in the calculation, the initial time is chosen as $U_\infty t_0/c = 0.01$ which corresponds to the spoiler velocity approximately equal to 2000 deg/sec. Therefore, the strength and length of the first vortex sheet depend on the spoiler deployment velocity. The present method gives results which are close to the experimental ones, unlike the other methods (Bearman et al., 1989; Tou and Hancock, 1987) in which the initial condition corresponds to the sudden appearance of the spoiler deployed into the pre-established airstream at $t_0 = 0$.

5 Results and Discussion

In all calculations presented here, an 11 percent thick Joukowsky airfoil fitted with a spoiler of 10 percent c in length above an airfoil surface and hinged at 70 percent c measured from the leading edge of the airfoil is considered. To compare the present results with an inviscid computation (Bearman et al., 1989), the Reynolds number is chosen as 6.0×10^7 where the spoiler deploys from 0 deg to δ = 90 deg at α = 12 deg. To compare other computations with measurements by Parkinson and Yeung (1987), the Reynolds number used in all other calculations are chosen to match the experimental value of 3×10^5.

The time-step $U_\infty \Delta t/c$ which directly affects the vortex shedding process, i.e., creation of nascent vortices, is an important parameter in the calculation. After some numerical calculations, the maximum allowable nondimensional time step $U_\infty \Delta t/c$ = 0.015 is prescribed to minimize numerical errors in the time integration.

When the spoiler is deployed instantaneously from 0 deg to δ = 90 deg and α = 12 deg, the nondimensional time increment is chosen as $U_\infty \Delta t/c$ = 0.002. The computed flow patterns at $U_\infty t/c$ = 0.434, 0.650, and 0.868 are given in Fig. 4. The flow patterns are similar to the computed results as reported by Bearman et al. (1989). For the other cases of computation, the nondimensional time increment is taken as $U_\infty \Delta t/c$ = 0.01. Figures 5 and 6 show the computed flow patterns for spoiler deployment 0 deg → 20 deg and 0 deg → 30 deg at α = 0 deg, respectively.

A strong vortex develops behind the spoiler growing in size until it starts to interact with the trailing edge. At that moment, the relatively weak vortex sheet shed from the trailing edge strengthens and starts to roll up due to the counterclockwise flow generated by the spoiler vortex. The spoiler tip vortices roll up after shedding and may mix with the vortices shed from the airfoil trailing edge. Subsequently, this trailing edge vortex starts to spread into the formation region of the spoiler vortex disrupting the vortex sheet from the spoiler tip. Eventually, the spoiler vortex may shed at a larger δ (Fig. 4) or form a long separation bubble at a smaller δ (Figs. 5 and 6). The flow patterns also show that when the spoiler angle is small, the flow behind the spoiler may reattach with the airfoil rear upper surface before the interaction of the two shedding vortices. This phenomenon was not observed in the calculations of Tou and

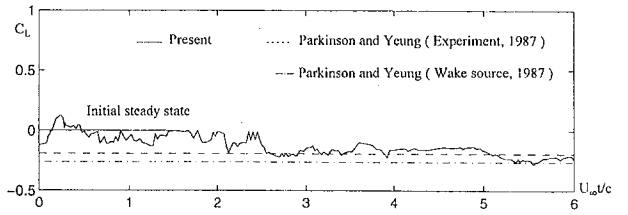

Fig. 12 The variation of the lift with time (α = 0 deg, δ = 30 deg)

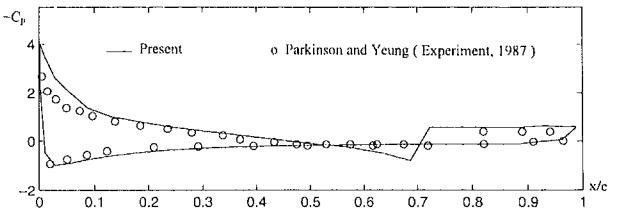

Fig. 10 Long-term pressure on the airfoil with time (α = 12 deg, δ = 60 deg)

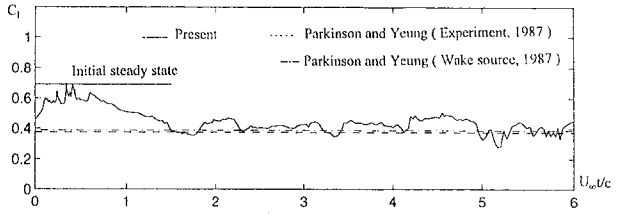

Fig. 13 The variation of the lift with time (α = 6 deg, δ = 30 deg)

Downloaded 04 May 2010 to 171.66.16.26. Redistribution subject to ASME license or copyright; see http://www.asme.org/terms/Terms_Use.cfm

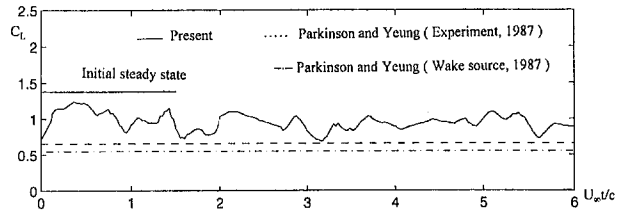

Fig. 14 The variation of the lift with time (α = 12 deg, δ = 60 deg)

Hancock (1987) and Bearman et al. (1989). The development of the spoiler vortex leads to a large suction pressure over the rear upper surface of the airfoil which lies beneath it.

The development of the pressure distributions over the airfoil surface calculated from the unsteady Bernoulli equation are shown in Figs. 7 and 8, respectively. The spoiler angle and position determine the strength and duration of the suction pressure generated. The higher the spoiler angle and the further forward the spoiler on the airfoil surface, the larger and longer duration generally is the suction pressure generated. The long-term averaged pressure distributions for a spoiler deployment 0 deg → 30 deg at α = 6 deg and 0 deg → 60 deg at α = 12 deg compared with experimental mean pressure measurements on the same thickness airfoil are shown in Figs. 9 and 10. Present computational results are in reasonable agreement with the experimental results (Parkinson and Yeung, 1987), except that an overprediction of the suction peak is found at the leading edge. This discrepancy is probably attributable to the presence of the boundary layer. The variation of the lift coefficient C_L from surface pressure integration with time is shown in Fig. 11 for a spoiler deployment 0 deg → 20 deg at α = 0 deg. The computed lift time histories corresponding to the case of the spoiler deployment 0 deg → 30 deg at α = 0 deg, 0 deg → 30 deg at α = 6 deg and 0 deg → 60 deg at α = 12 deg compared with experimental and theoretical (Parkinson and Yeung, 1987) long-term mean results are shown in Fig. 12, 13, and 14. The adverse positive lift phase due to the formation of the spoiler vortex is visible in each case of the computation. The lift first increases, owing to the continued reattachment of the flow downstream of the spoiler and the development of a strong vortex. The lift then starts to collapse at the time when the spoiler vortex starts to interact strongly with the trailing edge. After the vortex is shed, the lift oscillates as it decreases towards an asymptotically lower value. The degree of adverse lift attained depends on the spoiler deployment angle and the incidence of the airfoil. The large spoiler deployment angle and small airfoil incidence cause a large adverse lift. The computed result agrees with the experiment of Consigney et al. (1984).

Concluding Remarks

The separated time-dependent flow over an airfoil with a spoiler has been computed by the discrete vortex method. The main feature of the flow induced by a rapid spoiler deployment is the formation of a strong vortex behind the spoiler. This vortex grows rapidly causing a region of pressure suction on the rear upper surface of the airfoil behind the spoiler. The adverse lift continues to grow until the shear layer feeding the vortex starts to interact with the trailing edge. The spoiler vortex stops growing and starts to convect downstream causing the lift to drop. The adverse lift effects depend on the airfoil angle of incidence and the angle of spoiler deployment. Reasonable agreement is obtained where comparison is possible with experiment.

Acknowledgments

The suggestions of the referees led to improvements in the revised paper.

References

Anderson, C., and Greengard, C., eds., 1991, "Vortex Methods and Vortex Dynamics," *Lectures in Applied Mathematics,* Vol. 28, American Mathematical Society, Providence, RI.

Bearman, P. W., Graham, J. M. R., and Kalkanis, P., 1989, "Numerical simulation of separated flow due to spoiler deployment," *Int. Conference of Proc.: The Prediction and Exploitation of Separated Flow,* Royal Aeronautical Society, London, UK.

Brown, C. E., and Michael, W. H., 1955, "On Slender Delta Wings with Leading Edge Separation," NACA Technical Notes 3430.

Chorin, A. J., 1973, "Numerical Study of Slightly Viscous Flow," *Journal of Fluid Mechanics,* Vol. 57, pp. 785–796.

Consigney, H., Gravelle, A., and Molinaro, R., 1984, "Aerodynamic Characteristics of a Two-dimensional Moving Spoiler in Subsonic and Transonic Flow," *Journal of Aircraft,* Vol. 21, No. 9, pp. 687–693.

Edwards, R. H., and Cheng, H. K., 1982, "The Separation Vortex in the Weis-Fogh Circulation-generation Mechanism," *Journal of Fluid Mechanics,* Vol. 120, pp. 463–473.

Kiya, M., Sasaki, K., and Arie, M., 1982, "Discrete-vortex simulation of a turbulent separation bubble," *J. of Fluid Mechanics,* Vol. 120, pp. 219–244.

Lee, Y. T., Bein, T. W., Feng, J., and Merkle, C. L., 1993, "Unsteady Rotor Dynamics in Cascade," ASME *Journal of Turbomachinery,* Vol. 115, pp. 85–95.

Maixner, M. R., 1996, "Role of Secondary Vorticity in parallel Blade-Vortex Interactions," *AIAA Journal,* Vol. 34, No. 6, pp. 1195–1202.

Morino, L., and Tseng, K., 1978, "Time-Domain Green's Function Method for Three-dimensional Nonlinear Subsonic Flows," Presented at the AIAA 11th Fluid and Plasma Dynamics Conference, Seattle, WA, Paper No. 78-1204.

Nagano, S., Naito, M., and Takata, H., 1982, "A numerical analysis of two dimensional flow past a rectangular prism by a discrete vortex model," *Computer Fluids,* Vol. 10, pp. 243–259.

Parkinson, G. V., and Yeung, W., 1987, "Awake Source Model for Airfoils with Separated Flow," *Journal of Fluid Mechanics,* Vol. 179, pp. 41–57.

Rott, N., 1956, "Diffraction of a Weak Shock with Vortex Generation," *Journal of Fluid Mechanics,* Vol. 1, No. 111, pp. 111–128.

Sarpkaya, T., 1989, "Computational Method with Vortices—The 1988 Freeman Scholar Lecture," *Journal of Fluids Engineering,* Vol. 111, pp. 5–52.

Slaouti, A., and Stansby, P. K., 1992, "Flow Around Two Circular Cylinders by the Random-vortex Method," *Journal of Fluids and Structures,* Vol. 6, pp. 641–670.

Spalart, R. P., Leonard, A., and Baganoff, D., 1983, "Numerical Simulation of Separated Flows," NASA Tech. Memo. 84328.

Tou, H. B., and Hancock, G. J., 1987, "The Rapid Deployment of a Spoiler on a Two-dimensional Aerofoil," *Aeronautical Journal,* Dec., pp. 492–498.

Downloaded 04 May 2010 to 171.66.16.26. Redistribution subject to ASME license or copyright; see http://www.asme.org/terms/Terms_Use.cfm

S. Müftü
Massachusetts Institute of Technology,
Haystack Observatory,
Westford, MA 01886
Assoc. Mem. ASME

T. S. Lewis
Eastman Kodak Company,
Engineering Research Center,
901 Elmgrove Road,
Rochester, NY 14653

K. A. Cole
Eastman Kodak Company,
Web Dynamics Group,
Building 10, Kodak Park,
Rochester, NY 14652

R. C. Benson
Professor and Head of Mechanical Engineering,
Department of Mechanical Engineering,
The Pennsylvania State University,
University Park, PA 16802
Mem. ASME

A Two-Dimensional Model of the Fluid Dynamics of an Air Reverser

A theoretical analysis of the fluid mechanics of the air cushion of the air reversers used in web-handling systems is presented. A two-dimensional model of the air flow is derived by averaging the equations of conservation of mass and momentum over the clearance between the web and the reverser. The resulting equations are Euler's equations with nonlinear source terms representing the air supply holes in the surface of the reverser. The equations are solved analytically for the one-dimensional case and numerically for the two-dimensional case. Results are compared with an empirical formula and the one-dimensional air-jet theory developed for hovercraft. Conditions that maximize the air pressure supporting the web are analyzed and design guidelines are deduced.

1 Introduction

Products such as photographic film and paper are made and processed in continuous sheets known as webs. During these operations a web follows a complicated path over, under, and around various rollers, coaters, driers, and other devices. Air reversers are used in this path to change the moving direction of a coated wet web without touching it. As shown in Fig. 1, an air reverser is a large diameter hollow drum with holes in its surface. Air is pumped through these holes to create an air cushion on top of which the web can float. No contact is permitted between the web and the surface of the air reverser. The pressure distribution in the clearance between the web and the air reverser is determined by the size and distribution of the holes and the pressure inside the drum. In order to design air reversers that achieve adequate web flotation with minimum air flow, it is desirable to develop a theoretical model of the system.

Other applications of using an air cushion to float materials include externally pressurized bearings used in tape conveyance, air film conveyors used in transport of packages, and hovercraft. Even though the end result in these applications is to separate two surfaces, different hydrodynamic effects are at work. For example, at low operating clearances on the order of microns, common to tape and package conveyance, viscous forces dominate the air pressure generation. (Chandra et al., 1990; Gross, 1980, Chapter 6.5). On the other hand, in the air jet of a hovercraft, where the clearance is on the order of centimeters, the inertial forces are more important (Elsley and Devereux, 1968). In the former situation the air flow is commonly represented by the Reynolds equation and in the latter situation by Euler's equations. See Gross (1980, Chapter 5) for more on the classification of the externally pressurized interfaces. The ratio of the inertial to viscous forces in a narrow channel, given by the modified Reynolds number $\mathrm{Re}^* = \rho U h^2/\mu L$, is a good measure of which approach should be taken. In the definition of Re^*, ρ is the density and μ is the viscosity of the fluid, U is a speed representative of the flow, h is the clearance height, and L is a scale length in the flow field (Hamrock, 1994).

The weight of a hovercraft is balanced by the "cushion pressure" generated by the airjet(s) placed on the skirt of the vehicle. Analytical expressions for this pressure can be found in Elsley and Devereux (1968) for the incompressible case and in Pozzi et al. (1993) for the compressible case. An air reverser usually has a complicated hole pattern as shown in Fig. 1 and in general the flow is two-dimensional in the plane of the web. Therefore the expressions developed for the hovercraft has limited use only for air-reversers with a specific hole pattern. Here we report on the general equations governing the two-dimensional air flow in an air cushion without any restrictions on the hole pattern.

In this paper we assume that the location of the web is fixed and known. The coupling between a flexible moving web and the air flow will be presented later. The equations governing the air flow are Euler's equations for momentum balance and the mass continuity equation, both with nonlinear source terms representing the holes. These equations are averaged over the spacing between the web and the reverser to obtain a two-dimensional model of the air flow in the plane of the web. An analytical solution of these equations can be found for the one-dimensional case with a constant gap height. The two-dimensional case is solved numerically.

2 Governing Equations

A balance of the forces acting on a membrane-like web requires that the air pressure p and the "belt-wrap" pressure $T/(RL_y)$ be in equilibrium (Müftü and Benson, 1996). Here T is

Contributed by the Applied Mechanics Division of THE AMERICAN SOCIETY OF MECHANICAL ENGINEERS for publication in the ASME JOURNAL OF APPLIED MECHANICS.

Discussion on this paper should be addressed to the Technical Editor, Professor Lewis T. Wheeler, Department of Mechanical Engineering, University of Houston, Houston, TX 77204-4792, and will be accepted until four months after final publication of the paper itself in the ASME JOURNAL OF APPLIED MECHANICS.

Manuscript received by the ASME Applied Mechanics Division, Sept. 30, 1996; final revision, July 24, 1997. Associate Technical Editor: S. A. Berger.

 Copyright © 1998 by ASME

Downloaded 04 May 2010 to 171.66.16.26. Redistribution subject to ASME license or copyright; see http://www.asme.org/terms/Terms_Use.cfm

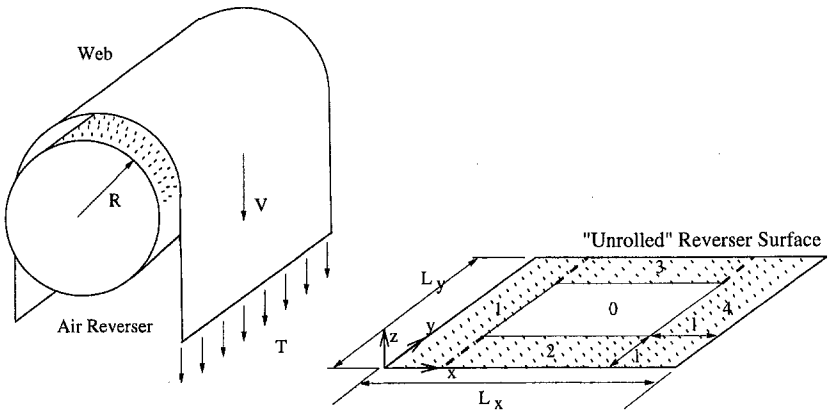

Fig. 1 Schematic view of a web moving over an air reverser under tension T and with speed V

the web tension, R is the reverser radius, and L_y is the web width, as shown in Fig. 1. For the typical values $R = 0.25$ m, $L_y = 1.5$ m, and $T = 200$ N, the pressure required to support the web is approximately $p = 533$ Pa.

The supply pressure inside the air reverser is typically $p_0 = 800$ Pa. The velocity U through one of the holes of the air reverser can be estimated from Bernoulli's equation

$$p + \tfrac{1}{2}\rho U^2 = p_0, \quad \text{or} \quad U = (2(p_0 - p)/\rho)^{1/2}, \qquad (1)$$

where ρ is the density of air, which is 1.2 kg/m^3 at room conditions (Gerhart et al., 1992). For $p_0 - p = 267$ Pa, this gives $U = 21$ m/s. Velocities throughout the flow field are generally of the same order of magnitude as U. The gap between the web and the surface of the reverser is typically about 4 mm. Using $L_x = 0.8$ m as the length scale we find Re* = 14.5. This indicates that inertial forces dominate over viscous forces. Moreover, the fact that the Reynolds number $\mathrm{Re} = \rho U h/\mu$ is 5450 indicates that the flow is turbulent ($\mu = 1.85 \times 10^{-5}$ Nsm^{-2}). Therefore, it is concluded that the effect of viscosity on pressure is negligible in the air reverser flow.

The diameter of the air reverser is large enough to make centrifugal effects negligible in the flow, so the cylindrical geometry of the problem can be unrolled onto a plane, as shown in Fig. 1. Here the x-axis is along the circumferential direction, the y-axis is along the axial direction, and the z-axis is perpendicular to the surface of the reverser. The flow field covers a rectangular region in the xy-plane. The web travels in the $+x$ direction, but its velocity ($\sim$2 m/s) is generally small compared to the velocity of the air under the web.

We assume that the clearance h between the web and the air reverser is small enough that the air flow can be considered two-dimensional. We thus neglect the velocity in the z direction and assume that the pressure p and the velocities u and v in the x and y directions, respectively, are functions of x and y but not z. The assumption of two-dimensional flow is not valid in the vicinity of each of the holes, but the details of the flow near the holes should not be important if the net effect of the mass and momentum flux through the holes is estimated correctly.

We assume that the holes in the reverser surface are sufficiently close together that they can be considered a uniform, distributed flow source. They can then be described by a single parameter α, the ratio of the total cross-sectional area of the holes to the total surface area. For circular holes of radius r_h arranged in a rectangular pattern with spacings b and c, as shown in Fig. 2(a), we have $\alpha = \pi r_h^2/bc$. At different parts of the reverser the hole density may be different. If there are no holes, $\alpha = 0$.

The equations describing the flow field can be derived by averaging the equations of conservation of mass and momentum over the clearance between the air reverser and the web (Lewis). We also assume that the flow is incompressible and neglect viscous forces. This gives

$$\frac{\partial h}{\partial t} + \frac{\partial hu}{\partial x} + \frac{\partial hv}{\partial y} = \alpha U \qquad (2a)$$

$$\rho \frac{\partial u}{\partial t} + \rho u \frac{\partial u}{\partial x} + \rho v \frac{\partial u}{\partial y} + \frac{\partial p}{\partial x} = -\alpha \rho U \frac{u}{h} \qquad (2b)$$

$$\rho \frac{\partial v}{\partial t} + \rho u \frac{\partial v}{\partial x} + \rho v \frac{\partial v}{\partial y} + \frac{\partial p}{\partial y} = -\alpha \rho U \frac{v}{h}. \qquad (2c)$$

Equation ($2a$) is a form of the mass continuity equation with a source term αU. The terms on the right-hand sides of ($2b$) and ($2c$) represent the effect of the momentum flux through the holes. The pressure gradients created by these terms are

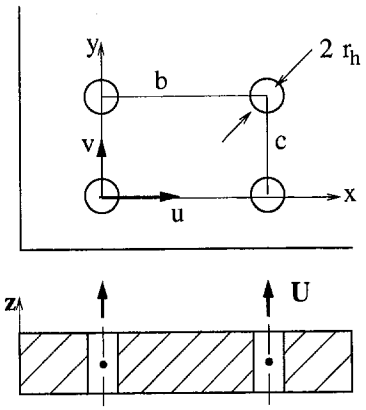

Fig. 2(a) Detail of the pressure holes

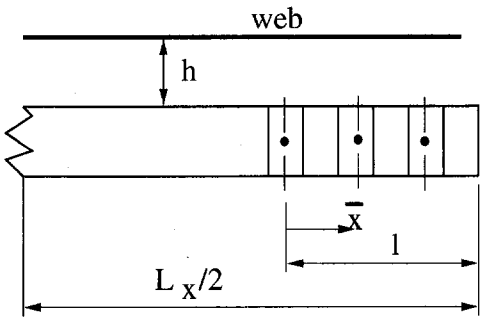

Fig. 2(b) One half of the one-dimensional problem

Fig. 2 Schematic view of the air reverser

Downloaded 04 May 2010 to 171.66.16.26. Redistribution subject to ASME license or copyright; see http://www.asme.org/terms/Terms_Use.cfm

proportional to the mass flow rate $\rho\alpha U$ and the local flow field velocities u and v.

In addition to Eqs. (2), it is necessary to specify the average velocity U through the holes. In general U is not constant, but varies from hole to hole and depends on the solution for the flow field. A reasonable first-order assumption is that U is a function of the pressure drop across the hole $p_0 - p$, where p_0 is the pressure inside the reverser (the supply pressure) and p is the local pressure under the web. In the absence of frictional losses, U would be given by Bernoulli's Eq. (1). If we assume that frictional losses are a fixed fraction of the original potential energy we get instead

$$U = \kappa(2(p_0 - p)/\rho)^{1/2} = \kappa U_0(1 - p/p_0)^{1/2} \qquad (3)$$

where $U_0 = \sqrt{2p_0/\rho}$, and where κ is an empirical constant, lying between 0 and 1, which is commonly called the discharge coefficient. This equation is generally used in calculating the flow rate across the orifice of a flow measuring device; κ accounts for the losses due to turbulence and the contraction of the effective flow area near the orifice (Gerhart et al., 1992).

In our problem there is a more complicated mechanism for both momentum loss and exchange near a pressure hole. In the reverser gap the air jet coming through a hole is affected by both the web and the cross flow present in the gap, creating a very complicated three-dimensional flow. In genèral a wall, such as the web, placed in front of a jet stagnates the flow and hence causes pressure to rise (Rajaratnam, 1976, p. 231). If the jet velocity U is a function of the pressure drop across the hole then the presence of the web would reduce the average jet exit velocity. A different effect occurs in the presence of cross flow. When a jet is injected into a cross flow it locally retards the cross flow on the upstream side of the jet and causes rarefaction on the downstream side. Thus the pressure in the mixing fluid rises on the upstream side and drops on the down stream side. This pressure difference causes the jet to deflect (Abramovich, 1963, p. 542). Trying to approximate the combined interaction of these two effects by a single parameter κ is obviously an oversimplification, but it allows us to circumvent the solution of a very complicated three-dimensional problem. A separate and more detailed study of the discharge coefficient under the conditions described in this paragraph would be useful.

In an experiment without the web, the discharge coefficient for typical air reverser holes was estimated to be 0.65 (Lewis). If the gap between the web and the air reverser were large compared to the hole diameter, we would expect this value to be valid here. In practice, however, the gap is approximately equal to the hole diameter, which produces the complicated flow pattern described above, and makes it reasonable to expect that a different value may be appropriate. In fact, as will be seen later using a higher value of κ gives a closer match to empirically obtained pressures.

We assume that for most practical applications air will be flowing out of the web-reverser interface. Therefore we have an "outflow boundary" situation, where it is sufficient to prescribe only one boundary condition to obtain a well-posed boundary value problem (Fletcher, 1991). Indicating the outer periphery of the air reverser by B, we set the pressure to the ambient value

$$p = 0 \quad \text{on} \quad B. \qquad (4)$$

Note that p is given in terms of gauge pressure.

3 Analytical Solution

Some insight into the full two-dimensional problem can be obtained by considering a one-dimensional model. The one-dimensional model can be expected to be approximately correct along and near the centerline of the web in either the x or y direction.

If we assume that the flow is only in the x direction, then the steady-state versions of Eqs. (2a) and (2b) become

$$\frac{d}{d\bar{x}}(hu) = \alpha U \qquad (5a)$$

$$\frac{dp}{d\bar{x}} + \rho u \frac{du}{d\bar{x}} + \frac{\rho\alpha U}{h} u = 0 \qquad (5b)$$

where U is again given by (3), and where $\bar{x}$ is a local coordinate for the region with sources, as shown in Figure 2(b). Equations (3) and (5) are still nonlinear, but if the clearance h between the air reverser and the web is constant, they can be solved exactly. In particular, substitution of (3) into (5a) gives

$$p = p_0\left[1 - \left(\frac{h}{\kappa\alpha U_0}\frac{du}{d\bar{x}}\right)^2\right]. \qquad (6)$$

Substitution of (3) and (6) into (5b) then gives the linear ordinary differential equation

$$\frac{d^2u}{d\bar{x}^2} - 2\left(\frac{\kappa\alpha}{h}\right)^2 u = 0. \qquad (7)$$

The symmetrical air reverser shown in Fig. 2(b) contains two regions of width l with holes and a central region without holes. The total width of the web is L_x. By symmetry, the solutions for the regions on the left and right will be identical, and the solution for the central region will be given by p = constant and $u = 0$. The appropriate boundary conditions for the region on the right are $u = 0$ at the edge of the central region $\bar{x} = 0$, and $p = 0$ at the edge of the web $\bar{x} = l$. Using these boundary conditions, the solution for the right-hand region can be found to be

$$u = U_0 \frac{\sinh(m\bar{x}/l)}{\sqrt{2}\cosh(m)} \qquad (8a)$$

$$p = p_0\left[1 - \left(\frac{\cosh(m\bar{x}/l)}{\cosh(m)}\right)^2\right] \qquad (8b)$$

where

$$m = \sqrt{2}\frac{\kappa\alpha l}{h}. \qquad (9)$$

The dimensionless parameter $\kappa\alpha l/h$ is the ratio of the effective area of the holes to the total exit area at the edge of the web. The higher this parameter, the more difficult it is for the flow to exit from under the web, and therefore the higher the pressure that is generated, as can be seen from Eq. (8b).

4 Numerical Solution

The full two-dimensional problem cannot be solved analytically. We used a numerical method, whose details can be found in Müftü et al. (1997), to solve the governing equations. This method employs a pseudo-transient iteration algorithm to calculate the steady-state solution where Eq. (2a) is replaced by

$$\frac{\partial ph}{\partial t} + \rho a^2\left(\frac{\partial hu}{\partial x} + \frac{\partial hv}{\partial y}\right) = \rho a^2\alpha U. \qquad (10)$$

In this equation a^2 is a constant which can be considered an artificial speed of sound (Fletcher, 1991, Vol. 2, p. 356). In this method the discrete time-step Δt which is introduced later and a^2 act like relaxation constants between the iterations.

Downloaded 04 May 2010 to 171.66.16.26. Redistribution subject to ASME license or copyright; see http://www.asme.org/terms/Terms_Use.cfm

During the solution iterations the air pressure p can sometimes become higher than the supply pressure p_0. When this occurs, the air velocity U is replaced by U^*;

$$U^* = \begin{cases} -\kappa(2|p_0 - p|/\rho)^{1/2} & \text{if} \quad p > p_0 \\ \kappa(2|p_0 - p|/\rho)^{1/2} & \text{if} \quad p_0 > p. \end{cases} \tag{11}$$

These sinks typically occur where two regions of substantially different hole densities α are placed close to each other. They disappear at steady state.

For convenience the following notation is used throughout this paper. The solution domain of the governing equation is indicated by $S = \{(x, y) : 0 \le x \le L_x \text{ and } 0 \le y \le L_y\}$ where x, y, L_x and L_y are as shown in Fig. 1. This domain is divided into two subdomains: $S = B \cup I$, where the inner domain is $I = \{(x, y) : 0 < x < L_x \text{ and } 0 < y < L_y\}$. The inner domain I is further subdivided into I_S where there are pressure sources and I_0 where there are no pressure sources. The boundary $B = B_1 \cup B_2 \cup B_3 \cup B_4$ is composed of the four edges:

$$B_1 = \{(x, y) : x = 0, 0 \le y \le L_y\},$$

$$B_2 = \{(x, y) : y = 0, 0 \le x \le L_x\},$$

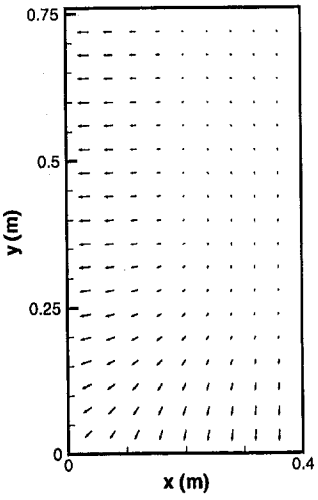

Fig. 3(*a*) Air velocity vector, V

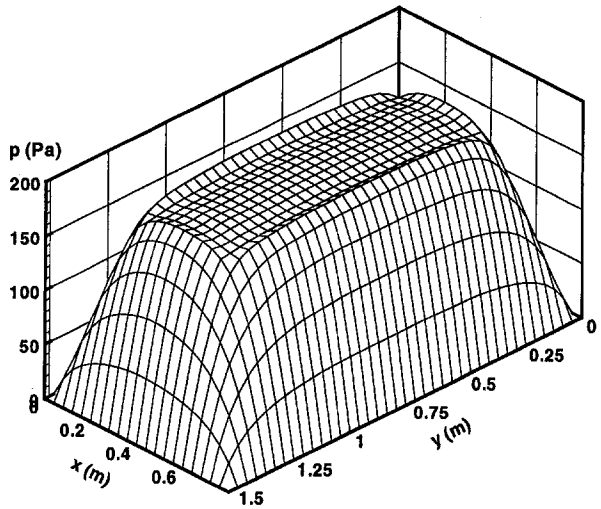

Fig. 3(*b*) Air pressure distribution

Fig. 3 Air velocity and pressure profiles at steady state. Note that (*a*) shows only the lower left quarter of the solution domain; the solution is symmetrical with respect to $x = L_x/2$ and $y = L_y/2$ (p_0 = 800 Pa, h_0 = 3 mm, and α_{1-4} = 0.0084).

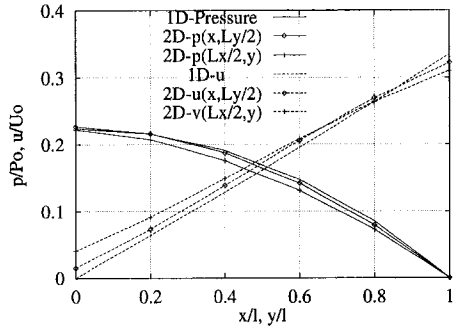

Fig. 4 Comparison of a one-dimensional analytical solution with two-dimensional numerical results (α_{1-4} = 0.0084, h_0 = 3 mm, and p_0 = 800 Pa)

$$B_3 = \{(x, y) : y = L_y, 0 \le x \le L_x\},$$

$$B_4 = \{(x, y) : x = L_x, 0 \le y \le L_y\}.$$

The solution domain is discretized using a uniform rectangular mesh with $\Delta x = L_x/(M - 1)$ and $\Delta y = L_y/(N - 1)$ spacing between the nodes in the x and y directions, respectively, where M and N are the total number of discretization points along the x and y-axes. In I, Eqs. (2b, c) and (10) are discretized using second-order accurate central finite difference formulas. On B, velocities u and v are extrapolated from the inside solution and p is given by the pressure boundary condition (4).

Using the central finite difference formulas to discretize the governing equations uncouples the grid points in an odd-even fashion. This uncoupling causes an aliasing error (Hirsch, 1988, Vol. 1, p. 325). The aliasing is eliminated by adding artificial viscosity which transforms the discretized equations to an upwind equivalent formulation (Kwak et al., 1986). The artificial viscosity is provided by the following matrix operators, whose use is shown later in Eq. (14),

$$-[C_i]\{\Delta q^{n+1}\} = -\epsilon_i(L_{xx} + L_{yy})\Delta q_k^{n+1} \tag{12a}$$

$$-[C_e]\{q^n\} = -\epsilon_e(L_{xxxx} + L_{yyyy})q_k^n \tag{12b}$$

where q_k^n is one of the u, v, and p at current time level n and mesh point k, and $\Delta q_k^{n+1} = q_k^{n+1} - q_k^n$. The parameters ϵ_i and ϵ_e are the implicit and explicit artificial viscosity constants and the $[C_i]$ and $[C_e]$ are the matrix representation of the viscosity operators. For example in the y direction the difference operators are $L_{yyyy}u_k = (u_{k+2} - 4u_{k+1} + 6u_k - 4u_{k-1} + u_{k-2})$ and $L_{yy}u_k = (u_{k+1} - 2u_k + u_{k-1})$. Using $\epsilon_i = 2\epsilon_e$ leads to unconditional stability (Pulliam, 1985). On nodes adjacent to B the artificial viscosity is applied using special forms for Eqs. (12) (Müftü et al., 1997).

We use the Crank-Nicholson method, which provides an unconditionally stable time-stepping algorithm (Fletcher, 1991), for the discretizing Eqs. (10), (2b, c) in time. This gives, for example, for Eq. (2b),

$$\rho\frac{v_k^{n+1} - v_k^n}{\Delta t} + \frac{1}{2}(r_k^{(2)^{n+1}} + r_k^{(2)^n}) = 0, \tag{13}$$

where $n + 1$ is the unknown time level, and Δt is the time-step size. The residuals $r^{(1)}$, $r^{(2)}$, and $r^{(3)}$ are obtained by collecting the time-independent terms of (10), (2b, c) on the left-hand side of the equations, respectively. The resulting equations are still nonlinear. They are linearized around a known time level t^n using Taylor series expansions.

After applying the time discretization, performing lineariza-

Downloaded 04 May 2010 to 171.66.16.26. Redistribution subject to ASME license or copyright; see http://www.asme.org/terms/Terms_Use.cfm

tion and adding the artificial viscosity operators given above, the system of equations can be represented in the following matrix form:

$$-\{R^n\} - [C_e]\{q^n\} = ([J^n] - [C_i])\{\Delta q^{n+1}\} \quad (14)$$

where $\{R^n\} = \{\{r^{(1)^n}\}\{r^{(2)^n}\}\{r^{(3)^n}\}\}^T$, $\{\Delta q^{n+1}\} = \{\{\Delta u^{n+1}\}\{\Delta v^{n+1}\}\{\Delta p^{n+1}\}\}^T$, and $[J^n]$ is the Jacobian matrix. The bandwidth of the matrix $([J^n] - [C_i])$ is $3N$. This matrix is nonlinear, therefore it is inverted at every time step. We use the successive-over-relaxation method to solve (14). The solution advances in time by

$$\{q^{n+1}\} = \{q^n\} + \{\Delta q^{n+1}\}. \quad (15)$$

The solution process starts with zero initial conditions, $\{q^0\} = 0$.

5 Results

Typically the pressure holes are distributed around the outer edges of the air reverser, and there is a large area in the middle with no holes as shown in Fig. 1; in terms of the notation introduced before we have four inner regions with sources, $I_{S1} - I_{S4}$, and one sourceless inner region, I_0 marked "0." The physical dimensions of the air reverser considered here are $L_x = 0.8$ m, $L_y = 1.52$ m, and $l = 0.2$ m. The hole density α varies from 0.008 to 0.05, and the supply pressure p_o varies from 200 to 800 Pa. The discharge coefficient is $\kappa = 0.65$, and the spacing between the web and the air reverser has a constant value $h(x, y) = h_0 = 3$ mm unless otherwise stated in the figure captions. The values $a = 139$ m/s, $\Delta t = 10^{-3}$ s, $\epsilon_e = 2.5 \times 10^{-2}$, $M = 21$ and $N = 39$ along with the relation $\epsilon_i = 2\epsilon_e$ were used in all of the cases shown here, and were selected based on numerical experiments (Müftü et al., 1997).

5.1 Comparison of the One-Dimensional and the Two-Dimensional Solutions. Figure 3 shows a typical steady-state solution. In part (a) we give the air velocity vector, $\mathbf{V}(x, y)$. In contrast to the one-dimensional analytical solution, where we assumed the air flow is zero at the inner edge of the source region, we make no assumptions about the flow conditions in I_0 in the numerical solution. Upon examining this figure we see that there is very little flow in I_0. Furthermore, the outflow from B is nearly uniform and perpendicular to each edge, thus approximately one-dimensional, except near the corner regions.

Figure 3(b) shows the two-dimensional air pressure profile corresponding to this case. Here we see that the pressure attains a constant value in the sourceless region, I_0, and in I_{S1-4} it gradually falls to ambient level on the outer edge, B. The pressure in the middle region is nearly uniform, and the one-dimensional assumption again seems to be valid, except near the corners of the reverser.

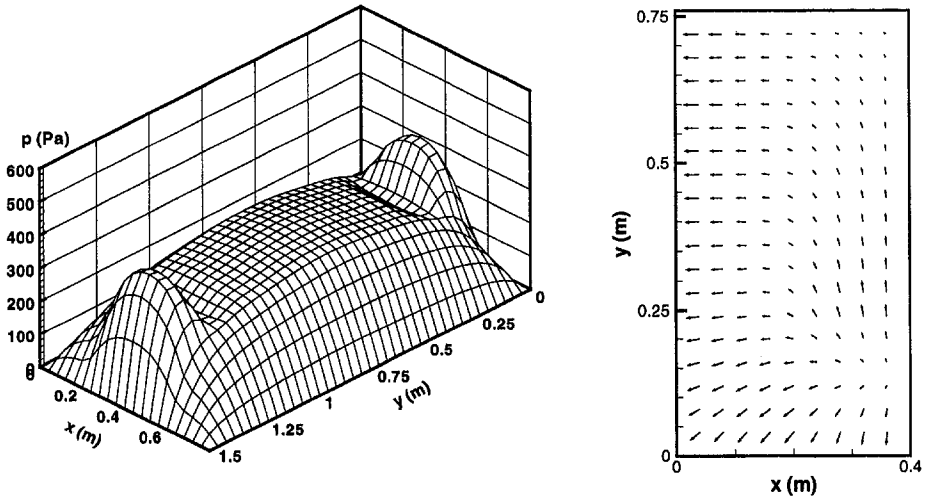

Fig. 5(a) $\alpha_{2,3} = 0.0252$, $\alpha_{1,4} = 0.0084$

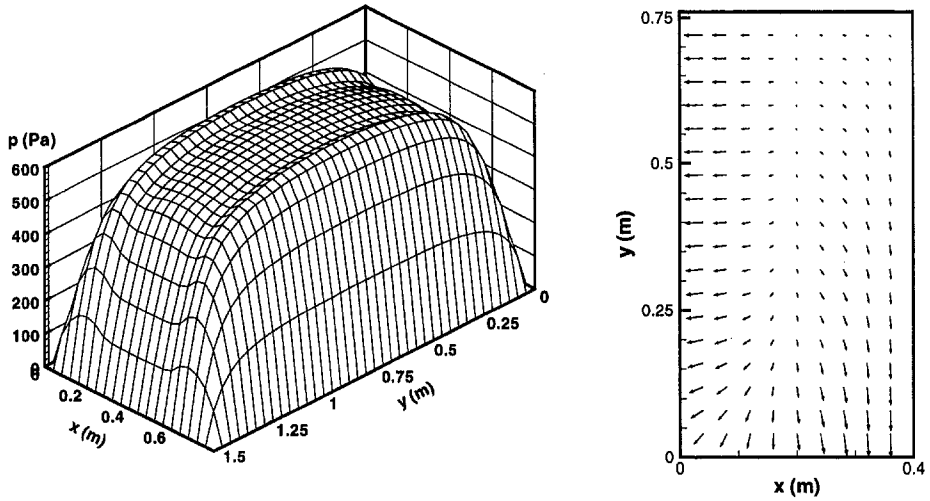

Fig. 5(b) $\alpha_{2,3} = 0.0084$, $\alpha_{1,4} = 0.0252$

Fig. 5 The effect of hole density on the steady-state pressure profile ($h_0 = 3$ mm and $p_0 = 800$ Pa)

Downloaded 04 May 2010 to 171.66.16.26. Redistribution subject to ASME license or copyright; see http://www.asme.org/terms/Terms_Use.cfm

In Fig. 4 we compare the velocity profile from a one-dimensional solution with a calculated two-dimensional solution along the lines $\bar{x}$ in I_{S4} and $\bar{y}$ in I_{S2}. In general, the two-dimensional solution shows slightly higher velocities and lower pressures than the one-dimensional solution. The pressure profile in $\bar{x}$ is slightly higher than in $\bar{y}$. This is caused by the fact that I_{S4} has 3.8 times larger hole area (thus air in-flow) compared to I_{S2}.

5.2 Maximizing the Average Pressure. The air pressure distribution under the web can be changed by adjusting the source densities in regions I_{S1-4}. Figure 5 shows the effect of using different densities in different regions. When the source density is tripled in I_{S2} and I_{S3} with respect to the case shown in Fig. 3, the steady-state pressure takes the rather interesting distribution shown in Fig. 5(a). Here we see that the pressure in regions I_{S2} and I_{S3} reach a maximum of 355 Pa and in regions I_{S1} and I_{S4} a maximum of 300 Pa. On the other hand, if we use the one-dimensional assumption, then the pressure at the inner edge of a source region ($\bar{x} = 0$) given by (8b)

$$p_1 = p_0\left[1 - \frac{1}{\cosh^2(m)}\right] \tag{16}$$

would be 666 Pa ($m = 1.54$) and 179 Pa ($m = 0.51$) in $I_{S2,3}$

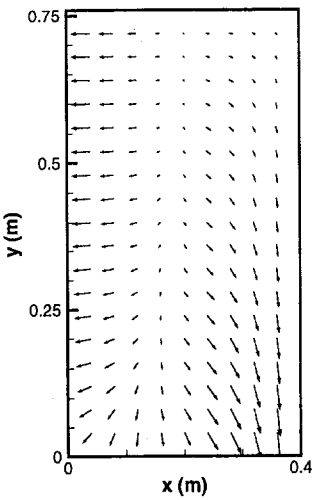

Fig. 6(a) $\alpha_{2,3} = 0$, $\alpha_{1,4} = 0.0274$

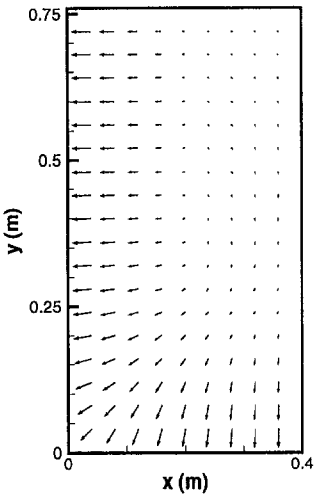

Fig. 6(b) $\alpha_{1-4} = 0.0217$

Fig. 6 These two cases and the case shown in Fig. 7(b) have equivalent total hole area. The flow pattern and subsequently the pressure profile are greatly affected by the location and density of the holes (h_0 = 3 mm and p_0 = 800 Pa).

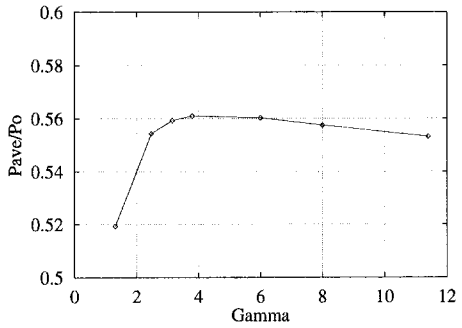

Fig. 7 The effect of the hole area ratio Γ = Gamma on the ratio P_{ave}/P_0 for a fixed total hole area of 0.0167 m². The maximum pressure occurs for a uniform α distribution (p_0 = 800 Pa, h_0 = 3 mm).

and $I_{S1,4}$, respectively. This indicates that the total average pressure in this situation is a suboptimal combination of the four source regions.

A more uniform pressure distribution is obtained, as shown in part (b) of Fig. 5, when we keep the source density in $I_{S2,3}$ at its original level of 0.0084 but increase the density in regions, $I_{S1,4}$. In this case the maximum of calculated pressure in regions I_{S1} and I_{S4} is 610 Pa and slightly lower in regions I_{S2} and I_{S3}. Note that this is very close to the p_1 value of the one-dimensional case mentioned above.

The air flow vectors **V** corresponding to these cases are also given in Fig. 5. In both these cases the air flow is from high-pressure regions to low-pressure regions, as would be expected. We see that the flow direction is reversed by increasing the source density in the side regions. This situation indicates that the air flow from the side source areas $I_{S2,3}$ can be used to "block" the main air-flow coming from the larger areas $I_{S1,4}$.

In order to show this blocking effect several cases with different $\alpha_{2,3}$ and $\alpha_{1,4}$ values were evaluated for a constant total air inflow area $2l(\alpha_{2,3}(L_x - 2l) + \alpha_{1,4}L_y) = 0.0167$. Figure 6 shows the air velocity profiles for $\Gamma = \infty$ and $\Gamma = 3.8$, where Γ is the ratio of the air flow rate into the different source regions

$$\Gamma = \frac{q_4}{q_2} = \frac{L_y}{L_x - 2l}\left(\frac{\alpha_4}{\alpha_2}\right). \tag{17}$$

The $\Gamma = \infty$ case has no holes in the side region, and the latter case has a uniform α value. When there are no holes in the side region the air can escape from the edges B_2 and B_3 with high velocity resulting in lower pressure. In contrast, when the side region has pressure holes the air flow in the no source region is reduced and the sources of the two regions are almost "separated" from each other. In this case the pressure generated in the mid region is higher. In order to evaluate the effect of the density distributions we use the average pressure p_{ave} obtained by dividing the numerically integrated two-dimensional pressure distribution by the total reverser area.

In fact, when we look at the effect of Γ on the average pressure, given in Fig. 7, we see that the maximum occurs at $\Gamma = 3.8$ (uniform α). In this case the pressure distribution on all four side regions is nearly identical. Thus very little pressure gradient exist to cause flow in the no-source region. Therefore, the average pressure attains the optimal value. This shows that, as the pressure in the no-source region is a function of the ratio $\alpha l/h$, *it is crucial to keep this ratio constant throughout the whole reverser surface, in order to optimize the average pressure in the clearance.*

5.3 The Effect of $\alpha l/h$ on Average Pressure. Figure 8 shows a plot of the average pressures as a function of the parameter $\alpha l/h$ calculated by the one-dimensional and two-dimensional solutions, an empirical relation and the air-jet the-

Downloaded 04 May 2010 to 171.66.16.26. Redistribution subject to ASME license or copyright; see http://www.asme.org/terms/Terms_Use.cfm

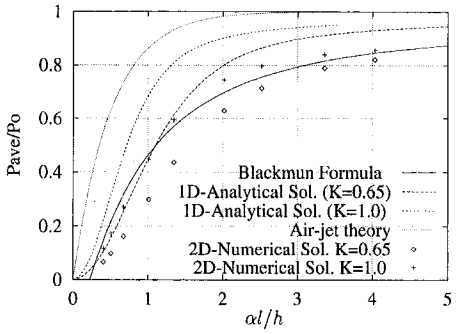

Fig. 8 Average pressure under the entire web as a function of dimensionless parameter $\alpha l/h$ ($\epsilon_a = 2.5 \times 10^{-2}$, $p_0 = 800$ Pa)

ory. A uniform α value was used in all four source domains for the two-dimensional calculations.

The average pressure for the one-dimensional solution over the entire web area is

$$p_{\text{ave}} = \left(1 - \frac{2l}{L_x}\right)p_1 + \left(\frac{2l}{L_x}\right)\bar{p}, \tag{18}$$

where

$$\bar{p} = \frac{1}{l}\int_0^l p\,dx = p_0\left[1 - \frac{1 + \dfrac{\sinh(2m)}{2m}}{1 + \cosh(2m)}\right]. \tag{19}$$

Blackmun's formula is a semi-empirical relation based on data for two-dimensional reversers with values of $\alpha l/h$ between about 0.4 and 1 given by

$$\bar{p} = p_0\left[1 - 1.24\,\frac{1 - e^{-2\alpha l/h}}{2\alpha l/h}\right] \tag{20}$$

(Blackmun).

An analytical expression for the cushion pressure p_1 for the hovercraft is obtained by integrating the Euler's equations along and across the stream lines of the air jet when the pressure on the inside of the air jet is assumed to be p_1 and on the outside of the air-jet it is assumed to be the ambient pressure P_a,

$$p_1 = p_0(1 - e^{-2\chi}). \tag{21}$$

Here p_0 is the supply pressure and $\chi = 2r_h/h$ when the jets are perpendicular to the ground (Elsley and Devereux, 1968). The diameter of the air-hole is given by $2r_h$. In Fig. 8 the air-jet Eq. (21) is used by assuming that $\chi = \alpha l/h$, (or $2r_h = \alpha l$).

Except for the air-jet formula, the results agree reasonably well. The two-dimensional solution is always lower than the one-dimensional solution due to the existence of the corner regions, where the actual pressure is lower than what the one-dimensional solution predicts. In the range $0 \le \alpha l/h \le 1$, both the one-dimensional and two-dimensional solutions for discharge coefficient $\kappa = 0.65$ predict lower average pressures than Blackmun's formula. If we increase κ to 1, the two-dimensional solution agrees quite well with Blackmun's formula. This suggests that the effective discharge coefficient may be higher than 0.65. Further experimentation to determine the discharge coefficient might be warranted.

6 Summary and Conclusions

The equations governing the air flow in an air reverser are derived. The flow is averaged across the clearance, which is much smaller than the other dimensions of the problem; the resulting equations apply in the plane of the reverser. An analytical solution for the governing equations is found for the case in which the flow is one-dimensional and web-reverser gap is constant. Comparing this solution with the two-dimensional numerical solution shows that the flow is approximately one-dimensional along each edge, except near the corners. As a result of this, the average pressure under the web is overestimated by the one-dimensional solution. The parameter $\kappa\alpha l/h$, the ratio of the effective hole area to the total exit area, is the main factor in controlling the average pressure under the web: in general, increasing $\kappa\alpha l/h$ results in higher average pressure. Two-dimensional analysis of the problem showed that dissimilar hole densities in the source regions may cause air flow in the no-source region, leading to reductions in the average pressure and a nonuniform pressure distribution. The average pressure is maximized when the ratio $\kappa\alpha l/h$ is kept uniform on the outer periphery of the reverser surface.

References

Abramovich, G. N., 1963, *The Theory of Turbulent Jets,* M.I.T. Press, Cambridge, MA.

Blackmun, R. C., 1997, "Correlation of Factors Affecting Web Clearance Around Air Reversers," private communication, Eastman Kodak Company, Rochester, NY.

Burden, R. L., and Faires, J. D., 1989, *Numerical Analysis,* PWS-Kent, Boston.

Chandra, C. J. G., Srinivas, Y. L., Seetharamu, K. H., and Parameswaran, M. A., 1990, "Investigation of Air Film Conveyor Pressurised Through Multiple Holes," *Finite Elements in Analysis and Design,* Vol. 6, pp. 235–243.

Elsley, G. H., and Devereux, A. J., 1968, *Hovercraft Design and Construction,* Cornell Maritime Press, Cambridge, MD.

Fletcher, C. A. J., 1991, *Computational Techniques for Fluid Dynamics,* Springer-Verlag, Berlin.

Gerhart, P. M., Gross, R. J., and Hochstein, J. I., 1992, *Fundamentals of Fluid Mechanics,* Addison-Wesley, Reading, MA.

Gross, W. A., ed., 1980, *Fluid Film Lubrication,* John Wiley and Sons, New York.

Hamrock, B. J., 1994, *Fundamentals of Fluid Film Lubrication,* McGraw-Hill, New York.

Hirsch, C., 1988, *Numerical Computation of Internal and External Flows,* John Wiley and Sons, Chichester, UK.

Kwak, D., Chang, J. L. C., Shanks, S. P., and Chakravarthy, S. R., 1986, "A Three-Dimensional Incompressible Navier-Stokes Solver Using Primitive Variables," *AIAA Journal,* Vol. 24, No. 3, pp. 390–395.

Lewis, T. S., 1997, "The Fluid Dynamics of Air Reversers," private communication, Eastman Kodak Company, Rochester, NY.

Müftü, S., and Benson, R. C., 1996, "A Study of Cross-Width Variations in the Two Dimensional Foil Bearing Problem," ASME *Journal of Tribology,* Vol. 118, pp. 407–414.

Müftü, S., Lewis, T. S., and Cole, K. A., 1997, "A Numerical Solution of the Euler's Equations with Non-linear Source Terms in Modeling the Fluid Dynamics of an Air Reverser," *Proceedings of the Information Storage and Processing Systems Symposium,* ASME Winter Annual Meeting, Dallas, TX.

Pozzi, A., Manzo, F., and Luchini, P., 1993, "Compressible Flow in a Hovercraft Air Cushion," *AIAA Journal,* Vol. 31, No. 3, pp. 528–533.

Pulliam, T. H., 1985, "Artificial Dissipation Models for the Euler Equations," AIAA-85-0438.

Rajaratnam, N., 1976, *Turbulent Jets,* Elsevier Scientific Publishing Co., Amsterdam.

Downloaded 04 May 2010 to 171.66.16.26. Redistribution subject to ASME license or copyright; see http://www.asme.org/terms/Terms_Use.cfm

Three-Dimensional Axisymmetric Piezothermoelastic Solution of a Transversely Isotropic Piezoelectric Clamped Circular Plate

S. Kapuria

P. C. Dumir

Applied Mechanics Department,
I.I.T. Delhi,
New Delhi 110016, India

S. Segupta
Engineers India, Ltd.,
New Delhi 110066, India

Three-dimensional solution in terms of potential functions is presented for a transversely isotropic piezoelectric clamped circular plate subjected to axisymmetric thermoelectromechanical load. The boundary conditions are satisfied using Fourier-Bessel expansions yielding two uncoupled infinite systems of algebraic equations for the arbitrary constants. These are solved to any desired degree of accuracy by truncating to finite set of equations. Results are presented to illustrate the effect of the thickness parameter. These would help assess two-dimensional theories of piezoelectric plates.

1 Introduction

The direct piezoeffect in piezoelectric materials is used in sensors in electromechanical transducers to infer deflection or stress. The converse piezoeffect is used in electromechanical actuators to control deflection or stress. Very few three-dimensional solutions for thermopiezoelectric response of piezoelectric elements are available. Ashida et al. (1993, 1994a–d) have presented potential function method for piezothermoelastic problems in cylindrical and Cartesian coordinates and obtained some solutions of direct and inverse problems of an infinite plate subjected to heating. Choi et al. (1995) have developed the solution for quasi-static transient thermoelastic response of a plate of crystal class 6 mm. Kapuria et al. (1996) have used the potential function method to obtain piezothermoelastic response of a finite transversely isotropic cylindrical shell.

We present a three-dimensional analytical solution for a transversely isotropic, axially polarized piezoelectric clamped circular plate subjected to static axisymmetric thermoelectric load. In the analysis, the temperature field is solved independently, without mechanical and electrical couplings, in terms of Bessel functions of the first kind so as to identically satisfy the thermal boundary condition at the lateral surface. The arbitrary constants in this solution are determined from the boundary conditions at the flat surfaces. The potential functions proposed by Ashida et al. (1993) are used to solve the equations of coupled piezothermoelectricity by a method similar to the one presented by Valov (1962). The complementary solution is obtained by combining two independent solutions involving, respectively, Bessel functions of the first kind and modified Bessel functions of the first kind and adding a solution which is independent of the axial coordinate. The particular solution is obtained in terms of Bessel functions of the first kind. The boundary conditions are satisfied termwise using Fourier-Bessel expansions to yield two uncoupled infinite systems of algebraic equations for the arbitrary constants. Results are presented for two thermoelectric loads to illustrate the effect of the thickness parameter.

2 General Solution for a Finite Circular Plate

Let (u, v, w), $(\sigma_r, \sigma_\theta, \sigma_z, \tau_{\theta z}, \tau_{zr}, \tau_{r\theta})$ and (D_r, D_θ, D_z) be the displacements, stresses, and electric displacements in cylindrical coordinates (r, θ, z). Let ϕ and T be the electric potential and temperature rise above the stress-free reference temperature. The general solution to the governing differential equations of piezothermoelasticity is expressed by Ashida et al. (1993) in terms of displacement potential functions as

$$u = (\psi_1 + \psi_2)_{,r}, \quad w = (\bar{k}_1\psi_1 + l\psi_2)_{,z},$$

$$\phi_{,z} = (\nabla_1\psi_2 + \nu_2\psi_{2,zz} - \delta_2 T)/\xi_2, \tag{1}$$

$$\psi_1 = \bar{\phi} + \bar{\psi}_1 + \bar{\psi}_2 + \bar{\psi}_3,$$

$$\psi_{2,zz} = (\nabla_1\psi_1 + \nu_1\psi_{1,zz} - \delta_1 T)/\xi_1, \tag{2}$$

$$\nabla_1\bar{\psi}_i + \mu_i\bar{\psi}_{i,zz} = 0, \quad i = 1, 2, 3, \tag{3}$$

where $\nabla_1(\ ) = (\ )_{,rr} + (\ )_{,r}/r$. $\bar{\phi}$ is the particular solution of the differential equation

$$\left(\nabla_1 + \mu_1\frac{\partial^2}{\partial z^2}\right)\left(\nabla_1 + \mu_2\frac{\partial^2}{\partial z^2}\right)\left(\nabla_1 + \mu_3\frac{\partial^2}{\partial z^2}\right)\bar{\phi}$$

$$= d_2\nabla_1^2 T + d_1\nabla_1(T_{,zz}) + d_0 T_{,zzzz}. \tag{4}$$

The expressions of $\bar{k}_i$, ξ_i, δ_i, l, d_i, ν_i, μ_i in Eqs. (1)–(4), are given in Ashida et al. (1993) in terms of elastic, piezoelectric-stress, permittivity, stress-temperature, and pyroelectric constants: C_{ij}, e_i, η_i, β_i, p_i.

Consider a clamped plate of radius R and thickness $2h$ with the midplane at $z = 0$. Its clamped surface at $r = R$ is electrically earthed and held at $T = 0$. Let $p_j(r)$, $T_j(r)$, $\phi_j(r)$ be the prescribed normal pressure, ambient temperature and ϕ at the bottom $[z = -h(j = 1)]$ and top $[z = h(j = 2)]$ surfaces. The boundary conditions of the plate are

$$T(R, z) = 0, \quad u(R, z) = 0,$$

$$w(R, z) = 0, \quad \phi(R, z) = 0, \tag{5}$$

Contributed by the Applied Mechanics Division of THE AMERICAN SOCIETY OF MECHANICAL ENGINEERS for publication in the ASME JOURNAL OF APPLIED MECHANICS.

Discussion on this paper should be addressed to the Technical Editor, Professor Lewis T. Wheeler, Department of Mechanical Engineering, University of Houston, Houston, TX 77204-4792, and will be accepted until four months after final publication of the paper itself in the ASME JOURNAL OF APPLIED MECHANICS.

Manuscript received by the ASME Applied Mechanics Division, Sept. 30, 1996; final revision, Oct. 30, 1997. Associate Technical Editor: W. K. Liu.

 Copyright © 1998 by ASME

Downloaded 04 May 2010 to 171.66.16.26. Redistribution subject to ASME license or copyright; see http://www.asme.org/terms/Terms_Use.cfm

$$\tau_{zr}(r, \mp h) = 0, \quad \phi(r, -h) = \phi_1(r),$$

$$\phi(r, h) = \phi_2(r), \tag{6a}$$

$$\sigma_z(r, -h) = -p_1(r), \quad \sigma_z(r, h) = -p_2(r), \tag{6b}$$

$$-T_{,z}(r, -h) + h_1 T(r, -h) = h_1 T_1(r),$$

$$T_{,z}(r, h) + h_2 T(r, h) = h_2 T_2(r), \tag{7}$$

h_1 and h_2 being the surface heat transfer coefficients at its bottom and top surfaces. Let $\bar{\lambda}_i$'s be thermal conductivities with $\alpha^2 = \bar{\lambda}_z/\bar{\lambda}_r$. The solution of the heat conduction equation, satisfying $T(R, z) = 0$, is

$$T(r, z) = \sum_{n=1}^{\infty} g_1^n(z) J_0(\lambda_n r), \tag{8}$$

where J_0 is the zero-order Bessel function of the first kind, $\lambda_n's$ are the roots of the equation $J_0(\lambda_n R) = 0$, and $g_1^n(z) = U^n \operatorname{ch}(\lambda_n z/\alpha) + V^n \operatorname{sh}(\lambda_n z/\alpha)$ with ch and sh being hyperbolic cosine and sine functions. U^n, V^n are arbitrary constants. Substituting T from (8) in Eq. (4), its particular solution $\bar{\phi}$ is obtained as

$$\bar{\phi} = -Z_1 \alpha^2 \sum_{n=1}^{\infty} g_1^n(z) J_0(\lambda_n r)/\lambda_n^2, \tag{9}$$

with $Z_1 = (d_2\alpha^4 - d_1\alpha^2 + d_0)/[(\alpha^2 - \mu_1)(\alpha^2 - \mu_2)(\alpha^2 - \mu_3)]$. The solution of Eq. (3) is represented as $\bar{\psi}_i = R_i(r) Z_i(z)$, where $R_i(r)$ and $Z_i(z)$ satisfy $R_{i,rr} + R_{i,r}/r + cR_i = 0$, $Z_{i,zz} - cZ_i/\mu_i = 0$, c being an arbitrary constant. Allowing c to be both positive and negative with $c = \lambda_n^2$ and $c = -\mu_i k_m^2$, respectively, the general solution for $\bar{\psi}_i$ is obtained, in terms of arbitrary constants A_i^n, B_i^n, and C_i^m as

$$\bar{\psi}_i = \sum_{n=1}^{\infty} g_{2i}^n(z) J_0(\lambda_n r) + \sum_{m=1}^{\infty} g_{3i}^m(z) I_0(\sqrt{\mu_i} k_m r), \tag{10}$$

where $g_{2i}^n(z) = A_i^n \operatorname{ch}(\lambda_n z/\sqrt{\mu_i}) + B_i^n \operatorname{sh}(\lambda_n z/\sqrt{\mu_i})$, $g_{3i}^m(z) = C_i^m \cos\{k_m(z - h)\}$, with $k_m = m\pi/2h$, $m = 1, 2, \ldots, \infty$. Putting $\bar{\psi}_i$ from Eq. (10) in Eq. (2) and defining $L_i = (\nu_1 - \mu_i)/\xi_1$, $Z_2 = [Z_1(\nu_1 - \alpha^2) + \delta_1]/\xi_1$, yields

$$\psi_1 = \sum_{i=1}^{3} [\sum_{n=1}^{\infty} g_{2i}^n(z) J_0(\lambda_n r) + \sum_{m=1}^{\infty} g_{3i}^m(z) I_0(\sqrt{\mu_i} k_m r)] - Z_1 \alpha^2 \sum_{n=1}^{\infty} g_1^n(z) J_0(\lambda_n r)/\lambda_n^2, \tag{11}$$

$$\psi_2 = \sum_{i=1}^{3} L_i [\sum_{n=1}^{\infty} g_{2i}^n(z) J_0(\lambda_n r) + \sum_{m=1}^{\infty} g_{3i}^m(z) I_0(\sqrt{\mu_i} k_m r)] - Z_2 \alpha^2 \sum_{n=1}^{\infty} g_1^n(z) J_0(\lambda_n r)/\lambda_n^2. \tag{12}$$

Substituting ψ_1, ψ_2 from Eqs. (11) and (12) in Eq. (1) and adding the z-independent solution given by $u = A_0 r$, $w = 0$, $\phi = 0$, where A_0 is an arbitrary constant, yields

$$u(r, z) = -\sum_{i=1}^{3} (1 + L_i)[\sum_{n=1}^{\infty} g_{2i}^n(z) \lambda_n J_1(\lambda_n R) - \sqrt{\mu_i} \sum_{m=1}^{\infty} g_{3i}^m(z) k_m I_1(\sqrt{\mu_i} k_m r)] + A_0 r + (Z_1 + Z_2)\alpha^2 \sum_{n=1}^{\infty} g_1^n(z) J_1(\lambda_n r)/\lambda_n, \tag{13}$$

$$w(r, z) = \sum_{i=1}^{3} (\bar{k}_1 + lL_i)[\sum_{n=1}^{\infty} g_{4i}^n(z) \lambda_n J_0(\lambda_n r)/\sqrt{\mu_i} - \sum_{m=1}^{\infty} g_{5i}^n(z) k_m I_0(\sqrt{\mu_i} k_m r)] - (\bar{k}_1 Z_1 + lZ_2)\alpha \sum_{n=1}^{\infty} g_2^n(z) J_0(\lambda_n r)/\lambda_n, \tag{14}$$

$$\phi(r, z) = \sum_{i=1}^{3} M_i [\sum_{n=1}^{\infty} g_{4i}^n(z) \lambda_n J_0(\lambda_n r)/\sqrt{\mu_i} - \sum_{m=1}^{\infty} g_{5i}^m(z) k_m I_0(\sqrt{\mu_i} k_m r)] - Z_3 \alpha \sum_{n=1}^{\infty} g_2^n(z) J_0(\lambda_n r)/\lambda_n, \tag{15}$$

with $g_2^n(z) = U^n \operatorname{sh}(\lambda_n z/\alpha) + V^n \operatorname{ch}(\lambda_n z/\alpha)$, $g_{4i}^n(z) = A_i^n \operatorname{sh}(\lambda_n z/\sqrt{\mu_i}) + B_i^n \operatorname{ch}(\lambda_n z/\sqrt{\mu_i})$, $g_{5i}^m(z) = C_i^m \sin\{k_m(z - h)\}$, $M_i = L_i(\nu_2 - \mu_i)/\xi_2$, $Z_3 = [Z_2(\nu_2 - \alpha^2) + \delta_2]/\xi_2$. Substituting these in the strain-displacement and constitutive equations yields the stresses in terms of following defined entities:

$$N_i = C_{33}(\bar{k}_1 + lL_i) - C_{13}\mu_i(1 + L_i) + e_3 M_i,$$

$$K_i = [C_{44}\{1 + \bar{k}_1 + (1 + l)L_i\} + e_4 M_i]\sqrt{\mu_i}$$

$$Q_{1i} = C_{11}(1 + L_i)\mu_i - C_{13}(\bar{k}_1 + lL_i) - e_1 M_i,$$

$$Q_{2i} = (C_{11} - C_{12})(1 + L_i)\sqrt{\mu_i},$$

$$Z_5 = (C_{11} - C_{12})\alpha(Z_1 + Z_2),$$

$$Z_4 = C_{11}(Z_1 + Z_2)\alpha^2 - C_{13}(\bar{k}_1 Z_1 + lZ_2) - e_1 Z_3 - \beta_1,$$

$$Z_7 = [C_{44}(\bar{k}_1 Z_1 + lZ_2 + Z_1 + Z_2) + e_4 Z_3]\alpha,$$

$$Z_6 = C_{13}(Z_1 + Z_2)\alpha^2 - C_{33}(\bar{k}_1 Z_1 + lZ_2) - e_3 Z_3 - \beta_3. \tag{16}$$

$$\sigma_r(r, z) = (C_{11} + C_{12})A_0 + \sum_{n=1}^{\infty} g_1^n(z)\{Z_4 J_0(\lambda_n r) - Z_5 \alpha J_1(\lambda_n r)/\lambda_n r\} + \sum_{i=1}^{3} [-\sum_{n=1}^{\infty} \{Q_{1i} J_0(\lambda_n r)/\mu_i - Q_{2i} J_1(\lambda_n r)/\sqrt{\mu_i}\lambda_n r\} g_{2i}^n(z)\lambda_n^2 + \sum_{m=1}^{\infty} \{Q_{1i} I_0(\sqrt{\mu_i} k_m r) - Q_{2i} I_1(\sqrt{\mu_i} k_m r)/k_m r\} k_m^2 g_{3i}^m(z)], \tag{17}$$

$$\sigma_z(r, z) = 2C_{13}A_0 + Z_6 \sum_{n=1}^{\infty} g_1^n(z) J_0(\lambda_n r) + \sum_{i=1}^{3} N_i [\sum_{n=1}^{\infty} g_{2i}^n(z)\lambda_n^2 J_0(\lambda_n r)/\mu_i - \sum_{m=1}^{\infty} g_{3i}^m(z) k_m^2 I_0(\sqrt{\mu_i} k_m r)] \tag{18}$$

$$\tau_{zr}(r, z) = Z_7 \sum_{n=1}^{\infty} g_2^n(z) J_1(\lambda_n r) - \sum_{i=1}^{3} K_i [\sum_{n=1}^{\infty} g_{4i}^n(z)\lambda_n^2 J_1(\lambda_n r)/\mu_i + \sum_{m=1}^{\infty} g_{5i}^m(z) k_m^2 I_1(\sqrt{\mu_i} k_m r)] \tag{19}$$

3 Algebraic Equations for Coefficients

$T_i(r), p_i(r), \phi_i(r)$ are expanded in the Fourier-Bessel series to satisfy the boundary conditions at $z = \mp h$:

$$[T_i(r), p_i(r), \phi_i(r)] = \sum_{n=1}^{\infty} [T_i^n, p_i^n, \phi_i^n] J_0(\lambda_n r). \tag{20}$$

Substitution of T from Eq. (8) and the expansions (20) into boundary conditions (7) yields the values of U^n and V^n. For convenience we introduce $\bar{A}_i^n$, $\bar{B}_i^n$, $\bar{C}_i^n$, $\bar{U}^n$, $\bar{V}^n$ which are related to A_i^n, B_i^n, C_i^n, U^n, V^n by

Downloaded 04 May 2010 to 171.66.16.26. Redistribution subject to ASME license or copyright; see http://www.asme.org/terms/Terms_Use.cfm

Table 1 Convergence study for load case 1 for $S = 20$

(N, M)	$\bar{w}(0, 0)$	$\bar{u}(R/2, -h)$	$\bar{\sigma}_r(0, h)$	$\bar{\sigma}_r(r_p, h)$	$\bar{\sigma}_r(0, -h)$	$\bar{\tau}_{zr}(r_p, 0)$
(140, 140)	−1.2991	0.43147	−16.98	−16.46	5.165	1.3754
(180, 150)	−1.2992	0.43148	−17.13	−16.49	5.167	1.3754
(220, 150)	−1.2992	0.43148	−17.23	−16.52	5.169	1.3754
(260, 150)	−1.2993	0.43149	−17.31	−16.54	5.170	1.3754
(280, 150)	−1.2993	0.43149	−17.34	−16.54	5.171	1.3754
(280, 160)	−1.2993	0.43149	−17.34	−16.54	5.171	1.3754

$$\bar{A}_i^n = A_i^n \text{ sh } (\lambda_n h/\sqrt{\mu_i}) J_1(\lambda_n R)\lambda_n^2,$$

$$\bar{B}_i^n = B_i^n \text{ ch } (\lambda_n h/\sqrt{\mu_i}) J_1(\lambda_n R)\lambda_n^2, \quad \bar{C}_i^m = C_i^m I_0(\sqrt{\mu_i} k_m R) k_m^2,$$

$$\bar{U}^n = U^n \text{ sh } (\lambda_n h/\alpha) J_1(\lambda_n R),$$

$$\bar{V}^n = V^n \text{ ch } (\lambda_n h/\alpha) J_1(\lambda_n R). \quad (21)$$

Substituting w and ϕ from Eqs. (14) and (15) into the last two boundary conditions of Eq. (5) yields $\sum_{i=1}^{3} (\bar{k}_1 + lL_i)\bar{C}_i^m = 0$, $\sum_{i=1}^{3} M_i \bar{C}_i^m = 0$ which are solved for $\bar{C}_2^m$ and $\bar{C}_3^m$ in terms of $\bar{C}_1^m$ as

$$\bar{C}_j^m = \delta_j \bar{C}_1^m, \quad j = 2, 3, \quad (22)$$

where $\delta_2 = [M_1(\bar{k}_1 + lL_3) - M_3(\bar{k}_1 + lL_1)]/D$, $\delta_3 = [M_2(\bar{k}_1 + lL_1) - M_1(\bar{k}_1 + lL_2)]/D$ with $D = [M_3(\bar{k}_1 + lL_2) - M_2(\bar{k}_1 + lL_3)]$. Substitution of τ_{zr} from Eq. (19) into boundary conditions (6a) yields

$$\sum_{i=1}^{3} K_i \bar{A}_i^n/\mu_i = Z_7 \bar{U}^n, \quad \sum_{i=1}^{3} K_i \bar{B}_i^n/\mu_i = Z_7 \bar{V}^n. \quad (23)$$

ϕ from Eq. (15) and ϕ_i from Eq. (20) are substituted in boundary conditions (6a) for ϕ to yield

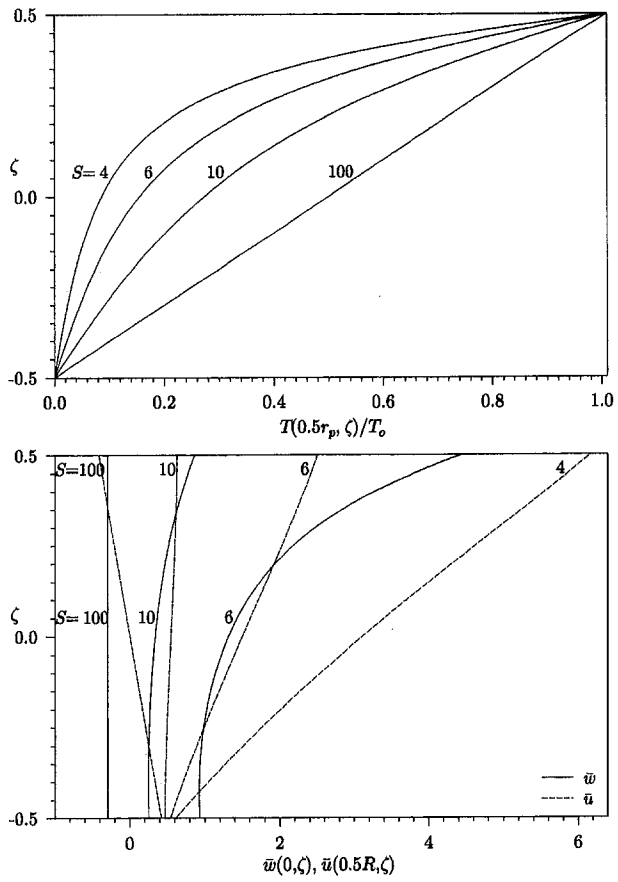

Fig. 1 Effect of S on the distributions of T, $\bar{w}$, and $\bar{u}$ under load case 1

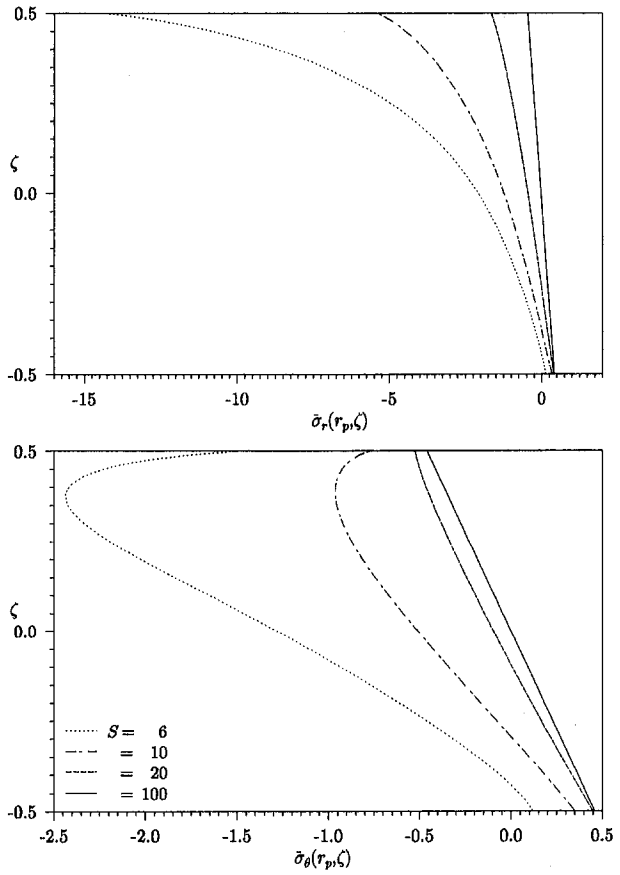

Fig. 2 Effect of S on the distributions of $\bar{\sigma}_r$ and $\bar{\sigma}_\theta$ under load case 1

$$\sum_{i=1}^{3} M_i \bar{A}_i^n/\sqrt{\mu_i} = Z_3\alpha \bar{U}^n + (\phi_2^n - \phi_1^n)\lambda_n J_1(\lambda_n R)/2,$$

$$\sum_{i=1}^{3} M_i \bar{B}_i^n/\sqrt{\mu_i} = Z_3\alpha \bar{V}^n + (\phi_1^n + \phi_2^n)\lambda_n J_1(\lambda_n R)/2. \quad (24)$$

Equations (23) and (24) are solved for $\bar{A}_2^n$, $\bar{A}_3^n$ in terms of $\bar{A}_1^n$ and $\bar{B}_2^n$, $\bar{B}_3^n$ in terms of $\bar{B}_1^n$:

$$\bar{A}_j^n = \bar{\alpha}_j \bar{A}_1^n + \bar{R}_j^{an}, \quad \bar{B}_j^n = \bar{\alpha}_j \bar{B}_1^n + \bar{R}_j^{bn}, \quad j = 2, 3, \quad (25)$$

$$\bar{R}_j^{an} = \Omega_j(\phi_2^n - \phi_1^n)\lambda_n J_1(\lambda_n R) + \bar{\delta}_j \bar{U}^n,$$

$$\bar{R}_j^{bn} = \Omega_j(\phi_1^n + \phi_2^n)\lambda_n J_1(\lambda_n R) + \bar{\delta}_j \bar{V}^n, \quad (26)$$

$$\bar{\alpha}_2 = \mu_2(K_3 M_1\sqrt{\mu_1} - K_1 M_3\sqrt{\mu_3})/\mu_1\Delta,$$

$$\bar{\alpha}_3 = \mu_3(K_1 M_2\sqrt{\mu_2} - K_2 M_1\sqrt{\mu_1})/\mu_1\Delta,$$

$$\Omega_2 = -\mu_2 K_3/2\Delta, \quad \Omega_3 = \mu_3 K_2/2\Delta,$$

$$\Delta = K_2 M_3\sqrt{\mu_3} - K_3 M_2\sqrt{\mu_2},$$

$$\bar{\delta}_2 = \mu_2(\sqrt{\mu_3} M_3 Z_7 - K_3 Z_3\alpha)/\Delta,$$

$$\bar{\delta}_3 = -\mu_3(\sqrt{\mu_2} M_2 Z_7 - K_2 Z_3\alpha)/\Delta. \quad (27)$$

Downloaded 04 May 2010 to 171.66.16.26. Redistribution subject to ASME license or copyright; see http://www.asme.org/terms/Terms_Use.cfm

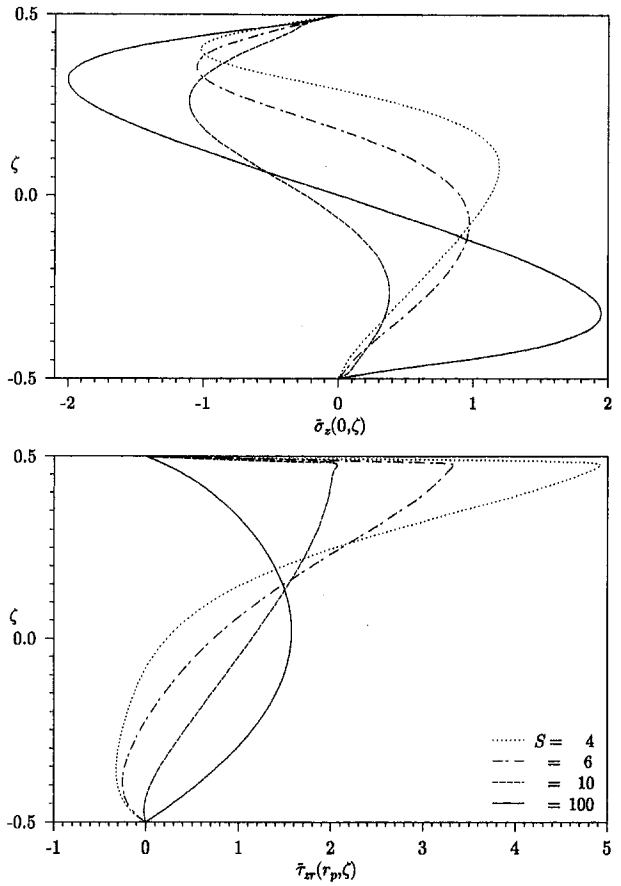

Fig. 3 Effect of S on the distributions of $\bar{\sigma}_z$ and $\bar{\tau}_{zr}$ under load case 1

The boundary condition, $u(R, z) = 0$, yields

$$A_0 R - \sum_{n=1}^{\infty} F_1(z, n) + \sum_{m=1}^{\infty} R_m^{(1)} \cos\{k_m(z-h)\} = 0, \quad (28)$$

$$F_1(z, n) = \lambda_n[\sum_{i=1}^{3}(1 + L_i) g_{2i}^n(z) - (Z_1 + Z_2)\alpha^2 g_1^n(z)/\lambda_n] J_1(\lambda_n R),$$

$$R_m^{(1)} = \sum_{i=1}^{3}(1 + L_i)\sqrt{\mu_i} I_1(\sqrt{\mu_i} k_m R) k_m C_i^m. \quad (29)$$

Using the expansions of hyperbolic cosine and sine functions in the range $-h \le z \le h$ in the cosine Fourier series in terms of $\cos\{k_m(z-h)\}$, and the relations (25), $F_1(z, n)$ is expanded in the Fourier series as

$$F_1(z, n) = F_0^{(1)}(n) + \sum_{m=1}^{\infty} F_m^{(1)}(n) \cos\{k_m(z-h)\} \quad (30)$$

$$F_0^{(1)}(n) = [\sum_{i=1}^{3} H_0^i \bar{\alpha}_i \bar{A}_i^n + \sum_{i=2}^{3} H_0^i R_i^{an} - \Gamma_0 \bar{U}^n]/\lambda_n^2,$$

$$F_m^{(1)}(n) = \sum_{i=1}^{3} H_{mn}^i \bar{\alpha}_i \bar{A}_i^n + \sum_{i=2}^{3} H_{mn}^i R_i^{an} - \Gamma_{mn} \bar{U}^n, \quad m = 2, 4, \ldots$$

$$F_m^{(1)}(n) = \sum_{i=1}^{3} H_{mn}^i \bar{\alpha}_i \bar{B}_i^n + \sum_{i=2}^{3} H_{mn}^i R_i^{bn} - \Gamma_{mn} \bar{V}^n, \quad m = 1, 3, \ldots \quad (31)$$

with $H_0^i = (1 + L_i)\sqrt{\mu_i}/h$, $H_{mn}^i = 2(1 + L_i)\sqrt{\mu_i}(\lambda_n^2 + \mu_i k_m^2)^{-1}/h$, $\bar{\alpha}_1 = 1$, $\Gamma_0 = (Z_1 + Z_2)\alpha^3/h$, $\Gamma_{mn} = 2(Z_1 + Z_2)\alpha^3(\lambda_n^2 + \alpha^2 k_m^2)^{-1}/h$. Substituting the expansion (30) for $F_1(z, n)$ in Eq. (28) and equating the Fourier coefficients yields

$$A_0 = [\bar{H}_0 \sum_{n=1}^{\infty} \bar{A}_1^n/\lambda_n^2 + \xi_0]/R; \quad (32)$$

$$\bar{C}_1^m = [\sum_{n=1}^{\infty} \bar{H}_{mn} \bar{B}_1^n + \xi_m^{(2)}]/X_m, \quad m = 1, 3, \ldots;$$

$$\bar{C}_1^m = [\sum_{n=1}^{\infty} \bar{H}_{mn} \bar{A}_1^n + \xi_m^{(1)}]/X_m, \quad m = 2, 4, \ldots \quad (33)$$

$$\xi_0 = \sum_{n=1}^{\infty} [\sum_{i=2}^{3} H_0^i R_i^{an} - \Gamma_0 \bar{U}^n]/\lambda_n^2,$$

$$\bar{H}_0 = \sum_{i=1}^{3} H_0^i \bar{\alpha}_i, \quad \bar{H}_{mn} = \sum_{i=1}^{3} H_{mn}^i \bar{\alpha}_i,$$

$$\xi_m^{(1)} = \sum_{n=1}^{\infty} [\sum_{i=1}^{2} H_{mn}^i R_i^{an} - \Gamma_{mn} \bar{U}^n], \quad m = 2, 4, \ldots;$$

$$\xi_m^{(2)} = \sum_{n=1}^{\infty} [\sum_{i=2}^{3} H_{mn}^i R_i^{bn} - \Gamma_{mn} \bar{V}^n], \quad m = 1, 3, \ldots$$

$$X_m = k_m^{-1} \sum_{i=1}^{3} \delta_i (1 + L_i)\sqrt{\mu_i} I_1(\sqrt{\mu_i} k_m R)/I_0(\sqrt{\mu_i} k_m R), \quad (34)$$

with $\delta_1 = 1$. Using the expansions (20), the boundary conditions for $\sigma_z(r, \mp h)$ yield

$$2C_{13}A_0 + \sum_{i=1}^{3}(N_i/\mu_i) \sum_{n=1}^{\infty} A_i^n \operatorname{ch}(\lambda_n h/\sqrt{\mu_i})\lambda_n^2 J_0(\lambda_n r) - \sum_{m=2,4}^{\infty} F_2(r, m) = -\sum_{n=1}^{\infty} [(p_1^n + p_2^n)/2 - Z_6 U^n \operatorname{ch}(\lambda_n h/\alpha)] J_0(\lambda_n r), \quad (35)$$

$$\sum_{i=1}^{3}(N_i/\mu_i) \sum_{n=1}^{\infty} B_i^n \operatorname{sh}(\lambda_n h/\sqrt{\mu_i})\lambda_n^2 J_0(\lambda_n r) - \sum_{m=1,3}^{\infty} F_2(r, m) = \sum_{n=1}^{\infty} [(p_1^n - p_2^n)/2 - Z_6 V^n \operatorname{sh}(\lambda_n h/\alpha)] J_0(\lambda_n r), \quad (36)$$

where $F_2(r, m) = \sum_{i=1}^{3} N_i C_i^m k_m^2 I_0(\sqrt{\mu_i} k_m r)$. Using the Fourier-Bessel expansion of $I_0(\sqrt{\mu_i} k_m r)$ in terms of $J_0(\lambda_n r)$ and relations (22), the Fourier-Bessel coefficients of $F_2(r, m)$ are obtained as

$$F_2(r, m) = \sum_{n=1}^{\infty} F_n^{(2)}(m) J_0(\lambda_n r) \quad (37)$$

with $F_n^{(2)}(m) = G_{mn} \bar{C}_1^m / J_1(\lambda_n R)$, $G_{mn} = 2 \sum_{i=1}^{3} \delta_i N_i (\lambda_n^2 + \mu_i k_m^2)^{-1} \lambda_n / R$. Substituting $F_2(r, m)$ from (37) in Eqs. (35) and (36) and using relations (25) and (33), we express these in terms of $\bar{A}_1^n$'s and $\bar{B}_1^n$'s alone. Using the Fourier-Bessel expansion of unity, $1 = 2/R \sum_{n=1}^{\infty} [\lambda_n J_1(\lambda_n R)]^{-1} J_0(\lambda_n r)$, in the resulting equations and equating the coefficients of the Fourier-Bessel series on the two sides, we obtain an uncoupled pair of an infinite system of algebraic equations for $\bar{A}_1^n$'s and $\bar{B}_1^n$'s:

$$\bar{A}_1^n = \Bigg[\sum_{m=2,4}^{\infty} \frac{G_{mn}}{X_m} (\xi_m^{(1)} + \sum_{s=1}^{\infty} \bar{H}_{ms} \bar{A}_1^s) - \frac{4C_{13}}{R^2 \lambda_n} (\xi_0 + \bar{H}_0 \sum_{s=1}^{\infty} \bar{A}_1^s/\lambda_s^2) - (p_1^n + p_2^n) J_1(\lambda_n R)/2 - Z_6 \bar{U}^n \coth(\lambda_n h/\alpha) - \bar{Q}_n^a \Bigg] \Big/ \bar{P}_n^a \quad (38)$$

Downloaded 04 May 2010 to 171.66.16.26. Redistribution subject to ASME license or copyright; see http://www.asme.org/terms/Terms_Use.cfm

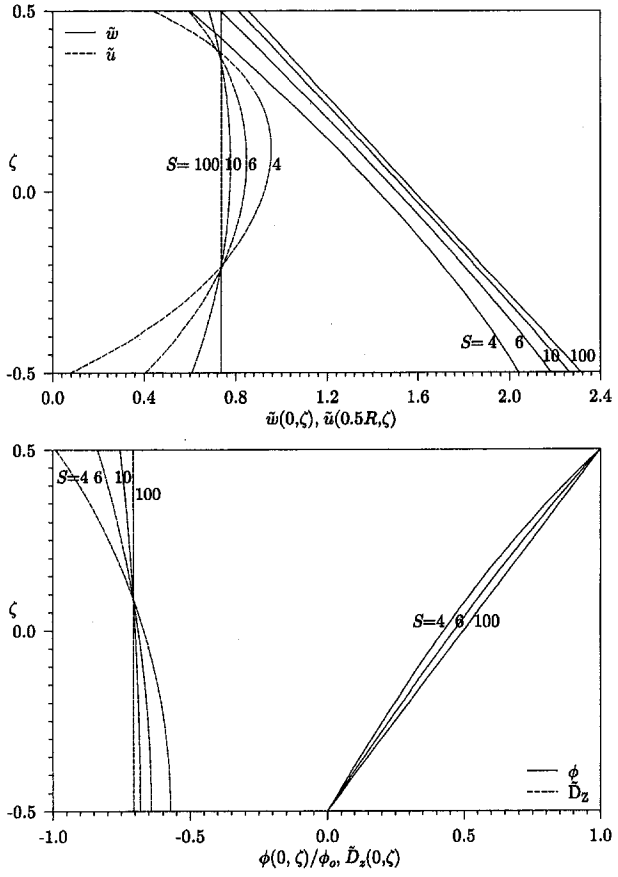

Fig. 4 Effect of S on the distributions of $\hat{w}$, $\hat{u}$, ϕ, and $\hat{D}_z$ under load case 2

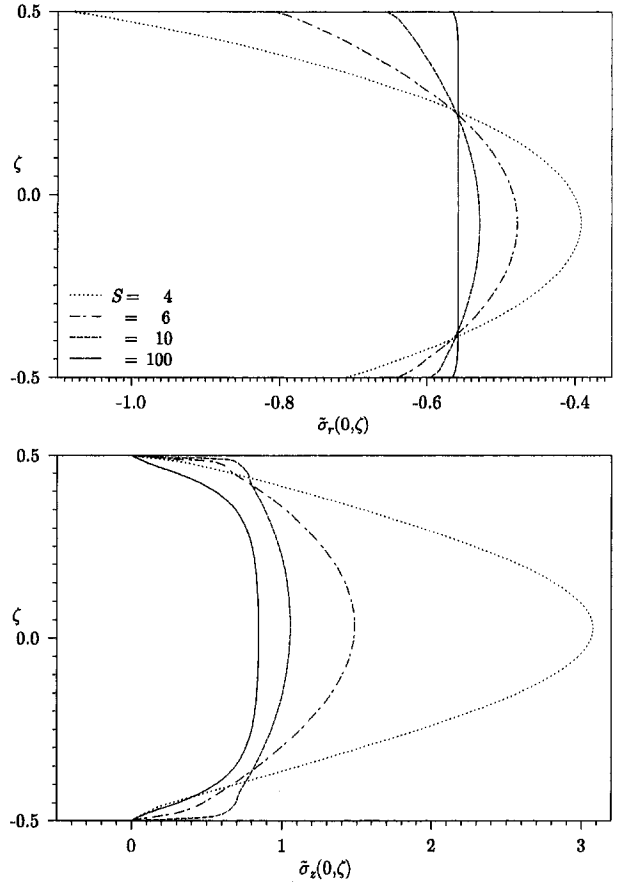

Fig. 5 Effect of S on the distributions of $\hat{\sigma}_r$ and $\hat{\sigma}_\theta$ under load case 2

$$\bar{B}_1^n = \left[\sum_{m=1,3}^{\infty} \frac{G_{mn}}{X_m} (\xi_m^{(2)} + \sum_{s=1}^{\infty} \bar{H}_{ms} \bar{B}_1^s) + (p_1^n - p_2^n) J_1(\lambda_n R) - Z_6 \bar{V}^n \tanh(\lambda_n h/\alpha) - \bar{Q}_n^b \right] \Big/ \bar{P}_n^b \quad (39)$$

with $\bar{P}_n^a = \sum_{i=1}^{3} \bar{\alpha}_i N_i / T_i^n \mu_i^2$, $\bar{Q}_n^a = \sum_{i=2}^{3} N_i \bar{R}_i^{an} / T_i^n \mu_i^2$, $\bar{P}_n^b = \sum_{i=1}^{3} \bar{\alpha}_i N_i T_i^n$, $\bar{Q}_n^b = \sum_{i=2}^{3} N_i \bar{R}_i^{bn} T_i^n$, where $T_i^n = \tanh(\lambda_n h/\sqrt{\mu_i})/\mu_i$. Equations (38) and (39) are solved numerically to desired accuracy by truncating the series after a finite number of terms with, say, N terms for n and M terms for m. The constants A_1^n, B_1^n, A_0, A_2^n, A_3^n, B_2^n, B_3^n, C_1^m are then determined from Eqs. (21), (32), (25), (22), and (33).

4 Numerical Results and Discussion

Results are presented for a piezoceramic cadmium selenide plate, with the material properties that are the same as in Ashida et al. (1993) for the following nonzero thermoelectric loads with its two faces traction free: (1) $T_2(r)$ is a central patch temperature of T_0 up to radius $r_p = 0.1R$ and (2) $\phi_2(r) = \phi_0 J_0(\lambda_n r)$. The results for these cases are nondimensionalized as (1) $(\bar{\sigma}_r, \bar{\sigma}_\theta, \bar{\sigma}_z, \bar{\tau}_{zr}) = 10^3(\sigma_r, \sigma_\theta, 0.1S^2\sigma_z, S\tau_{zr})/E_T\alpha_T S^2 T_0$, $(\bar{u}, \bar{w}) = 10^4(Su, w)/S^3\alpha_T R T_0$; and (2) $(\hat{\sigma}_r, \hat{\sigma}_\theta, \hat{\sigma}_z, \hat{\tau}_{zr}) = (\sigma_r, \sigma_\theta, 100\sigma_z, S\tau_{zr})h/E_T|d_1|\phi_0$, $(\hat{u}, \hat{w}) = (10u/S, w)/|d_1|\phi_0$, $\hat{D}_z = D_z h/100|d_1|^2 E_T \phi_0$, where $S = R/h$, $E_T = 42.8$ GPa, $\alpha_T = 4.4 \times 10^{-6}$ K^{-1}, $d_1 = -3.92 \times 10^{-12}$ CN^{-1}. Based on the convergence studies, for S from 4 to 100, all results are computed with $N = 300$, $M = 250$. A typical convergence study is given in Table 1 for $S = 20$.

The through-the-thickness distributions of some entities are shown in Figs. 1 to 3 for plates under the thermal load of case 1. Figure 1 shows that T varies nonlinearly across the thickness for $S \leq 10$. The variation of central deflection $\bar{w}$ becomes nonlinear for $S \leq 10$, due to stretching in the thickness direction. The radial displacement $\bar{u}$ follows approximately linear distribution, even for thick plates. It is observed from Fig. 2 that the variation of $\bar{\sigma}_r$ and $\bar{\sigma}_\theta$ becomes nonlinear across the thickness for $S < 10$. The nature of $\bar{\sigma}_r$ and $\bar{\sigma}_\theta$ is predominantly bending for very thin plates with $S \geq 100$. Figure 3 shows that $\bar{\sigma}_z$ changes in sign across the thickness at the center. Its distribution becomes skewsymmetric about the midplane for thin plates with $S \geq 100$. The peak value of $\bar{\tau}_{zr}$ increases and occurs at a location nearer to the thermally loaded surface as the plate becomes thicker.

The effect of S on the response of a piezoelectric plate under the potential load of case 2 is presented in Figs. 4 and 5. The contraction in the thickness direction is found to cause nonuniform central deflection $\hat{w}$ across the thickness, even for thin plates. The variation of $\hat{w}$ is almost linear up to $S = 6$. The variation of $\hat{u}$ and $\hat{\sigma}_r$ is nonlinear across the thickness for $S \leq 10$. The maximum value of $\hat{\sigma}_z$ occurs at the midplane for all S. The potential $\hat{\phi}$ varies almost linearly across the thickness even for a thick plate with $S = 6$. The distribution of $\hat{D}_z$ is nonuniform and nonlinear for $S \leq 10$. The stress $\hat{\tau}_{zr}$ (not presented for brevity) has an antisymmetric distribution about the midplane with peaks near the flat surfaces.

5 Conclusions

A three-dimensional series solution is presented for a transversely isotropic piezoelectric clamped circular plate subjected to an axisymmetric thermoelectric load. The systems of alge-

Downloaded 04 May 2010 to 171.66.16.26. Redistribution subject to ASME license or copyright; see http://www.asme.org/terms/Terms_Use.cfm

braic equations obtained are found to be well conditioned, even for a very large number of terms. The method can be used for similar problems of circular plates with other boundary conditions. The results for thermoelectric loads reveal that for the diameter-to-thickness ratio of less than 10, the three-dimensional solution deviates from the assumptions of two-dimensional theories regarding the nature of distributions across the thickness of u, w, σ_r, σ_θ, ϕ, and D_z. The solution would help assess two-dimensional theories of piezoelectric plates.

References

Ashida, F., Tauchert, T. R., and Noda, N., 1993, "Response of a piezothermoelastic plate of crystal class 6 mm subject to axisyimmetric heating," *International Journal of Engineering Science,* Vol. 31, pp. 373–384.

Ashida, F., Tauchert, T. R., and Noda, N., 1994a, "Potential function method for piezothermoelastic problems of solids of crystal class 6 mm in cylindrical coordinates," *Journal of Thermal Stresses,* Vol. 17, pp. 361–376.

Ashida, F., Noda, N., and Tauchert, T. R., 1994b, "A two-dimensional piezothermoelastic problem in an orthotropic plate exhibiting crystal class mm2," *JSME International Journal Series A,* Vol. 37, pp. 334–340.

Ashida, F., Noda, N., and Tauchert, T. R., 1994c, "Inverse problem of two-dimensional piezothermoelastic problem in an orthotropic plate exhibiting crystal class mm2," *JSME International Journal Series A,* Vol. 37, pp. 341–346.

Ashida, F., Tauchert, T. R., and Noda, N., 1994d, "A general technique for piezothermoelasticity of hexagonal solids of class 6 mm in Cartesian coordinates," *ZAMM,* Vol. 74, pp. 87–97.

Choi, J., Ashida, F., and Noda, N., 1995, "Transient piezothermoelasticity of a hexagonal plate of class 6 mm," *Archive of Applied Mechanics,* Vol. 65, pp. 24–37.

Kapuria, S., Dumir, P. C., and Sengupta, S., 1996, "Exact piezothermoelastic axisymmetric solution of a finite transversely isotropic cylindrical shell," *Computers and Structures,* Vol. 61, pp. 1085–1099.

Valov, G. M., 1962, "On the axially symmetric deformation of a solid circular cylinder of finite length," *PMM,* Vol. 26, pp. 975–999.

Downloaded 04 May 2010 to 171.66.16.26. Redistribution subject to ASME license or copyright; see http://www.asme.org/terms/Terms_Use.cfm

H. Cho
Graduate Student.

G. A. Kardomateas
Professor.
Mem. ASME.

C. S. Valle
Graduate Student.

School of Aerospace Engineering,
Georgia Institute of Technology,
Atlanta, GA 30332-0150

Elastodynamic Solution for the Thermal Shock Stresses in an Orthotropic Thick Cylindrical Shell

An elastodynamic solution for the thermal shock stresses in an orthotropic thick cylindrical shell is presented. The solution is achieved by the proper usage of integral transforms such as the finite Hankel transform and the Laplace transform. No restrictive assumptions on the shell thickness are placed. Results are presented for the well-formed wave propagation phenomenon of elastic stresses through the thickness of an orthotropic thick cylindrical shell. Thermal shock stresses become of significant magnitude due to stress wave propagation which is initiated at the boundaries by sudden thermal loading.

Introduction

In recent years, attention to thick composite shells has been continuously increased in several industrial areas. Thick composite cylindrical shells can be used in applications involving aerospace, offshore and submarine structures, pressure vessels, civil engineering structures, chemical pipes, and even automotive suspension components. These structures can be easily exposed to a variety of temperature fields in different environments. In high-temperature applications, thermal stresses, which are induced from the heat build up and cooling processes, may rise above the ultimate strength and lead to unexpected failures. Thus, the importance of thermal stresses in causing structural damage and changes in the functionality of the structure is well recognized whenever thermal environments are involved. Therefore, the capability to predict elastodynamic stresses induced by sudden thermal loading in composite structures is essential for the proper and safe design and the knowledge of its response during service in these severe thermal applications.

In the case of suddenly applied thermal loading, thermal deformation and the role of inertia become larger. Since the thermal stress changes very rapidly, the static analysis cannot capture its behavior. This dynamic thermoelastic stress response is significant and leads to the propagation of elastic stress waves in the solid.

Regarding related work, Sneddon (1951) introduced the finite Hankel transform to solve the heat conduction problems. The finite Hankel transform was successfully applied to the boundary value problem of heat conduction by Cinelli (1965) and later the usefulness of applications to dynamic problems for cylindrical and spherical shells was also studied (Cinelli, 1966).

The three-dimensional elasticity approach is the most powerful way to analyze the elastodynamic behavior when thick construction is involved. Elasticity approaches for orthotropic cylindrical shells have been used for static and dynamic stress analysis in several instances. Hyer and Cooper (1986) studied the static stresses and deformations induced by a circumferential temperature gradient in a composite tube. Kardomateas (1989, 1990) also used the elasticity approach to obtain the transient (but without the inertia term) thermal stresses in an orthotropic composite thick tube.

The thermal shock problem, which is a dynamic thermoelastic problem, was studied by Birman (1990) for a composite hollow cylinder based on the Donnell type of thin shell theory. Several other contributions using the elasticity approach to the thermal shock problem have been made, which are mostly related to an infinite elastic body with a spherical cavity (Sternberg and Chakravorty, 1959) and hollow spherical shells (Tsui and Kraus, 1965; Zaker, 1969). Another considerable work for the thermal shock stresses in a hollow sphere due to rapid uniform heating was performed by Hata (1991). The Ray theory was employed by taking the thermoelastic displacement potential for the thermoelastic equation and the displacement potential for the dynamic elasticity equation. The dynamic, thermoelastic response of thin cylindrical shells to suddenly applied and rotating thermal loadings was studied by McQuillen and Brull (1970). Sciuva and Carrera (1992) numerically investigated the elastodynamic behavior of relatively thick symmetrically laminated anisotropic circular shells as a plane-strain problem by the first-order shear deformation theory. Wang and Gong (1992) obtained the analytic solution using the finite Hankel transform and the Laplace transform for elastodynamic problems and presented the elastodynamic solution for a multilayered isotropic hollow cylinder. Wang (1993, 1995) dealt with the stress wave propagation problem in a two layered cylinder with initial interface pressure and investigated the thermal shock stresses caused by rapidly increasing uniform heating to an isotropic hollow cylinder as a plane-strain problem. But their studies were confined only to isotropic shell problems.

Even though several papers have been written in this area, the elastodynamic solution for a generally orthotropic cylindrical shell has not yet been reported. Thus, in this study, the finite Hankel transform and the Laplace transform are used to solve the uncoupled linear dynamic thermoelasticity problem for an orthotropic cylindrical shell. The advantage of this method is the ability to provide a closed-form solution which is applicable to a generally orthotropic cylinder of arbitrary thickness. This requires the use of the Bessel functions of the first and/or the second kind of arbitrary order due to the orthotropy of material constants.

Formulation

Consider a hollow cylinder subjected to a specific temperature environment with or without external pressure. The inner

Contributed by the Applied Mechanics Division of THE AMERICAN SOCIETY OF MECHANICAL ENGINEERS for publication in the ASME JOURNAL OF APPLIED MECHANICS.

Discussion on the paper should be addressed to the Technical Editor, Professor Lewis T. Wheeler, Department of Mechanical Engineering, University of Houston, Houston, TX 77204-4792, and will be accepted until four months after final publication of the paper itself in the ASME JOURNAL OF APPLIED MECHANICS.

Manuscript received by the ASME Applied Mechanics Division, Oct. 15, 1996; final revision, May 12, 1997. Associate Technical Editor: U. K. Kinra.

 Copyright © 1998 by ASME

Downloaded 04 May 2010 to 171.66.16.26. Redistribution subject to ASME license or copyright; see http://www.asme.org/terms/Terms_Use.cfm

and outer radii are denoted by r_1 and r_2, respectively. We denote by r the radial, θ the circumferential, and z the axial coordinate. The hollow cylinder is assumed to have zero initial temperature, but at $t > 0^+$, the shell is kept at a constant temperature through the thickness. Since there is only radial dependence of the temperature field, the hoop displacements are zero and the stresses and strains are independent of θ. Thus the thermoelastic stress-strain relations for the orthotropic body are

$$\begin{bmatrix} \sigma_{rr} \\ \sigma_{\theta\theta} \\ \sigma_{zz} \\ \tau_{\theta z} \\ \tau_{rz} \\ \tau_{r\theta} \end{bmatrix} = \begin{bmatrix} c_{11} & c_{12} & c_{13} & 0 & 0 & 0 \\ c_{12} & c_{22} & c_{23} & 0 & 0 & 0 \\ c_{13} & c_{23} & c_{33} & 0 & 0 & 0 \\ 0 & 0 & 0 & c_{44} & 0 & 0 \\ 0 & 0 & 0 & 0 & c_{55} & 0 \\ 0 & 0 & 0 & 0 & 0 & c_{66} \end{bmatrix} \begin{bmatrix} \epsilon_{rr} - \alpha_r \Delta T \\ \epsilon_{\theta\theta} - \alpha_\theta \Delta T \\ \epsilon_{zz} - \alpha_z \Delta T \\ \gamma_{\theta z} \\ \gamma_{rz} \\ \gamma_{r\theta} \end{bmatrix}, \tag{1}$$

where c_{ij} are the elastic constants and α_i are the thermal expansion coefficients (1, 2, and 3 represent r, θ, and z directions, respectively). The geometry of shell is assumed to be axisymmetric. Since the temperature doesn't depend on the axial coordinate, it is assumed that the stresses are independent of z. In addition to the constitutive Eq. (1), the elastic response of the cylinder must satisfy the dynamic equilibrium equations. Only one equilibrium equation remains, since $\tau_{\theta z} = \tau_{rz} = \tau_{r\theta} = 0$.

$$\frac{\partial \sigma_{rr}}{\partial r} + \frac{\sigma_{rr} - \sigma_{\theta\theta}}{r} = \rho \frac{\partial^2 u_r}{\partial t^2}, \tag{2}$$

where ρ denotes the density of material.

For the problem without the thermal effects, the expressions for the displacement field were derived by Lehknitskii (1963).

$$u_r = U(r, t) + z(w_y \cos\theta - w_x \sin\theta) + u_0 \cos\theta + v_0 \sin\theta, \tag{3}$$

$$u_\theta = -z(w_y \sin\theta + w_x \cos\theta) + w_z r - u_0 \sin\theta + v_0 \cos\theta, \tag{4}$$

$$u_z = zf(t) - r(w_y \cos\theta - w_x \sin\theta) + w_0, \tag{5}$$

where the function $U(r, t)$ represents the radial displacement accompanied by deformation. The constants u_0, v_0, w_0, w_x, w_y, and w_z denote the rigid-body translation and rotation along the x, y, and z directions in the Cartesian coordinate system, respectively. The time-dependent parameter $f(t)$ is determined from the boundary conditions.

The strains are expressed in terms of the displacements as follows:

$$\epsilon_{rr} = \frac{\partial U(r, t)}{\partial r}, \quad \epsilon_{\theta\theta} = \frac{U(r, t)}{r}, \quad \epsilon_{zz} = f(t),$$

$$\gamma_{\theta z} = \gamma_{rz} = \gamma_{r\theta} = 0. \tag{6}$$

Substituting (1) and (6) into the equilibrium Eq. (2) gives the following equation of dynamic thermoelasticity for the radial displacement $U(r, t)$:

$$c_{11}\left[\frac{\partial^2 U(r, t)}{\partial r^2} + \frac{1}{r}\frac{\partial U(r, t)}{\partial r}\right] - \frac{c_{22}}{r^2} U(r, t) = q_1 \frac{\partial T(r, t)}{\partial r} + q_2 \frac{T(r, t)}{r} + (c_{23} - c_{13}) \frac{f(t)}{r} + \rho \frac{\partial^2 U(r, t)}{\partial t^2}, \tag{7}$$

where, the q_i constants are given by

$$q_1 = c_{11}\alpha_r + c_{12}\alpha_\theta + c_{13}\alpha_z, \tag{8}$$

$$q_2 = (c_{11} - c_{12})\alpha_r + (c_{12} - c_{22})\alpha_\theta + (c_{13} - c_{23})\alpha_z, \tag{9}$$

and the initial conditions, as well as the boundary conditions due to the absence of external tractions, $\sigma_{rr}(r_i, t) = 0$, $i = 1, 2$, are

$$U(r, 0) = 0, \quad \frac{\partial U(r, 0)}{\partial t} = 0, \tag{10}$$

$$c_{11}\frac{\partial U(r_i, t)}{\partial r} + c_{12}\frac{U(r_i, t)}{r_i} + c_{13}f(t) - q_1 T(r_i, t) = 0, \quad i = 1, 2. \tag{11}$$

The axial force $P_z(t)$ is given by

$$P_z(t) = \int_{r_1}^{r_2} \sigma_{zz}(r, t) 2\pi r dr = \int_{r_1}^{r_2} \left[c_{13}\frac{\partial U(r, t)}{\partial r} + c_{23}\frac{U(r, t)}{r} + c_{33}f(t) - q_3 T(r, t)\right] 2\pi r dr, \tag{12}$$

where $q_3 = c_{13}\alpha_r + c_{23}\alpha_\theta + c_{33}\alpha_z$.

Consider now the thermoelastic equation of the present problem without the inertia term, which is described by the following inhomogeneous ordinary differential equation of second order in terms of the radial displacement $U_t(r, t)$:

$$c_{11}\left[\frac{\partial^2 U_t(r, t)}{\partial r^2} + \frac{1}{r}\frac{\partial U_t(r, t)}{\partial r}\right] - \frac{c_{22}}{r^2} U_t(r, t) = q_1 \frac{\partial T(r, t)}{\partial r} + q_2 \frac{T(r, t)}{r} + (c_{23} - c_{13}) \frac{f(t)}{r}. \tag{13}$$

Notice the absence of the dynamic term (last term in (7)). The associated initial conditions and boundary conditions are given as in (10) and (11) with U_t substituted in place of U. The axial force, $P_{z_t}(t)$, is also given by the same relation as in (12) with U_t substituted in place of U.

It is assumed that the general solution of the governing equation of linear dynamic thermoelasticity (7) can be separated into two parts, by the principle of superposition, namely,

$$U(r, t) = U_t(r, t) + U_d(r, t), \tag{14}$$

where $U_t(r, t)$ represents the thermoelastic radial displacement without the inertia term and $U_d(r, t)$ denotes the dynamic radial displacement.

As a particular case for the presented formulation, the temperature distribution which can be arbitrarily selected can be assumed as

$$T(r, t) = T_0 H(t) = \begin{cases} 0, & t < 0 \\ T_0, & t \geq 0^+ \end{cases}. \tag{15}$$

The function $f(t)$ is set in the same form, as

$$f(t) = f_0 H(t) = \begin{cases} 0, & t < 0 \\ f_0, & t \geq 0^+ \end{cases}, \tag{16}$$

Downloaded 04 May 2010 to 171.66.16.26. Redistribution subject to ASME license or copyright; see http://www.asme.org/terms/Terms_Use.cfm

where $H(t)$ is defined as the Heaviside step function. The general solution $U_t(r, t)$ of the inhomogeneous differential Eq. (13) is given by

$$U_t(r, t) = G_{10}r^{\lambda_1} + G_{20}r^{\lambda_2} + \frac{c_{23} - c_{13}}{c_{11} - c_{22}} f_0 r + U_t^*(r, t) \quad \text{for} \quad c_{11} \neq c_{22}, \quad (17)$$

or

$$U_t(r, t) = G_{10}r + G_{20}\frac{1}{r} + \frac{c_{23} - c_{13}}{2c_{11}} f_0 r \ln r + U_t^*(r, t) \quad \text{for} \quad c_{11} = c_{22}, \quad (18)$$

where $\lambda_{1,2} = \sqrt{c_{22}/c_{11}}$ and $U_t^*(r, t)$ is a particular solution, obtained as

$$U_t^*(r, t) = \begin{cases} T_0 q_2 r/(c_{11} - c_{22}) & \text{for} \quad c_{11} \neq c_{22}, t \geq 0^+ \\ T_0 q_2 r \ln r/(2c_{11}) & \text{for} \quad c_{11} = c_{22}, t \geq 0^+ \end{cases} \quad (19)$$

Using (7) with the associated initial and boundary conditions and the above definition, the following equation for the dynamic elasticity part in terms of displacement is obtained:

$$c_{11}\left[\frac{\partial^2 U_d(r, t)}{\partial r^2} + \frac{1}{r}\frac{\partial U_d(r, t)}{\partial r}\right] - \frac{c_{22}}{r^2} U_d(r, t) = \rho\left(\frac{\partial^2 U_t(r, t)}{\partial t^2} + \frac{\partial^2 U_d(r, t)}{\partial t^2}\right), \quad (20)$$

with the initial conditions

$$U_d(r, 0) = 0, \quad \frac{\partial U_d(r, 0)}{\partial t} = 0. \quad (21)$$

The boundary conditions for the traction-free surfaces of the cylinder and the axial force at the ends are given from (11) as follows:

$$c_{11}\frac{\partial U_d(r_i, t)}{\partial r} + c_{12}\frac{U_d(r_i, t)}{r_i} = 0, \quad i = 1, 2. \quad (22)$$

Moreover, the axial force condition is given from (12):

$$\int_{r_1}^{r_2}\left[c_{12}\frac{\partial U_d(r, t)}{\partial r} + c_{23}\frac{U_d(r, t)}{r}\right]2\pi r dr = 0, \quad (23)$$

where $r_i = r_1$, or r_2. The dynamic elasticity Eq. (20) is given in the form

$$\frac{\partial^2 U_d(r, t)}{\partial r^2} + \frac{1}{r}\frac{\partial U_d(r, t)}{\partial r} - \frac{\nu^2}{r^2} U_d(r, t) = \frac{1}{\bar{c}^2}\left(\frac{\partial^2 U_t(r, t)}{\partial t^2} + \frac{\partial^2 U_d(r, t)}{\partial t^2}\right), \quad (24)$$

where the parameter $\nu = \sqrt{c_{22}/c_{11}}$. Therefore $\nu = \lambda_1$ and the wave speed in the radial direction is denoted by $\bar{c} = \sqrt{c_{11}/\rho}$.

At this stage, in order to develop the procedure for solving the dynamic elasticity Eq. (24), let the solution be $U_{d_h}(r, t) = g(r)e^{-i\omega t}$, where ω is the natural frequency. Substituting $U_{d_h}(r, t)$ into (24), after assuming $U_t(r, t) = 0$ and setting $\xi = \omega/\bar{c}$, gives a standard Bessel equation as follows:

$$\frac{d^2 g(r)}{dr^2} + \frac{1}{r}\frac{dg(r)}{dr} + \left(\xi^2 - \frac{\nu^2}{r^2}\right)g(r) = 0, \quad (25)$$

with the Cauchy boundary conditions

$$\frac{dg(r_i)}{dr} + h_i g(r_i) = 0, \quad i = 1, 2, \quad (26)$$

where the constants are defined by

$$h_1 = \frac{c_{12}}{r_1 c_{11}}, \quad h_2 = \frac{c_{12}}{r_2 c_{11}}. \quad (27)$$

The general solution of the Bessel equation of arbitrary order ν is obtained by

$$g(r) = AJ_\nu(\xi r) + BY_\nu(\xi r), \quad (28)$$

where $J_\nu(x)$ is the Bessel function of the first kind of order ν and $Y_\nu(x)$ is the Bessel function of the second kind of order ν defined as

$$Y_\nu(\xi r) = \frac{J_\nu(\xi r)\cos \pi\nu - J_{-\nu}(\xi r)}{\sin \pi\nu}. \quad (29)$$

But when the order ν is an integer, the function $Y_n(z)$ should be taken by the limit definition

$$Y_n(z) = \lim_{\nu \to n} Y_\nu(z).$$

The definitions of $J_\nu(\xi r)$ and $J_{-\nu}(\xi r)$ are described in Appendix A. By using the boundary conditions, the general solution $g(r)$ of the Bessel equation can be written as the eigenfunction series

$$g(r) = \sum_i A_i D_\nu(\xi_i r), \quad i = 1, 2, \ldots, \infty, \quad (30)$$

where A_i are constants, the eigenfunction

$$D_\nu(\xi_i r) = J_\nu(\xi_i r)Y_a - Y_\nu(\xi_i r)J_a,$$

and ξ_i is a positive root of the transcendental equation:

$$J_a Y_b - J_b Y_a = 0, \quad (31)$$

where the parameters are defined as

$$J_a = \xi_i J_\nu'(\xi_i r_1) + h_1 J_\nu(\xi_i r_1), \quad J_b = \xi_i J_\nu'(\xi_i r_2) + h_2 J_\nu(\xi_i r_2),$$
$$Y_a = \xi_i Y_\nu'(\xi_i r_1) + h_1 Y_\nu(\xi_i r_1),$$
$$Y_b = \xi_i Y_\nu'(\xi_i r_2) + h_2 Y_\nu(\xi_i r_2). \quad (32)$$

After multiplying (30) by $D_\nu(\xi_i r)$ and r, and integrating in the finite range, we can find the constants A_i by using the orthogonality condition

$$A_i = \int_{r_1}^{r_2} r g(r) D_\nu(\xi_i r) dr \Big/ \int_{r_1}^{r_2} r[D_\nu(\xi_i r)]^2 dr. \quad (33)$$

In order to get the general solution of the Bessel equation, we use the finite Hankel transform of $g(r)$, denoted by $\hat{g}(\xi_i)$, defined by

$$\hat{g}(\xi_i) = \int_{r_1}^{r_2} r g(r) D_\nu(\xi_i r) dr. \quad (34)$$

Downloaded 04 May 2010 to 171.66.16.26. Redistribution subject to ASME license or copyright; see http://www.asme.org/terms/Terms_Use.cfm

Then the inverse of the finite Hankel transformation is given in the form

$$g(r) = \sum_i \frac{\hat{g}(\xi_i) D_\nu(\xi_i r)}{N(\xi_i)}, \tag{35}$$

where the normalizing factor $N(\xi_i) = \int_{r_1}^{r_2} r[D_\nu(\xi_i r)]^2 dr$ which is always positive. Therefore, setting $U_d(r, t)$ in place of $g(r)$, the radial displacement due to the dynamic elasticity contribution can be expressed as

$$U_d(r, t) = \sum_i \frac{\hat{u}_d(\xi_i, t) D_\nu(\xi_i r)}{N(\xi_i)}, \tag{36}$$

where the summation is taken over all the positive roots of the transcendental equation (31). The finite Hankel transform for the dynamic displacement is now written by

$$\hat{u}_d(\xi_i, t) = \int_{r_1}^{r_2} r U_d(r, t) D_\nu(\xi_i r) dr. \tag{37}$$

Taking the finite Hankel transform of the inhomogeneous Eq. (24) over r_1 and r_2, and using (31), the transformed equation results in

$$\frac{2J_a}{\pi J_b}\left[\frac{\partial U_d(r_2, t)}{\partial r} + h_2 U_d(r_2, t)\right] - \frac{2}{\pi}\left[\frac{\partial U_d(r_1, t)}{\partial r} + h_1 U_d(r_1, t)\right] - \xi_i^2 \hat{u}_d(\xi_i, t) = \frac{1}{\bar{c}^2}\left(\frac{\partial^2 \hat{u}_d(\xi_i, t)}{\partial t^2} + \frac{\partial^2 \hat{u}_t(\xi_i, t)}{\partial t^2}\right). \tag{38}$$

Since $U_d(r, t)$ satisfies the homogeneous boundary conditions (22) at each surface, the first two terms of the left-hand side of (38) should vanish. Thus the transformed equation becomes

$$-\xi_i^2 \hat{u}_d(\xi_i, t) = \frac{1}{\bar{c}^2}\left(\frac{\partial^2 \hat{u}_d(\xi_i, t)}{\partial t^2} + \frac{\partial^2 \hat{u}_t(\xi_i, t)}{\partial t^2}\right). \tag{39}$$

Using the Laplace transform, denoted by $\hat{u}_d^L$, with the zero initial conditions, the above equation can be transformed as

$$-\xi_i^2 \hat{u}_d^L(\xi_i, s) = \frac{s^2}{\bar{c}^2}[\hat{u}_d^L(\xi_i, s) + \hat{u}_t^L(\xi_i, s)]. \tag{40}$$

For convenience, the above equation can be written in the form

$$\hat{u}_d^L(\xi_i, s) = -\hat{u}_t^L(\xi_i, s) + \frac{\bar{c}^2 \xi_i^2}{\bar{c}^2 \xi_i^2 + s^2} \hat{u}_t^L(\xi_i, s). \tag{41}$$

By using the inverse Laplace transform, the following Hankel transformed dynamic displacement as a function of time is obtained from the previous equation

$$\hat{u}_d(\xi_i, t) = -\hat{u}_t(\xi_i, t) + \bar{c}\xi_i \sin \bar{c}\xi_i t * \hat{u}_t(\xi_i, t). \tag{42}$$

Since $U_t(r, t)$ is already known, the finite Hankel transform of $U_t(r, t)$, denoted by $\hat{u}_t(\xi_i, t)$, can be defined as follows:

$$\hat{u}_t(\xi_i, t) = \int_{r_1}^{r_2} r U_t(r, t) D_\nu(\xi_i r) dr. \tag{43}$$

Then, by using (17), the finite Hankel transform of the thermally induced displacement is described, for $c_{11} \neq c_{22}$, by

$$\hat{u}_t(\xi_i, t) = G_{10} I_1(\xi_i) + G_{20} I_2(\xi_i) + \frac{c_{23} - c_{13}}{c_{11} - c_{22}} f_0 I_3(\xi_i) + \hat{u}_t^*(\xi_i, t), \tag{44}$$

and, by using (18), for $c_{11} = c_{22}$,

$$\hat{u}_t(\xi_i, t) = G_{10} I_1(\xi_i) + G_{20} I_2(\xi_i) + \frac{c_{23} - c_{13}}{2c_{11}} f_0 I_3'(\xi_i) + \hat{u}_t^*(\xi_i, t). \tag{45}$$

Notice that the I_i's are the finite Hankel transforms, defined as

$$I_1(\xi_i) = \int_{r_1}^{r_2} r^{\nu+1} D_\nu(\xi_i r) dr,$$

$$I_2(\xi_i) = \int_{r_1}^{r_2} r^{-\nu+1} D_\nu(\xi_i r) dr. \tag{46}$$

These transforms can be analytically calculated from the recurrence formulas,

$$\frac{d}{dz}\{z^\nu J_\nu(z)\} = z^\nu J_{\nu-1}(z),$$

$$\frac{d}{dz}\{z^{-\nu} J_\nu(z)\} = -z^{\nu+1} J_{\nu+1}(z), \tag{47}$$

regardless of the range of arguments. Thus the finite Hankel transforms $I_1(\xi_i)$ and $I_2(\xi_i)$ can be easily carried out analytically as given in Appendix B. Here the finite Hankel transform for $U_t^*(r, t)$ is given as

$$\hat{u}_t^*(\xi_i, t) = H\{U_t^*(r, t)\} = \int_{r_1}^{r_2} r U_t^*(r, t) D_\nu(\xi_i r) dr. \tag{48}$$

The finite Hankel transform of the above expression, using the earlier definition, becomes, for $c_{11} \neq c_{22}$,

$$\hat{u}_t^*(\xi_i) = \frac{T_0 q_2}{c_{11} - c_{22}} I_3(\xi_i), \tag{49}$$

and, for $c_{11} = c_{22}$,

$$\hat{u}_t^*(\xi_i) = \frac{T_0 q_2}{2c_{11}} I_3'(\xi_i), \tag{50}$$

where q_2 becomes zero for the isotropic case, for which $\alpha_r = \alpha_\theta$ and $c_{11} = c_{22}$. In the previous expression, I_3 and I_3' are the finite Hankel transforms of the functions r and $r \ln r$, described by

$$I_3(\xi_i) = \int_{r_1}^{r_2} r^2 D_\nu(\xi_i r) dr \quad \text{for} \quad c_{11} \neq c_{22}, \tag{51}$$

$$I_3'(\xi_i) = \int_{r_1}^{r_2} r^2 \ln r D_\nu(\xi_i r) dr \quad \text{for} \quad c_{11} = c_{22}. \tag{52}$$

The integration given by Eqs. (52) and (51) can be performed in closed form with the recurrence formulas available, only if the argument is in the small arguments domain and the definition

Downloaded 04 May 2010 to 171.66.16.26. Redistribution subject to ASME license or copyright; see http://www.asme.org/terms/Terms_Use.cfm

of series expansions for Bessel functions is used. The closed-form integration cannot be obtained in the large argument region for Eqs. (51) and (52). In this case, numerical integration should be used. Therefore, the Bessel functions for integration need to be computed in the two regions. One is for small arguments, the other is for large arguments. For the large arguments of the Bessel functions, the Hankel asymptotic expansions are always numerically integrated regardless of the order of Bessel functions because the closed form of integration cannot be obtained due to the complexity of the asymptotic definition of Bessel functions in this range. It can be noted that the numerical Hankel transform is always possible for any arbitrary analytical functions if the appropriate scheme of numerical integration is used. The Bessel functions of the first kind of order ν for small and large arguments used in this work are defined in Appendix A. Further details on the numerical finite Hankel transform will be mentioned in the next section.

Combining all these expressions, the finite Hankel transform of the dynamic displacement part is obtained by

$$\widehat{u}_d(\xi_i, t) = -\widehat{u}_t(\xi_i, t) + \bar{c}\xi_i \sin \bar{c}\xi_i t * \widehat{u}_t(\xi_i, t). \quad (53)$$

Thus, the convolution integral $I_0(t) = \int_0^t \widehat{u}_t(\xi_i, \tau) \sin \bar{c}\xi_i(t - \tau)d\tau$ is used and gives

$$\widehat{u}_d(\xi_i, t) = -\widehat{u}_t(\xi_i) \cos \bar{c}\xi_i t. \quad (54)$$

Substituting $\widehat{u}_d(\xi_i, t)$ into the inverse formula (36), the general solution of the dynamic part of the equation of motion is obtained by

$$U_d(r, t) = \sum_i \frac{D_\nu(\xi_i r)}{N(\xi_i)} [-\widehat{u}_t(\xi_i) \cos \bar{c}\xi_i t]. \quad (55)$$

Therefore, the general solution for the elastodynamic radial displacements due to thermal shock in an orthotropic thick cylindrical shell is found to be

$$U(r, t) = G_{10} r^{\lambda_1} + G_{20} r^{\lambda_2} + \left(\frac{c_{23} - c_{13}}{c_{11} - c_{22}} f_0 + \frac{T_0 q_2}{c_{11} - c_{22}} \right) r + \sum_i \frac{D_\nu(\xi_i r)}{N(\xi_i)} [-\widehat{u}_t(\xi_i) \cos \bar{c}\xi_i t]. \quad (56)$$

After obtaining the displacement (19) and its finite Hankel transform (49)–(50), the total displacement field (56) can be obtained. Therefore the elastodynamic thermal shock stresses in each direction can be determined from the relations (1) and (6) when $c_{11} \neq c_{22}$. The radial stress is

$$\begin{aligned}\sigma_{rr}(r, t) &= c_{11} \frac{\partial U(r, t)}{\partial r} + c_{12} \frac{U(r, t)}{r} + c_{13} f(t) - q_1 T(r, t) \\ &= G_{10}(c_{11}\lambda_1 + c_{12}) r_i^{\lambda_1 - 1} + G_{20}(c_{11}\lambda_2 + c_{12}) r_i^{\lambda_2 - 1} \\ &\quad + f_0 \left[c_{13} + \frac{c_{23} - c_{13}}{c_{11} - c_{22}} (c_{11} + c_{12}) \right] \\ &\quad - T_0 \left[q_1 - q_2 \frac{(c_{11} + c_{12})}{c_{11} - c_{22}} \right] \\ &\quad + \sum_i \frac{[-\widehat{u}_t(\xi_i) \cos \bar{c}\xi_i t]}{N(\xi_i)} \\ &\quad \times \left[c_{11} \frac{\partial D_\nu(\xi_i r)}{\partial r} + \frac{c_{12}}{r} D_\nu(\xi_i r) \right], \quad (57)\end{aligned}$$

the hoop stress is given by

$$\begin{aligned}\sigma_{\theta\theta}(r, t) &= c_{12} \frac{\partial U(r, t)}{\partial r} + c_{22} \frac{U(r, t)}{r} + c_{23} f(t) - q_{\alpha 2} T(r, t) \\ &= G_{10}(c_{12}\lambda_1 + c_{22}) r_i^{\lambda_1 - 1} + G_{20}(c_{12}\lambda_2 + c_{22}) r_i^{\lambda_2 - 1} \\ &\quad + f_0 \left[c_{23} + \frac{c_{23} - c_{13}}{c_{11} - c_{22}} (c_{12} + c_{22}) \right] \\ &\quad - T_0 \left[q_{\alpha 2} - q_2 \frac{(c_{12} + c_{22})}{c_{11} - c_{22}} \right] \\ &\quad + \sum_i \frac{[-\widehat{u}_t(\xi_i) \cos \bar{c}\xi_i t]}{N(\xi_i)} \\ &\quad \times \left[c_{12} \frac{\partial D_\nu(\xi_i r)}{\partial r} + \frac{c_{22}}{r} D_\nu(\xi_i r) \right], \quad (58)\end{aligned}$$

and the axial stress is given by

$$\begin{aligned}\sigma_{zz}(r, t) &= c_{13} \frac{\partial U(r, t)}{\partial r} + c_{23} \frac{U(r, t)}{r} + c_{33} f(t) - q_3 T(r, t) \\ &= G_{10}(c_{13}\lambda_1 + c_{23}) r_i^{\lambda_1 - 1} + G_{20}(c_{13}\lambda_2 + c_{23}) r_i^{\lambda_2 - 1} \\ &\quad + f_0 \left(c_{33} + \frac{(c_{23}^2 - c_{13}^2)}{(c_{11} - c_{22})} \right) \\ &\quad - T_0 \left[q_3 - q_2 \frac{(c_{13} + c_{23})}{(c_{11} - c_{22})} \right] \\ &\quad + \sum_i \frac{[-\widehat{u}_t(\xi_i) \cos \bar{c}\xi_i t]}{N(\xi_i)} \\ &\quad \times \left[c_{13} \frac{\partial D_\nu(\xi_i r)}{\partial r} + \frac{c_{23}}{r} D_\nu(\xi_i r) \right], \quad (59)\end{aligned}$$

where $q_{\alpha 2} = c_{12}\alpha_r + c_{22}\alpha_\theta + c_{23}\alpha_z$.

At this stage the unknown coefficients are found from the boundary conditions available. We have assumed that no external tractions exist. Then the conditions in the contour bounding the cross section (at r_1 and r_2) can be written in the following form:

$$\sigma_{rr}(r_i, t) = \tau_{r\theta}(r_i, t) = \tau_{rz}(r_i, t) = 0, \quad i = 1, 2. \quad (60)$$

Only a condition for the stress σ_{rr} is not satisfied identically and this is written as Eq. (57). By (60), the following linear equations in unknown constants G_{10}, G_{20}, and f_0 are obtained:

$$G_{10}(c_{11}\lambda_1 + c_{12}) r_i^{\lambda_1 - 1} + G_{20}(c_{11}\lambda_2 + c_{12}) r_i^{\lambda_2 - 1} + f_0 B_1 = T_0 B_0, \quad i = 1, 2, \quad (61)$$

where

$$B_1 = \begin{cases} c_{13} + (c_{23} - c_{13})(c_{11} + c_{12})/(c_{11} - c_{22}) & \text{for } c_{11} \neq c_{22} \\ c_{13} + (c_{23} - c_{13})/2 + (c_{23} - c_{13})(c_{11} + c_{12}) \ln r/(2c_{11}) & \text{for } c_{11} = c_{22}, \end{cases} \quad (62)$$

$$B_0 = \begin{cases} q_1 - q_2(c_{11} + c_{12})/(c_{11} - c_{22}) & \text{for } c_{11} \neq c_{22} \\ q_1 - q_2/2 - q_2(c_{11} + c_{12}) \ln r/(2c_{11}) & \text{for } c_{11} = c_{22} \end{cases}. \quad (63)$$

Downloaded 04 May 2010 to 171.66.16.26. Redistribution subject to ASME license or copyright; see http://www.asme.org/terms/Terms_Use.cfm

The end boundary condition of zero resultant axial force, $P_z(t) = \int_{r_1}^{r_2} \sigma_{zz}(r, t) 2\pi r dr = 0$, gives the last set of equations that are needed to determine the unknown constants:

$$G_{10}\left(\frac{c_{31}\lambda_1 + c_{32}}{\lambda_1 + 1}\right)(r_2^{\lambda_1+1} - r_1^{\lambda_1+1}) + G_{20}E_2 + f_0E_1 = T_0E_0, \quad (64)$$

where the parameters used are described, for $c_{11} \neq c_{22}$, by

$$E_2 = \left(\frac{c_{13}\lambda_2 + c_{23}}{\lambda_2 + 1}\right)(r_2^{\lambda_2+1} - r_1^{\lambda_2+1});$$

$$E_1 = \left(\frac{c_{23}^2 - c_{13}^2}{c_{11} - c_{22}} + c_{33}\right)\frac{(r_2^2 - r_1^2)}{2}, \quad (65)$$

$$E_0 = \left(q_{\alpha 3} - q_2\frac{c_{13} + c_{23}}{c_{11} - c_{22}}\right)\frac{(r_2^2 - r_1^2)}{2}, \quad (66)$$

and, for $c_{11} = c_{22}$,

$$E_2 = (c_{13}\lambda_2 + c_{23}) \ln (r_2/r_1), \quad (67)$$

$$E_1 = \left(c_{33} + c_{31}\frac{c_{23} - c_{13}}{2c_{11}} - \frac{c_{23}^2 - c_{13}^2}{4c_{11}}\right)\frac{(r_2^2 - r_1^2)}{2} + \frac{c_{23}^2 - c_{13}^2}{4c_{11}}(r_2^2 \ln r_2 - r_1^2 \ln r_1), \quad (68)$$

and

$$E_0 = \left(q_{\alpha 3} - q_2\frac{c_{13}}{2c_{11}}\right)\frac{(r_2^2 - r_1^2)}{2} - (c_{31} + c_{32})\frac{q_2}{4c_{11}} \times \left[(r_2^2 \ln r_2 - r_1^2 \ln r_1) - \frac{(r_2^2 - r_1^2)}{2}\right]. \quad (69)$$

The boundary conditions for the time dependent terms in the sets of algebraic Eqs. (61) and (64) have already been satisfied by (22) and (23). Therefore there is no need for additional equations to determine the unknown constants.

Results and Discussion

In order to examine the present solution's validity, a numerical example was employed to analyze the elastodynamic thermal shock stresses propagating through the wall in the form of a stress wave. Before presenting results, it should be mentioned that the definition in the form of a series expansion for the Bessel functions cannot be used for large arguments. For large arguments, the Hankel asymptotic expansions of the Bessel functions should be used for the eigenvalues, eigenfunctions, and the evaluation of Hankel transforms as described in the Appendix A.

Table 1 The first ten roots of the transcendental Eq. (31) and the values of the arguments* at the boundaries

i	ξ_i	$r_1 \times \xi_i$	$r_2 \times \xi_i$
1	25.30	1.265	2.530
2	68.56	3.428	6.856
3	128.4	6.422	12.84
4	190.3	9.517	19.03
5	252.7	12.64	25.27
6	315.3	15.76	31.53
7	377.9	18.90	37.79
8	440.6	22.03	44.06
9	503.3	25.17	50.33
10	566.1	28.30	56.61

* In computing the Bessel functions, the Hankel asymptotic expansions are used above the value of 18.0 (large arguments region).

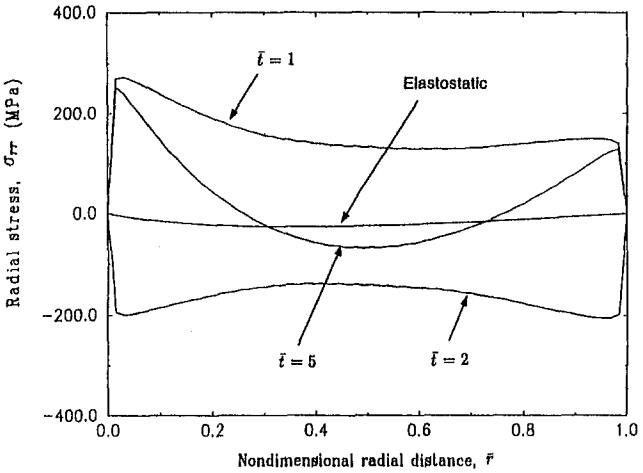

Fig. 1 The distribution of radial stress, σ_{rr}, from the elastodynamic solution at different times versus the nondimensional radial distance, $\bar{r} = (r - r_1)/(r_2 - r_1)$. Also the elastostatic solution is shown.

As an illustrative example, the distributions and histories of thermal shock stresses in the wall are determined for a glass/epoxy circular cylinder of inner radius $r_1 = 50$ mm and outer radius $r_2 = 100$ mm. It is supposed to be made, by filament winding, with the fibers oriented around the circumference of cylinder. The moduli in GN/m^2 and Poisson's ratios for the material are listed in the following, where 1 denotes the radial (r), 2 the circumferential (θ), and 3 the axial (z) direction:

$$E_1 = 13.7, \quad E_2 = 55.9, \quad E_3 = 13.7, \quad G_{12} = 5.6, \quad G_{23} = 5.6$$
$$G_{31} = 4.9, \quad \nu_{12} = 0.068, \quad \nu_{23} = 0.277, \quad \nu_{31} = 0.4.$$

The thermal expansion coefficients are $\alpha_r = 40 \times 10^{-6}$/°C, $\alpha_\theta = 10 \times 10^{-6}$/°C, and $\alpha_z = 40 \times 10^{-6}$/°C. The loading temperature of $T(r, t)$, causing thermal shock at the surface, is applied at $t = 0^+$ over the entire thickness of the hollow cylinder, and it is assumed that the applied temperature is kept constant thereafter. This type of thermal loading, causing the response of strong dynamic thermal stresses on the cylinder, can be developed by a strong chemical reaction, an absorption of infrared radiation, or an electromagnetic radiant energy from pulses.

For the eigenfunction series sum of the elastodynamic solution, roots of the transcendental Eq. (31) are needed. The first ten roots are shown in the Table 1 with the values of the arguments at both boundaries. Numerical finite Hankel transformations for arbitrary functions were carried out by using the Romberg's integration algorithm.

In order to show the results, the following nondimensional quantities are used: for radial distance (through the thickness), $\bar{r} = (r - r_1)/(r_2 - r_1)$, and for time, $\bar{t} = \bar{c}t/(r_2 - r_1)$, where $\bar{t}$ would physically represent the number of trips required by the stress wave in going through the thickness. The distribution of radial dynamic thermal stress is presented at each nondimensional time $\bar{t} = 1$, 2, and 5 in Fig. 1. Since the speed of wave $\bar{c}$ is calculated as 3,169 m/sec, the nondimensional time $\bar{t} = 1$ indicates 1.577×10^{-5} sec. The radial stress wave is initiated at the inside and outside boundaries simultaneously, propagates outward from the inside boundary and inward from the external boundary through the wall and reflects in the opposite direction towards the boundaries. Subsequently, this reflected wave is also reversed again at the boundaries. The tension in the first phase of travel is reversed into compression by the reflection

Downloaded 04 May 2010 to 171.66.16.26. Redistribution subject to ASME license or copyright; see http://www.asme.org/terms/Terms_Use.cfm

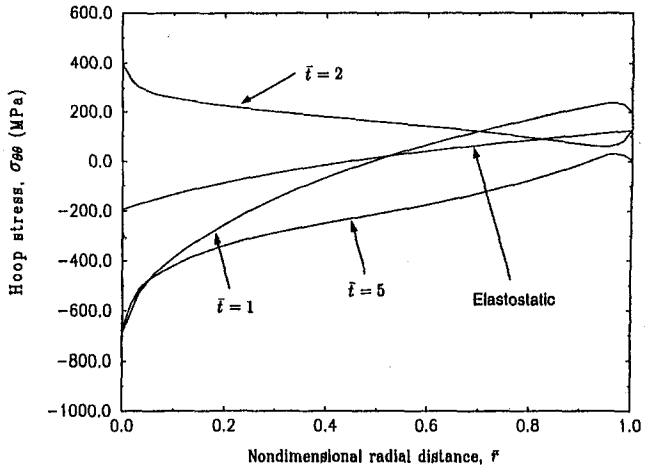

Fig. 2 The distribution of hoop stress, $\sigma_{\theta\theta}$, at different times versus the nondimensional radial distance, $\bar{r} = (r - r_1)/(r_2 - r_1)$

of waves, as shown in Figs. 4(*a*, *b*), and a dramatic change of radial stress through the thickness is observed. This effect is reduced with time. The first maximum peak radial stress is obtained at $\bar{r} = 0.5$ when $\bar{t} \approx 5.5$. As expected, the magnitude of dynamic radial stress is much higher than that in the static case.

The largest change of stresses through the shell thickness is observed in the circumferential direction during the first travel of the wave, as shown in Fig. 2. The magnitude of the hoop stresses near the boundaries increases with continuing wave propagation. The hoop stress near the midpoint in the wall is lower than that near the boundaries. The maximum dynamic thermal stress on a circumferentally wound orthotropic cylindrical shell occurs in the first travel in the circumferential direction at the inner boundary. This observation for an orthotropic cylindrical shell is still true as in the isotropic case which was observed in Wang (1995). It should be noted that the cylinder is most resistant in this direction, since it is circumferentially filament wound and the material strength in the fiber direction is usually the largest. Therefore, this dominant material characteristic affects to a large extent the elastodynamic response of the cylindrical shell structure. Of course, in addition to the stiffness and strength in the fiber direction, the thermal expansion coefficients are also important factors in determining the thermoelastic behavior of an orthotropic thick cylindrical shell. The axial stress in Fig. 3 is not significant in comparison with the radial and hoop stresses. Actually, the behavior of axial stress is similar to that of the radial stress.

The time history of the radial stress is shown at $\bar{r} = 0.1$ in Fig. 4(*a*) and $\bar{r} = 0.5$ in Fig. 4(*b*) (notice the high-frequency oscillations). The peaks of radial stress appear whenever the stress wave reaches the corresponding locations. The steep change of magnitude of radial stress is seen near each observing location. In Fig. 5, it is clear that the hoop stress at $\bar{r} = 0.5$ experiences a smaller change than that at $\bar{r} = 0$ and $\bar{r} = 1$. This phenomenon can be observed in Fig. 2, as well. The maximum stress is observed at $\bar{t} = 5$ and 10 in the circumferential direction. The time history of axial stress is given in Fig. 6. The axial stress also has sharp peaks at $\bar{r} = 0.5$ when a stress wave arrives at that location. This characteristic of axial stress isn't seen in Fig. 3 because the time selected corresponds to the absence of points when the waves arrive.

To compare the effects of stresses for an orthotropic thick cylindrical shell to that of the isotropic case, the distribution of radial stress at $\bar{t} = 1$, 2, 5, and 10 in Fig. 7 is carried out after selecting for the orthotropic moduli, in GN/m^2 and the other material constants:

$$E = E_i = 55.9, \quad \nu = \nu_{ij} = 0.277,$$

$$\alpha = \alpha_i = 10 \times 10^{-6}/°\text{C}, \quad i = 1, 2, 3,$$

i.e., the constants of the orthotropic shell in the circumferential direction. It is seen that a large amount of stress variation

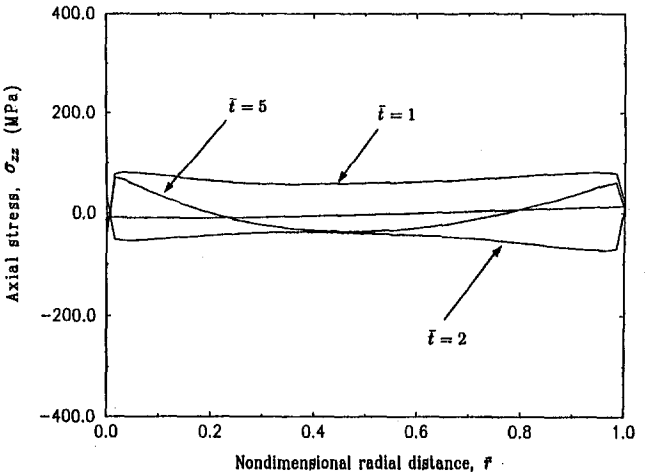

Fig. 3 The distribution of axial stress, σ_{zz}, at different times versus the nondimensional radial distance, $\bar{r}$

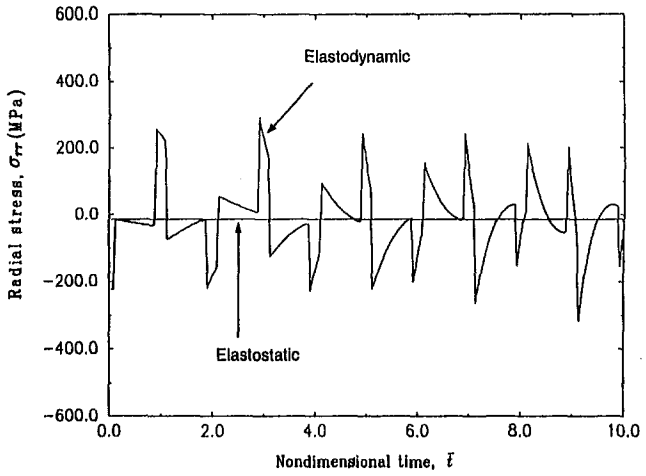

Fig. 4(*a*) The time history of radial stress, σ_{rr}, versus the nondimensional time $\bar{t} = \bar{c}t/(r_2 - r_1)$, at $\bar{r} = 0.1$

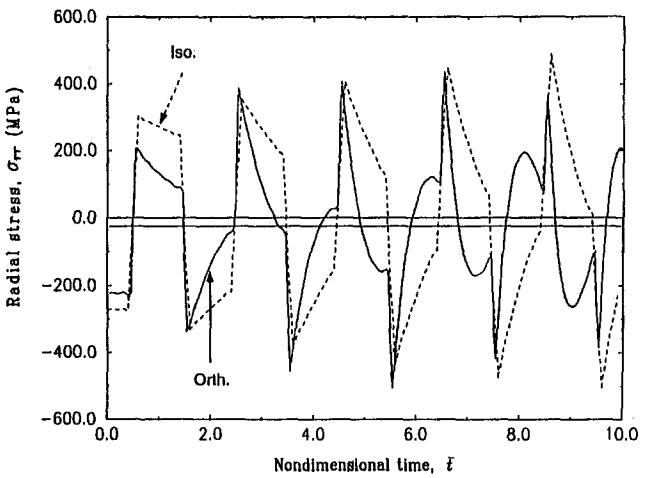

Fig. 4(*b*) The time history of radial stress, σ_{rr}, versus the nondimensional time $\bar{t} = \bar{c}t/(r_2 - r_1)$, at $\bar{r} = 0.5$

Downloaded 04 May 2010 to 171.66.16.26. Redistribution subject to ASME license or copyright; see http://www.asme.org/terms/Terms_Use.cfm

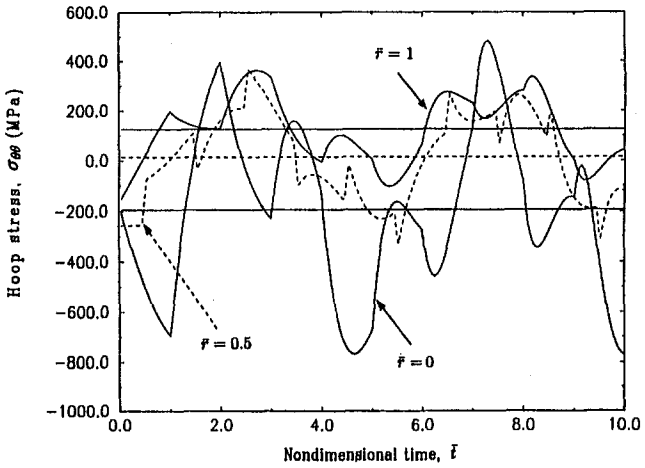

Fig. 5 The time history of hoop stress, $\sigma_{\theta\theta}$, versus the nondimensional time, $\bar{t} = \bar{c}t/(r_2 - r_1)$, at different positions through the shell thickness

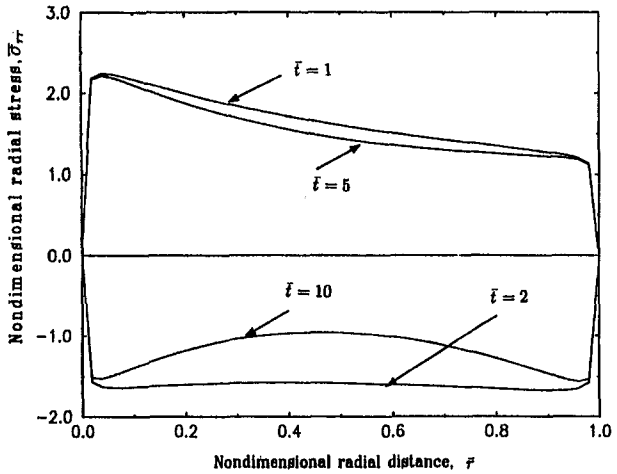

Fig. 7 The distribution of radial stress, $\bar{\sigma}_{rr}$, at $\bar{t}$ = 1, 2, 5, and 10

through the wall exists in an orthotropic cylindrical shell (Fig. 1). Thus, the peaks near the boundaries are much higher than these in other locations. The magnitude of radial stress in an orthotropic cylindrical shell drops near the center and has an oscillatory behavior attributed to the direct contribution of static stress and the orthotropic characteristics of elastic constants and thermal expansion coefficients. This effect can not be seen in the isotropic case. The oscillating behavior would come even at large time values due to the interference of the stress waves. The main difference between the two material systems appears in Figs. 1 and 7. The wavefront in an orthotropic shell is more rapidly interfered than that in an isotropic shell, as shown in Figs. 4(a, b). Also, Fig. 7, where the normalized radial stress is defined as $\bar{\sigma}_{rr} = \sigma_{rr}/E\alpha T$, and its plot shows almost the same shape and magnitude with the result given by Wang (1995). In Fig. 9, a comparison of the time history of the radial stress at $\bar{r}$ = 0.5, is shown. One of the differences between the two studies is that a plane-strain condition, $\epsilon_{zz} = 0$ was imposed in that study, unlike the present one. The differences between the two results, however, most likely should be due to the differences in the calculation points. The peak values of Wang's (1995) solution are on the present study's curves but the wave patterns are different after the first trip. This seems to be due to the fact that the plot in Wang (1995) was made from data at time values not closely enough, therefore missing the peaks values of the stress wave. This comparison also makes an important point: that the time scale of calculations of data points should be carefully examined to make sure the entire response of the stress wave and especially the peaks are captured.

Finally, one more result is presented regarding the phenomena of initial wave propagation. Figure 8 for an isotropic shell can help the understanding of the early phase of stress distribution due to wave occurrence and propagation. Since the thermal loading is applied to the entire hollow cylinder instantaneously, the stress disturbance is simultaneously generated all over the wall. In the vicinity of the boundary, the radial stress feels the strong discontinuity (wavefront) right after the loading. Each wavefront moves inward and the waves meet at the center location and cause a stress reversion and sudden jump in magnitude, as shown in Figs. 4(a, b). After that, the wavefronts proceed to the boundaries continuously. When the wavefronts reach the boundaries, they are reflected into the opposite direction as mentioned earlier.

In this study, it should be mentioned that the coupling effects between the thermal and mechanical energy in the system are neglected. This means that the uncoupled linear dynamic thermoelasticity problem was handled. Since the coupling effects always exist in the physical system under thermal environments, the coupled dynamic thermoelasticity is more realistic but too difficult and complex or sometimes impossible to obtain the closed-form solution. The uncoupled dynamic thermoelasticity problem, which was treated here, is, however, still valuable and

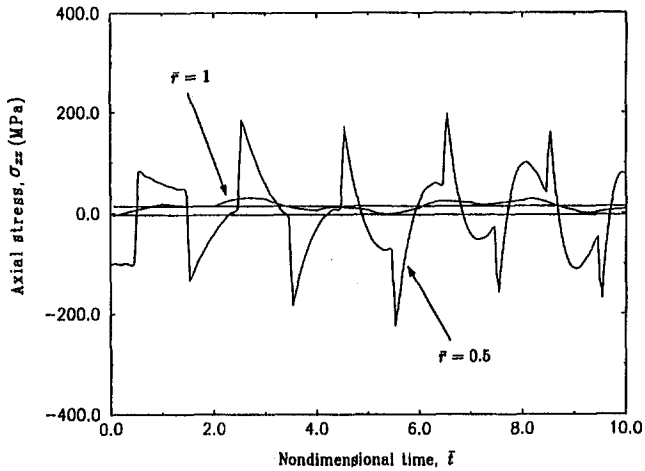

Fig. 6 The time history of axial stress, σ_{zz}, versus the nondimensional time, $\bar{t} = \bar{c}t/(r_2 - r_1)$, at $\bar{r}$ = 0.5 and 1.0

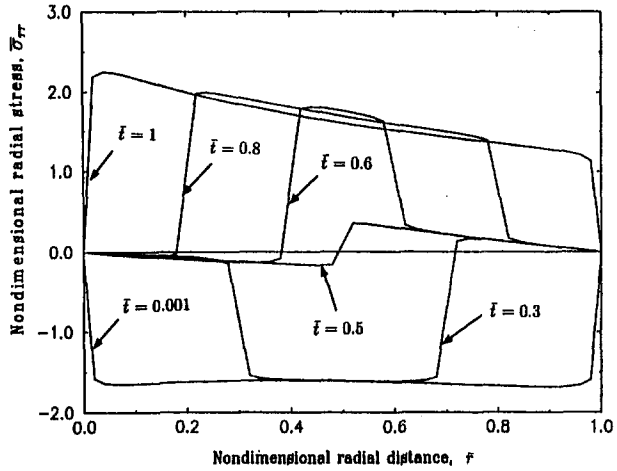

Fig. 8 The propagation of the radial stress wave, $\bar{\sigma}_{rr}$, versus $\bar{r}$ at different times

Downloaded 04 May 2010 to 171.66.16.26. Redistribution subject to ASME license or copyright; see http://www.asme.org/terms/Terms_Use.cfm

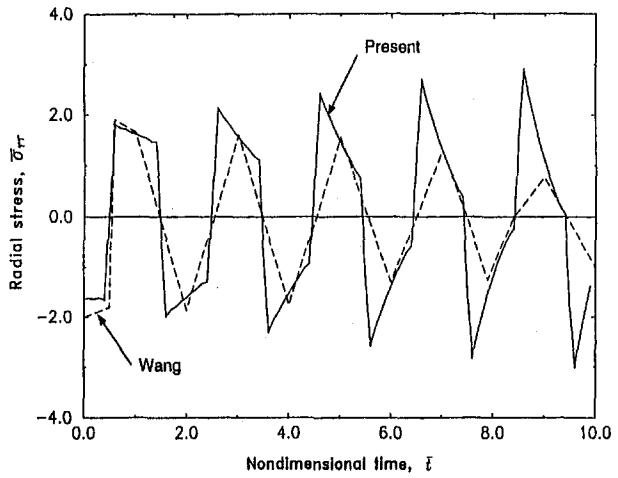

Fig. 9 Comparison of $\bar{\sigma}_{rr}$ at $\bar{r} = 0.5$, for the isotropic case, with the results of Wang (1995)

can provide a large amount of useful information on the thermal shock effects. Finally, the shell axisymmetry concept, in conjunction with the radial dependence of the thermal field, limit the applicability of the results to essentially infinitely long shells.

Summary

This work presents a method to analyze the uncoupled dynamic thermoelastic stress problem in an orthotropic thick cylindrical shell. In implementing the method, the linear dynamic thermoelasticity equations are used with the appropriate boundary and initial conditions, and the elastodynamic problem is solved by using the finite Hankel transform in the spatial variable and the Laplace transform in the time variable. In this paper, the temperature distribution was considered as the step function applied to the entire surface of the hollow cylinder. It is shown that a closed-form solution can be obtained for the thermal shock stresses in an orthotropic thick cylindrical shell. As seen in the results, a thermal stress wave occurs due to the thermal shock loading, and this plays an important role on the significant amount of dynamic thermal stresses generated through the wall. Important differences between an isotropic and orthotropic cylindrical shell exist, namely rapid variations of radial stresses in the orthotropic case, which are attributed to the orthotropy of the mechanical and thermal properties.

Acknowledgment

The financial support of the Office of Naval Research, Ship Structures and Systems, S&T Division, Grant N00014-91-J-1892, and the interest and encouragement of the Grant Monitor, Dr. Y. D. S. Rajapakse, are both gratefully acknowledged.

References

Abramowitz, M., and Stegun, I. A., 1972, *Handbook of Mathematical Functions with Formulas, Graphs and Mathematical Tables,* Dover, New York.

Achenbach, J. D., 1973, *Wave Propagation in Elastic Solids,* North-Holland, Amsterdam.

Birman, V., 1990, "Thermal Dynamic Problems of Reinforced Composite Cylinders," ASME JOURNAL OF APPLIED MECHANICS, Vol. 57, pp. 941–947.

Churchill, R. V., 1972, *Operational Mathematics,* 3rd. ed., McGraw-Hill, New York.

Cinelli, G., 1965, "An Extension of the Finite Hankel Transform and Applications," *International Journal of Engineering Science,* Vol. 3, pp. 539–559.

Cinelli, G., 1966, "Dynamic Vibrations and Stresses in Elastic Cylinders and Spheres," ASME JOURNAL OF APPLIED MECHANICS, Vol. 33, pp. 825–830.

Doxee, Jr., L. E., and Springer, G. S., 1989, "Hygrothermal Stresses and Strains in Axisymmetric Composite Shells," *Computers and Structures,* Vol. 32, No. 2, pp. 395–407.

Eringen, A. C., and Suhubi, E. S., 1975, *Elastodynamics* (Vol. II, Linear Theory), Academic Press, New York.

Graff, K. F., 1975, *Wave Motion in Elastic Solids,* Ohio State University Press, Columbus, OH.

Hata, T., 1991, "Thermal Shock in a Hollow Sphere Caused by Rapid Uniform Heating," ASME JOURNAL OF APPLIED MECHANICS, Vol. 58, pp. 64–69.

Hyer, M. W., and Cooper, D. E., 1986, "Stresses and Deformations in Composite Tubes due to a Circumferential Temperature Gradient," ASME JOURNAL OF APPLIED MECHANICS, Vol. 53, pp. 757–764.

Kardomateas, G. A., 1989, "Transient Thermal Stresses in Cylindrically Orthotropic Composite Tubes," ASME JOURNAL OF APPLIED MECHANICS, Vol. 56, pp. 411–417; also Errata, Ibid, 1991, Vol. 58, p. 909.

Kardomateas, G. A., 1990, "The Initial Phase of Transient Thermal Stresses due to General Boundary Thermal Loads in Orthotropic Hollow Cylinders," ASME JOURNAL OF APPLIED MECHANICS, Vol. 57, pp. 719–724; also Errata, Ibid, 1991, Vol. 58, p. 909.

Lebedev, N. N., 1972, *Special Functions and their Applications,* Dover, New York.

Lekhinitskii, S. G., 1981, *Theory of Elasticity of an Anisotropic Body,* Mir Publishers, Moscow.

McLachan, N. W., 1934, *Bessel Functions for Engineers,* Oxford, London.

McQuillen, E. J., and Brull, M. A., 1970, "Dynamic Thermoelastic Response of Cylindrical Shells," ASME JOURNAL OF APPLIED MECHANICS, Vol. 37, pp. 661–670.

Sciuva, M. D., and Carrera, E., 1992, "Elastodynamic Behavior of Relatively Thick, Symmetrically Laminated, Anisotropic Circular Cylindrical Shells," ASME JOURNAL OF APPLIED MECHANICS, Vol. 59, pp. 222–224.

Sneddon, I. N., 1995, *Fourier Transforms,* Dover, New York (original printed in 1951).

Sternberg, E., and Chakravorty, J. G., 1959, "Thermal Shock in an Elastic Body with a Spherical Cavity," *Quart. Applied Mathematics,* Vol. 17, pp. 205–218.

Tsui T., and Kraus H., 1965, "Thermal Stress Wave Propagation in Hollow Elastic Spheres," *Journal of the Acoustical Society of America,* Vol. 37, pp. 730–737.

Wang, X., and Gong, X. N., 1992, "An Elastodynamic Solution for Multilayered Cylinders," *International Journal of Engineering Science,* Vol. 30, No. 1, pp. 25–33.

Wang, X., 1995, "Thermal Shock in a Hollow Cylinder Caused by Rapid Arbitrary Heating," *Journal of Sound and Vibration,* Vol. 183, No. 5, pp. 899–906.

Wang, X., 1993, "Stress Wave Propagation in a Two Layered Cylinder with Initial Interface Pressure," *International Journal of Solids and Structures,* Vol. 30, No. 12, pp. 1693–1700.

Zaker, T. A., 1969, "Dynamic Thermal Shock in a Hollow Sphere," *Quart. Applied Mathematics,* Vol. 26, pp. 503–518.

APPENDIX A

The definition of Bessel functions of the first kind of order υ is for small arguments:

$$J_\nu(z) = \sum_{m=0}^{\infty} \frac{(-1)^m (1/2)^{2m+\nu}}{m!\Gamma(m+\nu+1)} z^{2m+\nu}, \quad m = 1, 2, 3, \ldots, \quad (A1)$$

$$J_{-\nu}(z) = \sum_{m=0}^{\infty} \frac{(-1)^m (1/2)^{2m-\nu}}{m!\Gamma(m-\nu+1)} z^{2m-\nu}, \quad m = 1, 2, 3, \ldots. \quad (A2)$$

The Hankel's asymptotic expansions for large arguments, when ν is fixed and $|z|$ goes to infinity, are described in the following:

$$J_\nu(z) = \sqrt{2/(\pi z)}\,[P(\nu, z)\cos\chi - Q(\nu, z)\sin\chi], \quad (A3)$$

$$Y_\nu(z) = \sqrt{2/(\pi z)}\,[P(\nu, z)\sin\chi + Q(\nu, z)\cos\chi], \quad (A4)$$

where the parameter $\chi = z - (\frac{1}{2}\nu + \frac{1}{4})\pi$, and, with $4\nu^2$ denoted by μ, P, and Q are defined by

$$P(\nu, z) = \sum_{k=0}^{\infty} (-1)^k \frac{(\nu, 2k)}{(2z)^{2k}} = 1 - \frac{(\nu-1)(\nu-9)}{2!(8z)^2} + \ldots, \quad (A5)$$

Downloaded 04 May 2010 to 171.66.16.26. Redistribution subject to ASME license or copyright; see http://www.asme.org/terms/Terms_Use.cfm

$$Q(\nu, z) = \sum_{k=0}^{\infty} (-1)^k \frac{(\nu, 2k+1)}{(2z)^{2k+1}}$$

$$= \frac{(\nu-1)}{(8z)} - \frac{(\nu-1)(\nu-9)(\nu-25)}{3!(8z)^3} + \ldots . \quad (A6)$$

APPENDIX B

The finite Hankel transformations of arbitrary functions can be evaluated analytically by using the series expansion form of the Bessel functions for small arguments. By the recurrence formula, the finite Hankel transforms for r^{ν} and $r^{-\nu}$ can be expressed as

$$I_1(\xi_i) = \int_{r_1}^{r_2} r^{\nu+1} D_{\nu}(\xi_i r) dr = J_{-a}\left[\frac{r^{\nu+1}}{\xi_i} J_{\nu+1}(\xi_i r)\right]_{r_1}^{r_2}$$

$$- J_a\left[-\frac{r^{\nu+1}}{\xi_i} J_{-\nu-1}(\xi_i r)\right]_{r_1}^{r_2}, \quad (B1)$$

$$I_2(\xi_i) = \int_{r_1}^{r_2} r^{-\nu+1} D_{\nu}(\xi_i r) dr = J_{-a}\left[-\frac{r^{-\nu+1}}{\xi_i} J_{\nu-1}(\xi_i r)\right]_{r_1}^{r_2}$$

$$- J_a\left[\frac{r^{-\nu+1}}{\xi_i} J_{-\nu+1}(\xi_i r)\right]_{r_1}^{r_2}. \quad (B2)$$

For r, the finite Hankel transform is given by

$$I_3(\xi_i) = \int_{r_1}^{r_2} r^2 D_{\nu}(\xi_i r) dr = J_{-a}\left[\sum_{m=0}^{\infty} \frac{A_m r^{2m+\nu+3}}{2m+\nu+3}\right]_{r_1}^{r_2}$$

$$- J_a\left[\sum_{m=0}^{\infty} \frac{A_{-m} r^{2m-\nu+3}}{2m-\nu+3}\right]_{r_1}^{r_2}, \quad (B3)$$

where

$$A_m = \frac{(-1)^m (1/2)^{2m+\nu}}{m!\Gamma(m+\nu+1)}, \quad A_{-m} = \frac{(-1)^m (1/2)^{2m-\nu}}{m!\Gamma(m-\nu+1)}. \quad (B4)$$

Downloaded 04 May 2010 to 171.66.16.26. Redistribution subject to ASME license or copyright; see http://www.asme.org/terms/Terms_Use.cfm

A. G. Chassiakos
School of Engineering,
California State University,
Long Beach, CA 90840

S. F. Masri
Mem. ASME.

A. W. Smyth

School of Engineering,
University of Southern California,
Los Angeles, CA 90089

T. K. Caughey
Division of Engineering
and Applied Science,
California Institute of Technology,
Pasadena, CA 91125
Mem. ASME

On-Line Identification of Hysteretic Systems

Using adaptive estimation approaches, a method is presented for the on-line identification of hysteretic systems under arbitrary dynamic environments. The availability of such an identification approach is crucial for the on-line control and monitoring of nonlinear structural systems to be actively controlled. In spite of the challenges encountered in the identification of the hereditary nature of the restoring force of such nonlinear systems, it is shown through the use of simulation studies and experimental measurements that the proposed approach can yield reliable estimates of the hysteretic restoring force under a very wide range of excitation levels and response ranges.

1 Introduction

1.1 Background. Problems involving the identification of structural systems exhibiting inelastic restoring forces with hereditary characteristics are widely encountered in the applied mechanics field. Representative examples include buildings under strong earthquake excitations or aerospace structures incorporating joints. Due to the hysteretic nature of the restoring force in such situations, the nonlinear force cannot be expressed in the form of an algebraic function involving the instantaneous values of the state variables of the system. Consequently, much effort has been devoted by numerous investigators to develop models of hysteretic restoring forces and techniques to identify such systems. Noteworthy contributions in this area have been made by Caughey (1960, 1963), Jennings (1964), Iwan (1966), Bouc (1967), Karnopp and Scharton (1966), Iwan and Lutes (1968), Kobori et al. (1976), Wen (1976), Masri and Caughey (1979), Baber and Wen (1981, 1982), Grossmayer (1981), Spanos (1981), Toussi and Yao (1983), Andronikou and Bekey (1984), Park et al. (1985), Spencer and Bergman (1985), Sues et al. (1985, 1988), Powell and Chen (1986), Iwan and Cifuentes (1986), Vinogradov and Pivovarov (1986), Iwan et al. (1987), Jayakumar and Beck (1987), Peng and Iwan (1987, 1992), Roberts (1987), Wen and Ang (1987), Yar and Hammond (1987a, 1987b), Worden and Tomlinson (1988), Capecchi (1990), Roberts and Spanos (1990), Masri et al. (1991), Loh and Chung (1993), Benedettini et al. (1995), and Chassiakos et al. (1995).

One of the challenges in actively controlling the nonlinear dynamic response of structural systems undergoing hysteretic deformations is the need for rapid identification of the nonlinear restoring force so that the information can be utilized by on-line control algorithms for determining the proper actuator forces needed to ensure stable response control of the oscillating flexible structure. Consequently, the availability of a method for the on-line identification of hysteretic restoring forces is crucial for the practical implementation of structural control concepts (Housner and Masri, 1990, 1993; Housner et al., 1995). It is precisely this problem that this paper addresses.

1.2 Scope. This paper presents a method for the on-line identification of hysteretic systems under arbitrary dynamic environments. Section 2 formulates the problem and Section 3 presents the on-line identification algorithm. Section 4 presents simulation results corresponding to a single-degree-of-freedom model to illustrate the use of the algorithm and to demonstrate its validity under test signals that differ from those used for identification. Additionally, the identification approach is applied to experimental measurements corresponding to a steel subassembly undergoing significant hysteretic deformations. Section 5 discusses the advantages and limitations of this approach compared to alternative identification methods.

2 Problem Formulation

The motion of the single-degree-of-freedom system in Fig. 1 to be identified is governed by

$$m\ddot{x}(t) + Q(x(t), \dot{x}(t)) = u(t) \tag{1}$$

where $x(t)$ is the system displacement, $Q(x(t), \dot{x}(t))$ is the restoring force, and $u(t)$ is the system's external excitation. The mass m of the system is assumed to be known or easily estimated, and measurements of $u(t)$ and $\ddot{x}(t)$ are assumed to be available at times t_k, $k = 1, \ldots$. The values of $\dot{x}(t)$ and $x(t)$ are available either by direct measurements at times t_k, $k = 1, \ldots$, or by integration of the signal $\ddot{x}(t)$.

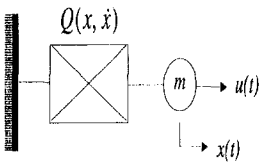

Fig. 1 Model of hysteretic system

Contributed by the Applied Mechanics Division of THE AMERICAN SOCIETY OF MECHANICAL ENGINEERS for publication in the ASME JOURNAL OF APPLIED MECHANICS.

Discussion on this paper should be addressed to the Technical Editor, Professor Lewis T. Wheeler, Department of Mechanical Engineering, University of Houston, Houston, TX 77204-4792, and will be accepted until four months after final publication of the paper itself in the ASME JOURNAL OF APPLIED MECHANICS.

Manuscript received by the ASME Applied Mechanics Division, Aug. 23, 1996; final revision, July 18, 1997. Associate Technical Editor: N. C. Perkins.

 Copyright © 1998 by ASME

Downloaded 04 May 2010 to 171.66.16.26. Redistribution subject to ASME license or copyright; see http://www.asme.org/terms/Terms_Use.cfm

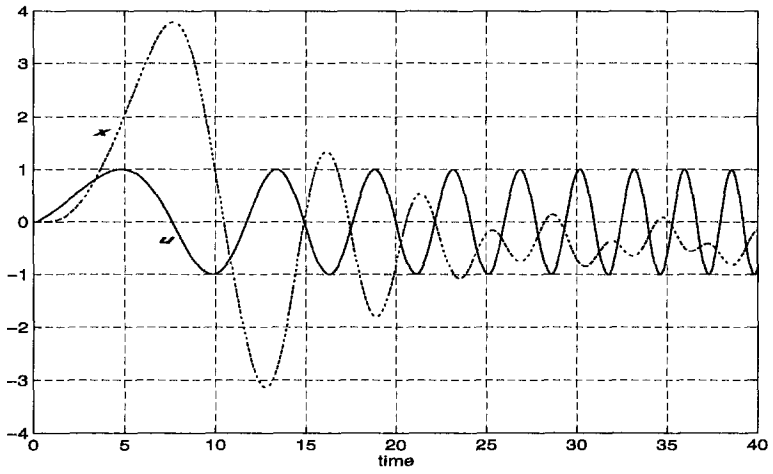

Fig. 2 Time-history records of the hysteretic system excitation and response under swept-sine excitation

If the restoring force $Q(x, \dot{x})$ has hysteretic characteristics, a model for such a force can be given by the following nonlinear differential equation (Wen, 1989):

$$Q(x, \dot{x}) = z \tag{2}$$

$$\dot{z} = (1/\eta)[A\dot{x} - \nu(\beta|\dot{x}||z|^{n-1}z - \gamma\dot{x}|z|^n)]. \tag{3}$$

Different combinations of the parameters η, A, ν, β, γ, and n will produce smooth hysteretic loops of various hardening or softening characteristics, with different amplitudes and shapes. The Bouc-Wen model was chosen as the identification model for its ability to capture the properties of a wide class of real nonlinear hysteretic systems.

Let

$$u(k) = u(t_k); \quad x(k) = x(t_k);$$

$$\dot{x}(k) = \dot{x}(t_k); \quad \ddot{x}(k) = \ddot{x}(t_k); \quad z(k) = z(t_k). \tag{4}$$

The system equation of motion (1) is rewritten as

$$Q(k) = z(k) = u(k) - m\ddot{x}(k); \tag{5}$$

hence the values of z at time t_k are available and the identification problem can be stated as follows: given the mass m and using the on-line measurements of x, $\dot{x}$, $\ddot{x}$, and u, determine on-line estimates of the unknown parameters of the hysteretic model expressed by Eq. (3).

3 On-Line Identification Algorithm

The hysteretic model described in Section 2 obeys the nonlinear differential equation (3). The model is parameterized linearly with respect to the coefficients $(1/\eta)A$, $(1/\eta)\nu\beta$, $(1/\eta)\nu\gamma$, but nonlinearly with respect to the power n. It is, however, desirable to use a linearly parameterized estimator for the on-line estimation of hysteretic behavior, hence the following modification of the model expressed by Eq. (3) will be used:

$$\dot{z} = (1/\eta)\left[A\dot{x} - \sum_{n=1}^{n=N} a_n\nu(\beta|\dot{x}||z|^{n-1}z - \gamma\dot{x}|z|^n)\right] \tag{6}$$

where the value of coefficient a_n determines the contribution of power n to the hysteresis, and N is a large enough integer. For example, if the value of power n in model (3) is $n = 3$, and N is chosen as $N = 4$, then the coefficients a_i in Eq. (6) will be $a_1 = 0$, $a_2 = 0$, $a_3 = 1$, and $a_4 = 0$.

Since measurements are taken at discrete-time intervals Δt, a discrete-time version model of the system defined by Eq. (6) will be used:

$$z(k) = z(k-1) + \Delta t(1/\eta)A\dot{x}(k-1) + \Delta t \sum_{n=1}^{n=N} (-a_n(1/\eta)\nu\beta|\dot{x}(k-1)||z(k-1)|^{n-1}z(k-1) + a_n(1/\eta)\nu\gamma\dot{x}(k-1)|z(k-1)|^n). \tag{7}$$

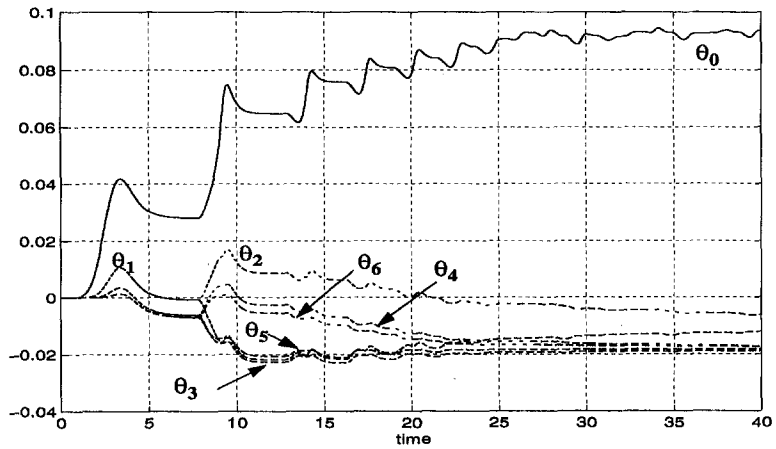

Fig. 3 On-line estimates of the identified hysteretic system parameters obtained through swept-sine input excitation

Downloaded 04 May 2010 to 171.66.16.26. Redistribution subject to ASME license or copyright; see http://www.asme.org/terms/Terms_Use.cfm

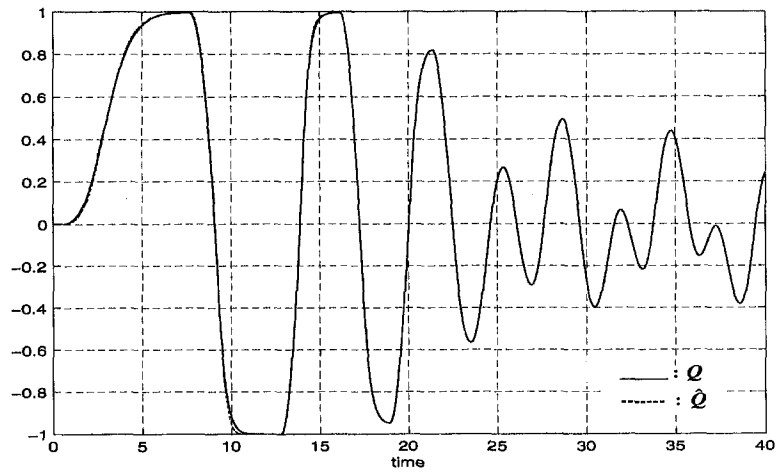

Fig. 4 Comparison between the measured $Q(t)$ and identified $\hat{Q}(t)$ hysteretic restoring force for system under swept-sine input excitation

This discrete-time model gives rise to the following discrete-time linearly parameterized estimator

$$\hat{Q}(k) = z(k-1) + \theta_0(k)\dot{x}(k-1) + \sum_{n=1}^{n=N} (\theta_{2n-1}(k)|\dot{x}(k-1)||z(k-1)|^{n-1}z(k-1) + \theta_{2n}(k)\dot{x}(k-1)|z(k-1)|^n) \quad (8)$$

where the coefficients $\theta_i(k)$, $i = 0, \ldots 2N$ are estimates at time t_k of the corresponding coefficients from Eq. (7); i.e., $\theta_0(k)$ is an estimate of $\Delta t(1/\eta)A$, $\theta_{2n-1}(k)$ is an estimate of $-(\Delta t)a_n(1/\eta)\nu\beta$, and θ_{2n} is an estimate of $(\Delta t)a_n(1/\eta)\nu\gamma$.

Let $\theta(k) = [\theta_0(k), \theta_1(k), \theta_2(k), \ldots, \theta_{2N}(k)]^T$ be the vector containing the parameter estimates at time t_k and $\theta^* = [\theta_0^*, \theta_1^*, \theta_2^*, \ldots, \theta_{2N}^*]^T$ the vector containing the true values of the parameters. Also let

$$\phi(k-1) = [\dot{x}(k-1), |\dot{x}(k-1)||z(k-1)|^0 z(k-1), \dot{x}(k-1)|z(k-1)|^1, |\dot{x}(k-1)||z(k-1)|^1 z(k-1), \dot{x}(k-1)|z(k-1)|^2, \ldots, |\dot{x}(k-1)||z(k-1)|^{N-1}z(k-1), \dot{x}(k-1)|z(k-1)|^N]^T \quad (9)$$

be a vector containing the system measurements at time t_k. Estimator model (8) is then expressed as

$$\hat{Q}(k) = z(k-1) + \phi^T(k-1)\theta(k) \quad (10)$$

and the estimation error will be

$$e(k) = \hat{Q}(k) - Q(k) = \phi^T(k-1)\theta(k) - \phi^T(k-1)\theta^* = \phi^T(k-1)\tilde{\theta}(k) \quad (11)$$

where $\tilde{\theta}(k) = \theta(k) - \theta^*$ is the $((2N+1) \times 1)$ vector of parameter errors between the actual and estimated values θ_i.

Based on Eq. (10), and using standard techniques found in the adaptive estimation and adaptive control literature (Ioannou and Datta, 1991; Narendra and Annaswamy, 1989; Polycarpou and Ioannou, 1992), use will be made of the following gradient projection adaptation law (12)–(13)

$$\theta(k) = \begin{cases} \mu(k), & \text{if } \|\mu(k)\| \le M_\theta \quad (12a) \\ (M_\theta/\|\mu(k)\|)\mu(k) & \text{if } \|\mu(k)\| > M_\theta \quad (12b) \end{cases}$$

with

$$\mu(k) = \theta(k-1) - \frac{\gamma_0}{\beta_0 + \|\phi(k-1)\|^2} e(k-1)\phi(k-1) \quad (13)$$

where $\gamma_0 > 0$ is the *learning rate* of the algorithm and $\beta_0 > 0$ is a design constant. The norms $\|\phi(k)\|$ and $\|\mu(k)\|$ are the usual Euclidean vector norms. The number M_θ is an upper bound on the norm $\|\theta^*\|$. Such an upper bound can be easily found, if some information about the order of magnitude of the elements of θ^* is a priori available.

The reason the adaptation law is switching from Eq. (12*a*) to Eq. (12*b*) is to avoid *parameter drift,* which could drive the estimate $\theta(k)$ to infinity and yield an unstable estimation scheme: If $\|\mu(k)\| \le M_\theta$ then the estimate $\theta(k)$ is equal to $\mu(k)$ which evolves according to Eq. (13); on the other hand, if $\|\mu(k)\| > M_\theta$ then the estimate $\theta(k)$ given by Eq. (12*b*), will

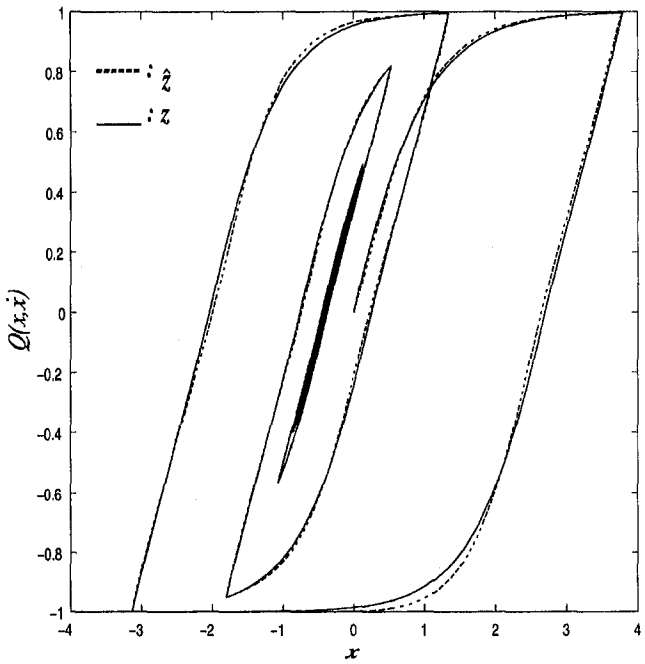

Fig. 5 Phase-plane comparison of the measured $Q(t)$ and identified $\hat{Q}(t)$ hysteretic restoring force for system under swept-sine input excitation

Downloaded 04 May 2010 to 171.66.16.26. Redistribution subject to ASME license or copyright; see http://www.asme.org/terms/Terms_Use.cfm

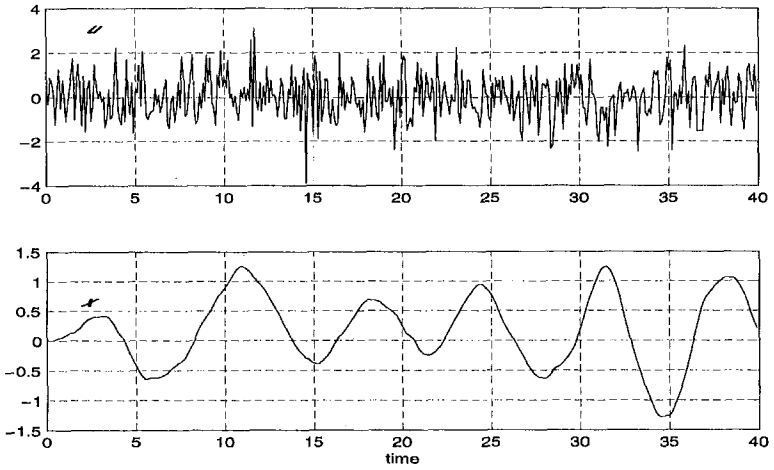

Fig. 6 Time-history records of the hysteretic system excitation and response under wide-band random excitation with level σ_0

remain small, so that the norm $\|\theta(k)\|$ does not exceed the number M_θ, hence $\theta(k)$ will not be driven to infinity.

The adaptive law expressed by Eqs. (12)–(13) guarantees that all the signals will remain bounded and that the error $e(k) \to 0$ as $k \to \infty$, if the model of Eq. (3) is a good representation of the unknown system.

It is worth repeating here that representation in Eq. (6) of Eq. (3) was introduced in order to obtain a *linearly parametrized* estimator. In this case recursive, on-line linear estimation techniques can be used and they provide fast identification and output tracking. Other techniques from the nonlinear estimation literature would be at a disadvantage if they were used in the context of the present study. For example, global search techniques, such as random search (Masri et al., 1980), can be used for *off-line nonlinear parameter estimation,* but they are not suited for on-line estimation, since they search over the whole parameter space, and search time can be quite long. Other nonlinear parameter estimation techniques such as the ones based on steepest descent would require the computation of the partial derivatives of $z(k)$ with respect to the unknown parameters at every iteration step (or the computation of the Hessian matrix in addition to the first partials, if a technique based on Newton's method is chosen), thus increasing computational complexity. A nonlinear estimation method similar to the one applied in this paper is the "sequential nonlinear least squares algorithm" (Goodwin and Sin, 1984), which is computationally more intensive since it requires calculations of the partial derivatives at every time step.

The representation in Eq. (6) of the hysteretic system of Eq. (3) increases the number of parameters to be estimated, but it should be noted that the unknown power n is relatively small (typically an integer less than 4), so that the total number of parameters remains relatively small. Concerning identifiability, it can be stated that the system of Eq. (3) under the parametric model Eq. (6) and under the algorithm of Eq. (12)–(13) is *system identifiable* (Soderstrom and Stoica, 1989) in the sense that the set of parameter vectors θ that satisfy Eq. (10) is nonempty: The on-line algorithm will converge to this parameter set. Because of overparametrization, this parameter set contains more than one point, hence convergence to a *unique* parameter vector cannot be guaranteed. It is noted, however, that tracking of the output signal is performed even with an overparametrized model.

4 Applications

In this section identification results from simulated systems and from real data of a hysteretic structure are presented. First,

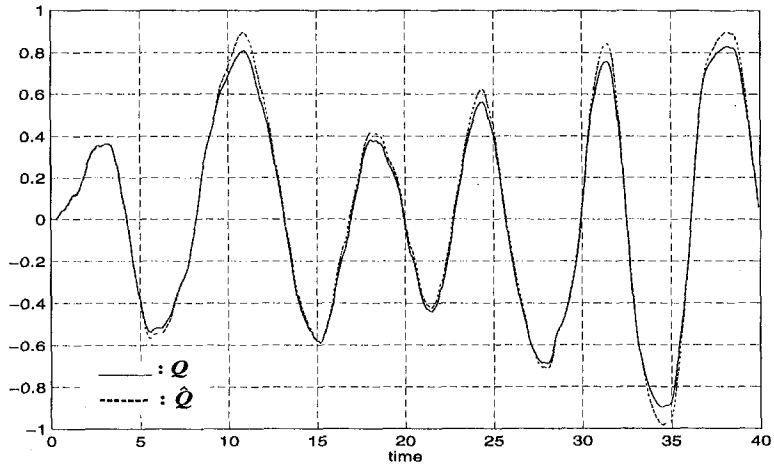

Fig. 7 Comparison of the time-history records of the measured and predicted hysteretic restoring force under random excitation of level σ_0. Here, the adaptation scheme is off, and the restoring force is predicted based upon fixed-system parameters obtained from the end of the swept-sine input simulation in Section 4.3.

Downloaded 04 May 2010 to 171.66.16.26. Redistribution subject to ASME license or copyright; see http://www.asme.org/terms/Terms_Use.cfm

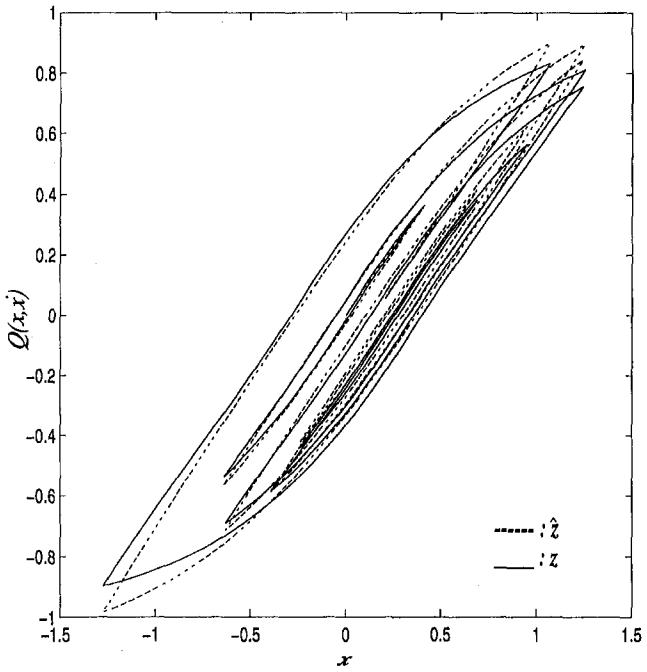

Fig. 8 Comparison of the phase-plane plots of the measured and predicted hysteretic restoring force under random excitation of level σ_0. Here, the adaptation scheme is off, and the restoring force is predicted based upon fixed-system parameters obtained from the end of the swept-sine input simulation in Section 4.3.

simulation results from a single-degree-of-freedom hysteretic system are shown, to illustrate the application of the on-line identification algorithm developed in Section 3. After the identification procedure is completed, the parameter values are frozen at their final values, and the identified model is validated and tested under various levels of wide-band random excitation. Next the identification and prediction scheme is used to track the output of a system which is phenomenologically different from the Bouc-Wen model, and it is seen to produce very good agreement between predicted output and system output. Finally, actual data acquired from testing on a full-scale structural steel subassembly are used, and the identification procedure is shown to identify the hysteretic characteristics and perform very good output prediction.

4.1 Model Characteristics. The identification procedure under discussion will be outlined in the context of the hysteretic system illustrated in Fig. 1. The model parameters of Eq. (3) used to characterize the present example were selected to have the following values:

$$\eta = 1, \quad A = 1, \quad \nu = 1, \quad \beta = 0.5,$$
$$\gamma = -0.5, \quad n = 1 \tag{14}$$

additionally, the system mass m had a value of unity.

4.2 Generation of "Experimental" Measurements. Assume that the experimental measurements for $u(t)$ and $\ddot{x}(t)$ are available over a time span much longer than the system characteristic period of interest. The corresponding system displacement $x(t)$ and velocity $\dot{x}(t)$ of m can be found by direct measurement or through integration of $\ddot{x}(t)$. By discretizing the measurements at the rate of Δt (which in this case was every 0.1 seconds), the values of $Q(k)$ can be obtained from Eq. (5).

The method under consideration imposes no restrictions on the nature of the excitation source to be used as a probing source signal. In the present example, the excitation used is the swept sine signal

$$u(t) = \sin((0.03t + 0.2)t). \tag{15}$$

The time-history records of the swept-sine input excitation and response displacement corresponding to the example single-degree-of-freedom hysteretic system are shown in Fig. 2.

4.3 Identification of the Hysteretic Restoring Force. The unknown parameter vector θ is initially set to 0. A value of $N = 3$ is chosen, so the algorithm will estimate a total of seven parameters (see Eq. (8)). The upper bound M_θ is taken equal to 1. Figure 3 shows the on-line estimates of parameters θ_0 to θ_6. In Fig. 4, the on-line prediction of $\hat{Q}(k)$ is shown (dashed line) and compared to the actual value of $Q(x(k), \dot{x}(k))$ (solid line). Similarly, in Fig. 5, the phase plane plots of $z(k)$ (solid line) and $\hat{z}(k)$ (dashed line) versus $x(t)$ (horizontal axis) are compared. The phase plane plot of z versus x in Fig. 5. shows clearly the hysteretic nature of the system. Note from Figs. 4 and 5 that the agreement between the measured and identified hysteretic restoring force is extremely good, over the whole domain of the motion. The algorithm is capable of accurately replicating the motion of the actual system immediately after the tracking begins; it requires only a few time samples for the accurate tracking of the observed response. It is interesting to note that even when the identified parameters had not settled to their constant values, their instantaneous combinations were able to generate an extremely good agreement within that local range of excitation.

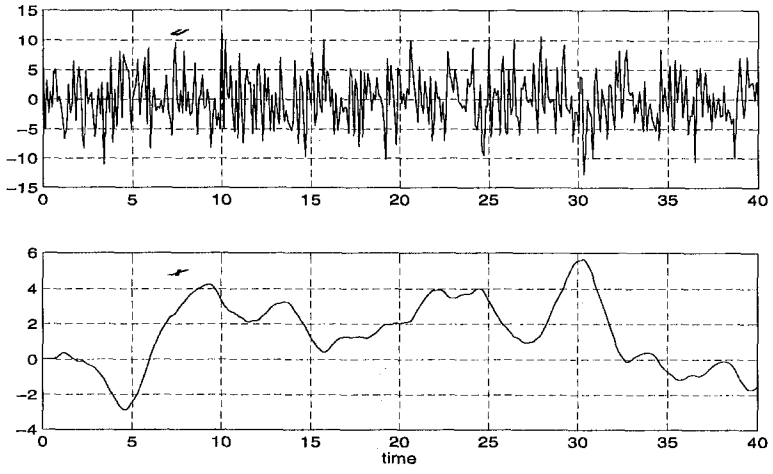

Fig. 9 Time-history records of the hysteretic system excitation and response under wide-band random excitation with level $\sigma \gg \sigma_0$

Downloaded 04 May 2010 to 171.66.16.26. Redistribution subject to ASME license or copyright; see http://www.asme.org/terms/Terms_Use.cfm

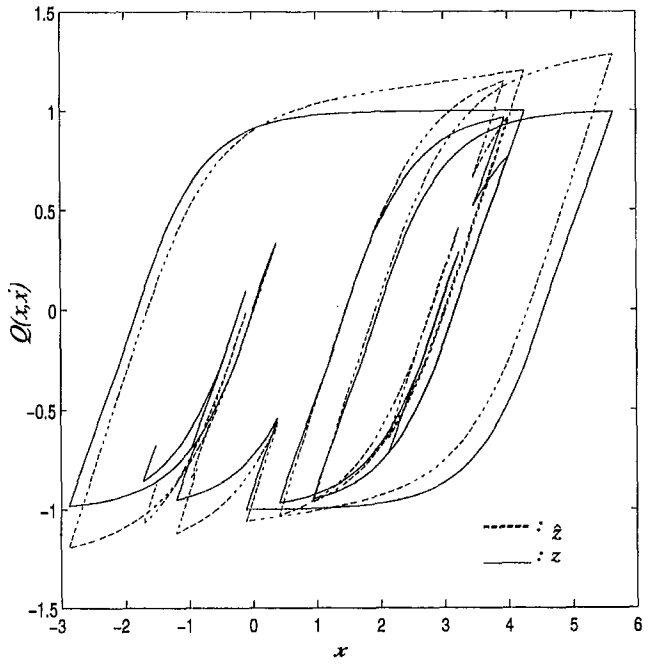

Fig. 10 Phase-plane plots of the hysteretic system response under wide-band random excitation with level $\sigma \gg \sigma_0$. Here, the adaptation scheme is off, and the restoring force is predicted based upon fixed-system parameters obtained from the end of the swept-sine input simulation in Section 4.3.

4.4 Model Validation Procedure. At this point, the model identified in Section 4.3 is to be validated. The parameters θ_i, $i = 0, \ldots 6$ are frozen to the values obtained during the identification phase. The system is subjected to a zero-mean wide-band random excitation $u(t)$ of rms level σ_0, as shown in Fig. 6. Using the system response data and the parameter values obtained previously under swept-sine excitation, the predicted values of $\hat{Q}(k)$ are computed. Figure 7 compares the actual $Q(x, \dot{x})$ with the predicted $\hat{Q}$. The agreement is very good, although the adaptation algorithm is now off. Figure 8 shows the phase plane plots of z (solid line) and $\hat{z}$ (dashed line) versus x (horizontal axis). Again the hysteretic features of the system are clearly seen and the agreement between actual and predicted values is very good. Similar results are obtained when the level of excitation is $\sigma \ll \sigma_0$ where σ_0 was the random excitation level used in the previous validation test.

From Fig. 3 it can be seen that the parameters reach a steady state in approximately 20–25 sec of simulation time, which corresponds to actual CPU time of 0.7–0.8 sec, on a 60 MHz Sun SparcStation20. This time estimate includes the time required to store the data in the ϕ vector. The total number of floating point operations required is about 30000 using MATLAB. This actual CPU time of 0.7–0.8 sec, required for convergence can be decreased significantly with a faster machine or a dedicated DSP that will undertake most of the calculations. It is noted that tracking and prediction of the restoring force is performed a lot faster, as seen from Fig. 4: Output tracking is achieved within a few cycles of iterations, which corresponds to real CPU time of a few msec on the same 60 MHz machine. Hence, for purposes of active control, on-line prediction of the unknown restoring force is achieved a lot faster than parameter convergence.

4.5 Model Validation With High-Level Random Excitation. The system is now subjected to wide-band random excitation $u(t)$ as shown in Fig. 9. The level of excitation in this case is $\sigma \gg \sigma_0$ where σ_0 was the random excitation level used in the previous validation test. This results in a system response level roughly an order of magnitude larger than the motion range corresponding to excitation level σ_0. In Fig. 10 the phase plots of the system response under this random excitation are shown. Note that the internal restoring force exhibits significant hysteretic behavior. Using these data and the parameter values obtained previously under swept-sine excitation, the predicted values of $\hat{Q}(k)$ are computed. Figure 11 compares the time histories of the actual $Q(x, \dot{x})$ with the predicted $\hat{Q}$, and Fig. 10 compares the phase plane plots of Q and $\hat{Q}$. Even though the adaptation algorithm is now off, the agreement is quite good within the region exhibiting predominantly linear behavior as well as the nonlinear behavior within the motion range corresponding to excitation level σ_0. However, in the highly nonlinear region, direct on-line identification is required to obtain good estimation results, as illustrated in Fig. 12: The erroneous prediction results are avoided if the tracking algorithm is turned on, rather than constraining the identified parameters to remain static.

4.6 Identification Results for Phenomenologically Different Models. The adaptive estimation technique used here, based upon the assumption of a Bouc-Wen model, can also capture the behavior of phenomenologically different systems.

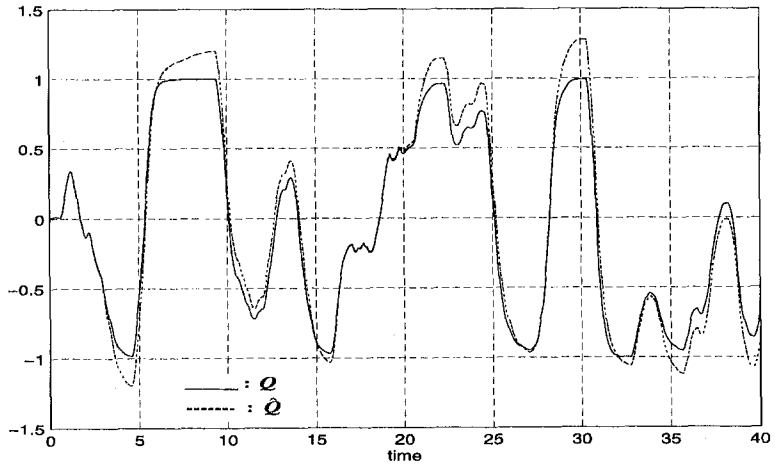

Fig. 11 Comparison of the time history records of the measured and predicted hysteretic restoring force under random excitation of level $\sigma \gg \sigma_0$. Here, the adaptation scheme is off, and the restoring force is predicted based upon fixed-system parameters obtained from the end of the swept-sine input simulation in Section 4.3.

Downloaded 04 May 2010 to 171.66.16.26. Redistribution subject to ASME license or copyright; see http://www.asme.org/terms/Terms_Use.cfm

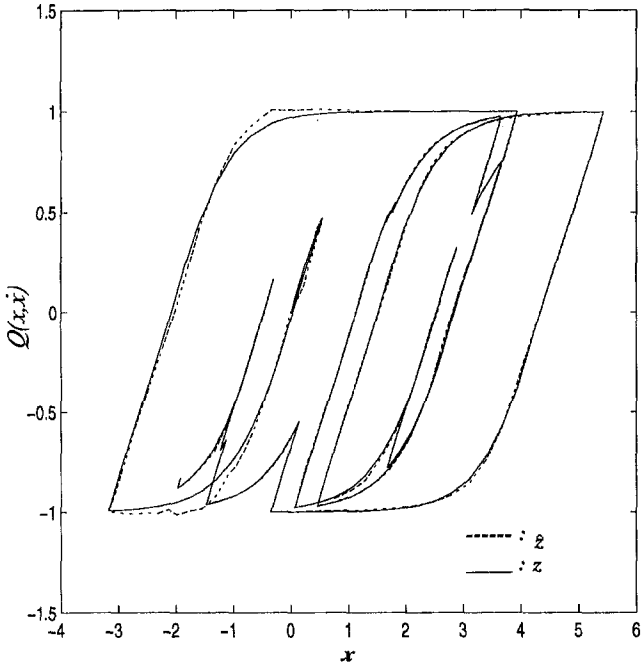

Fig. 12 Comparison of the time history records of the measured and predicted hysteretic restoring force under random excitation of level $\sigma \geqslant \sigma_0$. Here, the adaptive scheme is on.

From inspection, it is clear that a classical linear single-degree-of-freedom system with viscous damping is merely a special case of the Bouc-Wen model with one extra term for the damping. Indeed, parameter estimation results from linear system identification are very good. The damped hardening Duffing oscillator presents a more challenging problem for the identification scheme, and the results of such a simulation are shown here. The variation of the Bouc-Wen model parameter estimates in Fig. 13 is seen to be more irregular than before. This is not surprising, because the parameters are being pushed to best immitate polynomial terms in the Duffing oscillator expression which are not present in the Wen's model. Regardless of this, in both the time domain comparison shown in Fig. 14, and the phase plane illustration shown in Fig. 15, the agreement between the estimated and actual restoring force is extremely good.

4.7 Identification Results for Full-Scale Structural Steel Subassembly. The experimental tests were conducted by means of a full-scale structural steel subassembly (made of ASTM A36 steel), consisting of a W16X40 wide flange beam framing into an 11 inch square box column. Because the behavior of the column wall has an important effect on the overall behavior of the connection, an axial load was applied to the column to simulate the dead and live load in an actual building column. Hydraulic actuators were used to impose the vertical loads as well as the induced moment at the connection. The applied tip loads and beam displacements were monitored by suitable force and displacement sensors. Experimental measurements were later processed to extract the value of the applied moment and the corresponding joint rotation, which were subsequently used to develop the hysteretic characteristics of the connection. For the experimental data, a value of $N = 3$ was again chosen for the model of Eq. (6).

Figure 16 shows the phase-plane plots of the measured (solid) and identified (dashed) restoring forces. The agreement is seen to be extremely good, comparable to the results of the simulations. Figure 17 shows the convergence of the $(2N + 1)\theta$ vector parameter clusters. The smoothness of the "convergence" of the parameters and the prediction error are dependent upon the value of γ_0, i.e., the sensitivity of the adaptive law. One can see that the system is degrading, because not all of the θ-parameter clusters are converging to fixed values. The θ_0 term, for example, which basically represents the stiffness of the system, can be seen to be steadily decreasing in Fig. 17. This decrease in stiffness accounts for the slight clockwise rotation of the hysteretic loops in Fig. 16.

This case provides, to a degree, an example of how the identification algorithm performs with noisy measurements, since the real data used here are to a certain extent corrupted by measurement noise. To further examine the effects of noise on identification, a simulation case was run, using the same benchmark model as in Section 4.1, where the measurements of the restoring force were corrupted by high level noise. It was found that prediction of the restoring force was still very good, despite the high-level measurement noise.

5 Discussion

In all of the simulations, one can qualitatively regard the estimation scheme as very successful. Under the swept-sine input excitation, the model parameters converged with reasonable accuracy within about six cycles. The convergence can be shown to be considerably accelerated by introducing a "persis-

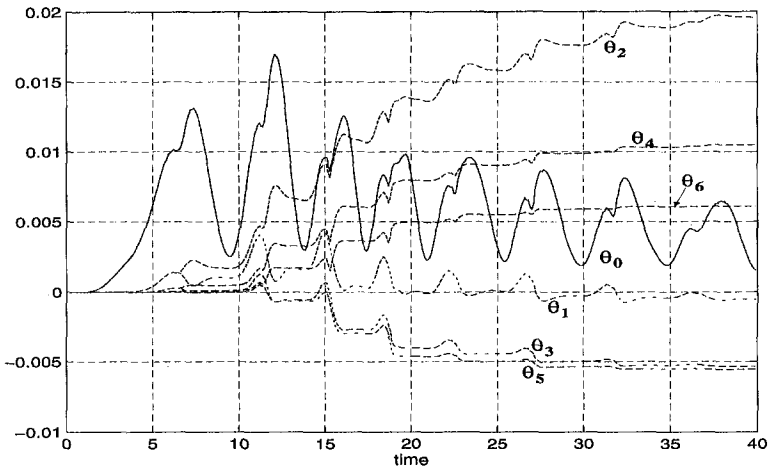

Fig. 13 On-line estimates of the identified system parameters for damped hardening Duffing oscillator under swept-sine excitation

Downloaded 04 May 2010 to 171.66.16.26. Redistribution subject to ASME license or copyright; see http://www.asme.org/terms/Terms_Use.cfm

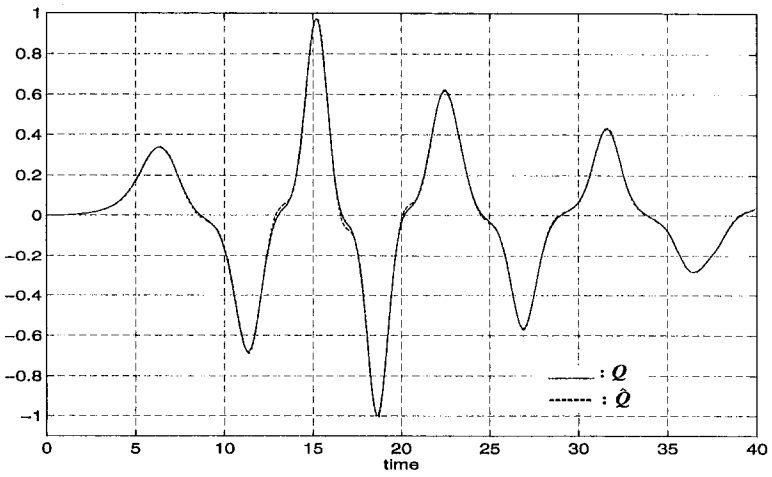

Fig. 14 Comparison between the measured $Q(t)$ and identified $\hat{Q}(t)$ restoring force for damped hardening Duffing oscillator under swept-sine excitation

tently exciting'' input excitation. For example, a wide-band random excitation is ideal because it will fully excite the system to be identified.

The results of Section 4.5 suggest that caution should be exercised when using this on-line estimation technique for off-line use. The parameter values to which the on-line model converged cannot always be used for precise off-line estimation of the hysteretic forces. While noting this, it also suggests that without precise information available on the system's response characteristics to high levels of excitation, that the best approach to take is to use on-line methods.

The importance of numerous variables involved in the adaptive scheme such as γ_0, β_0, and M_θ is not fully presented here. For this scheme, the variables affecting the learning rate and the parameter bounds are chosen to be constants. In this case they were chosen by trial and error, along with a priori knowledge of the approximate bound on the norm of the system parameter vector θ^*. In fact, in using this particular adaptive scheme it was found that the projection bound was not necessary in these simulations. However, setting the learning rate too high caused serious algorithmic instability with this projection method because the parameters were continuously pushed far outside of the bounded parameter space (due to the high learning rate) and projected back to the bound at each time step. Other adaptive schemes effectively contain adaptive learning rates, and these may prove to be even more successful.

The on-line identification of the system parameters for the data from the full-scale structural steel subassembly, presents an excellent example of the power of adaptive methods to identify time-varying systems. In this case the system can be said to be relatively slowly time-varying. Another attractive quality of these adaptive methods is that when used for closed-loop control, it is not essential to have parameter convergence to θ^*. Notice that throughout this paper the tracking has been very good even when the parameters were not the ''correct'' ones.

It should be noted that this particular formulation of the identification scheme could have been slightly altered to include the

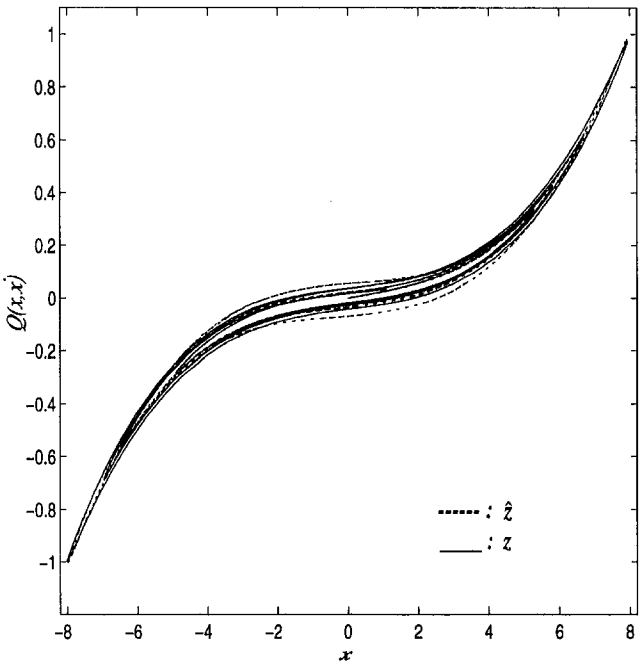

Fig. 15 Phase-plane comparison of the measured $Q(t)$ and identified $\hat{Q}(t)$ restoring force for damped hardening Duffing oscillator under swept-sine excitation

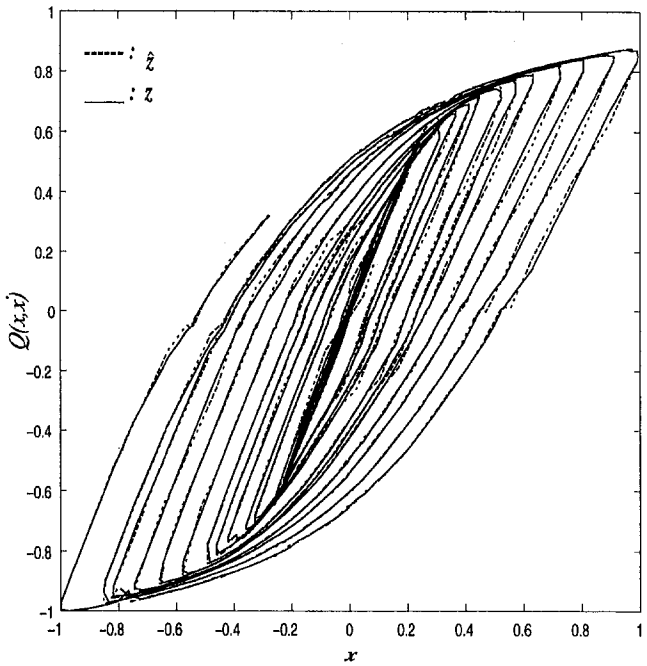

Fig. 16 Phase-plane comparison of the measured $Q(t)$ and identified $\hat{Q}(t)$ restoring force for structural steel subassembly

Downloaded 04 May 2010 to 171.66.16.26. Redistribution subject to ASME license or copyright; see http://www.asme.org/terms/Terms_Use.cfm

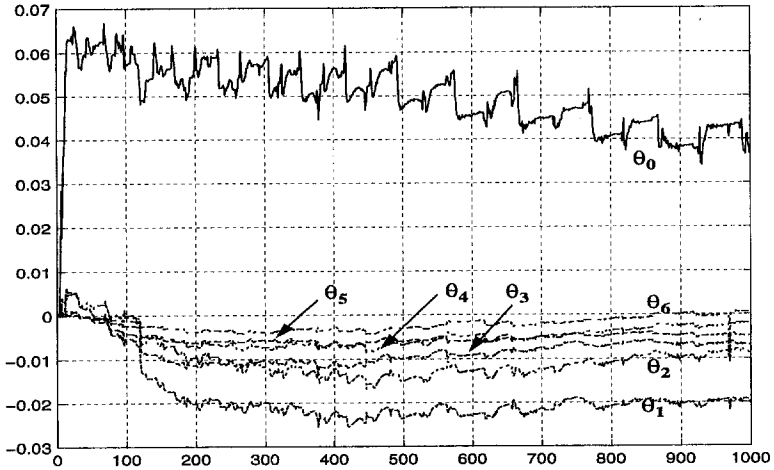

Fig. 17 On-line estimates of the identified system parameters for full-scale structural steel subassembly under cyclical loading

mass term from the equation of motion as an extra unknown parameter. Using such a scheme, the signal being tracked would be the input excitation, and the only additional information which would be required would be the rate of change of the acceleration. Other unknown parameters can also be arbitrarily added as long as a corresponding entry to the ϕ motion vector is inserted. For example, although the Wen's model was chosen for its ability to capture the hysteretic behavior of many types of real systems, a specific polynomial term could be added to the formulation in Eq. (8), and after running the identification problem, the estimate of that term's contribution could be determined.

Issues that require further investigation include the effects of over-parameterization, conditions on the parameter convergence, and application to distributed systems.

6 Conclusions

Using adaptive estimation approaches, a method is presented for the on-line identification of hysteretic systems under arbitrary dynamic environments. It is shown, through the use of simulation studies and experimental measurements, that the proposed approach can yield reliable estimates of the hysteretic restoring force under a very wide range of excitation levels and response ranges. The method is ideally suited for on-line control applications involving time-varying nonlinear systems typically encountered in the applied mechanics field.

Acknowledgments

This study was supported in part by grants from the National Science Foundation, the Air Force Office of Scientific Research, by NASA grant #NAGW-4103, and by FEMA HMGP. The assistance of Prof. J. C. Anderson of U.S.C. in the experimental phase of the studies is appreciated.

References

Andronikou, A. M., and Bekey, G. A., 1984, "Identification of Hysteretic Systems," *Proc. of the 18th IEEE Conf. on Decision and Control,* Dec., pp. 1072–1073.

Baber, T. T., and Noori, M. N., 1984, "Random Vibration of Pinching, Hysteretic Systems," ASCE *J. Eng. Mech Div.,* Vol. 110, No. 7, pp. 1036–1049.

Baber, T. T., and Wen, Y. K., 1981, "Random Vibration of Hysteretic Degrading Systems," ASCE *J. Eng. Mech. Div.* Vol. 107, No. EM6, pp. 1069–1087.

Baber, T. T., and Wen, Y. K., 1982, "Stochastic Response of Multistory Yielding Frames," *Earthquake Eng. Struct. Dyn,* Vol. 10, pp. 403–416.

Benedettini, F., Capecchi, D., and Vestroni, F., 1995, "Identification of hysteretic oscillators under earthquake loading by nonparametric models," *J. of Eng. Mech.* Vol. 121, pp. 606–612.

Bergman, L. A., and Spencer, B. F., 1987, "On the Solution of Several First Passage Problems in Nonlinear Stochastic Dynamics," *Proceedings, IUTAM Symposium on Nonlinear Stochastic Dynamic Engineering Systems,* Innsbruck, Austra, pp. 479–493.

Bouc, R., 1967, "Forced Vibration of Mechanical Systems with Hysteresis," *Proceedings, 4th Conference on Nonlinear Oscillation,* Prague, Czechoslovakia, abstract.

Capecchi, D., 1990, "Accurate Solutions and Stability Criterion for Periodic Oscillations in Hysteretic Systems," *Meccanica,* Vol. 25, pp. 159–167.

Caughey, T. K., 1960, "Random Excitation of a System with Bilinear Hysteresis," ASME JOURNAL OF APPLIED MECHANICS, Vol. 27, pp. 649–652.

Caughey, T. K., 1963, "Equivalent Linearization Techniques," *J. Acoustical Soc of America,* Vol. 35, pp. 1706–1711.

Chassiakos, A. G., Masri, S. F., Smyth, A., and Anderson, J. C., 1995, "Adaptive Methods for Identification of Hysteretic Structures," *Proceedings American Control Conference,* ACC95, June, Seattle, WA.

Goodwin, G. C., and Sin, K. S., 1984, *Adaptive Filtering, Prediction and Control,* Prentice-Hall, Englewood Cliffs, NJ.

Grossmayer, R. L., 1981, "Approximate Stochastic Analysis of Elasto-Plastic Systems," ASCE *J. Eng. Mech. Div.,* Vol. 107, No. EM1, pp. 97–116.

Housner, G. W., and Masri, S. F., eds., 1990, *Proceedings of the U.S. National Workshop on Structural Control Research,* Oct. 25–26, University of Southern California, U.S.C. Publication No. M9013.

Housner, G. W., and Masri, S. F., eds., 1993, *Proceedings of the International Workshop on Structural Control,* Aug. 3–5, Honolulu, HI, USC Publication No. CE-9311.

Housner, G. W., Masri, S. F., and Chassiakos, A. G., eds., 1995, *Proceedings of the First World Conference on Structural Control,* Aug. 3–5, Los Angeles, CA, *Civil Engineering Department, University of Southern California,* Los Angeles, ISBN 0-9628908-3-9.

Ioannou, P. A., and Datta, A., 1991, "Robust Adaptive Control: A Unified Approach," *Proceedings of the IEEE,* Vol. 79, pp. 1736–1768.

Iwan, W. D., 1966, "A Distributed-Element Model for Hysteresis and Its Steady-State Dynamic Response," ASME JOURNAL OF APPLIED MECHANICS, Vol. 33, pp. 893–900.

Iwan, W. D., and Cifuentes, A. O., 1986, "A Model for System Identification of Degrading Structures," *Jnl Earthquake Engineering and Structural Dynamics,* Vol. 14, No. 6, pp. 877–890.

Iwan, W. D., and Lutes, L. D., 1968, "Response of the Bilinear Hysteretic System to Stationary Random Excitation," *J. Acoust Soc. Am,* Vol. 43, No. 3, pp. 545–552.

Jayakumar, P., and Beck, J. L., 1987, "System Identification Using Nonlinear Structural Models," *Proceedings, Structural Safety Evaluation Based on System Identification Approaches,* Lambracht, Germany, pp. 82–102.

Jennings, P. C., 1964, "Periodic Response of a General Yielding Structure," ASCE *Journal of Engineering Mechanics Division,* Vol. 90, No. EM2, pp. 131–166.

Karnopp, D., and Scharton, T. D., 1966, "Plastic Deformation in Random Vibration," *J. Acost Soc Am,* Vol. 39, pp. 1154–1161.

Kobori, T., Minai, R., and Suzuki, Y., 1976, "Stochastic Seismic Response of Hysteretic Structures Pt. 1," *Bull Disaster Prevention Res Inst* Vol. 26, pp. 55–70.

Loh, C., and Chung, S., 1993, "A three-stage identification approach for hysteretic systems," *Earthquake Engineering & Structural Dynamics,* Vol. 22, pp. 129–150.

Masri, S. F., and Caughey, T. K., 1979, "A Nonparametric Identification Technique for Nonlinear Dynamic Problems," ASME JOURNAL OF APPLIED MECHANICS, 46(2), pp. 433–447.

Masri S. F., Bekey G. A., and Safford F. B., 1980, "A global optimization algorithm using adaptive random search," *Applied Math and Computation,* Vol. 7, pp. 353–375.

Downloaded 04 May 2010 to 171.66.16.26. Redistribution subject to ASME license or copyright; see http://www.asme.org/terms/Terms_Use.cfm

Masri, S. F., Miller, R. K., Traina, M.-I., and Caughey, T. K., 1991, "Development of Bearing Friction Models From Experimental Measurements," *Journal of Sound and Vibration,* Vol. 148, No. 3, pp. 455–475.

Narendra, K. S., and Annaswamy, A. M., 1989, *Stable Adaptive Systems,* Prentice-Hall, Englewood Cliffs, NJ.

Park, Y. J., Ang, A. H-S. and Wen, Y. K., 1987, "Seismic Damage Analysis of Reinforced Concrete Buildings," *ASCE J. Struct. Eng.* Vol. 3, No. 4, pp. 740–757.

Peng, C. Y., and Iwan, W. D., 1987, "Identification of Hysteretic Structural Behavior from Strong Motion Accelerograms," *Proceedings, Structural Safety Evaluation Based on System Identification Approaches,* Lambrecht, Germany, Friedr. Viewg & Sohn., Braunchweig/Wiesbaden F.R.G. pp. 103–117.

Peng, C. Y., and Iwan, W. D., 1992, "An identification methodology for a class of hysteretic structures," *Earthquake Engineering & Structural Dynamics,* Vol. 21, pp. 695–712.

Polycarpou, M. M., and Ioannou, P. A., 1992, "Neural Networks as On-line Approximators of Nonlinear Systems," *Proc. of the 31st IEEE CDC,* Tucson, AZ, pp. 7–12.

Powell, G. H., and Chen, P. F-S, 1986, "3-D Beam-Column Element with Generalized Plastic Hinges," *J. Eng. Mech,* ASCE Vol. 112, No. 76, pp. 627–641.

Roberts, J. B., 1987, "Application of Averaging Methods of Randomly Excited Hysteretic Systems," *Proceedings, IUTAM Symposium on Nonlinear Stochastic Dynamic Engineering Systems,* Innsbruck, Austria, pp. 361–380.

Roberts, J. B., and Spanos, P. D., 1990, *Random Vibration and Statistical Linearization,* John Wiley and Sons, New York.

Soderstrom T., and Stoica, P., 1989, *System Identification,* Prentice-Hall, Englewood Cliffs, NJ.

Spanos, P. D., 1981, "Stochastic Linearization in Structural Dynamics," ASME *Appl Mech Rev,* Vol. 34.

Spencer, B. F., and Bergman, L. A., 1985, "On the Reliability of a Simple Hysteretic System," ASCE *J. Eng. Mech. Div.,* Vol. 3, pp. 1502–1514.

Sues, R. H., Wen, Y. K., and Ang, A. H-S., 1985, "Stochastic Evaluation of Seismic Structural Performance," ASCE *J. Struct. Eng.* Vol. 3, No. 6, pp. 1204–1218.

Sues, R. H., Mau, S. T., and Wen, Y. K., 1988, "Systems identification of degrading hysteretic restoring forces," ASCE *J. Eng. Mech.,* Vol. 114, pp. 833–846.

Toussi, S., and Yao, J. T. P., 1983, "Hysteretic Identification of Existing Structures," ASCE *Jnl Engrg. Mech. Div.,* Vol. 109, No. 5, pp. 1189–1202.

Vinogradov, O., and Pivovarov, I., 1986, "Vibrations of a System with Non-Linear Hysteresis," *Jnl Sound and Vibration,* Vol. 111, No. 1, pp. 145–152.

Wen, Y. K., 1976, "Method for Random Vibration of Hysteretic Systems," ASCE *J. Eng. Mech. Div.,* Vol. 102, No. EM2, pp. 249–263.

Wen, Y. K., 1980, "Equivalent Linearization for Hysteretic Systems Under Random Excitations," ASME JOURNAL OF APPLIED MECHANICS, Vol. 47, pp. 150–154.

Wen, Y. K., and Ang, A. H-S., 1987, "Inelastic Modeling and System Identification," *Proceedings, Structural Safety Evaluation Based on System Identification Approaches,* International Workshop, Lambrecht, Germany, pp. 142–160.

Wen, Y. K., 1989, "Methods of Random Vibration for Inelastic Structures," ASME *Appl Mech Rev,* Vol. 43, pp. 39–52.

Worden, K., and Tomlinson, G. R., 1988, "Identification of Linear/Nonlinear Restoring Force Surfaces in Single- and Multi-Mode Systems," *Proc 3rd Int Conf on Recent Advances in Structural Dynamics,* Southampton, U.K., pp. 299–308.

Yar, M., and Hammond, J. K., 1987a, "Modelling and response of bilinear hysteretic systems," *ASCE J. Eng. Mech.,* Vol. 113, pp. 1000–1013.

Yar, M., and Hammond, J. K., 1987b, "Parameter Estimation for Hysteretic Systems," *Jnl Sound and Vibration,* Vol. 117, No. 1, pp. 161–172.

Downloaded 04 May 2010 to 171.66.16.26. Redistribution subject to ASME license or copyright; see http://www.asme.org/terms/Terms_Use.cfm

The Dependence of the Time Scale of Relative Lagrangian Motion on the Initial Separation

J. C. H. Fung
Department of Mathematics,
The Hong Kong University of
Science and Technology,
Clear Water Bay,
Kowloon, Hong Kong

Kinematic simulation of homogeneous isotropic turbulence are used to compute Lagrangian statistics of turbulence and, in particular, its time scales. The computed pseudo-Lagrangian velocity autocorrelation functions $\hat{R}^L_{11}(l, t)$ compare well with theory for a small initial separation l and short time t. We also demonstrate the feasibility of using kinematic simulation as a means of constructing Lagrangian statistics.

1 Introduction

The statistical theory of turbulence is usually treated in terms of the "hierarchy" of moment equations. For example, the equation for the second moment is formed by multiplying the Navier-Stokes equation by u_j, averaging the results over the ensemble of realizable flows; this equation involves term with third-order correlations because of the nonlinearity in the equations of motion. The equation for the third-order correlations involves the fourth-order correlations, and so on. Since this sequence of equations does not converge, a "closure hypothesis" (involving some statistical or dynamical assumption about the flow), such as supplementary equation between the moments, is needed to compute a sequence of moments of finite order. Usually, these equations involve moments at points in space that are separated from each other. When the averaged quantities are each defined at only one point $\mathbf{x}$ of the physical space, one talks of "one-point closure modeling." Although, most current methods of modeling practical turbulent flows involve only one-point moments, it has been recognized that the limitation of these methods as regards information given and approximations involved can only be improved by more complex models. At the next order of complexity, models involve the correlations (and their corresponding spectra) between the velocity at two points in space at the same time, or at two different times. The points may move with the local flow, in which case the correlations and spectra are described as Lagrangian.

The best known model for evolution of the two-point spectra is the so-called EDQNM approximation (Eddy-Damped Quasi-Normal Markovian approximation; see Bertoglio (1986) and Lesieur (1987)). One of the principal advantages of using these model equations for the spectra is that they provide the length scale information which is notoriously difficult to include in one-point turbulent closures. Also, there is no closure needed for the pressure fluctuations (which are calculated in term of the velocity) or of the viscous dissipation, in contrast to what happens in the "one-point closure modeling."

The aim of this study is to provide some new model computations and new theory for correlations that EDQNM predicts. The results should be a better understanding of some essential features of the model. The essence of the EDQNM model can be represented by equations for the mean moment $M_n(k)$ of the Fourier transforms of the velocity components of wave number, i.e.,

$$\frac{dM_2(k)}{dt} = f_2(M_2, M_3) \tag{1a}$$

and

$$\frac{dM_3(k)}{dt} = f_3(M_3, M_4), \tag{1b}$$

where f_2 and f_3 denote functional dependence. The essential feature introduced by Orszag (1970) is to represent M_4 in term of M_2 and M_3 with an inverse time scale factor $\mu(k)$ to account for eddy damping. This avoids exaggerated growth of the third order moment. The hypothesis is that Eq. (1b) is modified to

$$\frac{dM_3(k)}{dt} = f_4(M_2, M_2) - \mu(k)M_3, \tag{2}$$

where $\mu(k) \sim 1/\tau(k)$, and $\tau(k)$ is the unknown time scale for scales of $O(k^{-1})$.

For flows at Reynolds numbers sufficiently high to contain an inertial subrange in the energy spectrum, Kolmogorov's (1941) arguments show that the time scale of wave number k must have the form

$$\tau(k) = C_k \epsilon^{-1/3} k^{-2/3}, \tag{3}$$

where C_k is a constant and ϵ is the rate of dissipation of kinetic energy per unit mass. Here $\tau(k)$ (in EDQNM) may be interpreted as an effective relaxation time for nonlinear transfer between various scales of motion (Leslie, 1973). But this is not a precise definition, so the question is: how can $\tau(k)$ be defined precisely in a given flow and in an appropriate way for the EDQNM Eq. (2)? The present study addresses this question and provides a quantitative estimate for $\tau(k)$.

Bertoglio (1986) has suggested that the most appropriate definition for $\tau(k)$ is in terms of the two-time two-point Lagrangian velocity autocorrelation function defined by

$$R^L_{ij}(\mathbf{x}_0, t_0|t_0; \mathbf{x}_0 + \mathbf{l}, t_0|t) = \langle u_i(\mathbf{x}_0, t_0|t_0) u_j(\mathbf{x}_0 + \mathbf{l}, t_0|t)\rangle, \tag{4}$$

where $\langle\cdot\rangle$ denotes ensemble average, and in normalized form by

$$\hat{R}^L_{ij}(\mathbf{x}_0, t_0|t_0; \mathbf{x}_0 + \mathbf{l}, t_0|t) = \frac{\langle u_i(\mathbf{x}_0, t_0|t_0) u_j(\mathbf{x}_0 + \mathbf{l}, t_0|t)\rangle}{\langle u_i(\mathbf{x}_0, t_0|t_0) u_j(\mathbf{x}_0 + \mathbf{l}, t_0|t_0)\rangle}, \tag{5}$$

Contributed by the Applied Mechanics Division of THE AMERICAN SOCIETY OF MECHANICAL ENGINEERS for publication in the ASME JOURNAL OF APPLIED MECHANICS.

Discussion on this paper should be addressed to the Technical Editor, Professor Lewis T. Wheeler, Department of Mechanical Engineering, University of Houston, Houston, TX 77204-4792, and will be accepted until four months after final publication of the paper itself in the ASME JOURNAL OF APPLIED MECHANICS.

Manuscript received by the ASME Applied Mechanics Division, Dec. 5, 1996; final revision, July 25, 1997. Associate Technical Editor: Editor: S. Lichter.

 Copyright © 1998 by ASME

Downloaded 04 May 2010 to 171.66.16.26. Redistribution subject to ASME license or copyright; see http://www.asme.org/terms/Terms_Use.cfm

where $u_i(\mathbf{x}_0, t_0|t)$ is the velocity measured at time t in the fluid element whose space-time trajectory passes through $\mathbf{x}_0$ at time t_0. The Eulerian velocity $u_i(\mathbf{x}_0, t_0)$ is $u_i(\mathbf{x}_0, t_0|t_0)$ and the usual Lagrangian velocity is $u_i(\mathbf{x}_0, 0|t_0)$ if $t_0 = 0$ is the initial time. In other words, Eq. (5) is the correlation between the velocity of a particle at point $\mathbf{x}_0$ at time t_0 and the velocity at time t ($t \geq t_0$) of a particle that was at the point $\mathbf{x}_0 + \mathbf{l}$ at time t_0. It is not the usual Lagrangian autocorrelation function, as such we will refer to it as the pseudo Lagrangian autocorrelation function. Note also that the pseudo correlation $\hat{R}_{ij}^L$ as defined in Eq. (5) is not the usual correlation coefficient which have a product of r.m.s. fluctuations in its denominator. The present normalization factor in Eq. (5) is chosen because we would like to compare $\hat{R}_{ij}^L$ for different separations $\mathbf{l}$ (section 4) and it is easier to compare if $\hat{R}_{ij}^L(\mathbf{x}_0, t_0|t_0; \mathbf{x}_0 + \mathbf{l}, t_0|t_0) = 1$ for all $\mathbf{l}$.

The reason for considering $\hat{R}_{ij}^L$ is that it is possible to define a time scale with a dynamical significance. As t tends to t_0, the rate of change of $\hat{R}_{ij}^L$ is related to the *Eulerian* time scale associated with the cross correlation of velocity at $\mathbf{x}$ and pressure gradient at $\mathbf{x} + \mathbf{l}$ viz:

$$\left.\frac{d\hat{R}_{ij}^L}{dt}\right|_{t\to t_0} = -\frac{1}{\rho}\left\langle u_i(\mathbf{x})\frac{\partial p}{\partial x_j}(\mathbf{x}+\mathbf{l})\right\rangle \Big/ \langle u_i u_j\rangle = -\frac{1}{\tau_{ij}}. \quad (6)$$

In deriving Eq. (6), the viscous part of $\partial u_j/\partial t$ has been neglected because of high Reynolds number arguments. When $|\mathbf{l}| = 0$, it can be shown (see Eq. (7)) that $\tau_{ii} = u'^2/\pi C^L \epsilon \approx T_L$, where u'^2 is the turbulent intensity, T_L is the Lagrangian integral time scale of the flow, and C^L is a universal constant of order 1 with the value near 0.6 (Fung et al., 1992). Thus the time scale τ_{ij} indicates the dynamical time scale of different scales of eddy, which is required by EDQNM theory.

2 Hypothesis for the Pseudo-Velocity Correlation Function

There are two mechanisms to make the velocity of particle B decorrelate from that of the hypothetical particle A which is held fixed (see Figs. 1(a, b)).

(a) In high Reynolds number turbulence, the Lagrangian frequency spectrum (Fung et al., 1992) has the form $\phi_{ii}^L(\omega) = C^L \epsilon \omega^{-2}$ ($i = 1, 2$ or 3). The ω^{-2} spectrum in the inertial range means that the acceleration spectrum would be flat (see Borgas and Sawford, 1991) and hence the acceleration of fluid particles have "sudden jumps" (white noise) since in a homogeneous three-dimensional isotropic turbulent flow, the velocity gradients are not distributed in a uniform manner in space, and are intermittent. (In fact, the acceleration does have a finite, albeit short, memory time. Borgas and Sawford (1991) suggested that the two-particle acceleration correlation remains important for significant periods of time, decaying as t^{-1} in the inertial range. More recent work of DNS by Yeung (1997) offers qualitative support for a t^{-1} scaling suggested by Borgas and Sawford.) This intermittency is of a different nature from the "external intermittency" which characterizes the large scales of a turbulent flow at the frontier with the outer irrotational flow, in turbulent boundary layer or jets for instance. The existence of internal intermittency is characteristic of small scales at high Reynolds number turbulence as a result of the process of stretching of vortex filaments. By taking the Fourier transform of $\phi_{11}^L(\omega)$ yields the one particle autocorrelation

$$R_{11}^L(\tau) = \langle u(t)u(t+\tau)\rangle = \int_{-\infty}^{\infty} \phi_{11}^L(\omega) e^{i\omega\tau} d\omega = u'^2 - \pi C^L \epsilon \tau \quad \text{for} \quad l = 0, \quad (7)$$

i.e., the correlation decreases linearly with time τ for $\tau_L \ll \tau \ll T_L$ (where τ_L is the Lagrangian microscale). If we define T_L as $R_{11}^L(\tau = T_L) = 0$, then $T_L = u'^2/\pi C^L \epsilon$. Note that (7) also implies that

$$\left\langle u\frac{du}{dt}\right\rangle = -\pi C^L \epsilon \quad \text{as} \quad \tau \to 0. \quad (8)$$

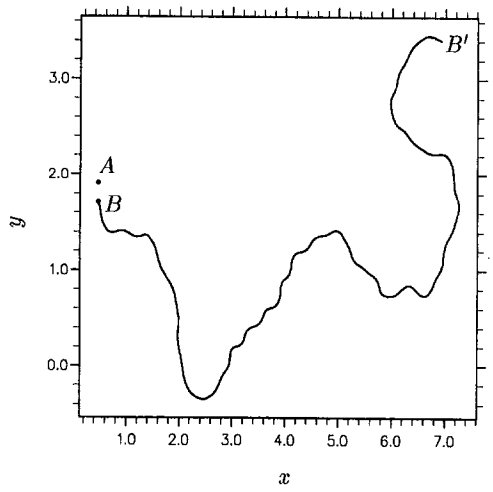

Fig. 1(a) Particles A and B separated at a distance l_0 apart initially. Particle B is tracked through the flow field while the hypothetical particle A is held fixed.

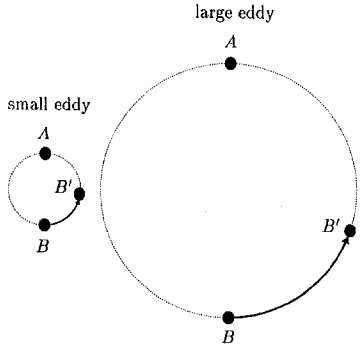

Fig. 1(b) The pseudo-velocity correlation function of Eq. (5) between point A and point B decreases more slowly for particle pairs of larger initial separation because they are advected by larger eddies in the flow which have a longer time scale

(b) The random spatial eddy structure of the flow means that the velocity of the two particles are not perfectly correlated with each other. The greater the value of l, the smaller is the correlation $\hat{R}_{ij}^L$ of the particles A and B at time t_0. Although when l is small $\hat{R}_{ij}^L$ is greater, and the decorrelation between the velocity of the pair of particles is rapid because the eddies contributing to $\hat{R}_{ij}^L$ have a smaller time scale. Consequently, the further they move apart the more they are decorrelated but the *larger* the time scale $\tau(l)$ of the eddies that do correlate the velocity of the particles. Therefore when they are at a distance l apart in the inertial range, the time scale, $\tau(l)$, for decorrelation of $\hat{R}_{ij}^L$ is given by

$$\tau(l) = C_l \epsilon^{-1/3} l^{2/3}. \quad (9)$$

Using the assumption that the Eulerian and Lagrangian time scales scale in the same way, then the constant $C_k = C_l/(2\pi)^{2/3}$ because $k = 2\pi/l$.

By combining the two effects, it is plausible that the asymptotic form for $\hat{R}_{ii}^L$ for small t (i.e., $t - t_0 \ll T_L$) and small l (i.e., $l \ll L$, where L is the integral length scale of the flow) has the form

Downloaded 04 May 2010 to 171.66.16.26. Redistribution subject to ASME license or copyright; see http://www.asme.org/terms/Terms_Use.cfm

$$\hat{R}_{ii}^{L}(\mathbf{x}_0, t_0|t_0; \mathbf{x}_0 + \mathbf{l}, t_0|t) = 1 - \frac{|t - t_0|}{\tau_l}$$

$$\text{for} \quad \tau_L \ll \tau \ll |t - t_0|, \quad (10)$$

where

$$\tau_l = \frac{u'^2}{\pi C^L \epsilon} + C_l \frac{l^{2/3}}{\epsilon^{1/3}}. \quad (11)$$

Note that for $l = 0$, Eq. (11) reduces to the one-particle results of Eq. (7).

In order to test the validity of Eq. (11), particularly its dependence on l, it may be rewritten as

$$\frac{1}{\tau_l\,(l=0)} - \frac{1}{\tau_l} = \left(\frac{\pi C^L \epsilon}{u'^2}\right)^2 C_l \epsilon^{-1/3} l^{2/3} \quad (12)$$

where $\tau_l\,(l = 0) = u'^2/(\pi C^L \epsilon)$.

It would be interesting to see if the dimensional and physical reasoning of Eq. (10) is consistent with the prediction of the EDQNM theory.

It is the purpose of this paper to find the value of the constant C_l. Is it a universal constant? Or is it a function of the Reynolds number?

3 Numerical Simulation

Fung et al. (1992) described a method for "kinematically" simulating a turbulent velocity field in space and time using only the information on the space-time Eulerian spectra—without computing the flow field from the dynamical equations. It is called kinematic simulation (KS); it is described in detail in Fung et al. (1992) and is merely summarized here. Any velocity field $u_i(\mathbf{x}, t)$ can be represented as the sum of N_k modes with random amplitudes a_{n_i} and mode functions $\phi^{n_i}(\mathbf{x}, t)$; its covariance $E_{n_{ij}}$ and functional form are both defined by the spatial-temporal spectra. The amplitude variables and the mode functions are not directly correlated with each other. The simulated turbulence is a stationary, isotropic, and homogeneous velocity field, and it is assumed that the probability distribution function is Gaussian. Then the mode function ϕ^{n_i} consists of sine and cosine functions for each wave number k_n and frequency ω_n, so that the velocity field is

$$\mathbf{u}(\mathbf{x}, t) = \sum_{n=1}^{n=N_k} [(\mathbf{a}_n \wedge \hat{\boldsymbol{\kappa}}_n) \cos\{\boldsymbol{\kappa}_n \cdot \mathbf{x} + \omega_n t\} + (\mathbf{b}_n \wedge \hat{\boldsymbol{\kappa}}_n) \sin\{\boldsymbol{\kappa}_n \cdot \mathbf{x} + \omega_n t\}]. \quad (13)$$

The essential features of the time dependence of the velocity field have been simulated in two ways: (*i*) by allowing each spatial Fourier component to vary with time at a frequency $\omega_n = \lambda \epsilon^{1/3} k_n^{2/3}$, where ϵ is the rate of dissipation of kinetic energy per unit mass and λ is a constant of order one; and (*ii*) by dividing the velocity into a large-scale velocity field $\mathbf{u}_l(k < k_c)$, and a small velocity field $\mathbf{u}_s(k_c < k)$ at some critical wave number k_c, and allowing the large-scale field to advect the small-scale field following Tennekes (1975). The "large-scale" velocity field can be obtained from dynamical simulations or from an idealized representation of large eddies moving randomly without much change of form. The Eulerian and Lagrangian frequency spectra, space structure function, and pressure spectra obtained from kinematic simulation all compare well with direct numerical simulation (DNS), and experimental data are not sensitive to the choice of k_c and λ.

KS has the same advantage as spectral methods over finite difference or finite element methods in representing the velocity field. But in a *dynamical* simulation using spectral methods it is necessary to include modes for every wave number in the representation where the number of points $N_p \propto k_\eta^3 \sim \mathrm{Re}^{9/4}$, whereas in KS a fewer number of modes are needed to represent all the major *kinematical* features of the flow field. It is found empirically that $N_k \propto k_\eta \sim \mathrm{Re}^{3/4}$.

Even though this is a random superposition of Fourier modes, it can generate localized regions of high vorticity or strain; two waves of different frequency travelling in the same direction will "beat" together to give high, local energy, while two orthogonal waves can form a vortical structure. In a straining region, this vortical structure will give rise to helical motion and spiral streamlines (Fung et al., 1990).

Since KS can simulate a turbulent velocity field with a prescribed Eulerian energy spectrum $E(k)$, it can simulate both high Reynolds number turbulent flow, i.e., with a Kolmogorov spectrum, for the inertial subrange and moderate Reynolds number of typical laboratory turbulence with an exponentially decaying spectrum.

Note that $E(k)$ is normalized to give

$$\int_0^\infty E(k)dk = \tfrac{1}{2}\langle \mathbf{u}(\mathbf{x}, t)^2 \rangle,$$

and, from Batchelor (1953), the integral length scale is given by

$$L_{11} = \frac{3\pi}{4} \int_0^\infty k^{-1} E(k)dk \Big/ \int_0^\infty E(k)dk.$$

Because we use a finite number of Fourier modes, the energy spectrum must be truncated at some cut-off wave number k_η. The choice of k_η determines both the Reynolds number and the integration time step. In a viscous flow at high Reynolds number, the micro and large scales are related through the Reynolds number by $\mathrm{Re}^{3/4} \sim l_e/\eta = k_\eta l_e$ (Batchelor, 1953), where $l_e \sim v^3/\epsilon$ is the length scale of the energy-containing eddies and $v^2 = \langle u_1^2 \rangle$ is the velocity variance. Thus increasing k_η increases the Reynolds number of the simulation. At separations less than k_η^{-1}, the velocity field is simply a uniform straining motion, as assumed in many previous models. Increasing k_η also decreases the time step which can be used in computing velocities and trajectories of fluid elements since the time step must be less than the inverse of the highest frequencies in the flow, and this increases the computational time.

4 Results

Two "kinematic simulation" (KS) of homogeneous isotropic turbulence (Fung et al., 1992) were used for this investigation with the Eulerian spectra of the form $E(k) = \alpha_k \epsilon^{2/3} k^{-5/3}$, and the Kolmogorov constant α_k is chosen to be 1.5 (Gibson, 1963). In the simulations used here, only the inertial subranges are simulated from $k_e < k < k_\eta$ with $k_e = 1$. Two ranges of wave numbers with $k_\eta/k_e = 10$ and $k_\eta/k_e = 50$ are used which corresponds to different Reynolds numbers. An inertial subrange of this length is only found when the Reynolds numbers is greater than 10^3.

Lagrangian statistic are obtained by tracking 6000 fluid particles in the flow. We integrate the equation of motion $\partial \mathbf{x}(t)/\partial t = \mathbf{u}(\mathbf{x}, t)$ using an extended Runge-Kutta scheme (for more details, see Fung et al., 1992).

Alternatively, particle trajectories can be generated directly using a stochastic model for Lagrangian velocities, an approach initiated by Taylor (1921). Various two-particle models have been proposed which involve a pair of coupled Langevin equations in which the rate of separation of the pair of particles is modulated according to their separation (Durbin, 1980) or their expected separation (Sawford, 1982) by a term involving the space structure function of the turbulence. The idea is to model the physical motion that particles tend to move together when their separation is small compared with the Eulerian length scale L and to move independently when their separation is large

Downloaded 04 May 2010 to 171.66.16.26. Redistribution subject to ASME license or copyright; see http://www.asme.org/terms/Terms_Use.cfm

compared with L and the rate of separation depends on the expected separation.

The pseudo correlation $\hat{R}_{ii}^{L}$ with $k_\eta/k_c = 10$ and 50 obtained are given as functions of dimensional time and different initial separations l which has been normalized by the large scale ($=1/k_c$) in the simulated flow in Figs. 2(a, b). For most values of l, $\hat{R}_{ii}^{L}(t)$ is seen to decrease steadily with time, and the time to complete decorrelation is clearly longer for increasing l, i.e., the correlations corresponding to small separation decrease more rapidly. It is interesting to note the recent DNS work of Yeung (1994) who studies the true two-particle, one-time statistics of relative displacement and velocity. The simulated particle-pair velocity correlation coefficients for different initial separations decrease steadily with time, but the time to complete decorrelation is shorter for increasing l. Moveover, for the larger values of l, the correlation coefficient initially increases slightly or remains nearly constant before it begins to decrease. Yeung pointed out that this behavior can be expected by recognizing that although the particles move apart on average, they do not do so at all times. The results of Yeung are not inconsistent with the present study.

It should also be noted that when $l = 0$, we obtain the Lagrangian auto-correlation function as in Fung et al. (1992), and as l increases but still smaller than the integral length scale L_{11}, the only mechanism to keep the two-particle correlated is the very large-scale eddy which has a very long Lagrangian integral time scale and hence $\hat{R}^{L}(l, t) \geq \hat{R}^{L}$ ($l = 0$, t) even for large t as shown in Figs. 2(a, b). Of course, if the particles are initially far apart ($l \gg L_{11}$), the two-point, two-time correlation between them would be nearly zero for all time.

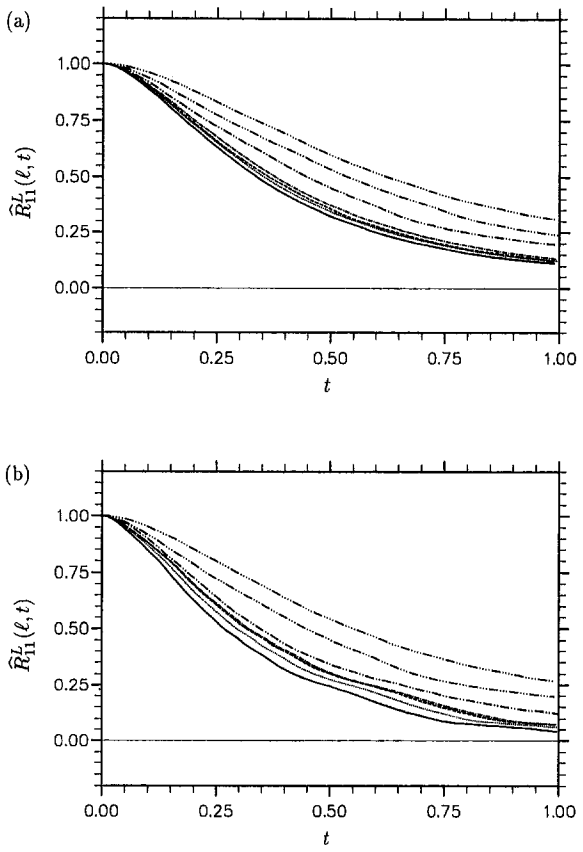

Fig. 2 The two-point pseudo Lagrangian velocity auto-correlation function $\hat{R}_{11}^{L}(l, t)$ as a function of time and initial separation l with (a) $k_\eta/k_c = 10$ and (b) $k_\eta/k_c = 50$: $l = 0.0$ (solid curve), $l = 1/50$ (dotted curve), $l = 1/30$ (dashed curve), $l = 1/20$ (dash-dotted curve), $l = 1/10$ (dash-dot-dotted curve), $l = 1/5$ (dash-dot-dot-dotted curve) and $l = 1/3$ (dash-dot-dot-dot-dotted curve), respectively.

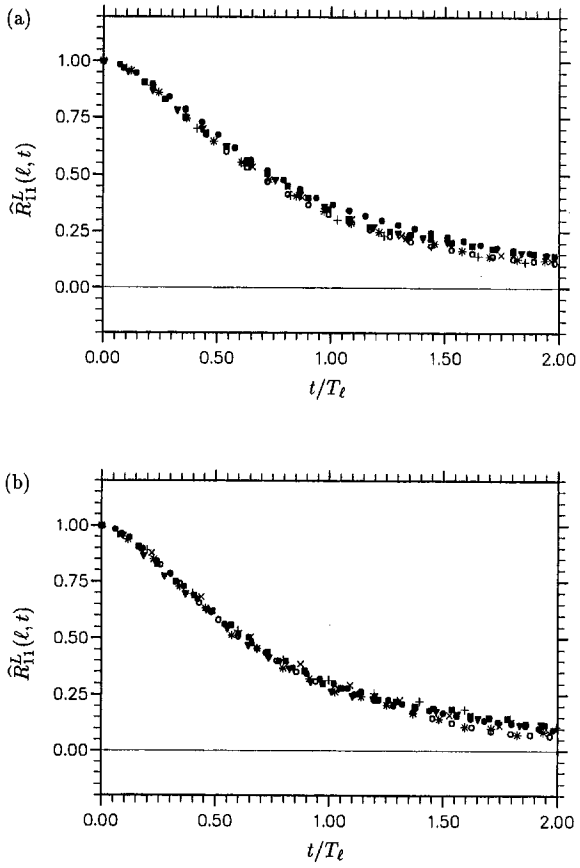

Fig. 3 The pseudo-velocity correlation of Fig. 2 as a function of time normalized by their time scale T_l. (a) $k_\eta/k_c = 10$ and (b) $k_\eta/k_c = 50$: $l = 0.0$ (○○○), $l = 1/50$ (***), $l = 1/30$ (+++), $l = 1/20$ (×××), $l = 1/10$ (●●●), $l = 1/5$ (■■■) and $l = 1/3$ (▼▼▼), respectively.

Note also that with the same initial separation l, the pseudo correlation $\hat{R}_{ii}^{L}$ in Fig. 2(b) which corresponds to a higher Reynolds number case, decreases more rapidly to zero than that of $\hat{R}_{ii}^{L}$ in Fig. 2(a) which corresponds to a lower Reynolds number case. This is expected since high Reynolds numbers would have a smaller Lagrangian integral time scale T_L, hence $\hat{R}_{11}^{L}$ ($l = 0$, t) decreases faster to zero.

We also plot the velocity correlations as functions of the time normalised by the time scales T_l (which is defined as the time taken for $\hat{R}_{11}^{L}(\tau)$ to fall to a value of zero. An accurate time scale should collapse the results to a single curve. Figures 3(a, b) show that this is indeed so.

The pseudo-correlation function $\hat{R}_{ii}^{L}$ in theory decreases linearly with time for small l (i.e., $l \ll L$) and small time $t - t_0$ (i.e., $t - t_0 \ll T_L$), see also Eq. (7). Therefore, by plotting the inverse slope of the pseudo-correlation function $\hat{R}_{ij}$ at small time (about $T_L/10$) against $l^{2/3}$, and estimating the slope of the curve at small l, the constant C_l can be estimated. In Fig. 4, the constant is determined by this method and found to be 0.31 ± 0.04 for $k_\eta/k_c = 10$ and 0.46 ± 0.05 for $k_\eta/k_c = 50$. Despite the inaccuracy of these estimates for the slopes, there seems to be a variation of C_l with the extent of the inertial subrange and therefore with the Reynolds numbers. This is consistent with our finding for the dispersion of particle pairs (Fung et al., 1992), and that the structure of the turbulence in the inertial range only becomes invariant with Reynolds numbers when k_η/k_c is significantly greater than 100.

5 Conclusion

We have presented here a simulation of an unsteady random velocity field whose statistics are adjusted to agree with the

Downloaded 04 May 2010 to 171.66.16.26. Redistribution subject to ASME license or copyright; see http://www.asme.org/terms/Terms_Use.cfm

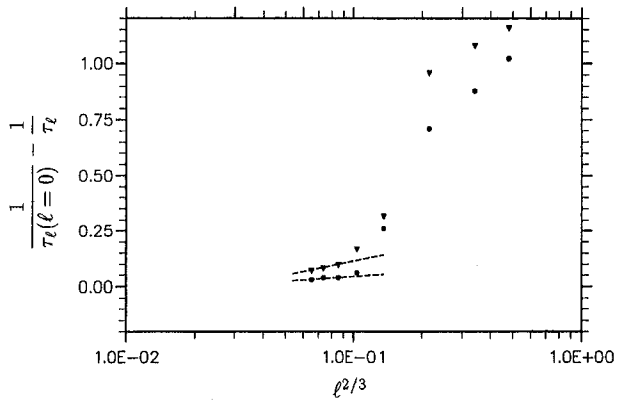

Fig. 4 The inverse slope of the pseudo-velocity correlation function $R^L_{11}(l, t)$ at small time as a function of initial separation l. $k_\eta/k_c = 10$ (●●●) and $k_\eta/k_c = 50$ (▼▼▼).

experimentally measured values of two-point, space-time Eulerian and Lagrangian statistics of homogeneous turbulence. Although they do not simulate the nonlinear dynamics of the flow field, such as the interaction between large and small-scale motion, they appear to simulate the random displacements of fluid particles, the time-dependent structure of turbulence (for two moments in time), and the pressure spectrum (Fung et al., 1992). Since it is not yet possible to simulate a high Reynolds number spectrum using DNS over more than one decade (Vincent and Meneguzzi 1991), we cannot yet compute directly how fluid elements move in a fully developed high Reynolds number turbulent flow. This is why we have had to use kinematic simulation. This kinematic simulation should be useful in many studies which require such flow fields, and where there is no model for the small scale at present—it is a kind of "small-eddy simulation" that might complement large-eddy simulation. In this study, we have demonstrated the feasibility of using kinematic simulation as means of constructing Lagrangian statistics (Fung and Vasslicos, 1998), and hence obtained "universal" and empirical constants for different models.

Further work could be done with more appropriate forms of spectra in KS to explore whether this would change the present results. Theoretical studies should explore whether the nonlinear interaction between different scales of motion significantly affect the constant C_l.

Acknowledgment

The author thanks Prof. J. C. R. Hunt for stimulating discussions and comments and the support of the Hong Kong Research Grant Council is gratefully acknowledged.

References

Batchelor, G. K., 1953, *The theory of homogeneous turbulence,* Cambridge University Press, London.

Bertogilo, J. P., 1986, "Etude d'une turbulence aniotrope; Modelisation de Sous-Maille et Approche Statistique," Thèse d'Etat, Universite C. Bernard, Lyon, France.

Borgas, M. S. and Sawford, B. L., 1991, "The small-scale structure of acceleration correlations and its role in the statistical theory of turbulence dispersion," *J. Fluid Mech.* Vol. 228, pp. 295–320.

Durbin, P. A., 1980, "A stochastic model of two-particle dispersion and concentration fluctuations in homogeneous turbulence," *J. Fluid Mech.* Vol. 100, pp. 279–302.

Fung, J. C. H., Hunt, J. C. R., Perkins, R. J., Wray, A. A., and Stretch, D. D., 1991, "Defining the zonal structure of turbulence using the pressure and invariants of the deformation tensor," *Proc. Third European Turbulence Conference, Stockholm, 1990,* Springer-Verlag, New York.

Fung, J. C. H., Hunt, J. C. R., Malik, N. A., and Perkins, R. J., 1992, "Kinematic Simulation of homogeneous turbulent flows generated by unsteady random Fourier modes," *J. Fluid Mech.,* Vol. 236, pp. 281–318.

Fung, J. C. H., and Vassilicos, J. C., 1998, "Two-particle dispersion in turbulent-like flows," *Physical. Rev. E,* to appear.

Gibson, M. M., 1963, "Spectra of turbulence in a round jet," *J. Fluid Mech.* Vol. 15, pp. 161–173.

Kolmogorov, A. N., 1941, "The local structure of turbulence in incompressible viscous fluid for very large Reynolds numbers," *Dokl. Akad. Nauk SSSR,* Vol. 30, pp. 301–305.

Lesieur, M., 1987, *Turbulence in fluids: Stochastic and numerical modelling,* M. Nijhoff, Dordrecht, Netherlands.

Leslie, D. C., 1973, *Developments in the theory of turbulence,* Clarendon Press, Oxford, UK.

Orszag, S. A. 1970 "Analytical theories of turbulence," *J. Fluid Mech.* Vol. 41, pp. 363–386.

Sawford, B. L., 1982, "Lagrangian Monte Carlo simulation of the turbulent motion of a pair of particles," *Quart. J. Roy. Meteor.,* Vol. 16, pp. 207–213.

Taylor, G. I., 1921, "Diffusion by continuous movements," *Proc. Lond. Math. Soc.,* Vol. 20, pp. 196–211.

Tennekes, H., 1975, "Eulerian and Lagrangian time microscales in isotropic turbulence," *J. Fluid Mech.,* Vol. 67, pp. 561–567.

Yeung, P. K., 1994, "Direct numerical simulation of two-particle relative diffusion in isotropic turbulence," *Phys. Fluid,* Vol. 6, pp. 3416–3428.

Yeung, P. K., 1997, "One- and two-particle Lagrangian acceleration correlations in numerically simulated homogeneous turbulence," *Phys. Fluid,* Vol. 9, pp. 2981–2990.

Downloaded 04 May 2010 to 171.66.16.26. Redistribution subject to ASME license or copyright; see http://www.asme.org/terms/Terms_Use.cfm

Canonical Perturbation of a Fast Time-Periodic Hamiltonian via Liapunov-Floquet Transformation

E. A. Butcher
Graduate Research Assistant,
Assoc. Mem. ASME.

S. C. Sinha[1]
Professor and Director,
Fellow ASME.

Nonlinear Systems Research Laboratory,
Department of Mechanical Engineering,
Auburn University,
Auburn, AL 36849

In this study a possible application of time-dependent canonical perturbation theory to a fast *nonlinear time-periodic Hamiltonian with* strong *internal excitation is considered. It is shown that if the time-periodic unperturbed part is quadratic, the Hamiltonian may be canonically transformed to an equivalent form in which the new unperturbed part is time-invariant so that the time-dependent canonical perturbation theory may be successfully applied. For this purpose, the Liapunov-Floquet (L-F) transformation and its inverse associated with the unperturbed time-periodic quadratic Hamiltonian are computed using a recently developed technique. Action-angle variables and time-dependent canonical perturbation theory are then utilized to find the solution in the original coordinates. The results are compared for accuracy with solutions obtained by both numerical integration and by the classical method of directly applying the time-dependent perturbation theory in which the time-periodic quadratic part is treated as another perturbation term. A strongly excited Mathieu-Hill quadratic Hamiltonian with a cubic perturbation and a nonlinear time-periodic Hamiltonian without a constant quadratic part serve as illustrative examples. It is shown that, unlike the classical method in which the internal excitation must be* weak, *the proposed formulation provides accurate solutions for an arbitrarily large internal excitation.*

1 Introduction

Previous works (Goldstein, 1980; Tabor, 1989; Rand, 1994; Hyams and Month, 1984; Month and Rand, 1980) have shown that canonical perturbation theory can be used to study the stability and obtain approximate solutions to systems with autonomous Hamiltonians of the form $H = H_0 + \epsilon H_1$ where the unperturbed part H_0 can be solved exactly, H_1 is the nonintegrable perturbation, and ϵ is a small parameter. In the event the perturbation contains a periodic time-dependence as $H(t) = H_0 + \epsilon H_1(t)$, $H_1(t + T) = H_1(t)$, at least two possible approaches (which yield equivalent results) exist. One option is to eliminate time via an extended phase space and employ canonical perturbation while another is to apply the time-dependent canonical perturbation theory directly as shown by Lichtenberg and Lieberman (1983). In these problems the unperturbed Hamiltonian H_0 always remains time independent. However, many problems in classical and quantum mechanics have a time-periodic Hamiltonian of the form $H(t) = H_0(t) + \epsilon H_1(t)$, $H(t + T) = H(t)$ in which the unperturbed part is time periodic as well. Time-dependent canonical perturbation or similar perturbation techniques cannot be applied in these cases unless (1) the time variation in $H_0(t)$ is *slow*, i.e., $H_0 = H_0(\epsilon t)$ (Lichtenberg and Lieberman, 1983); or (2) the pseudo-stationary states of $H_0(t)$ are known (Lo, 1991); or (3) $H_0(t)$ can be separated into constant and time-periodic parts as $H_0(t) = \bar{H}_0 + \epsilon\tilde{H}_0(t)$ where the time-periodic part is of the same (small) order as the perturbation. In the third case the internal excitation is *weak* and the time-dependent perturbation theory may be directly applied to $H(t) = \bar{H}_0 + \epsilon(\tilde{H}_0(t) + H_1(t))$ where the internal excitation term is treated as another perturbation. If the time-dependent part of $H_0(t)$ is not small or $\bar{H}_0 = 0$, however, then the internal excitation is *strong* and (if the first two cases above still do not hold) another procedure must be found.

Here we consider the case of a *fast* (i.e., not slow) time-periodic quadratic Hamiltonian with strong internal excitation (such that the cases mentioned above are not applicable) perturbed by nonlinear monomials of cubic or higher order which might have periodic coefficients. It is shown that the Hamiltonian may be canonically transformed to an equivalent form in which the unperturbed quadratic part is time-invariant and the perturbation is time periodic so that time-dependent canonical perturbation theory may be applied. For this purpose, the Liapunov-Floquet (L-F) transformation associated with the unperturbed time-periodic quadratic Hamiltonian $H_0(t)$ and its inverse are computed using a recently developed technique (Sinha and Joseph, 1994; Sinha and Pandiyan, 1994; Pandiyan and Sinha, 1995). While the formulation is applicable to systems of arbitrary dimension, a single-degree-of-freedom Mathieu-Hill quadratic Hamiltonian with an autonomous cubic perturbation is chosen here to illustrate the technique. It is shown that the proposed procedure enables one to obtain accurate solutions in action-angle coordinates which may be transformed back to the original phase-space coordinates for an arbitrarily large internal excitation. These solutions are compared to the results obtained using the classical method of direct perturbation analysis which diverge from the true solutions as the excitation strength is increased. An example with $\bar{H}_0 = 0$ is also presented where the L-F transformation approach is absolutely essential.

2 Problem Formulation and Analysis

Consider a nonlinear time-periodic Mathieu-Hill Hamiltonian of the form

$$H(x, p_x, t) = \frac{p_x^2}{2} + \frac{1}{2}(1 + \beta \sin(2\pi t))x^2 + \epsilon x^3 \quad (1)$$

[1] To whom all correspondence should be addressed. E-mail: ssinha@eng.auburn.edu.

Contributed by the Applied Mechanics Division of THE AMERICAN SOCIETY OF MECHANICAL ENGINEERS for publication in the ASME JOURNAL OF APPLIED MECHANICS.

Discussion on the paper should be addressed to the Technical Editor, Professor Lewis T. Wheeler, Department of Mechanical Engineering, University of Houston, Houston, TX 77204-4792, and will be accepted until four months after final publication of the paper itself in the ASME JOURNAL OF APPLIED MECHANICS.

Manuscript received by the ASME Applied Mechanics Division, Dec. 10, 1996; final revision, June 10, 1997. Associate Technical Editor: S. W. Shaw.

 Copyright © 1998 by ASME

Downloaded 04 May 2010 to 171.66.16.26. Redistribution subject to ASME license or copyright; see http://www.asme.org/terms/Terms_Use.cfm

where x and p_x are the generalized coordinate and momentum, respectively, β is the internal excitation strength (not necessarily small), and $\epsilon \ll 1$ is the small perturbation parameter. This Hamiltonian models various parametrically excited single-degree-of-freedom systems under the influence of asymmetric restoring forces. The mass and frequency of the quadratic autonomous ($\beta = \epsilon = 0$) Hamiltonian have been set to identity while the internal excitation frequency has been set to 2π. Thus, the system is away from the primary 2:1 resonance as shown in the stability diagram of the linearized ($\epsilon = 0$) system in Fig. 1. It can be seen that Eq. (1) is of the form $H(t) = H_0(t) + \epsilon H_1$; $H_0(t) = \bar{H}_0 + \beta \tilde{H}_0(t)$ where

$$\bar{H}_0 = \frac{p_x^2}{2} + \frac{x^2}{2}; \quad \tilde{H}_0(t) = \frac{1}{2}\sin(2\pi t)x^2; \quad H_1 = x^3. \quad (2)$$

The equations of motion for the system are

$$\dot{x} = \frac{\partial H}{\partial p_x} = p_x;$$

$$\dot{p}_x = -\frac{\partial H}{\partial x} = -(1 + \beta \sin(2\pi t))x - 3\epsilon x^2 \quad (3)$$

which may be written in vector-matrix form as

$$\dot{\mathbf{x}} = \mathbf{A}(\mathbf{t})\mathbf{x} - 3\epsilon \mathbf{f}(\mathbf{x}) \quad (4)$$

where the state vector, 1-periodic Hamiltonian system matrix, and nonlinear vector are

$$\mathbf{x} = \begin{pmatrix} x \\ p_x \end{pmatrix};$$

$$\mathbf{A}(t) = \mathbf{A}(t+1) = \begin{bmatrix} 0 & 1 \\ -(1 + \beta \sin(2\pi t)) & 0 \end{bmatrix};$$

$$\mathbf{f}(\mathbf{x}) = \begin{pmatrix} 0 \\ x^2 \end{pmatrix}. \quad (5)$$

The fundamental solution matrix $\Phi(t)$ of the linear part of Eq. (4) satisfies

$$\dot{\Phi}(t) = \mathbf{A}(t)\Phi(t); \quad \Phi(0) = \mathbf{I}_2 \quad (6)$$

and the eigenvalues (Floquet multipliers) $\mu_{1,2}$ of $\Phi(1)$ determine the stability of the (0, 0) fixed point where $|\mu_i| = 1$ for (neutral) stability. From Floquet theory, $\Phi(t)$ can be factored in two ways as

$$\Phi(t) = \mathbf{L}(t)\exp(\mathbf{C}t) = \mathbf{Q}(t)\exp(\mathbf{R}t);$$
$$\mathbf{L}(0) = \mathbf{Q}(0) = \mathbf{I}_2 \quad (7)$$

where $\mathbf{L}(t) = \mathbf{L}(t+1)$ is the 1-periodic Liapunov-Floquet (L-F) matrix and $\mathbf{Q}(t) = \mathbf{Q}(t+2)$ is the 2-periodic L-F matrix. If $\mathrm{Re}(\mu_{1,2}) > 0$, then $\mathbf{L}(t) = \mathbf{Q}(t)$ are both 1-periodic and the eigenvalues of $\mathbf{C} = \mathbf{R}$ are the characteristic exponents. If $\mathrm{Re}(\mu_{1,2}) < 0$, then $\mathbf{L}(t) \neq \mathbf{Q}(t)$, $\mathbf{C} \neq \mathbf{R}$, and only the eigenvalues of $\mathbf{C}$ are the characteristic exponents. If $\mu_{1,2}$ are negative real, then $\mathbf{L}(t)$ and $\mathbf{C}$ are complex while $\mathbf{Q}(t)$ and $\mathbf{R}$ remain real (Yakubovich and Starzhinskii, 1975). Equation (4) can be transformed using one of the L-F transformation matrices as

$$\mathbf{x} = \mathbf{P}(t)\mathbf{y} \quad (8)$$

which results in

$$\dot{\mathbf{y}} = \mathbf{G}\mathbf{y} - 3\epsilon \mathbf{P}^{-1}(t)\mathbf{f}(\mathbf{P}(t)\mathbf{y}) \quad (9)$$

where $\mathbf{P}(t) = \mathbf{L}(t)$ or $\mathbf{Q}(t)$ and $\mathbf{G} = \mathbf{C}$ or $\mathbf{R}$, respectively. It should be noted that the linear system matrix in Eq. (9) is time-invariant and that the nonlinear terms now have periodic coefficients with period 1 or 2. The transformation of Eq. (8) is canonical (i.e., preserves the form of the Hamiltonian) since $\det(\mathbf{P}(t)) = \det(\mathbf{P}(0)) = 1$ implies that $\mathbf{P}(t)$ is symplectic and $\mathbf{G}$ is Hamiltonian with $\mathrm{tr}(\mathbf{G}) = 0$ regardless of the L-F matrix used. Details on the computation of $\mathbf{L}(t)$, $\mathbf{Q}(t)$, $\mathbf{C}$, and $\mathbf{R}$ by expanding $\mathbf{A}(t)$ and $\Phi(t)$ in shifted Chebyshev polynomials can be found in the papers by Sinha and Joseph (1994), Sinha and Pandiyan (1994), and Pandiyan and Sinha (1995). It is also shown in these papers how the inverse transformation matrix $\mathbf{L}^{-1}(t)$ or $\mathbf{Q}^{-1}(t)$ can be computed from the linear adjoint system corresponding to Eq. (4).

A second linear canonical transformation

$$\mathbf{y} = \mathbf{M}\mathbf{z}; \quad \mathbf{z} = \begin{pmatrix} q \\ p \end{pmatrix} \quad (10)$$

is then made via the real constant symplectic modal transforma-

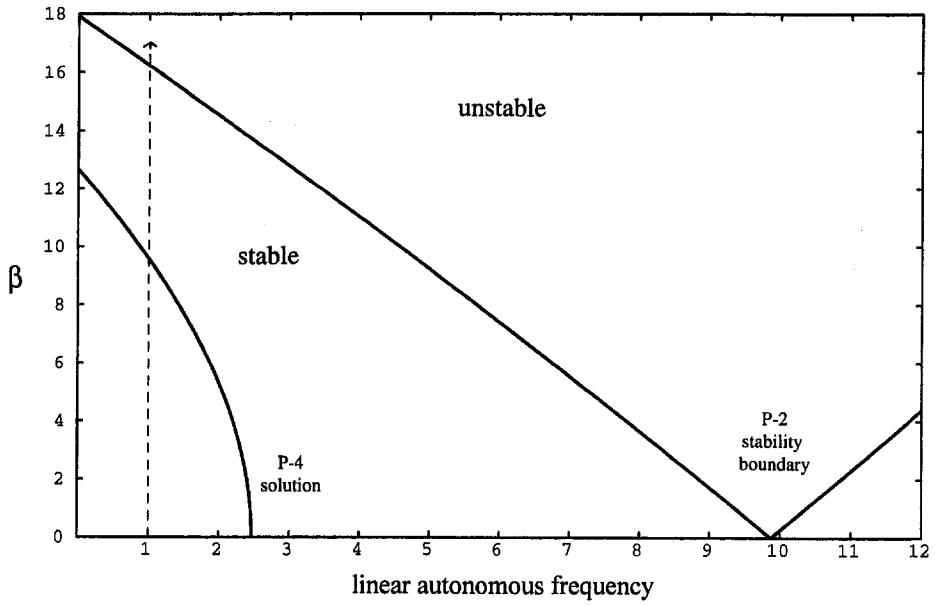

Fig. 1 Stability diagram with period 4 (P-4) solutions and the period-doubling (P-2) destabilization boundary for the linearized ($\epsilon = 0$) system. The linear autonomous frequency is held at one while β is increased.

Downloaded 04 May 2010 to 171.66.16.26. Redistribution subject to ASME license or copyright; see http://www.asme.org/terms/Terms_Use.cfm

tion matrix $\mathbf{M}$ which is normalized such that $\det(\mathbf{M}) = 1$. Applying Eq. (10) to Eq. (9) then yields

$$\dot{\mathbf{z}} = \mathbf{K}\mathbf{z} - 3\epsilon\mathbf{M}^{-1}\mathbf{P}^{-1}(t)\,\mathbf{f}(\mathbf{P}(t)\mathbf{M}\mathbf{z}) = \mathbf{J}\mathbf{S}\mathbf{z} - 3\epsilon\begin{pmatrix} g_{11}(t)q^2 + g_{12}(t)qp + g_{13}(t)p^2 \\ g_{21}(t)q^2 + g_{22}(t)qp + g_{23}(t)p^2 \end{pmatrix} \quad (11)$$

where the $g_{ij}(t)$'s are periodic functions of time with period 1 or 2 and

$$\mathbf{K} = \begin{bmatrix} 0 & \omega_0 \\ -\omega_0 & 0 \end{bmatrix}; \quad \mathbf{J} = \begin{bmatrix} 0 & 1 \\ -1 & 0 \end{bmatrix}; \quad \mathbf{S} = \begin{bmatrix} \omega_0 & 0 \\ 0 & \omega_0 \end{bmatrix}. \quad (12)$$

$\mathbf{K}$ is in real Jordan form (for stable cases) which is equivalent to real Hamiltonian normal form for the 2×2 case only. Higher dimensional problems require an additional permutation transformation from real Jordan form to real Hamiltonian normal form (Butcher and Sinha, 1995). ω_0 is the real number associated with one of the imaginary eigenvalues of the $\mathbf{C}$ or $\mathbf{R}$ matrix and is also the $\epsilon = 0$ approximation to the oscillation frequency in the transformed coordinates. The linear part of Eq. (11) has been also expressed in symplectic form via the symplectic coefficient matrix $\mathbf{J}$ and the symmetric matrix $\mathbf{S}$. In order to derive the transformed Hamiltonian, the nonlinear vector is also expressed in symplectic form as

$$\dot{\mathbf{z}} = \mathbf{J}\nabla H(\mathbf{z}, t) = \mathbf{J}\left[\mathbf{S}\mathbf{z} + 3\epsilon\begin{pmatrix} g_{21}(t)q^2 + g_{22}(t)qp + g_{23}(t)p^2 \\ -g_{11}(t)q^2 - g_{12}(t)qp - g_{13}(t)p^2 \end{pmatrix}\right]. \quad (13)$$

Equation (13) can be integrated to yield the transformed Hamiltonian

$$H(\mathbf{z}, t) = H_0(\mathbf{z}) + \epsilon H_1(\mathbf{z}, t) \quad (14)$$

where the new time-invariant unperturbed term and time-periodic perturbation are given by

$$H_0(\mathbf{z}) = \tfrac{1}{2}\omega_0(p^2 + q^2),$$

$$H_1(\mathbf{z}, t) = h_1(t)q^3 + h_2(t)q^2p + h_3(t)qp^2 + h_4(t)p^3,$$

$$h_1(t) = g_{21}(t), \quad h_2(t) = \tfrac{3}{2}g_{22}(t) - 3g_{11}(t),$$

$$h_3(t) = 3g_{23}(t) - \tfrac{3}{2}g_{12}(t), \quad h_4(t) = -g_{13}(t). \quad (15)$$

It should be observed that if the nonlinear perturbation in Eq. (1) had periodic coefficients, the form of the transformed Hamiltonian in Eqs. (14) and (15) would remain the same.

Equation (14) is now suitable for application of time-dependent perturbation theory. First, one of the phase-space variables is eliminated from the unperturbed Hamiltonian $H_0(\mathbf{z})$ via the canonical transformation

$$q = \sqrt{2I}\sin\theta, \quad p = \sqrt{2I}\cos\theta \quad (16)$$

to action-angle variables (I, θ). The Hamiltonian can thus be expressed as

$$H(I, \theta, t) = H_0(I) + \epsilon H_1(I, \theta, t), \quad H_0(I) = \omega_0 I,$$

$$H_1(I, \theta, t) = (2I)^{3/2}(h_1(t)\sin^3\theta + h_2(t)\sin^2\theta\cos\theta + h_3(t)\sin\theta\cos^2\theta + h_4(t)\cos^3\theta) \quad (17)$$

The canonical perturbation of Eq. (17) proceeds as shown by Goldstein (1980) and Tabor (1989) by finding a canonical near-identity transformation from the variables (I, θ) to new ones (J, ϕ) via a time-dependent mixed-variable generating function $S(J, \theta, t)$ which is expanded in powers of ϵ as

$$S(J, \theta, t) = J\theta + \epsilon S_1(J, \theta, t) + \epsilon^2 S_2(J, \theta, t) + \ldots. \quad (18)$$

Like $H(J, \theta, t)$, $S(J, \theta, t)$ is periodic in both the angle (with period 2π) and time (with period 1 or 2). The transformation equations for the old action and new angle are

$$I = \frac{\partial S}{\partial \theta} = J + \epsilon\frac{\partial S_1}{\partial \theta} + \epsilon^2\frac{\partial S_2}{\partial \theta} + \ldots$$

$$\phi = \frac{\partial S}{\partial J} = \theta + \epsilon\frac{\partial S_1}{\partial J} + \epsilon^2\frac{\partial S_2}{\partial J} + \ldots. \quad (19)$$

It is desired to chose $S(J, \theta, t)$ so that the new Hamiltonian $K(J)$, sometimes called the *Kamiltonian* (Goldstein, 1980; Rand, 1994), is only in terms of the new action thus making the solution to the equations of motion trivial. For this purpose, $K(J)$ is expanded in powers of ϵ and the time-dependent Hamiltonian-Jacobi equation

$$K(J) = K_0(J) + \epsilon K_1(J) + \epsilon^2 K_2(J) + \ldots = H_0(I) + \epsilon H_1(I, \theta, t) + \frac{\partial S}{\partial t} \quad (20)$$

is employed. Equations (18)–(20) yield

$$K_0(J) = H_0(J) = \omega_0 J$$

$$K_1(J) = H_1(J, \theta, t) + \omega_0\frac{\partial S_1}{\partial \theta} + \frac{\partial S_1}{\partial t}$$

$$K_2(J) = \frac{\partial S_1}{\partial \theta}\frac{\partial H_1}{\partial I}(J, \theta, t) + \omega_0\frac{\partial S_2}{\partial \theta} + \frac{\partial S_2}{\partial t} \quad (21)$$

where Taylor's series expansion and the formula $\omega_0 = \partial H_0/\partial I$ have been used. In order to eliminate the θ and t-dependence in $K_1(J)$ and $K_2(J)$, the averages

$$\langle H_1\rangle(J) = \frac{1}{2\pi T}\int_0^T\int_0^{2\pi} H_1(J, \theta, t)\,d\theta dt = 0$$

$$\left\langle \frac{\partial S_1}{\partial \theta}\frac{\partial H_1}{\partial I}\right\rangle(J) = \frac{1}{2\pi T}\int_0^T\int_0^{2\pi}\frac{\partial S_1}{\partial \theta}\frac{\partial H_1}{\partial I}(J, \theta, t)\,d\theta dt \quad (22)$$

and oscillations

$$\{H_1\}(J, \theta, t) = H_1(J, \theta, t) - \langle H_1\rangle(J) = H_1(J, \theta, t)$$

$$\left\{\frac{\partial S_1}{\partial \theta}\frac{\partial H_1}{\partial I}\right\}(J, \theta, t) = \frac{\partial S_1}{\partial \theta}\frac{\partial H_1}{\partial I}(J, \theta, t) - \left\langle \frac{\partial S_1}{\partial \theta}\frac{\partial H_1}{\partial I}\right\rangle(J) \quad (23)$$

are introduced where $T = 1$ or 2. It should be noted that the average of $H_1(I, \theta, t)$ in Eq. (17) is zero for this problem. Then from Eq. (21),

$$K_1(J) = \langle H_1\rangle(J) = 0, \quad K_2(J) = \left\langle \frac{\partial S_1}{\partial \theta}\frac{\partial H_1}{\partial I}\right\rangle(J) \quad (24)$$

Downloaded 04 May 2010 to 171.66.16.26. Redistribution subject to ASME license or copyright; see http://www.asme.org/terms/Terms_Use.cfm

and

$$-H_1(J, \theta, t) = \omega_0 \frac{\partial S_1}{\partial \theta} + \frac{\partial S_1}{\partial t},$$

$$-\left\{\frac{\partial S_1}{\partial \theta}\frac{\partial H_1}{\partial I}\right\}(J, \theta, t) = \omega_0 \frac{\partial S_2}{\partial \theta} + \frac{\partial S_2}{\partial t}. \quad (25)$$

To find $K_2(J)$, $S_1(J, \theta, t)$ must first be computed. This is accomplished by expressing it and $H_1(J, \theta, t)$ in real Fourier series as

$$H_1(J, \theta, t) = (2J)^{3/2} \sum_{lm} [a_{lm} \sin(l\theta + m\pi t) + b_{lm} \cos(l\theta + m\pi t)]$$

$$S_1(J, \theta, t) = (2J)^{3/2} \sum_{lm\neq 0} [c_{lm} \sin(l\theta + m\pi t) + d_{lm} \cos(l\theta + m\pi t)]. \quad (26)$$

Inserting this into Eq. (25) yields the Fourier coefficients of $S_1(J, \theta, t)$ as

$$c_{lm} = \frac{-b_{lm}}{l\omega_0 + m\pi}, \quad d_{lm} = \frac{a_{lm}}{l\omega_0 + m\pi} \quad (27)$$

It can be seen that an order $r = |l| + |m|$ resonance occurs if the denominators in Eq. (27) are zero and that this may occur to any degree of accuracy for sufficiently large r. However, while l and m run from -15 to 15 in these computations, resonances with orders r higher than 3 (the highest polynomial degree in $H(q, p, t)$) are not essential (Khazin and Shnol, 1985) and consequently a resonance is usually not encountered. After $S_1(J, \theta, t)$ is found, $K_2(J)$ is calculated from Eq. (24), and the Kamiltonian is known up to the second power in ϵ as

$$K(J) = K_0(J) + \epsilon^2 K_2(J) + \ldots = \omega_0 J + \epsilon^2 k_2 J^2 + \ldots \quad (28)$$

where both ω_0 and k_2 depend on the value of β. $S_2(J, \theta, t)$ may be found similarly from Eq. (25). Although the solutions are generally *not* periodic in the original (x, p_x) coordinates for $\beta \neq 0$, the process of averaging in Eq. (22) yields periodic motion in the transformed coordinates whose perturbed frequency can be found from

$$\omega(J) = \frac{\partial K}{\partial J} = \omega_0 + 2\epsilon^2 k_2 J + \ldots. \quad (29)$$

The equations of motion are

$$\dot{\phi} = \frac{\partial K}{\partial J} = \omega(J), \quad \dot{J} = -\frac{\partial K}{\partial \phi} = 0 \quad (30)$$

which have the solutions

$$\phi(t) = \omega(J)t + \phi_0, \quad J(t) = J_0 \quad (31)$$

where ϕ_0 and J_0 are arbitrary constants of integration. It can be seen that J (or any function of J) is an invariant of the motion. To express J and ϕ in terms of the original variables x, p_x, and t, Eq. (19) must be inverted to get the new variables in terms of the old ones as

$$J = I - \epsilon \frac{\partial S_1}{\partial \theta}(I, \theta, t) + \epsilon^2\left(\frac{\partial^2 S_1}{\partial \theta \partial J}(I, \theta, t)\frac{\partial S_1}{\partial \theta}(I, \theta, t) - \frac{\partial S_2}{\partial \theta}(I, \theta, t)\right) + \ldots$$

$$\phi = \theta + \epsilon \frac{\partial S_1}{\partial J}(I, \theta, t) + \epsilon^2\left(-\frac{\partial^2 S_1}{\partial J^2}(I, \theta, t)\frac{\partial S_1}{\partial \theta}(I, \theta, t) + \frac{\partial S_2}{\partial J}(I, \theta, t)\right) + \ldots \quad (32)$$

where expansion in Taylor's series has been used, and the inverse transformations of Eqs. (16), (10), and (8) are utilized. For a given initial condition (x^0, p_x^0) in original coordinates at time $t = 0$, these are used to find the values of J_0 and ϕ_0. The solution in the original variables may then be found by again inverting Eq. (19) to get the old variables in terms of the new ones as

$$I = J + \epsilon \frac{\partial S_1}{\partial \theta}(J, \phi, t) + \epsilon^2\left(-\frac{\partial^2 S_1}{\partial \theta^2}(J, \phi, t)\frac{\partial S_1}{\partial J}(J, \phi, t) + \frac{\partial S_2}{\partial \theta}(J, \phi, t)\right) + \ldots$$

$$\theta = \phi - \epsilon \frac{\partial S_1}{\partial J}(J, \phi, t) + \epsilon^2\left(\frac{\partial^2 S_1}{\partial J \partial \theta}(J, \phi, t)\frac{\partial S_1}{\partial J}(J, \phi, t) - \frac{\partial S_2}{\partial J}(J, \phi, t)\right) + \ldots \quad (33)$$

while the transformations of Eqs. (16), (10), and (8) are utilized directly in the back substitution. Disentangling the old and new variables in Eq. (19) becomes algebraically tedious for higher-order expansions, while the procedure for calculating higher-order Kamiltonians (and therefore the perturbed frequencies) is relatively straightforward (Lichtenberg and Lieberman, 1983).

It is also desired to find the approximate average amplitude A in the original coordinates which can be physically measured. Since $I = J$ to order $O(\epsilon^0)$, the amplitude is

$$A = \sqrt{2J} \quad (34)$$

in (q, p) coordinates. It was found that Eq. (34) also gives a reasonable amplitude in (x, p_x) coordinates for most values of β. When $\beta = 0$, then $\omega_0 = 1$, $\mathbf{L}(t) = \mathbf{Q}(t) = \mathbf{M} = \mathbf{I}_2$, $H(I, \theta) = I + \epsilon(2I)^{3/2} \sin^3\theta$, and Eq. (32) may be utilized to get $S_1(J, \theta) = (2I)^{3/2}(\cos\theta - (\frac{1}{3})\cos^3\theta)$. Then $K_2(J)$ is found to be $-12 < \sin^6\theta > J^2$, $k_2 = -15/4$ in Eq. (28), and the perturbed frequency is $\omega(J) = 1.0 - 7.5\epsilon^2 J + \ldots$, indicating the well-known frequency reduction with energy/amplitude in the autonomous problem. The numerical value of J or A is determined from the initial conditions, which in this case are $(x, p_x) = (1, 0)$, and the value of ϵ, which was set as $\epsilon = 0.01$. For $\beta = 0$ this yields to order of ϵ^2, $J = 0.5 + \epsilon + 0.9375\,\epsilon^2 = 0.510094$ and $\omega = 0.999617$, $A = 1.01004$ from Eqs. (29) and (34). For small values of the parameter β, $\mathbf{L}(t) = \mathbf{Q}(t) \approx \mathbf{I}_2$ with small periodic deviations and the motion in original coordinates is *almost* periodic. Although the motion appears more erratic as β becomes large, the proposed formulation still yields accurate solutions since the exact L-F transformation matrix (and its inverse) are utilized in obtaining the solutions. As will be seen in Section 3, when the excitation strength approaches the value for period-doubling destabilization at $\beta = 16.23$, a maximum amplitude results which significantly exceeds the value computed from Eq. (34).

As an example, the case of $\beta = 1$ is considered where all computations were performed using MATHEMATICA. Since the multipliers ($\mu_{1,2} = 0.53437 \pm 0.84525i$) are in the right half-plane, the L-F transformation matrices $\mathbf{L}(t) = \mathbf{Q}(t)$ are

Downloaded 04 May 2010 to 171.66.16.26. Redistribution subject to ASME license or copyright; see http://www.asme.org/terms/Terms_Use.cfm

identical and 1-periodic while the constant $\mathbf{C} = \mathbf{R}$ and $\mathbf{M}$ matrices were computed as

$$\mathbf{C} = \mathbf{R} = \begin{bmatrix} -0.177503 & 1.00104 \\ -1.04453 & 0.177503 \end{bmatrix};$$

$$\mathbf{M} = \begin{bmatrix} 0.981887 & 0.173071 \\ 0.0 & 1.01845 \end{bmatrix}. \quad (35)$$

It should be observed that tr $(\mathbf{C}) = 0$, det $(\mathbf{L}(t)) = 1 + O(10^{-9})$, and det $(\mathbf{M}) = 1$ implies that $\mathbf{C}$ is Hamiltonian while $\mathbf{L}(t)$ and $\mathbf{M}$ are symplectic. The eigenvalues (characteristic exponents) of $\mathbf{C}$ are $\pm 1.00703 * i$ and the transformed Hamiltonian in action-angle variables is given by Eq. (17) where $\omega_0 = 1.00703$ is the linear frequency. It should be noted that only a few terms in the Fourier series of $\mathbf{L}(t)$, $\mathbf{L}^{-1}(t)$, and the 1-periodic coefficients $h_{1-4}(t)$ (not shown) were required for an accuracy of 10^{-6}. Application of Eqs. (18) – (28) then yielded the $O(\epsilon^2)$ Kamiltonian

$$K(J) = 1.00703J - 4.30366\epsilon^2 J^2 \quad (36)$$

For the initial conditions $(x^0, p_x^0) = (1, 0)$ at $t = 0$ and $\epsilon = .01$, the integration constants were found to be $\phi_0 = 1.56170$ and $J_0 = 0.528913$ while the perturbed frequency is $\omega = 1.00658$. The solution given by Eq. (31) was then substituted back into the original coordinates where it is plotted in the (x, p_x) phase space as the thin solid line in Fig. 2. This phase plot is practically indistinguishable from that obtained from Eq. (3) by using an adaptive numerical integration routine. Finally, the average amplitude is $A = 1.02851$ from Eq. (34).

3 Comparison With Direct Perturbation

As discussed in Section 1, when β is small the internal excitation term is weak and can be grouped together with the perturbation as

$$H(x, p_x, t) = \tfrac{1}{2}(p_x^2 + x^2) + \epsilon(\gamma \sin(2\pi t)x^2 + x^3) \quad (37)$$

where the unperturbed $\bar{H}_0$ term is time-invariant and $\gamma = \beta/(2\epsilon)$ is assumed to have an order of unity. Action-angle variables can be directly applied in this case to yield

$$H(I, \theta, t) = \bar{H}_0(I) + \epsilon(\tilde{H}_0(I, \theta, t) + H_1(I, \theta))$$
$$= I + \epsilon(2\gamma I \sin^2\theta \sin 2\pi t + (2I)^{3/2} \sin^3\theta) \quad (38)$$

after which canonical perturbation yields the $O(\epsilon^2)$ Kamiltonian

$$K(J) = \left(1 + \frac{\beta^2}{16(\pi^2 - 1)}\right)J - \epsilon^2 \frac{15}{4} J^2 + \ldots \quad (39)$$

where the resonance condition is $l + m\pi = 0$. The perturbed frequency of periodic motion is

$$\omega = 1 + \frac{\beta^2}{16(\pi^2 - 1)} - \epsilon^2 \frac{15}{2} J + \ldots \quad (40)$$

which is equivalent to the expression in Eq. (29) when $\beta = 0$. With the initial conditions $(x, p_x) = (1, 0)$, the action invariant can be found to be

$$J = \frac{1}{2} + \epsilon + \epsilon^2 \frac{-15 + 90\pi^2 - 28\pi^2\beta^2 - 135\pi^4 + 40\pi^4\beta^2 + 60\pi^6}{16(\pi^2 - 1)^2(4\pi^2 - 1)} + \ldots \quad (41)$$

while the amplitude is again given by Eq. (34). With $\epsilon = 0.01$ and $\beta = 0$, the above equations yield $J = 0.5 + \epsilon + 0.9375\,\epsilon^2 = 0.510094$, $\omega = 0.999617$, and $A = 1.01004$, exactly the same results as in Section 2.

For $\beta = 1$, $J = 0.510101$, $\omega = 1.00666$, $A = 1.01005$, and the phase plot in (x, p_x) space is the thick solid ellipse in Fig. 2 superimposed on the true solution obtained via the L-F transformation in Section 2. It can be noticed that while Eq. (40) yields reasonable average frequencies for the perturbed problem, the action invariant and amplitude given by Eqs. (41) and (34) are generally too small where the error increases with β. This is shown graphically in Fig. 3 where the amplitudes calculated from the two formulations are plotted versus β up to the stability limit. For large β, the assumption of weak excitation in Eq. (37) is incorrect since it does not account for the true dynamics of the entire quadratic Hamiltonian. Consequently, the resulting solutions from this formulation are smoothed approximations with amplitudes that are smaller than the true values

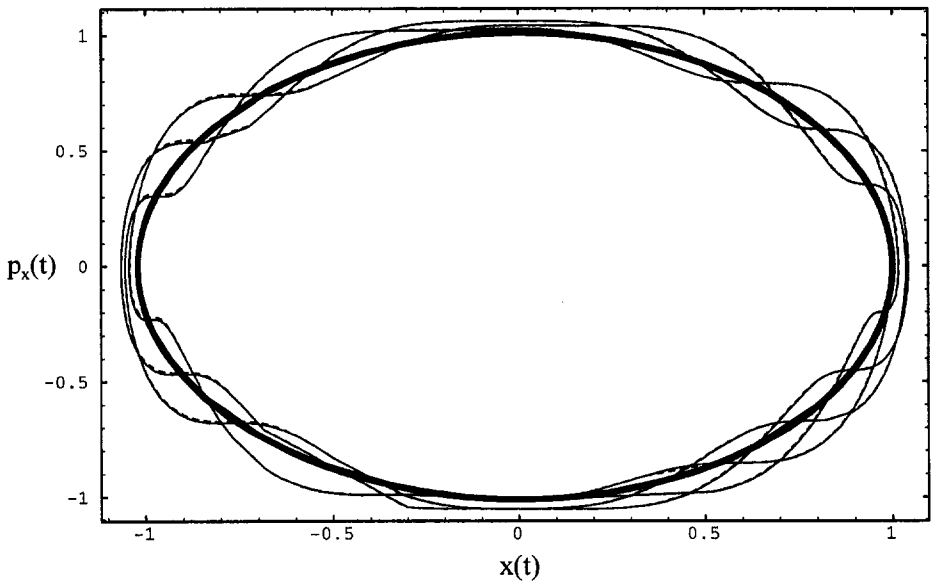

Fig. 2 Phase plots of the solution to Eq. (3) with $\beta = 1$ and $\epsilon = 0.01$ via the L-F transformation (thin solid), numerical integration (dashed), and direct perturbation (thick solid)

Downloaded 04 May 2010 to 171.66.16.26. Redistribution subject to ASME license or copyright; see http://www.asme.org/terms/Terms_Use.cfm

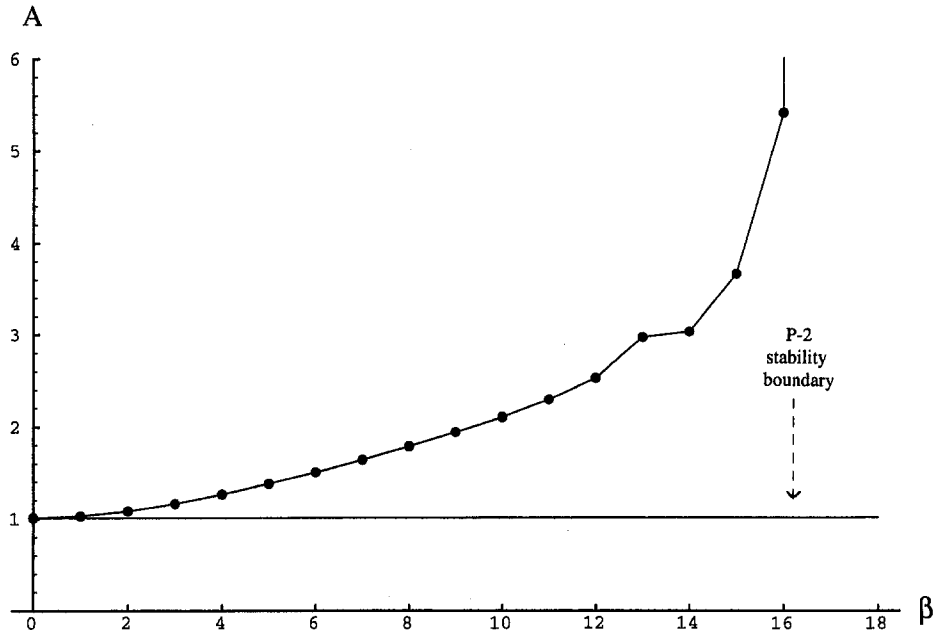

Fig. 3 Amplitudes versus β for the solution to Eq. (3) with $\epsilon = 0.01$ via the L-F transformation (with dots) and direct perturbation (which appears constant on this scale)

which are approximated much more accurately via the L-F transformation. This can easily be seen in Figs. 4 and 5 which contain phase plots in (x, p_x) space and x versus t time series plots, respectively, computed via the L-F and direct approaches for $\beta = 10$. The solutions obtained via the L-F transformation are again almost indistinguishable from that obtained by numerical integration. While the periodic motion of the direct perturbation approach represented by the thick solid ellipse in Fig. 4 has a frequency of 1.70427 close to the perturbed frequency in transformed coordinates ($\omega = 1.61954$, cf. Eq. (29)) computed using the 1-periodic $\mathbf{L}(t)$ matrix, the amplitude is clearly inaccurate as can be seen from Fig. 5. Again, the L-F transformation approach yields an accurate average amplitude of $A = 2.10228$. Since the multipliers ($\mu_{1,2} = -0.04941 \pm 0.99878i$) are now in the left half-plane, $\mathbf{L}(t) \neq \mathbf{Q}(t)$ and use of the 2-periodic L-F matrix results in the same solution and average amplitude but different perturbed frequency in the transformed coordinates ($\omega = -1.52205$, cf. Eq. (29)). The linear ($\epsilon = 0$) frequencies obtained from both L-F transformations are plotted versus β in Fig. 6 along with the linear frequency $1 + \beta^2/(16(\pi^2 - 1))$ of the direct approach which serves as an estimate for the magnitude of the characteristic exponent (eigenvalues of $\mathbf{C}$). For $\beta > 9.57$ (the period 4 solution point where $\omega_0 = \pi/2 = 1.5708$), the magnitude of the eigenvalues of $\mathbf{R}$ decrease to zero while the use of a real symplectic modal matrix in Eq. (10) forces ω_0 computed via the $\mathbf{Q}(t)$ matrix to be negative (indicated by the dashed line). Both the period 4 solution point (where $\mu_{1,2} = \pm i$) and the period-doubling destabilization boundary at $\beta = 16.23$ (where $\mu_{1,2} = -1$) can be seen in the stability diagram of Fig. 1.

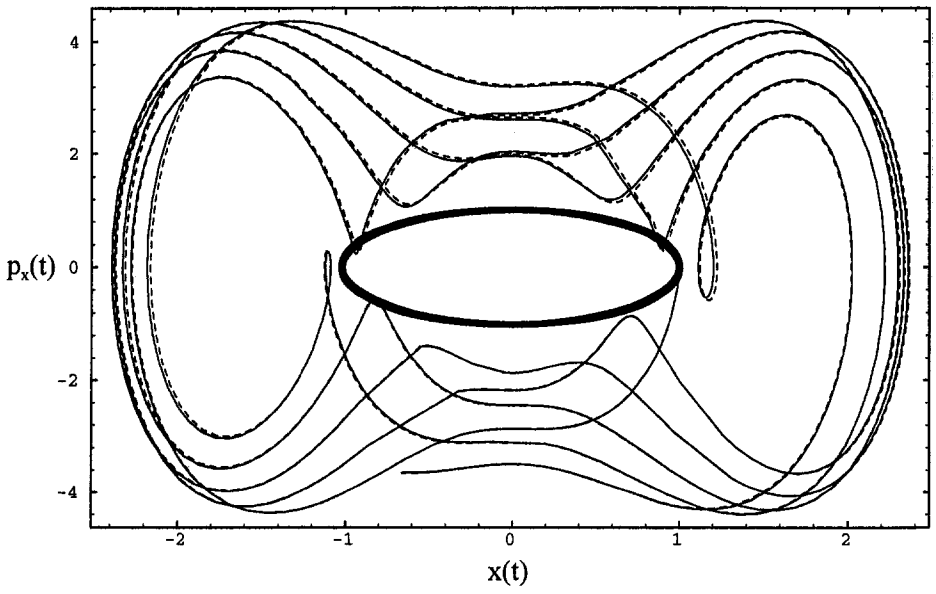

Fig. 4 Phase plots of the solution to Eq. (3) with $\beta = 10$ and $\epsilon = 0.01$ via the L-F transformation (thin solid), numerical integration (dashed), and direct perturbation (thick solid)

Downloaded 04 May 2010 to 171.66.16.26. Redistribution subject to ASME license or copyright; see http://www.asme.org/terms/Terms_Use.cfm

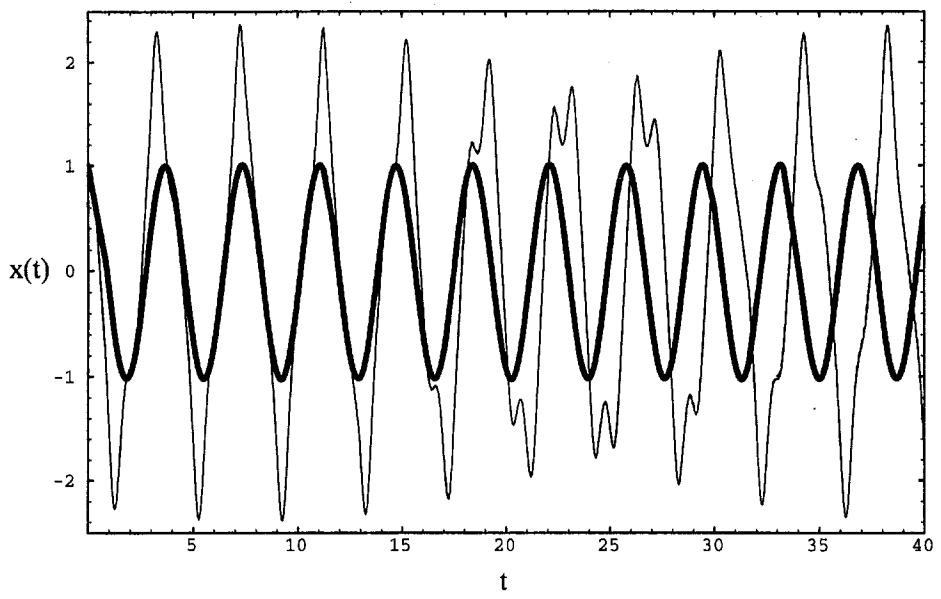

Fig. 5 Time series plots of the solution to Eq. (3) with $\beta = 10$ and $\epsilon = 0.01$ via the L-F transformation (thin solid), numerical integration (dashed), and direct perturbation (thick solid)

The solutions obtained in original coordinates in the $9.57 < \beta < 16.23$ region are mostly accurate compared to numerically integrated solutions where a significant error is apparent in solution plots only near the stability boundary. For example, when $\beta = 16$ the multipliers are $\mu_{1,2} = -0.95649 \pm 0.29175i$ and the linear and perturbed frequencies from the 1-periodic L-F transformation are $\omega_0 = 2.84554$ and $\omega = 2.79769$, respectively, while those obtained via the 2-periodic L-F transformation are $\omega_0 = -0.29605$ and $\omega = -0.34390$, respectively. The corresponding time series solution plotted in Fig. 7 consists of nearly $2\pi/2.79769 \approx 2.25$-periodic oscillations with amplitudes modulated by envelopes of approximate period $2\pi/0.34390 \approx 18.27$. The largest discrepancies with the numerically integrated solution occur near the nodes of the envelope while the solutions at maximum amplitude are relatively accurate. In this case it is seen that the perturbed frequencies computed via both L-F matrices are easily recognized in the resulting dynamics and that any perturbation procedure which results in a reasonably accurate solution must include the L-F transformation as a necessary step. Past the destabilization limit of $\beta = 16.23$ the eigenvalues of $\mathbf{C}$ and $\mathbf{R}$ split symmetrically along the $i\pi$ line and the real axis, respectively, of the complex plane and both L-F transformation approaches correctly yield an unstable solution. The direct approach, however, continues to yield stable periodic solutions (with continually increasing frequencies as shown in Fig. 6) which are clearly incorrect.

Finally, we consider another nonlinear time-periodic Hamiltonian given by

$$H(x, p_x, t) = \tfrac{1}{2}\alpha \sin(2\pi t)(p_x^2 - x^2) + \beta \cos(2\pi t) x p_x + \epsilon x^3 \quad (42)$$

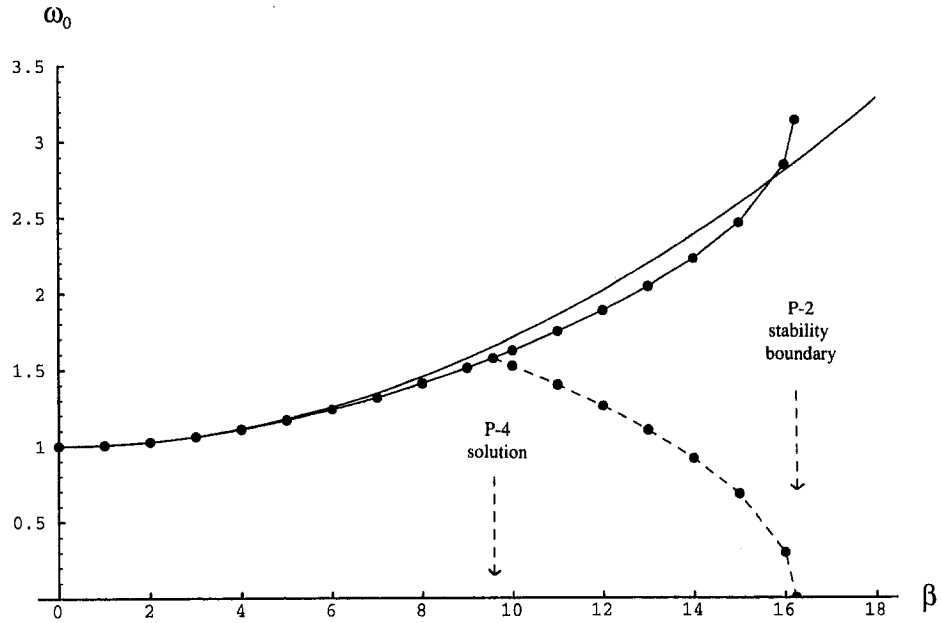

Fig. 6 Linear ($\epsilon = 0$) frequency magnitudes versus β for the solution to Eq. (3) via the 1-periodic L-F transformation (solid with dots), 2-periodic L-F transformation (dashed with dots), and direct perturbation (solid without dots)

Downloaded 04 May 2010 to 171.66.16.26. Redistribution subject to ASME license or copyright; see http://www.asme.org/terms/Terms_Use.cfm

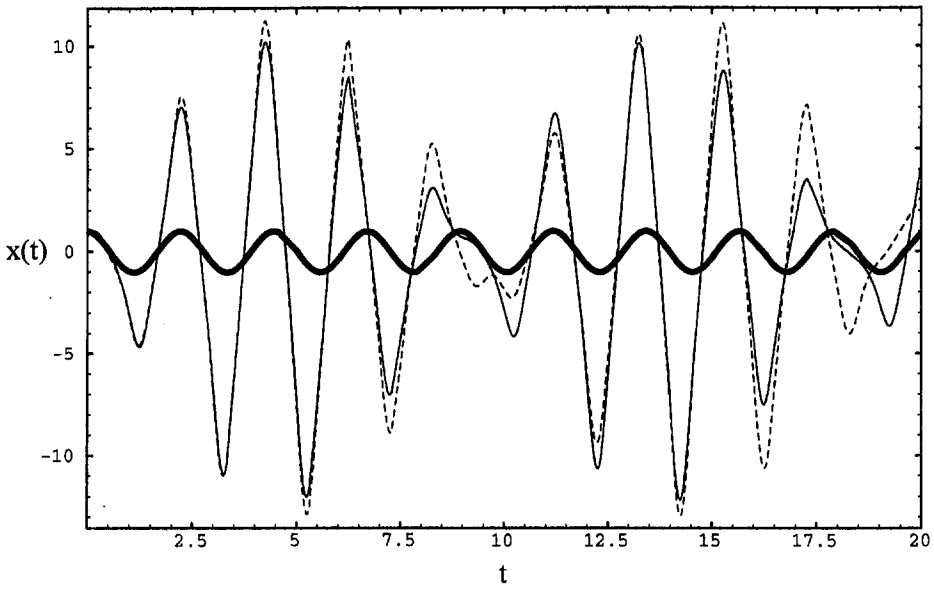

Fig. 7 Time series plots of the solution to Eq. (3) with $\beta = 16$ and $\epsilon = 0.01$ via the L-F transformation (thin solid), numerical integration (dashed), and direct perturbation (thick solid)

in which $\bar{H}_0 = 0$. It should be noted that no classical perturbation procedure can be directly applied in this case regardless of the values of α and β since no constant generating solution exists to start the perturbation. However, the solutions for the quadratic part of Eq. (44) are Liapunov stable for certain values of the two periodic parameters such that the L-F transformation approach may still be used to compute accurate solutions to the perturbed problem. When this is carried out for $\alpha = 1$, $\beta = 3$, and $\epsilon = 0.01$, the multipliers ($\mu_{1,2} = 0.85386 \pm 0.52048i$) are in the right half-plane so that the two L-F transformations are identical. The linear and perturbed frequencies are thus found to be $\omega_0 = -0.547419$ and $\omega = -0.54496$ while the action invariant is $J = 0.510405$. The corresponding time series plot in Fig. 8 is almost identical with the numerically integrated result and consists of oscillations of approximate period 1 (the period of the L-F matrix) with mean values modulated by oscillations of period $2\pi/|\omega| \approx 11.53$ and amplitude $A = (2J)^{1/2} = 1.01035$. It is obvious that application of the L-F transformation is absolutely necessary in this case when using time-dependent canonical perturbation theory or any other similar procedure.

4 Conclusions

A method for the application of time-dependent canonical perturbation theory to a fast nonlinear time-periodic Hamiltonian with strong internal excitation has been suggested. The example of a Mathieu-Hill Hamiltonian with a cubic perturbation has been used to show that, if the time-periodic unperturbed part is quadratic, the Hamiltonian may be canonically transformed to an equivalent form in which the new unperturbed quadratic part is time-invariant. This is achieved through an application of the Liapunov-Floquet (L-F) transformation associated with the system. The unperturbed linear frequency in the

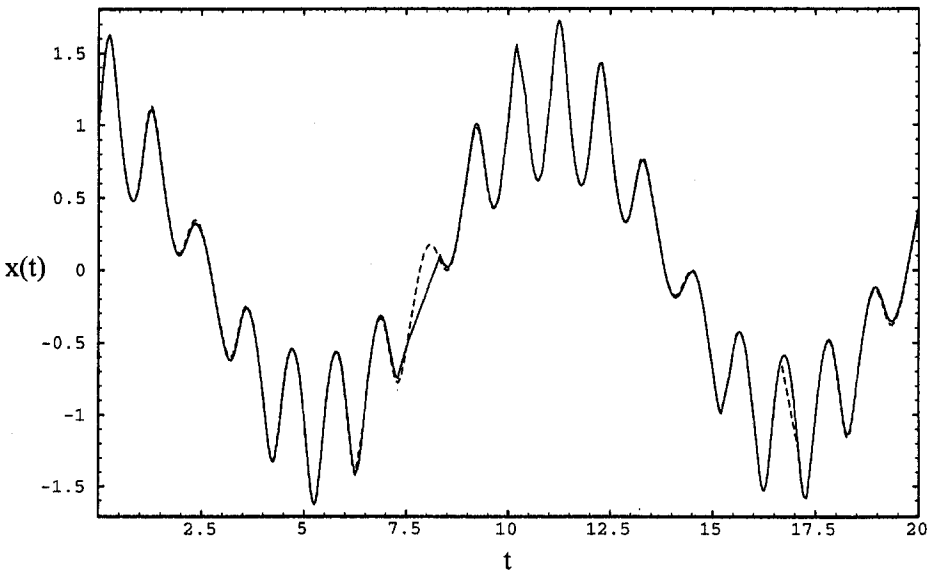

Fig. 8 Time series plots of the solution to the equations of motion for the Hamiltonian of Eq. (42) with $\alpha = 1$, $\beta = 3$, and $\epsilon = 0.01$ via the L-F transformation (solid) and numerical integration (dashed). Direct perturbation cannot be applied in this case.

Downloaded 04 May 2010 to 171.66.16.26. Redistribution subject to ASME license or copyright; see http://www.asme.org/terms/Terms_Use.cfm

transformed coordinates is the real number associated with one of the imaginary eigenvalues of the resulting constant linear matrix and is negative in some instances depending on the type of L-F transformation employed. Time-dependent canonical perturbation theory was then successfully applied to find the solution in the original coordinates where all computations were performed using MATHEMATICA. It was shown that these solutions were generally very accurate compared to numerically integrated results, while perturbation solutions obtained directly using the assumption of weak excitation were smoothed approximations with reasonable frequencies but inaccurate amplitudes. As expected, the error increased with an increase in the strength of internal excitation. Significant errors in the solutions computed via the proposed method were apparent only with the excitation strength close to the destabilization boundary while the physical meaning of the L-F transformation in the resulting dynamics at this location was obvious. This was also the case with a nonlinear time-periodic Hamiltonian with no constant quadratic part where use of the L-F transformation was absolutely essential since the lack of a generating solution prohibited the direct application of any perturbation procedure. With the excitation strength greater than the stability limit in the Mathieu-Hill Hamiltonian, only the L-F transformation correctly yielded an unstable solution. While the time-dependent perturbation method used here involved classical mixed-variable generating functions, it should be noted that the same results could also be obtained by using the L-F transformation in conjunction with time-dependent Lie transforms (Deprit, 1969) in which the canonical near-identity transformation (cf., Eq. (19)) expresses both old variables in terms of the new such that the complicated inversions of Eqs. (32) and (33) are avoided. Finally it must be pointed out that, while the examples presented here utilized constant nonlinear monomial perturbations, the proposed formulation works the same when the perturbation term in a quasi-linear system such as

$$H(x, p_x, t) = \frac{p_x^2}{2} + (1 + \beta \sin(2\pi t))\left(\frac{x^2}{2} - \epsilon x^4\right); \qquad \epsilon = \frac{1}{24} \quad (43)$$

also possesses time-periodic coefficients as is typically the case in real problems after expanding a nonlinear function such as $\cos(x)$ in a truncated Taylor series about a periodic solution.

Acknowledgments

Financial support for this work was provided by the Army Research Office, monitored by Dr. Gary L. Anderson under contract numbers DAAL03-92G-0364 and DAAH04-94G-0337.

References

Butcher, E. A., and Sinha, S. C., 1995, "On the Analysis of Time-periodic Nonlinear Hamiltonian Dynamical Systems," *Vibration of Nonlinear, Random, and Time-Varying Systems,* S. C. Sinha et al., eds., Proceedings of the Fifteenth ASME Biennial Conference on Mechanical Vibration and Noise, Sept. 17–21, Boston, MA, pp. 375–386.

Deprit, A., 1969, "Canonical Transformations Depending on a Parameter," *Celestial Mechanics,* Vol. 1, pp. 1–31.

Goldstein, H., 1980, *Classical Mechanics,* Addison-Wesley, Reading, MA.

Hyams, M. R., and Month, L. A., 1984, "The Origin of Stability Indeterminacy in a Symmetric Hamiltonian," ASME JOURNAL OF APPLIED MECHANICS, Vol. 51, pp. 399–405.

Khazin, L. G., and Shnol, E. E., 1985, *Stability of Critical Equilibrium States,* Manchester University Press, Manchester, U.K. (translated from Russian, 1991).

Lichtenberg, A. J., and Lieberman, M. A., 1992, *Regular and Chaotic Dynamics,* Springer-Verlag, New York.

Lo, C. F., 1991, "Perturbative Treatment of a General Driven Time-dependent Oscillator in a Time-dependent Basis," *American Journal of Physics,* Vol. 59, No. 3, pp. 254–258.

Month, L. A., and Rand, R. H., 1980, "An Application of the Poincaré Map to the Stability of Nonlinear Normal Modes," ASME JOURNAL OF APPLIED MECHANICS, Vol. 47, pp. 645–651.

Pandiyan, R., and Sinha, S. C., 1995, "Analysis of Time-periodic Nonlinear Dynamical Systems Undergoing Bifurcations," *Nonlinear Dynamics,* Vol. 8, pp. 21–43.

Rand, R. H., 1994, *Topics in Nonlinear Dynamics with Computer Algebra* (Computation in Education: Mathematics, Science, and Engineering, Vol. 1), Gordon and Breach, Langhorne, PA.

Sinha, S. C., and Joseph, P., 1994, "Control of General Dynamic Systems with Periodically Varying Parameters via Liapunov-Floquet Transformation," ASME *Journal of Dynamic Systems, Measurement, and Control,* Vol. 116, pp. 650–658.

Sinha, S. C., and Pandiyan, R., 1994, "Analysis of Quasilinear Dynamical Systems with Periodic Coefficients via Liapunov-Floquet Transformation," *International Journal of Non-Linear Mechanics,* Vol. 29, pp. 687–702.

Tabor, M., 1989, *Chaos and Integrability in Nonlinear Dynamics,* John Wiley and Sons, New York.

Yakubovich, V. A., and Starzhinskii, V. M., 1975, *Linear Differential Equations with Periodic Coefficients,* Parts I and II, John Wiley and Sons, New York.

Downloaded 04 May 2010 to 171.66.16.26. Redistribution subject to ASME license or copyright; see http://www.asme.org/terms/Terms_Use.cfm

Paradoxes in Rigid-Body Kinematics of Structures

L. Mentrasti
Senior Researcher,
Istituto di Scienza e Tecnica
delle Costruzioni,
Facoltà di Ingegneria,
Università di Ancona,
Via delle Brecce Bianche,
60131 Ancona, Italia
E-mail: mentrasti@popsci.unian.it

The paper discusses two paradoxes appearing in the kinematic analysis of interconnected rigid bodies: there are structures that formally satisfy the classical First and Second Theorem on kinematic chains, but do not have any motion. This can arise when some centers of instantaneous rotation (CIR) relevant to two bodies coincide with each other (first kind paradox) or when the CIRs relevant to three bodies lie on a straight line (second kind paradox). In these cases two sets of new theorems on the CIRs can be applied, pointing out sufficient conditions for the nonexistence of a rigid-body motion. The question is clarified by applying the presented theory to several examples.

Introduction

A primary problem of structural kinematics is to establish whether virtual rigid-body motion exists for a structure $\mathcal{S}$, near a prescribed configuration with fixed constraints (homogeneous problem). To answer this question several approaches can be devised.

The general method used in analytic mechanics (finite displacement with nonlinear constraint equations) leads to algebraic systems that are almost intractable even for few bodies (cf. Kuznetsov, 1988; Roberson and Schwertassek, 1988). Recently a number of paper discussed the possibility of obtaining information about the rigid-body motion of $\mathcal{S}$ by applying the methods of the general theory of elastic stability (cf. Salerno, 1992 and quoted references). On the other hand the (linear) small displacement kinematics formulation gives a first-order solution of the problem when the number of bodies is very large (Pellegrino et al., 1986; Pellegrino et al., 1992; Johnson, 1992).

Notwithstanding the theoretical value of the aforementioned general methods, it is beyond doubt that an analytical formulation scarcely suggests the mechanical behavior of the structure. Many engineering textbooks, dealing with *two-dimensional* structural mechanics, therefore suggest using a heuristic approach called the *kinematic chain method* (Skalmierski, Chapter 2, Timoshenko, Chapter 3): this rests on the fact that the absolute and relative centers of instantaneous rotation (hereinafter referred to as CIR for the sake of brevity) lie on straight lines during a motion (the next paragraph gives a precise statement of the first and second theorem).

In short, this graphic method makes it necessary to accomplish the following conditions: (i) locate the absolute and relative CIRs of each body as dictated by the actual active constraints; (ii) verify the above-mentioned theorems.

Once all the centers of rotation are determined, two alternatives can take place:

1 Any one of the theorems *is not verified;* this occurrence is of course a sufficient condition so that the structure *does not have* a rigid-body motion.

2 Proper applications of the first theorem (to every pair of bodies) and of the second theorem (to every triple of bodies) *are verified.*

This paper discusses the conclusions that can be reached in this last case.

In several applications an *incorrect* proposition was often tacitly used that read as follows: a *sufficient* condition for a structure to undergo a rigid motion is that all the *proper applications of the first and second theorems are satisfied* (see, e.g., the above-mentioned applications by Timoshenko about drawing influence lines, or by Skalmierski on determining velocities and accelerations in plane mechanisms).

The inconsistency of this approach will be proved in the following with reference to the cases in which two CIRs coincide or the CIRs relevant to three bodies lie on a straight line; new theorems will also be given, refining the classical results on kinematic chains.

First Kind Paradox. In order to prove the above statement by a counterexample, consider the structure depicted in Fig. 1, the kinematic analysis of which must be carried out in detail:

1 If Ω_1 exists, it is at point A, where a hinge constraint appears.

2 $\Omega_{2,1}$ is at C and $\Omega_{1,3}$ at D, if they exist, for the same reason.

3 By applying the first theorem to Ω_1, $\Omega_{2,1}$, and Ω_2, and taking into account that Ω_2 must belong to the vertical line passing through B, Ω_2 is the improper point in the vertical direction, if it exists (in Fig. 2 the symbol $\uparrow\infty$ denotes an improper point, the arrow indicating its direction).

4 Similarly, Ω_3 is the improper point in the vertical direction, if it exists.

5 An application of the second theorem to $\Omega_{2,1}$, $\Omega_{3,2}$, and $\Omega_{1,3}$, and considering the simple constraint at G, makes it possible to locate $\Omega_{3,2}$ at F, if it exists.

All the theorems are so satisfied, all the CIRs are uniquely located, but the motion is nil for every body, as can easily be verified.

Note that $\Omega_2 \equiv \Omega_3$ because these CIRs are the same (improper) point. The paradox is explained by the Theorem I.2 stating that $\Omega_{2,3}$ does not actually exist, that is $\mathcal{B}_2$ and $\mathcal{B}_3$ behave as a unique rigid body.

Second Kind Paradox. The structure sketched in Fig. 2 has a similar apparently strange behavior: a kinematic analysis, not reported here for the sake of conciseness, seems to state that all the *distinct* CIRs belong to the line *ABCDE* (the bodies $\mathcal{B}_1$, $\mathcal{B}_2$, and $\mathcal{B}_3$ are represented by the vertical segment at B, C, and D, respectively, while the inclined struts are devised as simple constraints). However, as in the previous case, it is easy to verify that the motion does not exist.

The aim of this paper is to explain these findings by proving two sets of sufficient conditions for the nonexistence of a rigid-

Contributed by the Applied Mechanics Division of THE AMERICAN SOCIETY OF MECHANICAL ENGINEERS for publication in the ASME JOURNAL OF APPLIED MECHANICS.

Discussion on this paper should be addressed to the Technical Editor, Professor Lewis T. Wheeler, Department of Mechanical Engineering, University of Houston, Houston, TX 77204-4792, and will be accepted until four months after final publication of the paper itself in the ASME JOURNAL OF APPLIED MECHANICS.

Manuscript received by the ASME Applied Mechanics Division, Dec. 17, 1996; final revision, July 12, 1997. Associate Technical Editor: J. N. Reddy.

 Copyright © 1998 by ASME

Downloaded 04 May 2010 to 171.66.16.26. Redistribution subject to ASME license or copyright; see http://www.asme.org/terms/Terms_Use.cfm

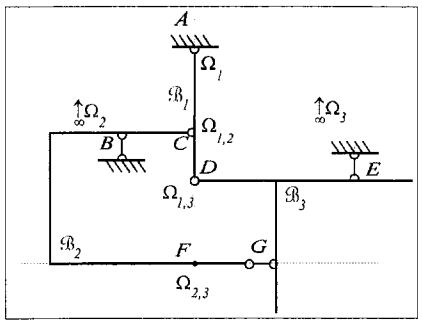

Fig. 1 The centers of instantaneous rotation are properly aligned according to the classical first and second theorems; nevertheless no motion exists because $\Omega_2 \equiv \Omega_3$ (at the vertical improper point $\uparrow\infty$), as explained by Theorem I.2

body motion: the first can be applied when *any pair* of the CIRs *coincides* (as in the first kind paradox); the second, when *all* the centers relevant to *three bodies* lay on the same straight line (second kind paradox).

Plane Motion Results

Let P be a *material point* whose placement is the vector $\mathbf{x}_P \in \mathcal{V}$, $\mathcal{V}$ being the vector space associated to a fixed frame of reference $\mathcal{F}_o$ in the euclidean affine space $\mathcal{E}$.

A *rigid-body* $\mathcal{B}$ is a set of material points P whose *placements* constitute a closed subset $\boldsymbol{B}(t) := \{\mathbf{x}_P(t), P \in \mathcal{B}\} \subset \mathcal{E}$, such that $\|\mathbf{x}_{Pi}(t) - \mathbf{x}_{Pj}(t)\| =$ constant, $t \in \mathcal{R}$ being a parameter (time).

In this paper a *structure* $\mathcal{S}$, $\mathcal{S} := \cup_i \mathcal{B}_i$ with $\mathcal{B}_i \cap \mathcal{B}_j = \varnothing$, $i \neq j$, is a system of *interconnected* rigid bodies: the placements $\boldsymbol{B}_i(t)$ and $\boldsymbol{B}_j(t)$ are not independent of one another, owing to the presence of absolute or relative (scleronomous) *constraints* restricting the motion of some point of the bodies of $\mathcal{S}$.

An *instantaneous (virtual) rigid-body motion* of $\mathcal{S}$ is the field of the velocity bound vectors $\boldsymbol{V}_S(t) := \{\mathbf{v}_P \in \mathcal{V}, P \in \mathcal{S}\}$ (associated to which, the infinitesimal displacement $d\mathbf{x}_P := \mathbf{v}_P dt$ can also be considered) such that:

$$\text{(i)} \quad \mathbf{v}_P = \mathbf{v}_{P_{oi}} + \boldsymbol{\omega}_i \times (\mathbf{x}_P - \mathbf{x}_{P_{oi}}), \quad \forall P \in \mathcal{B}_i \qquad (1)$$

where P_{oi} is an arbitrary (fixed) point of the body $\mathcal{B}_i$ and $\boldsymbol{\omega}_i$ is its angular velocity; and

(ii) the *relative* and *absolute* constraints are satisfied.

When the *motion is plane*, e.g., $\mathbf{v}_P \cdot \mathbf{e}_3 = 0$, $\forall P \in \mathcal{S}$, the problem can be regarded as being two-dimensional and, as a result of a fundamental theorem, each body only rotates about its absolute CIR Ω_i; strictly speaking, it is an improper point of the plane, Ω_i^∞, when $\mathcal{B}_i$ actually translates.

Relative Kinematics Results. Consider an *actual* motion of the structure: the field $\boldsymbol{V}_j$, relevant to the body $\mathcal{B}_j$, can be written as follows:

$$\mathbf{v}_P = \mathbf{v}_{A_j} + (\boldsymbol{\omega}_i + \boldsymbol{\omega}_{j,i}) \times (\mathbf{x}_P - \mathbf{x}_{A_j}), \quad \forall P \in \mathcal{B}_j \qquad (2)$$

in which $\mathbf{v}_{A_j}$ is the absolute velocity of an arbitrary point A_j rigidly linked to $\mathcal{B}_j$, and $\omega_{j,i}$ is the *relative* angular velocity of $\mathcal{B}_j$ with respect to $\mathcal{B}_i$ (namely, the angular velocity of the body $\mathcal{B}_j$ when it is observed in a frame of reference $\mathcal{F}_i$ fixed to the body $\mathcal{B}_i$).

When the motion is plane, Eq. (2) can be rearranged considering that $\mathcal{B}_i$ rotates about Ω_i and $\mathcal{B}_j$ rotates with respect to $\mathcal{B}_i$ about their *relative* CIR $\Omega_{j,i}$. By choosing $A_j \equiv \Omega_{j,i}$ then $\mathbf{v}_{\Omega_{j,i}} = \boldsymbol{\omega}_i \times (\mathbf{x}_{\Omega_{j,i}} - \mathbf{x}_{\Omega_i})$ and the velocity field can be written as

$$\mathbf{v}_P = \boldsymbol{\omega}_i \times (\mathbf{x}_P - \mathbf{x}_{\Omega_i}) + \boldsymbol{\omega}_{j,i} \times (\mathbf{x}_P - \mathbf{x}_{\Omega_{j,i}}), \quad \forall P \in \mathcal{B}_j; \qquad (3)$$

consequently the absolute CIR of $\mathcal{B}_j$ can be located by looking for a point Ω_j such that $\mathbf{v}_{\Omega_j} = \mathbf{0}$,

$$\mathbf{0} = \boldsymbol{\omega}_i \times (\mathbf{x}_{\Omega_j} - \mathbf{x}_{\Omega_i}) + \boldsymbol{\omega}_{j,i} \times (\mathbf{x}_{\Omega_j} - \mathbf{x}_{\Omega_{j,i}}). \qquad (4)$$

By taking the scalar product of this relationship with $(\mathbf{x}_{\Omega_j} - \mathbf{x}_{\Omega_{j,i}})$ and $(\mathbf{x}_{\Omega_{j,i}} - \mathbf{x}_{\Omega_i})$,

$$\boldsymbol{\omega}_{j,i} \cdot (\mathbf{x}_{\Omega_j} - \mathbf{x}_{\Omega_{j,i}}) \times (\mathbf{x}_{\Omega_j} - \mathbf{x}_{\Omega_i}) = 0, \qquad (5)$$

$$\boldsymbol{\omega}_i \cdot (\mathbf{x}_{\Omega_j} - \mathbf{x}_{\Omega_i}) \times (\mathbf{x}_{\Omega_j} - \mathbf{x}_{\Omega_{j,i}}) = 0, \qquad (6)$$

results, respectively.

Therefore, if $\|\boldsymbol{\omega}_i\| + \|\boldsymbol{\omega}_{j,i}\|$ is different to zero then Ω_i, $\Omega_{j,i}$, and Ω_j lie on a straight line; on the other hand, when the instantaneous motion of these rigid bodies is nil, $\boldsymbol{\omega}_i = \boldsymbol{\omega}_{j,i} = \mathbf{0}$, then the location of Ω_i, $\Omega_{j,i}$, and Ω_j is immaterial and they can therefore be chosen to be aligned again. This proves the following.

First Theorem: *During the rigid-body plane motion of a structure $\mathcal{S}$, the absolute (Ω_i, Ω_j) and relative $(\Omega_{j,i})$ CIRs of two bodies $\mathcal{B}_i, \mathcal{B}_j \subset \mathcal{S}$ lie on a straight line.*

According to the remark 3 below and using the principle of galilean relativity, by substituting the frame of reference $\mathcal{F}_o$ with $\mathcal{F}_k$, from Eq. (4)

$$\mathbf{0} = \boldsymbol{\omega}_{i,k} \times (\mathbf{x}_{\Omega_{j,k}} - \mathbf{x}_{\Omega_{i,k}}) + \boldsymbol{\omega}_{j,i} \times (\mathbf{x}_{\Omega_{j,k}} - \mathbf{x}_{\Omega_{j,i}}) \qquad (7)$$

results, and the following can immediately be obtained.

Second Theorem: *During the rigid-body plane motion of a structure $\mathcal{S}$, the relative CIRs $\Omega_{i,k}$, $\Omega_{j,i}$, and $\Omega_{j,k}$ of three bodies $\mathcal{B}_i, \mathcal{B}_j, \mathcal{B}_j \subset \mathcal{S}$, lay on a straight line.*

Remarks.

1 Some of the centers involved in the above theorems can, obviously, coincide; in this case the alignment is trivial.

2 The relative CIR $\Omega_{j,i}$ is a point of $\mathcal{B}_j$ that moves solidly with $\mathcal{B}_i$ and vice versa, so that $\Omega_{i,j} \equiv \Omega_{j,i}$; however, it is not the *only* point fulfilling this property when the relative motion is nil.

3 Since $\boldsymbol{\omega}_{j,i}$ is the angular velocity of the jth body when it is observed from $\mathcal{F}_i$, $\boldsymbol{\omega}_i$ can be regarded as the relative angular velocity of $\mathcal{B}_i$ when it is observed from $\mathcal{F}_o$; in particular, Eq. (1) is contained in Eq. (2) with $\boldsymbol{\omega}_i = \boldsymbol{\omega}_{i,o}$.

4 The first and second theorem also hold true when any one of the CIRs becomes an improper point, that is when the relevant absolute or relative motion is actually a translation; formal proof can easily be obtained by a limit procedure considering that $\|\mathbf{x} - \mathbf{x}_\Omega\| \to \infty$ and $\|\boldsymbol{\omega}\| \to 0$ in such a way that the typical velocity term $\boldsymbol{\omega} \times (\mathbf{x} - \mathbf{x}_\Omega)$ remains finite. The straight line containing the CIRs can eventually be improper (as happen when two distinct CIRs are improper).

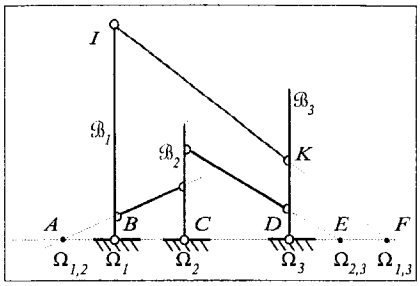

Fig. 2 All the centers of instantaneous rotation, relevant to the three vertical bodies (the inclined struts being regarded as simple constraints), are aligned on a straight line, but no motion exists

Downloaded 04 May 2010 to 171.66.16.26. Redistribution subject to ASME license or copyright; see http://www.asme.org/terms/Terms_Use.cfm

5 When the CIRs are determined, two relationships between the angular velocities are identically satisfied during the motion. Let $\mathbf{e}$ be an arbitrary unit vector of the plane, i.e., $\mathbf{e}\cdot\boldsymbol{\omega} = 0$, with $\boldsymbol{\omega} = \omega\mathbf{e}_3$; applying the identity

$$(\mathbf{e}_3 \times \mathbf{e})\cdot\boldsymbol{\omega} \times \mathbf{x} = [(\mathbf{e}_3 \times \mathbf{e}) \times \boldsymbol{\omega}]\cdot\mathbf{x} = [\mathbf{e}_3\cdot\boldsymbol{\omega}\,\mathbf{e}]\cdot\mathbf{x} = \omega\mathbf{e}\cdot\mathbf{x} \tag{8}$$

to Eq. (4) and (7) results in

$$\omega_i(\mathbf{x}_{\Omega_j} - \mathbf{x}_{\Omega_i})\cdot\mathbf{e} + \omega_{j,i}(\mathbf{x}_{\Omega_j} - \mathbf{x}_{\Omega_{j,i}})\cdot\mathbf{e} = 0, \tag{9}$$

$$\omega_{i,k}(\mathbf{x}_{\Omega_{j,k}} - \mathbf{x}_{\Omega_{i,k}})\cdot\mathbf{e} + \omega_{j,i}(\mathbf{x}_{\Omega_{j,k}} - \mathbf{x}_{\Omega_{j,i}})\cdot\mathbf{e} = 0. \tag{10}$$

A particular interesting case is given when $\mathbf{e}$ is chosen so that $\xi_\Omega := \mathbf{x}_\Omega\cdot\mathbf{e}$ is the abscissa of Ω on the line containing Ω_i, Ω_j, and $\Omega_{j,i}$. Considering that $\omega_{j,i} = \omega_j - \omega_i$, Eq. (9) can be finally be rewritten in the form

$$\omega_i(\xi_{\Omega_{j,i}} - \xi_{\Omega_i}) = \omega_j(\xi_{\Omega_{j,i}} - \xi_{\Omega_j}), \tag{11}$$

which has the following notable interpretation: the displacement of the point $\Omega_{j,i} \in \mathcal{B}_j$ must be equal to the displacement of the point $\Omega_{i,j} \in \mathcal{B}_i$.

Coinciding Centers of Instantaneous Rotation

This section presents the first group of theorems involving the *nonexistence* of some CIR when two or more of these points coincide with each other.

Basic Definitions. According to the considerations discussed in the previous paragraph, the first step must be the removal of the ambiguity about the location of a CIR (absolute or relative).

Definition 1. A point Ω_j, rigidly linked to the body $\mathcal{B}_j$, is an absolute CIR of $\boldsymbol{B}_i$ iff its (virtual) absolute velocity is nil.

Definition 1′. A point $\Omega_{j,i}$, rigidly linked to both the bodies $\mathcal{B}_j$ and $\mathcal{B}_i$, is a relative CIR of $\mathcal{B}_j$ with respect to $\mathcal{B}_i$ iff its (virtual) relative velocity, in the frame of reference $\mathcal{F}_i$, is nil.

Theorem 1. The CIR Ω_i exists iff it is the *only* point of $\mathcal{B}_i$ at rest.

Theorem 1′. The CIR $\Omega_{j,i}$ exists iff it is the *only* point of $\mathcal{B}_j$ that moves solidly with $\mathcal{B}_i$ (and vice versa).

Proof. The results follow from both definitions and remarks 2, 3 of the previous paragraph. □

Corollary 1. When the CIR Ω_i does not exist, the body $\mathcal{B}_i$ cannot be considered as belonging to the structure $\mathcal{S}$ because it is fixed to the frame of reference $\mathcal{F}_o$; consequently it *must be eliminated* from the kinematic analysis and its relevant relative constraints transformed in absolute constraints, accordingly.

Corollary 1′. When the CIR $\Omega_{j,i}$ does not exist, the body $\mathcal{B}_j$ cannot be considered as distinct from $\mathcal{B}_i$ because it is fixed to the frame of reference $\mathcal{F}_i$; consequently they *must be considered as a single body* $\{\boldsymbol{B}_i \cup \boldsymbol{B}_j\}$.

Coinciding CIRs in First Theorem.

Theorem I.1. If Ω_i coincides with $\Omega_{j,i}$, and $\Omega_{j,i}$ does not coincide with Ω_j, then Ω_j does not actually exist: $\Omega_i \equiv \Omega_{j,i} \not\equiv \Omega_j \Rightarrow \nexists\Omega_i$.

Theorem I.2. If Ω_i coincides with Ω_j, and Ω_j does not coincide with $\Omega_{j,i}$, then $\Omega_{j,i}$ does not actually exist: $\Omega_i \equiv \Omega_j \not\equiv \Omega_{j,i} \Rightarrow \nexists\Omega_{j,i}$.

Theorem I.3. If Ω_i coincides with $\Omega_{j,i}$, and $\Omega_{j,i}$ coincides with $\Omega_j(\Omega_i \equiv \Omega_{j,i} \equiv \Omega_j)$, then $\mathcal{B}_i$ and $\mathcal{B}_j$ must be considered as independent of one another (without relative constraints).

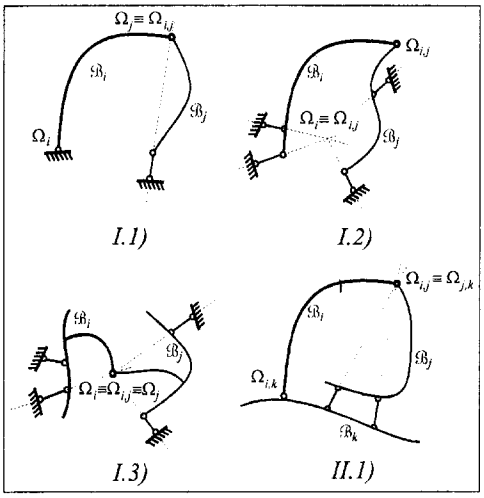

Fig. 3 Schemes of *coinciding* centers of instantaneous rotation: Theorems I.1, I.2, I.3, and II.1, respectively

Coinciding CIRs in Second Theorem.

Theorem II.1. If $\Omega_{i,k}$ coincides with $\Omega_{j,i}$ that does not coincide with $\Omega_{j,k}$, then $\Omega_{j,k}$ does not actually exist: $\Omega_{i,k} \equiv \Omega_{j,i} \not\equiv \Omega_{j,k} \Rightarrow \nexists\Omega_{j,k}$.

Theorem II.3. If $\Omega_{i,k}$ coincides with $\Omega_{j,i}$, and $\Omega_{j,i}$ coincides with $\Omega_{j,k}(\Omega_{i,k} \equiv \Omega_{j,i} \equiv \Omega_{j,k})$ then the relative motion of bodies $\mathcal{B}_i$ and $\mathcal{B}_j$ are actually dependent on two distinct parameters: $\mathcal{B}_i$ and $\mathcal{B}_j$ must be considered as independent of one another (without relative constraints).

Proof. Consider the points Ω_i, $\Omega_{j,i}$, and Ω_j as potential CIRs, in the following sense: by satisfying both the absolute and relative constraints and from possible previous applications of the first and second theorem involving bodies $\mathcal{B}_i$ and $\mathcal{B}_j$, the points Ω_i, $\Omega_{j,i}$ and Ω_j are the (absolute or relative) CIRs, *if they exist.*

Consider first the hypotheses of Theorem I.1. If $\Omega_i \equiv \Omega_{j,i} \not\equiv \Omega_j$ then body $\mathcal{B}_j$ has two distinct points at rest: Ω_j, because it is its absolute CIR; and $\Omega_{j,i}$, because it is the point of $\mathcal{B}_j$ that moves solidly with the point Ω_i of $\mathcal{B}_j$ (see remark 2), which is a point at rest by definition. As a result the whole body is at rest and $\nexists\Omega_i$; so Theorem I.1 is proved.

Regarding to Theorem I.3, note that when $\Omega_i \equiv \Omega_{j,i} \equiv \Omega_j$ then $\mathcal{B}_i$ and $\mathcal{B}_j$ are not subjected to any actual restriction on the relative motion about this point: consequently the mechanical constraints between them must be ignored (the motions of bodies $\mathcal{B}_i$ and $\mathcal{B}_j$ *can* depend on *two* distinct Lagrange parameters).

The remaining theorems are similarly proved (see Fig. 3). □

A simple application of Theorem I.2 to the case shown in Fig. 1 ($\Omega_1 \equiv \Omega_2 \not\equiv \Omega_{2,1}$), explains the paradox, taking into account the prescription of Corollary 1′.

Centers of Instantaneous Rotation on a Straight Line

In this paragraph the second kind of paradox is discussed. Consider the structures shown in Figs. 2 and 4: despite the fact that all the CIRs seem to be distinct and aligned on the same straight line, the rigid-body motion is actually nil.

This unexpected result occurs if the geometry of the structure $\mathcal{S}$ has the following property: *without* one of its simple constraints (e.g., the strut *IK* in Fig. 2 or 4) the *position* of a CIR, on the named straight line, *is undetermined* ($\Omega_{1,3}$ in Fig. 2, and $\Omega_{i,k}$ in Fig. 4); observe that the first and second theorem are in any case satisfied.

In order to render the discussion more precise, two definitions about some distinctive structures are in order.

Downloaded 04 May 2010 to 171.66.16.26. Redistribution subject to ASME license or copyright; see http://www.asme.org/terms/Terms_Use.cfm

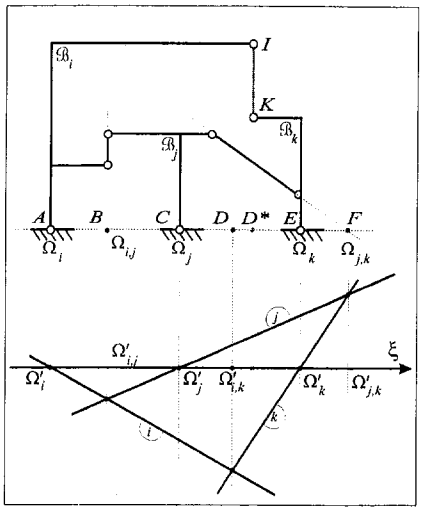

Fig. 4 Sketch of the proof of Theorem III: (1) the substructure {$\mathcal{B}_i$, $\mathcal{B}_j$, $\mathcal{B}_k$}; (2) its vertical displacement diagram, obtained by ignoring the constraint *IK* between the bodies $\mathcal{B}_j$, $\mathcal{B}_k$

Definition 2. A *plane* structure is a complete kinematic chain (CKC) when the following requirements are fulfilled:

1 A motion exists governed by only *one* Lagrange parameter (one-degree-of-freedom rigid-body motion).

2 None of the bodies is *at rest.*

Definition 3. A body $\mathcal{B}_i$ is said to be *simply supported on* $\mathcal{B}_j$, if

1 its (absolute and relative) constraints are *necessary and sufficient* to uniquely define its placement and

2 between $\mathcal{B}_i$ and $\mathcal{B}_j$ there is *only one* simple constraint.

Remarks.

1 A CKC can have an arbitrary number of redundant constraints, while a simply supported body has exactly three simple constraints.

2 A simply supported body on a complete kinematic chain certainly has a nontrivially nil motion.

The following discussion finally clarifies the paradox presented.

Theorem III. Let $\mathcal{C}'$ be the set of three bodies, $\mathcal{B}_i$, $\mathcal{B}_j$, and $\mathcal{B}_k$, components of a structures $\mathcal{S}$, with $\mathcal{B}_i$ and $\mathcal{B}_j$ belonging to a CKC. Let $\mathcal{B}_k$ be simply supported on $\mathcal{B}_j$ in such a way that Ω_k and $\Omega_{k,j}$ be aligned with Ω_i, Ω_j, and $\Omega_{j,i}$ on the straight line l. Moreover, let $\mathcal{C}$ be the substructure obtained by adding a simple constraint, say *IK*, between $\mathcal{B}_i$ and $\mathcal{B}_k$. Finally, suppose that none of the theorems on coinciding CIRs can be applied to $\mathcal{C}$.

Then, a *necessary* condition for the rigid-body motion *to exist* is that *IK* locates $\Omega_{i,k}$ on l in such a way that the following relationship holds true:

$$\frac{(\xi_{\Omega_{i,j}} - \xi_{\Omega_i})(\xi_{\Omega_{j,k}} - \xi_{\Omega_j})(\xi_{\Omega_{k,j}} - \xi_{\Omega_k})}{(\xi_{\Omega_{i,j}} - \xi_{\Omega_j})(\xi_{\Omega_{j,k}} - \xi_{\Omega_k})(\xi_{\Omega_{k,i}} - \xi_{\Omega_i})} = 1, \qquad (12)$$

where $\xi_\Omega := \mathbf{x}_\Omega \cdot \mathbf{e}$ is the abscissa of Ω, $\mathbf{e}$ being a unit vector lying on l.

Proof. Note first that, as a consequence of the hypotheses, $\Omega_{i,k}$ also belongs to l, despite the fact that the first and second theorems are not able to locate it uniquely.

Consider the substructure $\mathcal{C}'$ (the constraint *IK* in Fig. 4, locating $\Omega_{i,k}$ at D^*, must therefore be ignored); by using Eq. (11) the following equations hold:

$$\Omega_{i,j} \to (\xi_{\Omega_{i,j}} - \xi_{\Omega_i})\omega_i = (\xi_{\Omega_{i,j}} - \xi_{\Omega_j})\omega_j, \qquad (13)$$

$$\Omega_{j,k} \to (\xi_{\Omega_{j,k}} - \xi_{\Omega_j})\omega_j = (\xi_{\Omega_{j,k}} - \xi_{\Omega_k})\omega_k; \qquad (14)$$

furthermore, if $\Omega_{i,k}$ exists, the relationships with the absolute CIRs of bodies $\mathcal{B}_i$ and $\mathcal{B}_k$ is necessarily given by

$$\Omega_{i,k} \to (\xi_{\Omega_{i,k}} - \xi_{\Omega_k})\omega_k = (\xi_{\Omega_{i,k}} - \xi_{\Omega_i})\omega_i. \qquad (15)$$

By simplifying the angular velocities from these equations, relationship 4.1 results.

The CIR $\Omega_{j,k}$, which is located by Eq. (12) in $\mathcal{C}'$ (see also Eq. (16)), must therefore be compatible with the condition dictated by the simple constraint *IK*, in the complete substructure $\mathcal{C}$. □

Remarks.

1 Equation (12) also remains valid when *one* (and only one according to the hypotheses of the theorem) CIR is an improper point, because each abscissa ξ_Ω appears in both the numerator and denominator.

2 Despite the fact that Eq. (12) is derived by considering the relative CIR $\Omega_{i,k}$, the same relationship is also attained when an *absolute* CIR, say Ω_k, cannot be located by applying the first and second theorems since Ω_i, Ω_j, $\Omega_{i,j}$, $\Omega_{j,k}$ and $\Omega_{k,i}$ are aligned on the straight line l (a typical structure of this kind is sketched in Fig. 5).

3 It may be useful to explicitly derive the abscissa of $\Omega_{i,k}$, by considering that $(\xi_{\Omega_{i,k}} - \xi_{\Omega_i}) \equiv (\xi_{\Omega_{i,k}} + \xi_{\Omega_k}) + (\xi_{\Omega_k} - \xi_{\Omega_i})$, so that from Eq. (12)

$$\xi_{\Omega_{i,k}} - \xi_{\Omega_k} = \alpha(\xi_{\Omega_k} - \xi_{\Omega_i}), \qquad (16)$$

results, where

$$\alpha := \left[\frac{(\xi_{\Omega_{i,j}} - \xi_{\Omega_i})(\xi_{\Omega_{i,j}} - \xi_{\Omega_j})}{(\xi_{\Omega_{i,j}} - \xi_{\Omega_j})(\xi_{\Omega_{j,k}} - \xi_{\Omega_k})} - 1\right]^{-1}. \qquad (17)$$

In a similar manner,

$$\xi_{\Omega_{i,k}} - \xi_{\Omega_i} = (1 + \alpha)(\xi_{\Omega_k} - \xi_{\Omega_i}). \qquad (18)$$

Conclusion

The kinematic analysis of a plane structure, to ascertain if a virtual rigid-body motion exists near a prescribed configuration with fixed constraints, cannot be limited to verify whether the absolute and relative CIRs of the bodies of the structure are properly aligned according to the classical first and second theorem on kinematic chains.

The paper shows, by several counterexamples, that these theorems *do not give sufficient conditions* for a structure to undergo a rigid motion.

A set of results is obtained and applied to clarify the paradoxes presented; in particular:

1 Theorems I.1, I.2, and II.1 are applicable when *two* absolute or relative CIRs *coincide with one another;* they assert *sufficient*

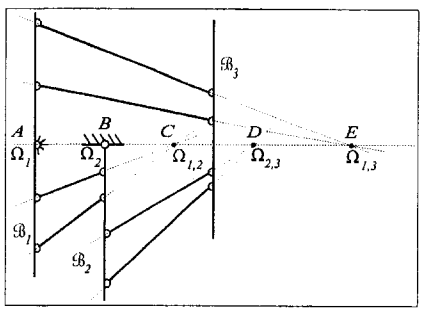

Fig. 5 Example of an application of Theorem III: the absolute center of instantaneous rotation Ω_3 is aligned with Ω_1, Ω_2, $\Omega_{1,2}$, $\Omega_{2,3}$, and $\Omega_{3,1}$, but a rigid-body motion does not exist

Downloaded 04 May 2010 to 171.66.16.26. Redistribution subject to ASME license or copyright; see http://www.asme.org/terms/Terms_Use.cfm

conditions for the nonexistence of a CIR, that is for *the nonexistence of an absolute (or relative) motion;*

2 Theorem III gives an algebraic necessary condition for the rigid-body motion when all the absolute and relative CIRs relevant to *three* bodies *are aligned* on the same straight line.

References

Johnson, A., 1992, "Mechanism Analysis by Matrix Reduction. II—Kinematics," *Proc. R. Soc. London,* Vol. A439, pp. 497–510.

Kuznetsov, E. N., 1988, "Underconstrained Structural Systems," *Int. J. Solids Structures,* Vol. 24, No. 2, pp. 153–163.

Pellegrino, S., and Calladine, C. R., 1986, "Matrix Analysis of Statically and Kinematically Indeterminate Frameworks," *Int. J. Solids Structures,* Vol. 22, No. 4, pp. 409–428.

Pellegrino, S., Kwan, A. S. K., Van Heerden, T. F., 1992, "Reduction of Equilibrium, Compatibility and Flexibility Matrices, in the Force Method," *Int. J. Numerical Methods in Engineering,* Vol. 35, pp. 1219–1236.

Roberson, R. E., and Schwertassek, R., 1988, *Dynamics of multibody systems,* Springer-Verlag, Berlin.

Salerno, G., 1992, "How to Recognize the Order of Infinitesimal Mechanisms: A Numerical Approach," *Int. J. Numerical Methods in Engineering,* Vol. 35, pp. 1351–1395.

Skalmierski, B., 1991, *Mechanics,* Elsevier, Amsterdam; Polish Scientific Publishers, Warszawa.

Timoshenko, S. P., and Young, D. H., 1965, *Theory of structures,* McGraw, Tokyo.

Downloaded 04 May 2010 to 171.66.16.26. Redistribution subject to ASME license or copyright; see http://www.asme.org/terms/Terms_Use.cfm

On the Dynamics of Vibration Absorbers With Motion-Limiting Stops

H. Luo
Post Doctoral Fellow,
Assoc. Mem. ASME.

S. Hanagud
Professor,
Mem. ASME.

School of Aerospace Engineering,
Georgia Institute of Technology,
Atlanta, GA 30332

The dynamics of a class of vibration absorbers with elastic stops is discussed in this paper. The mechanical model proposed in previously published papers are modified to explain certain nonlinear effects, chaotic vibrations, and lower damping observed in our studies. Refined contact-noncontact criteria are presented. Exact steady-state solutions are obtained for a piecewise linear system by using the proposed contact-noncontact criteria. Numerical simulations are presented and compared with the results of the previous work. Significant differences that have been found include some chaotic responses of the system. Experiments are conducted to validate the theoretical results. Chaotic and period-2 responses are also detected experimentally.

Introduction

During the past few years, the dynamic characteristics and the dynamic response of composite beams and plates with delaminations have been studied by the authors. In comparison to a beam without delaminations, a delaminated beam exhibits additional natural frequencies and modes (Nagesh Babu and Hanagud, 1990). The numerical value of these additional natural frequencies are located between the natural frequencies of a nondelaminated beam. The modes, however, are characterized by an opening of the delaminated surfaces (Fig. 1). In an attempt to experimentally identify the delamination modes (Hanagud and Luo, 1994), an enhanced damping due to the impact of the two sides of the delaminated surfaces and observed other nonlinear effects have been identified. In order to model and understand the enhanced damping of the delaminated beam in a very simple way, the model of vibration absorbers with motion limiting stops was considered. A more comprehensive modeling should consider the distributed parameter system with appropriate contact mechanics.

Vibration absorbers with motion-limiting stops have been studied in the past. The idea of using an elastic stop in vibration absorbers was proposed by Ormondroyed and Den Hartog (1928) more than 60 years ago. The purpose of the elastic stop is to limit the excessive motion of the auxiliary mass relative to the main mass. Masri (1972) presented an exact solution for the steady-state motion of the problem. In that model, the stiffness of the elastic stop was assumed to be infinite. The mechanical energy dissipation during the collision is governed by the coefficient of restitution.

The experimental verification of the elastic stop was also published by Masri et al. (1981). In this paper, a cantilever beam was used (Fig. 2), where the motion limiting stop was modeled as a spring with a finite spring constant k_s. An initial gap d between the stop and the beam was also assumed in the model. Thus the response of the beam was composed of a noncontact response and a contact response. The contact-noncontact criterion was $w(x_0, t) = d$, that is, if $w(x_0, t) > d$ the system is in a contact state, whereas if $w(x_0, t) < d$ the system is in a noncontact state.

In another model proposed by Masri (1978), the motion-limiting stop was modeled to include the damping effect as well (Fig. 3). The motion-limiting stop was represented by a massless stop s, a spring k_s, and a damper c_s. In that model, the contact-noncontact criterion was kept the same as in the case where the stop damper was not considered (Masri, 1972, 1981). The equation $x(t) = d$ was used as a contact-noncontact criterion for simplification. This assumption simplifies the model significantly so that one can derive analytical solutions for the dynamic response. In many cases, the simplified model and the resulting dynamic response approximate the observed experimental observations. However, in some other cases similar to the case of interest to us, such an assumption leads to contact forces that are not always realized in practice. In other words, we will have a tensile force between the stop s and the mass m_1 of Fig. 3 even when the stop s and the mass m_1 are still in contact. In fact, the condition for separation of the stop s from the mass m_1 is that the contact force becomes zero from a compressive force that is caused by the contact. This $x(t) = d$ assumption has been incorporated in recent papers by Galhoud et al. (1987), Natsiavas (1990a, 1990b, 1993), Natsiavas et al. (1992), etc., for several applications.

In this paper, previous models are improved by considering appropriate contact force conditions to obtain an improved model for the vibration absorber with the motion-limiting stop. The corresponding differential equations are derived. An appropriate contact-noncontact criterion is proposed. Analytical steady-state solutions are obtained by incorporating the proposed contact-noncontact criterion. Numerical simulations and the effective damping due to the addition of a motion-limiting stop have been compared with earlier results (e.g., Galhoud et al., 1987) in the range of our interest. In this range, we have also found period-4 bifurcation and chaotic vibrations at exciting frequencies that are close to the natural frequency of the main structure. Experiments have been designed and conducted. The experimental results support our numerical conclusions.

Mechanical Model and Dynamic Equations

The motion-limiting stop in a vibration absorber introduces nonlinearities due to the contact and noncontact motion states during vibrations. A two-degree-of-freedom vibration absorber system that has been discussed in Galhoud et al. (1987) is shown in Fig. 4. In that paper, the system is modeled as a main mass m_1 attached to a main spring with elastic constant k_1 and a main damper with damping constant c_1. An auxiliary mass

Contributed by the Applied Mechanics Division of THE AMERICAN SOCIETY OF MECHANICAL ENGINEERS for publication in the ASME JOURNAL OF APPLIED MECHANICS.

Discussion on this paper should be addressed to the Technical Editor, Professor Lewis T. Wheeler, Department of Mechanical Engineering, University of Houston, Houston, TX 77204-4792, and will be accepted until four months after final publication of the paper itself in the ASME JOURNAL OF APPLIED MECHANICS.

Manuscript received by the ASME Applied Mechanics Division, Oct. 25, 1996; final revision, July 21, 1997. Associate Technical Editor: J. W. Ju.

 Copyright © 1998 by ASME

Downloaded 04 May 2010 to 171.66.16.26. Redistribution subject to ASME license or copyright; see http://www.asme.org/terms/Terms_Use.cfm

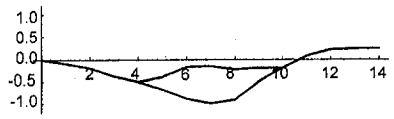

Fig. 1 Delamination mode exhibits opening of the delaminated surfaces

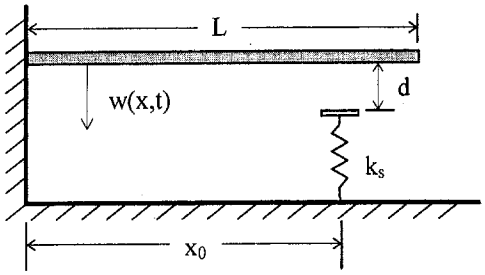

Fig. 2 Motion-limiting stop is modeled as a finite spring

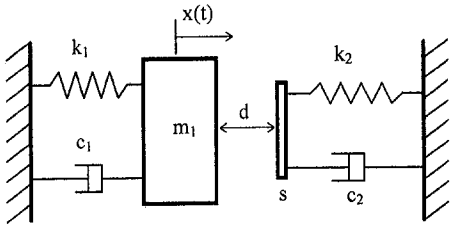

Fig. 3 Motion-limiting stop is modeled as a finite spring and a damper

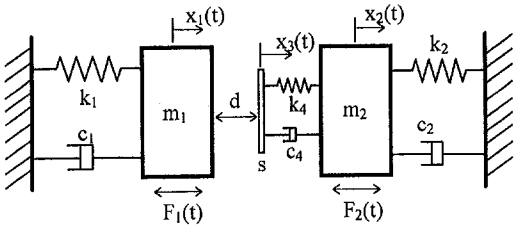

Fig. 4 Model of a vibration absorber with an elastic stop

m_2 is connected to an auxiliary spring with spring constant k_2 and an auxiliary damper with damping constant c_2. A massless stop s is modeled as a spring with elastic constant k_4 and a damper with damping constant c_4. The elastic stop is connected to the auxiliary mass m_2. In a free initial state, there is a gap d between the main mass m_1 and the stop s. Quantities $x_1(t)$, $x_2(t)$, and $x_3(t)$ are used to denote the displacements of the main mass m_1, the auxiliary mass m_2, and the stop s, respectively. Then $y = x_1 - x_2$ denotes the relative motion between the main mass m_1 and the auxiliary mass m_2. The relative motion between the stop s and the auxiliary mass m_2 can be represented by $z = x_3 - x_2$.

In the models described by Galhoud et al. (1987), it was assumed that as long as $y \geq d$, there always exists a contact force $f(t)$ (as shown in Fig. 5). The contact force $f(t)$ was expressed as

$$f(t) = k_4(y - d) + c_4\dot{y}, \quad y \geq d \tag{1a}$$

$$f(t) = 0, \quad y < d. \tag{1b}$$

Thus the equations of motion were expressed as follows

(1) In a noncontact state

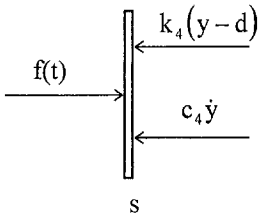

Fig. 5 Contact force calculation in Galhoud et al. (1987) when $y > d$

$$m_1\ddot{x}_1 = -k_1x_1 - c_1\dot{x}_1 + F_1(t) \tag{1c}$$

$$m_2\ddot{x}_2 = -k_2x_2 - c_2\dot{x}_2 + F_2(t). \tag{1d}$$

(2) In a contact state

$$m_1\ddot{x}_1 = -k_1x_1 - c_1\dot{x}_1 - f(t) + F_1(t) \tag{1e}$$

$$m_2\ddot{x}_2 = -k_2x_2 - c_2\dot{x}_2 + f(t) + F_2(t). \tag{1f}$$

Or eliminating $f(t)$ by substituting (1a) into (1e) and (1f), we get

$$m_1\ddot{x}_1 = -(k_1 + k_4)x_1 + k_4x_2 - (c_1 + c_4)\dot{x}_1 + c_4\dot{x}_2 + F_1(t) + k_4d \tag{1g}$$

$$m_2\ddot{x}_2 = -(k_2 + k_4)x_2 + k_4x_1 - (c_2 + c_4)\dot{x}_2 + c_4\dot{x}_1 + F_2(t) - k_4d. \tag{1h}$$

During vibrations, due to the existence of the stop spring k_4 and damper c_4, $(y - d)$ and $\dot{y}$ in Eq. (1a) are not necessarily in the same phase. Cases exist when even though $y > d$ is still satisfied, $\dot{y}$ could be negative and the contact force $f(t) = k_4(y - d) + c_4\dot{y} < 0$ in a certain configuration of k_4 and c_4 and in a certain period.

We have to discern the governing equations of the system (as shown in Fig. 4) depending on whether the stop is in contact with main mass m_1 or not. In a dynamic problem, the contact will take place only when the contact force $f(t)$ is compressive (positive in this case). When $f(t)$ turns zero, the contact ceases. Negative $f(t)$ (tensile force) is not a possible situation and implies that the separation should have taken place when $f(t)$ becomes zero. By using the example that was discussed in reference of Galhoud et al. (1987) for our cases of studies, we have found that $f(t)$ can be negative. In the cases where the stop s and main mass m_1 are not in contact, the stop s and the auxiliary mass m_2 cannot have the same displacement unless c_4 is zero (the stop spring k_4 need not be zero as long as we neglect the mass of the stop), because of the additional time constant introduced by c_4 and k_4. Therefore, we have modified the model by considering three generalized coordinates instead of two in the noncontact state. Similar simplifications as in Galnoud et al. (1987) can be seen in the references of Natsiavas (1990a, 1990b, 1993), Natsiavas et al. (1992), etc.

Improvement of Contact-Noncontact Criteria. The contact-noncontact criterion that are applicable to our studies should include the following considerations:

(1) From the contact state to noncontact state, the contact force $f(t)$ changes from positive to zero. A negative contact force is not possible.

(2) In the noncontact state, the displacement of the stop s is an additional degree-of-freedom. The relative motion of the stop s with respect to the auxiliary mass m_2, $z = x_3 - x_2$, is controlled by the stop spring k_4 and the damper c_4.

(3) From the noncontact state to contact state, the transition is determined by $y = d + z$ instead of $y = d$, since the elastic stop is an additional degree-of-freedom during the noncontact state of motion.

Downloaded 04 May 2010 to 171.66.16.26. Redistribution subject to ASME license or copyright; see http://www.asme.org/terms/Terms_Use.cfm

Table 1 Parameters of model 1

F_1	F_2	$d/(F_1/k_1)$	$\mu = m_2/m_1$	Ω/ω_1	ω_2/ω_1	ω_4/ω_1	ζ_1	ζ_2	ζ_4	τ
1.0	0.0	10.0	0.1	1.0	0.5	5.0	0.005	0.01	0.1	0.04

Based on the above considerations, the modified governing equations for the system shown in Fig. 4 are as follows:

(1) In a noncontact state

$$m_1\ddot{x}_1 = -k_1x_1 - c_1\dot{x}_1 + F_1(t) \quad (2a)$$

$$m_2\ddot{x}_2 = -k_2x_2 - c_2\dot{x}_2 + F_2(t) \quad (2b)$$

$$k_4(x_3 - x_2) + c_4(\dot{x}_3 - \dot{x}_2) = 0. \quad (2c)$$

(2) In a contact state

$$m_1\ddot{x}_1 = -k_1x_1 - c_1\dot{x}_1 - f(t) + F_1(t) \quad (3a)$$

$$m_2\ddot{x}_2 = -k_2x_2 - c_2\dot{x}_2 + f(t) + F_2(t) \quad (3b)$$

$$f(t) = k_4(x_3 - x_2) + c_4(\dot{x}_3 - \dot{x}_1) \quad (3c)$$

$$x_3 = x_1 - d. \quad (3d)$$

Equation $(2c)$ implies that in the state of noncontact motion, x_3 is an additional degree of the system. The motion of the stop s relative to the auxiliary mass m_2, $z = x_3 - x_2$, follows the exponential decay law in this region. The time constant is $\tau = c_4/k_4$. Equation $(3d)$ indicates that in the contact state, x_3 is no longer an independent degree-of-freedom. Its motion is prescribed by x_1 and the initial gap d through Eq. $(3d)$. Eliminating $f(t)$ and x_3 in Eqs. $(3a-d)$, we get, for the contact state, the same as Eqs. $(1g)$ and $(1h)$, as expected. Even though we obtain the same equations, the difference between the present model and the earlier work is as follows. If we use the previous model, for our calculation, we will be using these equations even when the system is already in a noncontact state.

Steady-State Solutions

In a nonlinear system, we may not always have a steady-state solution because of the possible existence of chaotic motions. If we assume that we have a steady-state solution, as discussed in the paper of Galhoud et al. (1987), we can proceed as fol-

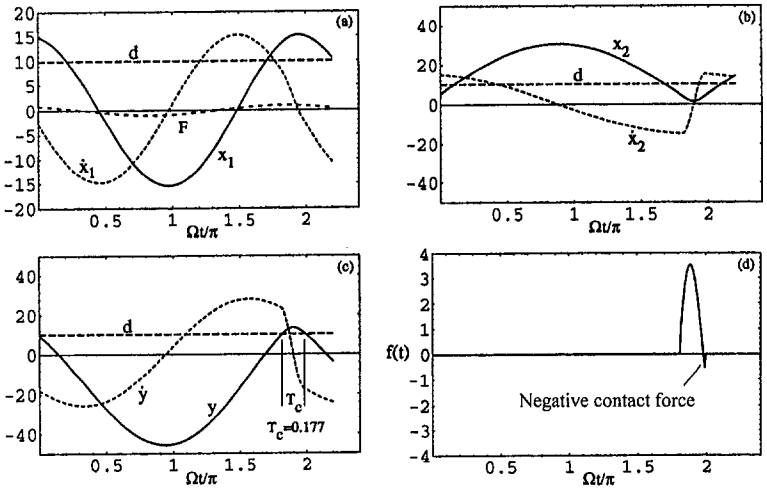

(I) One cycle of steady-state responses based on the contact criterion of Galhoud et al. (1987). Negative contact force is detected.

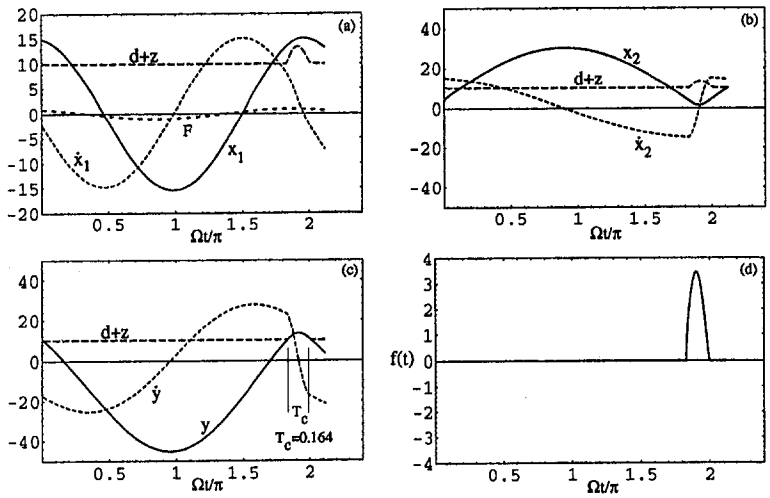

(II) One cycle of steady-state responses according to the present contact criterion. The contact force is always nonnegative.

Fig. 6 Steady-state solutions: (I) criterion I; (II) criterion II

Downloaded 04 May 2010 to 171.66.16.26. Redistribution subject to ASME license or copyright; see http://www.asme.org/terms/Terms_Use.cfm

Table 2 Parameters of model 2

F_1	F_2	$d/(F_1/k_1)$	$\mu = m_2/m_1$	Ω/ω_1	ω_2/ω_1	ω_4/ω_1	ζ_1	ζ_2	ζ_4	τ
1.0	0.0	2.0	0.1	0.8–1.2	0.5	5.0	0.01	0.1	0.1	0.04

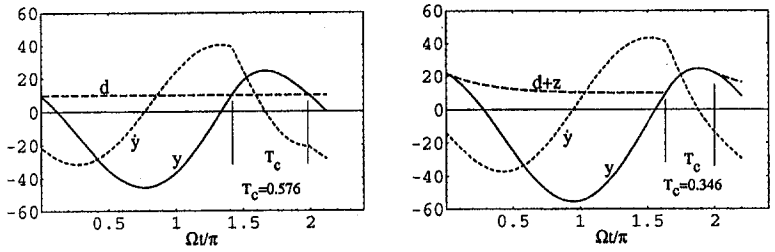

(a) Criterion I (b) Criterion II

Fig. 7 The contact time difference is increased with the increase of the stop time constant (τ = 1.0)

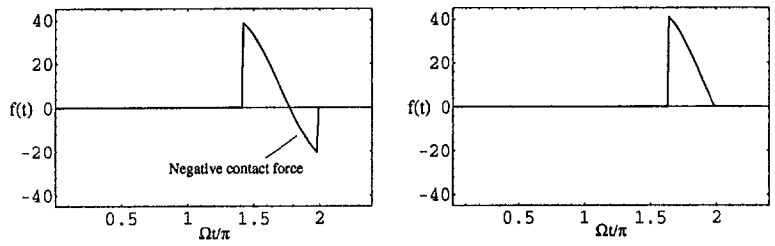

(a) Criterion I (b) Criterion II

Fig. 8 The contact force difference is increased with the increase of the stop time constant (τ = 1.0)

lows: Since the dynamic response of the system is governed by two sets of equations, the exact solution of the system needs to be solved in the time domain by treating the contact and noncontact cases separately. For convenience, we write Eqs. (2) and (3) in state-space representations as

(1) state-space representation in the noncontact state

$$\dot{\mathbf{u}} = \mathbf{A}_1\mathbf{u} + \mathbf{f}_1 \tag{4}$$

(2) state-space representation in the contact state

$$\dot{\mathbf{v}} = \mathbf{A}_2\mathbf{v} + \mathbf{f}_2 \tag{5}$$

where $\mathbf{u}$ and $\mathbf{v}$ are the state variables of the noncontact and contact states, respectively, and

$$\mathbf{u} = \{x_1 \quad \dot{x}_1 \quad x_2 \quad \dot{x}_2 \quad x_3\}^T, \quad \text{and} \quad \mathbf{v} = \{x_1 \quad \dot{x}_1 \quad x_2 \quad \dot{x}_2\}^T$$

where the superscript T stands for transpose. $\mathbf{A}_1$ and $\mathbf{A}_2$ are the system coefficient matrices of the state-space representation in the noncontact and contact states, respectively,

$$\mathbf{A}_1 = \begin{bmatrix} 0 & 1 & 0 & 0 & 0 \\ -\omega_1^2 & -2\omega_1\zeta_1 & 0 & 0 & 0 \\ 0 & 0 & 0 & 1 & 0 \\ 0 & 0 & -\omega_2^2 & -2\omega_2\zeta_2 & 0 \\ 0 & 0 & \dfrac{\omega_4}{2\zeta_4} & 1 & -\dfrac{\omega_4}{2\zeta_4} \end{bmatrix}$$

$$\mathbf{A}_2 = \begin{bmatrix} 0 & 1 & 0 & 0 \\ -\omega_1^2 - \mu\omega_4^2 & -2\omega_1\zeta_1 - 2\mu\omega_4\zeta_4 & \mu\omega_4^2 & 2\mu\omega_4\zeta_4 \\ 0 & 0 & 0 & 1 \\ \omega_4^2 & 2\omega_4\zeta_4 & -\omega_2^2 - \omega_4^2 & -2\omega_2\zeta_2 - 2\omega_4\zeta_4 \end{bmatrix}.$$

Quantities $\mathbf{f}_1$ and $\mathbf{f}_2$ are the state-space expressions of the external forcing vectors in the noncontact and contact states, respectively,

$$\mathbf{f}_1 = \left\{0 \quad \frac{\omega_1^2 F_1}{k_1} \quad 0 \quad \frac{\omega_2^2 F_2}{k_2} \quad 0\right\}^T$$

$$\mathbf{f}_2 = \left\{0 \quad \frac{\omega_1^2 F_1}{k_1} + \mu\omega_4^2 d \quad 0 \quad \frac{\omega_2^2 F_2}{k_2} - \mu\omega_4^2 d\right\}^T$$

where

$$\omega_1^2 = \frac{k_1}{m_1}, \quad \omega_2^2 = \frac{k_2}{m_2}, \quad \omega_4^2 = \frac{k_4}{m_2}$$

$$2\omega_1\zeta_1 = \frac{c_1}{m_1}, \quad 2\omega_2\zeta_2 = \frac{c_2}{m_2}, \quad 2\omega_4\zeta_4 = \frac{c_4}{m_2}, \quad \mu = \frac{m_2}{m_1}.$$

By denoting $T_1 = (t_1, t_2]$, $T_2 = (t_2, t_3]$ the consecutive noncontact and contact time regions, respectively, the initial conditions of the two sets of equations can be defined as

$$\mathbf{u}|_{t_1} = \{v_1 \quad v_2 \quad v_3 \quad v_4 \quad v_1 - d\}|_{t_1}, \quad \text{and}$$

$$\mathbf{v}|_{t_2} = \{u_1 \quad u_2 \quad u_3 \quad u_4\}|_{t_2}.$$

Then the solutions in the two regions can be expressed as

$$\mathbf{u}(t) = e^{\mathbf{A}_1(t-t_1)}\mathbf{u}(t_1) + \int_{t_1}^{t} e^{\mathbf{A}_1(t-\tau)}\mathbf{f}_1(\tau)d\tau, \quad t \in (t_1, t_2] \tag{6a}$$

$$\mathbf{v}(t) = e^{\mathbf{A}_2(t-t_2)}\mathbf{v}(t_2) + \int_{t_2}^{t} e^{\mathbf{A}_2(t-\tau)}\mathbf{f}_2(\tau)d\tau, \quad t \in (t_2, t_3]. \tag{6b}$$

If the initial conditions and the excitations and the external

Downloaded 04 May 2010 to 171.66.16.26. Redistribution subject to ASME license or copyright; see http://www.asme.org/terms/Terms_Use.cfm

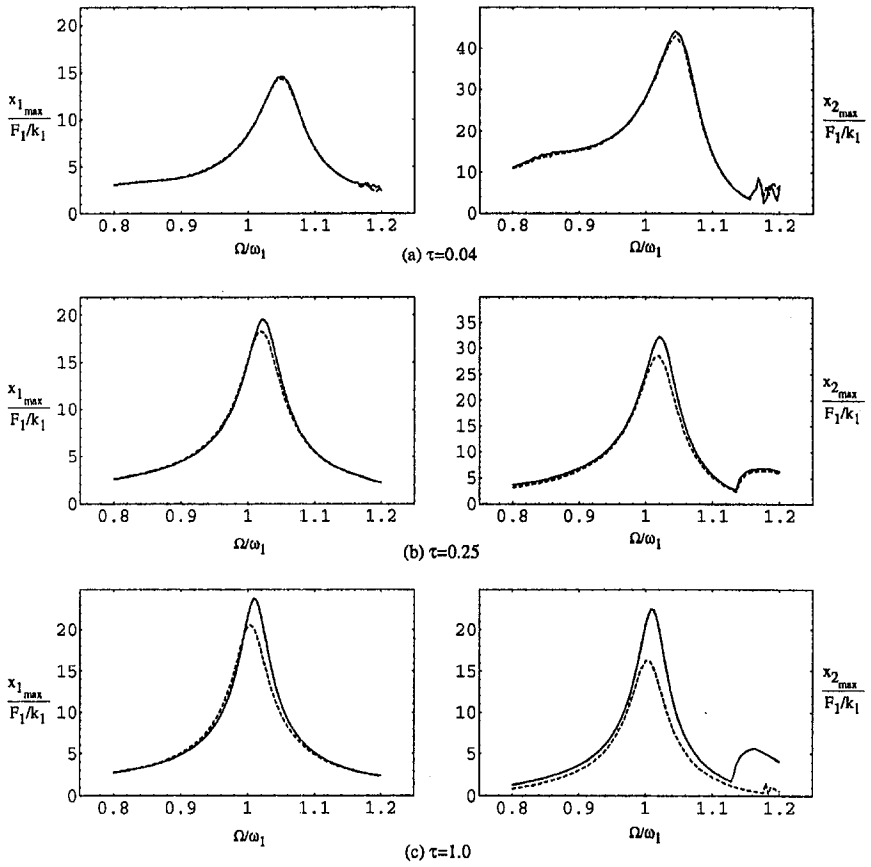

Fig. 9 Maximum responses versus external excitation frequencies (dashed lines: results of Galhoud et al. (1987); solid lines: present results)

excitations $F_1(t)$ and $F_2(t)$ of the system are known, the response of the system can be determined analytically.

If we are interested only in the steady-state motions, we can use the approach similar to that of Masri (1972) for a system with linear damping, in which the time origin of the external forcing term is shifted as follows:

$$F_i(t) = F_{i0} \sin(\Omega t + \varphi_0)$$

where φ_0 is the initial phase angle to be determined from the steady-state conditions. Assuming $t_1 = 0$ and $\Omega t_3 = 2\pi$, we can write the steady-state solutions as

$$\mathbf{u}(t) = e^{\mathbf{A}_1 t}\mathbf{u}(0) + \int_0^t e^{\mathbf{A}_1(t-\tau)}\mathbf{f}_1(\tau + \varphi_0)d\tau, \quad t \in (0, t_2] \quad (7a)$$

$$\mathbf{v}(t) = e^{\mathbf{A}_2(t-t_2)}\mathbf{v}(t_2) + \int_{t_2}^t e^{\mathbf{A}_2(t-\tau)}\mathbf{f}_2(\tau + \varphi_0)d\tau, \quad t \in \left(t_2, \frac{2\pi}{\Omega}\right]. \quad (7b)$$

To complete the solutions that are given by Eqs. (7*a*) and (7*b*) for a given system with a given forcing frequency, we need to know the initial conditions $\mathbf{u}(0)$, $\mathbf{v}(t_2)$, t_2, and φ_0. These quantities can be determined by the state-space variables continuity at contact

$$\mathbf{v}|_{t_2} = \{v_1 \quad v_2 \quad v_3 \quad v_4\}^T|_{t_2} = \{u_1 \quad u_2 \quad u_3 \quad u_4\}^T|_{t_2} \quad (8)$$

$$\mathbf{u}|_0 = \{u_1 \quad u_2 \quad u_3 \quad u_4 \quad u_5\}^T|_0 = \{v_1 \quad v_2 \quad v_3 \quad v_4 \quad v_1 - d\}^T|_{2\pi/\Omega} \quad (9)$$

together with the solutions from Eqs. (7*a*) and (7*b*)

$$\mathbf{u}|_{t_2} = e^{\mathbf{A}_1 t_2}\mathbf{u}(0) + \int_0^{t_2} e^{\mathbf{A}_1(t_2-\tau)}\mathbf{f}_1(\tau + \varphi_0)d\tau \quad (10)$$

$$\mathbf{v}|_{2\pi/\Omega} = e^{\mathbf{A}_2((2\pi/\Omega)-t_2)}\mathbf{v}(t_2) + \int_{t_2}^{2\pi/\Omega} e^{\mathbf{A}_2((2\pi/\Omega)-\tau)}\mathbf{f}_2(\tau + \varphi_0)d\tau \quad (11)$$

and the noncontact force conditions at $t = 2\pi/\Omega$ and $t = t_2$

$$f\left(\frac{2\pi}{\Omega}\right) = [k_4(v_1 - v_3) + c_4(v_2 - v_4)]|_{2\pi/\Omega} = 0 \quad (12)$$

$$f(t_2) = [k_4(v_1 - v_3) + c_4(v_2 - v_4)]|_{t_2} = 0. \quad (13)$$

Equations (8) through (13) are 20 transcendental equations which relate 20 unknowns of $\mathbf{u}(0)$, $\mathbf{u}(t_2)$, $\mathbf{v}(t_2)$, $\mathbf{v}(2\pi/\Omega)$, t_2, and φ_0. Theoretically, we can determine the initial phase shift φ_0 and the contact time t_2 through these equations. Once φ_0 and t_2 are known, the nonchaotic steady-state responses are determined by Eqs. (7*a*) and (7*b*).

Numerical Simulations: Chaotic Solutions

To study the possible chaotic solution of this nonlinear system, we used numerical integration schemes. The steady-state solutions are obtained after integrating through many cycles so that the transient response due to the initial conditions is fully damped out by the virtue of the dampers of the system. The numerical integration is based on Eq. (6*a*) or (6*b*), depending on the noncontact or contact state during vibrations. The contact-noncontact criterion is incorporated into the numerical integration scheme in the following way:

Downloaded 04 May 2010 to 171.66.16.26. Redistribution subject to ASME license or copyright; see http://www.asme.org/terms/Terms_Use.cfm

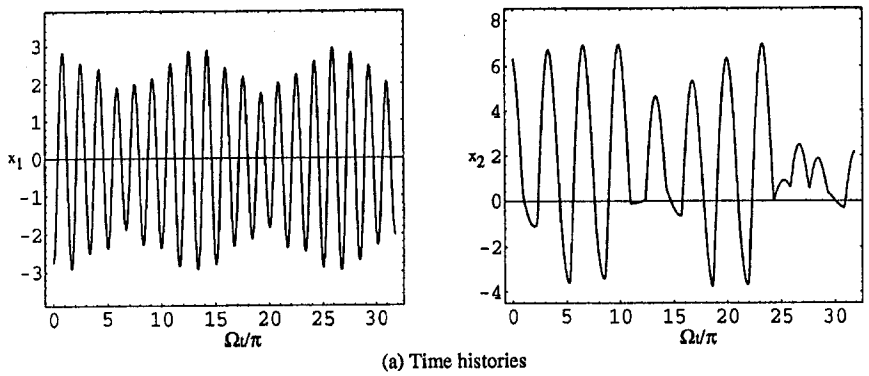

(a) Time histories

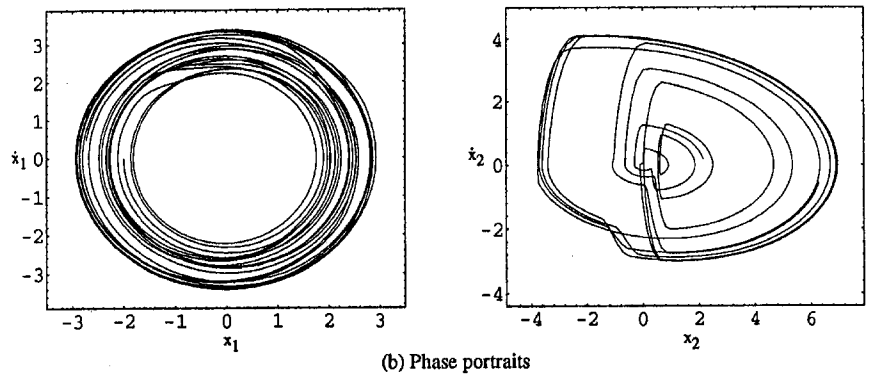

(b) Phase portraits

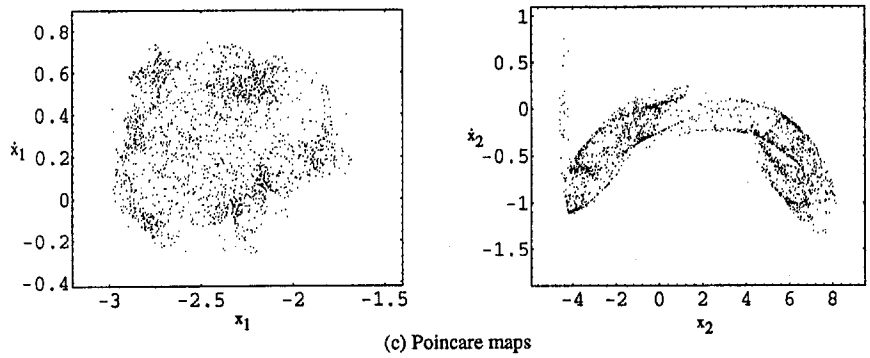

(c) Poincare maps

Fig. 10 Chaotic responses at $\Omega/\omega_1 = 1.1952$

(1) If the system is in a noncontact state, the integration follows Eq. (6*a*). In the noncontact state integration, contact condition $y = d + z$ is checked at each step of integration. Here $y = x_1 - x_2$ is the relative motion of the main mass m_1 with respective to the auxiliary mass m_2. $z = x_3 - x_2$ is the relative motion of the stop s with respective to the auxiliary mass m_2. If the condition $y = d + z$ is satisfied, then the following motions will be controlled by Eq. (6*b*).

(2) If the system is in a contact state, the integration follows (6*b*). The noncontact condition $f(t) \leq 0$ is checked. If the contact force $f(t)$ reaches zero, then the following integration will be based on Eq. (6*a*). If the contact force $f(t)$ is negative, it implies the noncontact happened in the past integration step.

Examples: In order to estimate the significance of the negative contact force, the first example used here is the same as that used by Galhoud et al. (1987). The parameters of the system are listed in Table 1. The numerical results are obtained by integrating numerically the state-space Eqs. (6*a*) and (6*b*) using the fourth-order Runge-Kutta method and double precision variables. The steady-state solutions are extracted after integrating 1000 external forcing cycles. Both the contact-noncontact criteria used in Galhoud et al. (1987) and the criteria modified and presented in this paper are used for purposes of comparison. The results are shown in Fig. 6. For convenience, we will call the contact-noncontact criterion used in Galhoud et al. (1987) the criterion I, whereas the contact-noncontact criterion presented in this paper is criterion II. A second model is used to calculate the maximum steady-state responses as the excitation frequency varies. The model was also the same as that used by Galhoud et al. (1987). Parameters used for this model are listed in Table 2. The results are shown in Fig. 9.

In Fig. 6, we have shown the results of the first model. Fig. 6(I) is the computational results of one cycle steady-state response and the contact force according to the criterion used in the paper of Galhoud et al. (1987) (criterion I). The corresponding results calculated based on the criterion presented in this paper (criterion II) are shown in Fig. 6(II). The abscissa in the figures is the normalized time $T = \Omega t/\pi$. The ordinate is the amplitude of the variables shown in the figure. By comparing the results shown in part (I) and part (II) of Fig. 6, we are able to find two major differences:

Downloaded 04 May 2010 to 171.66.16.26. Redistribution subject to ASME license or copyright; see http://www.asme.org/terms/Terms_Use.cfm

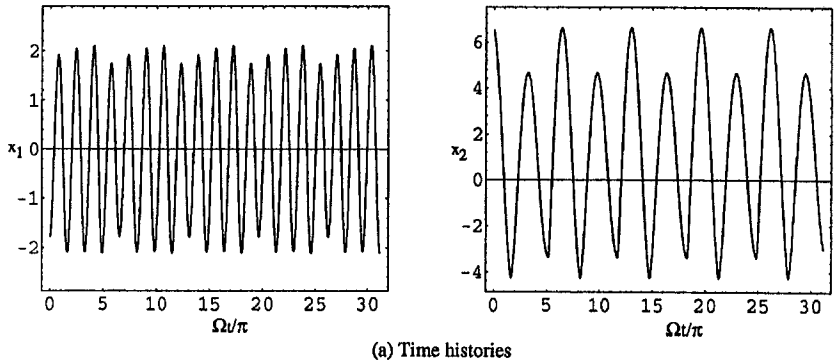

(a) Time histories

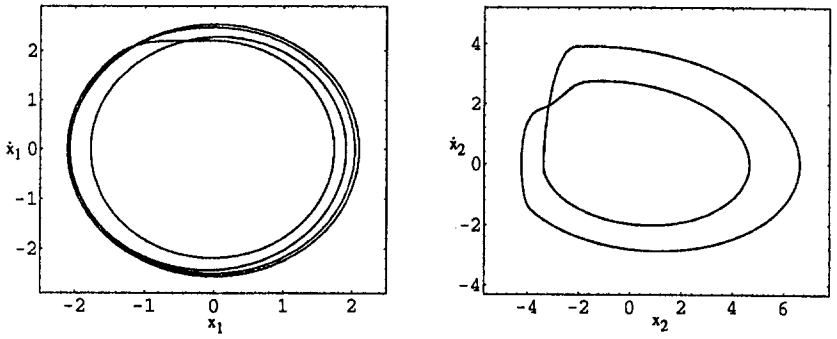

(b) Phase portraits

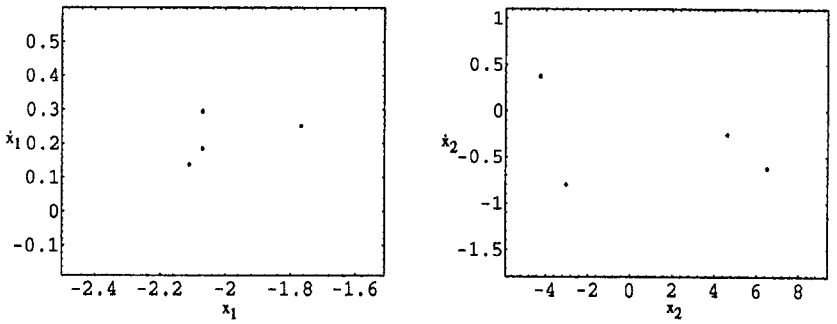

(c) Poincare maps

Fig. 11 Period-4 responses at $\Omega/\omega_1 = 1.2188$

(1) The contact time in one cycle of external excitation is different. The contact time of criterion I is longer than that of criterion II. In our example, the contact time is $T_c = 0.177$ by criterion I, as indicated in Fig. 6(I)(c) while it is $T_c = 0.164$ by criterion II, as marked in the Fig. 6(II)(c);

(2) The contact force in one cycle of external excitation is different. From Fig. 6(I)(d), we can see that there can be negative contact force in a cycle by using criterion I, which is not possible in a real situation. Whereas the contact force is always non-negative by using the contact criterion presented in this paper.

These differences are increased with the increase of the elastic stop time constant $\tau = c_4/k_4$. Figures 7 and 8 are shown the results of an example with the increased time constant. In this example, the parameters are the same as the first model except $\omega_4/\omega_1 = 1.0$ and $\zeta_4 = 0.5$, thus the time constant $\tau = 1.0$. In Fig. 7, we have shown the relative motion y and its velocity. In Fig. 7(a) with criterion I, the normalized contact time is T_c

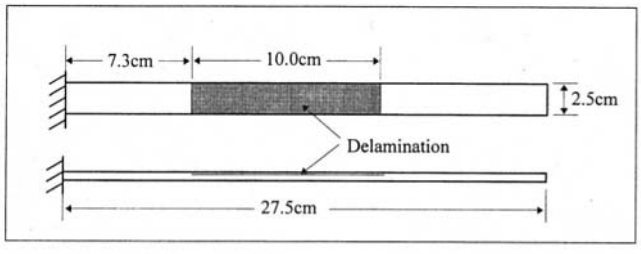

Fig. 12 Delamination specimen configurations

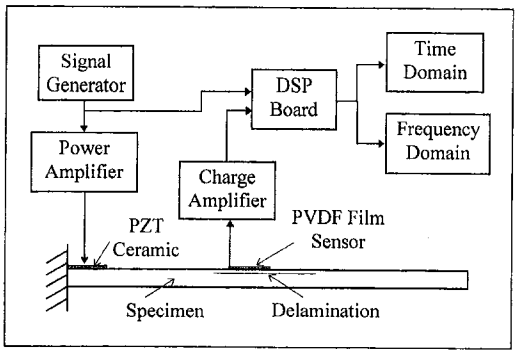

Fig. 13 Instrumentation setup for the dynamic response analysis

Downloaded 04 May 2010 to 171.66.16.26. Redistribution subject to ASME license or copyright; see http://www.asme.org/terms/Terms_Use.cfm

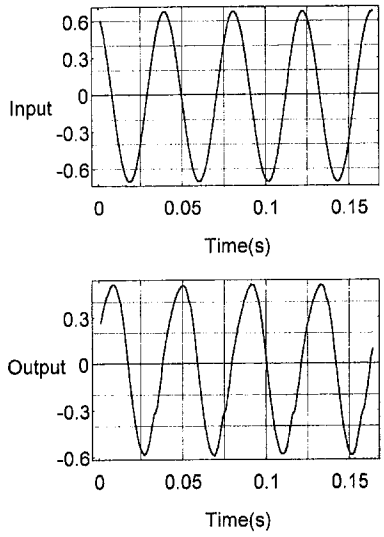

(a) Time Domain

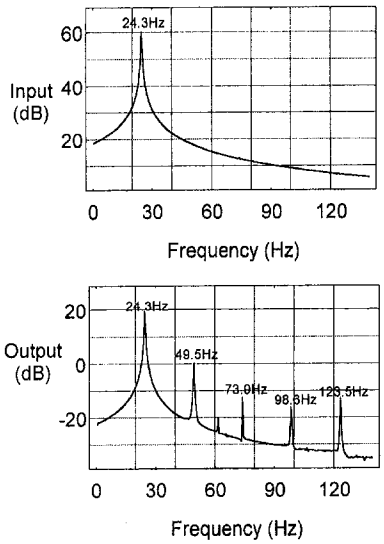

(b) Frequency Domain

Fig. 14 Nonlinear response of the delaminated beam case 2

= 0.567. In Fig. 7(b) with criterion II, the contact time is T_c = 0.346, which is significantly smaller than that of criterion I. More significant differences are also found in the magnitude of the contact force. In Fig. 8, we have shown the contact forces determined by the two criteria. In Fig. 8(a) with criterion I, a significant negative force is found in the "contact state"; In Fig. 8(b) with criterion II, we do not have any negative contact forces.

In Fig. 9, we have shown the maximum response verses the external excitation frequencies. The model used is the second model. The parameters are listed in Table 2. The maximum response is determined numerically as follows:

(1) For given excitation frequency Ω, the state Eq. (6a) or (6b) is integrated numerically according to the noncontact or contact states.

(2) Integration is over 1000 external force cycles to remove the transient response.

(3) Taking one cycle response out, the absolute maximum value in this cycle is assumed to be the maximum response under the given excitation.

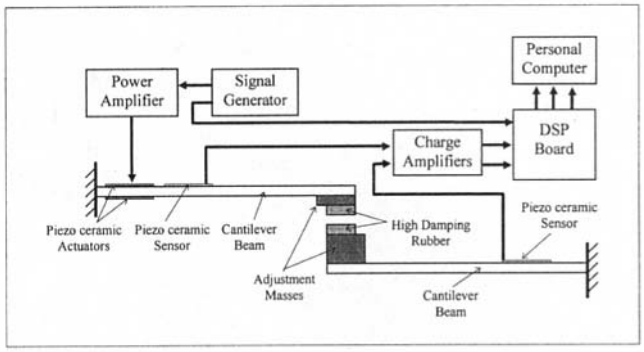

Fig. 15 Design and instrumentation of a vibration absorber system

The maximum response diagram of the second model is shown in Fig. 9(a). The dashed lines indicate the results of criterion I, whereas the solid lines denote the results from criterion II. It is seen that by using criterion I, the vibration absorber effect (damping) is overestimated. This is because in criterion I, the elastic stop provided a negative force which restricts the main mass m_1 and the elastic stop moving apart. This overestimation error will increase with the increase of the elastic stop time constant τ. The results of τ = 0.25 and τ = 1.0 cases are shown in Figs. 9(b) and (c), respectively. The more significant overestimations are seen from these figures.

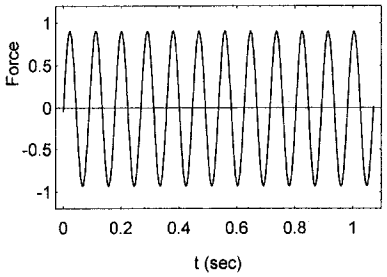

(a) Excitation

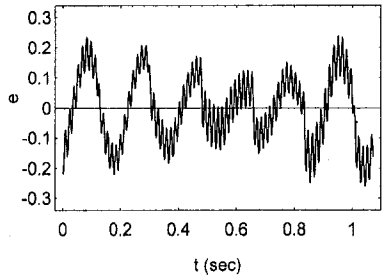

(b) Main Structure Response

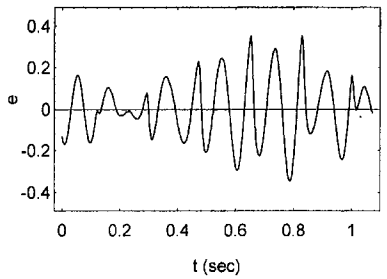

(c) Auxiliary Structure Response

Fig. 16 Time history of the system at chaotic motions, experimental detection

Downloaded 04 May 2010 to 171.66.16.26. Redistribution subject to ASME license or copyright; see http://www.asme.org/terms/Terms_Use.cfm

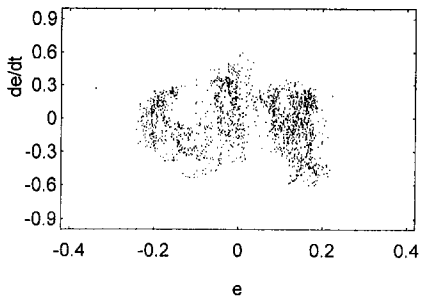

(a) Main Structure

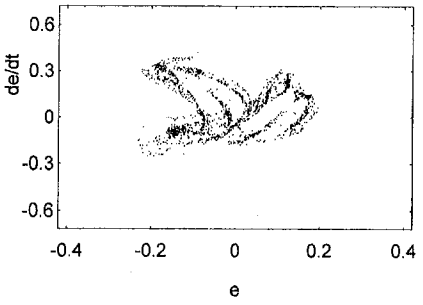

(b) Auxiliary Structure

Fig. 17 Poincaré maps of the main and auxiliary structures at chaotic motions, experimental detection

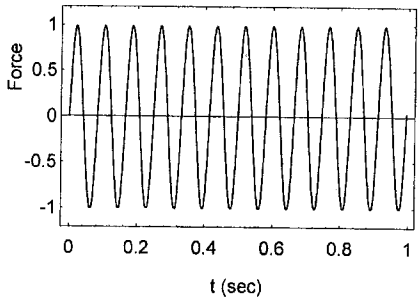

(a) Excitation

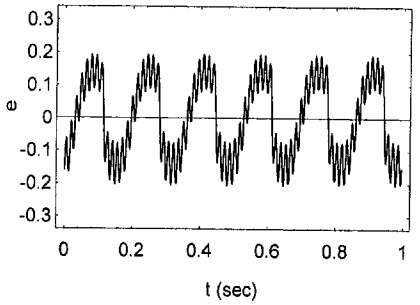

(b) Main Structure Response

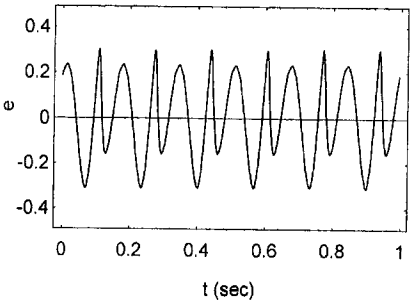

(c) Auxiliary Structure Response

Fig. 18 Time history of the system at period-2 motions, experimental detection

Another issue worth pointing out is in Fig. 9(a), the maximum response diagram displays irregularities in the region of $\Omega/\omega_1 \approx (1.155, 1.324)$. More detailed investigation indicates that in this region, the dynamic responses become irregular. For example, if we select $\Omega/\omega_1 = 1.1952$, the dynamic responses behave chaotically. In Fig. 10, we have shown the time histories, phase portraits, and Poincaré maps of the main mass m_1 and the auxiliary mass m_2 at the given external forcing frequency. At $\Omega/\omega_1 = 1.2188$, we detected period-4 responses. The corresponding time histories, phase portraits, and Poincaré maps are shown in Fig. 11.

Experimental Results

As indicated in the Introduction of this paper, the research of this paper is motivated by a simplified model for delaminated structures. In the following preliminary experiments we first demonstrate the existence of the nonlinearity in dynamic response in a delaminated beam with a delamination. Then, a vibration absorber system with a motion-limit stop is constructed by using cantilever beams. The dynamic response of the system is investigated experimentally.

Nonlinearity in a Delaminated Beam: Here we briefly present the experimental observations of the existence of the nonlinearity in a delaminated composite structural dynamic response. More detailed results can be found in Luo (1996).

The specimens in the experiment were made from the 0/90 woven glass cloth and epoxy matrix. The specimens were first prepared in a plate form with approximately 33 cm × 45 cm in in-plane dimensions and 12 layers of woven glass cloth in thickness. The delamination was simulated by placing a very thin Teflon film between glass cloth layers during the layup. The plate was then cut in beam specimens with dimension of 30 cm × 2.5 cm. Delaminations were centered at the specimen length. Boundary conditions are simulated cantilever boundary conditions. The effective beam length is about 27.5 cm.

A case we present here is a beam with a 10 cm delamination in lengthwise location. The thickness direction location of the delamination is between the second layer and the third layer from the beam top surface for all the three cases. The specimen configurations are shown in Fig. 12.

A PZT ceramic chip was bonded at the root of the delaminated beam as a vibration driver. A PVDF film was used as a sensor to pick up the curvature response signal. The DSP board installed in a PC was used for data acquisition and analysis. The instrumentation setup is shown in Fig. 13.

In Figs. 14, we have shown the input signal to the PZT actuator and the response signal of the delaminated beam case form the PVDF sensor. The time histories of the input and output signals are shown in Fig. 14(a). The corresponding FFT analyses of the input and response signals are shown in Fig. 14(b). It is clearly seen that even though the input signal is purely sinusoidal, higher harmonic components of the excitation frequency exist in the dynamic response of the delaminated beam. The response of a delaminated beam exhibits superharmonic frequency components of the excitation frequency, which is a typical nonlinear phenomenon.

The dynamics of a delaminated beam exhibits nonlinear behavior due to inherent nonlinearity and impact between the delaminated sublaminates. The dynamic behavior of a delaminated beam may be simplified by simple spring-mass-damper-

Downloaded 04 May 2010 to 171.66.16.26. Redistribution subject to ASME license or copyright; see http://www.asme.org/terms/Terms_Use.cfm

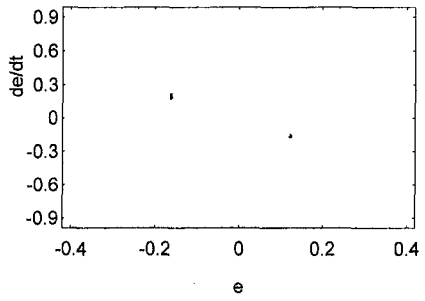

(a) Main Structure

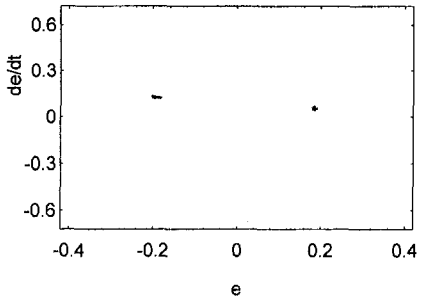

(b) Auxiliary Structure

Fig. 19 Poincaré maps of the main and auxiliary structures at period-2 motions, experimental detection

stop models by appropriately selecting of their physical parameters.

A Spring-Mass-Damper-Stop System Experiment: To experimentally investigate the dynamic behavior, especially the chaotic behavior of a vibration absorber system with motion-limiting stop, we constructed a system as shown in Fig. 15.

In Fig. 15 the vibration absorber system is constructed by using two cantilever beams. One beam is used to serve as the master structure and the other beam is considered as the auxiliary structure. Piezoceramics are bonded to the master structure to provide the driving force for the system. Another pair of piezoceramics are bonded to master and auxiliary structures to serve as sensors. To increase the stop-damping effect (increase c_4 in Fig. 4), small pieces of rubber are attached to the master structure and the auxiliary structure at the contacting points. Adjustment masses are used to tune the basic frequencies of the master structure and the auxiliary structure. As a result, the basic frequency of the master structure is 10.00 Hz and the basic frequency of the auxiliary structure is 5.00 Hz.

As shown in Fig. 15, the driving signal is generated by a signal generator, and then amplified by a power amplifier before it goes into the piezoceramic actuator. Sensor signals first pass through the charge amplifiers, then digitized by the digital signal processing (DSP) board. Further signal processing is conducted by a personal computer. According to Lee and Moon (1990), the sensor equation can be written as

$$Q(t) = -Gb \int_{x_1}^{x_2} E_p \kappa(x, t) \frac{h}{2} d_{31} dx \qquad (14)$$

where G is the amplifier gain, b is the beam width, E_p is Young's modulus of the sensor material, κ is the curvature, $h/2$ is the distance between the beam neutral plane and the sensor neutral plane, d_{31} is the sensor piezoelectric constants, and $x_2 - x_1$ is the sensor length. Assuming the sensor length is small compared to the vibration wavelength, Eq. (14) can be simplified as

Table 3 Parameters for the numerical calculation of the experimental model

$d/(F_1/k_1)$	$\mu = m_2/m_1$	ω_2/ω_1	ω_4/ω_1	ζ_1	ζ_2	ζ_4
1.974	4.0	0.5	3.0	0.02	0.02	0.2

$$Q(t) = -GAE_p d_{31} \frac{h}{2} \bar{\kappa}(x, t) \qquad (15)$$

where A is the sensor area and $\bar{\kappa}$ is the averaged curvature over the sensor area. Thus the response signals from the test setup shown in Fig. 15 are proportional to the curvatures at the measuring points.

At the excitation frequency = 11.86 Hz ($\Omega/\omega_1 = 1.186$), a chaotic vibration was detected in the system. In Fig. 16 we have shown the time histories of the input, the main structure response, and the auxiliary structure response. From Figs. 16(b) and 16(c), we can see the irregularities in the response signals. In Fig. 17 we have shown the Poincaré section map of the response signals. The curvature rates in the maps are derived from the curvature signals by numerical differentiation. To maintain numerical differentiation precision while keeping the signal long enough to produce a section map, the data sampling time interval is chosen as 0.002 seconds. About 1830 points were used to generate each of the section maps.

At the excitation frequency = 12.59 Hz ($\Omega/\omega_1 = 1.259$), a period-2 vibration was detected in the system. In Fig. 18 we have shown the time histories. In Fig. 19 we have shown the Poincare section maps of the main and the auxiliary structures. In this case, the data sampling time interval is chosen as 0.001 seconds. About 588 points were used to generate each of the section maps.

Numerical Simulations for the Experimental Model: Based on the experimental model, parameters for the numerical simulations are chosen as in the Table 3.

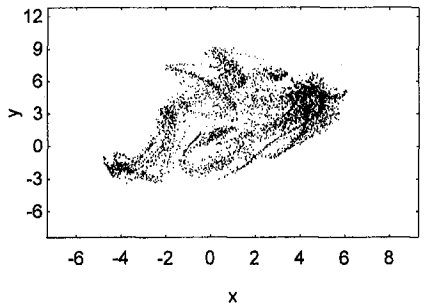

(a) Main Structure

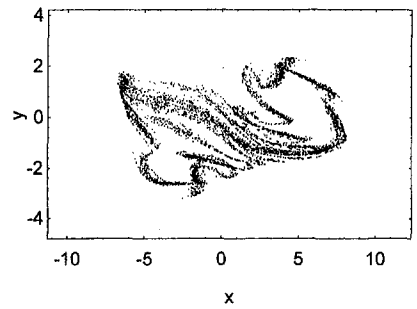

(b) Auxiliary Structure

Fig. 20 Poincaré maps of the main and auxiliary structures at chaotic motions, numerical simulation of the experimental model

Downloaded 04 May 2010 to 171.66.16.26. Redistribution subject to ASME license or copyright; see http://www.asme.org/terms/Terms_Use.cfm

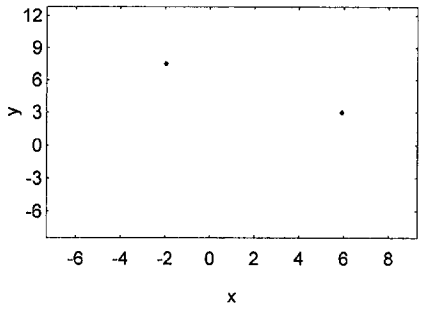

(a) Main Structure

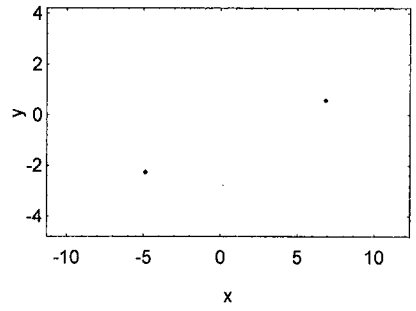

(b) Auxiliary Structure

Fig. 21 Poincaré maps of the main and auxiliary structures at period-2 motions, numerical simulation of the experimental model

A fourth-order Runge-Kutta method was used to calculate the response of the system which the parameters are listed in Table 3. At $f = 11.94$ Hz ($\Omega/\omega_1 = 1.194$) a chaotic motion was detected. The Poincaré maps of the chaotic motion are shown in Fig. 20, where 5000 section points were used. At $f = 12.40$ Hz ($\Omega/\omega_1 = 1.240$), a period-2 motion was detected and the corresponding Poincaré maps are shown in Fig. 21, where 1000 section points were calculated.

Through the comparison of the experimental detection and numerical simulation it is seen that the proposed model for nonlinear vibration absorber is able to simulate the important dynamic response features such as chaos and periodic doubling. The subtle differences between the experimental model and the numerical simulation can be expected due to the nature of chaotic motions. Other causes for the difference can be attributed to the following reasons:

(1) The experimental model is essentially a continuous system. Higher order vibration modes may have involved in the response.

(2) The selection of parameters for the numerical simulation are only approximations of the properties of the experimental model. The damping ratios were selected from experimental modal analysis.

(3) The excitation and detection are also slightly different. In numerical simulations, the excitation is a pure sinusoidal force and the response is described by the displacement and the velocity. In the experimental detection the excitation is applied through a surface bonded PZT ceramic wafer, which is essentially a couple of concentrated tangential shear forces to the beam surface. The response is detected using another piezosensor. The output of the sensor is proportional to the average of the local curvature.

Conclusions

We have investigated the dynamics of a class of vibration absorbers with motion-limiting stops. We have shown that the previous models need modifications for noncontact cases that are considered in our studies. In the models where the motion-limiting stop can be modeled as a damper and a spring, the $y = d$ contact-noncontact criterion is no longer valid. Instead, appropriate contact-noncontact criteria for such a system need to be considered. The zero-contact force at the transition from a contact state to a noncontact state and the additional degree-of-freedom of stop s in the noncontact state should be considered. Therefore, neither the transition point from a contact state to a noncontact state nor the transition point from a noncontact state to a contact state is necessarily expressed by the condition $y = d$. Keeping a $y = d$ contact-noncontact criterion in such a system can cause an overestimation of the damping effect of the motion-limiting stop as well as unreasonable contact forces in vibrations. Numerical studies based on our contact-noncontact criteria indicate that chaotic motions exist in certain system parameter combinations and excitation frequency ranges that are close to the natural frequency of the main system. Experimental investigations of a vibration absorber with motion-limiting stop support the existence of the chaotic and period-2 motions of such systems. Experimental observations were verified by numerical simulations.

References

Galhoud, L. E., Masri, S. F., and Anderson, J. C., 1987, "Transfer Function of a Class of Nonlinear Multi-degree of Freedom Oscillators," ASME JOURNAL OF APPLIED MECHANICS, Vol. 54, pp. 215–225.

Hanagud, S., and Luo, H., 1994, "Modal of a Delaminated Beam," *SEM Spring Conference on Experimental Mechanics,* Baltimore, MD.

Lee, C.-K., and Moon, F. C., 1990, "Modal Sensors/Actuators," ASME JOURNAL OF APPLIED MECHANICS, Vol. 57, pp. 434–441.

Luo, H., 1996, "Damage Detection and Health Monitoring of Structures Using Dynamic Response and Neural Network Techniques," Ph.D. dissertation, Georgia Institute of Technology, Atlanta, GA.

Masri, S. F., 1972, "Theory of the Dynamic Vibration Neutralizer with Motion-Limiting Stops," ASME JOURNAL OF APPLIED MECHANICS, Vol. 39, pp. 563–568.

Masri, S. F., 1978, "Analytical and Experimental Studies of a Dynamic System with a Gap," ASME *Journal of Mechanical Design,* Vol. 100, pp. 127–132.

Masri, S. F., Mariamy, Y. A., and Anderson, J. C., 1981, "Dynamic Response of a Beam With a Geometric Nonlinearity," ASME JOURNAL OF APPLIED MECHANICS, Vol. 48, pp. 404–410.

Nagesh Babu, G. L., and Hanagud, S., 1990, "Delamination in Smart Structures—A Parametric Study on Vibrations," 31st SDM Conference, pp. 2417–2426.

Natsiavas, S., 1990a, "Stability and Bifurcation Analysis for Oscillators with Motion Limiting Constraints," *Journal of Sound and Vibration,* Vol. 141, No. 1, pp. 97–102.

Natsiavas, S., 1990b, "On the Dynamic Oscillators with Bi-Linear Damping and Stiffness," *International Journal of Non-Linear Mechanics,* Vol. 25, No. 5, pp. 534–554.

Natsiavas, S., and Gonzalez, H., 1992, "Vibration of Harmonically Excited Oscillators With Asymmetric Constraints," ASME JOURNAL OF APPLIED MECHANICS, Vol. 59, pp. 284–290.

Natsiavas, S., 1993, "Dynamics of Multiple-Degree-of-Freedom Oscillators with Colliding Components," *Journal of Sound and Vibration,* Vol. 165, No. 3, pp. 439–453.

Ormondroyed, J., and Den Hartog, J. P., 1928, "The Theory of the Dynamic Vibration Absorber," *Transactions of ASME,* Vol. 50, pp. 9–15.

Downloaded 04 May 2010 to 171.66.16.26. Redistribution subject to ASME license or copyright; see http://www.asme.org/terms/Terms_Use.cfm

Viscoelastic Effects in Modeling Web Handling Systems: Unsteady-State Analysis

Xiaofeng Guan

M. S. High

D. A. Tree[1]

School of Chemical Engineering,
Oklahoma State University,
423 Engineering North,
Stillwater, OK 74078

A model to predict the tension in open spans of web handling systems during transient operations has been developed. Governing equations were developed by using the White-Metzner equation to describe the material response in conjunction with mass and force balances. The governing equations were nondimensionalized and solved via the MacCormack predictor/corrector technique. Two dimensionless parameters emerged from the analysis, the Deborah number, De, and the ratio of the viscous stress to the steady state stress, N. The resulting model is the companion to a previously reported model for steady-state operations (Guan et al., 1995). The model was used to predict the behavior of a web handling system during start-up, transition between steady states, and a periodic disturbance. During start-up and transition, systems responded more rapidly at low De. The system response during a periodic disturbance was correlated to De, the frequency, and the magnitude of the disturbance.

1 Introduction

During production and processing thin, flexible materials such as paper, polymer films, and metal foils are known collectively as webs. The production of any web involves a handling system to convey the material. The highly competitive nature of the web industry requires that the web be transported as rapidly as possible without damage, and that the capital investment in the handling system be kept at a minimum. Any web will break or be damaged if the applied tension is too high, resulting in downtime or unacceptable product quality. Therefore, models that can aid in the design, optimization, and control of web handling systems are of great importance.

Web handling operations are superficially similar to polymer processing operations, but can be differentiated on the basis of the magnitude of the permanent deformation imparted to the material, the desirability of a material deformation, the variety of materials involved, and the dimensionally of the deformation. In polymer processing operations the desired outcome is usually a large, multidimensional deformation in a polymeric material. In web handling operations, the intent is to convey the web, which may be a variety of materials, in such a manner as to prevent or minimize any permanent strains. Also, web handing operations cannot tolerate conditions that would result in significant cross machine stresses or velocities in the open spans. Normal web handling operations are primarily one dimensional. Therefore, modeling web handling systems is a distinct pursuit from modeling polymer processing operations.

Furthermore, the modeling of polymer processes has an extensive scientific literature (see, for example, Baird and Collias, 1995). Although web properties have been studied, particularly for paper (Pecht et al., 1984; Perkins and Porter, 1977; Roylance et al., 1980; Williams, 1983), web handling has received almost no attention in the mechanics literature despite being of great importance to several very large industries. Therefore, this paper and its companion paper (Guan et al., 1995) represent nearly unique contributions to the literature.

A web handling system model must account for the interactions of the web material with the components of the system. The most significant work in modeling system components has been presented by Shin (1991). Shin identified and modeled "primitive elements" including: unwind rollers, wind up rollers, driven rollers, idle rollers, open spans, and dancers. Shin demonstrated that the primitive elements could be assembled into any desired configuration to simulate a web handling system. Reid and Lin (1993) later demonstrated that control models could be added to Shin's primitive elements to simulate the effect of PID controllers.

Attempts to model the material behavior in web handling systems have usually assumed that web materials are purely elastic and obey Hooke's law (Campbell, 1958; Grenfell, 1963; Brandenburg, 1976; Taguchi et al., 1985; Shin, 1991; Reid and Lin, 1993). However, common web materials such as polymer films, paper, and even many metal foils show viscoelastic behavior (Ward, 1983; Hauptmann and Cutshall, 1977). Since the purely elastic response is a limiting case in the general behavior of viscoelastic materials, elastic models can describe only one extreme of the possible system behavior. However, in many cases, the viscoelastic effects are so pronounced that no realistic results can be obtained from an elastic model. The first attempt to account for viscoelasticity was reported by Whitworth and Harrison (1983) who suggested that an elastic model could be modified to account for viscoelastic effects by substituting the viscoelastic modulus for the elastic modulus. However, the results of this effort failed to capture any significant viscoelastic effects.

In previously reported work (Guan et al., 1995), a viscoelastic model was developed and applied to the steady-state operation of general multispan web handling systems. The results clearly showed that even a small degree of viscoelasticity had a significant effect on the behavior of multispan systems.

This paper is an extension of the previous study (Guan et al., 1995) on the effects of viscoelasticity on steady state operations into the area of transient web handling system operations. Significant transient operations in industrial settings include: start-up, transition from one steady state to another, shut-down, a temporary interruption, and a periodic disturbance about a

[1] To whom correspondence should be addressed.

Contributed by the Applied Mechanics Division of THE AMERICAN SOCIETY OF MECHANICAL ENGINEERS for publication in the ASME JOURNAL OF APPLIED MECHANICS.

Discussion on this paper should be addressed to the Technical Editor, Professor Lewis T. Wheeler, Department of Mechanical Engineering, University of Houston, Houston, TX 77204-4792, and will be accepted until four months after final publication of the paper itself in the ASME JOURNAL OF APPLIED MECHANICS.

Manuscript received by the ASME Applied Mechanics Division, May 24, 1996; final revision, July 24, 1997. Associate Technical Editor: S. A. Berger.

 Copyright © 1998 by ASME

Downloaded 04 May 2010 to 171.66.16.26. Redistribution subject to ASME license or copyright; see http://www.asme.org/terms/Terms_Use.cfm

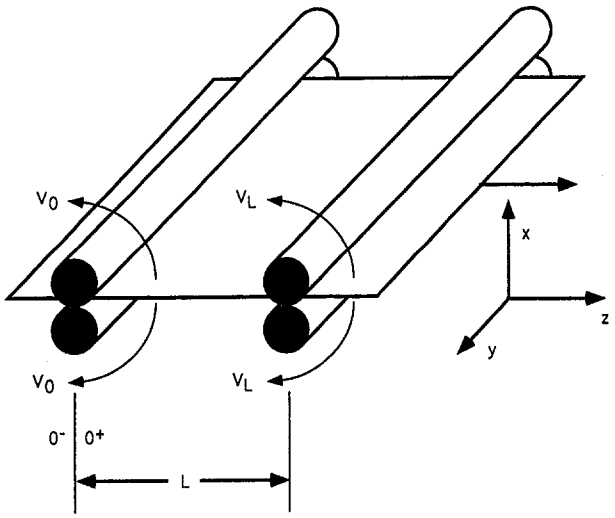

Fig. 1 Single open span with coordinate system

steady state. In practice, transient operations may represent only a small fraction of the operating time. However, the potential for difficulties is much greater than during steady-state operations and the need for theoretical guidance more acute.

2 Model Development

The primary goal of the model development was to predict the tension within the open spans during normal operations. A single span from a larger multispan web handling system and a Cartesian coordinate system are shown in Fig. 1. The positive z-axis coincides with the machine direction. The length of the span is L, and the tangential velocities of the first and second roller sets are v_0 and v_L, respectively. In practice, the roller sets are usually single rollers. The beginning of a span and the end of the previous span are designated 0^+ and 0^-, respectively. The isotropic pressure, p, was given by (Han, 1976):

$$p = -\tfrac{1}{3}(\sigma_{xx} + \sigma_{zz} + \sigma_{zz}), \tag{1}$$

where σ_{ij} $(i, j = x, y, z)$ are total stresses.

Several assumptions can be made in order to simplify the modeling:

1 The web materials are incompressible and isotropic.
2 Physical properties are constant within a span.
3 Stresses and velocity in the z-direction, v_z, are functions of z only.
4 The contact length between a roller and the web is zero.
5 No heat transfer or viscous heating.
6 No tram error.
7 Shear stresses are not present.
8 Gravitational, inertial, and air traction forces are insignificant.
9 No slip at the roller/web interface.

Assumption 3 does not preclude cross machine stresses or velocities. Significant cross machine stresses usually result from edge flutter or tram error. Cross machine velocities result from interactions of the web with the rollers, air drag, tram error, or necking. Cross machine velocities may cause lateral control problems or wrinkling. Significant edge flutter, lateral instability and wrinkling are unacceptable web handling regimes. The ability to predict when a system will cross over from a normal to an unacceptable operation mode would be of great value. However, the intent of this paper is to model tension during normal operations which would exclude regimes with any significant cross machine dependencies. Therefore, assumption 3 is a reflection of normal web handling operations.

As a consequence of assumption 4, no viscous deformations can occur in the web/roller contact regions. A multispan system can, therefore, be modeled as a series of open spans in which the material behaves viscoelastically, separated by the roller contact regions in which only elastic deformations can occur.

2.1 Governing Equations. A set of governing equations is developed below for the open spans followed by the development of the governing equation for the contact regions. In light of the goal to predict the tension, F, in each span, the first governing equation is a force balance. Assumption 8 allows the force balance to be written as

$$\sigma_{zz} = \frac{F}{A} - p_a \tag{2}$$

where A is the cross-sectional area of the web, σ_{ij} are total stresses, and p_a is the ambient pressure. In writing Eq. (2), one must recall that the total stress may be defined so as to include the ambient pressure (Bird et al., 1987). The total stresses are related to the deviatoric stresses, τ_{ij}, by

$$\tau_{ij} = \sigma_{ij} + p\delta_{ij} \tag{3}$$

where δ_{ij} are the coefficients of the identity tensor. Since $\sigma_{xx} = -p_a$ and $\sigma_{zz} - \sigma_{xx} = \tau_{zz} - \tau_{xx}$, the force balance can be rewritten as

$$F = A(\tau_{zz} - \tau_{xx}). \tag{4}$$

Assumption 8 also requires the tension within a span to be constant, therefore

$$\frac{\partial}{\partial z}[A(\tau_{zz} - \tau_{xx})] = 0. \tag{5}$$

By invoking assumption 1, the mass balance can be written as

$$\frac{\partial A}{\partial t} + \frac{\partial (Av_z)}{\partial z} = 0, \tag{6}$$

where t is time.

The White-Metzner equation, which was selected as the rheological equation of state, is described mathematically as

$$\underline{\underline{\tau}} + \frac{\eta}{G}\underline{\underline{\tau}}_{(1)} = \eta\underline{\underline{\dot{\gamma}}}, \tag{7}$$

where η is the viscosity function, G is the elastic modulus, $\underline{\underline{\dot{\gamma}}}$ is the rate of strain tensor defined as

$$\underline{\underline{\dot{\gamma}}} = \nabla\underline{v} + (\nabla\underline{v})^T, \tag{8}$$

where $\underline{v}$ is the velocity vector and $\underline{\underline{\tau}}_{(1)}$ is the upper convected derivative of the stress tensor:

$$\underline{\underline{\tau}}_{(1)} = \frac{D\underline{\underline{\tau}}}{Dt} - \{(\nabla\underline{v})^T \cdot \underline{\underline{\tau}} + \underline{\underline{\tau}} \cdot (\nabla\underline{v})\} \tag{9}$$

and

$$\frac{D\underline{\underline{\tau}}}{Dt} = \frac{\partial\underline{\underline{\tau}}}{\partial t} + \{\underline{v} \cdot \nabla\underline{\underline{\tau}}\}. \tag{10}$$

The White-Metzner equation was selected because it is a mathematically simple rheological equation of state that captures viscoelastic effects, preserves material objectivity, and allows some flexibility when attempting to model diverse materials such as paper, plastic films, and metal foils.

In this study, a power-law function (Bird et al., 1987) was chosen for the viscosity function:

Downloaded 04 May 2010 to 171.66.16.26. Redistribution subject to ASME license or copyright; see http://www.asme.org/terms/Terms_Use.cfm

$$\eta(\dot{\gamma}) = m(\dot{\gamma})^{n-1} \tag{11}$$

where m and n are the power-law coefficient and exponent, respectively; and $\dot{\gamma}$ is the second invariant of the rate of strain tensor defined as

$$\dot{\gamma} = (\tfrac{1}{2}\underline{\dot{\gamma}} : \underline{\dot{\gamma}})^{1/2}. \tag{12}$$

In the case of the elongational deformation that a web material would experience,

$$\dot{\gamma} = \sqrt{3}\left|\frac{\partial v_z}{\partial z}\right|. \tag{13}$$

When Eqs. (11) and (13) are substituted into the xx and zz-components of Eq. (7) and expanded the result is

$$\tau_{xx} + 3^{(n-1)/2}\left(\frac{m}{G}\right)\left|\frac{\partial v_z}{\partial z}\right|^{n-1}\left(\frac{\partial \tau_{xx}}{\partial t} + v_z\frac{\partial \tau_{xx}}{\partial z} + \tau_{xx}\frac{\partial v_z}{\partial z}\right) = -3^{(n-1)/2}m\left|\frac{\partial v_z}{\partial z}\right|^{n-1}\frac{\partial v_z}{\partial z} \tag{14}$$

and

$$\tau_{zz} + 3^{(n-1)/2}\left(\frac{m}{G}\right)\left|\frac{\partial v_z}{\partial z}\right|^{n-1}\left(\frac{\partial \tau_{zz}}{\partial t} + v_z\frac{\partial \tau_{zz}}{\partial z} - \tau_{zz}\frac{\partial v_z}{\partial z}\right) = 2\cdot 3^{(n-1)/2}m\left|\frac{\partial v_z}{\partial z}\right|^{n-1}\frac{\partial v_z}{\partial z}. \tag{15}$$

When time (t) and position (z) are specified, Eqs. (5), (6), (14), and (15) represent a set of four independent equations in four unknowns: v_z, A, τ_{xx}, and τ_{zz}.

In the contact region between the rollers and the web, the stress/strain relationship is given by Hooke's law:

$$\Delta\sigma_{zz} = E\Delta\epsilon_z \tag{16}$$

where E is Young's modulus and $\Delta\sigma_{zz}$ and $\Delta\epsilon_z$ are defined as

$$\Delta\sigma_{zz} = (\sigma_{zz})_{0^+} - (\sigma_{zz})_{0^-} \tag{17}$$

and

$$\Delta\epsilon_z = (\epsilon_z)_{0^+} - (\epsilon_z)_{0^-} \tag{18}$$

where ϵ_z is the extensional strain. An expression for $\Delta\sigma_{zz}$ can be found by subtracting the xx-component from the zz-component of Eq. (3) and recalling that $\sigma_{xx} = -p_a$:

$$\sigma_{zz} = (\tau_{zz} - \tau_{xx}) - p_a. \tag{19}$$

Substituting Eq. (19) into Eq. (17) yields

$$\Delta\sigma_{zz} = (\tau_{zz} - \tau_{xx})_{0^+} - (\tau_{zz} - \tau_{xx})_{0^-}. \tag{20}$$

An expression for $\Delta\epsilon_z$ can be found by considering the conservation of mass of an incompressible web undergoing an elongation. If a subscripted u denotes the undeformed state, and the subscripts 1 and 2 denote any two distinct elongated states, then

$$A_u = A_1[1 + (\epsilon_z)_1] = A_2[1 + (\epsilon_z)_2]. \tag{21}$$

If 0^- and 0^+ are substituted for 1 and 2, respectively, an expression for $(\epsilon_z)_{0^+}$ results after algebraic manipulation:

$$(\epsilon_z)_{0^+} = [1 + (\epsilon_z)_{0^-}]\frac{A_{0^-}}{A_{0^+}} - 1. \tag{22}$$

Since the web is incompressible and no mass accumulation is permitted in a contact region,

$$(v_z)_{0^-}A_{0^-} = (v_z)_{0^+}A_{0^+}. \tag{23}$$

Substitution of Eqs. (18), (20), (22), and (23) into Eq. (16) results in

$$(\tau_{zz} - \tau_{xx})_{0^+} = (\tau_{zz} - \tau_{xx})_{0^-} + E[1 + (\epsilon_z)_{0^-}]\left[\frac{(v_z)_{0^+}}{(v_z)_{0^-}} - 1\right]. \tag{24}$$

Equation (24) is the governing equation for the contact region and serves to link the current span of interest to the immediate up-stream span.

2.3 Boundary and Initial Conditions. Three boundary conditions were applied at $z = 0^+$

$$A(0^+, t) = A_{0^+}(t), \quad v_z(0^+, t) = v_{0^+}(t)$$
$$(\tau_{zz} - \tau_{xx})(0^+, t) = (\tau_{zz} - \tau_{xx})_{0^+}(t), \tag{25}$$

and a fourth boundary condition was applied at $z = L$.

$$v_z(L, t) = v_L(t) \tag{26}$$

In open loop control, the value of variables at the 0^+ position are initially unknown. However, the value of $v_{0^+}(t)$ may be determined during a trial and error solution. Once $v_{0^+}(t)$ is known, Eqs. (23) and (24) may then be used to find $A_{0^+}(t)$ and $(\tau_{zz} - \tau_{xx})_{0^+}$.

The initial conditions were

$$A(z, 0) = A_{00}(z), \quad v_z(z, 0) = v_{00}(z)$$
$$(\tau_{zz} - \tau_{xx})(z, 0) = (\tau_{zz} - \tau_{xx})_{00}(z) \tag{27}$$

where a subscripted 00 indicates a value at $t = 0$.

2.4 Nondimensionalization. Following the work of Fisher and Denn (1976), with appropriate modifications, a set of dimensionless variables was defined:

$$\phi = \frac{v_z}{(v_{zs})_{0^-}}, \quad T_{ij} = \tau_{ij}\frac{(A_s)_{0^+}}{F_s}, \quad a = \frac{A}{(A_s)_{0^+}}$$
$$\xi = \frac{z}{L}, \quad \theta = \frac{(v_{zs})_{0^-}}{L}t \tag{28}$$

where a subscripted s refers to steady-state values available from previous work (Guan et al., 1995). The dimensionless governing equations are

$$\frac{\partial}{\partial\xi}[a(T_{zz} - T_{xx})] = 0, \tag{29}$$

$$\frac{\partial a}{\partial\theta} + \frac{\partial(a\phi)}{\partial\xi} = 0, \tag{30}$$

$$T_{xx} + \mathrm{De}\left|\frac{\partial\phi}{\partial\xi}\right|^{n-1}\left(\frac{\partial T_{xx}}{\partial\theta} + \phi\frac{\partial T_{xx}}{\partial\xi} + T_{xx}\frac{\partial\phi}{\partial\xi}\right) = -N\left|\frac{\partial\phi}{\partial\xi}\right|^{n-1}\frac{\partial\phi}{\partial\xi}, \tag{31}$$

and

$$T_{zz} + \mathrm{De}\left|\frac{\partial\phi}{\partial\xi}\right|^{n-1}\left(\frac{\partial T_{zz}}{\partial\theta} + \phi\frac{\partial T_{zz}}{\partial\xi} - 2T_{zz}\frac{\partial\phi}{\partial\xi}\right) = 2N\left|\frac{\partial\phi}{\partial\xi}\right|^{n-1}\frac{\partial\phi}{\partial\xi}. \tag{32}$$

Downloaded 04 May 2010 to 171.66.16.26. Redistribution subject to ASME license or copyright; see http://www.asme.org/terms/Terms_Use.cfm

Two dimensionless groups naturally appear in Eqs. (31) and (32):

$$\mathrm{De} = 3^{(n-1)/2}\frac{m}{G}\left[\frac{(v_{zs})_{0^-}}{L}\right]^n, \tag{33}$$

and

$$N = \mathrm{De}G\frac{(A_s)_{0^+}}{F_s}. \tag{34}$$

De is the Deborah number which can be thought of as the ratio of the characteristic time of the material to the characteristic time of the operation in steady state. With caution, due to the complexity of Eqs. (29)–(32), the Deborah number may also be thought of as an indication of the length of the "memory" of the material. In the limit of De approaching infinity, the system will behave as if the material were purely elastic. If a purely elastic material is deformed under stress and some period of time passes before the stress is released, the material will regain the original shape regardless of the length of time it was under stress. In this context, an elastic material can be considered to have "infinite memory." In the limit of De going to zero, the system will behave as if the material response is purely viscous and there will be no memory of past states.

N may be regarded as the ratio of the characteristic viscous stress to the steady-state stress and in a purely mathematical sense is independent of De. However, in Eq. (34), $(A_s)_0^+$ and F_s are dependent on De. If comparisons are made between simulations of different operating conditions, but with the same material, G will be constant and N will be dependent on De. Therefore, only the effect of De or N need be considered. Since De is well known and has a more readily understood interpretation, the simulated results were correlated with De.

The dimensionless initial conditions for Eqs. (29) to (32) are

$$a(\xi, 0) = a_{00}(\xi), \quad \phi(\xi, 0) = \phi_{00}(\xi),$$
$$(T_{zz} - T_{xx})(\xi, 0) = T_{00}(\xi). \tag{35}$$

The dimensionless boundary conditions are

$$a(0^+, \theta) = a_{0^+}(\theta), \quad \phi(0^+, \theta) = \phi_{0^+}(\theta),$$
$$(T_{zz} - T_{xx})(0^+, \theta) = T_{0^+}(\theta), \tag{36}$$

and

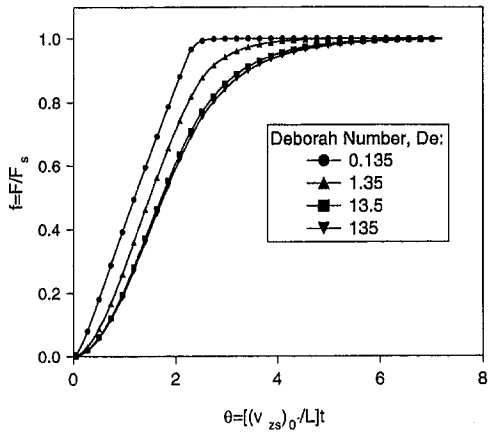

Fig. 2 Dimensionless tension as a function of dimensionless time with Deborah number as a parameter for a single open span in start-up

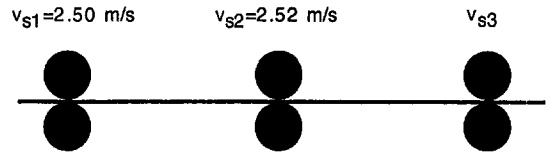

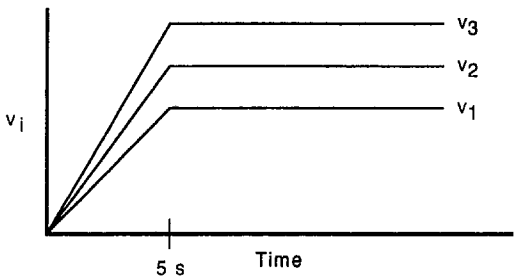

Fig. 3 Two span system in start-up

$$\phi(1, \theta) = \phi_1(\theta). \tag{37}$$

3 Solution of the Governing Equations

The governing equations were solved numerically by an explicit MacCormack finite difference scheme (MacCormack, 1969, 1982). Details of the discretization have been given elsewhere (Guan, 1995). The scheme had second-order accuracy and conditional stability. Since the boundary conditions for the viscoelastic response in the open span are unknown, the solution required a trial-and-error procedure and a shooting strategy to balance the elastic response in the contact regions with the viscoelastic response in the open spans.

4 Numerical Results and Discussion

Numerical simulations for start-up, transition between steady states, and a periodic disturbance about a steady state were conducted to examine the model performance. The behavior of viscoelastic webs was also compared to the behavior of purely elastic webs. In all of the following results, n was set equal to 1.

4.1 Start-Up Procedure. Start-up procedures vary from system to system depending on the configuration and control scheme. As a typical example, the tension was calculated in a single open span (Fig. 1) under the assumption of open loop control. The roller velocities were increased linearly from zero to their steady-state values over a dimensionless time period of $\theta_s = 2.25$ while the draw ratio ($D_R = v_L/v_{0^-}$) was held constant at 1.00222. The web material entered the system in an unstressed, unstrained state with a cross-sectional area of 1×10^{-4} m^2 and the value of n was set to 1.

The dimensionless tension, $f = F/F_s$, (where a subscripted "s" refers to steady state) in the span as a function of dimensionless time, with Deborah number as a parameter, can be seen in Fig. 2. The tension behavior clearly shows that the steady state tension is reached more rapidly in systems with smaller Deborah numbers. A decrease in Deborah number indicates that the web material adapts more rapidly to the current conditions and would be easier to control. Therefore, unlike steady-state operations (Guan et al., 1995), a low De would be more desirable in start up than a high De.

In order to investigate the important issue of tension transfer in a multispan system during start-up, the system shown in Fig. 3 was simulated. The system was configured with two 7.5-m

Downloaded 04 May 2010 to 171.66.16.26. Redistribution subject to ASME license or copyright; see http://www.asme.org/terms/Terms_Use.cfm

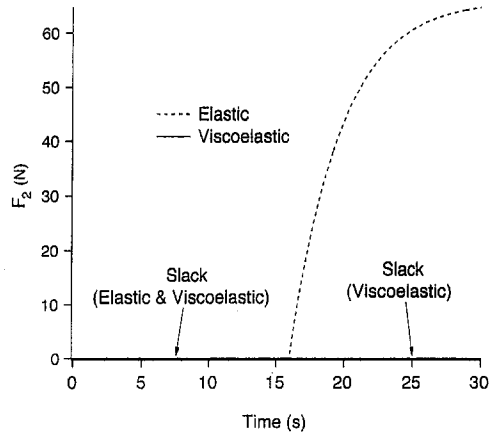

Fig. 4(a)

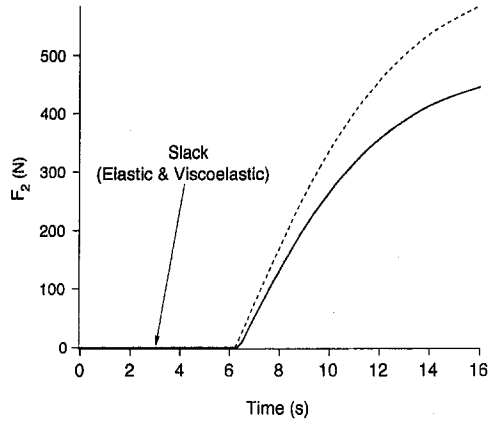

Fig. 4(b)

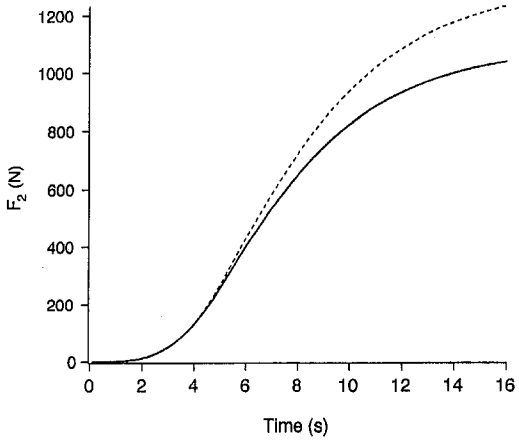

Fig. 4(c)

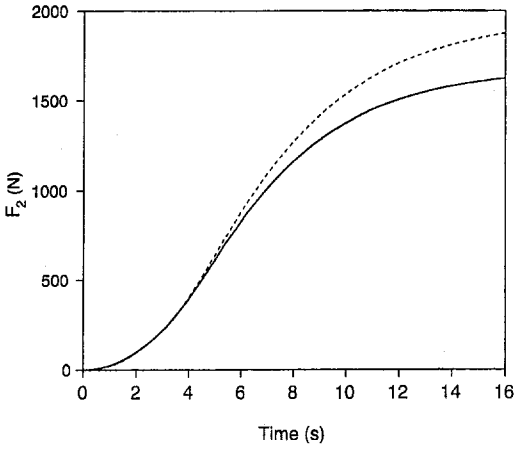

Fig. 4(d)

Fig. 4 Tension as function of time in the second span during start-up for (*a*) v_{s3} = 2.501 m/s, (*b*) v_{s3} = 2.51 m/s, (*c*) v_{s3} = 2.52 m/s, and (*d*) v_{s3} = 2.53 m/s

long spans. The rollers were linearly ramped from zero velocity to 2.50 m/s, 2.52 m/s and v_{s3}, respectively, over a start-up time, t_s, of five seconds. The Deborah numbers in each span were 10 and 10.08, respectively, with material properties: $G = 0.55 \times 10^9$ Pa, $m = 1.65 \times 10^{10}$ Pa·S, $n = 1$. The entry state was unstressed, unstrained with a cross-sectional area of 1×10^{-4} m^2.

In the limit of very small deformations, a precise relationship can be established between the Young's modulus, E, and the White-Metzner parameter, G, that allows comparisons of the viscoelastic model to the elastic model. In the limit of a very small deformation, Eq. (7) reduces to the Maxwell equation

$$\underline{\underline{\tau}} + \frac{\eta}{G}\frac{\partial \underline{\underline{\tau}}}{\partial t} = \eta \underline{\underline{\dot{\gamma}}}. \tag{38}$$

The elastic limit of the Maxwell equation is reached when η becomes very large compared to G. This is a counterintuitive observation, but can be understood by considering the mechanical analog to the Maxwell equation, which is a dash pot and spring in series, undergoing an elongational deformation. As η becomes very large there will be little or no deformation in the dash pot and the system will behave as though it were a spring alone. Therefore, in the elastic limit, Eq. (38) becomes

$$\frac{\partial \underline{\underline{\tau}}}{\partial t} = G \underline{\underline{\dot{\gamma}}}. \tag{39}$$

When the zz-component of Eq. (39) is integrated, the result is

$$\Delta \tau_{zz} = G \Delta \gamma_{zz}. \tag{40}$$

For uniaxial elongational deformation, Hooke's law states

$$\Delta \sigma_{zz} = E \Delta \epsilon_z, \tag{41}$$

where ϵ_z is the extension strain.

By writing Eq. (3), substituting Eq. (1) and recalling from the symmetry and nature of the deformation that $\sigma_{xx} = \sigma_{yy} = -p_a$, an expression for $\Delta \sigma_{zz}$ can be derived, if p_a is constant.

$$\Delta \sigma_{zz} = \tfrac{3}{2} \Delta \tau_{zz} \tag{42}$$

Also, by definition $\dot{\epsilon}_z = \partial v_z / \partial z$ and $\dot{\gamma}_{zz} = 2 \partial v_z / \partial z$, therefore

$$\Delta \epsilon_z = \tfrac{1}{2} \Delta \gamma_{zz}. \tag{43}$$

By substituting Eqs. (42) and (43) in Eq. (41)

$$\Delta \tau_{zz} = \frac{E}{3} \Delta \gamma_{zz}. \tag{44}$$

By comparing Eq. (44) to Eq. (40) E can be related to G:

$$E = 3G. \tag{45}$$

For comparison, simulations of an elastic web under the same conditions were run with $E = 1.65 \times 10^9$ Pa and extremely large values of η (i.e., large values of m).

In the first span, the tension showed the same general behavior as in the single span case (Fig. 2) since the tension in the first span is not affected by the downstream span. However, the

Downloaded 04 May 2010 to 171.66.16.26. Redistribution subject to ASME license or copyright; see http://www.asme.org/terms/Terms_Use.cfm

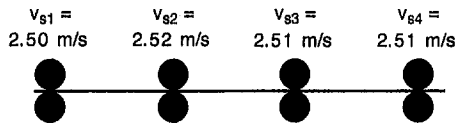

Fig. 5 A system with three open spans

tension behavior in the second span, as shown in Fig. 4, is different from the tension behavior in a single-span system. In Fig. 4(a), v_{s3} was set equal to 2.501 m/s. Since v_3 is greater than v_1 at all times, intuition leads to the conclusion that the tension in the second span will always be greater than zero. However, the simulation shows that the viscoelastic material is in an undesirable slack state at all times (including $t = \infty$) while elastic web is slack at $t < 16$ seconds. The persistent slackness in the viscoelastic web results from the fact that v_3 was too low to wind up the irrecoverable (viscous) deformation that occurred in the two spans. The period of slackness for the elastic web, on the other hand, is an example of the dynamic response of the tension transfer. At long times, under the conditions of Fig. 4(a), the value of F_2 asymptotically approaches 66 N which is in exact agreement with the steady state simulation (Guan et al. 1995).

When v_{s3} was increased to 2.51 m/s, (Fig. 4(b)) there was still slackness in both the viscoelastic and elastic materials a $t < 6.3$ seconds. However, the period of slackness was shorter and the velocity of the third roller was large enough to eventually wind up the viscous deformation. As v_{s3} was further increased, the period of slackness decreased (Fig. 4(c)), but reached zero (Fig. 4(d)) only when v_{s3} becomes sufficiently larger than v_{s2} to wind up the irrecoverable deformation.

Figure 4 demonstrates that periods of slackness may occur during start-up even though there is tension at steady state, and that the elastic model will predict normal operations under conditions that would cause sagging in a viscoelastic material.

4.2 Transition Between Two Steady States. Tension variations during transition from one steady state to another were illustrated by simulating the web line shown in Fig. 5. Initially the system was in steady-state operation with tangential rollers velocities of 2.50 m/s, 2.52 m/s, 2.51 m/s, and 2.51 m/s, respectively. The velocity of the third roller was linearly decreased by 0.009 m/s over 1.0 second. The tension in the second and third spans are plotted in Fig. 6.

Examination of Fig. 6 reveals three points. First, the third span (Fig. 6(b)) can be in tension even thought the upstream span (Fig. 6(a)) is slack. Second, the time required to reach a new steady state is considerably longer than the transition time, t_s. This conclusion can be drawn from the tension behavior of either span and is independent of the material being elastic or viscoelastic. Insights into how to reduce the time required to reach a new steady state can be drawn from the start up of a single span (Fig. 2) since start up is a special case of transition from one steady state to another. Therefore, a lower De would be expected to result in more rapid transitions. This conclusion is confirmed by noting in Figs. 6(a) and 6(b) that the new steady state is reached more rapidly by the viscoelastic material (De = 10 and 10.08 in spans 2 and 3, respectively) than for the elastic material that has De = ∞.

The third point of interest in Fig. 6 is the tension overshoot seen in Fig. 6(b). The tension overshoot results from the dynamic interactions of the system with the web and is independent of the rheological equation of state used to model the material. The significance of the tension overshot is that the web may be subjected to higher tensions than would be expected if only steady state simulation were considered, thereby damaging the web.

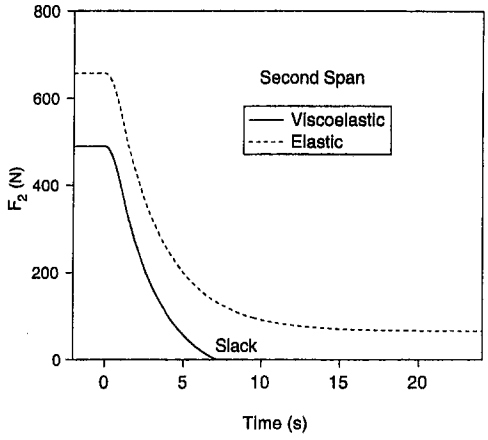

Fig. 6(a)

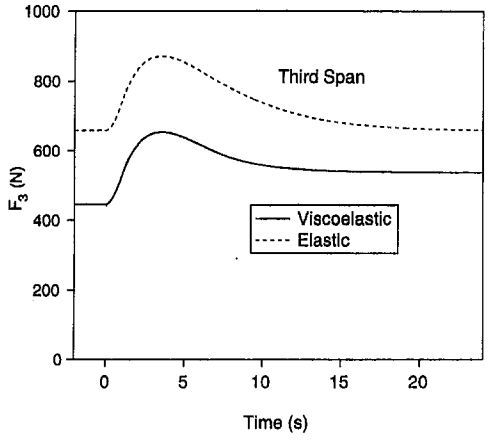

Fig. 6(b)

Fig. 6 Tension as a function of time for the (a) second span and (b) third span of a three-span system

4.3 Periodic Disturbance About a Steady State. Periodic disturbances in the roller velocity will result from eccentric mounting of a roller or from a nonideal roll geometry, known in the industry as flats and bumps. An eccentricity mounted roller, rotating with angular velocity ω, is depicted in Fig. 7. Based on the geometry, an average radius, R_{ave}, and an offset, δ_e, can be defined,

$$R_{ave} = \frac{R_{max} + R_{min}}{2}, \tag{46}$$

and

$$\delta_e = \frac{R_{max} - R_{min}}{2}. \tag{47}$$

The ratio, δ_e/R_{ave}, can be thought of as a dimensionless measure

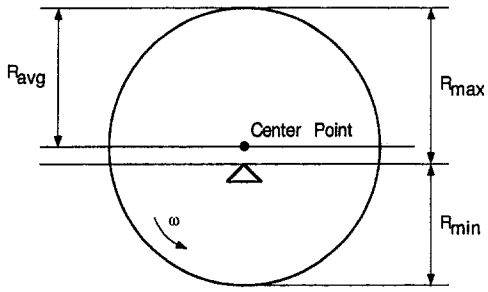

Fig. 7 Geometry of an eccentrically mounted roller

Downloaded 04 May 2010 to 171.66.16.26. Redistribution subject to ASME license or copyright; see http://www.asme.org/terms/Terms_Use.cfm

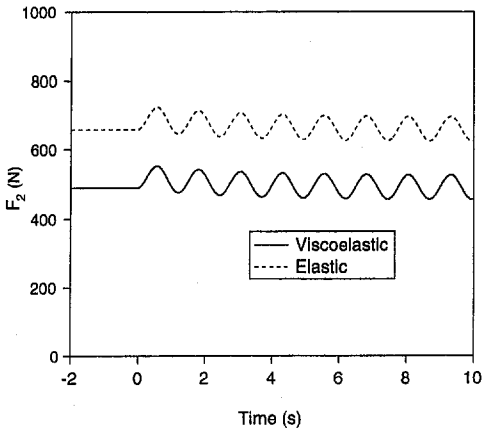

Fig. 8(*a*)

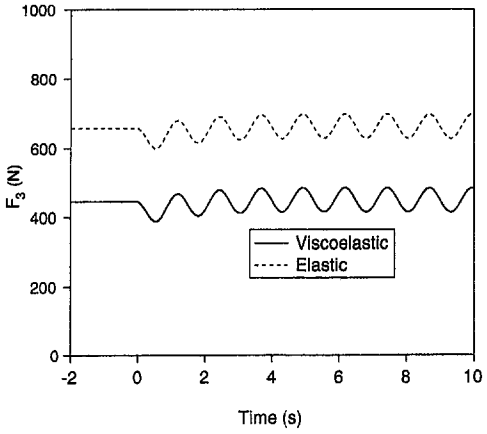

Fig. 8(*b*)

Fig. 8 Tension as a function of time in a three-span system due to a periodic disturbance in v_3: (*a*) span two, (*b*) span three

of the eccentricity. The tangential velocity of an eccentrically mounted roller, v, is

$$v = v_s + v_{\text{amp}} \sin(\omega t) \tag{48}$$

where v_{amp} is the amplitude of the velocity disturbance ($\omega\delta_e$), and ω is the angular velocity (v_s/R_{ave}). The draw ratio in the span immediately upstream of the eccentrically mounted roller is given by

$$D_R = \frac{v_{i+1}}{v_{si}} = D_{Rs}\left(1 + \frac{\delta_e}{R_{\text{avg}}} \sin \Omega\theta\right), \tag{49}$$

where D_{Rs} is the draw ratio at steady state; and $\Omega = [L/(v_{zs})_{0-}]\omega$, which can be thought of as dimensionless angular velocity. Ω can also be though of as the ratio of the characteristic time that the material spends in the open span to the characteristic time of the disturbance.

In order to examine the response of a system to an eccentrically mounted roller, the system shown in Fig. 5 was simulated. The system was at steady state until $t = 0$, when the third roller suddenly developed an eccentricity with velocity amplitude and angular velocity of 0.008367 m/s and 5.02 rad/s, respectively. The tension behavior as a function of time for the second and third spans is shown in Fig. 8. As would be expected, the tension shows sinusoidal behavior at $t > 0$. However, the average tension in each span rapidly returns to the same value as before the onset of the eccentricity. Therefore, the maximum tension within a span, but not the average tension, is affected by the eccentricity.

The effect of eccentricity on maximum tension was examined by allowing the second roller of Fig. 1 to be eccentrically mounted. The amplitude of the dimensionless tension, Δf, was plotted as a function of De, δ_e/R_{avg}, and Ω in Fig. 9. The value of Δf was taken at large values of time when the effect of any startup had decayed. Figure 9(a) demonstrates that Δf is greater for lower values of De. Figures 4, 6, and 8 all show that that the tension decreases as De decreases. Therefore, at low De, the tension will be small and the tension change due to a periodic disturbance will be relatively greater. Figure 9(b)

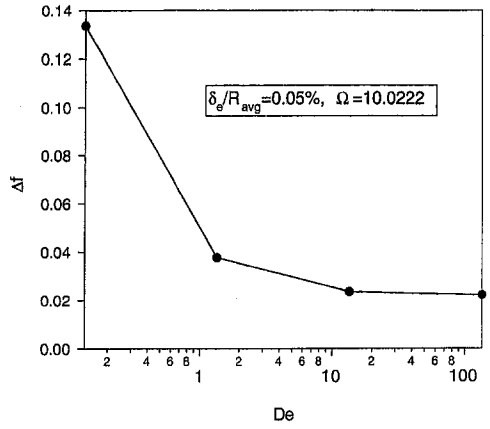

Fig. 9(*a*)

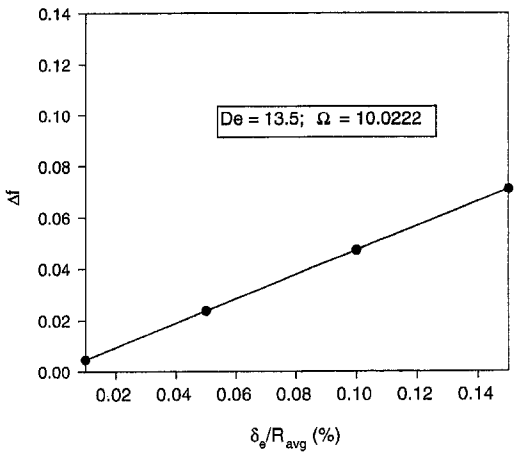

Fig. 9(*b*)

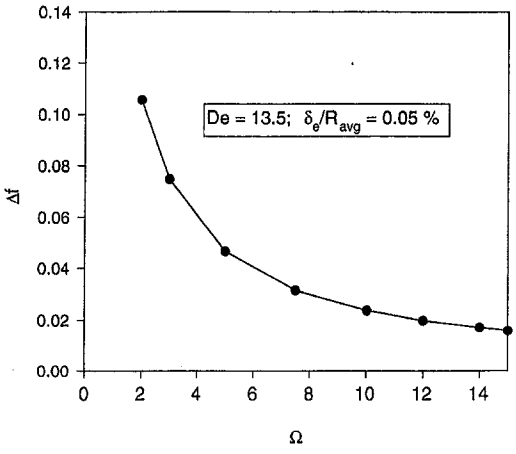

Fig. 9(*c*)

Fig. 9 Change in tension due to an eccentrically mounted roller in a single span system as a function of (*a*) Deborah number, (*b*) eccentricity, and (*c*) angular velocity

Downloaded 04 May 2010 to 171.66.16.26. Redistribution subject to ASME license or copyright; see http://www.asme.org/terms/Terms_Use.cfm

shows the effect of increasing the eccentricity. As would be expected, the tension fluctuation becomes greater as eccentricity increases. The decrease in Δf with increasing Ω, as shown in Fig. $9(c)$, can be understood by considering the definition of Ω and the fact that viscous stress is proportional to the rate of strain. Therefore, the tension difference due to a periodic disturbance would be proportional to the difference in the rate of strain that can be roughly approximated as $(v - v_{amp})/L$. If L decreases, the rate of strain and the tension will both increase, but Ω will decrease.

5 Conclusion

The dynamic behavior of elastic and viscoelastic webs has been modeled using the White-Metzner rheological equation of state. The behavior of viscoelastic webs with Deborah numbers ranging from near unity (highly viscous) to infinity (purely elastic) have been modeled for industrially important transient conditions.

In long time-scale dynamic transitions, such as start-up and transition between steady states, a system with viscoelasticity will respond to the change in operating conditions more rapidly than a system with a purely elastic material. A short time-scale disturbance of roller velocity, such as those found with an eccentric roller, does not affect the average response of the system, but produces variation of tension that can be correlated by the Deborah number and the geometry of the roller.

In general, accurate tension analysis and control of viscoelastic webs requires the use of the appropriate viscoelastic rheological models. Treating polymeric web materials as purely elastic is an oversimplification that can lead to improper processing of webs and reduced product quality.

Acknowledgment

The authors wish to acknowledge the Oklahoma Center for Integrated Design and Manufacture for supporting this work and Drs. Ku-Chin Lin and Karl N. Reid for many insightful discussions.

References

Baird, D. G., and Collias, D. I., 1995, *Polymer Processing Principles and Design,* Butterworth-Heinemann, Boston.

Brandenburg, G., 1976, "New Mathematical Models for Web Tension and Register Error," *Proc. 1, 3rd International IFAC Conf. on Instrumentation and Automation in the Paper, Rubber and Plastics Industries,* Brussels, May 24–26.

Campbell, D. P., 1958, *Process Dynamics,* John Wiley and Sons, New York.

Fisher, R. J., and Denn, M. M., 1976, "A Theory of Isothermal Melt Spinning and Draw Resonance," *AIChE Journal,* Vol. 22, No. 2, pp. 236–246.

Grenfell, K. P., 1963, "Tension Control on Paper-Making and Converting Machinery," *Proc., IEEE Ninth Annual Conference on Electrical Engineering in the Pulp and Paper Industry,* Boston, MA, June 20–21.

Guan, X., High, M. S., and Tree, D. A., 1995, "Viscoelastic Effects in Modeling Web Handling Systems: Steady-State Analysis," ASME JOURNAL OF APPLIED MECHANICS, Vol. 62, pp. 908–914.

Guan, X., 1995, "Modeling of Viscoelastic Effects on Web Handling System Behavior," Doctoral dissertation, Oklahoma State University, Stillwater, OK.

Han, C. D., 1976, *Rheology in Polymer Processing,* Academic Press, New York.

Hauptmann, E. G., and Cutshall, K. A., 1977, "Dynamic Mechanical Properties of Wet Paper Webs," *TAPPI Journal,* Vol. 60, No. 10, pp. 106–108.

MacCormack, R. W., 1969, "The Effect of Viscosity in Hypervelocity Impact Cratering," AIAA Paper No. 69–354, pp. 1–7.

MacCormack, R. W., 1982, "A Numerical Method for Solving the Equations of Compressible Viscous Flow," *AIAA Journal,* Vol. 20, No. 9, pp. 1275–1281.

Pecht, M. G., Johnson, M. W., Jr., and Rowlands, R. E., 1984, "Constitutive Equations for the Creep of Paper," *TAPPI Journal,* Vol. 67, No. 5, pp. 106–108.

Perkins, W. G., and Porter, R., 1977, "Review of Solid-State Deformation of Polyethylene and Nylon and Its Effects on Their Structure and Morphology," *Journal of Materials Science,* Vol. 12, pp. 2355–2388.

Reid, K. N., and Lin, K.-C., 1993, "Control of Longitudinal Tension in a Multi-Span Web Transport System During Start Up," *Proceedings of the Second International Conference on Web Handling,* Stillwater, OK.

Shin, K.-H., 1991, "Distributed Control of Tension in a Multi-Span Web Transport System," Doctoral dissertation, Oklahoma State University, Stillwater, OK.

Roylance, D., McElroy, P., and McGarry, F., 1980, "Viscoelastic Properties of Paper," *Fiber Science and Technology,* Vol. 13, pp. 411–421.

Taguchi, T., Morimoto, K., Terada, Y., and Sakamoto, Y., 1985, "Web Behavior on Newspaper Web Rotary Presses," Technical Review, Mitsubishi Heavy Industries, Ltd., Tokyo, Japan.

Ward, I. M., 1983, "Mechanical Properties of Solid Polymers, 2nd Ed., John Wiley and Sons, Chichester, UK.

Whitworth, D. P. D., and Harrison, M. C., 1983, "Tension Variations in Pliable Materials in Production Machinery," *Applied Mathematical Modeling,* Vol. 7, June, pp. 189–196.

Williams, D. G., 1983, "A Fiber Network Model Theory for the Wet Web Strength of Paper," *TAPPI Journal,* Mar., pp. 159–162.

Downloaded 04 May 2010 to 171.66.16.26. Redistribution subject to ASME license or copyright; see http://www.asme.org/terms/Terms_Use.cfm

A Variational Framework for Solution Method Developments in Structural Mechanics

K. C. Park
Fellow ASME.

C. A. Felippa
Mem. ASME.

Department of Aerospace Engineering Sciences
and Center for Aerospace Structures,
University of Colorado,
Campus Box 429,
Boulder, CO 80309

We present a variational framework for the development of partitioned solution algorithms in structural mechanics. This framework is obtained by decomposing the discrete virtual work of an assembled structure into that of partitioned substructures in terms of partitioned substructural deformations, substructural rigid-body displacements and interface forces on substructural partition boundaries. New aspects of the formulation are: the explicit use of substructural rigid-body mode amplitudes as independent variables and direct construction of rank-sufficient interface compatibility conditions. The resulting discrete variational functional is shown to be variationally complete, thus yielding a full-rank solution matrix. Four specializations of the present framework are discussed. Two of them have been successfully applied to parallel solution methods and to system identification. The potential of the two untested specializations is briefly discussed.

1 Introduction

Variational principles in structural mechanics have been seminal in the development of mathematical models and discretization methods such as finite elements. While a rich family of variational principles have been constructed and used for those purposes (Argyris and Kelsey, 1955; Washizu, 1968; Fraeijs de Veubeke, 1974; Atluri, 1975; Oden and Reddy, 1982; Felippa, 1994), a majority of general-purpose structural analysis computer programs have essentially embraced the displacement-based discretization and solution paradigm: generating the stiffness matrix and nodal forces, and solving for the nodal displacements from the resulting master stiffness equations.

Recent developments have motivated reexamination of that paradigm. Those developments include: parallel computations based on substructural domain decomposition, inverse problems in system identification and damage detection of large-scale structures, and analysis of coupled-field problems such as fluid-structure-control interaction and electromechanical problems. The conventional displacement method has been found to be deficient for various reasons noted below. These deficiencies have prompted research into discretization and solution procedures that can take advantage of parallel computing architectures, that are flexible and robust for large-scale identification and model updating, and that meet the demands of coupled-field analysis.

A common approach followed in that research is substructure-by-substructure decomposition. This decomposition naturally divides the problem into two: substructure-level or local, and partition interface or global. The local problem considers each substructure as a separate problem under substructure-level loading plus interface forces or interface displacements that are assumed to be known. This is solved by standard procedures. The interface problem solves for interface unknowns to satisfy equilibrium and compatibility equations of the assembled system. Here a great variety of methods is possible depending on the choice of interface unknowns. The complete solution is then obtained by superposing the local and interface solutions.

Decomposition into substructures has obvious appeal for massively parallel processing. If each substructure is assigned to a different processor, the local problem is trivially parallelizable. On the other hand, solving the interface problem necessarily entails processor intercommunication. Directly solving for the interface displacement unknowns, which is the common practice in multilevel finite element codes on sequential computers, leads to serious communication bottlenecks that eventually destroy scalability as the number of processors increases into the hundreds. In the case of system identification applications, purely displacement-based approaches can lead to modeling and robustness difficulties in processing experimental vibration records. In summary, while the direct stiffness equation solver constitutes a basic tool for each individual substructure, efficient interface solution procedures for the coupled substructures depend on how the coupling mechanisms are modeled and approximated.

We present here a variational framework of discrete structural mechanics that is primarily intended for the development of substructure-based solution algorithms. The starting point is the conventional displacement method and the associated direct stiffness equations. The decision is not accidental. It insures that the interior problem can be easily implemented into existing structural analysis programs, since the formation of those equations can make full use of existing finite element libraries and assembly procedures. The decomposition into substructures is translated into variational formalism using Lagrange multipliers that enforce the interface compatibility constraints. A novel aspect is then introduced: the substructural displacement is further decomposed into deformational and rigid-body components; a treatment motivated by the need to handle "floating" substructures. A general functional derived through these steps has four independent state variables: the substructural interaction forces, the deformational displacements at substructural interfaces, the amplitudes of the substructural rigid-body modes, and the total global displacements at interface nodes.

A number of special solution methods can be derived from the general functional either by invoking different interface compatibility conditions or by eliminating one or more of the unknown state variables. All such methods share the virtue of being able to use existing finite element libraries, because a common basis for all matrix manipulations at the substructure

Contributed by the Applied Mechanics Division of THE AMERICAN SOCIETY OF MECHANICAL ENGINEERS for publication in the ASME JOURNAL OF APPLIED MECHANICS.

Discussion on this paper should be addressed to the Technical Editor, Professor Lewis T. Wheeler, Department of Mechanical Engineering, University of Houston, Houston, TX 77204-4792, and will be accepted until four months after final publication of the paper itself in the ASME JOURNAL OF APPLIED MECHANICS.

Manuscript received by the ASME Applied Mechanics Division, Sept. 16, 1996; final revision, May 8, 1997. Associate Technical Editor: J. N. Reddy.

Copyright © 1998 by ASME

Downloaded 04 May 2010 to 171.66.16.26. Redistribution subject to ASME license or copyright; see http://www.asme.org/terms/Terms_Use.cfm

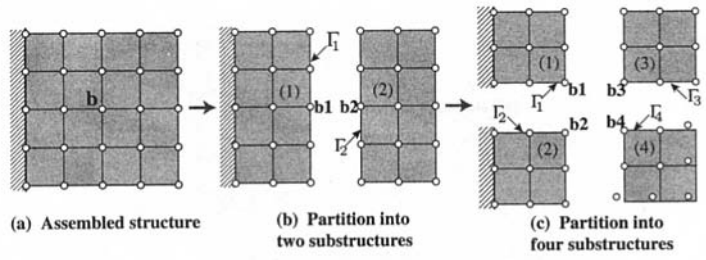

Fig. 1 Partitioning of a structure into substructures. (*a*) The assembled structure. (*b*) Partition into two substructures; for node b, the displacement compatibility condition is uniquely defined as given by Eq. (1). (*c*) Partition into four substructures; for node b, the displacement compatibility condition can be expressed in different forms exemplified by Eq. (4).

level is the construction of the free-free stiffness matrices and force vectors produced by those libraries. Four specializations are presented in some detail: (1) a direct flexibility method (DFM) that has been proven effective in parallel computations; (2) a substructural boundary-displacement method that may be viewed as dual of the DFM; (3) a minimally redundant flexibility method that offers potential for structural optimization; and (4) a method tailored for the inverse problem of extracting substructural flexibility from measured global flexibility data for damage detection and distributed control design.

2 Motivation

The objective of this paper is to present a variational framework for the formulation of the governing equations of structural mechanics for partitioned substructures, and to study specializations of those equations for the applications described in the Introduction. As shown below, a straightforward variational treatment may encounter formulation difficulties, which can adversely affect the computational implementation.

Consider the plane structure of Fig. 1(*a*), subjected to static loading. This is partitioned into two substructures as shown in Fig. 1(*b*). For this case, the displacements along the partitioned boundaries Γ_1 and Γ_2 must be the same because they represent the assembled structural displacements. Specifically,

$$\mathbf{u}_{\Gamma_1} - \mathbf{u}_{\Gamma_2} = 0 \tag{1}$$

which will be here called an interface displacement compatibility condition or simply an interface condition. In the above equation Γ_1 and Γ_2 refer to the substructural partition boundaries, and $\mathbf{u}_{\Gamma_1}$ and $\mathbf{u}_{\Gamma_2}$ designate the interface displacements pertaining to substructures 1 and 2, respectively.

The system of Fig. 1(*b*) can be modeled in terms of the two substructural discrete energy functionals augmented by the interface condition (1) treated by Lagrange multipliers:

$$\Pi(\mathbf{u}^{(1)}, \mathbf{u}^{(2)}, \boldsymbol{\lambda}) = (\tfrac{1}{2}\mathbf{u}^{(1)T}\mathbf{K}^{(1)}\mathbf{u}^{(1)} - \mathbf{u}^{(1)T}\mathbf{f}^{(1)}) + (\tfrac{1}{2}\mathbf{u}^{(2)T}\mathbf{K}^{(2)}\mathbf{u}^{(2)} - \mathbf{u}^{(2)T}\mathbf{f}^{(2)}) + \boldsymbol{\lambda}^T(\mathbf{u}_{\Gamma_1} - \mathbf{u}_{\Gamma_1}) \tag{2}$$

where the superscripts $\{(1), (2)\}$ designate substructures, $\mathbf{f}^{(s)}$ is the applied force vector acting on each substructure, $\mathbf{K}^{(s)}$ is the substructural stiffness matrix, and $\boldsymbol{\lambda}$ is the vector of Lagrange multipliers that enforces (1). The stationarity condition for Π leads to the following equations:

$$\begin{bmatrix} \mathbf{K}^{(1)} & \mathbf{0} & \mathbf{C}^{(1)} \\ \mathbf{0} & \mathbf{K}^{(2)} & -\mathbf{C}^{(2)} \\ \mathbf{C}^{(1)T} & -\mathbf{C}^{(2)T} & \mathbf{0} \end{bmatrix} \begin{Bmatrix} \mathbf{u}^{(1)} \\ \mathbf{u}^{(2)} \\ \boldsymbol{\lambda} \end{Bmatrix} = \begin{Bmatrix} \mathbf{f}^{(1)} \\ \mathbf{f}^{(2)} \\ \mathbf{0} \end{Bmatrix},$$

$$\mathbf{u}_{\Gamma_1} = \mathbf{C}^{(1)T}\mathbf{u}^{(1)}, \quad \mathbf{u}_{\Gamma_2} = \mathbf{C}^{(2)T}\mathbf{u}^{(2)}. \tag{3}$$

Here $\mathbf{C}^{(1)T}$ and $\mathbf{C}^{(2)T}$ are Boolean matrices that extract the substructural partition-boundary displacements $\mathbf{u}_{\Gamma_1}$ and $\mathbf{u}_{\Gamma_2}$ from the substructural displacements $\mathbf{u}^{(1)}$ and $\mathbf{u}^{(2)}$.

While it is straightforward to construct the interface condition (1) for the case of Fig. 1(*b*), the construction of interface conditions for more general partitions raises nonuniqueness issues. To illustrate this, consider the example structure now divided into four substructures as shown in Fig. 1(*c*). For the ensuing discussion we focus on the center node **b** shown in Fig. 1(*a*), which is called a "cross point" in some of the domain-decomposition literature. Because this node belongs to all four substructures, it is identified by labels ($b1$, $b2$, $b3$, $b4$) as depicted in Fig. 1(*c*). The interface kinematic conditions for this node can be expressed in many ways. Four possibilities are

$$\begin{aligned}
&\text{Case 1:} \quad \mathbf{u}_{b1} - \mathbf{u}_{b2} = 0, \quad \mathbf{u}_{b2} - \mathbf{u}_{b3} = 0, \quad \mathbf{u}_{b3} - \mathbf{u}_{b4} = 0 \\
&\qquad\qquad \mathbf{u}_{b4} - \mathbf{u}_{b1} = 0 \\
&\text{Case 2:} \quad \mathbf{u}_{b1} - \mathbf{u}_{b2} = 0, \quad \mathbf{u}_{b1} - \mathbf{u}_{b3} = 0, \quad \mathbf{u}_{b1} - \mathbf{u}_{b4} = 0 \\
&\qquad\qquad \mathbf{u}_{b2} - \mathbf{u}_{b3} = 0, \quad \mathbf{u}_{b2} - \mathbf{u}_{b4} = 0, \quad \mathbf{u}_{b3} - \mathbf{u}_{b4} = 0 \\
&\text{Case 3:} \quad \mathbf{u}_{b1} - \mathbf{u}_{b2} = 0, \quad \mathbf{u}_{b1} - \mathbf{u}_{b3} = 0, \quad \mathbf{u}_{b1} - \mathbf{u}_{b4} = 0 \\
&\text{Case 4:} \quad \mathbf{u}_{b1} - \mathbf{u}_{b2} = 0, \quad \mathbf{u}_{b2} - \mathbf{u}_{b3} = 0, \quad \mathbf{u}_{b3} - \mathbf{u}_{b4} = 0.
\end{aligned} \tag{4}$$

Cases 1 and 2 lead to redundant interface conditions, implying that the resulting Lagrange multipliers become linearly dependent. Cases 3 and 4 lead to linearly independent Lagrange multipliers. For a three-dimensional solid structure modeled by brick elements, there will be typically eight substructures meeting at a cross point. The number of nonunique interface conditions, and particularly the possibility of redundancies, grows rapidly as the number of substructures meeting at a cross point increases.

If the Lagrange multipliers are linearly dependent, the standard variational calculus no longer applies. One must resort to restricted variational principles (Finlayson, 1972) to handle the redundancies. In such principles, troublesome variations are carried out by ad hoc rules, and hence the "Euler equations" do not necessarily represent true stationarity conditions. The theoretical and computational implications of using restricted variational principles in structural mechanics are not well understood.

A second issue associated with the use of the principle of virtual work plus the interface condition in (2) is computational in nature. Since the number of interior substructural unknowns can be substantially larger than that of interface nodes, it is often computationally advantageous to eliminate $\mathbf{u}^{(1)}$ and $\mathbf{u}^{(2)}$ and solve for the interface Lagrange multipliers $\boldsymbol{\lambda}$. As illustrated

Downloaded 04 May 2010 to 171.66.16.26. Redistribution subject to ASME license or copyright; see http://www.asme.org/terms/Terms_Use.cfm

in Figure 1(b), substructure 1 is fully constrained so that $\mathbf{u}^{(1)}$ can be obtained simply through the ordinary inverse:

$$\mathbf{u}^{(1)} = \mathbf{K}^{(1)^{-1}}(\mathbf{f}^{(1)} - \mathbf{C}^{(1)}\boldsymbol{\lambda}). \tag{5}$$

But since substructure 2 is floating (in fact free-free), $\mathbf{u}^{(2)}$ is given by

$$\mathbf{u}^{(2)} = \mathbf{K}^{(2)^{+}}(\mathbf{f}^{(2)} + \mathbf{C}^{(2)}\boldsymbol{\lambda}) + \mathbf{R}^{(2)}\alpha,$$

$$\mathbf{R}^{(2)} = \mathbf{I} - \mathbf{K}^{(2)^{+}}\mathbf{K}^{(2)} \tag{6}$$

where $\mathbf{K}^{(2)^{+}}$ is the Moore-Penrose generalized inverse of $\mathbf{K}^{(2)}$, and α is an arbitrary vector.

Although a minimum-norm solution of $\mathbf{u}^{(2)}$ is achieved by choosing $\alpha = 0$ (Stewart and Sun, 1990), this choice generally leads to a physically incorrect solution. For the columns of $\mathbf{R}^{(2)}$ span the orthonormalized rigid-body motions of substructure 2. Vector α defines a rigid motion amplitude that brings, within a deformational motion, the interface nodes $\mathbf{u}_{\Gamma_2}$ of substructure 2 to coincide with $\mathbf{u}_{\Gamma_1}$ of substructure 1. Most existing variational principles for partitioned substructures have not dealt explicitly with the displacement decomposition (6).

It should be noted that the use of more general variational principles such as the Hu-Washizu and Hellinger-Reissner principles (Washizu, 1968) as well as parametrized variational principles (Felippa, 1994) face the same formulation and computational difficulties when they are applied to formulate the governing discrete equations of partitioned substructures. We now present a variational framework that alleviates the two difficulties identified above.

3 Variational Decomposition of Global Direct Stiffness Equation

The variational framework presented here utilizes the same mesh definition and finite element libraries available in existing structural analysis programs. To facilitate this reuse, we begin with the displacement-based discrete energy functional Π for a linear structure under static loading given by

$$\Pi(\mathbf{u}_g) = \tfrac{1}{2}\mathbf{u}_g^T\mathbf{K}_g\mathbf{u}_g - \mathbf{u}_g^T\mathbf{f}_g, \quad \mathbf{K}_g = \mathbf{L}^T\mathbf{K}\mathbf{L} \tag{7}$$

where $\mathbf{u}_g$ is the discrete global displacement vector, $\mathbf{f}_g$ is the global applied load, $\mathbf{K}_g$ is the assembled global stiffness matrix, $\mathbf{L}$ is the Boolean assembly matrix, and $\mathbf{K}$ is the block diagonal element-by-element stiffness matrix given by

$$\mathbf{K} = \begin{bmatrix} \mathbf{K}^{(1)} & & & \\ & \mathbf{K}^{(2)} & & \\ & & \ddots & \\ & & & \mathbf{K}^{(N_s)} \end{bmatrix} \tag{8}$$

in which $\{\mathbf{K}^{(i)}, i = 1, \ldots, N_s\}$ represent substructural stiffness matrices, and N_s is the number of partitioned substructures.

The stationarity of (7) leads to the well-known direct stiffness equation

$$\delta\Pi = 0 \Rightarrow \mathbf{K}_g\mathbf{u}_g = \mathbf{f}_g. \tag{9}$$

Next, we modify Π to accommodate substructural partitioning such as that illustrated in Fig. 2.

3.1 Construction of Partitioned Interface Condition. Consider an assembled structure built with N_s substructures, such as the one illustrated in Fig. 2 (in which $N_s = 4$). The substructural nodal displacements $\mathbf{u}$ are related to the assembled global displacements $\mathbf{u}_g$ through the assembly matrix $\mathbf{L}$:

$$\mathbf{u} = \mathbf{L}\mathbf{u}_g, \quad \mathbf{u}^T = \langle \mathbf{u}^{(1)^T} \ldots \mathbf{u}^{(N_s)^T} \rangle \tag{10}$$

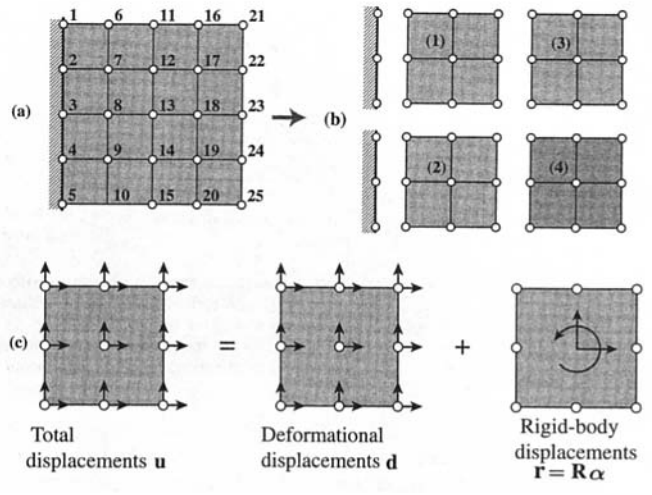

Fig. 2 Decomposition of complete structure into four substructures. (*a*) Total assembled structure for which the global displacements $\mathbf{u}_g$ are associated with each node. (*b*) Decomposition into four substructures. (*c*) Substructural displacements u are further decomposed into deformational displacements d and rigid-mode displacements r.

On the other hand, the global force vector $\mathbf{f}_g$ and the substructural force vector that is conjugate to the substructural displacement $\mathbf{u}$ are related by

$$\mathbf{L}^T\mathbf{f} = \mathbf{f}_g, \quad \mathbf{f}^T = \langle \mathbf{f}^{(1)^T} \ldots \mathbf{f}^{(N_s)^T} \rangle. \tag{11}$$

Observe that (10) represents a unique relation between the global displacement $\mathbf{u}_g$ and the substructural displacement $\mathbf{u}$ regardless of the number of nodes involved at any substructural interface (or partition-boundary) node. In other words, (10) can be used to uniquely define the substructural interface compatibility condition. To this end, we introduce a Boolean matrix $\mathbf{B}$ that relates the interface displacements $\mathbf{u}_b$ to substructural displacements by

$$\mathbf{u}_b = \mathbf{B}^T\mathbf{u}. \tag{12}$$

Combining (10) and (12) yields

$$\mathbf{B}^T(\mathbf{u} - \mathbf{L}\mathbf{u}_g) = 0. \tag{13}$$

The decomposition process to express the discrete energy functional in terms of partitioned substructures requires several steps. First, we partition the global stiffness matrix $\mathbf{K}_g$ in terms of the substructural stiffness matrix given by (8):

$$\Pi(\mathbf{u}_g) = \tfrac{1}{2}\mathbf{u}_g^T\mathbf{L}^T\mathbf{K}\mathbf{L}\mathbf{u}_g - \mathbf{u}_g^T\mathbf{f}_g. \tag{14}$$

Second, the global force vector $\mathbf{f}_g$ is substituted in terms of the substructural force vector $\mathbf{f}$ using (11):

$$\Pi(\mathbf{u}_g) = \tfrac{1}{2}\mathbf{u}_g^T\mathbf{L}^T\mathbf{K}\mathbf{L}\mathbf{u}_g - \mathbf{u}_g^T\mathbf{L}^T\mathbf{f}. \tag{15}$$

This equation represents the virtual work for the assembled structure.

To complete the physical separation in variational language the term $\mathbf{L}\mathbf{u}_g$ in (15) is replaced by the partitioned substructural displacement $\mathbf{u}$ using (10), and the resulting virtual work augmented with the interface condition (13) is treated by Lagrange multipliers $\boldsymbol{\lambda}_b$:

$$\Pi(\mathbf{u}, \mathbf{u}_g, \boldsymbol{\lambda}_b) = \tfrac{1}{2}\mathbf{u}^T\mathbf{K}\mathbf{u} - \mathbf{u}^T\mathbf{f} + \boldsymbol{\lambda}_b^T\mathbf{B}^T(\mathbf{u} - \mathbf{L}\mathbf{u}_g). \tag{16}$$

Remark 1. For the example partition of Fig. 1(c), the interface condition (13) provides

$$\langle \mathbf{u}_{b1}^T \quad \mathbf{u}_{b2}^T \quad \mathbf{u}_{b3}^T \quad \mathbf{u}_{b4}^T \rangle = \mathbf{u}_b^T[\mathbf{I} \quad \mathbf{I} \quad \mathbf{I} \quad \mathbf{I}] \tag{17}$$

Downloaded 04 May 2010 to 171.66.16.26. Redistribution subject to ASME license or copyright; see http://www.asme.org/terms/Terms_Use.cfm

where $\mathbf{u}_b$ is the displacement at node **b** for the assembled structure shown in Fig. 1(a), and **I** is an identity matrix whose dimension is the same as the number of degrees-of-freedom at that node. This and similar representations lead to rank-sufficient interface conditions at any cross point, providing an alternative to (4).

3.2 Decomposition of Substructural Displacements. Although the constrained virtual work derived in (16) is associated with linearly independent Lagrange multipliers, those substructural stiffness matrices corresponding to floating or partially floating substructures are singular. As illustrated in (6), this can lead to computational difficulties. To circumvent singularities, we decompose the substructural displacement **u** into the deformational and rigid-body components (see Fig. 2(c)):

$$\mathbf{u} = \mathbf{d} + \mathbf{r} \tag{18}$$

where **d** and **r** are the deformational and rigid-body displacements, respectively. The rigid-body displacement can be expressed in terms of the substructural rigid-body modes **R** and associated generalized amplitudes collected in vector $\boldsymbol{\alpha}$:

$$\mathbf{r} = \mathbf{R}\boldsymbol{\alpha} \quad \text{such that} \quad \mathbf{KR} = 0$$

$$\boldsymbol{\alpha} = \begin{Bmatrix} \boldsymbol{\alpha}^{(1)} \\ \cdot \\ \cdot \\ \boldsymbol{\alpha}^{(N_s)} \end{Bmatrix}, \quad \mathbf{R} = \begin{bmatrix} \mathbf{R}^{(1)} & & & \\ & \mathbf{R}^{(2)} & & \\ & & \cdot & \\ & & & \mathbf{R}^{(N_s)} \end{bmatrix} \tag{19}$$

where it is understood that $\mathbf{R}^{(k)}$ would be zero for substructures whose physical boundary, not partitioned interface boundary, conditions are fully constrained.

Substituting (19) and (18) into (16) leads to the four-variable functional

$$\Pi(\mathbf{d}, \boldsymbol{\lambda}_b, \boldsymbol{\alpha}, \mathbf{u}_g) = \tfrac{1}{2}\mathbf{d}^T\mathbf{K}\mathbf{d} - \mathbf{d}^T\mathbf{f} + \boldsymbol{\lambda}_b^T\mathbf{B}^T(\mathbf{d} - \mathbf{L}\mathbf{u}_g) + \boldsymbol{\alpha}^T\mathbf{R}^T(-\mathbf{f} + \mathbf{B}\boldsymbol{\lambda}_b). \tag{20}$$

The four state variables $(\mathbf{d}, \boldsymbol{\lambda}_b, \boldsymbol{\alpha}, \mathbf{u}_g)$ in the above functional are linearly independent because the substructural interface-node extraction matrix **B** has full row rank. In other words, it is variationally complete. Thus, it is legal to vary Π as

$$\delta\Pi = \delta\mathbf{d}^T(\mathbf{K}\mathbf{d} - \mathbf{f} + \mathbf{B}\boldsymbol{\lambda}_b) + \delta\boldsymbol{\lambda}_b^T\mathbf{B}^T(\mathbf{d} - \mathbf{L}\mathbf{u}_g + \mathbf{R}\boldsymbol{\alpha}) + \delta\boldsymbol{\alpha}^T\mathbf{R}^T(-\mathbf{f} + \mathbf{B}\boldsymbol{\lambda}_b) - \delta\mathbf{u}_g^T\mathbf{L}^T\mathbf{B}\boldsymbol{\lambda}_b. \tag{21}$$

Setting this variation to zero yields

$$\begin{bmatrix} \mathbf{K} & \mathbf{B} & 0 & 0 \\ \mathbf{B}^T & 0 & \mathbf{R}_b & -\mathbf{L}_b \\ 0 & \mathbf{R}_b^T & 0 & 0 \\ 0 & -\mathbf{L}_b^T & 0 & 0 \end{bmatrix} \begin{Bmatrix} \mathbf{d} \\ \boldsymbol{\lambda}_b \\ \boldsymbol{\alpha} \\ \mathbf{u}_g \end{Bmatrix} = \begin{Bmatrix} \mathbf{f} \\ 0 \\ \mathbf{R}^T\mathbf{f} \\ 0 \end{Bmatrix}$$

$$\mathbf{R}_b = \mathbf{B}^T\mathbf{R}, \quad \mathbf{L}_b = \mathbf{B}^T\mathbf{L}. \tag{22}$$

Remark 2. The preceding variationally decomposed Eq. (22) has a configuration similar to the well-known hybrid formulation linking two or more subdomains (see, e.g., p. 380 of Zienkiewicz and Taylor, 1989). Specifically, for two substructures the hybrid treatment yields

$$\begin{bmatrix} \mathbf{F}^{(1)} & \mathbf{D}^{(1)} & 0 & 0 & 0 \\ \mathbf{D}^{(1)^T} & 0 & 0 & 0 & \mathbf{C}^{(1)} \\ 0 & 0 & \mathbf{F}^{(2)} & \mathbf{D}^{(2)} & 0 \\ 0 & 0 & \mathbf{D}^{(2)^T} & 0 & \mathbf{C}^{(2)} \\ 0 & \mathbf{C}^{(1)^T} & 0 & \mathbf{C}^{(2)^T} & 0 \end{bmatrix} \begin{Bmatrix} \boldsymbol{\sigma}^{(1)} \\ \mathbf{u}^{(1)} \\ \boldsymbol{\sigma}^{(2)} \\ \mathbf{u}^{(2)} \\ \boldsymbol{\lambda} \end{Bmatrix} = \begin{Bmatrix} 0 \\ \mathbf{f}^{(1)} \\ 0 \\ \mathbf{f}^{(2)} \\ 0 \end{Bmatrix} \tag{23}$$

where **F**, **D** are stress and strain-displacement operators, respectively; **C** is the interface condition; and $\boldsymbol{\sigma}$ and **u** are the stress and displacement interface freedoms, respectively. Note, however, that the substructural matrix block

$$\mathbf{H} = \begin{bmatrix} \mathbf{F} & \mathbf{D} \\ \mathbf{D}^T & 0 \end{bmatrix} \tag{24}$$

becomes singular whenever that substructure is floating after partitioning, leading to computational difficulties. In addition to this succeptibility to rank-deficiency, matrix **D** appearing in (24) depends on element properties. On the other hand, the matrices **R** and **L** in (22) are *element-independent* because they are constructed directly from nodal connectivity and geometric information.

4 A Direct Flexibility Method for Parallel Computation

When the global structure is partitioned into substructures in which the number of interface nodes is substantially smaller than that of interior nodes, it is attractive to treat the interface force $\boldsymbol{\lambda}_b$ as the primary solution variable. To this end, first we solve for the substructural deformation **d** from the first row of (22):

$$\mathbf{d} = \mathbf{K}^+(\mathbf{f} - \mathbf{B}\boldsymbol{\lambda}_b) \tag{25}$$

where $\mathbf{K}^+$ is a generalized inverse of **K**. It should be emphasized that the singularity of the substructural stiffness matrix **K** does not affect the accuracy of the deformation vector **d** if $\mathbf{K}^+$ is computed as described in Section 9.

Second, we represent the interface displacement extraction matrix **B** as

$$\mathbf{B} = \begin{bmatrix} \mathbf{0}_i \\ \mathbf{I}_b \end{bmatrix} \quad \text{that corresponds to}$$

$$\mathbf{L} = \begin{bmatrix} \mathbf{L}_i & 0 \\ 0 & \mathbf{L}_b \end{bmatrix} \quad \text{and} \quad \mathbf{u}_g = \begin{Bmatrix} \mathbf{u}_i \\ \mathbf{u}_b \end{Bmatrix} \tag{26a, b, c}$$

where the subscripts (i, b) denote the substructural interior and partitioned interface nodes, respectively. Observe that the preceding choice of **B** precludes all the interior substructural nodes. However, selected interior nodes can be included by appending them to $\mathbf{I}_b$.

Substituting this into the second row of (22) leads to the so-called *direct flexibility method* (DFM) equation:

$$\begin{bmatrix} \mathbf{F}_b & -\mathbf{R}_b & \mathbf{L}_b \\ -\mathbf{R}_b^T & 0 & 0 \\ \mathbf{L}_b^T & 0 & 0 \end{bmatrix} \begin{Bmatrix} \boldsymbol{\lambda}_b \\ \boldsymbol{\alpha} \\ \mathbf{u}_b \end{Bmatrix} = \begin{Bmatrix} \mathbf{B}^T\mathbf{K}^+\mathbf{f} \\ -\mathbf{R}^T\mathbf{f} \\ 0 \end{Bmatrix},$$

$$\mathbf{F}_b = \mathbf{B}^T\mathbf{K}^+\mathbf{B} \tag{27}$$

where $\mathbf{u}_b$ represents the global displacement at the substructural boundaries.

The derivation steps outlined above are diagrammed in Fig. 3. The Decomposition step shown therein gives rise to the substructural equilibrium equation expressed by the first row of (22). The Flexibility Formation and the BC Application steps are realized by the choice of the interface displacement extraction matrix (26a) and the first row of (27). Finally, the Interconnection step performs the matching of substructural boundary nodes that satisfies the substructural static equilibrium equation and boundary compatibility conditions given by the second and last row of (27), respectively.

The DFM Eq. (27) becomes attractive for subdomains containing a large number (typically thousands) of elements and has been adopted for use in parallel computations. A parallel iterative algorithm is obtained by constructing a projected iterative residual vector $\mathbf{r}_p$ in terms of the interface force $\boldsymbol{\lambda}_b$ as

Downloaded 04 May 2010 to 171.66.16.26. Redistribution subject to ASME license or copyright; see http://www.asme.org/terms/Terms_Use.cfm

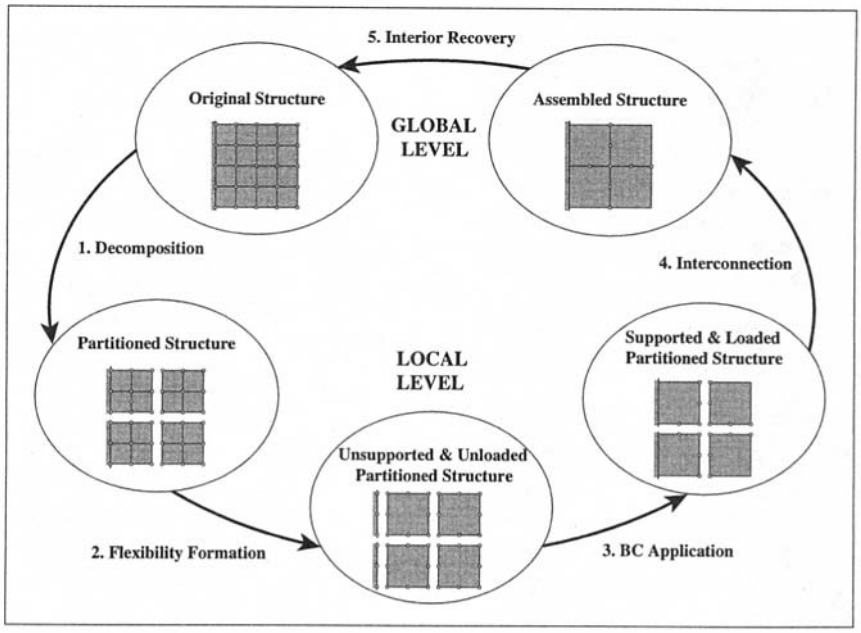

Fig. 3 The main steps of the direct flexibility method described by Felippa and Park (1997)

follows (Park, Justino, and Felippa, 1997; Justino, Park, Felippa, 1997):

$$\mathbf{r}_p = \mathbf{P}_l \mathbf{P}_r (\mathbf{b}_\lambda - \mathbf{F}_b \boldsymbol{\lambda}_b)$$

$$\mathbf{P}_r = \mathbf{I} - \mathbf{R}_b (\mathbf{R}_b^T \mathbf{R}_b)^{-1} \mathbf{R}_b^T$$

$$\mathbf{P}_l = \mathbf{I} - \mathbf{P}_r \mathbf{L}_b (\mathbf{L}^T \mathbf{P}_r \mathbf{L}_b)^{-1} \mathbf{L}_b^T \mathbf{P}_r$$

$$\mathbf{b}_\lambda = \mathbf{B}^T \mathbf{K}^+ \mathbf{f}. \tag{28}$$

A preconditioned iterative solution procedure utilizing the above residual is described in detail by Justino, Park, and Felippa (1997).

The foregoing developments in parallel computation methods have been motivated and influenced by the work of Farhat and his colleagues in the development of the Finite Element Tearing and Interconnecting (FETI) solution methods (Farhat and Roux, 1991, 1994). A two-level extension called FETI2, aimed at scalable parallel solution of models that contain plate and shell elements, has been recently presented by Farhat and Mandel (1995). These methods are also based on substructural decompositions, but the interface equations are obtained by an approach akin to the differential partitioning technique for coupled field problems (Park and Felippa, 1983): the floating substructures are initially treated as disconnected, and connection equations adjoined by force-like Lagrange multipliers. This technique has advantages when meshes on both sides of an interface are nonconforming. The state variables in the original FETI are the interface forces and the rigid-body mode amplitudes, a choice that leads to configurations similar to Eq. (45) below. The substructural displacement state decomposition exemplified by (6) is carried out by an algorithm that combines matrix factorization and singular-value decomposition (Farhat and Geradin, 1996).

The iterative solution algorithm based on (27) has been termed A-FETI in the cited references because the original derivation follows the algebraic partitioning technique of coupled field analysis (Park and Felippa, 1983): the complete system equations are initially assumed to be assembled, and then decomposed through appropriate releases. This technique works best for conforming meshes at substructural interfaces.

5 Substructural Interface-Displacement Method

Instead of retaining the interface forces $\boldsymbol{\lambda}_b$ as unknowns, we may decide to keep the substructural boundary displacement $\mathbf{u}_b$ by eliminating $\boldsymbol{\lambda}_b$ from (27):

$$\mathbf{K}^B \begin{Bmatrix} \mathbf{u}_b \\ \alpha \end{Bmatrix} = \begin{Bmatrix} \mathbf{L}_b^T \mathbf{F}_b^+ \mathbf{B}^T \mathbf{K}^+ \mathbf{f} \\ \mathbf{R}^T (\mathbf{I} - \mathbf{B} \mathbf{F}_b^+ \mathbf{B}^T \mathbf{K}^+) \mathbf{f} \end{Bmatrix}$$

$$\mathbf{K}^B = \mathbf{Q}_b^T \mathbf{F}_b^+ \mathbf{Q}_b, \quad \mathbf{Q}_b = [-\mathbf{L}_b \quad \mathbf{R}_b]. \tag{29}$$

A candidate preconditioner $\mathbf{K}^{-B}$ for the iterative solution of the above equation is

$$\mathbf{K}^{-B} = \mathbf{G} \mathbf{Q}_b^T \mathbf{F}_b \mathbf{Q}_b \mathbf{G}$$

$$\mathbf{G} = \begin{bmatrix} \mathbf{G}_{11} & \mathbf{G}_{12} \\ \mathbf{G}_{12}^T & \mathbf{G}_{22} \end{bmatrix}$$

$$\mathbf{G}_{11} = [\mathbf{D}_r - \mathbf{E}^T \mathbf{D}_l^{-1} \mathbf{E}]^{-1}, \quad \mathbf{D}_r = \mathbf{R}_b^T \mathbf{R}_b,$$

$$\mathbf{D}_l = \mathbf{L}_b^T \mathbf{L}_b, \quad \mathbf{E} = \mathbf{L}_b^T \mathbf{R}_b$$

$$\mathbf{G}_{22} = \mathbf{D}_l^{-1} (\mathbf{I} + \mathbf{E} \mathbf{G}_{11} \mathbf{E}^T \mathbf{D}_l^{-1}), \quad \mathbf{G}_{12} = \mathbf{G}_{11} \mathbf{E}^T \mathbf{D}_l^{-1}. \tag{30}$$

It should be noted that, if one applied the partitions (26*b*) and (26*c*) directly to the assembled Eq. (9), the following Guyan-reduced primal equation results:

$$\mathbf{L}_b^T \mathbf{K}_b^S \mathbf{L}_b \mathbf{u}_b = \mathbf{L}_b^T (\mathbf{f}_{gb} - \mathbf{K}_{bi} \mathbf{K}_{ii}^{-1} \mathbf{f}_{gi}), \quad \mathbf{K}_{bb}^S = \mathbf{K}_{bb} - \mathbf{K}_{bi} \mathbf{K}_{ii}^{-1} \mathbf{K}_{ib}$$

$$\mathbf{K}_g = \begin{bmatrix} \mathbf{K}_{bb} & \mathbf{K}_{bi} \\ \mathbf{K}_{ib} & \mathbf{K}_{ii} \end{bmatrix}, \quad \mathbf{f}_g = \begin{Bmatrix} \mathbf{f}_{gi} \\ \mathbf{f}_{gb} \end{Bmatrix} \tag{31}$$

where $\mathbf{K}_{bb}^S$ is the Guyan-reduced stiffness matrices in terms of the substructural interface nodes.

Comparing (31) with the substructural interface-displacement Eq. (30), one observes that the latter may be viewed as a rigid-body-mode augmented equation. This augmentation is thought to offer attractive convergence properties over the Guyan-reduced equation as the rigid-body modes are known to play a beneficial role in iterative solution procedures.

Computational aspects of the substructural boundary-displacement method (30) have not been investigated to date. The

Downloaded 04 May 2010 to 171.66.16.26. Redistribution subject to ASME license or copyright; see http://www.asme.org/terms/Terms_Use.cfm

form (30) may offer additional insight into the so-called primal domain-decomposition methods described by Przemieniecki (1968), Widlund (1988), Le Tallec (1994), Mandel (1993), and Le Tallec, Mandel, and Vidrascu (1994).

6 Minimally Redundant Direct Flexibility Method

In the two foregoing specializations of (22), the rigid-body modal amplitudes $\boldsymbol{\alpha}$ are kept as independent variables. In structural optimization, the primary variables of interest are the stresses and their perturbations due to design parameters. As the rigid-body displacements contribute nothing to the stress computations, it is desirable to eliminate them altogether. To this end, recall the kinematical relations (18)–(19)

$$\mathbf{u} = \mathbf{d} + \mathbf{R}\boldsymbol{\alpha}. \tag{32}$$

This can be partitioned as

$$\begin{Bmatrix} \mathbf{u}_c \\ \mathbf{u}_f \end{Bmatrix} = \begin{Bmatrix} \mathbf{d}_c \\ \mathbf{d}_f \end{Bmatrix} + \begin{Bmatrix} \mathbf{R}_c \\ \mathbf{R}_f \end{Bmatrix} \boldsymbol{\alpha} \tag{33}$$

where $\mathbf{R}_c$ is a square invertible submatrix. Thus, solving for $\boldsymbol{\alpha}$ from the first row of (33), we obtain

$$\boldsymbol{\alpha} = \mathbf{R}_c^{-1}(\mathbf{u}_c - \mathbf{d}_c). \tag{34}$$

Introduce now a deformation measure $\mathbf{v}$ that represents relative motions at nodes f with respect to nodes c:

$$\mathbf{v} = \mathbf{d}_f - \mathbf{R}_f\mathbf{R}_c^{-1}\mathbf{d}_c = \mathbf{T}\mathbf{u} = \mathbf{T}\mathbf{L}\mathbf{u}_g = \mathbf{T}_l\mathbf{u}_g$$
$$\mathbf{T} = [-\bar{\mathbf{R}} \quad \mathbf{I}], \quad \bar{\mathbf{R}} = \mathbf{R}_f\mathbf{R}_c^{-1}. \tag{35}$$

Using (35) with the relations

$$\mathbf{u}_g^T\mathbf{f}_g = \mathbf{v}^T\mathbf{f}_v, \quad \mathbf{f}_v = \mathbf{T}_l(\mathbf{T}_l^T\mathbf{T}_l)^{-1}\mathbf{f}_g,$$
$$\mathbf{K} = \mathbf{T}^T\mathbf{K}_v\mathbf{T}, \quad \mathbf{B} = \mathbf{T}^T\mathbf{B}_v \tag{36}$$

the discrete energy functional (16) is transformed into

$$\Pi = \tfrac{1}{2}\mathbf{v}^T\mathbf{K}_v\mathbf{v} - \mathbf{v}^T\mathbf{f}_v + \boldsymbol{\lambda}_v^T\mathbf{B}_v^T(\mathbf{v} - \mathbf{T}_l\mathbf{u}_g). \tag{37}$$

Stationarity of Π leads to

$$\begin{bmatrix} \mathbf{K}_v & \mathbf{B}_v & \mathbf{0} \\ \mathbf{B}_v^T & \mathbf{0} & \mathbf{B}_v^T\mathbf{T}_l \\ \mathbf{0} & \mathbf{T}_l^T\mathbf{B}_v & 0 \end{bmatrix} \begin{Bmatrix} \mathbf{v} \\ \boldsymbol{\lambda}_v \\ \mathbf{u}_g \end{Bmatrix} = \begin{Bmatrix} \mathbf{f}_v \\ 0 \\ 0 \end{Bmatrix}. \tag{38}$$

In order to determine a $\mathbf{B}_v$ that does not hinder matrix sparsity, we exploit the following partitioned form of $\mathbf{T}_l = \mathbf{T}\mathbf{L}$:

$$\mathbf{T}_l = \mathbf{T}\mathbf{L} = [-\bar{\mathbf{R}} \quad \mathbf{I}] \begin{bmatrix} \mathbf{L}_r \\ \mathbf{L}_v \end{bmatrix} \tag{39}$$

and select

$$\mathbf{B}_v = \text{nullspace}(\mathbf{L}_v), \quad \mathbf{B}_v^T\mathbf{L}_v = 0. \tag{40}$$

It can be shown that $\mathbf{B}_v$ is a column sum of column-by-column nullspaces of $\mathbf{L}_v$ (Park, Justino, and Felippa, 1997).

On eliminating $\mathbf{v}$ from (38), we obtains a minimally redundant DFM equation

$$\begin{bmatrix} \mathbf{B}_v^T\mathbf{F}_v\mathbf{B}_v & -\mathbf{G}_v \\ -\mathbf{G}_v^T & \mathbf{0} \end{bmatrix} \begin{Bmatrix} \boldsymbol{\lambda}_v \\ \mathbf{u}_g \end{Bmatrix} = \begin{Bmatrix} \mathbf{B}_v^T\mathbf{F}_v\mathbf{f}_v \\ 0 \end{Bmatrix}, \quad \mathbf{G}_v = \mathbf{B}_v^T\bar{\mathbf{R}}\mathbf{L}_r. \tag{41}$$

It is emphasized that $\bar{\mathbf{R}}$ is determined on an element-by-element basis. Matrix $\mathbf{L}$ is the element assembly operator, which is readily available in the direct stiffness method (7) and (9). Hence, the present choice (40) is applicable to frame-type as well as continuum cases.

The classical force method results from (41) if one chooses $\mathbf{B}_v$ to be a nullspace of $\mathbf{T}_l$, that is,

$$\mathbf{B}_v^T\mathbf{T}_l = \mathbf{0} \Rightarrow \mathbf{B}_v^T\mathbf{v} = 0. \tag{42}$$

It should be noted, however, that computation of the null space generally entails a heavy computational burden and, moreover, the matrix block $\mathbf{B}_v^T\mathbf{F}_v\mathbf{B}_v$ becomes dense. For continuum finite element models, the resulting solution procedure is not competitive with the direct stiffness method (Felippa and Park, 1997). Interested readers may consult a recent survey article by Kaveh (1992), who discusses several direct approaches to the construction of $\mathbf{B}_v$ for skeletal structures.

Nearly all classical force method formulations endeavor to build $\mathbf{T}_l$ as a single matrix. In the present formulation (41), the operator $\mathbf{T}_l$ is generated as the product of two matrices. This is computationally convenient because the $\mathbf{L}$-matrix is easily available in standard finite element programs. Furthermore, $\mathbf{T}$ is also computable in an element-by-element manner.

7 Computation of Substructural Flexibility From Measured Global Flexibility

So far we have focused on the use of substructure-based formulations for developing solution algorithms. The same principle can be used for the determination of substructural flexibility from a global flexibility matrix determined from experimental data and system identification. Applications of this technique include model updating, damage detection and synthesis of localized control laws (Farhat and Hemez, 1993; Alvin and Park, 1996; Alvin, 1997). System identification techniques typically yield a global flexibility matrix formed as

$$\mathbf{F}_g = \boldsymbol{\Phi}\boldsymbol{\Lambda}\boldsymbol{\Phi}^T \tag{43}$$

where $\boldsymbol{\Phi}$ are global deformation mode shapes, and the diagonal matrix $\boldsymbol{\Lambda}$ collects the inverse of identified eigenvalues of the global stiffness matrix. Our goal here is to determine the substructural flexibility in terms of the boundary nodes; that is, to compute $\mathbf{F}_b$ from the identified global flexibility $\mathbf{F}_g$. This is because sensor output locations can be defined to be at substructural interface nodes. Of several choices investigated to date, it has been found that the following basis transformation of the interface Lagrange multipliers is most convenient:

$$\boldsymbol{\lambda}_b = \mathbf{N}\boldsymbol{\lambda}_n, \quad \mathbf{N}^T\mathbf{L}_b = 0 \tag{44}$$

where $\mathbf{N}$ is a nullspace of $\mathbf{L}_b$. With this choice, together with the stipulation that the substructures possess no interior nodes ($\mathbf{B} = \mathbf{I}$, $\mathbf{L}_b = \mathbf{L}$), (27) reduces to

$$\begin{bmatrix} \mathbf{N}^T\mathbf{K}^+\mathbf{N} & \mathbf{R}_n \\ \mathbf{R}_n^T & \mathbf{0} \end{bmatrix} \begin{Bmatrix} \boldsymbol{\lambda}_n \\ \boldsymbol{\alpha} \end{Bmatrix} = \begin{Bmatrix} \mathbf{N}^T\mathbf{K}^+\mathbf{f} \\ \mathbf{R}^T\mathbf{f} \end{Bmatrix}$$

$$\mathbf{B}\mathbf{N} = \mathbf{N}, \quad \mathbf{R}_n = \mathbf{N}^T\mathbf{R}. \tag{45}$$

Solving for $\boldsymbol{\lambda}_n$ and $\boldsymbol{\alpha}$, substituting into (44), (32), (25), and (10) yields the following expression:

$$\mathbf{u}_g = \mathbf{F}_g\mathbf{f}_g$$

$$\mathbf{F}_g = \bar{\mathbf{L}}^T(\mathbf{F} - \mathbf{F}\mathbf{A} - \mathbf{A}^T\mathbf{F} - \mathbf{F}\mathbf{M}\mathbf{F} + \mathbf{F}_R)\bar{\mathbf{L}}, \quad \bar{\mathbf{L}} = \mathbf{L}(\mathbf{L}^T\mathbf{L})^{-1}$$

$$\mathbf{F} = \mathbf{K}^+, \quad \mathbf{A} = \mathbf{K}_n\mathbf{F}_R, \quad \mathbf{M} = \mathbf{K}_n - \mathbf{K}_n\mathbf{F}_R\mathbf{K}_n$$

$$\mathbf{K}_n = \mathbf{N}[\mathbf{N}^T\mathbf{F}\mathbf{N}]^{-1}\mathbf{N}^T, \quad \mathbf{F}_R = \mathbf{R}[\mathbf{R}^T\mathbf{K}_n\mathbf{R}]^{-1}\mathbf{R}^T. \tag{46}$$

Downloaded 04 May 2010 to 171.66.16.26. Redistribution subject to ASME license or copyright; see http://www.asme.org/terms/Terms_Use.cfm

The above system leads to the following Riccati-like equation for the determination of substructural flexibilities $\mathbf{F}$:

$$\mathbf{F} - \mathbf{F}\mathbf{A} - \mathbf{A}^T\mathbf{F} - \mathbf{F}\mathbf{M}\mathbf{F} + \mathbf{F}_R = \mathbf{L}\mathbf{F}_g\mathbf{L}^T \qquad (47)$$

which can be solved for $\mathbf{F}$ via a homotopy method (Alvin and Park, 1996).

8 Forming the Rigid-Mode Matrix R

The availability of the substructural rigid-body modes is a fundamental ingredient of the algorithms presented here. In principle they can be obtained as a nullspace of each substructural stiffness matrix (see Eq. (20)). For a large substructure, it has been found that nullspace computations based on the substructural stiffness matrices are not only expensive but also can lead to accuracy loss. For this reason, we describe a static equilibrium method based entirely on geometric information.

When the translation forces $\mathbf{F}_i^T = (F_x, F_y, F_x)_i$ and moments $\mathbf{M}_i^T = (M_x, M_y, M_x)_i$ are applied at nodes $(i = 1, \ldots, m)$ where m is the total number of nodes in substructure (s), the substructure (s) will be in equilibrium only if the following conditions are satisfied (see, e.g., Przemieniecki, 1968):

$$\sum_{i=1}^{m} \mathbf{R}_i^{(s)T} \begin{Bmatrix} \mathbf{F}_i \\ \mathbf{M}_i \end{Bmatrix} = 0 \qquad (48)$$

where $\mathbf{R}_i^{(s)}$ is given by

$$\mathbf{R}_i^{(s)T} = \begin{bmatrix} \mathbf{I}_3 & \mathbf{0} \\ \boldsymbol{\chi}_i & \mathbf{I}_3 \end{bmatrix},$$

$$\boldsymbol{\chi}_i = \begin{bmatrix} 0 & -(z_i - z_0) & (y_i - y_0) \\ (z_i - z_0) & 0 & -(x_i - x_0) \\ -(y_i - y_0) & (x_i - x_0) & 0 \end{bmatrix}. \qquad (49)$$

In the above equation, (x_i, y_i, z_i) and (x_0, y_0, z_0) are the coordinates at node i and the reference node 0, the first three rows correspond to three translational rigid-body modes, and the remaining three to three rotations, respectively. It should be noted that the rigid-body modes for a three-dimensional continuum element are obtained by eliminating the last three columns in each of the block submatrices of the $\mathbf{R}_i^{(s)}$ matrix.

Free-free rigid-body modes of the complete structure are obtained by grouping the substructural ones as

$$\mathbf{R} = \begin{bmatrix} \mathbf{R}^{(1)} & & & \\ & \mathbf{R}^{(2)} & & \\ & & \ddots & \\ & & & \mathbf{R}^{(N_s)} \end{bmatrix},$$

$$\mathbf{R}^{(s)T} = [\mathbf{R}_1^{(s)T} \quad \mathbf{R}_2^{(s)T} \ldots \mathbf{R}_m^{(s)T}]. \qquad (50)$$

9 Computation of Generalized Inverses

Throughout the present study one expression has been repeatedly used: the Moore-Penrose generalized inverse of the substructural stiffness matrix $\mathbf{K}^+$ for free-free substructures. (This is called the pseudo-inverse by some authors, such as Stewart and Sun (1990).) As this constitutes a major computational building block, we present an efficient procedure for its computation. Of various possibilities tested, we have found that the use of a natural stiffness to substructural stiffness relation (35) offers the most efficient computation. This relation is recalled for convenience:

$$\mathbf{K} = \mathbf{T}^T\mathbf{K}_v\mathbf{T}, \quad \mathbf{T} = [-\bar{\mathbf{R}} \quad \mathbf{I}] \qquad (51)$$

where $\mathbf{K}_v$ is obtained by eliminating the rows and columns of $\mathbf{K}$ that correspond to the degrees of freedom of $\mathbf{u}_c$ in (32). Therefore, a generalized inverse of $\mathbf{K}$ can be obtained as

$$\mathbf{K}^+ = \mathbf{T}^T\mathbf{D}_r\mathbf{K}_v^{-1}\mathbf{D}_r\mathbf{T}, \quad \mathbf{D}_r = \mathbf{I} - \bar{\mathbf{R}}[\mathbf{I} + \bar{\mathbf{R}}^T\bar{\mathbf{R}}]^{-1}\bar{\mathbf{R}}^T. \qquad (52)$$

It should be noted that $\mathbf{K}_v^{-1}$ is a sparse matrix and $[\mathbf{I} + \bar{\mathbf{R}}^T\bar{\mathbf{R}}]$ appearing in $\mathbf{D}_r$ is at most a (6×6) matrix, which contribute to making the computation of $\mathbf{K}^+$ efficient and accurate.

Another frequent requirement is the computation of a generalized inverse of $\mathbf{F}_b$. This can be based on the relation

$$\mathbf{F}_b^+ = \mathbf{P}_r(\mathbf{P}_r\mathbf{F}_b\mathbf{P}_r + \mathbf{R}_b(\mathbf{R}_b^T\mathbf{R}_b)^{-1}\mathbf{R}_b^T)^{-1} \qquad (53)$$

where $\mathbf{P}_r$ is given in (28). This and related matrices are used for preconditioning of the projected residuals for iterative solutions of several methods presented in the paper.

10 Concluding Remarks

We have presented a variational framework that can be used for the development of solution algorithms for linear or linearized structural analysis. The general variational Eq. (22) contains four independently varied state variables: the substructural deformational displacements and rigid-body mode amplitudes, the Lagrange multipliers representing substructural interaction forces, and the global displacements at the partition boundaries. The main contributions of the present formulation are: (1) an automatic way to construct rank-sufficient interface compatibility conditions, and (2) and the use of substructural rigid-body modal amplitudes as an independent variable.

Four specializations have been derived from the general variational framework: a direct flexibility method and its dual form for parallel computation, a minimal-order flexibility method as a candidate procedure for structural optimization, and an algorithm for extracting substructural flexibility from measured global flexibility. These specializations have been accomplished by retaining different sets of interface compatibility conditions. The first and the fourth specializations have been shown to lead to practical computational procedures (Justino, Park, and Felippa, 1997; Alvin and Park, 1996). The second and third ones are presently being evaluated.

The present variational framework can precipitate additional solution algorithms by seeking different interface constraint conditions heretofore untried. Some potential applications of the present variational framework include friction-contact-sliding problems, mechanics of granular materials, and dynamics and vibration eigenanalysis. We hope to extend this framework to treat those more ambitious applications.

Acknowledgments

The present research has been supported by the National Science Foundation under NSF/HPCC Grant ESC-9217394 and by Sandia National Laboratories under Accelerated Strategic Computational Initiative (ASCI) Contracts AS-5666 and AS-9991.

References

Alvin, K. F., 1997, "Finite element model update via Bayesian estimation and minimization of dynamic residuals," *AIAA Journal,* Vol. 35, No. 5, pp. 879–886.

Alvin, K. F., and Park, K. C., 1996, "Extraction of substructural flexibility from measured global frequencies and mode shapes," *Proc. 1996 AIAA SDM Conference,* Salt Lake City, UT, Apr. 15–16, Paper No. AIAA 96-1297.

Argyris, J. H., and Kelsey, S., 1960, *Energy Theorems and Structural Analysis,* Butterworths, London (reprinted from *Aircraft Engineering,* Vol. 26, Oct.–Nov. 1954 and Vol. 27, Apr.–May 1955).

Atluri, S. N., 1975, "On 'hybrid' finite-element models in solid mechanics," *Advances in Computer Methods for Partial Differential Equations,* R. Vichnevetsky, ed., Rutgers University, AICA, pp. 346–356.

Farhat, C., and Roux, F.-X., 1991, "A method of finite element tearing and interconnecting and its parallel solution algorithm," *International Journal for Numerical Methods in Engineering,* Vol. 32, pp. 1205–1227.

Downloaded 04 May 2010 to 171.66.16.26. Redistribution subject to ASME license or copyright; see http://www.asme.org/terms/Terms_Use.cfm

Farhat, C., and Hemez, F. M., 1993, "Updating finite element dynamic models using an element-by-element sensitivity methodology," *AIAA Journal,* Vol. 31, No. 9, pp. 1702–1711.

Farhat, C., and Roux, F.-X., 1994, "Implicit parallel processing in structural mechanics," *Computational Mechanics Advances,* Vol. 2, pp. 1–124.

Farhat, C., and Mandel, J., 1995, "The two-level FETI method for static and dynamic plate problems—Part I: an optimal iterative solver for biharmonic systems," Center for Aerospace Structures, University of Colorado, Report Number CU-CAS-95-23.

Farhat, C., and Geradin, M., 1996, "On the computation of the null space and generalized inverse of a large matrix and the zero energy modes of a structure," Center for Aerospace Structures, University of Colorado, Report Number CU-CAS-96-15.

Felippa, C. A., 1994, "A survey of parametrized variational principles and applications to computational mechanics," *Computer Methods in Applied Mechanics and Engineering,* Vol. 113, pp. 109–139.

Felippa, C. A., and Park, K. C., 1997, "A Direct Flexibility Method," *Computer Methods in Applied Mechanics and Engineering,* Vol. 149, pp. 319–337.

Finlayson, B. A., 1972, *The Method of Weighted Residuals and Variational Principles,* Academic Press, London, pp. 335–337.

Fraeijs de Veubeke, B. M., 1974, "Variational principles and the patch test," *Int. J. Numer. Meth. Engrg,* Vol. 8, pp. 783–801.

Justino, M. R., Park, K. C., and Felippa, C. A., 1997, "An algebraically partitioned FETI method for parallel structural analysis: Implementation and numerical performance evaluation," *International Journal for Numerical Methods in Engineering,* Vol. 40, pp. 2739–2758.

Kaveh, A., 1992, "Recent developments in the force method of structural analysis," ASME *Applied Mechanics Reviews,* Vol. 45, pp. 401–418.

LeTallec, P., 1994, "Domain decomposition methods in computational mechanics," *Computational Mechanics Advances,* Vol. 1, pp. 121–220.

LeTallec, P., Mandel, J., and Vidrascu, M., 1994, "Parallel domain decomposition algorithms for solving plates and shell problems," *Domain Decomposition Methods in Scientific and Engineering Computing,* D. E. Keyes and J. Xu, eds., American Mathematical Society, Providence, RI, pp. 515–524.

Mandel, J., 1993, "Balancing domain decomposition," *Communications in Numerical Methods in Engineering,* Vol. 9, pp. 233–241.

Oden, J. T., and Reddy, J. N., 1982, *Variational Methods in Theoretical Mechanics,* 2nd ed., Springer-Verlag, Berlin.

Park, K. C., and Felippa, C. A., 1983, "Partitioned analysis of coupled systems," *Computational Methods for Transient Analysis,* T. Belytschko and T. J. R. Hughes, eds., Elsevier New York, pp. 157–219.

Park, K. C., Justino, M. R., and Felippa, C. A., 1997, "An algebraically partitioned FETI method for parallel structural analysis: Algorithm description," *International Journal for Numerical Methods in Engineering,* Vol. 40, pp. 2717–2737.

Pian, T. H. H., and Tong, P., 1969, "Basis of finite element methods for solid continua," *International Journal for Numerical Methods in Engineering,* Vol. 1, pp. 3–28.

Przemieniecki, J. S., 1968, *Theory of Matrix Structural Analysis,* McGraw-Hill, New York.

Stewart, G. W., and Sun, J., 1990, *Matrix Perturbation Theory,* Academic Press, New York.

Washizu, K., 1968, *Variational Methods in Elasticity and Plasticity,* Pergamon Press, New York.

Widlund, O. B., 1988, "Iterative substructuring methods: Algorithms and theory for elliptic problems in the plane," *First International Symposium on Domain Decomposition Methods for Partial Differential Equations,* eds. by R. Glowinski, G. H. Golub, G. A. Meurant, and J. Périaux, eds., SIAM, Philadelphia, PA.

Zienkiewicz, O. C., and Taylor, R. E., 1989, *The Finite Element Method,* Vol. I, 4th ed. McGraw-Hill, New York.

Downloaded 04 May 2010 to 171.66.16.26. Redistribution subject to ASME license or copyright; see http://www.asme.org/terms/Terms_Use.cfm

Dynamical Friction Behavior in a Forced Oscillator With a Compliant Contact

J.-W. Liang
Department of Mechanical Engineering,
MingChi Institute of Technology,
Taipei, Taiwan, R.O.C.

B. F. Feeny
Department of Mechanical Engineering,
Michigan State University
A231 Engineering Building,
East Lansing, MI 84424-1226
Mem. ASME.

Contact compliance, which may arise from elastic deformation near the contact point or in the surrounding structure, affects the dynamical friction behaviors in mechanical oscillators. An idealized model consisting of a mass sliding harmonically on a massless compliant contact produces hysteresis in friction-velocity plots. Dynamical friction features, depending on the contact stiffness, friction level, and the frequency and amplitude of oscillation, are predicted and quantified. Contact compliance can also lead to oscillations at the transition from slip to stick. Experiments and simulations verify the model and tie together phenomena of both continuous sliding and stick-slip.

1 Introduction

This paper is devoted to the investigations of experimentally observed frictional hysteresis and stick-slip transition oscillations in a mechanical oscillator.

Hysteresis is observed during oscillations with "macroscopic" continuous sliding. We use the word macroscopic because the large-scale motion resembles pure sliding, although during velocity reversals, short-term microscale sticks occur. This is related to the "spring-like" sticking behavior in the literature (Canudas de Wit et al., 1995; Dahl, 1968; Marui and Kato, 1984; Courtney-Pratt and Eisner, 1957). Due to the fact that the displacement change in this elastofrictional event is often small, it has been called "preliminary displacement," "micro displacement," or "presliding displacement" (Oden and Martins, 1985; Canudas de Wit et al., 1995; Harnoy et al., 1994). However, we will denote this motion as "microsticking" so that it is consistent with our modeling details.

Among the modeling works regarding this problem are the following. Dahl's (1968) model is equivalent to the Coulomb friction model with a lag in the friction force change incorporated when the direction of motion reverses. Haessig and Friedland (1991) and Canudas de Wit et al. (1995) proposed a friction model which treats the friction interface as a contact between bristles. (Indeed, Coulomb had the same idea; see Dugas, 1955.) Such a model can numerically generate spring-like behaviors during a stick.

Harnoy et al. (1994) proposed a compliant-contact model incorporated with a hydrodynamic sliding model to study a journal bearing problem. Several important friction features were revealed in their simulation results, including the "Dahl effect" (presliding or elastic deformation motion), the hysteresis in sliding motion (frictional memory), and the effect of coupling between presliding and sliding modes.

The other phenomenon of focus is the transition oscillation seen during the stick-slip process (Polycarpou and Soom, 1992; Ko and Brockley, 1970; Rorrer, 1995; Marui and Kato, 1984). These studies attribute transition oscillations to the coupling of systems on either side of the contact.

In this paper, an idealized compliant contact model is added to the harmonically forced Coulomb oscillator. Our study addresses details of the dynamical effects of presliding motion on oscillations with macroscopic sliding, and includes quantitative experimental verifications. We show that the averaged tangential contact stiffness, when coupled with the main system parameters, can produce the high-frequency transition oscillations which are experimentally observed. We also observe two different scales of stick-slip, i.e., macroscopic and microscale stick-slip. The results of the sliding and stick-slip studies are complementary. As such, the frictional hysteresis and the stick-slip transition oscillations are tied through a common mechanism: contact compliance.

2 The Compliant-Contact Model

A schematic diagram illustrating the forced Coulomb oscillator together with the idealized massless contact model is presented in Fig. 1, where $x(t)$ and $z(t)$ represent the displacements of sliding mass and base excitation respectively, $y(t)$ denotes the displacement of the hypothetical contact surface, and K_y represents the stiffness of the contact joint. Linear contact stiffness is an approximation which will be less valid for elliptical contacts or asperity-born compliance (Threlfall, 1978; Johnson, 1985; Sanliturk and Ewins, 1996), and more valid for structural compliances, and is often used, for example, in turbine-blade studies (Griffin, 1980; Ferri and Heck, 1997; Guillen and Pierre, 1996; J.-H. Wang, 1996; Ferri, 1995). We use the Coulomb friction model with identical static and kinetic friction, namely $f_s = f_k$. The mass motion, $x(t)$, is approximated by a harmonic function.

During the sliding interval the mass moves relative to the contact surface, and the massless contact surface is assumed to be motionless, such that $y(t)$ is a constant, i.e. $\pm Y_m \equiv \pm f_k/K_y$. There are no dynamics in y during sliding. The "microsticking" starts when the relative velocity is zero, or $\dot{x}(t) = 0$. During microsticking, both the sliding mass and the contact surface undergo the same motion, namely $\dot{x}(t) = \dot{y}(t)$, until the static friction force can no longer sustain the stiffness force exerted by the compliant contact joint, i.e. $|K_y y(t)| > f_k$. The motion is called microsticking since when K_y is large, both the sticking interval and the elastic displacement are small.

Hypothetical time-domain traces of $x(t)$, $\dot{x}(t)$, $y(t)$, and $f(t)$ are shown in Fig. 2, where $f(t)$ depicts the friction force occurring at the interface, and varies implicitly in time due to its dependence on $\dot{x}(t)$ and $y(t)$. The dashed lines in this figure represent macroscopic sliding motion and solid lines represent the elastic deformation or the microsticking motion. In Fig. 2,

Contributed by the Applied Mechanics Division of THE AMERICAN SOCIETY OF MECHANICAL ENGINEERS for publication in the ASME JOURNAL OF APPLIED MECHANICS.

Discussion on this paper should be addressed to the Technical Editor, Professor Lewis T. Wheeler, Department of Mechanical Engineering, University of Houston, Houston, TX 77204-4792, and will be accepted until four months after final publication of the paper itself in the ASME JOURNAL OF APPLIED MECHANICS.

Manuscript received by the ASME Applied Mechanics Division, Jan. 6, 1997; final revision, June 23, 1997. Associate Technical Editor: N. C. Perkins.

 Copyright © 1998 by ASME

Downloaded 04 May 2010 to 171.66.16.26. Redistribution subject to ASME license or copyright; see http://www.asme.org/terms/Terms_Use.cfm

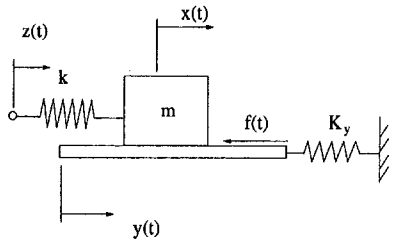

Fig. 1 A schematic diagram showing the massless compliant contact model

microsticking commences at the onset of each direction reversal. Upon this microsticking, the massless contact joint deforms in a linearly elastic manner such that the friction force equals the spring force exerted by the effective contact stiffness. Hence, $f(t) = K_y y(t)$. The schematic representations of $x(t)$, $y(t)$, and $f(t)$ possess similar features during the microsticking interval. A constant kinetic friction force is assumed during the sliding interval.

Because of the contact compliance, microsticking events replace the instantaneous jump events (which are caused by the discontinuity of the Coulomb law) seen during pure sliding against a rigid contact. The microsticking event occurs right after the mass changes its sliding direction but before sliding resumes. At the onset of sliding, the mass will have a certain velocity which will be called the "transition speed."

Based on the information collected from Fig. 2(*a*) and (*d*), a qualitative *f-x* characteristic can be established and is illustrated in Fig. 3. (See also Ferri and Heck (1997), Guillen and Pierre (1996) Ferri (1995), and Wang and Chen (1993) for example. The effect of contact mass on these *f-x* characteristics was addressed by Ferri and Heck (1997).) A constant magnitude of friction force, f_k, is assumed in the sliding interval and the friction force evolves in a linearly elastic way during the microsticking interval. The slope of the straight lines AB and CD in the *f-x* plot depicts the effective contact stiffness, K_y. In addition, the microdisplacement in the sticking interval is twice the amplitude of the contact motion. Thus, $2Y_m = 2f_k/K_y$. The amplitude of harmonic motion of the sliding mass is X_m.

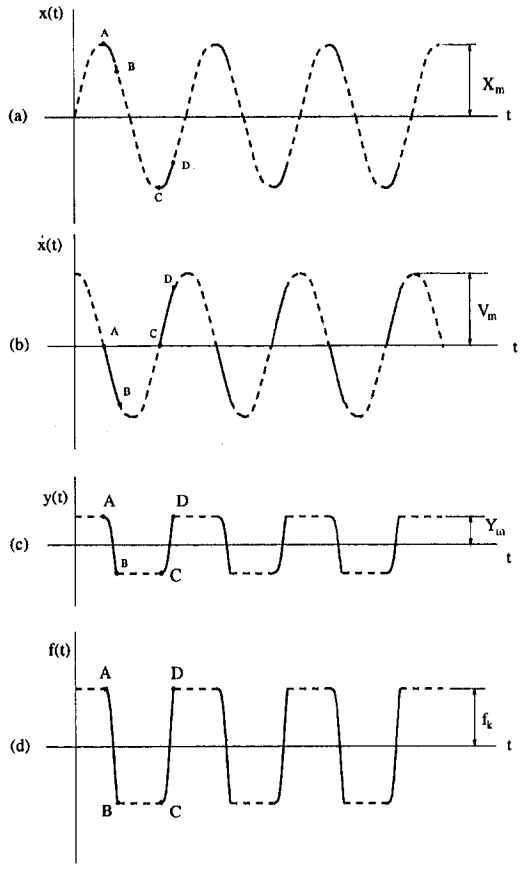

Fig. 2 Hypothetical responses of the idealized model during macroscopic sliding. Dashed lines indicate the sliding phase, and solid lines correspond to the microsticking phase. The mass displacement is *x*, the contact deformation is *y*, and the force at the interface is *f*.

Next, we consider the *f-ẋ* characteristic. By examining features in Figs. 2(*b*) and (*d*), a plot which dictates the *f-ẋ* relationship can be derived for the case of harmonic sliding motion, as shown in Fig. 4.

The maximum velocity of sliding is V_m. The transition speed, which distinguishes microsticking and sliding, is labeled as V_s. The slanted curves AB and CD describe microsticking motion, whereas the horizontal lines depict sliding motion.

If $f_s > f_k$ a jump occurs at each onset of sliding due to the transition from f_s to f_k. Stribeck friction models include a range of low relative velocities for which the friction characteristics have a negative slope, which usually induces instability in a friction system. If we substitute this relationship into the massless compliant contact model, the resulting *f-ẋ* and *f-x* plots have jumps from the static value of friction to the value of the friction at the transition velocity V_s (Liang and Feeny, 1996).

2.1 Transition Features in *f-ẋ* Plots. The transition speed V_s is the velocity of the mass when sliding begins. It characterizes the amount of hysteresis in the *f-ẋ* plots. Focusing on the sticking interval in Fig. 4, we note that the mass sticks at point C which corresponds to the time instant $t = t_1$, so that $\dot{x}(t_1) = 0$ and $x(t_1) = -X_m$. The contact then starts to deform elastically until sliding initiates at point D corresponding to $t = t_2$, at which the transition speed is defined. Nearly harmonic motion will be assumed to be preserved during this deformation process. Thus, for $t > t_1$, the following equation is assumed:

$$x(t) = -X_m \cos \omega(t - t_1). \tag{1}$$

Next, we consider the conditions which are required at the point D. The increment in displacement of the sliding mass during the interval CD is $2f_k/K_y$. Thus,

$$x(t_2) = -X_m + \frac{2f_k}{K_y} = -X_m \cos \omega(t_2 - t_1). \tag{2}$$

Furthermore, $V_s \equiv \dot{x}(t_2)$, which is expressed as

$$V_s = \omega X_m \sin \omega(t_2 - t_1). \tag{3}$$

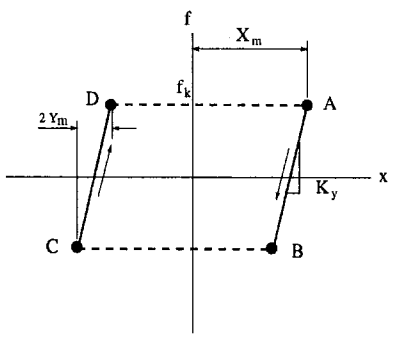

Fig. 3 A schematic diagram showing the *f-x* relationship in a compliant contact during harmonic motion of the sliding mass. Dashed and solid lines correspond to sliding and microsticking phases.

Downloaded 04 May 2010 to 171.66.16.26. Redistribution subject to ASME license or copyright; see http://www.asme.org/terms/Terms_Use.cfm

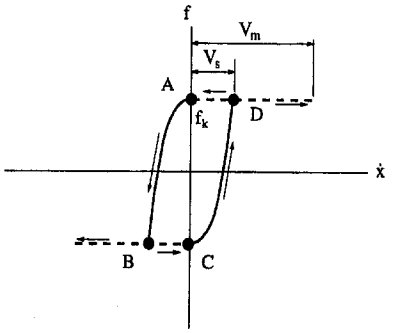

Fig. 4 A schematic diagram showing the *f-ẋ* relationship in a compliant contact during harmonic motion of the sliding mass. Dashed and solid lines correspond to sliding and microsticking phases.

Squaring and adding "ω times Eq. (2)" and "Eq. (3)", and solving for V_s, yields

$$V_s = 2\omega\sqrt{\frac{X_m f_k}{K_y} - \left(\frac{f_k}{K_y}\right)^2}. \quad (4)$$

This expression shows that the transition speed is proportional to the frequency of the harmonic oscillation. Thus, increasing the frequency increases the amount of hysteresis, as can be observed in practice. Furthermore, V_s can be used to cross check the contact stiffness. The qualitative and quantitative features of expression (4) will be investigated experimentally in Section 3.2.

Another specific feature of the idealized model is the horizontal tangency of *f-ẋ* plot in the transition from sliding to microsticking at both points C and A in Fig. 4. This characteristic is due to the fact that, during a stick,

$$f(t) = K_y y(t) = K_y\{Y_m \text{ sign } (\dot{x}(t_1^-)) + x - X_s\}, \quad (5)$$

where X_s represents the displacement at which microsticking starts, and t_1 corresponds to the time instant at which the mass sticks. From the above equation, we can write

$$\frac{df}{d\dot{x}} = \frac{df}{dt}\frac{dt}{d\dot{x}} = K_y\dot{x}\frac{1}{\ddot{x}}. \quad (6)$$

using Eq. (4), we have

$$\frac{df}{d\dot{x}} = \frac{K_y\dot{x}}{\omega\sqrt{X_m^2\omega^2 - \dot{x}^2}}. \quad (7)$$

Thus, there is a horizontal tangency at the onset of microsticking, i.e., $df/d\dot{x}|_{|\dot{x}|=0^+} = 0$.

3 Experiments

3.1 Apparatus. The apparatus (Fig. 5) consisted of a mass in an air track, helical springs, and the friction-contact mechanism. Motion in the air track had a nondimensional viscous damping factor equal to 0.0008. The friction-contact mechanism consisted of a pinched-flange structure which is designed for balancing the normal loads on both sliding surfaces. The contacts were mounted to 2 × 12.7 × 44.45 mm aluminum beams. Strain gages on the beams were used to sense the normal loads.

The displacements of both the sliding mass and the base excitation were sensed by a linear variable differential transformer (LVDT). This LVDT was made by Rabinson-Halpern Co. (Model 210A-0500) and had a resolution of 2.5 μm after quantization. The seismic accelerometer (PCB, Model 393C) was adopted to record the acceleration signal. This accelerometer had a frequency range from 0.025 to 800 Hz with five percent transverse sensitivity and a resonant frequency of 3.5 kHz. The friction force was measured by a piezoelectric load cell (PCB, Model 208B) which had 0.00089 N resolution in a range of 44.8 N in both tension and compression, and a stiffness of 1.75 × 10^9 N/m. The discharge time constant of this load cell was 50 sec and the resonant frequency was 70 kHz. The velocity signal was obtained by differentiating the displacement signal, and then smoothened with a five-point moving average. Considerable noise was still present despite smoothening the velocity signal. Special care was taken to ensure that the phases of the sensor signals were consistent.

The system was driven by an electromagnetic shaker (LDS, Model 400) associated with a power amplifier and signal generator. This unit produced a harmonic signal for exciting the sliding mass. The lowest operating frequency for which the shaker produced satisfactory harmonic signal was 1 Hz. The maximum displacement amplitude was 8 mm. The friction contact was steel-on-steel. The planar surfaces were ground and rubbed with 400-grit silicon-carbide paper. The other contact surfaces, attached to the loading beams, were hemispherical with 6.3-mm radii and were lathed with an engineering finish then rubbed by the same type of paper. Finally, the surfaces were cleaned by a degreaser (Measurement Group, Inc., Model CSM-1). The R_a surface roughness parameter, which measures the mean magnitude of deviation from the centerline of the surface (Chung, 1993), was estimated by using a Dektak IIA. The instrument moves a stylus across the surface and measures vertical stylus variations in the range of 100–655,000 Angstroms with an LVDT. The worn hemispherical contact had R_a values ranging from approximately one to eight microns for 1-mm scans, and the planar contact had R_a values ranging from 0.3–0.35 μm for 2-mm scans on the unworn surface, and 0.5–0.8 μm for 1-mm scans on the worn surface. The surfaces were engaged in sliding motion for at least 30 minutes to attain a steady-state friction characteristic before the data were recorded. During the whole experiment process, the nominal normal load was 3.53 N.

3.2 Macroscopic Sliding. The friction force was plotted against the displacement and velocity for excitation frequencies of 5.61 Hz, 8.7 Hz, and 11.1 Hz. The case of 8.7 Hz is shown in Fig. 6.

In order to verify that the displacement responses of these pure macroscopic sliding motions were close to harmonic func-

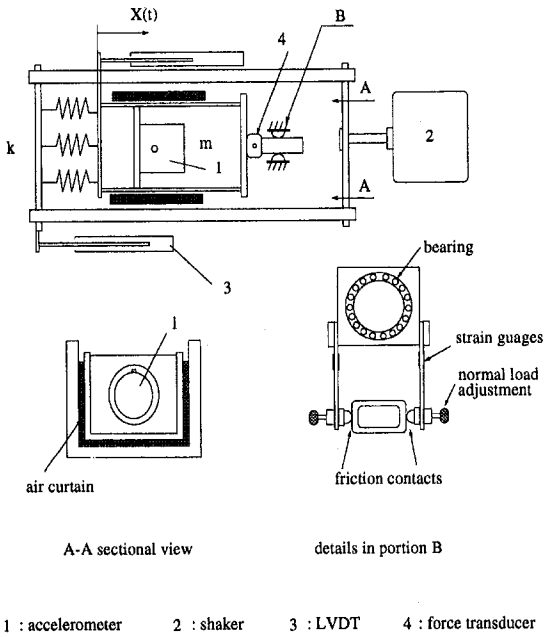

Fig. 5 A schematic diagram showing the outline of the experimental apparatus

Downloaded 04 May 2010 to 171.66.16.26. Redistribution subject to ASME license or copyright; see http://www.asme.org/terms/Terms_Use.cfm

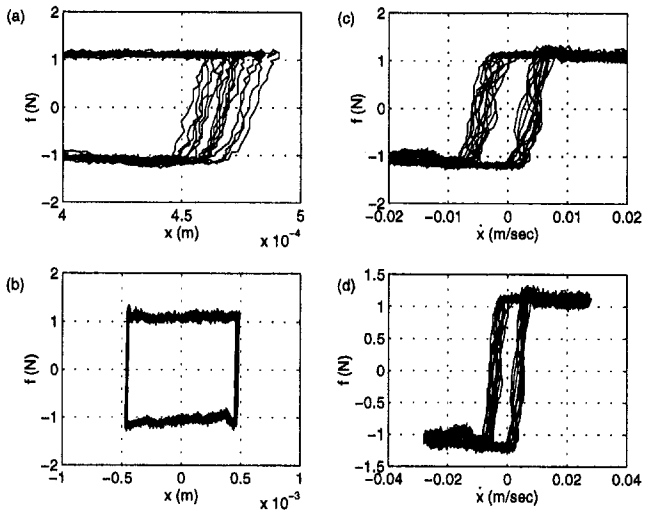

Fig. 6 Experimental *f-x* and *f-ẋ* characteristics for 8.7 Hz excitation: (*a*) detail of sticking in *f-x* plot, (*b*) *f-x* characteristics, (*c*) detail of sticking in *f-ẋ* plot, and (*d*) *f-ẋ* characteristics

tions as assumed in Section 2.1, the power spectrum of the displacement signal of the sliding mass corresponding to 5.61 Hz excitation was examined. The amplitude associated with the fundamental frequency was almost 100 times larger than that of the second harmonic.

3.2.1 Extraction of the Contact Stiffness. Plots from various excitation frequencies demonstrate similar microsticking characteristics; the slopes of sticking straight lines are almost indistinguishable. This implies that, during the microsticking, the contact deformed in a nearly linearly elastic manner.

Table 1 includes the following estimated information: (1) the average span of friction force, $2\tilde{f}_k$, which accounts for the friction-force changes right before and after the sticking events; (2) the micro displacement or the "elastic deformation," $2\tilde{Y}_m$, which is the cumulative displacement of the sliding mass during the microsticking interval; (3) the effective contact stiffness, $\tilde{K}_y$.

The estimated effective contact stiffnesses are taken as the average slope of the nearly vertical portion of the *f-x* plots. Thus, the estimates of the effective contact stiffness, $\tilde{K}_y$, for different cases are determined by dividing the average friction force span, $2\tilde{f}_k$, with the averaged elastic deformation, $2\tilde{Y}_m$. The average contact stiffness, $\tilde{K}_y$, from Table 1, is 192000 N/m.

3.2.2 Estimations of the Transition Speeds. Based on the *f-ẋ* plots from each case, the parameters for the computation process in Eq. (4) are shown in Table 2. In this table, the effective contact stiffnesses are taken to be the same as the estimated values listed in Table 1. The estimates of the transition speeds, $\hat{V}_s$, were obtained by directly applying the estimated parameters ω, $\hat{f}_k$, $\hat{K}_y$, and $\hat{X}_m$, to Eq. (4). Thus, these transition speed estimates are based on the ideal model. We would like to compare these values with the experimentally observed transition speeds as in Fig. 6(*c*) and the cases not shown. In the figure, the band of slanted trajectories, which denote microsticking, corresponds to the curves AB and CD of the ideal model

Table 1 Extraction of the effective contact stiffness

freq. ω (Hz)	$2\tilde{f}_k$ (N)	$2\tilde{Y}_m$ $(10^{-4}m)$	$\tilde{K}_y$ $(10^4 N/m)$	std. dev. σ $(10^4 N/m)$
5.61	2.42	0.110	20.1	2.63
8.7	2.36	0.116	18.1	2.51
11.1	2.60	0.125	19.4	2.72

Table 2 Estimation of the transition speed

freq. ω (Hz)	$\hat{f}_k$ (N)	$\hat{K}_y$ $(10^4 N/m)$	X_m $(10^{-3}m)$	$\hat{V}_s$ (m/sec)
5.61	1.06	20.1	0.49	0.0036
8.7	1.10	18.1	0.485	0.0058
11.1	1.28	19.4	0.48	0.0079

(Fig. 4). The microstick-slip transitions (corresponding to points B and D) are approximately centered at the estimated transition speeds from Table 2. The computed transition speeds in Table 2 were compared to the average transition speeds in the experiments, which were estimated to be 0.0035 m/sec, 0.0058 m/sec, and 0.0080 m/sec. The randomness surrounding these trends might be caused by surface roughness or the differentiation noise of the velocity signal.

3.3 Macroscopic Stick-Slip. The frequency of the base-excitation motion in this test was 2.5 Hz. Figure 7 shows the displacement, velocity, and acceleration responses of the sliding mass to a harmonic excitation. In Fig. 7, transition oscillations are evident in the acceleration and friction signals during intervals in which the displacement is nearly constant. Small-amplitude ripples also occurred during the macroscopic sticking interval of the velocity (apart from the differentiation noise) and displacement time histories, although they can barely be seen. In this investigation, the frequency of the transition oscillation is studied first.

To examine the frequency of the transition oscillation, a free-vibration test was carried out on the mass when stuck to the friction contact. This experiment was performed by releasing the sliding mass from an initial position. The presence of dry friction stopped the mass after some motion. At the onset of sticking, a high-frequency oscillation occurred. This oscillation was sensed by both the load cell and the accelerometer. An FFT of both signals showed that the frequency of this transition oscillation was 47.0 Hz.

In order to investigate the relationship between this oscillation frequency with the coupling effects, the main system parameters are required. These parameters are m = 2.42 kg and k = 2310 N/m. According to the sticking condition and the structure of the experimental apparatus, during sticking, the sliding mass is supported by the spring of the main system and an equivalent spring provided by the contact point. Therefore, a single-degree-of-freedom system connected to two springs provides a simple model for calculating the fundamental fre-

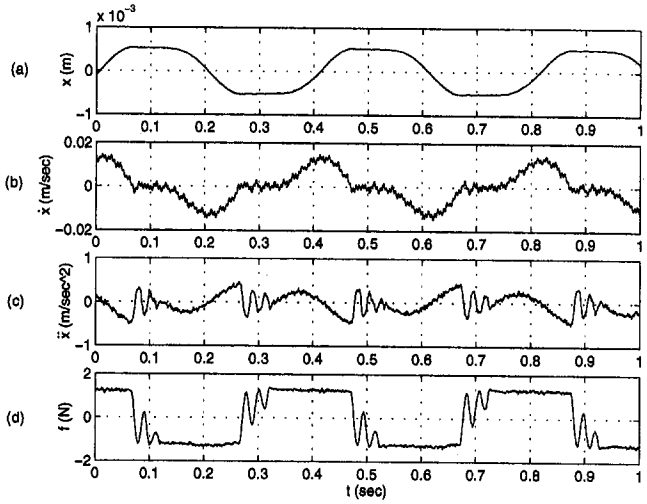

Fig. 7 Experimental stick-slip motion with 2.5 Hz excitation: time-domain responses of (*a*) displacement, (*b*) velocity, (*c*) acceleration, and (*d*) friction force

Downloaded 04 May 2010 to 171.66.16.26. Redistribution subject to ASME license or copyright; see http://www.asme.org/terms/Terms_Use.cfm

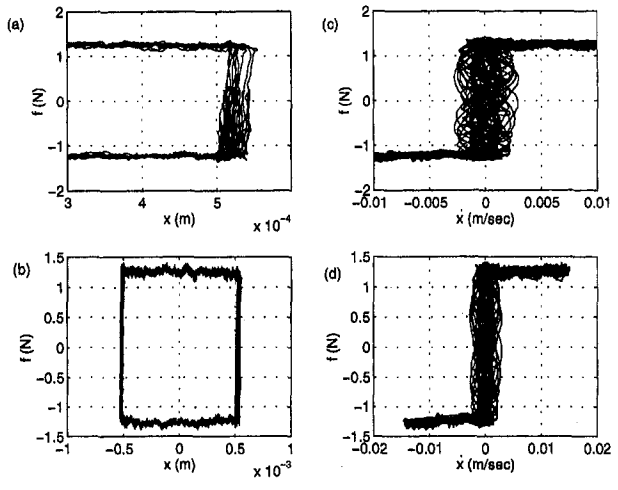

Fig. 8 Experimental *f-x* and *f-ẋ* characteristics with stick-slip process: (*a*) detail of sticking in *f-x* plot, (*b*) *f-x* characteristics, (*c*) detail of sticking in *f-ẋ* plot, and (*d*) *f-ẋ* characteristics

quency during a stick. Based on the averaged contact stiffness, $\bar{K}_y = 192000$ N/m, and main system parameters, the coupled fundamental frequency is equal to 45.1 Hz. This value is very close to the result from the free-vibration test. A viscous damping factor of $\zeta = 0.016$ (± 0.002) for the contact was estimated by logarithmic decrement.

Next, we explore the *f-x* and *f-ẋ* characteristics of the experimental stick-slip process, which are illustrated in Fig. 8. The sticking features are different from the macroscopic sliding cases. The occurrence of the transition oscillation (along with the noise in the velocity signal) gives rise to the tangle structures during the sticking regions in both *f-x* and *f-ẋ* plots. A more careful observation in the *f-x* plot (Fig. 8(*a*)) reveals that the friction force actually fluctuates before it moves from one extreme value to the other. This is again caused by the transition oscillation. The randomness of surface roughness, differentiation noise of velocity signal, and tangled structure conceal the transition behaviors in the *f-ẋ* plot. Such features are clear in the experiments of Hinrichs et al. (1997).

4 Numerical Studies

According to the idealized compliant-contact model, the system in Fig. 1 can be represented as

$$m\ddot{x} + kx + f(t) = kZ_e \cos(\omega t) \tag{8}$$

where Z_e is the amplitude of a harmonic base motion. It is reasonable to incorporate damping into the contact structure. The viscous damping factor of the contact is defined such that $\zeta = c/(2\sqrt{m(k + K_y)})$. Damping factors were employed in the simulations prior to its identification in Section 3.3, and hence differ from the estimated value. This damping effect is only added to the contact model, i.e., $f(t) = K_y y(t) + c\dot{y}(t)$, and is neglected during sliding, under the assumption that sliding contact dynamics are fast due to the large value of K_y (Vielsack, 1996, included contact damping in simulations). In addition, from Section 2, we know that $\dot{y}(t) = \dot{x}(t)$ during the microsticking interval. Thus, during sliding the model becomes

$$m\ddot{x} + kx + f_k \operatorname{sign}(\dot{x}) = kZ_e \cos(\omega t), \tag{9}$$

and during microsticking

$$m\ddot{x} + kx + c\dot{y} + K_y y(t) = kZ_e \cos(\omega t), \tag{10}$$

$$y(t) = Y_m \operatorname{sign}(\dot{x}(t_1^-)) + x(t) - X_s, \tag{11}$$

where Y_m (positive number) is the maximum deflection and X_s (number with a sign) is the displacement of the mass before microsticking begins. t_1 represents the time instant at which the mass sticks. The switching between microsticking and sliding occurs when the magnitude of $f(t) = K_y y(t) + c\dot{y}(t)$ exceeds f_k.

The numerical algorithm, based on a fifth-order Runge-Kutta method, carefully accounts for the switching between Eq. (9) and Eqs. (10) and (11) by checking for velocity reversals and whether the compliant-contact force has exceeded the static friction force, and iterating to precisely find the switching times. Similar algorithms are found in Shaw (1986) and Feeny and Moon (1994).

4.1 Macroscopic Sliding. The base amplitude Z_e is tuned such that both the experimental and simulated results possess similar macroscopic amplitudes X_m. At 5.61 Hz, 8.71 Hz, and 11.1 Hz, the measured base amplitudes were $\hat{Z}_e = 0.51$ mm, $\hat{Z}_e = 1.1$ mm, and $\hat{Z}_e = 2.0$ mm, while the simulation base amplitudes were $Z_e = 0.6$ mm, $Z_e = 1.1$ mm, and $Z_e = 2.0$ mm. The parameters K_y, m, k, and f_k are the same as those estimated from experimental studies. In this section, we will use a damping coefficient that has a nondimensional viscous damping factor equal to 0.0174.

We present the simulation results corresponding to 8.7 Hz excitation. The consistencies were similar in the other two cases, although the 5.61 Hz response magnitude was approximately 25 percent high when its simulated transition speed matched the experiment. In Fig. 9, the slanted hysteretic structure is present in the numerical versions of *f-ẋ* plots. This can be compared to Fig. 6. Aside from the random effects, the slanted structure in numerical studies corresponds to experimental results closely, particularly in the trend of frequency dependence of the transition speed, V_s. Furthermore, V_s matches the prediction given in Table 2, based on expression (4). There may be a small deviation caused by the presence of viscous damping which was absent in the derivation of expression (4), since V_s is defined as the velocity at which $K_y y(t) + c\dot{y}(t) = f_k$, and viscous damping will affect the evolution of $y(t)$. Moreover, horizontal tangency exists in the simulation results of the *f-ẋ* plots during the transition from sliding to microsticking.

4.2 Macroscopic Stick-Slip. The excitation amplitude input to the numerical model was chosen to produce a response magnitude similar to that of the experiment. The simulation excitation amplitude was $Z_e = 0.65$ mm while the experimentally measured amplitude was $\hat{Z}_e = 0.6$ mm. The discrepancy may compensate for simplifications in the friction modeling,

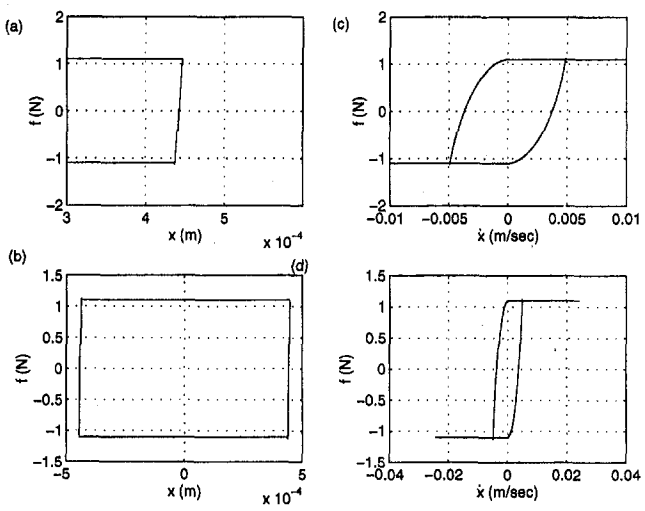

Fig. 9 Simulation of compliant contact model (ω = 8.7 Hz), numerical versions of (*a*) detail of sticking in *f-x* characteristic, (*b*) *f-x* plot, (*c*) detail of sticking in *f-ẋ* plot, and (*d*) *f-ẋ* characteristic

Downloaded 04 May 2010 to 171.66.16.26. Redistribution subject to ASME license or copyright; see http://www.asme.org/terms/Terms_Use.cfm

the presence of harmonics in the excitation, or other experimental errors.

The simulation results corresponding to a viscous-damping factor of 0.0174 are shown in Figs. 10 and 11. Comparing these plots with the equivalent experimental results shown in Figs. 7 and 8, the following observations can be made. (1) The numerical model matches the experimental macroscopic motion features of the friction and acceleration histories. For example, macroscopic stick-slip occurs with the the transition oscillation. (2) Numerical results in the f-x characteristics depict the transition features observed in experimental data. This includes the fluctuations in the friction force during the sticking interval, which can be observed in Fig. 11(a) as a darker portion in the lower part of the transition line. Furthermore, a multiple-loop structure present in the f-$\dot{x}$ characteristic manifests the transition oscillation. The presence of this multiple-loop structure replaces the slanted hysteretic structure occurring in the pure sliding case. This loop structure also states the existence of the oscillation ripple in the velocity response. These loops are also seen in the simulations of Hinrichs et al. (1997).

The simulation demonstrates that a microscale stick-slip occurs. This "double stick-slip" event is evident because the friction force, during the transition, temporarily reaches its maximum value twice before it finally stays at that value for a macroscopic sliding phase. Such a feature is apparent in the simulations of Vielsack (1996). This affects the f-$\dot{x}$ plots, where the loops have connected themselves with the sliding-friction levels in both signs. Similarly, the acceleration signal demonstrates some distortions corresponding to these "friction-bouncing" events.

Randomness of the friction process and velocity signal conceal part of the experimental transition features. However, the friction signal in Fig. 7(d), particularly in the transition regions, actually reached its static friction level during the transition region, which implies that microscale stick-slip did occur in the experiment.

The mechanism of this event can be roughly described as follows. At the onset of the macroscopic sticking, the contact point $y(t)$ is at its maximum deflection, i.e., $y(t_1) = Y_m$, if t_1 corresponds to the instant that the mass gets stuck and $\dot{x}(t_1^-) > 0$. Then, the contact starts to recoil from this extreme deflection and experiences the high-frequency transition oscillation as a mass/spring main system with an extra spring-damper system, modeled by $K_y y + c\dot{y}$. This transition oscillation is also influenced by the low-frequency excitation of the base. When the overall force exerted by the contact point, $K_y y(t) + c\dot{y}(t)$, during this transition oscillation, exceeds the static friction force, the mass will temporarily undergo a "micro slip." This micro slip takes place for a very short duration because during a micro slip, the behavior reverts from that of the sticking Eqs. (10) and (11) to the slip Eq. (9), which is independent of the compliance and damping of the contact. An important property of Eq. (9) alone (which models the case of rigid contact) is that it has sticking regions in the zero-velocity plane (Shaw, 1986). An interpretation of this sticking region is that, both below and above the $\dot{x} = 0$ plane, the vector field points toward the $\dot{x} = 0$ plane (Feeny, 1992). Thus, during a micro slip in the vicinity of the sticking region, the velocity is small and the vector field quickly pushes the oscillator back to zero velocity, where it may stick again. When x and $\dot{x}$ are no longer near the sticking region, a tiny slip leads to a macro slip.

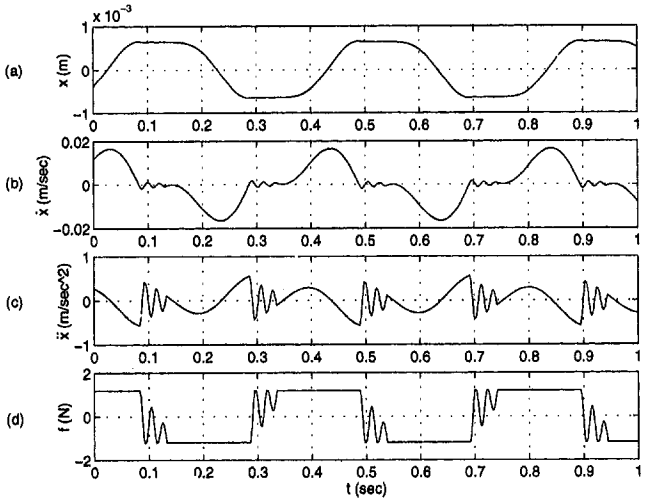

Fig. 10 Numerical simulations of stick-slip with the compliant-contact model with $\zeta = 0.0174$: responses of (a) displacement, (b) velocity, (c) acceleration, and (d) friction force

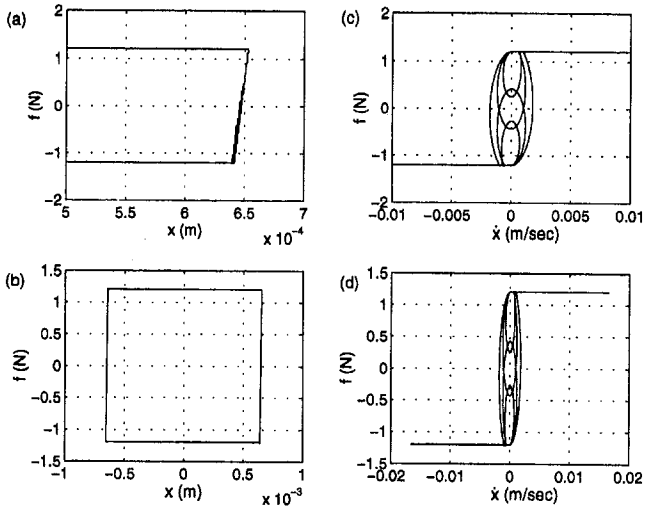

Fig. 11 Simulation of the compliant-contact model with $\zeta = 0.0174$: (a) detail of sticking in f-x characteristic, (b) f-x plot, (c) detail of sticking in f-$\dot{x}$ plot, and (d) f-$\dot{x}$ characteristic

Since the estimated damping factor is close to that used in the case presented, the occurrence of double stick slip in the experiment is consistent with the simulations. Simulations with $\zeta = 0.0558$ did not exhibit double stick-slip. Instead, transition oscillations decayed smoothly. f-$\dot{x}$ plots were still tangled, but the tangles did not connect themselves with sliding friction values in the same way as in the above case. The f-x plots had similar features to the case of lower damping.

5 Discussion

The energy dissipated per cycle of oscillation is equal to the area of the f-x loop, which equals the displacement span of sliding times twice the sliding friction force. Thus, the slope in this curve, K_y, has no effect on the energy dissipation, unless compliance significantly effects the span of sliding displacement. Hence, one might ask whether it is of any use to consider this model when the stiffness is relatively large. This would depend on the application and on the parameter range of interest.

Controller performance can be sensitive to modeling details. We see from the f-$\dot{x}$ plots that the dissipation power depends on the phase of the oscillation. This might be important in precision control, for example in the manufacturing of mirrors and other precise surfaces, which may need precision of a few nm (Cetinkunt and Donmez, 1993).

The transition velocity is an indicator of the amount of hysteresis in the f-$\dot{x}$ plots, and is approximated as proportional to the excitation frequency. In the case of dither, high frequencies are involved, and the force-velocity hysteresis is likely to be significant to the understanding of the dither mechanism.

Downloaded 04 May 2010 to 171.66.16.26. Redistribution subject to ASME license or copyright; see http://www.asme.org/terms/Terms_Use.cfm

Hysteresis in an f-$\dot{x}$ plot indicates instances for which the contact force does not oppose the motion. This results from the energy stored in the contact stiffness.

Recent works have shown that subtle force-velocity hysteresis can have an impact on the qualitative nonlinear behavior of oscillators. Oancea and Laursen (1996) reported that a simple oscillator exhibited different behaviors depending on whether a simple friction model or a hysteretic state-variable model was used. Kappagantu (1997) showed that the simulated dynamics of a frictionally excited beam matched the experimental dynamics better if contact compliance was included in the model. Such modeling details may be significant when considering, for example, the friction law used to model friction-induced squeak and squeal (Ibrahim, 1994), the occurrence of which varies from day to day as the temperature and humidity changes.

A frequency response would give some indication of the dependence of the amplitude of response on contact stiffness. Nonlinear frequency responses have been presented by Ferri and Heck (1997), which included the effect of contact mass, Griffin (1980), J.-H. Wang (1996), Y. Wang (1996), Guillen and Pierre (1996), and Sanliturk and Ewins (1996). The nonlinear response is greatly dependent on the amplitude of excitation.

The source of the contact compliance could be in the asperities, the contact material, or the surrounding structure. Each of these sources are viable, and likely to occur in mechanical systems. To distinguish this, one idea would be to conduct the experiments at various normal loads. If the contact compliance were part of an ideal hemispherical contact geometry, the stiffness would vary with the normal load N and also the tangential displacement (Johnson, 1985). Based on equations from Mindlin (1949), Cattaneo (1938), and Mindlin and Deresiewicz (1953), with a single coefficient of friction μ, tangential loading T would cause an annular region (in the contact area) of slip because of the normal load distribution, and the tangential displacement would vary with $N^{2/3}[1 - (1 - T/\mu N)^{2/3}]$, whence a compliance characteristic could be ascertained. There is some nonlinearity evident in our f-x plots, but it is not a dominating feature. Therefore it might be suspected that the surrounding structural elasticity is responsible for much of the contact compliance. Nonetheless, the normal-load effect would be an interesting issue for further study.

Sometimes researchers have used smoothened friction laws as useful approximations to discontinuous models and to model presliding displacement (Threlfall, 1978; Vielsack, 1996). In quasi-static or unidirectional sliding, the two ideas might be seen as equivalent, but the general dynamic features are different. Such smoothened functions of velocity only do not produce the f-$\dot{x}$ hysteresis that the contact compliance generates. Indeed, the addition of contact compliance in the model is akin to having an additional state in the system. Increasing the state-space dimension raises the potential diversity of dynamical behavior.

Experimentally observed hysteresis in force-velocity plots have led to some interesting state-variable modeling ideas (Ruina, 1985). In this case, a physically motivated model has been verified through several cross examinations.

6 Conclusion

A massless compliant contact model with Coulomb friction at the interface was used to interpret both the hysteretic behavior in the f-$\dot{x}$ measurements during macroscopic sliding oscillations and the transition oscillations in the stick-slip process. Consistency in experimental and numerical results ties both phenomena, usually treated separately in the literature, to contact compliance.

Hysteresis in the macroscopic sliding force-velocity plots was predicted in the analysis, observed in the sliding experiments, and reproduced in numerical simulations. Characteristics include a transition speed between microsticking and sliding motion. The transition speed indicates the degree of hysteresis, and was shown to depend on the amplitude and frequency of oscillation, the friction force, and the contact stiffness.

We experimentally and numerically observed transition oscillations during macroscopic stick-slip processes. The free-vibration frequency of oscillation while stuck matched the stick-slip-transition oscillation frequency, and agreed with the predicted frequency based on the contact stiffness estimated from the sliding experiments. Both experimental and simulated f-$\dot{x}$ plots revealed tangles in the friction force during the stick-slip transitions.

Micro-scale stick-slip occurred during the transition oscillations associated with the macroscopic stick phases in the experimental and simulated stick-slip processes. The occurrence of such events depended on the damping incorporated into the contact compliance.

The contact compliance is a physical modeling feature that explains observed behavior, which may be significant to controller performance, dither, noise generation, nonlinear response, and other applications.

Acknowledgment

This work was funded by the National Science Foundation (CMS-9624347), Ford Motor Co. and MSU. Access to the to Dektak IIA machine was provided by R. Loloee and the Physics and Astronomy Department at MSU.

References

Canudas de Wit C., Olsson H., Astrom K. J., and Lischinsky, 1995, "A New Model for Control of System with Friction," *IEEE Transactions on Automatic Control,* Vol. 40, No. 3, pp. 419–425.

Cattaneo, C., 1938, "Sul Contatto di due Corpi Elastici," *Accademia dei Lincei, Rendiconti,* Series 6, Vol. 27, pp. 342–348, 434–436, and 474–478.

Cetinkunt, S., and Donmez, A., 1993, "CMAC Learning Controller for Servo Control of High Precision Machine Tools," *Proceedings of the American Control Conference,* IEEE, San Francisco, pp. 1976–1980.

Chung, Y.-W., 1993, "Characterization of Topography of Engineering Surfaces," *Surface Diagnostics in Tribology,* K. Miyoshi and Y.-W. Chung, eds., World Scientific, Singapore, pp. 33–46.

Courtney-Pratt, J., and Eisner, E., 1957, "The Effect of a Tangential Force on the Contact of Metallic Bodies," *Proceedings of the Royal Society of London,* Vol. A238, pp. 529–550.

Dahl, P., 1968, "A Solid Friction Model," Tech. Rep. Tor-0158(3197-18)-1, Aerospace Corp., El Segundo, CA.

Dugas, R., 1955, *A History of Mechanics,* Éditions du Griffon, Neuchâtel.

Feeny, B. F., 1992, "A Nonsmooth Coulomb Friction Oscillator," *Physica D,* Vol. 59, pp. 25–38.

Feeny, B. F., and Moon, F. C., 1994, "Chaos in a Forced Dry-Friction Oscillator: Experiments and Numerical Modelling," *Journal of Sound and Vibration,* Vol. 170, No. 3, pp. 303–323.

Ferri, A. A., 1995, "Friction Damping and Isolation Systems," *Journal of Mechanical Design,* Vol. 117(B), pp. 196–206.

Ferri, A. A., and Heck, B. S., 1997, "Vibration Analysis of Dry Damped Turbine Blades Using Singular Perturbation Theory," *Journal of Vibration and Acoustics,* to appear.

Guillen, J., and Pierre, C., 1996, "Analysis of the Forced Response of Dry-Friction Damped Structural Systems Using an Efficient Hybrid Frequency-Time Method," *Nonlinear Dynamics and Controls,* DE-Vol. 91, pp. 41–50.

Griffin, J. H., 1980, "Friction Damping of Resonant Stresses in Gas Turbine Engine Airfoils," *Journal of Engineering for Power,* Vol. 102, pp. 329–333.

Harnoy, A., Friedland, B., and Rachoor, H., 1994, "Modeling and Simulation of Elastic and Friction Forces in Lubricated Bearing for Precise Motion Control," *Wear,* Vol. 172, pp. 155–165.

Hinrichs, N., Oestreich, M., and Popp., K., 1997, "Friction-Induced Vibrations: Experiments, Modeling and Analysis," *ASME Design Engineering Technical Conferences,* Sacramento, in press.

Ibrahim, R. A., 1994, "Friction-Induced Vibration, Chatter, Squeal and Chaos," ASME *Applied Mechanics Reviews,* Vol. 47, No. 7, pp. 209–253.

Kappagantu, R., 1997, *An "Optimal" Modal Reduction of Systems with Frictional Excitation,* Ph.D. thesis, Michigan State University, East Lansing, MI.

Ko, P. L., and Brockley, C. A., 1970, "The Measurement of Friction and Friction-Induced Vibration," *Journal of Lubrication Technology,* Oct., pp. 543–549.

Liang, J.-W., and Feeny, B. F., 1996, "The Effects of Tangential Contact Stiffness on a Harmonically Forced Oscillator," *Elasto-Impact and Friction in Dynamic Systems,* A. A. Ferri, G. T. Flowers, and S. C. Sinha, eds., ASME DE-Vol. 90, pp. 85–96.

Marui, E., and Kato, S., 1984, "Forced Vibration of a Base-Excited Single-Degree-of-Freedom System With Coulomb Friction," ASME *Journal of Dynamical Systems, Measurement, and Control,* Vol. 106, pp. 280–285.

Downloaded 04 May 2010 to 171.66.16.26. Redistribution subject to ASME license or copyright; see http://www.asme.org/terms/Terms_Use.cfm

Mindlin, R. D., 1949, "Compliance of Elastic Bodies in Contact," ASME JOURNAL OF APPLIED MECHANICS, Vol. 16, pp. 259–268.

Mindlin, R. D., and Deresiewicz, H., 1953, "Elastic Spheres in Contact Under Varying Oblique Forces," ASME JOURNAL OF APPLIED MECHANICS, Vol. 20, pp. 327–344.

Oancea, V. G., and Laursen, T. A., 1996, "Experimental and Numerical Study of Low Frequency Stick-Slip Motion," *Sixth Conference on Nonlinear Vibrations, Stability, and Dynamics of Structures,* Blacksburg, VA, June 9–13.

Oden, J. T., and Martins, J. A. C., 1985, "Models and Computational Methods for Dynamic Friction Phenomena," *Computer Methods in Applied Mechanics and Engineering,* Vol. 52, Nos. 1–3, pp. 527–634.

Polycarpou, A., and Soom, A., 1992, "Transitions Between Sticking and Slipping," *Friction-Induced Vibration, Chatter, Squeal, and Chaos,* ASME DE-Vol. 49, pp. 139–148.

Rorrer, R. A. L., 1995, "Friction-Induced Vibration of Multi-Degree of Freedom Sliding Subsystems," *ASME Design Engineering Technical Conference 3-A,* Boston, Sept., DE-Vol. 84-1, pp. 1179–1186.

Ruina, A. L., 1985, "Constitutive Relations for Frictional Slip," *Mechanics of Geomaterials,* Z. Bazant, ed., John Wiley and Sons, pp. 169–188.

Sanliturk, K. Y., and Ewins, D. J., 1996, "Modeling Two-Dimensional Friction Contact and its Application Using Harmonic Balance Method," *Journal of Sound and Vibration,* Vol. 193, No. 2, pp. 511–524.

Shaw, S. W., 1986, "On the Dynamic Response of a System with Dry Friction," *Journal of Sound and Vibration,* Vol. 108, No. 2, pp. 305–325.

Threlfall, D. C., 1978, "The Inclusion of Coulomb Friction in Mechanisms Programs with Particular Reference to DRAM," *Mechanisms and Machine Theory,* Vol. 13, pp. 475–483.

Vielsack, P., 1996, "Regularisierung des Halftzustandes bei Coulombscher Reibung," *Zeitschrift für angewandte Mathematik und Mechanik,* Vol. 76, No. 8, pp. 439–446.

Wang, J.-H., 1996, "Design of a Friction Damper to Control Vibration of Turbine Blades," *Dynamics with Friction: Modeling, Analysis, and Experiment,* A. Guran, F. Pfeiffer, and K. Popp, eds., World Scientific, Singapore, pp. 169–195.

Wang, J.-H., and Chen, W. K., 1993, "Investigation of the Vibration of a Blade with Friction Damper by HBM," *Journal of Engineering for Gas Turbines and Power,* Vol. 115, pp. 294–299.

Wang, Y., 1996, "An Analytical Solution for Periodic Response of Elastic-Friction Damped Systems," *Journal of Sound and Vibration,* Vol. 189, No. 3, pp. 299–313.

Downloaded 04 May 2010 to 171.66.16.26. Redistribution subject to ASME license or copyright; see http://www.asme.org/terms/Terms_Use.cfm

The Transient Response of Structures Using Asymptotic Modal Analysis

R. R. Reynolds
Assistant Professor of Mechanical Engineering, University of Arkansas, Fayetteville, AR 72701
Assoc. Mem. ASME

E. H. Dowell
Dean and J. A. Jones Professor of Mechanical Engineering and Materials Science, Duke University, Durham, NC 27708
Mem. ASME

The transient response of a structure is predicted using an asymptotic modal approximation of the classical modal solution. The method is aimed at estimating the impulse response problem for high frequency regimes where typical numerical methods (e.g., finite elements) are impractical. As an example, the response of a thin elastic panel is modeled in a frequency range that includes a sufficient number of modes. Both impulsive and arbitrary forms of excitation are considered. It is shown that the asymptotic modal analysis yields an excellent estimate of both the local displacement near the excitation location and of the spatially averaged transient response of the panel for moderate time spans after the excitation is applied. Furthermore, as this approach does not *require that the mode shapes or natural frequencies of the structure to be calculated, it is an* extremely *efficient technique.*

1 Introduction

As structural engineers attempt to assess the durability of their designs, one of the most valuable tools that they can have is an efficient method of predicting dynamic response. There are many methods available for predicting the response of a complex structure to *random* inputs or single frequency excitation. Statistical energy analysis (SEA) (Lyon, 1975) and, more recently, asymptotic modal analysis (AMA) (Dowell and Kubota, 1985; Kubota and Dowell, 1986; Kubota et al., 1990) are two such techniques. However, there are few approaches available today that can be applied when the excitation is transient. Of these, the finite element methods are most widely used and while they are very useful for characterizing the static and low-frequency dynamic behavior of structures, the model size and computational requirements become cumbersome at moderate to high frequencies due to the spatial resolution necessary to resolve the mode shapes. There have also been several efforts made to extend SEA to cope with transient structural excitations (Dalton, 1992; Pinnington and Lednik, 1996) that have had some success. However, these methods yield very approximate estimates of system behavior. Here, we present a new method for estimating the transient response of a structure based on AMA methods that is applicable to the moderate to high frequency ranges.

2 Analysis

To make the method easily accessible, we will use a thin elastic plate as a representative physical system. This is simply an example and in no way limits the applicability of the approach. For such a panel, the equation of motion of such a panel is typically written as

$$\frac{\partial^2 W}{\partial \tau^2} + C\frac{\partial W}{\partial \tau} + \left[\frac{1}{\gamma^2}\frac{\partial^4 W}{\partial \xi^4} + 2\frac{\partial^4 W}{\partial \xi^2 \partial \eta^2} + \gamma^2\frac{\partial^4 W}{\partial \eta^4}\right] = f(\xi, \eta, \tau) \quad (1)$$

where W is the nondimensional, transverse displacement of the panel, f is the nondimensional excitation function, γ is the panel aspect ratio, and ξ, η, and τ are the nondimensional spatial and time coordinates. It is also well known that the response of such a plate can be represented as

$$W(\xi, \eta, \tau) = \sum_{n=1}^{N} q_n(\tau)\psi_n(\xi, \eta) \quad (2)$$

where, q_n is the modal coefficient of the nth mode and ψ_n is the nth eigenmode of the plate. As is typical, we substitute Eq. (2) into (1) and use the orthogonality of the modes to arrive at the equation of motion for an individual mode. This has the form

$$\ddot{q}_n + 2\zeta_n\omega_n\dot{q}_n + \omega_n^2 q_n = Q_n(\tau) \quad (3)$$

where a dot indicates differentiation with respect to nondimensional time, ζ_n is the damping ratio, and ω_n is the natural frequency of mode n. Here the generalized force is

$$Q_n = \frac{\int_{\text{panel}} f(\tau)\psi_n dA}{\int_{\text{panel}} \psi_n^2 dA}. \quad (4)$$

For simplicity, the mass distribution of the plate is assumed to be uniform. However, the results are readily generalized to any smoothly varying distribution. At high frequencies, the displacements of the panel away from its boundaries are independent of the boundary conditions and the nondimensional frequencies can be expressed in terms of the modal numbers, n_ξ, n_η, and the panel aspect ratio, γ, as

$$\omega_n = \frac{1}{\gamma}\pi^2(n_\xi^2 + \gamma^2 n_\eta^2). \quad (5)$$

The time variation of the modal coefficients can be expressed using the standard convolution integral

$$q_n(\tau) = \int_0^{\tau_f} h_n(\tau - \tau')Q_n(\tau')d\tau' \quad (6)$$

where τ_f is the duration of the excitation and $h_n(\tau)$ is the nth classical unit impulse response

$$h_n(\tau) = \frac{\exp(-\zeta_n\omega_n\tau)\sin(\omega_n\sqrt{1-\zeta_n^2}\tau)}{\omega_n\sqrt{1-\zeta_n^2}}. \quad (7)$$

Contributed by the Applied Mechanics Division of THE AMERICAN SOCIETY OF MECHANICAL ENGINEERS for publication in the ASME JOURNAL OF APPLIED MECHANICS.

Discussion on this paper should be addressed to the Technical Editor, Professor Lewis T. Wheeler, Department of Mechanical Engineering, University of Houston, Houston, TX 77204-4792, and will be accepted until four months after final publication of the paper itself in the ASME JOURNAL OF APPLIED MECHANICS.

Manuscript received by the ASME Applied Mechanics Division, Jan. 28, 1997; final revision, July 11, 1997. Associate Technical Editor: M. Shinozuka.

 Copyright © 1998 by ASME

Downloaded 04 May 2010 to 171.66.16.26. Redistribution subject to ASME license or copyright; see http://www.asme.org/terms/Terms_Use.cfm

2.1 Local AMA Solution. We now, consider the response due to a point load on the plate. In this case, Q_n is

$$Q_n = \frac{\int_0^1 \int_0^1 f(\tau)\delta(\xi - \xi_f)\delta(\eta - \eta_f)\psi_n(\xi, \eta)d\xi d\eta}{\int_0^1 \int_0^1 \psi_n^2(\xi, \eta)d\xi d\eta} \quad (8)$$

where (ξ_f, η_f) is the point of application of the load. This simplifies to yield

$$Q_n = \frac{f(\tau)\psi_n(\xi_f, \eta_f)}{\langle\psi_n^2\rangle} \quad (9)$$

where $\langle \ldots \rangle$ indicates the spatial average. We may now write our classical solution to the point forcing problem as

$$W_{\mathrm{CMA}}(\xi, \eta, \tau) = \sum_{n=1}^{\infty} \frac{\psi_n(\xi, \eta)\psi_n(\xi_f, \eta_f)}{\langle\psi_n^2\rangle} \int_0^{\tau_f} h_n(\tau - \tau')f(\tau')d\tau' \quad (10)$$

which expresses the plate displacement at the location (ξ, η) due to the point load $f(\tau)$ at (ξ_f, η_f).

We now apply several simplifications. First, for the sake of definiteness, let us temporarily restrict our attention to impulsive loads. We will return to more general loading forms later. In this instance, Eq. (10) simplifies to

$$W_{\mathrm{CMA}}(\xi, \eta, \tau) = \hat{f} \sum_{n=1}^{\infty} \frac{\psi_n(\xi, \eta)\psi_n(\xi_f, \eta_f)}{\langle\psi_n^2\rangle} h_n(\tau) \quad (11)$$

where $\hat{f}$ is the magnitude of the impulse loading. We will focus on the response of the panel within a particular band of frequencies, $\Delta\omega$, placing no restrictions on the size of $\Delta\omega$. If the number of modes in this frequency band, ΔM, is sufficiently large[1], then for the response at the loading point, (ξ_f, η_f), we may apply a form of the asymptotic approximation of Dowell and Kubota (1985) and express the summation of modes as approximately the spatial average of a mode, i.e.,

$$\sum_{n=M}^{M+\Delta M-1} \frac{h_n(\tau)\psi_n^2(\xi_f, \eta_f)}{\langle\psi_n^2\rangle} \approx \frac{\langle\psi_c^2\rangle}{\langle\psi_c^2\rangle} \sum_{n=M}^{M+\Delta M-1} h_n(\tau) = \sum_{n=M}^{M+\Delta M-1} h_n(\tau) \quad (12)$$

where ψ_c is the eigenmode at the center frequency, ω_c, of $\Delta\omega$.

Now consider the behavior of the impulse response function and the sum of the right-hand side of Eq. (12). During a relatively short period of time after the application of the force, say $0 < \tau < (2\pi/\omega_c)$, the exponential portion of the impulse response function will be slowly varying compared to the sine function (cf. Eq. (7)). As τ is small, then $\exp(\xi_n\omega_n\tau) \approx 1$ and we may focus on the terms that vary more rapidly with $\omega\tau$. Let us now assume that the structural damping is also slowly varying with in $\Delta\omega$ and can be approximated by the damping at ω_c. That is, $\zeta_n \approx \zeta_c$. Therefore, this summation is essentially

$$S_1 \equiv \sum_{n=M}^{M+\Delta M-1} h_n(\tau) \approx \sum_{n=M}^{M+\Delta M-1} \frac{\sin(\omega_n\sqrt{1-\zeta_c^2}\tau)}{\omega_n\sqrt{1-\zeta_c^2}}. \quad (13)$$

Now, linearize S_1 in terms of $\delta\omega_n$ where $\omega_n = \omega_c + \delta\omega_n$.

$$S_1 \approx \sum_{n=M}^{M+\Delta M-1} \left\{ \frac{\sin(\omega_c\sqrt{1-\zeta_c^2}\tau)}{\omega_c\sqrt{1-\zeta_c^2}} + \frac{\tau\delta\omega_n \cos(\omega_c\sqrt{1-\zeta_c^2}\tau)}{\omega_c} - \frac{\delta\omega_n \sin(\omega_c\sqrt{1-\zeta_c^2}\tau)}{\omega_c^2\sqrt{1-\zeta_c^2}} \right\} + \text{H.O.T.} \quad (14)$$

Simplifying this further yields

$$S_1 \approx \Delta M \frac{\sin(\omega_c\sqrt{1-\zeta_c^2}\tau)}{\omega_c\sqrt{1-\zeta_c^2}} + \left\{ \frac{\tau\cos(\omega_c\sqrt{1-\zeta_c^2}\tau)}{\omega_c} - \frac{\sin(\omega_c\sqrt{1-\zeta_c^2}\tau)}{\omega_c^2\sqrt{1-\zeta_c^2}} \right\} \sum_{n=M}^{M+\Delta M-1} \delta\omega_n \quad (15)$$

or

$$S_1 \approx S_2 + \{\cdots\} \sum_{n=M}^{M+\Delta M-1} \delta\omega_n. \quad (16)$$

Recall that we have already restricted τ to be less than $(2\pi/\omega_c)$ so that the last term in Eq. (16) is of the order $(1/\omega_c^2)$ $\Sigma_{n=1}^{M+\Delta M-1}\ \delta\omega_n$ for small damping. Since our definition of $\delta\omega_n$ restricts its range to approximately

$$-\frac{\Delta\omega}{2} \le \delta\omega_n \le \frac{\Delta\omega}{2} \quad (17)$$

then, if the structural modes are distributed evenly throughout the frequency range $\Delta\omega$,

$$\sum_{n=M}^{M+\Delta M-1} \delta\omega_n \approx 0 \quad (18)$$

and we may say that

$$S_1 \approx S_2 = \Delta M \frac{\sin(\omega_c\sqrt{1-\zeta_c^2}\tau)}{\omega_c\sqrt{1-\zeta_c^2}}. \quad (19)$$

Equation (12) can now be written as

$$\sum_{n=M}^{M+\Delta M-1} \frac{h_n(\tau)\psi_n^2(\xi_f, \eta_f)}{\langle\psi_n^2\rangle} \approx \Delta M h_c(\tau). \quad (20)$$

We will show later that this is valid using a thin panel as an example. For now we note that the error of this approximation is small only if τ is small and the modes are nearly evenly distributed. Strictly speaking, the summation is no longer necessary, yet note that the error caused by unevenly distributed modes is now proportional to the number of modes and, therefore, the size of the frequency interval $\Delta\omega$. This error can be reduced by decreasing the range of modes over which the summation is taken. To do this we subdivide the frequency range, $\Delta\omega$, into a few, smaller frequency bands. Rather than summing over a frequency interval containing ΔM modes, the summation will be applied to ΔM^* subintervals each with approximately $\Delta M/\Delta M^*$ modes. This can be expressed as

$$\sum_{n=M}^{M+\Delta M-1} \frac{h_n(\tau)\psi_n^2(\xi_f, \eta_f)}{\langle\psi_n^2\rangle} \approx \left(\frac{\Delta M}{\Delta M^*}\right) \sum_{i}^{\Delta M^*} h_{ci}(\tau) \quad (21)$$

where h_{ci} is evaluated at the ΔM^* center frequencies distributed throughout $\Delta\omega$. Equation (21) essentially states that the superposition of the impulse response of the ΔM modes in the frequency band may be approximated by a very few, ΔM^*, appropriately spaced, false modes (i.e., modes that are *not* based on the actual natural frequencies of the structure). We note that to

[1] See (Dowell and Kubota, 1985,) for a more through discussion of the number of modes necessary. Here we will simply say that it is of order $\Delta M \approx 100$.

Downloaded 04 May 2010 to 171.66.16.26. Redistribution subject to ASME license or copyright; see http://www.asme.org/terms/Terms_Use.cfm

choose ΔM^* one must balance the improved estimate that is obtained by more subdivisions with the increased computational cost that evaluating the summation requires.

Together the two simplifications of Eqs. (12) and (21) result in an expression for the response of the panel at the forcing location

$$W_{\mathrm{AMA}}(\xi_f, \eta_f, \tau) = \hat{f}\left(\frac{\Delta M}{\Delta M^*}\right) \sum^{\Delta M^*} h_{ci}(\tau). \qquad (22)$$

This relation states that the displacement of the panel at the point of application of the force is independent of the particular mode shapes of the panel. In addition, if the modal density of the panel is sufficiently large (which is in accord with our requirement of sufficiently large ΔM), then the center frequencies used in the impulse response function need not be the actual eigenvalues of the system. In fact, they need only be distributed approximately evenly throughout the frequency range, $\Delta\omega$ and the eigenvalue solution is not needed at all. Lyon (1975) discusses various expressions for estimating ΔM based on material properties and structural dimensions.

Finally, it is noted that from Eq. (11) and using similar reasoning, one may show that the response for $(\xi, \eta) \neq (\xi_f, \eta_f)$ is smaller than (22) by a factor of order $(1/\Delta M)$. Hence Eq. (22) is the key result.

2.2 Spatially Averaged Mean-Square AMA Solution. The fact that the panel response is initially in phase with the panel excitation at the point of excitation is implicit in the derivation of Eq. (22). At other locations on the panel this is not true and calculating the panel displacement requires the true mode shapes and frequencies. However, we can determine the *spatially averaged* mean-square response of the panel due to the impulsive point force in the same way that $W_{\mathrm{AMA}}(\xi_f, \eta_f, \tau)$ was derived above.

Begin with Eq. (11) and square the response. Assuming (nondimensionalized) mass normalized modes and a uniform panel, we may neglect off-diagonal coupling between modes, and write

$$W^2_{\mathrm{CMA}}(\xi, \eta, \tau) = \hat{f}^2 \sum_{n=M}^{M+\Delta M-1} \frac{\psi^2(\xi, \eta)\psi^2(\xi_f, \eta_f)}{\langle \psi_n^2 \rangle^2} h_n^2(\tau). \quad (23)$$

Spatially averaging this response over the entire panel yields

$$\langle W^2 \rangle_{\mathrm{CMA}}(\tau) = \hat{f}^2 \sum_{n=M}^{M+\Delta M-1} \psi_n^2(\xi_f, \eta_f) h_n^2(\tau). \qquad (24)$$

If ΔM is sufficiently large (cf. Eqs. (12) and (20)), then this can be simplified to be

$$\langle W^2 \rangle_{\mathrm{AMA}}(\tau) = \hat{f}^2 \left(\frac{\Delta M}{\Delta M^*}\right) \sum^{\Delta M^*} h_{ci}^2(\tau). \qquad (25)$$

Here again, the average panel response is expressed in terms of the excitation, the number of modes in the frequency range and a few selected frequencies in that range. The absence of detailed information about the panel itself greatly reduces the computation effort necessary for the calculation. Whereas the number of calculations necessary to evaluate Eq. (23) is clearly of order ΔM in *addition* to those required to determine the ω_n and ψ_n, the effort necessary to evaluate the asymptotic modal solution of Eq. (25) is merely ΔM^* and, most importantly, needs none of the eigensolution information.

3 Results

To test the validity of the AMA method, the response of a sample panel is calculated using Eqs. (22) and (25) and compared to the CMA solution of Eqs. (11) and (24). The panel has an aspect an aspect ratio, γ of 1.5 and is excited at the single point $(\xi_f, \eta_f) = ((1/\pi), (1/\pi))$ by an impulsive load as well as by other longer duration transient loads.

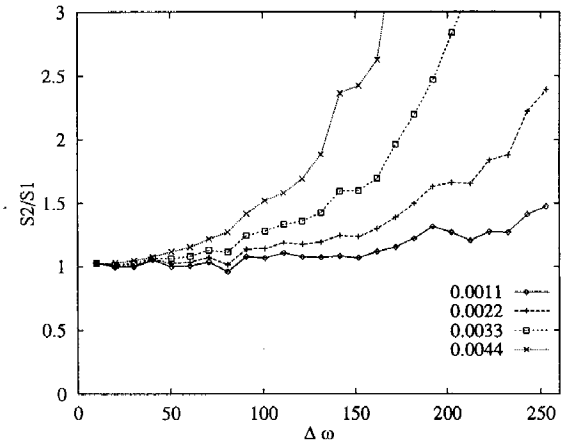

Fig. 1 Ratio of S_2 to S_1 (cf. Eq. (13) and (19)) for several values of nondimensional time, τ. The modal damping is $\zeta = 0.001$ and the center frequency is 506.

For reference, this example corresponds to a physical panel made of aluminum (modulus, E, of 70 GPa, Poisson's ratio, ν, of 0.346, and density, ρ, of 2700 kg/m^3) with dimensions of $a = 0.762$ meters by $b = 0.508$ meters by $h = 7.94 \times 10^{-4}$ meters thick. The dimensionless quantities can be related to their dimensional counterparts via the relations

$$W(\xi, \eta, \tau) = \frac{w(x, y, t)}{h}$$

$$f(\xi, \eta, \tau) = F(x, y, t)\left(\frac{a^2 b^2}{Dh}\right)$$

$$\tau = t\sqrt{\frac{D}{\rho h a^2 b^2}}$$

$$\omega = \tilde{\omega}\sqrt{\frac{D}{\rho h a^2 b^2}} \qquad (26)$$

where the dimensionless quantities on the left-hand sides of these relations are displacement, forcing, time, and frequency, respectively, and D is the panel bending stiffness.

As the type of structural damping model used was not of primary interest here, these calculations assume that the modal damping coefficient, ζ, is constant for all frequencies. In addition, although several frequency ranges were examined, there was no discernible sensitivity to frequency provided that the number of modes in the frequency band was sufficiently large. As such, only representative results are presented here for the nondimensional frequency range of $2387 < \omega < 3977$ (which corresponds to a range of from 1200 to 2000 Hertz for the physical panel described above). The corresponding number of modes is $\Delta M = 123$.

3.1 Impulsive Loading. Before comparing the local maximum or spatially averaged displacement let us first consider the approximation $S_1 \approx S_2$ of Eq. (19). Recall that S_1 is a sum of the impulse response functions and is calculated using the actual eigenmodes of the panel. S_2 is an abbreviated summation of impulse responses determined with a few frequencies distributed over the frequency range. To test the validity of this approximation we first excite the panel with an impulsive point load. The ratio S_2/S_1 is plotted in Fig. 1 for several values of τ and a center frequency of 506. These data show that the ratio remains nearly one when τ is small and provided that $\Delta\omega$ is not large. It is interesting to note that $S_2 \approx S_1$ even when τ is

Downloaded 04 May 2010 to 171.66.16.26. Redistribution subject to ASME license or copyright; see http://www.asme.org/terms/Terms_Use.cfm

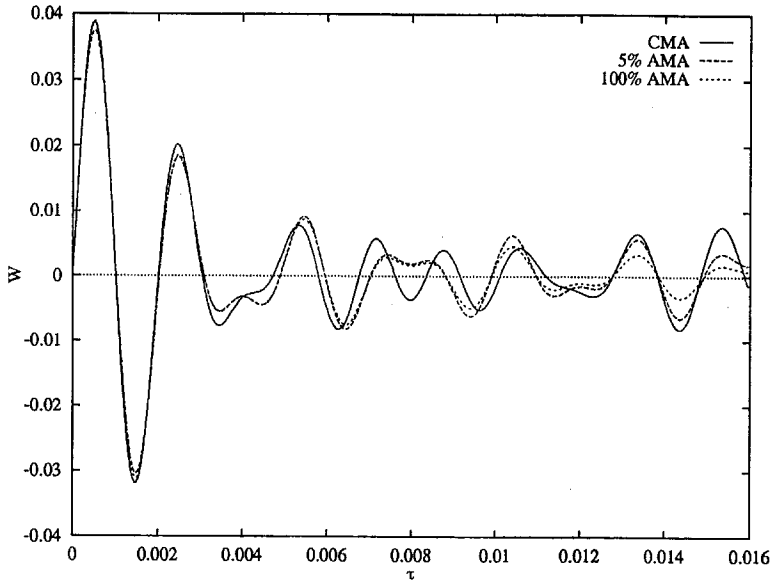

Fig. 2 Comparison of CMA, 5 percent and 100 percent AMA solutions (i.e., $\Delta M^* = (0.05)\,\Delta M$, and ΔM, respectively) for the nondimensional panel displacement, W, at (ξ_f, η_f). The modal damping is $\zeta = 0.001$ and the frequency range is $2387 < \omega < 3977$.

nearly equal to the period of the center frequency, 0.002, and that while the approximation degrades at large times, it is not highly sensitive to τ. Since the magnitude of the impulse response decays rapidly, the largest (and, typically the most important) part of the response occurs when τ is small. Thus we can expect that the AMA approximations for local and spatially averaged displacement in Eqs. (22) and (25) will agree well with the more lengthy CMA solutions.

Let us now consider the local, maximum response at the point of excitation on the panel. The displacement of the panel at this point is calculated via CMA and the AMA method using both $\Delta M^* = 0.05(\Delta M)$ and $\Delta M^* = \Delta M$. Figure 2 presents a comparison of these results where the modal damping is 0.1 percent. As the 100 percent AMA solution (i.e., $\Delta M^* = \Delta M$) agrees well with the CMA solution, we may conclude that using an equivalent number of evenly spaced frequencies rather than the actual eigenmodes yields a very good approximation of the local response. Further, the agreement between the five percent ΔM AMA solution (which was determined by using only 6 of the 123 frequencies) and the CMA solution indicates that we may abbreviate the solution substantially by using several frequency-range subdivisions. Since the AMA solutions use evenly spaced frequencies, there exists a periodic error at regular intervals that is proportional to the frequency spacing used in the solution (a beat phenomenon). However, even well after the excitation ceases the mean amplitudes of the AMA solutions are approximately the same magnitude as those of the CMA solution. As the five percent ΔM solution uses fewer modes

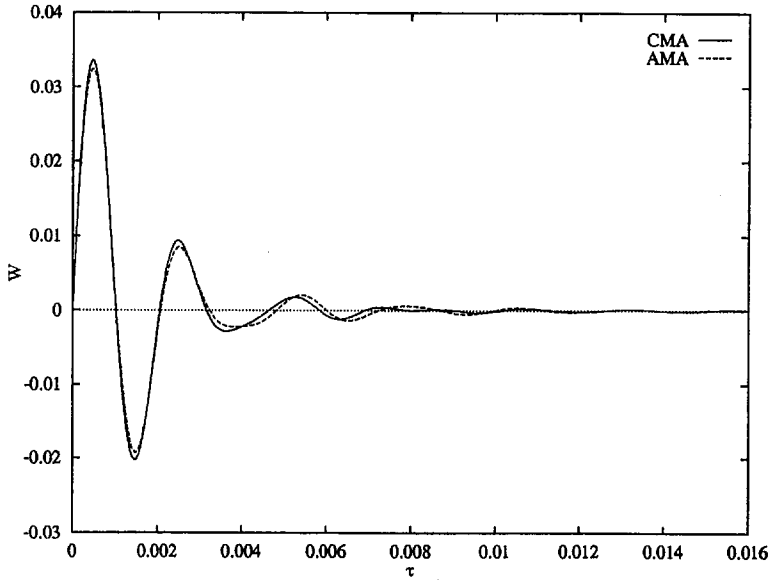

Fig. 3 Comparison of AMA and CMA solutions for the nondimensional panel displacement, W, at (ξ_f, η_f). The modal damping is $\zeta = 0.1$ and the frequency range is $2387 < \omega < 3977$.

Downloaded 04 May 2010 to 171.66.16.26. Redistribution subject to ASME license or copyright; see http://www.asme.org/terms/Terms_Use.cfm

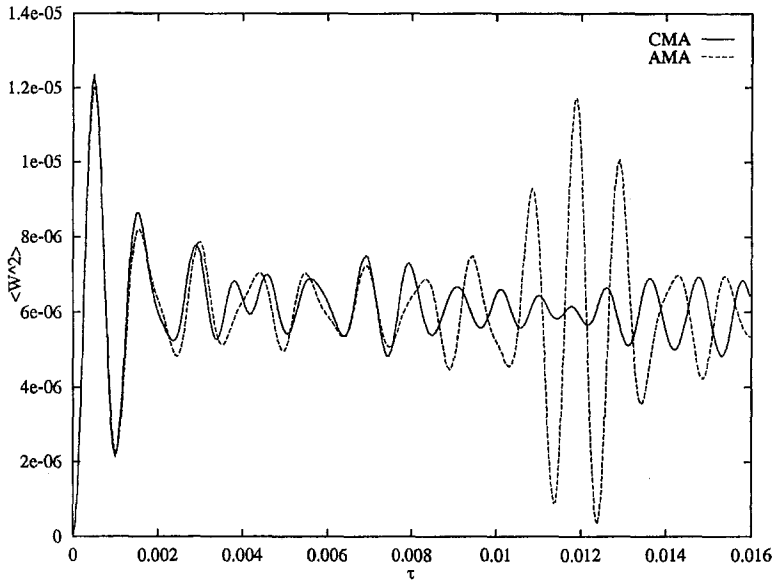

Fig. 4 Comparison of AMA and CMA solutions of the spatial average of the nondimensional panel displacement squared, $\langle W^2 \rangle$. The modal damping is $\zeta = 0.001$ and the frequency range is $2387 < \omega < 3977$.

and no eigenmodes, it requires less than (1/20) the computation time of the CMA estimate. The remaining results presented here use a value of ΔM^* equal to five percent of ΔM.

Figure 3 presents a comparison of AMA and CMA results for the local, maximum displacement for ten percent damping (i.e., $\zeta = 0.1$). Again, the two solutions are in very good agreement—particularly since the response has decayed significantly before the periodic error effects the solution. A comparison of Figs. 2 and 3 indicates that the accuracy of the AMA solution itself is not highly sensitive to the modal damping. In both cases, there is good agreement and it is clear that the AMA method provides a good estimate of the classical panel response near the excitation location. It is worth noting that different structural damping models can easily be incorporated into the AMA solution.

Consider now the panel response away from the excitation. Figures 4 and 5 present the spatial average of the panel displacement squared for low and high structural damping ratios ($\zeta = 0.001$ and $\zeta = 0.1$), respectively. In both cases the AMA solutions yield good estimates of the panel's response. For the lower damping case, there is some deviation between the solutions at large times where the frequency spacing error emerges. This occurs for two reasons, the first is the periodic error that is due to the choice of *evenly* spaced frequencies in the AMA solution as mentioned earlier. This error reoccurs periodically. In addition, the approximations of Eq. (19) are valid for short times after the excitation pulse and as τ increases, these simplifications begin to deteriorate. It is important to note, however, that these deviations occur well after the period of the most relevant portion (i.e., that con-

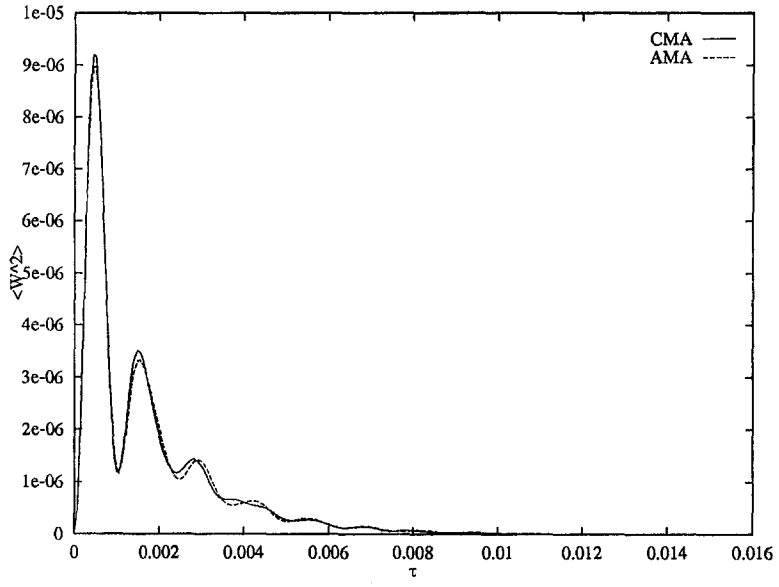

Fig. 5 Comparison of AMA and CMA solutions of the spatial average of the nondimensional panel displacement squared, $\langle W^2 \rangle$. The modal damping is $\zeta = 0.1$ and the frequency range is $2387 < \omega < 3977$.

Downloaded 04 May 2010 to 171.66.16.26. Redistribution subject to ASME license or copyright; see http://www.asme.org/terms/Terms_Use.cfm

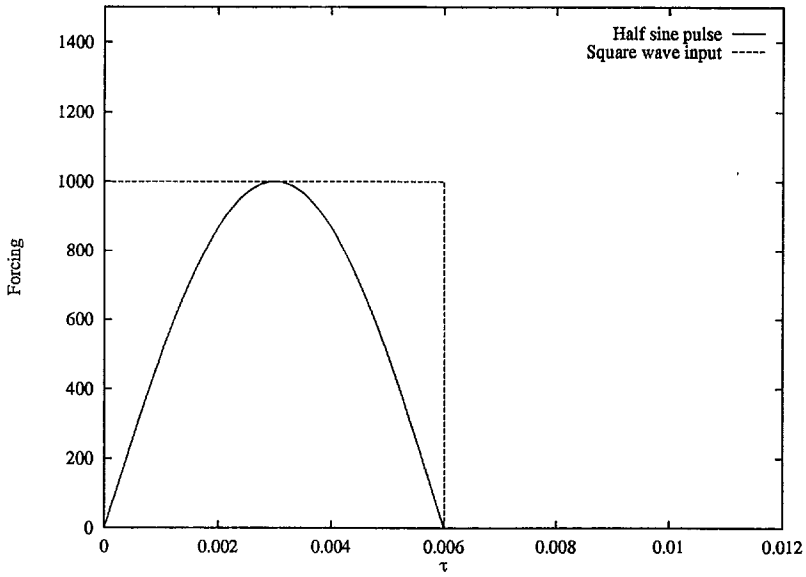

Fig. 6 Nondimensional excitation functions, $f(\tau)$, for the half-sine pulse and the square-wave excitation

taining the highest energy) of the response so the AMA solution still captures the most valuable behavior.

From these results we can conclude that the asymptotic approximations are valid for impulsive, point loading. We have also determined that the AMA solutions are a computationally efficient means of obtaining the local forcing and average panel responses as they require only two to four percent of the computer time of the CMA solutions. In a large, multiply connected structure the savings may be even greater since the eigensolution represents an overhead cost of the CMA method whose proportion increases with the model's size.

3.2 Arbitrary Excitation. The assumptions made to simplify the classical modal relations above are not related to the impulsive nature of the excitation used in the examples just presented. Therefore, a logical extension of the impulsive AMA method is to consider more complex forcing functions. The relationships for these calculations are similar to those noted above but are presented here for completeness. The local response at the forcing location is

$$W_{\mathrm{AMA}}(\xi_f, \eta_f, \tau) = \left(\frac{\Delta M}{\Delta M^*}\right) \sum^{\Delta M^*} \int_0^{\tau_f} h_n(\tau - \tau') f(\tau') d\tau' \quad (27)$$

and the spatially averaged response is

$$\langle W^2 \rangle_{\mathrm{AMA}}(\tau) = \left(\frac{\Delta M}{\Delta M^*}\right) \sum^{\Delta M^*} \left\{ \int_0^{\tau_f} h_n(\tau - \tau') f(\tau') d\tau' \right\}^2 . \quad (28)$$

To study the more general case of arbitrary excitation, two waveforms are used: a half-sine wave and a square wave (cf. Fig. 6) both of duration $\tau_f = 0.006$ and maximum magnitude

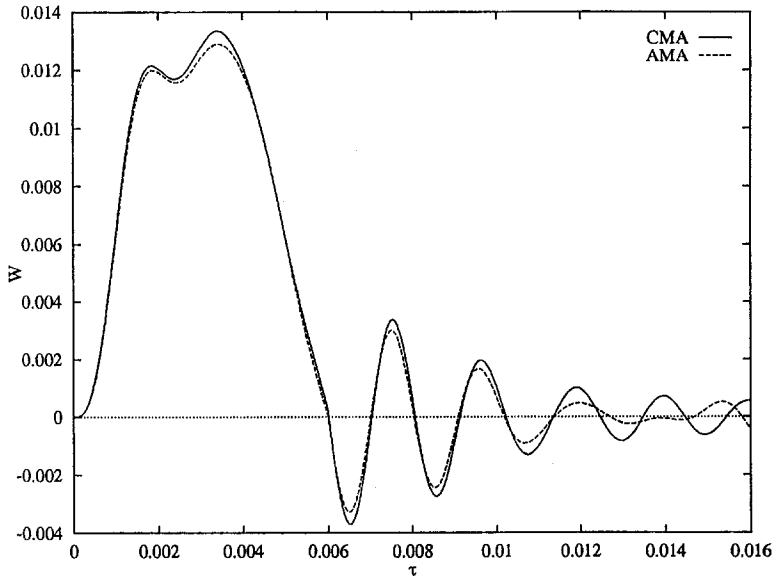

Fig. 7 Nondimensional panel displacement, W, at (ξ_f, η_f) due to a half-sine wave forcing function. The modal damping is $\zeta = 0.001$ and the frequency range is $2387 < \omega < 3977$.

Downloaded 04 May 2010 to 171.66.16.26. Redistribution subject to ASME license or copyright; see http://www.asme.org/terms/Terms_Use.cfm

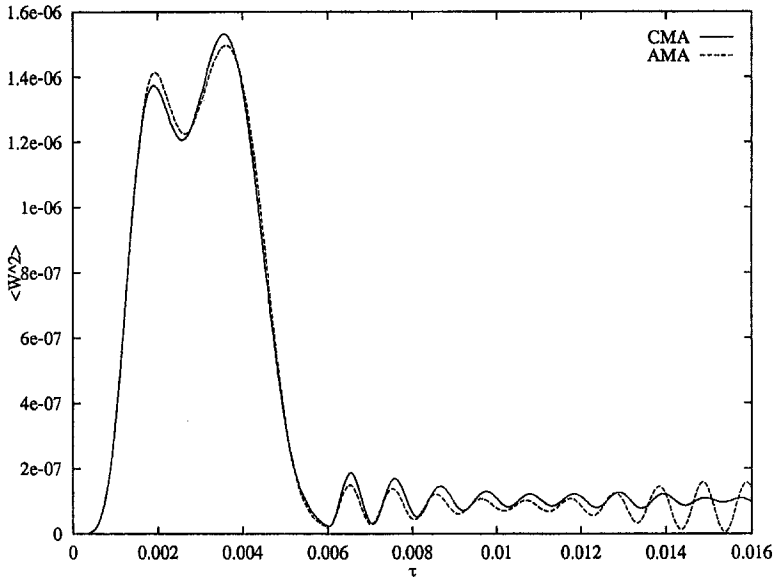

Fig. 8 Spatial average of nondimensional panel displacement squared, $\langle W^2 \rangle$, due to a half-sine-wave forcing function. The modal damping is $\zeta = 0.001$ and the frequency range is $2387 < \omega < 3977$.

1×10^3. All of the results presented here are, again, for the frequency range from 2387 to 3977 so that the duration of these inputs is nearly three times the length of the lowest modal period. This should provide some insight into the validity of the AMA method over moderate time spans relative to the frequency domain of interest.

Here we will focus on the low damping case, (i.e., $\zeta = 0.001$) as this results in a slower response decay and allows a better scrutiny of the complete response. For the half-sine-wave excitation, the local, maximum displacements are shown in Fig. 7. They indicate that the AMA estimate agrees very well with the CMA solution for a time span that is equal to several times the lowest modal period of the frequency interval. The spatially averaged panel displacements are presented in Fig. 8. Here again the AMA-CMA comparison of $\langle W^2 \rangle$ for the same parameters and loading show very good agreement. The smoothly varying half-sine input is well approximated by the asymptotic method.

While the impulse and half-sine waveforms represent the two extremes of excitation duration, the square-wave forcing function combines the broad frequency input of the impulse and the duration of the half-sine input. The comparison of AMA and CMA predictions of $W(\xi_f, \eta_f)$ and $\langle W^2 \rangle$ for this excitation are presented in Figs. 9 and 10, respectively. Again, there is good agreement between the AMA and CMA solutions for moderate time periods after the forcing ceases. Some of the periodic error due to the even frequency spacing of the AMA solution is again apparent at large values of time. This does not occur, however, until nearly three times the pulse duration when the response magnitude has decayed considerably and may be lessened if the AMA frequencies are chosen more randomly.

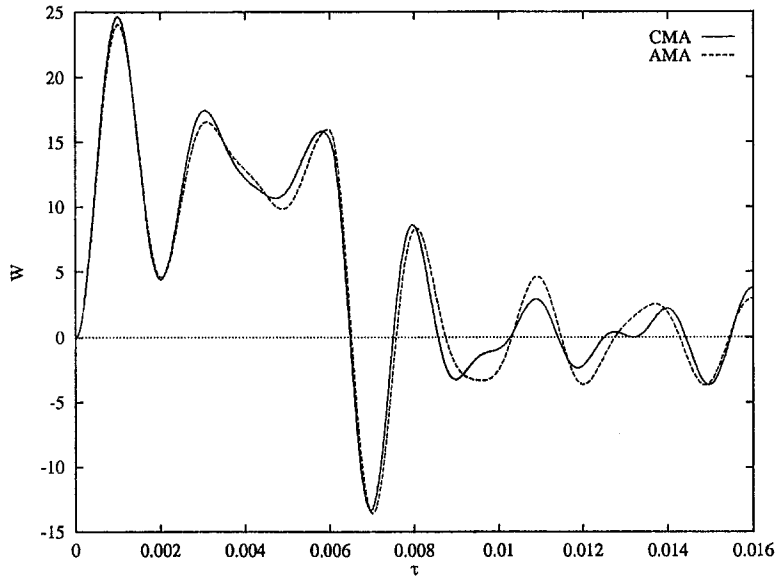

Fig. 9 Nondimensional panel displacement, W, at (ξ_f, η_f) due to a square wave forcing function. The modal damping is $\zeta = 0.001$ and the frequency range is $2387 < \omega < 3977$.

Downloaded 04 May 2010 to 171.66.16.26. Redistribution subject to ASME license or copyright; see http://www.asme.org/terms/Terms_Use.cfm

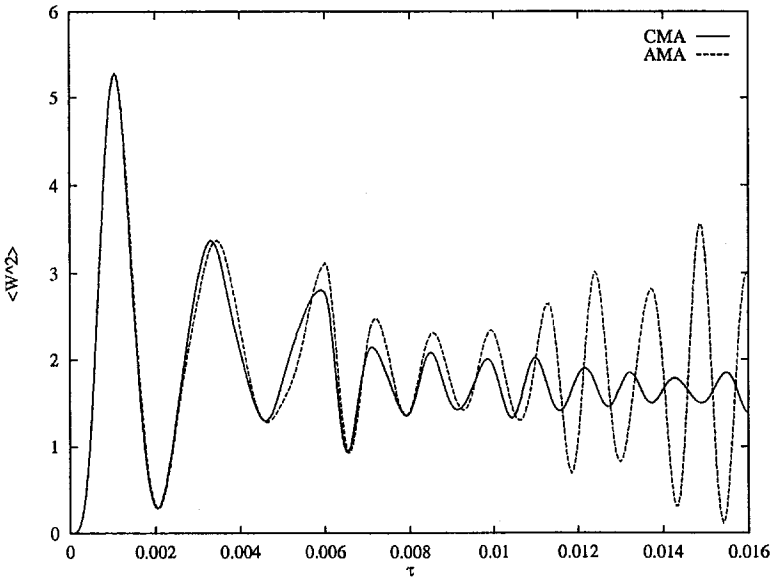

Fig. 10 Spatial average of nondimensional panel displacement squared, $\langle W^2 \rangle$, due to a square-wave forcing function. The modal damping is $\zeta = 0.001$ and the frequency range is $2387 < \omega < 3977$.

4 Conclusions

A new asymptotic method has been developed to model the response of continuous structures to transient or impulsive loads. The resulting relations were used to predict the band-limited response of a single continuous structure to point loads. Both impulsive and more general time-dependent excitations were considered and it was shown that the local response at the point of load application as well as the spatial average of the panel displacement squared were found to agree very well with the predictions of classical modal analysis for time spans of several times the lowest period of oscillation. It was noted that a periodic error appeared in the AMA solutions due to the choice of evenly spaced frequencies. This may be reduced by choosing these frequencies at uneven frequency intervals. Further, as the asymptotic solution does not rely upon the natural modes or natural frequencies of the system, detailed information about the system of interest is unnecessary. As a result, the asymptotic solution method requires significantly less physical information about the system and less computational effort than do classical methods.

The transient AMA method shows significant promise as a tool for predicting the response of much larger multiply connected structures. With further development, it could provide engineers with a much needed tool for predicting transient structural response at moderate to high frequencies where many modes contribute to the response.

References

Dalton, E. C., 1992, "Ballistic shock response by an extension of statistical energy analysis," *63rd Shock and Vibration Symposium,* Booz Allen & Hamilton, Inc., Arlington, VA.

Dowell, E. H., and Kubota, Y., 1985, "Asymptotic Modal Analysis and Statistical Energy Analysis of Dynamical Systems," ASME JOURNAL OF APPLIED MECHANICS, Vol. 52, pp. 949–957.

Kubota, Y., and Dowell, E. H., 1986, "Experimental investigation of asymptotic modal analysis for a rectangular plate," *Journal of Sound and Vibration,* Vol. 106, pp. 203–216.

Kubota, Y., Sekimoto, S., and Dowell, E. H., 1990, "The high-frequency response of a plate carrying a concentrated mass," *Journal of Sound and Vibration,* Vol. 138, pp. 321–333.

Lyon, R. H., 1975, *Statistical energy analysis of dynamical systems: theory and applications,* The M.I.T. Press, Cambridge, MA.

Pinnington, R. J., and Lednik, D., 1996, "Transient statistical energy analysis of an impulsively excited, two oscillator system," *Journal of Sound and Vibration,* Vol. 189, pp. 249–264.

Downloaded 04 May 2010 to 171.66.16.26. Redistribution subject to ASME license or copyright; see http://www.asme.org/terms/Terms_Use.cfm

Journal of Applied Mechanics

Brief Notes

A Brief Note is a short paper that presents a specific solution of technical interest in mechanics but which does not necessarily contain new general methods or results. A Brief Note should not exceed 1500 words *or equivalent* (a typical one-column figure or table is equivalent to 250 words; a one line equation to 30 words). Brief Notes will be subject to the usual review procedures prior to publication. After approval such Notes will be published as soon as possible. The Notes should be submitted to the Technical Editor of the JOURNAL OF APPLIED MECHANICS. Discussions on the Brief Notes should be addressed to the Editorial Department, ASME, United Engineering Center, 345 East 47th Street, New York, N. Y. 10017, or to the Technical Editor of the JOURNAL OF APPLIED MECHANICS. Discussions on Brief Notes appearing in this issue will be accepted until two months after publication. Readers who need more time to prepare a Discussion should request an extension of the deadline from the Editorial Department.

Performance Evaluation of Accelerometers to 200,000 G

T. C. Togami,[1] F. A. Brown,[2] M. J. Forrestal,[3] W. E. Baker[4]

Introduction

In a recent paper, Togami, Baker, and Forrestal (1996) present a Hopkinson bar technique to evaluate the performance of accelerometers for peak acceleration amplitudes between 20,000 and 120,000 G (1G = 9.81 m/s^2). We conducted that study at the University of New Mexico (Togami, 1994) and recently built a similar apparatus for the Shock Laboratory at Sandia National Laboratories. In this note, we report design improvements for our apparatus that extend performance evaluations to 200,000 G.

We now briefly describe our split Hopkinson bar technique to evaluate the performance of accelerometers that measure large-amplitude pulses. A nondispersive stress pulse propagates in an aluminum bar and interacts with a steel disk at the end of the bar. We measure stress at the aluminum bar-disk interface with a quartz gage and measure acceleration at the free end of the disk with an accelerometer. The rise time of the incident stress pulse in the aluminum bar is long enough and the disk length is short enough that the response of the disk can be approximated closely as rigid-body motion. Since the cross-sectional area and mass of the disk are known, we calculate acceleration of the rigid disk from the stress measurement and Newton's Second Law. Comparisons of accelerations calculated from the quartz gage data and measured acceleration data for this study show good agreement for acceleration pulses with the peak amplitudes between 12,000 and 200,000 G.

In the next sections, we review our apparatus and procedure, point out our design improvements, and report results for acceleration amplitudes between 12,000 and 200,000 G.

Experiment Description and Procedure

Figure 1 shows a schematic of the split Hopkinson bar apparatus. The 19.05-mm-diameter 7075-T651 aluminum incident bar is 1.83 m long. A 12.7-mm-long disk of steel has a 0.254-mm-thick x-cut quartz stress gage[5] bonded to one end with conductive epoxy and an accelerometer attached to the free end with screws, following the manufacturer's specifications.[6] The mass m of the steel disk and mounted accelerometer is 0.0309 kg. The diameters of the steel disk and stress gage are the same as the diameter for the incident bar. We call the stress gage, disk, and accelerometer assembly the fly-away. The fly-away is attached to the incident bar with a thin layer of vacuum grease and held in place with a vacuum collar. We made three changes to our previous design: (1) the thickness of the quartz gage was changed from 2.54 mm to 0.254 mm, (2) the length of the steel disk was changed from 17.8 mm to 12.7 mm, and (3) a thin layer of vacuum grease was included between the quartz stress gage and the incident bar.

A spherical-nose projectile is launched from a gas gun and strikes the pulse-shaper shown in Fig. 1. The pulse-shaper used for this study (Bateman, Leisher, Brown, and Davie, 1993) consists of several layers of index cards. After impact, a nondispersive sine-squared strain pulse propagates along the incident bar. The amplitude and duration of the strain pulse, measured with the strain gages (Togami, Baker, and Forrestal, 1996), are controlled by the projectile impact velocity and number of index cards. Next the pulse interacts with the fly-away. For a steel disk and an aluminum incident bar, a compression wave reflects back along the incident bar, and the quartz gage measures the sum of the incident and reflected stress pulses. The thin (0.254 mm) quartz gage has nearly the same impedance as aluminum (Togami, Baker, and Forrestal, 1996), so there are negligible disturbances due to the thin quartz gage. Eventually, the interface stress between the incident bar and the quartz gage becomes tensile, and the fly-away separates from the incident bar. The fly-

[1] Sandia National Laboratories, Albuquerque, NM 87185-0555. Assoc. Mem. ASME.
[2] Sandia National Laboratories, Albuquerque, NM 87185-0555.
[3] Sandia National Laboratories, Albuquerque, NM 87185-0315. Fellow ASME.
[4] Department of Mechanical Engineering, University of New Mexico, Albuquerque, NM 87171. Mem. ASME.

Contributed by the Applied Mechanics Division of THE AMERICAN SOCIETY OF MECHANICAL ENGINEERS for publication in the ASME JOURNAL OF APPLIED MECHANICS. Manuscript received by the ASME Applied Mechanics Division, Mar. 5, 1997; final revision, June 19, 1997. Associate Technical Editor: I. M. Daniel.

[5] Valpey-Fisher Corporation, 1994, *The User's Guide to Ultrasound Products*, 75 South Street, Hopkinton, MA 01748.
[6] Endevco General Catalog, 1991, 30700 Rancho Viejo Road, San Juan Capistrano, CA 92675.

Copyright © 1998 by ASME

Downloaded 04 May 2010 to 171.66.16.26. Redistribution subject to ASME license or copyright; see http://www.asme.org/terms/Terms_Use.cfm

Table 1 Data summary

Shot	T(μs)	A_q(G)	A_a(G)	% Diff.
1	49	12,247	12,900	5.33
2	48	26,089	26,540	1.73
3	49	53,193	57,448	8.00
4	43	97,255	101,746	4.62
5	41	138,925	144,680	4.12
6	35	205,235	209,865	2.26

away separates after the time duration of interest for the experiments and is caught in a foam catcher.

The rise time of the stress pulse in the incident bar is long enough and the length of the disk is short enough that the response of the disk and accelerometer with mass m can be closely approximated as rigid-body motion. Data and an analytical model (Togami, Baker, and Forrestal, 1996) support this assumption. Because the cross-sectional area and mass of the disk and mounted accelerometer are known, we calculate acceleration from the stress measurement and Newton's Second Law. Thus, acceleration calculated from the stress gage is

$$a(t) = \frac{\sigma(t)A}{m} \tag{1}$$

where $\sigma(t)$ is from the stress gage, A is the bar cross-sectional area, and m is the mass of the disk and mounted accelerometer. For our procedure, we compare accelerations calculated from the quartz stress gage with measured accelerations.

We now discuss two of the design changes that improved our apparatus. Our previous study (Togami, Baker, and Forrestal, 1996) used a 2.54-mm-thick quartz gage that fractured for peak acceleration pulses of about 120,000 G. Also, (1) shows that the stress in the quartz gage, $\sigma(t)$, is proportional to the mass of the steel disk and mounted accelerometer, m. For this study, we use a 0.254-mm-thick quartz gage and shorten the length of the steel disk from 17.8 mm to 12.7 mm. The 0.254-mm-thick quartz gage performed without fracturing for a smaller mass m and for peak acceleration pulses to 200,000 G, which is the largest acceleration recommended by the manufacturer.

Results

We conducted six experiments and summarize results in Table 1. In Table 1, T is the duration of the acceleration pulse, and A_q, A_a are the peak amplitudes measured from the quartz gage and accelerometer, respectively. The percent difference between measurements from the quartz gage and accelerometer is given by percent Diff.

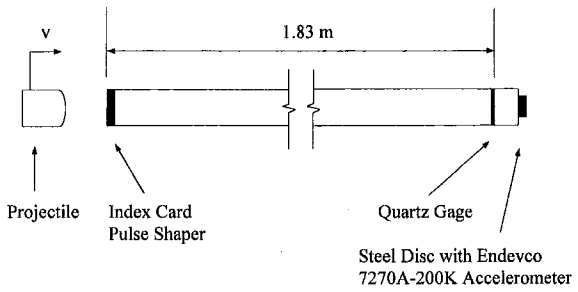

Fig. 1 Experimental apparatus

Figures 2 and 3 show comparisons of accelerometer data and acceleration versus time calculated from (1) that used input from the stress gage. As previously mentioned, we made three design changes for our new apparatus. The thinner (0.254 mm thick) quartz gage and shorter steel disk (12.7 mm long) have been discussed. For the third design change, we added a thin layer of vacuum grease between the quartz stress gage and the incident bar. This third change eliminated the high-amplitude vibrations at the mounted natural frequency (1.2 MHz) of the accelerometer after the fly-away separates from the incident bar (Togami, Baker, and Forrestal, 1996).

Summary

We modified our previous (Togami, Baker, and Forrestal, 1996) Hopkinson bar technique to evaluate the performance of accelerometers. The new apparatus extends performance evaluations to 200,000 G and eliminates the resonant high-frequency vibrations of the accelerometer after the fly-away separates from the incident bar. We found good agreement between accelerations calculated from (1) with the quartz gage and accelerations measured with the Endevco 7270A-200K accelerometer.

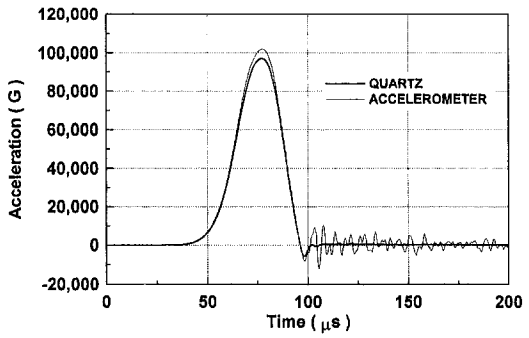

Fig. 2 Accelerometer data and prediction using the stress gage data with m = 0.0309 kg (Shot 4)

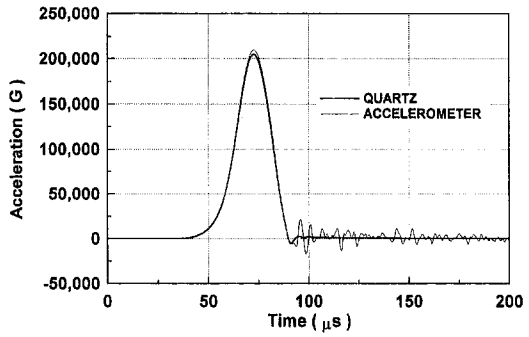

Fig. 3 Accelerometer data and prediction using the stress gage data with m = 0.0309 kg (Shot 6)

Downloaded 04 May 2010 to 171.66.16.26. Redistribution subject to ASME license or copyright; see http://www.asme.org/terms/Terms_Use.cfm

Acknowledgments

This work was supported by the United States Department of Energy under Contract DE-AC04-94AL85000 and the Joint DoD/DOE Munitions Technology Development Program. Sandia is a multiprogram laboratory operated by Sandia Corporation, a Lockheed Martin Company, for the United States Department of Energy.

References

Bateman, V. I., Leisher, W. B., Brown, F. A., and Davie, N. T., 1993, "Calibration of a Hopkinson Bar with a Transfer Standard," *Shock and Vibration,* Vol. 1, No. 2, pp. 145–152.

Togami, T. C., 1994, "Hopkinson Bar Method for Direct Evaluation of High G Accelerometers," thesis submitted in partial fulfillment for the Degree of Master of Science in Mechanical Engineering, University of New Mexico, Albuquerque, NM.

Togami, T. C., Baker, W. E., and Forrestal, M. J., 1996, "A Split Hopkinson Bar Technique to Evaluate the Performance of Accelerometers," ASME JOURNAL OF APPLIED MECHANICS, Vol. 63, pp. 353–356.

Polycrystalline Plasticity: Application to Earing in Cup Drawing of Al2008-T4 Sheet

S. Balasubramanian[7] and L. Anand[7,8]

Introduction

Ears which develop during the drawing of anisotropic sheets are important defects that form during the production of deep-drawn containers. The quantitative prediction of earing patterns is a classical outstanding problem in anisotropic plasticity (e.g., Wilson and Butler, 1961). Recently, Becker et al. (1993) have attempted to predict earing patterns in polycrystalline aluminum sheets. While their calculations are noteworthy, they were unable to obtain fully drawn cups in their simulations. The purpose of this brief note is to show that the recently developed theory for polycrystalline plasticity of f.c.c. materials deforming by crystallographic slip (e.g., Asaro and Needleman, 1985; Kalidindi et al., 1992; and references therein) is able to predict *quantitatively* (i) the punch force versus punch displacement, and (ii) the number of ears, their positions, and their heights during cup drawing of aluminum alloy Al2008-T4.

Constitutive Model

The governing variables in the constitutive model are

(i) the Cauchy stress $\mathbf{T}$.
(ii) the deformation gradient $\mathbf{F}$.
(iii) crystal slip systems, labeled by integers α. Each slip system is specified by a unit normal $\mathbf{n}_0^\alpha$ to the slip plane, and a unit vector $\mathbf{m}_0^\alpha$ denoting the slip direction. The slip systems $(\mathbf{m}_0^\alpha, \mathbf{n}_0^\alpha)$ are assumed to be known in the reference configuration.
(iv) the plastic deformation gradient, $\mathbf{F}^p$, with $\det \mathbf{F}^p = 1$. The local configuration defined by $\mathbf{F}^p$ is relaxed, that is $\mathbf{T} = \mathbf{0}$, and is chosen such that the crystal lattice in this configuration has the same orientation with respect to a fixed orthonormal basis in space as it had in the reference configuration.
(v) the slip system deformation resistance $s^\alpha > 0$, with units of stress.

In terms of $\mathbf{F}$ and $\mathbf{F}^p$ the quantity $\mathbf{F}^e \equiv \mathbf{F}\mathbf{F}^{p-1}$ defines an elastic deformation gradient. Next, with $\mathbf{E}^e \equiv \frac{1}{2}\{\mathbf{F}^{e^T}\mathbf{F}^e - 1\}$ and $\bar{\mathbf{T}} \equiv (\det \mathbf{F}^e)\,\mathbf{F}^{e-1}\,\mathbf{T}\mathbf{F}^{e-T}$ defining an elastic strain measure and its conjugate stress measure, respectively, where $\mathbf{T}$ is the Cauchy stress, the constitutive equation for the stress in the single crystal is taken as the linear relation

$$\bar{\mathbf{T}} = C\,[\mathbf{E}^e], \tag{1}$$

where C is a fourth-order anisotropic elasticity tensor.

The evolution equation for $\mathbf{F}^p$, the flow rule for single crystals, is given by

$$\dot{\mathbf{F}}^p\mathbf{F}^{p-1} = \sum_\alpha \dot{\gamma}^\alpha \mathbf{m}_0^\alpha \otimes \mathbf{n}_0^\alpha, \tag{2}$$

where $\dot{\gamma}^\alpha$ is the plastic shearing rate on slip system α. The plastic stress power per unit volume of the relaxed configuration is given by $\dot{\omega}^p = (\mathbf{C}^e\bar{\mathbf{T}})\cdot(\dot{\mathbf{F}}^p\mathbf{F}^{p-1})$. Using this and (2), we may write the plastic stress power as $\dot{\omega}^p = \sum_\alpha \tau^\alpha\dot{\gamma}^\alpha$, where

$$\tau^\alpha \equiv (\mathbf{C}^e\bar{\mathbf{T}})\cdot(\mathbf{m}_0^\alpha \otimes \mathbf{n}_0^\alpha) \tag{3}$$

defines the *resolved shear stress* for the slip system α. With the resolved shear stress so defined, we take the plastic shearing rate to be given by a simple power-law expression:

$$\dot{\gamma}^\alpha = \dot{\gamma}_0\left(\frac{|\tau^\alpha|}{s^\alpha}\right)^{1/m} \operatorname{sign}(\tau^\alpha), \tag{4}$$

where $\dot{\gamma}_0$ is a reference rate of shearing defined such that $|\dot{\gamma}^\alpha| = \dot{\gamma}_0$ when $|\tau^\alpha| = s^\alpha$, and the parameter m characterizes the material rate sensitivity.

Further, the slip system resistance parameters s^α are taken to evolve according to the simple hardening rule

$$\dot{s}^\alpha = \sum_\beta h^{\alpha\beta}\,|\dot{\gamma}^\beta|, \quad h^{\alpha\beta} = [q + (1-q)\delta^{\alpha\beta}]h^\beta. \tag{5}$$

Here, h^β is a single slip-hardening rate, and q is the latent-hardening ratio. The parameter q is taken to be equal to 1.0 for coplanar slip systems, and 1.4 for noncoplanar slip systems. For the single slip-hardening rate, the following specific form is adopted:

$$h^\beta = h_0\left\{1 - \frac{s^\beta}{s_s}\right\}^a, \tag{6}$$

where h_0, a, and s_s are slip system hardening parameters which are taken to be identical for all slip systems.

To make the transition from single crystal to polycrystals we invoke the classical Taylor assumption. According to this, the local deformation gradient in each grain is taken to be homogeneous and identical to the macroscopic deformation gradient. It then follows that the Cauchy stress at a macroscopic continuum polycrystalline material point is the volume-averaged stress response of the single crystalline grains constituting the material point:

[7] Department of Mechanical Engineering, Massachusetts Institute of Technology, Cambridge, MA 02139.
[8] Mem. ASME.

Contributed by the Applied Mechanics Division of THE AMERICAN SOCIETY OF MECHANICAL ENGINEERS for publication in the ASME JOURNAL OF APPLIED MECHANICS. Manuscript received by the ASME Applied Mechanics Division, Feb. 20, 1997; final revision, July 26, 1997. Associate Technical Editor: R. Becker.

Downloaded 04 May 2010 to 171.66.16.26. Redistribution subject to ASME license or copyright; see http://www.asme.org/terms/Terms_Use.cfm

Acknowledgments

This work was supported by the United States Department of Energy under Contract DE-AC04-94AL85000 and the Joint DoD/DOE Munitions Technology Development Program. Sandia is a multiprogram laboratory operated by Sandia Corporation, a Lockheed Martin Company, for the United States Department of Energy.

References

Bateman, V. I., Leisher, W. B., Brown, F. A., and Davie, N. T., 1993, "Calibration of a Hopkinson Bar with a Transfer Standard," *Shock and Vibration,* Vol. 1, No. 2, pp. 145–152.

Togami, T. C., 1994, "Hopkinson Bar Method for Direct Evaluation of High G Accelerometers," thesis submitted in partial fulfillment for the Degree of Master of Science in Mechanical Engineering, University of New Mexico, Albuquerque, NM.

Togami, T. C., Baker, W. E., and Forrestal, M. J., 1996, "A Split Hopkinson Bar Technique to Evaluate the Performance of Accelerometers," ASME JOURNAL OF APPLIED MECHANICS, Vol. 63, pp. 353–356.

Polycrystalline Plasticity: Application to Earing in Cup Drawing of Al2008-T4 Sheet

S. Balasubramanian[7] and L. Anand[7,8]

Introduction

Ears which develop during the drawing of anisotropic sheets are important defects that form during the production of deep-drawn containers. The quantitative prediction of earing patterns is a classical outstanding problem in anisotropic plasticity (e.g., Wilson and Butler, 1961). Recently, Becker et al. (1993) have attempted to predict earing patterns in polycrystalline aluminum sheets. While their calculations are noteworthy, they were unable to obtain fully drawn cups in their simulations. The purpose of this brief note is to show that the recently developed theory for polycrystalline plasticity of f.c.c. materials deforming by crystallographic slip (e.g., Asaro and Needleman, 1985; Kalidindi et al., 1992; and references therein) is able to predict *quantitatively* (i) the punch force versus punch displacement, and (ii) the number of ears, their positions, and their heights during cup drawing of aluminum alloy Al2008-T4.

Constitutive Model

The governing variables in the constitutive model are

(i) the Cauchy stress $\mathbf{T}$.
(ii) the deformation gradient $\mathbf{F}$.
(iii) crystal slip systems, labeled by integers α. Each slip system is specified by a unit normal $\mathbf{n}_0^\alpha$ to the slip plane, and a unit vector $\mathbf{m}_0^\alpha$ denoting the slip direction. The slip systems $(\mathbf{m}_0^\alpha, \mathbf{n}_0^\alpha)$ are assumed to be known in the reference configuration.
(iv) the plastic deformation gradient, $\mathbf{F}^p$, with $\det \mathbf{F}^p = 1$. The local configuration defined by $\mathbf{F}^p$ is relaxed, that is $\mathbf{T} = \mathbf{0}$, and is chosen such that the crystal lattice in this configuration has the same orientation with respect to a fixed orthonormal basis in space as it had in the reference configuration.
(v) the slip system deformation resistance $s^\alpha > 0$, with units of stress.

In terms of $\mathbf{F}$ and $\mathbf{F}^p$ the quantity $\mathbf{F}^e \equiv \mathbf{F}\mathbf{F}^{p-1}$ defines an elastic deformation gradient. Next, with $\mathbf{E}^e \equiv \frac{1}{2}\{\mathbf{F}^{e^T}\mathbf{F}^e - 1\}$ and $\bar{\mathbf{T}} \equiv (\det \mathbf{F}^e)\,\mathbf{F}^{e-1}\,\mathbf{T}\mathbf{F}^{e-T}$ defining an elastic strain measure and its conjugate stress measure, respectively, where $\mathbf{T}$ is the Cauchy stress, the constitutive equation for the stress in the single crystal is taken as the linear relation

$$\bar{\mathbf{T}} = C\,[\mathbf{E}^e], \tag{1}$$

where C is a fourth-order anisotropic elasticity tensor.

The evolution equation for $\mathbf{F}^p$, the flow rule for single crystals, is given by

$$\dot{\mathbf{F}}^p\mathbf{F}^{p-1} = \sum_\alpha \dot{\gamma}^\alpha \mathbf{m}_0^\alpha \otimes \mathbf{n}_0^\alpha, \tag{2}$$

where $\dot{\gamma}^\alpha$ is the plastic shearing rate on slip system α. The plastic stress power per unit volume of the relaxed configuration is given by $\dot{\omega}^p = (\mathbf{C}^e\bar{\mathbf{T}})\cdot(\dot{\mathbf{F}}^p\mathbf{F}^{p-1})$. Using this and (2), we may write the plastic stress power as $\dot{\omega}^p = \sum_\alpha \tau^\alpha\dot{\gamma}^\alpha$, where

$$\tau^\alpha \equiv (\mathbf{C}^e\bar{\mathbf{T}})\cdot(\mathbf{m}_0^\alpha \otimes \mathbf{n}_0^\alpha) \tag{3}$$

defines the *resolved shear stress* for the slip system α. With the resolved shear stress so defined, we take the plastic shearing rate to be given by a simple power-law expression:

$$\dot{\gamma}^\alpha = \dot{\gamma}_0\left(\frac{|\tau^\alpha|}{s^\alpha}\right)^{1/m} \operatorname{sign}(\tau^\alpha), \tag{4}$$

where $\dot{\gamma}_0$ is a reference rate of shearing defined such that $|\dot{\gamma}^\alpha| = \dot{\gamma}_0$ when $|\tau^\alpha| = s^\alpha$, and the parameter m characterizes the material rate sensitivity.

Further, the slip system resistance parameters s^α are taken to evolve according to the simple hardening rule

$$\dot{s}^\alpha = \sum_\beta h^{\alpha\beta}\,|\dot{\gamma}^\beta|, \quad h^{\alpha\beta} = [q + (1-q)\delta^{\alpha\beta}]h^\beta. \tag{5}$$

Here, h^β is a single slip-hardening rate, and q is the latent-hardening ratio. The parameter q is taken to be equal to 1.0 for coplanar slip systems, and 1.4 for noncoplanar slip systems. For the single slip-hardening rate, the following specific form is adopted:

$$h^\beta = h_0\left\{1 - \frac{s^\beta}{s_s}\right\}^a, \tag{6}$$

where h_0, a, and s_s are slip system hardening parameters which are taken to be identical for all slip systems.

To make the transition from single crystal to polycrystals we invoke the classical Taylor assumption. According to this, the local deformation gradient in each grain is taken to be homogeneous and identical to the macroscopic deformation gradient. It then follows that the Cauchy stress at a macroscopic continuum polycrystalline material point is the volume-averaged stress response of the single crystalline grains constituting the material point:

[7] Department of Mechanical Engineering, Massachusetts Institute of Technology, Cambridge, MA 02139.
[8] Mem. ASME.

Contributed by the Applied Mechanics Division of THE AMERICAN SOCIETY OF MECHANICAL ENGINEERS for publication in the ASME JOURNAL OF APPLIED MECHANICS. Manuscript received by the ASME Applied Mechanics Division, Feb. 20, 1997; final revision, July 26, 1997. Associate Technical Editor: R. Becker.

Copyright © 1998 by ASME

Downloaded 04 May 2010 to 171.66.16.26. Redistribution subject to ASME license or copyright; see http://www.asme.org/terms/Terms_Use.cfm

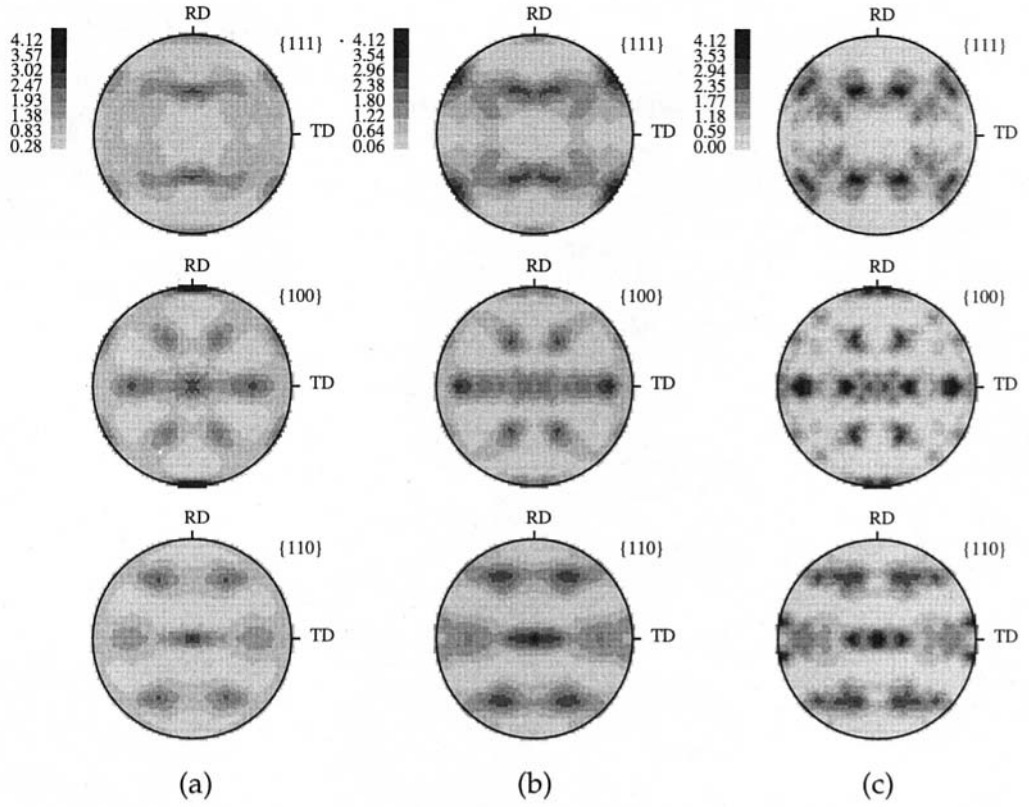

Fig. 1 (*a*) Experimentally measured initial texture of the sheet, (*b*) numerical representation of the measured texture using 192 weighted grains, (*c*) numerical representation of the measured texture using 34 weighted grains

$$\mathbf{T} = \sum_{k=1}^{N} v^{(k)}\, \mathbf{T}^{(k)}, \tag{7}$$

where $\mathbf{T}^{(k)}$ is the Cauchy stress in the kth grain, and $v^{(k)}$ is the volume fraction of the kth grain. When all grains are assumed to be of equal volume, the stress $\mathbf{T}$ is just the number average over all the grains.

We have implemented this constitutive model in the "dynamic explicit" finite element program ABAQUS/Explicit (1995). Since the sheet metal-forming process that we shall consider is essentially quasi-static, it would appear that a "static implicit" procedure is a more appropriate choice for modeling this process. However, it has been found that a dynamic explicit procedure, in which the solution of individual time increments is inexpensive, is computationally more efficient for large three-dimensional problems which are dominated by contact.

Application to Cup-Drawing

Polycrystalline Al2008-T4 sheet, 0.7874 mm in thickness, was kindly provided by ALCOA Technical Center. The initial crystallographic texture of the as-received sheet was measured using X-ray irradiation, and the data from the pole-figure measurements were processed using popLA (Kallend et al., 1991). Figure 1(*a*) shows the measured {111}, {100}, and {110} pole-figures (equal-area projections). Figure 1(*b*) shows a numerical representation of this texture using a weighted average over 192 components. Figure 1(*c*) shows a numerical representation of the texture using a weighted average over only 34 components. Although the texture representation using 192 components is more accurate, in our numerical calculations for cup drawing we shall use the computationally less expensive numerical representation which employs only 34 components.

For f.c.c. crystals, the anisotropic elasticity tensor C may be specified in terms of three elastic constants. For aluminum, the values of these constants are taken as (Simmons and Wang, 1971): C_{11} = 107 GPa, C_{12} = 61 GPa, and C_{44} = 28.3 GPa. Crystallographic slip is assumed to occur on the 12 {111} ⟨110⟩ slip systems.

For the plastic flow parameters, we set $\dot{\gamma}_0 = 0.001\ \text{sec}^{-1}$, and we estimated the value of the material rate-sensitivity parameter m by performing strain-rate jump experiments on sheet-tension specimens (ASTM E8) cut parallel to the rolling direction. The experimentally measured value is $m \approx 0.005$. The material parameters for the slip system deformation resistance

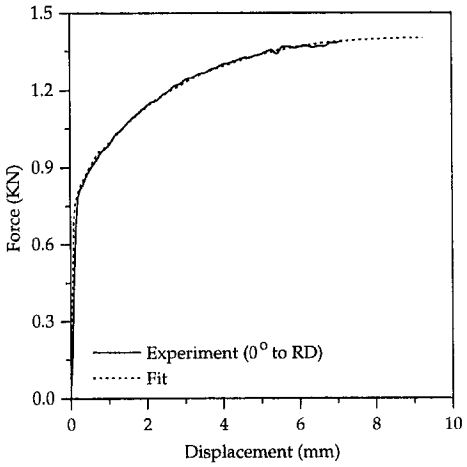

Fig. 2 Load-displacement response for sheet tension

Downloaded 04 May 2010 to 171.66.16.26. Redistribution subject to ASME license or copyright; see http://www.asme.org/terms/Terms_Use.cfm

and its evolution were obtained by fitting the load-displacement curves obtained from the sheet-tension tests. The measured load-displacement curve prior to the onset of diffuse-necking is shown in Fig. 2. A sheet tension specimen with a gauge length of 25.4 mm was modeled using 180 ABAQUS C3D8R continuum elements, with only one element in the thickness direction. The values for the hardening parameters were adjusted so that the numerical load-displacement results matched the corresponding experimental data. The numerical fit to the data is also shown in Fig. 2. The material parameters obtained from the fit are $s_0 = 55$ MPa, $h_0 = 445$ MPa, $s_s = 164$ MPa, and $a = 2$.

A schematic diagram of the geometry of the cup-drawing apparatus is shown in Fig. 3(a). Circular blanks of diameter 101.6 mm and thickness 0.7874 mm, were drawn in an apparatus comprising a round-nosed punch and die of diameters 50.8 mm and 53.035 mm, respectively. The cup-drawing experiments were performed on a double-action hydraulic press, powered by two dual-acting hydraulic cylinders. A constant binder force of 10 KN was applied and the cup was drawn with a punch speed of 1 mm/sec. Teflon sheets were used as lubricants to minimize the friction in the interfaces between the punch and the blank, the blank and the blankholder, and the blank and the die.

The cups showed four ears: two along the rolling direction and two along the transverse direction of the sheet, as shown in Fig. 4(a). Note that a cup drawn from a sheet with a rolling

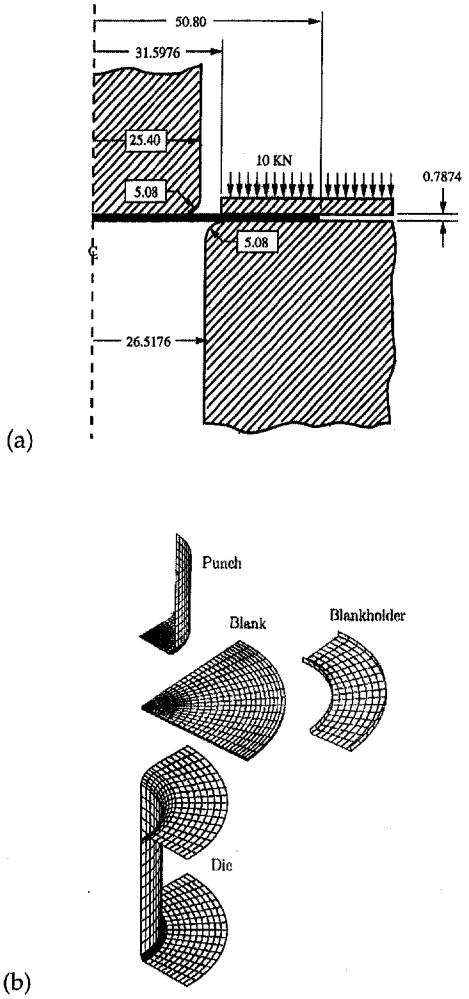

Fig. 3 (a) Geometry of the cup-drawing apparatus (all dimensions are in millimeters), (b) exploded view of the finite element mesh used in the simulation

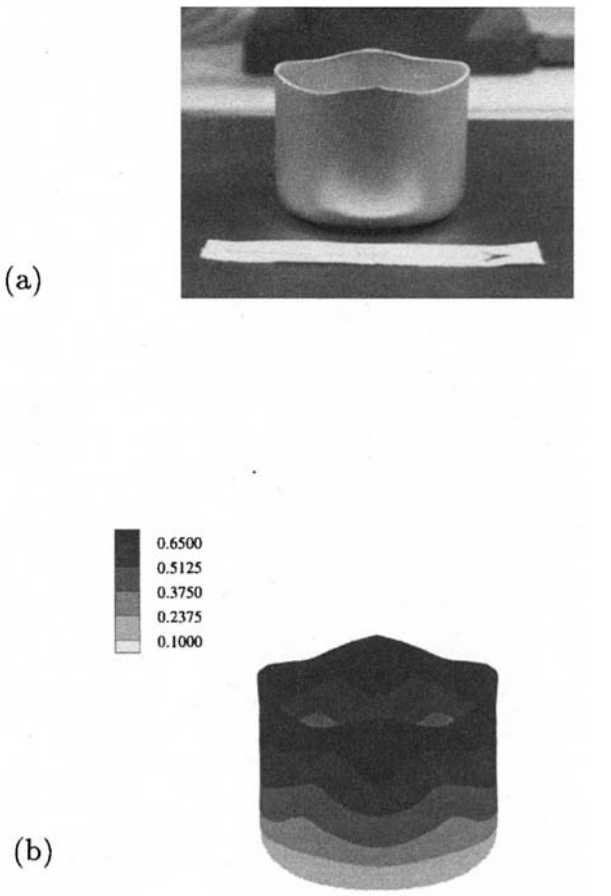

Fig. 4 Comparison of the predicted earing pattern with that observed in the experiment; (a) observed earing pattern (the rolling direction is from the left to the right), (b) numerical prediction. The numerical simulation also shows the equivalent plastic strain contours.

texture forms four ears at ~ 45 deg to the rolling direction. The difference in the earing pattern between that situation and the situation in our experiments, arises directly from the differences in the two initial textures. The texture in Fig. 1(a) contains a large volume-fraction of Goss and Cube-oriented grains, both of which are known to form ears at 0 deg and 90 deg to the rolling direction (Rollett et al., 1987).

Figure 3(b) shows the finite element mesh used for the numerical simulation. A total of 672 ABAQUS continuum C3D8R and C3D6 elements were used, with two elements through the thickness. Since the initial texture of the sheet possesses orthotropic symmetry, only a 90-deg sector of the circular blank was considered for the analysis. The die, blankholder, and punch were treated as rigid surfaces. A friction coefficient of $\mu = 0.1$ was used for the interface between the punch and the sheet top, and the interfaces between all other contacting surfaces were considered frictionless. Figure 4(b) shows the predicted shape of the fully drawn cup. This figure also shows the equivalent tensile plastic strain $\bar{\varepsilon}^p$ contours in the cup at the end of the drawing process. The prediction of the number of ears and their positions is accurate. Figure 5(a) shows a comparison of the predicted cup height with the experimentally measured height. The discrepancy in the predicted cup height is due to the small difference between the predicted and measured cup thickness which is not reported here. Figure 5(b) shows a comparison of the predicted punch load-displacement curve with the values measured in the experiments.

Overall, the *quantitative* prediction of (i) the punch force versus punch displacement, and (ii) the number of ears, their positions, and their heights, is very good.

Downloaded 04 May 2010 to 171.66.16.26. Redistribution subject to ASME license or copyright; see http://www.asme.org/terms/Terms_Use.cfm

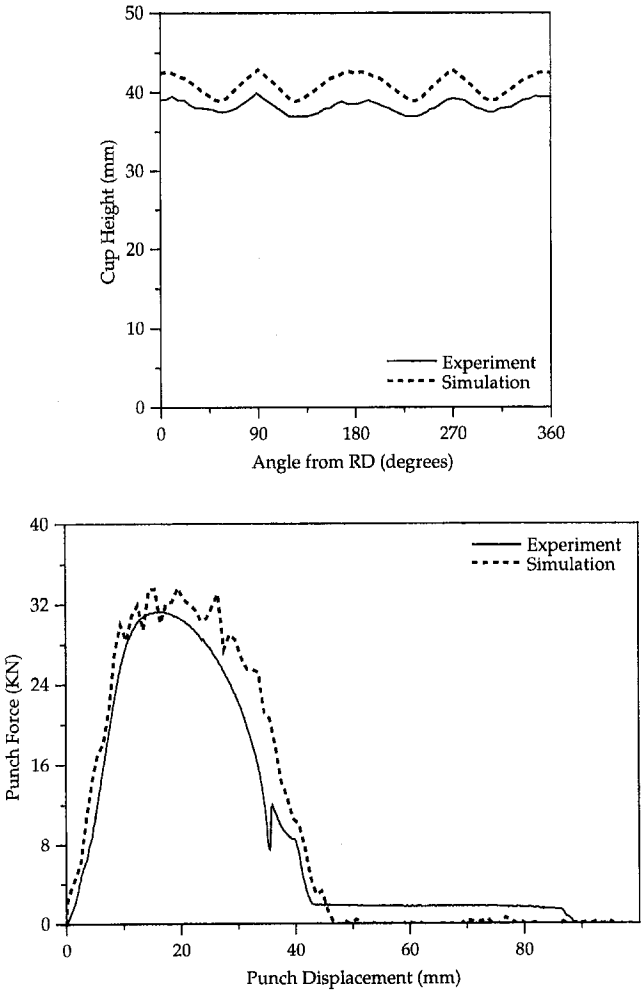

Fig. 5 (*a*) Comparison of the predicted cup-height profile with the experimentally measured height, (*b*) comparison of the measured load-displacement response during the cup-drawing process with the numerical prediction

Acknowledgment

Financial support for this work was provided by the U.S. National Science Foundation under Grant No. DMI-9215246.

References

ABAQUS, 1995, *Reference Manuals,* Hibbitt, Karlsson, & Sorensen Inc., Pawtucket, RI.

Asaro, R. J., and Needleman, A., 1985, "Texture Development and Strain Hardening in Rate-Dependent Polycrystals," *Acta Metallurgica,* Vol. 33, pp. 923–953.

Becker, R., Smelser, R. E., and Panchanadeeswaran, S., 1993, "Simulations of earing in aluminum single crystals and polycrystals," *Modelling and Simulations in Materials Science and Engineering,* Vol. 1, pp. 203–224.

Kalidindi, S. R., Bronkhorst, C. A., and Anand, L., 1992, "Crystallographic Texture Evolution During Bulk Deformation Processing of FCC Metals," *Journal of The Mechanics and Physics of Solids,* Vol. 40, pp. 537–569.

Kallend, J. S., Kocks, U. F., Rollett, A. D., and Wenk, H. R., 1991, "popLA: The Preferred Orientation Package from Los Alamos," Los Alamos National Laboratory, Los Alamos, NM.

Rollett, A. D., Canova, G. R., and U. F. Kocks, U. F., 1986, "The Effect of the Cube Texture Component on the Earing Behavior of Rolled f.c.c. metals," *Proceedings of the Conference on Formability and Metallurgical Structures,* Orlando, FL, 1987, pp. 147–155.

Simmons, G., and Wang, H., 1971, *Single Crystal Elastic Properties and Calculated Aggregate Properties: A HANDBOOK,* The MIT Press, Cambridge, MA.

Wilson, D. V., and Butler, R. D., 1961, "The role of cup-drawing tests in measuring drawability," *Journal of the Institute of Metals,* Vol. 90, pp. 473–483.

Finite Element Analysis of Rolling Contact Problems Using Minimum Dissipation of Energy Principle

S. K. Rathore[9] and N. N. Kishore[10]

In steady rolling motion, the loads and the fields of strain, stress, and deformations do not change with time at the contact region, as the contact region is continuously being formed by a new rolling surface. The principle of minimum dissipation of energy and the concept of traveling finite elements are made use of in solving such problems and the determination of micro-slips. The conditions of contact are discovered by use of the kinematic constraints and the Coulomb's law of friction. A two-dimensional plane-strain finite element method along with the iterative procedure is used. The results obtained are in good agreement with expected behavior.

Introduction

When a cylindrical body rolls on a rigid plane surface without sliding, contact develops between the roller and the ground. In free rolling, viz., rolling under the action of a purely normal load, the extent of slip is small, whereas when the contact surfaces transmit an externally applied tangential force or twisting couple, an appreciable amount of slip occurs. Several analytical and numerical solutions have been reported by Poritsky (1950), Kalker (1979), and Liu and Paul (1989). The rolling contact problem was also described by a variational inequality (hyperbolic/elliptic) and solved numerically using an incremental finite element method by Zochowski and Myslinki (1991). A recent method using the principle of minimum dissipation of energy (Kishore et al., 1994) to solve contact problem does not require any assumption regarding the distribution of tractions and contact conditions on the contact patch. This method, together with the concept of traveling finite elements (Padovan, Tovichakchaikul, and Zeid, 1984), are used to solve the present steady rolling contact problem employing only a coarse mesh.

Simulation of Rolling Motion

The method is based on the fact that every material point or node on the periphery of rolling body passes through the entire contact field during its period of contact. Therefore, instead of actually rolling the body, the contact field conditions are shifted rearward over the contact nodal points. This lets the contact zone be represented by the same set of nodal points for all iterations. The rolling is assumed to take place in steps of one degree, which coincides with the angular distance between the nodes in contact. To begin with, the initial configuration is taken to be the static solution. Thus, knowing the displacement component in the tangential direction at instant t at the i^{th} node, the response at instant $t + \Delta t$ can be taken as

[9] Reader, Department of Mechanical Engineering, Engineering College, Kota, India.

[10] Professor, Department of Mechanical Engineering, Indian Institute of Technology, Kanpur, India.

Contributed by the Applied Mechanics Division of THE AMERICAN SOCIETY OF MECHANICAL ENGINEERS for publication in the ASME JOURNAL OF APPLIED MECHANICS. Manuscript received by the ASME Applied Mechanics Division, Dec. 5, 1996; final revision, July 12, 1997. Associate Technical Editor: J. N. Reddy.

Downloaded 04 May 2010 to 171.66.16.26. Redistribution subject to ASME license or copyright; see http://www.asme.org/terms/Terms_Use.cfm

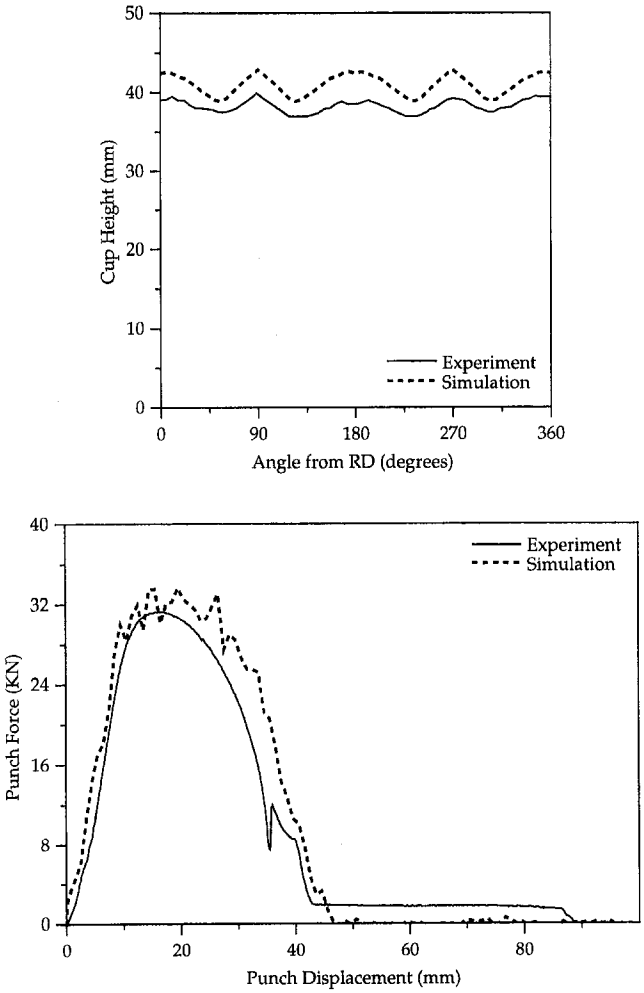

Fig. 5 (*a*) Comparison of the predicted cup-height profile with the experimentally measured height, (*b*) comparison of the measured load-displacement response during the cup-drawing process with the numerical prediction

Acknowledgment

Financial support for this work was provided by the U.S. National Science Foundation under Grant No. DMI-9215246.

References

ABAQUS, 1995, *Reference Manuals,* Hibbitt, Karlsson, & Sorensen Inc., Pawtucket, RI.

Asaro, R. J., and Needleman, A., 1985, "Texture Development and Strain Hardening in Rate-Dependent Polycrystals," *Acta Metallurgica,* Vol. 33, pp. 923–953.

Becker, R., Smelser, R. E., and Panchanadeeswaran, S., 1993, "Simulations of earing in aluminum single crystals and polycrystals," *Modelling and Simulations in Materials Science and Engineering,* Vol. 1, pp. 203–224.

Kalidindi, S. R., Bronkhorst, C. A., and Anand, L., 1992, "Crystallographic Texture Evolution During Bulk Deformation Processing of FCC Metals," *Journal of The Mechanics and Physics of Solids,* Vol. 40, pp. 537–569.

Kallend, J. S., Kocks, U. F., Rollett, A. D., and Wenk, H. R., 1991, "popLA: The Preferred Orientation Package from Los Alamos," Los Alamos National Laboratory, Los Alamos, NM.

Rollett, A. D., Canova, G. R., and U. F. Kocks, U. F., 1986, "The Effect of the Cube Texture Component on the Earing Behavior of Rolled f.c.c. metals," *Proceedings of the Conference on Formability and Metallurgical Structures,* Orlando, FL, 1987, pp. 147–155.

Simmons, G., and Wang, H., 1971, *Single Crystal Elastic Properties and Calculated Aggregate Properties: A HANDBOOK,* The MIT Press, Cambridge, MA.

Wilson, D. V., and Butler, R. D., 1961, "The role of cup-drawing tests in measuring drawability," *Journal of the Institute of Metals,* Vol. 90, pp. 473–483.

Finite Element Analysis of Rolling Contact Problems Using Minimum Dissipation of Energy Principle

S. K. Rathore[9] and N. N. Kishore[10]

In steady rolling motion, the loads and the fields of strain, stress, and deformations do not change with time at the contact region, as the contact region is continuously being formed by a new rolling surface. The principle of minimum dissipation of energy and the concept of traveling finite elements are made use of in solving such problems and the determination of micro-slips. The conditions of contact are discovered by use of the kinematic constraints and the Coulomb's law of friction. A two-dimensional plane-strain finite element method along with the iterative procedure is used. The results obtained are in good agreement with expected behavior.

Introduction

When a cylindrical body rolls on a rigid plane surface without sliding, contact develops between the roller and the ground. In free rolling, viz., rolling under the action of a purely normal load, the extent of slip is small, whereas when the contact surfaces transmit an externally applied tangential force or twisting couple, an appreciable amount of slip occurs. Several analytical and numerical solutions have been reported by Poritsky (1950), Kalker (1979), and Liu and Paul (1989). The rolling contact problem was also described by a variational inequality (hyperbolic/elliptic) and solved numerically using an incremental finite element method by Zochowski and Myslinki (1991). A recent method using the principle of minimum dissipation of energy (Kishore et al., 1994) to solve contact problem does not require any assumption regarding the distribution of tractions and contact conditions on the contact patch. This method, together with the concept of traveling finite elements (Padovan, Tovichakchaikul, and Zeid, 1984), are used to solve the present steady rolling contact problem employing only a coarse mesh.

Simulation of Rolling Motion

The method is based on the fact that every material point or node on the periphery of rolling body passes through the entire contact field during its period of contact. Therefore, instead of actually rolling the body, the contact field conditions are shifted rearward over the contact nodal points. This lets the contact zone be represented by the same set of nodal points for all iterations. The rolling is assumed to take place in steps of one degree, which coincides with the angular distance between the nodes in contact. To begin with, the initial configuration is taken to be the static solution. Thus, knowing the displacement component in the tangential direction at instant t at the i^{th} node, the response at instant $t + \Delta t$ can be taken as

[9] Reader, Department of Mechanical Engineering, Engineering College, Kota, India.

[10] Professor, Department of Mechanical Engineering, Indian Institute of Technology, Kanpur, India.

Contributed by the Applied Mechanics Division of THE AMERICAN SOCIETY OF MECHANICAL ENGINEERS for publication in the ASME JOURNAL OF APPLIED MECHANICS. Manuscript received by the ASME Applied Mechanics Division, Dec. 5, 1996; final revision, July 12, 1997. Associate Technical Editor: J. N. Reddy.

 Copyright © 1998 by ASME

Downloaded 04 May 2010 to 171.66.16.26. Redistribution subject to ASME license or copyright; see http://www.asme.org/terms/Terms_Use.cfm

u_i at time $t + \Delta t = u_{i+1}$ at time t

(subscript i refers to the i^{th} node in contact). (1)

The normal displacement boundary conditions which are the results of kinematic constraints are constant for all iterations. Using these conditions, the response at $t + \Delta t$ is obtained in terms of contact nodal forces. Now the Coulomb's friction condition is checked at all nodes in the contact zone. Those nodes for which the ratio of tangential to normal traction exceeds the coefficient of friction are allowed to slip. The direction of F_t opposes the slip at that node and slip is equal to the change in displacement of that node while body has rolled from instant t to $t + \Delta t$ viz., $u_i^{t+\Delta t} - u_{i+1}^t$. The extent of slip is determined following the minimum dissipation of energy principle (Kishore et al., 1994). This procedure is continued for subsequent iterations until the response converges to a steady-state solution.

Results

The flat bed was modeled as an infinite rigid bed and the roller was discretized into triangular elements. The finite element analysis was done under the assumption of plane strain. In what follows W and P represent normal and driving tangential loads on the cylinder and the F represents additional force to account for losses like windage, etc., and it is taken constant as $F/W = 0.02$ (inset in Fig. 1). As can be seen in the figure, the tangential stress in the contact zone varies linearly in the middle portion and attains large values near the edges before becoming zero at the ends. The maximum value occurs in the trailing edge and is higher for higher coefficients of friction. Figure 2 shows the size of slip and no-slip zones at different coefficients of friction and also shows a significant decrease in the slip zone size at edges as the coefficient of friction increases. It can also be seen that the extent of slip at the leading edge (L.E.) is very small (≈1 deg) and is of significant magnitude at the trailing edge (T.E.) (≈4 deg–5 deg), thus agreeing with the concept of micro and macro-slip over leading and trailing edges (Moore, 1975). This also brings out the fact that as P/W increases, the contact area shifts towards the leading edge. It was observed that the normal stress distribution essentially remains same whereas the tangential stress increases with P/W.

Energy dissipation per degree of rotation is presented in Fig. 3. The dissipation of energy is low at very low coefficient of friction and increases with μ, attains a maximum value, and decreases with further increase in μ. Thus, to achieve lower dissipation of energy it is a requirement to have high-value coefficient of friction and the same phenomenon is also expected at very low-value μ.

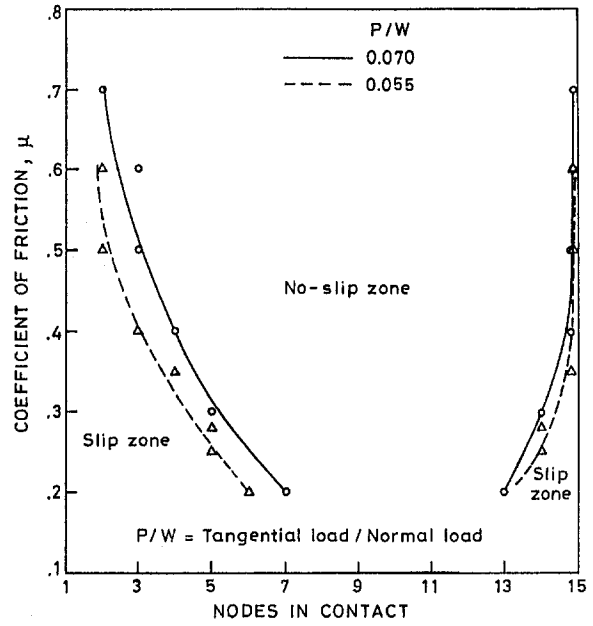

Fig. 2 Variation of slip and noslip zones over contact area with friction (at different P/W) (W/EDL = 0.834)

Conclusions

1 Use of minimum dissipation of energy approach makes it possible to get the solution even with coarse mesh.

2 The general behavior obtained is in agreement with rolling motion characteristics.

3 Quantitative analysis of energy dissipation at the contact area is presented.

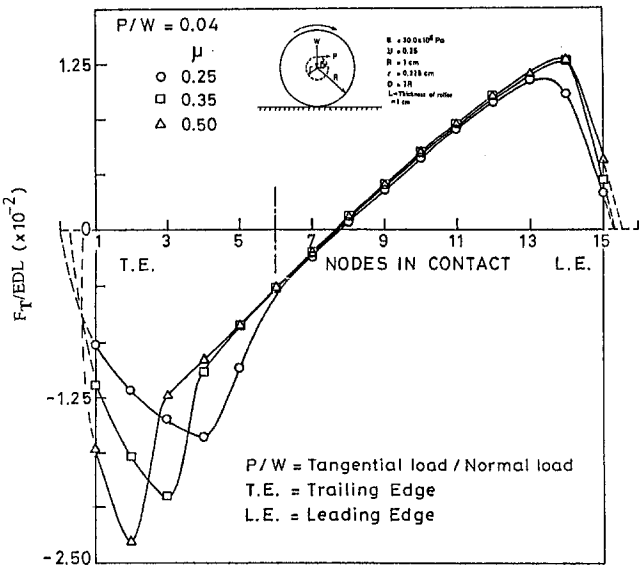

Fig. 1 Effect of friction on tangential contact force distribution (W/EDL = 0.834)

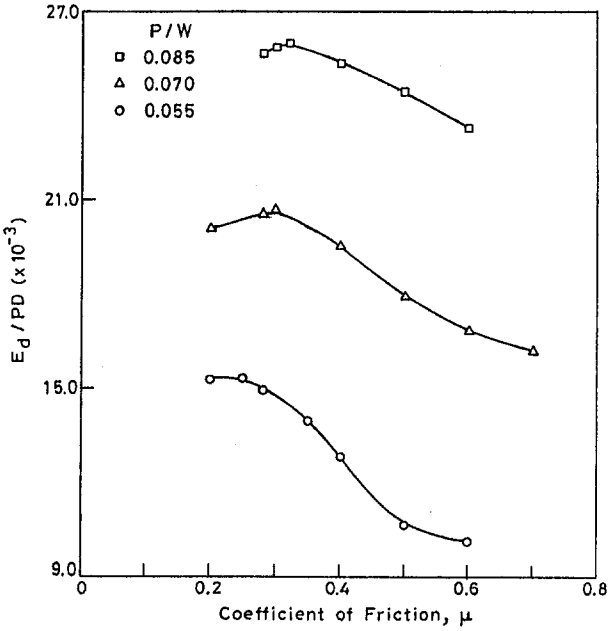

Fig. 3 Effect of friction upon energy of dissipation at different P/W (W/EDL = 0.834)

Downloaded 04 May 2010 to 171.66.16.26. Redistribution subject to ASME license or copyright; see http://www.asme.org/terms/Terms_Use.cfm

References

Kalker, J. J., 1979, "The Computation of Three Dimensional Rolling-Contact with Dry Friction," *Int. J. for Num. Methods in Eng.*, Vol. 14, pp. 1293–1307.

Kishore, N. N., Ghosh, A., Rathore, S. K., and Kishore, P. V., 1994, "Finite Element Analysis of Quasi-Static Contact Problems Using Minimum Dissipation of Energy Principle," ASME JOURNAL OF APPLIED MECHANICS, Vol. 61, pp. 642–648.

Liu, C., and Paul, B., 1989, "Rolling Contact with Friction and Non-Hertzian Pressure Distribution," ASME JOURNAL OF APPLIED MECHANICS, Vol. 56, pp. 814–820.

Moore, D. F., 1975, *The Friction of Pneumatic Tyres,* Elsevier Scientific Pub., Amsterdam.

Padovan, J., Tovichakchaikul, and Zeid, I., 1984, "Finite Element Analysis of Steadily Moving Contact Fields," *Computer and Structures,* Vol. 18, pp. 191–200.

Poritsky, H., 1950, "Stress and deflections of Cylindrical bodies in contact," ASME JOURNAL OF APPLIED MECHANICS, Vol. 18, p. 191.

Zochowski, A., and Myslinski, A., 1991, "Rolling Contact Problems using Quasi-static Variational Formulation," *Computers and Structures,* Vol. 40, pp. 1261–1266.

A Study of Solutions for the Anisotropic Plate Subjected to a Concentrated Force

B. LaMattina,[11,14] E. C. Klang,[12,14] and J. W. Eischen[13,14]

1 Introduction

The fundamental solution is an essential part of the boundary element method. Bending analysis of plates by the boundary element method requires the use of two fundamental solutions: (1) the displacement field due to a transverse point load, and (2) the displacement field due to a point moment, both for plates of infinite extent. Fundamental solutions for anisotropic plates utilize complex variable theory following groundwork laid by Lekhnitskii (1968). Mossakowski (1955) presented a solution for a point force on an infinite plate using complex parameters of the first kind, and Suchar (1964) presented the solutions for a point force and point moment in terms of complex parameters of the second kind. LaMattina (1997) derived a solution for the point force using the same mapping functions as Mossakowski that is more general than the other two solutions.

One of the objectives of this brief note is to present all three solutions and show how they are applied to the boundary element method formulation. Secondly, differences between these solutions are illustrated and discussed. The implications of these discrepancies is examined for the infinite plate as well as a typical boundary value problem. Another result of this work is related to an arbitrary constant sometimes referred to as the reference radius. This parameter is used to draw a connection between the three solutions. The purpose of the reference radius is discussed and suggestions are made on how to assign its value in numerical implementations of the boundary element method.

2 The Fundamental Solution and Boundary Element Method

The basis of the boundary element formulation are two boundary integral equations. The first integral equation is for the point force solution, and the second is for the point moment solution. The direct boundary element method DBEM uses meaningful physical quantities such as deflection, slope, shear forces, and moments in its boundary integral equations. In contrast, the indirect formulation uses functions that do not have a direct physical interpretation. The direct boundary element method integral equations for a generally anisotropic plate are based on the Rayleigh-Green identity. The boundary integral equation for the point force solution is given by Shi and Bezine (1988) as

$$\frac{1}{2} D_{22} w(P) + \int_\Gamma \left[V_n^f w - M_n^f \frac{\partial w}{\partial n} + \frac{\partial w^f}{\partial n} M_n - w^f V_n \right] ds + \sum_j^m [\,|T_n^f w - w^f T_n|\,]_j = \int_\Omega w^f q d\Omega. \quad (1)$$

The fundamental solution for the point load is represented by w^f and the other quantities with the superscript f are computed from the fundamental solution. The boundary element method solution process involves discretizing the boundary and using shape functions similar to finite element analysis. Subsequent to insertion of the fundamental solution and discretization of Eq. (1), the boundary conditions are applied and unknown constants are determined. The deflection at the interior of the plate is determined by another equation similar to Eq. (1).

3 Fundamental Solutions for a Point Load

In this section, the solutions for an infinite anisotropic plate subjected to a concentrated force are presented. The midplane of the plate coincides with the xy-plane and the concentrated force is directed in the positive z direction. The assumptions of classical plate theory are utilized in all the solutions, and the subscript f has been dropped from the fundamental solution ($w = w^f$) for the sake of brevity. The governing differential equation for an anisotropic plate subjected to a concentrated force is given by

$$D_{11} \frac{\partial^4 w}{\partial x^4} + 4D_{16} \frac{\partial^4 w}{\partial x^3 \partial y} + 2(D_{12} + 2D_{66}) \frac{\partial^4 w}{\partial x^2 \partial y^2} + 4D_{26} \frac{\partial^4 w}{\partial x \partial y^3} + D_{22} \frac{\partial^4 w}{\partial y^4} = P\delta(x - \xi, y - \eta) \quad (2)$$

where the lateral deflection, $w(x, y)$, is the fundamental solution used in Eq. (1). The magnitude of the concentrated force is P, and $\delta(x - \xi, y - \eta)$ is the Dirac delta function. The variables ξ and η give the x and y location of the force, respectively. For simplicity, the point load will be located at the origin of the coordinate system, so that ξ and η are zero.

The characteristic equation is given by

$$D_{22}\mu^4 + 4D_{26}\mu^3 + 2(D_{12} + 2D_{66})\mu^2 + 4D_{16}\mu + D_{11} = 0. \quad (3)$$

The roots μ_j of this equation, also known as complex parameters of the first kind, have been shown by Lekhnitskii to be either complex or purely imaginary.

[11] Graduate Student, Assoc. Mem. ASME.

[12] Assoc. Professor.

[13] Assoc. Professor, Mem. ASME.

[14] Mechanical and Aerospace Engineering, North Carolina State University, Raleigh, NC 27695.

Contributed by the Applied Mechanics Division of THE AMERICAN SOCIETY OF MECHANICAL ENGINEERS for publication in the ASME JOURNAL OF APPLIED MECHANICS. Manuscript received by the ASME Applied Mechanics Division, Mar. 20, 1996; final revision, May 23, 1997. Associate Technical Editor: J. N. Reddy.

Downloaded 04 May 2010 to 171.66.16.26. Redistribution subject to ASME license or copyright; see http://www.asme.org/terms/Terms_Use.cfm

References

Kalker, J. J., 1979, "The Computation of Three Dimensional Rolling-Contact with Dry Friction," *Int. J. for Num. Methods in Eng.*, Vol. 14, pp. 1293–1307.

Kishore, N. N., Ghosh, A., Rathore, S. K., and Kishore, P. V., 1994, "Finite Element Analysis of Quasi-Static Contact Problems Using Minimum Dissipation of Energy Principle," ASME JOURNAL OF APPLIED MECHANICS, Vol. 61, pp. 642–648.

Liu, C., and Paul, B., 1989, "Rolling Contact with Friction and Non-Hertzian Pressure Distribution," ASME JOURNAL OF APPLIED MECHANICS, Vol. 56, pp. 814–820.

Moore, D. F., 1975, *The Friction of Pneumatic Tyres*, Elsevier Scientific Pub., Amsterdam.

Padovan, J., Tovichakchaikul, and Zeid, I., 1984, "Finite Element Analysis of Steadily Moving Contact Fields," *Computer and Structures*, Vol. 18, pp. 191–200.

Poritsky, H., 1950, "Stress and deflections of Cylindrical bodies in contact," ASME JOURNAL OF APPLIED MECHANICS, Vol. 18, p. 191.

Zochowski, A., and Myslinski, A., 1991, "Rolling Contact Problems using Quasi-static Variational Formulation," *Computers and Structures*, Vol. 40, pp. 1261–1266.

A Study of Solutions for the Anisotropic Plate Subjected to a Concentrated Force

B. LaMattina,[11,14] E. C. Klang,[12,14] and J. W. Eischen[13,14]

1 Introduction

The fundamental solution is an essential part of the boundary element method. Bending analysis of plates by the boundary element method requires the use of two fundamental solutions: (1) the displacement field due to a transverse point load, and (2) the displacement field due to a point moment, both for plates of infinite extent. Fundamental solutions for anisotropic plates utilize complex variable theory following groundwork laid by Lekhnitskii (1968). Mossakowski (1955) presented a solution for a point force on an infinite plate using complex parameters of the first kind, and Suchar (1964) presented the solutions for a point force and point moment in terms of complex parameters of the second kind. LaMattina (1997) derived a solution for the point force using the same mapping functions as Mossakowski that is more general than the other two solutions.

One of the objectives of this brief note is to present all three solutions and show how they are applied to the boundary element method formulation. Secondly, differences between these solutions are illustrated and discussed. The implications of these discrepancies is examined for the infinite plate as well as a typical boundary value problem. Another result of this work is related to an arbitrary constant sometimes referred to as the reference radius. This parameter is used to draw a connection between the three solutions. The purpose of the reference radius is discussed and suggestions are made on how to assign its value in numerical implementations of the boundary element method.

2 The Fundamental Solution and Boundary Element Method

The basis of the boundary element formulation are two boundary integral equations. The first integral equation is for the point force solution, and the second is for the point moment solution. The direct boundary element method DBEM uses meaningful physical quantities such as deflection, slope, shear forces, and moments in its boundary integral equations. In contrast, the indirect formulation uses functions that do not have a direct physical interpretation. The direct boundary element method integral equations for a generally anisotropic plate are based on the Rayleigh-Green identity. The boundary integral equation for the point force solution is given by Shi and Bezine (1988) as

$$\frac{1}{2} D_{22} w(P) + \int_\Gamma \left[V_n^f w - M_n^f \frac{\partial w}{\partial n} + \frac{\partial w^f}{\partial n} M_n - w^f V_n \right] ds + \sum_j^m [\,|T_n^f w - w^f T_n|\,]_j = \int_\Omega w^f q \, d\Omega. \quad (1)$$

The fundamental solution for the point load is represented by w^f and the other quantities with the superscript f are computed from the fundamental solution. The boundary element method solution process involves discretizing the boundary and using shape functions similar to finite element analysis. Subsequent to insertion of the fundamental solution and discretization of Eq. (1), the boundary conditions are applied and unknown constants are determined. The deflection at the interior of the plate is determined by another equation similar to Eq. (1).

3 Fundamental Solutions for a Point Load

In this section, the solutions for an infinite anisotropic plate subjected to a concentrated force are presented. The midplane of the plate coincides with the xy-plane and the concentrated force is directed in the positive z direction. The assumptions of classical plate theory are utilized in all the solutions, and the subscript f has been dropped from the fundamental solution ($w = w^f$) for the sake of brevity. The governing differential equation for an anisotropic plate subjected to a concentrated force is given by

$$D_{11} \frac{\partial^4 w}{\partial x^4} + 4D_{16} \frac{\partial^4 w}{\partial x^3 \partial y} + 2(D_{12} + 2D_{66}) \frac{\partial^4 w}{\partial x^2 \partial y^2} + 4D_{26} \frac{\partial^4 w}{\partial x \partial y^3} + D_{22} \frac{\partial^4 w}{\partial y^4} = P\delta(x - \xi, y - \eta) \quad (2)$$

where the lateral deflection, $w(x, y)$, is the fundamental solution used in Eq. (1). The magnitude of the concentrated force is P, and $\delta(x - \xi, y - \eta)$ is the Dirac delta function. The variables ξ and η give the x and y location of the force, respectively. For simplicity, the point load will be located at the origin of the coordinate system, so that ξ and η are zero.

The characteristic equation is given by

$$D_{22}\mu^4 + 4D_{26}\mu^3 + 2(D_{12} + 2D_{66})\mu^2 + 4D_{16}\mu + D_{11} = 0. \quad (3)$$

The roots μ_j of this equation, also known as complex parameters of the first kind, have been shown by Lekhnitskii to be either complex or purely imaginary.

[11] Graduate Student, Assoc. Mem. ASME.

[12] Assoc. Professor.

[13] Assoc. Professor, Mem. ASME.

[14] Mechanical and Aerospace Engineering, North Carolina State University, Raleigh, NC 27695.

Contributed by the Applied Mechanics Division of THE AMERICAN SOCIETY OF MECHANICAL ENGINEERS for publication in the ASME JOURNAL OF APPLIED MECHANICS. Manuscript received by the ASME Applied Mechanics Division, Mar. 20, 1996; final revision, May 23, 1997. Associate Technical Editor: J. N. Reddy.

Copyright © 1998 by ASME

Downloaded 04 May 2010 to 171.66.16.26. Redistribution subject to ASME license or copyright; see http://www.asme.org/terms/Terms_Use.cfm

The solution to Eq. (2) has been presented by three authors for the case when the complex parameters are complex and different. LaMattina and Mossakowski write the solution in terms of the complex parameters of the first kind. Thus, they derive the solution using complex variables defined by

$$z_j = x + \mu_j y \quad \text{for} \quad j = 1, 2. \tag{4}$$

In contrast, Suchar uses complex parameters of the second kind, k_j, which are defined in terms of μ_j as

$$k_j = \frac{1 + i\mu_j}{1 - i\mu_j}. \tag{5}$$

In this case, the xy-plane is mapped into two planes z_{s1} and z_{s2} defined by the following transformation.

$$z_{sj} = (1 + k_j)x + i(1 - k_j)y \quad \text{for} \quad j = 1, 2. \tag{6}$$

The solution presented by LaMattina is given by

$$w = \text{Re} \sum_{j=1}^{2} A_j z_j^2 \ln\left(\frac{z_j}{a_j}\right). \tag{7}$$

The variables a_1, and a_2 are arbitrary constants which are sometimes referred to as reference radii. The constants A_1 and A_2 are given by

$$A_j = \frac{(-1)^j Pi}{2\pi D_{22}(\mu_2 - \mu_1)(\mu_j - \bar{\mu}_1)(\mu_j - \bar{\mu}_2)}. \tag{8}$$

The solution presented by Mossakowski is given by

$$w = \text{Re} \sum_{j=1}^{2} \left[A_j z_j^2 \ln\left(\frac{z_j}{a}\right) - \frac{3}{2} A_j z_j^2 \right] \tag{9}$$

where A_j is the same as Eq. (8).

Suchar writes the fundamental point load solution using the complex variables defined in Eq. (6) as

$$w = \text{Re} \sum_{j=1}^{2} B_j z_{sj}^2 \ln\left(\frac{z_{sj}}{b}\right) \tag{10}$$

where again the constant b is a reference radius.

Here the constants B_1 and B_2 are defined as

$$B_j = \frac{(-1)^j P(1 + k_1)(1 + k_2)(1 + \bar{k}_1)(1 + \bar{k}_2)}{16\pi D_{22}(1 - k_j\bar{k}_1)(1 - k_j\bar{k}_2)(k_2 - k_1)}. \tag{11}$$

4 Comparison of Fundamental Solutions

The three solutions presented above are plotted in Fig. 1 for a $[45/0/90/-45]_s$ carbon/epoxy composite laminate. The lamina properties, corresponding laminate flexural rigidities, and complex parameters are given in Table 1. Figure 1 shows the nondimensionalized deflection, wD_{22}/Ph^2 versus y/h, with the value of x equal to zero. The arbitrary constants a_1, a_2, a, and b are all set equal to one. The three curves have the same general shape but diverge as the distance from the origin increases. It is beneficial to examine the equations more closely in an effort to isolate these differences. Disregarding the reference radii for the moment, a comparison of the author's solution (Eq. (7)) and Mossakowski's solution (Eq. (9)) shows that they differ by the second-order polynomial $(-(3/2)A_j z_j^2)$.

Isolating the difference between the author and Suchar is more complicated since the solutions use different transformation equations. However, manipulation of Eqs. (4) – (6) results in an expression that relates the mapping function z_{sj} to z_j.

$$z_{sj} = (1 + k_j)z_j \tag{12}$$

Another necessary relationship is found by examining the constants A_j and B_j from Eqs. (8) and (11). Consequently,

$$A_j = (1 + k_j)^2 B_j. \tag{13}$$

By substituting Eqs. (12) and (13) into Eq. (10), Suchar's solution becomes

$$w = \text{Re} \sum_{j=1}^{2} \left[A_j z_j^2 \ln\left(\frac{z_j}{b}\right) + A_j z_j^2 \ln(1 + k_j) \right]. \tag{14}$$

Thus, if the reference radii are equal ($a_1 = a_2 = b$), comparing Eqs. (7) and (14) reveals that the solution derived by Suchar differs from the author's solution by the polynomial $[A_j z_j^2 \ln(1 + k_j)]$.

In order to explain the discrepancy in results, the solution process for boundary value problems must be examined from the beginning. A well-posed boundary value problem consists of the governing equation as well as the boundary conditions. To obtain a unique solution one must satisfy both the governing equation and the boundary conditions. The general solution to the governing differential equation consists of two parts. The first part satisfies the homogeneous differential equation and is often referred to as the complimentary solution. The complimentary solution usually contains unknown constants. The second part of the general solution is usually called a particular solution and is any solution that satisfies the nonhomogeneous governing equation. The particular solution does not contain unknown constants and is not unique. Particular solutions may differ from one another by a multiple of any of the terms of the complimentary solution. The general solution is a linear combination of the complimentary and particular solutions. Once the general solution is formed, the boundary conditions are applied, the unknown constants are determined, and the solution becomes unique.

The fundamental solutions presented in this note are particular solutions for a plate subjected to a concentrated force. They satisfy the nonhomogeneous Eq. (2) and were not subject to any boundary conditions. Therefore, if all of these solutions are valid they should only differ by some multiple of a term of the complimentary solution. It has been shown that both Mossakowski's and Suchar's solutions differ from

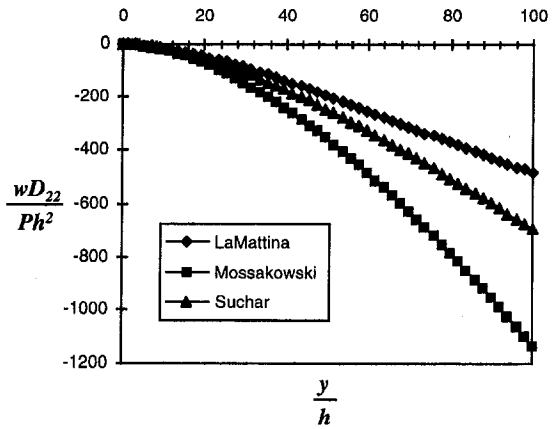

Fig. 1 Nondimensionalized deflection for the three solutions

Downloaded 04 May 2010 to 171.66.16.26. Redistribution subject to ASME license or copyright; see http://www.asme.org/terms/Terms_Use.cfm

Table 1 Composite properties and complex parameters

Lamina Properties, Composite Flexural Rigidities, and Complex Parameters
E_1=159.0 GPa E_2=10.0 GPa G_{12}=5.9 GPa ν_{12}=0.31
D_{11}=11.3 Nm D_{12}=3.4 Nm D_{16}=3.0 Nm D_{22}=7.2 Nm D_{26}=3.0 Nm D_{66}=3.8 Nm
μ_1=-0.134 + 0.903i μ_2=-0.706 + 1.171i k_1=0.046 - 0.074i k_2=-0.167 - 0.271i
Lamina Thickness=0.15mm

the author's by a multiple of the polynomial z_j^2. Thus, consider the function

$$w_{c1} = C_j z_j^2 \tag{15}$$

where C_j is any constant. Substituting Eq. (4) into (15) gives

$$w_{c1} = C_j(x + \mu_j y)^2. \tag{16}$$

The homogeneous version of the governing Eq. (2) is clearly satisfied by Eq. (16). Hence, this term is also a term of the complimentary solution and will therefore be inconsequential when considering a boundary value problem.

5 The Reference Radius

In this section, the consequences and purpose of the reference radius is examined more closely. Almost all the plate bending solutions that contain the natural log term include the reference radius (Lekhnitskii, 1968; Mossakowski, 1955; Suchar, 1964; Timoshenko et al., 1959). However, none of these publications state anything about this constant except that it is arbitrary.

Examination of any of the fundamental solutions shows that they will differ for different values of the reference radius. Thus, the obvious question one may ask is "How can this term be considered arbitrary if it changes the solution"? This is a valid question which can be answered by rewriting the solutions in a slightly different form. For example, Eq. (7) can be rewritten as

$$w = \mathrm{Re} \sum_{j=1}^{2} [A_j z_j^2 \ln z_j - A_j z_j^2 \ln a_j]. \tag{17}$$

Scrutiny of Eq. (17) reveals that the inclusion of the reference radius is equivalent to including the polynomial term $[-A_j z_j^2 \ln a_j]$. However, as is pointed out in the previous section, any second-order polynomial of the form $[C_j z_j^2]$ is a complimentary solution. Thus, its incorporation in the particular solution will have no effect on the uniqueness of a boundary value problem.

In fact, by a prudent choice of the reference radii the solution presented by the author can be made to match the solutions by Mossakowski or Suchar. By setting Eq. (7) equal to Eq. (9) and solving for a_j gives a relation for the reference radii that makes the solutions by the author and Mossakowski identical. The author's solution can be made to match Suchar's by equating Eq. (7) and (10). The relationships between the reference radii are summarized in Table 2. For the numerical example presented in Section 4 the values of the reference radii are given in Table 3. Tables 2 and 3 show that the solution presented by the author can be made to match either of the other solutions by choosing the proper reference radius. However, it is not possible to make the solutions by Mossakowski and Suchar match each other's by choosing a reference radius. This is because these solutions only contain one reference radius, whereas the author's solution has two.

Table 2 Connection between the reference radii

Mossakowski $\Rightarrow$ *LaMattina* : $a_j = ae^{1/4}$, a = *arbitrary*
Suchar $\Rightarrow$ *LaMattina* : $a_j = \dfrac{b}{1+k_j}$, b = *arbitrary*

6 Discussion

Three solutions for the generally anisotropic plate subjected to a concentrated force are presented. This paper illustrates that each of these solutions are different from one another. It also points out that they are particular solutions and that the lack of uniqueness among them is attributed to the addition of a term from the complementary solution. Hence, any of these three solutions given by Eqs. (7), (9), or (10), respectively, can be used as the fundamental solution for the boundary element method.

Perhaps the most obvious reason for including the reference radius is for dimensional consistency of the equations. By including a reference radius with units of length, the log term becomes dimensionless, and the units on the left and right sides of the equations will match. Another positive side effect of the reference radius comes into play for numerical solution methods, such as the boundary element method. The reference radius provides a variable that can be assigned a value that will aid in avoiding ill-conditioned equations. In the indirect boundary element method formulation presented by Wu and Alterio (1981), a range of values for the reference radius is given for which their results are accurate. The author believes that avoiding ill-conditioned equations is the reason for choosing these values. In the boundary element method it is sufficient to choose the reference radius to have the same order of magnitude as the largest plate dimension.

As illustrated in Eq. (7), it is not necessary to use the same value for the reference radius in both terms of the fundamental solution as indicated in the papers by Mossakowski and Suchar. Choosing different values will not effect the end result for a boundary value problem. Secondly, it is not necessary to restrict the reference radii to only real numbers, they can be complex. In fact, this is the case when the reference radii are defined according to Table 3.

Table 3 Values of the reference radii to match solutions for the [45/0/90/-45]$_s$ composite

Mossakowski $\Rightarrow$ *LaMattina* $a_1 = a_2 = e^{1/4}$ m, a = 1 m
Suchar $\Rightarrow$ *LaMattina* $a_1 = 0.9517 + 0.0671i$ m $a_2 = 1.0855 + 0.3531i$ m, b = 1 m

Downloaded 04 May 2010 to 171.66.16.26. Redistribution subject to ASME license or copyright; see http://www.asme.org/terms/Terms_Use.cfm

Acknowledgment

This work was funded in part by NASA grant NAGW-1331.

References

LaMattina, B., 1997, "Anisotropic Plate Bending Analysis Using Complex Variables Methods," Ph.D. dissertation, North Carolina State University, Raleigh, NC.

Lekhnitskii, S. G., 1968, *Anisotropic Plates,* Gordon and Breach, New York.

Mossakowski, J., 1955, "Singular Solutions of Anisotropic Plates," *Arch. Mech. Stos.,* Vol. 7, No. 1, pp. 97–110 (in Polish).

Shi, G., and Bézine, G., 1988, "A General Boundary Integral Formulation for the Anisotropic Plate Bending Problems," *Journal of Composite Materials,* Vol. 22, pp. 694–716.

Suchar, M., 1964, "On Singular Solutions in the Theory of Anisotropic Plates," *Bulletin de l'Académie Polonaise des Sciences. Série des Sciences Techniques,* Vol. 12, pp. 29–38.

Timoshenko, S., and Woinowsky-Krieger, S., 1959, *Theory of Plates and Shells,* McGraw-Hill, New York, pp. 325–328.

Wu, B. C., and Altiero, N. J., 1981, "A New Numerical Method for the Analysis of Anisotropic Thin-Plate Bending Problems," *Comp. Meth. Appl. Mech. and Eng.,* Vol. 25, pp. 343–353.

Downloaded 04 May 2010 to 171.66.16.26. Redistribution subject to ASME license or copyright; see http://www.asme.org/terms/Terms_Use.cfm

Journal of Applied Mechanics

Discussion

Shakedown Analysis for Trusses and Frames[1]

P. S. Symonds[2]. In the nearly 50 years since B. G. Neal and the writer made early contributions to shakedown analysis, advances have been made in directions such as: thermal loading, dynamic loading, second-order effects, and mathematical programming; and the range of structural applications has been extended beyond the beams and plane frames under general quasi-static loading, which we successfully treated. The writer thought he knew something about shakedown, but found the author's paper all but incomprehensible due, no doubt, to his own lack of mathematical erudition.

The author's abstract concludes with the statement: "The result implies that the methods available in plastic limit analysis, such as the method of hinge mechanisms, can be developed for use in shakedown analysis of the structure". He is evidently unaware that plastic hinge mechanisms are the basis of the kinematic method developed by Neal and the writer for determining the critical load factor for failure by incremental collapse of a continuous beam or rigid jointed frame under a general system of forces (Neal, 1950; Neal and Symonds, 1951; Symonds, 1950; Symonds and Neal, 1951). Laboratory experiments confirming this work were discussed by Neal and Symonds (1958). A full discussion of both our method and experiments is given in the treatise by Baker, Horne, and Heyman (1956); the method is outlined in books by Neal (1956), Hodge*[3] (1959), and Heyman (1971); see also Heyman (1996).

Martin* (1975) discusses our kinematic method as a special case of Koiter's theorem, which it predated; and also discussed it as a minimum problem of linear programming. Most other authors refer to Koiter as the originator of the kinematic approach. This may be traced to the statement (Koiter*, 1960, p. 213), that our method is "in effect a clever method of applying the first theorem". For beam and frame problems loaded by concentrated forces it seems obvious that our method furnishes upper bounds and finally the exact shakedown load factor; no reference in the argument need be made to Melan's theorem. Koiter's statement remains mystifying.

That the Neal-Symonds method furnishes an upper bound for incremental collapse under general loading by concentrated forces is clear by the same arguments used in the kinematic method for plastic collapse under proportional loading (see, e.g., Neal, 1950, 1956). Each proposed mechanism furnishes a load factor at which incremental collapse may occur. From that load factor, the moments throughout the frame may be computed. If all satisfy the fully plastic moment conditions, the load factor is the correct one. If not, the sections where the condition is violated may be imagined strengthened without otherwise affecting the behavior; it is axiomatic that the plastic collapse load of a strengthened frame is not less than that of the unstrengthened frame. Thus the correct load factor is the smallest of the load factors computed for the identified class of mechanisms. Proof that no alternative mechanism can be found that further lowers the load factor for incremental collapse is easily given (see Neal, 1956).

Incremental collapse under a general system of load forces can occur in the sense of increments of displacement that take place *in the same direction* each time a cycle of load applications is repeated. The force system must consist of at least two independent forces. Contrary to the caption of Fig. 1(*b*) of the author's paper, a single force cannot perform a cyclic loading in the sense required for incremental collapse. The only (non-shakedown) failure possible in the author's example is that of alternating plasticity (with plastic flow in equal positive and negative increments occurring successively in some member). It seems unfortunate to mix failure by incremental collapse with that by alternating plasticity, which leads to fracture; the two kinds of failure are easily separable mathematically and physically. Mathematical compactness here adds confusion, not clarity.

References

Baker, J. F., Horne, M. R., and Heyman, J., 1956, *The Steel Skeleton, Volume Two: Plastic Behaviour & Design,* Cambridge University Press, Cambridge, UK, Chapter 9.

Heyman, J., 1971, *Plastic Design of Frames, Volume 2: Applications,* Cambridge University Press, Cambridge, UK, Chapter 6.

Heyman, J., 1996, *Elements of the Theory of Structures,* Cambridge University Press, Cambridge, UK, Chapter 10.

*Hodge, P. G., Jr., 1959, *Plastic Analysis of Structures,* McGraw-Hill, New York, Chapter 5.

*Koiter, W. T., 1960, "General Theorems for Elastic-Plastic Solids," *Progress in Solid Mechanics,* I. N. Sneddon, and R. Hill, eds., North-Holland, Amsterdam, pp. 167–221.

*Martin, J. B., 1975, *Plasticity: Fundamentals and General Results,* M.I.T. Press, Cambridge, MA, Chapter 19.

Neal, B. G., 1950, "Plastic Collapse and Shakedown Theorems for Structures of Strain-Hardening Material," *Journal of the Aeronautical Sciences,* Vol. 17, pp. 297–306.

Neal, B. G., 1956, *The Plastic Methods of Structural Analysis,* Chapman and Hall, London, Chapter 8.

Neal, B. G., and Symonds, P. S., 1951, "A Method for Calculating the Failure Load for a Framed Structure Subjected to Fluctuating Loads," *Journal of the Institute of Civil Engineers,* Vol. 35, pp. 186–197.

Neal, B. G., and Symonds, P. S., 1958, "Cyclic Loading of Portal Frames: Theory and Tests," *Pub. of the International Association for Bridge & Structural Engineering,* Vol. 18, pp. 171–199.

Symonds, P. S., 1950, "The Basic Theorems in the Plastic Theory of Structures," Readers' Forum, *Journal of the Aeronautical Sciences,* Vol. 17, pp. 669–670.

Symonds, P. S., and Neal, B. G., 1951, "Recent Progress in the Plastic Methods of Structural Analysis," *Journal of the Franklin Institute,* Vol. 252, Nos. 5 and 6, pp. 383–492.

[1] Chinh, Pham Duc, 1997, "Shakedown Analysis for Trusses and Frames," ASME JOURNAL OF APPLIED MECHANICS, Vol. 64, pp. 415–419.

[2] Professor of Engineering (Research), Brown University, Providence, RI 02912, Fellow ASME.

[3] The references starred (*) are the author's list of references. Note that Koiter's (1960) paper is incorrectly dated "1963" in the author's paper.

 Copyright © 1998 by ASME

Downloaded 04 May 2010 to 171.66.16.26. Redistribution subject to ASME license or copyright; see http://www.asme.org/terms/Terms_Use.cfm

Elastic Fields in a Polygon-Shaped Inclusion With Uniform Eigenstrains[4]

Gregory J. Rodin.[5] The authors consider Eshelby's inclusion problem for polygonal domains. The interest in this problem was ignited by Mura's et al. (1994) claim that pentagonal inclusions are similar to the ellipsoids in the sense that their interior Eshelby's tensor is constant. Subsequently this claim was proven to be incorrect (Rodin, 1996; Markenscoff, 1997).

In addition to an introduction, the paper under discussion contains two sections concerned with computational procedures for inclusions and inhomogeneities and a section in which these procedures are applied to various problems.

First we note that the computational procedure for inclusions proposed by Nozaki and Taya is not as general as that proposed earlier by Rodin (1996) since the former procedure can compute the strain field only inside convex polygonal inclusions whereas the latter procedure can compute the strain field both inside and outside of arbitrary polygonal and polyhedral inclusions. Furthermore, the equations derived by Rodin (1996) are much simpler than those derived by Nozaki and Taya.

More importantly, the computational procedure for inhomogeneities proposed by Nozaki and Taya contains an apparently irreconcilable flaw. To expose this flaw let us recall that the perturbation strain field ϵ due to the inhomogeneity ω can be expressed in the form (e.g., Mura, 1982)

$$\boldsymbol{\epsilon}(\mathbf{x}) = \int_{\omega} \mathbf{K}(\mathbf{x}, \mathbf{y})\boldsymbol{\epsilon}^*(\mathbf{y})d\mathbf{y} \qquad (1)$$

where the fourth rank tensor $\mathbf{K}(\mathbf{x}, \mathbf{y})$ involves second derivatives of Green's functions and elastic constants and $\boldsymbol{\epsilon}^*$ is the equivalent eigenstrain. For reference, Eshelby's tensor can be expressed as

$$\mathbf{S}(\mathbf{x}) = \int_{\omega} \mathbf{K}(\mathbf{x}, \mathbf{y})d\mathbf{y}.$$

Upon averaging (1) over the domain ω we obtain

$$\langle\boldsymbol{\epsilon}\rangle = \frac{1}{\omega}\int_{\omega}\int_{\omega} \mathbf{K}(\mathbf{x}, \mathbf{y})\boldsymbol{\epsilon}^*(\mathbf{y})d\mathbf{y}d\mathbf{x}$$

$$= \frac{1}{\omega}\int_{\omega} \mathbf{S}(\mathbf{y})\boldsymbol{\epsilon}^*(\mathbf{y})d\mathbf{y} = \langle\mathbf{S}\boldsymbol{\epsilon}^*\rangle.$$

It is clear that the relationship

$$\langle\mathbf{S}\boldsymbol{\epsilon}^*\rangle = \langle\mathbf{S}\rangle\langle\boldsymbol{\epsilon}^*\rangle, \qquad (2)$$

which is central to the analysis of Nozaki and Taya, should not hold in general although it does hold for the ellipsoidal inhomogeneities since $\mathbf{S}$ is constant. Thus, unless (2) is proved, results presented by Nozaki and Taya for polygonal inhomogeneities are incorrect.

References

Markenscoff, X., 1997, "On the Shape of the Eshelby Inclusions," *J. Elasticity,* in press.

Mura, T., 1982, *Micromechanics of Defects in Solids,* Martinus Nijhoff, Dordrecht, The Netherlands.

Mura, T., Shodja, H. M., Lin, T. Y., Safadi, A., and Makkawy, A., 1994, "The Determination of the Elastic Field of a Pentagonal Star Shaped Inclusion," *Bull. Tech. Univ. Istanbul,* Vol. 47, pp. 267–280.

Nozaki, H., and Taya, M., 1997, "Elastic Fields in a Polygon-Shaped Inclusion With Uniform Eigenstrains," ASME JOURNAL OF APPLIED MECHANICS, Vol. 64, pp. 495–502.

Rodin, G. J., 1996, "Eshelby's Inclusion Problem for Polygons and Polyhedra," *J. Mech. Phys. Solids,* Vol. 44, No. 12, pp. 1977–1995.

[4] Nozaki, N., and Taya, M., 1997, "Elastic Fields in a Polygon-Shaped Inclusion With Uniform Eigenstrains," ASME JOURNAL OF APPLIED MECHANICS, Vol. 64, pp. 495–502.

[5] Department of Aerospace Engineering and Engineering Mechanics, The University of Texas at Austin, Austin, TX 78712.

Copyright © 1998 by ASME

Downloaded 04 May 2010 to 171.66.16.26. Redistribution subject to ASME license or copyright; see http://www.asme.org/terms/Terms_Use.cfm